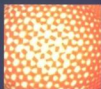


Nanoporous Materials

Science and Engineering

edited by

G. Q. Lu
X. S. Zhao



Imperial College Press

Nanoporous Materials

Science and Engineering

edited by

G. Q. Lu

University of Queensland, Australia

X. S. Zhao

National University of Singapore, Singapore



Imperial College Press

Published by

Imperial College Press
57 Shelton Street
Covent Garden
London WC2H 9HE

Distributed by

World Scientific Publishing Co. Pte. Ltd.

5 Toh Tuck Link, Singapore 596224

USA office: 27 Warren Street, Suite 401–402, Hackensack, NJ 07601

UK office: 57 Shelton Street, Covent Garden, London WC2H 9HE

British Library Cataloguing-in-Publication Data

A catalogue record for this book is available from the British Library.

NANOPOROUS MATERIALS: SCIENCE AND ENGINEERING

Series on Chemical Engineering

Copyright © 2004 by Imperial College Press

All rights reserved. This book, or parts thereof, may not be reproduced in any form or by any means, electronic or mechanical, including photocopying, recording or any information storage and retrieval system now known or to be invented, without written permission from the Publisher.

For photocopying of material in this volume, please pay a copying fee through the Copyright Clearance Center, Inc., 222 Rosewood Drive, Danvers, MA 01923, USA. In this case permission to photocopy is not required from the publisher.

ISBN 1-86094-210-5

ISBN 1-86094-211-3 (pbk)

Editor: Tjan Kwang Wei

Preface

In the last decade, we have witnessed a rapid growth in research and development of nanotechnology, especially nanostructured materials. Nanoporous materials as an important class of nanostructured materials possess high specific surface area, large pore volume, uniform pore size, and rich surface chemistry. These materials present great promises and opportunities for a new generation of functional materials with improved and tailorable properties for applications in adsorption, membranes, sensors, energy storage, catalysis and photocatalysis, and biotechnology, etc.

Interest in making materials from nanoscale building blocks arose from discoveries that by controlling the size in the range of 1-100 *nm* and the assembly of such constituents, one could alter and prescribe the properties of the assembled nanostructures. Nanoscale phenomena and objects have been around for some time. Catalysts, for example, are mostly nanoscale particles, and catalysis is a nanoscale phenomenon. What is new and different now is the degree of understanding and deliberate control and precision that the new nanoscale techniques afford. Instead of discovering new materials by random search (trial-and-error), we can now design them systematically. Nanoporous materials can have long-range structural order or disordered structure and contain pores of the dimension of a few nanometers to tens of nanometers. Some applications such as catalysis take advantage of high surface area and pore confinement effects. Synthesis and processing of nanoporous materials with controllable structures and properties require new approaches such as molecular templating and intercalation in a bottom-up manner.

From a practical standpoint, a large specific surface for nanoparticles is most desired for catalysis. However, fine powder catalysts can cause serious operational problems such as agglomeration, difficulties in loading, pressure drop, and separation of catalyst from the reaction products. A feasible approach to generating a large and accessible surface area of catalyst but avoiding the morphology of fine powder is to create a composite or immobilized structure. One can disperse nanoparticles of metals or oxides in an inorganic support to stabilize the discrete nanoparticles, meanwhile maintaining most of their surface accessible to reactant molecules. However, the conventional methods of preparing the catalysts such as impregnation often result in agglomerated catalyst particles in the support, thus decreasing the active surface area, and

uniformity of the active centers. With nanostructuring techniques, active metal or oxide precursors can be incorporated or grafted on the nanoporous support during synthesis thus not only increase the control in catalyst particle size, surface area and dispersion, but also eliminating the cost and problems associated with impregnation.

Since the early 1990s, a large number of microporous and mesoporous materials have found wide applications in catalysis. Major breakthroughs in materials synthesis such as the templated synthesis of mesoporous molecular sieves M41S and porous clay heterostructures have opened exciting avenues for designing new classes of nanoporous materials based on molecular templating and self-assembly principle (with pore dimensions between 1 to 10 nm). These materials offer great potential for applications in separation and catalysis, particularly reactions involving large and bulky molecules. We are excited at the prospect of an explosion of revolutionary discoveries at nanoscale. The new millennium presents opportunities as well as challenges to scientists and engineers working in this dynamic field of nanoporous materials in terms of the tailor-design, synthesis and characterization for specific functionalities and applications.

The main objectives of this book are to provide the readers with an overview of the field of nanoporous materials and to present the latest advances in various areas from synthesis, characterization, surface modification to adsorption and separation processes, and biological and catalytic applications. Fundamentally, this book contains chapters dealing with important issues in synthesis of nanoporous materials of various compositions, characterization techniques, surface modification/functionalization, catalyst design and nanostructure tailoring, and adsorption/separation application including bioseparation. This book presents 28 comprehensive chapters reviewing the state of the art in the field of nanoporous materials contributed by some of the finest scientists in the world in this field.

With an overview of nanoporous materials in chapter 1, chapters 2-10 describe some general strategies for the synthesis of nanoporous materials such as the nonionic block copolymer template method, the synthesis of composite materials with a zeolite framework, preparation of hydrophobic membranes using sol-gel technique, macroporous materials templated by colloidal crystals, and carbon nanotubes. The advances in characterization of nanoporous materials by physical adsorption in combination with simulation, and modification and functionalization of nanoporous

materials are covered in chapters 11-16. In addition to traditional pore evaluation methods such as the BJH method based on Kelvin equation for pore size determination, the development of microscopic methods, such as the non-local-density functional theory (NLDFT) or computer simulation methods (e.g. monte-carlo and molecular-dynamic simulations), which allow the description of the configuration of adsorbed molecules in pores on a molecular level (elaborated in chapters 11 and 12). Surface functionalization of nanoporous materials by grafting, co-condensation routes, and molecularly designed dispersion methods, surface alumination to alter acidity, as well as measurement of surface acidity can be found in chapters 13-16. Recent developments in the catalytic applications of nanoporous materials, ranging from acidic catalysis to base catalysis, from shape-selective catalysis to environmentally friendly catalysis, are presented in chapters 17-21. Adsorption- and separation processes involving nanoporous materials are subjects of chapters 22-28. Nanoporous materials for the removal of pollutants in gas or liquid phase are elaborated. Separation and immobilization of enzymes are reviewed in chapters 26 and 27.

We would like to thank the authors of the chapters for their valuable and timely contributions, and for their patience and cooperation in the editing process. We hope that this book would be a useful reference for senior students, graduate students and researchers in materials chemistry, physical and colloid chemistry, chemical engineering, materials science, biotechnology and nanotechnology.

Finally, we would like to express our sincere thanks to Professor Ralph T Yang, University of Michigan, the Series Editor of Chemical Engineering for Imperial College Press for his kind invitation to contribute this volume. We would also like to thank the Editor in Imperial College Press, Tjan Kwang Wei for his great assistance. We are very grateful to Sharon Mathiesen for her wonderful help with manuscript management and editing. Last but not the least, to our respective families for their love, understanding and support in this endeavor.

G.Q (Max) Lu
Brisbane, Australia

George X S Zhao
Singapore

November, 2003

Contents

Preface v

1. Nanoporous Materials-an Overview **1**

1.1 Introduction 1

1.2 Classification of Nanoporous Materials 4

1.3 Properties and Characterization of Nanoporous Materials 5

1.4 Major Opportunities in Applications 6

1.5 Concluding Remarks 11

References 13

2. Advances in Mesoporous Materials Templated by Nonionic Block Copolymers **14**

2.1 Introduction 14

2.2 Siliceous Mesoporous Materials 16

2.3 Wall Structures of Mesoporous Materials Templated by Amphiphilic Block Copolymers 22

2.4 Morphology of Mesoporous Materials Templated by Block Copolymers 24

2.5 Non-siliceous Structures 28

2.6 Applications 33

2.7 Conclusion Remarks 38

2.8 Acknowledgements 38

References 39

3. Zeolite/Mesoporous Molecular Sieve Composite Materials **47**

3.1 Introduction 47

3.2 Mechanisms of Zeolite Germination 48

3.3	Synthesis Strategies for Zeolite/MMS Composites	51
3.4	Catalytic Properties	84
3.5	Future Challenges	90
3.6	Conclusion	93
3.7	Acknowledgements	93
	References	93
4.	Chromium-containing Ordered Nanoporous Materials	101
4.1	Introduction	101
4.2	Materials and Methods	103
4.3	Results and Discussion	106
4.4	Conclusion	118
4.5	Acknowledgements	119
	References	119
5.	Surfactant-templated Mesostructured Materials: Synthesis and Compositional Control	125
5.1	Introduction	125
5.2	Synthesis Routes	126
5.3	Compositions of Mesostructured and Mesoporous Materials	140
5.4	Conclusions and Outlook	151
5.5	Acknowledgments	152
	References	152
6.	Organic Host-guest Structures in the Solid State	165
6.1	Introduction	166
6.2	Host Design Principles	168
6.3	C ₃ Symmetry and Halogen...Halogen Interaction in Host Design	170
6.4	Wheel-axle Host Lattice	177
6.5	Design of Layered Host: Crystal Engineering	179
6.6	Gas Storage in Interstitial Voids	182
6.7	Guest Selectivity in Inclusion	184

6.8	Conclusions	185
6.9	Acknowledgement	185
	References	185
7.	Nonsurfactant Route to Nanoporous Phenyl-modified Hybrid Silica Materials	188
7.1	Introduction	188
7.2	Methods	191
7.3	Results and Discussion	192
7.4	Conclusions	202
7.5	Acknowledgements	202
	References	202
8.	3D Macroporous Photonic Materials Templated by Self Assembled Colloidal Spheres	206
8.1	Introduction	206
8.2	A Survey of Photonic Bandgap	207
8.3	Nanolithography for Photonic Crystals	211
8.4	Self-assembly Approaches to 3D Photonic Crystals	212
8.5	Fabrication of Intentional Defects in 3D Photonic Crystals	226
8.6	Acknowledgements	228
	References	228
9.	Hydrophobic Microporous Silica Membranes for Gas Separation and Membrane Reactors	237
9.1	Introduction	237
9.2	Inorganic Membranes	238
9.3	Hydrothermal Stability and Hydrophobicity-key Areas of Improvement	243
9.4	Membrane Reactors	251
9.5	Perspective and Concluding Remarks	256
9.6	Acknowledgement	257
	References	257

10. Synthesis and Characterization of Carbon Nanotubes for Hydrogen Storage	263
10.1 Introduction	264
10.2 Construction, Structure and Unique Properties of Carbon Nanotubes	266
10.3 Synthesis of Carbon Nanotubes	271
10.4 Surface and Pore Structure of Carbon Nanotubes	279
10.5 Experimental Investigations on Hydrogen Uptake in Carbon Nanotubes	286
10.6 Theoretical Predictions and Simulations of Hydrogen Uptake in Carbon Nanotubes	295
10.7 Possible Hydrogen Adsorption Sites in Carbon Nanotubes	303
10.8 Future Research Topics and Remarks	308
10.9 Acknowledgement	309
References	309
11. Physical Adsorption Characterization of Ordered and Amorphous Mesoporous Materials	317
11.1 Introduction	317
11.2 Surface and Pore Size Analysis by Physisorption: General Aspects	322
11.3 Pore Condensation and Adsorption Hysteresis	328
11.4 Pore Size Analysis of Mesoporous Solids	345
11.5 Concluding Remarks	355
11.6 Acknowledgements	356
11.7 References	356
12. Molecular Simulation of Adsorption in Porous Materials	365
12.1 Introduction	366
12.2 Simulation Techniques	366
12.3 Thermodynamics	369
12.4 Adsorption in Spaces with Simple Geometries	372
12.5 Adsorption Heterogeneity	380

12.6	Adsorption in Zeolites	382
	Conclusions	387
	References	387
13.	Surface Functionalization of Ordered Nanoporous Silicates	393
13.1	Introduction	394
13.2	Functionalization of ONSs by Grafting	396
13.3	Functionalization by co-condensation	407
13.4	Concluding Remarks	417
13.5	Acknowledgements	418
	References	418
14.	Surface Alumination of Mesoporous Silicates	427
14.1	Introduction	427
14.2	Direct Mixed-gel Synthesised Mesoporous Aluminosilicates	428
14.3	Methods for the Surface Alumination of Mesoporous Silicas	429
14.4	Acidity and Catalytic Activity of Al-grafted Mesoporous Silicates	439
14.5	Stability of Al-grafted Mesoporous Aluminosilicates	446
14.6	Alumination of Mesoporous Silica via Composite Materials	455
14.7	Concluding Remarks	457
14.8	Acknowledgements	458
	References	458
15.	Acidity Measurement of Nanoporous Aluminosilicates – Zeolites and MCM-41	464
15.1	Introduction	464
15.2	Titration Methods	466
15.3	Thermodynamic Methods	468
15.4	Infrared Spectroscopic (IR) Methods	473
15.5	Nuclear Magnetic Resonance (NMR) Methods	477

15.6	Other Spectroscopic Methods	480
15.7	Concluding Remarks	482
15.8	Acknowledgements	483
	References	483
16.	Nanocatalysts Prepared by the Molecularly Designed Dispersion Process	487
16.1	Introduction	487
16.2	Molecular Designed Dispersion Approach	488
16.3	Applications: Designed Dispersions of Metal Oxides on Porous Solids	499
16.4	Conclusions	515
16.5	Acknowledgement	515
	References	516
17.	Acidity-enhanced Nanoporous Catalytic Materials	519
17.1	Introduction	519
17.2	Heteropolyacids (HPAs) Supported on Mesoporous Materials	520
17.3	Sulfated Zirconia Supported on Mesoporous Materials	522
17.4	Acidity-enhanced Mesoporous Materials by Posttreatments	527
17.5	Strongly Acidic Mesoporous Aluminosilicates Assembled from Preformed Nanosized Zeolite Precursors	537
17.6	Acknowledgements	546
	References	546
18.	Modified Mesoporous Materials as Acid and Base Catalysts	553
18.1	Introduction	553
18.2	Synthesis of Materials	554
18.3	Acid Catalysts	557
18.4	Base Catalysis	575
18.5	Conclusions and Perspectives for Future Directions	586

18.6	Acknowledgements	587
	References	587
19.	Lewis Acid/Base Catalysts Supported on Nanoporous Silica as Environmental Catalysts	596
19.1	Introduction	596
19.2	Synthesis of Mesoporous Silicas with or without Heterometallic Elements	597
19.3	Preparation and Characterization of Lewis Acid/Base Containing Mesoporous Silica Catalysts	598
19.4	Application of Lewis Acid Catalysts Supported on Mesoporous Silica	604
19.5	Applications of Basic Catalysts Supported on Mesoporous Silica	611
19.6	Concluding Remarks	612
19.7	Acknowledgement	613
	References	613
20.	Nanoporous Catalysts for Shape-selective Synthesis of Specialty Chemicals: a Review of Synthesis of 4,4'-dialkylbiphenyl	623
20.1	Introduction	623
20.2	Shape-selective Preparation of 4,4'-diisopropylbiphenyl (4,4'-DIBP)	627
20.3	Ethylation and Transethylation of Biphenyl and Its Derivate into 4,4'-diethylbiphenyl (4,4'-DEBP)	634
20.4	Preparation of 4,4'-dimethylbiphenyl (4,4'-DMBP)	636
20.5	Conclusion	645
20.6	Acknowledgments	646
	References	646
21.	Catalysis Involving Mesoporous Molecular Sieves	649
21.1	Introduction	649
21.2	Acid/Base Catalysis	650
21.3	Redox Catalysis	660

21.4	Enantioselective Catalysis	668
21.5	Other Catalytic Applications	677
21.6	Acknowledgements	677
	References	682
22.	Adsorption and Transport in Nanoporous Materials	694
22.1	Introduction	694
22.2	Intraparticle Transport Mechanisms	695
22.3	Combined Bulk and Knudsen Diffusion	697
22.4	Viscous Flow	699
22.5	Diffusion within Micropores	703
22.6	Particle Uptake Rate Models	714
22.7	Conclusions	722
	References	722
23.	Adsorption of Organic Molecules in Nanoporous Adsorbents from Aqueous Solution	727
23.1	Introduction	727
23.2	Characterisation of Nanoporous Adsorbents in View of Their Use for Adsorption in Aqueous Solution	729
23.3	Thermodynamics and Kinetics of Adsorption in Aqueous Solution	736
23.4	Other Methods	740
23.5	Applications	741
23.6	Conclusions	748
	References	749
24.	Functionalized Nanoporous Adsorbents for Environmental Remediation	756
24.1	Introduction	756
24.2	Synthesis of Ordered Materials	757
24.3	Functionalization	760
24.4	Remediation	763
24.5	Conclusions	768
24.6	Acknowledgements	768

References	769
25. Nanoporous Adsorbents for Air Pollutant Removal	772
25.1 Introduction	772
25.2 Mechanism Approaches	773
25.3 Some Adsorbents Used in Air Treatments	786
25.4 Adsorption and Fixed Bed Adsorbers	788
25.5 Industrial Systems and Design Approaches	801
25.6 Activated Carbon Regeneration	805
References	809
26. Bioadsorption and Separation with Nanoporous Materials	812
26.1 Introduction	812
26.2 Separations, Adsorption and Solutes	816
26.3 Adsorption Capacity and Kinetics	820
26.4 Access to Pores	824
26.5 Size Exclusion	827
26.6 Adsorption Mechanisms	829
26.7 Regeneration and Reuse	836
26.8 Stability	837
26.9 Challenges Remaining	839
26.10 Concluding Remarks	840
References	841
27. Nanoporous Materials as Supports for Enzyme Immobilization	849
27.1 Introduction	849
27.2 Immobilization Methods for Enzymes	851
27.3 General Considerations in the Application of Nanoporous Materials for Enzyme Immobilization	852
27.4 Microporous Molecular Sieves as Carriers	853
27.5 Mesoporous Molecular Sieves as Carriers	855
27.6 Mesocellular Foam (MCF) Materials as Carriers	866

27.7	Future Developments	868
27.8	Acknowledgements	870
	References	870
28.	A Novel Nonsurfactant Route to Nanoporous Materials and Its Biological Applications	873
28.1	Introduction	873
28.2	Nonsurfactant-templating Route to Mesoporosity	874
28.3	Selected Applications of Nonsurfactant-templating Approach	878
28.4	Nanoencapsulation of Enzymes and Other Bioactive Substances	880
28.5	Protein Folding/Unfolding in Nanoporous Host Materials and Rigid Matrix Artificial Chaperones	882
28.6	Summary	886
28.7	Acknowledgements	887
	References	887
Author Index		893
Index		895

NANOPOROUS MATERIALS – AN OVERVIEW

G. Q. LU

The Nanomaterials Centre, The University of Queensland, Brisbane 4072, Australia
E-mail: maxlu@cheque.uq.edu.au

X. S. ZHAO

Department of Chemical and Environmental Engineering, National University of
Singapore, 10 Kent Ridge Crescent, Singapore 119260
E-mail: chezxs@nus.edu.sg

1 Introduction

In recent years, nanomaterials have been a core focus of nanoscience and nanotechnology – which is an ever-growing multidisciplinary field of study attracting tremendous interest, investment and effort in research and development around the world. Nanoporous materials as a subset of nanostructured materials possess unique surface, structural, and bulk properties that underline their important uses in various fields such as ion exchange, separation, catalysis, sensor, biological molecular isolation and purifications. Nanoporous materials are also of scientific and technological importance because of their vast ability to adsorb and interact with atoms, ions and molecules on their large interior surfaces and in the nanometer sized pore space. They offer new opportunities in areas of inclusion chemistry, guest-host synthesis and molecular manipulations and reaction in the nanoscale for making nanoparticles, nanowires and other quantum nanostructures.

To provide a comprehensive overview of the area of nanoporous materials, this chapter will begin with a brief introduction to nanoscience and nanotechnology, and the importance of nanomaterials. The basic concepts and definitions in relation to porous materials and nanoporous materials will be given to understand the context of nanoporous materials. Following this introduction, a systematical classification of the types and scope of nanoporous materials will be presented. The properties and their characterisation and measurement methods will be briefly described before major applications in various fields are reviewed. Finally in this chapter, key scientific and engineering issues and future directions are identified as challenges and opportunities to researchers in this field.

1.1 Nanotechnology and nanomaterials

Nanoscale is fascinating because it is on this scale that atoms and molecules interact and assemble into structures that possess unique properties, which are dependent on the size of the structures. It is at this scale that molecular interactions, processes, and phenomena can be controlled and directed to form the desired geometries of the materials building blocks with desirable properties. Nanoscale phenomena and objects have, of course, been utilized for some time. Small metal or metal oxide crystallites supported on a ceramic material, for example, are mostly nanoscale particles that have been used to crack crude oil into fuels for many years. However, what distinguishes cutting-edge nanoscience is the degree of understanding, deliberate control, and precision that new nanostructuring techniques afford. Instead of discovering new materials by serendipity or by trial-and-error, we can now design them systematically.

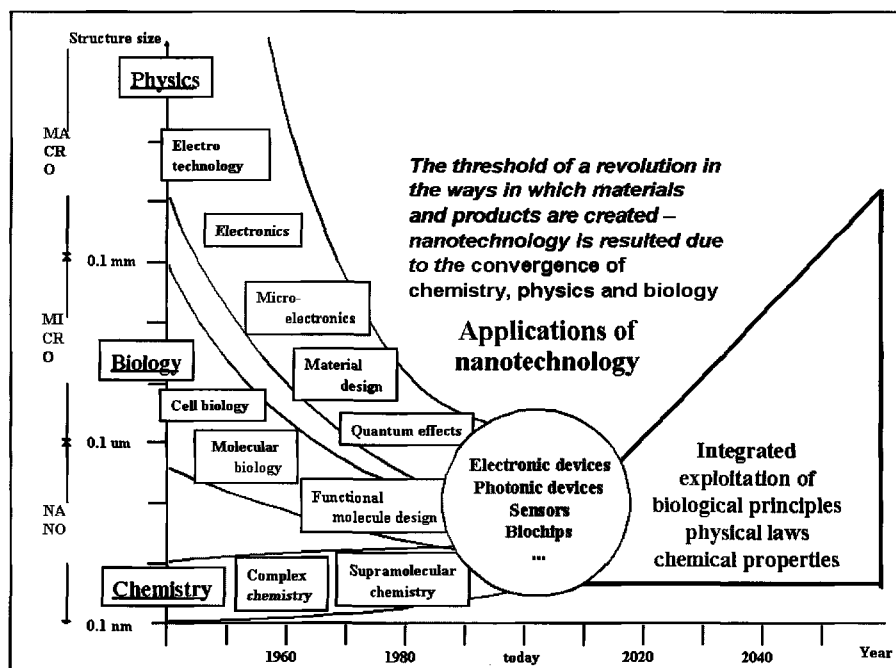


Figure 1. Threshold of nanotechnology as basic sciences converges to the nanoscale (adapted from [1])

What makes nanoscale building blocks interesting is that by controlling the size in the range of 1-100 nm and the assembly of such constituents, one could alter and prescribe the properties of the assembled nanostructures. As Professor Roald Hoffmann – the Chemistry Nobel Laureate put it, “*Nanotechnology is the way of ingeniously controlling the building of small and large structures, with intricate properties; it is the way of the future, with incidentally, environmental benignness built in by design*”. Nanostructured materials may possess nanoscale crystallites, long-range ordered or disordered structures or pore space. Nanomaterials can be designed and tailor-made at the molecular level to have desired functionalities and properties. Manipulating matter at such a small scale with precise control of its properties is one of the hallmarks of nanotechnology. The potential and importance of nanoscale science and technology has clearly been recognized worldwide as evidenced by significant investments in nanotechnology R&D in the USA, Europe, Japan and other Asia-Pacific countries since 2000 when the US Nation Nanotechnology Initiative was announced.

1.2 Definitions of pores and porous materials

Porous materials are like music: the gaps are as important as the filled-in bits. The presence of pores (holes) in a material can render itself all sorts of useful properties that the corresponding bulk material would not have [2]. Generally porous materials have porosity (volume ratio of pore space to the total volume of the material) between 0.2-0.95 [3]. Pores are classified into two types: open pores which connect to the surface of the material, and closed pores which are isolated from the outside. In functional applications such as adsorption, catalysis and sensing, closed pores are not of any use. In separation, catalysis, filtration or membranes, often penetrating open pores are required. Materials with closed pores are useful in sonic and thermal insulation, or lightweight structural applications. Pores have various shapes and morphology such as cylindrical, spherical and slit types. There are also pores taking more complex shapes such a hexagonal shape. Pores can be straight or curved or with many turns and twists thus having a high tortuosity.

The definition of pore size according to the International Union of Pure and Applied Chemistry (IUPAC) is that micropores are smaller than 2 nm in diameter, mesopores 2 to 50 nm and macropores larger than 50 nm. However this definition is somewhat in conflict with the definition of nanoscale objects. Nanoporous materials are a subset of porous materials, typically having large porosities (greater than 0.4), and pore diameters

between 1- 100 nm. In the field of chemical functional porous materials, it is better to use the term “nanoporous” consistently to refer to this class of porous materials having diameters between 1 and 100 nm. For most functional applications, pore sizes normally do not exceed 100 nm anyway. It is noted that nanoporous materials actually encompass some microporous materials to all mesoporous materials.

So what are the unique properties of those materials? Nanoporous materials have specifically a high surface to volume ratio, with a high surface area and large porosity, of course, and very ordered, uniform pore structure. They have very versatile and rich surface composition, surface properties, which can be used for functional applications such as catalysis, chromatography, separation, and sensing. A lot of inorganic nanoporous materials are made of oxides. They are often non-toxic, inert, and chemically and thermally stable, although in certain applications the thermal stability requirement is very stringent so you have to have a very highly thermal stable catalyst.

2 Classification of Nanoporous Materials

Porous materials can be classified according to their materials constituents (such as organic or inorganic; ceramic or metal) or their properties. Table 1 summarizes the available nanoporous materials according to their chemical compositions and their technical characteristics.

Table 1. Classification of nanoporous materials

	Polymeric	Carbon	Glass	Alumino-silicate	Oxides	Metal
Pore size	Meso-macro	Micro-meso	Meso-macro	Micro-meso	Micro-meso	Meso-macro
Surface area / Porosity	Low >0.6	High 0.3-0.6	Low 0.3-0.6	High 0.3-0.7	Medium 0.3-0.6	Low 0.1-0.7
Permeability	Low-medium	Low-medium	High	Low	Low-medium	High
Strength	Medium	Low	Strong	Weak	Weak-medium	Strong
Thermal stability	Low	High	Good	Medium-high	Medium-high	High
Chemical stability	Low-medium	High	High	High	Very high	High
Costs	Low	High	High	Low-medium	Medium	Medium
Life	Short	Long	Long	Medium-long	Long	Long

3 Properties and characterization of nanoporous materials

Nanoporous materials possess a unique set of properties that the bulk correspondent materials do not have such as high specific area, fluid permeability and molecular sieving and shape-selective effects. Different nanoporous materials with varying pore size, porosity, pore size distribution and composition have different pore and surface properties that will eventually determine their potential applications. For different applications there are different sets of performance criteria that would require different properties.

For example, the performance criteria for a good adsorbent include

(1) High adsorption capacity. Fundamental properties that affect this parameter are specific surface area, surface chemical nature, and pore size. These parameters determine how much adsorbates can be accumulated by per unit mass of adsorbents.

(2) High selectivity. For multicomponent mixture, selectivity is highly desired for separation. The selectivity of an adsorbent will depend on the pore size, shape and pore size distribution as well as the nature of the adsorbate components.

(3) Favorable adsorption kinetics. Adsorption kinetics is determined by the particle (crystallite) size, the macro-, meso and microporosity of the adsorbent. Sometimes, binder type and amount would also affect the interparticle transport thus the global adsorption process kinetics. A favorable kinetics means that the adsorption rate is fast or controllable depending on the requirement of a particular application.

(4) Excellent mechanical properties. Obviously, adsorbents need to be mechanically strong and robust enough to stand attrition, erosion and crushing in adsorption columns or vessels. High bulk density and crushing strength, and attrition resistance are desirable.

(5) Good stability and durability in use. Adsorbents are often subject to harsh chemical, pressure and thermal environments. Good stability in those environments is essential in ensuring long life or durable utilization. As synthesized nanoporous materials may or may not have all these desirable properties depending on the synthesis systems, methods and processing conditions. Obviously the practical challenges in making good adsorbent materials will be to obtain high-adsorption-capacity adsorbents in a simple and cost effective manner, to make sure the above requirements/criteria are met as much as possible. In many cases, post-synthesis modification is required to impart certain functionality or

improve certain property due to the inability of the synthesis route to achieve them during the process of synthesis. There are many research efforts devoted to this area.

If used as catalyst support or catalysts, nanoporous materials involved are required to have not only the above properties but also suitable surface chemistry characteristics such as acidity or basicity, and shape selectivity is often important.

4 Major opportunities in applications

There are ever expanding applications for nanoporous materials besides the traditional areas of adsorption separation, catalysis and membranes. This chapter is not intended to cover the details of applications of nanoporous materials but will provide an overview of the main application opportunities and market potentials. Many promising applications and processes are dealt with in the subsequent chapters in this book by the contributing authors.

4.1 Environmental separations

As the regulatory limits on environmental emissions become more and more stringent, industries have become more active in developing separation technologies that could remove contaminants and pollutants from waste gas and water streams. Adsorption processes and membrane separations are two dominating technologies that have attracted continuous investment in R&D. Adsorbent materials and membranes (typically nanoporous) are increasingly being applied and new adsorbents and membranes are constantly being invented and modified for various environmental applications such as the removal of SO₂, NO_x, and VOCs emissions [4]. Adsorbents of the traditional types such as commercially available activated carbons, zeolites, silica gels, and activated alumina have estimated worldwide market exceeding US\$1.5 billion per year [5].

New adsorbent materials with well defined pore sizes and high surface areas are being developed and tested for potential use in energy storage and environmental separation technologies. Table 2 lists some examples of new adsorbents for energy and environmental applications as identified by Yang [5].

Table 2. Examples of emerging processes for environmental separations

Energy and Environmental Applications	Adsorbents and technology
CH ₄ storage for on-board vehicular storage	Super-activated carbon and activated carbon fibers; Near or meeting DOE target storage capacity
H ₂ storage for on-board vehicular storage	Carbon nanotubes possible candidate
N ₂ /CH ₄ separation for natural gas upgrading	Clinoptilolite, Sr-ETS-4 by kinetic separation
Sulfur removal from transportation fuels (gasoline, diesel and jet fuels)	π -complexation sorbents such as Cu(I)Y, AgY
CO removal from H ₂ to <10 ppm for fuel cell applications	π -complexation sorbents such as CuCl/ γ -Al ₂ O ₃ , CuY, and AgY; silica molecules sieve membranes
NO _x removal	Fe-Mn-Ti oxides, Fe-Mn-Zr oxides, Cu-Mn oxides
Removal of dienes from olefins (to<1 ppm)	π -complexation sorbents such as Cu(I)Y, AgY

4.2 Clean energy production and storage

Future energy supply is dependent on hydrogen as a clean energy carrier. Hydrogen can be produced from fossil fuels, water electrolysis and biomass. However, the current debates on the hydrogen economy are intimately linked to the clean production of hydrogen from fossil fuels such as natural gas and coal. Due to the low cost and wide availability of coal, coal gasification to syngas and then to hydrogen through the water gas shift reaction is a promising route to cheap hydrogen. The success of such a hydrogen production route will be only possible provided that carbon dioxide is sequestered safely and economically. Key to the cost-effective conversion of coal to hydrogen and carbon capture is nanomaterials development such as catalyst for the WGS reaction and inorganic membranes for hydrogen/CO₂ separation.

In the future hydrogen economy, hydrogen will be the dominant fuel, and converted into electricity in fuel cells, leaving only water a product. Fuel cell development has been very rapid in recent year. However, there are many technological challenges before fuel cells become commercially viable and widely adopted. Many of the problems are associated with materials notably related to electrocatalyst, ion-conducting membranes and porous supports for the catalyst. Certain nanoporous materials such as carbon nanotubes and zirconium phosphates have already shown promise for application in fuel cells.

Hydrogen storage will be also essential in hydrogen economy infrastructure. Currently there are no optimal systems for hydrogen storage. Hydrogen can be stored in gaseous, liquid or more recently in solid forms. Nanostructured materials such as carbon nanotubes again show promise as an adsorbent. Despite many controversial reports in the literature, hydrogen storage in carbon nanotubes may one day become competitive and useful. Another type of nanostructured carbons is templated by using 3-D ordered mesoporous silicates. It has been shown that this type of carbons exhibit interesting and superior performance as supercapacitor and electrode materials for Li-ion battery applications [6]. The clean energy market is a huge one already and according to the Austin Business Journal [7] the worldwide "clean energy" market is expected to grow from US\$9.5 billion in 2002 to US\$89 billion by 2012. Fuel cell products will expand from a US\$500 million business in 2002 to US\$12.5 billion by 2012.

4.3 Catalysis and photocatalysis

Heterogeneous catalysis has had a major impact on chemical and fuel production, environmental protection and remediation, and processing of consumer products and advanced materials [8]. A survey of U.S. industries revealed that the annual revenue from chemical and fuel production topped all other industrial sectors at \$210 billion. The survey also showed that over 60% of the 63 major products and 90% of the 34 process innovations from 1930-80 involved catalysis, illustrating the critical role of this field in the fuel and chemical industry. The significance of catalytic processes can be further demonstrated by the value of their products, which amounted to \$1 trillion in the United States alone in 1989 [9].

More efficient catalytic processes require improvement in catalytic activity and selectivity. Both aspects will rely on the tailor-design of catalytic materials with desired microstructure and active site dispersion. Nanoporous materials offer such possibilities in this regard with controlled

large and accessible surface area of catalyst but avoiding standalone fine particles. The traditional methods of impregnation of metal ions in nanoporous supports are not as effective in achieving high dispersion of active centers, whereas incorporation in template synthesis or intercalation are more advanced techniques rendering high activity owing high surface area of the active components and selectivity due to the narrow pore size distribution.

Transition metal oxides exhibit a wide range of physical, chemical and optical properties. One of the most widely studied metal oxides is semi-conducting TiO_2 . Titania in anatase form exhibits strong photocatalytic effect, which generates electron-hole pairs. As a result the material can harvest photos in the near UV region ($<410\text{nm}$) to render its surface strong oxidizing power to decompose organic molecules. Photocatalysis is a rapid growing field of study that has attracted intense attention of chemical and materials researchers in recent years. It is estimated that the TiO_2 photocatalyst market in Japan alone could exceed US\$5billions [10].

4.4 Sensors and actuators

Nanoparticles and nanoporous materials possess large specific surface areas, and high sensitivity to slight changes in environments (temperature, atmosphere, humidity, and light). Therefore such materials are widely used as sensor and actuator materials. Gas sensors rely on the detection of electric resistivity change upon change in gas concentration and their sensitivity is normally dependent on the surface area. Gas sensors based on nanoporous metal oxides such as SnO_2 , TiO_2 , ZrO_2 , and ZnO are being developed and applied in detectors of combustible gases, humidity, ethanol, and hydrocarbons. Zirconia is typically a good sensor material for oxygen. According to the market projection by Freedonia group [11], the market demand for chemical sensors is forecast to grow 8.6% per year to \$3.4 billion in 2006.

4.5 Biological applications

Nanomaterials that are assembled and structured on the nanometer scale are attractive for biotechnology applications because of the potential to use material topography and the spatial distribution of functional groups to control proteins, cells, and tissue interactions, and also for bioseparations. Bionanotechnology is all about creating nanomaterials or biomaterials for biological applications [12]. Many studies are underway in fundamental

understanding and exploiting the nature of nanoscale systems and processes to

- Develop improved chemical separations and isolation media using nanoporous materials
- Integrate engineered and self-assembled materials into useful devices ranging from biosensors to drug delivery systems
- Develop new products and biomedical devices by manipulating biomolecules enzymes, other proteins, and biochemical processes at the nanoscale.

Proteins have been used by nature for billions of years to create the incredibly complex nanoscale structures within a living cell. Molecular scale scaffolding, cables, motors, ion pores, pumps, coatings, and chemically powered levers composed primarily of proteins are all found in nature. Proteins provide superior catalytic abilities over traditional inorganic type catalysts and the simplified reaction conditions of enzymes require less complex engineering than catalytic reactors. Nanoporous materials being porous and some often found bio-compatible afford the capability to build enzymatic nanomaterials that mimic natural biological reactions. Immobilizing recombinant enzymes into nanoporous materials can be used for long-lifetime biological reactors for a variety of applications. The possibilities for using enzymes in small-scale reactors for producing drugs, energy, decontaminating wastes, and creating complicated synthetic reactions are limitless [13].

Nanopores embedded in an insulating membrane fabricated by using a physical method has been demonstrated useful to examine biomolecules one by one, achieving single-molecule analysis [14]. Li et al. [14] are able to use an ion beam to shrink a pore of micrometer size in a silicon nitride membrane down to nanoscale dimensions for measuring the motion of single DNA molecules through the nanopores. The most supervising result of the work is that the DNA molecules do not thread meekly through these nanopores like a noodle of spaghetti that one sucks up, but instead come through the pores in several configurations. This is an important breakthrough towards DNA sequencing, demonstrating the potential applications of nanoporous materials in bioengineering.

Another area of applications that is exciting as far as nanoporous materials is concerned, is biosensors. Piezoelectric biosensors utilizing high surface area nanoporous coatings exhibit increased sensitivity in detection. Immobilized biological molecules on the surface of nanoporous silica can serve as biological detection systems [15, 16]; microscale

piezoelectric cantilevers serve as the transducer. There is a shift in resonance frequency of the cantilever when molecules adsorb onto its surface. The shift in frequency results from the change in mass of the cantilever; and the sensitivity is directly related to the ratio of the mass of the adsorbed analyte to the mass of the cantilever. Thus by incorporating nanoporous silica, between the transducer and biological detection system, the increased surface to volume ratio of the cantilever increases the sensitivity of the resonant frequency of the oscillator to changes in mass [17]. Biosensors have major potential in the healthcare industry where, for example, real-time *in vivo* sensing could be used for insulin pumps, drug detection in emergency situations. Rapid methods for detecting pathogens in food products and animal feed could save billions of dollars in medical costs. It is estimated that the world market for biosensors in 2001 was US\$1.44 billion [11]. The estimated market for bionanotechnology products in 2003 is US\$930 m, and is expected to reach over US\$3 billion in 2008 (http://www.frontlinesmc.com/nano/Nano_PressRelease.pdf).

4.6 Other applications

Besides the above applications, there are also tremendous opportunities for nanoporous materials in the following areas [18].

- (1) high efficiency filtration and separation membranes
- (2) catalytic membranes for chemical processes
- (3) porous electrodes for fuel cells
- (4) high efficiency thermal insulators
- (5) electrode materials for batteries
- (6) porous electronic substrates for high speed electronics

5 Concluding remarks

Nanomaterials will have a profound impact on many industries including microelectronics, manufacturing, medicine, clean energy, and environment. In these industries, there are already many examples of applications of microporous zeolites and molecular sieves as nanoscale catalysts and gas separation membranes. Expanding the pore dimensions to mesopores range will increase the scope of their applications in these fields. In particular, mesoporous materials will have wider applications into biological separation, biosensors, and nanoreactors for conducting multiple and controlled biological reactions on microchips. In the fields of clean energy production and storage, nanoporous materials as catalysts and

storage media and electrode materials will have tremendous potential in enabling process innovations in areas such as gas to liquid conversion, hydrogen production, alternative solar cells, fuel cells and advanced batteries. In the environmental field, nanoporous and nanocrystalline semiconductors are the key to cost-effective photocatalytic purification of water and air, economic removal and recovery of organic vapors, greenhouse gas reduction and utilization. In health care, biomaterials for orthopedic, and cardiovascular applications, tissue repair, biosensors, and controlled drug delivery are likely to be developed and applied in the near future, all of which will depend on the development of new nanoporous substrates or coatings one way or the other.

In the science of nanoporous materials, there are many challenges and opportunities ahead of us. For example, in catalysis, one of the key goals is to promote reactions to have a high selectivity with a high yield. To meet this goal, tailoring a catalyst particle via nanoparticle synthesis and self-assembly so that it catalyzes only a specific chemical conversion with a higher yield a greater energy efficiency is imperative. For adsorption and catalysis selectivity, a relatively narrow pore size distribution is desirable. Traditional amorphous nanoporous materials such as silica gels, alumina, and activated carbons are limited in shape selectivity because of their broad pore size distribution and fixed pore geometries. Microporous zeolites and pillared clays are the only class of nanocrystalline materials with uniform pores. However, their pore sizes are limited to below 1.0–1.2 nm. The mesostructured molecular sieves and oxides that have been developed since the invention of MCM-41 by Mobil scientists [19] have shown great promises for separation, catalysis and biological applications where large molecules are involved. The supramolecular templating techniques and processing have revolutionized the synthesis and application opportunities of nanoporous materials. There are many templating pathways in making mesostructured materials. New synthesis strategies are constantly being revealed and trailed for improving the pore size range, chemical composition, thermal and hydrothermal stabilities. Structural modification either via isomorphous substitution or post-synthesis grafting can improve the surface chemistry characteristics and thermal stability [20]. Surface functionalization is particularly important for selective adsorption, and biomolecular immobilization and separation. All these topics are exciting and scientifically challenging, which are well addressed in the subsequent contributions in this book.

References

1. Bachmann G., Market Opportunities at the Boundary From Micro to Nanotechnology, *MST News* **3** (1) (2001) pp. 13-14.
2. Ball P., Made to Measure, *Princeton University Press*, 1997, Princeton, NJ, USA.
3. Ishizaki K., Komarneni S., Nanko M., *Porous Materials –Process technology and applications*, Kluwer Academic Publishers, Boston, 1998, p. 2.
4. Cohen Y., and Peters R.W., Novel adsorbents and their environmental applications, *AIChE Symposium Series*, **91** (1995) New York.
5. Yang R.T., *Adsorbents: Fundamentals and Applications*, 2003, Brisbane, John Wiley & Sons, Inc.
6. Xing W., Yan Z.F., Ryoo R. and Lu G.Q., *Advanced materials*, submitted, 2003.
7. <http://austin.bizjournals.com/austin/stories/2003/02/17/daily32.html>.
8. Ying Jackie Y., Nanostructure Processing of Advanced Catalytic Materials, in *WTEC Workshop Report on R&D Status and Trends in Nanoparticles, Nanostructured Materials, and Nanodevices in the United States*, Proceedings of the May 8-9, 1997 Workshop, Ed. Richard W. Siegel, Evelyn Hu, and M.C. Roco, January 1998 (http://www.wtec.org/loyola/nano/us_r_n_d/04_07.htm)
9. Cusumano J.A., In *Perspectives in catalysis*, ed. J.M. Thomas and K.I. Zmoraev. Blackwell Scientific Publication, Boston, 1992
10. Fujishima A., Hashimoto K. and Watanabe T., *TiO₂ Photocatalysis –Fundamentals and Applications*, BKC Inc. Tokyo, 1999.
11. Freedonia Industry Study, #1547 *Chemical Sensors: Liquid, Gas & Biosensors* April 2002 (http://www.gii.co.jp/english/fd10075_chemical_sensors_toc.html).
12. Sarikaya M., Tamerler C., Jen A. K.-Y., Schulten K., Baneyx F., Molecular biomimetics: nanotechnology through biology, *Nature Mater.* **2** (2003) pp. 577-585.
13. Pacific Northwest National Laboratory, Institutional Plan FY2001-2005, USDOE, (<http://www.pnl.gov/nano/bio/>).
14. Li J., Gershow G., Stein D., Brandin D. and Golovchenko J. A. DNA molecules and configurations in a solid-state nanopore microscope, *Nature Mater.* **2** (2003) pp. 611-615.
15. Collings A. F. and Caruso F., Biosensors: recent advances, *Rep. Prog. Phys.* **60** (1997) p. 1397.
16. Diaz J.F. and Balkus K.J., *J. Mol. Catal. B: Enzymatic* **2** (1996).
17. McGrath K.M., Dabbs D.M., Yao N., Edler K.J., Aksay I.A. and Gruner S.M., *Langmuir* **16** (2000).
18. Schaefer D.W., Engineered Porous Materials, *MRS Bulletin*, **19** (4) April (1994) p. 14.
19. Kresge C.T., Leonowicz M.E., Roth W.J., Vartuli, J.C. and Beck J.S., *Nature* **359** (1992) p. 710.
20. Zhao X.S. and Lu G.Q., *J. Phys. Chem B* **102**, 1556-1561, 1998.

ADVANCES IN MESOPOROUS MATERIALS TEMPLATED BY NONIONIC BLOCK COPOLYMERS

C. YU, B. TIAN, X. LIU, J. FAN, H. YANG AND D. Y. ZHAO*

Shanghai Key Laboratory of Molecular Catalysis and Innovative Materials, Department of Chemistry, Fudan University, Shanghai, 200433, P. R. China
E-mail: dyzhao@fudan.edu.cn

Advances in the synthesis and applications of mesoporous materials templated by nonionic block copolymers have been reviewed. In the past few years, different synthetic methodologies have been developed to fabricate periodic mesoporous silica materials with controllable morphologies. The wall structures of mesoporous silica materials templated by block copolymers represent quite different properties compared to that of mesoporous silica templated by ionic surfactants and therefore are discussed separately in this chapter. Recent research efforts have been devoted to the fabrication of non-siliceous mesostructures, the use of nonionic surfactants and amphiphilic block copolymers has resulted in non-siliceous mesoporous materials with a large variety of compositions. Mesoporous materials with uniform and tunable pore size, highly ordered pore structures, adjustable morphologies, ultra large surface areas and various wall compositions have shown potential applications in catalysis, adsorption, separation, optics, sensors and nano-reactors.

1 Introduction

Traditional microporous zeolite materials have been widely used in gas separation, ion-exchanging agents and petroleum industries [1]. However, the relatively small pore size restricts their future use in separation and catalytic process where large molecules are involved. In 1992, Mobil researchers reported the synthesis of a family of ordered mesoporous aluminosilicates (denoted as M41S) [2, 3]. This surfactant supramolecular templating approach has led to a breakthrough to extend porous materials to meso-scale with relatively large, uniform and adjustable pore sizes.

In the initial report of the synthesis of mesoporous M41S [2, 3], long-chain quaternary ammonium surfactants such as cetyltrimethyl ammonium bromide (CTAB) were employed as the structure-directing agents under basic conditions, where the electrostatic charge matching between cationic surfactant (S^+) and anionic inorganic precursors (Γ^-) may generate organic/inorganic hybrid mesostructures. Later, the synthesis approaches have been extended to ST^+ (anionic surfactants such as

sulfonates and cationic inorganic precursors), $S^-M^+T^-$ (M^+ = metal ion) and $S^+X^-T^+$ (X^- = counter anion) to synthesize mesoporous materials with various compositions [4]. Pinnavaia and coworkers firstly demonstrated that neutral amine surfactants (S^0) and neutral inorganic precursors (T^0) could be used to prepare mesoporous metal oxides by a S^0T^0 pathway [5]. However, these ionic surfactants and neutral amine surfactants are relatively expensive and toxic, which may limit the future applications of mesoporous materials in industries. A careful search in the surfactant categories by the same group shortly led to the nonionic polyethylene oxide (PEO) surfactants, which are relatively low-cost, nontoxic and biodegradable [6] and can also be used as templates to synthesize disordered mesoporous materials MSU-X in a near neutral condition [7]. While the above-mentioned synthesis was carried out at relatively low surfactant concentrations, Attard and coworkers reported a liquid crystal templating approach [8] to synthesize highly ordered mesoporous materials where high concentration (50 wt%) oligomeric PEO surfactants were also utilized. In an organic solvent system, Wiesner and coworkers synthesized organically modified aluminosilicate mesostructures with the use of specially designed poly(isoprene-*b*-ethylene oxide) (PI-*b*-PEO) block copolymers as the structure-directing agents [9]. By increasing the fraction of the inorganic precursors with respect to the polymers, mesostructures expected from the phase diagrams of diblock copolymers were obtained.

Stucky and coworkers employed commercial PEO block copolymers under acidic aqueous solutions and successfully synthesized a family of mesoporous materials (SBA-X) with various ordered structures and large pore sizes (up to 30 nm) [10, 11]. Göltner and coworkers also employed block copolymers in the synthesis of mesoporous materials with thick walls and large pore sizes [12, 13]. Since then, much attention has been paid to the synthesis, property characterization and application of mesoporous materials by using PEO amphiphilic block copolymers as the templates.

In fact, compared to the commonly used small molecular surfactants, PEO amphiphilic copolymers are much richer in both quantities and properties such as association properties, phase behaviors, *etc.* Generally, amphiphilic copolymers of hydrophilic PEO with hydrophobic propylene oxide (PO), 1,2-butylenes oxide (BO) or styrene oxide (SO) can be synthesized by anionic polymerization with narrow molecular weight distribution (usually $M_w/M_n < 1.1$). The first two classes of amphiphilic block copolymers are now commercially available from BASF-Wyandotte and Dow Chemical Company, respectively. Since the block architecture (*e.g.*, diblock EO_mPO_n , EO_mBO_n , triblock $EO_mPO_nEO_m$, $EO_mBO_nEO_m$,

triblock $\text{PO}_n\text{EO}_m\text{PO}_n$, $\text{BO}_n\text{EO}_m\text{BO}_n$ and cyclic EO_mBO_n) and the repeating number of hydrophilic block and hydrophobic block (m and n , respectively) can be elegantly controlled, it offers a wide range of PEO block copolymers with various compositions and properties (commercial or synthesized in lab). Moreover, the association properties [14] and phase behaviors (both theoretical [15] and experimental [16, 17]) are well documented in literatures, which can be utilized as useful predictions in the design of mesoporous materials.

The recent advances in mesoporous materials templated by nonionic PEO type surfactants are reviewed in this chapter and focused on nonionic amphiphilic block copolymers. In the literature alkyl PEO oligomeric surfactants are sometimes referred to as diblock copolymers (EO_mC_n) and such surfactants are also involved in the discussion. Ionic block copolymer surfactants such as cationic polybutadiene-*b*-poly(vinylpyridinium) and anionic poly(ethylethylene)-*b*-polystyrenesulfonate, which are rarely used in the synthesis of mesoporous materials [18], are not included in this section.

2 Siliceous mesoporous materials

Nonionic block copolymers become more and more important in the synthesis of mesoporous materials because of their diverse structural characteristics and rich phase behaviors. Different synthetic methodologies have been developed to fabricate periodic mesoporous silica materials in the past few years. By carefully manipulating the processing variables such as temperature, pH, ionic strength, reaction time and solution composition, ordered mesoporous silica materials have been obtained from different nonionic amphiphilic block copolymers with variable structures and adjustable physical properties.

From the point view of the pore arrangement, mesoporous materials can be divided into ordered and disordered structures. Some of the ordered mesostructures reported in the literature synthesized by using amphiphilic block copolymers are listed in Table 1.

Using nonionic oligomeric surfactants C_{12}EO_8 and C_{16}EO_8 in 1995, Attard and coworkers [8] synthesized hexagonal mesoporous silica under an acidic condition with a surfactant concentration of ~50 wt%. The resulting ordered materials exhibit pore sizes up to 3.0 nm. In an acidic and nonaqueous medium, the syntheses of highly ordered hexagonal and lamellar aluminosilicate-copolymer mesostructures were carried out by

Wiesner and coworkers [9]. Later, a cubic $Im\bar{3}m$ mesoporous silica with bicontinuous "Plumber's Nightmare" morphology was synthesized from a block copolymer-hybrid mesophase by the same group [19]. Under a mild acidic condition, Su and coworkers [20] have obtained a well-ordered mesoporous silica CMI-1 from $C_{16}EO_{10}$ in a relatively wide range of surfactant concentrations.

In acidic media, a number of highly ordered mesoporous silica materials with various mesopore packing symmetries and well defined pore connectivities have been prepared by Zhao and coworkers [10, 11, 21, 22]. By using alkyl PEO oligomeric surfactants, mesostructures with hexagonal, cubic and lamellar symmetries were obtained. Cubic SBA-11 with a space group of $Pm\bar{3}m$ [11] was synthesized from $C_{16}EO_{10}$ template; SBA-12 [11] and SBA-14 [11] were prepared by using $C_{16}EO_{10}$ and $C_{12}EO_4$ as the templates [11], respectively. In the presence of triblock copolymers such as $EO_{20}PO_{70}EO_{20}$ (P123), $EO_{106}PO_{70}EO_{106}$ (F127), $EO_{132}PO_{50}EO_{132}$ (F108) and $EO_{39}BO_{47}EO_{39}$ (B50-6600) as structure-directing agents, highly ordered large pore (up to 30 nm) mesoporous silica materials SBA-15 (space group $p6mm$, Figure 1), SBA-16 [11] (space group $Im\bar{3}m$), FDU-1 [21] (space group $Im\bar{3}m$) and FDU-5 [22] (space group $Ia\bar{3}d$) were obtained.

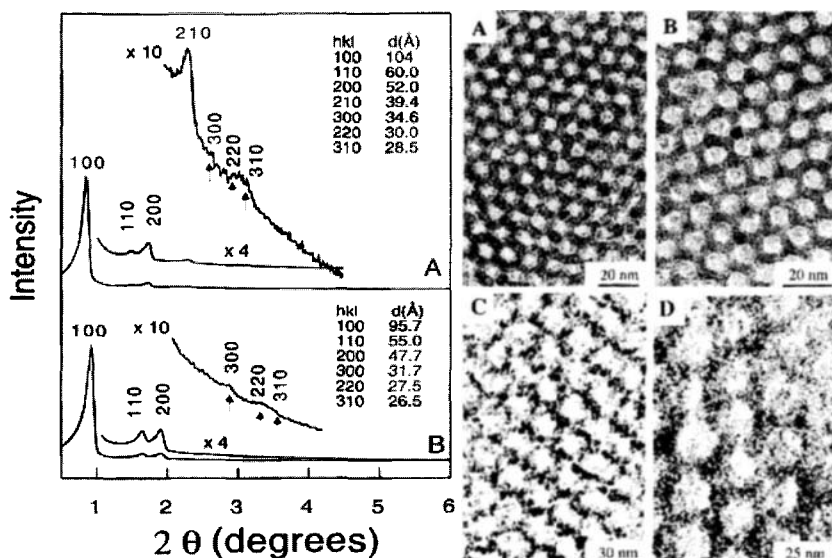


Figure 1. (left) X-ray diffraction patterns (XRD) of (A) as-synthesized and (B) calcined SBA-15 materials. (right) Transmission electron microscopy (TEM) images of calcined hexagonal SBA-15 mesoporous silica with different average pore sizes. (A) 60 Å, (B) 89 Å, (C) 200 Å, and (D) 260 Å. Adapted with permission from ref. [10].

SBA-11 was synthesized over a wide range of reactant compositions at room temperature with a mean pore size of 2.5 nm. SBA-12 has a BET surface area of 1150 m²/g, a pore volume of 0.83 cm³/g and a mean pore size of 3.1 nm. SBA-12 was originally assumed to have a space group of *P6₃/mmc*, later it was revealed by using TEM techniques that the SBA-12 specimens usually contained mixed *hcp* and *ccp* phases. [23]

Highly ordered mesoporous materials SBA-15 have attracted more and more attention not only because they have high quality structure regularity, thick inorganic walls, excellent thermal and hydothermal stability, but also because the template is economically cheap and nontoxic, and the synthesis is quite simple and reproducible [10, 11]. The pore size of the materials can be tuned easily through hydrothermal treatment, namely higher heating temperature achieves larger pore sizes [10, 11]. More importantly, people recently revealed that the wall structure of SBA-15 is quite different from that of MCM-41, although the two materials have the same space group (*p6mm*). A large number of disordered micropores are distributed within the walls of SBA-15, even mesopores with the diameters between 2 ~ 3 nm can be observed [24-26]. This feature will be discussed in greater detail in the following section.

Table 1. Ordered mesoporous silica materials synthesized by using amphiphilic block copolymers

Researchers or materials	Surfactant(s)	Structure	Reference
Attard <i>et al</i>	C ₁₂ EO ₈ , C ₁₆ EO ₈	<i>p6mm</i>	[8]
Wiesner <i>et al</i>	PI- <i>b</i> -PEO	<i>p6mm</i> , <i>Im3m</i> and lamellar L	[9, 19]
CMI-1	C ₁₆ EO ₁₀	<i>p6mm</i>	[20]
SBA-11	C ₁₆ EO ₁₀	<i>Pm3m</i>	[11]
SBA-12	C ₁₈ EO ₁₀	<i>P6₃/mmc</i>	[11]
SBA-14	C ₁₂ EO ₄	Cubic	[11]
SBA-15	EO ₂₀ PO ₇₀ EO ₂₀	<i>p6mm</i>	[10]
SBA-16	EO ₁₀₆ PO ₇₀ EO ₁₀₆	<i>Im3m</i>	[11]

Table continued

FDU-1	EO ₃₉ PO ₄₇ EO ₃₉	<i>Im3m</i>	[21]
FDU-5	EO ₂₀ PO ₇₀ EO ₂₀	<i>Ia3d</i>	[22]
Voegtlin <i>et al</i>	C ₈ Ph(EO) ₁₀		[27]

C: carbon chain; PI: poly (isoprene)

SBA-16 is a cubic mesophase with a symmetry of *Im3m* and a large cell parameter (*a*) of 16.6 nm [11]. The structure-directing agent is triblock copolymer EO₁₀₆PO₇₀EO₁₀₆ with large hydrophilic segments. Calcined specimen has a large pore size of 5.4 nm, a pore volume of 0.45 cm³/g and a BET surface area of 740 m²/g.

FDU-1 is prepared by using EO₃₉BO₄₇EO₃₉ amphiphilic triblock copolymers [21] and has a space group *Im3m* with unit cell parameter *a* = 22 nm. The pore size is about 12 nm, pore volume about 0.77 cm³/g and a BET surface area about 740 m²/g. The structure is similar to that of SBA-16 except that FDU-1 has a significantly larger pore size and unit cell dimensions, the largest among all the known cubic mesoporous silica materials.

FDU-5 [22] was prepared in a non-aqueous solution by using P123 as a template and by adding a small amount of organosilicates, for example, mercapto-propyltrimethoxysilane (MPTS), or a fraction of non-polar organic molecules, for example, ethylbenzene, toluene, TMB, etc., at room temperature under an acidic condition. The resultant materials have a bicontinuous cubic *Ia3d* space symmetry that is analogous to the structure of MCM-48 prepared by using cationic surfactant under a basic condition (Figure 2). However, the pore size (up to 10 nm) of the materials is much larger than that for MCM-48. These large pore mesoporous silica materials FDU-5 have been used as hard templates to prepare mesoporous carbon materials with bicontinuous cubic structure (space group *Ia3d*) [28].

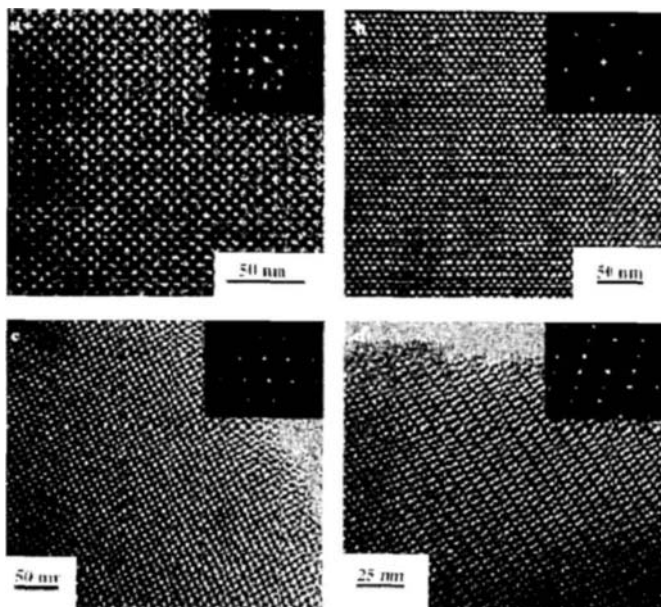


Figure 2. TEM images and corresponding Fourier diffractograms of calcined FDU-5 prepared at room temperature under acidic conditions with triblock copolymer P123 as template and MPTS as additive. The images were recorded along the directions [100] (a), [111] (b), [110] (c), and [331] (d). Adapted with permission from ref. [22]

From the materials discussed above, we can see that all the syntheses were carried out in acidic media. This is related to the assembly characteristics of PEO type nonionic amphiphilic block copolymers. However, it is worth to mention that some researchers have prepared ordered periodic mesoporous silica in a quite different system. An example is the mesoporous silica prepared by Voegtlin *et al.* under near-neutral conditions employing nonionic oligomeric surfactants in the presence of fluoride ions [27]. In a wide range of pH conditions (pH = 0-9), Stucky and coworkers have developed a one-step synthesis of ordered hexagonal silica-surfactant mesostructured composites by using nonionic amphiphilic block copolymers with fluorides by controlling the rates of hydrolysis and condensation of tetramethoxysilane (TMOS) as a silica source [29].

The ordered mesoporous silicas templated by nonionic amphiphilic block copolymers have greatly enlarged the family of mesostructures. It is

important for researchers to investigate the assembly pathways during the formation of mesostructures as well. The syntheses of disordered sponge-like or wormhole-like mesoporous silica materials have also contributed a lot to the exploiting of organization principles in inorganic-surfactant reaction systems. Pinnavaia and coworkers [7, 30] have brought forward a nonionic, surfactant neutral, inorganic precursor templating pathway to synthesize mesoporous materials. Disordered structures, designated as MSU-X, with uniform pore diameters in the range of 2.0-5.8 nm have been obtained by using PEO surfactants in neutral conditions. Su and coworkers have also obtained disordered wormhole mesostructures (DWM) analogous to MSU materials with the surfactant weight percentage of 50% using $C_{18}EO_{10}$, $C_{13}EO_n$ ($n = 6, 12, 18$) or $C_{16}EO_{10}$ templates [31, 32].

In summary, the successful preparations of a variety of both ordered and disordered mesoporous silica materials from nonionic PEO type block copolymer surfactants have demonstrated their essential role in the development of mesoporous materials. This family of block copolymers has been widely employed by the researchers in the fabrication of mesostructures. For example, templated by blends of diblock oligomeric C_nEO_x and Pluronic triblock $EO_xPO_{70}EO_x$ amphiphilic copolymers, a series of mesostructures have been successfully obtained by changing the volume proportion of the hydrophilic EO groups which was defined by varying mixed ratios of the two surfactants [33]. It was found that the mesostructures changed from lamellar to 2D hexagonal, 3D hexagonal, a cubic phase, and another cubic $Im3m$ mesophase with the increase of the EO volumes. Nonionic oligomeric surfactants were also used in a non-aqueous synthesis procedure along with Pluronic block copolymers to improve the quality of mesoporous silica materials [34]. It has been demonstrated that the total pore volumes, surface areas of the resulted silica materials were increased by this approach. By using alkyl poly (oxyethylene) oligomer as a co-surfactant, many researchers [35-37] have observed that in basic media the structural quality can be improved for mesoporous silica materials templated by cationic surfactants especial ammonium halogenides. Moreover, employing amphiphilic triblock copolymer as a structure-directing agent, periodic organosilicas have been synthesized in acidic media [38, 39]. Recently, preparations of $Ia3d$ cubic mesoporous silica materials have been carried out by using diblock copolymers poly (ethylene oxide)-*b*-poly (methyl acrylate) ($EO_{17}MA_{23}$) as structure-directing agents [40]. The resulted mesoporous silica materials have pore size >5.0 nm and wall thickness >3.0 nm.

3 Wall structures of mesoporous materials templated by amphiphilic block copolymers

In spite of the fact that both MCM-41 and SBA-15 materials possess honeycomb mesopore arrays, the differences between two mesostructures are distinct in composition, pore diameter, wall thickness and therefore stability. However, its wall structure, which is the most important and unique structural character of SBA-15, was not elucidated during its first report, although this feature has been cognized by the authors. A large number of disordered micropores might be inferred from the extra high surface area of SBA-15 ($\sim 850 \text{ m}^2/\text{g}$) [10]. A purely mesoporous SBA-15 with hexagonally arrayed pore diameter of 8.9 nm and wall thickness of 3.1 nm [10] should theoretically have a specific surface area of $204 \text{ m}^2/\text{g}$, suggesting that larger than 70% surface area for mesoporous SBA-15 materials is arisen from the microporosity within the inorganic walls. Similar phenomenon has been observed in poly(butadiene-*b*-ethylene oxide) (PB-PEO) copolymer templating systems [41].

The presence of microporosity and relatively small mesopores within the walls of SBA-15 was first indicated by Lukens *et al.* based on calculations performed from reference data of quartz [42]. Later, systematic studies including nitrogen adsorption [24, 26], selective pore blocking technique via organosilane modification [26], inverse platinum replica [26] and carbon replica [43] of ordered SBA-15 materials have been carried out by Ryoo and coworkers. It is found that the structure of SBA-15 is different from that of cylindrical or hexagonal pores, the uniform hexagonally arrayed primary pores are accompanied by a certain amount of significantly smaller pores (1-3.4 nm) with a broad distribution, which are in the micropore or/and small-mesopore range and sometimes referred to as complementary pores. It is suggested that an appreciable fraction of such disordered complementary pores is located in the walls of SBA-15, providing connectivity between the ordered large primary mesopore channels. This structure is unambiguously supported by the successful synthesis of hexagonally ordered mesoporous carbon CMK-3 by using SBA-15 as a hard template (Figure 3) [43]. By quantitatively exploiting the XRD reflection intensities of SBA-15 materials, Imperor-Clerc *et al.* suggested that a “corona” region of low density around the cylindrical organic aggregates existed in as-synthesized samples [44], and this corona becomes microporous upon calcination. However, the speculation of the distinct boundary of the corona and solid silica matrix cannot be used to

explain the formation of highly ordered mesoporous carbon CMK-3 reversed from silica SBA-15.

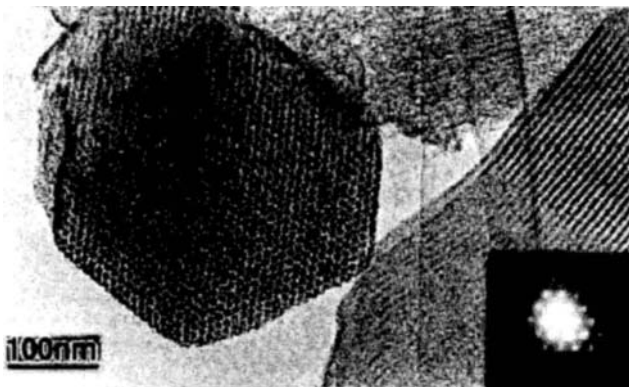


Figure 3. Typical TEM images of the ordered mesoporous carbon molecular sieve, CMK-3. Adapted with permission from ref. [43]

The complementary pores are suggested to be resulted from the penetration of PEO chains of the amphiphilic triblock copolymer templates within the silica framework of as-synthesized SBA-15. Actually the partially occlusion of hydrophilic PEO chains in inorganic matrix has been investigated before by TEM with elemental mapping technique [9] and by *in situ* $^{29}\text{Si}\{^1\text{H}\}$ and $^{13}\text{C}\{^1\text{H}\}$ two-dimensional (2D) solid-state heteronuclear correlation nuclear magnetic resonance (NMR) techniques together with ^1H NMR relaxation measurements [45]. It should be noted that in the latter two reports different PEO block copolymers and/or solvent systems compared to the synthesis of SBA-15 were employed, suggesting that the entrapping of PEO chains by inorganic matrix is quite general for all PEO surfactant synthesis systems.

Considering the interaction like $[(\text{EO})\text{H}_3\text{O}^+]\text{XT}^+$ pathway for the formation of SBA-15 materials under aqueous solutions [11], the potential of hydration of PEO chains is directly correlated to wall structure of SBA-15. Dehydration of PEO segments may occur at high ionic strength [46] and high temperatures [16]. In this context, it is reasonable that the use of high concentration of inorganic salts results in low microporosity SBA-15 materials [47]. The relationship between pore size, wall thickness and temperature has already been explained [10], however, the influence of temperature on the wall structure is more complicated. It should be kept in mind that the complementary pores have a size of 1-3.4 nm, ranging from

micropore scale to small mesopores scale. Therefore, it can be postulated that the PEO blocks within the silica matrix are aggregated; moreover, these PEO chains may be somehow different in aggregation number. It was revealed that, as the synthesis/aging temperature increased, the total volume of the complementary pores decreased only slightly relative to the primary mesopore volume, but the relative amount of the micropore volume within the complementary pores decreased significantly [24], suggesting that higher temperature results in more hydrophobe for EO segments and their redistribution from small aggregation number to large number and consequently the change in complementary pore size distributions from micropores to small diameter mesopores. At even higher temperatures such as 303 K, the micropore region in the complementary pores is almost eliminated, leaving only relatively larger mesopores (3-8 nm) within the walls of SBA-15 materials [48].

Complementary porosity of SBA-15 was retained to a significant extent even after calcination at 1173 K, but most likely completely disappeared at 1273 K [24], resulting a wall structure and therefore nitrogen adsorption properties similar to those of MCM-41 materials.

The above discussion has been focused on the wall structure of SBA-15 materials, however, the origin of complementary pores and the factors that may be used to control these complementary pores should be general in other nonionic block copolymer templating systems. This structural feature of SBA-15 will be further discussed in following section.

4 Morphology of mesoporous materials templated by block copolymers

Besides the success in the synthesis of mesoporous materials with various structures by using amphiphilic block copolymers, [10] the simultaneously efficient control of morphologies (including thin films, spheres, rods, fibers and monoliths) of these materials has also been achieved.

4.1 Fibers, rods, and spheres

Mesoporous silica materials with fiber, rod and spherical morphologies have also been obtained in the presence of amphiphilic block copolymer templates. When using TMOS as a silica source, the condensation rate of silicate species is fast, SBA-15 with fiber-like morphology was synthesized (Figure 4a) [49]. The addition of co-surfactants facilitated the formation of curved morphologies for SBA-15 such as sphere-, gyroid-, and discoid-like

macrostructures. Millimeter sized SBA-16 spheres have also been synthesized by using amphiphilic block copolymers as the templates in the presence of inorganic salts such as NaCl. The use of inorganic salts improved the structure regularity of mesoporous spheres [50], Zhao *et al.* have synthesized hollow spheres with ultra large mesopore (50 nm) wall structures by reverse emulsion templating [51].

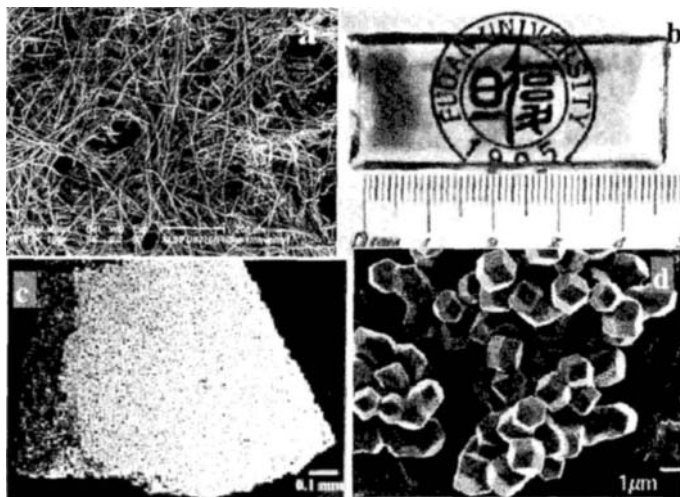


Figure 4. Selective scanning electron microscopy (SEM) images of mesoporous materials synthesized in the presence of block copolymer templates with different morphologies. (a) fibers; (b) monoliths; (c) meso-macrostructured membrane; and (d) single crystals.

Prouzet and co-workers have reported spherical MSU-1 with desired particle sizes from a new two-step synthesis approach by using PEO-based nonionic surfactants. The particle sizes can be tuned from 1 ~ 10 microns by controlling the fluoride to silica ratio [52]. Brinker and co-workers have developed a rapid, aerosol-base process for synthesizing spherical mesoporous silica with various mesostructures [53, 54]. Using this rapid aerogel method, they generate nanometer-sized, highly ordered mesoporous silica spheres with hexagonal or cubic structures within a quite short time (6 second). Amphiphilic block copolymers can be used as the templates in this novel synthesis. Most recently, Ward and coworkers reported an evaporation-driven surface templating approach to synthesize monodisperse mesoporous silica microspheres by means of a vibrating orifice aerosol generator (VOAG), a device that produces microdroplets [55]. Particle and pore size as well as mesoscopic order are controllable by varying the experimental conditions, precursor chemistry, and VOAG parameters.

4.2 Monoliths and Membranes

Transparent mesostructured silica monoliths and membranes with bulk sizes are ideal host materials for optical devices, such as lens, chromophores, lasers and nonlinear optical devices [56, 57].

Mesoporous silica monoliths with enhanced elasticity and ductibility have been synthesized by using amphiphilic block copolymers as the templates in a non-aqueous solution based on the sol-gel process [7, 58]. The details of the syntheses and characterizations of these transparent block copolymer/silica monoliths were reported by Chmelka and co-workers. [45] They have synthesized a transparent mesostructured silica/EO₁₀₆PO₇₀EO₁₀₆ monolith with large ordered domains [59]. 2D X-ray diffraction analyzes revealed that the well ordered hexagonal domains are greater than 1 cm × 1 mm × 1 mm in size. Melosh *et al.* have used a simple capillary shear-flow technique to form macroscopic aligned bulk transparent mesostructured silica [60]. The alcohols produced by the hydrolysis of alkoxide precursors were removed under vacuum prior to mixing with the block copolymer solution in order to obtain a viscous fluid.

The simultaneous control of pore size and morphology in monolithic structures has been hampered by the lack of a generalized synthetic method. Feng *et al.* reported a general method for the synthesis of periodic monolithic silica mesostructure by direct liquid crystal templating in multi-components (inorganic, surfactants and co-surfactant) systems [61]. The advantage of this method is the feasibility of fabricating large size monoliths with controllable periodic mesostructures and adjustable pore size.

Normally, the formation of crack-free mesoporous monoliths is time-consuming, which takes several days or even one month. [45, 60] Zhao and co-workers created a liquid paraffin medium protected solvent evaporation method to fast yield transparent, crack-free, large sized, highly ordered mesoporous monoliths by using amphiphilic block copolymers as the templates (Figure 4b) [28]. This technique is expected to provide practical methods to the fabrication of monolithic materials aimed at optic and separation applications.

Stucky and coworkers [62] have produced a novel mesoporous silica membrane with 3D sponge-like macrostructures (Figure 4c). The synthesis was especially interested in that the macropore dimensions were established by the sizes of droplets of aqueous electrolytes, such as NaCl, LiCl, KCl, NH₄Cl, or NiSO₄. The hierarchical pore structures may be important for mass transportations in catalysis and separation.

4.3 Films

Continuous and crack-free films with accessible mesopores may offer important potential applications in separation, adsorption and electronic-optical devices. Generally, dip-coating or spin-coating methods have been utilized to synthesize mesoporous silica films by using an evaporation-induced self-assembly process [63-65]. By using the amphiphilic block copolymers as the templates, Stucky and co-workers reported the syntheses of highly ordered, large pore, 2D and 3D mesoporous silica or/and transitional metal oxide films [64, 66]. It was interesting to note that the dielectric constants (k) of the calcined mesoporous silica films deposited on heavily n -doped (100) silicon substrates has a low value of 1.45 ± 2.1 . The structure and porosity of the films greatly influenced this property. Larger porosities generally give lower k values for the same structure [64]. Recently, Sanchez and coworkers reported the syntheses of mesoporous thin films with TiO_2 , ZrO_2 , Al_2O_3 , and VO_x compositions by dip-coating methods [67-70].

4.4 Mesoporous crystals and polyhedrons

It is not common that mesoporous materials possess a crystal-like morphology. Since the first report of MCM-48 single crystals [71], Guan and Sayari *et al.* have reported the synthesis of hybrid cubic mesoporous crystals ($Pm\bar{3}n$) with well-defined decaoctahedron shape [72]. SBA-1 ($Pm\bar{3}n$) has also been synthesized with crystal morphologies of large number of faces [73, 74]. In the above cases, ionic surfactants have been utilized to synthesize mesoporous crystals. An exception has been reported by Zhao and coworkers, where cubic mesoporous silica single crystals were synthesized by using a commercial non-ionic amphiphilic block copolymer as a template under acidic conditions (Figure 4d) [75]. These single crystals possess exclusively uniform rhombdodecahedron shapes ($\sim 1 \mu\text{m}$) with $\sim 100\%$ crystal yield and uniform large pores (up to 7.4 nm). The mesopore arrays in each crystal face are resolved from TEM, further confirming that these crystals are perfect single crystals with a body-centered cubic space group ($Im\bar{3}m$). It is assumed that the introduction of inorganic salts into the synthesis system increased the interaction between silicate species and non-ionic block copolymers, which is essential to the successful synthesis of mesoporous single crystals by using nonionic block copolymers.

5 Non-siliceous structures

Since the first synthesis of mesoporous M41S materials [2, 3], research efforts have been devoted to the fabrication of non-siliceous mesostructures. Recently, nonionic surfactants and amphiphilic block copolymers have been increasingly used to organize mesostructured composite solids with non-siliceous frameworks.

After the pioneering efforts for the syntheses of mesostructured W and Pb oxides in 1994 [4], a stable mesoporous Nb oxide molecular sieve was reported in 1996 by Ying *et. al.* [76]. This material had an advantage over the W and Pb oxide materials in that the pore structures remained intact after template removal. The syntheses of related mesoporous Ta, Hf and Mn oxides were also reported thereafter [76-78]. Such non-siliceous mesoporous materials have important features in many catalytic and electronic applications. For all of these non-siliceous materials, low molecular weight surfactants were used for the assembly of the mesostructures and the resulting mesoporous materials generally have small pore sizes (< 4 nm). Moreover, the channel walls of the inorganic framework were amorphous. Most of the above syntheses were carried out in aqueous solution by using metal alkoxides as inorganic precursors and the existence of a large amount of water makes the hydrolysis and condensation of the reactive metal alkoxides and the subsequent mesostructure assembly process difficult to control. The major problem, however, lies in the fact that most of those non-siliceous oxide mesostructured composites are thermally unstable. The surfactant removal by calcination always leads to structure collapse. Incomplete re-condensation, fast re-crystallization and redox reactions during the calcination process are responsible for this thermal stability.

Some examples using nonionic surfactants shed new light in the syntheses of non-siliceous mesostructured materials. Stupp *et. al.* [79] used oligoethylene oxide oleyl ether mixed with an equal volume of aqueous cadmium salt, and prepared mesostructured CdS products via diffusion of H_2S into the above mesophase. This procedure adopted the TLCT (true liquid crystal templating) approach, where a lyotropic liquid crystalline phase was loaded with the metallic salt precursors. They further extended this route to the syntheses of mesostructured CdSe and ZnS [80]. However, so far, no porous structure has been obtained with a chalcogenide framework. Attard and coworkers employed the similar approach, where a lyotropic liquid crystalline phase was loaded with the metal precursor ion

and then reduced within the liquid crystals, and successfully prepared ordered platinum mesostructured networks [81].

Dag *et al.* showed that oligo (ethylene oxide) type surfactants exhibit liquid crystal behavior in the presence of $[M(H_2O)_n](NO_3)_m$ type transition metal aqua complexes which functioned as the second component of the lyotropic liquid crystalline (LLC) phase [82]. Therein, the coordinated water molecules of the transition metal aqua complexes induced the aggregation and self-assembly of the surfactant molecules into hexagonal and/or cubic mesostructures and allowed the transition metal ions to be distributed into those structures uniformly in the form of free ions and ion pairs with the NO_3^- counterion. Unfortunately the organic template cannot be removed in such systems.

Concerning the fact that the interactions between the nonionic block copolymers and the inorganic species are relatively weaker than that of ionic surfactant templating systems, and that most metal alkoxides readily hydrolyze when attacked by water, it is crucial to conduct the syntheses under non-aqueous conditions. Stucky *et al.* developed a simple and general procedure for the syntheses of ordered large pore (up to 14 nm) mesoporous metal oxides in alcoholic media, by using the amphiphilic poly (alkylene oxide) block copolymers as the structure-directing agents [83, 84]. They use inorganic salts rather than alkoxides or organic metal complexes as the soluble and hydrolysable inorganic precursors to construct the metal oxide framework. In a typical synthesis, 1 g of poly (alkylene oxide) block copolymer was dissolved in 10 g of ethanol. Then 0.01 mole of the anhydrous inorganic chloride precursor was added with vigorous stirring. The resulting sol solution was gelled in an open petri dish at 40-60°C in air. The as-made bulk samples were then calcined at 300-600 °C for hours to decompose the block copolymers. This novel method has generated several large pore, ordered mesoporous composites, including TiO_2 , ZrO_2 , Nb_2O_5 , Ta_2O_5 , Al_2O_3 , SiO_2 , SnO_2 , WO_3 , HfO_2 , and mixed oxides $SiAlO_y$, Al_2TiO_y , $ZrTiO_y$, $SiTiO_y$ and $ZrWO_y$. The organic templates in as-made bulk samples can be easily removed due to the much lower decomposition temperature of block copolymers compared with ionic surfactants or long chain amines, therefore a true hollowed out and impurity free inorganic framework can be achieved. Moreover, those materials are thermally stable probably due to their much thick inorganic walls. The most important feature, according to the authors, is the semicrystalline framework where nano-crystallites nucleated within the amorphous inorganic mattress (Figure 5).

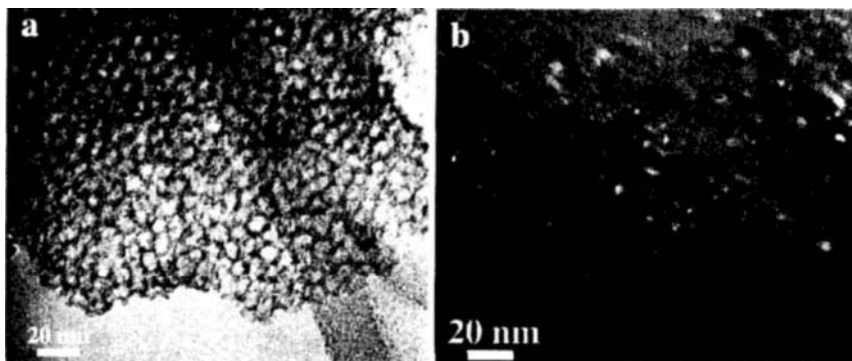


Figure 5. (a) Bright-field TEM image of a thin slice of the hexagonal mesoporous TiO₂ sample. (b) Dark-field image obtained on the same area of the same TiO₂ sample. The bright spots in the image correspond to TiO₂ nanocrystallites. Adapted with permission from ref. [84]

The syntheses of homogeneous and multi-component mesoporous oxides were demonstrated by Tilley and coworkers using single molecular precursors (such as $\text{Zr}[\text{OSi}(\text{O}-t\text{-Bu})_2]_4$, $\text{Fe}[\text{OSi}(\text{O}-t\text{-Bu})_3]_3 \cdot \text{THF}$, and $[\text{Al}(\text{O}-i\text{-Pr})_2\text{O}_2\text{P}(\text{O}-t\text{-Bu})_2]_4$, *etc.* ($\text{O}-t\text{-Bu}$ = *t*-butoxy, *i*-Pr = *i*-propoxy, THF = tetrahydrofuran) in non-polar media solvent via post thermolytic transformation to the final oxide composites [85, 86]. The obtained inorganic frameworks are molecular homogeneous, but the lack of long range mesostructural order was reflected by the relatively poor XRD patterns and TEM images.

Various nonsiliceous thin films, e.g. TiO₂, ZrO₂, Al₂O₃, and VO_x were prepared by dip-coating from ethanol-water solutions by Sanchez *et al.* [67-70] They employed tri-block copolymers or oligo (ethylene oxide) surfactants to direct the formation of 2 D hexagonal (*p6m*) or 2 D centered rectangular (*c2m*) mesostructures. Using *in situ* time-resolved small angle XRD techniques, they clearly demonstrated the film formation process and uniaxial contraction phenomena. The most distinct result might be the successful syntheses of mesostructured vanadium-oxo based thin films. It was found that V(IV) species had crucial influences on the structural stability upon calcinations, which greatly influenced the partially template-out vanadia mesostructures.

Table 2. The inorganic precursors, structure-directing agents (SDA) and resultant nonsiliceous mesoporous materials (NMM)

NMM	Precursor	SDA	Mesophase	Ref.
TiO ₂	TiCl ₄	P123, B50-1500	Hex, cubic	[83]
	TiCl ₄	F127, Brij58	Hex	[67]
	Ti(OR) ₄	P123	Hex	[87]
	Ti(OR) ₄	P123	Lam, Hex, cubic	[66]
	Anatase nanoparticle	Brij58	Wormlike	[88]
	TiCl ₄ and Ti(OR) ₄	P123, F108	Hex, cubic	[34]
Al ₂ O ₃	AlCl ₃	P123	Wormlike	[83]
	AlCl ₃	Brij58	Hex	[69]
	Al(OR) ₃	Triton, Igepal, Tergitol, Pluronic	Wormlike	[30]
	AlCl ₃ and Al(OR) ₃	P123, F108	Hex, cubic	[34]
ZrO ₂	ZrCl ₄	P123, B50-1500	Hex, cubic	[83]
	ZrCl ₄	Brij58	Hex	[68]
	ZrO ₂ nanoparticle	P123	Wormlike	[89]
	ZrCl ₄ and Zr(OR) ₄	P123, F108	Hex, cubic	[34]
Nb ₂ O ₅	NbCl ₅	P123	Hex	[83]
WCl ₆	P123	Hex	[83]	
	WCl ₆	P123	Wormlike	[90]
VOx-Surfactant	VCl ₄	P123		[83]
	VCl ₄ /VCl ₅	Brij56 or Brij58	Hex	[70]
AlPO	Mixed alkoxides	P123	Wormlike	[85]
	AlCl ₃ and H ₃ PO ₄	P123, F127	Hex, 3D hex	*
TiPO	TiCl ₄ and OP(OR) ₃	P123, F108	Hex, cubic	*
	or Ti(OR) ₄ and PCl ₃			
ZrPO	ZrCl ₄ and OP(OR) ₃	F108	Cubic	*
	Zr(OR) ₄ and PCl ₃	F108	Cubic	*
NbPO	NbCl ₅ and OP(OR) ₃	F108	Cubic	*
	Nb(OR) ₅ and PCl ₃	F108	Cubic	
CePO	CeCl ₃ and OP(OR) ₃	P123	Hex	*
Mixed oxides	Mixed alkoxides	Triblock copolymer	Wormlike	[85]
	Mixed metal chlorides	Triblock copolymer	Hex	[83]
	Alkoxides and chlorides	Triblock copolymer	Hex, cubic	*

Hex: hexagonal, Lam: lamellar. *: unpublished data.

Very recently, Zhao and coworkers developed a new versatile method to prepare a large family of nonsiliceous mesoporous materials, including metal phosphates TiPO , AlPO , NbPO , ZrPO , CePO , etc.; silico-aluminophosphates (SAPO , MeSAPO , $\text{Me} = \text{V}, \text{W}, \text{Sn}, \text{In}, \text{Mn}, \text{Fe}, \text{Co}, \text{Ni}$, etc.); ordered mesostructured metal borates, as well as various metal oxide and mixed metal oxides mesostructured phases. The syntheses strategy took a different perspective into the acid-base chemistry and a new concept of 'Acid-Base Pairs' was brought forward. The simple and general method has led to highly ordered, homogeneous and ultrastable mesostructured materials. For example, starting from TiCl_4 (acid) and $\text{Ti}(\text{OC}_2\text{H}_5)_4$ (base), they prepared highly ordered mesoporous titania with better crystallined walls compared with that from single TiCl_4 source. They also show that the highly ordered mesoporous materials prepared in this way can be molded into desirable morphologies and exhibit novel physicochemical properties, which make them of considerable interest for potential practical applications.

The structure-directing agents, inorganic precursors and resultant non-siliceous mesoporous materials are listed in Table 2. Despite the fact that a lot of non-siliceous mesostructures have been obtained, the syntheses of non-siliceous mesoporous materials still meet some challenges. First, the surface areas and pore volumes of such materials should be significantly increased. Many of reported non-siliceous mesoporous materials actually show much lower surface areas and much smaller pore volumes even taking density into account compared with that for mesoporous silica materials, which may be resulted from some disordered structure domains and some structural clog. This problem may be solved by the post treatment, *e. g.* hydrothermal re-crystallization. Another consideration is that the microporous nature of mesoporous silica templated by amphiphilic block copolymers may be not true in the case of non-siliceous materials. In this regard, the relatively low surface area in the latter materials is reasonable. Second, the inorganic framework should be better crystallized. It has long been realized that fully crystallized porous materials are much more useful than amorphous or semi-crystallized ones. For some applications, such as photocatalysis, the percentage of nanocrystallites makes a strike difference. One has to address this problem probably by choosing more proper inorganic precursors or employing a different thermal treatment process. Third, the family of non-siliceous mesoporous materials should be further extended. For example, ABO_3 materials, pure organic materials, superconductive materials and some semiconductive materials are still difficult to synthesize into mesostructures.

6 Applications

Because of the large and uniform pore size, highly ordered pore structures, ultra large surface areas and rich surface groups that are convenient to functionalize, mesoporous materials templated by nonionic block copolymer have shown potential applications in catalysis, adsorption, separation, optics, sensors and nano-reactors. The recent results of the applications of mesoporous materials are discussed in this section.

Generally, the mesoporous materials used for catalysis are functionalized with organic groups as solid acid catalysts or incorporated with transition metal oxide as a catalyst substrate. Large surface area of the materials is especially beneficial for the catalyst to disperse and their large pore size favors the catalytic conversion of large molecules.

6.1 Catalysis

MSU-X can be functionalized with phenyl groups and used as the catalysts in acetalization of aldehydes and ketones with ethylene glycol or methanol, which showed that cyclohexanone could be converted to the corresponding dimethylacetals in high conversion and selectivity. They also performed well in the isopropylation reactions of naphthalene with isopropanol [91]. Another case is that propanesulfonic acid-derivatized mesoporous SBA-15 catalysts show high selectivity for alcohol coupling to form ethers, specifically from methanol and isobutanol coupling to form methyl isobutyl ether [92].

Most of the reports about catalysis application are focused on Al-, Ti-, V-, Co-mesoporous silica materials. Al-containing mesoporous molecular sieves are often used as supports for acidic catalytic reactions. The catalytic behavior of the alumina-promoted sulfated zirconia supported on mesoporous silica SBA-15 was studied in isomerization of *n*-butane [93]. Epoxidation catalyzed by Ti-mesoporous silica has also been reported. Titanium supported on SBA-15 mesoporous silica was synthesized by chemical grafting. This material upon calcination was catalytically active for the epoxidation of styrene with *tert*-butylhydroperoxide (TBHP) exhibiting a significant selectivity towards the epoxide with negligible leaching of Ti species [94]. Ti-SBA-15 catalysts show catalytic activity and selectivity for the epoxidation of cyclohexene with cumene hydroperoxide as oxidant, compared Ti/amorphous silica [95]. Photocatalysis is an interesting property of V-containing mesoporous silica. VOx/SBA-15 catalysts have been prepared by different impregnation methods and the photocatalytic reactivity evaluated for the selective oxidation of methane

with oxygen at 220°C under UV irradiation. Both the formation rate and selectivity of formaldehyde were improved when vanadium was impregnated on the SBA-15 supports from a vanadyl sulfate methanolic solution. VOx/SBA-15 catalysts were seemingly more effective for the selective photo-assisted oxidation of methane than VOx/SiO₂ catalysts [96]. Novel cobalt catalysts supported on MSU-1 and SBA-12 are developed for Fischer-Tropsch synthesis in a fixed bed reactor, and the reactivity of Co/MSU-1 and Co/SBA-12 is compared with that of Co/HMS. It is found that the selectivity of C₁₉ hydrocarbon product for Co/MSU-1 and Co/SBA-12 is higher than that of Co/HMS and the chain propagation ability of Co/MSU-1 and Co/SBA-12 is also higher than that of Co/HMS possibly due to the stability [97].

There are also some other reports about the catalytic applications of mesoporous materials templated by non-ionic surfactants. The catalytic activity and selectivity of Cr₂O₃ supported on mesoporous SBA-15 for non-oxidative and oxidative dehydrogenation of propane by O₂ and CO₂ have been studied and compared with those of Cr₂O₃/ZrO₂ and Cr₂O₃/gamma-Al₂O₃ catalysts. Cr₂O₃/SBA-15 and Cr₂O₃/ZrO₂/SBA-15 catalysts show higher selectivity to propene, furthermore, they can be more resistant to coking in comparison with Cr₂O₃/ZrO₂ and Cr₂O₃/γ-Al₂O₃ for non-oxidative dehydrogenation of propane. In oxidative dehydrogenation of propane by O₂ and CO₂, Cr₂O₃/SBA-15 also displays better activity, selectivity and stability than the amorphous silica and γ-alumina supports [98].

6.2 Adsorption

Mesoporous materials functionalized with organic groups are good absorbents for heavy metal ions. Thiol- and amino-functionalized SBA-15 silicas were employed for removing heavy metal ions from waste water. The thiolated SBA-15 exhibited a higher complexation affinity for Hg²⁺, while the other metal ions (Cu²⁺, Zn²⁺, Cr³⁺ and Ni²⁺) showed exceptional binding ability with its aminated analogue [99]. Similar report is related with the SBA-15 materials functionalized with ethyl-, carboxylate-, and ethylene-diaminetriacetic acid groups which are efficient for Cu²⁺ adsorption [100].

It is more interesting that mesoporous silica materials prepared by block copolymers can be used in the adsorption/desorption of biomolecules that is the basis of further separation application [101]. As Yiu *et al.* reported, mesoporous silica SBA-15 functionalised with propylthiol groups during synthesis shows strong and size selective adsorption of proteins, selectively

excluding those with molecular weights of *ca.* 40000 *u* or/and above. A model for the adsorption process has been proposed, in which reversible physicosorption is followed by irreversible chemisorption. Adsorption of proteins on an unfunctionalized SBA-15 (mean pore diameter 5.6 nm) shows shape selective and reversible adsorption of proteins with molecular weights of *ca.* 43000 *u* and below [102]. Adsorption of cytochrome *c* was also studied. The immobilization of the protein was influenced by the molecular sieve structure and the proteins adsorbed in the channels of mesoporous molecular sieve could be stable even under conditions that would denature the protein in solution. The immobilized cytochrome *c* retained its redox activity following immobilization for several months as demonstrated by cyclic voltammetry (CV) [103].

6.3 Separation

As we mentioned above, mesoporous silica with ordered large pores exhibits excellent characteristics for absorption and desorption of large biomolecules such as proteins. Recently, It has been demonstrate by Zhao *et al.* that functionalized large pore SBA-15 as a satisfactory substrate in high performance liquid chromatography (HPLC) to separate peptides and proteins [104]. Dimethyloctadecylchlorosilane ($\text{CH}_3(\text{CH}_2)_{17}\text{Si}(\text{CH}_3)_2\text{Cl}$) (C_{18}) was used to produce the C_{18} modified SBA-15 (C_{18} -SBA-15) and this functionalized SBA-15 was further used as the substrate of capillary LC. Separation performance of myoglobin peptides (horse) and four proteins, lysozyme, bovine serum albumin (BSA), myoglobin (horse) and ovalbumin (chicken) with different mass weights and structures were studied and the C_{18} -SBA-15 was proved to be a promising substrate for various biomolecular separation.

6.4 Optics

Mesostructured materials with different macroscopical morphology such as films, fibers, and monoliths have been utilized as optical materials. Marlow *et al.* have studied optic character of mesoporous fibers coated with dye molecules [105, 106]. The results showed that this fiber with good optical waveguides and resonant structure can emit parallel to its longitudinal axis and amplified light, which makes it have a prospect as laser materials. Yang *et al.* have prepared a mesoporous material with low refractive index by combining sol-gel chemistry and soft-lithography technique [107]. This new material has an applied prospect for constructing optic loop. Wirnsberger *et al.* coated mesoporous film containing dye molecules on

general glass fibers [108], and found that the emission with low value and much singles can be observed when the functionalized fibers were activated by laser. It is expected that the new materials can be applied to analyze the gas molecules absorbed by mesopores. Recently, Stucky and coworkers reported a one-step synthesis of mesoporous titania films doped with Eu^{3+} ions [109]. It was observed that the excitation of the anatase nanocrystallites within their band gap led to nonradiative energy transfer to the europium ions, which exhibit a bright red luminescence (Figure 6). Since the europium ions were located at the crystalline \pm amorphous interface, concentration quenching of the europium emission was prevented.

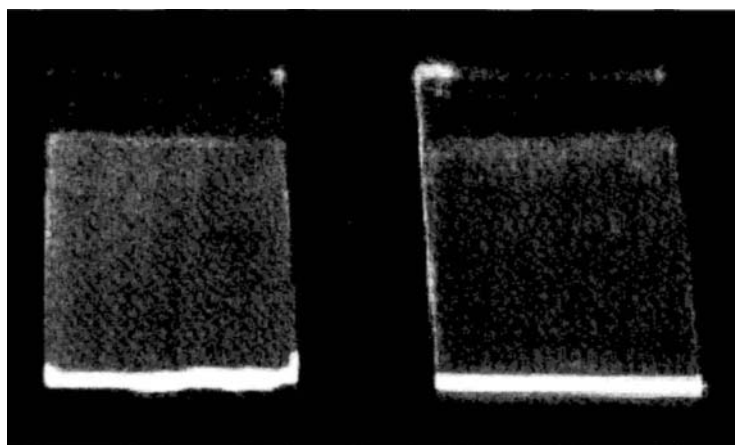


Figure 6. Photograph of mesoporous silica (left) and titania (right) films, both doped with 8 mol% Eu^{3+} . The films are excited with a UV lamp at 300 nm. Adapted with permission from ref. [109].

6.5 Sensors

Zhou *et al.* published several papers related with sensor application for mesoporous materials. They demonstrated that mesoporous silica thin films fabricated in a metal-insulator-semiconductor (such as $\text{Au}/\text{mesoporous SiO}_2/\text{Si}_3\text{N}_4/\text{SiO}_2/\text{Si}$) device based on the surface photovoltage (SPV) system can be applied as a gas sensor [110-114]. A size controlled silica mesoporous film was synthesized by spin coating on a $\text{Si}_3\text{N}_4/\text{SiO}_2/\text{Si}$ silicon wafer and using PEO triblock copolymers as templates (P123 for hexagonal or F127 for cubic). The sensing properties of the self-ordered hexagonal mesoporous SPV system have been investigated by repeated exposure to

NO gas and air. The changes in the average value and phase of the AC photocurrent (I-ph) have been observed after exposure of the films to 100 ppm NO gas. The response of the alternative photocurrent results from the physical adsorption and chemical interaction between detected NO gases and the self-ordered hexagonal mesoporous films. Cubic structured mesoporous film shows better accessibility for the gas and is considered better to be used for a sensor device. Another NO gas sensor SPV system from metal-hexagonal mesoporous silica-Si is also under investigation by the same group.

6.6 Nanoreactors

Mesoporous materials are always considered to be ideal nanoreactors because their ordered channels provide an excellent confined space for controlling the size and shape of materials on the nanoscale. Yang and coworkers have synthesized Ag nanowires with 5 ~ 6 nm diameter within the 1D ordered channels of SBA-15 [115]. After that, Stucky and coworkers have employed SBA-15 as the templates to achieve metal Pt, Ag and Au nanorods. Moreover, a group from Korea have obtained ordered mesostructured Pd network in small domains by using SBA-15 as a template [116]. More recently, an *in situ* adsorption synthesis route is reported by Gao *et al.* Mesoporous silica SBA-15 templates are functionalized with sulfur-containing organic group which directly serves as a sulfur source and metal ion adsorbents. By this way, binary surfides such as CdS and PbS have been successfully filled in the pores of mesoporous materials. By well controlling the number of OH groups on SBA-15 surface and reaction condition, semiconductor CdS and PbS nanoparticles and nanowires can be prepared consequently [117, 118].

An outstanding contribution is the mesoporous carbons that can be prepared by using mesoporous materials as templates. As Ryoo and coworkers reported, ordered mesoporous carbons can be obtained by using mesoporous silica SBA-15 as a hard template in a simple sucrose carbonization process [43]. This material is denoted as CMK-3 which proved to be the first true replica structure of all the reported mesoporous materials [119]. It is even more interesting that Ryoo and co-workers have carefully coated a layer of amorphous carbons on the walls of the channels of SBA-15 through a well-controlled process and obtained ordered carbon tubes after removal of the silica. This material has bi-modal pore size distribution, namely two sets of mesopores with uniform pore size distribution [120]. These novel carbon materials have shown excellent

properties in electrochemical double-layered capacity (EDLC), which is expected to achieve breakthroughs in the area of advanced electronic devices. [120]

7 Conclusion remarks

By employing amphiphilic block copolymers as structure-directing agents, highly ordered mesoporous materials with uniform and adjustable pore sizes (2-50 nm), variable pore structures, defined pore connectivity and huge surface area and pore volumes have successfully been synthesized. The frameworks of mesoporous materials can be variable in different compositions and the morphologies can be engineered in desired shapes. Such functionalized mesoporous materials are potential to be use in catalysis, separation of large molecular, sensors and optic-electric devices.

Despite the great advances that have been achieved in amphiphilic block copolymer templating systems, some challenges remain to be further explored. First of all, PEO type block copolymers are usually utilized in acidic conditions. In order to synthesize mesoporous materials with crystalline frameworks, one strategy may include the use of ionic block copolymers with amine groups. It is expected that with such templating systems the synthesis may be carried out under basic conditions, the block copolymers may template the formation of mesostructures and the occlusion of hydrophilic amine groups within the inorganic may be further used as the templates to produce crystalline inorganic frameworks. Another challenge for the mesoporous materials community is to step from laboratory studies further to industrial applications. Mesoporous materials templated by amphiphilic block copolymers with large pore sizes are much useful in large molecular separation process. It is anticipated that with more research efforts in the area, much more exciting developments will be delivered in block copolymer templated systems.

8 Acknowledgements

We acknowledge the financial supports by the National Science Foundations of China, State key research program, Shanghai Science and Technology Committee, Ministry of Education of Chinese.

References

1. Szostak R., *Molecular Sieves: Principles of Synthesis, and Identification*. London: Blackie Academic and Professional (1998).
2. Kresge C. T., Leonowicz M. E., Roth W. J., Vartuli J. C. and Beck J. S., Ordered Mesoporous Molecular Sieves Synthesized by a Liquid-Crystal Template Mechanism, *Nature* **359** (1992) pp. 710-712.
3. Beck J. S., Vartuli J. C., Roth W. J., Leonowicz M. E., Kresge C. T., Schmitt K. D., Chu C. T. W., Olson D. H., Sheppard E. W. and et al., A new family of mesoporous molecular sieves prepared with liquid crystal templates, *J. Am. Chem. Soc.* **114** (1992) pp. 10834-43.
4. Huo Q. S., Margolese D. I., Ciesla U., Feng P. Y., Gier T. E., Sieger P., Leon R., Petroff P. M., Schuth F. and Stucky G. D., Generalized Synthesis of Periodic Surfactant Inorganic Composite Materials, *Nature* **368** (1994) pp. 317-321.
5. Tanev P. T. and Pinnavaia T. J., A Neutral Templating Route to Mesoporous Molecular Sieves, *Science* **267** (1995) pp. 865-867.
6. Porter M. R., *Handbook of Surfactants* (Chapman and Hall, New York, 1991).
7. Bagshaw S. A., Prouzet E. and Pinnavaia T. J., Templating of Mesoporous Molecular Sieves by Nonionic Polyethylene Oxide Surfactants, *Science* **269** (1995) pp. 1242-1244.
8. Attard G. S., Glyde J. C. and Goltner C. G., Liquid-Crystalline Phases as Templates for the Synthesis of Mesoporous Silica, *Nature* **378** (1995) pp. 366-368.
9. Templin M., Franck A., DuChesne A., Leist H., Zhang Y. M., Ulrich R., Schadler V. and Wiesner U., Organically modified aluminosilicate mesostructures from block copolymer phases, *Science* **278** (1997) pp. 1795-1798.
10. Zhao D. Y., Feng J. L., Huo Q. S., Melosh N., Fredrickson G. H., Chmelka B. F. and Stucky G. D., Triblock copolymer syntheses of mesoporous silica with periodic 50 to 300 angstrom pores, *Science* **279** (1998) pp. 548-552.
11. Zhao D. Y., Huo Q. S., Feng J. L., Chmelka B. F. and Stucky G. D., Nonionic triblock and star diblock copolymer and oligomeric surfactant syntheses of highly ordered, hydrothermally stable, mesoporous silica structures, *J. Am. Chem. Soc.* **120** (1998) pp. 6024-6036.
12. Goltner C. G., Henke S., Weissenberger M. C. and Antonietti M., Mesoporous silica from lyotropic liquid crystal polymer templates, *Angew. Chem.Int. Ed.* **37** (1998) pp. 613-616.
13. Goltner C. G., Berton B., Kramer E. and Antonietti M., Nanoporous silica from amphiphilic block copolymer (ABC) aggregates: control over correlation and architecture of cylindrical pores, *Chem. Commun.* (1998) pp. 2287-2288.
14. Booth C. and Attwood D., Effects of block architecture and composition on the association properties of poly(oxyalkylene) copolymers in aqueous solution, *Macromol. Rapid Commun.* **21** (2000) pp. 501-527.
15. Bates F. S. and Fredrickson G. H., Block copolymers - Designer soft materials, *Physics Today* **52** (1999) pp. 32-38.
16. Alexandridis P. and Hatton T. A., Poly(Ethylene Oxide)-Poly(Propylene Oxide)-Poly(Ethylene Oxide) Block Copolymer Surfactants in Aqueous Solutions and at Interfaces - Thermodynamics, Structure, Dynamics, and Modeling, *Colloids and Surface A* **96** (1995) pp. 1-46.

17. Hamley I. W., Mai S. M., Ryan A. J., Fairclough J. P. A. and Booth C., Aqueous mesophases of block copolymers of ethylene oxide and 1,2-butylene oxide, *Phys. Chem. Chem. Phys.* **3** (2001) pp. 2972-2980.
18. Kramer E., Forster S., Goltner C. and Antonietti M., Synthesis of nanoporous silica with new pore morphologies by templating the assemblies of ionic block copolymers, *Langmuir* **14** (1998) pp. 2027-2031.
19. Finnefrock A. C., Ulrich R., Du Chesne A., Honeker C. C., Schumacher K., Unger K. K., Gruner S. M. and Wiesner U., Metal oxide containing mesoporous silica with bicontinuous "Plumber's Nightmare" morphology from a block copolymer-hybrid mesophase, *Angew. Chem. Int. Ed.* **40** (2001) pp. 1207-1211.
20. Blin J. L., Leonard A. and Su B. L., Well-ordered spherical mesoporous materials CMI-1 synthesized via an assembly of decaoxyethylene cetyl ether and TMOS, *Chem. Mater.* **13** (2001) pp. 3542-3553.
21. Yu C. Z., Yu Y. H. and Zhao D. Y., Highly ordered large caged cubic mesoporous silica structures templated by triblock PEO-PBO-PEO copolymer, *Chem. Commun.* (2000) pp. 575-576.
22. Liu X., Tian B., Yu C., Feng Gao, Xie S., Tu B., Che R., Peng L.-M. and Zhao D., Room-Temperature Synthesis in Acidic Media of Large-Pore Three-Dimensional Bicontinuous Mesoporous Silica with Ia3d Symmetry, *Angew. Chem. Int. Ed.* **41** (2002) pp. 3876.
23. Sakamoto Y., Diaz I., Terasaki O., Zhao D. Y., Perez-Pariente J., Kim J. M. and Stucky G. D., Three-dimensional cubic mesoporous structures of SBA-12 and related materials by electron crystallography, *J. Phys. Chem. B* **106** (2002) pp. 3118-3123.
24. Kruk M., Jaroniec M., Ko C. H. and Ryoo R., Characterization of the porous structure of SBA-15, *Chem. Mater.* **12** (2000) pp. 1961-1968.
25. Ravikovitch P. I. and Neimark A. V., Characterization of micro- and mesoporosity in SBA-15 materials from adsorption data by the NLDFT method, *J. Phys. Chem. B* **105** (2001) pp. 6817-6823.
26. Ryoo R., Ko C. H., Kruk M., Antochshuk V. and Jaroniec M., Block-copolymer-templated ordered mesoporous silica: Array of uniform mesopores or mesopore-micropore network, *J. Phys. Chem. B* **104** (2000) pp. 11465-11471.
27. Voegtlin A. C., Ruch F., Guth J. L., Patarin J. and Huve L., F⁻ mediated synthesis of mesoporous silica with ionic- and non- ionic surfactants. A new templating pathway, *Microporous Mater.* **9** (1997) pp. 95-105.
28. Yang H., Shi Q., Liu X., Xie S., Jiang D., Zhang F., Yu C., Tu B. and Zhao D., Synthesis of ordered mesoporous carbon monoliths with bicontinuous cubic pore structure of Ia3d symmetry, *Chem. Commun.* **23** (2002) pp. 2842.
29. Kim J. M., Han Y. J., Chmelka B. F. and Stucky G. D., One-step synthesis of ordered mesocomposites with non-ionic amphiphilic block copolymers: implications of isoelectric point, hydrolysis rate and fluoride, *Chem. Commun.* (2000) pp. 2437-2438.
30. Bagshaw S. A. and Pinnavaia T. J., Mesoporous Alumina Molecular Sieves, *Angew. Chem. Int. Ed.* **35** (1996) pp. 1102-1105.
31. Blin J. L., Herrier G., Otjacques C. and Su B. L., Synthesis and characterization of ordered mesoporous MCM-41 materials, *Characterization of Porous Solids V* **128** (2000) pp. 269-277.
32. Blin J. L., Becue A., Pauwels B., Van Tendeloo G. and Su B. L., Non-ionic surfactant (C13EO_m, m = 6, 12 and 18) for large pore mesoporous molecular sieves preparation, *Micropor. Mesopor. Mater.* **44** (2001) pp. 41-51.

33. Kim J. M., Sakamoto Y., Hwang Y. K., Kwon Y. U., Terasaki O., Park S. E. and Stucky G. D., Structural design of mesoporous silica by micelle-packing control using blends of amphiphilic block copolymers, *J. Phys. Chem. B* **106** (2002) pp. 2552-2558.
34. Tian B. Z., Liu X. Y., Zhang Z. D., Tu B. and Zhao D. Y., Syntheses of high-quality mesoporous materials directed by blends of nonionic amphiphiles under nonaqueous conditions, *J. Solid State Chem.* **167** (2002) pp. 324-329.
35. Ryoo R., Joo S. H. and Kim J. M., Energetically favored formation of MCM-48 from cationic-neutral surfactant mixtures, *J. Phys. Chem. B* **103** (1999) pp. 7435-7440.
36. Dai L. R., Wang T. W., Bu L. T. and Chen G., Mixed surfactant templating route for mesoporous silica, *Colloids and Surface A* **181** (2001) pp. 151-157.
37. Song M. G., Kim J. Y., Cho S. H. and Kim J. D., Mixed cationic-nonionic surfactant templating approach for the synthesis of mesoporous silica, *Langmuir* **18** (2002) pp. 6110-6115.
38. Zhu H. G., Jones D. J., Zajac J., Roziere J. and Dutartre R., Periodic large mesoporous organosilicas from lyotropic liquid crystal polymer templates, *Chem. Commun.* (2001) pp. 2568-2569.
39. Kapoor M. P. and Inagaki S., Synthesis of cubic hybrid organic-inorganic mesostructures with dodecahedral morphology from a binary surfactant mixture, *Chem. Mat.* **14** (2002) pp. 3509-3514.
40. Chan Y.-T., Lin H.-P., Mou C.-Y. and Liu S.-T., Ia3d Cubic mesoporous silicas using EO17MA23 diblock copolymers made from ATRP, *Chem. Commun.* **23** (2002) pp. 2878.
41. Goltner C. G., Berton B., Kramer E. and Antonietti M., Nanoporous silicas by casting the aggregates of amphiphilic block copolymers: The transition from cylinders to lamellae and vesicles, *Adv. Mater.* **11** (1999) pp. 395-398.
42. Lukens W. W., Schmidt-Winkel P., Zhao D. Y., Feng J. L. and Stucky G. D., Evaluating pore sizes in mesoporous materials: A simplified standard adsorption method and a simplified Broekhoff-de Boer method, *Langmuir* **15** (1999) pp. 5403-5409.
43. Jun S., Joo S. H., Ryoo R., Kruk M., Jaroniec M., Liu Z., Ohsuna T. and Terasaki O., Synthesis of new, nanoporous carbon with hexagonally ordered mesostructure, *J. Amer. Chem. Soc.* **122** (2000) pp. 10712-10713.
44. Imperor-Clerc M., Davidson P. and Davidson A., Existence of a microporous corona around the mesopores of silica-based SBA-15 materials templated by triblock copolymers, *J. Amer. Chem. Soc.* **122** (2000) pp. 11925-11933.
45. Melosh A., Lipic P., Bates F. S., Wudl F., Stucky G. D., Fredrickson G. H. and Chmelka B. F., Molecular and mesoscopic structures of transparent block copolymer-silica monoliths, *Macromolecules* **32** (1999) pp. 4332-4342.
46. Desai P. R., Jain N. J., Sharma R. K. and Bahadur P., Effect of additives on the micellization of PEO/PPO/PEO block copolymer F127 in aqueous solution, *Colloids and Surface A* **178** (2001) pp. 57-69.
47. Newalkar B. L. and Komarneni S., Control over microporosity of ordered microporous-mesoporous silica SBA-15 framework under microwave-hydrothermal conditions: effect of salt addition, *Chem. Mater.* **13** (2001) pp. 4573-4579.
48. Fan J., Yu C., Wang L., Tu B., Zhao D. Y., Sakamoto Y. and Terasaki O., Mesotunnels on the silica wall of ordered SBA-15 to generate three-dimensional large pore mesoporous networks, *J. Am. Chem. Soc.* **123** (2001) pp. 12113-12114.

49. Zhao D. Y., Sun J. Y., Li Q. Z. and Stucky G. D., Morphological control of highly ordered mesoporous silica SBA-15, *Chem. Mater.* **12** (2000) pp. 275-279.
50. Yu C. Z., Fan J. and Zhao D. Y., Block copolymer synthesis of high-quality cubic, large pore mesoporous millimeter spheres in the presence of inorganic salts, *Acta Chim. Sin.* **60** (2002) pp. 1357-1360.
51. Yu C., Tian B., Fan J., Stucky G. D. and Zhao D., Synthesis of Siliceous Hollow Spheres with Ultra Large Mesopore Wall Structures by Reverse Emulsion Templating, *Chem. Lett.* (2002) pp. 62-63.
52. Boissiere C., Kummel M., Persin M., Larbot A. and Prouzet E., Spherical MSU-1 mesoporous silica particles tuned for HPLC, *Adv. Funct. Mater.* **11** (2001) pp. 129-135.
53. Brinker C. J., Lu Y. F., Sellinger A. and Fan H. Y., Evaporation-induced self-assembly: Nanostructures made easy, *Adv. Mater.* **11** (1999) pp. 579-585.
54. Lu Y. F., Fan H. Y., Stump A., Ward T. L., Rieker T. and Brinker C. J., Aerosol-assisted self-assembly of mesostructured spherical nanoparticles, *Nature* **398** (1999) pp. 223-226.
55. Rao G. V. R., Lopez G. P., Bravo J., Pham H., Datye A. K., Xu H. F. and Ward T. L., Monodisperse mesoporous silica microspheres formed by evaporation-induced self assembly of surfactant templates in aerosols, *Adv. Mater.* **14** (2002) pp. 1301-1304.
56. Klein L. C., Sol-Gel Optical-Materials, *Annu. Rev. Mater. Sci.* **23** (1993) pp.437-452.
57. Scott B. J., Wirnsberger G. and Stucky G. D., Mesoporous and mesostructured materials for optical applications, *Chem. Mater.* **13** (2001) pp. 3140-3150.
58. Goltner C. G. and Antonietti M., Mesoporous materials by templating of liquid crystalline phases, *Adv. Mater.* **9** (1997) pp. 431-436.
59. Melosh N. A., Davidson P. and Chmelka B. F., Monolithic mesophase silica with large ordering domains, *J. Am. Chem. Soc.* **122** (2000) pp. 823-829.
60. Melosh N. A., Davidson P., Feng P., Pine D. J. and Chmelka B. F., Macroscopic shear alignment of bulk transparent mesostructured silica, *J. Am. Chem. Soc.* **123** (2001) pp. 1240-1241.
61. Feng P. Y., Bu X. H., Stucky G. D. and Pine D. J., Monolithic mesoporous silica templated by microemulsion liquid crystals, *J. Am. Chem. Soc.* **122** (2000) pp. 994-995.
62. Zhao D. Y., Yang P. D., Chmelka B. F. and Stucky G. D., Multiphase assembly of mesoporous-macroporous membranes, *Chem. Mater.* **11** (1999) pp. 1174-1178.
63. Zhao D. Y., Yang P. D., Margolese D. I., Chmelka B. F. and Stucky G. D., Synthesis of continuous mesoporous silica thin films with three-dimensional accessible pore structures, *Chem. Commun.* (1998) pp. 2499-2500.
64. Zhao D., Yang P., Melosh N., Feng J., Chmelka B. F. and Stucky G. D., Continuous mesoporous silica films with highly ordered large pore structures, *Adv. Mater.* **10** (1998) pp. 1380-1385.
65. Lu Y. F., Ganguli R., Drewien C. A., Anderson M. T., Brinker C. J., Gong W. L., Guo Y. X., Soyez H., Dunn B., Huang M. H. and Zink J. I., Continuous formation of supported cubic and hexagonal mesoporous films by sol gel dip-coating, *Nature* **389** (1997) pp. 364-368.
66. Alberius P. C. A., Frindell K. L., Hayward R. C., Kramer E. J., Stucky G. D. and Chmelka B. F., General predictive syntheses of cubic, hexagonal, and lamellar silica and titania mesostructured thin films, *Chem. Mater.* **14** (2002) pp. 3284-3294.

67. Grosso D., Soler-Illia G., Babonneau F., Sanchez C., Albouy P. A., Brunet-Bruneau A. and Balkenende A. R., Highly organized mesoporous titania thin films showing mono- oriented 2D hexagonal channels, *Adv. Mater.* **13** (2001) pp. 1085-1090.
68. Crepaldi E. L., Soler-Illia G., Grosso D., Albouy P. A. and Sanchez C., Design and post-functionalisation of ordered mesoporous zirconia thin films, *Chem. Commun.* (2001) pp. 1582-1583.
69. Pídel L., Grosso D., Soler-Illia G., Crepaldi E. L., Sanchez C., Albouy P. A., Amenitsch H. and Euzen P., Hexagonally organised mesoporous aluminium-oxo-hydroxide thin films prepared by the template approach. In situ study of the structural formation, *J. Mater. Chem.* **12** (2002) pp. 557-564.
70. Crepaldi E. L., Grosso D., Soler-Illia G., Albouy P. A., Amenitseh H. and Sanchez C., Formation and stabilization of mesostructured vanadium-oxo- based hybrid thin films, *Chem. Mater.* **14** (2002) pp. 3316-3325.
71. Kim J. M., Kim S. K. and Ryoo R., Synthesis of MCM-48 single crystals, *Chem. Commun.* (1998) pp. 259-260.
72. Guan S., Inagaki S., Ohsuna T. and Terasaki O., Cubic hybrid organic-inorganic mesoporous crystal with a decaoctahedral shape, *J. Amer. Chem. Soc.* **122** (2000) pp. 5660-5661.
73. Huang L. M., Guo W. P., Deng P., Xue Z. Y. and Li Q. Z., Investigation of synthesizing MCM-41/ZSM-5 composites, *J. Phys. Chem. B* **104** (2000) pp. 2817-2823.
74. Che S., Sakamoto Y., Terasaki O. and Tatsumi T., Control of crystal morphology of SBA-1 mesoporous silica, *Chem. Mater.* **13** (2001) pp. 2237-2239.
75. Yu C., Tian B., Fan J., Stucky G. D. and Zhao D. Y., Non-ionic block copolymer synthesis of large pore cubic mesoporous single crystals by use of inorganic salts, *J. Am. Chem. Soc.* **124** (2002) pp. 4556-4557.
76. Antonelli D. M. and Ying J. Y., Synthesis of a stable hexagonally packed mesoporous niobium oxide molecular sieve through a novel ligand-assisted templating mechanism, *Angew Chem. Int. Ed.* **35** (1996) pp. 426-430.
77. Antonelli D. M. and Ying J. Y., Synthesis and characterization of hexagonally packed mesoporous tantalum oxide molecular sieves, *Chem. Mater.* **8** (1996) pp. 874-881.
78. Tian Z. R., Tong W., Wang J. Y., Duan N. G., Krishnan V. V. and Suib S. L., Manganese oxide mesoporous structures: Mixed-valent semiconducting catalysts, *Science* **276** (1997) pp. 926-930.
79. Braun P. V., Osenar P. and Stupp S. I., Semiconducting Superlattices Templated by Molecular Assemblies, *Nature* **380** (1996) pp. 325-328.
80. Braun P. V. and Stupp S. I., CdS mineralization of hexagonal, lamellar, and cubic lyotropic liquid crystals, *Mater. Res. Bull.* **34** (1999) pp. 463-469.
81. Attard G. S., Bartlett P. N., Coleman N. R. B., Elliott J. M., Owen J. R. and Wang J. H., Mesoporous platinum films from lyotropic liquid crystalline phases, *Science* **278** (1997) pp. 838-840.
82. Celik O. and Dag O., A new lyotropic liquid crystalline system: Oligo(ethylene oxide) surfactants with [M(H₂O)_n]-X-m transition metal complexes, *Angew. Chem. Int. Ed.* **40** (2001) pp. 3799-3803.
83. Yang P. D., Zhao D. Y., Margolese D. I., Chmelka B. F. and Stucky G. D., Generalized syntheses of large-pore mesoporous metal oxides with semicrystalline frameworks, *Nature* **396** (1998) pp. 152-155.

84. Yang P. D., Zhao D. Y., Margolese D. I., Chmelka B. F. and Stucky G. D., Block copolymer templating syntheses of mesoporous metal oxides with large ordering lengths and semicrystalline framework, *Chem. Mater.* **11** (1999) pp. 2813-2826.
85. Kriesel J. W., Sander M. S. and Tilley T. D., General route to homogeneous, mesoporous, multicomponent oxides based on the thermolytic transformation of molecular precursors in non-polar media, *Adv. Mater.* **13** (2001) pp. 331-335.
86. Kriesel J. W., Sander M. S. and Tilley T. D., Block copolymer-assisted synthesis of mesoporous, multicomponent oxides by nonhydrolytic, thermolytic decomposition of molecular precursors in nonpolar media, *Chem. Mater.* **13** (2001) pp. 3554-3563.
87. Soler-Illia G., Louis A. and Sanchez C., Synthesis and characterization of mesostructured titania-based materials through evaporation-induced self-assembly, *Chem. Mater.* **14** (2002) pp. 750-759.
88. Hwang Y. K., Lee K. C. and Kwon Y. U., Nanoparticle routes to mesoporous titania thin films, *Chem. Commun.* (2001) pp. 1738-1739.
89. Wong M. S., Huang H. C. and Ying J. Y., Supramolecular-templated synthesis of nanoporous zirconia-silica catalysts, *Chem. Mater.* **14** (2002) pp. 1961-1973.
90. Cheng W., Baudrin E., Dunn B. and Zink J. I., *Synthesis and electrochromic properties of mesoporous tungsten oxide*, *J. Mater. Chem.* **11** (2001) pp. 92-97.
91. Gong Y. J., Li Y., Wu D. and Sun Y. H., Multiphasic acetalization and alkylation on organically modified MSU-X silica, *Catal. Lett.* **74** (2001) pp. 213-216.
92. Shen J. G. C., Herman R. G. and Klier K., Sulfonic acid-functionalized mesoporous silica: Synthesis, characterization, and catalytic reaction of alcohol coupling to ethers, *J. Phys. Chem. B* **106** (2002) pp. 9975-9978.
93. Chen C. L., Li T., Cheng S. F., Xu N. P. and Mou C. Y., Catalytic behavior of alumina-promoted sulfated zirconia supported on mesoporous silica in butane isomerization, *Catal. Lett.* **78** (2002) pp. 223-229.
94. Calleja G., van Grieken R., Garcia R., Melero J. A. and Iglesias J., Preparation of titanium molecular species supported on mesostructured silica by different grafting methods, *J. Mol. Catal. A* **182** (2002) pp. 215-225.
95. Jarupatrakorn J. and Tilley J. D., Silica-supported, single-site titanium catalysts for olefin epoxidation. A molecular precursor strategy for control of catalyst structure, *J. Am. Chem. Soc.* **124** (2002) pp. 8380-8388.
96. Lopez H. H. and Martinez A., Selective photo-assisted oxidation of methane into formaldehyde on mesoporous VOx/SBA-15 catalysts, *Catal. Lett.* **83** (2002) pp. 37-41.
97. Yang W. S., Gao H. Y., Xiang H. W., Yin D. H., Yang Y., Xu Y. Y., Zhong B. and Li Y. W., Reactivity and hydrocarbon distribution of novel cobalt catalysts supported on mesoporous molecular sieves for F-T synthesis, *Chem. J. Chin. Univ.-Chin.* **23** (2002) pp. 1748-1752.
98. Zhang X. Z., Yue Y. H. and Gao Z., Chromium oxide supported on mesoporous SBA-15 as propane dehydrogenation and oxidative dehydrogenation catalysts, *Catal. Lett.* **83** (2002) pp. 19-25.
99. Liu A. M., Hidajat K., Kawi S. and Zhao D. Y., A new class of hybrid mesoporous materials with functionalized organic monolayers for selective adsorption of heavy metal ions, *Chem. Commun.* (2000) pp. 1145-1146.
100. Markowitz M. A., Klachn J., Hendel R. A., Qadriq S. B., Gollledge S. L., Castner D. G. and Gaber B. P., Direct synthesis of metal-chelating mesoporous silica: Effects of

- added organosilanes on silicate formation and adsorption properties, *J. Phys. Chem. B* **104** (2000) pp. 10820-10826.
101. Han Y. J., Stucky G. D. and Butler A., Mesoporous silicate sequestration and release of proteins, *J. Am. Chem. Soc.* **121** (1999) pp. 9897-9898.
 102. Yiu H. H. P., Botting C. H., Botting N. P. and Wright P. A., Size selective protein adsorption on thiol-functionalised SBA-15 mesoporous molecular sieve, *Phys. Chem. Chem. Phys.* **3** (2001) pp. 2983-2985.
 103. Washmon-Kriel L., Jimenez V. L. and Balkus K. J., Cytochrome c immobilization into mesoporous molecular sieves, *J. Mol. Catal. B* **10** (2000) pp. 453-469.
 104. Zhao J. W., Gao F., Fu Y. L., Jin W., Yang P. Y. and Zhao D. Y., Biomolecule separation using large pore mesoporous SBA-15 as a substrate in high performance liquid chromatography, *Chem. Commun.* (2002) pp. 752-753.
 105. Marlow F., Optical materials based on nanoscaled guest/host composites, *Mol. Cryst. Liquid Cryst.* **341** (2000) pp. 1093-1098.
 106. Marlow F., Zhao D. Y. and Stucky G. D., Doped mesoporous silica fibers: the internal structure, *Micropor. Mesopor. Mater.* **39** (2000) pp. 37-42.
 107. Yang P. D., Wirnsberger G., Huang H. C., Cordero S. R., McGehee M. D., Scott B., Deng T., Whitesides G. M., Chmelka B. F., Buratto S. K. and Stucky G. D., Mirrorless lasing from mesostructured waveguides patterned by soft lithography, *Science* **287** (2000) pp. 465-467.
 108. Wirnsberger G. and Stucky G. D., Ordered mesostructured materials with optical functionality, *Chem. Phys. Chem.* **1** (2000) pp. 90-92.
 109. Frindell K. L., Bartl M. H., Popitsch A. and Stucky G. D., Sensitized luminescence of trivalent europium by three- dimensionally arranged anatase nanocrystals in mesostructured titania thin films, *Angew. Chem. Int. Ed.* **41** (2002) pp. 959-962.
 110. Yamada T., Zhou H. S., Uchida H., Tomita M., Ueno Y., Asai K., Honma I. and Katsube, T., An application possibility of self-ordered mesoporous silicate for surface photo voltage type NO gas sensor (I): The characterization of nonionic triblock copolymer templated self- ordered mesoporous silicates and preparation their film for device application, *IEICE Trans. Electron.* **E85C** (2002) pp. 1298-1303.
 111. Yamada T., Zhou H. S., Uchida H., Tomita M., Ueno Y., Asai K., Honma I. and Katsube, T., An application possibility of self-ordered mesoporous silicate for surface photo voltage (SPV) type NO gas sensor (II): Self- ordered mesoporous silicate incorporated SPV device and its sensing property dependence on mesostructure, *IEICE Trans. Electron.* **E85C** (2002) pp. 1304-1310.
 112. Yamada T., Zhou H. S., Uchida H., Tomita M., Ueno Y., Honma I., Asai K. and Katsube T., Application of a cubic-like mesoporous silica film to a surface photovoltage gas sensing system, *Micropor. Mesopor. Mater.* **54** (2002) pp. 269-276.
 113. Yamada T., Zhou H. S., Uchida H., Tomita M., Ueno Y., Ichino T., Honma I., Asai K. and Katsube T., Surface photovoltage NO gas sensor with properties dependent on the structure of the self-ordered mesoporous silicate film, *Adv. Mater.* **14** (2002) pp. 812-815.
 114. Zhou H. S., Yamada T., Asai K., Hodma I., Uchida H. and Katsube T., Ordered mesoporous silicate materials from a template of triblock copolymer (II): Synthesis of film and application for gas sensor, *Euro Ceramics VII, Pt 1-3* **206-2** (2002) pp. 1985-1988.
 115. Huang M. H., Choudrey A. and Yang P. D., Ag nanowire formation within mesoporous silica, *Chem. Commun.* (2000) pp. 1063-1064.

116. Han Y. J., Kim J. M. and Stucky G. D., Preparation of noble metal nanowires using hexagonal mesoporous silica SBA-15, *Chem. Mater.* **12** (2000) pp. 2068-2069.
117. Gao F., Lu Q. Y., Liu X. Y., Yan Y. S. and Zhao D. Y., Controlled synthesis of semiconductor PbS nanocrystals and nanowires inside mesoporous silica SBA-15 phase, *Nano. Lett.* **1** (2001) pp. 743-748.
118. Gao F., Lu Q. Y. and Zhao D. Y., In situ adsorption method for synthesis of binary semiconductor US nanocrystals inside mesoporous SBA-15, *Chem. Phys. Lett.* **360** (2002) pp. 585-591.
119. Ryoo R., Joo S. H., Kruk M. and Jaroniec M., Ordered mesoporous carbons, *Adv. Mater.* **13** (2001) pp. 677-681.
120. Joo S. H., Choi S. J., Oh I., Kwak J., Liu Z., Terasaki O. and Ryoo R., Ordered nanoporous arrays of carbon supporting high dispersions of platinum nanoparticles, *Nature* **412** (2001) pp. 169-172.

ZEOLITE/MESOPOROUS MOLECULAR SIEVE COMPOSITE MATERIALS

DO TRONG ON AND SERGE KALIAGUINE

Department of Chemical Engineering, Laval University, Quebec G1K 7P4, Canada

E-mail: kaliagui@gch.ulaval.ca

Up to recently, mesostructured materials were considered as lacking hydrothermal stability, which was a real drawback for many catalytic applications. Recent efforts in trying to impart these materials with thermal properties comparable to those of zeolites have resulted in a variety of zeolite/MMS composite materials. A review of these recent efforts is presented here with a special emphasis on the composites which involve nanozeolites. In order to allow a rational presentation of the concepts behind the various synthesis procedures, a brief review of the recent advances in the field of zeolite nucleation/growth phenomena is first presented. Then a systematic discussion of the various synthesis strategies reported in the literature is made, followed by a rapid presentation of the existing literature on the catalytic properties of zeolite/MMS composites. Some future challenges are then outlined.

1 Introduction

The almost fortuitous discovery of the M41-S family [1,2] of mesostructured aluminosilicates was a result of attempts to make very large pore zeolites [3]. It was soon recognized however that these early mesoporous molecular sieves (MMS's) did not display some of the key properties which made the success of zeolites as catalysts and adsorbants. Indeed the amorphous nature of the walls of MCM-41 and MCM-48 aluminosilicates resulted in low acid strength and low hydrothermal stability compared to zeolites [4]. This was thus a strong incentive to try to prepare new materials that would combine both the regular mesopore structure of MMS's and the crystalline character of zeolites. In the present chapter, we intend to review these efforts and the various composite materials they generated. In order to make a comprehensive report of a large fraction of the strategies that have been proposed, we felt important to discuss briefly the nucleation/growth phenomena associated with the crystallization of zeolites. In particular recent developments in zeolite nucleation and the formation of zeolite nanoseeds have had important impact on the orientations adopted in the synthesis of zeolite/MMS composites.

It was also deemed important to review some recent literature exploring views on how mesostructured materials having fully crystalline zeolitic

walls could eventually be directly synthesized. These views may lead to the next developments in this field in a near future.

2 Mechanisms of zeolite germination

Zeolites are usually crystallized under hydrothermal conditions, at basic pH and at temperatures in the range 60–200 °C, from gels containing the silica and alumina sources, basic agents and alkali metal cations. In many cases, the zeolite synthesis requires also the presence of organic compounds that may play the role of structure-directing agents (templates).

Two extreme mechanisms have been considered in the past to describe the nucleation and growth of zeolite crystals [5,6]. In the first approach (heterogeneous mechanism), it is assumed that the zeolite crystallization proceeds by the reorganization of an amorphous solid phase, usually referred to as the hydrogel that is already present at the onset of the zeolite synthesis. Therefore, in this first approach, nucleation is considered to take place within the hydrogel and the crystals to be formed by solid–solid transformations. In the second alternative (homogeneous mechanism), the nucleation is supposed to occur directly from the liquid phase and, once the nuclei reach a critical size to form stable nanoparticles, they grow into crystals by the progressive incorporation of dissolved species. These two extreme descriptions of the nucleation process may apply differently whether or not the hydrogel is present in the crystallization medium. In the first case, the purely heterogeneous mechanism may proceed or the amorphous solid gel may act as a reservoir of nutrients, which are first dissolved to the liquid phase and give rise there to a homogeneous nucleation/growth process. When a clear gel is the initial crystallization medium, the homogeneous mechanism is believed to apply in most cases. Below we will review in some details the present state of knowledge about to these different zeolite crystallization processes.

2.1 Crystallization by solid-solid transformation

Solid–state transformation in zeolite synthesis could be carried out by the vapor-phase transport (VPT) method [7]. An aluminosilicate dry gel was transformed into a zeolite with MFI topology by contact with water amine mixed vapors. By mixing aluminum sulfate, sodium silicate and sodium hydroxide, an amorphous gel was formed and placed in a sieve-bottomed container inside an autoclave. An ethylenediamine–triethylamine aqueous solution was placed in the bottom of the autoclave. This disposition allowed one to avoid any direct contact between the solid and liquid

phases. The XRD patterns of the product showed the MFI topology, even for a gel completely dried before synthesis. The resulting ZSM-5 samples had similar Si/Al ratio compared to the initial gel. This suggested a solid-phase transformation process.

Kim et al. [8] and Matsukata et al. [9] have applied the VPT technique to the synthesis of a variety of zeolite topologies including ANA, FER, MFI, MOR and CHA. The above described crystallization device allows to contact the solid gel with the vapor generated at the synthesis temperature and to avoid any direct contact with the liquid phase. In some instances the starting gel was however impregnated with the template. Selecting proper synthesis conditions, the dry gel may be completely converted to zeolite. In some other preparations, an excess of water was present in the liquid phase, which promoted the crystallization. The success of the VPT technique illustrates the truly heterogeneous nucleation growth process although the presence of water in the gas phase may indicate that adsorbed water plays a role in the solid phase transport process.

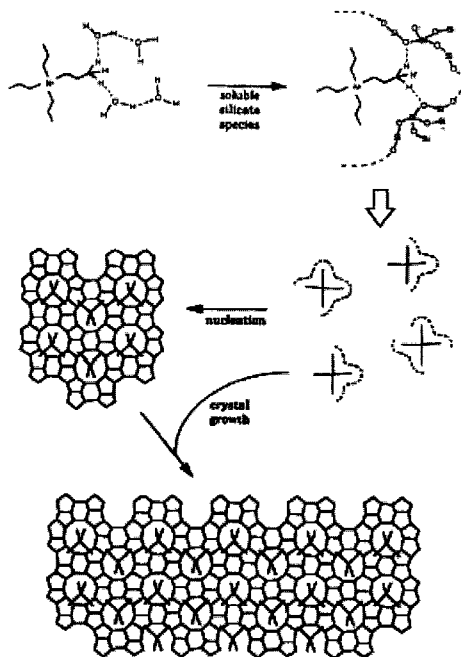
Another example for the solid-solid transformation mechanism in zeolite synthesis was reported by Serrano et al. [10-13]. The procedure involves the transformation of a $\text{SiO}_2\text{-TiO}_2$ xerogel into TS-1, by wetness impregnation with a TPAOH solution followed by heating to the synthesis temperature. A two-step sol-gel route was implemented for the preparation of the $\text{SiO}_2\text{-TiO}_2$ cogels, used as raw materials. Acid hydrolysis of the Si and Ti precursors (to avoid TiO_2 precipitation) was followed by addition of a base to accelerate the condensation of the species in solution, which yielded a solid cogel. This material was finally transformed into the zeolite using the appropriate template by autoclaving. The raw $\text{SiO}_2\text{-TiO}_2$ solids exhibited Ti atoms dispersed in a polymeric SiO_2 network. Si-O-Ti bonds were formed prior to the zeolite synthesis. The generated TS-1 samples showed properties, which depended on the cogel preparation [6,10-13].

2.2 Crystallization from clear solutions

The synthesis of silicalite-1 (MFI topology) has been commonly selected as a model system for the study of the crystallization mechanism due to its simplicity. The clear gel solutions are usually obtained by the hydrolysis of monomeric silica species, although in some cases they are derived from the depolymerization of polymeric silica sources. Several research groups [14-26, 53] investigated the early stages of the crystallization of silicalite-1 from clear solutions, prepared by hydrolysis of TEOS with TPAOH indicating that subcolloidal particles were formed in clear gel solutions even at room temperature. The presence of subcolloidal particles with

sizes around 3 nm is evidenced by cryo-TEM in such raw clear solutions. In a further work, the subcolloidal silica particles were extracted from the precursor solution, as a powder. The extracted solid was characterized by a number of techniques such as Raman and DRIFT spectroscopies, N_2 adsorption and electron diffraction during TEM analysis. Raman spectra indicate the presence of TPA^+ cations entrapped in the silicate structure of the subcolloidal particles. It is proposed that the TPA^+ cations are incorporated within the silica particles during polymerization of the silica species arising from TEOS hydrolysis.

The crystallization mechanism of silicalite-1 from clear solutions was also investigated in detail using both small- and wide angle X-ray scattering measurements (SAXS and WAXS, respectively) [17-26, 53]. The authors indicate the presence of particles with sizes around 3 nm during the whole silicalite-1 crystallization process. The 3.0 nm size particles tend to form some aggregates yielding larger particles, with diameters in the range 7–10 nm. The formation of these colloidal aggregates is dependent on the basicity of the synthesis medium [22]. At relatively low basicity, colloidal aggregates were formed. However, under more basic conditions, no aggregates were detected.



Scheme 1. Proposed mechanism of structure direction and crystal growth involving inorganic–organic composite species in the TPA-mediated synthesis of silicalite-1 [26].

Based on these results [14-26, 53], the authors proposed a possible crystallization mechanism for the MFI zeolite synthesis. It is considered that subcolloidal particles and aggregates are directly involved in the crystallization. The primary units are formed by dissolution of the silicic acid in the TPAOH solution. These subcolloidal particles are assumed to be composite organic-inorganic units, which show some degree of ordering, but are not still completely organized in a crystalline lattice. A second population of particles, with sizes around 10 nm, is formed by aggregation of the primary units (scheme 1) [26]. The concentration of aggregates depends on the alkalinity of the synthesis medium and it shows also a strong correlation with the number of crystals finally formed, i.e. with the nucleation rate. Accordingly, the formation of the aggregates is an essential step in the nucleation process. It can be concluded that the crystal growth step proceeds by incorporation of the primary units, with 2.8 nm size, at the crystal surface.

This crystallization mechanism was also shown valid for the synthesis of other pure silica zeolites [14-26]. For the BEA structure, these primary units show a size of 2.6 nm, whereas in the MTW synthesis, particles with a diameter of 1.5 nm are detected [21]. These results suggest that the same general mechanism may account for the organic-mediated crystallization of different high-silica zeolite structures based on nanometer sized primary units. The exact size of these primary particles depends on the zeolite topology [14-26]. Different approaches of using zeolitic nanoparticles involving the two extreme mechanisms of crystallization for the synthesis of various types of zeolite/MMS composites are discussed in the following section.

3 Synthesis strategies for zeolite/ MMS composites

Over the past few years, several groups have discussed the preparation of zeolite/MMS composite materials. Interestingly, a whole variety of synthesis strategies has been reported [56]. The earlier approaches included the mere mixing of zeolite crystals in the MMS synthesis gel and the dual templating with cationic surfactants and a zeolite template introduced simultaneously or successively during the synthesis. Then a series of other strategies involved the secondary crystallization of zeolites from the material of a mesostructured aluminosilica. In some instances, this crystallization was performed as the precursor MMS was as a suspension in a liquid medium, in some others the secondary zeolite crystallization was performed in the solid state. A whole series of works has also described the autoassembly of either polyanions or the

protozeolite seeds. Finally a technique proposed in our laboratory involves the coating of the mesopore walls of a mesoporous molecular sieve with the clear gel of zeolite nanoseeds. The composite materials resulting from these various strategies will be discussed below.

The so-called ITQ materials reported recently by Corma et al. are worth mentioning here because, even though they are not zeolite/MMS composites, they display most of the target properties of these composites. They are obtained by delamination of layered zeolite precursors such as MCM-22 and ERB-1 zeolites and are thus constituted by a population of high external surface area ($\sim 700 \text{ m}^2/\text{g}$) nano-sheets of these zeolites. The external surface of these nanoparticles is indeed accessible through large meso- and macropores [27-29].

3.1 Early attempts

All the disadvantages of mesoporous materials are closely associated with the amorphous nature of their frameworks. To upgrade the performance of these materials, early studies have attempted to synthesize a zeolite/MCM-41 composite, which would combine the advantages of zeolites and mesoporous materials. Kloetstra et al. [31] reported FAU/MCM-41 composite prepared by over-growing the thin walls of MCM-41 and by adding FAU crystals to the MCM-41 synthesis gel. These composites showed good activities in cracking of vacuum gas oil. The formation of MFI/MCM-41 composites was also reported by Karlsson et al. [32,33] using a two-template gel system [$\text{C}_6\text{H}_{13}(\text{CH}_3)_3\text{NBr}$ and $\text{C}_{14}\text{H}_{29}(\text{CH}_3)_3\text{NBr}$ for MFI and MCM-41], respectively. The relative amounts of both MFI and MCM-41 phases in the final products can be controlled by varying the ratio of the templates and by tuning the synthesis temperature. The XRD spectra and N_2 adsorption/desorption isotherms from samples synthesized with various combinations of C_6 and C_{14} at the same temperature and synthesis time indicate that the isotherms reveal gradual transition from Type IV (MCM-41) to Type I (MFI-type), and the XRD peaks, which are characteristic of the MCM-41 structure, are gradually less well resolved, with increasing the C_6/C_{14} ratio. Because $\text{C}_6\text{H}_{13}(\text{CH}_3)_3\text{N}^+$ was known as a structure-directing agent to produce MFI zeolite at 200°C , however amorphous material at 100°C ; while $\text{C}_{14}\text{H}_{29}(\text{CH}_3)_3\text{N}^+$ gave amorphous material at 200°C and MCM-41 at 100°C . The strategy of sequential low/high ($100^\circ\text{C}/175^\circ\text{C}$) or high/low temperatures was also performed using $\text{C}_6=75\%$ and $\text{C}_{14}=25\%$ to synthesize the MFI/MCM-41 materials (Fig. 1). Because of the protozeolitic unit cell size of around 3.0 nm [14-29], this size is larger than the wall thickness of MCM-41 ($\sim 1.5 \text{ nm}$).

Clearly, once a zeolite phase is formed from MCM-41, the MCM-41 framework was partially destroyed. It was likely to appear as a separate zeolite phase and/or MFI-type crystals embedded partly in MCM-41 aggregates. No test of the hydrothermal stability and acidity were performed for these samples.

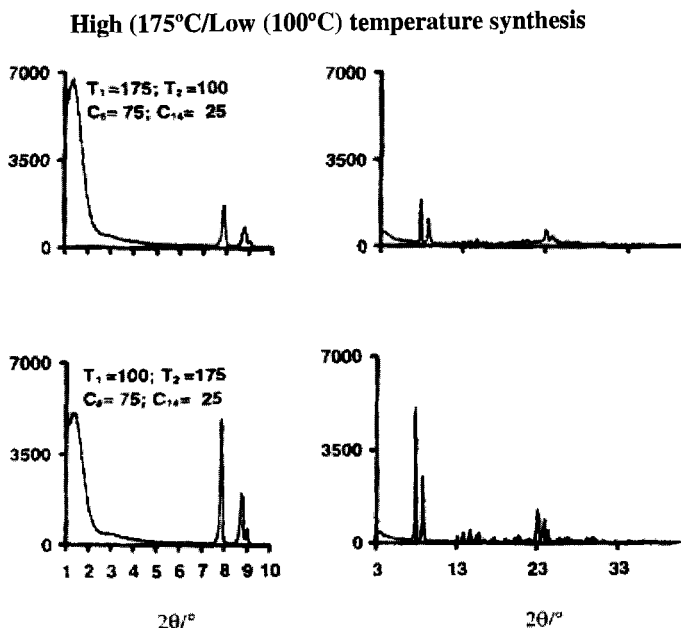


Figure 1. XRD patterns of mesoporous (left) and microporous (right) structures. The samples (calcined) were obtained using a high (175°C/Low (100°C) synthesis temperature scheme (top) and vice versa (bottom) and a $C_6=75\%$, $C_{14}=25\%$ combination of ammonium cations in the syntheses gels [33].

Furthermore, Li et al. [34-35] propose a two-step crystallization process for the syntheses of ZSM-5/MCM-41 composites. In this process, the mesoporous MCM-41 phase was first prepared and followed by addition of a structure-directing agent as tetra-propylammonium cations (TPA^+) and subsequently re-crystallization of the amorphous walls MCM-41 at an appropriate temperature (between 100°C and 150°C). A solid to solid-phase transformation mechanism was presented in this re-crystallization. With the increase of re-crystallization time and temperature, some discrete micron-sized ZSM-5 crystals were produced. Because of the thin wall thickness of MCM-41, it is difficult for nanometer-sized ZSM-5 to remain in the mesopore walls while preserving the mesopore structure. However, these MCM-41/ZSM-5 composites containing interconnected mesopore

and micropore were observed. Figure 2 shows the ^{129}Xe NMR spectra of the mechanical mixture and composite of MCM-41/ ZSM-5. For the sample of the mechanical mixture, three chemical shifts at 174.0, 84.6 and 0 ppm corresponding to the xenon adsorbed in the microporous channels of ZSM-5, mesoporous channels of MCM-41 and non-adsorbed xenon in the gas phase, respectively. However, the ^{129}Xe NMR spectrum of the composite sample is quite different. The peaks corresponding to the xenon adsorbed in micropore and mesopore structures were shifted. Compared to those of the mixture sample. This could be due to the existence of micropore/mesopore interconnected; xenon molecules can be rapidly exchanged between the micro-and mesopore, thus resulting in a lower chemical shift (159.4 ppm) for the mesopore and a higher chemical shift (at 90.5 ppm) for the micropore. Furthermore, the composite samples showed improved acidity and cracking activity of n-dodecane compared to the amorphous Al- MCM-41 and the mechanical mixture of MCM-41 and ZSM-5 [34,35].

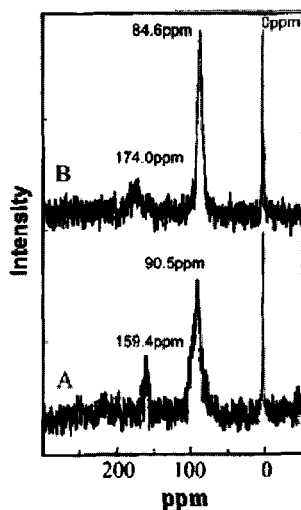


Figure 2. ^{129}Xe NMR spectra of (A) sample S2 and (B) mechanical mixture of MCM-41/ZSM-5 [34].

On the other hand, the same research group reported another synthetic approach, which was based on the sequential synthesis of colloids of zeolite Beta followed by adding this viscous gel to a solution of cetyltrimethylammonium bromide [36,37]. The resulting Beta/MCM-41 composites with various crystallinities of zeolite beta possess the bimodal mesopore system and the zeolite Beta structure. With increasing crystallinity of zeolite Beta, the number and strength of the acid sites

increase. As a result, Beta/MCM-41 composites with higher Beta crystallinity exhibit higher catalytic activity for n-heptane cracking [37]. Zeolite/MCM-41 composites were also made using dissolved zeolites as silica-alumina source [38]. The mesostructure could be formed by dissolved zeolite crystals in the solution. The XRD spectra of these materials show the peaks characteristic of both zeolite and MCM-41. Their catalytic activity of n-hexane is higher than that of the zeolite precursor and the corresponding Al-MCM-41.

3.2 MMS as precursors of zeolites

3.2.1 Recrystallization in the presence of a liquid phase

One approach to the synthesis of composite MMS/zeolite materials introduced by van Bekkum et al. [39] is to transform the pre-assembled walls of Al-MCM-41 and Al-HMS to subunit zeolite structure by post-assembly treatment with a micro-porous zeolite structure-directing agent, such as the tetrapropylammonium cation. In contrast to the parent samples (e.g., Al-MCM-41 and Al-HMS), the resulting products, denoted as PNA-1 and PNA-2 respectively, displayed FTIR spectra with a distinct vibration at $\sim 550\text{ cm}^{-1}$ indicative of the five-membered ring subunits of a pentasil zeolite. XRD patterns showed however no crystalline feature, which must result from small zeolite nanodomains having characteristic lengths below 5 nm. Support for the formation of ZSM-5 structure was also gained from ^{13}C NMR. TPA^+ confined in ZSM-5 showed a characteristic splitting of the methyl ^{13}C NMR signal at 10 ppm. This is ascribed to the different surroundings of the propyl chains extending in the two different channels of the ZSM-5 crystalline. ^{13}C NMR performed on as-synthesized recrystallized MCM-41 showed a small splitting of the signal at 10 ppm [40]. Such splitting of the methyl signals was indeed absent in the spectrum of MCM-41 impregnated with TPA^+ before hydrothermal treatment.

The walls in MCM-41 have a thickness of $\sim 1.5\text{ nm}$ which is smaller than the zeolite subunit cell ($\sim 3.0\text{ nm}$). Once a zeolite nuclei is formed, a separate phase can appear. This was also reported by van Beckkum et al. [40]. After 1 h of hydrothermal treatment, the Al-MCM-41 impregnated with TPAOH was found to be severely damaged and its surface area dropped from $855\text{ m}^2/\text{g}$ for the parent material to $74\text{ m}^2/\text{g}$. This suggests that the ZSM-5 crystallites are growing from the MCM-41 pore wall followed by aggregating and collapsing the MCM-41 structure. Increasing the precursor wall thickness would allow multiple zeolite units to be

formed at the wall surface, thus increasing crystallinity, stability and catalytic activity, while preserving the mesopore structure. Thus it appears that the process involved here is a heterogeneous nucleation in the mesopore wall followed by growth at the expense of the wall material. It is interesting that the earlier preparation [39] used glycerol as a recrystallization medium presumably to avoid the dissolution of silicate oligomers and the homogeneous nucleation/growth process to proceed away from the mesopore surface.

3.2.2 Solid phase recrystallization

We recently reported an alternative approach to the production of a new type of materials with semi-crystalline zeolitic mesopore walls, designated as UL-zeolites [41-44]. This procedure involves a templated solid-state secondary crystallization of zeolites starting from an amorphous mesoporous material. As discussed above, it is of special concern that the walls of the amorphous mesoporous precursor material should be as thick as possible. References [45-52] provide methods for the preparation of mesoporous precursors, such as SBA-15 and MCF, which are useful in this context. Moreover, the solid-state recrystallization using the sieve-bottomed autoclave discussed above [7], ensures that the germination/growth process is indeed fully heterogeneous and that the zeolite nanocrystals are actually part of the mesopore wall surface.

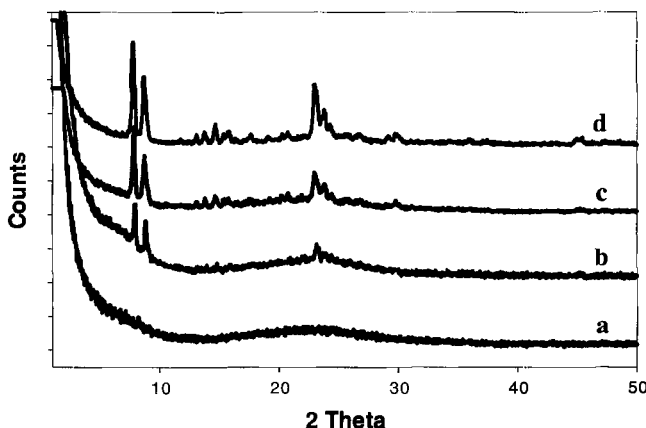


Figure 3. XRD patterns of the calcined UL-ZSM-5 samples after different lengths of crystallization time: a) 0 day, b) 1 day, c) 2 days and d) 5 days (ref. 41).

UL-ZSM-5 was synthesized using a mesostructured aluminosilicate (Si/Al=100) prepared by hydrolysis of chlorides in ethanol described by

Stucky et al. [47,48], as a precursor. The solid-state crystallization was performed at 130°C in the presence of TPAOH. Upon crystallization, the crystalline phase in UL-ZSM-5 was characterized by wide-angle XRD patterns, as shown in Fig. 3. The mesoporous precursor with amorphous walls provides a starting material from which nano-crystalline domains can nucleate within the walls (Fig.3a). The XRD pattern of the calcined sample in Fig. 3b shows broad peaks, which match those of ZSM5. These peaks grow in intensity as the crystallization time is increased (Fig. 3c,d). Considering the ZSM-5 sample as 100% crystalline, the crystallinity of the UL-ZSM-5 samples was estimated from XRD peak intensity (Fig. 3). ~42 % crystallinity was reached after 5 days of solid-state crystallization at 130°C. These data indicate that the initially amorphous walls of the mesoporous material are progressively transformed into crystalline nanoparticles. Furthermore, the UL-ZSM-5 sample after 5 days of crystallization shows a FTIR absorption band at 561/547 cm^{-1} (doublet) which is not present in the mesoporous precursor. The band at ~550 cm^{-1} has been assigned to the asymmetric stretching mode in five membered ring blocks. Splitting of this lattice-sensitive band into a doublet at 561/547 cm^{-1} is characteristic of nanocrystals of the MFI structure (ZSM-5) [53].

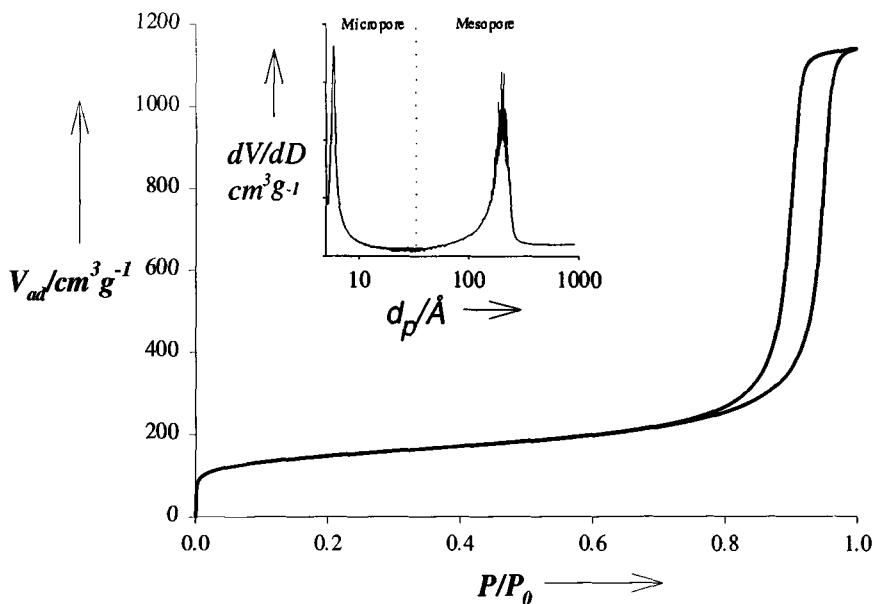


Figure 4. Adsorption/desorption isotherms of nitrogen at -196°C on the calcined UL-ZSM-5 sample after 2 days of crystallization at 130°C . Inset: Horváth-Kawazoe (HK) micropore and Barrett-Joyner-Halenda (BJH) mesopore size distributions (ref. 41).

Fig. 4 shows the nitrogen adsorption/desorption isotherm from a calcined UL-ZSM-5 sample obtained after 2 days of crystallization at 130°C, which exhibits a typical type IV adsorption/desorption isotherm with a H_1 hysteresis loop and steep rises at low relative P/P_0 pressure indicating the presence of both mesopore and micropore structures. The micropore and mesopore size distributions were calculated using Horváth-Kawazoe (HK) and Barrett-Joyner-Halenda (BJH) methods, respectively and are presented in Figure 4 as an inset. It shows narrow pore size distributions of both micro- and mesopores. With increasing crystallization time, the samples exhibit nitrogen adsorption/desorption isotherms with similar inflection but a shift toward higher P/P_0 values over a larger P/P_0 range. A significant increase in the pore diameter and a broader pore size distribution were observed with increasing crystallization time, while the micropore volume increased from 0.020 to 0.158 cm^3/g with no essential change in the micropore diameter (~ 0.57 nm). The evolution of the pore diameters is shown in Fig. 5. The micropore diameter is comparable to the value known for the crystallographic aperture of the 10 membered ring zeolite ZSM-5. Note that for highly crystalline ZSM-5, the micro-pore volume is approximately 0.20 cm^3/g (see Fig. 5).

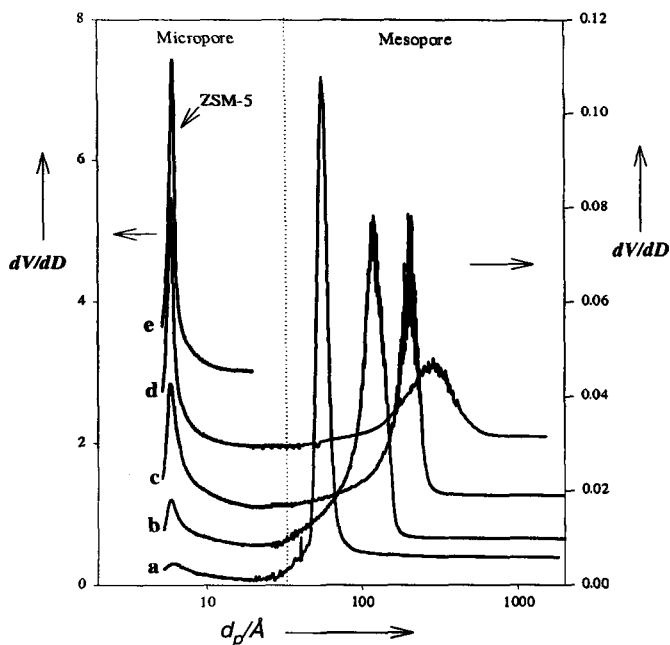


Figure 5. HK micropore and BJH mesopore size distributions for the UL-ZSM-5 sample at different lengths of crystallization time: a) 0 day, b) 1 day, c) 2 days, d) 5 days and e) ZSM-5 [41].

The increase in micropore volume suggests that particles of this zeolite have grown at the expense of the mesopore walls. Furthermore, as the crystallization time is increased, the total surface area of the sample (S_{BET}) varies from 865 to 565 m^2/g and the mesopore surface area S_{BJH} varies from 745 to 130 m^2/g . Concomitantly, the micropore surface area increases from 120 to 435 m^2/g for this series of samples. This indicates some rearrangement of the tubular channels of these materials during crystallization [41,42].

Fig. 6 shows bright-field and dark-field TEM images recorded on the same area of a UL-ZSM-5 obtained after 5 days of crystallization. As seen in the dark-field image (Fig.6B), the bright spots correspond to ZSM-5 nanocrystallites. The nanocrystals are embedded in the continuous amorphous inorganic matrix to form semicrystalline wall structures while preserving the mesoporous structure. The wormhole pore lattice is however still present and micro-domains of the order of $\sim 10\text{-}30$ nm are observed. This indicates that the pore walls consist of nanocrystals of this zeolite. However, some agglomerations of segregated zeolite crystals were seen in the dark field images.

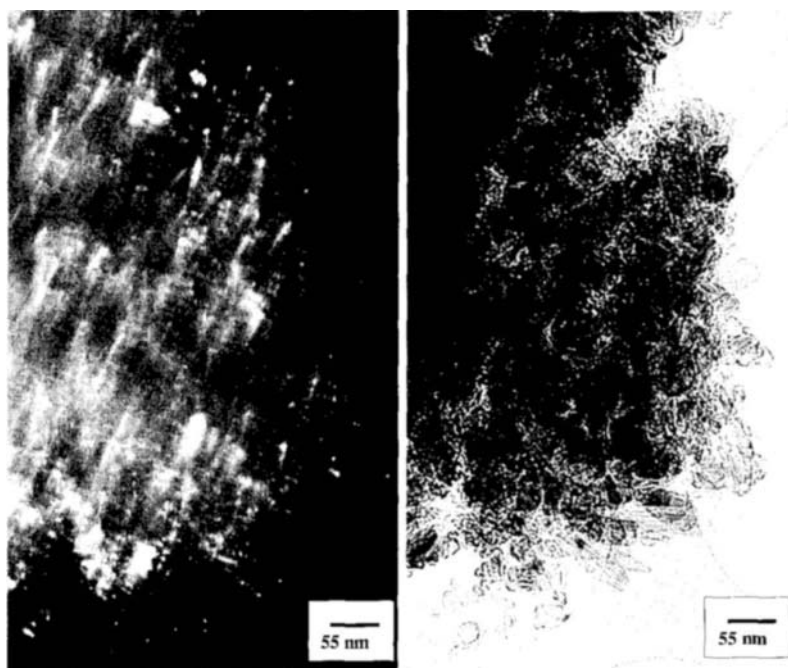


Figure 6. Bright-field (A) and dark-field (B) TEM images on the same area of the UL-ZSM-5 sample after 5 days of crystallization (the bright spots in the image correspond to ZSM-5 nanocrystals) [41].

^{27}Al MAS NMR spectra of UL-ZSM-5 samples (atomic Si/Al=100) exhibit a single resonance centered at 54-58 ppm, which is characteristic of tetrahedral aluminum. To determine the acidity, pyridine adsorption/desorption experiments were performed. The IR spectra of the pyridine adsorbed on the parent sample and UL-ZSM-5 sample after crystallization for 5 days (e.g. 42% crystallinity), and using ZSM-5 (atomic Si/Al = 57) as the reference, in the 1350-1800 cm^{-1} range are shown in Fig. 7. For the parent sample after evacuation at 150°C, two very weak IR bands at 1547 cm^{-1} and 1455 cm^{-1} , which are characteristic of Brönsted and Lewis acid sites respectively [54], were observed. However, the FTIR spectra of the UL-ZSM-5 and ZSM-5 samples show two intense bands at 1547, 1455 cm^{-1} and which were still retained even after evacuation at 200°C, while these bands had disappeared from the spectrum of the parent sample. This suggests a much stronger acidity in UL-ZSM-5 and ZSM-5 than in the parent mesoporous aluminosilicate. The order of acid strength was found to be ZSM-5>UL-ZSM-5(~42% crystallinity)>> mesoporous aluminosilicate.

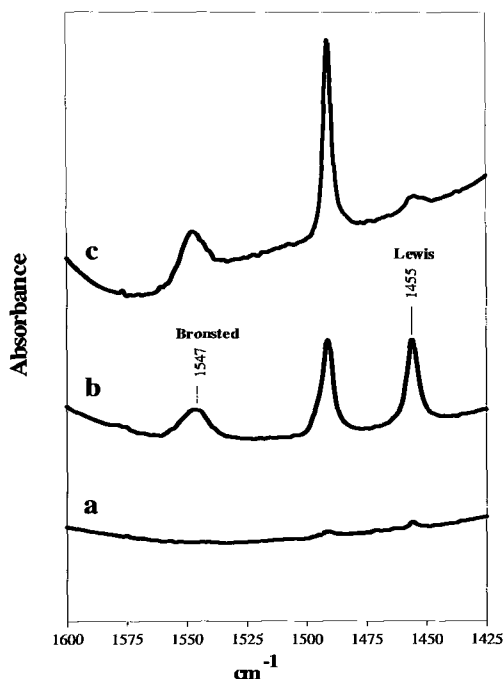


Figure 7. FTIR spectra of the adsorbed pyridine in the 1350-1800 cm^{-1} range after pyridine desorption at 150°C: a) parent mesoporous aluminosilicate, b) UL-ZSM-5 after 5 days of crystallization and c) ZSM-5 [41].

A series of UL-ZSM-5 (Si/Al=50) with different crystallinities were also steamed with 20% water vapour in N_2 at 800°C for 24 h [55,56]. As seen in Fig. 8, the hydrothermal stability of this series of UL-ZSM-5 increases with crystallinity. The 60% crystalline solid shows very little degradation of its pore structure after 24 h at 800 °C in the presence of 20 % water vapour.

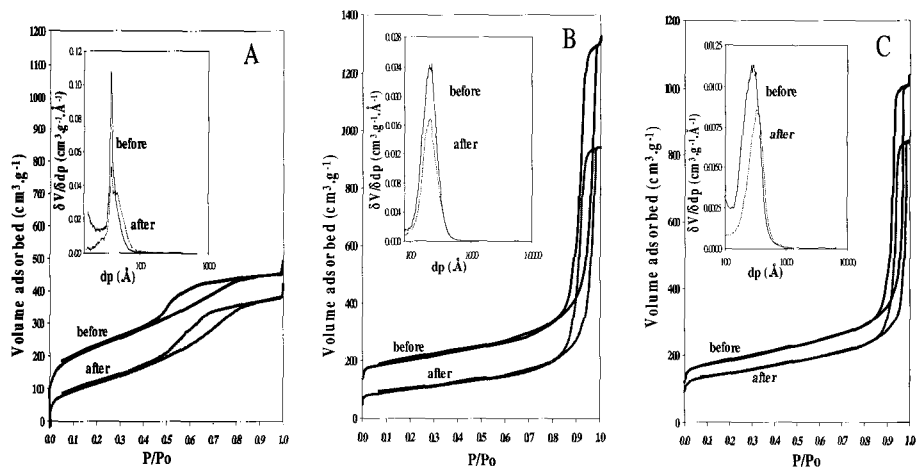


Figure 8. N_2 sorption isotherms of the UL-ZSM-5 samples with different crystallinities before and after steaming for 24 h at 800°C with 20% water vapor in N_2 : A) precursor Al-SBA-15 (Si/Al=50), B) UL-ZSM-5 with ~24% crystallinity and C) UL-ZSM-5 with ~60% crystallinity (inset: BJH pore diameter distribution) (refs. 55,56).

Our approach of using thicker wall mesoporous aluminosilicates as precursors and of a solid-state crystallization to the formation of nanozeolite particles within the mesopore walls has also been used to partially transform mesostructured titano-silica into embedded nanoparticle of the titanium silicalite (TS-1) yielding UL-TS-1 [42,43]. Well-ordered hexagonal and wormhole-like pore structures were observed for the titano-silicate precursors (atomic Si/Ti= 65) prepared from tetraethyl orthosilicate, TEOS (route I) [45,46] and $SiCl_4$ (route II) [47,48], respectively. Fig. 9 shows the TEM images of the UL-TS-1 samples prepared from route I and route II after 10 days of crystallization at 120°C. It is seen that the hexagonal structure of the precursor SBA-15 phase is transformed after the crystallization step. The diameter of the regularly arranged pores is significantly enlarged compared to that of the parent precursors. The pore walls themselves show a discontinuous structure suggesting that nucleation of TS-1 begins in these walls.

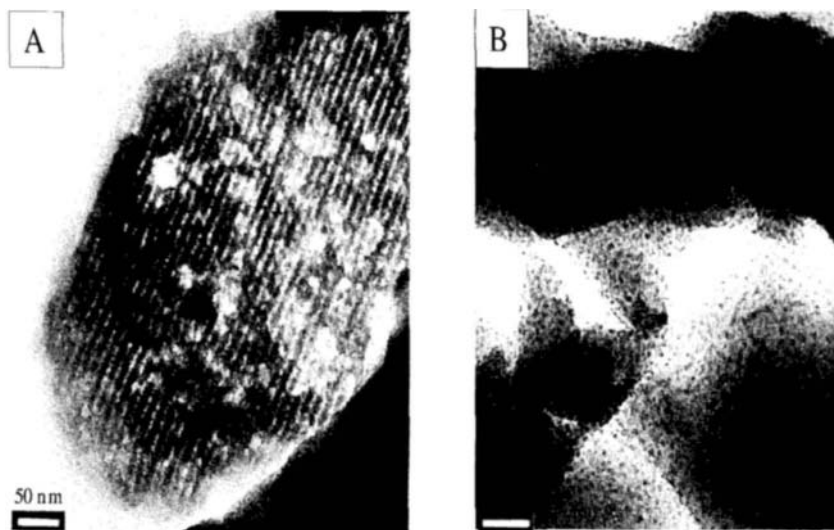


Figure 9. TEM images of the calcined UL-TS-1 (atomic Si/Ti = 66) samples after 10 days of crystallization in the presence of TPAOH, A) UL-TS1 prepared from TEOS, route I (~ 80% crystallinity) and B) UL-TS1 prepared from SiCl₄, route II (~ 65% crystallinity) [42].

The FTIR spectra of a series of UL-TS1 samples prepared from TEOS (route I) with various times of crystallization are shown in Fig. 10. The pure SBA-15 silica sample exhibits spectroscopic features similar to those of amorphous mesoporous silica. A broad band at 985 cm^{-1} assigned to the vibration mode of a SiO₄ tetrahedron perturbed by the bond to a silanol group on the wall surface is present (Fig. 10a). However, for the mesoporous titano-silicate precursor before crystallization, a band at 965 cm^{-1} , which is characteristic of titanium framework, is shown and no band at 550 cm^{-1} was observed. The band at 985 cm^{-1} disappears progressively, while the bands at 550 and 965 cm^{-1} develop with increasing crystallization time. The FTIR spectra of the samples show the bands at 550 and 965 cm^{-1} , which are characteristic of zeolite crystals and titanium framework, respectively. The UV-visible spectra of the UL-TS1 sample with different lengths of crystallization time show that only a single intense large band at 230 nm was observed. No band at 330 nm characteristic of octahedral extra-framework titanium was observed. This also suggests that all titanium is essentially incorporated in the UL-TS1 framework.

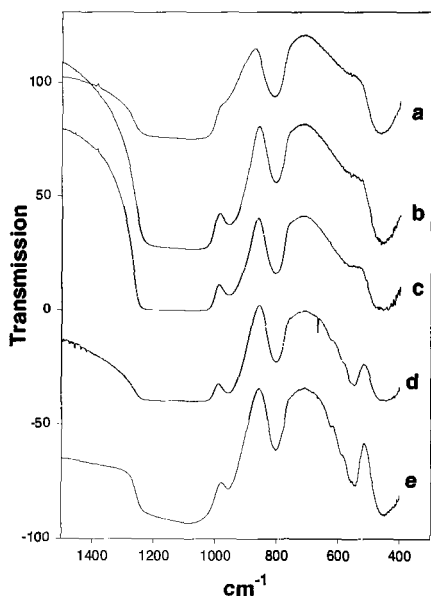


Figure 10. FTIR spectra of: a) the calcined SBA silica sample and the UL-TS1 (atomic Si/Ti = 65) sample prepared from TEOS (route1) after various times of crystallization at 120°C b) 0 day, c) 5 days, d) 8 days and e) 10 days [42].

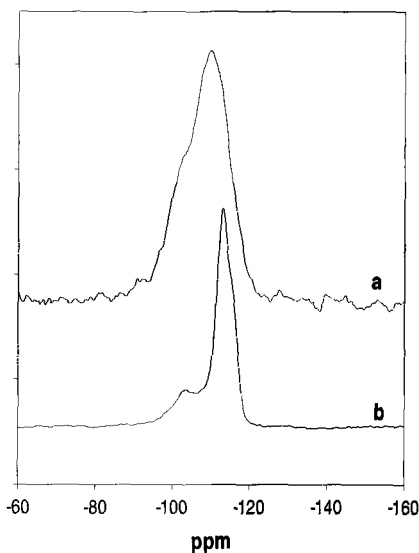


Figure 11. ^{29}Si MAS-NMR spectra of: a) the calcined mesoporous titanasilicate precursor prepared from TEOS (route I) and b) the calcined UL-TS-1 sample after 10 days of crystallization at 120°C (~ 80% crystallinity) [42].

Fig. 11 shows the ^{29}Si MAS NMR spectra of an amorphous mesoporous titano-silicate prepared from TEOS (route I), and of the UL-TS-1 sample obtained after 10 days of crystallization of this precursor at 120°C. The mesoporous titano-silicate exhibits a ^{29}Si MAS NMR spectrum typical of amorphous materials; two main resonances at -114 and -104 ppm, and a very weak peak at -98 ppm correspond to $\text{Si}(\text{OSi})_4$ (Q^4), $\text{Si}(\text{OSi})_3$ (Q^3) and $\text{Si}(\text{OSi})_2$ (Q^2) silicate species, respectively. Upon crystallization for 10 days, the ^{29}Si MAS NMR spectrum showed the main resonance (Q^4) at -114 ppm along with only a weak resonance (Q^3) at -104 ppm associated with residual surface hydroxyl groups and the resonance (Q^2) at -98 ppm had disappeared. The increase in the intensity of the Q^4 resonance and concomitant decrease in the intensity of the Q^3 resonance reflect the crystallization process and the transformation of the hydrophilic surface into a hydrophobic one.

Finally, this approach is not limited to the MFI zeolite structure and other zeolite structures such as beta, X and mordenite have been

synthesized in our laboratory. The resulting bimodal porous materials display a mesoporous surface constituted of zeolite nanoparticles so that a large zeolite surface is accessible to bulky molecules. Moreover, the relatively short diffusion pathways through the thin walls and isolated nanoparticles are expected to improve mass transfer and catalytic reaction efficiency, while minimizing channel blocking. These materials are not only hydrothermally stable, but they also possess the strong acidic sites of zeolites [41-43,55,56].

3.3 Auto-assembly of polyanions

In 1995, Fyfe et al. [57,58] used cubic silicate polyanions $\text{Si}_8\text{O}_{20}^{8-}$ (D4R) with cationic surfactants to synthesize mesoporous materials. The auto-assembly of silicate or aluminosilicate polyanions by the cationic surfactant, $\text{CH}_3(\text{CH}_2)_{15}\text{N}(\text{CH}_3)_3^+$ (C_{16}TA^+) led to mesophasic precipitates with layer or rod-based structures depending on the conditions of precipitation. Further structure ordering of these precipitates was achieved by acidic vapour treatment leading to more stable ordered materials with cubic (MCM-48), lamellar and hexagonal (MCM-41) mesostructures. The phase transformations between these mesophases were also observed in a systematic manner during vapour phase treatments: layered precipitates (namely L_0) \rightarrow cubic (V_1) \rightarrow lamellar (L_1) \rightarrow hexagonal (H_1). It is believed that the electrostatic interaction and the matching of charge density at the inorganic-surfactant interfaces should govern the cooperative assembly of these structures [59-61].

3.3.1 Mesoporous Materials from cubic silicate polyanions

The synthetic procedure of this type of materials consists of two steps; i) preparation of clear concentrated solution of TMA- Si_8 crystals ($[\text{N}(\text{Me})_4]_8\text{Si}_8\text{O}_{20} \cdot 65\text{H}_2\text{O}$), followed by adding a cationic CTA^+ solution at room temperature, which results in rapid precipitate of a mesophase. The resulting solid is then filtered and dried; ii) acidic vapour treatment of the precipitates at 105-130°C for enhancement of the structural order or even mesostructural transformation [57,58].

Figure 12 presents the XRD patterns and ^{29}Si MAS NMR spectra of the $\text{Si}_8\text{C}_{16}\text{TA}$ precipitates obtained by varying the pH of the TMA- Si_8 solution adding different amounts of either TMAOH (tetramethylammonium hydroxide) or HCl before the addition of the surfactant (CTAC) solution [57]. The reaction conditions were otherwise identical. Different mesophases were indeed obtained. In basic or neutral surfactant solutions

(Figure 12, a and b) a layer-based structure designated as L_0 is formed. Its ^{29}Si NMR spectrum shows a single, narrow peak at -99 ppm, indicating the Si_8 structural units are perfectly intact in this layered mesophase. When acid is added to the surfactant solution, another mesophase appears in addition to L_0 (Figure 12, c and d) and the ^{29}Si NMR spectrum shows the expected Q^3 resonance at -99 ppm, and an additional peak at about -110 ppm in the Q^4 Si region [57]. This indicates that condensation between Si_8 cubes has indeed taken place. When a relatively large amount of acid is added, the second hexagonal mesophase (designated as H_0) is virtually the only one observable in the precipitates (Figure 12, e and f). The XRD pattern of this phase is very close to that of MCM-41 but with less well-defined higher order peaks. However, there is no evidence in the ^{29}Si MAS NMR spectrum for any Q^2 . It should be noted that the degree of silicate condensation as indicated by the ^{29}Si NMR spectra can vary considerably depending on precipitation conditions (Figure 12, e and f).

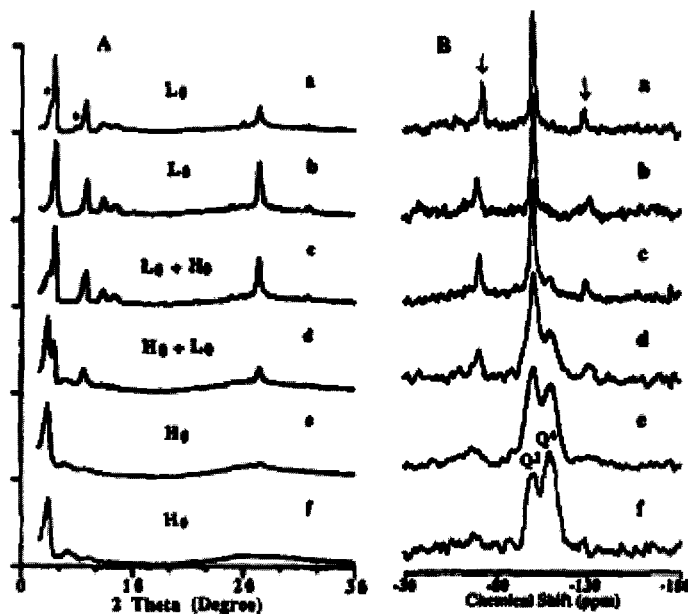


Figure 12. (A) XRD patterns and (B) ^{29}Si MAS NMR spectra of $\text{Si}_8\text{C}_{16}\text{TA}$ precipitates prepared at room temperature by addition of solutions of $(\text{NMe}_4)_8\text{Si}_8\text{O}_{20} \cdot 65\text{H}_2\text{O}$ crystals (typically, 2 g in 20 ml of H_2O) into C_{16}TACl solutions (typically, 100 ml of 5 wt %) which contain (a) 5 g of $\text{TMAOH} \cdot 5\text{H}_2\text{O}$, (b) no additional reagents, and (c - f) 0.1, 0.2, 0.4, and 0.6 ml of 38% HCl solution, respectively. The XRD peaks indicated "*" in (a) are due to an additional layered mesophase. The NMR peaks indicated "↓" are spinning sidebands [57].

To prove the integrity of the Si_8 system in these phases, the FTIR spectra of the precipitates were investigated. In the case of zeolites, a peak in the region $500\text{--}650\text{ cm}^{-1}$ is characteristic of double ring systems [62,63]. In Fyfe et al.'s work, the FTIR spectrum of Si_8 shows strong absorptions in the range $610\text{--}555\text{ cm}^{-1}$ analogous to the spectra of completely siliceous zeolite A. These lines are considered due to the D4R moieties. The layered precipitate (L_0) phase precipitated at high pH shows a strong absorption at 593 cm^{-1} suggesting the presence of a high concentration of D4R in agreement with the ^{29}Si spectra of Figure 12B. The hexagonal precipitate obtained at lower pH also shows an absorption at 574 cm^{-1} indicating the presence of a substantial concentration of D4R units. In contrast, amorphous silica gel shows no clear absorption in this region. These observations indicate a considerable degree of stability of the D4R units in these materials and during reactions.

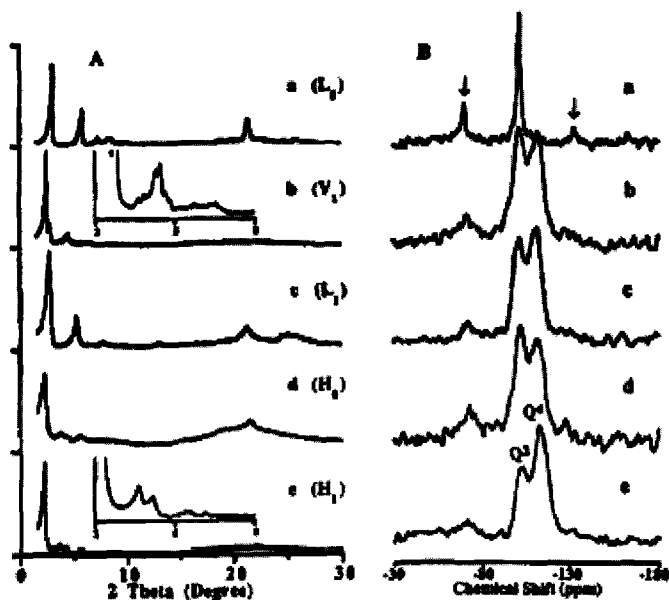


Figure 13. (A) XRD patterns and (B) ^{29}Si MAS NMR spectra of the $\text{Si}_8\text{C}_{16}\text{TA}$ mesophases: (a) layered L_0 phase obtained by direct precipitation (see Figure 12 for details), (b) the cubic V_1 produced by acidic vapor treatment of L_0 at 110°C for 7 days, (c) the lamellar L_1 phase from treating L_0 at 128°C for 8 days, (d) the rod-based precipitate H_0 prepared by precipitation under acidic conditions (see Figure 12), and (e) the hexagonal H_1 phase obtained from H_0 by acidic vapor treatment at 110°C for 7 days. The insets in patterns b and e show the higher order XRD peaks enlarged. The NMR peaks indicated " \downarrow " are spinning sidebands [57].

Fig. 13 shows the XRD patterns and ^{29}Si NMR spectra of the highly ordered mesostructures obtained through the acidic vapor-phase treatment of L_0 and H_0 materials. The treatment of the material having lamellar phase L_0 yields a cubic-Ia3d phase (designated as V_1) at 110°C and another lamellar phase (designated L_1) at 128°C . Treating the H_0 precipitate produces a higher order hexagonal phase (designated as H_1). The ^{29}Si NMR spectrum (Fig. 13) shows that in L_1 more than 50% of the Si atoms are in Q^4 sites indicating condensed silicate layers. In this sense, L_1 is quite different from L_0 where the silicate layers are formed by individual Si_8 anions, although both phases show comparable interlayer distances and both consist of surfactant monolayers.

Fig. 14 shows the XRD patterns of a series of L_0 samples (pattern a) treated with acidic vapor as a function of time under the conditions given in the caption. It can be seen that the patterns c, e, and g correspond to the cubic (V_1), lamellar (L_1) and hexagonal (H_1) structures, respectively. The patterns b, d, and f show an intermediate structure (b) or mixtures of structures (d and f) observed during transformation. Therefore, these mesophases transform in the following order: $L_0 \rightarrow V_1 \rightarrow L_1 \rightarrow H_1$ [57].

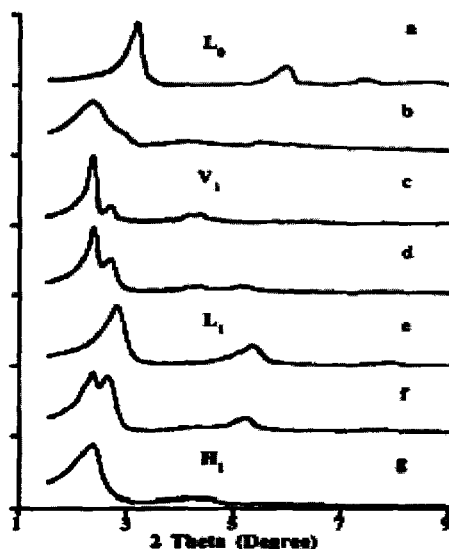


Figure 14. XRD patterns showing the structural transformations of the L_0 precipitate phase during an acidic vapor treatment. (a) The layered L_0 used for experiments (b-g) under the following conditions: (b-d) treatment with 0.44% HCl solution at 110°C for 1, 5, and 10 days, respectively; (e-g) treatment with 0.44% HCl solution at 130°C for 8, 12, and 24 days, respectively. (c), (e), and (g) are typical patterns of the V_1 , L_1 , and H_1 mesophases, respectively [57].

3.3.2 Mesoporous materials from cubic aluminosilicate polyanions

Using the two-step synthetic procedure described above, a hexagonal aluminosilicate mesostructured was also prepared by Fyfe et al. with a Si/Al ratio close to 1 from the known aluminosilicate analogue of Si_8 , the $\text{Al}_4\text{Si}_4(\text{OH})_8\text{O}_{12}^{4-}$ (denoted Al_4Si_4) species (with 4 Al replacing 4 Si atoms in alternating corners of the cube) [63,64]. The structure of the Al_4Si_4 anion is shown schematically in Fig. 15. The ^{27}Al NMR spectra (Fig. 16) show that these mesoporous materials contain mostly tetrahedrally coordinated Al centers even after calcination. One interesting aspect of the behavior of the Al_4Si_4 anions was also observed; for Al_4Si_4 , when mixed with C_{16}TA^+ , the rod-based precipitate phase (AS- H_0) is always the dominant product even under basic conditions ($\text{pH} \sim 10$). However, under these conditions for Si_8 (see above), only the layered precipitate phase (L_0) is formed. This is understandable because $\text{Al}_4\text{Si}_4^{4-}$ has a lower charge than Si_8^{8-} , and since all the terminal groups in the Al_4Si_4 structure are OH (compared to O^- in Si_8) condensation can take place much more easily even under basic conditions, which further lowers the charge density. Obviously, such a precursor is unfavorable for an L_0 phase, which requires highly charged inorganic layers. This observation provides additional evidence that in the presence of a cationic surfactant the charge density of the inorganic precursor is one of the important factors that determine the formation of the mesophase structure. The corresponding hexagonal phases formed from Al_4Si_4 cubes, which are the stable species at different pH values of their formation, exhibit a FTIR strong absorption at 584-590 cm^{-1} . Even after calcination, this hexagonal mesophase also shows a strong absorption at 585 cm^{-1} confirming the stability of D4R cubes in these materials [58]. However, no information about hydrothermal stability and acidity was reported for this type of mesoporous materials.

It is important to note that using Al_4Si_4 as precursor, a Si/Al very close to 1 was achieved, which is the lowest ratio possible for an aluminosilicates with tetrahedrally coordinated Al centers without the formation of unstable Al-O-Al linkage. Clearly, in comparison to the conventional methods based on gel precursors, it is advantageous to incorporate Al at the oligomer stage using aluminosilicate polyanions as precursors. In addition to the Al_4Si_4 species, aluminosilicate polyanions with the same cubic structure, AlSi_7 , Al_2Si_6 , and Al_3Si_5 were reported and characterized [64], and could be used as precursors. Other polysilicates are also known such as double three-ring $\text{Si}_6\text{O}_{15}^{6-}$ (D3R) and double five-ring cage anion $\text{Si}_{10}\text{O}_{25}^{10-}$ (D5R) [65,66]. Such systems are also of particular interest in the synthesis of zeolites, such as zeolite A, ZSM-5, ZSM-11,

ZK-4, omega and offretite etc [67]. Incorporation of other metallic elements in the polyanion structure should also be possible. By selection of appropriate precursor species in terms of both structure and composition, it should be possible to synthesize mesostructured and mesoporous materials with desired properties and some degree of local structure [57,58].

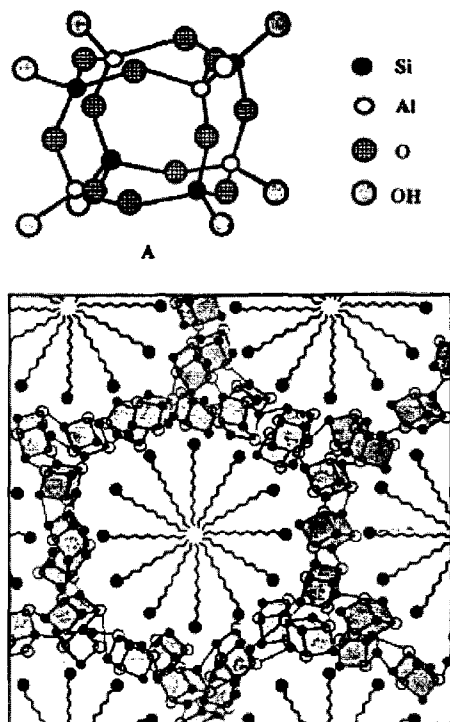


Figure 15. *Top:* Schematic representation of the $\text{Al}_4\text{Si}_4\text{O}_{12}(\text{OH})_8^{4-}$ structure; *bottom:* Schematic representation of the structure of the $\text{Al}_4\text{Si}_4\text{-C}_n\text{TA}$ hexagonal phase (AS- H_1) in the plane perpendicular to the cylindrical channels showing the arrangement of templates and precursor cubes [58].

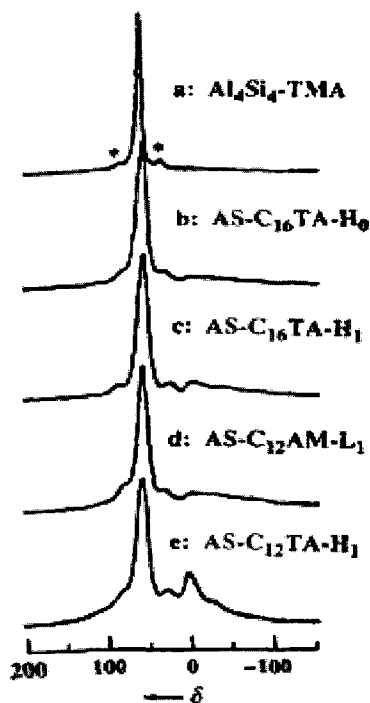


Fig. 16: ^{27}Al MAS NMR spectra of a) $(\text{NMe}_4)_4\text{Al}_4\text{Si}_4\text{O}_{12}(\text{OH})_8 \cdot x\text{H}_2\text{O}$, b) the aluminosilicate precipitate phase (AS- H_0) formed by C_{16}TACl and c) the aluminosilicate hexagonal phase (AS- H_1) obtained from AS- H_0 by vapour phase treatment at 110°C for 3 days, d) the lamellar phase (AS- L_1) obtained by first precipitating Al_4Si_4 followed by treating in refluxing isopropyl alcohol for 24 h and e) the hexagonal phase of $\text{Al}_4\text{Si}_4\text{-C}_{12}\text{TA}$ obtained by C_{12}TACl [58].

3.4 Auto-assembly of zeolite seeds

The use of protozeolitic nanoclusters (also known as zeolite seeds, which normally nucleate zeolite crystallization) to directly assemble hydrothermally stable and strongly acidic aluminosilicate mesostructures was first reported by Pinnavaia et al. [68]. These initial studies were based on the arrangement of faujasitic zeolite (FAU) seeds into a mesostructured framework. Following this approach, several studies successfully assembled steam-stable and strongly acidic hexagonal MCM-41 derivatives by using ZSM-5, TS-1 (MFI) and Beta (BEA) zeolite seeds as building materials (denoted as MSU-S, MAS-5) [69-76]. The idea of using zeolite seeds as precursors to assemble large pore materials has been extended more recently to include hexagonal SBA-15 analogs, denoted MSUS/ H, MAS-7 and MAS-9. Moreover, strongly acidic mesostructured cellular foam (MCF) analogs, denoted MSU-S/F, have also been assembled using ZSM-5, Beta, and faujasitic zeolite seeds at pH <2–6.5 [80-84]. In a recent review paper [30], Pinnavaia and Liu discussed in detail the interest of this type of materials. We therefore outline here only the major synthesis pathways and refer the reader to this excellent review paper for further information.

3.4.1 MCM-41 analog from Y zeolite seeds

Hexagonal mesoporous aluminosilicates were assembled from faujasitic-type Y zeolite seeds and cetyltrimethylammonium bromide (CTAB) as the structure director (nanoclustered zeolite Y seeds were prepared by reacting sodium hydroxide, sodium aluminate, and sodium silicate under vigorous stirring at 100°C overnight). The steam-stable mesoporous aluminosilicate (denoted MSU-S) was obtained by exchanging the as-synthesized material with NH_4NO_3 and then calcining at 540°C for 7 h [68]. Fig. 17 shows the XRD patterns of calcined 10%Al-MSU-S before and after exposure to 20% (v/v) water vapor in N_2 at 800°C for 5 h. Included in Fig. 17, for comparison, are the corresponding patterns for a MCM-41 prepared according to the grafting method of Mokaya (denoted CAH5) [77] and a disordered 10%Al- MCM-41 obtained by the same direct assembly route as MSUS, except that the 100°C aging step leading to the formation of zeolite Y seeds was eliminated. Clearly, 10%Al-MSU-S assembled from nanoclustered zeolite Y seeds retained a well-ordered hexagonal structure upon steam treatment. In contrast, the conventional 10%Al-MCM-41 and the Al-grafted CAH5 were almost totally destroyed by steaming. These results are also supported by N_2 sorption isotherms. The 10%Al-MSU-S

retained 90 and 75% of its surface area and pore volume, respectively. Evidence for the presence of zeolite connectivities in Al-MSU-S was provided by the observation of a single tetrahedral aluminum peak at ca. 61 ppm in the ^{27}Al NMR spectrum of the calcined mesoporous materials, which was consistent with the ^{27}Al chemical shift of the zeolite Y seeds solution and the Al environment of crystalline zeolite Y [78]. A similar study was reported by Pérez Pariente et al. [79], except that nanoclustered zeolite Y seeds were prepared in the presence of tetramethylammonium (TMA^+) cations as a structure-directing agent. The FTIR spectrum of the pyridine adsorbed on this sample indicates its acidity is higher than that of the corresponding MCM-41 [79]. Aside from the improved steam stability and acidity of Al-MSU-S, well-ordered hexagonal Al-MSU-S with a low Si/Al ratio could be readily assembled from nanoclustered faujasitic seeds. This composition is difficult to obtain from conventional aluminosilicate precursors.

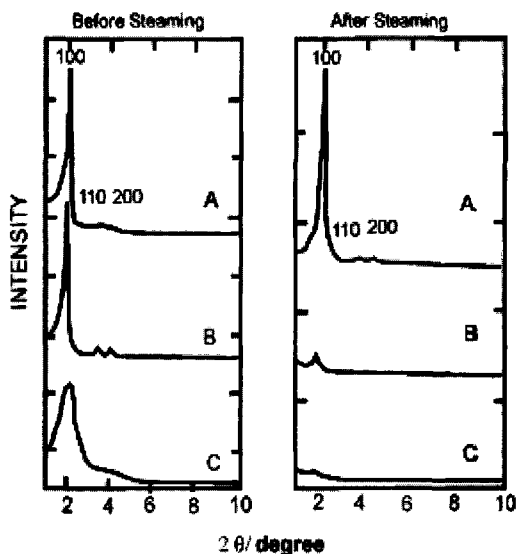


Figure 17. XRD patterns of calcined mesoporous aluminosilicate molecular sieves before and after steaming (800°C, 5 h): (A) hexagonal 10%Al-MSU-S prepared from zeolite Y seeds; (B) "ultrastable" hexagonal 14%Al-MCM-41 prepared by grafting; (C) disordered 10%Al-MCM-41 prepared by direct synthesis from conventional silicate and aluminate precursors [68].

3.4.2 MCM-41/MCM-48 analogs from MFI structure and Beta seeds

Several studies have used zeolite seeds as precursors for the assembly of steam-stable mesostructures, especially BEA and MFI-type seeds [69-76].

In comparison to faujasitic zeolite seeds, which are nucleated by sodium ions, pentasil zeolite seeds are nucleated by specific tetraalkylammonium ions as structure-directing agents. The structural evolution of nanoclusters leading to the nucleation of MFI silicalite, was discussed in section II. Presumably, related structures containing subunits with five-membered rings are encountered before nanoslab formation in pentasil zeolite seed solutions. In further developing the concept of using protozeolitic nanoclusters for mesostructure assembly, hydrothermally stable and strongly acidic MCM-41 analogs were prepared from zeolite ZSM-5, and Beta seeds, which are nucleated by tetrapropylammonium and tetraethylammonium cations, respectively, denoted MSU-S_(MFI), MSU-S_(BEA), MAS-5 and UMA-1.

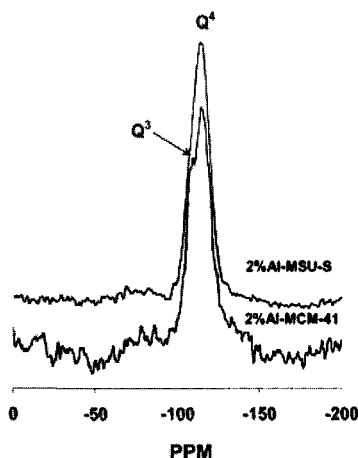


Figure 18. Comparison of ^{29}Si MAS NMR spectra for calcined 2%Al- MSU-S_{BEA} prepared from zeolite Beta seeds and for calcined 2%Al-MCM-41 [69].

Upon steaming at 800°C, the MSU-S analogs still retained long-range hexagonal order and substantial mesoporosity, whereas the mesoporosity of Al-MCM-41 was totally destroyed [69]. It can be proposed that the hydrothermal stability and catalytic activity of MSU-S_(MFI) and MSU-S_(BEA) arise from the presence of zeolitic subunits of AlO_4 and SiO_4 tetrahedra in the framework walls of the mesostructures. Support for the retention of a protozeolitic connectivity of tetrahedra was provided by a FTIR band at 550 – 600 cm^{-1} characteristic of five -membered ring subunits apparent in the FTIR spectra of MSU-S_(MFI) and MSU-S_(BEA), but not for conventional Al-MCM-41. Moreover, in accord with the high hydrothermal stability, the ^{29}Si MAS NMR spectra indicated that the framework walls of 2%Al-MSU-S were essentially fully condensed

whereas this was not the case for a 2%Al-MCM-41. As shown in Fig. 18, only one line at -114 ppm (Q^4) was found in the spectrum of 2%Al-MSU-S, whereas two well-resolved lines at -114 (Q^4) and -104 (Q^3) ppm were observed in the spectrum for 2%Al-MCM-41. The high Q^4 intensity for 2%Al-MSU-S signifies the presence of highly crosslinked walls.

MCM-41 (denoted MAS-5)⁷⁰ and MCM-48 (denoted UAM-1) [74,75] were assembled from zeolite Beta seeds. After boiling in water for 300 h or steaming with 100% water vapor at 800°C for 2 h, still retained well-ordered hexagonal arrays. These materials also exhibited stronger acidity than corresponding Al-MCM-41 and Al-MCM-48 and were found to be similar to Beta zeolite, as judged by temperature programmed desorption of ammonia. Five-membered ring vibrations also were observed in MAS-5 and UAM-1 by FTIR technique, which indicated the incorporation of Beta zeolite subunits in the framework. Note that no zeolite phases were observed by XRD for MSU-S(MFI), MSU-S(BEA), MAS-5 and UAM-1. These materials should be distinguished from microporous/mesoporous composites. The acidity and hydrothermal stability are attributed to the incorporation of pentasil zeolite subunits into the framework walls of the resultant mesostructures [68-76].

3.4.3 Mesostructured cellular foams (MCF) and SBA-15 from zeolite seeds

Hexagonal SBA-15 and mesostructured cellular foams (MCF) are substantially larger pore (7–35 nm) mesostructures that are assembled under strongly acidic conditions, which is not compatible with zeolite seeds. An effort to assemble larger pore SBA-15 and MCF analogs with improved hydrothermal stability and acidity was nevertheless undertaken. The synthesis of SBA-15 analogs (denoted MAS-7 and MAS-9) was reported using beta zeolite and TS-1 seeds, respectively, in strong acidic media [71,72,83,84]. These materials exhibited ordered hexagonal structure and high hydrothermal stability.

Pinnavaia et al. studied the possibility of using nanoclustered faujasite, ZSM-5, and Beta seeds as precursors under mildly acidic pH conditions. The resulting large-pore hexagonal SBA-15 and foam-like MSU-S materials exhibited exceptional hydrothermal stability in boiling water and under steaming conditions. Foam-like MSU-S/ F_{FAU} , MSU-S/ F_{MFI} , and MSU-S/ F_{BEA} are much more stable than Al-MCF [80-82].

Evidence for the retention of foam structures was provided by the TEM images shown in Fig. 19. Consistent with the structural features of MCF reported by Stucky's group [49-52], the MSU-S/F foams are comprised of

large spherical cells interconnected by narrow windows defined by aluminosilicate struts. The struts are 4–6 nm in thickness, which is larger than the anticipated size of nanoclustered zeolite seeds.

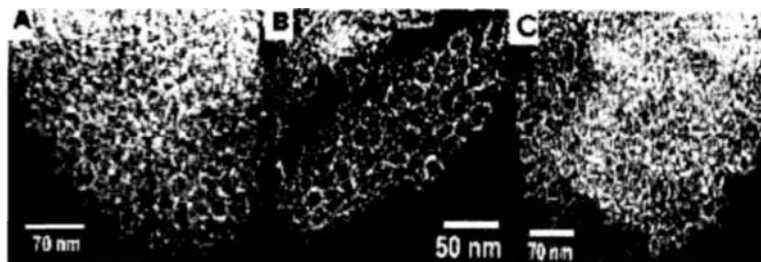


Figure 19. TEM images of (A) MSU-S/F_{FAU}, (B) MSU-S/F_{MFI}, and (C) MSU-S/F_{BEA} [30].

3.5 Zeolite coated mesoporous molecular sieves

Recently we described the preparation of a new family of materials, which we designated as zeolite coated mesoporous molecular sieves (denoted ZCMS). This new type of zeolite/MMS composites is obtained by contacting a mesostructured aluminosilicate with a diluted clear solution containing primary zeolite units. Hydrothermally ultra-stable and highly acidic ZCMS were achieved due to the nano-crystalline zeolitic nature of their pore wall surface [85-89]. These features open new possibilities for high temperature acid catalysis applications. It is of special concern that due to the size of the primary zeolite units, (for example, primary ZSM-5 units templated by tetrapropylammonium ions are of 2.8 nm in diameter [14-29]), the pore diameter of the mesoporous precursor molecular sieves should be higher than 30 Å. The methods described in references [45-52] are therefore useful in this context for the preparation of large pore mesoporous precursors such as SBA15 and mesostructured cellular foams (MCFs). The synthesis of zeolite coated mesoporous materials consists in two steps: the first step is the preparation of both the mesoporous precursor and the desired clear zeolite gel and the second step is the coating of zeolite nanocrystals on the mesopore surface by contacting the mesoporous precursor with the zeolite gel.

3.5.1 ZSM-5 coated mesoporous aluminosilicate SBA-15

ZSM-5 coated samples (denoted ZCMesoAS) were synthesized from mesoporous aluminosilicate SBA-15 [45-48] and diluted clear ZSM-5 gel

solutions [14-29] with desired chemical composition, as described in references. [85,86]. The N_2 adsorption/desorption isotherms obtained from the calcined sample before and after coating are shown in Fig. 20. The parent and ZSM-5 coated samples have the typical isotherm of a mesoporous molecular sieve and a mesopore volume capacity of ~ 1.56 and $0.78 \text{ cm}^3/\text{g}$ respectively (Table 1). A narrower pore diameter distribution of the coated sample compared to that of the parent sample was observed (Fig. 20B). Furthermore, a decrease in pore diameter (from 70 to 54 \AA) and in surface area (from 800 to $465 \text{ m}^2/\text{g}$) could conceivably be ascribed to the ZSM-5 nanocrystals coated inside the mesopore channels of the host. After coating, a uniform pore size with a highly ordered structure was retained from TEM observations.

Table 1. Physico-chemical properties of the parent mesoporous aluminosilicate (PMesoAS) and ZSM-5 coated mesoporous aluminosilicate(ZCMesoAS) samples [85].

Entry	Materials	Si/Al* (atomic)	S_{BET} (m^2g^{-1})	S_{BJH} (m^2g^{-1})	Mesopore volume (cm^3g^{-1})	BJH pore diameter (\AA)
1	PMesoAS	65	1080	800	1.56	20
2	ZCMesoAS	50	495	465	0.78	54

* atomic Si/Al ratios obtained by atomic absorption spectroscopy

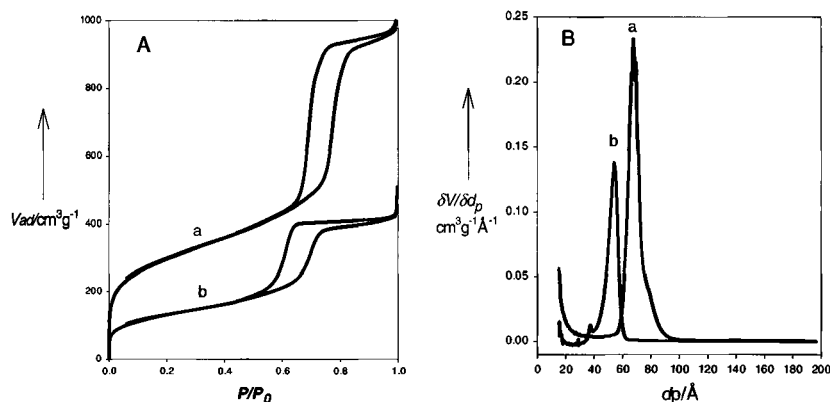


Figure 20. N_2 adsorption/desorption isotherms of nitrogen at -196°C (A) and BJH pore diameter distributions calculated from the desorption branch of the isotherm (B) for a) parent MesoAS, b) ZSM-5 coated MesoAS [85].

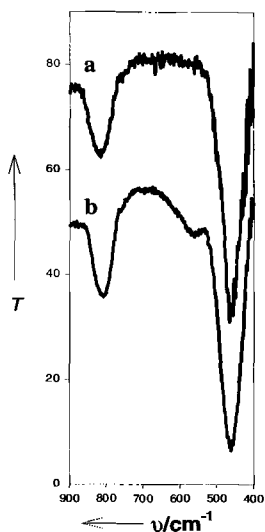


Figure 21. FTIR spectra of a) parent MesoAS, b) ZSM-5 coated MesoAS [85].

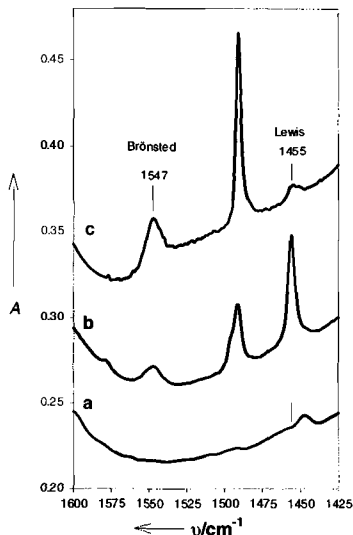


Fig. 22: FT-IR spectra of adsorbed pyridine in the $1350\text{--}1600\text{ cm}^{-1}$ range after pyridine adsorption and then desorption at 150°C : a) parent MesoAS in H-form, b) H-ZSM-5 coated MesoAS, c) H-ZSM-5 [85].

The ZCMesoAS sample shows a FTIR absorption band at 550 cm^{-1} , which is not present in the parent MesoAS sample (Fig. 21). The band around 550 cm^{-1} has been assigned to the asymmetric stretching mode in double five-membered ring in the pentasil secondary building units [19]. Its occurrence indicates therefore that ZSM-5 nanocrystals are present within the mesostructured material. These are however too small to be detected by XRD.

The FTIR spectra of pyridine adsorbed on the parent MesoAS (atomic Si/Al=65/1) in H-form and H-ZSM-5 coated MesoAS (Si/Al=50/1) samples and on H-ZSM-5 (Si/Al=57/1) as the reference after desorption at 150°C , are shown in Figure 22 (the samples in H-form were obtained by the ion exchange of Na^+ by NH_4^+ followed by calcination at 550°C). Two intense bands at 1547 cm^{-1} and 1455 cm^{-1} which are characteristic of Brønsted and Lewis acid sites respectively are observed for the H-ZSM-5 coated MesoAS sample and the H-ZSM-5 reference; however, no such bands are observed for the parent MesoAS sample in H-form. This suggests the acidity of the coated sample is comparable to that of the H-ZSM-5 reference with a larger fraction of Lewis acid sites, much higher

than that of the parent sample. The order of the acid site density is H-ZSM-5 > H-ZSM-5 coated MesoAS >> parent MesoAS.

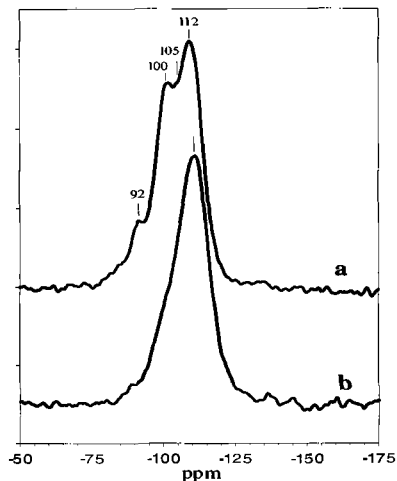


Figure 23. ^{29}Si MAS NMR spectra of: a) parent MesoAS, b) ZSM-5 coated MesoAS [85].

The ^{27}Al MAS NMR spectra of the parent MesoAS and ZSM-5 coated samples exhibit a single resonance centered at about 56 ppm, which is characteristic of tetrahedral aluminum. This indicates that most of the aluminum is incorporated into the material framework. As seen in Figure 23, the ^{29}Si MAS NMR spectrum of the parent MesoAS sample (atomic Si/Al = 65/1) shows a ^{29}Si MAS NMR spectrum typical of mesoporous aluminosilicates, which contains four main features [90,91] (Fig. 23a). Two main resonances at -112 and -100 ppm and a weak peak at -92 ppm correspond to $\text{Si}(\text{OSi})_4$ (Q^4), $(\text{HO})\text{Si}(\text{OSi})_3$ (Q^3), $(\text{HO})_2\text{Si}(\text{OSi})_2$ (Q^2) silicate species, respectively; a shoulder at -105 ppm has been assigned to $(\text{AlO})_1\text{Si}(\text{OSi})_3$ species due to the tetrahedral aluminum structure. By contrast, the ^{29}Si MAS NMR spectrum of the coated sample (atomic Si/Al = 50/1) shows a main resonance centered at -112 ppm, which is attributed to Q^4 silicon of the silicalite framework and a shoulder $(\text{AlO})_1\text{Si}(\text{OSi})_3$ band at -105 ppm (Fig. 23b). Only a weak resonance attributable to Q^3 silicon from surface hydroxyl groups is observed at ~-100 ppm. The increase in intensity of the Q^4 resonance and concomitant decrease in intensity of the Q^3 and Q^2 resonances reflect the transformation of the hydrophilic surface of the precursor into a more hydrophobic one upon coating. These changes reflect the strong chemical interaction of the zeolite seeds with the precursor surface.

Table 2. Physico-chemical properties of the parent mesoporous alumino-silicates (PMesoAS) and ZSM-5 coated mesoporous alumino-silicates (ZCMesoAS) before and after hydrothermal treatment [85].

Entry	Materials	Treatment time (h)	S_{BJH} (m^2g^{-1})	Mesopore volume (cm^3g^{-1})	BJH Pore diameter (\AA)
Boiling water at 100°C					
1	PMesoAS-0-W*	0	800	1.56	70
2	PMesoAS-48-W	48	375	1.72	120
3	ZCMesoAS-0-W	0	465	0.78	52
4	ZC MesoAS-48-W	48	485	0.85	55
5	ZC MesoAS-120-W	120	495	1.35	58
Steaming of 20% vapor water in N_2 at 800°C					
6	ZCMesoAS-24-S	24	400	0.70	53

* PMesoAS-x-y where: x treatment time in h, y: boiling water (W) or steaming (S).

The hydrothermal stability in boiling water at 100°C and steam stability with 20% water vapor in N_2 at 800°C of the parent MMS sample and the ZCMesoAS sample were also studied (Table 2). The pore diameter distributions of the parent MMS sample before and after 48 h of treatment in boiling water at 100°C are shown in Figure 24, inset. The mesopore structure of the parent MesoAS sample was collapsed after 48 h of this treatment. By contrast, no significant collapse of the mesopore structure was observed for the ZSM-5 coated MMS sample after 48 h in the same treatment conditions. The pore volume and BJH surface area slightly varied from 0.78 to 0.85 cm^3/g and from 465 to 485 m^2/g , respectively (Fig. 24A); even after 120 h, the mesopore structure was still uniform. This indicates that the coated sample is much more hydrothermally stable than the conventional MesoAS sample. Furthermore, the coated sample was also steamed with 20% water vapor in N_2 at 800°C for 24 h (Fig. 24B). No essential change in the pore size distribution after 24h of steaming indicates that the coated sample is hydrothermally ultra-stable. The remarkable hydrothermal stability observed here involves therefore the zeolite seeds coated on the mesopore surface, which act to heal defect sites in the MesoAS framework. It is likely that the 2.8 nm sized ZSM-5 seeds templated by TPA^+ cations could electrostatically interact with tetrahedral Al sites in the silica framework and as consequence of this interaction, migrate inside the mesopore channels. It is also apparent that this electrostatic interaction, which provides enough mobility to the zeolite nanoparticles for their initial migration within the mesopores, does not

leave these nanoparticles with sufficient mobility for their sintering during crystallization. Calcination of these materials led to grafting nanoclustered ZSM-5 particles on the mesopore surface by the condensation reaction of silanol groups at the interface. Such coating procedure reduces the concentration of silanols, as confirmed by the ^{29}Si MAS NMR results reported in Fig. 23. Consequently, the high hydrothermal stability of the coated samples should be associated with this lowered silanol surface concentration since several treatments known to decrease the silanol concentration of MMS have been shown to improve their thermal and hydrothermal stability. Finally, the strong acidity combined with an ultra-stable, well-ordered uniform mesopore structure also opens up new opportunities in the use of these coated materials as catalysts [85-87].

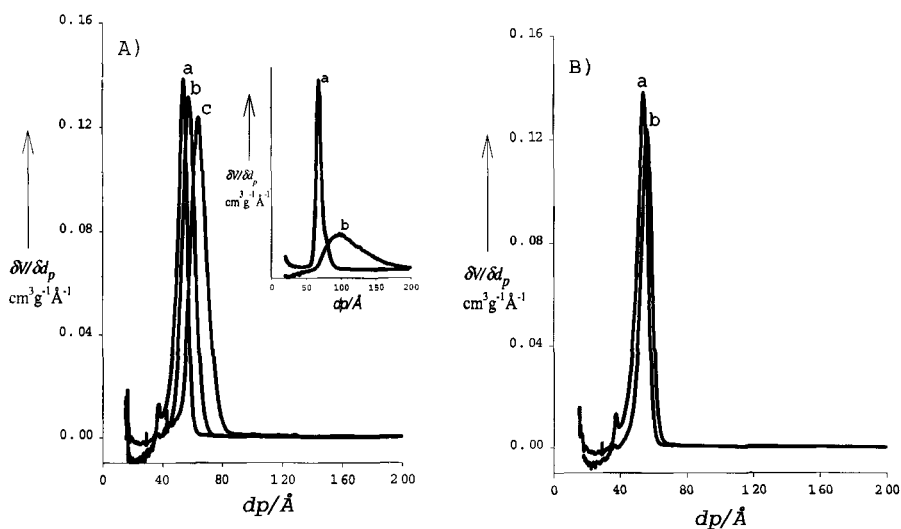


Figure 24. BJH pore diameter distributions calculated from the desorption branch of the isotherm for (A) ZSM-5 coated MesoAS treated in boiling water at 100°C for 48 h: a) before and b) after treatment for 48 h and c) for 120 h; (inset: the parent MesoAS sample treated in boiling water at 100°C for 48 h: a) before and b) after treatment for 48 h) and (B) ZSM-5 coated MesoAS: a) before and b) after steaming with 20% in N_2 at 800°C for 24 h [85].

3.5.2 Zeolite coated mesostructured cellular foams (MCF)

Unlike MCM-41 and SBA-15, which have mono-dimensional mesopore structures leading to mass transfer limitations, mesostructured cellular silica foams (MCF) are composed of uniformly sized, large spherical cells (up to 500 Å) with high surface area that are interconnected by uniformly sized windows to create a continuous 3-D pore system [49-52]. It would

therefore be also of interest to impart to these new larger pore materials the high hydrothermal stability already obtained by zeolite coating of SBA-15. Our objective was thus to prepare zeolite coated MCF using a mesostructured cellular foam precursor (MCF) and desired clear gel solutions containing zeolite seeds such as ZSM-5, TS-1 (MFI structure) and faujasitic zeolite type Y (FAU). The detailed synthesis procedure is better described in references [87-89].

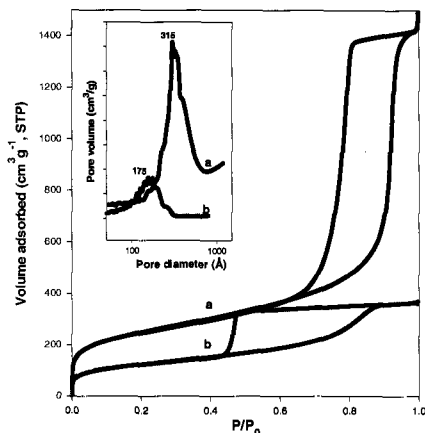


Figure 25. N_2 adsorption/desorption isotherms at -196°C and BdB-FHH pore diameter distributions calculated from the adsorption branch of the isotherm (Inset) for a) parent MCF and b) ZSM-5 coated MCF [87].

Figure 25 shows the N_2 adsorption/desorption isotherms and BdB-FHH cell size distributions calculated from the adsorption branch of the isotherm for the MCF sample before and after coating using a clear ZSM-5 gel solution. Table 3 summarizes for the same samples the BdB-FHH spherical cell sizes along with the BET surface areas and pore volumes. Significant decreases in surface area, spherical cell size and pore volume clearly indicate that zeolite nano-clusters were located inside the mesopore channels. XRD diagrams of the coated samples show no peaks in the 2θ range of $10\text{--}50^\circ$ indicating that the coating contains no crystals having diameters above ~ 50 Å. Figure 26 shows TEM photos of the parent MCF and ZSM-5 coated MCF samples. The parent sample presents a typical strut-like MCF structure (Fig. 26A). For the coated sample, slight deformation of the spherical cells was observed. However, some spots of $30\text{--}50$ Å in size (due to a higher density of zeolite particles compared to the amorphous mesopore walls) become visible as distributed homogeneously over the coated sample (Fig. 26B). The formation of ~ 30 Å particles is in

agreement with the initial stage of the ZSM-5 crystal growth mechanism reported in the literature [14-29].

Table 3. Physico-chemical properties of the parent meso-cellular alumino-silica foam (PMCF) and zeolite coated meso-cellular foam (zeolite-MCF) samples [87].

Materials	Si/Al ^a (atom.)	S _{BET} (m ² g ⁻¹)	Meso. vol. (cm ³ g ⁻¹)	Spheri. cavity diameter (Å) ^b
PMCF	200	875	2.35	315
ZSM-5Coated MCF	125	435	0.70	175
NaY Coated MCF	115	455	0.55	155

^a atomic Si/Al ratios obtained by atomic absorption spectroscopy.

^b cell diameter determined according to the BdB-FHH method using the spherical pore model.

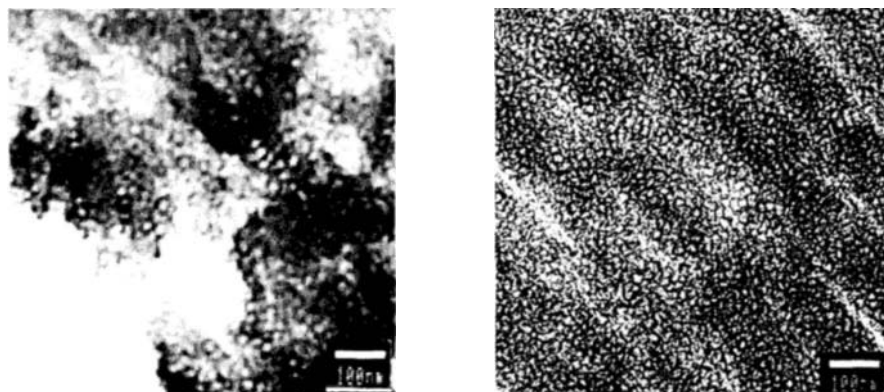


Figure 26. TEM image of (A) parent MCF and (B) ZSM-5 coated MCF [87].

Furthermore, ¹²⁹Xe NMR was also used as a probing technique for studying the internal pore structure of these materials. A weak band at ~174 ppm, which is characteristic of xenon adsorbed in the ZSM-5 micropore channels was observed for the ZSM-5 coated sample. Such band was indeed not present in the parent MCF sample [92]. Similar trends were also observed for the NaY coated MCF sample (Table 3). The ²⁹Si MAS spectrum of the parent MCF sample exhibited two broad resonances at -110 ppm for a Q⁴ environment and at -100 ppm for a Q³ environment together with a shoulder at 90 ppm ascribable to Q² species. However, the spectra of the coated MCF samples show a main Q⁴ peak at -108.5 ppm and a small Q³ shoulder peak at ~ -98 ppm and essentially no Q₂ peak was found (Fig. 27). These reflect a lower OH concentration in

the coated samples, which indicates the coating procedure led to grafting nano-clustered zeolite particles on the mesopore surface by the condensation reaction of silanol groups at the interface. Aluminum environments in these materials were also quantified by ultra-high field ^{27}Al MAS and MQMAS (750 MHz for ^1H) NMR [57]. For the parent MCF sample, two distinct aluminium environments were detected; a broad peak at ~ 53 ppm is a typical tetrahedral aluminum in amorphous materials and the second at ~ 0 ppm is extra-framework aluminum species. However, the coated samples (e. g., ZSM-5 and NaY coated MCF) show an additional sharp peak at ~ 56 ppm, which is characteristic of the tetrahedral aluminum in the zeolite framework [92,93]. The combination of these results suggests that zeolite nano-particles were located within the mesopore channels. The actual decrease in spherical cavity diameter (Table 3) indicates that this coating encompasses more than one monolayer of nanoparticles.

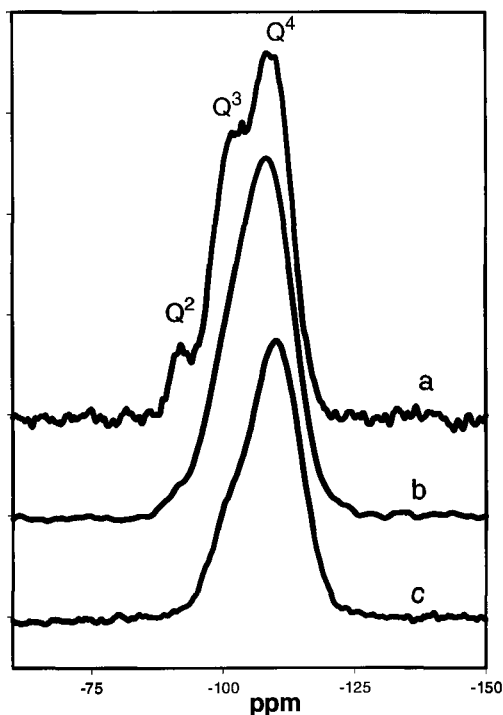


Figure 27. ^{29}Si MAS NMR spectra of a) parent MCF, b) NaY coated MCF and c) ZSM-5 coated MCF [87].

The IR spectra of pyridine adsorbed on protonated samples in the region 1600-1400 cm^{-1} after evacuation at different temperatures show that both Brönsted and Lewis acid sites of the coated samples are in much higher concentration than those of the corresponding MCF sample. The higher acidity can be attributed to secondary building units characteristic of zeolite within the mesopore walls. The order of the acid site density is HY coated MCF > H-ZSM-5 coated MCF >> parent MCF. The higher acid site density of the HY-coated sample could be due to the high aluminium loading in the faujasite gel (Si/Al=10) compared to that in ZSM-5 gel (Si/Al=50). The N_2 adsorption/desorption isotherms for the parent MCF, ZSM-5 and NaNaY coated samples were recorded before and after exposure to 20% steam at 800°C for 2 h. The mesopore structure of the parent sample had collapsed after this treatment. By contrast, no significant change in the mesopore structure under the same treatment conditions indicates that the coated samples are much more hydrothermally stable than the parent MCF sample. This is associated with the zeolite seeds coated on the mesopore surface, which create valence bonds with the precursor and heal defect sites reducing consequently the concentration of silanol groups. It can be concluded that zeolite coated MCF's are promising as new acid catalysts for the conversion of bulky molecules at high temperature [87].

TS-1 coated Ti-MCF materials have also been prepared by the same coating procedure using Ti-MCF and a diluted clear gel solution containing primary TS-1 nano-crystal units (atomic Si/Ti = 65) [88,89]. Similar results were also observed for these samples. Table 4 summarizes the physico-chemical properties of the mesostructured cellular titano-silica foam (parent Ti-MCF) sample and the same samples after a first (denoted as TS-1 coated Ti-MCF1) and a second coating (TS-1 coated Ti-MCF2). The spherical cell size decreases from 305 to 255 and 245 Å, and the BET surface area from 675 to 540 and 410 m^2/g for the first and second coating of the Ti-MCF sample, respectively. The mesopore volume also decreases accordingly from 2.05 to 1.40 and 1.20 cm^3/g . This again suggests that TS-1 nano-particles were located within the mesopore channels and not sufficiently mobile to allow their aggregation.

Finally, our results also illustrate the potential importance of zeolite seeds as precursors for the design of this new class of materials. Indeed, our methodology is not limited to the coating of MFI and FAU seeds, since primary units with diameters of 2.8 nm for MFI/MEL structures, 2.6 nm for zeolite beta, 1.5 nm for ZSM-12 and 1.6 nm for zeolite sodalite etc. have been reported [14-29]. They can potentially be used to prepare a large variety of zeolite coated mesoporous molecular sieves.

Table 4. Physico-chemical properties of the parent Meso-Cellular Foam (Ti-MCF) and TS-1 coated Meso-Cellular Foam (TS1-MCF) samples [88,89].

N ^o	Materials	Si/Ti ^a (atomic ratio)	S _{BET} (m ² /g)	Meso. vol. (cm ³ /g)	Cell dia. (Å) ^b
1	Ti-MCF	65	675	2.05	305
2	TS-1 coated Ti-MCF1	64	540	1.40	255
3	TS-1 coated Ti-MCF2 ^c	65	410	1.20	245
4	Ti-MCF recycled ^d	72	580	1.85	325
5	TS-1 coated Ti-MCF1 recycled	64	530	1.40	255
6	TS-1 coated Ti-MCF2 recycled	66	415	1.25	245

^a atomic Si/Ti ratios obtained by atomic absorption spectroscopy.

^b pore diameter determined according to the BdB-FHH method.

^c TS-1 coated Ti-MCF1 followed by a second coating.

^d catalyst after 24 h of 1-naphtol hydroxylation by H₂O₂ reaction in the conditions of Table 3 and calcined at 550°C for 4 h.

4 Catalytic properties

For a comprehensive review of the catalytic properties of mesostructured materials, we refer the reader to the various review papers published between 1997 and 2001, references [4,104-108]. They all discuss the need for a steam stable mesoporous molecular sieve materials that could perform such high temperature acid catalyzed reactions as cracking and hydrocracking or play the role of a support for hydrotreating catalysts. With the recent development of composite zeolite/MMS materials, this goal is indeed essentially met. Another interesting potential application of such composites is the liquid phase oxidation of organic molecules by titanium zeolites such as TS-1. The hydrodynamic diameter of the organics, which can be oxidized this way, is limited by the pore apertures of MFI and Beta zeolites. Thus a composite where-by a substantial external surface area of TS-1 nanocrystals is accessible through mesopores is certainly a potentially interesting catalyst. In the text below we discuss briefly the results in these two areas.

Table 4. Physico-chemical properties of the parent Meso-Cellular Foam (Ti-MCF) and TS-1 coated Meso-Cellular Foam (TS1-MCF) samples [88,89].

N ^o	Materials	Si/Ti ^a (atomic ratio)	S _{BET} (m ² /g)	Meso. vol. (cm ³ /g)	Cell dia. (Å) ^b
1	Ti-MCF	65	675	2.05	305
2	TS-1 coated Ti-MCF1	64	540	1.40	255
3	TS-1 coated Ti-MCF2 ^c	65	410	1.20	245
4	Ti-MCF recycled ^d	72	580	1.85	325
5	TS-1 coated Ti-MCF1 recycled	64	530	1.40	255
6	TS-1 coated Ti-MCF2 recycled	66	415	1.25	245

^a atomic Si/Ti ratios obtained by atomic absorption spectroscopy.^b pore diameter determined according to the BdB-FHH method.^c TS-1 coated Ti-MCF1 followed by a second coating.^d catalyst after 24 h of 1-naphtol hydroxylation by H₂O₂ reaction in the conditions of Table 3 and calcined at 550°C for 4 h.

4 Catalytic properties

For a comprehensive review of the catalytic properties of mesostructured materials, we refer the reader to the various review papers published between 1997 and 2001, references [4,104-108]. They all discuss the need for a steam stable mesoporous molecular sieve materials that could perform such high temperature acid catalyzed reactions as cracking and hydrocracking or play the role of a support for hydrotreating catalysts. With the recent development of composite zeolite/MMS materials, this goal is indeed essentially met. Another interesting potential application of such composites is the liquid phase oxidation of organic molecules by titanium zeolites such as TS-1. The hydrodynamic diameter of the organics, which can be oxidized this way, is limited by the pore apertures of MFI and Beta zeolites. Thus a composite where-by a substantial external surface area of TS-1 nanocrystals is accessible through mesopores is certainly a potentially interesting catalyst. In the text below we discuss briefly the results in these two areas.

4.1 Acid catalysts

The ZSM-5/MCM-41 and Beta/MCM-41 composites prepared through a two-step crystallization process [34] show enhanced catalytic cracking activity of bulky molecules, as compared to those of the analogous MCM-41, ZSM-5 and the mechanical mixture of MCM-41 and zeolite. For example, the conversion of n-dodecane was 25% at 500°C over H-form ZSM-5/MCM-41 composite, compared to 9% over analogous H-form MCM-41 with the same Si/Al ratio (Si/Al = 14) [34,35]. The catalytic activities over Beta/MCM-41 composites with different % crystallinities for n-hexane cracking at 400°C are also summarized in Table 5. It can be seen that the catalytic activity increases with increasing % crystallinity. This is in agreement with an enhancement of their acidity observed by the NH₃-TPD results [36,37].

Table 5. Acidity of Beta/MCM-41 composites with different % crystallinities measured by NH₃-TPD and catalytic activity for n- heptane cracking at 400°C [37].

Sample	Peak temp./K		Acidity ($\times 10^{20} \text{ g}^{-1}$)			n-Heptane* conver. (%)
	I	II	I	II	I+II	
S1	498	654	0.77	1.07	1.84	51
S2	517	652	0.75	1.16	1.91	63
S3	519	676	0.81	1.27	2.08	75
S4	507	664	0.87	1.43	2.30	84

conversion of n-heptane cracking over zeolite Beta under the same conditions is 95%.

*Catalytic activities for n-heptane cracking were tested in a pulse microreactor with a catalyst load of 15 mg (60–80 mesh) after being activated at 400°C for 2 h. Hydrogen was used as the carrier gas at a flow rate of $45 \text{ cm}^3 \text{ min}^{-1}$. Following this procedure 1 μl of the reactant was injected into the catalyst bed through a microsyringe. The cracking products were analyzed by an on-line gas chromatograph equipped with a flame ionization detector.

Cumene cracking was also carried out over mesoporous aluminosilicates (10% Al-MSU) assembled from nanoclustered zeolite Y seeds, compared to those of a conventional 10%Al-MCM-41 before and after steaming (20% water vapor in N₂ at 800 °C for 5 h). Although the two calcined mesostructures are nearly equivalent in activity (Fig. 28), after exposure to steam, 10%Al-MSU is much more active than 10%Al-MCM-41. On the other hand, Pérez Pariente et al. [79] synthesized

mesoporous aluminosilicate using the same above procedure except that the building blocks precursors of faujasite zeolite were obtained in the presence of tetramethylammonium (TMA^+) cations. The catalytic activity of this sample in *m*-xylene conversion is nearly two orders of magnitude higher than that of analogous Al-MCM-41 and approaches that of USY. These results suggest that the synthesis route in the presence of TMA^+ cations gives rise to mesostructured aluminosilicates of enhanced acidity [79].

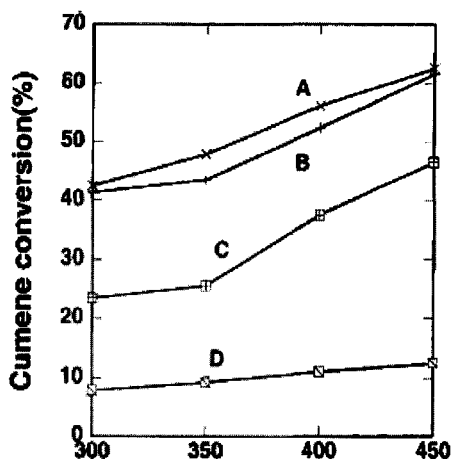


Figure 28. Cumene conversions over mesoporous aluminosilicates in the temperature range 300–450°C: (A and C) conversions obtained for calcined and steamed samples of 10%Al-MSU-S, respectively; (B and D) conversions for calcined and steamed samples, respectively, for analogous 10%Al-MCM-41. Reaction conditions: 6 mm i.d. fixed bed quartz reactor; 200 mg catalyst; cumene flow rate, 4.1 $\mu\text{mol}/\text{min}$; N_2 carrier gas, 20 cm^3/min ; conversions reported after 60 min on stream (ref. 68).

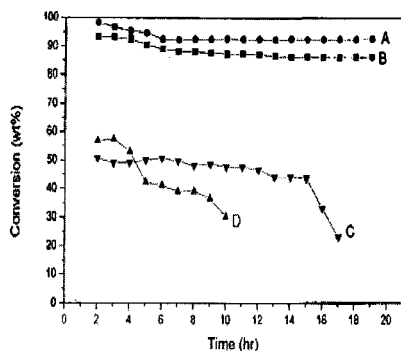


Figure 29. Catalytic conversion of 2-butene in alkylation of isobutene with butene vs reaction time over various catalysts (each of 0.5 g) of (A) MAS-5, (B) H-Beta, (C) MCM-41, and (D) HZSM-5 at a reaction temperature of 25 °C with a isobutane/butene molar ratio of 12/1, a 1-butene/2-butene molar ratio of 8/1, and WHSV of 9 h^{-1} (ref. 70).

Zhang et al. [70–72] have also reported various MCM-41 analogs (denoted MAS-5) which were assembled from zeolite Beta seeds, also exhibiting stronger acidity and higher activity than conventional Al-MCM-41 for 1,3,5-triisopropylbenzene cracking. The calcined MAS-5 gives both higher activity and longer catalyst life than MCM-41 (Table 6). Even after treatment in boiling water for 300 h, at 600 °C for 4 h, or

steaming at 800 °C for 2 h, MAS-5 still showed high catalytic activity. By contrast MCM-41 completely lost its activity after these treatments. In addition, MAS-5 showed higher catalytic activity than Beta zeolite and MCM-41 at a similar Si/Al ratio for the alkylation of 2-butene with isobutene (Fig. 29). The acidity of MAS-5 was reported to be very similar to Beta zeolite, as judged by temperature programmed desorption of ammonia. The higher catalytic activity for the alkylation was attributed to the easier diffusion of products in the mesoporous channels of MAS-5 than in microporous Beta zeolite.

Table 6. Catalytic activities in cracking of 1,3,5-triisopropylbenzene* on various catalysts [70].

Sample	SiO ₂ / Al ₂ O ₃	Treatment	Conversion (%)	Reaction temp., °C
HZSM-5	84		1.7	250
HMCM-41	80		65.8	250
HMCM-41	80	boiling water for 6 h	<1.0	250
HMCM-41	80	treated with 100% water vapor at 600 °C for 2 h	<1.0	250
MAS-5	81		78.8	250
MAS-5	81	boiling water for 300 h	79.1	250
MAS-5	81	treated with 100% water vapor at 600 °C for 4 h	78.9	250
MAS-5	80	treated with 100% water vapor at 800 °C for 2 h	77.5	250
MAS-5	123		87.0	320
MAS-5	81		90.1	320
MAS-5	59		95.2	320

* Catalytic reactions were performed by pulse injections, and the data presented in this table are the average values of 5 injections. In each run, 50 mg of catalyst was used, pulse injection of the reactant was 0.4 µl, and the reaction flow rate was 53.7 ml/min.

4.2 Redox Catalysts

Catalytic activities for the oxidation of aromatics using H₂O₂ as an oxidant over various mesoporous titanasilicates derivatives were also reported. For example, MAS-9, which was assembled from TS-1 seeds and triblock copolymers (Pluronic P123) in a strong acidic medium, showed very high catalytic activity in phenol hydroxylation, with 26% of phenol conversion,

which is comparable with that of TS-1. In styrene epoxidation, MTS-9 shows activity and selectivity similar to those of TS-1, which are much lower from those of conventional Ti-MCM-41. However, in bulkier molecule hydroxylation such as 2,3,6-trimethylphenol, conventional Ti-MCM-41 is inactive due to the relatively low oxidation ability of Ti species in the amorphous wall of Ti-MCM-41, and TS-1 is also inactive due to the inaccessibility of the small micropores of TS-1 to the large diameter bulky molecule of 2,3,6-trimethylphenol under the conditions given in Table 7. However, MTS-9 is very active for this reaction with a conversion of 18.8% under the same reaction conditions, indicating that MTS-9 is an effective catalyst for the oxidation of bulky molecules (Table 7) [71-73].

Table 7. Catalytic Activities in Oxidation Reactions using H_2O_2 over MTS-9, Ti-MCM-41 and TS-1 samples (ref. 71).

Samples	Reactions	TOF	Product selectivity (%)			
			conv. (%)	P1	P2	P3
MTS-9	phenol hydroxylation ^c	6.8	26.3	59.5	39.8	0.7
Ti-MCM-41	phenol hydroxylation ^c	0.5	2.5	60.1	38.0	1.9
Ti-HMS ^a	phenol hydroxylation ^c	0.1	0.5	58.5	41.5	0.5
TS-1	phenol hydroxylation ^c	5.5	28.0	50.4	48.6	1.0
MTS-9	styrene epoxidation ^d	9.4	56.4	28.0	29.3	42.7
Ti-MCM-41	styrene epoxidation ^d	6.1	48.3			100
TS-1 ^b	styrene epoxidation ^d	5.2	54.6	13.3	58.3	29.0
MTS-9	trimethylphenol hydroxylation ^e	7.4	18.8	66.7	21.1	12.2
Ti-MCM-41	trimethylphenol hydroxylation ^d	1.4	4.1	25.5	69.8	4.6
Ti-HMS ^a	trimethylphenol hydroxylation ^e	0.5	2.0	25.0	70.0	5.0
TS-1 ^b	trimethylphenol hydroxylation ^e	0.3	1.2	71.1	17.6	11.3

^a Ti-HMS with Si/Ti ratio of 30, ^b TS-1 with Si/Ti ratio of 30. Reaction conditions: water as a solvent, reaction temperature at 80 °C, phenol/ H_2O_2 3/1 (molar ratio), reaction time for 4 h, catalyst/phenol) 5% (weight ratio). The products are catechol (P1), hydroquinone (P2), and benzoquinone (P3). The product of tar is not included. ^d Reaction conditions: acetone as a solvent, reaction temperature at 45 °C, styrene/ H_2O_2 3/1 (molar ratio), reaction time for 5 h, catalyst/phenol) 5% (weight ratio). The products are styrene epoxide (P1), phenylacetaldehyde (P2), and benzaldehyde (P3). ^e Reaction conditions: acetonitrile as a solvent, reaction temperature at 80 °C, trimethylphenol/ H_2O_2 3/1 (molar ratio), reaction time for 4 h, catalyst/phenol) 5% (weight ratio). The product are trimethylhydroquinone (P1), trimethylbenzoquinone (P2), others (P3).

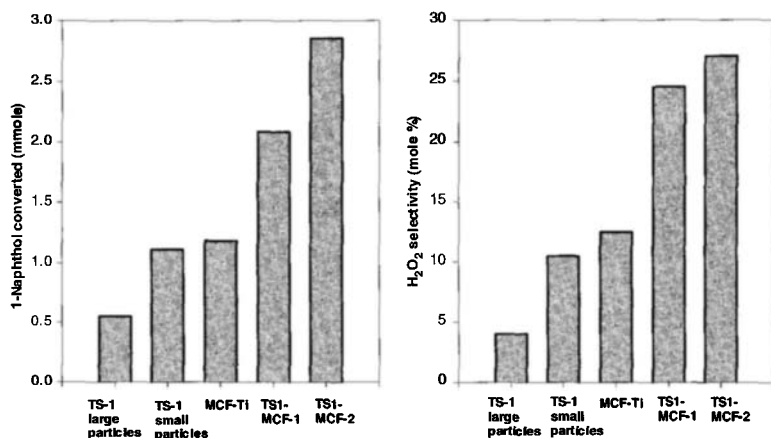


Figure 30. Catalytic activity of the parent Ti-MCF and TS-1 coated Ti-MCF samples in 1-naphthol hydroxylation using TS-1 samples as references. Reaction conditions: catalyst 0.1 g, 1-naphthol 1.0 g (6.95 mmole), H₂O₂ 30% aqueous solution 2.36 g (20.85 mmole), solvent CH₃CN 10g, temperature 333 K, reaction time 24 h (refs. 88,89).

In a recent study [88,89], we showed that TS-1 coated Ti-MCF materials could be prepared by the coating procedure using a diluted clear gel solution containing primary TS-1 nano-crystal units and Ti-MCF. These coated samples exhibit higher activity and H₂O₂ selectivity for bulky substrates such as 1-naphthol compared to those of both the parent Ti-MCF and TS-1 samples. The oxidation of 1-naphthol that cannot diffuse inside the TS-1 micropore channels was performed over the parent Ti-MCF and TS-1 coated Ti-MCF using hydrogen peroxide (H₂O₂) as the oxidant. Two TS-1 samples with small crystal size (~0.2 μm) and large crystal size (~10 μm) were used as references to yield information on the influence of the external surface (e. g., 105 m²/g and 35 m²/g, respectively) on the catalytic reaction. The catalytic activities of these samples in the 1-naphthol hydroxylation, expressed as a number of moles of 1-naphthol converted after 24 h are summarized in Table 8. The TS-1 samples exhibit lower activity and H₂O₂ selectivity than the MCF samples. However, the 1-naphthol conversion over small crystal TS-1 is higher than that over large crystal TS-1 (0.55 mmol. and 1.11 mmol. for the small and large crystal samples, respectively). The increase in the 1-naphthol conversion can be attributed to the increase in the external surface from 35 m²/g to 105 m²/g (see Table 8). As seen in Fig. 30, even having a very high mesopore surface area (675 m²/g), the parent Ti-MCF sample is only

slightly more active than the small crystal TS-1 under the same reaction conditions. However, the coating procedure greatly increased the activity and the H_2O_2 selectivity. About two and half times higher 1-naphthol conversion and two times higher H_2O_2 selectivity on TS-1 coated Ti-MCF2 compared to the parent uncoated Ti-MCF sample were demonstrated (Fig. 30 and Table 8).

Table 8: Catalytic activity of the Parent Meso-Cellular Foam (Ti-MCF) and TS-1 coated Ti-MCF (TS-1 coated Ti-MCF) samples in 1-naphthol hydroxylation for 24 h [88,89].

Nº	Materials	1-naphthol converted (in mmole)	H_2O_2 selectivity (mole %)
1	Ti-MCF	1.18	12.5
2	TS-1 coated Ti-MCF1	2.08	24.5
3	TS-1 coated Ti-MCF2 ^a	2.85	27.0
4	TS-1 (large crystals)	0.55	4.0
5	TS-1 (small crystals)	1.11	10.5

^a obtained by a second coating of TS-1 coated MCF1.

Reaction conditions: catalyst 0.1 g, 1-naphthol 1.0 g (6.95 mmole), H_2O_2 30% aqueous solution 2.36 g (20.85 mmole), solvent CH_3CN 10g, temperature 333 K, reaction time 24 h.

The activity enhancement is reasonable because the coating process changes the amorphous hydrophilic surface of the parent sample into to a crystalline relatively hydrophobic surface by reducing its silanol groups surface density, as seen by ^{29}Si MAS NMR spectra before and after coating. This makes both the substrate and oxidant molecules easily accessible to the Ti active sites. These results also suggest that these novel TS-1 coated Ti-MCF's are promising as new catalysts for the oxidation of bulky molecules.

5 Future Challenges

Generally, the strategies discussed in section III lead to materials having improved thermal stability and better properties as catalytic materials in comparison with the originally reported M41-S materials. Nevertheless, the acidity and hydrothermal stability of composite mesostructured

aluminosilicates are still lower than those of crystalline microporous zeolites.

To date, a large number of mesoporous materials of a variety of oxides with different, pore size and inorganic wall thickness is available. According to Davis [94], it remains unclear why the vast majority of ordered mesoporous materials cannot be synthesized in fully crystalline form. The syntheses of inorganic mesoporous materials occur under thermodynamic conditions comparable to those encountered during the syntheses of the more open zeolite frameworks (such as VPI-5 and cloverite [95]), suggesting that thermodynamic barriers in the assembly process are not causing the lack of crystallinity. Ordered mesoporous materials were first prepared using charged organic components, and charge matching between the organic and inorganic components influence the assembly of ordered mesoporous solids. This aspect of their synthesis may be an impediment to crystallinity [96]. However, the ordered mesoporous materials can now be prepared using non-ionic organic surfactants. These assemblies would suggest that charge matching is not the only impediment to crystallinity. Likewise, it is now known that not only ordered mesoporous materials can form through intermediate phases that are layered, but also zeolites (examples include MCM-22 [97] and ferrierite [98]). The involvement of layered intermediates during formation thus does not seem to be the reason why ordered mesoporous materials do not crystallize.

A plausible explanation for the lack of crystallinity may lie in the correlation between the framework density (FD, the number of atoms per nm^3) and the structural features of porous materials (parameter MINR, minimum ring size for every T-atom) [99]. If the structure has T-atoms in rings of different sizes, then a “+” is assigned.

For example, $\text{MINR} = 4+$ denotes that some of the T-atoms are in 4-membered rings, while others are in rings of larger size. All crystalline and ‘tetrahedral’ materials follow this relationship. In the case of oxide-based solids, most structures have $\text{MINR} > 4+$, which would correlate with a maximum void fraction of about 0.5. The correlation does not hold for crystalline structures built from units containing non-tetrahedral atoms, which have indeed been shown to exceed this void fraction [100-102]. Regardless of the phenomena that are the origin of the correlation between the FD and MINR, they may be the reasons why the ordered mesoporous materials are not crystalline (void fractions violate this relationship).

Table 9: Synthetic framework materials with numerous three-membered rings [94].

Material	Composition	FD(atoms per nm ³)	Pore size	Year
Lovdarite	Beryllosilicate	18.4	9 MR	1986
VPI-7	Zincosilicate	17.1	9 MR	1991
RUB-17	Zincosilicate	16.8	9 MR	1995
VPI-9	Zincosilicate	16.7	8MR	1996
VPI-10	Zincosilicate	15.3	9 MR	1996
RUB-23	Lithosilicate	17.7	8 MR	2000
RUB-29	Lithosilicate	17.7	10 MR	2001
ASU-15	Ge ₂ ZrO ₆ F	9.1	10 MR	2000
OSB-1	Beryllosilicate	13.3	14 MR	2001
OSB-2	Beryllosilicate	12.7	8 MR	2001

FD, framework density; MR, membered rings.

In order to obey the correlation, ordered mesoporous materials would need to have MINR = 3+, and they would need to contain a large number of three-membered rings (3MRs). Table 9 lists the synthetic crystalline materials that possess a significant number of 3MRs, which include zincosilicates, lithium silicates and a Ge₂ZrO₆F material. The materials listed illustrate the significant progress in the synthesis of MINR = 3+ materials, which now provides routes to new porous solids [94]. Crystalline materials with the pore volumes of the ordered mesoporous materials would require MINR = 3+ if they were to be tetrahedral frameworks, so it is possible that the appropriate oxide chemistry that would allow the realization of such materials has not yet been explored. A recently reported ordered mesoporous zincosilicate [103] did not contain sufficient amounts of zinc to facilitate the formation of a significant number of 3MRs, and further exploration of zinc-based materials might thus allow the preparation of ordered mesoporous materials that are crystalline.

As mentioned above, it is not known why ordered mesoporous materials do not form crystalline frameworks. Fully crystalline structures containing structured mesopores and exhibiting thermal and hydrothermal stability are highly desirable, especially if the pore system is more than one-dimensional. A major challenge facing the porous materials community is therefore the development of tetrahedral T-atom frameworks containing crystalline mesopore walls in a multidimensional network. The largely unexplored approach of creating mesopore structures that are based on 3-membered rings might prove successful in this regard.

6 Conclusion

Less than two years ago, it was thought that none of the MMS materials synthesized at that time was adequate for high temperature acid catalysis of reactions such as cracking and hydrocracking as they lacked both strong acidity and hydrothermal stability. Several of the various zeolite/MMS composites synthesized in the meantime are indeed solving this important problem. At the present time, actual experimental illustrations of these catalytic properties are still search but very encouraging. This research activity must therefore be actively pursued and various suggestions were made this text as to the possible trends, which could lead to still enhanced catalytic materials. Among these the suggestion to fully explore the autoassembly and coating of polyanions and nano-seeds of zeolites and the possibilities to synthesize crystalline mesostructured materials based on 3-membered rings, are certainly worth pursuing.

7 Acknowledgements

Some of the work in this review was supported by the Natural Science and Engineering Research Council of Canada (NSERC) through a strategic grant.

References

1. Kresge C. T., Leonowicz M. E., Roth W. J., Vartuli J. C. and Beck J. S., Ordered mesoporous molecular sieves synthesized by a liquid-crystal template mechanism, *Nature* **359** (1992) pp. 710-712.
2. Beck J. S., Vartuli J. C., Roth W. J., Leonowicz M. E., Kresge C. T., Schmitt K. D., Chu C. T.-W., Olsen D. H., Sheppard E. W., McCullen S. B., Higgins J. B. and Schlenker J. L., A new family of mesoporous molecular sieves prepared with liquid crystal templates, *J. Am. Chem. Soc.* **114** (1992), pp. 10834-10843.
3. Vartuli J. C., Mesoporous molecular sieves: The past, present and future, *Stud. Surf. Sci. Catal.* (2003) in press.
4. Trong On D., Giscard D., Danumah C. and Kaliaguine S., Perspectives in catalytic applications of mesostructured materials, *Appl. Catal. A: General* **222**, (2001) pp. 299-357.
5. Szostak R., *Molecular Sieves: Principles of Synthesis and Identification*, Van Nostrand Reinhold, New York, (1989) pp. 190-205.
6. Serrano D. P. and van Grieken R., Heterogenous events in the crystallization of zeolites, *J. Mater. Chem.* **11** (2001), pp. 2391-2407.
7. Xu W., Dong J., Li J., Li J. and Wu F., A novel method for the preparation of zeolite ZSM-5, *J. Chem. Soc., Chem. Commun.* (1990) pp. 755-756.
8. Kim M. H., Li H. X. and M. E. Davis, Synthesis of zeolites by water-organic vapor-phase transport, *Micropor. Mater.* **1** (1993) pp. 191-200.

9. Matsukata M., Nishiyama N. and Ueyama K., Synthesis of zeolites under vapor atmosphere : Effect of synthetic conditions on zeolite structure, *Micropor. Mater.* **1** (1993) pp. 219-222.
10. Uguina M. A., Ovejero G., van Grieken R., Serrano D. P. and Camacho M., Synthesis of Titanium Silicalite-1 from an $\text{SiO}_2\text{-TiO}_2$ cogel using a wetness impregnation method, *J. Chem. Soc., Chem. Commun.* (1994) pp. 27-28.
11. Serrano D. P., Uguina M. A., Ovejero G., van Grieken R. and Camacho M., Synthesis of TS-1 by wetness impregnation of amorphous $\text{SiO}_2\text{-TiO}_2$ solids prepared by the sol-gel method, *Micropor. Mater.* **4** (1995) pp. 273-282.
12. Serrano D. P., Uguina M. A., Ovejero G., van Grieken R. and Camacho M., Evidence of solid-solid transformations during the TS-1 crystallization from amorphous wetness impregnated $\text{SiO}_2\text{-TiO}_2$ xerogels, *Micropor. Mater.* **7** (1996) pp. 309-321.
13. Serrano D. P., Uguina M. A., Ovejero G., van Grieken R. and Camacho M., Crystallization of TS-1 and TS-2 zeolites with contribution of solid-solid transformations, *J. Chem. Soc., Chem. Commun.* (1996) pp. 1097-1098.
14. Persson A. E., Schoeman B. J., Sterte J. and Otterstedt J.-E., The synthesis of discrete colloidal particles of TPA-silicalite-1, *Zeolites* **14** (1994) pp. 557-567.
15. B. J. Schoeman, J. Sterte and J.-E. Otterstedt, Analysis of the crystal growth mechanism of TPA-silicalite-1, *Zeolites* **14** (1994) pp. 568-575; Schoeman B. J., A high temperature in situ laser light-scattering study of the initial stage in the crystallization of TPA-silicalite-1, *Zeolites* **18** (1997) pp. 97-105; Schoeman B. J. and Regev O., A study of the initial stage in the crystallization of TPA-silicalite-1, *Zeolites* **17** (1996) pp. 447-456.
16. Schoeman B. J., The homogeneous nature of clear TPA-silicalite-1 precursor solutions, *Microporous Mater.* **9** (1997) pp. 267-271; Schoeman B. J., *Stud. Surf. Sci. Catal.* **105** (1997) pp. 647; Schoeman B. J., Analysis of the nucleation and growth of TPA-silicalite-1 at elevated temperatures with the emphasis on colloidal stability, *Microporous Mesoporous Mater.* **22** (1998), pp. 9-22.
17. Dokter W. H., van Garderen H. F., Beelen T. P. M., van Santen R. A. and Brass W., ggregates of fractal dimension, *Angew. Chem., Int. Ed. Engl.* **34** (1995) pp. 73-75.
18. de Moor P.-P. E. A., Beelen T. P. M. and van Santen R. A., SAXS/WAXS study on the formation of precursors and crystallization of silicalite, *Microporous Mater.* **9** (1997) pp. 117-130; de Moor P.-P. E. A., Beelen T. P. M., Komanschek B. U., Diat O. and van Santen R. A., In situ investigation of Si-TPA-MFI crystallization using (Ultra-) Small- and Wide-Angle X-ray scattering, *J. Phys. Chem. B* **101** (1997) pp. 11077-11086.
19. de Moor P.-P. E. A., Beelen T. P. M., van Santen R. A., Insitu obervation of nucleation and crystal growth in zeolite synthesis. A Small-Angle X-ray scattering investigation on Si-TPA-MFI, *J. Phys. Chem. B* **103** (1999) pp. 1639-1650; de Moor P.-P. E. A., Beelen T. P. M., van Santen R. A., Beck L. W., Davis M. E., Si-MFI crystallization using a "Dimer" and "Trimer" of TPA studied with Small-Angle X-ray scattering, *J. Phys. Chem. B* **104** (2000) pp. 7600-7611.
20. de Moor P.-P. E. A., Beelen T. P. M., van Santen R. A., Tsuji K., Davis M. E., SAXS and USAXS investigation on nanometer-scaled precursors in organic-mediated zeolite crystallization from gelating systems, *Chem. Mater.* **11** (1999) pp. 36-43.
21. de Moor P. P. E. A., Beelen T. P. M., Komanschek B. U., Beck L. W., Wagner P., Davis M. E. and van Santen R. A., Imaging the assembly process of the organic-mediated synthesis of a zeolite *Chem. Eur. J.* **5** (1999) pp. 2083-2088.

22. Ravishankar R., Kirschhock C. E. A., Knops-Gerrits P.-P., Feijen E. J. P., Grobet P. J., Vanoppen P., De Schryver F. C., Mieke G., Fuess H., Schoeman B. J., Jacobs P. A. and Martens J. A., Characterization of nanosized materials extracted from clear suspension for MFI zeolite synthesis, *J. Phys. Chem. B* **103** (1999) pp. 4960-64.
23. Kirschhock C. E. A., Ravishankar R., Verspeurt F., Grobet P. J., Jacobs P. A., Martens J. A., Identification of precursor species in the formation of MFI zeolite in the TPAOH-TEOS-H₂O system, *J. Phys. Chem. B* **103** (1999) pp. 4965-71; Kirschhock C. E. A., Ravishankar R., Van Looveren L., Jacobs P. A., Martens J. A., Mechanism of transformation of precursors into nanoslab in the early stages of MFI and MEL zeolite formation from TPAOH-TEOS-H₂O and TBAOH-TEOS-H₂O mixtures, *J. Phys. Chem. B* **103** (1999) pp. 4972-4978.
24. Knight C. T. G. and Kinrade S. D., Comment on "Identification of precursor species in the formation of MFI zeolite in the TPAOH-TEOS-H₂O system", *J. Phys. Chem. B* **106** (2002) pp. 3329-3332; Kirschhock C. E. A., Ravishankar R., Verspeurt F., Grobet P. J., Jacobs P. A. and Martens J. A., Reply to the comment on "Identification of precursor species in the formation of MFI zeolite in the TPAOH-TEOS-H₂O system", *J. Phys. Chem. B* **106** (2002) pp. 3333-3334.
25. Kirschhock C. E. A., Buschmann V., Kremer S., Ravishankar R., Houssin C. J. Y., Mojet B. L., van Santen R. A., Grobet P. J., Jacobs P. A., Martens J. A., Zeosil nanoslabs: Building blocks in *n*Pr₄N⁺-mediated synthesis of MFI zeolite, *Angew. Chem. Int. Ed.* **40** (2001) pp. 2637-2640.
26. Burkett S. L., Davis M. E., Mechanism of structure Direction in the synthesis of Si-ZSM-5: An investigation by intermolecular ¹H-²⁹Si CP MAS NMR *J. Phys. Chem.* **98** (1994) pp. 4647-4653.
27. Corma A., Fornés V., Pergher S. B., Maesen T. L. M., Buglass J. G., Delaminated zeolite precursors as selective acidic catalysts, *Nature* **396** (1998) pp. 353-356.
28. Corma A., Diaz U., Domine M. E., Fornés V., AlITQ-6 and TiITQ-6: Synthesis, characterization, and catalytic activity, *Angew. Chem., Int. Ed. Engl.* **39** (2000) pp. 1499-1501; Corma A., Díaz-Cabanas M. J., Fornés V., Synthesis, characterization and catalytic activity of a large-pore tridirectional zeolite, H-ITQ-7, *Angew. Chem., Int. Ed. Engl.* **39** (2000) pp. 2346-2349.
29. Corma A., Diaz U., Domine M. E., Fornés V., New aluminosilicate and titanosilicate delaminated materials active for acid catalysis, and oxidation reaction using H₂O₂, *J. Am. Chem. Soc.* **122** (2000) pp. 2804-2809.
30. Liu Y., Pinnavaia T. J., Aluminosilicate mesostructures with improved acidity and hydrothermal stability, *J. Mater. Chem.* **122** (2002) pp. 3179-3190.
31. Kloetstra K. R., Zandbergen H. W., Jansen J. C., van Bekkum H., Overgrowth of mesoporous MCM-41 on faujasite, *Microporous Mater.* **6** (1996) pp. 287-293.
32. Karlsson A., Stocker M., Schmidt R., Attempts of structuring the pore walls of mesoporous MCM-41 materials in *Proceedings of the 12th International Zeolite Conference*; MRS: Warrendale, PA, Vol. 1, (1999) pp. 713-718.
33. Karlsson A., Stocker M., Schmidt R., Composites of micro- and mesoporous materials: simultaneous syntheses of MFI/MCM-41 like phases by a mixed template approach, *Micropor. Mesopor. Mater.* **27** (1999) pp. 181-192.
34. Huang L., Guo W., Deng P., Xue Z., Li Q., Investigation of synthesizing MCM-41/ZSM-5 composites, *J. Phys. Chem. B* **104** (2000) pp. 2817-2823.
35. Huang L., Li Q., Synthesis and characterization of composite MCM-41/ZSM-5 material in *Proceedings of the 12th International Zeolite Conference*; MRS: Warrendale, PA, Vol. 1 (1999) pp. 707-712.

36. Guo W., Huang L., Deng P., Xue Z., Li Q., Characterization of Beta/MCM-41 composite molecular sieve compared with the mechanical mixture, *Micropor. Mesopor. Mater.* **44-45** (2001) pp. 427-434; Guo W., Huang L., Ha C. S., Li Q., Cubic mesoporous aluminosilicate assembled from nanoclustered zeolite Beta seeds, *Stud. Surf. Sci. Catal.* (2003), in press.
37. Guo W., Xiong C., Huang L., Li Q., Synthesis and characterization of composite molecular sieves comprising zeolite Beta with MCM-41 structures, *J. Mater. Chem.* **11** (2001) pp.1886-1890.
38. Goto Y., Fukushima Y., Ratu P., Imada Y., Kubota Y., Sugi Y., Ogura M., Matsukata M., Mesoporous material from zeolite, *J. Porous. Mater.* **9** (2002) pp. 43-48.
39. Kloetstra K. R., van Bekkum H., Jansen J. C., Mesoporous material containing framework tectosilicate by pore-wall recrystallization, *Chem. Commun.* (1997) 2281-2282.
40. Verhoef M. J., Kooyman P. J., van der Waal J. C., Rigutto M. S., Peters J. A. and van Bekkum H., Partial transformation of MCM-41 material into zeolites: Formation of nanosized MFI type crystalites, *Chem. Mater.* **13** (2001) pp. 683-687.
41. Trong On D. and Kaliaguine S., Large pore mesoporous materials with semicrystalline zeolitic framework, *Angew. Chem. Int. Ed.* **40** (2001) pp. 3248-3251.
42. Trong On D., Lutic D. and Kaliaguine S., An example of mesostructured zeolitic material: UL-TS-1, *Micropor. Mesopor. Mater.* **44-45** (2001) 435-444.
43. Trong On D., Reinert P., Bonneviot L. and Kaliaguine S., Hierarchically mesostructured zeolitic materials with the MFI structure, *Stud. Surf. Sci. Catal.* **135** (2001) pp. 929-936.
44. Ungureanu A., Hoang T. V., Trong On D., Dumitriu E. and Kaliaguine S., Transalkylation of toluene with trimethylbenzenes over UL-ZSM-5, in preparation.
45. Zhao D., Feng J., Huo Q., Melosh N., Fredrickson G. H., Chmelka B. F. and Stucky G. D., Triblock copolymer syntheses of mesoporous silica with periodic 50 to 300 Angstrom pores, *Science* **279** (1998) pp. 548-552.
46. Zhao D., Huo Q., Feng J., Chmelka B. F. and Stucky G. D., Nonionic triblock and star diblock copolymer and oligomeric surfactant syntheses of highly ordered, hydrothermally stable, mesoporous silica structures, *J. Am. Chem. Soc.* **120** (1998) pp. 6024-6036.
47. Yang P., Zhao D., Margolese D. I., Chmelka B. F., Stucky G. D., Generalized syntheses of large-pore mesoporous metal oxides with semicrystalline frameworks, *Nature* **396** (1998) 152-155.
48. Yang P., Zhao D., Margolese D., Chmelka B. F., Stucky G. D., Block copolymer templating syntheses of mesoporous metal oxides with large ordering lengths and semicrystalline framework, *Chem. Mater.* **11** (1999) pp. 2813-2826.
49. Schmidt-Winkel P., Lukens W. W. Jr., Zhao D., Yang P., Chmelka B. F. and Stucky G. D., Mesocellular siliceous foams with uniformly sized cells and windows, *J. Am. Chem. Soc.* **121** (1999) pp. 254-255.
50. Schmidt-Winkel P., Glinka C. J. and Stucky G. D., Microemulsion templates for mesoporous silica, *Langmuir* **16** (2000) pp. 356-361.
51. Schmidt-Winkel P., Lukens W. W. Jr., Yang J. P., Margolese D. I., Lettow J. S., Ying J. Y. and Stucky G. D., Microemulsion templating of siliceous mesostructured cellular foams with well-defined ultralarge mesopores, *Chem. Mater.* **12** (2000) pp. 686-696.
52. Lukens W. W. Jr., Schmidt-Winkel P., Zhao D., Feng J. and Stucky G. D., Evaluating pore sizes in mesoporous materials: A simplified standard adsorption

- method and a simplified Broekhoff-de Boer method, *Langmuir* **15** (1999) pp. 5403-5409.
53. Ravishankar R., Kirschhock C. E. A., Schoeman B. J., Vanoppen P., Grobet P. J., Storck S., Maier W. F., Martens J. A., De Schryver F. C., Jacobs P. A., Physicochemical characterization of solicalite-1 nanophase material, *J. Phys. Chem. B* **102** (1998) pp. 2633-2639.
54. Trong On D., Nguyen S. V., Hulea V., Dumitriu E., Kaliaguine S., Mono- and bifunctional MFI, BEA and MCM-41 titanium-molecular sieves. Part 1. Synthesis and characterization, *Micropor. Mesopor. Mater.* **57** (2003) pp. 169-180.
55. Hoang V. T., Trong On D., Kaliaguine S., Hydrothermal stability and Diffusive behavior of UL-zeolites, (2003) in preparation.
56. Hamoudi S., Trong On D., Kaliaguine S., Mesostructured solid acids, *Stud. Surf. Sci. Catal.* (2003) in press.
57. Fyfe C. A., Fu G., Structure Organization of silicate polyanions with surfactants: A new approach to the Syntheses, structure transformations and formation mechanisms of mesostructural materials, *J. Am. Chem. Soc.* **117** (1995) pp. 9709-9714.
58. Fu G., Fyfe C. A., Schwieger W., Kokotailo G. T., Structure organization of aluminosilicate polyanions with surfacetants: Optimization of Al incorporation in aluminosilicate mesostructural materials, *Angew. Chem. Int. Ed.* **34** (1995) pp. 1499-1502.
59. Monnier A., Schüth F., Huo Q., Kumar D., Margolese D. I., Maxwell R. S., Stucky G. D., Krishnamurty M., Petroff P., Firouzi A., Janicke M., Chmelka B. F., Cooperative formation of inorganic-organic interfaces in the synthesis of silicate mesostructures, *Science* **261** (1993) pp. 1299-1303.
60. Huo Q., Margolese D., Ciesla U., Demuth D. G., Feng P., Gier T. E., Sieger P., Firouzi A., Chmelka B. F., Schüth F., Stucky G. D., Organization of organic molecules with inorganic molecular species into nanocomposite biphasic arrays, *Chem. Mater.* **6** (1994) pp. 1176-1191.
61. Trong On D., A simple route for the synthesis of mesostructured lamellar and hexagonal phosphorus-free titania (TiO_2), *Langmuir* **15** (1999) pp. 8561-8564.
62. Flanigen E. M. in *Zeolite Chemistry and Catalysis*; Rabo J. A., Ed.; ACS Monograph No. 171; American Chemical Society: Washington, DC, (1976) pp. 80.
63. Flanigen E. M., Khatami H., Szymanski H. A., Infrared structural studies of zeolite framework, *Adv. Chem. Ser.* **101** (1971) pp. 201-229.
64. Yitzchaik S., Lundquist P. M., Lin W., Marks T. J., Wong G. K., X(2) dispersion and wavequiding measurements in acentric chromophoric self-assembled NLO materials, *SPIE Proc.*, **2285** (1994) pp. 282-289.
65. Engelhardt G., Structure-forming effects of cations in sodium tetramethylammonium silicate solution. A silicon-29 NMR study, *J. Mol. Liq.* **27** (1984) pp. 125-131.
66. Harris R. K., Knight C. T. G., Silicon-29 NMR studies of aqueous silicate solutions, *J. Mol. Struct.* **78** (1982) pp. 273-278; Kinrade S. D., Knight C. T. G., Pole D. L. and Syvitski R. T., Silicon-29 NMR studies of tetraalkylammonium silicate solutions. 1. Equilibria, ^{29}Si Chemical shifts and ^{29}Si relaxation, *Inorg. Chem.* **37** (1998) 4272-4277; Kinrade S. D., Knight C. T. G., Pole D. L. and Syvitski R. T., Silicon-29 NMR studies of tetraalkylammonium silicate solutions. 2. Polymerization kinetics, *Inorg. Chem.* **37** (1998) 4278-4283.
67. Barrer R. M., *Hydrothermal Chemistry of Zeolite*, Academic Press, London (1982).
68. Liu Y., Zhang W., Pinnavaia T. J., Steam-stable aluminosilicate mesostructures assembled from zeolite type Y seeds, *J. Am. Chem. Soc.* **122** (2000) pp. 8791-8792.

69. Liu Y., Zhang W., Pinnavaia T. J., Steam-stable MSU-S aluminosilicate mesostructures assembled from zeolite ZSM-5 and zeolite Beta seeds, *Angew. Chem. Int. Ed.* **40** (2001) pp. 1255-1258.
70. Zhang Z., Han Y., Zhu L., Wang R., Yu Y., Qiu S., Zhao D., Xiao F.-S., Strongly acidic and high temperature hydrothermally stable mesoporous aluminosilicates with ordered hexagonal structure, *Angew. Chem. Int. Ed.* **40** (2001) pp.1258-1262.
71. Xiao F.-S., Han Y., Yu Y., Meng X., Yang M. and Wu S., Hydrothermally stable ordered mesoporous titanosilicates with highly active catalytic sites, *J. Am. Chem. Soc.* **124** (2002) pp. 888–889.
72. Zhang Z. T., Han Y., Xiao F. S., Qiu S. L., Zhu L., Wang R. W., Yu Y., Zhang Z., Zou B. S., Wang Y. Q., Sun H. P., Zhao D. Y., Wei Y., Mesoporous aluminosilicates with ordered hexagonal structure, strong acidity, and extraordinary hydrothermal stability at high temperatures, *J. Am. Chem. Soc.* **123** (2001) pp. 5014–5021.
73. Xiao F.-S., Han Y., Yu Y., Meng X., Yang M. and Wu S., Stable ordered mesoporous titanosilicates with highly active catalytic sites, *Stud. Surf. Sci. Catal.* (2003) in press.
74. Shih P.C., Lin H. P., Mou C. Y., Ultrastable acidic mesoporous aluminosilicates (UAM-1) with ordered cubic structure assembled from zeolite seeds, *Stud. Surf. Sci. Catal.* (2003) in press.
75. Guo W., Huang L., Ha C. S., Li Q., Investigation of the internal pore structures of Beta/MCM-41 and ZSM-5/MCM-41 composites by ^{129}Xe NMR, *Stud. Surf. Sci. Catal.* (2003) in press.
76. Guo W., Kong L., Ha C. S., Li Q., Enhanced acidity and hydrothermal stability of mesoporous aluminosilicate with secondary building units characteristic of zeolite Beta. *Stud. Surf. Sci. Catal.* (2003) in press.
77. Mokaya R., Ultrastable mesoporous aluminosilicates by grafting routes, *Angew. Chem., Int. Ed.*, **38** (1999) pp. 2930–2934.
78. Lippmaa E., Samoson A. and Magi M., High-resolution aluminum-27 NMR of aluminosilicates, *J. Am. Chem. Soc.* **108** (1986) 1730–1735.
79. Agundez J., Diaz I., Marquez-Alvarez C., Sastre E., Pérez-Pariente J., Ordered assembling of precursors of colloidal faujasite mediated by a cationic surfactant, *Stud. Surf. Sci. Catal.* **142** (2002) pp. 1267-1274; Agundez J., Diaz I., Marquez-Alvarez C., Pérez-Pariente J., Sastre E., High acid catalytic activity of aluminosilicate molecular sieves with MCM-41 structure synthesized from precursors of colloidal faujasite, *Chem. Commun.* (2003) pp. 150-151.
80. Liu Y. and Pinnavaia T. J., Assembly of hydrothermally stable aluminosilicate foams and large pore hexagonal mesostructures from zeolite seeds under strongly acidic conditions, *Chem. Mater.* **14** (2002) pp. 3–5.
81. Liu Y., Pinnavaia T. J., Mesocellular aluminosilicate foams (MSU-S/F) and large pore hexagonal mesostructured (MSU-S/H) assembled from zeolite seeds: hydrothermal stability and properties as cumene cracking catalysts, *Stud. Surf. Sci. Catal.* **142** (2002) pp. 1075-1082.
82. Liu Y., Zhang Z., Pinnavaia T. J., Recent advances in the assembly of mesostructured aluminas and aluminosilicates, *Stud. Surf. Sci. Catal.* (2003) in press.
83. Han Y., Xiao F. S., Wu S., Sun Y., Meng X., Li D., Lin S., Deng F., Ai X., A novel method for incorporation of heteroatoms into the framework of ordered mesoporous silica materials synthesized in strong acidic media, *J. Phys. Chem. B* **105** (2001) pp. 7963-7966.

84. Han Y., Wu S., Sun Y., Li D., Xiao F.-S., Liu J. and Zhang X., Hydrothermally stable ordered hexagonal mesoporous aluminosilicates assembled from a triblock copolymer and preformed aluminosilicate precursor in strongly acidic media, *Chem. Mater.* **14** (2002) pp. 1144-1148.
85. Trong On D., Kaliaguine S., Ultrastable and highly acidic zeolite coated mesoporous aluminosilicates, *Angew. Chem., Int. Ed. Engl.* **41** (2002) pp. 1036-1040.
86. Trong On D., Kaliaguine S., Acidic zeolite coated mesoporous aluminosilicates, *Stud. Surf. Sci. Catal.* (2003) in press.
87. Trong On D., Kaliaguine S., Zeolite-coated mesostructured cellular silica foams, *J. Am. Chem. Soc.* **125** (2003) pp. 618-619.
88. Trong On D., Ungureanu A., Kaliaguine S., TS-1 coated mesocellular titano-silica foams as new catalysts for oxidation of bulky molecules, *J. Phys. Chem. B* (2003) submitted.
89. Ungureanu A., Trong On D., Dumitriu E., Kaliaguine S., Hydroxylation of 1-naphthol by hydrogen peroxide over UL-TS-1 and TS-1 coated MCF, *Appl. Catal. A: General* (2003) in press.
90. Luan Z., Cheng C.-F., Zhou W. and Klinowski J., Mesopore Molecular Sieve MCM-41 Containing Framework Aluminum, *J. Phys. Chem.* **99** (1995) pp. 1018-1024.
91. Trong On D., Zaidi S. M. J., Kaliaguine S., Stability of mesoporous aluminosilicate MCM-41 under vapor treatment, acidic and basic conditions, *Micropor. Mesopor. Mater.* **22** (1998) pp. 211.
92. Trong On D., Kaliaguine S., Springuel-Huet M. A., Fyfe C. A., Characterization and quantification of the ZSM-5 phase and aluminum environment in zeolite coated mesoporous aluminosilicate SBA-15 by ^{129}Xe NMR and ^{27}Al MAS and MQMAS at very high field, (2003) in preparation.
93. Fyfe C. A., Bretherton J. L., Lam L. Y., Solid-state NMR detection, characterization, and quantification of the multiple aluminum environments in US-Y catalysts by ^{27}Al MAS and MQMAS experiments at very high field, *J. Am. Chem. Soc.* **123** (2001) pp. 5285-5291.
94. Davis, M. E., Ordered porous materials for emerging applications, *Nature* **2002** **417**, 813-824.
95. Navrotsky A., Petrovic I., Hu Y., Chen C. Y. and Davis M. E., Little energetic limitation to microporous and mesoporous materials, *Microporous Mater.* **4** (1995) pp. 95-98.
96. Davis M. E., Chen C. Y., Burkett S. L. and Lobo, R. L., Synthesis of (alumino)silicate materials using organic molecules and self-assembled organic aggregates as structure-directing agents, *Mater. Res. Soc. Symp. Ser. Proc.* **346** (1994) pp. 831-842.
97. Leonowicz M. E., Lawton J. A., Lawton S. L., Rubin M. K., MCM-22, a molecular-sieve with 2 independent multidimensional channel systems, *Science* **264** (1994) pp. 1910-1913.
98. Schreyeck L., Caullet P., Mougénel J. C., Guth J. L., Maler B., A layered microporous aluminosilicate precursor of FER-type zeolite, *J. Chem. Soc. Chem. Commun.* (1995) pp. 2187-2188.
99. Brunner G. O., Meier W. M., Framework density distribution of zeolite-type tetrahedral nets, *Nature* **337** (1989) pp. 146-147.
100. Li H., Eddaoudi M., O'Keeffe M., Yaghi O. M., Systematic design of pore size and functionality in isorecticular MOFs and their application in methane storage, *Nature* **402** (1999) pp. 276-279.

101. Chen B., Eddaoudi M., Hyde S. T., O'Keeffe M., Yaghi O. M., Interwoven metal-organic framework on a periodic minimal surface with extra-large pores, *Science* **291** (2001) pp. 1021–1023.
102. Eddaoudi M., Kim J., Rosi N., Vodak D., Wachter J., O'keeffe M., Yaghi O. M., Systematic design of pore size and functionality in isorecticular MOFs and their application in methane storage, *Science* **295** (2002) pp. 469–472.
103. Katovic A., Stawinski K., Mackowiak A., Preparation and characterization of mesoporous molecular sieves containing Al, Fe or Zn, *Micropor. Mesopor. Mater.* **44-45** (2001) pp. 275–281.
104. Corma A., From microporous to mesoporous molecular sieve materials and their use in catalysis, *Chem. Rev.* **97** (1997) pp. 2373–2419.
105. Biz S., Occelli M. L., Synthesis and characterization of mesostructured materials, *Catal. Rev.- Sci. Eng.* **40** (1998) pp. 329-408.
106. Ying J. Y., Mehnert C. P., Wong M. S., Synthesis and applications of supramolecular templated mesoporous materials, *Angew. Chem., Int. Ed. Engl.* **38** (1999) pp. 56-77.
107. De Vos D. E., Sels B. F., Jacobs P. A., Immobilization of homogeneous oxidation catalysts *Adv. Catal.* **46** (2001) pp. 1-76.
108. Ciesla U., Schüth F., Ordered mesoporous materials, *Micropor. Mesopor. Mater.* **27** (1999) pp. 131-149.

CHROMIUM-CONTAINING ORDERED NANOPOROUS MATERIALS

P. SELVAM[†]

*Department of Chemistry, Indian Institute of Technology, Powai, Mumbai
400 076, India*

[†]*Also at Department of Materials Chemistry, Graduate School of Engineering,
Tohoku University, Aoba-yama 07, Sendai 980-8579, Japan*

E-mail: selvam@iitb.ac.in; selvam@aki.che.tohoku.ac.jp

Chromium compounds are attractive owing to their potential oxidizing ability in many organic reactions. However, their use in stoichiometric quantities or catalytic (homogenous) amounts has adverse effects owing to the toxic nature of chromium besides affecting the selectivity. Hence, attention has been focused towards the development of chromium-based heterogeneous catalysts. However, the stability of chromium ions in the solid matrix is a subject of considerable discussion and debate as they can leach out under the reaction conditions. On the other hand, chromium containing mesoporous molecular sieves exhibit excellent activity and stability. Furthermore, the leaching of active chromium ions from the matrix is absent as compared to almost all the chromium-based heterogeneous catalysts reported so far. In this study, a comparative account of the catalytic properties of various chromium-containing mesoporous silicates, viz., (Cr)MCM-41 and (Cr)MCM-48, and aluminophosphates, e.g., (Cr)HMA, is presented. The activities of these catalysts are also compared with chromium-containing microporous silicate (MFI), aluminosilicate (BEA), and aluminophosphate (APO-5) molecular sieves.

1 Introduction

The potential of chromium compounds in various organic reactions has been tremendous [1-9]. However, their use as oxidizing agents in stoichiometric quantities has led to serious problems associated with chromium containing effluents. Thus, attention has been focused on the use of homogeneous catalysts wherein catalytic amounts of soluble chromium compounds can be used in conjunction with certain eco-friendly oxidants [2,4,7-9]. However, such established traditional processes also generate solid/liquid wastes in alarming levels that the disposal of which pose serious threat to the environment. Moreover, the use of such catalysts often cause inconvenience during reaction and work-up. Furthermore, these processes also lead to several other problems like difficulty in separation, recovery and recycling of the catalysts after reaction as well as the disposal of wastes, deactivation complications, etc., which makes them

highly unattractive. Owing to the limitations of chromium-based stoichiometric reagents/homogeneous catalysts, and in the wake of increasingly stringent environmental legislation, attention is being focused towards the design and development of greener processes such as heterogeneous catalytic oxidation. Many solid supports like silica, alumina, pillared clays, microporous molecular sieves containing active chromium species have been identified for this purpose [7-28]. In particular, the chromium containing microporous molecular sieve-based catalysts such as (Cr)S-1[16,20], (Cr)APO-5 [20], (Cr)APO-11 [20], (Cr)SAPO-37 [26] and (Cr)Beta [19,23], have shown promise and contributed significantly to the progress of new methodologies in organic transformations. However, one of the major problems associated with all these catalyst systems has been the extensive leaching of the active chromium ions into solution and pore blockage by the formation of bulky products [20,29-34]. Furthermore, the reactions do not take place in the micropores or at the outer surface of these solid catalysts, but are homogeneously catalyzed by the leached chromium. Therefore, the development of highly efficient processes/catalysts that generates no (or low amounts of) residues/byproducts with good activity is one of the main challenges to the scientific community.

On the other hand, the discovery of the so-called periodic mesoporous silicate/aluminosilicate materials in early 1990s [35,36], viz., thermally stable MCM-41 having a hexagonal structure with one-dimensional pore structure, and MCM-48 displaying a cubic structure with three-dimensional pore system, has opened wide range of opportunities in porous solids [37-43]. The unique flexibility in terms of synthetic conditions, pore size tuning (2-20 nm), high surface area (1000-1500 m²g⁻¹), large internal hydroxyl groups (40-60 %), framework substitution, etc. has created new avenues not only in catalysis but also in the areas of advanced materials, environmental pollution control strategies and separation processes. Moreover, these materials not only broaden the scope of their use but also overcome some of the drawbacks encountered by the microporous materials. On the other hand, the recent reports, on the successful synthesis of hexagonal mesoporous aluminophosphates (HMA) [44,45], having hexagonal MCM-41 structure with one-dimensional pores with high surface area and large pore openings, has given a new direction to incorporate and stabilize transition metal ions in the matrix. It is now well established that the mesoporous materials exhibit novel properties, and that they can very well be used to carry out certain important organic transformations more efficiently [46-69] than the corresponding microporous analogues or supported metal oxide systems. Moreover,

unlike many other systems based on microporous molecular sieves [16,19,20,23,26,31,32] and pillared clays [13,24], the mesoporous molecular sieves stabilize chromium ions in the matrix [70-76], thus they can act as true heterogeneous catalysts. In order to demonstrate the high activity and the stability towards leaching of chromium-based mesoporous catalysts, a representative reaction, viz., cyclohexane oxidation, was chosen as the reaction has also attracted much attention owing to the importance high value of the products, viz., cyclohexanol and cyclohexanone, which are key intermediates in the production caprolactam (a monomer in the manufacture of nylon-6) and adipic acid (a building block for a number of polyamide fibers, e.g., nylon-66, and polyurethane resins) [77]. In the past, several chromium-based catalysts such as (Cr)S-1 [17], (Cr)APO-5 [17], (Cr)SAPO-37 [25], silica gels, e.g., (Cr)-SiO₂ [78] have been reported. Although, all these catalysts have shown promise for this reaction, in most cases, extreme reaction conditions such as high pressures and high temperatures in conjunction with low activity make the process undesirable. Moreover, the catalysts often suffer from the disadvantage of extensive leaching of active chromium ions under the reaction conditions. However, it is to be noted here that the chromium-containing mesoporous molecular sieves, viz., hexagonal silicate, designated as (Cr)MCM-41, cubic silicate, designated as (Cr)MCM-48 and hexagonal mesoporous aluminophosphates, designated as (Cr)HMA, showed remarkable activity and stability for the chosen reaction. Therefore, in this presentation and attempt has been made to give a comparative account of the performance of these different chromium-containing mesoporous catalysts. In addition, the resistance against leaching under various reaction conditions of the mesoporous catalysts were also evaluated against the frequently encountered microporous molecular sieve catalysts such as (Cr)Silicalite-1, designated as (Cr)S-1, (Cr)Beta, and (Cr)APO-5.

2 Materials and Methods

The experimental procedures employed for the preparation and characterization of various chromium-based mesoporous molecular sieve catalysts as well as the reaction details are presented elsewhere [70-76,79,80].

2.1 Starting Materials

In general, the following chemicals are used for the synthesis of various mesoporous and microporous molecular sieves: tetradecyltrimethyl ammonium (TDTMA) bromide, cetyltrimethylammonium bromide (CTAB), cetyltrimethylammonium chloride (CTAC), tetrapropyl ammonium (TPA) bromide, tetraethyl ammonium (TEA) hydroxide, tripropylamine (Pr_3N) were used as templates. Sodium hydroxide (NaOH) and tetramethyl ammonium hydroxide (TMAOH) are used as the inorganic and organic bases, respectively. Tetraethyl orthosilicate (TEOS) and fumed silica are employed as the silicon source. Aluminium isopropoxide, pseudoboehmite and sodium aluminate were used as the aluminium sources for the synthesis of (Cr)HMA, (Cr)APO-5 and (Cr)Beta, respectively. In all the cases, chromium nitrate nonahydrate is used as the chromium source.

2.2 Synthesis

The various chromium-containing mesoporous, (Cr)MCM-41(1), (Cr)MCM-41(2), (Cr)MCM-48 and (Cr)HMA, as well as chromium-free MCM-4, MCM-48 and HMA, and microporous, (Cr)APO-5, (Cr)Beta and (Cr)S-1, materials are hydrothermally synthesized with a typical silicon-to-chromium (molar) ratio of ~ 50 [70-76]. The as-synthesized samples are normally calcined under air/nitrogen/oxygen atmosphere. It is, however, important to mention here that for the preparation (Cr)MCM-41, two different procedures employed: For (Cr)MCM-41(1), fumed silica, NaOH and TDTMA are used as the silicon, base and surfactant sources, respectively [71-73]. On the other hand, for the preparation (Cr)MCM-41(2), tetraethyl orthosilicate (TEOS), TMAOH and CTAB are employed as silicon, base and surfactant sources, respectively [74]. In addition, a third (Cr)MCM-41(3) sample is also synthesized using fumed silica, NaOH, TDTMA, and a different chromium nitrate source, viz., $\text{Cr}(\text{NO}_3)_3 \cdot \text{Cr}(\text{NO}_3)_3 \cdot 9\text{H}_2\text{O}$ [70].

2.3 Characterization

The molecular sieves materials are usually characterized by various analytical techniques, viz., X-ray diffraction (XRD), transmission electron microscopy (TEM), electron diffraction (ED), thermogravimetry-differential analysis (TG-DTA), and spectroscopic techniques such as Fourier transform-infrared (FT-IR), diffuse reflectance ultraviolet-visible

(DRUV-VIS), and electron paramagnetic resonance (EPR), and inductively coupled plasma-atomic emission spectroscopy (ICP-AES). By and large, the Brunauer-Emmett-Teller (BET) method is employed for the determination of surface area and the pore size is calculated using the Horvath-Kawazoe (H-K) procedure.

2.4 Reaction Procedure

The oxidation of cyclohexene is carried out in presence of H_2O_2 (30 %; oxidant), chlorobenzene (solvent), methyl ethyl ketone (initiator) and catalyst at 393 K for 12 h under ambient pressure [73-76]. The reaction is also carried out in the absence of the catalysts as well as using chromium-free catalysts. The catalyst is separated after the reaction, and the reaction products are analyzed by gas chromatography (GC) with SE-30 and carbowax column. This is further confirmed by combined gas chromatography-mass spectrometry (GC-MS) with HP-5 capillary column.

2.5 Leaching Studies

In order to check the classically encountered problem of leaching of chromium from the mesoporous matrix, several filtrate, quenching, recycling and washing experiments were carried out over the calcined catalysts as per the procedure given elsewhere [70-76]. Further, the performance of the various chromium-containing solutions/catalysts is also evaluated.

2.5.1 Filtrate Solutions

The calcined/washed catalyst is treated with oxidant and solvent at room temperature. The filtrate solution is then obtained by simple filtration.

2.5.2 Quenched Solutions

This is obtained by separating the reactant mixture containing the catalyst, substrate, solvent and oxidant under the reaction temperature after 2 h by filtration. The reaction is then continued as per the standard procedure on this quenched solution without any further addition of the oxidant.

2.5.3 Washed Catalysts

The calcined samples are treated with ammonium acetate solution at room temperature and filtered. This procedure is repeated for a couple of times so as to ensure all the non-framework chromium ions are removed from the catalyst. Finally, it is dried and recalcined, and the resulting catalyst is designated as washed catalyst.

2.5.4 Recycled Catalysts

The recycling experiments are performed as per the following procedure. After the first reaction, the catalyst is recovered from the reaction mixture by filtration and washed with acetone. It is then dried and calcined. This regenerated catalyst is referred as recycled catalyst, which is used for further studies.

3 Results and Discussion

Figures 1-4 depict the XRD patterns of various chromium-containing mesoporous materials. The diffraction patterns are typical of mesoporous MCM-41 and MCM-48 structures [35,36,43-45]. The XRD patterns chromium-free mesoporous materials [79,80] also show typical characteristic of mesoporous structures. It is to be noted here that the diffraction pattern of calcined (Cr)HMA (Fig. 4b) shows a single broad reflection characteristic of disordered mesoporous structure [43,81]. At this juncture, it is also noteworthy here that unlike (Cr)MCM-41(1), which is prepared using fumed silica, NaOH and TDTMA, the (Cr)MCM-41(2) catalyst, prepared using TEOS, TMAOH and CTAB, showed much higher crystallinity (*see* Figs. 1 and 2). Figure 5 illustrates the representative TEM (Fig. 5) image of the mesoporous samples, which clearly indicate the good quality of the materials. This is also well supported by ED studies. The nitrogen sorption isotherms follow type IV isotherm and give huge surface area ($1066 \text{ m}^2\text{g}^{-1}$ for (Cr)MCM-41; $1140 \text{ m}^2\text{g}^{-1}$ for (Cr)MCM-48 and $760 \text{ m}^2\text{g}^{-1}$ for (Cr)HMA), typical of mesoporous materials.

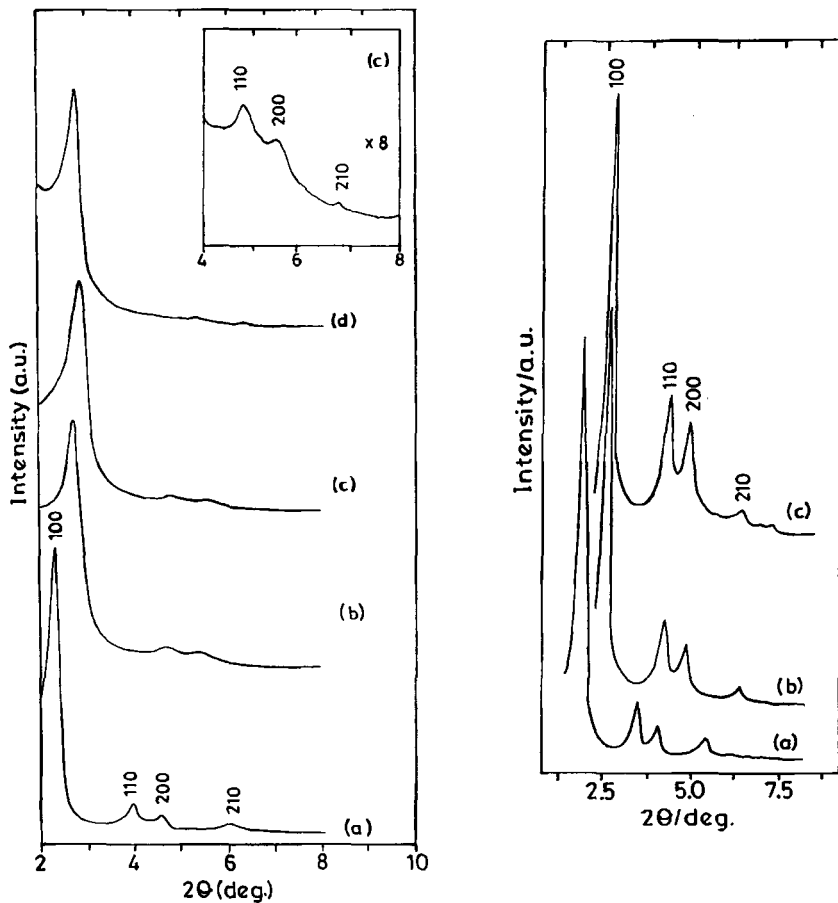


Figure 1. (Left): XRD patterns of (Cr)MCM-41(1): (a) as-synthesized, (b) calcined, (c) washed, and (d) recycled [75].

Figure 2. (Right): XRD patterns of (Cr)MCM-41(2): (a) as-synthesized, (b) calcined, and (c) recycled [74].

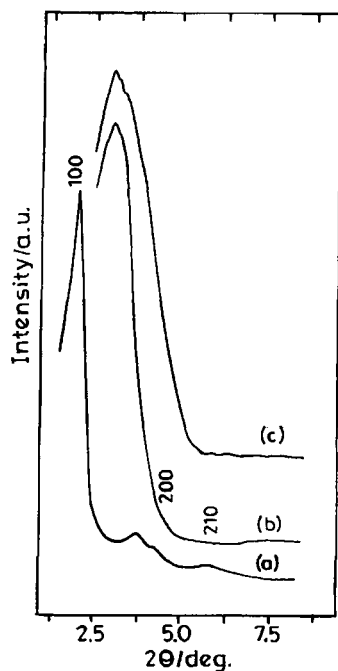
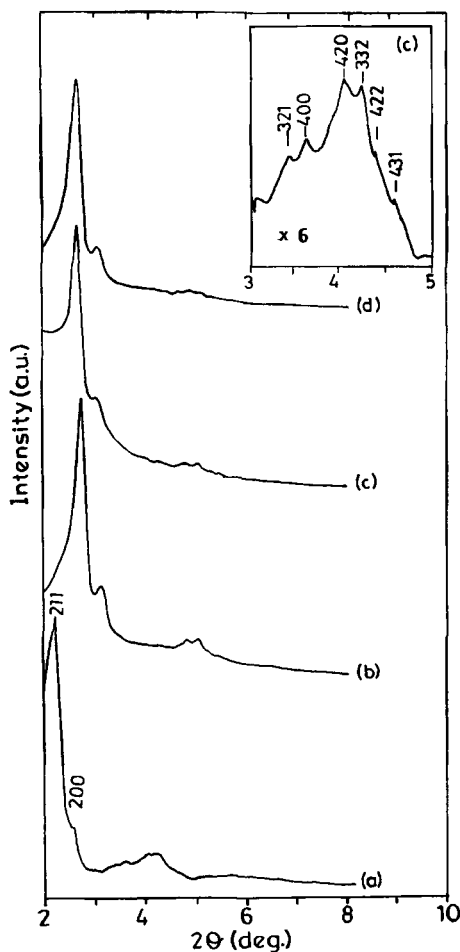


Figure 3. (Left): XRD patterns of (Cr)MCM-48(50): (a) as-synthesized, (b) calcined, (c) washed, and (d) recycled. Inset: XRD pattern of washed (Cr)MCM-48 [75].

Figure 4. (Right): XRD patterns of (Cr)HMA: (a) as-synthesized, (b) calcined, and (c) recycled [74].

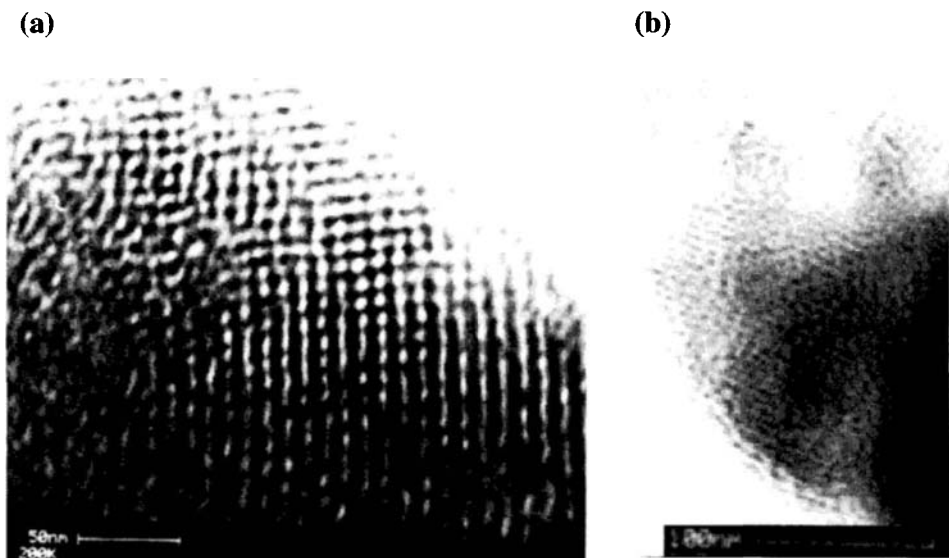


Figure 5. TEM image of calcined: (a) (Cr)MCM-48 [76], and (b) (Cr)HMA [74].

The TG of the calcined samples give relatively a small weight loss for the chromium-containing samples as compared to the chromium-free ones suggesting that part of the silanol groups (defect sites) are consumed for stabilization of chromium ions in the matrix. This conjecture is well supported by the ^{29}Si MAS-NMR studies of calcined (Cr)MCM-41(1) (Fig. 6a) and MCM-41 (Fig. 6b), where the distinct signals at -111 and -100 ppm, which are assigned to Q_4 and Q_3 ($\equiv\text{Si}-\text{OH}$) sites, respectively [82], and that the intensity of Q_3 signal for MCM-41 is much larger than that for (Cr)MCM-41(1) suggesting that the hydroxyl groups are consumed for the grafting of chromium ions in the matrix. This is also a clear indication that the silanol groups play an important role in stabilizing chromate, dichromate or polychromate species (Fig. 7) in a similar way to that reported for the chromium supported silica catalysts [83,84] or tetravalent titanium grafted on the walls of MCM-41 [46].

All the as-synthesized samples were green in colour and changed to yellow upon calcination. The former is due to the presence of trivalent chromium ions and the latter is due to the presence of higher valent chromium ions such as chromate, dichromate and/or polychromates. DRUV-VIS spectra of the as-synthesized samples (not reproduced here) show two bands at ~ 630 and ~ 460 nm. They are assigned as $^4A_{2g} \rightarrow ^4T_{2g}$ (F) and $^4A_{2g} \rightarrow ^4T_{1g}$ (F) transitions, respectively. A third band appears at ~ 300 nm, which is assigned as $^4A_{2g} \rightarrow ^4T_{1g}$ (P). The three spectral bands are

typical of trivalent chromium in octahedral coordination [85]. On calcination, a prominent band at ~ 375 nm ($1t_1 \rightarrow 2e$ symmetry allowed) along with a shoulder at ~ 445 nm ($1t_1 \rightarrow 2e$ symmetry forbidden) is observed (Figs. 8 and 9). These bands are assigned to the $O^{2-} \rightarrow Cr^{6+}$ (d^0) charge-transfer transitions due to the presence of chromate and/or dichromate like species [85-88].

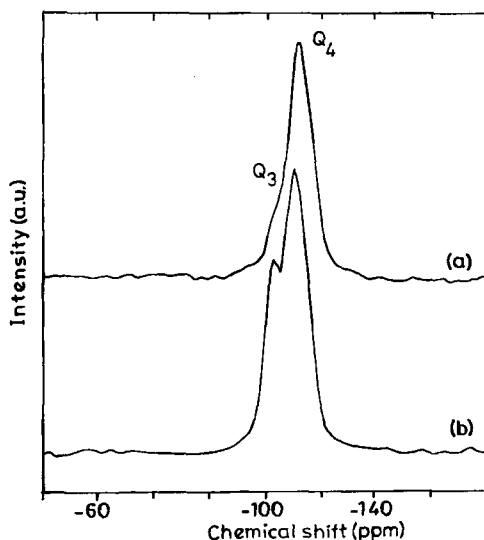


Figure 6. ^{29}Si MAS-NMR spectra of [72]: (a) (Cr)MCM-41 and (b) MCM-41.

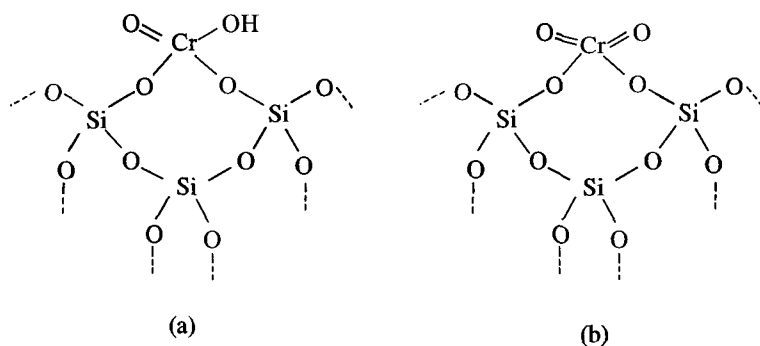


Figure 7. Schematic representation of stabilized chromium species in mesoporous silicates [73]: (a) Cr(V), and (b) Cr(VI).

The EPR spectra (not reproduced here) of as-synthesized samples show a broad spectrum with $g_{eff} = 1.98$ indicating the presence of trivalent chromium in octahedral coordination, while for the calcined samples a sharp signal appeared at $g_{eff} = 1.97$, which is characteristic of pentavalent chromium in tetrahedral coordination [13,27,28]. However, a notable exception is that isolated chromate-type species can be observed for a carefully prepared sample, (Cr)MCM-41(3) employing a different chromium source, viz., $(\text{Cr}(\text{NO}_3)_3 \cdot \text{Cr}(\text{NO}_3)_3 \cdot 9\text{H}_2\text{O}$ [13]. In this case, a complete oxidation of trivalent to hexavalent chromium is evidenced, which is well supported by the absence of EPR signal (Fig. 10a) while all other catalysts (e.g., see Fig. 2b) show a clear signal at $g_{eff} = 1.97$ due to the presence of pentavalent chromium. This observation of hexavalent chromium is corroborated by the DRUV-VIS studies, where the bands at ~ 430 nm is diffused while for the pentavalent species it is pronounced (Fig. 10b).

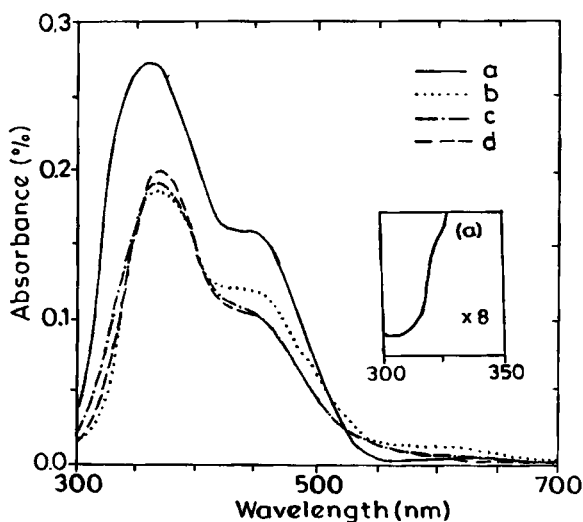


Figure 8. DRUV-VIS spectra of (Cr)MCM-41 [73] (a) calcined, (b) recycled, (c) washed, and (d) washed and recycled.

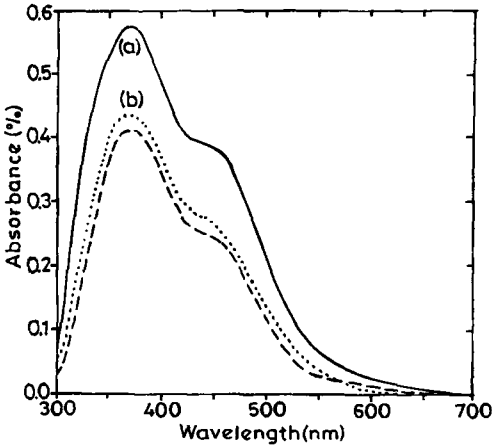


Figure 9. DRUV-VIS spectra of (Cr)MCM-48 [76] (a) calcined, (b) washed, and (c) recycled.

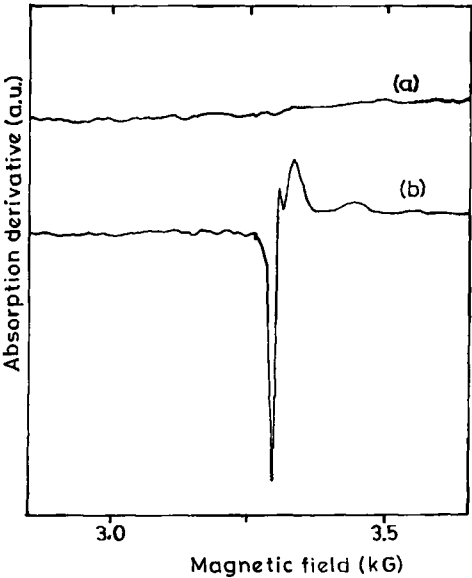


Figure 10. EPR spectra of [72]: (a) (Cr)MCM-41(3) and (b) (Cr)MCM-41(1).

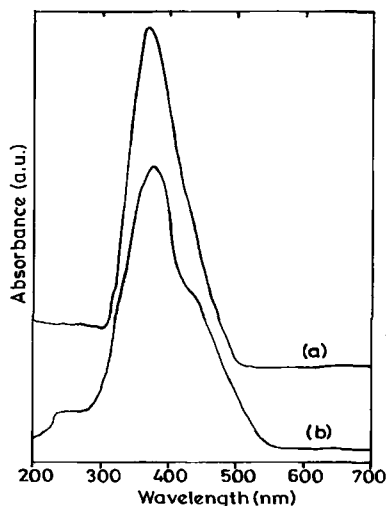


Figure 11. DRUV-VIS spectra of [72]: (a) (Cr)MCM-41(3), and (b) (Cr)MCM-41(1).

Tables 1-4 summarize the results of the oxidation of cyclohexane over various catalysts. It can be seen from these tables that the catalysts show excellent activity for the selective oxidation cyclohexane. The observed high conversion and selectivity of the catalysts may well be explained on the basis of coordination environment and oxidation states of Cr ions in the matrix. That is, under the reaction conditions, the higher valent chromium in the matrix (Fig. 12a) may interact with H_2O_2 to form catalytically active peroxo-complex of the type shown in (Fig. 12b). Subsequently, the substrate molecules interact with this reactive intermediate to give the final product. The reactions are also carried out over chromium-free materials as well as without the use of the catalyst. In both the cases, only ~ 10 % conversion was noted thus indicating that the observed high activity of the chromium-containing catalysts is only due to the presence of chromium ions in the matrix. It is also to be noted here that the catalytic activity remains nearly the same after first cycle or after washing experiments indicating no further leaching of chromium ions from the mesoporous matrix, which is in good agreement with ICP-AES results (*cf.* Tables 1-4) of the filtrate / quenched / washed solutions where no chromium was detected. It is also noteworthy here that the diffraction patterns (*see* Figs. 1-4) are not affected by the various treatments of recycling and washing thus suggesting the intactness of the structure.

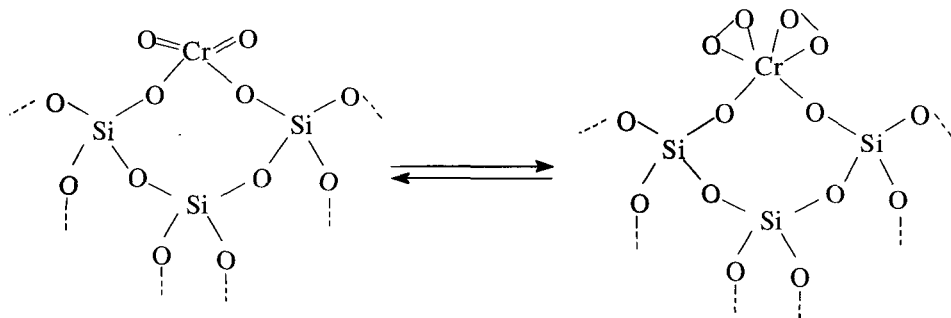


Figure 12. Schematic representation of [72] (a) stabilized hexavalent chromium, and (b) peroxo-species.

It can also be seen from Tables 1-4 that the calcined catalysts showed high activity while, a considerable decrease in activity was noticed, first time, for the recycled samples owing to leaching of active (non-framework) chromium ions under reaction conditions. On the other hand, the activity remains nearly the same in the subsequent cycles. However, the lower conversion during recycling experiments could, however, be attributed to lower chromium content. Interestingly, the washed catalysts also showed a similar result (*cf.* Tables 1 and 2). This observation of loss of chromium content upon recycling / washing treatments is well supported by DRUV-VIS studies where the initial decrease in absorption band intensity was noted for the calcined catalysts (*see* Figs. 8 and 9). However, spectra remain nearly the same for the washed and recycled samples. Further, the results are corroborated by the filtrate as well as the quenching studies carried out on washed catalysts (*see* Table 1) are in line with the above findings. At this point, it is also noteworthy to mention here that a similar observation was also made for the oxidation of phenols [70], alkylaromatics [71,72] and cyclohexen [73] over these chromium-containing mesoporous molecular sieves. It is also noteworthy to mention here that unlike many other chromium-based heterogeneous catalysts [13,16,19,20,23-26,31,32], the mesoporous silicates and aluminophosphates stabilize chromium ions in the matrix, which do not leach under the reaction conditions, albeit an initial loss in the case of calcined catalysts, and hence they can act as true heterogeneous catalysts.

Table 1. Cyclohexane oxidation over (Cr)MCM-41(1) [72,76].[†]

Catalyst	Cr content (wt %)	Conversion (wt %)	Cyclohexanol selectivity (wt %)
Calcined (Cr)MCM-41	1.23	98.9	92.9
After 2h	----	71.3	91.6
Filtrate solution	----	----	----
Quenched solution	0.3-0.4	85.5	94.6
Recycled catalyst [‡]	0.76	74.5	95.3
Washed (Cr)MCM-41	0.77	72.2	90.7
After 2h	----	42.1	89.4
Filtrate solution	----	4.7	87.1
Quenched solution	----	48.6	83.3
Recycled catalyst [‡]	----	71.1	98.5
Calcined MCM-41	----	11.6	96.4
No catalyst	----	9.0	78.1

[†] Reaction conditions: Substrate : Oxidant = 1:1; Catalyst = 3.3 wt %; T = 373 K; t = 12 h.

[‡] 2nd recycle or 3rd run.

Table 2. Cyclohexane oxidation over (Cr)MCM-41(2) [74].[‡]

Catalyst	Cr content (wt %)	Conversion (wt %)	Cyclohexanol selectivity (wt %)
Calcined (Cr)MCM-41	1.25	95.6	93.4
After 2h	----		
Filtrate solution	0.52	30.2	85.6
Quenched solution [‡]	0.48	25.1	87.2
Recycled catalyst [§]	0.75	72.8	90.5
Washed (Cr)MCM-41	0.72	73.5	89.6

[†] Reaction conditions: *see* Table 1. [‡] Conversion due to leached chromium. [§] 3rd recycle or 4th run.

Table 3. Cyclohexane oxidation over (Cr)MCM-48 [76].[†]

Catalyst	Cr content (wt %)	Conversion (wt %)	Cyclohexanol selectivity (wt %)
Calcined (Cr)MCM-48	1.58	97.1	98.8
After 2h	----	80.4	90.9
Filtrate solution	----	----	----
Quenched solution	0.3-0.4	92.0	94.4
Recycled catalyst [‡]	----	91.9	93.9
Washed (Cr)MCM-48	0.98	90.2	95.9
After 2h	----	52.6	96.8
Filtrate solution	----	5.0	94.3
Quenched solution	----	57.4	97.4
Recycled catalyst [‡]	----	91.5	95.6
Calcined MCM-48	----	10.9	95.1
No catalyst	----	9.0	78.1

[†] Reaction conditions: *see* Table 1. [‡] 2nd recycle or 3rd run.

Table 4. Cyclohexane oxidation over (Cr)HMA [74].[†]

Catalyst	Cr content (wt %)	Conversion (wt %)	Cyclohexanol Selectivity(wt %)
Calcined (Cr)HMA	1.10	93.5	96.3
After 2h	----		
Filtrate solution	0.11	12.4	84.0
Quenched solution [‡]	0.10	11.0	89.2
Recycled catalyst [§]	0.96	85.8	95.5
Washed (Cr)HMA	0.98	87.5	97.6
Calcined HMA	----	9.8	82.8
No catalyst	----	9.0	78.1

[†] Reaction conditions: *see* Table 1. [‡] Conversion due to leached chromium. [§] 3rd recycle or 4rd run.

As can be seen from Tables 1-4, a systematic recycling, washing and quenching experiments are performed under reaction conditions so as to check the classically encountered problems of active metal ion leaching as well as the stability of the chromium ions in the mesoporous matrix. Figure 8 illustrates the results of a representative oxidation reaction over various chromium-containing catalysts. It is interesting to note that, unlike the microporous-based catalysts, the mesoporous catalysts exhibit only a marginal loss in activity in the 1st recycling (or 2nd run) as due to a very little leaching of the active species from the matrix. This is very well supported by the washed catalysts where no loss in activity upon recycling was noticed (*see* Table 1) thus indicating that the chromium ions are intact in the mesoporous framework structure. It is also noteworthy here that the ICP-AES analysis of the filtrates obtained from the washed catalysts showed no leaching of active chromium species. On the other hand, the observed loss in activity for (Cr)MCM-41 is attributed for the leaching of active chromium ions, which is very well supported by the filtrate experiments (under reaction conditions) where the washed chromium ions showed substantial activity. However, both (Cr)MCM-48 and (Cr)HMA show only a very little amount of leaching of chromium and therefore display the high activity. Further, the ICP-AES results on the chromium analysis support these findings clearly (*see* Tables 1-4). Among the mesoporous catalysts, the (Cr)MCM-48 show much higher activity, which could be attributed to the three-dimensional pore system. The superior performance of the former could, however, be attributed to the three-dimensional pore system as well as to the stabilization of large amount of chromium (*cf.* Table 3). As depicted in Fig. 13, a continuous decrease in activity is noticed for the microporous-based catalysts, viz., (Cr)APO-5, (Cr)- β and (Cr)S-1 catalysts as due to leaching of chromium, which is in good agreement with literature reports [6]. It is also interesting to note that the mesoporous catalysts do not lose the stability even after recycling or washing treatments thus behaving truly as heterogeneous catalysts. This is clearly reflected from the XRD patterns (*see* Fig. 1c & 3c) where the catalysts, before and after reaction, show the prominent reflections characteristic of disordered (HMA) and ordered (MCM-41 and MCM-48) structures.

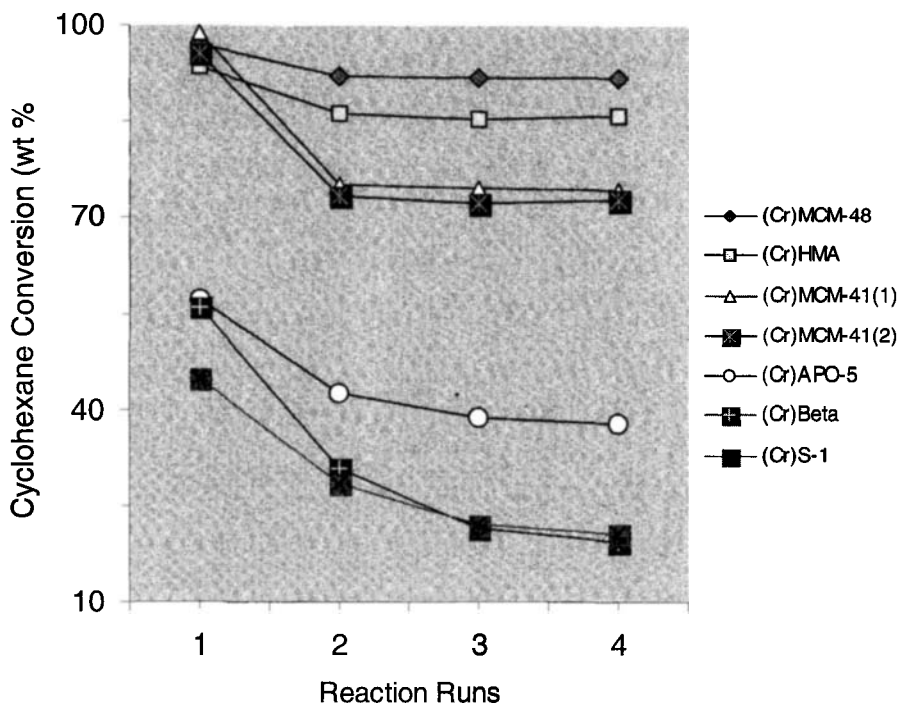


Figure 13. Catalytic activity of chromium-based mesoporous and microporous catalysts.

4 Conclusion

In summary, it can be concluded that the activity of the chromium-containing mesoporous catalysts, viz., (Cr)MCM-41 and (Cr)MCM-48, and aluminophosphates, e.g., (Cr)HMA, is much higher any other chromium-based catalysts reported so far. Further, it is also clear from this study that the microporous catalysts, viz., (Cr)APO-5, (Cr)-Beta and (Cr)S-1, showed much lower activity in addition to a continuous decrease in conversion, as a consequence of leaching of active chromium ions. On the other hand, it is also interesting to note that only a marginal loss or no loss in activity was noticed for the (washed) mesoporous catalysts. Thus, the chromium-based mesoporous molecular sieves opens up new possibility as a potential heterogeneous catalyst and that the application of these catalysts can further be extended for the oxidation of bulkier molecules.

5 Acknowledgements

I thank all my co-workers listed in the references who have contributed significantly towards the progress and understanding of the chromium-based mesoporous materials. I would also like to thank Prof. A. Miyamoto for his support and encouragement.

References

1. Wilberg K.B. in *Oxidation in Organic Chemistry A*, Academic Press, New York, 1965.
2. Sheldon R.A., and Kochi J.K., *Metal-Catalyzed Oxidations of Organic Compounds*, Academic Press, New York, 1981.
3. Cainelli G. and Cardillo G., *Chromium Oxidation in Organic Chemistry*, Springer-Verlag, Berlin, 1984.
4. Muzart J., Chromium^{VI} oxide - 70% tert.butyl hydroperoxide, a simple catalytic system for oxidation of alcohols to carbonyl compounds, *Tetrahedron Lett.* **28** (1987) pp. 2133; Practical chromium^{VI} oxide-catalyzed benzylic oxidations using 70% tert-butylhydroperoxide, *Tetrahedron Lett.* **28** (1987) pp. 2133; Synthesis of unsaturated carbonyl compounds via a chromium-mediated allylic oxidation by 70% tert.butylhydroperoxide, *Tetrahedron Lett.* **28** (1987) p. 4665; Chromium-catalyzed oxidations in organic synthesis, *Chem. Rev.* **92** (1992) p. 113.
5. Choudary B.M., Prasad A.D. and Valli V.L.K., Selective oxidation of alcohols by chromia-pillared : Montmorillonite catalyst, *Tetrahedron Lett.* **31** (1990) p. 5785.
6. Hudlicky, M., *Oxidation in Organic Chemistry*, ACS Monograph, Washington DC, Vol. 186, 1990.
7. Sheldon R.A., van Santen R.A., (ed.), *Catalytic Oxidation: Principles and Applications*, World Scientific, Singapore, 1995.
8. De Vos D.E., Sels B.F., Jacobs P.A., Immobilization of homogeneous oxidation catalysts, *Adv. Catal.* **46** (2001) p.1.
9. Thomas J.M. and Raja R., Catalytically active centres in porous oxides: design and performance of highly selective new catalysts, *Chem. Commun.* (2001) p. 675.
10. Choudary B.M., Kantam M.L., and Santhi P.L., New and ecofriendly options for the production of speciality and fine chemicals, *Catal. Today* **57** (2000) p. 17.
11. Murphy E.F., Mallat T., and Baiker A., Allylic oxofunctionalization of cyclic olefins with homogeneous and heterogeneous catalysts, *Catal. Today* **57** (2000) p. 115.
12. Schuchardt U., Cardoso D., Sercheli R., Pereira R., Cruz R.S., Guerreiro M.C., Mandelli D., Spimace E.V. and Pires E.L., Cyclohexane oxidation continues to be a challenge, *Appl. Catal. A* **211** (2001) p. 1.
13. Choudary B.M., Prasad A.D., Bhuma V., and Swapna V., Chromium-pillared clay as a catalyst for benzylic oxidation and oxidative deprotection of benzyl ethers and benzylamines: a simple and convenient procedure, *J. Org. Chem.* **57** (1992) p. 5841.
14. Kawi S. and Te M., MCM-48 supported chromium catalyst for trichloroethylene oxidation, *Catal.Today* **44** (1998) p. 101.
15. Weckhuysen B.M., I.E. Wachs I.E. and Schoonheydt R.A., Surface Chemistry and Spectroscopy of Chromium in Inorganic Oxides, *Chem. Rev.* **96** (1996) p. 3327.

16. Singh A.P. and Selvam T., Liquid phase oxidation reactions over chromium silicalite-1 (CrS-1) molecular sieves, *J. Mol. Catal. A* **113** (1996) p. 489.
17. Zhang W., Wang J., Tanev P.T. and Pinnavaia T.J., Catalytic hydroxylation of benzene over transition metal substituted hexagonal mesoporous silicas, *Chem. Commun.* (1996) p. 979.
18. Ulagappan N. and Rao C.N.R., Synthesis and characterization of the mesoporous chromium silicates, Cr-MCM-41, *Chem. Commun.* (1996) p. 1047.
19. Yuvaraj S., Palanichamy M. and Krishnasamy V., Chromium substitution in a large-pore high-silica zeolite BEA: synthesis, characterisation and catalytic activity, *Chem. Commun.* (1996) p. 2707.
20. Lempers H.E.B. and Sheldon R.A., The stability of chromium in CrAPO-5, CrAPO-11, and CrS-1 during liquid phase oxidations, *J. Catal.* **175** (1998) p. 62.
21. Das T.K., Chaudhari K., Nandan E., Chandwadkar A.J., Sudalai A., Ravindranathan T. and Sivasanker S., Cr-MCM-41-catalyzed selective oxidation of alkylarenes with TBHP, *Tetrahedron Lett.* **38** (1997) p. 3631.
22. Carvalho W.A., Valardo P.B., Wallau M. and Schuchardt U., Mesoporous redox molecular sieves analogous to MCM-41, *Zeolites* **18** (1997) p. 408.
23. Sakthivel A., Badamali S.K., Driver Z., and Selvam P., in *Recent Trends in Catalysis*, ed. V. Murugasen, B. Arabindoo, M. Palanichamy, Narosa, New Delhi, (1999) p. 539.
24. Xiao J., Xu J. and Gao Z., Selective oxidation on chromia-pillared zirconium phosphate and phenylphosphonate, *Catal. Lett.* **57** (1999) p. 37.
25. Spinacé E.V., Schuchardt U. and Cardoso D., Oxidation of hydrocarbons with peroxides catalyzed by chromium(III) and iron(III) incorporated in SAPO-37 framework, *Appl. Catal. A* **185** (1999) p. L193.
26. Srinivas N., Rani V.R., Kulkarni S.J. and Raghavan K.V., Liquid phase oxidation of anthracene and *trans*-stilbene over modified mesoporous (MCM-41) molecular sieves, *J. Mol. Catal. A* **179** (2002) p. 221.
27. Richter M. and Öhlmann G., Conversion of Propan-2-ol on Silica Supported Chromium Oxide: II. Catalytic Results, *Appl. Catal.* **36** (1988) p.81.
28. Dakka J. and Sheldon R.A., Selective decomposition of cyclohexyl hydroperoxide to cyclohexanone catalyzed by chromium aluminophosphate-5, *Appl. Catal. A* **108** (1994) p. L1.
29. Haanepen M.J. and Van Hooft J.H.C., VAPO as catalyst for liquid phase oxidation reactions Part I: preparation, characterisation and catalytic performance, *Appl. Catal.* **152** (1997) pp. 183.
30. Haanepen M.J., Elemans-Mehring A.M. and Van Hooft J.H.C., VAPO as catalyst for liquid phase oxidation reactions. Part II: stability of VAPO-5 during catalytic operation, *Appl. Catal.* **152** (1997) p. 203.
31. Sheldon R.A., Wallau M., Arends I.W.C.E. and Schuchardt U., Heterogeneous Catalysts for Liquid-Phase Oxidations: Philosophers' Stones or Trojan Horses? *Acc. Chem. Res.* **31** (1998) p. 485.
32. Arends I.W.C.E. and Sheldon R.A., Activities and stabilities of heterogeneous catalysts in selective liquid phase oxidations: recent developments, *Appl. Catal. A* **212** (2001) p. 175.
33. Sakthivel A., Arunkumar N. and Selvam P., Ethylbenzene oxidation over chromium-incorporated silicalite-1 molecular sieves, *Bull. Catal. Soc. India* **1** (2002) p. 136.

34. Vidya K., Mahalingam R.J. and Selvam P., Oxidation of aromatics over microporous (Cr)APO-5 molecular sieves, *Bull. Catal. Soc. India* **1** (2002) p. 142.
35. Kresge C.T., Leonowicz M.E., Roth W.T., Vartuli J.C. and Beck J.S., Ordered Mesoporous Molecular Sieves Synthesised by a Liquid-Crystal Template Mechanism, *Nature* **359** (1992) p. 710.
36. Beck J.S., Vartuli J.S., Roth W.J., Leonowicz M.E., Kresge C.T., Schmitt K.D., Chu C.T.-W., Olson, D.H., Sheppard, E.W., McCullen, S.B., Higgins, J.B. and Schlenker, J.L., A New Family of Mesoporous Molecular Sieves Prepared with Liquid Crystal Templates, *J. Am. Chem. Soc.* **114** (1992) p. 10834.
37. Zhao X. S., Lu G. Q. and Miller G. J., Advances in Mesoporous Molecular Sieve MCM-4, *Ind. Eng. Chem. Res.* **35** (1996) p. 2075.
38. Sayari A., Periodic Mesoporous Materials: Synthesis, Characterization and Potential Applications, *Stud. Surf. Sci. Catal.* **102** (1996) p. 1.
39. Corma A., Microporous to Mesoporous Molecular Sieve Materials and Their Use in Catalysis, *Chem. Rev.* **97** (1997) p. 2413.
40. Ryoo R.; Ko C.-H.; Park I.-S., Synthesis of Highly Ordered MCM-41 by Micelle-Packing Control with Mixed Surfactants, *Chem. Commun.* (1999) p. 1413.
41. Ying J. Y., Mehnert C. P. and Wong M. S., Synthesis and Applications of Supramolecular-Templated Mesoporous Materials, *Angew. Chem. Int. Ed.* **38** (1999) p. 56.
42. Trong On D., Desplandier D., Danumah C. and Kaliaguine S., Perspectives in catalytic applications of mesostructured materials, *Appl. Catal. A* **222** (2001) p. 299.
43. Selvam P., Bhatia S.K. and Sonwane C.G., Recent Advances in Processing and Characterization of Periodic Mesoporous MCM-41 Silicate Molecular Sieves, *Ind. Eng. Chem. Res.* **40** (2001) p. 3237.
44. Zhao D., Luan Z., and Kevan L., Synthesis of thermally stable mesoporous hexagonal aluminophosphate molecular sieves, *Chem. Commun.* (1997) p. 1009.
45. Kimura T., Sugahara Y., and Kuroda K., Synthesis and Characterization of Lamellar and Hexagonal Mesostructured Aluminophosphates Using Alkyltrimethylammonium Cations as Structure-Directing Agents, *Chem. Mater.* **11** (1999) p. 508.
46. Maschmeyer T., Rey F., Sankar G., Thomas J. M., Heterogeneous Catalysts Obtained by Grafting Metallocene Complexes onto Mesoporous Silica, *Nature* **378** (1995) p. 159.
47. Mohapatra S.K., Hussain F. and Selvam P., Titanium substituted hexagonal mesoporous aluminophosphates: Highly efficient and selective heterogeneous catalysts for the oxidation of phenols at room temperature, *Catal. Commun.* **4** (2003) p. 57.
48. Walker J. V., Morey M., Carlsson H., Davidson A., Stucky G. D., Butler A., Peroxidative Halogenation Catalyzed by Transition-Metal-Ion-Grafted Mesoporous Silicate Materials, *J. Am. Chem. Soc.* **119** (1997) p. 6921.
49. Selvam P., Badamali S.K., Mahalingam R.J. and Sakthivel A., Ecofriendly molecular sieve based heterogeneous catalysts for liquid-phase oxidation of aromatic compounds, *16th Meeting of North American Catalysis Society Meeting*, Boston, (1999) p. PI-011.
50. Sakthivel A., Badamali S.K. and Selvam P., in: *Recent Trends in Catalysis*, eds. V. Murugesan, B. Arabindoo and M. Palanichamy (Narosa, New Delhi, 1999) p. 96.

51. Zhou X. G., Yu X. Q., Huang J. S., Li L. S. and Che C. M., Asymmetric epoxidation of alkenes catalysed by chromium binaphthyl Schiff base complex supported on MCM-41, *Chem. Commun.* (1999) p. 1789.
52. Shyu S. G.; Cheng S. W. and Tzou D. L., Immobilization of $\text{Rh}(\text{PPh}_3)_3\text{Cl}$ on phosphinated MCM-41 for catalytic hydrogenation of olefins, *Chem. Commun.* (1999) p. 2337.
53. Badamali S.K., Sakthivel A. and Selvam P., Tertiary butylation of phenol over mesoporous FeMCM-41, *Catal. Lett.* **65** (2000) p. 153.
54. Sakthivel A., Badamali S.K. and Selvam P., *para*-Selective *t*-butylation of phenol over mesoporous H-AlMCM-41, *Micropor. Mesopor. Mater.* **39** (2000) p. 457.
55. Badamali S.K., Sakthivel A. and Selvam P., Influence of Aluminum Sources on the Synthesis and Catalytic Activity of Mesoporous AlMCM-41 Molecular Sieves, *Catal. Today* **63** (2000) p. 291.
56. Sakthivel A., Dapurkar S.E. and Selvam P., Mesoporous VMCM-41: Zeo-type heterogeneous catalysts for liquid phase oxidation of cyclohexane, *Advances in Environmental Materials, Vol. I, Pollution Control Materials* (ed. T. White and D. Sun), Materials Research Society, Singapore, (2001) p.67.
57. Subrahmanyam Ch., Louis B., Fabio R., Viswanathan B., Renken A. and Varadarajan T.K., Partial oxidation of toluene by O_2 over mesoporous Cr–AlPO, *Catal. Commun.* **3** (2002) p. 45.
58. Mohapatra S.K., Sahoo B., Keune W. and Selvam P., Synthesis, characterization and catalytic properties of trivalent iron substituted hexagonal mesoporous aluminophosphates, *Chem. Commun.* (2002) p. 1466.
59. Sakthivel A. and Selvam P., Vapour-phase tertiary butylation of phenol over mesoporous gallosilicate molecular sieves, *Catal. Lett.* **84** (2002) p. 37.
60. Mohapatra S.K., Sonavane S.U., Jayaram R.V. and Selvam P., Regio- and chemoselective catalytic transfer hydrogenation of aromatic nitro and carbonyl as well as reductive cleavage of azo compounds over novel mesoporous NiMCM-41 molecular sieves, *Org. Lett.* **4** (2002) p. 4297; Addition/Correction – Regio- and chemoselective catalytic transfer hydrogenation of aromatic nitro and carbonyl as well as reductive cleavage of azo compounds over novel mesoporous NiMCM-41 molecular sieves, *Org. Lett.* **5** (2003) p. 233; Reductive cleavage of azo dyes and reduction of nitroarenes over trivalent iron incorporated hexagonal mesoporous aluminophosphate molecular sieves, *Appl. Catal. B* **44** (2003) in press. Available online 24 June 2003.
61. Mohapatra S.K., Sonavane S.U., Jayaram R.V. and Selvam P., Heterogeneous catalytic transfer hydrogenation of aromatic nitro and carbonyl compounds over cobalt(II) substituted hexagonal mesoporous aluminophosphate molecular sieves, *Tetrahedron Lett.* **43** (2002) pp. 8527; Corrigendum to "Heterogeneous catalytic transfer hydrogenation of aromatic nitro and carbonyl compounds over cobalt(II) substituted hexagonal mesoporous aluminophosphate molecular sieves": [*Tetrahedron Lett.* **43** (2002) 8527], *Tetrahedron Lett.* **44** (2003) p. 1107.
62. Sonavane S.U., Mohapatra S.K., Jayaram R.V. and Selvam P., Catalytic transfer hydrogenation of nitro and carbonyl compounds over novel Fe(III) substituted hexagonal mesoporous aluminophosphates, *Chem. Lett.* **32** (2003) p. 142.
63. Mohapatra S.K. and Selvam P., Synthesis, characterization and catalytic properties of mesoporous cobalt aluminophosphate molecular sieves, *Top. Catal.* **22** (2003) p. 17.

64. Zhao X.S., Lu G.Q. and Song C., Immobilization of aluminum chloride on MCM-41 as a new catalyst system for liquid-phase isopropylation of naphthalene, *J. Mol. Catal. A* **191** (2003) p. 67.
65. Ishitani H. and Iwamoto M., Selective aldol reactions of acetals on mesoporous silica catalyst, *Tetrahedron Lett.* **44** (2003) p. 299.
66. Subrahmanyam Ch., Louis B., Rainone F., Viswanathan B., Renken A. and Varadarajan T.K., Catalytic oxidation of toluene with molecular oxygen over Cr-substituted mesoporous materials, *Appl. Catal. A* **241** (2003) p. 205.
67. Kugita T., Jana S.K., Owada T., Hashimoto N., Onaka M. and Namba S., Mesoporous Al-containing MCM-41 molecular sieves: highly active catalysts for Diels–Alder reaction of cyclopentadiene with α,β -unsaturated aldehydes, *Appl. Catal. A* **245** (2003) p. 353.
68. Maheswari R., Shanthi K., Sivakumar T. and Narayanan S., Beckmann rearrangement over phosphotungstic acid/SiMCM-41 cyclohexanone oxime to ϵ -caprolactam, *Appl. Catal. A* **248** (2003) p. 291.
69. Părvulescu V., Anastasescu C. and Su B.L., Liquid phase oxidation of aromatic hydrocarbons using highly ordered Nb and NbCo-MCM-41 nanoreactors, *J. Mol. Catal. A* **202** (2003) p. 171.
70. Mahalingam R.J., Badamali S.K. and Selvam P., Oxidation of phenols over mesoporous (Cr)MCM-41 molecular sieves, *Chem. Lett.* (1999) p. 1121.
71. Sakthivel A., Dapurkar S.E. and Selvam P., Mesoporous (Cr)MCM-41 and (Cr)MCM-48 molecular sieves: Promising heterogeneous catalysts for liquid phase oxidation reactions, *Catal. Lett.* **77** (2001) p. 155.
72. Sakthivel A., Badamali S.K. and Selvam P., Catalytic Oxidation of Alkylaromatics over Mesoporous (Cr)MCM-41, *Catal. Lett.* **80** (2002) p. 73.
73. Sakthivel A. and Selvam P., Mesoporous (Cr)MCM-41: A mild and efficient heterogeneous catalyst for selective oxidation of cyclohexane, *J. Catal.* **211** (2002) p. 134.
74. Mohapatra S.K., Hussain F. and Selvam P., Synthesis, characterization and catalytic properties of chromium containing hexagonal mesoporous aluminophosphate molecular sieves, *Catal. Lett.* **85** (2003) p. 217.
75. Sakthivel A., Dapurkar S.E., and Selvam P., Allylic oxidation of cyclohexene over chromium containing mesoporous molecular sieves, *Appl. Catal. A* **246** (2003) p. 283.
76. Dapurkar S.E., Sakthivel A. and Selvam P., Novel mesoporous (Cr)MCM-48 molecular sieves: Promising heterogeneous catalysts for selective oxidation reactions, *New. J. Chem.* **27** (2003) p. 1184.
77. Fisher W.B., Vanpappen J.F., A.S. Inc, in: *Kirk-Othmer Encyclopedia of Chemical Technology*, Vol.7, eds. M. Howe-Grant, Kroschwitz J.I., (Wiley, New York, 1992) p. 851.
78. da Cruz R.S., e Silva J.M.D.S., Arnol U. and Schuchardt, U., Catalytic activity and stability of a chromium containing silicate in liquid phase cyclohexane oxidation, *J. Mol. Catal. A* **171** (2001) p. 251.
79. Dapurkar S.E., Badamali S.K. and Selvam P., Nanosized metal oxides in the mesopores of MCM-41 and MCM-48 silicates, *Catal. Today* **68** (2001) p. 63.

80. Vidya K., Dapurkar S.E., Selvam P., Badamali S.K. and Gupta N.M., The entrapment of UO_2^{2+} in the mesoporous MCM-41 and MCM-48 molecular sieves, *Micropor. Mesopor. Mater.* **50** (2001) p. 173.
81. Khimyak Y.J. and Klinowski J., Synthesis of mesostructured aluminophosphates using cationic templating, *Phys. Chem. Chem. Phys.* **2** (2000) p. 5275.
82. Chen C.-Y., Li H.-X. and Davis M.E., Studies on mesoporous materials : I. Synthesis and characterization of MCM-41, *Micropor. Mater.* **2** (1993) pp. 17; Chen C.-Y.; Burkett S.L.; Li H.-X.; Davis M. E. Studies on Mesoporous Materials. II. Synthesis Mechanism of MCM-41, *Microporous Mater.* **2** (1993) p. 27.
83. Zecchina A., Garrone E., Ghiotti G., Morterra C. and E. Borello E., Chemistry of silica supported chromium ions. I. Characterization of the samples, *J. Phys. Chem.* **79** (1975) p. 966.
84. McDaniel M.P., Witt D.R. and Benham E.A., The Effect of Alkali Metal Doping on the Performance of Cr/Silica Catalysts in Ethylene Polymerization, *J. Catal.* **176** (1981) p. 344.
85. Weckhuysen B.M., De Ridder L.M., Grobet P.J. and Schoonheydt R.A., Redox Behavior and Dispersion of Supported Chromium Catalysts, *J. Phys. Chem.* **99** (1995) p. 320.
86. Weckhuysen B.M. and Schoonheydt R.A., Recent progress in diffuse reflectance spectroscopy of supported metal oxide catalysts, *Catal. Today* **49** (1999) p. 441.
87. Frunza L., Pelgrims J., Leeman H., Van Der Voort P., Vansant E. F., Schoonheydt R. A. and Weckhuysen B. M., Incorporation of Transition Metal Ions in Aluminophosphate Molecular Sieves with AST Structure, *J. Phys. Chem. B.* **105** (2001) p. 2677.
88. Zhu Z., Chang Z. and Kevan L., Synthesis and Characterization of Mesoporous Chromium-Containing Silica Tube Molecular Sieves CrMCM-41, *J. Phys. Chem. B* **103** (1999) p. 2680.

SURFACTANT-TEMPLATED MESOSTRUCTURED MATERIALS: SYNTHESIS AND COMPOSITIONAL CONTROL

MICHAEL S. WONG^{1,2} AND WILLIAM V. KNOWLES¹

*¹Department of Chemical Engineering, ²Department of Chemistry
Rice University, 6100 Main St., Houston, TX 77005-1892, USA
E-mail: mswong@rice.edu*

The compositional variety in surfactant-templated mesostructured and mesoporous materials widened tremendously since the initial reports on MCM-41 and the M41S aluminosilicate mesoporous molecular sieve materials came out. In this chapter the current state of synthesis and compositional control of mesostructured and mesoporous metal oxides is presented. New surfactant templating synthesis routes, especially those that lead to the formation of non-silicates, are described, and a comprehensive update on the available types of such materials is presented. General trends are noted, which could provide insights towards surfactant-templated materials as yet synthesized.

1 Introduction

The use of surfactant molecules in the preparation of nanoporous metal oxides has received tremendous attention since the initial publications on MCM-41 [1-6] (and FSM-16 [7], to a lesser extent) in the early 1990s. Since then, surfactant templating (or supramolecular templating) has proven to be an extremely useful materials design strategy, in which materials properties of

- high surface areas ($>1000 \text{ m}^2\text{g}^{-1}$);
- tunable, uniform pore sizes (2-10 nm);
- liquid crystal-like, long-range ordering of the pores;
- structural stability;
- ease in surface functionalization; and
- compositional tailoring of the inorganic framework

can be achieved. Due to such desirable characteristics, silicate-based surfactant-templated mesoporous materials have been extensively studied for a variety of applications, such as heterogeneous catalysis, separations, energy generation, electronics, and sensing [8-20]. In contrast, non-silica-containing mesoporous materials have not been studied as much, because (1) they do not fully display the above materials properties, and (2) they are more difficult to prepare [9, 13, 14].

The two-step preparation of surfactant-templated mesoporous materials is conceptually simple: form the surfactant/inorganic mesostructure, and remove the surfactant from the mesostructure to form the mesoporous material. The actual kinetics, of course, are much more complex [21-23]. Mesoporous silicates are easy to prepare because the surfactant templating chemistry can accommodate a wide range of synthesis parameters (*e.g.* aging temperature, aging time, pH of synthesis medium, and initial precursor ratios) to produce surfactant/silicate mesostructures, and because the silicate framework can resist structural collapse through various surfactant removal schemes (*e.g.*, solvent wash and calcination). Difficulties in preparing mesoporous materials can arise in either of the two steps, especially when the desired framework composition deviates significantly from pure silica. If a surfactant/inorganic mesostructure is formed, surfactant removal could lead to structural collapse, or at the very least, undesired structural rearrangement. Currently, it is not possible to prepare surfactant-templated mesoporous materials out of any arbitrary composition.

Reflecting the high level of activity in this field of materials research, many thorough reviews on various aspects of mesoporous materials – synthesis, characterization, properties, and applications – have been published [8-20, 24-29]. In this Chapter, we present the state-of-the-art developments in synthesis and compositional control of surfactant-templated mesostructured and mesoporous inorganic materials, which encompass metal oxides, metal chalcogenides, and metals. We limit our discussions to materials prepared using surfactants and amphiphilic block copolymers, and not using other types of sacrificial porogens (*e.g.*, microemulsions and latex spheres [30]). We discuss the many variations of surfactant templating synthesis routes, and describe general trends in the surfactant-templated synthesis of surfactant/inorganic mesostructures. We also discuss the current challenges in synthesizing mesoporous materials and some interesting approaches to address these issues.

2 Synthesis routes

Much work has been done on developing new surfactant-templated synthesis procedures and on understanding the formation mechanism of mesoporous materials, especially those of silicate compositions [29]. Several generalizations can be made at this point:

1. The various preparation methods can be distilled to a small number of synthesis routes.
2. The kinetics of surfactant templating via cooperative assembly formation are still not completely known.
3. Surfactant molecules can engage inorganic precursors to form surfactant/inorganic mesostructures, but their mesophase may not have long-range order.
4. Roughly 50% of the metal elements (and ~60% of transition metal elements) in the periodic table have been incorporated into a mesostructure, and roughly 50% of these mesostructures lead to mesoporous materials.
5. Mesostructures that retain long-range order upon surfactant removal are still difficult to prepare.
6. The macroscopic morphology of mesoporous materials *e.g.*, powders, monolithic, thick films, and patterned films, can be tailored towards specific applications.
7. Surfactant-templated mesostructures typically lead to materials with mesopores (diameter of 2-50 nm) after surfactant removal, but can also lead to materials with micropores (<2 nm), due to condensation of the framework during calcination.

This Chapter focuses on surfactant/inorganic composites produced through surfactant templating and the resultant porous materials, which may not be strictly mesoporous. No distinction will be made between surfactant-templated microporous and mesoporous materials, especially if the pore sizes are near the IUPAC-defined demarcation of 2 nm [31].

2.1 Surfactant templating routes

2.1.1 Cooperative assembly

Surfactant/inorganic interactions The attractive interactions between the surfactant and inorganic precursor molecules are critical to the formation of the surfactant/inorganic mesostructure. A convenient way to classify the different types of interactions is to consider how the surfactant head group (S) binds to the inorganic precursor (I), as shown in Table 1. Based on the nature of the precursors and synthesis conditions, the categories refer to the likely surfactant/inorganic chemical interactions: electrostatic (S^+I^- , S^-I^+ , $S^+X^-I^+$, $S^-M^+I^-$) [32, 33], hydrogen-bonding (S^0I^0 , N^0I^0) [34-37], hydrogen-bonding/electrostatic ($(S^0H^+)(X^-I^+)$) [38-40], and covalent (S-I) [41-43].

The surfactant/inorganic interactions are not definite or exclusive of other chemical interactions, though. For example, the synthesis of HMS mesoporous silica was hypothesized to take place through hydrogen-bonding of the hydrolyzing TEOS (I^0) and primary amine surfactant (S^0) [34, 35]. However, at neutral pH in water, soluble silicate intermediates are expected to be negatively charged (point of zero charge ~ 2) and amine compounds to be protonated (pK_a of alkylamines ~ 10). The possibility of electrostatic interactions between charged amine surfactant (S^+) and silicate (I^-) precursors during mesostructure formation could not be ruled out [35].

Table 1. Various surfactant/inorganic (S/I) interactions found in the cooperative assembly reaction pathways of surfactant templating.

S/I interactions	Example of surfactant/inorganic mesostructure and reaction conditions
S^+I^-	MCM-41 mesoporous SiO_2 , prepared with sodium silicate and CTAB ¹ at basic pH
S^-I^+	Al-dodecylphosphate mesostructure, prepared at acidic pH
$S^+X^-I^+$	SBA-3 mesoporous SiO_2 , prepared with CTAB at low pH; counterion X^- is Cl^-/Br^-
$S^-M^+I^-$	Al-dodecylphosphate mesostructure, prepared at basic pH; counterion M^+ is Na^+
S^0I^0	HMS mesoporous SiO_2 , prepared with TEOS ² and dodecylamine at neutral pH
N^0I^0	MSU-1 mesoporous SiO_2 , prepared with nonionic Tergitol T15-S-9 surfactant ³ at neutral pH
$(S^0H^+)(X^-I^+)$	SBA-15 mesoporous SiO_2 , prepared with nonionic triblock copolymer Pluronic P123 ⁴ at acidic pH
$S-I$	Nb-TMS1 mesoporous Nb_2O_5 , prepared with niobium ethoxide and dodecylamine

¹ cetyltrimethylammonium, or hexadecyltrimethylammonium, bromide

² tetraethylorthosilicate

³ $HO-(EO)_{15}-C_{11-15}H_{23-31}$, EO = ethylene oxide

⁴ $HO-(ethylene\ oxide)_{20}-(propylene\ oxide)_{70}-poly(ethylene\ oxide)_{20}-H$, or $EO_{20}PO_{70}EO_{20}$

As a second example, the formation of mesostructured aluminum phosphate is classified as occurring through electrostatic interactions ($S^- =$ dodecylphosphate, $I^+ = Al^{3+}$). It can also be considered to occur through

covalent S–I interactions, since phosphates are known to bind covalently to aluminum, as well as other metal cations [32, 43]. Still, the surfactant/inorganic interaction categories have provided a successful starting point in the design and synthesis of surfactant/inorganic mesostructures.

The synthesis of MCM-41 and the M41S materials occurs through S^+I^- interactions, making use of the attractive nature of ammonium-based cations (S^+) to hydrated silica oligomers (I^-) and surfaces under basic conditions, which is well-known in silica chemistry [44–46]. It is worth noting that similar (but less publicized) mesoporous silicates were reported around the same time period as MCM-41 [7, 47], and that a preparation method disclosed in a 1971 patent invention of “low-bulk density silica” was shown to yield MCM-41 [48, 49].

Mesophases The long-range arrangement, or mesophase, of the mesostructure (with and without the surfactant) is a unique characteristic of surfactant-templated materials. Mesostructures can be disordered or ordered, and ordered mesostructures can be a lamellar, cubic, or hexagonal phase. These materials possess long-range ordering of the pores but, unlike zeolites, they are not crystalline, lacking long-range ordering of the framework atoms [50]. Examples of mesostructured materials with the various phases are provided in Figure 1.

Ordered surfactant-templated materials have structures that correlate closely with the liquid crystal (LC) mesophases of surfactant solutions. The lamellar mesophase comprises an alternating stack of inorganic sheets and surfactant bilayers, which is quite common for surfactant/non-silicate mesostructures [16, 32]. With increasing degrees of curvature in the organic/inorganic interface as compared to the lamellar phase, the hexagonal and cubic phases can be regarded as containing, respectively, rod-like and spherical micelles that are close-packed within an inorganic matrix. A dimensionless number that accounts for surface curvature known as the effective surfactant packing parameter $g (= V \cdot a_0^{-1} \cdot l^{-1})$, where V is the overall volume of the surfactant, a_0 is the effective head group area, and l is the surfactant chain length) is used to explain the appearance of surfactant bilayer sheets ($1/2 < g \leq 1$), rods ($1/3 < g < 1/2$), and spheres ($g < 1/3$) in LC phases, and of the mesophases in surfactant-templated materials [51].

There are several common mesophases of surfactant-templated materials. The hexagonal-phase silicate (*e.g.*, MCM-41 and SBA-15) and non-silicate (*e.g.*, Nb-TMS1) mesoporous materials have the same spatial

pattern of pores and pore walls (space group $p6mm$, two-dimensional hexagonal). The hexagonal symmetry can be reduced, for example, by preparing it as a film on a flat substrate such that the pore packing is slightly flattened [52]. SBA-15 has now been conclusively shown to contain an additional set of pores which connect the primary mesopore channels (which are unconnected in MCM-41) [53, 54]. These micropores come from the poly(EO) ends of the block copolymer that extend into the framework from the micellar rods. A cubic-phase mesostructure can be one of several space groups, as shown in Figure 1(c) for MCM-48 ($Ia\bar{3}d$), SBA-6 ($Pm\bar{3}n$), and SBA-16 ($Im\bar{3}m$).

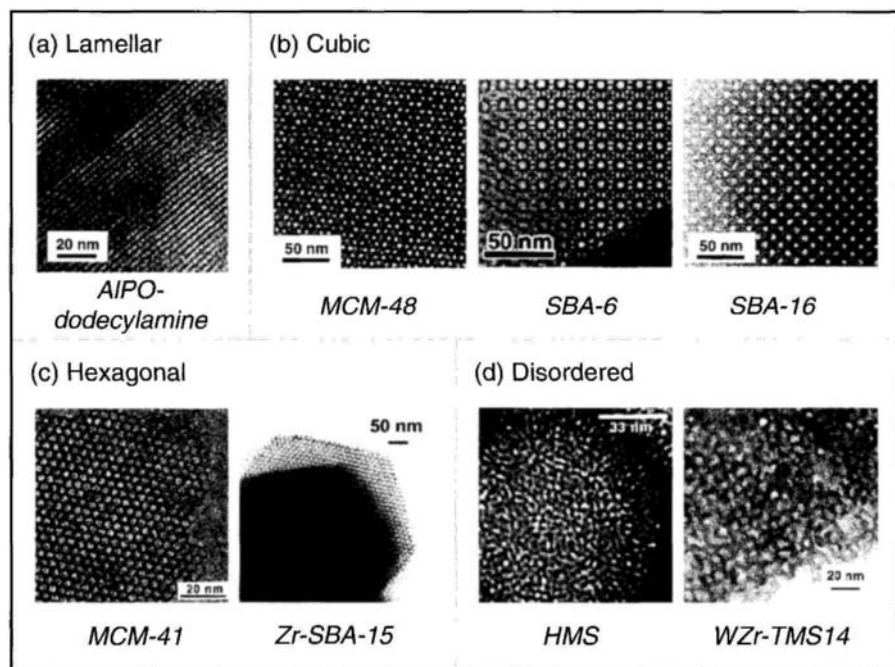


Figure 1. Examples of ordered and disordered phases of mesostructured materials: (a) AIPO-dodecylamine mesostructure (adapted with permission from [55], © 1996 American Chemical Society); (b) MCM-48 (adapted with permission from [56], © 2001 American Chemical Society), SBA-6, and SBA-16 (adapted with permission from [57], © 2000 Nature Publishing Group); (c) MCM-41 (adapted with permission from [58], © 2000 American Chemical Society) and Zr-doped SBA-15 (adapted with permission from [59], © 2002 American Chemical Society); and (d) HMS (adapted with permission from [60], © 2001 American Chemical Society) and WZr-TMS14 (adapted with permission from [61], © 2001 American Chemical Society).

In contrast, a disordered mesophase contains no long-range ordering and has no assignable crystallographic space group, such as the MSU [36, 37] and TMS14 materials [61]. The disorder can come from the use of a disordered LC phase (see Section 2.1.2), or from synthesis conditions that promote the improper packing of surfactant molecules within the surfactant/inorganic mesostructure.

Surfactant-templated materials can be found with a mixture of mesophases, which can pose a problem in structural analysis. A mesoporous silicate material called SBA-2 [62] was originally concluded to have a three-dimensional hexagonal close packing (hcp) of spherical micelles, with the space group $P6_3/mmc$. SBA-2 was later shown to be composed of an intergrown mixture of hcp and fcc (face-centered cubic) mesostructures [63], which led to the possibility that the synthesis procedure could be modified towards one mesophase ($P6_3/mmc$) or the other ($Fm\bar{3}m$ [64]). A modified preparation method was shown to yield a surfactant-templated mesoporous silica similar to SBA-2 (called STA-10) but with more pronounced $P6_3/mmc$ characteristics [65].

Mechanism of formation Many studies on elucidating the mechanism of surfactant/silicate mesostructure (specifically MCM-41) formation have been published, although comparatively less work has been done on surfactant/non-silicate mesostructure formation. Seemingly contradictory results can be found, which can be due to deviations from the typical synthesis procedures (in order to simplify the reaction system for the mechanistic studies), and to differences in precursors used in sample preparation (since there is no “standard” recipe for MCM-41). Still, a convergence of results from the various studies has led to a greater mechanistic understanding of MCM-41, and therefore, of other surfactant-templated mesostructures [9, 29, 66].

The surfactant templating of MCM-41 has some similarities to CTAB surfactant aggregation. The first and second critical micelle concentrations (cmc1 and cmc2) represent values above which solubilized surfactant molecules aggregate into spherical micelles and then into rod-like micelles, respectively. CTAB in water has reported cmc1 values of 9.2×10^{-4} M [67] and 8.9×10^{-4} M (0.032 wt%) at 28 °C [68], and a cmc2 value of 2.0×10^{-2} M (0.72 wt%) at 28 °C [68]. A different study showed that CTAB micelles in deuterated water elongated into short rod-like micelles (prolate ellipsoid with aspect ratio < 1.4) in the range of $\sim 3.0 \times 10^{-2}$ – 2×10^{-1} M, and into longer micelles (aspect ratio > 1.4) in the range of ~ 0.2 – 0.3 M [69].

A CTAB concentration of ~ 0.7 M (~ 20 wt%) was reported to be the cmc for LC phase formation at 25°C [4, 70, 71], and a 30 wt% CTAB solution was confirmed to be a hexagonal LC phase [72, 73]. The phase diagram for the CTAB/water system becomes complicated with the addition of ethanol (Figure 2), a co-solvent generated from the hydrolysis of TEOS during mesostructure formation.

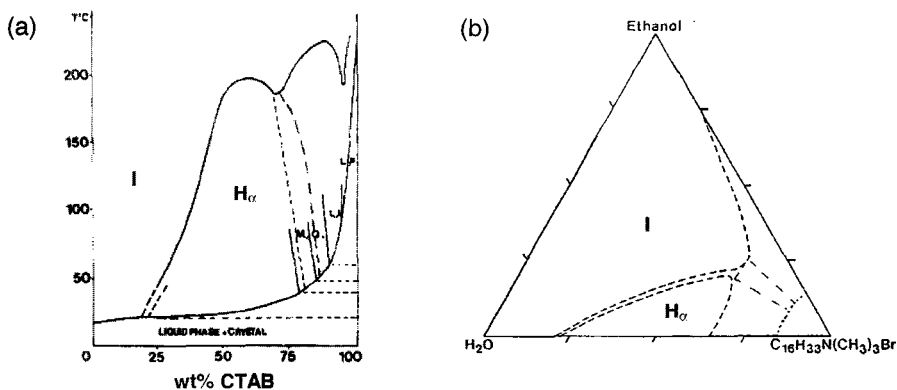


Figure 2. Phase diagrams for binary and ternary systems involving CTAB: (a) CTAB/water (adapted with permission from [70], © 1989 American Chemical Society) and (b) CTAB/water/ethanol at 25°C (adapted with permission from [71], © 1991 Springer-Verlag). Notations: isotropic solution (I) and hexagonal LC phase (H_{II}).

Like charged surfactants, nonionic block copolymer surfactants (*e.g.*, Pluronic P105) can have complex phase diagrams, forming various LC phases as a function of concentration, temperature, and co-solvent concentration (Figure 3). They can participate in mesostructure formation at concentrations (~ 5 – 10 wt%) below the LC cmc, indicating a cooperative assembly mechanism. Nonionic alkylamine surfactants, on the other hand, form only a lamellar mesophase with water [74].

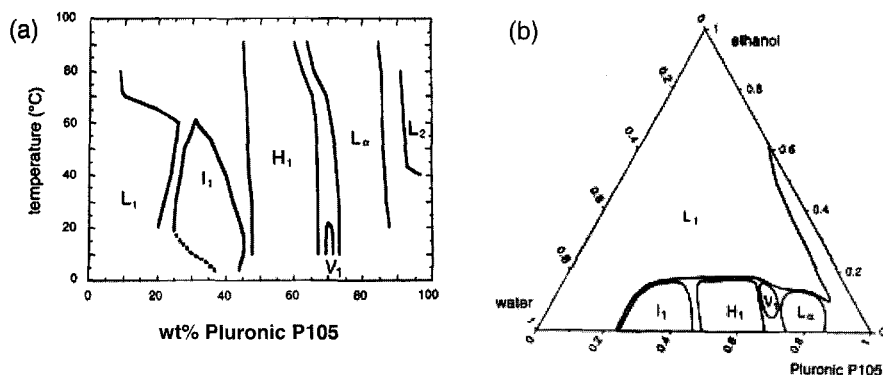


Figure 3. Phase diagrams for binary and ternary systems involving Pluronic P105 ($\text{EO}_{37}\text{PO}_{58}\text{EO}_{37}$): (a) P105/water and (b) P105/water/ethanol at 25 °C (adapted with permission from [75], © 2001 Elsevier). Compositions outside the single-phase regions are multiphased. Notations: isotropic solution (L_1 , L_2) and hexagonal (H_1), cubic (I_1 , V_1), and lamellar (L_α) LC phases.

The original synthesis procedure for MCM-41 called for a ~30 wt% aqueous solution of CTACl/OH (cetyltrimethylammonium chloride partially ion-exchanged with OH^- groups) [1, 2], but the existence of a LC phase under synthesis conditions was unlikely, based on a number of different measurements (see Ref. [29] and [66] for further details). Furthermore, CTACl was reported to form a hexagonal LC phase in the concentration range of 40–70 wt% at 25 °C, higher concentrations than the 20–65 wt% range for the CTAB LC phase [4].

A cooperative assembly mechanism for MCM-41 mesostructure formation in the absence of a LC demands the following conditions: the transition of surfactant molecules into micelles; the binding of the silicate to the CTAB micelle surface; and charge density matching during silicate polymerization [72, 73, 76]. These conditions have been detected under extreme synthesis conditions in various studies, providing reasonable assurance that MCM-41 mesostructure formation under typical preparation procedures also occurs via cooperative assembly. A 6.8 wt% CTAB solution contains spherical and rod-like micelles (Figure 2), and this solution was found to rapidly separate into two clear phases upon silicate precursor addition, a dilute (~0.3 wt% CTAB) and a concentrated surfactant phase (~33 wt% CTAB) [72, 73]. The concentrated surfactant phase was found also to contain double-four-ring silicate (D4R , $[\text{Si}_8\text{O}_{20}]^{8-}$) oligomers that ion-exchanged completely with the bromide anions, forming a silicate-surfactant hexagonal LC phase. The synthesis mixture pH of 12.5 was sufficiently high to prevent silicate condensation and

mesostructure precipitation. It was noted that the silicate precursor was not found to ion-exchange significantly with CTAB in high-pH surfactant/silicate precursor solutions that lack a surfactant/silicate LC phase, leading to the suggestion that the silicates underwent oligomerization prior to ion-exchanging with CTAB [23].

Charge density matching plausibly describes the appearance of curvature in a CTAB/silicate lamellar mesostructure, in which the charge *and* charge density of the CTA^+ (cetyltrimethylammonium) head group and silicate precursor are considered, according to Monnier *et al.* [76]. This lamellar mesophase restructuring shares some characteristics of the FSM-16 formation mechanism (see Section 2.3.1). The negative surface charge density of the interface reduces with continued condensation of the silicate framework ($\text{Si-O}^- + \text{HO-Si} \rightarrow \text{Si-O-Si} + ^-\text{OH}$). This is thought to lead to a larger, effective CTA^+ head group area (and therefore, to a smaller g), allowing the CTA^+ to aggregate into rod-like micelles instead of bilayers (Figure 4). A smooth transition between different mesophases is expected due to charge density matching, and has been observed through *in situ* x-ray diffraction studies [77, 78].

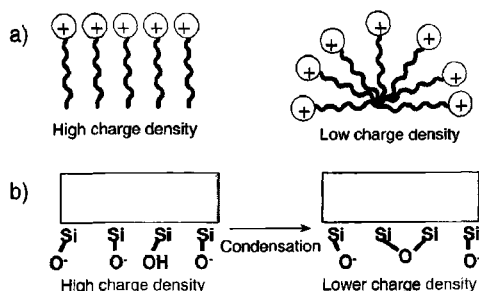


Figure 4. Schematic representation of charge densities for (a) a lamellar and spherical/rod-like packing of cationic surfactant molecules; and (b) a silicate framework undergoing condensation (reprinted with permission from [78], © 2001 American Chemical Society).

The mesophase is affected by the presence of silicate precursors and co-solvents, by silicate condensation kinetics, and by reaction conditions, such as surfactant/metal precursor ratios [4, 42]. Co-solvents, such as methanol and ethanol, can reduce the long-range ordering of a mesostructure and can induce mesophase transitions [79-81]. As long as surfactant aggregation can still take place, the replacement of water with non-aqueous solvents as the synthesis medium can be useful in the preparation of non-silicate mesostructures in which precursor solubility is a problem. For example, germanium sulfide-based mesostructures were

successfully prepared in formamide, a polar solvent with which CTAB forms LC phases [70, 82].

2.1.2 Liquid crystal (LC) templating

Whereas the surfactant/inorganic interactions drive mesostructure formation via cooperative assembly, surfactant LC phases guide mesostructure formation via LC templating (or “nanocasting” [30]; see Section 2.3.2). The formation of M41S materials was originally thought to occur through LC templating rather than cooperative assembly [1, 2], but the surfactant concentration was below the LC cmc. At high enough concentrations, the pre-formed surfactant LC phase can set the surfactant/inorganic mesophase, which is a major advantage of LC templating over cooperative assembly. LC phases span the volume of the surfactant solution, and can lead to large continuous domains (~millimeters) of LC-templated mesostructures. Thus, a difference in macroscopic form can often be observed (monoliths and thin films *v.* precipitated powders).

The first demonstration of true LC templating was reported by Attard *et al.* [83]. A ~50 wt% aqueous solution of octaethylene glycol dodecyl ether (HO-(EO)₈-C₁₂H₂₅, similar to Tergitol, Table 1) was a hexagonal LC, and it was shown to yield mesoporous silica that mimicked the repeat distance and mesophase of the parent LC. The surfactant LC phase was disrupted by the methanol generated by TMOS (tetramethylorthosilicate) hydrolysis, but was restored by removing the methanol. LC templating without interference from alcohols was demonstrated with the preparation of mesostructured CdS from a hexagonal LC phase comprising a ~50 wt% decaethylene glycol oleyl ether (HO-(EO)₁₀-C₁₈H₃₅) solution [84].

The surfactant/inorganic interaction is vital to mesostructure formation via LC templating, without which the inorganic phase would exclude the surfactant aggregates during condensation. Attard, Göltner, and co-workers later showed that the rapid reduction of platinum salt within a hexagonal LC phase of HO-(EO)₈-C₁₆H₃₃ produced stable, mesostructured Pt powders [85]. Slow reduction did not lead to the mesostructured Pt, suggesting that the surfactant/inorganic interaction was weak. Rapid reduction was possible through electrodeposition, through which mesoporous Pt films were produced [86]. To explain mesostructure formation for some semiconductor non-oxide compositions and not for others, Stupp and co-workers proposed that surfactant head group affinity

with both the inorganic precursor and the condensed inorganic phase was a necessary condition in LC templating [84, 87].

Other examples of LC systems used in LC templating include polystyrene-poly(EO) diblock copolymer/water [88], poly(EO)-poly(PO)-poly(EO) Pluronic triblock copolymer/water/ethanol [89], and cetylpyridinium chloride/NaCl/water/hexanol [90, 91]. The last system is the interesting L_3 phase, which has no long-range ordering (*i.e.*, not a LC phase) and can be described as a bicontinuous random pore network. This was used successfully as a “LC” template in the preparation of a disordered silica mesostructure.

2.1.3 Evaporation-induced surfactant templating

Solvent removal via evaporation is a common step in mesostructure formation. It can aid in the formation by (1) forcing the long-range self-assembly of block copolymer in the bulk; (2) shifting the charged surfactant concentration of the synthesis solution above the LC cmc; and (3) driving the condensation of the inorganic framework.

With block copolymers, solvent evaporation causes the inorganic precursor to localize and condense preferentially in one of the copolymer block regions, yielding a gelled product. Thick mesostructured aluminosilicate films (~1 mm) were produced by blending a polyisoprene-poly(EO) diblock copolymer with silicon and aluminum alkoxides and evaporating the non-aqueous solvent mixture at mild temperatures [92]; the copolymer could be removed without structural collapse [93]. A different approach used a silicon-containing triblock copolymer, polyisoprene-poly(pentamethyldisilylstyrene)-polyisoprene, to produce thick mesoporous films of silicon oxycarbide [94]. In these block copolymer-based evaporation routes, the processing steps of evaporation, condensation, and calcination lead to unavoidable shrinking and cracking of the films.

Thick, transparent films of mesostructured silica were prepared from a solution containing commercially available Pluronic F127 ($\text{EO}_{106}\text{PO}_{70}\text{EO}_{106}$), ethanol, HCl, and TEOS [89]. These films were mostly the hexagonal mesophase, with a small amount of cubic and disordered mesophases located near the edge and top-most surface of the films [95]. The mesophase was preserved after calcination, but transparency was not. By replacing HCl and TEOS with metal chlorides, this chemistry led to mesostructured and mesoporous films and powders of a wide variety of pure and mixed non-silicate compositions [96, 97] (see Section 3.7).

Dip-coating, which is based on solvent evaporation, can be used to prepare thin mesostructured films supported on substrates. Brinker and co-workers drew a film of synthesis solution onto a piece of silicon wafer, and a careful balance between the draining and evaporation of the film led to mesostructured silica (Figure 5a). The CTAB surfactant concentration (0.06 M) in the drawn film was below cmc1 (~ 0.1 M, for this water/ethanol solution) initially, but increased up along the wafer length, until the hexagonal LC cmc was reached and exceeded [98]. The surfactant concentration at various positions along the wafer progressed along a trajectory in the CTAB ternary diagram (Figure 5b) [99]. The mesostructured film reached a steady-state thickness of (~ 0.2 μm) and could be calcined to produce mesoporous silica films.

Surfactant templating induced by solvent evaporation can be incorporated easily into different methods to produce mesostructures of controlled macroscopic forms. For example, aerosol particles of synthesis solutions were sent through a heated reactor to produce surfactant/silica mesostructured nanoparticles [98], and ink-jet and microcontact printing methods were used to create patterned features on surfaces [100-102].

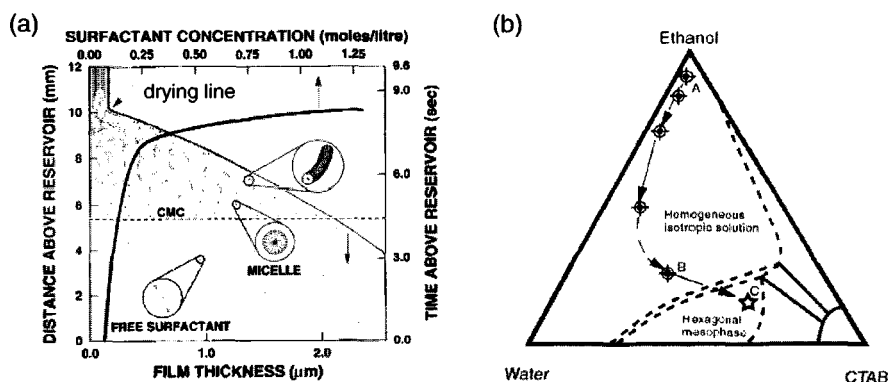


Figure 5. (a) Schematic representation of CTAB surfactant concentration in the dip-coating process, and (b) approximate concentrations during film drying: initial concentration of synthesis solution (point A), concentration at drying line (point B), and concentration of dried film (point C) (adapted with permission from [99], © 1999 Wiley VCH).

2.2 Electrodeposition with surfactant templating

The electrodeposition of other mesostructured metals besides Pt has been reported, such as Se and Ni [103-105]. The metals were formed from

the electroreduction of the metal salt precursors, with the film mesophase ordering imposed by the surfactant LC phase. Mesoporous films were formed by washing out the surfactant with water; there was some indication of surface oxidation of the mesoporous Ni film [105].

The electrodeposition of a lamellar ZnO mesostructured film was recently reported by Choi et al. [106]. Zn nitrate was used as the source of Zn cations and nitrate anions. The anions were reduced at the electrode surface to release hydroxyl groups, which reacted with Zn cations to form ZnO (cathodic deposition). The mesostructure ordering was suggested to arise from cooperative assembly at the electrode (via surface-adsorbed micelles), since the bulk sodium dodecyl sulfate concentration (0.1 wt%) was below the hexagonal LC phase cmc (~40 wt%) and below even cmc1 (8.0×10^{-3} M, 0.23 wt%) [107]. An electrodeposition mechanism combining cooperative assembly with cathodic deposition was thus proposed.

2.3 Other related routes to mesostructured materials

2.3.1 Layered materials and surfactants

Pillared interlayered clays (PILCs) have been studied since the late 1970s as microporous materials with larger pore sizes (0.4–2.0 nm, but less uniform) and more tunable compositions than those of zeolites [108, 109]. The parent clay materials are composed of negatively-charged aluminosilicate sheets sandwiching charge-balancing cations. PILCs are prepared by swelling the clay sheets, ion-exchanging the cations with $[\text{AlO}_4\text{Al}_{12}(\text{OH})_{24}(\text{H}_2\text{O})_{12}]^{7+}$ aluminum polyoxocations, and calcining the material to create aluminum oxide pillars within the clay sheets. It was shown that PILC-like materials termed PCHs (porous clay heterostructures) could be prepared by carrying out surfactant templating within the clay sheets [110]. The PCH had controllable, uniform pore sizes of 1.4–2.2 nm and retained the sheet-like characteristics of the original clay material.

In comparison, FSM-16 hexagonal-phase mesoporous silica is prepared from kanemite, a polysilicate composed of single silica sheets intercalated by sodium cations (nominal composition of $\text{NaHSi}_2\text{O}_5 \cdot 3\text{H}_2\text{O}$ [111]). The sheets are thin compared to clay sheets, leading to a proposed formation mechanism in which CTAB molecules intercalate within the kanemite sheets and force the sheets to fold around the CTAB micelles into a hexagonal-phase mesoporous structure [7].

This lamellar-to-hexagonal mesophase transition for FSM-16 formation is consistent with the charge density matching requirement of cooperative surfactant templating, but has not been conclusively shown yet [112]. Alkyltrimethylammonium bromides, like CTAB, were found to intercalate into kanemite, yielding a lamellar-like, disordered mesoporous material (now called KSW-1) [5, 47, 113]. Under slightly modified synthesis conditions, FSM-16 was synthesized [7]. It was reported later that different kanemite/solution weight ratios can yield both KSW-1 and FSM-16 materials [114]. ^{29}Si MAS NMR analysis of the synthesis mixture supported the hypothesis that kanemite broke into fragmented sheets during the folding process [113]. Partial dissolution of kanemite (which is composed of only one type of Si, $(\text{SiO})_3\text{SiO}^-$ [115]) was indicated, as uncondensed silicate species in the form of $\text{Si}(\text{OH})_4$, $(\text{SiO})\text{Si}(\text{OH})_3$, and $(\text{SiO})_2\text{Si}(\text{OH})_2$ were detected.

2.3.2 Mesoporous silica as a hard template

Surfactant-templated mesoporous silicates with three-dimensionally connected pore networks have been used as cast materials in the preparation of mesoporous carbons [116]. This technique and LC templating can be referred to as nanocasting, but the former uses a hard template (the silica framework) and the latter uses a soft template (the surfactant LC). As an example of preparation, sugar is dehydrated within the MCM-48 mesopores with sulfuric acid, leaving behind carbonaceous deposits. The material is calcined at high temperatures in the absence of oxygen, and the silica framework is dissolved to give CMK-1, a mesoporous carbon with an inverse imprint of the MCM-48 framework. Other suitable mesoporous materials that were found to yield mesoporous carbon are SBA-1, HMS [117], and SBA-15 [118]; materials with non-connected pore networks like MCM-41 are not suitable. The mesoporous carbon materials were found with BET surface areas as high as $1500 \text{ m}^2 \text{ g}^{-1}$. The SBA-15-derived mesoporous carbon (CMK-3) was composed of bundles of carbon nanowires (7 nm diameter), held in place presumably by carbon formed in the SBA-15 micropores (see Section 3.6.1). Similarly, bundles of connected Pt nanowires were observed experimentally [54].

This synthesis route has developed into a useful characterization technique for indirectly studying the structure of porous inorganic templates. Its application revealed the three-dimensional interconnects within the HMS mesoporous silica pore structure [117] and the micropores within SBA-15 [119].

3 Compositions of mesostructured and mesoporous materials

We analyzed the surfactant templating literature published as recently as December 2002 to gain a comprehensive outlook on the current state of compositional control of mesostructured and mesoporous materials. As can be noted in Tables 2 and 3 and the periodic tables of Figures 6 and 7, the compositions of surfactant-templated materials are remarkably varied. In this Section, we summarize and provide general comments on our findings.

Table 2 and Figure 6 present elements that have been reported as the main component of surfactant-templated materials (*ca.* 50%). Most of the reported elements are metals, and many can be prepared into mesostructures as pure metals, metal oxides, or metal non-oxides. The listings include composition of the inorganic, the existence of porosity, and the type of long-range order, if any. Of the listed mesostructure compositions, *ca.* 50% can be treated for surfactant removal to yield mesoporous materials. Each entry was listed according to the following criteria: mesoporous > mesostructured; ordered > disordered; and cubic/hexagonal phases > lamellar phase, for mesostructured materials. For example, hexagonal-phase mesoporous WO_3 is listed, but earlier reports of mesostructured WO_3 are not [146, 147]. For surfactant/inorganic mesostructures, the noted compositions are those of the precursors if the compositions were not specifically addressed in the referenced work.

Only materials of “pure” compositions were considered in Table 2 and Figure 6. Doped mesoporous non-silicates and mesoporous mixed metal oxides were not counted unless the other metal elements were essential to mesostructure formation and were part of (and not external to) the framework (*e.g.*, Mn/Ge/S mesostructure); they are considered in Section 3.7.

Table 2. Compositions of surfactant-templated mesostructured and mesoporous materials.

Element	Composition	S/P ¹	Long-range order ²	Reference
Aluminum	Al_2O_3	P	D	[120]
Antimony	Sb_2O_5	S	H	[33]
Antimony	$\text{Sb}_{1.3}\text{Ge}_4\text{S}_{11}$ species	S	H	[121]
Antimony	Sb_2S_3	S	H	[122]
Cadmium	CdO_2	S	–	[96]
Cadmium	CdS , CdSe	S	H	[84]

Table continued

Element	Composition	S/P ¹	Long-range order ²	Reference
Carbon	C (elemental)	P	C,H,L	[123]
Cerium	CeO ₂	P	D	[124]
Chromium	Cr chloride species	S	–	[96]
Cobalt	Co (elemental)	P	H	[125]
Cobalt	Co species	S	L	[33]
Cobalt	Co ₂ Ge ₄ S ₁₀ anion	S	H	[82]
Copper	Cu chloride species	S	L	[96]
Dysprosium	Dy ₂ O ₃	P	D	[124]
Erbium	Er ₂ O ₃	P	D	[124]
Europium	Eu ₂ O ₃	P	D	[124]
Gadolinium	Gd ₂ O ₃	P	D	[124]
Gallium	Ga chloride species	S	–	[96]
Gallium	Ga _{1.3} Ge ₄ S ₁₁ anion	S	H	[126]
Germanium	Ge chloride species	S	–	[96]
Germanium	Ge sulfide	S	L	[127]
Hafnium	HfO ₂	S	–	[96]
Holmium	Ho ₂ O ₃	P	D	[124]
Indium	In chloride species	S	–	[96]
Indium	In _{1.3} Ge ₄ S ₁₁ anion	S	H	[126]
Iron	Fe ₂ O ₃	P	D	[128]
Iron	Fe _{1.28} SnSe ₄ anion	S	–	[129]
Lanthanum	La ₂ O ₃	P	D	[124]
Lead	Pb species	S	H	[33]
Lead	PbS	S	L	[130]
Lutetium	Lu ₂ O ₃	P	D	[124]
Magnesium	MgO	S	L	[33]
Manganese	Mn ₂ O ₃ + Mn ₃ O ₄	P	H	[131]
Manganese	MnGe ₄ S ₁₀ anion	S	H	[132]
Mercury	HgGe ₄ Se ₁₀ anions	S	D	[133]
Molybdenum	MoO ₂	P	L	[134]
Molybdenum	MoS ₂	S	L	[135]
Neodymium	Nd ₂ O ₃	P	D	[124]
Nickel	Ni (elemental)	P	H	[105]
Nickel	Ni species	S	L	[33]
Niobium	Nb ₂ O ₅	P	H	[42]
Palladium	Pd (elemental)	P	H	[136]

Table continued

Element	Composition	S/P ¹	Long-range order ²	Reference
Platinum	Pt (elemental)	P	H	[86]
Praseodymium	Pr oxide	P	D	[124]
Rhenium	ReO ₂	S	D	[137]
Ruthenium	Ru chloride species	S	–	[96]
Samarium	Sm ₂ O ₃	P	D	[124]
Selenium	Se (elemental)	P	H	[103]
Silicon	SiO ₂	P	C,H	[2]
Silicon	Si(NH) ₂	P	D	[138]
Tantalum	Ta ₂ O ₅	P	H	[139]
Tellurium	Te (elemental)	P	H	[140]
Terbium	Tb oxide	P	D	[124]
Thulium	Tm ₂ O ₃	P	D	[124]
Tin	Sn (elemental)	P	D	[141]
Tin	SnO ₂	P	H	[96]
Tin	SnS ₂	S	L	[142]
Titanium	TiO ₂	P	C,H	[96]
Tungsten	WO ₃	P	H	[96]
Tungsten	WS ₂	S	L	[135]
Vanadium	V species	S	H	[143]
Ytterbium	Yb ₂ O ₃	P	D	[124]
Yttrium	Y ₂ O ₃	P	D	[144]
Zinc	Zn species	S	L	[33]
Zinc	Zn _x SnSe ₄ anion	S	C	[129]
Zinc	Zn ₂ Ge ₄ S ₁₀ anion	S	H	[82]
Zinc	ZnS	S	H	[87]
Zirconium	ZrO ₂	P	D	[145]

¹ S = mesostructured, P = mesoporous

² C = cubic, H = hexagonal, L = lamellar, D = disordered, – = not reported

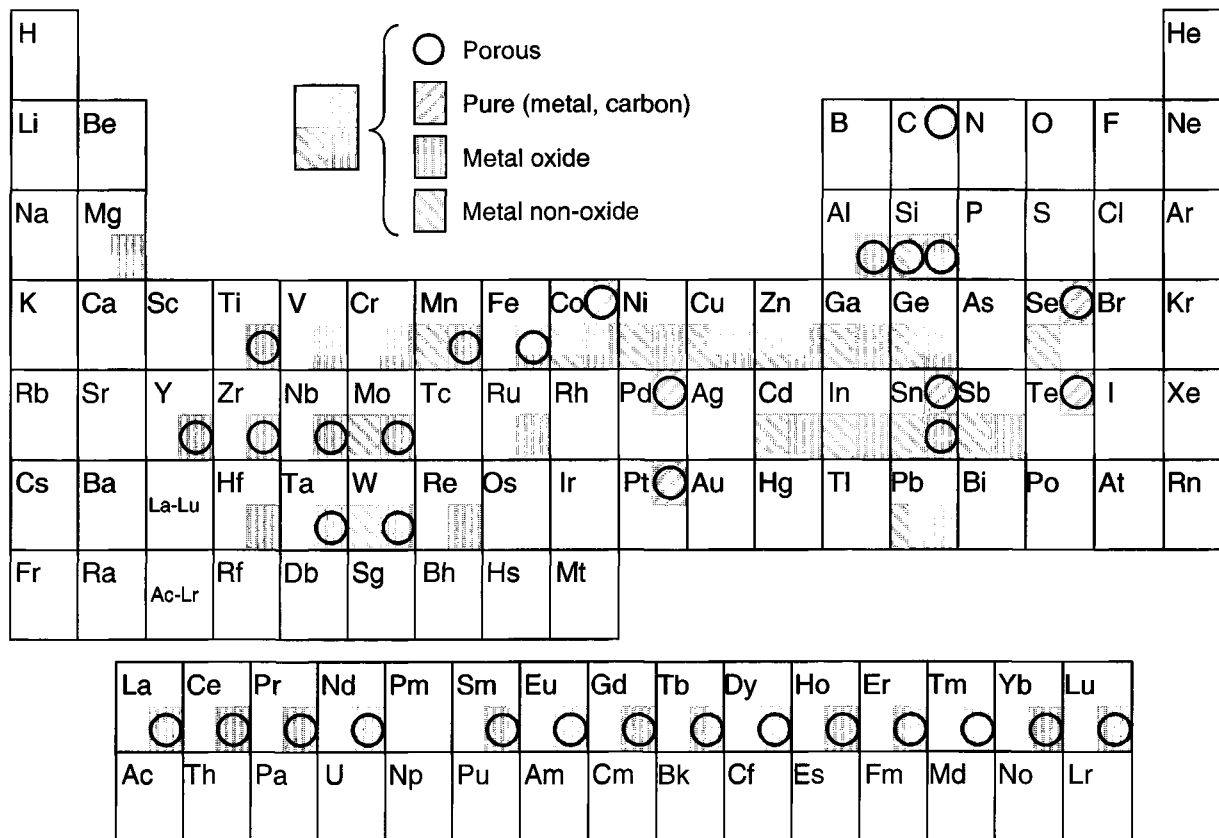


Figure 6: Compositions of surfactant-templated mesostructured and mesoporous materials.

3.1 Aluminum oxide

Alumina, a metal oxide available in at least seven different crystalline forms, is widely used as a catalyst and catalyst support. Mesoporous γ -alumina, for example, with a disordered pore structure can be obtained through traditional (non-surfactant-templated) routes with typical specific surface areas of $\sim 300 \text{ m}^2\text{g}^{-1}$ and stabilities up to 900°C [148]. Surfactant templating of mesoporous alumina is possible, but the gain in surface area is countered by a loss in thermal stability (due to lack of framework crystallinity). A major advantage of surfactant templating comes from pore size uniformity and tunability, but ordered, mesoporous alumina has not been achieved thus far.

Early synthesis efforts using anions of aluminum alkoxide species at high pH yielded amorphous frameworks of hexagonal mesostructures unstable to template removal [149], or disordered mesoporous materials [120, 150]. Recent attempts have enjoyed more success at introducing framework crystallinity. Working at pH below the isoelectric point of aluminum (iep ~ 9), Al^{3+} or Keggin ion building blocks $[\text{AlO}_4\text{Al}_{12}(\text{OH})_{24}(\text{H}_2\text{O})_{12}]^{7+}$ were found to form disordered mesoporous materials with crystalline frameworks after calcination at 450°C . Specific surface areas ranged between $300\text{--}800 \text{ m}^2\text{g}^{-1}$ [151]. A multi-step transformation process, also starting with Keggin ion clusters, obtained $\gamma\text{-Al}_2\text{O}_3$ nanocrystallites within the framework upon calcination at 550°C while maintaining mesoporosity. Specific surface areas were $\leq 350 \text{ m}^2\text{g}^{-1}$ [152]. The thermal stability limits of these mesoporous aluminas were not reported.

3.2 Transition metal oxides

Figure 2 illustrates the wide range of mesostructured and mesoporous transition metal oxides prepared to date. Roughly 60% of the transition metals can be prepared as mesostructured oxides, and almost 50% can be mesoporous.

Framework instability remains a significant problem for mesostructured transition metal oxides. Incomplete condensation of the inorganic precursors and crystallization of the amorphous framework have been noted as significant reasons. An example of a synthesis approach to bypass the crystallization problem is the use of crystalline transition metal oxide nanoparticles instead of molecular precursors [61]. For redox-active transition metals, template removal via calcination could partially reduce

the framework, causing the pore walls to restructure and collapse. For materials that collapse upon calcination, gentler methods of template removal have been used to obtain mesoporous materials *e.g.*, ion exchange [153], liquid extraction [33], supercritical fluid extraction [154], and oxygen plasma treatment [155].

3.3 Metal phosphates, sulfates, and sulfonates

Phosphate, sulfate, and sulfonate groups can be considered either extra- or intra-framework species. The distinction is blurry because the pore walls are so thin (~1 nm), but it can help to differentiate between either a surface-rich distribution or a homogeneous distribution within the framework. The extra-framework species are believed to stabilize the underlying metal oxide framework onto which they are surface-bound. Extra-framework phosphate, sulfate, and sulfonate ions are delivered to the inorganic framework in the form of surfactant head groups [43, 156], as anions in the reaction mixture [157], or anions that ion-exchange during post-synthesis acid washes [158, 159].

With phosphate anions as the intra-framework species, mesoporous metallophosphates (*e.g.*, aluminophosphates and metalloaluminophosphates) are similar to their crystalline zeolitic counterparts [160]. One of the most investigated phosphate materials is aluminum phosphate (AlPO). Zeolitic AlPO materials have a relatively narrow range of molar ratios, $0.8 \leq \text{Al/P} \leq 1.2$ [161]. In contrast, surfactant-templated AlPO mesostructure display greater compositional flexibility ($0.5 \leq \text{Al/P} \leq 5.9$), and presumably greater tunability of Lewis acid properties [162, 163]; however, these mesostructures exhibit poorer thermal stability and long-range order. Most reported materials are lamellar mesostructures [162, 164] or hexagonal-phase mesostructures that lose long-range order upon calcination [165, 166]. A few exceptions are hexagonal-phase mesoporous silicoaluminophosphate (SAPO) [167], aluminoborate (AlBO) [168], and titanoaluminophosphate (TiAPO) materials [169]. These materials are less stable than other surfactant-templated mesoporous materials.

3.4 Metal chalcogenides

Metal chalcogenides (*i.e.*, containing framework S, Se, or Te) represent the largest class of non-oxide mesoporous materials; mesoporous metal telluride has not been reported yet. Some metal chalcogenide

mesostructures are stable to partial removal of the surfactant, but none are stable upon total surfactant removal.

One approach to preparing metal chalcogenide mesostructures uses a metal salt dissolved in a LC phase, which is contacted with the chalcogenide precursor. The chalcogenide is introduced as an acid gas (e.g., H_2S and H_2Se) or a salt (e.g., Na_2S and Na_2Se). Lamellar and hexagonal-phase mesostructures of CdS , CdSe , ZnS [84, 170] and, later, SnS_2 and Sb_2S_3 [122] were obtained in this manner.

Another approach uses anionic chalcogenide molecular clusters linked together by metal cations in cooperatively assembled surfactant templating. These building blocks have tetrahedral coordination (like SiO_4^{4-} units in silicate frameworks), and have been used in the preparation of crystalline, microporous open frameworks since 1989 [171].

Early investigations focused on nonaqueous preparations using $[\text{Ge}_4\text{S}_{10}]^{4-}$ clusters and divalent metal salts ($\text{M} = \text{Zn}^{2+}$, Co^{2+} , Ni^{2+} , Cu^{2+}) to produce hexagonal mesostructures of the form $(\text{R})\text{M}/[\text{Ge}_4\text{S}_{10}]^{4-}$ (R = organic template) that were stable up to 40% surfactant removal [82, 172]. Later, molecular clusters of $[\text{Ge}_4\text{Q}_{10}]^{4-}$ ($\text{Q} = \text{S}$ or Se) led to different mesostructures produced in aqueous reaction mixtures [121, 126, 132, 133]. Stable to 70% surfactant removal, these hexagonal-phase mesostructures of the form $(\text{R})_2\text{M}_{1-1.7}\text{Ge}_4\text{Q}_{10-12.3}$ were obtained from $\text{M} = \text{Mn}^{2+}$, Sb^{3+} , Sn^{4+} counterions; $\text{M} = \text{Zn}^{2+}$, Cd^{2+} , Hg^{2+} , Co^{2+} , Ni^{2+} , Ga^{3+} , In^{3+} generated disordered wormhole structures. $[\text{SnSe}_4]^{4-}$ building blocks also successfully led to hexagonal-phase mesostructures with a composition of $(\text{R})_{4-2x}\text{M}_x\text{SnSe}_4$, where $\text{M} = \text{Mn}^{2+}$, Fe^{2+} , Cd^{2+} , Hg^{2+} , Co^{2+} ; with $\text{M} = \text{Zn}^{2+}$, a cubic-phase non-oxide mesostructure was shown for the first time [129]. Most recently, $[\text{Sn}_2\text{S}_6]^{4-}$ led to hexagonal-phase mesostructures of the form $(\text{R})_{1.1-1.4}\text{M}_{0.9-1.4}\text{Sn}_2\text{S}_6$ ($\text{M} = \text{Ga}^{2+}$, Zn^{2+} , Cd^{2+}), which were unstable to template removal [173].

Other examples of non-oxide mesostructures include lamellar germanium sulfide [127] and lamellar MoS_2 and WS_2 [135]. The latter sulfides were prepared by decarbonylating $\text{M}(\text{CO})_6$ ($\text{M} = \text{Mo}$ and W) with elemental sulfur in an alkylamine melt.

3.5 Metals

Mesoporous metals can be prepared through nanocasting of LCs (soft template) or of mesoporous silica (hard template). Metal mesostructures produced through LC templating are stable to template removal via solvent washing (see Section 2.1.2). Those produced through a combined

electrodeposition/LC templating were found to possess hexagonal-phase long-range order, relatively high surface areas, smooth surface topography, and in the case of alloys, uniform metal distribution [86, 103, 125, 136, 140, 141] (see Section 2.2).

Hard template nanocasting involves filling the pore channels of mesoporous silica with a metal salt, and reducing the metal salt to zero-valent metal [174, 175]. A three-dimensional pore network like MCM-48 and SBA-15 leads to a three-dimensional metal nanowire network, whereas silica templates without interchannel connectivity like MCM-41 lead to unconnected, one-dimensional metal nanowires. In the case of Pt, nanowire diameter and silica pore diameter matched very closely [174, 176].

3.6 Other compositions

3.6.1 Carbon

Disordered mesoporous carbon has been produced via conventional routes for two decades [177, 178], but it has lacked periodic three-dimensional structure and uniform pore size; moreover, acquiring high specific surface area requires a subsequent activation step. Ordered mesoporous carbon is prepared using the hard template nanocasting route used for mesoporous metals (see Section 3.5). However, despite similar synthesis routes, the topology differs slightly between the mesoporous carbon and metal product.

The general procedure requires filling a mesoporous inorganic template with organic material (with sulfuric acid as a dehydrating aid [116]), pyrolyzing the organic species to carbon in the absence of oxygen, and finally removing the inorganic framework. Carbonaceous precursor organic feedstocks have included sucrose, furfuryl alcohol, formaldehyde, and *in situ* polymerized phenol resin [116, 179]. To release the carbon imprint, the silica framework is dissolved in hydrogen fluoride or in a basic solution [116]. The carbon materials are mesoporous, have ordered domains, and have extremely high surface areas. The presence of pore openings with uniform size and shape should depend on the mesoporous silicate hard template used; a perfect imprint of MCM-48 would have uniform pore openings, whereas that of SBA-15 would not.

Crosslinked organic LC phases can be considered carbon-based mesoporous materials that retain the chemical identity of the carbon precursor, unlike nanocast mesoporous carbon. The formation of

mesoporous polymer proceeds with the formation of an *inverted* hexagonal LC phase of specially designed polymerizable surfactant molecules. The surfactant tail group is photopolymerized to form a connected organic framework (akin to the MCM-41 framework); the mesopores come from removing water from the cylindrical channels [180].

Mesoporous organosilicates are hybrid mesoporous silicates integrated with hydrocarbon species bound on, or embedded within, the pore walls. They are covered extensively in reviews [181] and elsewhere in this Book.

3.6.2 Nitrides

A recently reported mesoporous non-oxide, silicon imido nitride, $\text{Si}(\text{NH})_2$, can be prepared via two separate mechanisms, neither of which strictly fit the definition of surfactant-templated mesoporous materials. However, they have been included based on their interesting chemistry and surfactant-assisted formation. In both cases, these materials exhibit activity as base catalysts.

Microporous $\text{Si}(\text{NH})_2$ has been produced via long-chain amine templating [138]. Alkylamine, $\text{CH}_3(\text{CH}_2)_n\text{NH}_2$ ($n = 11-17$), participates both as the structure-directing template and condensation catalyst under thermal conditions. Added to boiling acetonitrile, tris(dimethylamino)-silylamine ($(\text{CH}_3)_2\text{N})_3\text{SiNH}_2$) undergoes ammonolysis and condensation, to yield porous $\text{Si}(\text{NH})_2$ after calcination. TEM and ^{29}Si MAS NMR revealed long-range pore disorder and amorphous short-range order which were preserved even after exposure to 1000 °C. Pore sizes were estimated in the microporous regime, but specific surface areas were not reported. The amine was speculated to participate via molecular templating and not supramolecular templating. Mesoporous silicon imido nitride was obtained by using *in situ* formed salt nanocrystals to template mesopores of 5.6-9.1 nm; no long-range ordering of the pores was found [182].

3.7 Mixed compositions

Table 3 and Figure 7 identify 24 elements used as the framework dopant in mesoporous silica. Surface grafted or functionalized materials were not considered. Materials containing less than 5 wt% dopant generally possess long range pore order, and materials with higher dopant content are predisposed to be disordered and less structurally stable. The uniformity in dispersion within the framework and dopant concentrations are limited by dissimilar hydrolysis and condensation rates typically exhibited by the silica and secondary metal oxide precursor [183].

H																	He
Li	Be											B	C	N	O	F	Ne
Na	Mg											Al	Si	P	S	Cl	Ar
K	Ca	Sc	Ti	V	Cr	Mn	Fe	Co	Ni	Cu	Zn	Ga	Ge	As	Se	Br	Kr
Rb	Sr	Y	Zr	Nb	Mo	Tc	Ru	Rh	Pd	Ag	Cd	In	Sn	Sb	Te	I	Xe
Cs	Bs	La-Lu	Hf	Ta	W	Re	Os	Ir	Pt	Au	Hg	Tl	Pb	Bi	Po	At	Rn
Fr	Ra	Ac-Lr	Rf	Db	Sg	Bh	Hs	Mt									
			La	Ce	Pr	Nd	Pm	Sm	Eu	Gd	Tb	Dy	Ho	Er	Tm	Yb	Lu
			Ac	Th	Pa	U	Np	Pu	Am	Cm	Bk	Cf	Es	Fm	Md	No	Lr

Figure 7: Elements doped into surfactant-templated mesoporous silica.

Table 3. Elements doped into surfactant-templated mesoporous silica

Element	Order ¹	Reference	Element	Order ¹	Reference
Aluminum	C, H	[1]	Niobium	H	[184]
Boron	H	[185]	Rhenium	H	[186]
Cerium	D	[187]	Ruthenium	H	[188]
Chromium	H	[189]	Tantalum	D	[183]
Cobalt	C	[190]	Thorium	H	[191]
Copper	H	[192]	Tin	H	[193]
Gallium	D	[194]	Titanium	D	[195]
Iron	D	[194]	Tungsten	H	[196]
Lanthanum	D	[187]	Uranium	H	[191]
Manganese	H	[197]	Vanadium	D	[198]
Molybdenum	D	[189]	Zinc	C	[199]
Nickel	H	[200]	Zirconium	D	[201]

¹ Long-range order: C = cubic, H = hexagonal, D = disordered

One approach to increasing the dopant level while maintaining structural stability is to prepare the doped mesoporous silicate under highly acidic conditions instead of basic conditions [59]. Up to 20 wt% Zr was successfully incorporated into mesoporous silica using Zr salt and TEOS precursors; above 10 wt%, significant contraction of the framework was observed after calcination, which led to microporous Zr-doped silicates.

Another approach to highly doped mesoporous materials, and to mesoporous mixed metal oxides, involves the use of two-metal-containing single-molecule precursors in evaporation-induced surfactant templating. This surfactant templating route to pure non-silicates was extended to mixed non-silicates (*e.g.*, silicon oxide/titanium oxide [96, 97] and niobium oxide/tantalum oxide [202]), but the degree of metal oxide dispersion is not known for all mixed materials. By using a single-molecule precursor like $\text{Zr}[\text{OSi}(\text{O-tert-Bu})_3]_4$ in a non-hydrolytic route, mesoporous $\text{ZrO}_2 \cdot 4\text{SiO}_2$ was produced. This material was found to be compositionally homogeneous, as inferred from the crystallization temperature of 1100 °C [183, 203]. With the ability to prepare mesoporous non-silicates, it is conceivable the entire compositional spectrum for a mesoporous material containing two metal oxides can be accessed *e.g.*, pure silica, metal-doped silicate, mixed metal oxide, silicon-doped metal oxide, and pure metal oxide.

The use of nanoparticles as the precursor to the framework was shown to be a viable route to two-metal-containing mesoporous materials [61]. ZrO_2 and TiO_2 nanoparticles (in addition to $[\text{AlO}_4\text{Al}_{12}(\text{OH})_{24}(\text{H}_2\text{O})_{12}]^{7+}$ molecular clusters) were used to prepare the corresponding tungstated metal oxides. Unlike the other bi-component mesoporous metal oxides, the second component (WO_3) was distributed throughout the material near the framework surface; also, these materials were nanocrystalline before heat treatment.

4 Conclusions and outlook

Mesoporous materials of various compositions can be achieved, with the templating chemistry tailored towards the type of inorganic precursors and surfactants used. It is critical that the interactions between the surfactant head group and inorganic precursor (and those between the surfactant head group and polymerizing inorganic framework) are favorable for mesostructure formation to occur. By observing this and other synthesis guidelines, new compositions can be prepared into a mesostructure, especially with designed inorganic precursors.

The favorable binding of the surfactant to the inorganic precursor is a necessary condition for mesostructure formation; however, it is an insufficient one for mesoporous materials formation. The lack of structural stability (*i.e.*, thermal and hydrothermal) is particularly troublesome for non-silicates and mixed metal oxides, which restricts the utility of these materials. Fortunately, there are opportunities in circumventing the instability problem of mesoporous materials, such as using pre-crystallized nanoparticle precursors [61, 204] and using novel metal precursors to form the mesostructure non-hydrolytically [183, 203].

The range, uniformity, and tunability of pore sizes, and the ordered pore structure are unique aspects of surfactant-templated materials. Reliable methods to produce materials with ordered mesopore channels with sizes > 15 nm are sought, which may require new types of templating agents. New mesophases could be possible with a better understanding of how inorganic condensation perturbs surfactant solution phase diagrams. The morphology of the mesostructured or mesoporous materials can be reliably controlled, an important consideration in particular applications. New morphologies and better control of pore orientation (*e.g.*, within mesoporous films) would increase the utility of surfactant-templated materials.

In short, the field of surfactant-templated materials remains vibrant, and research activity will remain high in the near future. What will motivate continued interest in surfactant templating chemistry and surfactant-templated materials are applications that can take full advantage of the mesostructure/mesoporosity, pore ordering, uniform pore size, and/or framework composition of these materials.

5 Acknowledgments

The authors gratefully acknowledge the financial support of Rice University and the Nanoscale Science and Engineering Initiative of the National Science Foundation under NSF Award Number EEC-0118007 through the Center for Biological and Environmental Nanotechnology (CBEN).

References

1. Kresge C. T., Leonowicz M. E., Roth W. J., Vartuli J. C. and Beck J. S., Ordered mesoporous molecular sieves synthesized by a liquid-crystal template mechanism, *Nature* **359** (1992) pp. 710-712.
2. Beck J. S., Vartuli J. C., Roth W. J., Leonowicz M. E., Kresge C. T., Schmitt K. D., Chu C. T.-W., Olson D. H., Sheppard E. W., McCullen S. B., Higgins J. B. and Schlenker J. L., A new family of mesoporous molecular sieves prepared with liquid crystal templates, *J. Am. Chem. Soc.* **114** (1992) pp. 10834-10843.
3. Beck J. S., Vartuli J. C., Kennedy G. J., Kresge C. T., Roth W. J. and Schramm S. E., Molecular or supramolecular templating: defining the role of surfactant chemistry in the formation of microporous and mesoporous molecular sieves, *Chem. Mat.* **6** (1994) pp. 1816-1821.
4. Vartuli J. C., Schmitt K. D., Kresge C. T., Roth W. J., Leonowicz M. E., McCullen S. B., Hellring S. D., Beck J. S., Schlenker J. L., Olson D. H. and Sheppard E. W., Effect of surfactant/silica molar ratios on the formation of mesoporous molecular sieves: inorganic mimicry of surfactant liquid-crystal phases and mechanistic implications, *Chem. Mat.* **6** (1994) pp. 2317-2326.
5. Vartuli J. C., Kresge C. T., Leonowicz M. E., Chu A. S., McCullen S. B., Johnson I. D. and Sheppard E. W., Synthesis of mesoporous materials: liquid-crystal templating versus intercalation of layered silicates, *Chem. Mat.* **6** (1994) pp. 2070-2077.
6. Kresge C. T., Leonowicz M. E., Roth W. J. and Vartuli J. C. (1990), *U.S. Patent No. 5,098,684*.
7. Inagaki S., Fukushima Y. and Kuroda K., Synthesis of highly ordered mesoporous materials from a layered polysilicate, *J. Chem. Soc. Chem. Commun.* (1993) pp. 680-682.
8. Zhao X. S., Lu G. Q. M. and Millar G. J., Advances in mesoporous molecular sieve MCM-41, *Ind. Eng. Chem. Res.* **35** (1996) pp. 2075-2090.

9. Ying J. Y., Mehnert C. P. and Wong M. S., Synthesis and applications of supramolecular-templated mesoporous materials, *Angew. Chem. Int. Edit.* **38** (1999) pp. 56-77.
10. Liu G. and Ding J., Diblock thin films with densely hexagonally packed nanochannels, *Adv. Mater.* **10** (1998) pp. 69-71.
11. Hayward R. C., Alberius-Henning P., Chmelka B. F. and Stucky G. D., The current role of mesostructures in composite materials and device fabrication, *Microporous Mesoporous Mat.* **44** (2001) pp. 619-624.
12. He X. and Antonelli D., Recent advances in synthesis and applications of transition metal containing mesoporous molecular sieves, *Angew. Chem. Int. Edit.* **41** (2001) pp. 214-229.
13. Schuth F., Non-siliceous mesostructured and mesoporous materials, *Chem. Mat.* **13** (2001) pp. 3184-3195.
14. Sayari A. and Liu P., Non-silica periodic mesostructured materials: recent progress, *Microporous Mater.* **12** (1997) pp. 149-177.
15. Corma A., From microporous to mesoporous molecular sieve materials and their use in catalysis, *Chem. Rev.* **97** (1997) pp. 2373-2419.
16. Sayari A., Catalysis by crystalline mesoporous molecular sieves, *Chem. Mat.* **8** (1996) pp. 1840-1852.
17. Pang J. B., Qiu K. Y. and Wei Y., Recent progress in research on mesoporous materials I: Synthesis, *J. Inorg. Mater.* **17** (2002) pp. 407-414.
18. Vartuli J. C., Shih S. S., Kresge C. T. and Beck J. S., Potential applications for M41S type mesoporous molecular sieves. In *Mesoporous Molecular Sieves 1998* (1998) pp. 13-21.
19. On D. T., Desplandier-Giscard D., Danumah C. and Kaliaguine S., Perspectives in catalytic applications of mesostructured materials, *Appl. Catal. A-Gen.* **222** (2001) pp. 299-357.
20. Scott B. J., Wirnsberger G. and Stucky G. D., Mesoporous and mesostructured materials for optical applications, *Chem. Mat.* **13** (2001) pp. 3140-3150.
21. Zhang J., Luz Z., Zimmermann H. and Goldfarb D., The formation of the mesoporous material MCM-41 as studied by EPR line shape analysis of spin probes, *J. Phys. Chem. B* **104** (2000) pp. 279-285.
22. Sicard L., Lebeau B., Patarin J. and Zana R., Study of the mechanism of formation of a mesostructured hexagonal alumina by means of fluorescence probing techniques, *Langmuir* **18** (2002) pp. 74-82.
23. Frasc J., Lebeau B., Soulard M., Patarin J. and Zana R., In situ investigations on cetyltrimethyl ammonium surfactant/silicate systems, precursors of organized mesoporous MCM-41-type siliceous materials, *Langmuir* **16** (2000) pp. 9049-9057.
24. Dabbs D. M. and Aksay I. A., Self-assembled ceramics produced by complex-fluid templation, *Annu. Rev. Phys. Chem.* **51** (2000) pp. 601-622.
25. Oye G., Sjoblom J. and Stocker M., Synthesis, characterization and potential applications of new materials in the mesoporous range, *Adv. Colloid Interface Sci.* **89** (2001) pp. 439-466.
26. Kruk M. and Jaroniec M., Gas adsorption characterization of ordered organic-inorganic nanocomposite materials, *Chem. Mat.* **13** (2001) pp. 3169-3183.

27. Lin H.-P. and Mou C.-Y., Structural and morphological control of cationic surfactant- templated mesoporous silica, *Accounts Chem. Res.* **35** (2002) pp. 927-935.
28. Ciesla U. and Schüth F., Ordered mesoporous materials, *Microporous Mesoporous Mat.* **27** (1999) pp. 131-149.
29. Patarin J., Lebeau B. and Zana R., Recent advances in the formation mechanisms of organized mesoporous materials, *Curr. Opin. Colloid Interface Sci.* **7** (2002) pp. 107-115.
30. Polarz S. and Antonietti M., Porous materials via nanocasting procedures: innovative materials and learning about soft-matter organization, *Chem. Commun.* (2002) pp. 2593-2604.
31. McCusker L. B., Liebau F. and Engelhardt G., Nomenclature of structural and compositional characteristics of ordered microporous and mesoporous materials with inorganic hosts (IUPAC Recommendations 2001), *Pure Appl. Chem.* **73** (2001) pp. 381-394.
32. Huo Q., Margolese D. I., Ciesla U., Demuth D. G., Feng P., Gier T. E., Sieger P., Firouzi A., Chmelka B. F., Schüth F. and Stucky G. D., Organization of organic-molecules with inorganic molecular species into nanocomposite biphasic arrays, *Chem. Mat.* **6** (1994) pp. 1176-1191.
33. Huo Q., Margolese D. I., Ciesla U., Feng P., Gier T. E., Sieger P., Leon R., Petroff P. M., Schüth F. and Stucky G. D., Generalized synthesis of periodic surfactant/inorganic composite materials, *Nature* **368** (1994) pp. 317-321.
34. Tanev P. T. and Pinnavaia T. J., A neutral templating route to mesoporous molecular sieves, *Science* **267** (1995) pp. 865-867.
35. Tanev P. T. and Pinnavaia T. J., Mesoporous silica molecular sieves prepared by ionic and neutral surfactant templating: a comparison of physical properties, *Chem. Mat.* **8** (1996) pp. 2068-2079.
36. Bagshaw S. A., Prouzet E. and Pinnavaia T. J., Templating of mesoporous molecular sieves by nonionic polyethylene oxide surfactants, *Science* **269** (1995) pp. 1242-1244.
37. Prouzet E., Cot F., Nabias G., Larbot A., Kooyman P. and Pinnavaia T. J., Assembly of mesoporous silica molecular sieves based on nonionic ethoxylated sorbitan esters as structure directors, *Chem. Mat.* **11** (1999) pp. 1498-1503.
38. Zhao D., Feng J., Huo Q., Melosh N., Fredrickson G. H., Chmelka B. F. and Stucky G. D., Triblock copolymer syntheses of mesoporous silica with periodic 50 to 300 angstrom pores, *Science* **279** (1998) pp. 548-552.
39. Zhao D., Huo Q., Feng J., Chmelka B. F. and Stucky G. D., Nonionic triblock and star diblock copolymer and oligomeric surfactant syntheses of highly ordered, hydrothermally stable, mesoporous silica structures, *J. Am. Chem. Soc.* **120** (1998) pp. 6024-6036.
40. Bagshaw S. A., Kemmitt T. and Milestone N. B., Mesoporous [M]-MSU-x metallo-silicate catalysts by non-ionic polyethylene oxide surfactant templating acid $[N^0(N^+)XT^-]$ and base $(N^0M^+T^-)$ catalysed pathways, *Microporous Mesoporous Mat.* **22** (1998) pp. 419-433.
41. Antonelli D. M. and Ying J. Y., Synthesis of a stable hexagonally packed mesoporous niobium oxide molecular sieve through a novel ligand-assisted templating mechanism, *Angew. Chem. Int. Edit. Engl.* **35** (1996) pp. 426-430.

42. Antonelli D. M., Nakahira A. and Ying J. Y., Ligand-assisted liquid crystal templating in mesoporous niobium oxide molecular sieves, *Inorg. Chem.* **35** (1996) pp. 3126-3136.
43. Wong M. S. and Ying J. Y., Amphiphilic templating of mesoporous zirconium oxide, *Chem. Mat.* **10** (1998) pp. 2067-2077.
44. Iler R. K., The chemistry of silica: solubility, polymerization, colloid and surface properties, and biochemistry (Wiley, New York, 1979).
45. Brinker C. J. and Scherer G. W., Sol-gel science: the physics and chemistry of sol-gel processing (Academic Press, Boston, 1990).
46. Hunter R. J., Foundations of colloid science (Oxford University Press, Oxford, 2001).
47. Yanagisawa T., Shimizu T., Kuroda K. and Kato C., The preparation of alkyltrimethylammonium-kanemite complexes and their conversion to microporous materials, *Bull. Chem. Soc. Jpn.* **63** (1990) pp. 988-992.
48. Chiola V., Ritsko J. E. and Vanderpool C. D. (1971), *U.S. Patent No.* 3,556,725.
49. Di Renzo F., Cambon H. and Dutartre R., A 28-year-old synthesis of micelle-templated mesoporous silica, *Microporous Mater.* **10** (1997) pp. 283-286.
50. Breck D. W., Zeolite molecular sieves: structure, chemistry, and use (Wiley, Malabar, Fla., 1984).
51. Israelachvili J. N., Intermolecular and surface forces (Academic Press, London, 1992).
52. Yang H., Kuperman A., Coombs N., Mamiche-Afara S. and Ozin G. A., Synthesis of oriented films of mesoporous silica on mica, *Nature* **379** (1996) pp. 703-705.
53. Imperor-Clerc M., Davidson P. and Davidson A., Existence of a microporous corona around the mesopores of silica-based SBA-15 materials templated by triblock copolymers, *J. Am. Chem. Soc.* **122** (2000) pp. 11925-11933.
54. Ryoo R., Ko C. H., Kruk M., Antochshuk V. and Jaroniec M., Block-copolymer-templated ordered mesoporous silica: array of uniform mesopores or mesopore-micropore network?, *J. Phys. Chem. B* **104** (2000) pp. 11465-11471.
55. Sayari A., Moudrakovski I., Reddy J. S., Ratcliffe C. I., Ripmeester J. A. and Preston K. F., Synthesis of mesoporous lamellar aluminophosphates using supramolecular templates, *Chem. Mat.* **8** (1996) pp. 2080-2088.
56. Thomas J. M., Terasaki O., Gai P. L., Zhou W. and Gonzalez-Calbet J., Structural elucidation of microporous and mesoporous catalysts and molecular sieves by high-resolution electron microscopy, *Accounts Chem. Res.* **34** (2001) pp. 583-594.
57. Sakamoto Y. H., Kaneda M., Terasaki O., Zhao D. Y., Kim J. M., Stucky G., Shin H. J. and Ryoo R., Direct imaging of the pores and cages of three-dimensional mesoporous materials, *Nature* **408** (2000) pp. 449-453.
58. Kruk M., Jaroniec M., Sakamoto Y., Terasaki O., Ryoo R. and Ko C. H., Determination of pore size and pore wall structure of MCM-41 by using nitrogen adsorption, transmission electron microscopy, and X-ray diffraction, *J. Phys. Chem. B* **104** (2000) pp. 292-301.
59. Wong M. S., Huang H. C. and Ying J. Y., Supramolecular-templated synthesis of nanoporous zirconia-silica catalysts, *Chem. Mat.* **14** (2002) pp. 1961-1973.
60. Pauly T. R. and Pinnavaia T. J., Pore size modification of mesoporous HMS molecular sieve silicas with wormhole framework structures, *Chem. Mat.* **13** (2001) pp. 987-993.

61. Wong M. S., Jeng E. S. and Ying J. Y., Supramolecular templating of thermally stable crystalline mesoporous metal oxides using nanoparticulate precursors, *Nano. Lett.* **1** (2001) pp. 637-642.
62. Huo Q., Leon R., Petroff P. M. and Stucky G. D., Mesostructure design with Gemini surfactants: supercage formation in a three-dimensional hexagonal array, *Science* **268** (1995) pp. 1324-1327.
63. Zhou W., Hunter H. M. A., Wright P. A., Ge Q. and Thomas J. M., Imaging the pore structure and polytypic intergrowths in mesoporous silica, *J. Phys. Chem. B* **102** (1998) pp. 6933-6936.
64. Sakamoto Y., Díaz I., Terasaki O., Zhao D., Pérez-Pariente J., Kim J. M. and Stucky G. D., Three-dimensional cubic mesoporous structures of SBA-12 and related materials by electron crystallography, *J. Phys. Chem. B* **106** (2002) pp. 3118-3123.
65. Garcia-Bennett A. E., Williamson S., Wright P. A. and Shannon I. J., Control of structure, pore size and morphology of three-dimensionally ordered mesoporous silicas prepared using the dicationic surfactant $[\text{CH}_3(\text{CH}_2)_{15}\text{N}(\text{CH}_3)_2(\text{CH}_2)_3\text{N}(\text{CH}_3)_3]\text{Br}_2$, *J. Mater. Chem.* **12** (2002) pp. 3533-3540.
66. Edler K. J. and Roser S. J., Growth and characterization of mesoporous silica films, *Int. Rev. Phys. Chem.* **20** (2001) pp. 387-466.
67. Raman N. K., Anderson M. T. and Brinker C. J., Template-based approaches to the preparation of amorphous, nanoporous silicas, *Chem. Mat.* **8** (1996) pp. 1682-1701.
68. Li N., Liu S. and Luo H. Q., A new method for the determination of the first and second CMC in CTAB solution by resonance Rayleigh scattering technology, *Anal. Lett.* **35** (2002) pp. 1229-1238.
69. Quirion F. and Magid L. J., Growth and counterion binding of cetyltrimethylammonium bromide aggregates at 25 °C - a neutron and light scattering study, *J. Phys. Chem.* **90** (1986) pp. 5435-5441.
70. Auvray X., Petipas C., Anthore R., Rico I. and Lattes A., X-ray diffraction study of mesophases of cetyltrimethylammonium bromide in water, formamide, and glycerol, *J. Phys. Chem.* **93** (1989) pp. 7458-7464.
71. Fontell K., Khan A., Lindström B., Maciejewska D. and Puang-Ngern S., Phase equilibria and structures in ternary systems of a cationic surfactant (C_{16}TABr or $(\text{C}_{16}\text{TA})_2\text{SO}_4$), alcohol, and water, *Colloid Polym. Sci.* **269** (1991) pp. 727-742.
72. Firouzi A., Kumar D., Bull L. M., Besier T., Sieger P., Huo Q., Walker S. A., Zasadzinski J. A., Glinka C., Nicol J., Margolese D., Stucky G. D. and Chmelka B. F., Cooperative organization of inorganic-surfactant and biomimetic assemblies, *Science* **267** (1995) pp. 1138-1143.
73. Firouzi A., Atef F., Oertli A. G., Stucky G. D. and Chmelka B. F., Alkaline lyotropic silicate-surfactant liquid crystals, *J. Am. Chem. Soc.* **119** (1997) pp. 3596-3610.
74. Karlsson S., Friman R., Björkqvist M., Lindström B. and Backlund S., Phase behavior and characterization of the system acetic acid-dodecylamine-water, *Langmuir* **17** (2001) pp. 3573-3578.
75. Ivanova R., Lindman B. and Alexandridis P., Modification of the lyotropic liquid crystalline microstructure of amphiphilic block copolymers in the presence of cosolvents, *Adv. Colloid Interface Sci.* **89** (2001) pp. 351-382.

76. Monnier A., Schuth F., Huo Q., Kumar D., Margolese D., Maxwell R. S., Stucky G. D., Krishnamurty M., Petroff P., Firouzi A., Janicke M. and Chmelka B. F., Cooperative formation of inorganic-organic interfaces in the synthesis of silicate mesostructures, *Science* **261** (1993) pp. 1299-1303.
77. Landry C. C., Tolbert S. H., Gallis K. W., Monnier A., Stucky G. D., Norby P. and Hanson J. C., Phase transformations in mesostructured silica/surfactant composites. Mechanisms for change and applications to materials synthesis, *Chem. Mat.* **13** (2001) pp. 1600-1608.
78. Tolbert S. H., Landry C. C., Stucky G. D., Chmelka B. F., Norby P., Hanson J. C. and Monnier A., Phase transitions in mesostructured silica/surfactant composites: Surfactant packing and the role of charge density matching, *Chem. Mat.* **13** (2001) pp. 2247-2256.
79. Anderson M. T., Martin J. E., Odinek J. G. and Newcomer P. P., Effect of methanol concentration on CTAB micellization and on the formation of surfactant-templated silica (STS), *Chem. Mat.* **10** (1998) pp. 1490-1500.
80. Anderson M. T., Martin J. E., Odinek J. G. and Newcomer P. P., Surfactant-templated silica mesophases formed in water:cosolvent mixtures, *Chem. Mat.* **10** (1998) pp. 311-321.
81. Gallis K. W. and Landry C. C., Synthesis of MCM-48 by a phase transformation process, *Chem. Mat.* **9** (1997) pp. 2035-2038.
82. MacLachlan M. J., Coombs N. and Ozin G. A., Non-aqueous supramolecular assembly of mesostructured metal germanium sulphides from $(\text{Ge}_4\text{S}_{10})^{4-}$ clusters, *Nature* **397** (1999) pp. 681-684.
83. Attard G. S., Glyde J. C. and Göltner C. G., Liquid-crystalline phases as templates for the synthesis of mesoporous silica, *Nature* **378** (1995) pp. 366-368.
84. Braun P. V., Osenar P. and Stupp S. I., Semiconducting superlattices templated by molecular assemblies, *Nature* **380** (1996) pp. 325-328.
85. Attard G. S., Göltner C. G., Corker J. M., Henke S. and Templer R. H., Liquid-crystal templates for nanostructured metals, *Angew. Chem. Int. Edit. Engl.* **36** (1997) pp. 1315-1317.
86. Attard G. S., Bartlett P. N., Coleman N. R. B., Elliott J. M., Owen J. R. and Wang J. H., Mesoporous platinum films from lyotropic liquid crystalline phases, *Science* **278** (1997) pp. 838-840.
87. Braun P. V., Osenar P., Tohver V., Kennedy S. B. and Stupp S. I., Nanostructure templating in inorganic solids with organic lyotropic liquid crystals, *J. Am. Chem. Soc.* **121** (1999) pp. 7302-7309.
88. Goltner C. G., Henke S., Weissenberger M. C. and Antonietti M., Mesoporous silica from lyotropic liquid crystal polymer templates, *Angew. Chem. Int. Edit.* **37** (1998) pp. 613-616.
89. Melosh N. A., Lipic P., Bates F. S., Wudl F., Stucky G. D., Fredrickson G. H. and Chmelka B. F., Molecular and mesoscopic structures of transparent block copolymer-silica monoliths, *Macromolecules* **32** (1999) pp. 4332-4342.
90. McGrath K. M., Dabbs D. M., Yao N., Aksay I. A. and Gruner S. M., Formation of a silicate L_3 phase with continuously adjustable pore sizes, *Science* **277** (1997) pp. 552-556.

91. McGrath K. M., Dabbs D. M., Yao N., Edler K. J., Aksay I. A. and Gruner S. M., Silica gels with tunable nanopores through templating of the L₃ phase, *Langmuir* **16** (2000) pp. 398-406.
92. Templin M., Franck A., Du Chesne A., Leist H., Zhang Y., Ulrich R., Schädler V. and Wiesner U., Organically modified aluminosilicate mesostructures from block copolymer phases, *Science* **278** (1997) pp. 1795-1798.
93. Finnefrock A. C., Ulrich R., Du Chesne A., Honeker C. C., Schumacher K., Unger K. K., Gruner S. M. and Wiesner U., Metal oxide containing mesoporous silica with bicontinuous "Plumber's Nightmare" morphology from a block copolymer-hybrid mesophase, *Angew. Chem. Int. Edit.* **40** (2001) pp. 1207-1211.
94. Chan V. Z.-H., Hoffman J., Lee V. Y., Iatrou H., Avgeropoulos A., Hadjichristidis N., Miller R. D. and Thomas E. L., Ordered bicontinuous nanoporous and nanorelief ceramic films from self assembling polymer precursors, *Science* **286** (1999) pp. 1716-1719.
95. Melosh N. A., Davidson P. and Chmelka B. F., Monolithic mesophase silica with large ordering domains, *J. Am. Chem. Soc.* **122** (2000) pp. 823-829.
96. Yang P., Zhao D., Margolese D. I., Chmelka B. F. and Stucky G. D., Generalized syntheses of large-pore mesoporous metal oxides with semicrystalline frameworks, *Nature* **396** (1998) pp. 152-155.
97. Yang P., Zhao D., Margolese D. I., Chmelka B. F. and Stucky G. D., Block copolymer templating syntheses of mesoporous metal oxides with large ordering lengths and semicrystalline framework, *Chem. Mat.* **11** (1999) pp. 2813-2826.
98. Lu Y., Ganguli R., Drewien C. A., Anderson M. T., Brinker C. J., Gong W., Guo Y., Soye H., Dunn B., Huang M. H. and Zink J. I., Continuous formation of supported cubic and hexagonal mesoporous films by sol-gel dip-coating, *Nature* **389** (1997) pp. 364-368.
99. Brinker C. J., Lu Y., Sellinger A. and Fan H., Evaporation-induced self-assembly: nanostructures made easy, *Adv. Mater.* **11** (1999) pp. 579-585.
100. Fan H., Lu Y., Stump A., Reed S. T., Baer T., Schunk R., Perez-Luna V., López G. P. and Brinker C. J., Rapid prototyping of patterned functional nanostructures, *Nature* **405** (2000) pp. 56-60.
101. Yang P., Deng T., Zhao D., Feng P., Pine D., Chmelka B. F., Whitesides G. M. and Stucky G. D., Hierarchically ordered oxides, *Science* **282** (1998) pp. 2244-2246.
102. Yang P., Wirmsberger G., Huang H. C., Cordero S. R., McGehee M. D., Scott B., Deng T., Whitesides G. M., Chmelka B. F., Buratto S. K. and Stucky G. D., Mirrorless lasing from mesostructured waveguides patterned by soft lithography, *Science* **287** (2000) pp. 465-467.
103. Nandhakumar I., Elliott J. M. and Attard G. S., Electrodeposition of nanostructured mesoporous selenium films (H₂-cSe), *Chem. Mat.* **13** (2001) pp. 3840-3842.
104. Attard G. S., Leclerc S. A. A., Maniguet S., Russell A. E., Nandhakumar I. and Bartlett P. N., Mesoporous Pt/Ru alloy from the hexagonal lyotropic liquid crystalline phase of a nonionic surfactant, *Chem. Mat.* **13** (2001) pp. 1444-1446.
105. Nelson P. A., Elliott J. M., Attard G. S. and Owen J. R., Mesoporous nickel/nickel oxide - a nanoarchitected electrode, *Chem. Mat.* **14** (2002) pp. 524-529.
106. Choi K.-S., Lichtenegger H. C., Stucky G. D. and McFarland E. W., Electrochemical synthesis of nanostructured ZnO films utilizing self-assembly of

- surfactant molecules at solid-liquid interfaces, *J. Am. Chem. Soc.* **124** (2002) pp. 12402-12403.
107. Guo R., Tianqing L. and Weili Y., Phase behavior and structure of the sodium dodecyl sulfate/benzyl alcohol/water system, *Langmuir* **15** (1999) pp. 624-630.
108. Cheng S., From layer compounds to catalytic materials, *Catal. Today* **49** (1999) pp. 303-312.
109. Ma Y., Tong W., Zhou H. and Suib S. L., A review of zeolite-like porous materials, *Microporous Mesoporous Mat.* **37** (2000) pp. 243-252.
110. Galarneau A., Barodawalla A. and Pinnavaia T. J., Porous clay heterostructures formed by gallery-templated synthesis, *Nature* **374** (1995) pp. 529-531.
111. Hayashi S., Solid-state NMR study of locations and dynamics of interlayer cations and water in kanemite, *J. Mater. Chem.* **7** (1997) pp. 1043-1048.
112. Inagaki S., Sakamoto Y., Fukushima Y. and Terasaki O., Pore wall of a mesoporous molecular sieve derived from kanemite, *Chem. Mat.* **8** (1996) pp. 2089-2095.
113. Kimura T., Itoh D., Shigeno T. and Kuroda K., Transformation of layered dicosyltrimethyl- and dicosyltriethylammonium silicates derived from kanemite into precursors for ordered mesoporous silicas, *Langmuir* **18** (2002) pp. 9574-9577.
114. Chen C.-Y., Xiao S.-Q. and Davis M. E., Studies on ordered mesoporous materials III. Comparison of MCM-41 to mesoporous materials derived from kanemite, *Microporous Mater.* **4** (1995) pp. 1-20.
115. Almond G. G., Harris R. K. and Franklin K. R., A structural consideration of kanemite, octosilicate, magadiite and kenyaite, *J. Mater. Chem.* **7** (1997) pp. 681-687.
116. Ryoo R., Joo S. H., Kruk M. and Jaroniec M., Ordered mesoporous carbons, *Adv. Mater.* **13** (2001) pp. 677-681.
117. Lee J., Yoon S., Oh S. M., Shin C.-H. and Hyeon T., Development of a new mesoporous carbon using an HMS aluminosilicate template, *Adv. Mater.* **12** (2000) pp. 359-362.
118. Jun S., Joo S. H., Ryoo R., Kruk M., Jaroniec M., Liu Z., Ohsuna T. and Terasaki O., Synthesis of new, nanoporous carbon with hexagonally ordered mesostructure, *J. Am. Chem. Soc.* **122** (2000) pp. 10712-10713.
119. Ryoo R., Ko C. H., Kruk M., Antochshuk V. and Jaroniec M., Block-copolymer-templated ordered mesoporous silica: Array of uniform mesopores or mesopore-micropore network?, *J. Phys. Chem. B* **104** (2000) pp. 11465-11471.
120. Bagshaw S. A. and Pinnavaia T. J., Mesoporous alumina molecular sieves, *Angew. Chem. Int. Edit. Engl.* **35** (1996) pp. 1102-1105.
121. Rangan K. K., Trikalitis P. N., Bakas T. and Kanatzidis M. G., Hexagonal mesostructured chalcogenide frameworks formed by linking $[\text{Ge}_4\text{Q}_{10}]^{4+}$ (Q = S, Se) clusters with Sb^{3+} and Sn^{4+} , *Chem. Commun.* (2001) pp. 809-810.
122. Neeraj and Rao C. N. R., Metal chalcogenide-organic nanostructured composites from self-assembled organic amine templates, *J. Mater. Chem.* **8** (1998) pp. 279-280.
123. Ryoo R., Joo S. H. and Jun S., Synthesis of highly ordered carbon molecular sieves via template-mediated structural transformation, *J. Phys. Chem. B* **103** (1999) pp. 7743-7746.

124. Yada M., Kitamura H., Ichinose A., Machida M. and Kijima T., Mesoporous magnetic materials based on rare earth oxides, *Angew. Chem. Int. Edit.* **38** (1999) pp. 3506-3510.
125. Bartlett P. N., Birkin P. N., Ghanem M. A., de Groot P. and Sawicki M., The electrochemical deposition of nanostructured cobalt films from lyotropic liquid crystalline media, *J. Electrochem. Soc.* **148** (2001) pp. C119-C123.
126. Rangan K. K., Trikalitis P. N. and Kanatzidis M. G., Light-emitting mesostructured sulfides with hexagonal symmetry: supramolecular assembly of $[\text{Ge}_4\text{S}_{10}]^{4-}$ clusters with trivalent metal ions and cetylpyridinium surfactant, *J. Am. Chem. Soc.* **122** (2000) pp. 10230-10231.
127. Froba M. and Oberender N., First synthesis of mesostructured thiogermanates, *Chem. Commun.* (1997) pp. 1729-1730.
128. Srivastava D. N., Perkas N., Gedanken A. and Felner I., Sonochemical synthesis of mesoporous iron oxide and accounts of its magnetic and catalytic properties, *J. Phys. Chem. B* **106** (2002) pp. 1878-1883.
129. Trikalitis P. N., Rangan K. K., Bakas T. and Kanatzidis M. G., Varied pore organization in mesostructured semiconductors based on the $[\text{SnSe}_4]^{4-}$ anion, *Nature* **410** (2001) pp. 671-675.
130. Leontidis E., Kyprianidou-Leodidou T., Caseri W., Robyr P., Krumeich F. and Kyriacou K. C., From colloidal aggregates to layered nanosized structures in polymer-surfactant systems. 1. Basic phenomena, *J. Phys. Chem. B* **105** (2001) pp. 4133-4144.
131. Tian Z.-R., Tong W., Wang J.-Y., Duan N.-G., Krishnan V. V. and Suib S. L., Manganese oxide mesoporous structures: mixed-valent semiconducting catalysts, *Science* **276** (1997) pp. 926-930.
132. Rangan K. K., Billinge S. J. L., Petkov V., Heising J. and Kanatzidis M. G., Aqueous mediated synthesis of mesostructured manganese germanium sulfide with hexagonal order, *Chem. Mat.* **11** (1999) pp. 2629-2632.
133. Wachhold M., Rangan K. K., Lei M., Thorpe M. F., Billinge S. J. L., Petkov V., Heising J. and Kanatzidis M. G., Mesostructured metal germanium sulfide and selenide materials based on the tetrahedral $[\text{Ge}_4\text{S}_{10}]^{4-}$ and $[\text{Ge}_4\text{Se}_{10}]^{4-}$ units: Surfactant templated three-dimensional disordered frameworks perforated with worm holes, *J. Solid State Chem.* **152** (2000) pp. 21-36.
134. Antonelli D. M. and Trudeau M., Phase changes and electronic properties in toroidal mesoporous molybdenum oxides, *Angew. Chem. Int. Edit.* **38** (1999) pp. 1471-1475.
135. Vanchura B. A., He P., Antochshuk V., Jaroniec M., Ferryman A., Barbash D., Fulghum J. E. and Huang S. D., Direct synthesis of mesostructured lamellar molybdenum disulfides using a molten neutral n-alkylamine as the solvent and template, *J. Am. Chem. Soc.* **124** (2002) pp. 12090-12091.
136. Bartlett P. N., Gollas B., Guerin S. and Marwan J., The preparation and characterisation of $\text{H}_1\text{-e}$ palladium films with a regular hexagonal nanostructure formed by electrochemical deposition from lyotropic liquid crystalline phases, *Phys. Chem. Chem. Phys.* **4** (2002) pp. 3835-3842.
137. Froba M. and Muth O., Nanostructured rhenium dioxide: Synthesis and characterization, *Adv. Mater.* **11** (1999) pp. 564+.

138. Farrusseng D., Schlichte K., Spliethoff B., Wingen A., Kaskel S., Bradley J. S. and Schüth F., Pore-size engineering of silicon imido nitride for catalytic applications, *Angew. Chem. Int. Edit.* **40** (2001) pp. 4204-4207.
139. Antonelli D. M. and Ying J. Y., Synthesis and characterization of hexagonally packed mesoporous tantalum oxide molecular sieves, *Chem. Mat.* **8** (1996) pp. 874-881.
140. Gabriel T., Nandhakumar I. S. and Attard G. S., Electrochemical synthesis of nanostructured tellurium films, *Electrochem. Commun.* **4** (2002) pp. 610-612.
141. Whitehead A. H., Elliott J. M., Owen J. R. and Attard G. S., Electrodeposition of mesoporous tin films, *Chem. Commun.* (1999) pp. 331-332.
142. Li J., Delmotte L. and Kessler H., Synthesis and characterization of a novel mesostructured layered tin(IV) sulfide, *Chem. Commun.* (1996) pp. 1023-1024.
143. Yagi Y., Zhou H., Miyayama M., Kudo T. and Honma I., Mesostructural transformation of vanadium oxide-hexadecyltrimethylammonium composite by low-temperature calcination, *Langmuir* **17** (2001) pp. 1328-1330.
144. Yada M., Kitamura H., Machida M. and Kijima T., Yttrium-based porous materials templated by anionic surfactant assemblies, *Inorg. Chem.* **37** (1998) pp. 6470-6475.
145. Trens P., Hudson M. J. and Denoyel R., Formation of mesoporous, zirconium(IV) oxides of controlled surface areas, *J. Mater. Chem.* **8** (1998) pp. 2147-2152.
146. Stein A., Fendorf M., Jarvie T. P., Mueller K. T., Benesi A. J. and Mallouk T. E., Salt-gel synthesis of porous transition-metal oxides, *Chem. Mat.* **7** (1995) pp. 304-313.
147. Ciesla U., Demuth D., Leon R., Petroff P., Stucky G., Unger K. and Schüth F., Surfactant controlled preparation of mesostructured transition-metal oxide compounds, *Chem. Commun.* (1994) pp. 1387-1388.
148. Schüth F. and Unger K., Precipitation and coprecipitation. In *Handbook of Heterogeneous Catalysis*, ed. by Ertl G., Knözinger H. and Weitkamp J. (Wiley-VCH, Weinheim, 1997) pp. 72-86.
149. Yada M., Machida M. and Kijima T., Synthesis and deorganization of an aluminium-based dodecyl sulfate mesophase with a hexagonal structure, *Chem. Commun.* (1996) pp. 769-770.
150. Cabrera S., El Haskouri J., Alamo J., Beltrán A., Beltrán D., Mendioroz S., Marcos M. D. and Amorós P., Surfactant-assisted synthesis of mesoporous alumina showing continuously adjustable pore sizes, *Adv. Mater.* **11** (1999) pp. 379-381.
151. Valange S., Guth J.-L., Kolenda F., Lacombe S. and Gabelica Z., Synthesis strategies leading to surfactant-assisted aluminas with controlled mesoporosity in aqueous media, *Microporous Mesoporous Mat.* **35-6** (2000) pp. 597-607.
152. Zhang Z. R. and Pinnavaia T. J., Mesostructured γ - Al_2O_3 with a lathlike framework morphology, *J. Am. Chem. Soc.* **124** (2002) pp. 12294-12301.
153. Whitehurst D. D. (1992), *U.S. Patent No. 5,143,879*.
154. Kawi S. and Lai M. W., Supercritical fluid extraction of surfactant template from MCM-41, *Chem. Commun.* (1998) pp. 1407-1408.
155. Schüth F., Surface-properties and catalytic performance of novel mesostructured oxides, *Ber. Bunsen-Ges. Phys. Chem. Chem. Phys.* **99** (1995) pp. 1306-1315.

156. Wong M. S., Antonelli D. M. and Ying J. Y., Synthesis and characterization of phosphated mesoporous zirconium oxide, *Nanostruct. Mater.* **9** (1997) pp. 165-168.
157. Ciesla U., Fröba M., Stucky G. and Schüth F., Highly ordered porous zirconias from surfactant-controlled syntheses: zirconium oxide-sulfate and zirconium oxo phosphate, *Chem. Mat.* **11** (1999) pp. 227-234.
158. Ciesla U., Schacht S., Stucky G. D., Unger K. K. and Schüth F., Formation of a porous zirconium oxo phosphate with a high surface area by a surfactant-assisted synthesis, *Angew. Chem. Int. Edit. Engl.* **35** (1996) pp. 541-543.
159. Chen H.-R., Shi J.-L., Hua Z.-L., Ruan M.-L. and Yan D.-S., Parameter control in the synthesis of ordered porous zirconium oxide, *Mater. Lett.* **51** (2001) pp. 187-193.
160. Martens J. A., Souverijns W., Van Rhijn W. and Jacobs P. A., Acidity and basicity in zeolites. In *Handbook of Heterogeneous Catalysis*, ed. by Ertl G., Knözinger H. and Weitkamp J. (Wiley-VCH, Weinheim, 1997) pp. 324-365.
161. Cheetham A. K., Férey G. and Loiseau T., Open-framework inorganic materials, *Angew. Chem. Int. Edit.* **38** (1999) pp. 3269-3292.
162. Oliver S., Kuperman A., Coombs N., Lough A. and Ozin G. A., Lamellar aluminophosphates with surface patterns that mimic diatom and radiolarian microstructures, *Nature* **378** (1995) pp. 47-50.
163. Gao Q., Xu R., Chen J., Li R., Li S., Qiu S. and Yue Y., Synthesis and characterization of an unusual lamellar aluminophosphate synthesized from an alcohol system, *J. Chem. Soc.-Dalton Trans.* (1996) pp. 3303-3307.
164. Ozin G. A. and Oliver S., Skeletons in the beaker—synthetic hierarchical inorganic materials, *Adv. Mater.* **7** (1995) pp. 943-947.
165. Kimura T., Sugahara Y. and Kuroda K., Synthesis of mesoporous aluminophosphates and their adsorption properties, *Microporous Mesoporous Mat.* **22** (1998) pp. 115-126.
166. Khimyak Y. Z. and Klinowski J., Synthesis of mesostructured aluminophosphates using cationic templating, *Phys. Chem. Chem. Phys.* **2** (2000) pp. 5275-5285.
167. Chakraborty B., Pulikottil A. C., Das S. and Viswanathan B., Synthesis and characterization of mesoporous SAPO, *Chem. Commun.* (1997) pp. 911-912.
168. Ayyappan S. and Rao C. N. R., Mesoporous aluminoborates, *Chem. Commun.* (1997) pp. 575-576.
169. Kapoor M. P. and Raj A., Synthesis of mesoporous hexagonal titanium aluminophosphate molecular sieves and their catalytic applications, *Appl. Catal. A-Gen.* **203** (2000) pp. 311-319.
170. Tohver V., Braun P. V., Pralle M. U. and Stupp S. I., Counterion effects in liquid crystal templating of nanostructured CdS, *Chem. Mat.* **9** (1997) pp. 1495-1498.
171. Bedard R. L., Vail L. D., Wilson S. T. and Flanigan E. M. (1989), *U.S. Patent No. 4,880,761*.
172. MacLachlan M. J., Coombs N., Bedard R. L., White S., Thompson L. K. and Ozin G. A., Mesostructured metal germanium sulfides, *J. Am. Chem. Soc.* **121** (1999) pp. 12005-12017.
173. Rangan K. K., Trikalitis P. N., Canlas C., Bakas T., Weliky D. P. and Kanatzidis M. G., Hexagonal pore organization in mesostructured metal tin sulfides built with $[\text{Sn}_2\text{S}_6]^{4-}$ cluster, *Nano Lett.* **2** (2002) pp. 513-517.

174. Shin H. J., Ko C. H. and Ryoo R., Synthesis of platinum networks with nanoscopic periodicity using mesoporous silica as template, *J. Mater. Chem.* **11** (2001) pp. 260-261.
175. Shin H. J., Ryoo R., Liu Z. and Terasaki O., Template synthesis of asymmetrically mesostructured platinum networks, *J. Am. Chem. Soc.* **123** (2001) pp. 1246-1247.
176. Liu Z., Sakamoto Y., Ohsuna T., Hiraga K., Terasaki O., Ko C. H., Shin H. J. and Ryoo R., TEM studies of platinum nanowires fabricated in mesoporous silica MCM-41, *Angew. Chem. Int. Edit.* **39** (2000) pp. 3107-3110.
177. Gilbert M. T., Knox J. H. and Kaur B., Porous glassy carbon, a new columns packing material for gas chromatography and high-performance liquid chromatography, *Chromatographia* **16** (1982) pp. 138-148.
178. Kyotani T., Control of pore structure in carbon, *Carbon* **38** (2000) pp. 269-286.
179. Lee J., Yoon S., Hyeon T., Oh S. M. and Kim K. B., Synthesis of a new mesoporous carbon and its application to electrochemical double-layer capacitors, *Chem. Commun.* (1999) pp. 2177-2178.
180. Gin D. L., Gu W. Q., Pindzola B. A. and Zhou W. J., Polymerized lyotropic liquid crystal assemblies for materials applications, *Accounts Chem. Res.* **34** (2001) pp. 973-980.
181. Sayari A. and Hamoudi S., Periodic mesoporous silica-based organic-inorganic nanocomposite materials, *Chem. Mat.* **13** (2001) pp. 3151-3168.
182. Kaskel S., Schlichte K. and Zibrowius B., Pore size engineering of mesoporous silicon nitride materials, *Phys. Chem. Chem. Phys.* **4** (2002) pp. 1675-1681.
183. Kriesel J. W., Sander M. S. and Tilley T. D., Block copolymer-assisted synthesis of mesoporous, multicomponent oxides by nonhydrolytic, thermolytic decomposition of molecular precursors in nonpolar media, *Chem. Mat.* **13** (2001) pp. 3554-3563.
184. Gao X., Wachs I. E., Wong M. S. and Ying J. Y., Structural and reactivity properties of Nb-MCM-41: comparison with that of highly dispersed Nb₂O₅/SiO₂ catalysts, *J. Catal.* **203** (2001) pp. 18-24.
185. Oberhagemann U., Kinski I., Dierdorf I., Marler B. and Gies H., Synthesis and properties of boron containing MCM-41, *J. Non-Cryst. Solids* **197** (1996) pp. 145-153.
186. Piquemal J.-Y., Briot E., Vennat M., Brégeault J.-M., Chottard G. and Manoli J.-M., Evidence for the presence of Mo(VI), W(VI) or Re(VII) species in silica-based materials. New approaches to highly dispersed oxo-species in mesoporous silicates, *Chem. Commun.* (1999) pp. 1195-1196.
187. Araujo A. S. and Jaroniec M., Synthesis and properties of lanthanide incorporated mesoporous molecular sieves, *J. Colloid Interface Sci.* **218** (1999) pp. 462-467.
188. Mulukutla R. S., Asakura K., Kogure T., Namba S. and Iwasawa Y., Synthesis and characterization of rhodium oxide nanoparticles in mesoporous MCM-41, *PCCP Phys. Chem. Chem. Phys.* **1** (1999) pp. 2027-2032.
189. Zhang W., Wang J., Tanev P. T. and Pinnavaia T. J., Catalytic hydroxylation of benzene over transition-metal substituted hexagonal mesoporous silicas, *Chem. Commun.* (1996) pp. 979-980.
190. Vinu A., Dedeczek J., Murugesan V. and Hartmann M., Synthesis and characterization of CoSBA-1 cubic mesoporous molecular sieves, *Chem. Mat.* **14** (2002) pp. 2433-2435.

191. Tismaneanu R., Ray B., Khalfin R., Semiat R. and Eisen M. S., Synthesis, characterization and catalytic activity of actinide Th-MCM-41 and U-MCM-41 hexagonal packed mesoporous molecular sieves, *J. Mol. Catal. A-Chem.* **171** (2001) pp. 229-241.
192. Karakassides M. A., Bourlinos A., Petridis D., Coche-Guerentè L. and Labbè P., Synthesis and characterization of copper containing mesoporous silicas, *J. Mater. Chem.* **10** (2000) pp. 403-408.
193. Chaudhari K., Das T. K., Rajmohan P. R., Lazar K., Sivasanker S. and Chandwadkar A. J., Synthesis, characterization, and catalytic properties of mesoporous tin-containing analogs of MCM-41, *J. Catal.* **183** (1999) pp. 281-291.
194. Tuel A. and Gontier S., Synthesis and characterization of trivalent metal containing mesoporous silicas obtained by a neutral templating route, *Chem. Mat.* **8** (1996) pp. 114-122.
195. Corma A., Navarro M. T. and Pariente J. P., Synthesis of an ultralarge pore titanium silicate isomorphous to MCM-41 and its application as a catalyst for selective oxidation of hydrocarbons, *Chem. Commun.* (1994) pp. 147-148.
196. Zhang Z., Sue J., Zhang X. and Li S., Synthesis, characterization, and catalytic testing of W-MCM-41 mesoporous molecular sieves, *Appl. Catal. A-Gen.* **179** (1999) pp. 11-19.
197. Zhang J. and Goldfarb D., Manganese incorporation into the mesoporous material MCM-41 under acidic conditions as studied by high field pulsed EPR and ENDOR spectroscopies, *J. Am. Chem. Soc.* **122** (2000) pp. 7034-7041.
198. Reddy J. S., Liu P. and Sayari A., Vanadium containing crystalline mesoporous molecular sieves: leaching of vanadium in liquid phase reactions, *Appl. Catal. A-Gen.* **148** (1996) pp. 7-21.
199. Hartmann M., Racouchot S. and Bischof C., Characterization of copper and zinc containing MCM-41 and MCM-48 mesoporous molecular sieves by temperature programmed reduction and carbon monoxide adsorption, *Microporous Mesoporous Mat.* **27** (1999) pp. 309-320.
200. Parvulescu V. and Su B.-L., Iron, cobalt or nickel substituted MCM-41 molecular sieves for oxidation of hydrocarbons, *Catal. Today* **69** (2001) pp. 315-322.
201. Gontier S. and Tuel A., Novel zirconium containing mesoporous silicas for oxidation reactions in the liquid phase, *Appl. Catal. A-Gen.* **143** (1996) pp. 125-135.
202. Katou T., Lu D. L., Kondo J. N. and Domen K., Synthesis of 2D-hexagonally ordered mesoporous niobium and tantalum mixed oxide, *J. Mater. Chem.* **12** (2002) pp. 1480-1483.
203. Kriesel J. W., Sander M. S. and Tilley T. D., General route to homogeneous, mesoporous, multicomponent oxides based on the thermolytic transformation of molecular precursors in non-polar media, *Adv. Mater.* **13** (2001) pp. 331-335.
204. Liu Y., Zhang W. Z. and Pinnavaia T. J., Steam-stable aluminosilicate mesostructures assembled from zeolite type Y seeds, *J. Am. Chem. Soc.* **122** (2000) pp. 8791-8792.

ORGANIC HOST-GUEST STRUCTURES IN THE SOLID STATE

ASHWINI NANGIA

School of Chemistry, University of Hyderabad, Hyderabad 500 046, India

E-mail: ansc@uohyd.ernet.in

Inclusion of small guest molecules in the cavity or channel formed by host lattice is a phenomenon of fundamental and applied importance. Clathrate compounds have applications in the design of tailored catalysts, supramolecular materials for magnetism, electrooptics and NLO, chemical separation and gas storage technologies, and targeted drug delivery. They also serve as chemical models to understand complex phenomenon such as chirality evolution, nucleation and crystallisation, and ligand-receptor binding. The status of organic host-guest structures is surveyed to show the diversity of supramolecular architectures, rational design strategies, and control of pore size/shape that is possible with crystal engineering. Recent examples of one-dimensional channel and two-dimensional layer frameworks from our research laboratory are highlighted.

1 Introduction

Supramolecular chemistry has come of age since the award of Nobel Prize to Charles J. Pedersen, Donald J. Cram and Jean-Marie Lehn in 1987 for their work in this area. Supramolecular chemistry is 'chemistry beyond the molecule', or the chemistry of molecular aggregates assembled by noncovalent interactions [1]. Supramolecular chemistry is an important branch of science today encompassing a broad range of concepts with significant overlap towards physics and biology. At the root of this interdisciplinary science lies the field of host-guest chemistry [2]. Humphrey Davy discovered chlorine hydrate as far back as 1810 and the H₂S clathrate of β -quinol by Wöhler dates back to 1849. Powell introduced the term 'clathrate' or the inclusion of one compound within the framework of another in 1948 in the context of X-ray crystal structures of β -quinol inclusion compounds. Research on macrocyclic and molecular hosts in the second half of the 20th century by Pedersen, Cram, Atwood, Gokel, Vögtle, Toda, and Weber, to name a few, led to the development of host-guest chemistry as an important topic within supramolecular chemistry [3]. Host-guest compounds are of two major types. Cavitands, or molecular host compounds with intramolecular cavities; the cavity is an intrinsic property of the molecule and exists in solution and in the solid state. Clathrands are hosts with extramolecular cavities that result from the aggregation of two or more molecules; lattice inclusion hosts exist only in the crystalline or solid state. The corresponding host-guest adducts are referred to as cavitates and clathrates. This review article deals with lattice

inclusion host structures held together by hydrogen bonds and van der Waals forces. Single crystal X-ray diffraction [4] is usually the method of choice to characterise the host framework, determine the guest orientation, and analyse the hydrogen bonds that stabilise the supramolecular structure.

The types of hydrogen bonds and non-covalent interactions that will appear in this article are briefly reviewed. Hydrogen bonding is the master key in molecular recognition and supramolecular chemistry. Hydrogen bonds of O–H...O, N–H...O and O–H...N type are strong and directional (H...O 1.5–2.0 Å, O...O 2.5–2.8 Å, \angle O–H...O 150–180°) with energy between 8–15 kcal/mol [5]. Hydrogen bonded to the less electronegative carbon atom participate in weak C–H...O interactions with moderate directionality (H...O 2.0–2.8 Å, O...O 3.0–4.0 Å, \angle O–H...O 120–180°, energy 2–5 kcal/mol) [6]. Strong and weak hydrogen bonds are important during recognition between molecules in solution and the solid state. Halogen...halogen [7] and other heteroatom interactions are anisotropic, with a moderate directionality and energy comparable to weak hydrogen bonds (<4 kcal/mol). Hydrophobic interactions (van der Waals forces, energy 1–2 kcal/mol) are isotropic and determine close packing in the crystal. The idea of close packing is universal in crystals and there are very few frameworks that have empty space. Words such as ‘porous’, ‘void’, ‘cavity’, ‘channel’ used in the description of host–guest structures refer to the host framework that is filled with guest species. Zeolites (aluminosilicate open frameworks) are an example of a truly porous lattice that does not collapse in the empty state.

Open networks may be constructed in purely inorganic systems, with metal atom bonded to organic ligand (coordination polymers), and with organic molecules. A typical example from each category is illustrated in Figure 1 [8–10]. Inorganic and metal–organic frameworks are strong and robust because they have ionic and metal–ligand bonds compared to organic host lattices that are stabilised by hydrogen bonds. There are many advantages in working with lattice inclusion hosts built from an organic core. (1) Structural diversity can be grafted on the molecule by functional group addition and/or manipulation using synthetic reactions and reagents. (2) Supramolecular synthons (hydrogen bond motifs) permit the design and engineering of diverse host lattices from functionalised molecules. (3) The nature, size and shape of pores and cavities may be systematically altered with hydrogen bonding and hydrophobic interactions. (4) The inclusion of guest occurs via self-assembly in organic hosts (a mild process) compared to zeolites wherein the guest molecule is introduced into a pre-existing lattice (usually with pressure). Thanks to these

advantages research on organic host-guest systems [11] is an active and contemporary theme in crystal engineering and supramolecular chemistry.

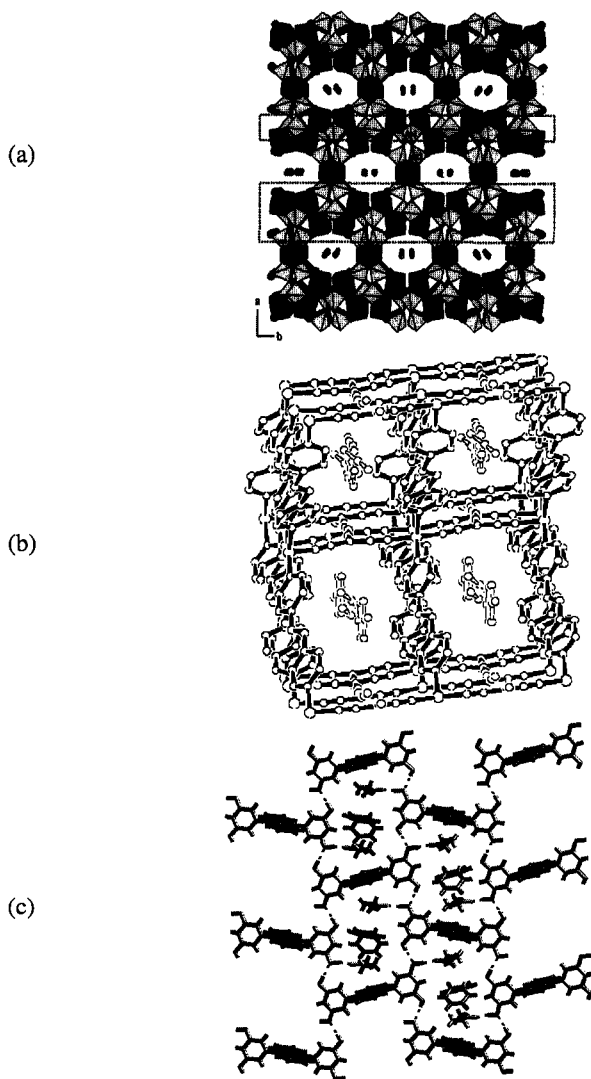


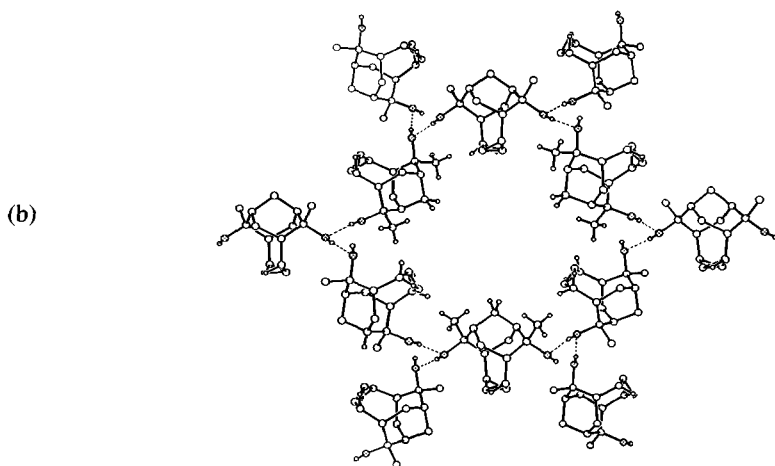
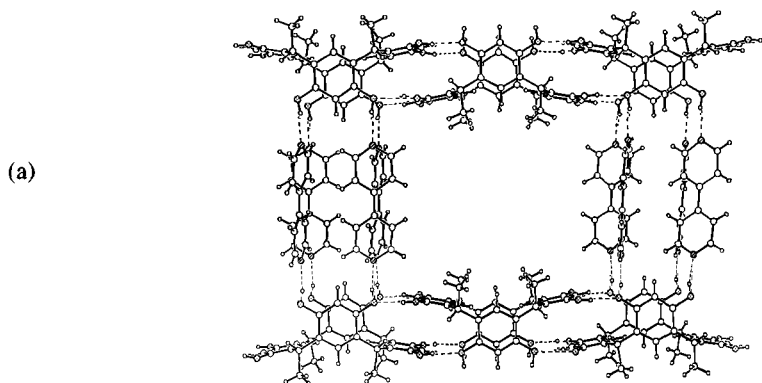
Figure 1. (a) Crystal structure of $\text{Rb}_2(\text{MoO}_2)_3(\text{As}_2\text{O}_7)_2 \cdot 2\text{H}_2\text{O}$ showing elliptical tunnels filled with Rb^+ cations and water molecules. MoO_6 octahedra are shown as dark polyhedra and AsO_4 tetrahedra as grey polyhedra [8]. (b) Intercalation of biphenylethylene (bpe) and MeCN guest in the rectangular channels of $[\text{Cu}(\text{tcm})(\text{bpe})] \cdot 0.25\text{bpe} \cdot 0.5\text{MeCN}$ (tcm = tricyanomethanide) formed by the stacking of $\text{Cu}(\text{tcm})(\text{bpe})$ sheets [9]. (c) Hydrogen bonded sheet in bisresorcinol-anthracene derivative with benzene and ethyl acetate guests encapsulated in the cavity [10].

2 Host design principles

Many of the early examples of host lattices were discovered by chance. These include urea inclusion compounds, β -hydroquinone clathrates, trimesic acid, gossypol, and gas hydrates. The deliberate use of symmetry, shape and intermolecular interactions in host design is about three decades old. The concept of hexa-host symmetry (hexa-substituted benzene) was introduced by MacNicol [12] in the 1970s in analogy with hydrogen-bonded hexamer of phenol, hydroquinone and Dianin's compound. Hexakis(phenylthio)benzene, designed as the first member of this series, exhibited wide-ranging enclathration property and number of related analogues were subsequently synthesised. The up-down orientation of adjacent groups in hexa-hosts led to the concept of Piedfort unit or the stacking of two trigonal benzene rings juxtaposed at van der Waals contact. Independently, Weber [13] proposed rules for the design of new host frameworks based on an examination of several aromatic hydrocarbon molecules. A typical host molecule should have these characteristics: (1) bulky in constitution and awkward shape; (2) rigid structure to maintain the cavity so that it does not collapse to a close-packed structure; (3) high affinity functional groups (OH, COOH, CONH₂) for specific and directional hydrogen bonding; and (4) an overall balanced shape to achieve close packing in the host-guest crystal. Desiraju [14] has suggested that crystal engineering principles may be applied for the design of host lattices by a consideration of molecular and crystal symmetry, supramolecular synthon concept [15], and the phenomenon of solvation in crystals (pseudopolymorphism). With the best of planning in rational approaches to design open structures one should remember that solvent (guest) inclusion is only one of the ways in which crystals solve the open framework vs. close packing dilemma. Nature uses other ways to reconcile the conflict between hydrogen bonding and space filling, e.g. interpenetration [16], multiple molecules in the asymmetric unit and disordered crystals

Significant progress has been made in the last decade using the above mentioned ideas to discover host lattices with novel architecture and guest inclusion properties. The emphasis in recent studies has been to discover organic host lattices with a robust (recurring) supramolecular synthon for diverse guest species, yet are flexible enough for structural tuning of cavity dimension, and also exhibit supramolecular isomerism. It is convenient to classify host lattices according to the dimensionality of the cavity: discrete voids or pockets surrounded by host molecules, one-dimensional channel or nanotube architecture, and two-dimensional sheet with porous gallery region. These are illustrated with examples from recent literature. Discrete

voids that house guest molecules in a brick framework constructed with calix[4]resorcinarene and 4,4'-bipyridine via O–H...N hydrogen bonds is exemplified in Figure 2a [17]. Molecules are hydrogen bonded by O–H...O trimer in chiral helical tubuland (space group $P3_121$ or its enantiomorph $P3_221$) from C_2 -symmetric diols. A slice of the *ab*-layer has empty tube (Figure 2b) with cross-sectional area of ca. 30 \AA^2 for guest inclusion [18]. Complementary guanidinium and sulfonate ions (GS) produce GS ribbons connected by N–H...O hydrogen bonds that serve as hinge (corrugated sheet). Organodisulfonate pillars project up or down from S sites on these sheets to afford porous framework architectures with variable height in the gallery region (8–12 Å, Figure 2c) [19].



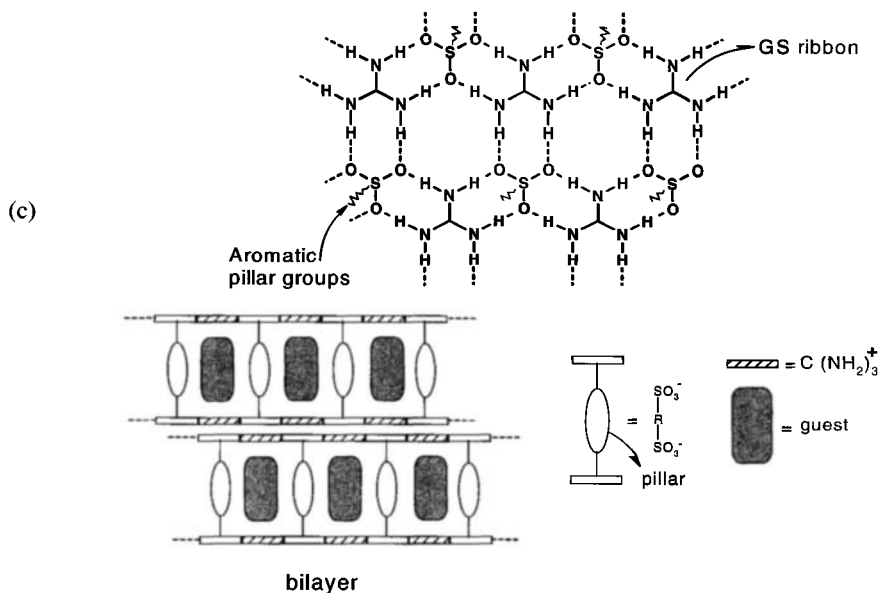


Figure 2. (a) Brick-shaped cavity in *C*-methylcalix[4]resorcinarene•4,4'-bipyridine of $14 \times 11 \times 6$ Å. The cavity is closed because adjacent layers are staggered. *m*-Xylene guest molecules are not shown for clarity [17]. (b) 1D channels of ca. 30 Å^2 area in C_2 -symmetric diol sustained by O–H...O helical trimer. The hollow tube is chiral because crystallisation takes place in enantiomorphous space group [18]. (c) 2D quasi-hexagonal layer formed by guanidinium cation and aromatic disulfonate anion with rigid aromatic groups serving as the pillar in the bilayer region [19]. Structural tuning of cavity size, tube area and gallery width is possible in these organic host architectures.

3 C_3 symmetry and halogen...halogen interaction in host design

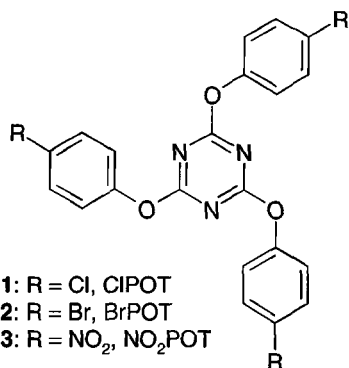
Symmetrical C_3 -substituted benzene rings are attractive starting materials for host lattices. The classical examples are 1,3,5-benzenetricarboxylic acid (trimesic acid, TMA), tri-*o*-thymotide (TOT chiral lattice), cyclotriphosphazene (CTP analogues). We have recently shown that a combination of molecular symmetry and intermolecular interaction geometry may be exploited for the design of crystal structures in high symmetry space groups [20,21]. Crystallisation of 2,4,6-tris(4-halophenoxy)-1,3,5-triazine **1** and **2** (halo = chloro, bromo; CIPOT, BrPOT) from a variety of solvents and guest molecules (e.g. benzene,

mesitylene, collidine, trinitrobenzene, hexamethylbenzene, hexachlorobenzene, hexamethylphosphoramide, etc.) afforded diffraction quality crystals that solve in the hexagonal space group $P6_3/m$. A slice of the honeycomb layer consists of alternating triazine molecule and halogen trimer synthon **I** at the nodes of the hexagon. Such layers may be stacked without offset to give a continuous channel ($P6_3/m$) or a finite cavity such that triazine and halogen trimers cap the guest ($R\bar{3}$). The diameter of cavity is 12-13 Å with an area of 100-110 Å². A stereoview of the hexagonal layer in CIPOT•TNB (2:1, TNB = 1,3,5-trinitrobenzene) is shown in Figure 3. The halogen trimer is a cooperative array of C–X...X interactions having polarisation-induced type II geometry (Cl...Cl 3.42 Å, θ_1 170.6°, θ_2 110.6°), the difference between the two angles being 120° because of crystallographic symmetry. In idealised type I approach $\theta_1 = \theta_2 \approx 150^\circ$ (halogen atoms related across inversion centre) and in type II approach $\theta_1 \approx 180^\circ$, $\theta_2 \approx 90^\circ$ (halogen atoms related by screw axis or glide plane). Molecular and supramolecular nodes occupy the $\bar{6}$ site and ordered TNB molecules are located at $z = \frac{1}{4}$ and $\frac{3}{4}$ in a staggered orientation within each channel. The fully ordered structure is ascribed to the numerous host–guest heteroatom interactions (N–O...O 3.16 Å, N–O...Cl 3.53 Å). TNB guest molecules are stacked at a distance of 3.5 Å in the 1D channel of CIPOT. This is the only example of π -stacked electron-deficient aromatic rings at van der Waals separation in the Cambridge Structural Database [22], an archive of over quarter of a million crystal structures. Interestingly, the nitro groups of TNB lie in the plane of the aromatic ring in an all-planar conformation. The isolation of TNB in a π -stacked planar conformation is ascribed to the numerous weak interactions that stabilise this high-energy conformation of the guest in the narrow channel of the host. In contrast to the channel structure of CIPOT•TNB and CIPOT•HCB (HCB = hexachlorobenzene), the crystal structure of BrPOT•HCB (space group $R\bar{3}$) is layered because host molecules are stacked with offset in adjacent layers. Once again, the host–guest structure is fully ordered because of numerous weak heteroatom interactions (O...Cl 3.53 Å). That the ordered arrangement of guest molecule is due to specific intermolecular interaction is suggested by the inclusion adduct of CIPOT and BrPOT with hexamethylbenzene (HMB). Both these structures have disordered guest molecules. Comparison of guest molecules with chloro to methyl exchange provides useful structural information because these groups have a similar size (Cl 20 Å³, Me 24 Å³), and hence occupy the same volume in the channel, but their intermolecular interactions (C–H...O vs. Cl...O) are quite different. The absence of specific weak interactions

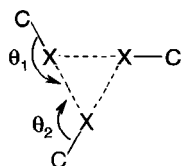
between heteroatoms on the host wall and CH₃ groups of the guest leads to guest disorder. Guest inclusion in cavities and channels of Cl/Br-POT host lattice is the norm and we have so far not been able to crystallise the solvent-free material for X-ray diffraction.

Table 1. Crystal data for halo- and nitro-phenoxytriazines ClPOT, BrPOT and NO₂POT.

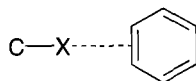
	Host/ guest	Space group	$a = b$ (Å)	c (Å)
BrPOT·½HCB	2:1	$R\bar{3}$	15.381(1)	18.402(2)
BrPOT·CLN	1:1	$P6_3/m$	15.468(2)	7.087(1)
BrPOT·MNP	1:1	$P6_3/m$	15.569(2)	7.064(1)
BrPOT·MES	1:1	$P6_3/m$	15.573(2)	7.042(1)
ClPOT·½HCB	2:1	$P6_3/m$	15.435(2)	6.876(1)
ClPOT·½HMB	2:1	$P6_3/m$	15.411(2)	6.867(1)
BrPOT·½HMB	2:1	$P6_3/m$	15.554(4)	6.951(3)
ClPOT·½TNB	2:1	$P6_3/m$	15.255(2)	7.005(2)
BrPOT·½TNM	2:1	$P6_3/m$	15.719(2)	7.034(1)
ClPOT·½HMPA	2:1	$P6_3/m$	15.234(2)	6.880(1)
BrPOT·2HMPA·½CA	2:4:1	$R3c$	15.615(2)	63.670(1)
BrPOT·½HBB	2:1	$R\bar{3}$	15.550(2)	7.511(1)
ClPOT·TBB	1:1	$P6_3$	15.250(2)	6.815(2)
ClPOT·TIB	1:1	$P6_3$	15.482(1)	7.011(1)
BrPOT·TBB	1:1	$P6_3$	15.442(1)	6.991(1)
BrPOT·TIB	1:1	$P6_3$	15.627(2)	7.046 (1)
2NO ₂ POT·benzene	2:1	$R\bar{3}$	14.195(2)	20.941(5)
NO ₂ POT·3CHCl ₃	1:3	$P6_3$	14.617(1)	8.383(1)
2NO ₂ POT·HCB	2:1	$R\bar{3}$	14.660(1)	20.210(2)
NO ₂ POT·TBB	1:1	$P\bar{3}$	14.524(1)	8.287(1)
3NO ₂ POT·HMB	3:1	$P6_3/m$	14.443(1)	22.593(2)



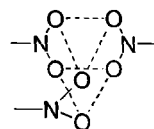
BrPOT.hexamethylbenzene (HMB), (2:1)
 BrPOT.trinitromesitylene (TNM), (2:1)
 BrPOT.2,4,6-collidine (CLN), (1:1)
 BrPOT.1-methylnaphthalene (MNP), (1:1)
 BrPOT.mesitylene (1:1)
 BrPOT.hexachlorobenzene (HCB), (2:1)
 BrPOT.hexabromobenzene (HBB), (2:1)
 BrPOT.hexamethylphosphoramide (HMPA)
 .cyanuric acid (CA), (2:4:1)
 CIPOT.hexachlorobenzene (HCB), (2:1)
 CIPOT.hexamethylbenzene (HMB), (2:1)
 CIPOT.trinitrobenzene (TNB), (2:1)
 CIPOT.hexamethylphosphoramide (HMPA), (2:1)
 CIPOT.1,3,5-tribromobenzene (TBB), (1:1)
 CIPOT.1,3,5-triiodobenzene (TIB), (1:1)
 BrPOT.1,3,5-tribromobenzene (TBB), (1:1)
 BrPOT.1,3,5-triiodobenzene (TIB), (1:1)
 NO₂POT.chloroform (1:3)
 NO₂POT.tribromobenzene (TBB), (1:1)
 NO₂POT.hexachlorobenzene (HCB), (2:1)
 NO₂POT.benzene (2:1)
 NO₂POT.hexamethylbenzene (HMB), (3:1)



I
halogen trimer



II
halogen... π



III
nitro trimer

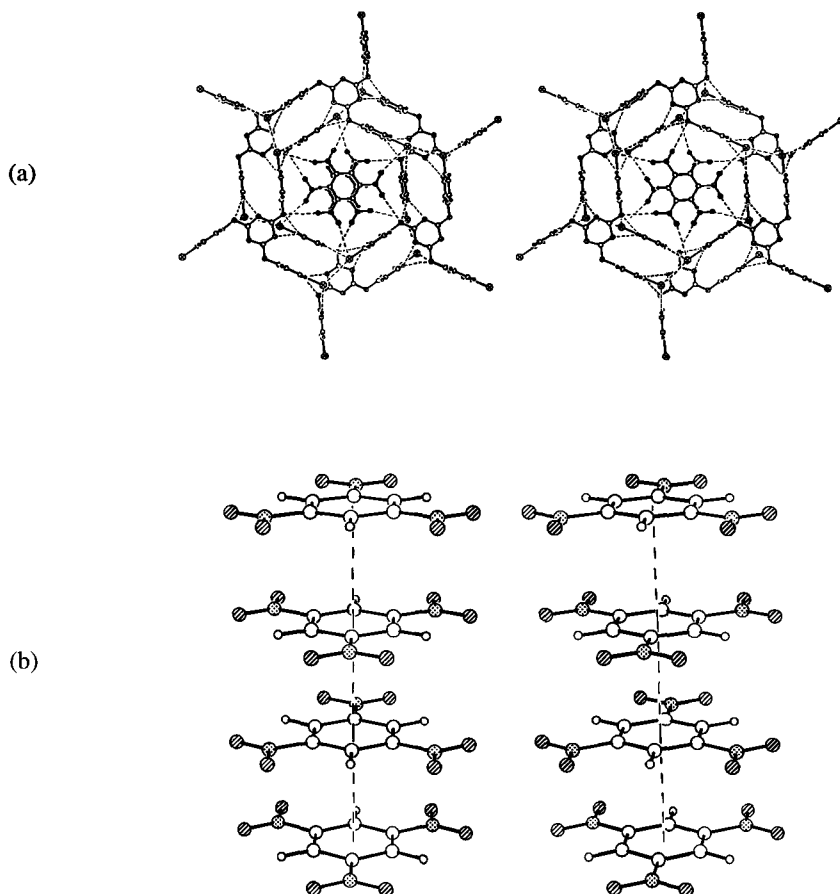


Figure 3. (a) Stereoview of the hexagonal network formed by alternating triazine **1** and halogen trimer **I** synthons at the nodes in the crystal structure of ClPOT•TNB (2:1). Note the O...Cl and O...O host–guest interactions. (b) Planar conformation of 1,3,5-trinitrobenzene (phenyl ring and nitro oxygen atoms occupy the same plane) in the 1D channel of ClPOT. The centroid-to-centroid distance of adjacent phenyl rings is 3.5 Å ($=c/2$).

Channels with van der Waals diameter at the nanometer scale (ca. 12 Å) have the potential to include larger guest molecules, such as fullerenes. Co-crystallisation of BrPOT and C₆₀ (or C₇₀) from toluene afforded hexagonal prism single crystals by temperature lowering technique [23]. The crystals are stable at room temperature. The crystal structure of 2•(C₆₀)_{0.2}(toluene)_{0.6} solve in the hexagonal space group *P6₃/m* with

disordered C_{60} and solvent molecules accommodated in the channels of BrPOT (Figure 4). The slightly larger a and b values (15.81 Å) compared to crystal data described above (Table 1) indicate flexibility of the channel to adapt to larger guests. Partial desolvation of toluene at 200 °C and 10^{-2} Torr gave material with ca. 10% solvent but in an amorphous state. It appears that toluene- C_{60} interactions are necessary to stabilise the guest species in the 1D channel.

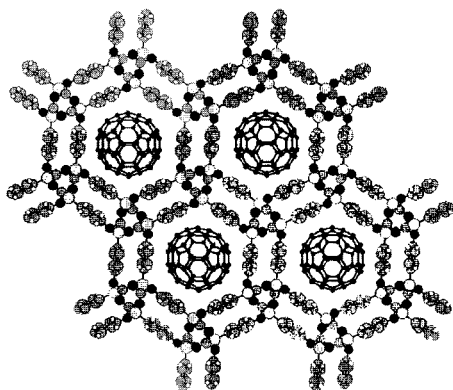


Figure 4. Inclusion of C_{60} in the channels of BrPOT **2**. The position of disordered C_{60} molecules is chosen arbitrarily and disordered toluene molecules are not shown for clarity [23]. © Royal Society of Chemistry.

Crystallisation of achiral molecules in polar or enantiomorphous space groups is an active research area for fundamental and applied reasons. Understanding the evolution of chirality in Nature, the phenomenon of spontaneous resolution, and the design of polar solids for electrooptic and nonlinear materials are important goals in supramolecular chemistry. In this context, crystallisation of 1,3,5-trihalobenzene (halo = Br, I) with ClPOT and BrPOT in 1:1 stoichiometry afforded diffraction quality crystals that solve in the polar space group $P6_3$ [24]. The hexagonal framework of the host lattice in these four structures is identical to the centrosymmetric crystal structures in $P6_3/m$ space group (Cl...Cl 3.56 Å, θ_1 167.0°, θ_1 107.0°). However, because of the asymmetric orientation of guest molecules and the tilted conformation of host phenyl rings the mirror plane is absent and the overall packing is non-centrosymmetric. In effect, inclusion of trihalobenzene guest induces significant structural changes in the arrangement of host phenyl rings but the unit cell dimensions of the crystal are unchanged. The guest molecules form short C-halogen... π interaction with the C=C bond of host phenoxy ring (3.43 Å, 158.3°; Σ_{vdw} 3.7 Å). The geometry of halogen... π interaction **II** is reminiscent of the polarisation-induced type **II** halogen...halogen interaction. In this

approach, the $C-X^{(\delta+)}$ vector points towards the mid-point of $\pi^{(\delta-)}$ bond of phenyl ring. A closer examination of these four isomorphous structures suggests that the host phenyl group is tilted with respect to the channel c -axis to optimise the halogen $\cdots\pi$ interaction. This tilting of phenyl group is transmitted to adjacent channels via the edge-to-face herringbone motif between phenoxy rings related by 2-fold screw axis. Thus, the recurring halogen $\cdots\pi$ interaction in these host–guest structures is the minimum ensemble necessary to amplify chirality in the entire crystal, in other words the synthon may be termed a supramolecular chiron. Supramolecular chiron [25] is defined as the smallest structural unit capable of generating through self-assembly topologically distinct enantio- or diastereopure architectures.

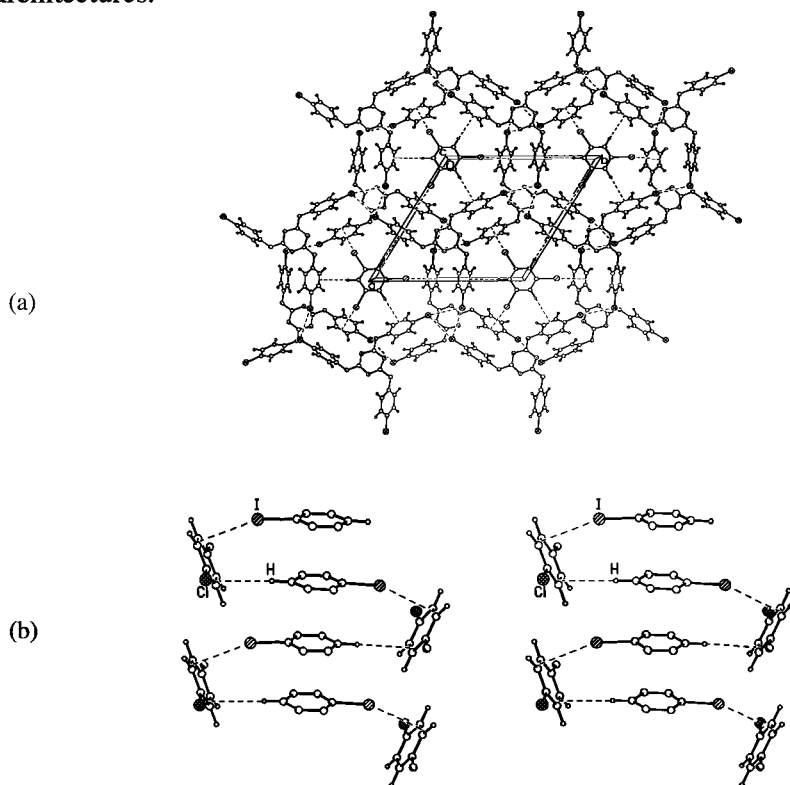


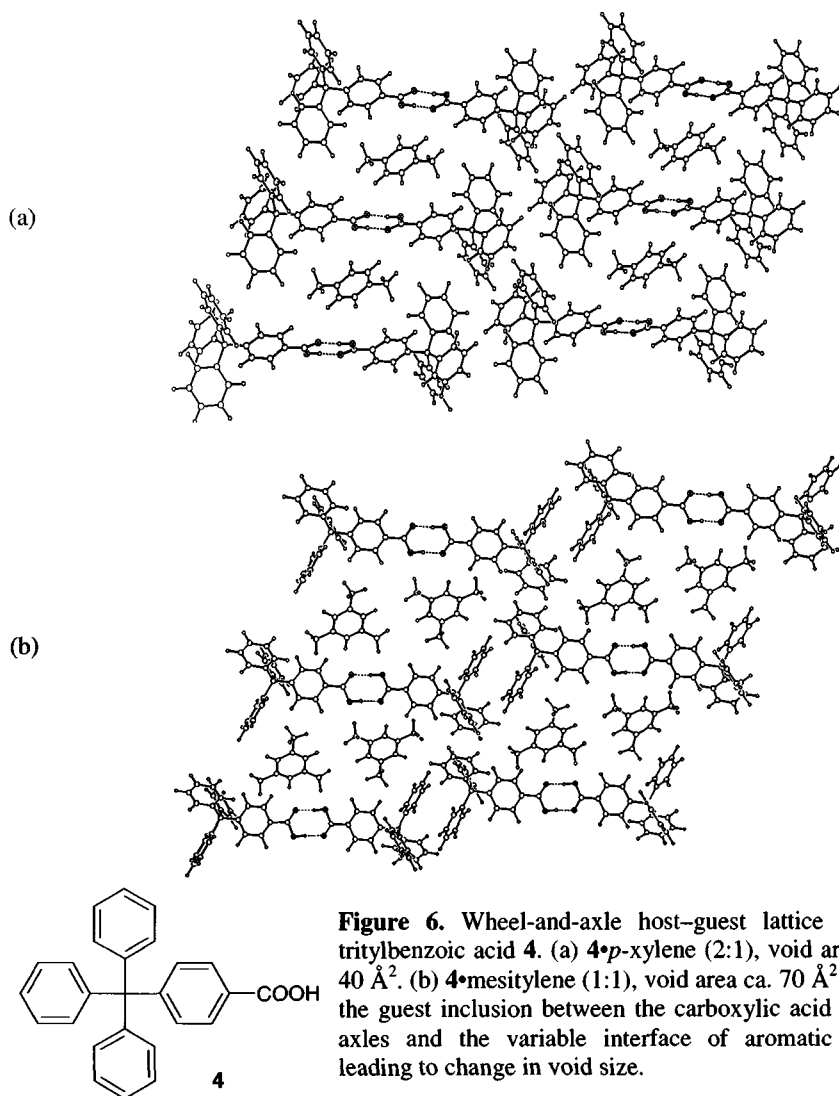
Figure 5. (a) Crystal structure of CIPOT•1,3,5-triiodobenzene (1:1). Note that the hexagonal host layers are identical but the phenoxy rings are tilted compared to Figures 3 and 4. C–I $\cdots\pi$ and C–H $\cdots\pi$ interactions are shown as dotted lines. (b) The spiral of C–I $\cdots\pi$ and C–H $\cdots\pi$ guest–host interactions in a channel (shown as stereoview) is the supramolecular chiron.

Noting that high symmetry hexagonal/rhombohedral space groups are routinely adopted in C_3 -symmetrical halophenoxytriazines, we reasoned that it should be possible to replace halogen with another functional group and obtain a new trimer supramolecular synthon. This design scheme was successful with the NO_2 group. Crystallisation of 2,4,6-tris(4-nitrophenoxy)-1,3,5-triazine **3** from a variety of solvents afforded crystalline adducts as detailed in Table 1 [26]. The notable features in these five adducts are: (1) the crystal structures are similar to the halogen series in terms of architecture (channel or layer) and crystal symmetry (hexagonal or rhombohedral space group); (2) the halogen trimer synthon **I** is replaced by nitro-trimer motif **III** in the hexagonal layer; (3) weak intermolecular host-guest interactions in **3** ($\text{C-H}\cdots\text{O/N}$, $\text{Cl}\cdots\text{O}$, $\pi\cdots\pi$) are similar to the halogen series **1** and **2**. The nitro trimer synthon **III** is stabilised by numerous $\text{O}\cdots\text{O}$ and $\text{O}\cdots\text{N}$ electrostatic interactions between the oxygen atom of one nitro group and the C-NO_2 fragment of a neighbouring molecule. Optimised energy of symmetrical synthon **III** in H-NO_2 calculated with RHF/6-31G** basis set (Spartan) is -8.6 kcal/mol, comparable to the energy of a strong hydrogen bond. Therefore, cumulative stabilisation from numerous weak interactions may be exploited in crystal design with appropriate consideration of symmetry factors. Supramolecular synthons involving the nitro group include $\text{O}\cdots\text{H}\cdots\text{O}_2\text{N}$, $\text{N}\cdots\text{H}\cdots\text{O}_2\text{N}$, $\text{C-H}\cdots\text{O}_2\text{N}$ and $\text{C-I}\cdots\text{O}_2\text{N}$ interactions. The nitro trimer synthon is a useful addition to the crystal engineer's tool kit.

4 Wheel-axle host lattice

An advantage in organic host-guest adducts assembled with robust supramolecular synthons is that the pore size, cavity shape and final 3D architecture can be systematically manipulated through spacer units and hydrophobic groups. Wheel-and-axle or dumb-bell shaped molecules are a typical example of open frameworks [27,28]. The mismatched size of wheel (rigid, bulky) and axle (long, linear) groups prevent self-inclusion (interpenetration), thereby resulting in voids that are occupied by small guest molecules. In a conceptual advance, the axle of 4-tritylbenzoic acid **4** was assembled supramolecularly through aggregation via the robust carboxy dimer synthon [29]. Acid **4** includes a variety of aromatic solvents in its microporous voids of $40\text{--}70$ Å² dimensions (Figure 6). The recurrence of wheel-axle host architecture is a result of the strong and robust $\text{O-H}\cdots\text{O}$ dimer (energy ca. 15 kcal/mol), further assisted in this case by aromatic-aromatic interactions. The cavity size is altered through

numerous edge-to-face and vertex-to-face arrangements (herringbone motif, T-geometry) that are possible between the triphenylmethyl groups of **4**. In effect, strong and weak hydrogen bonds play distinct structural role in these crystalline adducts: O–H...O dimer gives reproducibility and phenyl–phenyl interactions impart adaptive behaviour. The robustness of wheel–axle topology is further illustrated in clathrates of 4-tritylbenzamide with amide N–H...O dimer as the non-covalent axis [30].



5 Design of layered host: crystal engineering

Based on the C–H...O hydrogen-bonded tape **IV** in the crystal structure of benzoquinone we reasoned that it should be possible to design a family of layered structures if one of the carbonyl groups is replaced with geminal diaryl groups as in molecule **5**. Thus, a series of diphenylcyclohexadienones were synthesised ($R = H, F, Cl, Br, I, Me, \text{phenyl}$) and their crystal structures determined by X-ray diffraction. Crystal structures of the chloro- and bromophenyl derivatives (isomorphous structures in space group $C2/c$) are mediated by C–H...O interactions between activated phenyl C–H donors and C=O acceptor group. The halogen atoms participate in polarisation-induced type II interaction and C–H...X contacts. The tolyl derivative has different crystal packing in $P2_1/c$ space group [31]. We were unable to obtain single crystals of the fluorophenyl derivative. Thus, the halogen and methyl substituted analogues of **5** do not show the expected tape motif **IV** in their crystal structures.

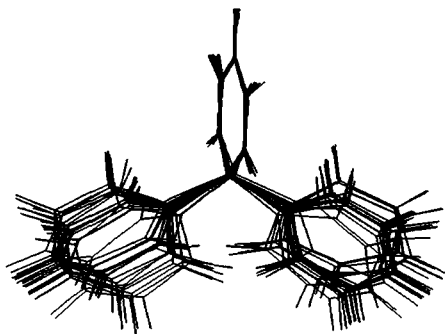
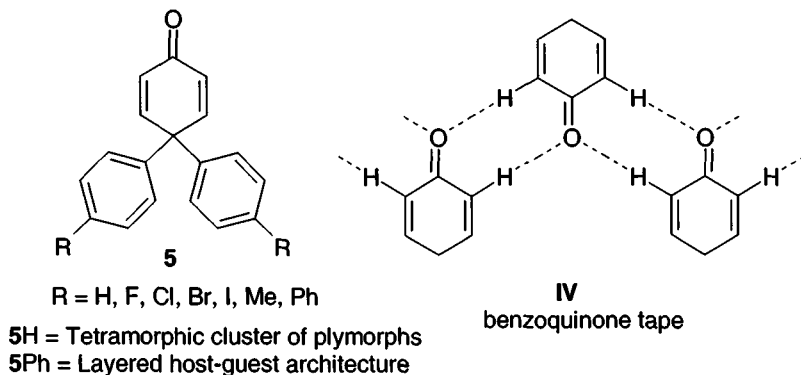


Figure 7. Overlay of 19 crystallographic independent conformations of **5H** in four polymorphs. The gearing of geminal phenyl rings leads to different conformations, which in turn results in crystallisation of conformational polymorphs.

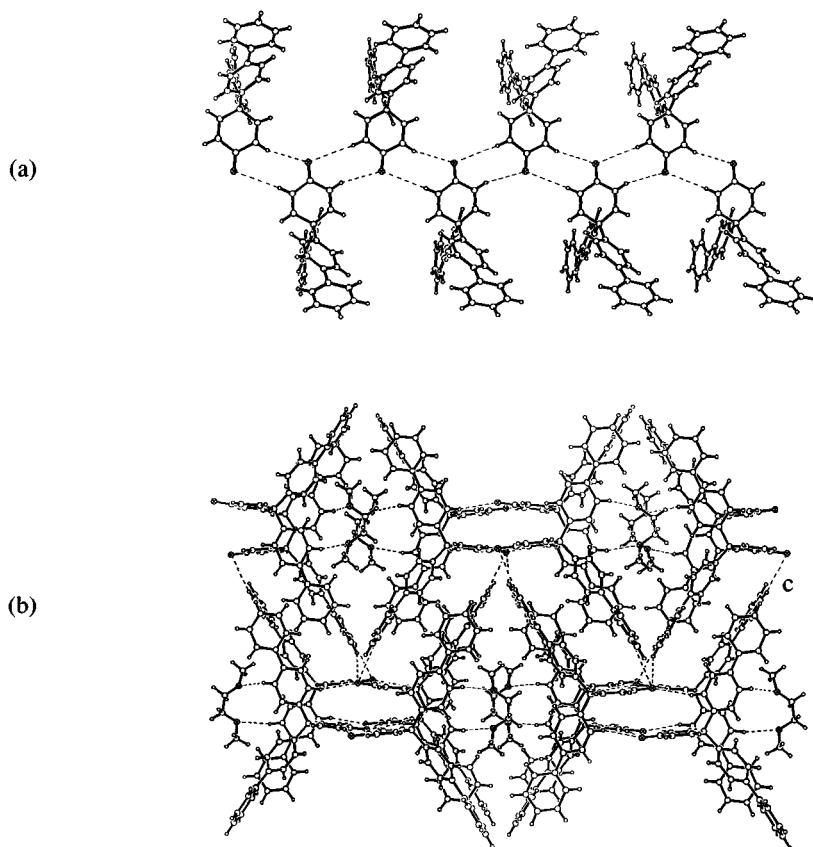
The parent compound **5H** exhibits fascinating structural behaviour in its own right but none of the diverse motifs in its crystal structures contain the C–H...O tape characteristic of benzoquinone. 4,4-Diphenyl-2,5-cyclohexadienone crystallises as four polymorphs with a total of 19 symmetry-independent molecular conformations [32]. These polymorphs (Table 2) may be classified as conformational polymorphs (forms B, C and D) and also concomitant polymorphs (forms A, B and C) [33] thus providing a unique example wherein these phenomenon are simultaneously present in the same polymorphic cluster. The existence of polymorphism in **5H** is ascribed to the geared rotation of geminal phenyl rings that results in small yet subtle changes in molecular conformations which in turn influence hydrogen bonding and close packing in the crystal.

Table 2. Crystallographic data on tetramorphs of 4,4-diphenyl-2,5-cyclohexadienone **5H**.

Polymorph	A	B	C	D
Space group	$P2_1$	$P\bar{1}$	$P\bar{1}$	$Pbca$
Z	2	8	24	16
<i>a</i> (Å)	7.9170(6)	10.0939(2)	18.3788(4)	10.7921(6)
<i>b</i> (Å)	8.4455(6)	16.2592(3)	19.9701(4)	17.4749(12)
<i>c</i> (Å)	10.3086(9)	16.2921(4)	24.4423(5)	27.9344(19)
α (°)	90	88.257(1)	95.008(1)	90
β (°)	105.758(2)	85.338(1)	111.688(1)	90
γ (°)	90	83.645(1)	105.218(1)	90

Success towards the design of a layered host with C–H...O hydrogen bonds forming the tape and aryl groups acting as the inter-layer spacer was achieved in the crystal structure of biphenyl analogue. The close-packed structures of phenyl derivative **5H** suggested that a longer aryl group is necessary to obtain a microporous architecture. Crystallisation of **5Ph** from a variety of solvents afforded diffraction quality crystals from 1,2-dimethoxyethane (DME) [34]. The crystal structure of **5Ph**•DME (2:1) in space group $C2/c$ contains the C–H...O hydrogen-bonded benzoquinone tape motif **IV** along [001] (H...O 2.66 Å, C...O 3.70 Å, \angle C–H...O 160.6°; Figure 8). Biphenyl groups form parallelepiped channels of 8×5 Å down the *c*-axis that are filled with ordered DME molecules. The ordered arrangement of guest molecules in the channel is ascribed to host–guest C–H...O hydrogen bond (2.57 Å, 3.60 Å, 159.5°). When **5Ph** was recrystallised from *n*-hexane, a solvent isosteric with DME but devoid of

oxygen atoms for hydrogen bonding, isomorphous 2:1 crystal structure of **5Ph**•hexane (2:1) was obtained. Structure solution and refinement converged to *R*-factor of 6.7%. *n*-Hexane molecules are disordered over two conformations with 55% and 45% occupancy. DME and *n*-hexane are present in folded conformations in the channel with end-to-end C...C distance of 5.3–5.5 Å. The presence of guest molecules in high-energy gauche and eclipsed conformations is forced by the narrow and rigid host cavity of 8×5 Å flanked by biphenyl groups (Figure 8). Interestingly, the hydrophobic cavity is selective towards the inclusion of long chain guests (e.g. DME, *n*-hexane, 1,4-dibromobutane) because co-solvents such as EtOAc, CH₂Cl₂, Et₂O, CHCl₃ are not included even though they are present in large excess. Given the disordered nature of guest species in the bilayer gallery region, **5Ph** may be viewed as an organic clay mimic.



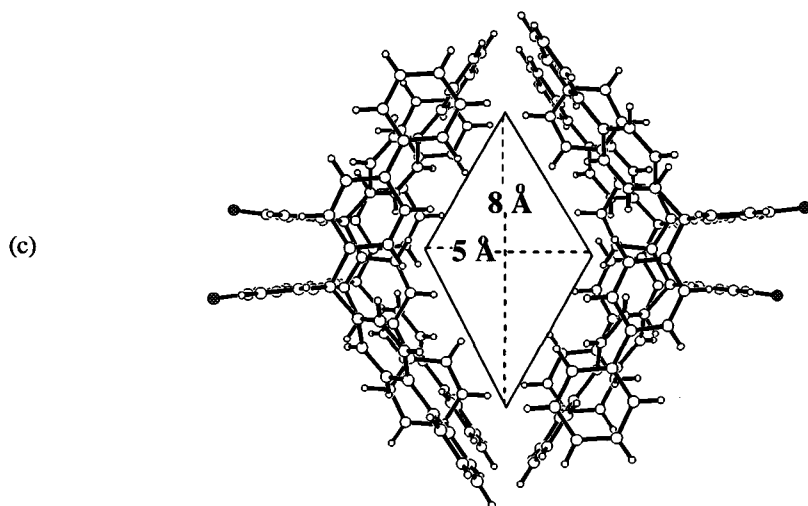
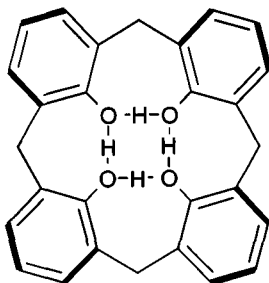


Figure 8. (a) C–H...O hydrogen-bonded tape motif along [001] in the crystal structure of 5Ph•DME (2:1). (b) Inversion-related biphenyl groups form parallelepiped-shaped channels that are filled with ordered 1,2-dimethoxyethane molecules. (c) The rigid cavity of host constrains long chain guest molecules in folded conformation.

6 Gas storage in interstitial voids

Host–guest compounds find application in the entrapment of volatile liquids and gases, the first example of this phenomenon being the solid with formula $\text{Cl}_2 \cdot 10\text{H}_2\text{O}$ (chlorine hydrate) mentioned in the Introduction. The water molecules form a hydrogen-bonded cage in which the gas is imprisoned without engaging in any strong interactions with the host lattice. Calixarenes are an extremely important class of macrocyclic compounds in host–guest inclusion chemistry. These bowl-shaped molecules with a shallow cleft have been used as molecular receptors and as lattice inclusion hosts. The simplest member calix[4]arene has a cone conformation stabilised by a cyclic array of intramolecular O–H...O hydrogen bonds as in **6**. Since solvent molecules are readily included in **6** during crystallisation, diffraction quality crystals of guest-free **6** were grown by sublimation at 300 °C [35]. Pure **6** crystallises in the hexagonal space group $P6_3/m$. Three calixarene molecules form a trimer arrangement that is approximately spherical in shape. All O–H...O hydrogen bonds are intramolecular and the structure is held together by weak van der Waals forces. Two types of channels run parallel to the *c*-axis: type ‘a’ channels are continuous and link the above trimer in an anti-prismatic arrangement

of six spheres; type 'b' channels (with solvent accessible void of ca. 150 Å³) are finite being surrounded by five spheres of **6** in a trigonal bipyramidal geometry. A large number of isomorphous guest inclusion structures of **6** are obtained in space group *P*6₃/*m* (Table 3).



Calix[4]arene **6**

Table 3. Inclusion compounds of calix[4]arene **6** with volatile guest molecules and gases, and hexagonal unit cell parameters.

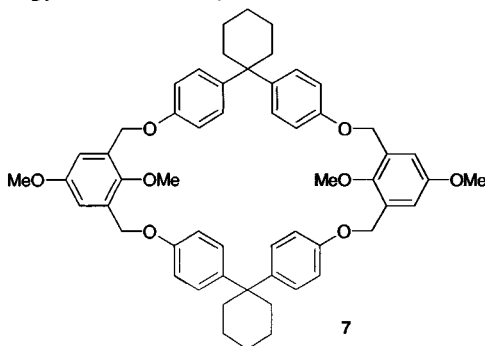
Complex	Guest b.p. (°C)	<i>a</i> = <i>b</i> (Å)	<i>c</i> (Å)
6 (pure)	---	14.3443	18.6271
6 •CCl ₄	76.8	14.5923	18.3862
6 •CHCl ₃	61.2	14.6975	17.9534
6 •CH ₂ Cl ₂	39.8	14.698	17.99
6 •CFCl ₃	23.7	14.6369	18.2454
6 •CF ₂ ClBr	-4	14.6432	18.2357
6 •CF ₃ CH ₂ F	-15	14.6401	18.2204
6 •CF ₃ Br	-57.7	14.4878	18.2273
6 •C ₂ F ₆	-78.2	14.6474	18.1957
6 •CF ₄	-127.9	14.6153	18.2847
6 •(CH ₄) ₂	-160	14.5991	18.2832

Thermogravimetric analysis (TGA) of hcp inclusion compounds shows that volatile guest species are released at a very high temperature from the cage (*T*_{on}) compared to the normal boiling point of pure guest (*T*_b). The parameter *T*_{on} - *T*_b is taken as a measure of the relative thermal stability in host-guest systems [36]. Methane is released from the hcp lattice at 160 °C giving a *T*_{on} - *T*_b value of 320 °C (values for CF₃Br and CF₄ are 260 °C and 370 °C, respectively). The high thermal stability of these host-guest adducts is attributed to the host lattice being isomorphous with its pure

phase. There is not much gain in energy for the host structure by releasing the guest from its interstitial voids and, moreover, the guest cannot escape easily from the void because it is surrounded on all sides by host spheres. This type of entrapment is even better than zeolites in which guest molecules can escape from the porous channels with the application of temperature or pressure.

7 Guest selectivity in inclusion

Competition experiments on the inclusion of picoline and lutidine isomers in a cyclophane host were reported recently [37]. Both host and guest molecules are devoid of strong hydrogen-bonding groups and all intermolecular association and stabilisation is due to weak C–H...O, C–H...N hydrogen bonds and van der Waals interactions. The rectangular box of molecular host cyclophane **7** show strong concentration-dependent selectivity for guest inclusion. Inclusion of 4-picoline is strongly favoured when its mole fraction in solution is >0.4 but disfavoured at concentration <0.2 . The lattice energy of **7**•(picoline)₂ clathrates is -31.60 , -31.17 and -38.44 kcal/mol for 2-, 3- and 4-picoline, respectively. Thus stability of clathrate with 4-picoline < 2 -picoline \approx 3-picoline. The extra stability of 4-picoline clathrate explains why inclusion is strongly favoured. Additionally, analysis of the three crystal structures shows that the cavity has different orientation of host methoxy groups for 4-picoline compared to 2- and 3-picoline. Furthermore, weak C–H...O and C–H...N hydrogen bonds involving CH₃ and N groups of 4-picoline constrain the guest molecule in the cavity but 2- or 3-picoline guest is not so tightly held to the host scaffold. In the lutidine series, inclusion of 2,4-lutidine is favoured in all cases when the mole fraction is >0.3 . This shows that weak C–H...O/N interactions are able to discriminate between guest isomers with preference for CH₃ group in 4-position to pyridine N. These ideas are advantageous in separation technology with macrocyclic hosts.



8 Conclusions

The traditional view is that host lattices must be assembled with strong hydrogen bonds to sustain the open architecture for guest inclusion. Recent examples from among those discussed in this article and by others [38,39] convincingly demonstrate that weak hydrogen bonds and heteroatom interactions can be equally effective design elements in the crystal engineering of host lattices. An advantage of using hydrogen bonding in host design is that strong multi-point recognition synthons provide reproducibility and robustness to the framework (invariant architecture) while the weak interactions give flexibility and adaptivity (lattice breathing), with variation of guest molecule as an additional parameter for supramolecular isomerism. The strong binding of gases and the high selectivity in isomer separation offered by organic host lattices bode well for further studies on the structures and properties of these materials.

9 Acknowledgement

I thank the Department of Science and Technology, Government of India for funding my research in the area of nanostructures (SP/S1/G29/98).

References

1. Lehn J.-M., *Supramolecular Chemistry* (VCH, Weinheim, 1995).
2. Atwood J. L., Davies J. E. D., MacNicol D. D. and Vögtle F. (series executive editors), *Comprehensive Supramolecular Chemistry*, Vol. 6, *Solid-State Supramolecular Chemistry: Crystal Engineering* ed. by MacNicol, D. D., Toda, F. and Bishop, R., (Pergamon, Oxford, 1996).
3. Steed J. W. and Atwood J. L., *Supramolecular Chemistry* (Wiley, Chichester, 2000).
4. Glusker J. P. and Trueblood K. N., *Crystal Structure Analysis. A Primer* (OUP, Oxford, 1985).
5. Jeffrey G. A., *An Introduction to Hydrogen Bonding* (OUP, Oxford, 1997).
6. Desiraju G. R. and Steiner T., *The Weak Hydrogen Bond in Structural Chemistry and Biology* (OUP, Oxford, 1999).
7. Bosch E. and Barnes C. L., Triangular halogen-halogen-halogen interactions as a cohesive force in the structures of trihalomesitylenes, *Cryst. Growth Des.* **2** (2002) pp. 299-302.
8. Hsu K.-F. and Wang S.-L., Synthesis and characterization of $\text{Rb}_2(\text{MoO}_4)_3(\text{As}_2\text{O}_7)_2 \cdot 2\text{H}_2\text{O}$: The first rubidium molybdenum(VI) diarsenate with a porous structure, *Inorg. Chem.* **39** (2000) pp. 4654-4657.

9. Batten S. R., Hoskins B. F. and Robson R., Interdigitation, interpenetration and intercalation in layered cuprous tricyanomethanide derivatives, *Chem. Eur. J.* **6** (2000) pp. 156-161.
10. Kobayashi K., Endo K., Aoyama Y. and Masuda H., Hydrogen-bonded network formation in organic crystals as effected by perpendicular and divergent hydroxyl groups: The crystal structure of a bisresorcinol derivative of anthracene, *Tet. Lett.* **34** (1993) pp. 7929-7932.
11. Nangia A., Organic nanoporous structures, *Curr. Opin. Solid State Mater. Sci.* **5** (2001) pp. 115-122.
12. MacNicol D. D. and Downing G. A., Symmetry in the evolution of host design. In *Comprehensive Supramolecular Chemistry*, Vol. 6, *Solid-State Supramolecular Chemistry: Crystal Engineering* ed. by MacNicol, D. D., Toda, F. and Bishop, R., (Pergamon, Oxford, 1996) pp. 421-464.
13. Weber E., Shape and symmetry in the design of new hosts. In *Comprehensive Supramolecular Chemistry*, Vol. 6, *Solid-State Supramolecular Chemistry: Crystal Engineering* ed. by MacNicol, D. D., Toda, F. and Bishop, R., (Pergamon, Oxford, 1996) pp. 535-592.
14. Desiraju G. R., *Crystal Engineering. The Design of Organic Solids* (Elsevier, Amsterdam, 1989).
15. Desiraju G. R., Supramolecular synthons in crystal engineering—A new organic synthesis, *Angew. Chem. Int. Ed. Engl.* **34** (1995) pp. 2311-2327.
16. Batten S. R. and Robson R., Interpenetrating nets: ordered, periodic entanglement, *Angew. Chem. Int. Ed.* **37** (1998) pp. 1461-1494.
17. MacGillivray L. R., Reid J. L. and Ripmeester J. A., Conformational isomerism leads to supramolecular isomerism and nanoscale inclusion in 2D extended framework solids based on *C*-methylcalix[4]resorcinarene, *Chem. Commun.* **11** (2001) pp. 1034-1035.
18. Kim S., Bishop R., Craig D. C., Dance I. G. and Scudder M. L., Crystal engineering of hydroxy group hydrogen bonding: Design and synthesis of new diol lattice inclusion hosts, *J. Org. Chem.* **67** (2001) pp. 3221-3230.
19. Holman K. T., Pivovar A. M., Swift J. A. and Ward M. D., Metric engineering of soft molecular host frameworks, *Acc. Chem. Res.* **34** (2002) pp. 107-118.
20. Jetti R. K. R., Xue F., Mak T.C.W. and Nangia A., 2,4,6-tris-4-(Bromophenoxy)-1,3,5-triazine: a hexagonal host framework assembled with robust Br \cdots Br synthons, *Cryst. Eng.* **2** (1999) pp. 215-224.
21. Jetti R. K. R., Xue F., Mak T.C.W. and Nangia A., Hexagonal nanoporous host structures based on 2,4,6-tris-(4-halophenoxy)-1,3,5-triazine (halo = chloro, bromo), *Tetrahedron* **56** (2000) pp. 6707-6719.
22. Allen F. H., The Cambridge Structural Database: a quarter of a million crystal structures and rising, *Acta Crystallogr. Sect. B* **58** (2002) pp. 380-388.
23. Süß H. I., Lutz M. and Hulliger J., Inclusion of fullerenes into channels of 2,4,6-tris(4-bromophenoxy)-1,3,5-triazine (BrPOT), *Cryst. Eng. Comm.* **4** (2002) pp. 610-612.
24. Jetti R. K. R., Nangia A., Xue F. and Mak T.C.W., Polar host-guest assembly mediated by halogen $\cdots\pi$ interaction: Inclusion complexes of 2,4,6-tris(4-halophenoxy)-1,3,5-triazine (halo = chloro, bromo) with trihalobenzene (halo = bromo, iodo), *Chem. Commun.* **10** (2001) pp. 919-920.

25. Hanessian S., Saladino R., Margarita R. and Simard M., Supramolecular chirons based on enantiodifferentiating self-assembly between amines and alcohols (supraminols), *Chem. Eur. J.* **5** (1999) pp. 2169-2183.
26. Jetli R. K. R., Thallapally P. K., Nangia A., Lam C.-K. and Mak T.C.W., 2,4,6-tris(4-Nitrophenoxy)-1,3,5-triazine: a hexagonal host framework stabilised by the NO₂-trimer supramolecular synthon, *Chem. Commun.* **9** (2002) pp. 952-953.
27. Müller T., Hulliger J., Seichter W., Weber E., Weber T. and Wübberhorst M., A new nanoporous architecture: Dumb-bell-shaped molecules with guests in parallel channels, *Chem. Eur. J.* **6** (2000) pp. 54-61.
28. Weber E., Nitsche S., Wierig A. and Csöregi I., Inclusion compounds of diol hosts featuring two 9-hydroxy-9-fluorenyl or analogous groups attached to linear spacer units, *Eur. J. Org. Chem.* (2002) pp. 856-872.
29. Jetli R. K. R., Xue F., Mak T.C.W. and Nangia A., 4-Tritylbenzoic acid. A molecular scaffold for wheel-and-axle host-guest inclusion compounds with a supramolecular axis, *J. Chem. Soc., Perkin Trans 2* (2000) pp. 1223-1232.
30. Reddy C. M., Nangia A., Lam C.-K. and Mak T.C.W., An engineered N-H... π interaction: crystal structure of 4-tritylbenzamide-*p*-xylene, *Cryst. Eng. Comm.* **4** (2002) pp. 323-325.
31. Kumar V. S. S., Polymorphism, pseudopolymorphism and networks in organic crystals, (Ph.D thesis, University of Hyderabad, India, 2002).
32. Kumar V. S. S., Addlagatta A., Nangia A., Robinson W. T., Broder C. K., Mondal R., Evans I. R., Howard J. A. K. and Allen F. H., 4,4-Diphenyl-2,5-cyclohexadienone: Four polymorphs and nineteen crystallographically independent molecular conformations, *Angew. Chem. Int. Ed.* **41** (2002) pp. 3848-3851.
33. Bernstein J., Davey R. J. and Henck J.-O., Concomitant polymorphs, *Angew. Chem. Int. Ed.* **38** (1999) pp. 3440-3461.
34. Kumar V. S. S. and Nangia A., Inclusion adducts of 4,4-bis(4'-biphenyl)-2,5-cyclohexadienone: a clay mimic organic host, *Chem. Commun.* **22** (2001) pp. 2392-2393.
35. Atwood J. L., Barbour L. and Jerga A., Storage of methane and freon by interstitial van der Waals confinement, *Science* **296** (2002) pp. 2367-2369.
36. Caira M. R. and Nassimbeni, L. R., Phase transformations in inclusion compounds, kinetics and thermodynamics of enclathration. In *Comprehensive Supramolecular Chemistry*, Vol. 6, *Solid-State Supramolecular Chemistry: Crystal Engineering* ed. by MacNicol, D. D., Toda, F. and Bishop, R., (Pergamon, Oxford, 1996) pp. 825-850.
37. Apel, S., Lennartz M., Nassimbeni L. R. and Weber E., Weak hydrogen bonding as a basis for concentration-dependent guest selectivity by a cyclophane host, *Chem. Eur. J.* **8** (2002) pp. 3678-3686.
38. Crystal engineering involving weak C-H...N hydrogen bonds: a diquinoline lattice inclusion host with a preference for polychlorocarbon guests, *Eur. J. Org. Chem.* (2001) pp. 863-873.
39. Thaimattam R., Xue F., Sarma J. A. R. P., Mak T. C. W. and Desiraju G. R., Inclusion compounds of tetrakis(4-nitrophenyl)methane: C-H...O networks, pseudopolymorphism, and structural transformations, *J. Am. Chem. Soc.* **123** (2001) pp. 4432-4445.

NONSURFACTANT ROUTE TO NANOPOROUS PHENYL-MODIFIED HYBRID SILICA MATERIALS

YEN WEI*, HUA DONG, JIGENG XU, CE WANG AND QIUWEI FENG

Department of Chemistry, Drexel University, Philadelphia, PA 19104, USA

E-mail: weiyen@drexel.edu

KUN-YUAN QIU AND ZI-CHEN LI

Department of Polymer Science & Engineering, Peking University, Beijing 100871 China

SUSAN A. JANSEN

Department of Chemistry, Temple University, Philadelphia, PA 19122, USA

Phenyl-modified mesoporous sol-gel materials have been successfully synthesized through the co-condensation of tetramethyl orthosilicate (TMOS) with up to 10 mol% of phenyltrimethoxysilane (PhTMS) under acid catalysis in the presence of fructose as a neutral nonsurfactant template. The phenyl group was incorporated into the silica matrix via the non-hydrolyzable Si-C covalent bond and functioned as network modifier. After solvent extraction to remove the template, the hybrid sol-gels synthesized from 5 mol% PhTMS and 95 mol% TMOS with over 50 wt% fructose had a BET surface area of $\sim 800 \text{ m}^2 \text{ g}^{-1}$, pore volume of $\sim 0.6 \text{ cm}^3 \text{ g}^{-1}$ and BJH pore diameter of around 3 nm. Although smaller than that of pure silica matrix under otherwise identical conditions, the hybrids still have characteristic of mesoporous materials. The mesoporosity of the materials was also evidenced by transmission electron microscopy (TEM). This one-step synthesis can produce mesoporous matrix with reasonably high loadings of organic functional groups. The phenyl-modification significantly alters thermodynamic properties, such as hydrophobicity, of the internal surface of the mesoporous materials, which could be useful in the encapsulation of enzymes for biocatalysis applications.

1 Introduction

Conventional sol-gel silicas derived from the hydrolysis and condensation (i.e. sol-gel reactions) of tetramethyl orthosilicate (TMOS) or tetraethyl orthosilicate (TEOS) are hydrophilic, transparent and microporous materials with reasonable chemical and mechanical stability as well as biocompatibility [1]. In most cases, they are appropriate matrices for bioencapsulation even though they are brittle in nature. Organically functionalized hybrid sol-gel materials, obtained from the hydrolysis and co-condensation of TMOS or TEOS with other organosiloxanes, e.g. $\text{R}'_x\text{Si}(\text{OR})_{4-x}$, where generally R is alkyl, R' is alkyl, aryl, vinyl, other functional groups or even polymers, and x is 1, 2 or 3, has attracted ever

increasing attention in recent years because of their potential applications in various fields such as hard coating for optics, catalysis, selective membranes, molecular recognition, dentistry, etc. [2-9]. In these materials, TMOS/TEOS precursors function as building blocks to construct the framework while the organosiloxanes with non-hydrolyzable organic groups are integrated into the silica framework and provide organic surface groups with a variety desired functionalities. Various organic-inorganic structures are formed depending on the functionality of the organosiloxane and its proportion in the reactant mixture.

The synthesis of the ordered mesoporous silica and aluminosilicate materials MCM-41 (hexagonal symmetry) and MCM-48 (cubic symmetry) represents an important breakthrough in the research on inorganic molecular sieves [10-13]. Since then considerable attention has been focused on tailoring the chemical composition of the mesoporous materials due to their promising applications in gas separation membranes, ion exchange, catalyst supports, hosts for proteins, adsorbents, etc. The mesopore size is generally in the range of 2-100 nm and hence the materials are nanoporous. The organic functionalization of the internal surface of MCM-41 type host can be achieved either by post-synthesis grafting method [14-19] or by directly incorporating organosiloxanes in the reactants during the preparation [20-30]. Currently, the most common and direct synthesis route to the introduction of organic groups into silica network in sol-gel chemistry involves the co-condensation of mixtures of alkoxysilane and organosiloxane as precursors in the surfactant-templated sol-gel reactions. Among the first successful examples was phenyl-modified MCM-41 type of silica materials at room temperature by the hydrolysis and co-condensation of TEOS with phenyltrimethoxysilane (PhTES) in the presence of cationic surfactant, hexadecyltrimethylammonium bromide ($C_{16}H_{33}N(CH_3)_3Br$), followed by the acid extraction [20,28]. Nitrogen sorption and XRD studies showed the resultant materials using 20 mol% PhTES in the initial reactant mixture was microporous and of high hydrophobicity. The incorporation of organic groups into TMOS gels reduces the surface area and pore volume, but increases the hydrophobicity of the modified silicate gels. By probing the internal pore structure of vinyl-functionalized MCM-41 using bromination reaction, Mann and co-workers proposed that the vinyl groups are mostly located within the internal surface of mesoporous channels [25]. Such a single-step synthesis can produce mesoporous solids with high loadings of organic

functional groups and homogeneous surface coverage within a relatively short preparation time [26].

Phenyltrimethoxysilane (PhTMS) and phenyltriethoxysilane (PhTES) are preferred organosiloxanes for controlling the thermal stability, glass transition temperature, or refractive index of organic-inorganic hybrid materials. Furthermore, they can also act as a pre-structured starting material for further chemical modifications. For instance, after sulfonation of the phenyl-containing silicas, solid ion exchangers can be readily obtained, which have many advantages over conventional polymeric sulfonic acids, including high surface area, controllable pore size, mechanical stability, as well as reduced swelling or contraction upon ion exchange, compared to polymeric sulfonic acids [25]. The sulfonic acid functionalized materials was found to be an efficient heterogeneous catalyst for the protection of alcohols by tetrahydropyranlation.

Recently, our group has developed a versatile, biocompatible nonsurfactant-templating sol-gel route to mesoporous materials, where nonsurfactant organic compounds, such as D-glucose, D-fructose, D-maltose, dibenzoyl-L-tartaric acid, etc., were employed as the templates or pore-forming agents followed by solvent extraction [31-33]. The resultant silica materials are mesoporous with pore size of 2-6 nm at high template concentrations and have large specific areas of $\sim 1000 \text{ m}^2 \text{ g}^{-1}$ and pore volume of $\sim 0.6 \text{ cm}^3 \text{ g}^{-1}$, which can be readily tuned by varying the template concentration. Furthermore, since the synthesis can be achieved at room temperature and near neutral pH, a variety of bioactive substances such as enzymes and other proteins have been encapsulated directly into mesoporous inorganic matrices [34-36]. Protein folding and unfolding in mesopore-confined space have also been studied [37,38]. Because the thermodynamic properties of the internal surface of the host matrix have significant influences on both enzymatic activity and protein folding-unfolding, it is very important to develop the capability of preparing mesoporous host materials with various designable hydrophobicity.

In this paper, we extend the nonsurfactant-templating approach to the preparation of transparent, phenyl-modified hydrophobic mesoporous materials. The synthesis was achieved by acid-catalyzed hydrolysis and co-condensation of TMOS with PhTMS in the presence of fructose as the neutral nonsurfactant template followed by removing fructose template through solvent extraction. The effect of the molar content of the PhTMS in the feeds and the fructose concentration on the final mesostructure was investigated by infrared spectroscopy, N_2 adsorption-desorption isotherms, thermogravimetric analysis and transmission electron microscopy.

2 Methods

2.1 Materials and Synthesis

Tetramethyl orthosilicate (TMOS, 99%) and phenyltrimethoxysilane (PhTMS, 97%) were purchased from Aldrich (Milwaukee, WI). D(-) Fructose was supplied by Sigma (St. Louis, MO). HCl was product of Fisher Scientific (Fair Lawn, NJ). All chemicals and reagents were used as received without further purification. Distilled and de-ionized water (dd water) was used in all the procedures.

The preparation of phenyl-modified mesoporous sol-gel materials followed the similar procedures as reported previously for the HCl-catalyzed sol-gel reactions of TMOS [31,32], except that fructose was used as the pore-forming agent or template. To minimize the possibility of macroscopic phase separation, TMOS and PhTMS were prehydrolyzed under HCl catalysis before adding fructose. Two series of samples were synthesized. One series was prepared by fixing the concentration of fructose at 50 wt% while varying the molar proportion of PhTMS in the initial precursors from 5 to 25 mol%. Another series was synthesized by fixing the molar proportion of PhTMS at 5 mol% and varying the concentration of fructose between 0 and 60 wt%. In a typical procedure for preparing 5 mol% phenyl-modified hybrid mesoporous materials, denoted as HIIIF50-5, TMOS and PhTMS was prehydrolyzed with deionized H₂O under HCl catalysis (at the TMOS:PhTMS:HCl:H₂O molar ratio of 0.95:0.05:0.01:4) at ~60°C till a homogeneous solution was obtained. Upon cooling to room temperature, 1.25 g of fructose solution (pre-dissolved in 1.25 g of distilled water) was added to the reaction under agitation. The resultant homogeneous sol was sealed with paraffin film, which had 15 pinholes punched with a syringe needle to allow for the evaporation of volatile byproduct molecules such as methanol and water. After gelation and drying in air then in vacuum to reach constant weight at room temperature, a transparent, monolithic disk of sample was obtained. Control sample was also prepared from the co-condensation of TMOS and 5 mol% PhTMS without addition of fructose (denoted as HIIIF0-5). The other control sample containing no phenyl groups was synthesized using TMOS as the only silica source in the presence of 50 wt% of fructose (denoted as F50). After gelation, all samples were aged and dried at room temperature until no further weight loss.

To remove the fructose template, the fructose-containing samples (0.2–0.4 g) were ground into powder and immersed in 15 ml dd water under magnetic stirring. After 1 hr, the mixture was centrifuged and decanted, followed by adding another 15 ml of dd water. This procedure was repeated for at least 5 times plus an addition overnight extraction. Such an extraction procedure was found to have little effect on the chemical structure of the matrix materials. After extraction, the samples were dried at 120°C overnight to afford porous materials. The infrared (IR) spectroscopy was employed to monitor the extraction process and to confirm the complete removal of fructose template.

2.2 Characterization and Instrumentation

The infrared spectra of both as-synthesized and water-extracted samples were recorded on a Perkin-Elmer 1600 FT-IR spectrophotometer (Norwalk, CT) with a resolution of 4 cm^{-1} in the form of KBr powder-pressed pellets. The contents of fructose before extraction and phenyl moiety in the hybrid matrix (i.e., after extraction) were determined from the weight loss at 600°C in air by means of thermogravimetric analysis (TGA) on a DuPont TA 2000 thermal analysis system with 950 TGA module. The BET (Brunauer-Emmett-Teller) surface areas were determined from N_2 adsorption-desorption isotherms at 77 K on a Micrometrics ASAP 2010 analyzer (Micromeritics, Inc., Norcross, GA). Prior to the measurements, the samples were degassed at 100 °C and 1 Pa overnight. BJH (Barrett-Joyner-Halenda) pore size distributions were plotted using desorption branch of the isotherms. Transmission electron microscopy (TEM) image for the hybrid samples after removing the fructose template were obtained on a Hitachi H-9000 NAR HRTEM microscope operating at an accelerating voltage of 300 kV. The TEM samples were prepared by dipping an ethanol suspension of the finely ground sample powders onto a Cu grid coated with a holey C film.

3 Results and Discussion

3.1 Synthesis and compositions

Transparent, phenyl-modified mesoporous hybrid silica materials have been prepared via the acid-catalyzed hydrolysis and co-condensation of TMOS with PhTMS in the presence of fructose as the nonsurfactant template followed by water extraction under ambient condition. The

compositions of phenyl-modified silica materials (as represented by the fructose concentrations in the as-synthesized materials) prepared via the nonsurfactant-templated sol-gel reactions and the pore parameters of the porous matrix upon water extraction are summarized in Tables 1 and 2. The fructose contents calculated from the initial feed stoichiometry (Table 1, with PhTMS fixed at 5 mol%) are comparable to those experimentally found from TGA measurements. There are some discrepancies between the calculated and experimentally determined values. Such discrepancies could be attributed to incomplete hydrolysis of TMOS/PhTMS and/or incomplete removal of the volatile solvents and by-products (e.g. water and methanol) that were tightly bound to the silica matrix, particularly in the cases when the fructose template was absent (HIIIF0-5) or at low concentrations. As the fructose content increases, the discrepancy becomes smaller and negligible.

Gelation time is the time interval between the initial mixing of the reactants and the occurrence of gel formation (i.e., the system loses its fluidity). Shorter gelation time is indicative of higher rate of the sol-gel reactions. As listed in Table 2, the gelation time for the TMOS and PhTMS binary system was much longer than that of the pure TMOS system under otherwise identical conditions. There is a general trend that the gelation time increases with the molar proportion of PhTMS in the initial feed and decreases as the fructose concentration is increased. This further confirms that the sugar molecules can facilitate or catalyze the sol-gel reactions as were previously observed in our laboratory [32,35]. These observations suggest that the hydrogen bonding between the fructose molecules or aggregates and intermediate silicate species promotes the sol-gel reactions, while the presence of phenyl groups hinders the co-condensation of PhTMS owing probably to the steric hindrance, lowered hydrophilicity and fewer surface silanol groups on phenyl-modified silica matrix. It seems that there is an upper limit for the amount of PhTMS, which could be incorporated into the silica matrix. In our case, as the amount of PhTMS was greater than 20 mol% in the initial mixture of precursors, macroscopic phase separation occurred as evidenced by the formation of translucent and opaque gels. It is clear that the hydrophobicity of the matrix has been appreciably modified.

Table 1. Pore Parameters of Water-Extracted PhTMS Hybrid Materials Prepared at Various Fructose Concentrations.

Sample ID ^a	D-fructose (wt%)		$S_{\text{BET}}^{\text{d}}$ (m^2g^{-1})	V_{SP}^{e} (cm^3g^{-1})	$D_{\text{BET}}^{\text{f}}$ (Å)	Micropore ^g	
	Calc ^b	Found ^c				Vol. (cm^3g^{-1})	Area (m^2g^{-1})
F50	50	51	915	0.6	35	--	--
HIIF0-5	0	11	114	0.077	--	0.042	76
HIIF33-5	33	37	544	0.305	22	0.222	402
HIIF38-5	38	43	666	0.370	22	0.205	366
HIIF46-5	46	48	756	0.418	23	0.110	193
HIIF52-5	52	54	878	0.601	27	--	--
HIIF60-5	60	67	808	0.638	34	--	--

^a PhTMS content in the initial precursors was fixed at 5 mol%. ^b Theoretical value from the feed composition of the reaction mixture. ^c Values from the weight loss of the sample, which represent total contents of volatile compounds. ^d The BET surface area using the Kelvin equation in the relative pressure (P/P_0) of 0.10-0.30. ^e The single point pore volume determined at $P/P_0 \approx 1$. ^f The BET pore diameter calculated from $4V/S$. ^g Determined by the t -plot method.

Table 2. Pore Parameters of Fructose-Templated, Water-Extracted Hybrid Sol-Gel Materials with Various Contents (mol%) of PhTMS in the Feed.

Sample ID ^a	PhTMS Content (mol%)	$S_{\text{BET}}^{\text{b}}$ (m^2g^{-1})	V_{SP}^{c} (cm^3g^{-1})	Micropore ^d		Gelation time (hrs)
				Vol. (cm^3g^{-1})	Area (m^2g^{-1})	
HIIF50-0	0	915	0.596	--	--	10
HIIF50-5	5	882	0.506	--	--	15
HIIF50-10	10	829	0.494	0.052	93	26
HIIF50-20	20	669	0.412	0.092	162	48
HIIF50-25	25	424	0.261	0.126	225	66

^a The content of fructose was fixed at 50 wt%. ^b The BET surface area using the Kelvin equation at the relative pressure (P/P_0) range of 0.10-0.30. ^c The single point pore volume determined at $P/P_0 \approx 1$. ^d Determined by the t -plot method.

3.2 Infrared spectroscopy

Fig. 1 shows a typical set of infrared spectra of the phenyl-modified hybrid materials with different molar ratios of PhTMS (varied between 5 to 25 mol%) in the initial feeds of precursors. Before the IR measurement, all the samples were extracted with water to remove the fructose and then dried at 100 °C in an oven overnight. The spectra show the major absorption bands associated with network Si-O-Si vibrational modes at 460, 790, 1080 and 1220 cm^{-1} , along with Si-OH asymmetrical stretching at $\sim 960 \text{ cm}^{-1}$. The absorptions associated with the vibration of phenyl ring C-H and out-of-plane bending of C-H bonds are clearly identifiable at 1430, 699 and 740 cm^{-1} . As anticipated, the intensities of these bands increase proportionally as the molar concentration of PhTMS in the initial feed of precursors is increased. These observations suggest qualitatively that the phenyl groups have been successfully incorporated into the silicate network via the non-hydrolyzable Si-C covalent bond. The appearance of an additional shoulder at $\sim 1140 \text{ cm}^{-1}$ in the Si-O-Si stretching region (1000-1200 cm^{-1}) indicates the presence of Si-C bonds [39,40].

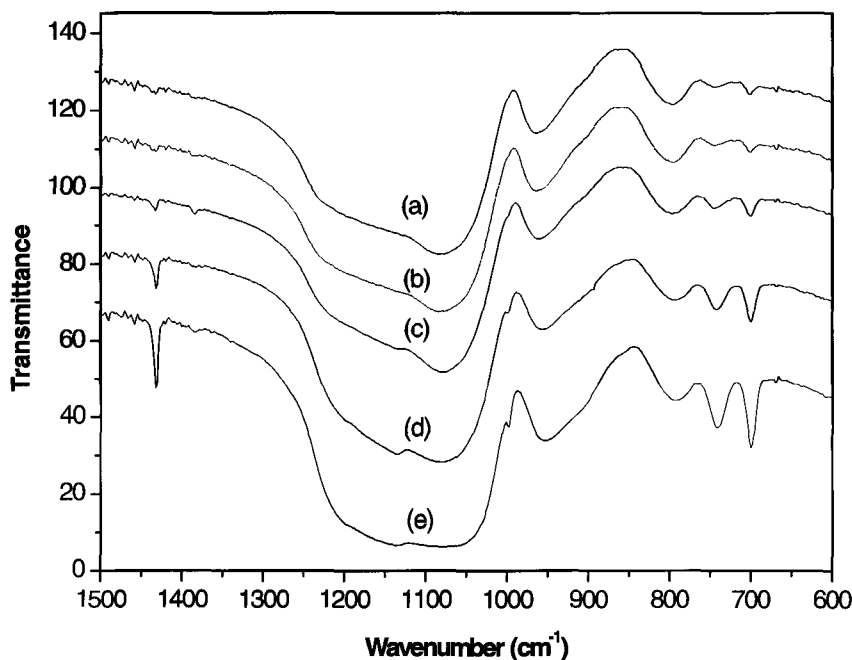


Figure 1. FT-IR of water-extracted phenyl-modified hybrid materials prepared using 50 wt% of fructose and (a) 0, (b) 5, (c) 10, (d) 20, and (e) 25 mol% of PhTMS in the initial precursor feeds.

3.3 Nitrogen adsorption-desorption isotherms

The silica materials derived from TMOS or TEOS in the presence of 50 wt% of fructose was mesoporous with surface area of $915 \text{ m}^2\text{g}^{-1}$, pore volume of $0.6 \text{ cm}^3\text{g}^{-1}$ and average pore diameter of $\sim 35 \text{ \AA}$ (control sample, F50 in Table 2). The modification of the silica matrix by incorporating phenyl groups into the sol-gel matrixes resulted in a significant decrease in the surface area (e.g., to $424 \text{ m}^2\text{g}^{-1}$) and pore volume (e.g., to $0.26 \text{ cm}^3\text{g}^{-1}$). This is in agreement with the observed trends for introducing organic groups to inorganic matrices as reported in the literature [20].

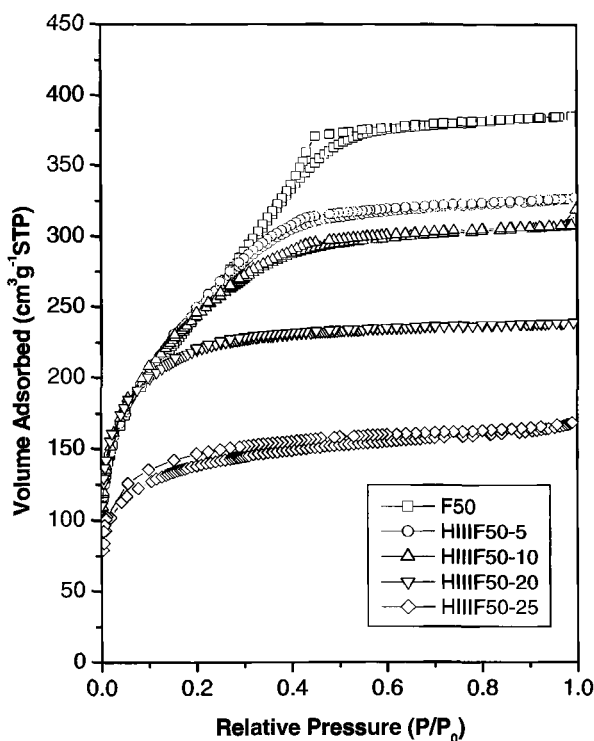


Figure 2. N_2 adsorption-desorption isotherms for water-extracted phenyl-modified hybrid materials with various molar concentrations (i.e., 0, 5, 10, 20 and 25 mol%) of PhTMS at a fixed fructose content of 50 wt%.

Fig. 2 shows the N_2 adsorption-desorption isotherms for the sample series synthesized with varied molar content of PhTMS and fixed fructose concentration of 50 wt%. As the PhTMS content decreases, the mesoporous characteristics of the materials become more noticeable. This

is characterized by the likeness to the type IV isotherms with H2 hysteresis, which is an indicative of the capillary condensation occurring in the mesopores [41]. Pore size distributions obtained from the BJH model [42] (Figure 3) indicate the hybrid silica made with <10 mol% PhTMS has a narrowly distributed pore size around 30 Å.

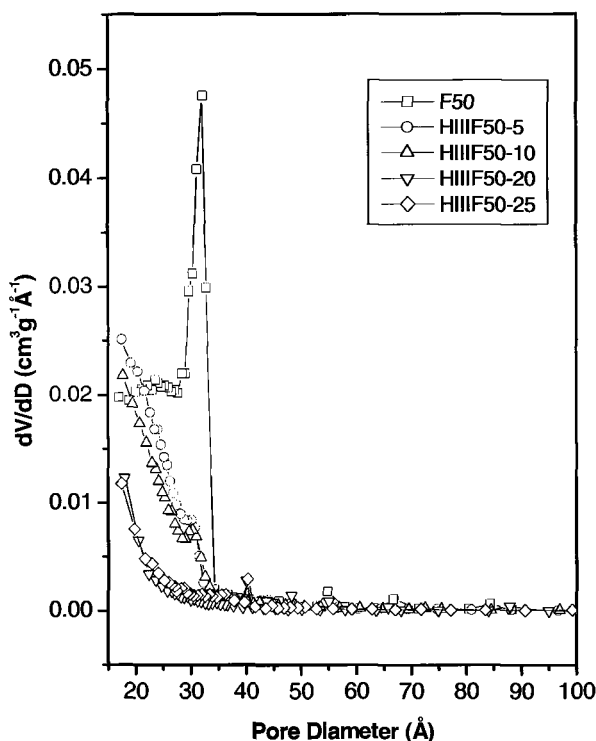


Figure 3. The BJH pore size distributions for water-extracted phenyl-modified hybrid materials with various molar concentrations (i.e., 0, 5, 10, 20 and 25 mol%) of PhTMS at a fixed fructose content of 50 wt%.

Figures 4 and 5 are the N_2 adsorption-desorption isotherms and BJH pore size distribution, respectively, of 5 mol%-PhTMS modified sol-gel materials with varied fructose concentrations. As the fructose concentration is increased, the N_2 adsorption-desorption isotherms transform gradually from reversible type I, typical for the microporous or nonporous materials (i.e. HIIIF0-5, HIIIF33-5, HIIIF38-5, HIIIF46-5), to the isotherms that resemble type IV with H2 hysteresis [41] which is typical for the mesoporous materials (i.e. HIIIF52-5, HIIIF60-5). The H2 hysteresis loop becomes greater in magnitude and shift to higher relative

pressure (P/P_0). There is also a well-defined plateau at a relative pressure $P/P_0 > 0.8$, suggesting the occurrence of pore filling by capillary condensation of nitrogen in the framework-confined mesopores instead of adsorption in the interparticle textural pores.

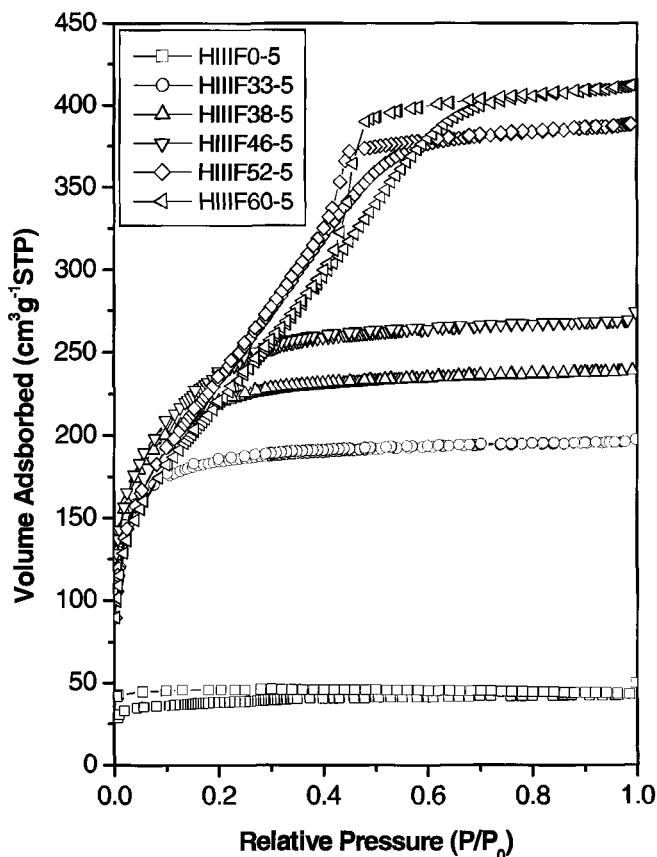


Figure 4. N_2 adsorption-desorption isotherms for water-extracted 5 mol%-phenyl-modified hybrid materials at various concentrations (i.e., 33, 38, 46, 52 and 60 wt%) of fructose template.

Compared with pure mesoporous silica materials prepared from TMOS at the same template content, the phenyl-modified silica materials showed a lower sorption capacities and smaller hysteresis loops. For example, at the fructose content of >50 wt% (sample HIIIF52-5), the material had large BET surface area of $\sim 800 \text{ m}^2 \text{ g}^{-1}$ and pore volume of $\sim 0.6 \text{ cm}^3 \text{ g}^{-1}$ with pore diameter of $\sim 30 \text{ \AA}$ (Table 2). These pore parameters, even though somewhat smaller than those of TMOS-derived pure silica counterpart, still suggest the mesoporosity of these hybrid materials.

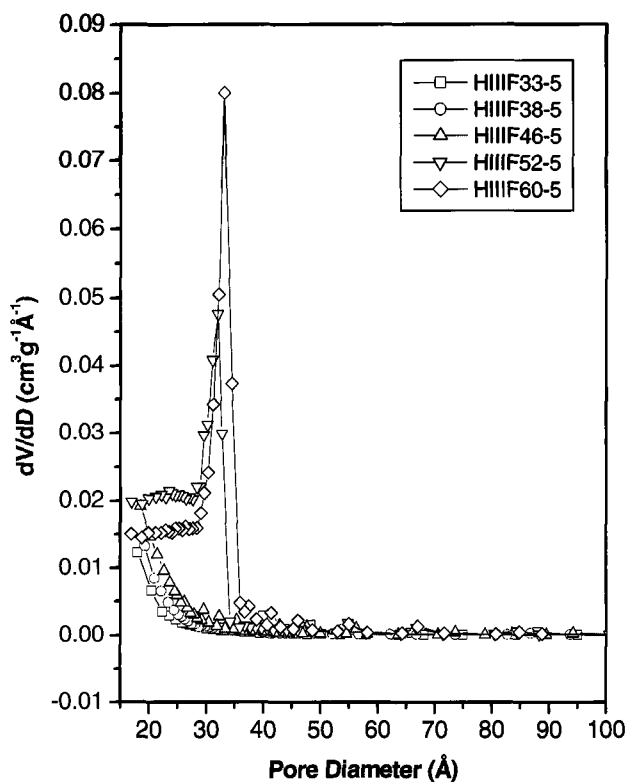


Figure 5. The BJH pore size distributions for water-extracted 5 mol%-phenyl-modified hybrid materials at various concentrations (i.e., 33, 38, 46, 52 and 60 wt%) of fructose template.

3.4 TEM and relationship between pore structural parameters and fructose concentration

A representative TEM image of the mesoporous hybrid silica samples is shown in Figure 6 for sample HIIIF52-5, prepared with 5 mol% PTMS in the feed and 52 wt% of fructose. There are numerous interconnected mesopores and channels, typical of the nonsurfactant templated silica materials [31-33] and similar to the wormhole-like channel motif in MSU-1 and other materials prepared via the neutral surfactant or block polymer pathway [43-45]. The pore or channel diameters are quite regular at about 30 Å, which is in reasonably agreement with the BJH pore diameter obtained from nitrogen adsorption-desorption measurements.

The pores or channels in the hybrid mesoporous materials after removing fructose template by solvent extraction come from the space previously occupied by the templating molecules. In the traditional surfactant templated ordered mesoporous system [10-13], the content of the surfactants does not have much effect on the final pore parameters. In contrast, in our nonsurfactant approach, the concentration of the template molecules seems to have a very significant effect on pore parameters. Analysis on the net pore volume and BET surface area, which are the differences between the water-extracted and as-synthesized 5 mol% phenyl-containing samples, reveals that both pore volume and surface area are linearly dependent on the fructose concentration with reasonably good correlation coefficients of $R^2=0.97$ and 0.98 (Figures 7 and 8), respectively. Hence, the observed total surface areas and pore volumes in the extracted materials are mainly contributed from the internal voids in the silica matrix previously occupied by the fructose molecules. These observations are consistent with our postulations that the template aggregates or assembly of aggregates, rather than the single molecule, may be responsible for the mesophase formation [31-33].

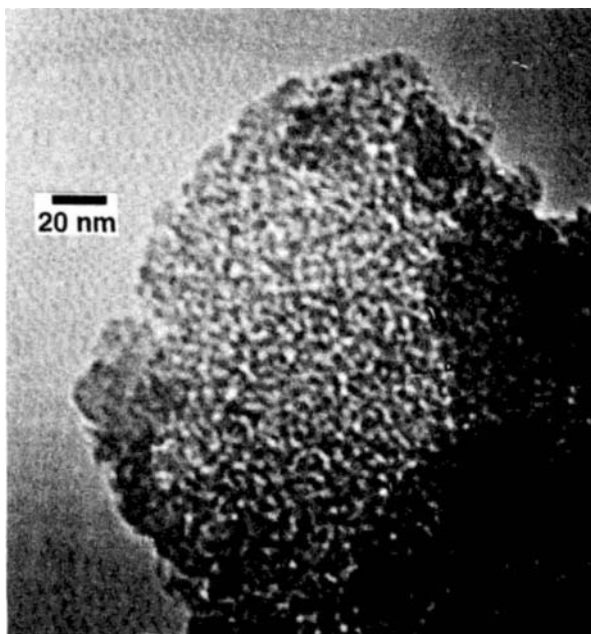


Figure 6. TEM image of water-extracted 5 mol%-phenyl-modified hybrid material in the presence of 52 wt % of fructose. The lighter features are mesopores as interconnected channels and the darker features are the phenyl-modified silica matrix.

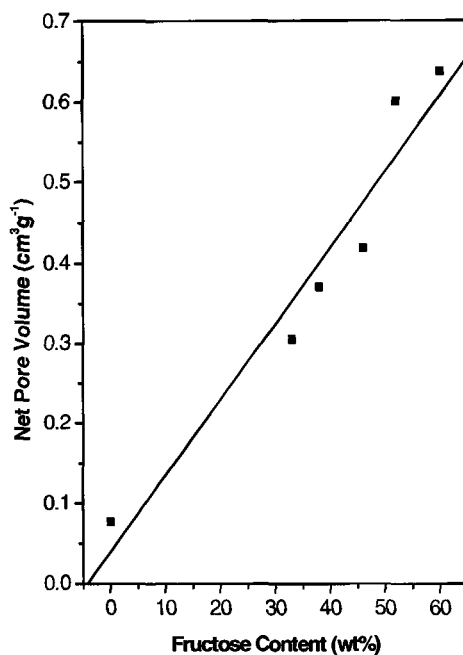


Figure 7. Correlation of the net pore volume of the 5 mol% phenyl-modified hybrid mesoporous silica materials and the content of the fructose content.

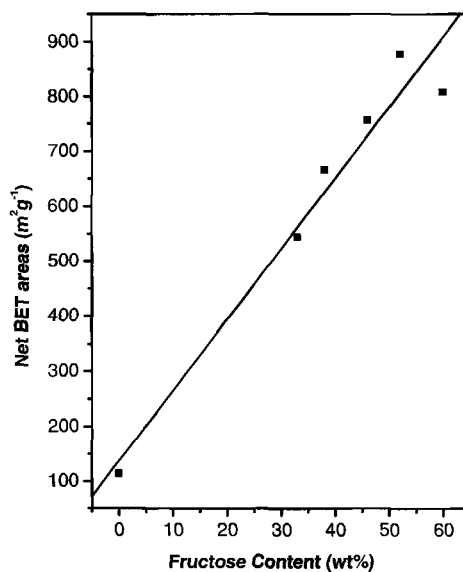


Figure 8. Correlation between the net BET surface areas and the fructose content for 5 mol% phenyl-containing (HIIIF-5) samples.

4 Conclusions

Transparent, phenyl-modified mesoporous silica materials have been synthesized via the acid-catalyzed sol-gel reactions of TMOS and PhTMS in the presence of fructose, a neutral nonsurfactant template. The template molecules can be removed by water extraction to afford mesoporous solid. Based on N_2 adsorption-desorption measurements, the hybrid materials synthesized from 5 mol% PhTMS and 95 mol% TMOS at 50 wt% fructose had BET surface area of $\sim 800 \text{ m}^2 \text{ g}^{-1}$, pore volume of $\sim 0.6 \text{ cm}^3 \text{ g}^{-1}$ and BJH pore diameter of around 3 nm with narrow pore size distribution. Up to 10 mol% of PhTMS in the initial feed of precursors, the hybrid gels before extraction were transparent. As the PhTMS content was increased, the surface area, pore size and volume of the hybrid materials decreased. FT-IR results of the as-synthesized and extracted samples confirmed the incorporation of phenyl groups into the silica matrix through non-hydrolyzable Si-C covalent bonds. TEM image of the materials showed numerous interconnected mesopores and channels, typical of the nonsurfactant templated silica materials and similar to the wormlike channel motif in MSU-1 and other materials prepared via a neutral surfactant or block polymer pathway. The existence of phenyl groups increases the surface hydrophobicity and modifies the internal microstructures of the silica matrix.

5 Acknowledgements

This work was supported in part by the National Institutes of Health (No. DE09848), by the Nanotechnology Institute of Southeastern Pennsylvania, and by the National Natural Science Foundation of China (NSFC Nos. 29874002, 19810760343 and 29825504). Part of the results in this article was presented at the 219th American Chemical Society meeting in San Francisco, CA, March 26-30, 2000.

References

1. Brinker C. J., Sherer G. W., Sol-Gel Science. (Academic Press, San Diego, 1990).
2. Yan Y., Hoshino Y., Duan Z., Chaudhuri S. R., and Sarkar A., Design and characterization of interconnected, microporous hybrid thin films by a sol-gel process, *Chem. Mater.* **9** (1997) p. 2583.
3. Schubert U., Hüsing N., and Lorenz A., Hybrid inorganic-organic materials by sol-gel processing of organofunctional metal alkoxides, *Chem. Mater.* **7** (1995) p. 2010.

4. Husing N., Schwertfeger F., Tappert W., and Schubert U., Influence of supercritical drying fluid on structure and properties of organically modified silica aerogels, *J. Non-Cryst. Solids* **186** (1995) p. 37.
5. Wen J. and Wilkes G.L., Organic/inorganic hybrid network materials by the sol-gel approach, *Chem. Mater.* **8** (1996) p. 1667.
6. Liu C.L., Chen H.X., Komarneni S., and Pantano C. G., High surface area SiC/silicon oxycarbide glasses prepared from phenyltrimethoxysilane-tetramethoxysilane gels, *J. Porous Mater.* **2** (1996) p. 245.
7. Smiaili M., Jermoumi T., Marignan J., and Noble R. D., Organic-inorganic gas separation membranes: preparation and characterization, *J. Membrane Sci.* **116** (1996) p. 211.
8. Mark J.E., Lee C. Y.-C. and Bianconi P.A. (eds) Hybrid organic-inorganic composites, (*Am. Chem. Soc. Symp. Ser. 585*, ACS, DC, 1995).
9. Wei Y., Polymer-modified ceramics, In *Encyclopedia of Materials: Science and Technology*, ed by Buschow K.H.J., Cahn R.W., Flemings M.C., Hschner B., Kramer E.J. and Mahajan S. (Elsevier Science Ltd., Oxford, UK 2001) pp. 7594-7605.
10. Kresge C. T., Leonowicz M. E., Roth W. J., Vartuli J. C. and Beck J. S., Ordered mesoporous molecular sieves synthesized by a liquid-crystal template mechanism, *Nature* **359** (1992) pp. 710-12.
11. Beck J. S., Vartuli J. C., Roth W. J., Leonowicz M. E., Kresge C. T., Schmitt K. D., Chu C. T. W., Olson D. H. and Sheppard E. W., A new family of mesoporous molecular sieves prepared with liquid crystal templates, *J. Am. Chem. Soc.* **114** (1992) pp. 10834-43.
12. Ying J.Y., Mehnert C.P. and Wong M.S., Synthesis and applications of supramolecular-templated mesoporous materials, *Angew. Chem. Int. Ed.* **38** (1999) pp. 56-77.
13. Raman N.K., Anderson M.T. and Brinker C.J., Template-based approaches to the preparation of amorphous, nanoporous silicas, *Chem. Mater.* **8** (1996) pp. 1682-1701.
14. Carati A., Ferraris G., Guidotti M., Moretti G., Psaro R., and Rizzo C., Preparation and characterisation of mesoporous silica-alumina and silica-titania with a narrow pore size distribution, *Catalysis Today* **77** (2003) pp. 315-323.
15. Mercier L. and Pinnavaia T., Access in mesoporous materials. Advantages of a uniform pore structure in the design of a heavy metal ion adsorbent for environmental remediation, *Adv. Mater.* **9** (1997) p. 500.
16. Sutra P. and Brunel D., Preparation of MCM-41 type silica-bound manganese(III) Schiff-base complexes, *Chem. Commun.* (1996) p. 2485.
17. Moller K. and Bein T., Inclusion chemistry in periodic mesoporous hosts, *Chem. Mater.* **10** (1998) p. 2950.
18. Feng X., Fryxell G. E., Wang L. Q., Kim A. Y., Liu J., and Kemner K. M., Functionalized monolayers on ordered mesoporous supports, *Science* **276** (1997) p. 923.
19. Shepard D. S., Zhou W., Maschmeyer T., Matters J. M., Roper C. L., Parsons S., Johnson B. F. G., and Duer M. J., Site-directed surface derivatization of MCM-41: Use of high-resolution transmission electron microscopy and molecular recognition for determining the position of functionality within mesoporous Materials, *Angew. Chem., Int. Ed. Engl.* **37** (1998) p. 2719.

20. Burkett S.L., Sims S.D., and Mann S., Interfacial synthesis of hollow microspheres of mesostructured silica, *Chem. Commun.* (1996) p. 1367.
21. Macquarrie D. J., Direct preparation of organically modified MCM-type materials. Preparation and characterisation of aminopropyl-MCM and 2-cyanoethyl-MCM, *Chem. Commun.* (1996) p. 1961.
22. Huo Q. S., Margolese D. I., and Stucky G. D., Surfactant control of phases in the synthesis of mesoporous silica-based materials, *Chem. Mater.* **8** (1996) p. 1147.
23. Mann S., Burkett S.L., Davis S.A., Fowler C.E., Menselson N. H., Sims S.D., Walsh D., and Whilton N. T., Sol-gel synthesis of organized matter, *Chem. Mater.* **9** (1997) p. 2300.
24. Fowler C.E., Burkett S.L., and Mann S., Synthesis and characterization of ordered organo-silica-surfactant mesophases with functionalized MCM-41-type architecture, *Chem. Commun.* (1997) p. 1769.
25. Rhijn W. M., DeVos D. E., Sels B.F., Bossaert W.D., and Jacobs P.A., Sulfonic acid functionalised ordered mesoporous materials as catalysts for condensation and esterification reactions, *Chem. Commun.* (1998) p. 317.
26. Lim M. H., Branford C. F. and A. Stein, Synthesis and characterization of a reactive vinyl-functionalized MCM-41: Probing the internal pore structure by a bromination reaction, *J. Am. Chem. Soc.* **119** (1997) p. 4090.
27. Lim M. H., Branford C. F., and Stein A., Synthesis of ordered microporous silicates with organosulfur surface groups and their applications as solid acid catalysts, *Chem. Mater.* **10** (1998) p. 467.
28. Bamnrough C. M., Slade R. C., Williams R. T., Burkett S. L., Sims S. D., and Mann S., Sorption of nitrogen, water vapor, and benzene by a phenyl-modified MCM-41 sorbent, *J. Colloid Interface Sci.* **201** (1998) p. 220.
29. Melde B. J., Holland B. T., Branford C. F. and Stein A., Mesoporous sieves with unified hybrid inorganic/organic frameworks, *Chem. Mater.* **11** (1999) p. 3302.
30. Husing N. and Schubert U., Formation and structure of porous gel networks from $\text{Si}(\text{OMe})_4$ in the presence of $\text{A}(\text{CH}_2)_n\text{Si}(\text{OR})_3$ (A = functional group), *Chem. Mater.* **10** (1998) p. 3024.
31. Wei Y., Jin D., Ding T., Shih W.H., Liu Q., Cheng S.Z.D., and Fu Q., A novel templating route to mesoporous materials, *Adv. Mater.* **10** (1998) pp. 313-316.
32. Wei Y., Xu J., Dong H., Dong J.H., Qiu K.Y., and Jansen-Varnum S.A., Preparation and physisorption characterization of D-glucose-templated mesoporous silica materials via base-catalyzed sol-gel process, *Chem. Mater.* **11** (1999) pp. 2023-2029.
33. Wei Y., Feng Q.W., Xu J., Dong H., Li S., Qiu K.Y., Jansen S.A., Yin R., and Ong K.K., Polymethacrylate-silica hybrid mesoporous materials: a bridge between the inorganic and polymeric molecular sieves, *Adv. Mater.* **12** (2000) pp. 1448-1450.
34. Wei Y., Xu J., Feng Q.W., Dong H., and Lin M., Encapsulation of enzymes in mesoporous host materials via the nonsurfactant-templated sol-gel process, *Mater. Lett.* **44** (2000) pp. 6-11.
35. Wei Y., Xu J., Feng Q.W., Lin M., Dong H., Zhang W.J., and Wang C., A novel method for enzyme immobilization: direct encapsulation of acid phosphatase in nanoporous silica host materials, *J. Nanosci. Nanotech.* **1** (2001) pp. 83-94.
36. Wei Y., Dong H., Xu J., and Feng Q.W., Simultaneous immobilization of horseradish peroxidase and glucose oxidase in mesoporous sol-gel host materials, *Chem. Phys. Chem.* **3** (2002) pp. 803-808.

37. Wei Y., Sun Z.F., Zheng J.Y., Dong H., Yuan J.M. and Ping G., Rigid matrix artificial chaperone (RMAC)-mediated refolding of heme proteins, *Polym. Mater. Sci. Eng.* **87** (2002) pp. 252-253.
38. Ping G., Yuan J. M., Vallieres M., Sun Z., Dong H., Wei Y., Li F. Y., and Lin S. H., Effects of confinement on protein folding and protein stability, *J. Chem. Phys.* **118** (2003) pp. 8042-8048.
39. Cappozzi C. A., Pye L. D. and Condrate Sr. R. A., Vibrational spectral/structural changes from the hydrolysis/polycondensation of methyl-modified silicates. I. Comparisons for single monomer condensates, *Mater. Lett.* **15** (1992) p. 130.
40. Cappozzi C. A., Condrate Sr. R. A., Pye L. D. and Hapanowicz R. P., Vibrational spectral/structural changes from the hydrolysis/polycondensation of methyl-modified silicates. II. Comparisons for condensates from the binary diethoxydimethylsilane/tetramethoxysilane system, *Mater. Lett.* **15** (1992) p. 233.
41. Gregg S. J., Sing K. S., Adsorption, Surface Area and Porosity, 2nd Edition, (Academic Press Inc., San Diego, 1982).
42. Barrett E. P., Joyner L. and Halenda P. P., The determination of pore volume and area distributions in porous substances. i. computations from nitrogen isotherms, *J. Am. Chem. Soc.* **73** (1951) p. 373.
43. Bagshaw S. A., Prouzet E., and Pinnavaia T. J., Templating of mesoporous molecular sieves by nonionic polyethylene oxide surfactants, *Science* **269** (1995) p. 1242.
44. Walsh D., Hopwood J. D., Mann S., Crystal tectonics: Construction of reticulated calcium phosphate frameworks in bicontinuous reverse microemulsions, *Science* **264** (1994) p. 1576.
45. Chan V. Z.-H., Hoffman J., Lee V.Y., Latrou H., Avgeropoulos A., Hadjichristidis N., Miller R.D., and Thomas E.L. Ordered bicontinuous nanoporous and nanorelief ceramic films from self assembling polymer precursors, *Science* **286** (1999) pp. 1716-1719.

3D MACROPOROUS PHOTONIC MATERIALS TEMPLATED BY SELF ASSEMBLED COLLOIDAL SPHERES

Z. C. ZHOU AND X. S. ZHAO*

*Department of Chemical and Environmental Engineering, National University of
Singapore, 10 Kent Ridge Crescent, Singapore 119260*

E-mail: chezxs@nus.edu.sg

Macroporous materials with three-dimensional (3D) ordered structure are a family of porous materials over which photonic bandgap (PBG) could be observed. They provide a foundation for the development of novel optical devices and integration of such devices into a microchip. In the past few years, one-dimensional (1D) and two-dimensional (2D) PBG materials have been successfully fabricated by using the conventional “top-down” techniques such as lithography. Optical devices based on 1D and 2D PBG materials are now available. However, fabrication of 3D PBG materials has been a great challenge because traditional lithography method has trouble making thick 3D structures. By contrast, self-assembly approach, a “bottom-up” method, has been explored and demonstrated a simple and inexpensive route to make 3D PBG materials. During the past decade, tremendous research effort has been made at self-assembly of colloidal crystals and the use of the crystals as a template to replicate 3D macroporous networks. This chapter provides a brief overview on the self assembly approaches to 3D macroporous materials. It focuses on the aspect of materials fabrication and photonic applications.

1 Introduction

Just as research in semiconductors led to a revolution in the electronic industry, a new family of periodically structured materials known as photonic bandgap (PBG) materials promise a similar revolution in photonics – where photons instead of electrons are the fundamental carriers and processors for information [1-12].

Photonic crystals are non-light-absorbing structures with a spatial periodicity on an optical-length scale. If a PBG exists in the materials, they are called PBG materials. When their periodicity expands to three dimensions, the structure can form a complete PBG, in which a range of frequencies or energy cannot propagate in any direction. With this property, 3D PBG materials allow one to inhibit unwanted spontaneous emission and manipulate the flow of electromagnetic (EM) waves. Thus, these materials would result in a revolutionary technology in the photonic era. Photonic devices, from high-speed optical switches to low-power microlasers, from light-emitting diodes to optical transistors, would be

useful ingredients in all-optical communications and high-speed computations.

In the past few years, breakthroughs have been made in the fabrication of one-dimensional (1D) and two-dimensional (2D) PBG materials because they are relatively easy to fabricate using the conventional “top-down” techniques such as lithography. For example, 1D photonic distributed Bragg reflectors have been used in building optical and near-infrared (IR) photonic devices [13,14]. Although 2D PBG materials require somewhat more fabrication, relatively mature conventional techniques can be employed to achieve such structures, and there are several examples of 2D PBG devices operating at mid- and near-IR wavelengths [15,16]. However, conventional lithography technique has trouble making thick 3D PBG materials. By contrast, self-assembly approach, a “bottom-up” method, has recently been explored and demonstrated as a simple and inexpensive route to make 3D photonic crystals [1-12, 17-41].

Self-assembly describes a spontaneous process by which colloidal spheres organize into ordered arrays. Such arrays, the so-called artificial opal, can be used as a template to structurally direct the creation of 3D photonic crystals, namely inverse opal. By infiltration of the voids in the artificial opal with a material of high refractive index such as silicon, followed by removal of the template, the inverse opal is created. The formation of the template is of importance in terms of the photonic properties of the final products. Sedimentation, evaporation, electrophoresis, etc. are the common methods for self-assembly of colloidal microspheres. Liquid infilling, chemical vapor deposition (CVD), and electrodeposition, etc. represent the frequently used techniques for infiltration. The inverse opal can be metals, metal oxides, semiconductors, polymers, carbons, organic-inorganic composites, etc.

This chapter provides an overview of self assembly approaches to 3D photonic crystals.

2 A survey of photonic bandgap

Yablonovitch [42a] first theoretically predicted the existence of the forbidden gap for EW waves in crystals and suggested the spherical air imbedded face-centered-cubic (fcc) structure with large enough refractive indexes could have the best effect [42b]. This structure is similar to an atomic fcc crystalline structure except for a scale of about a thousand times larger. At the same time, John [43] reported that a strong Anderson localization of photons exists in a carefully prepared disordered dielectric

superlattice. In addition, the author hypothesized that bandgaps for photons can form in the superlattice in 3D.

These two pioneer theoretical works resulted in the foundation of PBG materials. The EM waves traveling in these periodic dielectric structures are analogous to electronic waves in atomic crystals. By controlling the spatial periodicity of dielectric constant of the PBG materials, the propagation of the EM waves of a given wavelength along a certain direction can be stopped. When this termination is wide enough and overlaps for both polarization states along all crystal directions, the material possesses a complete PBG. This unique property provides the possibility of controlling the flow of photons as precisely as that semiconductors control electrons. In comparison to electrons, photons have a number of advantages in terms of information processing and transport [42b]: (1) the dispersion of electrons is parabolic while photons are linear; (2) the interaction between photons can be neglected; (3) photons have a larger angular momentum with a vector-wave character. With these advantages, the PBG materials can be tailored to achieve many functions such as inhibiting the spontaneous emission, directing the propagation of the photons, and localizing photons in a specific area at a restricted frequency. Thus, it is not surprising that a great deal of research interest has been directed towards PBG materials [1-12].

To explicitly elucidate how a PBG forms in a PBG material is a tired work because there are so many factors that have to be taken into account. In addition, complex mathematics simulation has to be used. In the work of Joannopoulos's group, they illustrate the formation of the photonic bandgap clearly using the simplest structure model, 1D photonic crystal [45], as shown in Fig. 1(a). This 1D photonic crystal is a multilayer film with alternating layer of different dielectric constants. Each layer has the same thickness and the difference of dielectric constants is only periodic in z direction. Fig. 1(b) is the band structure of on-axis propagation of EM wave. The dark region between band $n = 1$ and $n = 2$ is the photonic bandgap. It is known that the speed of light propagation depends on the refractive index of its traveling medium and the wave frequency:

$$\omega(k) = ck/(\epsilon)^{1/2} \quad (1)$$

where $\omega(k)$ is the frequency, c is the speed of light, k is a wave vector, and ϵ is the dielectric constant of the medium. Thus, a sharp change of the refractive index will cause a discontinuation of the band structure. The larger the difference of the refractive index contrast is, the wider the bandgap is.

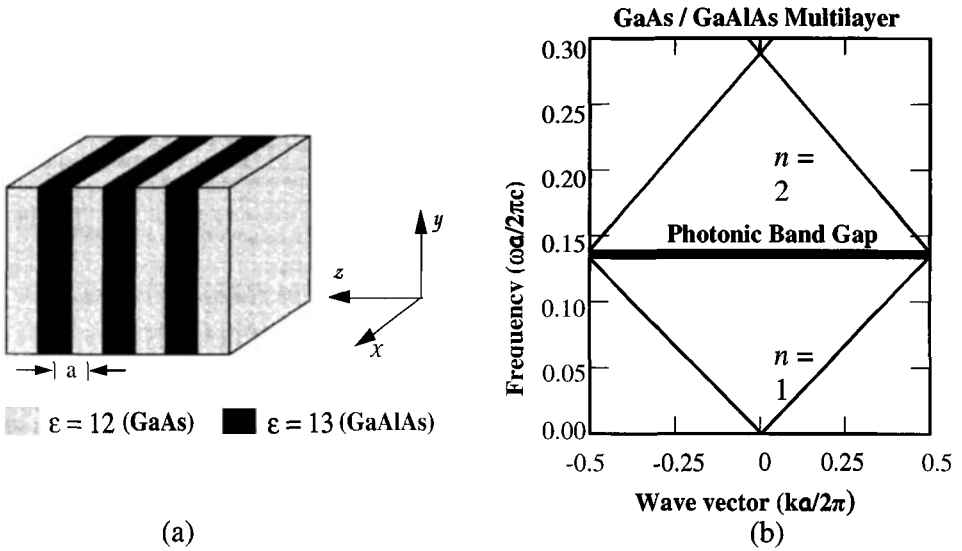


Figure 1. (a) Structural model of 1D photonic crystal, and (b) the bandgap formed in the structure, where the dark region is the bandgap [45].

Because the fcc structure is the most common atomic crystal, the early theoretical works mainly focused on fcc lattices of dielectric microspheres embedded in a uniform host medium. Various computation methods [46] have been used to investigate the band structures. Having conducted a broad experimental survey, Yablonovitch and co-workers [44b] claimed that a full bandgap in the fcc structure between the second and the third bands was observed. In addition, the bandgap structure, the optimal volume-filling fraction of spheres and the minimum refractive index constant ratio were obtained.

During the course of studying the formation of photonic bandgap, there have been many disputations. The reality and existence of bandgap in the fcc lattices of microsphere arrays were firstly questioned by a couple of research groups [47-49]. As criticized, the earlier theoretical calculations were solely based upon scalar-wave approximation whereas the vector nature of EM wave was ignored. When the vector character is taken into account, photonic bandgap extending throughout the whole Brillouin zone can not be observed because of the presence of a symmetry-induced degeneracy at the *W* point between the second and the third bands and a crossing of band lines at the *U* point [48,49].

Ho *et al.*[49] reported a remedy solution to solve the symmetry problem by using a diamond structure model. The authors observed that when high dielectric-constant spheres were arranged into a diamond

structure, a full photonic bandgap between the second and the third bands was observed. A subsequent study [50] confirmed the conclusion of Ho and co-workers, where Li *et al.* replaced the spherical building blocks with dimeric units that consisted of two interconnected dielectric spheres and obtained a complete bandgap.

In 1992, Sözüer and Haus [51] addressed the limitations of the plane-wave model and a Gaussian sphere model was proposed. A complete bandgap for air-sphere-embedded fcc structure between the 8th and 9th bands was observed, in agreement with the previous numerical studies [49,50]. The study of Busch and John [52] further confirmed work of Sözüer and Haus by using a plane wave expansion (PWE) method. Although the refractive index contrast had to be greater than 5.8 according to the Gaussian sphere model, the discovery attracted research attention back to the fcc structure.

Many computational simulation techniques employed for modeling electrons in solid-state semiconductors have been applied to investigate the properties of photons in PBG materials. These include plane-wave (PW) method [46c,46d], Korringa-Kohn-Rostoker (KKR) method [46a], augmented-plane-wave (APW) method [46b], and PWE method [46c]. Different from electrons in solids that have strong interactions, photons do not affect each other. Thus, these computational works can provide a very precise description and prediction of the behaviors of photons in PBG materials, offering a useful and complementary tool to experimental observations. Among these techniques, PWE method is the most commonly used one, which is briefed below.

In a PBG material the dielectric constant $\varepsilon(r)$ is position-dependent. Thus the propagation of EM waves in the material can be expressed using the Maxwell equations:

$$\begin{aligned} \nabla \cdot \mathbf{H}(r,t) &= 0 & \nabla \times \mathbf{E}(r,t) + \frac{1}{c} \frac{\partial \mathbf{H}(r,t)}{\partial t} &= 0 \\ \nabla \cdot \varepsilon(r) \mathbf{E}(r,t) &= 0 & \nabla \times \mathbf{H}(r,t) - \frac{\varepsilon(r)}{c} \frac{\partial \mathbf{E}(r,t)}{\partial t} &= 0 \end{aligned} \quad (2)$$

where H and E are the electric and magnetic fields, respectively.

By expanding the fields into a set of harmonic modes with a complex exponential, Eq. (2) can be solved as

$$\begin{aligned} \mathbf{H}(r,t) &= \mathbf{H}(r)e^{i\alpha x} \\ \mathbf{E}(r,t) &= \mathbf{E}(r)e^{i\alpha x} \end{aligned} \quad (3)$$

Further simplification can be made with Maxwell equations

$$\nabla \cdot \mathbf{H}(r) = \nabla \cdot \mathbf{D}(r) = 0 \quad (4)$$

to obtain:

$$\begin{aligned}\nabla \times E(r) + \frac{i\omega}{c} H(r) &= 0 \\ \nabla \times H(r) - \frac{i\omega}{c} \epsilon(r) E(r) &= 0\end{aligned}\quad (5)$$

Eqs. (5) are very important because they establish the relationship between $E(r)$ and $H(r)$. Solving these two equations by eliminating $E(r)$ to obtain an equation entirely in $H(r)$:

$$\nabla \times \left[\frac{1}{\epsilon(r)} \nabla \times H(r) \right] = \left[\frac{\omega}{c} \right] H(r) \quad (6)$$

This is the master equation. By solving it one can obtain the allowed mode frequencies for a given crystal structure and the wave vector k associated with the mode, which means one can determine the band structure.

3 Nanolithography for photonic crystals

To experimentally testify the above theories, many conventional lithography techniques have been applied to make 3D periodic structures, among which cutting and drilling were the early methods being used. Yablonovitch and Gmitter [42b] machined dozens of fcc structures out of low-loss dielectric materials. These crystals were different in filling fraction and refractive index contrast. The authors claimed that they opened bandgap in air spheres embedding fcc structures. However, most of these structures fabricated by using the micromachining techniques can only form bandgaps at the microwave, millimeter and submicron wave scales. In application, PBG materials should be used in a wide range of wavelength scales such as infrared and a much small lattice constant is required [16b]. As a result, nanolithography has not been successful in making PBG materials with a PBG at the visible wavelength scale. In addition, nanolithography approaches are very painstaking and expensive, having troubles in fabrication of thick 3D structures.

By contrast, self-assembly approaches have recently been explored and demonstrated as a simple and inexpensive route to make 3D photonic crystals. Self-assembly happens in nature, e.g. gemstone opal [56]. Artificial colloids have been well documented in the literature [57]. By controlling the colloid properties such as crystalline lattice and dielectric contrast, the colloidal particles can be fabricated to produce PBG. Unfortunately, a complete PBG has not yet been observed from these structures. However, by employing colloidal crystals as a template, an inverse opal structure has emerged that has potential to open a complete PBG between the 8th and 9th bands [51].

4 Self-assembly approaches to 3D photonic crystals

During the past few years, many research groups have been able to fabricate 3D photonic crystals using self-assembly approaches and various structures with different compositions have been obtained (see Table 1).

Table 1. Fabrication techniques for 3D photonic crystals from various self-assembly approaches.

Template	Self assembly	Framework material	Infiltration method	Ref.
Silica spheres	Evaporation	Si	CVD	17
	Sedimentation	Si /Ge	CVD	18
	Electrophoretic sedimentation	Ge	Soaking	19
	Sedimentation	Se	Soaking	20
	Evaporation	Au	Soaking	21
	Sedimentation	CdSe	Soaking	22
	Sedimentation	TiO ₂	Soaking	23
	Filtration	Polymer	Soaking	24
	Evaporation	Polymer	Soaking	25
	Sedimentation	Polymer	Soaking	26, 27
PS or PMMA spheres	Evaporation	Fe ₃ O ₄	Evaporation	28
	Evaporation	TiO ₂ /SiO ₂	Mixing	29,30
	Centrifugation/ sedimentation	TiO ₂	Soaking	31
	Centrifugation/ sedimentation	TiO ₂ , V ₂ O ₅ , etc.	Soaking	31
	Centrifugation	TiO ₂ , Si, etc	Filtration	33
	Filtration	Au/ SiO ₂	Filtration	34
	Evaporation	Au	Mixing	35
	Sedimentation	CdSe	Electro deposition	36
	Evaporation	BaTiO ₃	Filtration	37
	Filtration	Zeolites	Filtration	38
	Sedimentation	Conducting polymer	Electro deposition	39,40
Emulsion droplets	Centrifugation/ sedimentation	TiO ₂	Mixing	41

Schematically illustrated in Fig. 2 are the self assembly approaches to photonic crystals. Colloidal spheres spontaneously organize themselves into 3D arrays, namely artificial opal. The opal is then annealed to form necks connecting the adjacent spheres [58]. The annealed opal serves as a template containing voids that can be infiltrated by a material of high refractive index. Removal of the template leaves behind an inverse opal. From self-assembly approaches, a number of 3D structures consisting of various materials such as semiconductors [17-20,22], metals [21,32-35], metal oxide [23,28-34], polymers [24-27] etc. have been fabricated and the presence of PBGs in the structures has been observed. An excellent example is the work of Norris et al. [17], where Si photonic crystals were fabricated by using the self-assembly method and the optical properties of the Si materials were measured. A complete bandgap between the 8th and 9th bands in the wavelength region of about 1.3 μm was observed (Fig. 3).

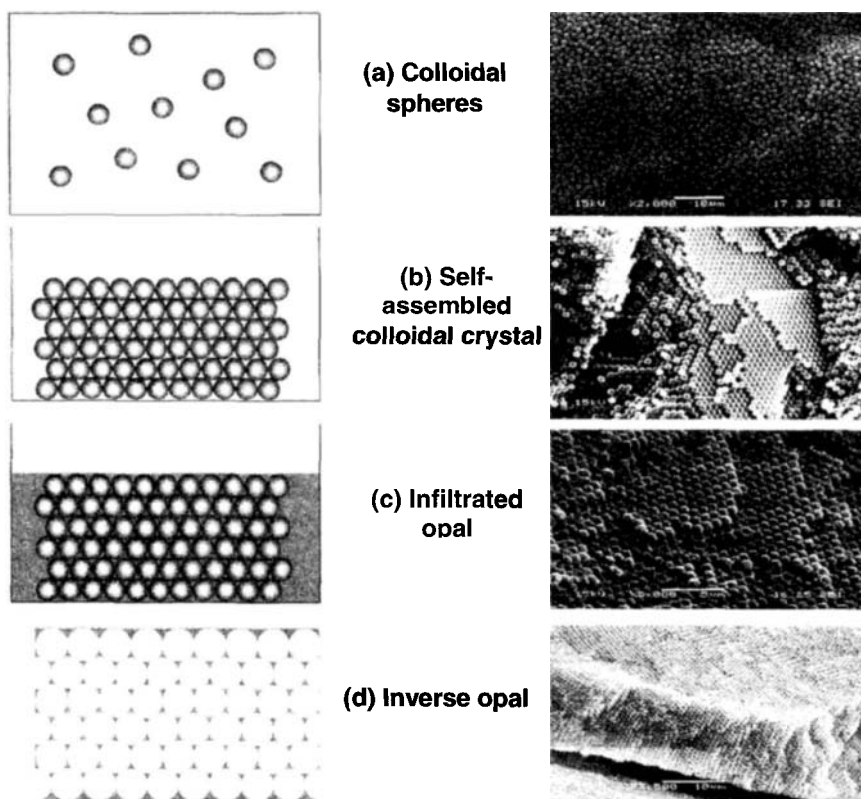


Figure 2. Schematic representation of self-assembly approaches to 3D photonic crystals, together with SEM images of representative experimental results of each step.

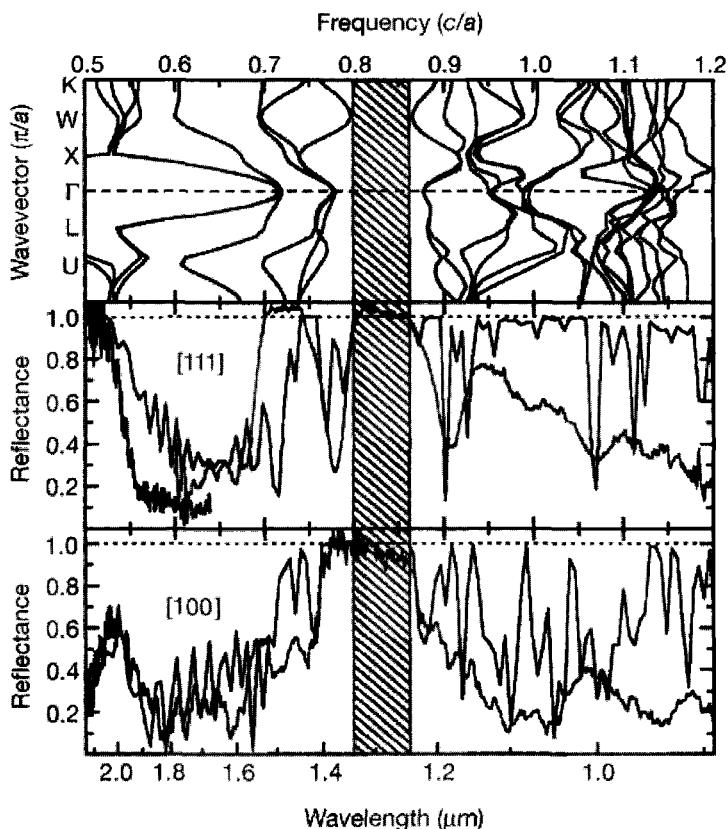


Figure 3. Middle and bottom image: Experimental reflection spectra for Si inverted opals measured normal to the (111) and (100) plane separately. Top image: the photonic band diagram calculated from experimental data [17].

4.1 Colloidal microspheres and artificial opals

Colloidal microspheres of uniform size with various surface properties are commercially available [5]. Polystyrene (PS) latex and silica colloids are the most frequently used spheres, which can be synthesized in laboratory [59, 60].

Silica spheres can disperse in water or ethanol steadily and be easily etched by hydrofluoric acid solution. As a result, they have been widely used as a template. The synthesis of silica spheres has been well described [60, 61]. The pioneering work of Stöber and co-workers [60] has been demonstrated to be the simplest and most effective method. By adjusting synthesis parameters, spherical silica colloids with a wide range of size can be synthesized [60-63].

Colloidal polymer latexes are another family of template having been widely used. The convenience of using polymer spheres is that they can be removed from infiltrated opals by heat or solvent treatment. The synthesis of polymer spheres has been studied thoroughly and many techniques have been developed, such as emulsion polymerization, dispersion polymerization and suspension polymerization [64, 65]. With these methods mono-disperse polymer spheres with diameter from nanometer to micrometer are obtainable. Styrene (PS) and methyl methacrylate (PMMA) is the mainly used monomer and their spheres are often synthesized by the emulsion polymerization method.

Recently core-shell composite spheres have attracted a great deal of interest. For example, Tissot *et al.* [66] functionalized PS spheres with 3-(trimethoxysilyl)-propyl methacrylate, followed by hydrolysis of TEOS on the surface of the spheres to obtain silica-coated PS spheres. The core-shell composites have been shown to offer an interesting avenue to make 3D photonic crystals with tunable optical properties [67,68].

Many methods have been developed to induce the formation of artificial opal (see Table 1). Irrespective of the methods, preparation of a suitable suspension of colloidal particles is a prerequisite. The suspension must meet the following requirements: (1) stability; (2) mono-distribution of the colloids without any aggregates, and (3) an easily removable solvent. Stability of the suspension is of importance, especially when evaporation and sedimentation techniques are used for self-assembly because the suspension is generally left alone for days to months. Mono-dispersion of the colloids ensures the opal structure to be highly ordered without the presence of defects. Previous studies [23,32b] have showed that polydispersity could destroy the ordered structure eventually. A removable solvent allows one to readily obtain an artificial opal.

4.2 Fabrication of artificial opals

Through self-assembly, colloidal microspheres can spontaneously arrange themselves into an ordered array, namely artificial opal. The properties of the artificial opal have a drastic impact on the photonic properties of the inverse opal. Li *et al.* [69] studied the effect of disorder in PBG materials on the optical properties. It was concluded that the bandgap is highly sensitive to the geometrical disorder. A disorder strength of even less than 2% of the lattice constant will destroy the bandgap completely. Thus, fabrication of defect-free artificial opal is a very challenging work. Nevertheless, the last few years have seen a number of simple and inexpensive routes that allow one to prepare the opal crystal.

4.2.1 Sedimentation method

Sedimentation is a self-assembly process during which colloidal microspheres dispersed in a solvent precipitate down to the bottom of a holding vessel to form closely packed structure due to gravitation and non-covalent interactions [70].

Thermodynamically, atoms or molecules tend to adopt the structure with the lowest Gibbs free energy. Self-assembly of spheres tends to form closely packed crystalline structures, such as fcc and hexagonal close packed (hcp) lattices. It has been demonstrated that the fcc structure has a slightly lower Gibbs free energy than the hcp structure with a difference of about $0.005 RT$ [71-73]. Because this difference is so small that the product of sedimentation is hardly a pure crystalline phase. However, careful control over particle sedimentation velocity can allow one to obtain a single crystalline phase. To control the sedimentation velocity, two methods can be applied. One is to use a proper solvent. Although both silica and polymer spheres can disperse in water, water is sometimes not a suitable solvent for sedimentation. For small particles, ethanol, which has a lower density and viscosity than water, has been found to be a good solvent. With large particles, a mixture of water and ethyl glycol is a good choice [11,18a]. The other method is to use electrophoretic deposition [74]. When colloidal particles in suspension are away from zero charge point, they will have a surface charge density. If they are placed in an electric field that parallels to the gravity, their deposition by sedimentation can be manipulated.

Although sedimentation is relatively simple and widely used, it is very time-consuming and delicate. The whole process can take weeks to months depending upon the size of spheres because sedimentation is a close-to-equilibrium process. In addition, any disturbance will result in the formation of a mixture of colloidal crystal phases or destroy the formation of a colloidal crystal.

The sedimentation method we have discussed above can only afford the formation of fcc opal with (111) plane parallel to the supporting substrate. How about those planes other than the (111) plane? This is a critical issue and has recently been addressed by patterning the surface of the substrate with ordered structure [72,75-78]. In these studies, the (100) plan of Si wafers was etched with square pyramidal pits, and then used it as a substrate for the fabrication of fcc opal. With this method, fcc structure with plane (100) parallel to substrate has been obtained [78].

4.2.2 Filtration

Another frequently used method for self-assembly of colloids is filtration (illustrate in Figure 4). By using extra forces, the assembly speed of colloids can be dramatically enhanced. For example, in Velve's group [34], a suspension of PS spheres (size ranging from 200 to 1000 nm) was filtered slowly through a smooth narrow-pore membrane. The particles accumulated on the membrane surface. The increased concentration led the suspension be apt to form crystal structures. The products were closely packed, ordered layers of thickness up to 10- μm . Apart from the advantage of high speed, the crystalline layers can be easily treated with different liquid media such as solution of nanoparticles. However it is hard to control the surface topology and the number of layers because flow pressure breaks equilibrium.

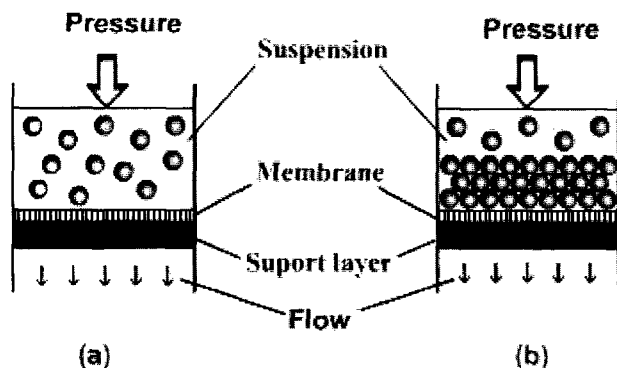


Figure 4. Schematic representation of filtration method for self-assembly

Xia *et al.* [24,79] designed a simple device to fabricate artificial opal. As schematically illustrated in Fig. 5, a photoresist frame was sandwiched into two glass plates to form a cell. A hole in the upper plate connecting with a tube and channels were opened at the bottom of the photoresist frame. During the experiments, suspension of colloidal spheres was injected in from the tube and nitrogen was filled in simultaneously. Because of the pressure of nitrogen, the flow (solvent) was forced to go through the channels. Thus the spheres within the flow accumulated at the bottom of the cell to assemble into a closed packed crystalline lattice. A pure fcc structure with large domain was created in 1-2 days. Most importantly, the number of the layers was controllable because it is solely determined by the distance between the two substrates and the diameter of the spheres.

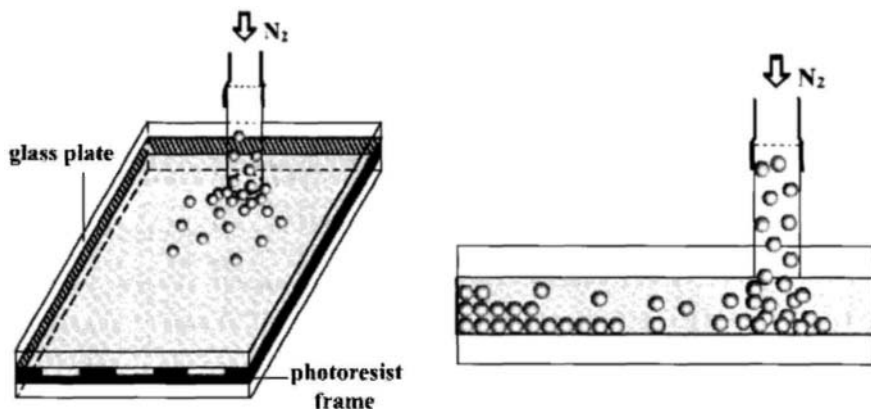


Figure 5. A scheme showing the device by designed by Xia's group [24]: (a) top view, (b) side view.

4.2.3 Solvent evaporation

It has long been noticed that colloidal particles can assemble into 2D ordered structures when the top of the particle protrudes into thin liquid films [80,81]. This observation has been further developed and has become the foundation of solvent evaporation method.

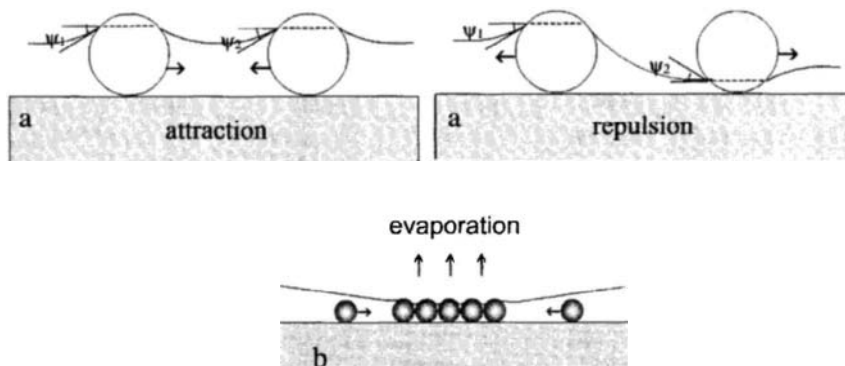


Figure 6. Schemes showing self-assembly of colloidal spheres into 2D order arrays: (a) the formation of capillary forces: $\sin\psi_1\sin\psi_2 > 0$, attractive forces; $\sin\psi_1\sin\psi_2 < 0$, repulsive forces [80], and (b) the mechanism of forming 2D arrays.

Evaporation-induced particle packing can be explained by surface tension and capillary forces. Two adjacent spherical particles of similar size may interact with each other when they are partially immersed in a liquid layer on a substrate. The liquid meniscus between the particles,

which is due to surface tension, plays a significant role. Because of the presence of the meniscus, strong capillary force is generated [80]. The immersion forces can be either attractive or repulsive (see Fig. 6a). It has been demonstrated by Kralchevsky *et al.* [82] that the type of immersion forces is determined by the meniscus slope angles ψ – when $\sin\psi_1\sin\psi_2 > 0$, the capillary force is attractive, and when $\sin\psi_1\sin\psi_2 < 0$, the capillary force is repulsive.

Many research groups have been able to use solvent evaporation method to organize colloidal microspheres into 2D hexagonal arrays [83,84]. In general, a suspension of colloid spheres is spread over the surface of a solid substrate and the solvent evaporates slowly under a controlled condition. When the thickness of solvent is equal to the diameter of the particle, a nucleus of 2D crystal forms. With progressing of evaporation, a thinner layer forms at the center of the solution, which drives more particles to flow to the nucleus by convective transport. Eventually self-organization around the nucleus occurs due to the attractive capillary forces (see Fig. 6b). Other forces may also be involved during the packing process. For example, polymer spheres that are copolymerized with styrene and methacrylic acid have carboxyl groups on surface [85]. Hydrogen bonding might play a role in self-assembly of the polymer spheres.

Dimitrov and Nagayama [86] studied the formation of 2D arrays on the surface of a vertical substrate by using Langmuir-Blodgett (LB) technique [87]. The substrate was firstly dipped into a suspension of monodisperse spheres, followed by withdrawal. Because the substrate is hydrophilic, a thin film of suspension formed on the surface. Evaporation of the solvent led to solvent flowing to compensate the area of the film, driving the colloids towards the film area. Simultaneously, the neighboring particles were attracted to each other due to lateral capillary immersion forces, which caused dense hexagonal packing. Because the crystal formed on the vertical placed substrate, the method also named as vertical deposition (VD) method.

Jiang *et al.* [25,87] and Gu *et al.* [30] further improved Nagayama's method. Instead of withdrawal, the substrate was put in a colloidal suspension. With the evaporation of the solvent, a meniscus between the vertically placed substrate and the colloidal sol swept slowly across the surface of the substrate. Strong capillary forces induced crystallization of spheres into ordered arrays on the substrate. Repeating the process and varying the concentration and the evaporation rate allowed the control of the number of the layers. Jiang *et al.* [25] also fabricated multiplayer 3D structures with spheres of different sizes. Unfortunately, the improvement

is only effective for small spherical particles with size less than $0.4\ \mu\text{m}$ because larger spheres deposit rapidly. For the self-assembly of larger spheres (say larger than $\sim 0.8\ \mu\text{m}$), other techniques have to be coupled with solvent evaporation method such as introduction of temperature gradient [17,88]. In addition, in VD method, the concentration of a colloidal suspension increases during the course of solvent evaporation, resulting in variable thickness of the resultant colloidal array over a large area because the number of layers of the array is dependent upon the concentration of the colloidal suspension.

A flow-controlled vertical deposition (FCVD) method has been developed in our laboratory [89], which can overcome the shortcomings of VD method. As schematically shown in Fig. 7, a peristaltic pump is used to control the flow rate of a colloidal suspension. Because a pump instead of solvent evaporation is used to control the decrease of the liquid level, concentration gradient of the suspension is substantially avoided. This method allows us to fabricate colloidal crystals of large spheres up to $1.5\ \mu\text{m}$ (Fig. 8).

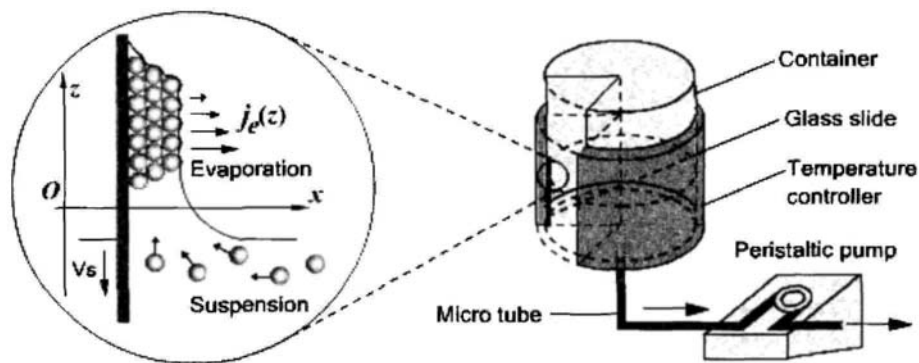


Figure 7. An illustration of the setup used in flow-controlled vertical deposition (FCVD) method. The surface dropping velocity of a colloidal suspension is controlled by a peristaltic pump instead of solvent evaporation [89].

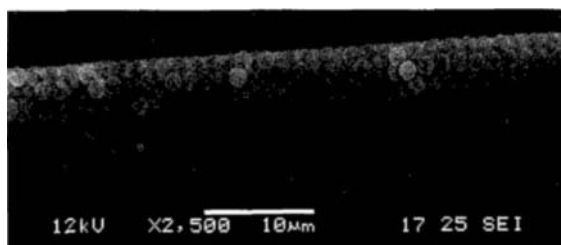


Figure 8. SEM image of uniform film fabricated with PS spheres of $1.5\ \mu\text{m}$ [89].

4.2.4 Electrohydrodynamic deposition

When an electrical field is applied to a colloidal suspension, the colloids particles will assemble together to form stable, 2D arrays due to lateral attraction, which was first observed by Richetti *et al.* [90]. As schematically shown in Fig. 9 (where R_E is the motion rate of deposition, which is dependent on the particle charge and the electric field; R_L is the motion rate of lateral attraction, which is dependent on the current density passing through the particle layers), a colloidal suspension is placed in the electrical field. The electrodynamic force leads to the electrophoresis of the suspension and the electrical current through the suspension accumulates ions on the electrode, which results in a pressure gradient on fluid to force the colloids to deposit on the electrode, forming a crystalline lattice. To obtain multilayers of colloidal particles, R_E should be less than or equal to R_L . Using this method, Trau *et al.* [91] fabricated ordered layers of both silica spheres ($0.9\ \mu\text{m}$ in diameter) and PS spheres ($2\ \mu\text{m}$ in diameter).

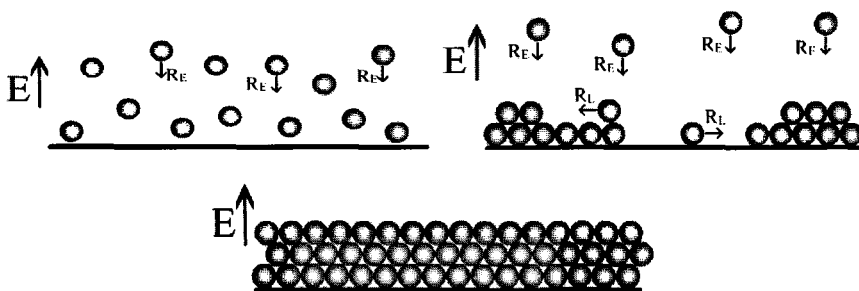


Figure 9. Schematic illustration of electrohydrodynamic method.

Based on the principles of the electrohydrodynamics, Hayward *et al.* [92] developed an alternative approach. The authors applied photochemical process to modulate electrophoretic deposition. An ITO (indium tin oxide) anode was exposed in illumination, an increase in both charge transfer rate and current density took place between the solution and electrode. Because of the gradient of current density, the colloids swept into the regions of higher current density.

Like other techniques, the electrohydrodynamic method has its own drawbacks: (1) the packing density is normally less than 50% because of the repulsive electrostatic forces among particles; (2) only a few layers of spheres can be formed, and (3) the facility used is relatively complicated and costly.

4.2.5 Emulsion assembly method

Artificial opal can also be made with the aid of emulsion droplets [93]. The emulsion droplets act as cells for self-assembly of colloidal spheres. An ordered structure is formed on the surface or inside the droplets. The whole process can be briefed as follows. First, colloidal particles in a suspension are hydrophobized by treating with surfactant, such as sodium dodecylsulfate. Second, the particles are mixed with an oil/water emulsion. Because of the surface hydrophobicity, the colloidal particles can easily adsorb in the bulk of the emulsion droplets. Third, a stabilizer is subsequently added to protect the oil droplets against coalescence and prevent the latex balls from coagulation. Finally, the oil droplets are removed and particle balls with an ordered structure are formed. Recently, emulsion template method has been further improved [94].

4.2.6 Float packing method

We have discussed so far, the artificial opals are contacted with the substrate first and then assembled into ordered structure. However, in float packing method, the ordered structure forms firstly on the surface of the solvent [95,96]. Due to the constraints of density, only polymer spheres can be used with this method.

4.3 Annealing of artificial opal

The 3D ordered arrays obtained by self-assembly are mechanically unstable because there is only Van der Waals force between the spheres. Subsequent infiltration easily destroys the ordered arrays. Consequently, slight annealing of the artificial opal is required to strengthen the opal arrays at a temperature slightly above the glass transition temperature (T_g) for polymer spheres [28-40] and between 700 and 750 °C for silica spheres [17-22]. Annealing gives rise to interconnections between the spheres, which are formed by slight melting of the sphere surfaces to form necks, providing the opal with necessary mechanical stability as well as transport channels for the products during removal of the spheres. Shown in Fig. 10 is a SEM image of PS opal annealed at 110 °C for 10 min. The formation of necks between spheres is clearly seen. It should be noted that annealing also affects the optical properties of the artificial opal as well as the inverted opal. With increase in annealing temperature, a blue shift of transmission spectra has been observed, which is due to the modification the filling volume fraction of the structure [97,98]. This offers a feasible way to control the optical properties of synthetic opal in a wide frequency range of visible light.

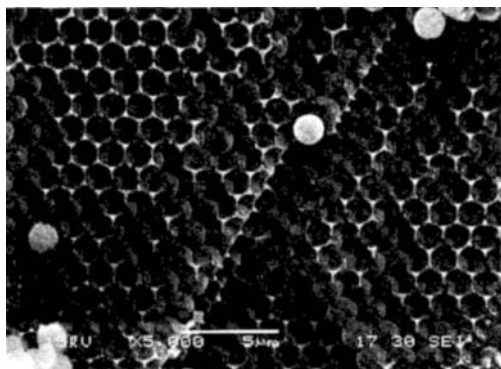


Figure 10. Artificial opal after annealing at an appropriate temperature

4.4 Infiltration

After the artificial opal is fabricated, the next step is to infiltrate the interstices between the spheres with a material of high refractive index. Because incomplete infiltration may lead to the collapse of the inverse opal structure, complete and uniform infiltration is thus of vital importance. Towards this goal, many infiltration techniques have been developed and they are discussed below.

4.4.1 Soaking

Soaking is an effective and simple means to infiltrate materials into artificial opal. The voids are filled with a desired material by capillary force. Because soaking is conducted in a liquid phase, a proper solution or suspension containing an infiltration material has to be available. This largely limits its application. There are mainly two soaking ways. One is to infiltrate the synthetic opal with a precursor followed by further reactions (e.g. polymerization, carbonization, hydrolysis, etc.) to obtain a desired material. This is termed precursor infiltration. The other one is to infiltrate the opal directly with metal or semiconductor nanoparticles, which is called nanoparticles infiltration.

Monomers are perfect precursor as they can be easily cured to a solid material. In addition, their elasticity is a great advantage in practical applications. Before infiltration, a monomer is dispersed in a solvent. After soaking, it can be solidified easily with thermal treatment (such as for PS) or UV irradiation (such as for polyacrylates or polyurethanes) [24-27,39,40]. Another advantage of using polymer is that during the treatment processes, the volume shrinkage is much less than other materials [25b], thus the structure as well as its photonic properties can be maintained to

the largest extent. Unfortunately, polymers normally have a lower refractive index than inorganic materials. This holds back their applications as an infiltration precursor.

Alkoxides are another kind of precursor that has been frequently used. For photonic applications, metals, metal oxides and semiconductors with a high refractive index are the desired materials. For example, Miguez *et al.* [19] employed tetramethoxygermane (TMOG) as a precursor to infiltrate silica opal. TMOG hydrolyzed at room temperature to form GeO_2 , which was subsequently reduced to metal Ge in a H_2 atmosphere at high temperatures. Because the reduction process led to free space, the infiltration-hydrolysis-reduction recycle was repeated.

Soaking with alkyloxide solution has its own drawbacks: (1) the reduction process brings about shrinkage (about 30% - 40%) of the inverted opal material, resulting in a large number of cracks; (2) the infiltration process has to be carried in a closed system because of the sensitivity of the alkyloxides to moisture; (3) most of the metal alkoxides are expensive and not commercially readily available.

Colloidal nanoparticles can be directly infiltrated into the voids of ordered opals by using liquid infilling method. The method is relatively straightforward and does not require subsequent chemical treatments. The size, shape and size distribution of the nanoparticles can have effects on the optical properties of the inverted opal. To enable the colloids to infiltrate into the voids of artificial opal, the size of the colloids should be much less than the size of the void between spheres [22]. Many synthetic strategies for making nanoparticles for this purpose have been available [99-101]. However, as the framework is formed with the nanoparticles its refractive index will suffer loss.

4.4.2 Filtration

Filtration is a method that can overcome some of the drawbacks of the liquid infilling method [32,34]. As we discussed earlier, colloidal microspheres are first packed on the surface of a membrane. Then a metal alkoxide (e.g., titanium ethoxide, zirconium *n*-propoxide, or aluminum tri-*sec*-butoxide) or nanoparticles solution [32] is filtrated through the membrane. To ensure a complete and quick infiltration, negative pressure is often applied.

4.4.3 Emulsion droplets

Mono-dispersed emulsion droplets have also been used as a template for fabricating 3D ordered structures [41,102]. The oil droplet template has the advantage of easy removal by evaporation or dissolution. In addition, it is

highly deformable that can avoid cracking and pulverization during drying and aging steps. Imhof & Pine [41b] prepared a metal oxide sol in pure formamide containing a little amount of water without the presence of alcohol (alcohol is deemed to have a negative effect on emulsion). The emulsion was dispersed in the sol. Then ammonia was added and gelation took place. Unfortunately, because of the polydispersity and deformity of the emulsion droplets, it is hard to form bandgap.

4.4.4 Electrodeposition

Electrodeposition is an ideal method to fully fill the requirements of making 3D ordered complex structures [12,103]. Here we use the device that was used by Braun and Wiltzius (see Fig. 11) as an example to show this method [36]. An artificial opal is placed on the cathode and a semiconductor can deposit directly in the voids of the opal. The most obvious advantage is that the deposition grows from the bottom to the top of the template, leading to a complete filling. In addition, during the template-removal process, framework shrinkage is minor - only about 2 % [36]. Furthermore, electrodeposition can be used for making II-VI, III-V and IV group semiconductors such as CdS and ZnO, etc. and metallic materials such as Pt [104,105], Pd [105], Ni [104,106], Ag [107], Au [106,108]. Macroporous polymeric materials have also been fabricated by using electrodeposition [39,40,109]. However, although electrodeposition could in principle be used to fill the opal with many different materials, only a handful have been demonstrated (e.g. CdS and CdSe). This is because other materials do not grow from the bottom to the top of the opal.

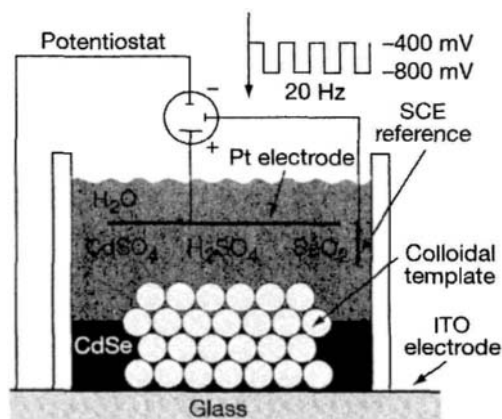


Figure 11. Schematic illustration of electrodeposition for infiltration of opal [36]

4.4.5 Chemical vapor deposition (CVD)

Chemical vapor deposition (CVD) is a widely used materials-processing technology [110] and it has been used for making Si PBG materials by using disilane as a precursor [18,111-113]. With moderate temperature and pressure, the infiltrated disilane decompose and form Si nanoclusters in the void. High temperatures are then applied to improve crystallization and to allow diffusion of the silicon inside the void structure. For example, Vlsov *et al.* [17] used a low-pressure chemical vapor deposition (LPCVD) rig to grow beautiful Si framework. Besides silicon materials, germanium photonic crystals have also been made by using CVD [18b].

4.5 Removal of template

Template removal is the final step of fabricating 3D PBG materials of self-assembly approaches. Calcination is used to remove organic template such as polymers while wet etching is effective to both inorganic and organic template.

Calcination could have a tremendous impact on the optical properties of the inverse opal [33b], which can transform the backbone materials both physically and chemically. For example, anatase phase can be transformed into rutile phase during calcination of which the later has a higher refractive index [41b]. As we mentioned earlier, calcined in a hydrogen environment can turn oxides into metals. Calcination may also lead to strong structural shrinkage because of condensation, transformation, crystallization, etc.

Silica is often removed by etching with a low-concentration hydrofluoric acid solution [17-27]. The main problem of HF-etching is that HF is extremely toxic and corrosive.

5 Fabrication of intentional defects in 3D photonic crystals

One of the applications of 3D PBG materials is as a waveguide [14]. This property can only be realized with introduction of artificial defects into the 3D PBG materials. Because 3D PBG materials can stop EM wave of certain wavelength completely, a line defect is the only route which allows the light to go through. As a result, 3D PBG materials can be designed as a circuit for photons.

Recently, Braun and co-workers have successfully fabricated line defect in 3D photonic crystal [114]. The defect they created is shown in Fig 12 [115,116]. The key of their fabrication is multi-photon polymerization. The authors first infiltrated the opal with monomer and

photoinitiator and then cure the monomer into rigid polymer with numbers of laser pulse. Because the polymerization only occurred on the intersection of the laser pulses, artificial defects were introduced into the materials and waveguide function was observed.



Figure 12. Photonic crystals with artificial defect fabricated by Lee *et al.* [115,116]

Although nanolithography is not an ideal technique for fabrication of complex 3D structures, the combination of it with self-assembly offers many possibilities for creation of unique properties. Using different modes of lithography-patterned substrates, various ordered arrays have been constructed such as lines, and micro-blocks with rectangular or triangular cross section [78,117a-c]. Infiltration and template removal results in the formation of molded photonic crystals [117c,117d]. Ye *et al.* [118] employed this method and fabricated linear artificial defects in PBG materials. As demonstrated in Fig. 13, Ye and co-workers coated a narrow photoresist layer on a substrate. After infiltration and removal of the photoresist layer, a linear defect formed between the photonic crystal and the substrate.

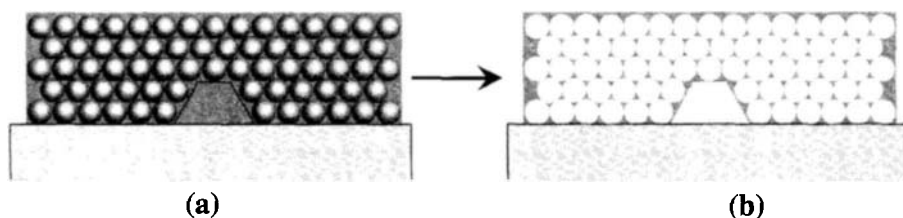


Figure. 13 Illustration of incorporating linear defects in photonic crystal. (a) Colloid spheres assemble on the substrate with linear photoresist layer and then infiltrate with SiO_2 . (b) After removing the template and the photoresist layer photonic crystal with linear defect is obtained [118].

6 Acknowledgements

We thank Agency for Science, Technology and Research (A*STAR), Singapore, for financial support.

References

1. John S. and Busch K., Photonic bandgap formation and tunability in certain self-organizing systems, *J. Lightwave Technol.* **17** (1999) pp. 1931-1943.
2. Koenderink A. F., Johnson P. M., López J. F. G. and Vos W. L., 3D photonic crystals as a cage for light, *C. R. Physique* **3** (2002) pp. 67-77.
3. Shen Y. Z., Friend C. S., Jiang Y., Jakubczyk D., Swiatkiewicz J. and Prasad P. N., Nanophotonics: interactions, materials, and applications, *J. Phys. Chem. B* **104** (2000) pp. 7577-7587.
4. Velez O. D. and Kaler E. W., Structured porous materials via colloidal crystal templating: from inorganic oxides to metals, *Adv. Mater.* **12** (2000) pp. 531-534.
5. Xia Y., Gates B., Yin Y. and Lu Y., Monodispersed colloidal spheres: old materials with new applications, *Adv. Mater.* **12** (2000) pp. 693-713.
6. Birner A., Wehrspohn R. B., Gösele U. M. and Busch K., Silicon-based photonic crystals, *Adv. Mater.* **13** (2001) pp. 377-388.
7. Xia Y., Gates B. and Li Z.-Y., Self-assembly approaches to three-dimensional photonic crystals, *Adv. Mater.* **13** (2001) pp. 409-413.
8. Norris D. J. and Vlasov Y. A., Chemical approaches to three-dimensional semiconductor photonic crystals, *Adv. Mater.* **13** (2001) pp. 371-376.
9. Stein A., Sphere templating methods for periodic porous solids, *Micropor. Mesopor. Mater.* **44-45** (2001) pp. 227-239.
10. Velez O. D. and Lenhoff A. M., Colloidal crystals as templates for porous materials, *Current Opinion Colloid Int. Sci.* **5** (2000) pp. 56-63.
11. Meseguer F., Blanco A., Míguez H., García-Santamaría F., Ibañeta M. and López C., Synthesis of inverse opals, *Colloids and Surf. A* **202** (2002) pp. 281-290.
12. Braun P. V. and Wiltzius P., Macroporous materials-electrochemically grown photonic crystals, *Current Opinion in Colloid & Interface Sci.* **7** (2002) pp. 116-123.
13. Dowling J. P., Mirror on the wall: you're omnidirectional after all? *Science* **282** (1998) pp. 1841-1842.
14. Fink Y., Winn J. N., Fan S., Chen C., Michel J., Joannopoulos J. D. and Thomas E. L., A dielectric omnidirectional reflector, *Science* **282** (1998) pp. 1679-1682.
15. Painter O., Lee R. K., Scherer A., Yariv A., O'Brien J. D., Dapkus P. D. and Kim I., Two-dimensional photonic band-gap defect mode laser, *Science* **284** (1999) pp. 1819-1821.
16. (a) Mekis A., Chen J. C., Kurland I., Fan S., Villeneuve P. R. and Joannopoulos J. D., High transmission through sharp bends in photonic crystal waveguides, *Phys. Rev. Lett.* **77** (1996) pp. 3787-3790. (b) Joannopoulos J. D., Villeneuve P. R. and Fan S., Photonic crystals: putting a new twist on light, *Nature* **386** (1997) pp. 143-147. (c) Lin S.-Y., Chow E., Hietala V., Villeneuve P. R. and Joannopoulos J. D., Experimental demonstration of guiding and bending of electromagnetic waves in a photonic crystal, *Science* **282** (1998) pp. 274-276. (d) Povinelli M. L., Johnson S.

- G., Fan S. and Joannopoulos J. D., Emulation of two-dimensional photonic crystal defect modes in a photonic crystal with a three-dimensional photonic band gap, *Phys. Rev. B* **64** (2001) pp. 075313.
17. Vlasov Y. A., Bo X.-Z., Sturm J. C. and Norris D. J., On-chip natural assembly of silicon photonic bandgap crystals, *Nature* **414** (2001) pp. 289-293.
 18. (a) Blanco A., Chomski E., Grabtchak S., Ibisate M., John S., Leonard S. W., López C., Meseguer F., Míguez H., Mondia J. P., Ozin G. A., Toader O. and van Driel H. M., Large-scale synthesis of a silicon photonic crystal with a complete three-dimensional bandgap near 1.5 micrometers, *Nature* **405** (2000) pp. 437-439. (b) Míguez H., Chomski E., García-Santamaría F., Ibisate M., John S., López C., Meseguer F., Mondia J. P., Ozin G. A., Toader O. and van Driel H. M., Photonic bandgap engineering in germanium inverse opals by chemical vapor deposition, *Adv. Mater.* **13** (2001) pp. 1634-1637.
 19. Míguez H., Meseguer F., López C., Holgado M., Andreasen G., Mifsud A. and Fornés V., Germanium FCC structure from a colloidal crystal template, *Langmuir* **16** (2000) pp. 4405-4408.
 20. Braun P. V., Zehner R. W., White C. A., Weldon M. K., Kloc C., Patel S. S. and Wiltzius P., Epitaxial growth of high dielectric contrast three-dimensional photonic crystal, *Adv. Mater.* **13** (2001) pp. 721-724.
 21. Jiang P., Cizeron J., Bertone J. F., Colvin V. L., Preparation of macroporous metal films from colloidal crystals, *J. Am. Chem. Soc.* **121** (1999) pp. 7959-7958.
 22. Vlasov Y. A., Yao N. and Norris D. J., Synthesis of photonic crystals for optical wavelengths from semiconductor quantum, *Adv. Mater.* **11** (1999) pp. 165-169.
 23. Ni P., Dong P., Cheng B., Li X. and Zhang D., Synthetic SiO₂ opals, *Adv. Mater.* **13** (2001) pp. 437-441.
 24. (a) Park S. H. and Xia Y., Macroporous membranes with highly ordered and three-dimensionally interconnected spherical pores, *Adv. Mater.* **10** (1998) pp. 1045-1048. (b) Park S. H. and Xia Y., Fabrication of three-dimensional macroporous membranes with assemblies of microspheres as templates, *Chem. Mater.* **10** (1998) pp. 1745-1747. (c) Xia Y., Gates B. and Park S. H., Fabrication of three-dimensional photonic crystals for use in the spectral region from ultraviolet to near-infrared, *J. Lightwave Tech.* **17** (1999) pp. 1956-1962. (d) Gates B., Yin Y. and Xia Y., Fabrication and characterization of porous membranes with highly ordered 3D periodic structures, *Chem. Mater.* **11** (1999) pp. 2827-2836.
 25. (a) Jiang P., Hwang K. S., Mittleman D. M., Bertone J. F. and Colvin V. L., Template-directed preparation of macroporous polymers with oriented and dcrySTALLINE arrays of voids, *J. Am. Chem. Soc.* **121** (1999) pp. 11630-11637. (b) Bertone J. F., Jiang P., Hwang K. S., Mittleman D. M. and Colvin V. L., Thickness dependence of the optical properties of ordered silica-air and air-polymer photonic crystals, *Phys. Rev. Lett.* **83** (1999) pp. 300-303. (c) Jiang P., Ostojic G. N., Narat R., Mittleman D. M. and Colvin V. L., The fabrication and bandgap engineering of photonic multilayers, *Adv. Mater.* **13** (2001), 389-393.
 26. Míguez H., Meseguer F., López C., López-Tejiera F. and Sánchez-Dehesa J., Synthesis and photonic bandgap characterization of polymer inverse opals, *Adv. Mater.* **13** (2001) pp. 393-396.
 27. Deutsch M., Vlasov Y. A. and Norris D. J., Conjugated-polymer photonic crystals, *Adv. Mater.* **12** (2000) pp. 1176-1180.
 28. Gates B. and Xia Y., Photonic crystals that can be addressed with an external magnetic field, *Adv. Mater.* **13** (2001) pp. 1605-1608.

29. (a) Subramanian G., Manoharan V. N., Thorne J. D. and Pine D. J., Ordered macroporous materials by colloidal assembly: a possible route to photonic bandgap materials, *Adv. Mater.* **11** (1999) pp. 1261-1265. (b) Subramania G., Constant K., Biswas R., Sigalas M. M. and Ho K.-M., Optical photonic crystals fabricated from colloidal systems, *Appl. Phys. Lett.* **74** (1999) pp. 3933-3935. (c) Subramania G., Constant K., Biswas R., Sigalas M. M. and Ho K.-M., Optical photonic crystals synthesized from colloidal systems of polystyrene spheres and nanocrystalline titanic, *J. Lightwave Tech.* **17** (1999) pp. 1970-1974. (d) Subramania G., Constant K., Biswas R., Sigalas M. M. and Ho K.-M., Inverse face-centered cubic thin film photonic crystals, *Adv. Mater.* **13** (2001) pp. 443-446. (e) Subramania G., Constant K., Biswas R., Sigalas M. M. and Ho K.-M., Synthesis of thin film photonic crystals, *Syn. Metal* **116** (2001) pp. 445-448.
30. (a) Meng Q.-B., Gu Z.-Z. and Sato O., Fabrication of highly ordered porous structures, *Appl. Phys. Lett.* **77** (2000) pp. 4313-4315. (b) Gu Z.-Z., Kubo S., Qian W., Einaga Y., Tryk D. A., Fujishima A. and Sato O., Varying the optical stop band of a three-dimensional photonic crystal by refractive index control, *Langmuir* **17** (2001) pp. 6751-6753.
31. (a) Wijnhoven J. E. G. J. and Vos W. L., Preparation of photonic crystals made of air spheres in titania, *Science* **281** (1998) pp. 802-804. (b) Wijnhoven J. E. G. J., Bechger L. and Vos W. L., Fabrication and characterization of large macroporous photonic crystals in titania, *Chem. Mater.* **13** (2001) pp. 4486-4499.
32. (a) Holland B. T., Blanford C. F. and Stein A., Synthesis of macroporous minerals with highly ordered three-dimensional arrays of spherical voids, *Science* **281** (1998) pp. 538-540. (b) Holland B. T., Blanford C. F., Do T. and Stein A., Synthesis of highly ordered, three-dimensional, macroporous structures of amorphous or crystalline inorganic oxides, phosphates and hybrid composites, *Chem. Mater.* **11** (1999) pp. 795-805.
33. (a) Yan H., Blanford C. F., Holland B. T., Parent M., Smyrl W. H. and Stein A., A chemical synthesis of periodic macroporous NiO and metallic Ni, *Adv. Mater.* **11** (1999) pp. 1003-1006. (b) Yan H., Blanford C. F., Holland B. T., Smyrl W. H. and Stein A., General synthesis of periodic macroporous solids by templated salt precipitation and chemical conversion, *Chem. Mater.* **12** (2000) pp. 1134-1141. (c) Yan H., Blanford C. F., Smyrl W. H. and Stein A., Preparation and structure of 3D ordered macroporous alloys by PMMA colloidal crystal templating, *Chem. Comm.* (2000) pp. 1477-1478. (d) Blanford C. F., Yan H., Schroden R. C., Al-Daous M. and Stein A., Gems of chemistry and physics: macroporous metal oxides with 3D order, *Adv. Mater.* **13** (2001) pp. 401-407. (e) Yan H., Blanford C. F., Lytle J. C., Carter C. B., Smyrl W. H. and Stein A., Influence of processing conditions on structures of 3D ordered macroporous metals prepared by colloidal crystal templating, *Chem. Mater.* **13** (2001) pp. 4314-4321.
34. (a) Velev O. D., Jede T. A., Lobo R. F. and Lenhoff A. M., Porous silica via colloidal crystallization, *Nature* **389** (1997) pp. 447-448. (b) Velev O. D., Jede T. A., Lobo R. F. and Lenhoff A. M., Microstructured porous silica obtained via colloidal crystal templates, *Chem. Mater.* **10** (1998) pp. 3597-3602. (c) Velev O. D., Tessier P. M., Lenhoff A. M. and Kaler E. W., A class of porous metallic nanostructures, *Nature* **401** (1999) pp. 548.
35. Tessier P. M., Velev O. D., Kalambur A. T., Lenhoff A. M., Rabolt J. F. and Kaler E. W., Structured metallic films for optical and spectroscopic applications via colloidal crystal templating, *Adv. Mater.* **13** (2001) pp. 396-400.

36. Davidoff J., Davies I. and Roberson D., Electrochemically grown photonic crystals, *Nature* **402** (1999) pp. 603-604.
37. Harkins P., Eustace D., Gallagher J. and McComb D. W. J., Synthesis of multifunctional photonic crystals, *J. Mater. Chem.* **12** (2002) pp. 1247-1249.
38. Zhu G., Qiu S., Gao F., Li D., Li Y., Wang R., Gao B., Li B., Guo Y., Xu R., Liu Z. and Terasaki O., Template-assisted self-assembly of macro-micro bifunctional porous materials, *J. Mater. Chem.* **11** (2001) pp. 1687-1697.
39. Bartlett P. N., Birkin P. R., Ghanem M. A. and Toh C. S., Electrochemical syntheses of highly ordered macroporous conducting polymers grown around self-assembled colloidal templates, *J. Mater. Chem.* **11** (2001) pp. 849-853.
40. Cassagneau T. and Caruso F., Semiconducting Polymer Inverse opals prepared by electropolymerization, *Adv. Mater.* **14** (2002) pp. 34-38.
41. (a) Imhof A. and Pine D. J., Ordered macroporous materials by emulsion templating, *Nature* **389** (1997) pp. 948-951. (b) Manoharan V. N., Imhof A., Thorne J. D. and Pine D. J., Photonic crystals from emulsion templates, *Adv. Mater.* **13** (2001) pp. 447-450.
42. (a) Yablonovitch E., Inhibited spontaneous emission in solid-state physics and electronics, *Phys. Rev. Lett.* **58** (1987) pp. 2059-2062. (b) Yablonovitch E. and Gmitter T. J., Photonic band structure: the face-centered-cubic case, *Phys. Rev. Lett.* **63** (1989) pp. 1950-1953.
43. John S., Strong localization of photons in certain disordered dielectric superlattices, *Phys. Rev. Lett.* **58** (1987) pp. 2486-2489.
44. (a) Yablonovitch E., Gmitter T. J. and Leung K. M., Photonic band structure: the face-centered-cubic case employing nonspherical atoms, *Appl. Phys. Lett.* **67** (1991) pp. 2295-2298. (b) Sievenpiper D. F., Sickmiller M. E. and Yablonovitch E., 3D wire mesh photonic crystals, *Phys. Rev. Lett.* **76** (1996) pp. 2480-2483.
45. Joannopoulos J. D., Meade R. D. and Winn J. N. Photonic Crystals: Molding the Flow of Light (Princeton University Press, N. J., 1995).
46. (a) John S. and Rangarajan R., Optimal structures for classical wave localization: an alternative to the Ioffe-Regel criterion, *Phys. Rev. B* **38** (1988) pp. 10101-10104. (b) Economou E. N. and Zdetsis A., Classical wave propagation in periodic structures, *Phys. Rev. B* **40** (1989) pp. 1334-1337. (c) Satpathy S., Zhang Z. and Salehpour M. R., Theory of photon bands in three-dimensional periodic dielectric structures, *Phys. Rev. Lett.* **64** (1990) pp. 1239-1242. (d) Leung K. M. and Liu Y. F., Photon band structures: the plane-wave method, *Phys. Rev. B* **41** (1990) pp. 10188-10190.
47. (a) Zhang Z. and Satpathy S., Electromagnetic Wave propagation in periodic structures: Bloch wave solution of Maxwell's Equations, *Phys. Rev. Lett.* **65** (1990) pp. 2650-2653.
48. Leung K. M. and Liu Y. F., Full vector wave calculation of photonic band structures in fcc dielectric media, *Phys. Rev. Lett.* **65** (1990) pp. 2646-2649.
49. Ho K. M., Chan C. T. and Soukoulis C. M., Existence of a photonic gap in periodic dielectric structure, *Phys. Rev. Lett.* **65** (1990) pp. 3152-3155.
50. Li Z. Y., Wang J. and Gu B. Y., Creation of partial band gaps in anisotropic photonic-band-gap structures, *Phys. Rev. B* **58** (1998) pp. 3721-3729.
51. Sözüer H. S. and Haus J. W., Photonic bands: convergence problems with the plane-wave method, *Phys. Rev. B* **45** (1992) pp. 13962-13972.
52. Busch K. and John S., Photonic band gap formation in certain self-organizing systems, *Phys. Rev. E* **58** (1998) pp. 3896-3908.

53. Fan S., Villeneuve P. R., Meade R. D. and Joannopoulos J. D., Design of three-dimensional photonic crystals at submicron length scales, *Appl. Phys. Lett.* **65** (1994) pp. 1466-1468.
54. (a) Özbay E., Michel E., Tuttle G., Biswas R., Sigalas M. M., and Ho K.-M., Inhibited spontaneous emission in solid-state physics and electronics, *Appl. Phys. Lett.* **64** (1994) pp. 2059-2062. (b) Özbay E., Abeyta A., Tuttle G., Tringides M., Biswas R., Chan C. T., Soukoulis C. M. and Ho K.-M., Measurement of a three-dimensional photonic band gap in a crystal structure made of dielectric rods, *Phys. Rev. B* **50** (1994) pp. 1945-1949. (c) Özbay E., Tuttle G., Sigalas M. M., Soukoulis C. M. and Ho K.-M., Defect structures in a layer-by-layer photonic band-gap crystal, *Phys. Rev. B* **51** (1995) pp. 13961-13965.
55. Sigalas M. M., McCalmont J. S., Ho K.-M. and Tuttle G., Theoretical and experimental study of silicon-based angular filters, *Appl. Phys. Lett.* **68** (1996) pp. 3525-3527.
56. Sanders J. V., Color of precious opal, *Nature* **204** (1964) pp. 1151-1153.
57. (a) Tarhan İ. İ. and Watson G. H., Photonic band structure of fcc colloidal crystals, *Phys. Rev. Lett.* **76** (1996) pp. 315-318. (b) Tarhan İ. İ., Zinkin M. P. and Watson G. H., Interferometric technique for the measurement of photonic band structure in colloidal crystals, *Opt. Lett.* **20** (1995) pp. 1571-1573. (c) Pradhan R. D., Tarhan İ. İ. and Watson G. H., Impurity modes in the optical stop bands of doped colloidal crystals, *Phys. Rev. B* **54** (1996) pp. 13721-13725. (d) Pradhan R. D., Bloodgood J. A. and Watson G. H., Photonic band structure of bcc colloidal crystals, *Phys. Rev. B* **55** (1997) pp. 9503-9507.
58. Zakhidov A., Baughman R. H., Iqbal Z., Cui C., Khayrullin I., Dantas S. O. J., Marti and Ralchenko V. G., Carbon structures with three-dimensional periodicity at optical wavelengths, *Science* **282** (1998) pp. 897-901.
59. Kang S., Hong S., Choe C. R., Park M., Rim S. and Kim J., Preparation and characterization of epoxy composites filled with functionalized nanosilica particles obtained via sol-gel process, *Polymer* **42** (2001) pp. 879-887.
60. Stöber W., Fink A. and Bohn E., Controlled growth of monodisperse silica spheres in the micron size range, *J. Colloid. Interface Sci.* **26** (1968) pp. 62-69.
61. Reculasa S., Poncet-Legrand C., Ravaine S., Mingotaud C., Duguët E. and Bourgeat-Lami E., Syntheses of raspberry like silica/polystyrene materials, *Chem. Mater.* **14** (2002) pp. 2354-2359.
62. Bogush G. H. and Zukoski C. F., Studies of the kinetics of the precipitation of uniform silica particles through the hydrolysis and condensation of silicon alkoxides, *J. Colloid Interface Sci.* **142**, 1 (1991) pp. 1-18.
63. Okubo T., Miyamoto T., Umemura K. and Kobayashi K., Seed polymerization of tetraethyl orthosilicate in the presence of colloidal silica spheres, *Colloid Polym. Sci.* **279** (2001) pp. 1236-1240.
64. Piirma I. *Emulsion Polymerization* (Academic press, N. Y., 1982).
65. (a) Shim S.-E., Cha Y.-J., Byun J.-M. and Choe S., Size Control of Polystyrene beads by multistage seeded emulsion polymerization, *J. Appl. Polym. Sci.* **71** (1999) pp. 2259-2269. (b) Zou D., Ma S., Guan R., Park M., Sun L., Aklonis J. J. and Salovey R., Model filled polymers. V. Synthesis of crosslinked monodisperse polymethacrylate beads, *J. Polym. Sci. Part A: Polym. Chem.* **30** (1992) pp. 137-144. (c) Bamnolker H. and Margel S., Dispersion polymerization of styrene in polar solvents: effect of reaction parameters on microsphere surface composition and surface properties, size and size distribution, and molecular weight, *J. Polym. Sci. Part A: Polym. Chem.* **34** (1996) pp. 1857-1871.

66. (a) Tissot I., Novat C., Lefebvre F. and Bourgeat-Lami E., Hybrid latex particles coated with silica, *Macromolecules* **34** (2001) pp. 5737-5739. (b) Tissot I., Reymond J. P., Lefebvre F. and Bourgeat-Lami E., SiOH-functionalized polystyrene latexes: a step toward the synthesis of hollow silica nanoparticles, *Chem. Mater.* **14** (2002) pp. 1325-1331.
67. Hotta Y., Alberius P. C. A. and Bergström L., Coated polystyrene particles as templates for ordered macroporous silica structures with controlled wall thickness, *J. Mater. Chem.*, **13** (2003) pp. 496-501.
68. Graf C. and van Blaaderen A., Metallo-dielectric Colloidal Core-Shell Particles for Photonic Applications, *Langmuir* **18** (2002) pp. 524-534.
69. Li Z.-Y. and Zhang Z.-Q., Photonic bandgaps in disordered inverse-opal photonic crystals, *Adv. Mater.* **13** (2001) pp. 433-436.
70. Mayoral R., Requena J., Moya J. S., López C., Cintas A., Míguez H., Meseguer F., Vázquez L., Holgado M. and Blanco Á., 3D long-range ordering in a SiO₂ submicrometer-sphere sintered superstructure, *Adv. Mater.* **9** (1997) pp. 257-260.
71. Woodcock L. V., Entropy difference between the face-centered cubic and hexagonal close-packed crystal structures, *Nature* **385** (1997) pp. 141-142.
72. Van Blaaderen A., Ruel R. and Wiltzius P., Template-directed colloidal crystallization, *Nature* **385** (1997) pp. 321-324.
73. Míguez H., Meseguer F., López C., Mifsud A., Moya J. S. and Vázquez L., Evidence of FCC crystallization of SiO₂ nanospheres, *Langmuir* **13** (1997) pp. 6009-6011.
74. Holgado M., Garcia-Santamaría F., Blanco A., Ibisate M., Cintas A., Míguez H., Serna C. J., Molpeceres C., Requena J., Mifsud A., Meseguer F. and López C., Electrophoretic deposition to control artificial opal growth, *Langmuir* **15** (1999) pp. 4701-4704.
75. Yin Y. and Xia Y., Growth of Large colloidal crystals with their (100) planes orientated parallel to the surfaces of supporting substrates, *Adv. Mater.* **14** (2002) pp. 605-608.
76. Van Blaaderen A. and Wiltzius P., Growing large, well-oriented colloidal crystals, *Adv. Mater.* **9** (1997) pp. 833-835.
77. Yang S. M. and Ozin G. A., Opal chips: vertical growth of colloidal crystal patterns inside silicon wafers, *Chem. Comm.* **24** (2000) pp. 2507-2508.
78. Yin Y., Lu Y., Gates B. and Xia Y., Template-assisted self-Assembly: a practical route to complex aggregates of monodisperse colloids with well-defined sizes, shapes, and structures, *J. Am. Chem. Soc.* **123** (2001) pp. 8718-8729.
79. Gates B., Qin D., and Xia Y., Assembly of nanoparticles into opaline structures over large areas, *Adv. Mater.* **11** (1999) pp. 466-469.
80. (a) Nagayama K., Two-dimensional self-assembly of colloids in thin liquid film, *Colloid. Surf. A* **109** (1996) pp. 363-374. (b) Kralchevsky P. A. and Nagayama K., Capillary forces between colloidal particles, *Langmuir* **10** (1994) pp. 23-36.
81. Dimitrov A. S., Dushkin C. D., Yoshimura H. and Nagayama K., Observations of latex particle two-dimensional-crystal nucleation in wetting films on mercury, glass, and mica, *Langmuir* **10** (1994) pp. 432-440.
82. (a) Kralchevsky P. A., Paunov V. N., Denkov N. D., Ivanov I. B. and Nagayama K., Energetical and force approaches to the capillary interactions between particles attached to a liquid-fluid interface, *J. Colloid Interface Sci.* **155** (1993) pp. 420-437. (b) Paunov V. N., Kralchevsky P. A., Denkov N. D. and Nagayama K.,

- Lateral capillary forces between floating submillimeter particles, *J. Colloid Interface Sci.* **157** (1993) pp. 100-112.
83. Denkov N. D., Velev O. D., Kralchevsky P. A., Ivanov I. B., Yoshimura H. and Nagayama K., Two-dimensional crystallization, *Nature* **361** (1993) pp. 26.
 84. Micheletto R., Fukuda H. and Ohtsu M., A simple method for the production of a two-Dimensional, ordered array of small latex particles, *Langmuir* **11** (1995) pp. 3333-3336.
 85. Chen X., Cui Z., Chen Z., Zhang K., Lu G., Zhang G. and Yang B., The synthesis and characterizations of monodisperse cross-linked polymer microspheres with carboxyl on the surface, *Polymer* **43** (2002) pp. 4147-4152.
 86. Dimitrov A. S. and Nagayama K., Continuous convective assembling of fine particles into 2D arrays on solid surfaces, *Langmuir* **12** (1996) pp. 1303-1311.
 87. Jiang P., Bertone J. F., Hwang K. S. and Colvin V. L., Single-crystal colloidal multilayers of controlled thickness, *Chem. Mater.* **11** (1999) pp. 2132-2140.
 88. Cheng Z., Russel W. B. and Chalkin P. M., Controlled growth of hard-sphere colloidal crystals, *Nature* **401** (1999) pp. 893-895.
 89. Zhou Z. and Zhao X. S., unpublished results.
 90. Richetti P., Prost J. and Barois P., *J. Phys. Lett.* **45** (1984) pp. L-1137.
 91. Trau M., Saville D. A. and Aksay I. A., Field-induced layering of colloidal crystal, *Science* **272** (1996) pp. 706-709.
 92. Hayward R. C., Saville D. A. and Aksay I. A., Electrophoretic assembly of colloidal crystal with optically tunable micropatterns, *Nature* **404** (2000) pp. 56-59.
 93. (a) Velev O. D., Furusawa K. and Nagayama K., Assembly of latex particles by using emulsion droplets as templates 1. Microstructured hollow spheres, *Langmuir* **12** (1996) pp. 2374-2384. (b) Velev O. D., Furusawa K. and Nagayama K., Assembly of latex particles by using emulsion droplets as templates. 2. ball-like and composite aggregates, *Langmuir* **12** (1996) pp. 2385-2391. (c) Velev O. D. and Nagayama K., Assembly of latex particles by using emulsion droplets. 3. Reverse (water in oil) system, *Langmuir* **13** (1997) pp. 1856-1859. (d) Velev O. D., Lenhoff A. M. and Kaler E. W., A class of microstructured particles through colloidal crystallization, *Science* **287** (2000) pp. 2240-2243.
 94. Yi G.-R., Moon J. H. and Yang S.-M., Ordered macroporous particles by colloidal templating, *Chem. Mater.* **13** (2001) pp. 2613-2618.
 95. Zeng F., Sun Z., Wang C., Ren B., Liu X. and Tong Z., Fabrication of Inverse opal via ordered highly charged colloidal spheres, *Langmuir* **18** (2002) pp. 9116-9120.
 96. (a) Im S. H., Lim Y. T., Suh D. J. and Park O. O., Three-dimensional self-assembly of Colloids at a water-air interface: a novel technique for the fabrication of photonic bandgap crystals, *Adv. Mater.* **19** (2002) pp. 1367-1369. (b) Im S. H. and Park O. O. Effect of evaporation temperature on the quality of colloidal crystals at the water-air interface, *Langmuir* **18** (2002) pp. 9642-9646. (c) Im S. H., Kim M. H. and Park O. O., Thickness control of colloidal crystals with a substrate dipped at a tilted angle into a colloidal suspension, *Chem. Mater.* **15** (2003) pp. 1797-1802.
 97. (a) Míguez H., López C., Meseguer F., Blanco A., Vázquez L., Mayoral R., Ocaña M., Fornés V. and Mifsud A., Photonic crystal properties of packed submicrometric SiO₂ spheres, *Appl. Phys. Lett.* **71** (1997) pp. 1148-1150. (b) Míguez H., Meseguer F., López C., Blanco A., Moya J. S., Requena J., Mifsud A. and Fornés V., Control of the photonic crystal properties of fcc-packed submicrometer SiO₂ spheres by sintering, *Adv. Mater.* **10** (1998) pp. 480-483.

98. Gates B., Park S. H. and Xia Y., Tuning the photonic bandgap properties of crystalline arrays of polystyrene beads by annealing at elevated temperatures, *Adv. Mater.* **12** (2000) pp. 653-656.
99. Steigerwald M. L., Selective syntheses of iron monotelluride and iron ditelluride from organometallic precursors. Synthesis and pyrolysis of $[\text{Cp}(\text{Et}_3\text{P})(\text{CO})\text{Fe}]_2(\text{Te})_n$, *Chem. Mater.* **1** (1989) pp. 52-57.
100. Bawendi M. G., Kortan A. R., Steigerwald M. L. and Brus L. E. J., X-ray structural characterization of larger CdSe semiconductor clusters, *Chem. Phys. Lett.* **91** (1989) pp. 7282-7290.
101. Murray C. B., Norris D. J. and Bawendi M. G., Synthesis and characterization of nearly monodisperse CdE (E=S, Se, Te) semiconductor nanocrystallites, *J. Am. Chem. Soc.* **115** (1993) pp. 8706-8715.
102. Imhof A. and Pine D. J., Uniform macroporous ceramics and plastics by emulsion templating, *Adv. Mater.* **10** (1998) pp. 697-700.
103. Klein J. D., Herrick R. D., Palmer D. and Sailor M. J., Electrochemical fabrication of cadmium chalcogenide microdiode arrays, *Chem. Mater.* **5** (1993) pp. 902-904.
104. Luo Q., Liti Z., Li L., Xie S., Kong J. and Zhao D., Creating highly ordered metal, alloy, and semiconductor macrostructures by electrodeposition, Ion spraying, and laser spraying, *Adv. Mater.* **13** (2001) pp. 286-289.
105. Bartlett P. N., Birkin P. R. and Ghanem M. A., Electrochemical deposition of macroporous platinum, palladium and cobalt films using polystyrene latex sphere templates, *Chem. Comm.* (2000) pp. 1671-1672.
106. Xu L., Zhou W. L., Frommen C., Baughma R. H., Zakhidov A. A., Malkinski L., Wang J. Q. and Wiley J. B., Electrodeposited nickel and gold nanoscale metal meshes with potentially interesting photonic properties, *Chem. Comm.* (2000) pp. 997-998.
107. Lellig C., Hartl W., Wagner J. and Hempelmann R., Immobilized highly charged colloidal crystals: a new route to three-dimensional mesoscale structured materials, *Angew. Chem. Int. Ed.* **41** (2002) pp. 102-104.
108. Wijnhoven J. E. G. I., Zevenhuizen S. J. M., Hendriks M. A., Vanmackelbergh D., Kelly J. J. and Vos W. L., Electrochemical assembly of ordered macropores in gold, *Adv. Mater.* **12** (2000) pp. 888-890.
109. Sumida T., Wada Y., Kitamura T. and Yanagida S., Electrochemical preparation of macroporous polypyrrole films with regular arrays of interconnected spherical voids, *Chem. Comm.* (2000) pp. 1613-1614.
110. Park J. H. and Sudarshan T. S., Chemical vapor deposition (Materials Park, O. H., 2001).
111. Bag Ö., Ozin G. A., Yang H., Reber C. and Bussière G., Photoluminescent silicon clusters in oriented hexagonal mesoporous silica film, *Adv. Mater.* **11** (1999) pp. 474-480.
112. Chomski E. and Ozin G. A., Panoscopic silicon-a material for "all" length scales, *Adv. Mater.* **12** (2000) pp. 1071-1078.
113. Yates H. N., Pemble M. E., Míguez H., Blanco A., López C., Meseguer F. and Vázquez L., Atmospheric pressure MOCVD growth of crystalline InP in opals, *J. Crystal Growth* **193** (1998) pp. 9-15.
114. Lee W., Pruzinsky S. A. and Braun P. V., Multi-photon polymerization of waveguide structures within three-dimensional photonic crystals, *Adv. Mater.* **14** (2002) pp. 271-274.

115. Taton T. A. and Norris D. J., Defective promise in photonics, *Nature* **416**, (2002) pp. 685-686.
116. Service R. F., Building better photonic crystals, *Science* **295** (2002) pp. 2399.
117. (a) Ozin G. A. and Yang S. M., The race for the photonic chip: colloidal crystal assembly in silicon wafers, *Adv. Funct. Mater.* **11** (2001) pp. 95-103. (b) Yang S. M. and Ozin G. A., Opal chips: vectorial growth of colloidal crystal patterns inside silicon wafers, *Chem. Commun.* (2000) pp. 2507-2508. (c) Yang S. M., Míguez H. and Ozin G. A., Opal circuits of light – planarized microphotonic crystal chips, *Adv. Funct. Mater.* **12** (2002) pp. 425-431. (d) Míguez H., Yang S. M., Tétreault N. and Ozin G. A., Oriented free-standing three-dimensional silicon inverted colloidal photonic crystal microfibers., *Adv. Mater.* **14** (2002) pp. 1805-1808.
118. Ye Y. -H., Mayer T. S., Khoo I. -C., Divliansky I. B., Abrams N. and Mallouk T. E., Self-assembly of three-dimensional photonic-crystals with air-core line defects, *J. Mater. Chem.* **12** (2002) pp. 3637-3639.

HYDROPHOBIC MICROPOROUS SILICA MEMBRANES FOR GAS SEPARATION AND MEMBRANE REACTORS

SABINE GIESSLER, JOÃO C. DINIZ DA COSTA AND G. Q. LU

*The NanoMaterials Centre, School of Engineering, The University of Queensland,
Brisbane, QLD 4072, Australia
E-mail: joedac@cheque.uq.edu.au*

This chapter reviews the recent literature in the field of silica membranes for gas separation and membrane reactors. The gap in performance between silica membranes and palladium (Pd) membranes has been substantially closed in the last decade. For silica membranes, H_2 permeation is typically $10^{-6} \text{ molm}^{-2}\text{s}^{-1}\text{Pa}^{-1}$ and H_2/CO_2 selectivity in the range of 5-70, resulting from an average pore diameter of 3.0-3.8 Å. Silica membranes are also good candidates for membrane reactor applications, including hydrogenation and dehydrogenation reactions. However, there is little attention given to the improvement of the hydrothermal stability of inorganic membranes among the increasing number of reports on microporous inorganic membranes. Furthermore, studies relating to the mass transfer of H_2 in gas mixtures containing water vapour are also limited. Nevertheless, major research effort remains to scale up defect-free thin films ($<1 \mu\text{m}$) which are hydrothermally stable (up to 600°C) with molecular pore dimensions ($d_p < 5 \text{ Å}$). This review also addresses methods to improve the hydrophobicity of silica membranes and xerogels, and discusses the influences of the synthesis methods on the pore size tailorability.

1 Introduction

Membranes are molecular scale filters with the purpose to separate a small molecule and hinder the passage of a larger molecule. Membrane technology therefore finds applications in process industries, energy and transportation sectors, and sensor applications. Although the use of membrane materials appeared some 30 years ago, only the last decade has seen the development of high quality ultrathin and defect-free inorganic membranes. For practical reasons, membranes should have very high fluxes and selectivities, which are often conflicting goals in membrane design. In addition, gas streams containing steam often cause structure collapse. i.e., water generally attacks the hydroxyl groups in silica derived membranes resulting in structural changes and pore closure. Despite of this, new generation of hybrid materials and synthesis processes have allowed these limitations to be overcome. The recently development of hydrophobic membranes have opened a window of research opportunities and industrial application in membrane reactor technology, in particular when it is imperative to find new membrane materials more permeable to

H₂ and less expensive than palladium¹. Clearly the choice of materials plays a vital role for further improvements in membrane design [2] due to the fact that there is a real transition to the hydrogen economy in the transportation and energy sector [3]. In view of these potential important issues, this review will be mainly focused on membrane performance, in particular when H₂ separation and hydrothermal stability are major technical goals.

2 Inorganic membranes

2.1 Overview

Inorganic membranes can be classified into two types: dense and porous membranes. Typical dense membranes are made of metals, mainly palladium and its alloys. Porous inorganic membranes are made of carbon, metals, glass and oxides such as alumina, titania and zirconia. Porous membranes can also be classified into asymmetric and symmetric membranes. Symmetric membranes have a homogeneous structure, whereas asymmetric membranes consist of a very thin top layer (thickness < 5 μm) supported by a porous sub-layer (thickness 50–200 μm) (Mulder, 1991). These layers are deposited as thin films on macroporous or mesoporous supports, usually γ- or α-alumina, which provide the mechanical integrity for the membrane module. Membrane synthesis can be carried out by phase separation and leaching, anodic oxidation, pyrolysis, particle dispersion, polymerization, dip coating, sol-gel impregnation, or chemical vapor deposition (CVD). Microporous ceramic membranes (3 < d_p < 20 Å) include amorphous oxides such as zeolithes, silica and carbon.

2.2 Sol-gel methods

The sol-gel method is the most suitable method to synthesise high quality silica membranes. The sol-gel method is also flexible as it allows the use of template agents to enable the pore size tailoring. Templates employed by various research groups to produce high quality membranes include organic covalently bonded templates such as methyl groups (de Vos et al [4], Raman and Brinker [5], da Costa et al [6]) and non-covalently bonded organic templates such as C6- and C16-surfactants (Tsai et al [7] and alkyl-tri-ethoxy-silanes Kusakabe et al [8]).

2.2.1 Polymeric sol-gel route

The standard sol-gel process is controlled by hydrolysis and condensation reactions [12]. Various research groups have produced high quality membranes using a single-step catalysed hydrolysis [13] or a two-step catalysed hydrolysis sol-gel process [14, 7]. The catalysed hydrolysis process employs tetraethylorthosilicate (TEOS) and precursors mixed with ethanol (EtOH), an acid catalyst (HCl or HNO₃) and distilled water. Diniz da Costa et al [6] reported that sol-gel derived films with a large contribution of silanol groups (SiOH) have much smaller pore sizes with molecular dimensions in the region of 3-4 Å than those with a large contribution of siloxane bonds (Si-O-Si). Hence, these materials are ideal precursors to be used for membranes with pores of the molecular dimensions required to separate a large gas molecule from a small one.

Brinker and Scherer [15] extensively reviewed the sol-gel process and its science. Depending on the pH and the H₂O:Si molar ratio ($r < 5$), weakly branched networks can be formed with a high contribution of silanol groups. In this case, there is a tendency for the framework structures to interpenetrate forming micropore apertures of molecular size. The hydrolysis and condensation reactions in the sol-gel process lead to the growth and aggregation of clusters resulting in gel formation. The film microstructure depends upon the formulation and preparation procedures of sols to the gel point, as well as the proceeding aging, drying, and heat treatment of the gels. During heat treatment continuing condensation reactions lead to the strengthening of the network due to polymeric cross-linking. Buckley and Greenblatt [16] investigated the pore characteristics of xerogels prepared with TEOS, ethanol and water. They found that by increasing the ethanol content of the solution, the particle size decreased. They also reported that increasing the alkyl chain of the alcohol solvent, the xerogel structure changed from microporous to mesoporous. In addition, they showed that a low water content favored mesoporosity, whereas a high water content favored macroporosity.

2.2.2 Modified polymeric template method

An important technique to tailor the pore size of intermediate or top layers of membranes is to add organic template agents during the sol-gel process. This field has been reviewed by Raman et al [17]. Baker et al [18] explored the potential of xerogel composites by investigating various organic oligomers and surfactants as possible modifying agents. The incorporation of organic molecules within the sol-gel process leads to

composites that can help to produce crack-free materials and improve coating-substrate adhesion. There are two methods of sol-gel composites with template agents. The first one is a covalently bonded organic template, such as methyl groups (CH_3) in methyltriethoxysilane (MTES), which has a co-monomer non-hydrolysable functionality. The second method employs an organic oligomer or surfactant, which interact with the sol by weak van der Waals forces, hydrogen or ionic bonds, or hydrophilic-hydrophobic routes.

During gel formation, organic templates are trapped in the gel structure. By heating xerogel above 400°C organic templates such as $-\text{CH}_3$ groups are burned off leaving in the xerogel matrix a cavity with similar dimensions to those of the template molecules. The characterisation of MTES templated silica xerogels for molecular sieve applications in MTES:TEOS molar ranges of 10:90 to 50:50, carried out by da Costa et al [6] showed that a higher template concentration induces the collapse of the xerogel matrix due to capillary stress promoting dense xerogels as well as a broader pore size distribution (PSD). This trend has a significant effect on the separation properties of membranes as reported by Raman and Brinker [5]. By increasing MTES molar ratio from 10 to 40mol%, their membranes showed that CO_2 permeation increased from 3.3×10^{-6} to $8.6 \times 10^{-6} \text{ cm}^3 \cdot \text{cm}^{-2} \cdot \text{s}^{-1} \cdot \text{cmHg}^{-1}$ whereas CO_2/CH_4 separation factor decreased by a factor of four. Hence, the pore size increased.

Kusakabe et al [8] used three different templates (octyldodecyl- and octadecyltriethoxy-silanes) in order to test the role of templates in tailoring pore sizes. They reported that the short alkyl chain of the templates resulted in narrow pore size distributions. Lu et al [19] trapped methacryloxypropyl groups into the silica matrix of xerogels. They showed that as long as the template ligand volume was kept below a critical percolation threshold, the secondary microporosity was inaccessible to N_2 . The amount of primary pores only accessible to CO_2 decreased with the amount of added organic ligands (covalently bonded templates). Lu's group also attempted to decrease the secondary pore size (around 5\AA) by using bridged templates with the form $(\text{RO})_3\text{-Si-R}'\text{-M}(\text{OR})_3$. Kim et al [20] prepared microporous silica membranes by reacting TEOS and methacryloxypropyltrimethoxysilane (MOTMS), where the later one controlled the pore structure formation in the region of pore size of 6\AA .

A number of research groups have used non-covalently bonded organic templates, such as C6- and C16-surfactants [7] and alkyltriethoxysilanes [8]. Tsai et al [7] claimed that by applying surfactants the flow resistance through the layers can be minimized, the

inherent support defects be overcome as well as that a narrow PSD can be attained. They used a C6-surfactant (triethyl-hexylammonium bromide) resulting in microporous ($d_p=10\text{--}12\text{ \AA}$) membranes with a high surface area ($575\text{ m}^2\cdot\text{g}^{-1}$). With an additional TEOS sol top layer with a pore size of about $3\text{--}4\text{ \AA}$, the membranes showed improved CO_2 flux of about $2\times 10^{-4}\text{ cm}^3\cdot\text{s}^{-1}\text{cm}^{-2}\text{cmHg}^{-1}$ and the CO_2/CH_4 separation factor around 200–600. However, by increasing the carbon chain from C6 to C16 (cetyltrimethylammonium bromide), the membrane performance could not be repeated. Yuan et al [21] used dodecyldimethylbenzylammonium chloride surfactants to achieve surface areas larger than $1000\text{ m}^2\cdot\text{g}^{-1}$ and uniform pore sizes around 10 \AA . Ayral et al [22] prepared silica membranes using TEOS and amphiphilic surfactants (Triton with varying polyoxyethylene chains). By increasing the chain length of the surfactants, the wider the PSD gets. This leads to poor performance as far as separation capabilities of membranes concern. On the other hand, surface area and porous volume increased which facilitates the transport of diffusing molecules through the membrane.

2.2.3 Hybrid materials

The synthesis of hybrid organic-inorganic membranes has been explored by various research groups, in particular to improve adsorption characteristics, pore size tailoring, surface area, and the reduction of membrane defects such as cracks and pin holes. In so-called hybrid materials, the chemical and thermal stability of the siloxane network is combined with the physical properties of the organic group. Therefore these materials prepared by the hydrolysis of organoalkoxysilanes (Baker) [18], silsesquioxanes, or bridged poly-silsesquioxanes have high specific surface areas, with pores between micro- and mesoporous, and a highly hydrophobic surface. Hence, these materials have the potential to be used as catalyst supports.

Yasuda et al [23] prepared silica-based hybrid membranes (i.e. amide groups) with H_2/CO_2 separation factor greater than 100 at 400°C for over 720 hours and a H_2 permeability of $10^{-7}\text{ molm}^{-2}\text{s}^{-1}\text{Pa}^{-1}$. Boury and Corriu [24] used $[\text{R}(\text{SiO}_{1.5})_n]$, with $n>2$ to control pore size between $4\text{--}20\text{ \AA}$, where the organic group was a dialkylene carbonate group. Despite the good results achieved, these xerogels were not tested for gas separation. Hybrid materials comprising of molecular sieve entities embedded in a polymer matrix offer the potential to combine the processibility of polymers with the superior gas separation properties of rigid molecular sieving materials. The challenges of these cross-linked polymers and

blends of molecular sieving domains in polymers are discussed by Koros and Mahajan [25].

2.2.4 Chemical vapor deposition (CVD) and other synthesis methods

Precursors for the CVD process are TEOS, phenyltriethoxysilane (PTES) or diphenyl-diethoxysilane (DPDES). The supports used are mostly Vycor glass or more recently α - and γ -alumina. The most recent properties achieved for CVD derived silica membranes are listed by Tsapatsis et al [26]. In average the achievable selectivity factor for H_2/N_2 vary between 30-1500 whereas the permeability reaches $2 \times 10^{-8} \text{ molm}^{-2}\text{s}^{-1}\text{Pa}^{-1}$. The CVD method has attracted a lot of attention for the synthesis of palladium-based composite membranes leading to a higher resistance towards embrittlement.

Microporous or dense silica membranes prepared by CVD have been mainly studied for selective hydrogen separations, but less commonly for other molecular sieve separations. The main research groups publishing in this area are Gavalas [27] and Morooka [28]. For the H_2 and water vapor separation, a silicon carbide-based membrane formed by CVD of triisopropylsilane showed good performance. The H_2 permeance tested between 50-400°C was $6 \times 10^{-7} \text{ molm}^{-2}\text{s}^{-1}\text{Pa}^{-1}$ and the H_2/H_2O selectivity 3-5 [29]. Sea et al [30] synthesized CVD membranes by placing the silica derived precursors inside the pores of α - and γ -alumina tubes resulting in hydrogen permeances around $3 \times 10^{-8} \text{ molm}^{-2}\text{s}^{-1}\text{Pa}^{-1}$ and a H_2/H_2O selectivity of 7.6 at 400°C.

So et al [31] combined sol-gel dip, soaking and vapor deposition (SVD) processes. First the silica membrane was formed through the sol-gel process. Then palladium particles were impregnated into the sol by using Pd-acetate as a Pd precursor. The membrane was stable up to temperatures of 400°C and pressures up to 280kPa. The selectivity increased with the number of layers prepared through SVD and at 150kPa the selectivity for H_2/N_2 was about 10 and the H_2 permeance about $5.8 \times 10^{-7} \text{ molm}^{-2}\text{s}^{-1}\text{Pa}^{-1}$. Doucoure et al [32] claimed that gas separation through mesoporous silica membranes, which they plasma-treated with C_4F_8 , CHF_3 and CF_3-CH_2F was dominated by the molecular sieving effect. Table 1 summarizes the permeance and selectivity data reviewed so far.

Table 1. Comparison of H₂ selective silica membranes prepared by different methods*.

Type of membrane	H ₂ permeance [molm ⁻² s ⁻¹ Pa ⁻¹]	Selectivity	Hydrothermal stability	Reference
• Pd impregnated alumina	3x10 ⁻⁶	9.86 H ₂ /N ₂	-	Lee ³³
• Pd SVD	3x10 ⁻⁸	11 H ₂ /N ₂		So ³¹
• CVD TEOS	0.89-9.8x10 ⁻⁸	>1000 H ₂ /N ₂	7% moisture no degradation	Yan ³⁴
• CVD TEOS	2x10 ⁻⁸	10-230 H ₂ /N ₂		Hwang ³⁵
• CVD	5.5x10 ⁻⁷	70-300 H ₂ /N ₂	-H ₂ -H ₂ O-HI	Sea ²⁹
TEOS,PTES,DPDES	0.34-2x10 ⁻⁸	12-72 H ₂ /N ₂		Wu ³⁶
• CVD SiO ₂	2x10 ⁻⁸	30-1500	per>60% lower in 2h	Tsapatsis ²⁶
• CVD SiO ₂	10 ⁻⁸			Gavalas ²⁷
• CVD Vycor	10 ⁻⁸	3000 H ₂ /N ₂		Morooka ²⁸
• thermal decomposition of TEOS	1.3x10 ⁻⁶	-	-very	Naito ⁹
• colloidal silica	2x10 ⁻⁶	70 H ₂ /CO ₂	hydrophobic	deVos ¹⁴
• sol-gel TEOS	1.5x10 ⁻⁶	40-200 H ₂ /CH ₄	-increased	Lange ¹³
• sol-gel TEOS	2x10 ⁻⁶	9-15 H ₂ /CO ₂	hydrophobicity	deVos ⁴
• adopted TEOS-MTES sol	1.5x10 ⁻⁶	10 H ₂ /N ₂	-	Tsai ⁷
		1265 H ₂ /CH ₄		
• C6 surfactant	1x10 ⁻⁷			Kusakabe ⁸
• sol-gel TEOS and alkyltriethoxysilanes	3.8x10 ⁻⁷	100 H ₂ /N ₂		Caro ³⁷
• silylated γ-alumina	4x10 ⁻⁷	3.5 H ₂ /N ₂		Kim ²⁰
• sol-gel TEOS+MOTMS	300 barrer	11-36 H ₂ /CO ₂		Doucoure ³²
• plasma treatment of mesoporous silica membrane	10 ⁻⁶	1.6CO ₂ /N ₂ 15 H ₂ /N ₂		Collins ³⁸
• Sol-gel				

*Unless mentioned else, the supports are α- or γ-alumina.

3 Hydrothermal stability and hydrophobicity -key areas of improvement

Hydrothermal stability of molecular sieve silica (MSS) materials is an area of increasing research interest, in particular for applications in catalysis, membrane reactors and membrane gas separation. In these applications, gas streams are likely to contain water vapour, which reacts with the hydrophilic sites in the silica thin films resulting in chemical and microstructural instability. Until now the importance of the hydrothermal stability for membranes has been mostly neglected and has been tested mainly for the supports of microporous membranes such as zirconia, alumina and titania membranes [39, 40, 41]. Gallaher [41] showed that γ-

alumina membranes had a hydrothermal stability under 90mol% steam up to 640°C. Nevertheless not much is reported on the testing of the hydrophobicity of microporous membranes.

Membrane supports have been modified, so that a hydrophilic top layer is combined with a hydrophobic support as reported by Caro et al [37]. The hydrophobic behavior was obtained through silylation or reaction of the γ -alumina layer with alacyl/aryl phosphoric acids. Silica undergoes densification above 800°C, but at temperatures around 600°C long-term permeation of helium and nitrogen showed no changes as investigated by Wu et al [36]. In contrast, when about 20mol% of water vapor is present structural densification occurred at temperatures above 300°C. This effect was shown to have a greater impact on the helium permeance within the first hours of exposure than the nitrogen permeance, suggesting closure of pores with $dp < 3.5 \text{ \AA}$.

3.1 Structural influences of water vapor on the membranes and xerogels

The interaction of water molecules with the silica surface depends on the type of the functional groups, which are mainly hydroxyl groups in the case of the silica materials. There are two types of silica surface hydroxyls, isolated hydroxyls and vicinal (geminal) hydroxyls [42]. The latter can form hydrogen bonds to each other and can retain water on the surface. Isolated hydroxyls do not hydrogen bond to water molecules (no infrared shift) and therefore contribute little to water adsorption. However, Lewis base compounds are preferentially adsorbed at these locations [43]. The vicinal hydroxyls can be destroyed by raising the calcination temperature and eliminating water at a temperature range of 450-800°C. The water uptake of a sample is controlled firstly by the hydroxylation state of the surface and secondly by the rate of water condensation to form multi-layers. The surface of freshly calcined samples may consist of siloxane and isolated silanols, which both have a hydrophobic character, and geminal silanols which are hydrophilic. However, once water molecules condense in the pores, the siloxane bonds might be hydrolysed resulting in silanol groups. The initial water adsorption most likely occurs at the geminal hydroxyl groups due to the strong chemisorption. Further water adsorption then takes place via hydrogen bonding.

Da Costa et al [6] used $[29\text{Si}]$ NMR results on sol-gel derived xerogels to show a high contribution of geminal silanols for high quality membranes. The advantage of silanol bonds is that they form weakly branched fractal systems, causing the collapse of the film structure and therefore resulting in low pore volume with molecular dimensions. The

disadvantage, however, is that geminal silanol groups are highly hydrophilic, they easily react with water molecules resulting in further changes in the matrix of xerogels. For instance, Fotou et al [39] reported complete densification of pure silica membranes at 800°C in a 50mol% steam atmosphere.

Table 2. [29] Si NMR spectra for xerogel samples calcined at 500°C [44].

Sample ID	Q ⁴ ; % area peak centre	Q ³ ; % area Peak centre	Q ² ; % area peak centre	T ³ ; % area peak centre	T ² ; % area peak centre
hydrophobic	53.7% -110.8	25.6% -102.0	2.27% -91.6	17.0% -63.0	1.4% -54.5
hydrophilic	28.2% -111.0	60.36% -101.8	11.42% -92.6	-	-

The [29] Si NMR spectra data of species Qⁿ and Tⁿ for a hydrophobic silica sample (molar ratio TEOS:EtOH:H₂O:HNO₃=1:3.8:5.0:0.004, and 4.2wt% C6 surfactant) and a hydrophilic one (molar ratio TEOS:EtOH:H₂O:HNO₃=1:3.8:5.0:0.004) are shown in Table 2. The peaks observed with chemical shifts in the region -90 to -120 ppm show the presence of Q², Q³ (silanols) and Q⁴ (siloxane bonds) species. The peaks with chemical shifts between -60 to -70 ppm are associated with Me(OH)₂Si-O-Si bonds. The latter peaks are referred to as T³, which are species bound by three Si-O-Si links and one carbon, while T² species are formed by two Si-O-Si links, one Si-OH and one carbon. It is observed that the contribution of uncondensed species (Q² and Q³) is higher for the hydrophilic sample than for the hydrophobic one. The contribution of fully condensed groups (Q⁴ species) is higher for the hydrophobic sample, which also has high percentage of methyl functional groups (T² and T³). As water does not attack the siloxane groups, the Q⁴ species are able to resist structural collapse. This point is clearly evidenced by the PSD determined by Giessler et al [44] before and after a hydro-treatment (see Figure 1). For the hydro-treatment the calcined xerogel samples were placed in a closed container at 75°C and a relative humidity of 96%. In previous water adsorption experiments with these xerogels it was shown that the water uptake and structure change occurs within the first few hours. Therefore the hydro-treatment was carried out for 50 hours. The results showed that the PSD of the hydro-treated xerogel derived by the surfactant method was similar to the non-hydrated sample. By the same token, the hydrophilic xerogel samples (derived by standard silica sols), which exhibit a high concentration of weakly branched systems (Q² and Q³ species), favoured further collapse of their structure and reduction in micropore surface area and pore volume. According to Brinker and

Scherer [15], Q^4 species form strongly branched fractal systems while Q^3 and Q^2 species form weakly branched fractal systems. Hence, Giessler and co-workers suggest that the Q^4 groups are responsible for maintaining to a large extent the integrity of the xerogel structure under hydro-treatment. Furthermore, Q^4 and methyl groups are responsible for enhancing the hydrophobicity.

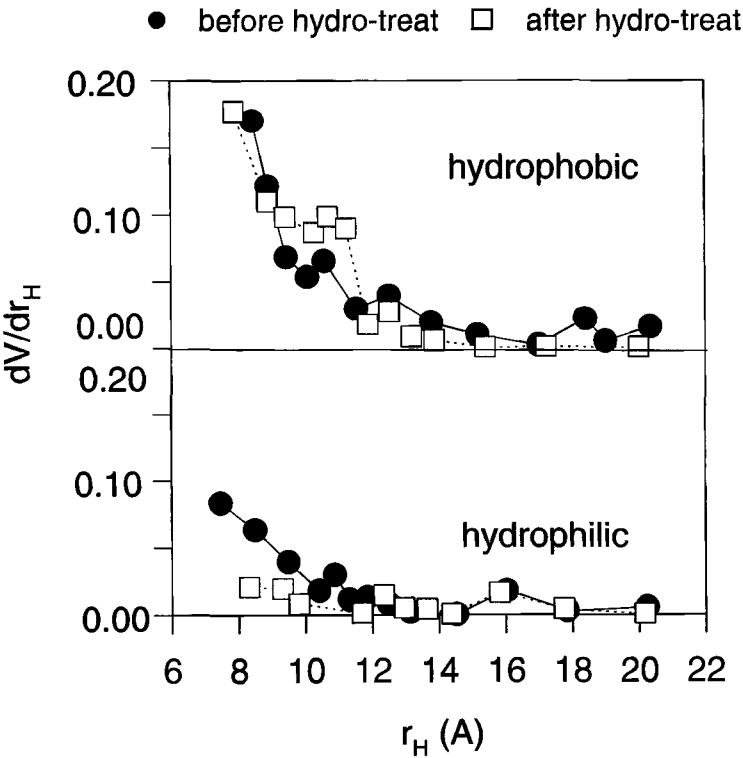


Figure 1. PSD before and after hydro treatment of a hydrophilic and hydrophobic silica sample [44].

3.2 Improvement of the thermal stability

Morooka et al [28] reported a temperature resistance of CVD derived silica membranes up to 650°C. The crystallization of amorphous silica membranes occurs at 874°C above which they are not usable anymore. The prolonged exposure of silica materials to humid air at temperatures higher than the calcination temperature of silica (400-500°C) causes rapid densification. Fotou et al [39] tried to increase the thermal stability by doping the starting silica sol with traces of Al_2O_3 or MgO nitrate salts. They reported that doping with alumina increased the thermal stability up to 600°C, whereas the magnesia-doped samples underwent a strong decrease in surface area. As magnesia is a network modifier it promoted sintering and densification, not like alumina which is a network former. In spite of the increased thermal stability, the pore size remained around 0.6nm.

The increase in thermal stability of sol-gel derived silica membranes was achieved by Yoshida et al [45] with the addition of zirconia. The membranes were tested for H_2 permeation. It was shown that the activation energy of gas permeation increased with increasing content of zirconia, which indicates membrane densification. In addition, Yoshida et al [45] also observed that another densification occurred under hydrothermal conditions which made the membranes unsuitable for N_2 permeation. Chai et al [46] prepared a microporous Al-based membrane through repeated dip-coating on a α -alumina support. The membranes were based on BaO- Al_2O_3 and La_2O_3 - Al_2O_3 layers prepared by the sol-gel process. The stability was reported to be up to 1100 °C. The raise in the phase transformation temperature of about 200°C was observed to be due to the addition of lanthanum as a pore structure stabilizer.

The doping of the silica network with titania is a method reported by Mariscal et al [47] resulting in xerogels consisting of oxides with high surface areas and pore size in the mesoporous range. This method suggested that the high surface area supports could be used as intermediate layers for membranes and catalysts. As the thermal expansion coefficient was constant over a wide range of temperatures, these materials are suitable for temperature dependent applications. Nevertheless these sols were not used for membrane synthesis and gas separation.

3.3 Methods to improve the hydrophobicity

3.3.1 Modified sols

De Vos et al [4] embedded MTES into a sol-gel process prepared with TEOS, water, ethanol and acid. This process introduced methyl groups to the silica matrix as template agents to enhance hydrophobicity. In contrast to the polymeric template route described above, the methyl groups of the MTES were not burned off as the calcination process was carried out under a nitrogen rich atmosphere. The membranes synthesized by this method showed good permeances while selectivities decreased due to a broader PSD compared with membranes prepared without MTES. The N_2 permeance was $7 \times 10^{-7} \text{ molm}^{-2}\text{s}^{-1}\text{Pa}^{-1}$ and the CO_2/O_2 permselectivity of 5. The resulting film structure showed a thickness for a double-silica layer of 60nm and an average pore diameter of 7Å. The preparation of a 50mol%TEOS/50mol%MTES membrane resulted in 10% increase in hydrophobicity, which is judged by comparing the hydrophobicity indices of the methylated sample and the standard silica material. Although the hydrophobicity index HI obtained by de Vos et al [4] (HI=3.0) were very good in terms of membrane performance, this area warrants further improvement as the hydrophobicity index HI for silicalite I (HI=10.3) is much higher.

Schwertfeger et al [48] prepared aerogels from various compositions of methyltrimethoxy-silane (MeTMOS e.g. MeSi(OMe)_3) or tetramethylorthosilicate (TMOS e.g. Si(OMe)_4) and analysed them in terms of hydrophobicity. They claimed that in order to increase the hydrophobicity significantly, the starting mixture for the base catalysed hydrolysis should contain 20mol% MeSi(OMe)_3 . Giessler et al [44] studied the hydrophobicity of three types of xerogels (see Table 3): (i) standard TEOS; (ii) modified TEOS plus MTES mixed at molar ratio 50/50; and (iii) modified TEOS plus C6-surfactant (tri-ethyl-hexylammonium bromide). They found that the surfactant xerogel, derived by the method of Tsai et al [7], was highly hydrophobic compared with the other xerogel samples as shown in Figure 2. The modified xerogels (ii and iii) resulted in up to 25% concentration of methyl functional groups (T^3 and T^2 species) resulting in hydrophobic xerogels. In terms of structural integrity and hydrophobicity, best results were also obtained with C6-surfactant xerogels. The results suggested that the surfactant enhanced condensation reactions, which led to structures with high contributions of Q^4 groups. In terms of improved hydrophobicity, increased surface area and smaller pore size, a mixture of the two modified

sols (ii and iii) seems to be a promising way as showed by Giessler et al [44]. The nitrogen adsorption results for these xerogels calcined at 500°C are depicted in Table 3. It is observed that the mixed sample, which incorporates the surfactant, has a higher surface area. The PSD is narrow compared to the MTES templated sample prepared using de Vos et al [4] method. The hydrophobicity of the mixed xerogel proved to be very high by water adsorption experiments.

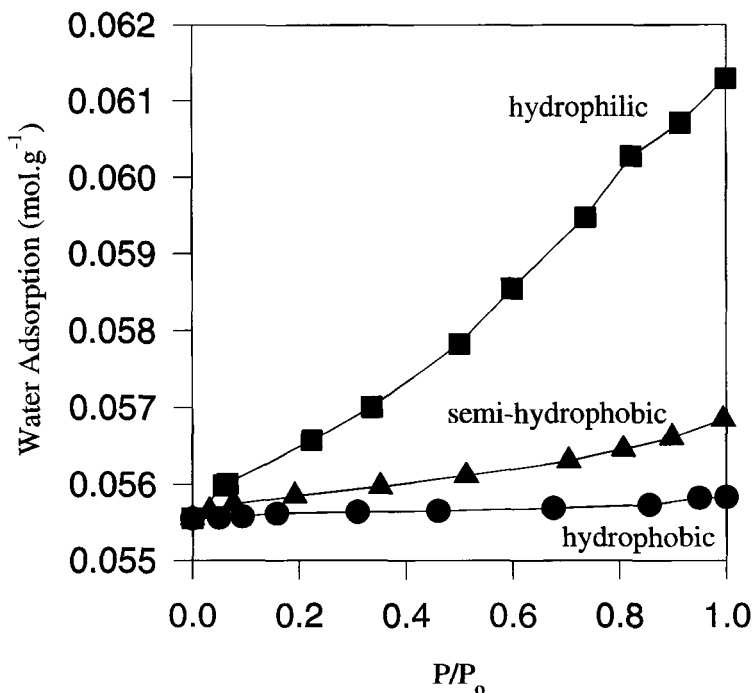


Figure 2. Water adsorption isotherms of methylated (hydrophobic and semi-hydrophobic samples) and non-methylated (hydrophilic) microporous silica samples [44].

A sol-gel method using fluoro-alkyl-alkoxysilane and TEOS also resulted in hydrophobic silica films as demonstrated by Nakagawa and Soga [49]. The films produced were temperature resistant up to 300°C. Hydrophobicity tests resulted in an unchanged water contact angle after 250h exposure to water vapor. Nevertheless the films were not tested for membrane preparation. As the applied silanes have a high critical diameter, the work reported by Kusakabe et al [8], which deals with the influence of the alkyl length of templates, should be considered in order to evaluate suitable chemicals for the synthesis of high quality membranes.

Composite films with crack-free and smooth surfaces were prepared by the sol-gel technique using branched chain polyfluoroalkylsilane and TEOS as starting materials [50]. It was found that these fluorosilane-containing films had thermal stability and surface energies as small as polytetrafluoroethylene (PTFE) up to 400°C. In this case, large hydrophobicity was resulted from the large contact angle of water as compared to films derived from methyltrimethoxysilane and TEOS. Wu et al [36] developed a CVD Si-based membrane for hydrogen permeation stable up to 600°C. A hydrothermal stability test showed that the membrane structure approached a new steady state immediately after exposing it to water vapor.

Table 3. Nitrogen adsorption results [44].

Sample ID	Micropore volume [cm ³ /g]	Spec. surface area [m ² /g]	Average pore radius [Å]	Total pore volume [cm ³ /g]
Standard (i)	0.153	350.20	8.9	0.161
Surfactant (iii)	0.297	662.75	8.9	0.298
De Vos (ii)	0.060	121.92	9.8	0.072
Mixed xerogel	0.064	248.21	9.5	0.1068

3.3.2 Silylation

One method of improving the hydrophobicity of a silica surface has been introduced by Takei et al [51]. They used the reaction of hexamethyldisilazane with the surface hydroxyl groups of silica glass in *n*-hexane. The decomposition of the trimethylsilyl (TMS) groups occurred at 400°C in air. It was observed that the thermal stability of the TMS groups was higher than that of alkoxy groups. However, the surface area decreased with an increase in the surface concentration of the TMS groups and even after the silylation water molecules could interact with the residual hydroxyl groups situated under the umbrellas of the TMS groups. Therefore an initial adsorption of water has been observed. The reduction of the pore radius of the porous silica glass by this surface modification has been around 0.44nm. The obtained mean pore size was around 1.8nm, which is outside the pore size range of microporous top layers necessary for gas separation applications.

Impens et al [52] reviewed the silylation of micro-meso- and non-porous oxides. They found that silanes and disilanes could be used to modify the pore channels in zeolites as pore sizes were reduced from 0.62nm to 0.35nm. If tetramethoxysilane as the silylation agent was used,

an external modification of the sample was attained. Wang et al [53] carried out a post-treatment of polydiethoxysiloxane by trimethylchlorosilane (TMCS) and dimethyl-dimethoxy-silane (DMMOS). The peak pore size shifted from 23.2 to 18.2 nm. They showed that the silylation with DMMOS which resulted in increased surface area, was more effective than using TMCS. This kind of post treatment is often applied for zeolitic molecular sieves such as MCM-41, where the average pore size is about 2nm after the silylation.

Prakash et al [54] prepared a standard silica sol with ammonium hydroxide ethanol. After gelation and aging at 50°C, the gel was washed in ethanol, followed by hexane, and derivatised with TMCS in hexane. The derivatised gel (methyl:Si=1:1.83) was then sonicated for 25min to create a sol slurry suitable for dip-coating. The thickness of the film they formed was analysed by ellipsometric imaging and was below 1 μm . As checked by [29] Si NMR, the film consisted of 60-70% of fully condensed species Q^4 , approximately up to 30% of Q^3 species. Further chemicals suitable for the organo-modification of silica for increasing the hydrophobicity as well as applications and procedures are given by Vansant et al [42].

4 Membrane Reactors

4.1 Applications

Many catalytic processes of industrial importance involve the combination of high temperature and chemically harsh environments, two factors that strongly favor inorganic membranes. As porous inorganic membranes are now becoming commercially available, there has been an immense surge of interest in this technology for use in catalysis. Economic factors also play an important role, particularly driven by the enormous payoff envisaged from using inorganic membrane reactors. In addition, inorganic membranes have the advantage of high H_2 permselectivity, ideal for fulfilling the increasing hydrogen demand in the refinery industry and for the fuel cell technology. Thus, they are optimal candidates for the large amount of H_2 applications including separation/reaction as discussed by Hsieh [66].

A review by Sirkar et al [81] showed the broad arrays of membranes in membrane reactors, ranging from biochemical through environmental to petrochemical applications. The membranes can be employed for the permeation of the products to shift equilibrium limitations or the distribution of reactants for the control of concentration of selected species, increasing reactor safety. Membranes with thin metallic layers have been

used so far for the permeation of the reaction products, though silica microporous membranes offer good separation qualities as shown in Table 1. An overview of catalytic reactors and configurations based on porous ceramic membranes is given by Coronas and Santamaria [82]. Some details of porous membranes application in catalysis are listed in Table 4.

There are two main types of inorganic membranes used in membrane reactors. Dense membranes made of palladium or its alloys, or porous membranes derived from silica or alumina. Regarding the design of membranes used in membrane reactors, Moon et al [90] found that an increase in selectivity at the expense of permeability could be validated. They claimed that this is valid only when the increase in selectivity is greater than that of the Peclet number (which indicates the ratio of the convective transport to the permeation rate through the membrane) in ratio. The flux of mass through membranes is inversely proportional to the thickness of membranes. Hence, the flux of permeate gases can be optimised by reducing the thickness of membranes. In the case of dense palladium membranes, thin films turn out to be very fragile while hydrogen diffusion depends on dissociation into atoms, which can be retarded by other components [91].

Prabhu et al [92] recently reviewed hydrogen selective ceramic membranes derived through various synthesis methods. They described the effect of water on the permeability and highlighted a new type of silica membrane prepared by the chemical vapor deposition (CVD) method, which showed 100% selectivity for H_2 with respect to CH_4 , CO and CO_2 . Using this membrane, the conversion for steam reforming could be increased above the equilibrium value. In addition, they emphasized that these membranes have a hydrothermal stability up to 10% H_2O at 600 °C for over 150 hours. Prabhu [92] pointed out that the introduction of membrane reactors in an industrial context is still dependent on membrane cost. Therefore, future research directions may be focussed on finding new membrane materials with high H_2 permeability and selectivity and manufacturing costs lower than those of palladium [91,93]. Tennison [102] analysed the area of membrane reactors and claimed that microporous membranes only would be financially viable if the production costs would be less than $\text{€}1000/\text{m}^2$. Therefore he suggested that, according to a list of publications for reactions considered so far, the direction and goals of research should be reviewed and refocused again.

Although Yildirim et al [100] stated that a high hydrogen permselectivity is a key factor in the reactor performance, there are also some advantages of having the membrane and catalyst as separate process units. Ross et al [94] showed through simulation that when re-circulation

is used in such a system, separation of a hydrogen-rich stream is the preferred option rather than a catalytic membrane reactor. Very detailed reviews are given by Saracco et al [95, 96], elucidating the potentials and problems still existing in regards to membrane reactors. They pointed out that a lot of progress has been done in the area of film formation and the formation of defect-free membrane films, whereas the areas of high-temperature sealing and scaling-up have been neglected. A categorization of membrane technologies for different types of reactions is given by Hsieh [66] and Zaman et al [86]. Hsieh especially focused on hydrogen consuming or generating reactions. A review highlighting the importance of the H_2 production in refineries is given by Armor [97], in particular directed towards the limitations of palladium and palladium alloys. The characteristics of ceramic membranes used in membrane reactors are described and discussed by Julbe et al [2].

Simulations showed that the conversion efficiency depends on the H_2 permeation through the membrane. Harold et al [98] reported that for the dehydrogenation of cyclohexane the membranes with very large separation factors, such as microporous membranes, exhibited a maximum in the conversion. They explained this effect by plotting the cyclohexane conversion against the ratio of the permeation to the reaction rate. The decrease in conversion was due to a loss of reactant from the feed side to the permeate side. In comparison to membranes with infinite separation factors they claimed that the combination of reasonable permeability and high selectivity makes sol-gel derived SiO_2 membranes an attractive candidate for equilibrium-shift applications. Harold et al [98] additionally listed all basic material properties for a number of reaction types suitable for the application in membrane reactor technology.

Table 4. Applications of porous membranes in gas vapor phase reactions.

Reaction	Type of membrane	Reference
• WGS	• Sol-gel silica	• Giessler ⁸³
• steam reforming of methane	• Composite alumina	• Minet ⁸⁴
• dehydrogenation of cyclohexane	• Composite alumina	• Okubo ⁸⁵
• dehydrogenation of ethane, butane	• Composite alumina	• Zaman ⁸⁶
• decomposition of hydrogen iodide	• silica membrane	• Collins ³⁸
• dehydrogenation of isobutene	• MFI microporous zeolithe	• Ciavarella ⁸⁷
• dehydrogenation of methanol	• Silica	• Ioannides ⁸⁸
• dehydrogenation of propane	• tubular CVI-silica membrane	• Weyten ⁸⁹

4.2 Comparison of various membrane reactors

In the literature, various comparisons of porous inorganic membranes and dense membranes have been carried out [3, 99, 100]. However, the comparison has been focused on porous membranes with a pore diameter of about 4nm. When comparing the performance of these porous membranes with Palladium membranes, e.g. in a membrane reactor for the steam reforming, dense membranes showed a better performance. These porous membranes have much lower permselectivities for H_2/CO_2 and H_2/N_2 than the MSS or CVD derived membranes described in this review because pore sizes of 4nm are too large to allow the membrane to have good separation capabilities. Criscuoli et al [93] claimed that the better performance of the palladium membrane was due not only to the selectivity but also the hydrogen permeation. However, Table 1 indicates that currently microporous silica membrane permeances are similar to one order of magnitude higher than Pd membranes. The gap in performance between palladium and silica membranes in the last decade is now slightly favouring silica membranes. In addition, several reactions can be carried out in a membrane reactor at lower temperatures compared to packed bed reactors. Therefore most of the suitable reactions for membrane reactors only demand temperatures between 160-400°C. This range of working temperature is ideal for silica membranes, in particular for feed streams containing H_2S or H_2O vapor. In contrast, Pd membranes are prone to poisoning and the H_2 permeability decreases when the feed contains CO [101], steam or H_2S^3 .

One clear example related to comparison between Pd and silica membranes is the work of Basile et al [99] and Giessler et al [83] for Water Gas Shift (WGS) reaction. Basile and co-workers prepared composite Pd membrane with a H_2 permeation of $6.25 \times 10^{-8} \text{ mol.s}^{-1}.\text{m}^{-2}.\text{Pa}^{-1}$ and a H_2/N_2 selectivity of 3. Using nitrogen as a sweep gas, the maximum conversion rate for the WGS reaction that they could obtain was 99.89%. At 300°C, a molar ratio of CO to H_2O equal to one with an optimum sweep flow, a 94% conversion of CO was reached. The MSS membranes of Giessler and co-workers had H_2/N_2 separation factors of 35 and H_2 permeances of $2.6 \times 10^{-7} \text{ mol.s}^{-1}.\text{m}^{-2}.\text{Pa}^{-1}$. Under the same experimental conditions as above-mentioned, it was possible to achieve CO conversions 98% for optimal sweep flow. These results suggest that the MSS membranes performed slightly better than the Pd-composite membrane.

Another problem still existing in the area of catalytic membrane reactors is the lack of real performance data. In particular data for reaction

conditions and the comparison of dense and porous membranes which so far only have been obtained by mathematical modelling [100, 103]. For the dehydrogenation of ethylbenzene to styrene, simulations presented by Burggraaf et al [76] showed that microporous silica membranes could achieve the same yield and conversion than palladium membranes. For the steam reforming of methane, Oklany et al [3] and Prabhu et al [104] modelled the behaviour of microporous silica membranes in various membrane reactor set-ups. Oklany et al [3] claimed that Pd/Ag membranes gave better performances than the silica membranes in terms of working parameters such as temperature, pressure, sweep gas ratio and membrane thickness, whereas the performance of the microporous membrane was better when steam has been used as a sweep gas. Godina [105] mentioned the possibility for microporous silica composite membranes to be applied in coal conversion processes where H_2 production is required.

Collins et al [38] applied and compared experimentally microporous silica-based membranes with palladium thin film membranes for the dehydrogenation of propane. They showed that the initial hydrogen permselectivity of the palladium membrane was higher (770) than that of the silica-membranes (15), even so the permeance has been of one order of magnitude lower. Nevertheless, with longer exposure to the reaction conditions the palladium membranes deactivated. In addition, Collins and co-workers observed a 10% increase in yield in the membrane reactor compared to the conventional packed-bed reactor. The same reaction has been examined by Weyten et al [89] using a tubular CVI-silica membrane with a H_2/N_2 selectivity of 84 at $500^\circ C$ and a hydrogen permeance of $1.4 \times 10^{-7} \text{ molm}^{-2} \text{Pa}^{-1} \text{s}^{-1}$. The propene yield was constant for 10h and twice as high as in the conventional reactor. The same authors conducted a further research by testing Pd/Ag membranes for the dehydrogenation [90]. These membranes showed better characteristics than the silica membranes and obtained the same yield than the silica ones even so the propane feed stream here ($\sim 105 \mu\text{mol/s}$) was six times higher than the optimal feed flow rate used with the CVI-silica membrane.

The good chemical stability of inorganic microporous silica membranes is advantageous in environments containing hydrogen iodide or hydrogen sulfide. Hwang et al [35] measured the hydrogen separation through a silica membrane, which showed a permeance of $6 \times 10^{-9} \text{ molm}^{-2} \text{Pa}^{-1} \text{s}^{-1}$ and 5-160 H_2/N_2 selectivity at $600^\circ C$. These membranes showed a good stability in a one-day exposure to a mixture of H_2 - H_2O -HI. Similar results were reported for a mixture of H_2 - H_2O -HBr. The permselectivity of H_2 to H_2O was reported to be one hundred [70].

5 Perspective and concluding remarks

The key issues associated with membrane and membrane reactors are generally known and current and future research efforts are and will be mainly to increase the hydrophobicity of aerogels/xerogels/films rather than testing these methods for membrane formation and further gas separation applications. The use of membrane reactors for industrial applications is potentially increasing, in particular for hydrogenation, dehydrogenation and fuel cell applications. However, scale up problems and costs are still the main limitations of this technology.

In recent years, mesoporous / microporous silica or alumina membranes have been extensively tested regarding their hydrophobicity characteristics. As these membranes had large pores, they performed quite poorly against palladium membranes. It is anticipated that silica membranes will become competitive against palladium membranes, especially when they are resisting to H_2S , CO and water vapour, while maintaining thermal stability up to 400°C and high selectivities and permeances. The employment of silica membranes in membrane reactors needs further research, to address industrial application concerns coupled with the need to acquire experimental data to validate computer simulations.

The hydrophobicity enhancement of molecular sieve silica membranes is an area that merits further research in tandem with permeation and permselectivity performance. This is an area where nanoscience and nanotechnology plays a vital role in further development of inorganic membrane. Of particular attention, covalently ligand templates such as CH_3 functional groups and C6 surfactants are showing great potential in achieving the design characteristics required for membrane reactors. There is a need to tailor materials with small pore sizes and narrow PSD while these materials should have high surface area and pore volume and hydrophobic properties. The resultant material will show high permeation and selectivities, and at the same time will be able to cope with harsh industrial conditions such as vapour, high temperature and pressures. In addition to this, transport studies with gas mixtures that contain water vapor have rarely been carried out. Therefore further studies of water vapor permeation and adsorption as well as the water vapor resistance of microporous samples at high temperature are very much desirable in future research in this area.

6 Acknowledgement

The authors would like to acknowledge the support from the Australia Research Council (IREX and ARC Large Grants) and the Alexander von Humboldt Foundation for the Feodor-Lynen Fellowship awarded to Sabine Giessler.

References

1. Criscuoli A., Basile A., Drioli E. and Loiacono O., An economic feasibility study for water gas shift membrane reactor, *J. Membr. Sci.* **181** (2001) p. 21.
2. Julbe A., Farrusseng D. and Guizard C., Porous ceramic membranes for catalytic reactors-overview and new ideas, *J. Membr. Sci.* **181** (2001) p. 3.
3. Oklany J. S., Hou K. and Hughes R. A., simulative comparison of dense and microporous membrane reactors for the steam reforming of methane, *Applied Catalysis A: General* **170** (1998) p. 13.
4. De Vos R., Maier W. F. and Verweij H., Hydrophobic silica membranes for gas separation, *J. Membr. Sci.* **158** (1999) p. 277.
5. Raman N. K. and Brinker C. J., Organic template approach to molecular sieving silica membranes, *J. Membr. Sci.* **105** (1995) p. 273.
6. Da Costa J. C. D., Lu G. Q. and Rudolph V., Characterisation of templated xerogels for molecular sieve application. *Colloids and Surfaces A: Physicochemical and Engineering Aspects.* **179** (2001) p. 243.
7. Tsai C., Tam S., Lu Y. and Brinker C. J., Dual-layer asymmetric microporous silica membranes, *J. Membr. Sci.* **169** (2000) p. 255.
8. Kusakabe K., Sakamoto S., Saie T. and Morooka S., Pore structure of silica membranes formed by a sol-gel technique using tetraethoxysilane and alkyltriethoxysilanes, *Separation and Purification Technology* **16** (1999), p. 139.
9. Naito M., Nakahira K., Fukuda Y., Mori H. and Tsubaki J., Process conditions on the preparation of supported microporous SiO₂ membranes by sol-gel modification techniques, *J. Membr. Sci.* **129** (1997) p. 263.
10. Tsuru T., Wada S., Izumi S. and Asaeda M., Silica-zirconia membranes for nanofiltration, *J. Membr. Sci.* **149** (1998) p. 127.
11. Chu L., Tejedor-Tejedor M. I. and Anderson M. A., Particulate sol-gel route for microporous silica gels, *Micropor. Mater.* **8** (1997) p. 207.
12. Nair B. N., Yamaguchi T., Okubo T., Suematsu H., Kaizer K. and Nakao S. I., Sol-gel synthesis of molecular sieving silica membranes, *J. Membr. Sci.* **135** (1997) p. 237.
13. De Lange R. S. A., Keizer K. and Burggraaf A. J., Analysis and theory of gas transport in microporous sol-gel derived ceramic membranes, *J. Membr. Sci.* **104** (1995) p. 81.
14. De Vos R. M., Verweij H., Improved performance of silica membranes for gas separation, *J. Membr. Sci.* **143** (1998) p. 37.
15. Brinker C. J. and Scherer G. W., Sol Gel Science: the physics and chemistry of the sol gel processing, *Academic Press: San Diego, USA*, 1990.
16. Buckley A. M., Greenblatt M., A comparison of the microstructural properties of silica aerogels and xerogels. *J. Non-Crystalline Solids* **143** (1992) p. 1.

17. Raman N. K., Anderson M. T. and Brinker C. J., Template-Based approaches to the preparation of amorphous, nanoporous silicas, *Chem. Mater.* **8** (1996) p. 1682.
18. Baker G. A., Pandey S., Maziarz E. P. and Bright F. V., Toward tailored xerogel composites: local dipolarity and nanosecond dynamics with binary composites derived from tetraethylorthosilane and ORMOSILs, oligomers or surfactants, *J. Sol-Gel Science and Technology* **15** (1999) p. 37.
19. Lu Y., Cao G., Kale R. P. and Prabakar S., Microporous silica prepared by organic templating: relationship between the molecular template and pore structure, *Chem. Mater.* **11** (1999) p. 1223.
20. Kim Y. S., Kusakabe K., Morooka S. and Yang S. M., Preparation of microporous silica membranes for gas separation, *Korean Journal of chemical Engineering* **18** (2001) p. 106.
21. Yuan Z.Y., Zhou W.Z. and Peng, L.M., Synthesis of microporous silica in the presence of dodecyldimethylbenzylammonium chloride surfactant, *Chemistry Letters* **10** (2000) p. 1150.
22. Ayril A., Balzer C., Dabadie T., Guizard C. and Julbe A., Sol-gel derived silica membranes with tailored microporous structures, *Catalysis Today* **25** (1995) p. 219.
23. Yasuda Y., Moritsuka H. and Izaki Y., Preparation and Evaluation of CO₂-permselective membrane for high temperature gas separation, *JSME International Journal, Series B* **41** (1998) p. 1012.
24. Boury B. and Corriu J. P., Adjusting the porosity of a silica-based hybrid material. *Adv. Mater.* **12** (2000) p. 989.
25. Koros W. J. and Mahajan R., Pushing the limits on possibilities for large scale gas separations: which strategies?, *J. Membr. Sci.* **175** (2000) p. 181.
26. Tsapatsis M., Gavalas G. R. and Xomeritakis G., Chemical Vapor Deposition Membranes, in *Recent advances in gas separation by microporous ceramic membranes*, edited by Kanellopoulos, N.K., Elsevier, Amsterdam, 2000.
27. Gavalas, G.; Megiris, C. E.; Nam, S. W. Deposition of H₂ permselective SiO₂-films, *Chem. Eng. Sci.* **44** (1989) p. 1829.
28. Morooka S., Yan S., Kusakabe K. and Akiyama Y., Formation of hydrogen-permselective SiO₂ membrane in macropores of α alumina support tube by thermal decomposition of TEOS, *J. Membr. Sci.* **101** (1995) p. 89.
29. Sea B. K., Ando K., Kusakabe K. and Morooka S., Separation of hydrogen from steam using a SiC-based membrane formed by chemical vapor deposition of triisopropylsilane, *J. Membr. Sci.* **146** (1998) p. 73.
30. Sea B. K., Watanabe M., Kusakabe K., Morooka S. and Kim S.S., Formation of hydrogen permselective silica membrane for elevated temperature hydrogen recovery from a mixture containing steam, *Gas. Sep. Purif.* **10** (1996) p. 187.
31. So J. H., Yang S. M. and Park S. B., Preparation of silica-alumina composite membranes for hydrogen separation by multi-step pore modifications, *J. Membr. Sci.* **147** (1998) p. 147.
32. Doucoure A., Guizard C., Durand J., Berjoan R. and Cot L., Plasma ploymerization of fluorinated monomers on mesoporous silica membranes and application to gas separation, *J. Membr. Sci.* **117** (1996) p. 143.
33. Lee S. J., Yang S. M. and Park S. B., Synthesis of palladium impregnated alumina membrane for hydrogen separation, *J. Membr. Sci.* **96** (1994) p. 223.
34. Yan S., Maeda H., Kusakabe K. and Morooka S., Thin palladium membrane formed in support pores by metal-organic chemical-vapor-deposition method and application to hydrogen separation, *Ind. Eng. Chem. Res.* **33** (1994) p. 2096.

35. Hwang G. J., Onuki K., Shimizu S. and Ohya H., Hydrogen separation in H₂-H₂O-HI gaseous mixture using the silica membrane prepared by chemical vapor deposition, *J. Membr. Sci.* **162** (1999) p. 83.
36. Wu J.C.S., Sabol H., Smith G.W., Flowers D.L. and Liu P. K. T., Characterization of hydrogen permselective microporous ceramic membranes, *J. Membr. Sci.* **96** (1994) p. 275.
37. Caro J., Noack M. and Koelsch P., Chemically modified ceramic membranes, *Microporous and Mesoporous Materials* **22** (1998) p. 321.
38. Collins J. P., Catalytic dehydrogenation of propane in hydrogen permselective membrane reactors, *Ind. Eng. Chem. Res.* **35** (1996) p. 4398.
39. Fotou G. P., Lin Y. S. and Pratsinis S. E., Hydrothermal stability of pure and modified microporous silica membranes, *J. Mater. Sci.* **30** (1995) p. 2803.
40. Chang C. H., Gopalan R. and Lin Y. S., A comparative study on thermal and hydrothermal stability of alumina, titania and zirconia membranes, *J. Membr. Sci.* **91** (1994) p. 27.
41. Vansant E. F., van der Voort P. and Vrancken K. C., Characterization and chemical modification of the silica surface, *Studies in Surface Science and Catalysis* Vol. 93, Elsevier, Amsterdam, 1995.
42. Gallaher G. R. and Liu P. K. T., Characterization of ceramic membranes I. Thermal and hydrothermal stabilities of commercial 40 μ m membranes, *J. Membr. Sci.* **92** (1994) p. 29.
43. Johnson R. E. and Ford D. I., in *Chemically modified surfaces*, (eds) Persek J. J. and Leigh I., The Royal Society of Chemistry, 1994.
44. Giessler S., Da Costa J. C. D. and Lu G. Q., Hydrophobicity of Templated Silica Xerogels for Molecular Sieving Applications, accepted in *Journal of Nanoscience and Nanotechnology* **2001**.
45. Yoshida K., Hirano Y., Fujii H., Tsuru T. and Asaeda M., Hydrothermal stability and performance of silica-zirconia membranes for hydrogen separation in hydrothermal conditions, *J. Chem. Eng. Japan* **34** (2001) p. 523.
46. Chai M., Machida M., Eguchi K. and Arai H., Preparation and characterization of sol-gel derived microporous membranes with high thermal stability, *J. Membr. Sci.* **96** (1994) p. 205.
47. Mariscal et al., Morphology and surface properties of titania-silica hydrophobic xerogels, *Langmuir* **16** (2000) p. 9460.
48. Schwertfeger F., Glaubitt W. and Schubert U., Hydrophobic aerogels from Si(OMe)₄/MeSi(OMe)₃ mixtures, *J. Non-Crystalline Solids* **145** (1992) p. 85.
49. Nakagawa T. and Soga M., A new method for fabricating water repellent silica films having high heat-resistance using the sol-gel method, *J. Non-Crystalline Solids* **260** (1999) p. 167.
50. Monde T., Fukube H., Nemoto F., Yoko T. and Konakahara T., Preparation and surface properties of silica-gel coating films containing branched-polyfluoroalkylsilane, *J. Non-Crystalline Solids* **246** (1999) p. 54.
51. Takei T., Yamazaki A., Watanabe T. and Chikazawa M., Water adsorption properties on porous silica glass surface modified by trimethylsilyl groups, *J. Colloid and Interface Sci.* **188** (1997) p. 409.
52. Impens N. R. E. N., van der Voort P. and Vansant E. F., Silylation of micro-, meso- and non-porous oxides: a review, *Microporous and Mesoporous Materials* **28** (1999) p. 217.

53. Wang J., Deng Z. S., Shen J. and Chen L. Y., Silylation of polydiethoxysiloxane derived silica aerogels, *J. Non-Crystalline Solids* **271** (2000) p. 100.
54. Prakash S. S., Brinker C. J., Hurd A. J. and Rao S. M., Silica aerogel films prepared at ambient pressure by using surface derivation to induce reversible drying shrinkage, *Nature* **374** (1995) p. 439.
55. Legrand A. P., The surface properties of silica; John Wiley: New York, 1998.
56. Muster T. H., Prestidge C. A. and Hayes R. A., Water adsorption kinetics and contact angles of silica particles, *Colloids and Surfaces A: Physicochemical and Engineering Aspects* **176** (2001) p. 253.
57. Riegel B., Hartmann I., Kiefer W., Gross J. and Fricke J., Raman spectroscopy on silica aerogels, *Journal of Non-Crystalline Solids* **211** (1997) p. 294.
58. Gregg S. J. and Sing K. S. W., *Adsorption, surface area and porosity*, 2nd Ed, Academic Press, New York, 1982.
59. Do D. D. and Do H. D., A model for water adsorption in activated carbon, *Carbon* **38** (2000) p. 767.
60. Malla P. B., Komarneni S. and Taguchi H., Probing the nature and the structure of pores in silica xerogels by water sorption: The tetramethyl-orthosilicate-hydrogen chloride/fluoride system, *J. Am. Ceram. Soc.* **74** (1991) p. 2988.
61. Burneau A., Lepage J. and Maurice G., Porous silica-water interactions. I. Structural and dimensional changes induced by water adsorption, *J. Non-Cryst. Solids* **217** (1997) p. 1.
62. Turov V. V., Chodorowski S. and Leboda R., Thermogravimetric and ¹H NMR spectroscopy studies of water on silicalites, *Colloids and Surfaces, A: Physicochemical and Engineering Aspects* **158** (1999) p. 363.
63. Rouquerol F., Rouquerol J. and Sing K., Adsorption by powders & porous solids, principles, methodology and applications, Academic press, London, 1999.
64. Llewellyn P., Characterisation of microporous materials by adsorption microcalorimetry, in Recent advances in gas separation by microporous ceramic membranes, edited by Kanellopoulos, N.K., Elsevier, Amsterdam, 2000.
65. Matsumoto A., Sasaki T., Nishimiya N. and Tsutsumi K., Evaluation of the hydrophobic properties of mesoporous FSM-16 by means of adsorption calorimetry, *Langmuir* **17** (2001) p. 47.
66. Hsieh H. P., Inorganic membranes for separation and reaction, Membrane Science and Technology Series, 3, Elsevier: Amsterdam 1996.
67. Bessarabov D.G., Membrane gas-separation technology in the petrochemical industry, *Membrane Technology* **107** (1999) p. 9.
68. Morooka S. and Kusakabe K., Inorganic membranes for gas separation at elevated temperatures, *Industrial Ceramics* **20** (2000) p. N1.
69. Soria R., Overview on industrial membranes, *Catalysis Today* **25** (1995) p. 285.
70. Morooka S. and Kusakabe K., Microporous inorganic membranes for gas separation, *MRS Bulletin* **3** (1999) p. 25.
71. Shelekhin A. B., Dixon A. G. and Ma Y. H., Theory of gas diffusion and permeation in inorganic molecular-sieve membranes, *AIChE J.* **41** (1995) p. 58.
72. Robeson L. M., Correlation of separation factor versus permeability for polymeric membranes, *J. Membr. Sci.* **62** (1991) p.165.
73. Freeman B. D., Basis of Permeability/Selectivity tradeoff relations in polymeric gas separation membranes, *Macromolecules* **32** (1999) p. 375.
74. Alentiev A.Y., Yampolskii Y. P., Free volume model and tradeoff relations of gas permeability and selectivity in glassy polymers, *J. Membr. Sci.* **165** (2000) p. 201.

75. Pandey P. and Chauhan R. S., Membranes for gas separation, *Progress in Polymer Science* **26** (2001) p. 853.
76. Burggraaf A. J. and Cot L., Fundamentals of inorganic membrane science and Technology, *Membrane Science and Technology Series 4*, Elsevier: Amsterdam, 1996.
77. Benes N., Nijmeijer A. and Verweij H., in *Membrane Science and Technology Series 6*, edited by Kanellopoulos, N.K., Elsevier, Amsterdam, 2000.
78. Barrer R. M., Porous crystal membranes, *J. Chem. Soc. Faraday Transaction* **86** (1990) p. 1123.
79. Uchtyl P., Schramm O. and Seidel-Morgenstern A., Influence of the transport direction on gas permeation in two-layer ceramic membranes, *J. Membr. Sci.* **170** (2000) p. 215.
80. Thomas S., Schaefer R., Caro J. and Seidel-Morgenstern A., Investigation of mass transfer through inorganic membranes with several layers, *Catalysis Today* **67** (2001) p. 205.
81. Sirkar K. K., Shanbhag P. V. and Kovaly A. S., Membrane in a reactor: a functional perspective, *Ind. Eng. Chem. Res.* **38** (1999) p. 3715.
82. Coronas J. and Santamaria J., Catalytic reactors based on porous ceramic membranes, *Catalysis Today* **51** (1999) p. 377.
83. Giessler S., Jordan L., Diniz da Costa J. C. and Lu G. Q., Performance of Hydrophobic and Hydrophilic Silica Membrane Reactor for the Water Gas Shift Reaction, *Sep. Pur. Tech.*, **32** (2003) p. 255.
84. Minet R. G. and Tsotsis T. T., U.S. Patent 4,981,676, 1991.
85. Okubo T. and Inoue H., Introduction of specific gas selectivity to porous glass membranes by treatment with tetraethylorthosilicate, *J. Membr. Sci.* **42** (1989) p. 109.
86. Zaman J. and Chakma A., Inorganic membrane reactors, *J. Membr. Sci.* **92** (1994) p. 1.
87. Ciavarella P., Casanave D., Moueddeb H., Miachon S., Fiaty K. and Dalmon J. A., Isobutane dehydrogenation in a membrane reactor; Influence of the operating conditions on the performance, *Catalysis Today*, **67** (2001) p. 177.
88. Ioannides T. and Gavalas G. R., Catalytic isobutane dehydrogenation in a dense silica membrane reactor, *J. Membr. Sci.* **77** (1993) p. 207.
89. Weyten H., Luyten J., Keizer K., Willems L. and Leysen R., Membrane performance: the key issues for dehydrogenation reactions in a catalytic membrane reactor, *Catalysis Today* **56** (2000) p. 3.
90. Moon W. S. and Park S. B., Design guide of a membrane for a membrane reactor in terms of permeability and selectivity, *J. Membr. Sci.* **170** (2000) p. 43.
91. Armor J. N., Membrane catalysis: where is it now, what needs to be done?, *Catalysis Today* **25** (1995) p. 199.
92. Prabhu A. K. and Oyama S. T., Highly hydrogen selective ceramic membranes: application to the transformation of greenhouse gases, *J. Membr. Sci.* **176** (2000) p. 233.
93. Criscuoli A., Basile A. and Drioli E., An analysis of the performance of membrane reactors for the water-gas shift reaction using gas feed mixtures, *Catalysis Today* **56** (2000) p. 53.
94. Ross J. R. H. and Xue E., Catalysis with membranes or catalytic membranes?, *Catalysis Today* **25** (1995) p. 291.
95. Saracco G. and Speechia V., Catalytic inorganic membrane-reactors present experience and future opportunities, *Catal. Rev. Sci. Engng.*, **36** (1994) p. 304.

96. Saracco G., Neomagus H. W. J. P., Versteeg G. F. and van Swaaij W. P. M., High-temperature membrane reactors: potentials and problems, *Chem. Eng. Sci.* **54** (1999) p. 1997.
97. Armor J. N., Applications of catalytic inorganic membrane reactors to refinery products, *J. Membr. Sci.* **147** (1998) p. 217.
98. Harold M. P., Catalysis with inorganic membranes, *MRS Bulletin* **19** (1994) p. 34.
99. Basile A., Criscuoli A., Santella F. and Drioli E., Membrane reactor for water gas shift reaction, *Gas. Sep. Purif.* **10** (1996) p. 243.
100. Yildirim Y., Gobina E. and Hughes R., An experimental evaluation of high-temperature composite membrane systems for propane dehydrogenation, *J. Membr. Sci.* **135** (1997) p. 107.
101. Li A., Liang W. and Hughes R., The effect of carbon monoxide and steam on the hydrogen permeability of a Pd/stainless steel membrane, *J. Membr. Sci.* **165** (2000) p. 135.
102. Tennison S., Current hurdles in the commercial development of inorganic membrane reactors, *Membrane Technology* **128** (2000) p. 4.
103. Schramm O. and Seidel-Morgenstern A., Comparing porous and dense membranes for the application in membrane reactors, *Chem. Eng. Sci.* **54** (1999) p. 1447.
104. Prabhu A. K., Liu A., Lovell L. G. and Oyama S. T., Modeling of the methane reforming reaction in hydrogen selective membrane reactors, *J. Membr. Sci.* **177** (2000) p. 83.
105. Gobina E., Multifunctionality in chemical reactors incorporating high-temperature membrane technology, *Membrane Technology* **86** (1997) p. 8.

SYNTHESIS AND CHARACTERIZATION OF CARBON NANOTUBES FOR HYDROGEN STORAGE

HUI-MING CHENG, CHANG LIU, FENG LI AND HAI-TAO FANG

Shenyang National Laboratory for Materials Science, Institute of Metal Research

Chinese Academy of Sciences, 72 Wenhua Road, Shenyang 110016, CHINA

Email: cheng@imr.ac.cn

QUAN-HONG YANG

Institute of Multidisciplinary Research for Advanced Materials, Tohoku University

Katahira, Sendai 980-8577, JAPAN

Hydrogen is a clean and renewable energy carrier, and in the 21st century it is expected to progressively replace the existing fossil fuels that are quickly depleted and cause heavy environmental problems. One of the potential uses of hydrogen lies in zero-emission vehicles powered by a proton exchange membrane fuel cell stack. However, the most serious barrier to achieve this goal is the development of feasible onboard hydrogen storage systems. The discovery of high hydrogen storage capacity of carbon nanotubes makes an onboard hydrogen storage system based on carbon nanotubes very promising. In this chapter, the basics and unique properties of carbon nanotubes are firstly introduced, and the development of synthesis technologies of this novel material is summarized. Then the unique pore and surface structures of carbon nanotubes are evaluated, and finally the experimental and theoretical investigations on the hydrogen storage behaviour of carbon nanotubes are reviewed. Carbon nanotubes are a novel nanoporous material with inner cavities, interstitial pores between single-walled nanotubes in a bundle, aggregated pores among nanotube bundles and among multi-walled carbon nanotubes, and "carbon island" structure in large diameter multi-walled carbon nanotubes. Some experimental results and theoretical predictions show that hydrogen can be effectively adsorbed in carbon nanotubes and after suitable pretreatment, carbon nanotubes may achieve a hydrogen storage capacity higher than 6.5 wt% and 63 kgH₂/m³. Nevertheless, efforts have to be made to reproduce and verify the hydrogen storage capacity of carbon nanotubes both theoretically and experimentally, to investigate their volumetric capacity and cycling characteristics, to elucidate their adsorption/desorption dynamics, kinetics and mechanism, and finally to clarify the feasibility of carbon nanotubes as a practical onboard hydrogen storage material.

1 Introduction

The start of a new millennium presents human beings with countless opportunities and challenges. On one hand, the ever-fast progresses of science and technology accelerate the development of world economy and culture, and as a result, rapidly bring many of us a higher living standard. On the other hand, our world is facing a rapid depletion of natural resources and serious global environmental pollution, mostly due to the overuse of fossil fuels. Nowadays, public concern about the global environmental problems caused by the utilization of fossil fuels and the over-dependence of the economy on fossil fuels is increasing, and many countries including USA, European Union, Japan, China, etc., are funding in an increasing budget year by year for the searches of possible alternative energy sources to replace fossil fuels.

There are quite a number of primary non-fossil-fuel energy sources available, such as thermonuclear energy, solar energy, wind energy, hydropower, geothermal energy, etc. In contrast to fossil fuels, these new primary energy sources cannot be directly used in many cases (e.g. used as fuels for transportation). Thus they must be converted into a form that can be easily transported and diversified. That is to say, an energy carrier is needed. Among a few choices, hydrogen is one of the best candidates. Hydrogen is an ideal fuel and versatile energy carrier, and its advantages are summarized as below [1,2]:

- (a) Easy to produce;
- (b) Convenient fuel for transportation;
- (c) Versatile, converts easily to other energy forms at the user end;
- (d) High utilization efficiency;
- (e) Environmentally compatible (zero- or low-emission).

Presently, hydrogen can be produced not only from fossil fuels, such as coal and natural gas, but also from wind, solar, hydroelectric, biomass or municipal solid wastes without consumption of non-renewable resources. Therefore, hydrogen provides the best route to a sustainable energy world, and in particular, for transportation sector and some other mobile uses.

In order to decrease the air pollution in metropolitan areas, the most important and urgent application of hydrogen is connected with transportation and automobiles. Hydrogen-powered vehicles can be

realized with power from:

- (1) Metal-hydride battery in which hydrogen is combined with metals as a metal hydride;
- (2) A spark-ignition engine in which hydrogen is combusted; and
- (3) A fuel cell stack burning pure hydrogen chemically.

In the last case, hydrogen can be converted to electricity with emission of only water at a very high efficiency because the process is not subjected to the limitation of the Carnot Cycle. Thus true zero-emission vehicles can be produced. However, several barriers have to be overcome before hydrogen electric vehicles can be put into large-scale practical utilization. One of the most severe challenges is the lack of a safe and efficient onboard storage technology, which may dramatically influence the vehicle's cost, range, performance, and fuel economy, as well as the scale, investment requirements, energy use, and potential emissions of a hydrogen-refueling infrastructure. This indicates that the development of onboard storage technologies will directly determine the schedule and speed of hydrogen-powered vehicles into market.

The US Department of Energy (DOE) Hydrogen Plan has set a benchmark for the amount of reversible hydrogen adsorption in a fuel cell vehicle. The benchmark requires a system-weight efficiency (the ratio of stored hydrogen weight to system weight) of 6.5 wt% hydrogen and a volumetric density of $63 \text{ kg H}_2/\text{m}^3$, since a vehicle powered by a fuel cell stack would require more than 3.1 kg of hydrogen for a normal 500 km driving range [3].

In hydrogen fuel cell-driven concept vehicles proposed by major automobile manufacturers, three technologies for storing hydrogen fuel are currently considered:

- (1) Cryogenic liquid hydrogen (LH_2) storage;
- (2) Ultra-high pressured hydrogen gas (PH_2) storage; and
- (3) Metal hydride (MH_2) storage technology.

However, these three technologies not only cannot reach the benchmarks just mentioned, but also have some significant disadvantages. Liquefying hydrogen wastes at least 1/3 of the stored energy of LH_2 itself, and the LH_2 storage also suffers from significant hydrogen loss due to vaporization. The hydride-based approach suffers from weight and cost

concerns, and the crucial issues connected with the PH_2 storage are tank volume limitation and safety. In fact, about twenty years ago some scientists turned their eyes to hydrogen adsorption in carbonaceous materials with high surface area [4-6], hoping that the inclusion of porous carbon materials in a hydrogen storage tank can enhance the overall hydrogen storage density by physisorption under certain pressure and temperature conditions. In the past ten years, great advances have been made and 3-6 wt% hydrogen adsorption capacities can be obtained for high surface area activated carbons at cryogenic temperatures of liquid nitrogen or lower [7-8], but at ambient temperature, activated carbons have very low hydrogen adsorption capacity. More recently, tremendous interests have been aroused by the discovery [3] and reproduction [9-13] of the high hydrogen storage capacity of a novel nanoporous carbon material---carbon nanotubes.

2 Construction, Structure and Unique Properties of Carbon Nanotubes

2.1 Construction and structure

In 1991, Dr. S. Iijima at NEC Fundamental Research Laboratory of Japan found a needle-like carbeneous substance that was 4-30 nm in diameter and up to 1 micron in length, and showed a hollow core under high-resolution transmission electron microscope (HRTEM) [14]. This needle-like substance is a new form of carbon named carbon nanotubes (CNTs). CNTs can be generally classified as multi-walled carbon nanotubes (MWNTs) and single-walled carbon nanotubes (SWNTs), depending on the layers of carbon atoms that make up of the tube walls. SWNTs were discovered in 1993 by Iijima *et al.* and Bethune *et al.* independently almost at the same time [15, 16], and a SWNT is defined by a cylindrical graphene sheet with a diameter of about 0.4 to 3.0 nm and a length of several hundred nanometers to tens of microns, respectively.

A SWNT can be imagined to be a seamless hollow tube that is rolled up from a two dimensional (2D) graphene sheet (Figure 1).

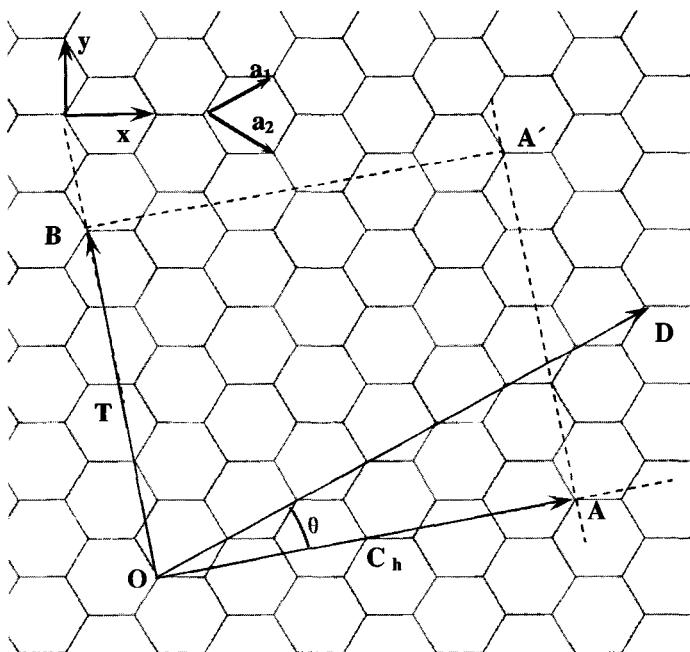


Figure 1. Construction of a SWNT from a 2D graphene sheet

Supposing that we roll the square “OAA'B” (see Figure 1) into a cylinder along vector \overrightarrow{OA} , we obtain a SWNT without caps. The vector \overrightarrow{OA} can be expressed as:

$$\overrightarrow{OA} = m\overrightarrow{a_1} + n\overrightarrow{a_2} \quad (1)$$

Where \mathbf{a}_1 and \mathbf{a}_2 are unit vectors in the two dimensional hexagonal lattice, and m and n are integers. Depending on how the graphene sheet is rolled up, or their chiral angle, which denotes the orientation of the hexagons of the nanotube with respect to the nanotube axis, SWNTs can be defined as armchair, zigzag, or chiral [17]. When $m=0$ or $n=0$, the chiral angle of the SWNT is zero, and the SWNT is defined as “Zigzag”; when $m=n$, the chiral angle is 30° , and the SWNT is defined as “Armchair”; In other cases, the SWNT is defined as “Chiral”. In Figure 2 [17], we show a schematic diagram of the molecular structures of the above three kinds of SWNTs. These hollow cylinders can be capped with half a fullerene molecule at each end. The diameter d and chiral angle θ of a SWNT can be expressed with m and n as follows:

$$d = \frac{\sqrt{3}d_{c-c}}{\pi} \sqrt{m^2 + mn + n^2} \quad (2)$$

$$\theta = \arccos \left(\frac{2m + n}{2\sqrt{m^2 + mn + n^2}} \right) \quad (3)$$

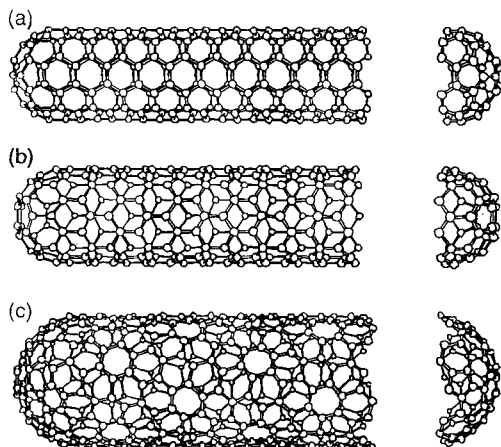


Figure 2. Schematic diagram of the molecular structures of single-walled carbon nanotubes. (a) Armchair, (b) Zigzag, (c) Chiral [17]

As classified above, there are two kinds of CNTs: MWNTs and SWNTs. MWNTs consist of more than two coaxial nanotubes of carbon with a structure similar to a Russian Doll. Transmission electron microscopic (TEM) image obtained from a SWNT or a MWNT is pair(s) of dark lines representing a longitudinal slice of tubes, as shown in Figure 3 [18]. The number of pairs of lines corresponds to the number of graphene sheets constructing the tube, and the distance between two adjacent straight lines corresponds to the (002) spacing of two graphitic sheets (normally 0.34 nm, a little larger than the ideal (002) spacing of a single crystal graphite).

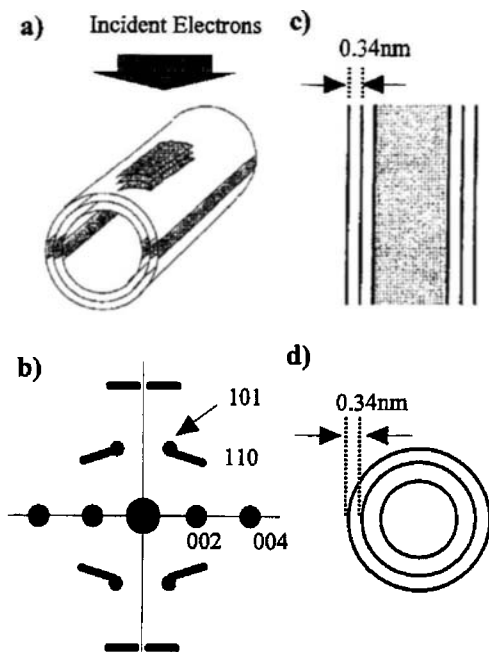


Figure 3. (a) Geometrical relationship between incident electron beams in TEM and a CNT, (b) typical transmission electron diffraction (TED) pattern, (c) schematic illustration of the image of a CNT, and (d) cross-sectional view of the CNT. In the TED pattern, the indexes follow those of graphite [18].

2.2 Main properties and promising applications

Theoretical studies indicate that the physical and chemical properties of SWNTs are directly related to their structures. For example, when $n=m$ or $2n+m=3k$ (k is integer), the SWNT is metallic; in other cases, the SWNT is semi-conducting [19-21]. In 1998, this prediction was experimentally confirmed by two groups with scanning tunnelling microscopy (STM) and scanning tunnelling spectroscopy (STS) [22, 23].

Since the C-C covalent bond is very strong and CNTs have few structural defects, it has been predicted that CNTs possess very high tensile strength and Young's modulus. Theoretical studies show that the Young's modulus of SWNTs is at least 1 TPa [24], much higher than that of conventional carbon fibres. Combining with low density, the specific

tensile strength of SWNTs can be about 100 times that of steel. Unlike brittle carbon fibres, CNTs have high bending strength, because their hexagonal network can partly transform into pentagons and heptagons to release the exerted stress [25]. Because of their high specific strength and large aspect ratio, CNTs are expected to be an ideal reinforcement, and are considered to be the only candidate for the construction of the cable of space elevators [26]. Furthermore, CNTs not only have very thin diameters, high strength and good toughness, but also possess high electrical conductivity, therefore they can be used as the probe of scanning probe microscopy (SPM), showing the advantages of higher resolution and longer lifetime [27].

The unique electronic properties of CNTs are due to the quantum confinement of electrons normal to the nanotube axis, since electrons can only propagate along the nanotube axis. Theoretical predictions show that about one-third of SWNTs are metallic, while the rest are semi-conducting [19-21]. Because of their remarkable electronic property and nano-scale dimension, CNTs are promising for the fabrication of various nanodevices. For instance, Tans *et al.* fabricated a field-effect transistor (FET) based on a semi-conducting SWNT that could operate at room temperature [28]. Room-temperature single-electron transistors within individual metallic SWNT molecules, logic circuits with CNT transistors, chemical sensors based on individual SWNTs, concept of CNT-based non-volatile random access memory for molecular computing, and entire arrays of nanoscale field-effect transistors based solely on the fraction of semi-conducting SWNTs were successfully developed [29-32].

CNTs can also be used as electrodes of supercapacitors [33] and electromechanical actuators [34]. A supercapacitor has the advantages of high specific capacitance and high power density compared to conventional capacitors and batteries. They can be used in hybrid power sources for electric vehicles, providing rapid acceleration and storing braking energy electrically. SWNT actuators function at only a few volts, much lower than that needed for piezoelectric stacks and electro-strictive actuators.

CNTs are excellent field emitters, owing to their nano-scale radius, physical and chemical stability, and good electrical conductivity [35]. A CNT field emitter has the advantages of low threshold electric field, large

emission current density and good emission stability. Therefore, CNTs have a bright application prospect in field emission flat panel displays, cathode-ray tube (CRT) type lighting-elements, gas discharge tubes providing surge protection, and X-ray generators.

Furthermore, CNTs have unique pore and surface structures and exhibit unique adsorption/absorption behaviours, such as high hydrogen adsorption capability, which will be the main subject discussed in the following sections. In a summary, the most promising application fields of carbon nanotubes are listed in Table 1.

3 Synthesis of Carbon Nanotubes

3.1 General classification

With the endless efforts of scientists for more than ten years, many methods and techniques have been developed to synthesize carbon nanotubes. The main methods and techniques developed can be classified into two categories:

- (1) Carbon vaporization method, including electric arc discharge[14], laser ablation[36], plasma ablation, solar energy vaporization, etc. The common characteristic of these methods is to prepare CNTs through vaporizing pure carbon or carbon-rich raw materials such as artificial and natural graphite or different types of coals with or without transition metal catalysts at very high temperature and different atmospheres.
- (2) Catalytic vapour decomposition of hydrocarbons and metallo-organic compounds. In this category, catalysts such as Fe, Co, Ni and rare-earth metals have to be applied. This technology is the most active and effective one, and it can be used for the synthesis of various kinds of CNTs such as SWNTs, MWNTs, and aligned MWNT arrays. Moreover, many techniques have been developed according to the different deposition space and position of CNTs (substrate method, floating catalyst method, *in-situ* catalysis method, micropore template method, fluid bed method, etc.) and different heating sources (plasma injection vapour deposition, plasma-enhanced chemical vapour deposition, etc.).

Among all these techniques, the laser ablation method, arc discharge method and catalytic vapour decomposition method are most important and widely investigated. At present, MWNTs can be synthesized in a quite large scale and with high quality, but the large-scale, low cost and controllable synthesis of SWNTs still remains a great challenge.

Table 1. The most promising application fields of carbon nanotubes

Scale	Fields	Promising applications
Nanotechnology	Nano-fabrication and nano-detection	Probes for SPM, templates for nanomaterials, nano-pumps, nano-channels, nano-tweezers, nano-gears and parts for nano-machines, etc.
	Electronic materials and devices	Nano-transistors, nanowires, molecular switches, memory devices, digital logic circuits, etc.
	Bio-technology	Injection devices, bio-sensors, nano-capsules, etc.
	Chemistry	Nanochemistry, nano-reactors, chemical sensors, etc.
Macrotechnology	Composite materials	Reinforcements for polymer, metallic, ceramic and carbon composites, conductive composites, electromagnetic shielding materials, wave-absorbing materials, etc.
	Electrode materials	Supercapacitors, lithium ion batteries, etc.
	Electron sources	Field emitters, flat display panels, cold cathode X-ray tubes, etc.
	Energy	Materials for hydrogen storage in gas phase or in electrochemical state, and for CH ₄ gas storage, etc.
	Chemistry	Catalyst and catalyst supports, etc.

3.2 Electric arc discharge method

CNTs were first synthesized by Iijima in 1991 by an electric arc discharge method, and the obtained MWNTs were 4-30 nm in diameter, up to 1 micron in length [14]. In 1992, Ebbesen and Ajayan [37] reported the mass synthesis of MWNTs with high purity in gram quantities by a modification of the conventional electric arc discharge technique for preparing fullerenes in a helium atmosphere. In 1993, Iijima *et al.* [15] and Bethune *et al.* [16] synthesized SWNTs by the electric arc discharge method independently, where they used iron and cobalt, respectively, as the catalyst. It should be noted that a metallic catalyst is necessary for the growth of SWNTs by the arc discharge method, while not for MWNTs. In 1997, Journet *et al.* used Y and Ni as co-catalyst and obtained SWNTs in a much higher yield and purity [38]. In 1999, Liu *et al.* developed a semi-continuous hydrogen arc discharge method for the synthesis of SWNTs [39, 40]. They displaced helium [16] and argon [15] inert gas with hydrogen as the buffer gas in the arc discharge chamber as shown in Figure 4, and succeeded in growing SWNTs with large diameter (Figure 5). Both HRTEM observations and resonant Raman measurements proved the existence of larger diameter SWNTs (1.6~2.0 nm). Meanwhile, high-resolution nitrogen adsorption measurements showed that the sample has abundant micropores with size similar to the nanotube diameter, indicating much more open tubes [41]. In 2000, they further developed a hydrogen/argon arc discharge method, and well-aligned freestanding SWNT ropes with length up to 20 cm were successfully prepared (Figure 6) [42]. The diameters of these ropes range from tens of micrometers to about 100 micrometers.

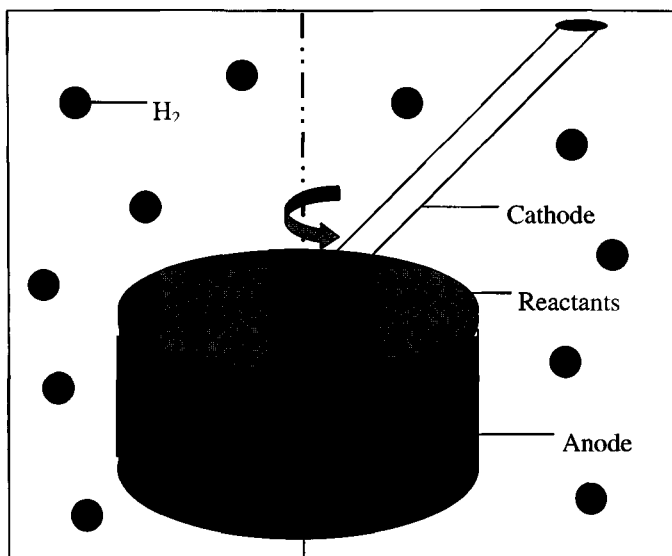


Figure 4. Schematic diagram of the apparatus used for the synthesis of SWNTs by the semi-continuous hydrogen arc discharge method [39].

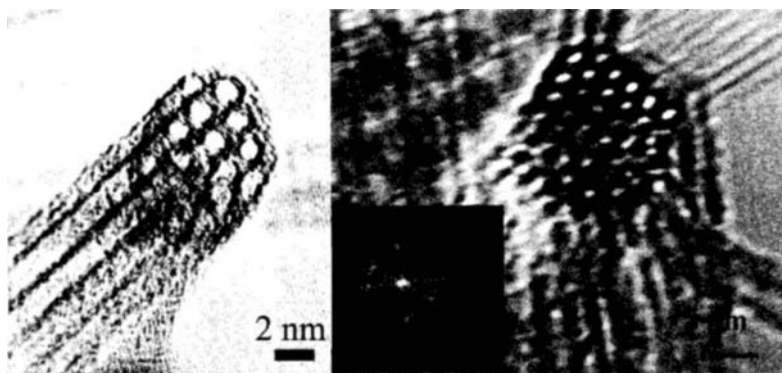


Figure 5. HRTEM images of the ends of SWNT bundles, showing the closely-packed individual SWNTs.

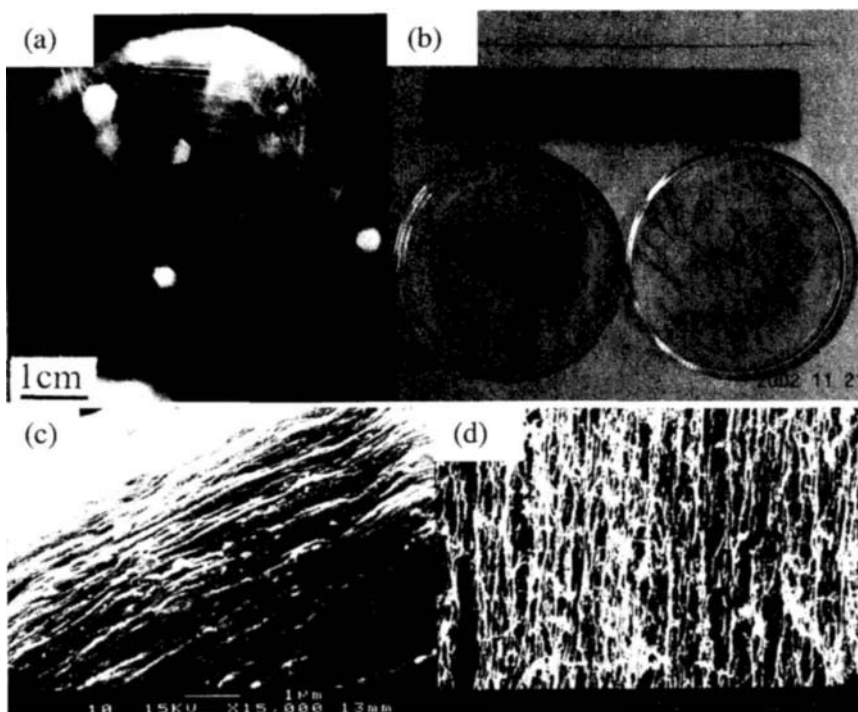


Figure 6. Optical images of the growing SWNT ropes (a and b), which can be up to 200 mm long and their SEM images (c and d) showing the sound alignment of SWNT bundles [43].

Huang *et al.* [43] also modified the conventional arc discharge method, and achieved the large-scale rooted growth of aligned super bundles of SWNTs. They used a bowl-shaped cathode directing the arc plasma in a specified direction and a combination of cobalt, nickel, iron and cerium as an efficient catalyst, with sulphur as a promoter and tin as a nanowelding element. In addition, Kiang *et al.* prepared SWNTs with different diameters by introducing different growth promoters such as S, Y, Bi or Pb-containing compounds [44]. More recently, Zhong *et al.* [45] synthesized SWNTs with higher purity and yield by the hydrogen arc discharge method using MWNTs and carbon nanofibres (CNFs) as carbon feedstock instead of graphite powder.

3.3 Laser ablation method

Laser ablation is another important technique to prepare SWNTs with structural perfection in high yield. In fact, the first achievement of the large-scale synthesis of SWNTs was realized using this method in 1996 [36]. The SWNTs with a mean diameter of 1.38 nm were produced, mostly in form of ropes consisting of tens of individual nanotubes closely packed into hexagonal crystals via van der Waals interactions (Figure 7) [36]. Because of their high quality and relatively large quantity, these samples have been regarded as good touchstone to prove many theoretical predictions. The typical mean diameter of the SWNTs synthesized from laser ablation is ~ 1.2 – 1.5 nm. Laser vaporization of carbon doped with Pd or Rh was reported to produce smaller diameter nanotubes [46], and Lebedkin *et al.* [47] prepared SWNTs with large diameter up to 6 nm by the pulsed laser vaporization of carbon rods doped with Co, Ni and FeS in an atmosphere of Ar and H₂.

3.4 Catalytic vapour decomposition of hydrocarbons

This method can be used to prepare vapour-grown carbon nanofibres (VGCNFs) [48], MWNTs [49], and SWNTs [50–52]. At present, the mass production of MWNTs at kilograms even to ton level has been achieved. The general process is to make hydrocarbon vapours decomposed at high temperature (e.g., 873 K–1473 K) with the presence of nano-sized metal catalysts (e.g. Fe, Co, Ni).

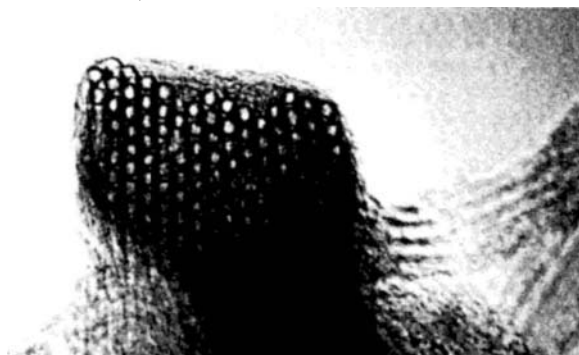


Figure 7. HRTEM image shows that each rope contains a bundle of SWNTs with diameter of about 1.4 nm, arranged in a triangular lattice (with lattice constant 1.7 nm) [36].

Cheng *et al.* prepared high quality MWNTs of different diameters by adjusting the processing parameters using a floating catalyst method, as shown in Figure 8. In their method, benzene was used as carbon feedstock, hydrogen as carrier gas, ferrocene as catalyst precursor and thiophene as growth promoter. Cheng *et al.* and Kong *et al.* succeeded in synthesizing SWNTs by this method with floating catalysts (floating catalyst technique) [50,51] and supported catalysts (substrate technique) [52], respectively. The prepared SWNT ropes by the catalytic decomposition of benzene at temperatures of 1373-1473 K using the improved floating catalyst method are shown in Figure 9. The SWNTs have relatively large diameter centered at 1.7 nm, and it was predicted that the large-diameter SWNTs possibly are a good gas storage material [51].

Many groups have been endeavouring to investigate different catalysts (including the support and promoter) [53, 54] and carbon sources (including different hydrocarbons and other carbon-containing compounds such as CO) [53-58] for the fabrication of CNTs. SWNTs, double-walled carbon nanotubes (DWNTs) and MWNTs with different diameters and macroscopic morphologies have been prepared, and in particular, many advances in the controllable growth of CNTs have been made.

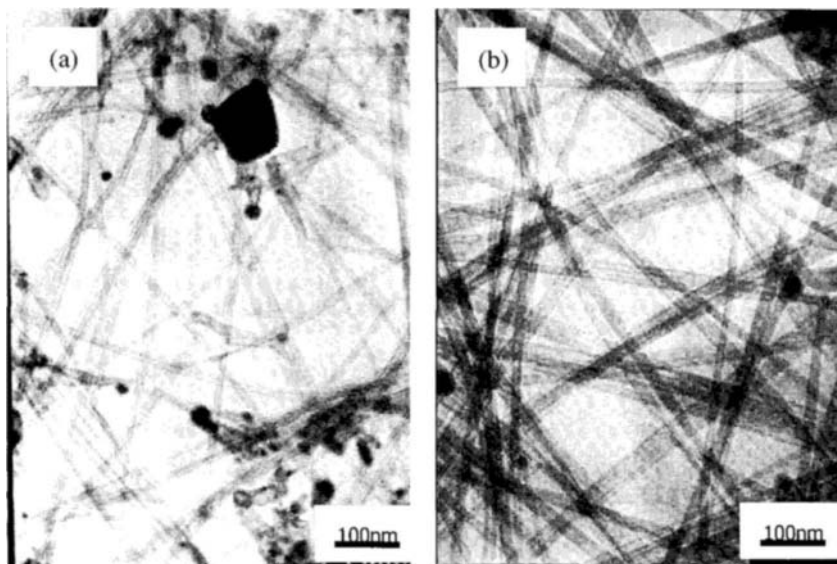


Figure 8. TEM images of MWNTs with average diameter of 7 nm (a) and 13 nm (b) obtained from the floating catalyst method.

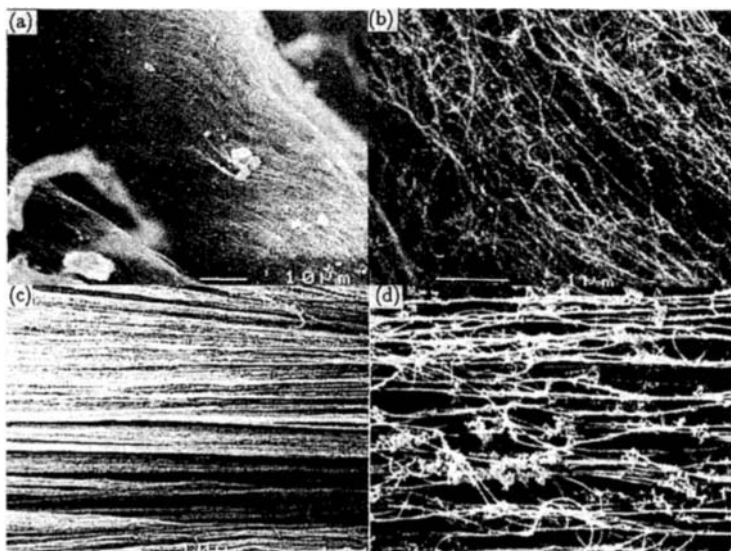


Figure 9. SEM images of the SWNT ropes and ribbons synthesized by the catalytic grown decomposition of hydrocarbons by the floating catalyst technique [51].

Wang *et al.* [59] prepared monosized SWNTs of 0.4 nm in diameter by pyrolysing tripropylamine molecules in the channels of a porous zeolite single crystal. Ren *et al.* [60] prepared DWNTs by catalytic vapour decomposition of methane with the floating catalyst technique, and investigated their special resonant Raman characteristics. Zhu *et al.* [61] prepared long SWNT strands by catalytic pyrolysis of n-hexane, and Bacsá *et al.* [62] prepared SWNTs with high specific surface area ($800\text{m}^2/\text{g}$) by catalytic vapour decomposition of methane. More recently, Yang *et al.* [63] prepared large diameter SWNTs (average diameter over 3 nm) by catalytic chemical vapour decomposition of benzene, and found that the aggregation mode of large diameter SWNTs differs from that of small diameter SWNTs. The preparation of high surface area and large diameter SWNTs will be helpful for the improvement of their hydrogen storage capacity.

Another important development is the fabrication of aligned or ordered MWNT arrays or patterns [64-69]. Usually, aligned MWNTs are prepared by catalytic decomposition of hydrocarbons on a matrix with catalyst particles embedded.

The catalytic vapour decomposition method has the obvious advantages of easier modification of substrates, reaction space and reaction

positions, and easier control of synthesis parameters. With these two advantages, VGCNFs, MWNTs, DWNTs, SWNTs, or aligned MWNTs can be synthesized, and it is expected that the commercial scale production of CNTs can be achieved soon by this method.

Besides the above techniques and methods, CNTs can be synthesized by many other techniques, such as electrolysis [70], solar vaporization [71], ball milling [72], etc. Our investigations have demonstrated that the hydrogen storage capacity of CNTs is closely related to their synthesis and pretreatment techniques. Therefore, efforts should be continuously endeavoured to the synthesis of CNTs for high efficient hydrogen storage.

4 Surface and Pore Structure of Carbon Nanotubes

Whatever, physical or chemical, the adsorption process of hydrogen in carbon nanotubes is, the adsorption process is surely an interaction process between hydrogen and the surface of carbon nanotubes. Therefore, a deep understanding to the surface and pore structures of carbon nanotubes will be helpful to understand the hydrogen adsorption mechanism and to direct the efficient development of carbon nanotube-based hydrogen storage systems.

4.1 Pore structure

CNTs have been found to possess many distinguished properties and potential applications, and many of them are related to the one-dimensional nano-scale cavities of their hollow cores. Experiments and calculations show that the inner hollow cavities of CNTs can hold atoms or molecules through capillarity and adsorption [73,74], which thus brings out the unique possibility of using CNTs as nano-sized super-adsorbents (hydrogen and other gas storage materials) [3, 9-13, 75], nano-sized reactors (offering the possibility of experimental realization of a one-dimensional reactor system) [73] and templates for the fabrication of novel one-dimensional nanomaterials [76] .

The inner hollow cavity is regarded as a fundamental pore structure in carbon nanotubes. However, the ends of pristine CNTs are usually capped with half a fullerene molecule, and the inner cavities of CNTs are not

available for adsorption and capillarity in many cases [77]. Thus, researchers have been managing to remove the ends of CNTs to create adsorption and capillarity in their inner cavities [78]. Moreover, some simulations and calculations predict that the interstices in SWNT bundles can be another domain to hold adsorbate molecules such as H_2 , He, Xe and N_2 [79-81]. MWNTs usually do not exist such bundles except for aligned nanotubes[82], leading to the absence of this type of porosity.

The pore structure of CNTs is often studied using a nitrogen cryo-adsorption method. Yang *et al.* [83] presented the nitrogen cryo-adsorption isotherm of the purified MWNTs, and it can be divided into four parts as shown in Figure 10, indicating a multi-stage adsorption process [83].

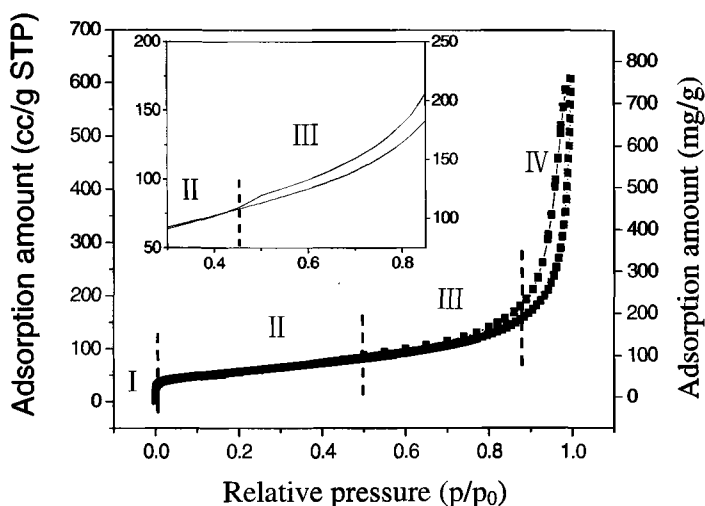


Figure 10. Nitrogen cryo-adsorption isotherm of MWNTs (Above curve: desorption branch; below: adsorption branch) [83].

In Part I, the isotherm is of Type I characteristic indicated by the fact that the adsorption amount increases rapidly at ultra-low pressure. Such a process occurs in pores with a molecular size, suggesting that there are micropores that may be contributed by the opened inner cavities of the MWNTs with very small diameter. Nitrogen molecules whose diameter is about 0.364 nm can fill in these pores under ultra-low adsorption pressures. Part II of the isotherm shows a surface adsorption process (monolayer formation), in which the nitrogen adsorption amount increases slowly. A

hysteresis loop is clearly visible in Part III and IV of the isotherm, which is associated with the capillary condensation in mesopores. Both ranges show Type IV isotherm characteristics. Part III corresponds to the capillary condensation occurring at the medium pressure range ($p/p_0=0.45-0.85$). A much more apparent hysteresis loop is shown in Part IV of the isotherm in the pressure range of $p/p_0=0.85-0.99$, and the adsorption amount of nitrogen sharply increases from 160 to 750 mg/g, resulting from an enhanced capillary condensation in larger pores, which is 78.5% of the total adsorption amount. According to the Kelvin equation, the corresponding pore size is about 20-40 nm, which is likely to be contributed by aggregated pores (confined pores formed in aggregated structure), since there are no carbon nanotubes with so large an inner diameter. The isolated nanotubes of different diameters and orientations interact to form an aggregated structure by inter-molecular force, and the so-called aggregated pores are the confined space among the isolated nanotubes in the relatively stable aggregated texture. The aggregated pores plays an important role on the adsorption and capillarity behaviour of MWNTs.

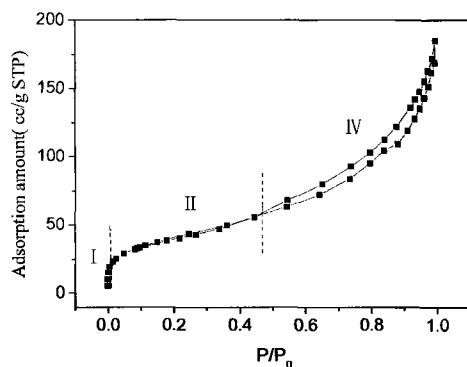


Figure 11. Nitrogen cryo-adsorption isotherm of SWNT bundles

Pore structures in SWNTs based on the adsorption investigations were also reported [84]. As shown in Figure 11, the nitrogen cryo-adsorption isotherm of the SWNTs employed can be divided into three ranges, and the isotherm in every range has different characteristics according to different

adsorption pressure, which indicates that nitrogen adsorption in the SWNTs is a multi-stage process and the SWNTs have different types of pores. In Part I corresponding to the ultra-low pressure range ($p/p_0=10^{-6}\sim 0.01$), the isotherm is of Type I characteristic. As mentioned above, such a process occurs in pores with a molecular size, indicative of the existence of micropores (less than 2 nm in diameter). Part II of the isotherm corresponding to the medium pressure zone ($p/p_0=0.01\sim 0.48$) shows a surface adsorption process (monolayer formation). In the high partial pressure zone (Part III), the isotherm is characterized by a hysteresis loop, resulted from the capillarity in mesopores.

In fact, except that the open inner hollow cavities of less than 2 nm in CNTs are one of the basic pores, the second kind of basic pores is the interstices among SWNT bundles, which, however, is hard to be explicated by the nitrogen cryo-adsorption method because nitrogen molecule is relatively large compared to the interstices. The third kind of pores is large pores formed by the interaction between SWNT bundles, which can be characterized by the nitrogen adsorption method and can be divided into ordered inter-bundle pores and disordered inter-bundle pores, whose sizes range from several nanometers to several hundred nanometers.

Compared to the slit-pore system of conventional activated carbons, a general pore formation model of carbon nanotubes was schematically proposed on the basis of the above experimental results and discussion [85], as shown in Figure 12.

4.2 Surface Area

Carbon nanotubes are regarded as materials with high surface area. In particular, isolated SWNTs with open tube tips are predicted to have the highest surface area ($2630\text{ m}^2/\text{g}$) in carbon materials [86]. In this case, every carbon atom is on the surface. However, in fact, the real CNTs including SWNTs and MWNTs show much lower specific surface areas (measured by the gas adsorption method) than the predicted limit value.

SWNTs usually interact with one another to form bundles, and most nanotube ends are closed, leading to a lower specific surface area.

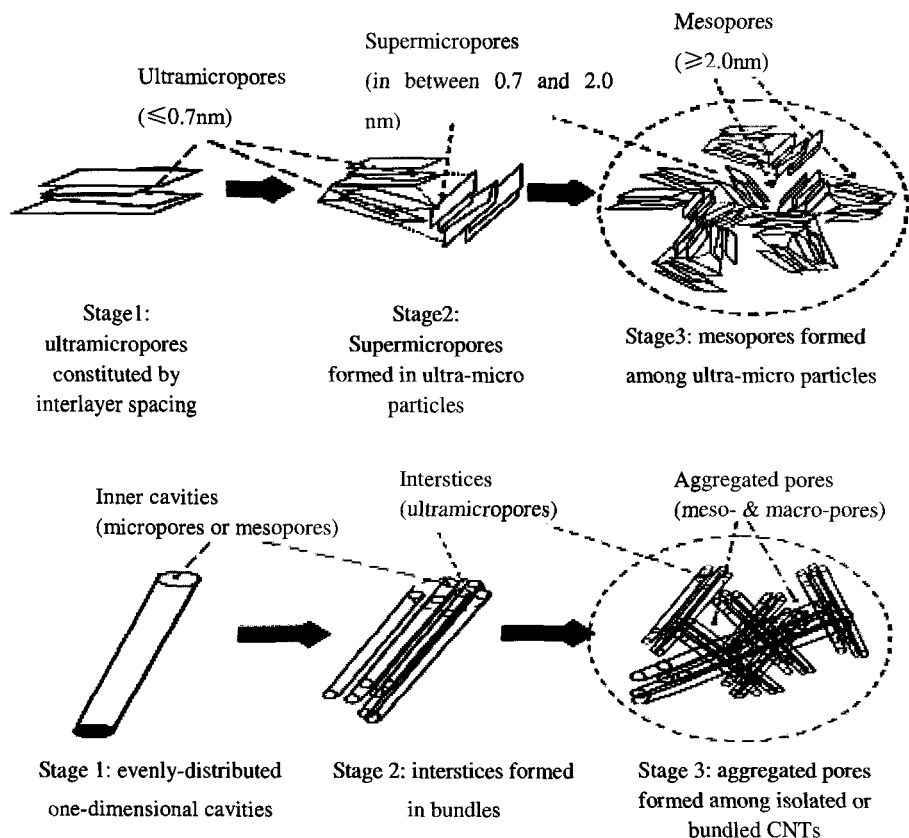


Figure 12. Schematic representation of proposed pore formation model in carbon nanostructures (upper: Porous carbon; lower: Carbon nanotubes) [85].

Experimentally, the highest specific surface area of SWNTs was measured to be $800 \text{ m}^2/\text{g}$, usually lower than $400 \text{ m}^2/\text{g}$ [62], and much lower than conventional activated carbons. As for MWNTs, it is hard for gas adsorbate molecules to enter the inter-layer spacing of the concentric carbon layers, and the calculated results indicate that the specific surface area decreases with increasing tube wall number and tube diameter, as shown in Figure 13 [86]. Our work shows that purification and pretreatment can increase the specific surface area of CNTs, but it is still far away from the theoretically predicted limit.

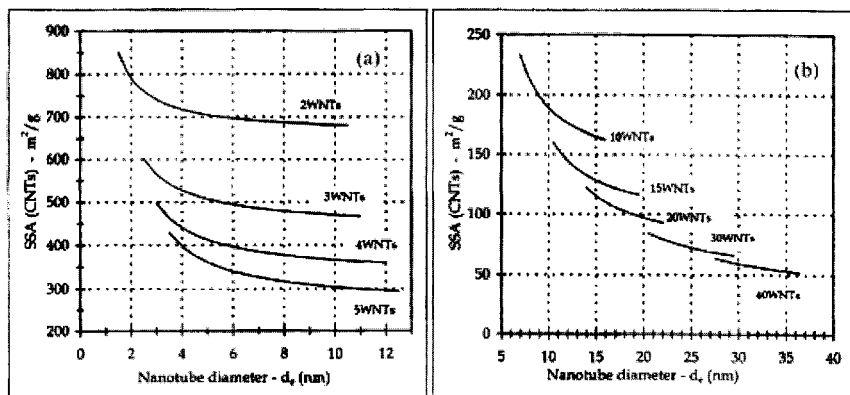


Figure 13. Specific surface area of CNTs versus their diameter and number of walls [86].

4.3 Surface heterogeneity

Gas adsorption on solid surfaces and in pore spaces is a complex process between adsorbate molecules and adsorbent surface molecules, involving both mass and energy interaction. Not only the pore structure but also the surface structure of the solid determines the adsorption process, and the adsorption isotherm provides a great deal of information both for the pore structure and surface energy distribution of the adsorbent materials. Eklund *et al.* [87] have reached a conclusion that there are many kinds of adsorption sites with different surface energy coexisting in SWNT bundles: the inner surface of cylindrical cavities, the outer surface of SWNT bundles and isolated nanotubes, and the interstice among nanotubes in a bundle that is hard to be characterized by the nitrogen adsorption method. The multi-stage characteristics of the isotherm of CNTs also suggest that there are many kinds of adsorption sites with different surface energy. In other words, the adsorption isotherm conveys a great deal of information about the energetic heterogeneity of the solid adsorbent and provides a sensitive indicator of its surface properties.

The integral adsorption isotherm can be interpreted as the convolution of a distribution of the adsorbate-adsorbent interaction intensity with a local isotherm for which the interaction (resulted from surface energy) is a parameter. The local isotherm can be calculated by the modified density functional theory (DFT) and the measured integral isotherm can be

inverted into the distribution of surface energy [88]. Assuming that only the first adsorption layer is determined from the surface energy of adsorption sites, the integral equation of adsorption for energetic heterogeneity can be written as:

$$\theta(p) = \int \theta(p, \varepsilon) f(\varepsilon) d\varepsilon \quad (4)$$

where $\theta(p)$ is the total quantity of adsorbate per gram of adsorbent at pressure p , $\theta(p, \varepsilon)$, the kernel function (the local isotherm), describes the adsorption isotherm for an ideally homotetic surface characterized by energy ε as the quantity of adsorbate per square meter of surface, and $f(\varepsilon)$ is the surface area distribution function with respect to ε [89].

Based on the above equation, Yang *et al.*[90] obtained a multiple surface area distribution $f(\varepsilon)$ for SWNTs and MWNTs with respect to ε . Figure 14 shows the surface energy distribution of SWNTs before and after hydrogen adsorption at high pressure [84]. The surface energy mainly ranges from 3.5 to 13.6 kJ/mol ($\varepsilon/k=20\sim 85$ K), suggesting the existence of heterogeneous surfaces in the SWNTs. By the same method, they obtained the surface energy of a planar graphite as 9 kJ/mol($\varepsilon/k=57$ K), lower than the average surface energy of SWNTs. Similarly, MWNTs were also proved to have multiple-distributed surface energy [90].

Generally, CNTs have a wide surface energy distribution, showing the existence of multiple pore structures and multiple surface structures, and consequently multiple adsorption sites. The information above is helpful to elucidate hydrogen storage mechanism of CNTs.

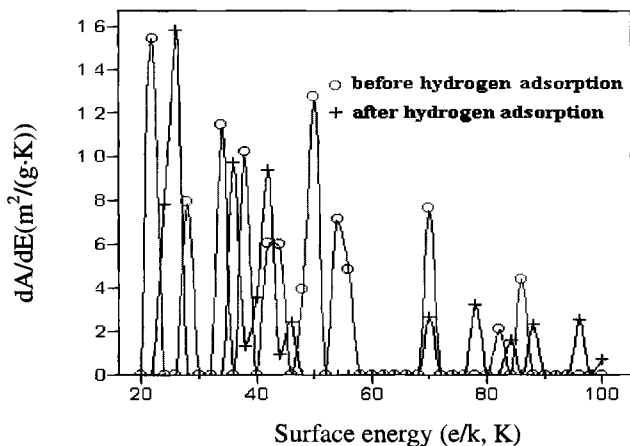


Figure 14. Surface energy distribution of SWNT bundles before and after hydrogen adsorption-desorption cycle [84].

5 Experimental Investigations on Hydrogen Uptake in Carbon Nanotubes

5.1 Gas phase hydrogen adsorption in carbon nanotubes

In 1997, Dillon *et al.* first claimed that SWNTs have a high reversible hydrogen storage capacity [3], which attracts great attentions from all over the world. They showed that hydrogen could condense to a high density (estimated to 5~10 wt%) inside narrow SWNTs with a diameter of 12 Å at room temperature and ambient atmosphere, and predicted that the SWNTs with diameters of 16.3 and 20 Å would come close to the target hydrogen uptake density of 6.5 wt %. The adsorption of hydrogen in SWNT soot was probed with temperature programmed desorption (TPD) spectroscopy and the TPD experiment suggested that physisorption of hydrogen mainly occurred within the cavities of SWNTs. The activation energy for hydrogen desorption was found to be 19.6 kJ/mol, which is much higher than the theoretical predicted value discussed previously, or approximately five times higher than that for a planar graphite surface, thereby promoting hydrogen storage at higher temperature. They have also developed a method to produce short laser-generated SWNTs with open ends that are accessible for the entry of hydrogen molecules, and these purified cut

SWNTs adsorbed 3.5~4.5 wt% hydrogen under ambient conditions in several minutes [91]. More recently, the same group reported that the hydrogen storage densities up to 7 wt% could be achieved for arc-generated SWNTs when the cutting procedure was optimised [92]. As to hydrogen storage mechanism, they thought that the interaction between hydrogen and SWNTs is mid-way between conventional van der Waals adsorption and chemical bond. Infrared absorption spectroscopic measurements on pristine and hydrogen-charged samples indicated that no C-H bonds were formed in the process. These experimental results are in agreement with an earlier TPD analysis showing that hydrogen molecules were not dissociated when bound to SWNT surfaces.

Ye *et al.* [11] reported that a ratio of H to C atoms of about 1.0 was obtained for the crystalline ropes of laser-generated SWNTs at 80 K and pressures >12 MPa. At a pressure of 4 MPa, a sudden increase in the hydrogen adsorption capacity of the SWNT samples was reported, and they suspected that a structural phase transition was responsible for this effect. Hydrogen was believed to be physisorbed on the exposed surfaces of the tubes.

Liu *et al.* [13] reported that the SWNTs with a large diameter (c.a.1.8 nm) by the hydrogen arc discharge method have a high hydrogen storage capacity at room temperature and high pressure. Figure 15 [13] shows the change of hydrogen pressures as a function of time under an initial hydrogen pressure of 10 MPa at room temperature in the first adsorption cycle of the SWNTs. The hydrogen uptake is completed within 5 hours. It is shown that even the as-synthesized SWNTs have a hydrogen uptake capacity of about 2 wt%, possibly resulting from the open tubes in the sample. Meanwhile, it has been proved that a notable change of their pore structure occurred in the course of hydrogen uptake in SWNTs [84]. By comparison of the pore structure and energy distribution of the SWNTs before and after hydrogen adsorption, it is preliminarily proposed that the hydrogen adsorption occurs in micropores and mesopores with smaller diameter.

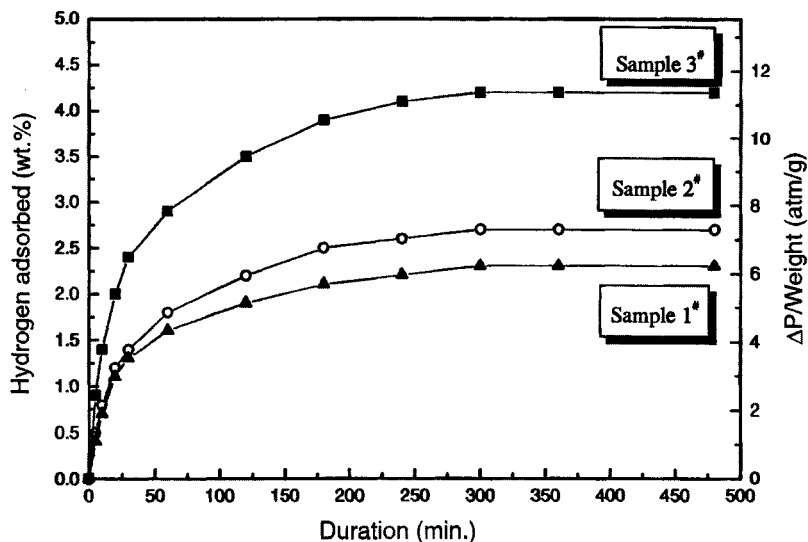


Figure 15. The amount of hydrogen in weight % stored in SWNT samples, and the pressure change versus the adsorption time. Sample 1 was used as synthesized. Sample 2 was soaked in 37% HCl acid for 48 hrs, rinsed with deionised water, and dried at 423 K. Sample 3 was pretreated in the same way as sample 2, then vacuum heat-treated for 2 hrs at 773 K [13].

The hydrogen storage behaviours of arc-generated and laser-generated SWNTs were investigated under different conditions. Dillon considered that the arc generated as-prepared SWNTs might have more defects and open inner hollow cavities than the laser-generated SWNTs to accommodate hydrogen, and therefore, the arc-generated SWNTs could adsorb hydrogen at room temperature, while the laser-generated SWNTs had to undergo cutting and opening procedure to adsorb hydrogen [92].

During the course, a striking experimental result about the hydrogen storage in graphite nanofibres (GNFs) was reported by Chambers *et al* [9]. They claimed that tubular, platelet, and herringbone forms of GNFs were capable of adsorbing in excess of 11, 45, and 67 wt % H₂, respectively, at room temperature under a pressure of about 12 MPa. In a further report [93], they considered that the GNFs possess special structural conformation, which is composed entirely of nanopores that accommodate

small-sized adsorbate molecules such as hydrogen and the non-rigid pore walls of which can expand to accommodate hydrogen molecules. They also pointed out that the pretreatment before hydrogen storage was very important and that ambient humidity was deadly harmful to the hydrogen uptake performance.

Chen *et al.* [10] reported in their TPD experiments that a high hydrogen uptake of 20 and 14 wt% could be achieved in milligram quantities of Li-doped and K-doped MWNTs, respectively, under ambient pressure. The K-doped MWNTs could adsorb hydrogen at room temperature, but they were chemically unstable, whereas the Li-doped MWNTs were chemically stable, but required elevated temperatures (473 to 673 K) for the maximum adsorption and desorption of hydrogen. Yang [94] reproduced the above experiments for dry hydrogen, and he showed that the K-doped MWNTs could only adsorb nearly 2 wt% hydrogen, but the experiment for wet hydrogen gave a value of 21 wt%. Therefore, Yang considered that it was moisture in hydrogen that drastically increased the weight gain by reactions with (or adsorption on) the alkali species on carbon [94].

Fan *et al.* [12] found that carbon nanofibres (CNFs) of 100 nm in diameter possessed high hydrogen storage capacity (5~10 wt%) at room temperature under moderate high pressure. Recently, Hou *et al.* at the same group [95] systematically investigated the influence of purification and pretreatment procedures, oxygen-containing surface functional groups, and pore structure on the hydrogen storage capacity of MWNTs. It was found that the hydrogen storage capacity of MWNTs was decreased with the increase of oxygen functional groups on the surface of the MWNTs, and various post-treatment methods could modify the pore structure and surface microstructure of the MWNTs to enhance their hydrogen adsorption capacity to a considerable extent, although there was no direct relationship between the hydrogen storage capacity of MWNTs and their pore volume and specific surface area. It is, therefore, believed that the pore and surface structures exert a large influence on the hydrogen storage performance of CNFs, MWNTs and SWNTs.

Furthermore, some groups reported that aligned MWNTs have higher hydrogen storage capacities. Cao *et al.* [96] and Zhu *et al.* [97] compared the hydrogen adsorption behaviours of aligned MWNTs (c.a. 2.4 wt% and

3 wt%) with randomly-ordered MWNTs (c.a. 0.5 wt%) at 290 K and 10 MPa, and argued that inter-tube channels in the well-aligned MWNTs were the effective domain for the hydrogen adsorption. Chen *et al.* [98] prepared aligned CNTs with diameters of 50-100 nm by plasma-assisted hot filament chemical vapour deposition, and obtained a hydrogen storage capacity of 5-7 wt%.

In contrast to the above positive results, there have been negative results less than 1 wt% on hydrogen storage in CNTs. For example, Hischer *et al.* argued that it was the metal particles introduced into SWNTs during a sonication process that were responsible for most of the hydrogen storage capacity of a SWNT sample [99].

All above results focus on the gravimetric hydrogen storage density of CNTs. From the viewpoint of practical applications, the volumetric hydrogen storage density of nano-structured carbon materials may be even more important, since their apparent density seems to be extremely low. Probably limited by the small amount of samples available or poor moulding ability of CNTs, the volumetric hydrogen storage capacity of CNTs have not been reported until Liu *et al.* [100] and Hou *et al.* [101] presented their results on the volumetric hydrogen storage densities of SWNTs and MWNTs, respectively, in 2002.

Liu *et al.* [100] found that macroscopically long SWNT ropes, synthesized by the hydrogen/argon arc discharge method, showed excellent moulding properties and they could be easily cold pressed into tablets, as shown in Figure 16, not using any binder without damaging their intrinsic pore structure. Their volumetric hydrogen storage capacity was measured at 11 MPa and ambient temperature. A high volumetric hydrogen storage capacity of $68 \text{ kgH}_2/\text{m}^3$ was achieved, and more than 70% of the adsorbed hydrogen could be released at room temperature. Hou *et al.* [101] performed similar experimental test on the purified MWNTs with mean diameter of 5.1 nm, and the gravimetric and volumetric hydrogen storage capacities of the bulk sample reached 6.3 wt % and $31.6 \text{ kg}/\text{m}^3$ at room temperature under an equilibrium pressure of 14.9 MPa, respectively.

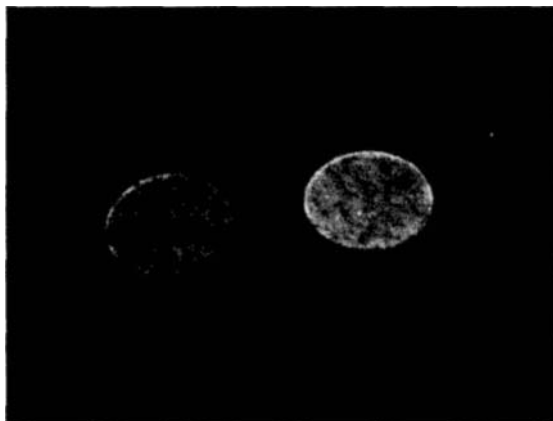


Figure 16. Optical image of the SWNT tablets cold compacted from SWNT ropes, and the diameter of the tablets is 10 mm [100].

Most of the current experimental results of hydrogen storage in carbon nanotubes are summarized in Table 2. Generally, the problems for hydrogen storage in CNTs lie in wide scattering of the results obtained by different groups, and the experimental results cannot match theoretical predictions. The quite diversified results of the hydrogen storage capacity of CNTs may be caused by the different samples from different synthesis techniques and pretreatment methods, and the different measurement methods employed by different research groups. It is in high demand to establish a standard method for the evaluation of the hydrogen storage capacity of CNTs.

Table 2. Summary of the experimentally reported hydrogen storage capacities of carbon nanotubes

Materials	Synthesis method	Measure - ment Method	H ₂ storage amount (wt%)	Storage temp. (K)	Storage pressure (MPa)	Reference
SWNTs (low purity)	Arc-discharge	TPD	5-10	273	0.040	3
GNFs (tubular)	CVD	VM	11.26	298	11.35	9
Li-MWNTs	CVD	TPD	20.0	473-673	0.1	10
K-MWNTs	CVD	TPD	14.0	<313	0.1	10
SWNTs (high purity)	Laser-ablation	VM	8.25	80	7.18	11
SWNTs (50% purity)	H ₂ arc discharge	VM	4.2	300	10.1	13
SWNTs (high purity)	Laser-ablation	TPD	3.5~4.5	298	ambient	91
SWNTs (high purity)	Laser-ablation	TPD	7	298	ambient	92
Li-MWNTs	CVD	TPD	2.5	473-673	0.1	94
K-MWNTs	CVD	TPD	1.8	<313	0.1	94
Aligned MWNTs	CVD	VM	2.4	298	10	96
Aligned MWNTs	CVD	VM	3	290	10	97
Pretreated-aligned MWNTs	Plasma-assisted CVD	TGA	13	298	1.0	98
CNFs	CVD	VM	6.5	300	14.8	101
GNFs	CVD	VM	10	300	8~12	102
GNFs	CVD	VM	6.5	~300	~12	103
SWNTs	Arc-discharge	TPD	0.1	300~520	0.1	104
MWNTs (80nm)	CVD	MW	0.7-0.8	300	7.0MPa	105

CVD: Catalytic vapour decomposition of hydrocarbons

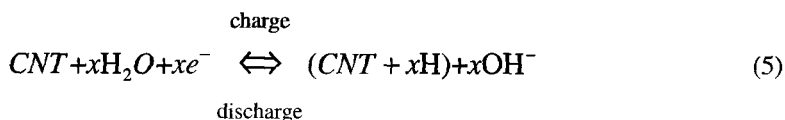
TPD: Temperature-programmed desorption

VM: Volumetric method

MW: Microbalance weighing

5.2 Electrochemical hydrogen storage in carbon nanotubes

Besides the gas phase hydrogen storage behaviour of CNTs, electrochemical hydrogen storage behaviours of CNTs have been also investigated. Nutzenadel *et al.* [106], for the first time, reported the electrochemical hydrogen storage behaviours of the as-produced SWNTs containing a few percent of SWNTs at room temperature and found a maximum discharge capacity of 110 mAh/g, corresponding to 0.41 wt% hydrogen storage capacity. The charge-discharge behaviour of hydrogen into CNTs can be represented as follows [107]:



where hydrogen enters CNTs during charging and releases during discharging. Later, they reported an electrochemical discharge capacity of 550 mAh/g for the sample with 70 wt% of SWNTs [108]. Rajalakshmi *et al.* [109] performed electrochemical hydrogen storage experiments using the purified and open arc-generated SWNTs, and a high electrochemical reversible charging capacity up to 800 mAh/g was obtained, corresponding to a hydrogen storage capacity of 2.9 wt%. Fazle Kibria *et al.* [107] compared the electrochemical behaviour of various CNTs prepared by different methods. They found that the laser-generated SWNTs had an electrochemical hydrogen storage capacity of 1.6 wt%, and that the Li-doped CNTs showed higher hydrogen storage capacity of 2.4 wt%.

Dai *et al.* [110] investigated the electrochemical hydrogen storage behaviour of the SWNTs (average diameter of 1.8 nm) synthesized by the hydrogen arc discharge method, and a maximum discharge capacity of 316 mAh/g (1.2 wt%) was obtained for the purified SWNTs. After 100 charge-discharge cycles, more than 81% of the maximum capacity was retained. They also found that pretreatment, especially heat-treatment, evidently improved the electrochemical capacity of the SWNTs. Moreover,

they employed the SWNT ropes made by the hydrogen/argon arc discharge method for the electrochemical measurement, and obtained the maximum discharge capacity of 503 mAh/g, corresponding to 1.84 wt% [111]. The entangled SWNTs and the SWNT ropes have different pore structure, which may lead to their different electrochemical hydrogen storage performance. The electrochemical hydrogen storage behaviour of MWNTs was investigated by Qin *et al.* [112], and they obtained a discharge capacity of 200 mAh/g from the MWNTs with outer diameter of 15-50 nm.

Table 3. Summary of the experimental results of electrochemical hydrogen storage in CNTs

Material	Synthesis method	Discharge capacity (mAh/g)	Weight hydrogen storage capacity (wt.%)	Reference
SWNTs(low purity)	Arc discharge	110	0.41	[106]
SWNTs (purity 90%)	Laser-ablation	440	1.6	[107]
Li-MWNTs+SWNTs	CVD	160	0.59	[107]
Li-SWNTs	Laser-ablation	640	2.3	[107]
SWNT(50~70% purity)	Arc-discharge	550	2	[108]
SWNTs (purity 80%)	Arc discharge	800	2.9	[109]
SWNTs (purity 95%)	H ₂ arc discharge	316	1.2	[110]
SWNT ropes	H ₂ -Ar arc discharge	503	1.84	[111]
MWNTs	CVD	200	0.74	[112]
SWNTs	unknown	160	0.59	[113]

Similar to gas phase hydrogen adsorption on CNTs, results on electrochemical hydrogen storage in CNTs also show diversity as revealed in Table 3, which is considered to be also due to the structural difference between different samples prepared by different synthesis and treatment methods at different groups. Electrochemical and gas phase hydrogen storage processes are dominated by different mechanisms, but both processes are connected with the surface and pore structure of CNTs.

6 Theoretical Predictions and Simulations of Hydrogen Uptake in Carbon Nanotubes

Due to their high surface area and abundant pore volume, conventional porous carbons such as activated carbons and activated carbon fibres are considered as good adsorbents. For the conventional porous carbons, their hydrogen uptake capacity is found to be proportional to their specific surface area and pore volume, while, regretfully, a high hydrogen adsorption capacity (3~6 wt%) can only be obtained at very low temperature such as liquid nitrogen temperature [7], consistent with theoretical calculations.

In contrast, in spite of their relatively low specific surface area and small pore volume compared to activated carbons, carbon nanotubes and carbon nanofibres show a surprisingly high hydrogen storage capacity. In the search of reasonable interpretations for this phenomenon, scientists employed different theoretical calculations and simulations. The intentions of the theoretical work are to answer the following important questions:

- (1) How do structural characteristics of CNTs influence their physical/chemical hydrogen storage process?
- (2) Where does the adsorption occur, in inner hollow cavities and/or other pore spaces (e.g. inter-tube space and aggregated pores) of CNTs?
- (3) During the adsorption of hydrogen onto carbon nanotubes, what interaction, chemical or physical, occurs between hydrogen and carbon?
- (4) What is the hydrogen adsorption mechanism of CNTs?
- (5) How high can the maximum hydrogen adsorption capacity of CNTs be reached?

6.1 Simplistic geometric estimate and qualitative discussion

Since hydrogen molecules at elevated pressures on a solid surface are expected to form a close-packed configuration, Dresselhaus *et al.* [114] obtained a simple geometric estimate for the close-packing capacity of hydrogen molecules above a plane of graphite using purely geometric arguments, which yielded 2.8 wt% ($\sqrt{3} \times \sqrt{3}$ commensurate stacking,

Figure 17, top) or 4.1 wt% (dense triangular structure, incommensurate with the graphite, observed for higher hydrogen pressure, Figure 17, bottom) hydrogen uptake for one layer of hydrogen adsorbed on a single graphene layer [114,115].

As for carbon nanotubes, one important issue currently being debated is whether hydrogen adsorption also occurs in the interstitial channels between adjacent nanotubes in a rope of SWNTs. Dresselhaus *et al.* [114] presented two geometrical estimates for the filling of a rope (crystalline lattice) of SWNTs. One assumes that hydrogen is a completely deformable fluid that fills the space not occupied by the carbon nanotubes, and then the packing of hydrogen molecules of kinetic diameter 0.29 nm on the inner walls and in the interstitial volume of the nanotubes can be accomplished, as shown in Figure 18 [87]. Using the geometrical model for a close-packing of hydrogen molecules within the core of a (10,10) tube leads to 3.3 wt% hydrogen adsorption within the tube and 0.7 wt% adsorption within the interstitial space, or a total of 4.0 wt% hydrogen adsorption [87,114].

It is considered that under high-pressure conditions (e.g. 10 MPa), the high compressibility of hydrogen and the attractive intermolecular interactions should lead to a closer packing of hydrogen molecules [114], which is consistent with the detailed calculation by Stan *et al.* [116].

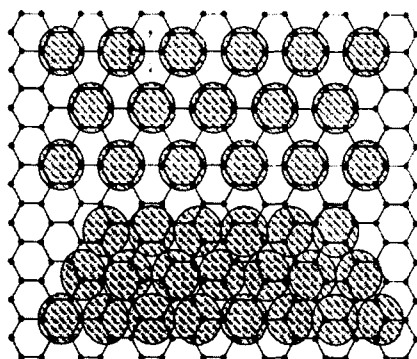


Figure 17. Relative density of a $\sqrt{3} \times \sqrt{3}$ commensurate (top) and an incommensurate (bottom) monolayer of H_2 on a graphite surface [114].

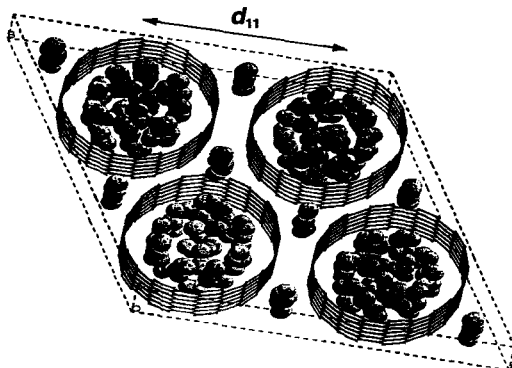


Figure 18. A typical configuration of H_2 molecules adsorbed on a triangular array of CNTs with a lattice constant of d_{11} [114].

Based on this, the hydrogen adsorption amount under high pressures would be higher than the simplistic geometric estimation. Moreover, Dresselhaus considered that a hydrogen molecule adsorbed in the interstitial space undergoes much stronger surface attraction than on a single planar graphene surface, since it is in close proximity to three graphene surfaces [114]. Therefore, the hydrogen adsorbed in the interstitial space would be expected to be denser than on a single graphene surface.

In a short summary, through a simple physical discussion, it is concluded that for SWNTs hydrogen is stored in the pores formed by the inner tube cavities and the inter-tube space, and the storage density is possibly higher than that on a planar graphene surface. Accordingly, the hydrogen adsorption amount may be higher than 4 wt%, consistent with some experimental results.

6.2 Simulations and calculations on physisorption of hydrogen in carbon nanotubes

Grand canonical Monte Carlo (GCMC) simulations and other simulations and calculations [81,87,115,117-131] have been carried out to verify and predict the adsorption capacity of hydrogen in carbon nanotubes based on

the assumption of physical adsorption. Parallel to the experimental results, the results of theoretical calculations and simulations on the hydrogen storage capacity of CNTs also scatter, as shown in Table 4. For all these approaches, the most important factor is the selection of intermolecular potential function describing the molecular interactions between hydrogen and carbon atoms. In spite of the use of different calculation methods and diversified results, some common points can be reached.

(1) Hydrogen adsorption possibly occurs at sites of different binding energy in SWNTs. Williams *et al.* [87] conducted quantitative examinations of the maximum potential energies in a 7-SWNT rope at 10 MPa and 77 K. They found that the strongest average attractive potential energy was in the interstice (-1443 K), followed by the endohedral sites along the inner (-758 K) and outer (-603 K) cylindrical surface of the nanotubes. Besides, their results showed that the attractive potential energies along the “grooves” (the wedge-shaped channel running along the outer surface of the rope where two nanotubes meet) was -1088 K, comparable to the energy at the interstitial sites. These estimates suggest that treatment of the outer surface of SWNT ropes in the simulation of physisorption is important not only for the obvious geometrical reason (high surface area), but for the energetic reason as well, since typical ropes possess many “wedge” channels on their exterior surface.

Table 4. Summary of the calculated results of hydrogen physisorbed in carbon nanotubes

Materials	Tube diameter/pore size (nm), or (m,n) parameter	Inter-tube spacing, nm	H ₂ adsorption capacity (wt%)	Temp. (K)	Pressure (MPa)	Reference
SWNTs	(9,9), (12,12) (18,18)	1.2	9~10	77	50	81
SWNTs	(9,9), (12,12) (18,18)	1.2	0.8~1.0	298	50	81

Table continued

SWNTs	0.7 1.0		1 2.5	77	10	118
SWNTs	0.7 1.0		0.8 1.0	300	10	118
Slit-shaped pores	0.9 2.0		7.5 12.5	77	10	120
Slit-shaped pores	0.9 2.0		1.4 2.4	298	10	120
SWNTs	(9, 9) (18, 18)		1.8 4.5	77	10	120
SWNTs	(9,9) (18,18)		0.4 0.9	298	10	120
SWNTs	6	1.0	4.7	298	10	125
SWNTs	2.2, 1.1		11.24	77	10	132
SWNTs	0.352 0.578 0.9785	1.0	0.7 0.9 1.1	293.1 5	10	133
SWNTs	(5,5)		5.0		10	135

(2) The inner-tube cavities have high adsorption potentials for hydrogen, compared with the planar surface and slit-pores of a similar size. SWNTs have a very narrow diameter distribution, and their diameter is in the same order of the interaction range between carbon atoms [117]. Figure 19 shows that the depth of the potential well for a (9,9) tube (1.22 nm in diameter) array is larger than that for a slit pore 0.9 nm in diameter because the curvature of the tube increases the number of nearest neighbour carbon atoms [120].

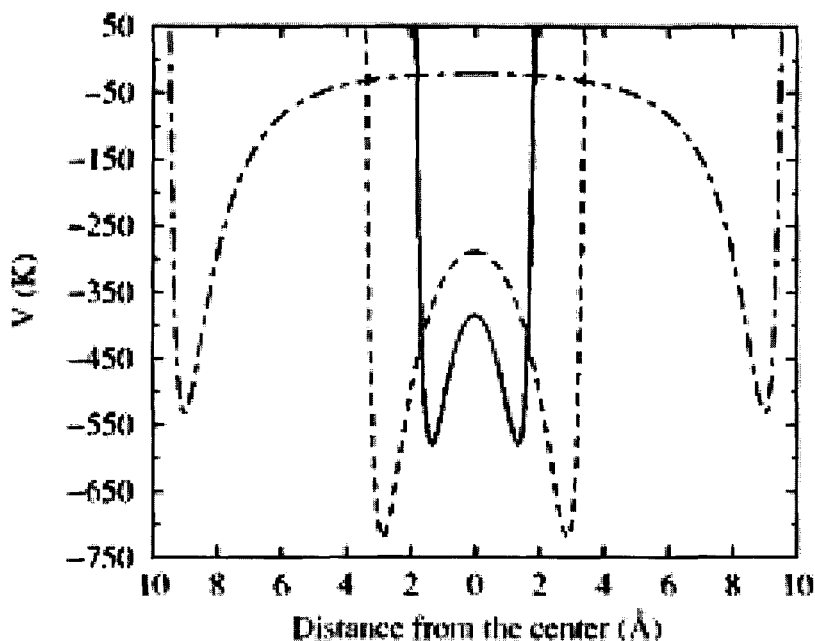


Figure 19. Adsorption potentials for hydrogen in tube arrays and idealized slit pores. The solid line denotes the idealized carbon slit pore with a pore width of 0.9 nm. The dashed line is the potential for a (9,9) tube array, and the dot-dashed line represents a (18,18) tube array. [120]

(3) The packing geometry of SWNTs plays an important role in hydrogen adsorption. The simulation of Williams *et al.* [87] suggested that the strong dependence of the gravimetric adsorption on the packing geometry and diameter of a SWNT rope correlated with the calculated values of the specific surface area, and the delamination of nanotube ropes should increase the gravimetric hydrogen storage capacity. The packing geometry of SWNTs also exerts great influence on their volumetric adsorption capacity. Wang *et al.* [81] optimised the packing geometry of SWNTs to maximize the hydrogen adsorption amount. They have found that (9,9) tube triangular arrays with an inter-tube spacing of 0.6 and 0.9 nm reached the highest volumetric densities at both 298 K and 77 K, and the (9,9) SWNTs with an inter-tube distance of 0.9 nm had gravimetric and volumetric densities at 77 K and 5 MPa very close to the DOE targets.

(4) The calculated heat of adsorption by some simulations (6.3 kJ/mol by Wang *et al.* [120], 1082 K by Stan *et al.* [126]) is much less than the experimental value of Dillon *et al.* (19.63 kJ/mol, or 2360 K) [3]. However, Cheng *et al.* [130] proposed a mechanism that yielded calculated adsorption energy (31.39 kJ/mol for H₂ onto the inner surface of SWNTs at 300 K) comparable to or higher than the experimental value, by quantum-mechanical molecular dynamics (MD) simulations. They thought that partial electron-transfer interaction between H₂ and instantaneously distorted carbon atoms in the SWNT wall was the primary reason responsible for the high hydrogen-SWNT adsorption energy.

Although many simulation results based on physisorption do not confirm the high hydrogen uptake capacity obtained experimentally for CNTs, some of recent simulations have shown that hydrogen can be physisorbed in SWNT bundles in high capacity at cryogenic temperature and under high pressure. For example, the results of Williams *et al.* [87] showed that the maximum gravimetric adsorption capacity of hydrogen onto an isolated (10,10) nanotube could reach 9.6 wt% at 77K and 10 MPa. The GCMC simulations by Darkrim [132] showed that SWNT bundles (individual diameter: 2.2 nm, and inter-tube spacing: 1.1 nm) exhibited high hydrogen adsorption of 11.24 wt% at 77 K and moderate pressure. Yin *et al.* [125] performed GCMC simulations on hydrogen storage in triangular arrays of SWNTs and in slit pores at 298 and 77 K. As for very large diameter SWNTs (6.0 nm in diameter) with large inter-tube spacing of 1.0 nm, 4.7 wt% hydrogen adsorption capacity at 298 K and 10 MPa was obtained. Their results also revealed that the potential of SWNTs for hydrogen storage is superior to that of activated carbons and the interstices may contribute to hydrogen adsorption. Although these results cannot yet thoroughly explain the hydrogen adsorption in common SWNTs (diameter less than 2 nm) at ambient temperature, it may provide scientists with confidence to narrow the discrepancy between the observed hydrogen storage capacities in CNTs and the physisorption simulations.

Table 4 illustrates the main simulation results for hydrogen physisorption in various nanostructured carbons in the past several years.

6.3 Simulations and calculations on chemisorption of hydrogen in carbon nanotubes

Although many simulation results based on physisorption do not confirm the high hydrogen uptake capacity obtained experimentally for CNTs, theoretical calculations based on chemisorption assumption seem to be more positive. Lee *et al.* [134] investigated the hydrogen storage behaviour of SWNTs by density functional calculations, and proposed that the adsorption of hydrogen in SWNTs was a chemisorption process. Their calculation predicted that the hydrogen storage capacity in (10,10) nanotubes could exceed 14 wt% ($160 \text{ kgH}_2/\text{m}^3$), which is much higher than the experimental values. By the density function calculation, Lee *et al.* [136] also proposed electrochemical hydrogen storage and extraction, corresponding to charge-discharge process, in SWNTs as follows: H atoms are first adsorbed on the tube wall by breaking the C-C midbond to form C-H bond and then stored in the hollow cavities as a form of hydrogen molecule by capillary force at higher coverage. In the hydrogen-extraction process, hydrogen molecules condensed by capillarity force in the hollow cavities first dissociated, adsorbed onto the inner wall, and is further extracted to the outer wall by the flip-out mechanism. Figure 20 represents this process of hydrogen insertion into SWNTs.

Bauschlicher *et al.* [137] calculated the C-H bond energy for a (10,0) SWNT, and obtained a value of 57.3 kJ/mol for the most stable 50% coverage, which is responsible for about 4 wt% hydrogen chemisorption amount.

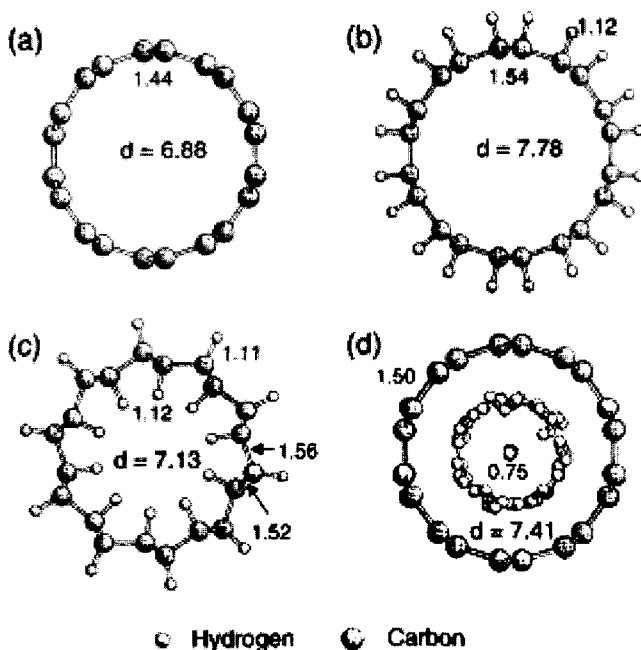


Figure 20. Top views of various hydrogen adsorptions in (5,5) nanotube with ball-and-stick forms. (a) Pristine, (b) *arch*-type, (c) *zigzag* type, and (d) the molecular hydrogen inside the CNT with coverage to 1.0 [136]. The d indicates an average diameter of the CNT. Bond lengths are in units of Å.

Above calculations based on chemisorption can partly explain the high hydrogen adsorption capacity of CNTs, and especially, the proposed mechanism of hydrogen electrochemical charge-discharge in SWNTs is of importance for final elucidation of the hydrogen storage mechanism of CNTs. However, the affirmation of the nature of hydrogen adsorption in CNTs remains a long way to go.

7 Possible Hydrogen Adsorption Sites in Carbon Nanotubes

There are many types of pores in carbon nanotubes as discussed above. It can be preliminarily concluded from the theoretical calculations and experimental results that inner cavities, interstices in SWNT bundles, small aggregated pores of several nanometers among CNTs and carbon islands on the surface of MWNTs are possible sites for hydrogen adsorption.

(1) The inner cavities of CNTs are primary hydrogen adsorption sites. Many simulations reveal that nano-sized inner cavities in SWNTs and MWNTs (with small diameter) have strong adsorption potentials for hydrogen adsorption and the inner cavities of SWNTs with larger diameter will hold more hydrogen molecules. Experimental results also have proved that cutting and tips-removing process [78,91,92] improves the hydrogen storage capacity of CNTs. Figure 21 shows that a tip-removing process leads to the great increase of small mesopore volume that can be attributed to inner cavities, consistent with the improved hydrogen storage capacity of the MWNTs [101].

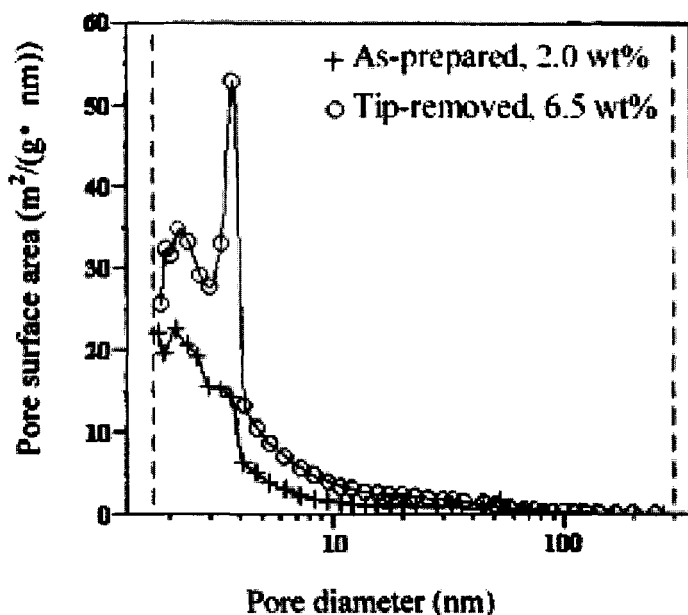


Figure 21. Pore size distribution and hydrogen storage capacities of the MWNTs in the as-prepared state and after tip-removing process [101].

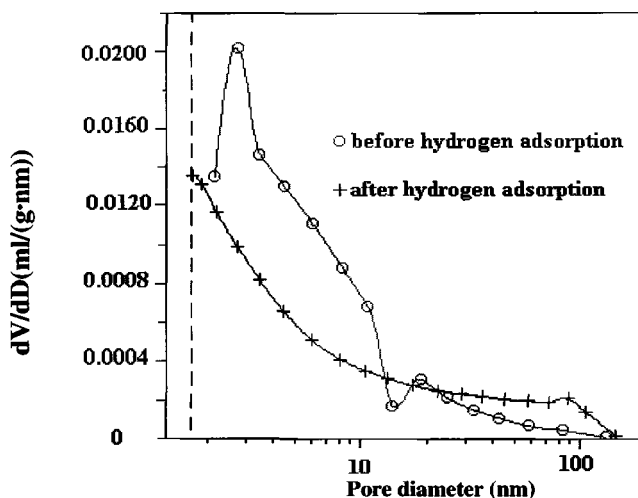


Figure 22. Pore size distributions of the SWNT bundles before and after the first hydrogen adsorption-desorption cycle [84].

(2) Interstices in SWNT bundles are an important domain for hydrogen storage. Some simulations proved that interstices among large diameter SWNTs (e.g. (18,18) SWNTs) had strong adsorption potentials for hydrogen [120], and that adjusting inter-tube spacing could influence the hydrogen storage capacity of SWNTs. For example, small diameter SWNTs (tube diameter 0.6 nm) with an inter-tube spacing of 3.0 nm has a surprisingly high hydrogen adsorption capacity of 33 wt% at 77 K under 7 MPa [125].

(3) Small aggregated pores (several nm) between CNTs or CNT bundles are responsible for part of hydrogen uptake. Figure 22 [84] represents the pore size distribution curves of the SWNTs by hydrogen arc discharge before and after hydrogen adsorption/desorption cycle, where ordered inter-bundle pores (small aggregated pores) of 3 nm in diameter disappeared after the first run of the hydrogen storage experiment, leading to a lower hydrogen uptake cycling capacity. Experiments showed that the small aggregated pores among the aligned carbon nanotubes would be more stable [96].

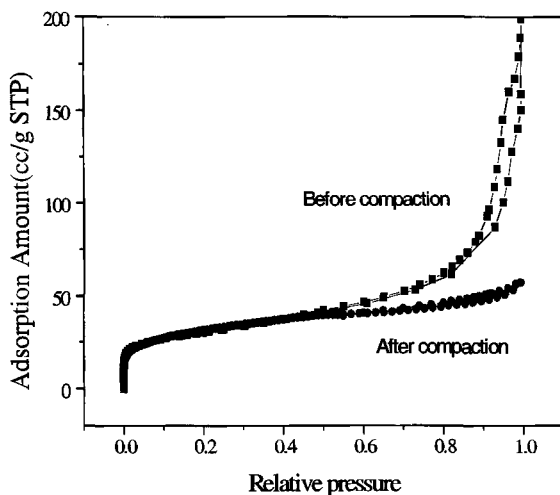


Figure 23. Comparison of nitrogen cryo-adsorption isotherms of the SWNTs before and after cold-pressing under high pressure (0.7 TPa) [100].

(4) Large aggregated pores (tens of nanometers) in CNTs have no contributions to hydrogen adsorption. In Liu's work [100], after cold compaction of SWNT ropes, the aggregated pores leading to high-pressure capillarity disappear, as shown in Figure 23, while the hydrogen adsorption capacity kept stable.

(5) Yang [90] carefully investigated the surface structure and pore structure of CNTs, and he observed a common structure defined as "Carbon Island", as shown in Figure 24, in MWNTs obtained by catalytic vapour decomposition of hydrocarbons. Carbon Island consists of some well-oriented graphitic layers in a size of several nanometers in length and in thickness, but the border between Carbon Islands is full of defects and disordered carbons. However, these micropores (defects, disordered carbons and spacing between graphitic layers) cannot be characterized by the nitrogen cryo-adsorption method. The Carbon Island structures can be considered as another main domain for hydrogen storage because the defects provide smooth channels for hydrogen entering the graphitic layers of the well-oriented small nano-islands [95]. Hou *et al* [95] measured the hydrogen storage capacity of MWNTs with different diameters and found

that the capacity increased with increasing MWNT outer diameter in the range of 10–53 nm. They attributed this increase of hydrogen storage capacity to the rich Carbon Island structures on the walls of larger diameter MWNTs observed by HRTEM.

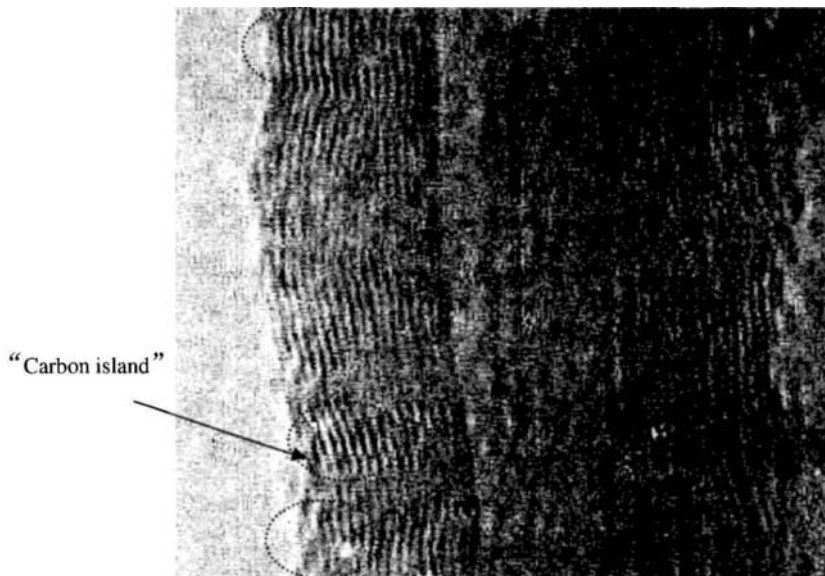


Figure 24. HRTEM image of a confined zone of MWNTs. The circled confined zones are called “Carbon Island” [90].

Generally, both recent experimental and theoretical results have proved the surface and pore structures play important roles in the hydrogen adsorption of CNTs. However, the detailed hydrogen adsorption process in different types of pores will not be fully elucidated until the mechanism of hydrogen-carbon interaction is understood.

It is quite difficult to reach a common conclusion for the maximum hydrogen adsorption capacity and explain the experimental observations from the results obtained by the present theoretical calculations and simulations. However, the information obtained from these calculations and simulations will be helpful for experimental investigations. Meanwhile, deep understanding into the pore and surface structure and the adsorption process of CNTs will benefit to choose the optimum intermolecular potential function used in theoretical calculations and simulations.

8 Future Research Topics and Remarks

More and more experimental results and theoretical predictions, both positive ones and negative ones, have been deepening our understanding about the hydrogen adsorption in carbon nanotubes. Comparative investigations at different research labs on the same sample or comparative investigations with the same measurement method at the same lab on different samples from different research labs are highly expected. To use carbon nanotubes as a practical hydrogen storage medium, the following essential works have to be accomplished:

- (1) Mass production of SWNTs, MWNTs and other nanostructured carbons with a controllable microstructure for excellent hydrogen storage at a reasonable cost.
- (2) Purification and surface fictionalisation of carbon nanotubes, and development and optimisation of pretreatment methods for opening nanotube caps and creating suitable hydrogen adsorption sites to improve their hydrogen storage capacity.
- (3) Elucidation of the microstructure, especially the pore and surface microstructures of carbon nanotubes in the viewpoint of hydrogen adsorption/desorption process.
- (4) Further improvement of volume storage capacity of carbon nanotubes.
- (5) Thorough investigations of adsorption/desorption process, thermodynamics, kinetics and cycling behaviours of carbon nanotubes.
- (6) Interpretation and understanding of hydrogen adsorption mechanism of carbon nanotubes.
- (7) Development of practical CNT-based hydrogen storage systems for proton exchange membrane fuel cell-powered vehicles and other applications.

In summary, hydrogen fuel is clean, versatile, efficient and safe, and is the best fuel for transportation. Hydrogen energy will play an important role in the energy structure of the future world. Preliminary experimental results and some of the theoretical predictions indicate that carbon nanotubes can be a promising candidate for efficient hydrogen storage, which may accelerate the development of hydrogen fuel cell-driven vehicles. Nevertheless, many efforts have to be made to reproduce and verify the hydrogen storage capacity of carbon nanotubes both

theoretically and experimentally, to investigate their volumetric capacity, cycling characteristics and release behaviour, to correlate the surface and pore structure with hydrogen adsorption behaviour, to elucidate the adsorption/desorption mechanism, and finally to clarify the feasibility of carbon nanotubes as a practical onboard hydrogen storage material.

9 Acknowledgement:

We acknowledge NSFC grants (No. 50025204 and 50032020) and the Special Fund for Major Basic Research Projects of MOST, China (G2000026403) for their financial support to the work accomplished at HMC group.

References

1. Veziroglu T. N., Hydrogen energy system as a permanent solution to global energy-environmental problems, *Chem. Ind.* **53** (1999) pp. 383-393.
2. Veziroglu T. N. and Barbir F., Hydrogen---the wonder fuel, *Int. J. Hydrogen Energy* **17** (1992) pp. 391-404.
3. Dillon A. C., Jones K. M. and Bekkedahl TA, Kiang C.H., Bethune D. S., Heben M. J., Storage of hydrogen in single walled carbon nanotubes, *Nature* **386** (1997) pp. 377-379.
4. Carpentis C. and Peschka W., A study on hydrogen storage by use of cryoadsorbents, *Int. J. Hydrogen Energy* **5** (1980) pp. 539-554.
5. Agarwal R. K., Noh J. S. and Schwarz J.A., Effect of surface-acidity of activated carbon on hydrogen storage, *Carbon* **25** (1987) pp. 219-226.
6. Noh J. S., Agarwal R. K. and Schwarz J. S., Hydrogen storage---systems using activated carbon, *Int. J. Hydrogen Energy* **12** (1987) pp. 693-707.
7. Schwarz J. A., Proc. 1993 DOE/NREL Hydrogen Program Review 1993, P. 89.
8. Schwarz J. A., Final Report for the Tasks XC-1-1108-1 and XAE-3-13346-01 (National Renewable Energy Laboratory, Golden Colorado, 1994).
9. Chambers A., Park C., Baker R. T. K., Rodriguez Nelly M., Hydrogen storage in graphite nanofibers, *J. Phys. Chem. B* **102** (1998) pp. 4253-4256.
10. Chen P., Wu X., Lin J., Tan K. L., High H₂ uptake by alkali-doped carbon nanotubes under ambient pressure and moderate temperatures, *Science* **285** (1999) pp. 91-93.
11. Ye Y., Ahn C. C., Witham C., Fultz B., Liu J., Rinzler A. G., Colbert D., Smith K. A., Smalley R. E., Hydrogen adsorption and cohesive energy of single-walled carbon nanotubes, *Appl. Phys. Lett.* **74** (1999) pp. 2307-2309.
12. Fan Y. Y., Liao B., Liu M., Wei Y. L., Lu M. Q., Cheng H. M., Hydrogen uptake in vapor-grown carbon nanofibers, *Carbon* **37** (1999) pp. 1649-1652.
13. Liu C., Fan Y. Y., Liu M., Cong H. T., Cheng H. M., Dresselhaus M. S., Hydrogen storage in single-walled carbon nanotubes at room temperature, *Science* **286** (1999) pp. 1127-1129.

14. Iijima S., Helical microtubules of graphitic carbon, *Nature* **354** (1991) pp. 56-58.
15. Iijima S. and Ichihashi T., Single shell carbon nanotubes of 1nm diameter, *Nature* **363** (1993) pp. 603-605.
16. Bethune D. S., Kiang C. H., De Vires M. S., Goman G., Savoyr, Vazquez J., Beyers R., Cobalt catalyzed growth of carbon nanotubes with single atomic layer walls, *Nature* **363** (1993) pp. 605-607.
17. Dresselhaus M. S., Dresselhaus G. and Eklund P. C., *Science of fullerenes and carbon nanotubes* (San Diego: Academic Press, 1996).
18. Hanada T., Okada Y. and Yase K., Structure of multi-walled and single-walled carbon nanotubes—EELS study, In *The Science and Technology of Carbon Nanotubes*, (Elsevier, 1999) pp. 29-39.
19. Mintmire J. W., Dunlap B. I. and White C. T., Are fullerene tubules metallic, *Phys. Rev. Lett.* **68** (1992) pp. 631-634
20. Hamada N., Sawada S. and Oshiyama A., New one-dimensional conductors – graphitic microtubules, *Phys. Rev. Lett.* **68** (1992) pp. 1579-1581.
21. Saito T., Fujita M., Dresselhaus G., Dresselhaus M. S., Electronic structure of chiral graphene tubules, *Appl. Phys. Lett.* **60** (1992) pp. 2204-2206.
22. Wildoer J. W. G., Venema L. C., Rinzler A. G., Smalley R. E., Dekker C., Electronic structure of atomically resolved carbon nanotubes, *Nature* **391** (1998) pp. 59-62.
23. Odom T. W., Huang J. L., Kim P., Lieber C. M., Atomic structure and electronic properties of single-walled carbon nanotubes, *Nature* **391** (1998) pp. 62-64.
24. Zhou X., Zhou J. J. and Ou-Yang Z. C., Strain energy and Young's modulus of single-wall carbon nanotubes calculated from electronic energy-band theory, *Phys. Rev. B* **62** (2000) pp. 13692-13696.
25. Zhang P. H., Lammert P. E. and Crespi V. H., Plastic deformations of carbon nanotubes, *Phys. Rev. Lett.* **81** (1998) pp. 5346-5349.
26. Yakobson B. I. and Smalley R. E., Fullerene nanotubes: C-1000000 and beyond, *Sci. Am.* **85** (1997) pp. 324-337.
27. Woolley A. T., Cheung C. L., Hafner J. H. and Lieber C. M., Structural biology with carbon nanotube AFM probe, *Chemistry & Biology* **7** (2000) pp. 193-204.
28. Tans S. J., Verschuere A. R. M. and Dekker C., Room-temperature transistor based on a single carbon nanotubes, *Nature* **393** (1998) pp. 49-53.
29. Bachtold A., Hadley P., Nakanishi T., Dekker C., Logic circuits with carbon nanotube transistors, *Science* **294** (2001) pp. 1317-1320.
30. Kong J., Franklin N. R., Zhou C. W., Chapline M. G., Peng S., Cho K. J., Dai H. J., Nanotube molecular wires as chemical sensors, *Science* **287** (2000) pp. 622-625.
31. Rueckes T., Kim K., Joselevich E., Tseng G. Y., Cheung C. L., Lieber C. M., Carbon nanotube-based nonvolatile random access memory for molecular computing, *Science* **289** (2000) pp. 94-97.
32. Collins P. G., Arnold M. S. and Avouris P., Engineering carbon nanotubes and nanotube circuits using electrical breakdown, *Science* **292** (2001) pp. 706-709.
33. Liu C., Bard A. J., Wudl F., Weitz I., Heath J., Electrochemical characterization of films of single-walled carbon nanotubes and their possible application in supercapacitors, *Electrochem Solid State Lett.* **2** (1999) pp. 577-578.
34. Baughman R. H., Cui C. X., Zakhidov A. A., Iqbal Z., Barisci J. N., Spinks G. M., Wallace G. G., Mazzoldi A., De Rossi D., Rinzler A. G., Jaschinski O., Roth S., Kertesz M., Carbon nanotube actuators, *Science* **284** (1999) pp. 1340-1344.
35. Deheer W. A., Chatelain A. and Ugarte D., A carbon nanotube field-emission electron source, *Science* **270** (1995) pp. 1179-1180.
36. Thess A., Lee R., Nikolaev P., Dai H. J., Petit P., Robert J., Xu C. H., Lee Y. H., Kim S. G., Rinzler A. G., Colbert D. T., Scuseria G. E., Tomanek D., Fischer J. E.,

- Smalley R. E., Crystalline ropes of metallic carbon nanotubes, *Science* **273** (1996) pp. 483-487.
37. Ebbesen T. W. and Ajayan P. M., Large scale synthesis of carbon nanotubes, *Nature* **358** (1992) pp. 220-222.
38. Journet C., Master W. K., Bernier P., Loiseau A., De La Chapelle M. L., Lefrant S., Deniard P., Lee R., Fischer J. E., Large scale production of single walled carbon nanotubes by the electric arc technique, *Nature* **388** (1997) pp.756-758.
39. Liu C., Cong H. T., Li F., Tan P. H., Cheng H. M., Lu K., Zhou B. L., Semi-continuous synthesis of single-walled carbon nanotubes by a hydrogen arc discharge method, *Carbon* **37** (1999) pp. 1865-1868.
40. Cheng H. M., Liu C., Fan Y. Y., Liu M., Cong H. T., Synthesis, characterization and hydrogen uptake of single- and multi-walled carbon nanotubes and carbon nanofibers, *Z. Metallkd.* **91** (2000) pp. 306-315.
41. Yang Q. H., Li F., Hou P. X., Liu C., Liu M., Cheng HM, Evaluation of diameter distribution of inside cavities of open carbon nanotubes by analyses of nitrogen cryo-adsorption isotherm, *Chin. Sci. Bull.* **46** (2001) pp. 1317-1320.
42. Liu C., Cheng H. M., Cong H. T., Li F., Su G., Zhou B. L., Dresselhaus M. S., Synthesis of macroscopically long Ropes of well-aligned single-walled carbon nanotubes, *Adv. Mater.* **12** (2000) pp. 1190-1192.
43. Huang H. J., Kajiura H. , Tsutsui S., Hirano Y., Miyakoshi M., Yamada A., Ata M., Large-scale rooted growth of aligned super bundles of single-walled carbon nanotubes using a directed arc plasma method, *Chem. Phys. Lett.* **343** (2001) pp. 7-14.
44. Kiang C.H., Growth of large-diameter single-walled carbon nanotubes, *J. Phys. Chem. A* **104** (2000) pp. 2454-2456.
45. Zhong R., Cong H. T. and Liu C., Fabrication of single-walled carbon nanotubes from multi-walled carbon nanotubes and carbon nanofibers, *Carbon* **40** (2002) pp. 2970-2973.
46. Kataura H., Kimura A., Ohtsuka Y., Suzuki S., Maniwa Y., Hanyu T., Achiba Y., Formation of thin single-wall carbon nanotubes by laser vaporization of Rh/Pd-graphite composite rod, *Jpn. J. Appl. Phys.* **237** (1998) pp. L616-L618.
47. Lebedkin S., Schweiss P., Renker B., Malik S., Hennrich F., Neumaier M., Stoermer C., Kappes M. M., Single-wall carbon nanotubes with diameters approaching 6 nm obtained by laser vaporization, *Carbon* **40** (2002) pp. 417-423.
48. Rodriguez N. M., A review of catalytically grown carbon nanofibers, *J. Mater. Res.* **8** (1993) pp. 3233-3250.
49. Fan Y. Y., Li F., Cheng H. M., Su G., Yu Y. D., Shen Z. H., Morphology and microstructure of diameter-controllable vapor-grown carbon nanofibers, *J. Mater. Res.* **113** (1998) pp. 2342-2346.
50. Cheng H. M., Li F., Su G., Pan H. Y., He L. L., Sun X., Dresselhaus M. S., Large-scale and low-cost synthesis of single-walled carbon nanotubes by the catalytic pyrolysis of hydrocarbons, *Appl. Phys. Lett.* **72** (1998) pp. 3282-3284.
51. Cheng H. M., Li F., Sun X., Brown S. D. M., Pimenta M. A., Marucci A., Dresselhaus G., Dresselhaus M. S., Bulk morphology and diameter distribution of single-walled carbon nanotubes synthesized by catalytic decomposition of hydrocarbons, *Chem. Phys. Lett.* **289** (1998) pp. 602-610.
52. Kong J., Cassell A. M. and Dai H. J., Chemical vapor deposition of methane for single-walled carbon nanotubes, *Chem. Phys. Lett.* **292** (1998) pp. 567-574.
53. Flahaut E., Govindaraj A., Peigney A., Laurent C., Rousset A., Rao C. N. R., Synthesis of single-walled carbon nanotubes using binary (Fe, Co, Ni) alloy nanoparticles prepared *in situ* by the reduction of oxide solid solutions, *Chem. Phys. Lett.* **300** (1999) pp. 236-242.

54. Su M., Zheng B. and Liu J., A scalable CVD method for the synthesis of single-walled carbon nanotubes with high catalyst productivity, *Chem. Phys. Lett.* **322** (2000) pp. 321-326.
55. Colomer J. F., Piedigrosso P., Fonseca A., Nagy J. B., Different purification methods of carbon nanotubes produced by catalytic synthesis, *Synth. Metal.* **103** (1999) pp. 2482-2483.
56. Nikolaev P., Bronikowski M. J., Bradley R. K., Rohmund F., Colbert D. T., Smith K. A., Smalley R. E., Gas-phase catalytic growth of single-walled carbon nanotubes from carbon monoxide, *Chem. Phys. Lett.* **313** (1999) pp. 91-97.
57. Kong J., Soh H., Cassell A. M., Quate C. F., Dai H. J., Synthesis of individual single-walled carbon nanotubes on patterned silicon wafers, *Nature* **395** (1998) pp. 878-881.
58. Hafner J., Bronikowski M., Azamian B., Nikolaev P., Rinzler A. G., Colbert D. T., Smith K. A., Smalley R. E., Catalytic growth of single-wall carbon nanotubes from metal particles, *Chem. Phys. Lett.* **296** (1998) pp.195-202.
59. Wang N., Tang Z. K., Li G. D., Chen J. S., Single-walled 4 Å carbon nanotube arrays, *Nature* **408** (2000) pp. 51.
60. Ren W. C., Li F., Chen J. A., Bai S., Cheng H. M., Morphology, diameter distribution and Raman scattering measurements of double-walled carbon nanotubes synthesized by catalytic decomposition of methane, *Chem. Phys. Lett.* **359** (2002) pp. 196-202.
61. Zhu H. W., Xu C. L., Wu D. H., Wei B. Q., Vajtai R., Ajayan P. M., Direct synthesis of long single-walled carbon nanotube strands, *Science* **296** (2002) pp. 884-886.
62. Bacsa R. R., Laurent C., Peigney A., Bacsa W. S., Vaugien T., Rousset A., High specific surface area carbon nanotubes from catalytic chemical vapor deposition process, *Chem. Phys. Lett.* **323** (2000) pp. 566-571.
63. Yang Q. H., Bai S., Sauvajol J. L., Bai J.B., Large diameter single-walled carbon nanotubes synthesized by CVD, submitted.
64. Heer W. A., Bacsa W. S., Chatelain A., Gerfin T., Humphreybaker R., Forro L., Ugarte D., Aligned carbon nanotube films production and optical and electronic properties, *Science* **268** (1995) pp. 845-847.
65. Li W. Z., Xie S. S., Qian L. X., Chang B. H., Zou B. S., Zhou W. Y., Zhao R. A., Wang G., Large scale synthesis of aligned carbon nanotubes, *Science* **274** (1996) pp. 1701-1703.
66. Ren Z. F., Huang Z. P., Xu J. W., Wang J. H., Bush P., Siegal M. P., Provencio P. N., Synthesis of large arrays of well-aligned carbon nanotubes on glass, *Science* **282** (1998) pp. 1105-1107.
67. Fan S. S., Chapline M. G., Franklin N. R., Tomblor T. W., Cassell A. M., Dai H. J., Self-oriented regular arrays of carbon nanotubes and their field emission properties, *Science* **283** (1999) pp. 512-514.
68. Pan Z. W., Xie S. S., Lu L., Chang B. H., Sun L. F., Zhou W. Y., Wang G., Zhang D. L., Tensile tests of ropes of very long aligned multiwall carbon nanotubes, *Appl. Phys. Lett.* **74** (1999) pp. 3152-3154.
69. Kanzow H., Schmalz A. and Ding A., Laser-assisted production of multi-walled carbon nanotubes from acetylene, *Chem. Phys. Lett.* **295** (1998) pp. 525-530.
70. Hsu W. K., Terrones M., Hare J. P., Terrones H., Kroto H. W., Walton D. R. M., Electrolytic formation of carbon nanostructures, *Chem. Phys. Lett.* **262** (1996) pp. 161-166.
71. Guillard T., Cetout S., Alvarez L., Sauvajol J. L., Anglaret E., Bernier P., Flamant G., Laplaze D., Production of carbon nanotubes by the solar route, *Euro. Phys. J. Appl. Phys.* **5** (1999) pp. 251-256.

72. Chen Y., Gerald J. F., Chadderton L. T., Chaffron L., Nanoporous carbon produced by ball milling, *Appl. Phys. Lett.* **74** (1999) pp. 2782-2784.
73. Ugarte D., Chatelain A., Deheer W. A., Nanocapillarity and chemistry in carbon nanotubes, *Science* **274** (1996) pp. 1897-1899.
74. Dujardin E., Ebbesen T. W., Hiura H., Tanigaki K., Capillarity and wetting of carbon nanotubes, *Science* **265** (1994) pp. 1850-1852.
75. Gadd G., Blackford M., Morica S., Webb N., Evans P. J., Smith A. N., Jacobsen G., Leung S., Day A., Hua Q., The world's smallest gas cylinders? *Science* **277** (1997) pp. 933-936.
76. Han W. Q., Fan S. S., Li Q. Q., Hu Y. D., Synthesis of gallium nitride nanorods through a carbon nanotube confined reaction, *Science* **277** (1997) pp. 1287-1289.
77. Talapatra S., Zambano A. Z., Weber S. E., Migone A. D., Gases do not adsorb on the interstitial channels of closed-ended single-walled carbon nanotube bundles, *Phys. Rev. Lett.* **85** (2000) pp. 138-141.
78. Hou P. X., Bai S., Yang Q. H., Liu C., Cheng H. M., Multi-step purification of carbon nanotubes, *Carbon* **40** (2002) pp. 81-85.
79. Yin Y. F., Mays T. J. and McEnaney B., Adsorption of nitrogen in carbon nanotube arrays, *Langmuir* **15** (1999) pp. 8714-8718.
80. Teizer W., Hallock R. B., Dujardin E., Ebbesen T. W., He desorption from single wall carbon nanotube bundles: a one dimensional adsorbate, *Phys. Rev. Lett.* **82** (1999) pp. 5305-5308.
81. Wang Q. Y. and Johnson J. K., Optimization of carbon nanotube arrays for hydrogen adsorption, *J. Phys. Chem. B* **103** (1999) pp. 4809-4813.
82. Ebbesen T. W., Hiura H., Fujita J., Ochiai Y., Matsui S., Tanigaki K., Patterns in the bulk growth of carbon nanotubes, *Chem. Phys. Lett.* **209** (1993) pp.83-90.
83. Yang Q. H., Hou P. X., Bai S., Wang M. Z., Cheng H. M., Adsorption and capillarity of nitrogen in aggregated multi-walled carbon nanotubes, *Chem. Phys. Lett.* **345** (2001) pp. 18-24.
84. Yang Q. H., Liu C., Liu M., Fan Y. Z., Cheng H. M., Wang M. Z., Pore structure of SWNTs with high hydrogen storage capacity, *Science in China (Ser. E)* **45** (2002) pp. 561-568.
85. Yang Q. H., Liu M., Cheng H. M., Wang M. Z. Nano-pore structure, physical properties, and applications of carbon nanotubes, *Chinese J. Mater. Res.* **15** (2001) pp.375-386.
86. Peigney A., Laurent C., Flahaut E., Bacsá R. R., Rousset A., Specific surface area of carbon nanotubes and bundles of carbon nanotubes, *Carbon* **39** (2001) pp. 507-514.
87. Williams K. A. and Eklund P. C., Monte Carlo simulations of H₂ physisorption in finite-diameter carbon nanotube ropes, *Chem. Phys. Lett.* **320** (2000) pp. 352-358.
88. Oliver J. P., The determination of surface energetic heterogeneity using model isotherms calculated by density functional theory, The fifth international conference on the fundamentals of adsorption, Pacific Grove, Ca, 1995.
89. Webb P. A. and Orr C., Analytical methods in fine particle technology (Micromeritics Instrument Corp., Norcross, USA, 1997) pp. 89-91.
90. Yang Q. H., Relationship between hydrogen uptake and surface and pore structure of carbon nanotubes, *Report for Post-doc Research*, Institute of Metal Research, CAS, China, Sept. 2001.
91. Dillon A. C., Gennett T., Alleman J. Z. L., et al., Proceedings of the 1999 U.S. DOE Hydrogen program Review. 1999.
92. Dillon A. C. and Heben M. J., Hydrogen storage using carbon adsorbents: past, present and future, *Appl. Phys. A* **72** (2001) pp. 133-142.
93. Park C., Anderson P. E., Chambers A., Tan C. D., Hidalgo R., Rodriguez N. M.,

- Further studies of the interaction of hydrogen with graphite nanofibers, *J. Phys. Chem. B* **103** (1999) pp. 10572-10581.
94. Yang R. T., Hydrogen storage by alkali-doped carbon nanotubes---revisited, *Carbon* **38** (2000) pp. 623-626.
95. Hou P. X., Large-scale synthesis, purification and hydrogen storage capacity investigations of multi-walled carbon nanotubes, *Ph. D Dissertation*, Institute of Metal Research, CAS, China, Jan. 2003.
96. Cao A. Y., Zhu H. W., Zhang X. F., Li X. S., Ruan D. B., Xu C. L., Wei B. Q., Liang J., Wu D. H., Hydrogen storage of dense-aligned carbon nanotubes, *Chem. Phys. Lett.* **342** (2001) pp. 510-514.
97. Zhu H. W., Cao A. Y., Li X. S., Xu C. L., Mao Z. Q., Ruan D. B., Liang J., Wu D. H., Hydrogen adsorption in bundles of well-aligned carbon nanotubes at room temperature, *Appl. Surf. Sci.* **178** (2001) pp.50-55.
98. Chen Y., Shaw D. T., Bai X. D., Wang E. G., Lund C., Lu W. M., Chung D. D. L., Hydrogen storage in aligned carbon nanotubes, *Appl. Phys. Lett.* **78** (2001) pp. 2128-2130.
99. Hirscher M., Becher M., Haluska M., Dettlaff-Weglikowska U., Quintel A., Duesberg G. S., Choi Y. M., Downes P., Hulman M., Roth S., Stepanek I., Bernier P., Hydrogen storage in sonicated carbon materials, *Appl. Phys. A* **72** (2001) pp.129-132.
100. Liu C., Yang Q. H., Tong Y., Cong H. T., Cheng H. M., Volumetric hydrogen storage in single-walled carbon nanotubes, *Appl. Phys. Lett.* **80** (2002) pp.2389-2391.
101. Hou P. X., Yang Q. H., Bai S., Xu S. T., Liu M., Cheng H. M., Bulk storage capacity of hydrogen in purified multiwalled carbon nanotubes, *J. Phys. Chem. B* **106** (2002) pp. 963-966.
102. Gupta B. K. and Srivastav O. N., Synthesis and hydrogenation behaviour of graphitic nanofibres, *Int. J. Hydrogen Energy* **25** (2000) pp. 825-830.
103. Browning D. J., Gerrard M. L., Lakeman J. B. Mellor I. M., Mortimer R. J. Turpin M. C., Investigation of the hydrogen storage capacities of carbon nanotubes prepared from an ethylene precursor, Hydrogen Energy Progress XIII, In *Proceedings of the 13th World hydrogen energy conference*, (International Association for Hydrogen Energy, Beijing China, 2000) pp. 554-559.
104. Hirscher M., Becher M., Quintel A., Skakalova V, Choi Y. M., Roth S., Stepanek I., Bernier P., Leonhardt A., Fink J., Hydrogen desorption measurements on carbon nanotubes and graphite, In *Extended Abstracts of Eurocarbon 2002*, (German Carbon Group, DKG, Berlin German, 2000) pp. 91-92.
105. Badzian A., Badzian T., Breval E., Piotrowski A., Nanostructured nitrogen-doped carbon materials for hydrogen storage, *Thin Solid Film* **398-399** (2001) pp. 170-174.
106. Nützenadel C., Züttel A., Chartouni D., Schlapbach L., Electrochemical storage of hydrogen in nanotube materials, *Electrochem Solid State Lett.* **2** (1999) pp. 30-32.
107. Kibria A. K. M. F., Mo Y. H., Park K. S., Nahm K. S., Yun M. H., Electrochemical hydrogen storage behaviors of CVD, AD and LA grown carbon nanotubes in KOH medium, *Inter. J. Hydrogen Energy* **26** (2001) pp. 823-829.
108. Nützenadel C., Züttel A., Emmenegger C., Sudan P. Schlapbach L., Electrochemical storage of hydrogen in carbon single wall nanotubes, In *Science and application of nanotubes*, ed. by Tománek D., Enbody R. J., (Kluwer Academic Publishing/Plenum Press, New York, 2000) pp. 205-213.
109. Rajalakshmi N., Dhathathreyan K. S., Govindaraj A., Satishkumar B. C., Electrochemical investigation of single-walled carbon nanotubes for hydrogen storage, *Electrochimica Acta.* **45** (2000) pp. 4511-4515.

110. Dai G. P., Liu M., Chen D. M., Hou P. X., Tong Y., Cheng H. M., Electrochemical charge-discharge capacity of purified single-walled carbon nanotubes, *Electrochem. Solid State Lett.* **5** (2002) pp. E13-E15.
111. Dai G. P., Liu C., Liu M., Wang M. Z., Cheng H. M., Electrochemical hydrogen storage behaviour of ropes of aligned single-walled carbon nanotubes, *Nano Letters* **2** (2002) pp. 503-506.
112. Qin X., Gao X. P., Liu H., Yuan H. T., Yan D. Y., Gong W. L., Song D. Y., Electrochemical hydrogen storage of multiwalled carbon nanotubes, *Electrochem. Solid State Lett.* **3** (2000) pp. 532-535.
113. Lee S. M., Park K. S., Choi Y. C., Park Y. S., Bok J. M., Bae D. J., Nahm K. S., Choi Y. G., Yu S. C., Kim N. G., Fraunheim T., Lee Y. H., Hydrogen adsorption and storage in carbon nanotubes, *Synth. Metal.* **113** (2000) pp. 209-216.
114. Dresselhaus M. S., Williams K. A. and Eklund P. C., Hydrogen adsorption in carbon materials, *MRS Bull* **24** (1999) pp. 45-50.
115. Brown S. D. M., Dresselhaus G. and Dresselhaus M. S., Recent advances in catalytic materials, In *Mater. Res. Soc. Symp. Proc.*, ed. by Rodriguez N. M., Soled S. L., Hrbek J., (Warrendale, PA., 1998) pp. 157-163.
116. Stan G. and Cole M., Low coverage adsorption in cylindrical pores, *Surface Science* **395** (1998) pp. 280-291.
117. Rzepka M., Zlamp P. and De La Casa-lillo M. A., Physisorption of hydrogen on microporous carbon and carbon nanotubes, *J Phys Chem B* **102** (1998) pp. 10894-10898.
118. Darkrim F. and Levesque D., Monte Carlo simulations of hydrogen adsorption in single-walled carbon nanotubes, *J. Chem. Phys.* **109** (1998) pp. 4981-4984.
119. Wang Q. Y. and Johnson J. K., Optimization of carbon nanotube arrays for hydrogen adsorption, *J. Phys. Chem. B* **103** (1999) pp. 4809-4813.
120. Wang Q. Y. and Johnson J. K., Molecular simulation of hydrogen adsorption in single-walled carbon nanotubes and idealized carbon slit pores, *J Chem Phys* **110** (1999) pp. 577-586.
121. Wang Q. Y., Johnson J. K. and Broughton J. Q., Thermodynamic properties and phase equilibrium of fluid hydrogen from path integral simulations, *Mol. Phys.* **89** (1996) pp. 1105-1119.
122. Wang Q. Y. and Johnson J. K., Phase equilibrium of quantum fluids from simulation: Hydrogen and neon, *Fluid Phase Equilibria* **132** (1997) pp. 93-116.
123. Wang Q. Y., Johnson J. K. and Broughton J. Q., Path integral grand canonical Monte Carlo, *J. Chem. Phys.* **107** (1997) pp. 5108-5117.
124. Wang Q. Y. and Johnson J. K., Hydrogen adsorption on graphite and in carbon slit pores from path integral simulations, *Mol. Phys.* **95** (1998) pp. 299-309.
125. Yin Y. F., Mays T. J. and McEnaney B., Molecular simulations of hydrogen storage in carbon nanotube arrays, *Langmuir* **16** (2000) pp. 10521-10527.
126. Stan G. and Cole M. W., Hydrogen adsorption in nanotubes, *J. Low Temp. Phys.* **110** (1998) pp. 539-544.
127. Arellano J. S., Molina L. M., Rubio A., Alonso J. A., Density functional study of adsorption of molecular hydrogen on graphene layers, *J. Chem. Phys.* **112** (2000) pp. 8114-8119.
128. Gordon P. A. and Saeger R. B., Molecular modeling of adsorptive energy storage: hydrogen storage in single-walled carbon nanotubes, *Ind. Eng. Chem. Res* **38** (1999) pp. 4647-4655.
129. Dodziuk H. and Dolgonos G., Molecular modeling study of hydrogen storage in carbon nanotubes, *Chem. Phys. Lett.* **356** (2002) pp. 79-83.
130. Cheng H., Pez G. P. and Cooper A. C., Mechanism of hydrogen sorption in single-walled carbon nanotubes, *J. Am. Chem. Soc.* **123** (2001) pp. 5845-5846.

131. Simonyan V. V., Diep P. and Johnson J. K., Molecular simulation of hydrogen adsorption in charged single-walled carbon nanotubes, *J. Chem. Phys.* **111** (1999) pp. 9778-9783.
132. Darkrim F. and Levesque D., High adsorptive property of opened carbon nanotubes at 77 K, *J. Phys. Chem. B* **104** (2000) pp. 6773-6776.
133. Gu C., Gao G. H., Yu Y. X., Mao Z. Q., Simulation study of hydrogen storage in single walled carbon nanotubes, *Inter. J. Hydrogen Energy* **26** (2001) pp. 691-696.
134. Lee S. M. and Lee Y. H., Hydrogen storage in single-walled carbon nanotubes, *Appl. Phys. Lett.* **76** (2000) pp. 2877-2879.
135. Ma Y. C., Xia Y. Y., Zhao M. W., Wang R. J., Mei L. M., Effective hydrogen storage in single-wall carbon nanotubes, *Phys. Rev. B* **63** (2001) pp. 115422.
136. Lee S. M., An K. H. and Lee Y. H., Seifert G, Frauenheim T, A hydrogen storage mechanism in single-walled carbon Nanotubes, *J. Am. Chem. Soc.* **123** (2001) pp. 5059-5063.
137. Bauschlicher C. W., High coverages of hydrogen on a (10,0) carbon nanotube, *Nano-lett.* **1** (2001) pp. 223-226.

PHYSICAL ADSORPTION CHARACTERIZATION OF ORDERED AND AMORPHOUS MESOPOROUS MATERIALS

MATTHIAS THOMMES

Quantachrome Instruments, 1900 Corporate Drive, Boynton Beach FL-33426, USA
E-mail: Matthias.thommes@quantachrome.com

Gas adsorption is a widely used method for the characterization of mesoporous materials with regard to the determination of surface area, pore size, pore size distribution, and porosity. Significant progress was achieved during recent years with regard to the understanding of sorption phenomena in narrow pores and the subsequent improvement in the pore size analysis of porous materials, mainly because of the following reasons: (i) the discovery of novel ordered mesoporous materials, such as MCM-41, MCM-48, SBA-15, which exhibit a uniform pore structure and morphology and can therefore be used as model adsorbents to test theories of gas adsorption; (ii) carefully performed adsorption experiments (iii) the development of microscopic methods, such as the Non-Local Density Functional Theory (NLDF) or computer simulation methods (e.g. Monte-Carlo – and Molecular-Dynamic simulations), which allow to describe the configuration of adsorbed molecules in pores on a molecular level. However, the influence of pore geometry, geometrical and chemical disorder (as present in many adsorbents) on adsorption, pore condensation and sorption hysteresis, and thus the shape of the sorption isotherm, remains under investigation.

1 Introduction

Porous materials are of great practical interest for applications in the chemical, oil and gas, food and pharmaceutical industries. Microporous materials (pore width < 2 nm [1]) such as zeolites are widely used in industry as heterogeneous catalysts, in oil refining and petrochemistry, however their applications are limited because of the narrow sizes of their cavities and channels. Mesoporous materials (pore widths: 2-50 nm [1]) as for instance silica gels, porous glasses, aerogel, mesoporous titania and alumina and others are widely used in applications related to separation science, catalysis etc. The successful performance of these applications requires a comprehensive characterization of these porous materials with regard to pore size, surface area, porosity and pore size distribution. Common mesoporous materials such as silica gels and porous glasses are amorphous; in contrast materials like zeolites are crystalline, i.e., every atom can be located in a microscopically-sized unit cell. Such symmetry is not present in amorphous materials. Whereas a complete and comprehensive characterization can be performed in case of crystalline

materials, amorphous nanoporous materials vary considerably in their microstructure and a complete and comprehensive characterization is problematic. However, average properties such as porosity, specific surface area, mean pore size and pore size distribution can still be determined.

Within this context, silicate/aluminosilicate mesoporous molecular sieves of the M41S family (i.e., MCM-41, MCM-48, MCM-50) are very interesting [e.g., 2-4]. (Discovered in 1992 by Mobil scientists) [2]. These materials are synthesized by using surfactants as structure directing agents and can be characterized by well defined pores of tunable sizes in the range between 2 nm and 10 nm, and specific surface areas between 600 m²/g and 1300 m²/g. The most prominent representatives of M41S materials are MCM-41 and MCM-48. MCM-41 consists of regular pseudo-one-dimensional pores in a honeycomb arrangement while MCM-48 exhibits cubic symmetry consisting of two interwoven, but unconnected three-dimensional pore systems of cylindrical pores. MCM-50 comprises a lamellar phase. Independently, a family of mesoporous silica materials of similar properties as MCM-41 was discovered by Japanese researchers [5,6]; a prominent member of this family is for instance FSM-16 [6]. These mesoporous molecular sieves are essentially amorphous on a microscopic scale (i.e., the pore walls) but can be considered as highly ordered on larger (macroscopic) length scales, and exhibit therefore properties of both zeolites and mesoporous solids such as silica gels and porous glasses. While the pore diameter range of MCM-41 materials is restricted to ca. 10 nm, ordered mesoporous silica molecular sieves with pore diameter up to ca. 30 nm (SBA-15) can be obtained by using amphiphilic block copolymers as templates [e.g.,7]. SBA-15 similar to MCM-41 consists of a hexagonal packing of cylindrical channels – but depending on details of the synthesis procedure this material can possess irregular intrawall micro-mesopores, which connect adjacent channels [8,9]. MCM-48 material is more difficult to synthesize and typically high-quality materials can be obtained in the pore size range between 2 and ca. 5 nm [12]. Meanwhile a great variety of mesoporous molecular sieve materials has been synthesized among them also materials with well defined cage-like structures (e.g., SBA-2, SBA-12, SBA-16). Mesoporous molecular sieves have potential applications in catalysis, separations [10], guest-host technologies etc [11,12]. Other recently developed ordered mesoporous materials include periodic mesoporous organosilicas (PMO's) [e.g., 13,14,15], nanoporous carbons with ordered mesostructure (e.g., CMK1, CMK3) [e.g.,16, 17] porous metal-organic framework materials [18] and carbon nanotubes [e.g.,19].

The high degree of order in M41S materials compared to conventional mesoporous materials is reflected in a narrow pore size distribution, which is determined by assuming that the porous material consists of pores having the same (cylindrical) shape, but varying only in size. This is illustrated in figure 1, which shows the extremely sharp pore size distribution curves (PSD) of MCM-41, and SBA-15 compared to the much broader PSD's for controlled-pore glass samples (CPG). The pore size distributions shown in figure 1 were obtained from nitrogen adsorption isotherms (at 77 K) [20]. Gas adsorption is one of many experimental methods available for the characterization of porous materials. These include small angle x-ray and neutron scattering (SAXS and SANS), mercury porosimetry, electron microscopy (scanning and transmission), thermoporometry, NMR-methods, and others. Each method has a limited length scale of applicability for pore size analysis. An overview of different methods for pore size characterization and their application range was recently given by IUPAC [21]. Among these methods gas adsorption is the most popular one because it allows to assess a wide range of pore sizes (from 0.35 nm up to 100 nm) including the complete range of micro- and mesopores and even macropores. In addition, gas adsorption techniques are convenient to use and are not that cost intensive as compared to some of the other methods.

The adsorbed amount as a function of pressure can be obtained by volumetric (manometric) and gravimetric methods, carrier gas and calorimetric techniques, nuclear resonance as well as by a combination of calorimetric and impedance spectroscopic measurements [22 - 24]. Surface area and pore size analysis is usually based on nitrogen, argon and krypton adsorption isotherms obtained with the volumetric (manometric) method at temperatures of liquid nitrogen (77.35 K) and liquid argon (87.27 K). The shape of adsorption/desorption isotherms (i.e., sorption isotherm) depends on pore size and temperature, i.e., differences in the thermodynamic states of the pore fluid and the bulk fluid (which includes critical point and triple point shifts of the pore fluid as compared to the bulk fluid; see section 3.2) as well as on the chemical and geometrical heterogeneity (i.e. the degree of disorder) of the porous material. For instance, the pore size characterization of mesoporous materials is based on an accurate understanding of the pore condensation phenomenon, which is characterized by a step in the sorption isotherm. Pore condensation represents a confinement induced shifted gas-liquid phase transition, i.e., condensation occurs at a pressure P less than the saturation pressure P_0 of the fluid. The P/P_0 -value where pore condensation occurs depends on the

liquid-interfacial tension, the strength of the attractive interactions between the fluid and pore walls, the pore geometry and the pore size.

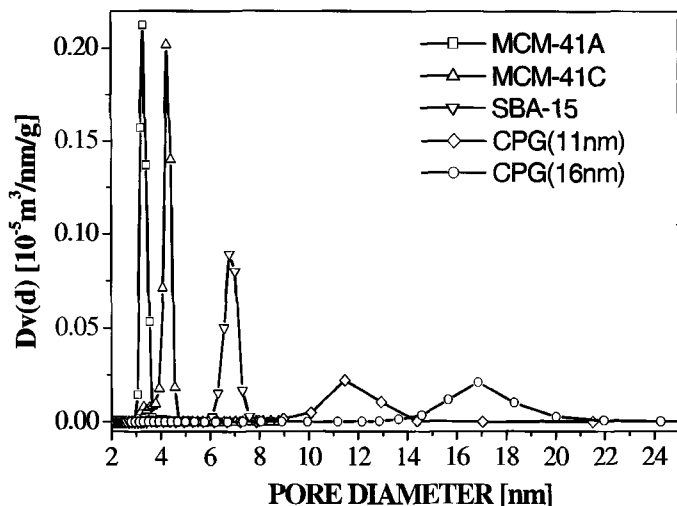


Figure 1. Pore size distribution curves for mesoporous molecular sieves (MCM-41 SBA-15), and controlled-pore glasses obtained from N_2 (77K) sorption isotherms. From [20].

A relation between the pore size and the pore condensation/evaporation pressure for a given fluid/pore system is for instance given by the classical Kelvin equation. Pore condensation is often accompanied by hysteresis, i.e., evaporation of the condensed fluid (desorption branch of the hysteresis loop) occurs at a lower pressure as compared to pore condensation, which complicates the situation. The decision whether the adsorption – or desorption branch of the sorption isotherm should be taken for the pore size analysis is often crucial for an accurate pore size analysis.

Despite the sometimes very complex microstructure of adsorbents the theoretical models and methods, which are applied to analyse sorption isotherms are commonly based on extremely simplified assumptions of the texture of the porous material. In almost all cases it is assumed that the adsorbent consists of an assembly of independent pores of given geometry (e.g., cylindrical or slit-like) with the additional assumption that the pore walls are chemically and geometrically homogeneous. Hence, the total adsorption isotherm consists of a sum of adsorption isotherms over a distribution of narrow pores. In order to test theoretical models which describe the relationship between the shape of an isotherm, pore size and texture, model adsorbents are needed, which reflect the assumptions made in the theoretical models. Mesoporous molecular sieves and in particular

MCM-41 were already early recognized as good candidates for the testing of theoretical models of gas adsorption, mainly because of two reasons: (i) the periodicity of mesoporous molecular sieves allows to use other techniques such as high resolution transmission electronic microscopy (TEM) and methods based on X-ray diffraction (XRD) to compare with pore size results obtained from gas adsorption; (ii) MCM-41 consists of independent pseudo-one-dimensional pores of well defined (hexagonal /cylindrical) pore geometry. Despite the fact that the pore channels may exhibit some curvature [25], MCM-41 silica material still captures the most important features of theoretical models currently used for pore size analysis.

Within this framework extensive experimental and theoretical studies on the sorption and phase behavior of fluids in ordered mesoporous molecular sieves have been performed since the first systematic sorption studies on MCM-41 had been published in 1993 [26,27]. Most of the following work focussed again on the adsorption properties of MCM-41 materials [e.g., 26-37], but somewhat later (starting at ca. 1996), systematic adsorption studies were also performed on other mesoporous silica molecular sieves such as SBA-15 [e.g, 9,38-40], MCM-48 [41-48], FSM-16 etc.. [e.g., 49,50]. The systematic evaluation of the adsorption properties of PMO and CMK adsorbents [e.g, 51] is in progress.

In particular, the studies involving MCM-41 materials have revealed, that classical methods for mesopore size analysis based on macroscopic, thermodynamic assumptions (e.g., methods based on the Kelvin equation) cannot describe the sorption and phase behavior of fluids in narrow mesopores correctly, which leads to an underestimation of the pore size up to ca. 25 % for materials consisting of pores < ca. 10 nm. Subsequently performed corrections of the Kelvin equation based methods have indeed led to some improvement in the accuracy, but only over a limited pore size range. An accurate mesopore size analysis over the complete micro- and mesopore size range is possible by applying microscopic methods based on statistical mechanics, such as the Non-Local Density Functional Theory (NLDFT) or computer simulation methods (Grand Canonical Monte Carlo (GCMC) and Molecular-Dynamic (MD) simulations). These methods allow to describe the configuration of adsorbed molecules in pores on a molecular level. Pore size analysis data for mesoporous molecular sieves obtained with these methods agree very well with the results obtained from independent methods (based on XRD, TEM etc..). In contrast to the classical methods, the microscopic methods for pore size analysis take into account details of the fluid-fluid interactions and the adsorption

potential (which depends on the strength of the fluid-wall interactions and the pore geometry). Appropriate methods for pore size analysis based on NLDFT and GCMC are meanwhile commercially available for many important fluid/substrate systems.

Despite this progress, a satisfying verification of theoretical models for mesopore size analysis is only achieved so far for highly ordered materials (e.g. mesoporous molecular sieves), which can be modeled within the framework of an independent pore model. Theories based on a single pore models may be in some cases (to some extend) applicable to describe the sorption and phase behavior of fluids in disordered materials, but this is not generally the case. The mechanisms of adsorption, pore condensation and hysteresis in disordered mesoporous materials is still not completely understood and more theoretical and experimental work is clearly required to understand the combined effects of confinement, pore geometry, connectivity etc., on the origin of pore condensation and hysteresis. The application of models which attempt to describe the microstructure of porous materials at length scales beyond that of a single pore is under investigation.

The paper is organized as follows: In section 2 we discuss some general aspects of the application of physical adsorption for surface and pore size analysis. Recent advances in the understanding of sorption, pore condensation, hysteresis phenomena, and critical behavior of fluids confined to mesoscopic systems will be reviewed in section 3. Important consequences for pore size calculation will be discussed in section 4. A discussion of the accuracy and applicability of classical, thermodynamic methods for pore size analysis compared to microscopic models (e.g. NLDFT) can also be found in section 4. Concluding remarks will be given in section 5.

2 Surface and pore size analysis by physisorption: General aspects

2.1 Physisorption measurement

Physical adsorption of gases on solid surfaces is caused by the attractive van der Waals interactions (i.e., dispersion forces) of gas molecules (adsorptive) with a solid (adsorbent). The interaction energy $U_s(z)$ of a gas molecule at distance z from a solid surface is approximately given as:

$$U_s(z) = -(\pi/6)C_{sf}\rho_s/z^3 \quad (1)$$

where C_{sf} is a measure for the strength of attractive fluid-wall interactions

and ρ_s represents the solid density. At sufficiently low temperatures (typically at and below the normal boiling temperature of the adsorptive), the adsorption of gases can be analyzed in terms of a two-phase model in which an adsorbed phase (adsorbate) coexists with the bulk phase. This is the typical situation encountered for nitrogen, argon and krypton adsorption at the temperatures of liquid nitrogen (ca. 77.35 K) and liquid argon (ca. 87.27 K), respectively. The amount of adsorbed fluid can be expressed by the adsorbed mass of gas or volume (often given in STP per unit mass; STP: standard temperature and pressure, namely 273.15 K, 760 Torr, i.e. 1.01325×10^5 Pa).

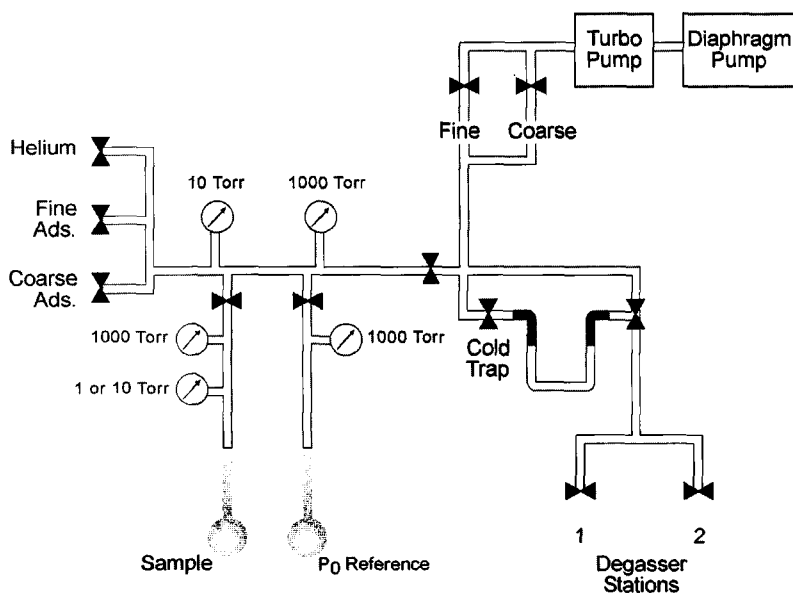


Figure 2. Schematic illustration of a volumetric (manometric) adsorption apparatus.

The volumetric (manometric) method is generally applied for adsorption measurements at cryogenic temperatures. The method is based on the measurement of the gas pressure in a calibrated constant volume, at known temperature. An example for a state-of-the-art volumetric adsorption apparatus is given in the schematic figure 2. The analysis station of the volumetric sorption apparatus is equipped - in addition to the obligatory pressure transducers in the dosing volume (manifold) of the apparatus - with high precision pressure transducers dedicated to read the pressure just in the sample cell. Hence, the sample cell is isolated during equilibration,

which ensures a very small effective void volume and therefore a highly accurate determination of the adsorbed amount. The saturation pressure P_0 is measured throughout the entire analysis by means of a dedicated saturation pressure transducer, which allows the vapor pressure to be monitored for each data point. This leads to high accuracy and precision in the determination of P/P_0 and thus in the determination of the pore size distribution. It is of advantage to use a diaphragm pump as a foreline pump for the turbomolecular pump in order to guarantee a complete oil-free environment for (i) the adsorption measurement and (ii) the outgassing of the sample, prior to the analysis.

2.2 Characterization of mesoporous materials

The International Union of Pure and Applied Chemistry (IUPAC) [1] proposed to classify pores by their internal pore width (the pore width defined as the diameter in case of a cylindrical pore and as the distance between opposite walls in case of a slit pore). *Micropore*: pore of internal width less than 2 nm; *mesopore*: pore of internal width between 2 and 50 nm; *macropore*: pore of internal width greater than 50 nm. In the same paper the IUPAC classification of sorption isotherms was published. The different shapes of the 6 isotherms in the classification reveal the influence of the interplay between the strength of attractive fluid-wall and fluid-fluid interactions as well as the effects of confined pore space on the shape of adsorption isotherms.

An analysis of gas adsorption isotherms allows to determine surface area, pore size, pore size distribution, pore volume, and porosity. In addition some information about the roughness of the adsorbent surfaces and fractal dimension can be obtained. The *specific surface area* is usually determined by the method of Brunauer Emmett and Teller (BET). By applying the BET equation in a relative pressure range between 0.05 – 0.3, the monolayer capacity N_m is determined. The specific surface area S is obtained from the monolayer capacity by the application of the simple equation: $S = N_m L \sigma$, where L is the Avogadro constant and σ is the so-called cross-sectional area (the average area occupied by each molecule in a completed monolayer). The BET equation is applicable for surface area analysis of nonporous- and mesoporous materials consisting of pores of wide pore diameter, but is in a strict sense not applicable in case of microporous adsorbents (a critical appraisal of the BET method is given in refs. [52-54]). In addition it seems that the BET method is inaccurate for estimating the surface area of mesoporous molecular sieves of pore widths

< ca. 4 nm, because pore filling is observed at pressures very close to the pressure range where monolayer-multilayer formation on the pore walls occurs, which may lead to a significant overestimation of the monolayer capacity in case of an BET analysis. In addition, the result depends very much on the assumed cross-sectional area. For instance, recent experimental sorption studies on MCM-41 silica materials suggest strongly, that the cross-sectional area of nitrogen on a hydroxylated surface (as it is the case for MCM-41) might differ from the commonly adopted value of 0.162 nm^2 [55]. Similar observation were already made in the past and it was assumed, that the quadrupole moment of the nitrogen molecule leads to specific interactions with the hydroxyl groups on the surface causing an orientating effect on the adsorbed nitrogen molecule [56]. A cross-sectional area of 0.135 nm^2 was proposed, which was obtained by measuring the volume of N_2 adsorbed on silica spheres of known diameter [57].

Because of the roughness of amorphous surfaces the determination of the *fractal dimension* by gas adsorption can be considered as a useful and characteristic parameter, which complements the surface and pore size characterization [58 - 60]. The determination of the surface roughness in the scale range of molecular sizes (usually less than 10 \AA) can be obtained by means of the method of molecular tiling which is based on a comparison of the monolayer capacities of different adsorbents. The scale range from $10\text{-}20 \text{ \AA}$ to 1000 \AA can be investigated by analyzing the multilayer region of a sorption isotherm by means of the Frenkel-Halsey Hill method. A thermodynamic method (the so-called Neimark-Kiselev (NK) method) allows to sense fractal properties of mesoporous materials in the range of scales from ca. 4 \AA – 1000 \AA . For instance, a characterization of MCM-41 with regard to roughness and fractality over a wide range of length scales can be found in ref. [60]. Please note that the interpretation of fractal dimension parameters obtained by gas adsorption in the context of fractal self-similarity (and/or self-affinity) is not always justified.

In case that the sorption isotherm exhibits a distinct plateau (see isotherms in figure 2a, i.e., so-called IUPAC type IV and type V sorption isotherms), the *total specific pore volume* can be obtained by converting the amount adsorbed after the pore filling step into liquid volume assuming that the density of the adsorbate is equal to the bulk liquid density at saturation (so-called Gurvich rule). The gas adsorption technique allows of course only to determine the volume of open pores. Closed porosity cannot be accessed, but can be derived if the true density and particle(bulk)

density of the materials are known. *Porosity* is defined as the ratio of the volume of pores and voids to the volume occupied by the solid. If a cylindrical pore geometry can be assumed, the *average pore diameter* of a porous materials can be calculated by the following relation:

$$D_{4V/s} = 4V_p / (S_{total} - S_{ext}) \quad (2)$$

The total surface area S_{total} can be calculated either from the BET-method, from t-plot or α_s comparison plot methods [52]. The external surface area can be determined by applying for instance the comparison plot method in the region of relative pressure above the pore condensation step.

In order to obtain a comprehensive surface and pore size analysis from sorption isotherms, details about the pore condensation and hysteresis mechanism need to be known. This will be discussed in section 3.

2.3 Adsorptives other than nitrogen for mesopore analysis

Generally, nitrogen adsorption at liquid nitrogen temperature (77 K) is used for surface and pore size characterization. Krypton adsorption at 77 K is more or less exclusively used for low surface area analysis [52-54]. Argon adsorption at 77 K and liquid argon temperature (87 K) is also often used for micro- and mesopore size analysis. The use of argon adsorption is of advantage for the pore size analysis of zeolites and other microporous materials because the filling of pores of dimension 0.5 - 1 nm occurs at much higher relative pressure as compared to nitrogen adsorption. This phenomenon is related to the fact, that the nitrogen molecule possesses a quadrupole moment, which leads to specific fluid-wall interactions [54]. However, a combined and complete micro- and mesopore size analysis with argon is not possible at liquid nitrogen temperature (which is ca. 6.5 K below the triple point temperature of bulk argon). Systematic sorption experiments indicate that the pore size analysis of mesoporous silica by argon adsorption at 77 K is limited to pore diameters smaller than ca. 15 nm, i.e., pore condensation cannot be observed anymore above this pore size limit [20, 44]. This behavior is related to confinement effects on the location of the (quasi)-triple point of the pore fluid (see section 3.2). Of course, such a limitation does not exist for argon sorption at 87.27 K; pore filling and pore condensation can be observed here over the complete micro- and mesopore size range. Argon sorption isotherms obtained at 87 K and 77 K in ordered and disordered mesoporous silica materials of

various mean pore size are shown in Figures 3a and b (the pore size distribution curves of these materials are given in Figure 1.) The argon sorption data at 87 K (in MCM-41, SBA-15 and controlled pore glasses) shown in Figure 3a reveal that pore condensation shifts to higher relative pressures with increasing pore diameter. In addition, hysteresis occurs in all materials, with the exception of MCM-41 A (pore size: 3.3 nm), which exhibits reversible pore condensation. With increasing pore diameter, hysteresis begins to develop and is present for MCM-41 C (4.2 nm), and a wide hysteresis loop is observed for SBA-15 (6.7 nm).

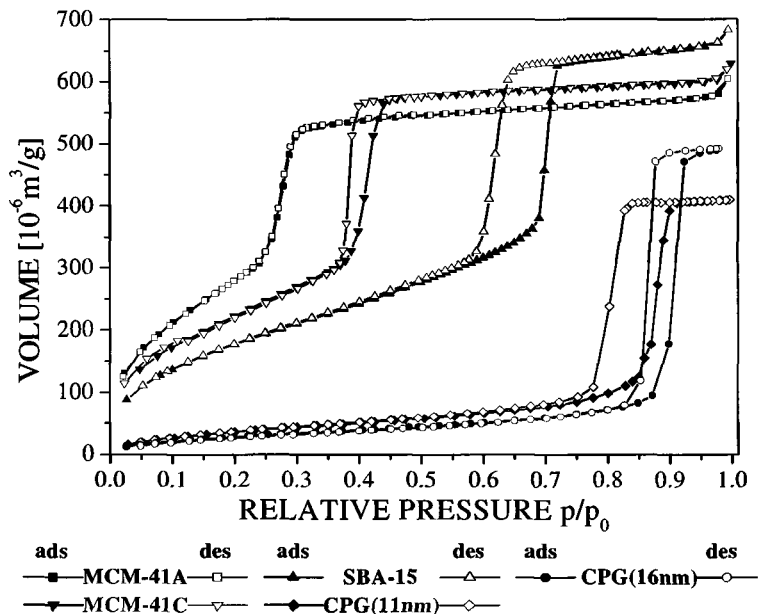


Figure 3a. Argon sorption isotherms at 87 K on MCM-41, SBA-15 and controlled-pore glasses (CPG) From [20].

The data also clearly reveal, that the width of the hysteresis loop increases with increasing pore size (details of the pore condensation and hysteresis mechanism will be discussed in section 3). Lowering the measurement temperature to 77 K (Figure 3b) leads to a widening of the hysteresis loops for the MCM-41 and SBA-15 silica samples (hysteresis appears also for MCM-41 A), but pore condensation and hysteresis cannot be observed anymore in the controlled pore glass of mode pore diameter 16 nm (the small deviations between the two argon sorption isotherms for CPG (16 nm) at 77 K are attributed to small differences in the temperature of the liquid nitrogen bath. A detailed analysis of the data in combination

with the pore size distribution curves has led to the conclusion that pore condensation does not occur anymore for pore sizes larger than ca. 15 nm [20], which limits (as indicated before) the pore diameter range over which mesopore size analysis can be performed using argon as adsorptive at 77 K.

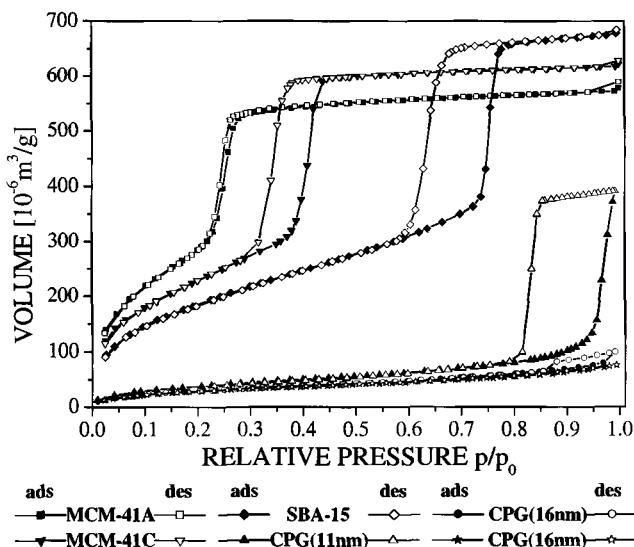


Figure 3b. Argon sorption at 77 K on MCM-41, SBA-15 and CPG. (P_0 refers to solid argon). From [20].

3 Pore condensation and adsorption hysteresis

3.1 The modified Kelvin equation

For pores of uniform shape and width (ideal slit-like or cylindrical mesopores) pore condensation can be described on the basis of the Kelvin equation, i.e., the shift of the gas-liquid phase transition of a confined fluid from bulk coexistence, is expressed in macroscopic quantities like the surface tension γ of the bulk fluid, the densities of the coexistent liquid ρ^l and gas ρ^g ($\Delta\rho = \rho^l - \rho^g$) and the contact angle θ of the liquid meniscus against the pore wall. For cylindrical pores the modified Kelvin equation [52-54] is given by

$$\ln(P/P_0) = -2\gamma\cos\theta / RT\Delta\rho(r_p - t_c), \quad (3)$$

where R is the universal gas constant, r_p the pore radius and t_c the thickness of an adsorbed multilayer film, which is formed prior to pore condensation. The occurrence of pore condensation is expected as long as the contact angle is below 90° . A contact angle of 0° is usually assumed in case of nitrogen and argon adsorption at 77 K and 87 K, respectively.

The Kelvin equation provides a relationship between the pore diameter and the pore condensation pressure, and predicts that pore condensation shifts to a higher relative pressure with increasing pore diameter and temperature. The modified Kelvin equation (eq. 3) serves as the basis for many methods applied for mesopore analysis, including the Barrett-Joyner Halenda method (BJH) [61], which is widely used. In order to account for the preadsorbed multilayer film, the Kelvin equation is combined with a standard isotherm or a so-called t -curve, which usually refers to adsorption measurements on a non-porous solid. Accordingly, the preadsorbed multilayer film is assessed by the statistical (mean) thickness of an adsorbed film on a nonporous solid of a surface similar to that of the sample under consideration (such statistical thickness equations were derived for instance by Halsey, Harkins-Jura and de-Boer [52-54]). However, it is obvious that assuming the situation of a nonporous, planar surface for the evaluation of the preadsorbed film thickness cannot be valid anymore in case of narrow pores, where the curvature of the pore walls and their adsorption potential has a pronounced effect on the film thickness and its interfacial tension. The corresponding inaccuracy in the pore size analysis is discussed in section 4.

3.2. Sorption and phase behavior of fluids in mesopores: multilayer adsorption, pore condensation and critical behavior

In case of complete wetting, the pore walls are covered by a multilayer adsorbed film at the onset of pore condensation. The stability of this film is determined by the attractive fluid-wall interactions, the surface tension and curvature of the liquid-vapor interface. Multilayer adsorption can for instance be described in the spirit of the Frenkel-Halsey-Hill theory [52,54]. One of the basic assumptions is that the (sufficiently thick) adsorbed multilayer film can be considered as a slab of liquid, which reveals the same properties (i.e., density etc.) as the bulk liquid would have at this temperature. The only modification to its free energy arises from the interaction with the solid, i.e. the adsorption forces (dispersion forces). The chemical potential difference $\Delta\mu = \mu - \mu_0$ of an adsorbed, liquid-like film of thickness t compared to the chemical potential of the appropriate bulk

liquid (μ_0) is given according to the Frenkel-Halsey-Hill (F.H.H) equation by

$$\Delta\mu = \mu - \mu_0 = -\alpha t^{-m} \quad (4)$$

where α is the fluid-wall interaction parameter, and the t^{-m} law results from the long-range van der Waals interactions between a fluid molecule and a semi-infinite planar wall. In case of non-retarded van der Waals fluid-wall interactions the exponent m has a theoretical value of 3. However, experimental values for m are often significantly smaller than the theoretical value, even for strongly attractive adsorbents like graphite, i.e., $m = 2.5 - 2.7$. Among other reasons these deviations from the theoretical value are correlated with the surface roughness and the fractal nature of the pore wall [58,59].

The film thickness cannot grow unlimited in pores. The stability of the multilayer adsorbed film is determined by the long-range van der Waals interactions, and by the surface tension and curvature of the liquid-vapor interface. The chemical potential difference $\Delta\mu$ is then given by

$$\Delta\mu = \Delta\mu_a + \Delta\mu_c \quad (5)$$

For small film thickness the first term $\Delta\mu_a$ associated with multilayer adsorption dominates. When the adsorbed film becomes thicker, the adsorption potential will become less important, and $\Delta\mu$ will be dominated almost entirely by the curvature contribution $\Delta\mu_c$ (i.e., the Laplace term), which is given for cylindrical pores by $\Delta\mu_c = -(\gamma/a \Delta\rho)$, a is the core radius ($a = r_p - t$). At a certain critical thickness t_c pore condensation occurs in the core of the pore, controlled by intermolecular forces in the core fluid.

Figure 4 shows a (schematic) sorption isotherm as it is expected for adsorption/desorption of a pure fluid in a single mesopore of cylindrical shape in combination with a schematic representation of the appropriate sorption and phase phenomena occurring in the pore. Please note, that the schematic isotherm reveals a vertical pore condensation step. However, a truly vertical step in the adsorption isotherm is not to be expected for any real porous material with a nonvanishing pore-size distribution, i.e., the wider the pore size distribution, the less sharp is the observed pore condensation transition. The adsorption mechanism in mesopores is at lower relative pressures absolutely similar as in case of adsorption on planar surfaces. After completion of the monolayer formation (A),

multilayer adsorption commences (B). After reaching a critical film thickness (C) capillary condensation occurs essentially in the core of the pore (transition from configuration C to D). The plateau region of the isotherm reflects the situation of a pore completely filled with liquid. The pore liquid is separated from the bulk gas phase by a hemispherical meniscus. Pore evaporation therefore occurs by a receding meniscus (E) at a pressure, which is less than the pore condensation pressure.

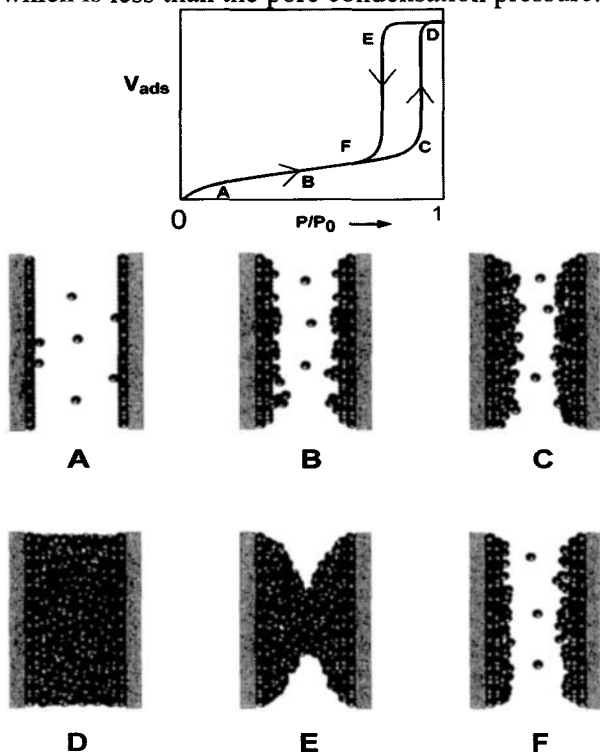


Figure 4. Schematic representation of multilayer adsorption, pore condensation and hysteresis in a single pore.

The pressure where the hysteresis loop closes corresponds again to the situation of an adsorbed multilayer film which is in equilibrium with a vapor in the core of the pore and the bulk gas phase. In the relative pressure range between (F) and (A) adsorption and desorption are reversible.

In contrast to the Kelvin approach, the Broeckhoff and de Boer [62 - 64] as well as the Saam-Cole theory [65] capture essentially the mechanism of pore condensation and hysteresis as it is described in Figure 4. These theories take into account the (i) influence of the adsorption

potential on the chemical potential where pore condensation occurs in the pores and (ii) the effect of curvature on the thickness of the adsorbed multilayer film. In agreement with experimental observations, these theories predict that an increase in the strength of the attractive fluid-wall interaction, a lowering of the experimental temperature as well as decreasing the pore size will shift the pore condensation transition to lower relative pressures.

However, all these thermodynamic, macroscopic theories do not account for the peculiarities of the critical region. As discussed before, the Kelvin approach considers pore condensation as a gas-liquid phase transition in the core of the pore between two homogenous, bulk like gas and liquid phases. The density difference $\Delta\rho = \rho^l - \rho^g$ is considered to be equal to the difference in orthobaric densities of coexisting bulk phases, i.e., pore condensation and hysteresis are expected to occur up to the bulk critical point, where $\Delta\rho = 0$.

In contrast, microscopic approaches such as DFT [66], lattice model calculation [67] and various computer simulation studies [68-70] suggest that a fluid confined to a single pore can exist with two possible density profiles corresponding to inhomogeneous gas- and liquid configurations in the pore. In this sense pore condensation reflects a first order phase transition between an inhomogeneous gas configuration, which consists of vapor in the core region of the pore in equilibrium with a liquid like adsorbed film (corresponds to configuration **C** in figure 4), and a liquid configuration, where the pore is filled with liquid (corresponds to configuration **D** in figure 4). At the pore critical point of the confined fluid, these two hitherto distinct fluid configurations will become indistinguishable, i.e., a pore condensation step cannot be observed anymore. The suggested order parameter for this phase transition is here the difference in surface excess (or adsorbed amounts at low bulk gas densities, i.e., $\Delta V_{(l,g)} = V_{\text{ads(liquid)}} - V_{\text{ads(gas)}}$) between the two inhomogeneous gas and liquid phases and not the difference in orthobaric densities $\Delta\rho$ as it is the case for the correspondent bulk phase transition, which occurs between homogeneous gas and liquid phases. Accordingly, at the pore critical point $\Delta V_{(l,g)} = 0$ and pore condensation cannot be observed anymore. The critical temperature of the confined fluid is shifted to lower temperatures, i.e., in contrast to the predictions of the Kelvin equation pore condensation and hysteresis will vanish already at temperatures below T_c . The shift of the critical temperature can be rationalized by the argument that a fluid in narrow pores is an intermediate between a three-dimensional fluid and a one-dimensional fluid for which

no critical point exists at $T > 0$. Hence, the shift of the pore critical temperature is correlated with the pore width, i.e., the more narrow the pore, the lower the pore critical temperature. Consequently, at a given subcritical temperature pore condensation is only possible in pores which are wider than the critical pore size W_c .

Adsorption experiments of pure fluids in porous glasses [71-73], silica gel [74] and MCM-41-type of materials [28b,75-77] revealed that pore condensation and hysteresis indeed disappears below the bulk critical temperature. Furthermore, systematic adsorption studies of SF_6 in controlled-pore glasses indicated already, that hysteresis already disappears below the pore critical temperature T_{cc} , i.e., reversible pore condensation could be observed (the criterion applied here to determine pore criticality was the disappearance of the pore condensation step) [73]. An experimental study on nitrogen adsorption in MCM-41 silica in combination with the application of density functional theory clearly revealed that the experimental disappearance of hysteresis is indeed not identical with having achieved the pore critical point [33]. Nitrogen sorption hysteresis (at 77 K) disappears when the pore diameter is smaller than 4 nm, however based on the theoretical results the (pseudo)-pore critical point is achieved at a much smaller pore diameter, i.e. 1.8 nm (the bulk critical temperature of nitrogen is 126.2 K). This picture was supported by subsequent experimental sorption studies of pure fluids in ordered mesoporous silica materials [75-77]. For instance, experiments to study the temperature dependence of argon adsorption in a MCM-41 materials with pore channels of 2.2 nm diameter revealed a hysteresis critical temperature T_h of ca. 62 K, whereas the pore critical temperature was located at ca. 98 K (the bulk critical temperature T_c for argon is 150.7 K), i.e., substantial downward shifts in the pore critical- and hysteresis critical temperatures are observed for such narrow pores [76,77]. These systematic studies also revealed that temperature and pore size can be considered as complementary variables with regard to their influence on the occurrence of hysteresis: an increase in temperature has qualitatively a similar effect as a decrease in pore size. Both lead to a decrease in the width of the hysteresis loop, which eventually disappears at certain critical pore size and temperature, which is illustrated in Figure 5.

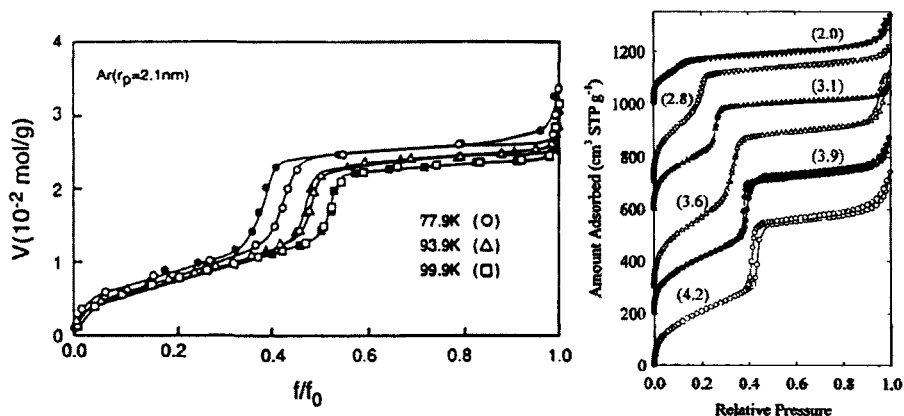


Figure 5. (a) Argon sorption as a function of temperature in a MCM-41 silica sample of pore radius 2.1 nm. From [76]. (b) Argon sorption at 87 K as a function of pore diameter in MCM-41 silica. From [116].

We can separate the following regimes: (i) Continuous pore filling without pore condensation step occurs below a certain critical pore width (W_c), at a given temperature $T < T_c$. For a given pore size (W) continuous pore filling can be observed above the pore critical temperature T_{Wc} . (and of course above the bulk critical temperature); (ii) Reversible pore condensation occurs for pore sizes between the critical pore size W_c and the pore size where hysteresis disappears (W_h), i.e., in the pore size range $W_c < W < W_h$; or in case of fixed pore size in the temperature range between the hysteresis critical temperature T_h and the pore critical temperature T_{Wc} ; (iii) Pore condensation with hysteresis occurs for pore sizes larger than W_h (for a given pore size) and at temperatures below T_h .

In addition to the shift in critical temperature, experiments and theory indicate that as a result of the combined effects of fluid-wall forces and finite-size the freezing temperature and triple point of the pore fluid may also be shifted to lower temperature relative to the bulk triple point, if the wall-fluid attraction is not too strong, i.e., the pore wall does not prefer the solid phase [70]. Hence, pore condensation can be also observed at temperature below the bulk triple point temperature (an example is argon pore condensation at 77 K in mesoporous silica materials of diameters $< 15 \text{ nm}$, see figure 3b [20,44]). Theoretical and experimental studies have led to the conclusion that the complete coexistence curve of a fluid confined to mesoporous silica materials is shifted to lower temperature and higher mean density [71,73,75] (see also the review of Gelb et al [70]). Please note, that an elevation of the freezing temperature is however observed in

case of strong adsorption forces (e.g, cyclohexane adsorption in carbon pores [78]). Figure 6 shows the schematic phase diagrams of bulk- and pore fluid and illustrates the influence of confinement on the sorption and phase behavior as it can be found for instance in case of mesoporous silica.

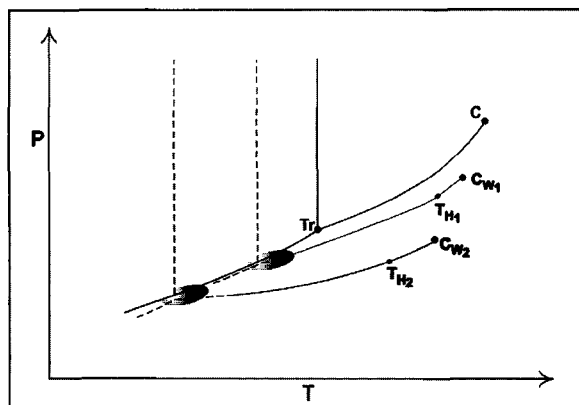


Figure 6. Schematic phase diagram of a bulk and pore fluid confined to different sized pores of widths $W_1 > W_2$. The pore condensation lines, i.e., the locus of states of the unsaturated vapour at which pore condensation will occur end in the appropriate pore critical points C_{w1} and C_{w2} , with $T_{Cw1} > T_{Cw2}$. For a given experimental temperature pore condensation will occur first in the pore of width W_2 , and a higher (relative) pressure in the larger pore W_1 . The temperatures T_{H1} and T_{H2} are the hysteresis critical temperatures, where experimental hysteresis disappears. Details of the sorption and phase behavior below the bulk triple point as well as the nature of pore triple points is still under investigation [20,48,70, 76, 78-83]. Hence, these regions of the phase diagram are indicated by dashed lines and the grey areas. (Please note, that from a theoretical point of view, real phase transitions and therefore real criticality cannot occur in pseudo-onedimensional cylindrical pores, i.e., pore condensation and the pore critical point should therefore be considered here as pseudo-phase transition and pseudo-critical point, respectively).

These observations reveal clearly that the shape of sorption isotherms does not depend only on the texture of the porous material, but also on the difference of thermodynamic states between the confined fluid and bulk fluid phase. This has to be taken into account for the characterization of porous media by gas adsorption, i.e., macroscopic, thermodynamic approaches based on the Kelvin equation, Broeckhoff and de Boer and Cole-Saam theories fail to predict correctly the influence of confinement on the phase and critical behavior of pore fluids. They are therefore inaccurate for pore size analysis in a temperature and pore size range where hysteresis disappears, i.e., close to the hysteresis- and pore critical temperature (this will be discussed in more detail in section 4).

3.3 Pore condensation hysteresis

3.3.1 IUPAC classification of hysteresis loops

It is widely accepted that there is a correlation between the shape of the hysteresis loop and the texture (e.g., pore size distribution, pore geometry, connectivity) of a mesoporous adsorbent. An empirical classification of hysteresis loops was given by the IUPAC [1], which is based on an earlier classification by de Boer [84]. The IUPAC classification is shown in figure 7. According to the IUPAC classification type H1 is often associated with porous materials consisting of well-defined cylindrical-like pore channels or agglomerates of compacts of approximately uniform spheres. It was found that materials that give rise to H2 hysteresis are often disordered and the distribution of pore size and shape is not well defined. Isotherms revealing type H3 hysteresis do not exhibit any limiting adsorption at high P/P_0 , which is observed with non-rigid aggregates of plate-like particles giving rise to slit-shaped pores.

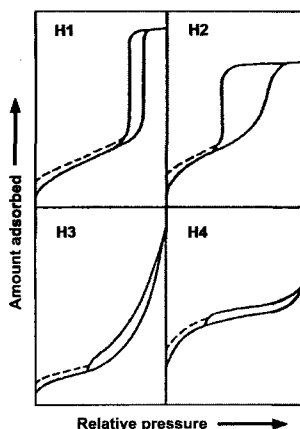


Figure 7. IUPAC classification of hysteresis loops. From [1].

The desorption branch for type H3 hysteresis contains also a steep region associated with a (forced) closure of the hysteresis loop, due to the so-called tensile strength effect. This phenomenon occurs for nitrogen at 77 K in the relative pressure range from 0.4 – 0.45 [52]. Similarly, type H4 loops are also often associated with narrow slit pores, but now including pores in the micropore region.

3.3.2 Origin of hysteresis

The mechanism and origin of sorption hysteresis is still under investigation. There are essentially three models which contribute to the understanding of sorption hysteresis: (i) *Independent (single) pore model*: Sorption hysteresis is considered as an intrinsic property of a phase transition in a single, idealized pore, reflecting the existence of metastable gas states. The hysteresis loop expected for this case is of type H1, according to the IUPAC classification [4]; (ii) *Network model*: Sorption hysteresis is explained as a consequence of the interconnectivity of a real porous network with a wide distribution of pore sizes. If network- and pore blocking effects are present a hysteresis loop of type H2 (IUPAC classification) is expected; (iii) *Hysteresis in disordered porous materials*: A more realistic picture takes into account that the thermodynamics of the pore fluid is determined by phenomena spanning the complete pore network: Hysteresis is here associated with thermodynamic metastability of low and high density phases of the pore fluid. In addition the occurrence of long time dynamics was suggested, which is so slow that on (experimentally) accessible time scales, the systems appear to be equilibrated. Typically, hysteresis loops of types H1 and H2 are observed in disordered porous materials.

Below we discuss the different models for hysteresis in more detail.

(a) Independent pore model

Different approaches, which would explain the occurrence of hysteresis in a single pore can be found in the literature since *ca.* 1900. Cohan [see refs. 52, 54] assumed that pore condensation occurs by filling the pore from the wall inward (for a cylindrical pore model). It was suggested that pore condensation would be controlled by a cylindrical meniscus once the pore is filled, whereas evaporation of the liquid would occur from a hemispherical meniscus, which would lead according to the Kelvin equation to different values of P/P_0 for condensation and evaporation.

Theories by Foster [see ref. 52,54], Everett [86], Cole and Saam (CS) [65] and Ball and Evans [87] suggested that hysteresis may be caused by the development of metastable states of the pore fluids associated with the capillary condensation transition in a manner analogous to superheating or supercooling of a bulk fluid. Theoretical studies applying Non Local Density Functional Theory (NLDFT) revealed that in principle both, pore condensation and pore evaporation can be associated with metastable states

of the pore fluid [89]. This is consistent with the classical van der Waals picture, which predicts that the metastable adsorption branch terminates at a vapor-like spinodal, where the limit of stability for the metastable states is achieved and the fluid spontaneously condenses into a liquid-like state. Accordingly, the desorption branch would terminate at a liquid-like spinodal, which corresponds to spontaneous evaporation. In practice however, metastabilities occur only on the adsorption branch. Assuming a pore of finite length (which is always the case in real adsorbents) vaporization can occur via a receding meniscus, a nucleation problem and therefore metastability is not expected to occur during desorption (evaporation). This situation is illustrated in Figure 8 [89]. The NLDFT adsorption isotherm of Ar at 87 K in a cylindrical pore is shown in comparison with the appropriate experimental sorption isotherm on a MCM-41 silica material. Good agreement is obtained; however the small steps in the theoretical isotherm are a consequence of assuming a structureless (i.e., chemically and geometrically smooth) pore wall model, which neglects the heterogeneity of the MCM-41 pore walls.

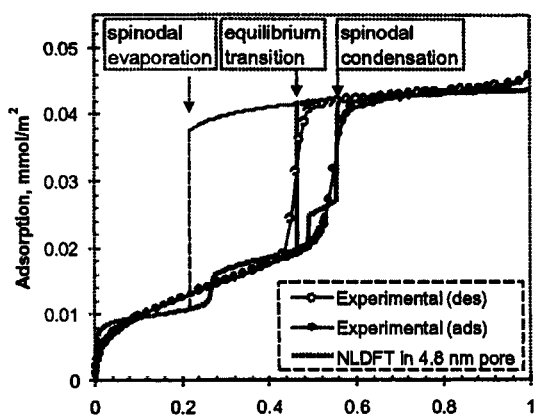


Figure 8. NLDFT adsorption isotherm of argon at 87 K in a cylindrical pore of diameter 4.8 nm in comparison with the appropriate experimental sorption isotherm on MCM-41. From [89].

It can be clearly seen, that the experimental desorption branch is associated with the equilibrium gas-liquid transition (the equilibrium transition corresponds to the condition at which the two states have equal grand potential), whereas the condensation step corresponds to the spinodal spontaneous transition.

These results clearly indicate that the H1 hysteresis generally observed in MCM-41 material can be attributed to the occurrence of metastable states associated with the pore condensation transition (spinodal condensation). According to the situation described in figure 8, the desorption branch should be chosen for pore size analysis if theories/methods are applied, which describe the equilibrium transition (e.g., BJH, conventional NLDFT). In addition, Ravikovitch and Neimark developed recently a NLDFT based method, which correlates the location of the spinodal transition with the pore size [89], i.e., the model takes into account the existence of metastable states of the pore fluid. This method is accurate for pore sizes larger ca. 5 nm and can be applied to the adsorption branch. Application examples of this method for pore size analysis are given in section 4.2.

Hysteresis of type H1 is not only observed in materials consisting of independent cylindrical-like pores, this type of hysteresis can also be observed in ordered three dimensional pore systems such as MCM-48. Argon adsorption hysteresis of type H1 was found at 77.35 K for pore diameters larger than ca. 3.0 nm, and for argon adsorption at 87.27 K for materials of pore size larger than ca. 4.1 nm [20,48]. A combined analysis of a reversible nitrogen isotherm (at 77 K) with an hysteretic argon sorption isotherm (at 87 K) revealed clearly that – although MCM-48 consists of a unique, three dimensional pore network – hysteresis can be described within the independent pore model, and the desorption branch of the argon sorption hysteresis loop corresponds to the equilibrium transition. Hence, similar as in case of MCM-41 the desorption branch appears to be correlated with the pore diameter, if a method for pore size analysis is applied, which is based on the equilibrium liquid-gas phase transition (e.g., BJH, NLDFT).

Other materials consisting of ordered pore networks, as for instance controlled pore glasses and some types of sol-gel glasses also reveal H1 hysteresis loops. Awschalom et al [90] investigated the adsorption behavior of krypton (at 118 K) and oxygen (at 90 K) in highly ordered sol-gel porous glass. The remarkable oxygen isotherm, which reveals H1 hysteresis of almost vertical adsorption and desorption branches is shown in Figure 9. The data were analysed within the framework of the Saam-Cole (SC) theory [65]. In the Saam-Cole (SC) theory, pore condensation and the hysteresis connected with this transition is explained by considering the limits of stability and metastability of an adsorbed multilayer film in a cylindrical pore. The SC theory yields a map of regions of stability, metastability, and instability in terms of the fluid-wall

interaction parameter α , surface tension γ , density difference $\Delta\rho$ between gas and liquid. According to the SC theory, pore condensation occurs at a critical film thickness t_c (i.e., $a_c = r - t_c$; r is the pore radius) where the cylindrical adsorbed film becomes unstable. Evaporation occurs at lower P/P_0 and the remaining film thickness is t_m (i.e., $a_m = r - t_m$). Hence, the range of metastable film thickness is given by the difference $a_m - a_c$.

The hysteresis of both, krypton and oxygen isotherms were in agreement with the predictions of the Saam-Cole theory (see figure 9), i.e., hysteresis is attributed to the existence of metastable pore fluid associated with pore condensation. This indicates again, that in ordered pore networks hysteresis can still be dominantly caused by the existence of metastable states. Accordingly, classical networking and pore blocking effects are not necessarily present in an interconnected pore system.

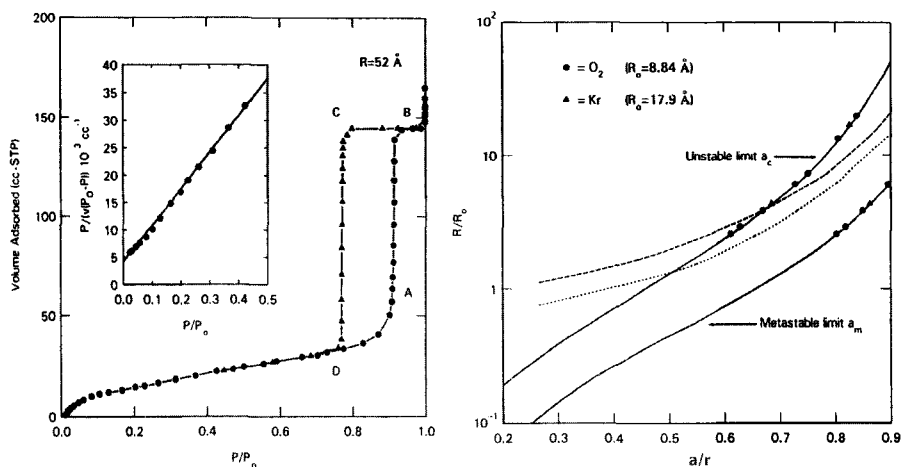


Figure 9. (a) Oxygen sorption isotherm at 90 K in highly ordered sol-gel porous glass of pore radius $r = 52 \text{ \AA}$. From [90]. (b) Comparison of the SC theory with experimental results. The solid lines represent the predictions of the SC theory for adsorbed film thickness at the relative pressures where pore condensation (a_c) and evaporation (a_m) occurs. The dependence of the unstable limit a_c/r and the metastable limit a_m/r is plotted in units of the dimensionless variables R_0 , which is a scaling factor depending on details of the fluid-solid system (e.g., fluid-wall interaction parameter α , surface tension γ , density difference $\Delta\rho$ between gas and liquid). Dashed and dotted lines are Kelvin equation predictions for pore condensation and evaporation. From [90].

The applicability of the Cole-Saam theory has been tested in detail by Findenegg et al. based on sorption isotherms obtained with organic vapours on controlled-pore glasses [128]. In this systematic experimental study some predictions of the SC theory could be confirmed.

(b) Network model

Network models take into account, that in many materials the pores are connected and form a three-dimensional network. An important feature of the network model is the possibility of pore blocking effects during evaporation, which occurs if a pore has access to the external gas phase only via narrow constrictions (e.g., an ink-bottle pore). The basis for the understanding of sorption hysteresis in ink-bottle pores and networks can be found in the work of McBain (see description in [52]). The wide inner portion of an ink-bottle pore is filled at high relative pressures, but it cannot empty during desorption until the narrow neck of a pore first empties at lower relative pressure. Thus, in a network of ink-bottle pores the capillary condensate in the pores is obstructed by liquid in the necks. The relative pressure at which a pore empties now depends on the size of the narrow neck, the connectivity of the network and the state of neighboring pores. Hence, the desorption branch of the hysteresis loops does here (in contrast to the single pore model) not occur at thermodynamic equilibrium, but reflects a percolation transition. In such a case the desorption branch of the hysteresis loop is much steeper as compared to the adsorption branch) leading to H2 hysteresis according to the IUPAC classification. Work by Everett [86] and others have led to the development of several specific network models. Advanced network or percolation models were introduced for instance by Mason [91] Wall and Brown [92], Neimark [93] Parlar and Yortsos [94], Ball and Evans [87], Seaton et al. [95] and Rojas et al. [96]. Page et al [97] suggested the existence of a percolation mechanism in case of the observed H2 hysteresis in porous vycor glass based on experimental results obtained by combining gravimetric and volumetric adsorption measurements with ultrasonic and optical measurements. Hoinkis et al [98] performed *in situ small angle* neutron scattering experiments in a disordered mesoporous silica glass (Gelsil 75). A H2 hysteresis loop was observed together with clear evidence of differences in the mechanisms of capillary condensation and evaporation, i.e., the latter was indicative of a percolation transition.

However, the existence of the conventional pore blocking mechanism as described above was recently questioned by Sarkisov and Monson [99]. They used molecular dynamics to study the adsorption and desorption of fluids in various simple geometries, including a simple ink-bottle pore geometry. Their data indicated clearly that the shape of the obtained H2 hysteresis loop was not caused by the occurrence of conventional pore blocking. The large cavities could be emptied by a diffusional mass transport

process from the fluid in the large cavity to the narrow neck and from there into the gas phase, hence the pore body can empty even while the pore neck remains filled.

A very recent experimental study of N_2 , Ar and Kr at 77.4 and 87.4 K in ordered mesoporous materials with 3D cage-like structure (FDU-1 and SBA-16) combined with a NLDFT study (applying NLDFT) by Ravikovitch and Neimark focussed on a detailed description of the effect of an ink-bottle pore geometry on adsorption hysteresis. This work suggests that both, conventional pore blocking and cavitation (i.e., spinodal evaporation, see figure 5) can occur depending on temperature and pore size. The cavitation effect is correlated with the occurrence of a lower limit of hysteresis (classically described as the so-called tensile strength effect, which we will discuss in section 3.3.3).

(c) Pore condensation and hysteresis in disordered systems

Even with the incorporation of network and percolation effects the adsorption thermodynamics is still modeled at a single pore level, i.e., the behavior of the fluid in the entire pore space is not assessed. In order to achieve this one needs to consider models which attempt to describe the microstructure of porous materials at length scales beyond that of a single pore. According to Gubbins et al. [100] there are two general approaches to construct a model of nanoporous materials by methods of molecular simulation. The first is the so-called mimetic simulation, and involves the development of a simulation strategy, that mimics the development of the pore structure in the materials preparation. The second approach is the reconstruction method. Here one seeks a molecular model, whose structure matches available experimental structure data. Monson and Co-workers investigated by Monte Carlo simulation the condensation and hysteresis phenomena of a Lennard Jones fluid in a reconstructed model of silica xerogel [101]. Their adsorption isotherms exhibited hysteresis loops of type H1 and H2 in agreement with experimental results obtained on the same type of material. The observed hysteresis was attributed to thermodynamic metastability of the low and high density phases of the adsorbed fluid – however these phases span the entire void space of the porous material and are therefore not associated with the individual pores. Pellenq et al [102] studied the pore condensation and hysteresis behavior of argon in a pseudo-vycor glass, which was obtained by a off-lattice reconstruction method over a wide temperature range via Monte Carlo simulation. Hysteresis loops of type H2 were observed; the steep

evaporation/desorption branch was associated with a first-order phase transition in a disordered system (no pore blocking effects were invoked).

Gelb and Gubbins [103,104] have recently reproduced the complex network structure of porous glasses such as vycor and controlled-pore glass by applying molecular simulation. Grand Canonical Monte Carlo simulation results for xenon adsorption in these pores suggest strongly that the shape of the adsorption/desorption hysteresis does here not depend on the connectivity of the material model, supporting the hypothesis that in materials of this type (e.g., a porous Vycor glass with a porosity of 30%) the fluid in different pores behaves quasi-independently, and that no system-spanning phase transitions occur during adsorption or desorption [104]. The origin of hysteresis in disordered porous glasses was recently also investigated by lattice DFT models [105] and Monte Carlo simulations [106]. These studies indicate that hysteresis is due to the presence of a large number of metastable states. It was concluded that the origin of the hysteresis is associated with long time dynamics, which is so slow that on (experimentally) accessible time scales, the systems appear to be equilibrated, which leads to the observed reproducible results in the observation of the hysteresis loop.

These results discussed above indicate that the nature of hysteresis in disordered systems is very complex. More theoretical and experimental work is necessary to (i) clarify what determines the shape of the hysteresis loop in such disordered systems to be H2 and (ii) to obtain a clearer picture of the nature of phase and also critical behavior of fluids in disordered porous systems.

3.3.3 Lower limit of the hysteresis loop - tensile strength hypothesis

It was observed already a long time ago, that the hysteresis loop for nitrogen adsorption at 77.35 K closed at relative pressure at or above 0.42, apparently independent of the porous material (see [54]). Experimental results with other adsorptives also supported the view, that for a given temperature this lower closure point of hysteresis is never located below a certain critical relative pressure. It was suggested that the lower closure point of hysteresis is determined by the tensile strength of the capillary condensed liquid, i.e., there exists a mechanical stability limit below which a macroscopic meniscus cannot exist anymore and which leads to a spontaneous evaporation of the pore liquid. This is in contrast to the situation of pore blocking where the evaporation of the liquid is controlled by the necks of the ink-bottle pores. The tensile strength theory was

analysed by Burgess and Everett [107] and very recently by Sonwane and Bhatia [108], Ravikovitch and Neimark [109], as well as by Findenegg et al [110]. Based on an extensive theoretical (by NLDFT) and experimental studies on capillary condensation of N_2 , Ar and Kr in materials with well defined ink-bottle pores (SBA-16, and FDU-1) Neimark and Ravikovitch found that the lower limit of the hysteresis loop also depends on the pore geometry, which questions the conventional assumption, that the lower limit of the hysteresis loop is a unique function of the adsorbate and the temperature.

Findenegg et al. [110] performed a systematic experimental study of the pore condensation hysteresis of CHF_3 and C_2F_6 in mesoporous silica with open cylindrical pores of uniform size (MCM-41 and SBA-15) and in a silica material consisting of large cellular mesopores, which are accessible only via narrow mesopores (which resembles an ink-bottle geometry). Their sorption results show that the lower closure point of hysteresis observed in the materials with ink-bottle geometry and the pore condensation pressure observed at the hysteresis critical temperature (i.e., the temperature at which hysteresis disappears) for the sorption isotherms in ordered MCM-41 and SBA-15 almost coincide. Hence, there appears to be a relation between the lower closure point of the hysteresis loop and the hysteresis critical temperature in uniform cylindrical pores. A correlation between the lower closure point of hysteresis and the hysteresis critical temperature was also suggested by Bhatia et al. [108].

Despite the fact, that the occurrence of the lower closure point of hysteresis is still not sufficiently understood, it is clear that it leads to a problem for pore size calculations. The existence of a lower closure point affects primarily the position of the desorption branch with regard to its position and steepness, i.e., the desorption isotherm exhibits a characteristic step at the lower closure point. Hence a pore size calculation based on an analysis of the desorption branch is here not straightforward.

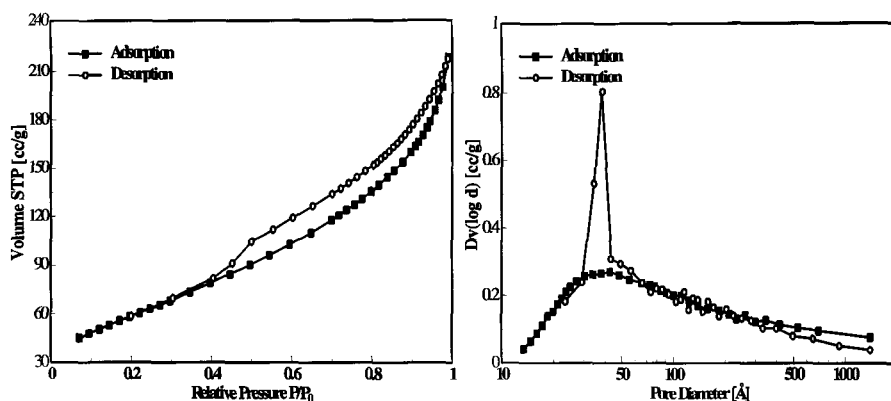


Figure 10. Nitrogen adsorption/desorption at 77.35 K on a disordered alumina catalyst and BJH pore size distribution curves from adsorption and desorption branches.

A typical example is given in Figure 10, which shows nitrogen sorption data on a highly disordered alumina catalyst sample together with BJH pore size distribution curves obtained from both, adsorption and desorption branches. As it can be clearly seen the hysteresis loop closes at a relative pressure of ca. 0.4-0.45 and exhibits the mentioned characteristic step down. This step is not associated with the evaporation of pore liquid from a specific group of pores, i.e., the spike in the desorption pore size distribution curve (PSD) reflects an artifact, caused by the spontaneous evaporation of metastable pore liquid (cavitation, i.e., the tensile strength effect). In contrast, the PSD derived from the adsorption branch does not reveal this artificial peak and represents the wide pore size distribution curve, which is characteristic for such an disordered sample.

4 Pore size analysis of mesoporous solids

4.1 Classical, macroscopic thermodynamic methods versus microscopic models (NLDFT) for pore size analysis

Among the classical methods for mesopore size analysis, the method of Barrett-Joyner-Halenda (BJH), which was proposed in 1951 is certainly the most popular one. The BJH-approach provides an algorithm to calculate the pore size distribution (PSD) by assuming a cylindrical pore geometry from nitrogen desorption data (obtained at 77.35 K). The BJH-approach attracted much attention and was later modified by Dollimore and Heal, Cranston-Inkley [52,53] and others.

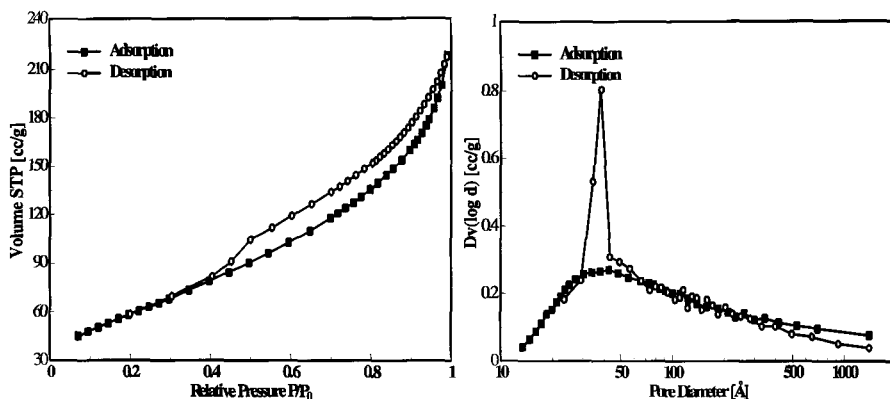


Figure 10. Nitrogen adsorption/desorption at 77.35 K on a disordered alumina catalyst and BJH pore size distribution curves from adsorption and desorption branches.

A typical example is given in Figure 10, which shows nitrogen sorption data on a highly disordered alumina catalyst sample together with BJH pore size distribution curves obtained from both, adsorption and desorption branches. As it can be clearly seen the hysteresis loop closes at a relative pressure of ca. 0.4-0.45 and exhibits the mentioned characteristic step down. This step is not associated with the evaporation of pore liquid from a specific group of pores, i.e., the spike in the desorption pore size distribution curve (PSD) reflects an artifact, caused by the spontaneous evaporation of metastable pore liquid (cavitation, i.e., the tensile strength effect). In contrast, the PSD derived from the adsorption branch does not reveal this artificial peak and represents the wide pore size distribution curve, which is characteristic for such an disordered sample.

4 Pore size analysis of mesoporous solids

4.1 Classical, macroscopic thermodynamic methods versus microscopic models (NLDFT) for pore size analysis

Among the classical methods for mesopore size analysis, the method of Barrett-Joyner-Halenda (BJH), which was proposed in 1951 is certainly the most popular one. The BJH-approach provides an algorithm to calculate the pore size distribution (PSD) by assuming a cylindrical pore geometry from nitrogen desorption data (obtained at 77.35 K). The BJH-approach attracted much attention and was later modified by Dollimore and Heal, Cranston-Inkley [52,53] and others.

All methods related to the original BJH approach are based on the modified Kelvin equation and the accuracy of the calculated PSD depends on the applicability and the deficiencies of the Kelvin equation, which were already discussed to some extent in sections 3.1 and 3.2. In narrow pores attractive fluid-wall interactions are dominant and the macroscopic, thermodynamic concept of a smooth liquid-vapor interface and bulk-like core fluid cannot realistically be applied. In addition, methods based on the modified Kelvin equation do not take into account the influence of the adsorption potential on the position of the pore condensation transition. It is further assumed that the pore fluid has essentially the same thermophysical properties as the correspondent bulk fluid. For instance, the surface tension of the pore liquid is thought to be equal to the properties of the corresponding bulk liquid, but the surface tension of the pore liquid depends on the radius of curvature. Significant deviations from the bulk surface tension are however expected to occur in narrow mesopores [52,55, 111]. Another problem is that the thickness of the preadsorbed multilayer film is assessed by the statistical thickness of an adsorbed film on a nonporous solid of a surface similar to that of the sample under consideration. However, in particular for narrow pores of widths $< \text{ca.} 10 \text{ nm}$ this mean thickness does not reflect the real thickness of the preadsorbed multilayer film, because curvature effects are not taken into account.

A direct experimental test of the validity of the Kelvin equation and its modifications became possible (as indicated before) after mesoporous molecular sieves became available, where the pore diameter could be derived by independent methods (such as x-ray-diffraction, high resolution transmission electronic microscopy). It is found that the BJH- and related approaches based on the modified Kelvin equation underestimate the pore size up to 25 % for pores smaller than 10 nm.

Corrections of the modified Kelvin equation in the spirit of the Broeckhoff de Boer and Cole-Saam approach were for instance developed by Lu et al. [111], Lukens et al. [38], Galarneau et al [56], Bhatia et al.[112], Groen et al [113]. These modified classical models were tested using MCM-41 and/or SBA-15 materials in combination with pore size data derived from the aforementioned independent experimental methods. In general good agreement, but only over a limited pore size range was found. An empirical approach, which is meanwhile widely used was proposed by Kruk, Jaroniec and Sayari (KJS) [36,114]. This method is based on a corrected (modified) BJH equation, which was properly *calibrated* using MCM-41 mesoporous silica materials. Series of MCM-41

silicas of cylindrical pores of size between 2 and ca. 7 nm were originally used to establish a relation between capillary condensation/evaporation pressures and pore size. A pore size assessment independent from the pore condensation pressure could be obtained from XRD interplanar spacing and the primary mesopore volume. The KJS approach is strictly valid only for MCM-41 type silica materials over a pore size range which reflects the range over which a calibration curve exists (i.e., meanwhile 2 – ca. 12 nm), however the KJS-approach tends to overestimate the pore size for diameters > 8 nm [110]. The method is meanwhile also available for argon adsorption in MCM-41 silica at 87.27 K [116] and 77.35 K [117], as well as for the analysis of hydrophobized mesoporous solids [118].

In contrast to the Kelvin equation based methods, microscopic methods based on Density Functional Theory [119-125] and the Grand Canonical Monte Carlo simulation (GCMC) [68,69] methods correctly describe the local fluid structure near curved solid walls on a microscopic level. These methods also capture correctly (as discussed before in section 3.2) that the thermodynamics of the confined fluid is altered as compared to the bulk fluid (e.g., critical point shifts) and consequently that pore condensation and hysteresis disappear already below the so-called hysteresis critical temperature and for pore sizes below a certain critical pore width. This is important for an accurate pore size analysis of narrow mesopores. Because the equilibrium density profiles are known for each pressure along an isotherm (i.e., these isotherms are calculated by integrating of the equilibrium density profiles, $\rho(r)$, of the fluid in the model pores) no assumptions about the pore filling mechanism are required as in case of the macroscopic methods. As a consequence these microscopic methods can be applied for pore size analysis over a large range of pore widths, i.e., from micropores up to well into the meso-macropore range. It is a general practice to adjust interaction parameters (fluid-fluid and fluid-solid) in such a way that the model would correctly reproduce fluid bulk properties (e.g., bulk liquid-gas equilibrium densities and pressures, liquid-gas interfacial tensions) as well as standard adsorption isotherms on well-defined non-porous adsorbents. A set of isotherms calculated for a set of pore sizes in a given range for a given adsorbate constitutes a model database, which is called a so-called kernel.

The calculation of pore size distribution is based on a solution of the Generalized Adsorption Isotherm Equation (GAI), which correlates the kernel of theoretical adsorption/desorption isotherms with the experimental sorption isotherm:

$$N(P/P_0) = \int_{W_{MIN}}^{W_{MAX}} N(P/P_0, W) f(W) dW \quad (6)$$

where, $N(P/P_0)$ = experimental sorption isotherm data, W = pore width

$N(P/P_0, W)$ = theoretical sorption isotherm on a single pore of width W
 $f(W)$ = pore size distribution function.

The GAI equation reflects the assumption that the total isotherm consists of a number of individual single pore isotherms multiplied by their relative distribution, $f(W)$, over a range of pore sizes. The set of $N(P/P_0, W)$ isotherms (kernel) for a given system (adsorptive/adsorbent) can be obtained, as indicated above, by either Density Functional Theory or by Monte Carlo computer simulation. The pore size distribution is then derived by solving the GAI equation numerically. In general, the solution of the GAI represents an ill-posed problem, which requires some degree of regularization. However, existing regularization algorithms allow to obtain meaningful and stable solutions of the GAI equation [89]

Figures 11 [126] and 12 [127] compare the predictions of various methods such as BJH, 4V/S (i.e., pore volume determined by Gurvitch rule, S is the BET surface area), Broeckhoff and de Boer (BDB), and DFT for the pore size analysis of MCM-41 and SBA-15 samples with pore diameters determined by experimental methods which are independent of the position of the pore condensation/evaporation steps of adsorption isotherms (e.g., XRD + V_{meso}). The data displayed in figure 11 reveal that both the DFT and BDB method agree quite well with the pore size values obtained from the independent method, whereas the BJH results clearly disagree. Figure 12 shows clearly, that over the complete pore size range good agreement exists between the experimental pore sizes and the ones determined by NLDFT from adsorption and desorption branch. It is also visible, that the BJH method significantly underestimates the pore sizes over a wide pore diameter range. Again, better agreement is obtained with methods based on the Broeckhoff and de Boer approach. However, significant deviations between the BDB- and NLDFT methods occur for pore diameters < 7 nm [126], mainly due to the fact that the Broeckhoff and de Boer method cannot predict the existence of pore criticality and the associated disappearance of sorption hysteresis below a certain critical pore diameter at given temperature (see section 3.2).

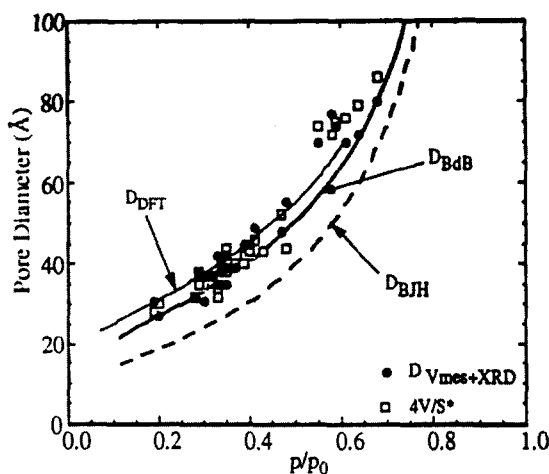


Figure 11. Pore size dependence of the relative pressure of evaporation (desorption) of nitrogen in MCM-41: Comparison of predictions of BJH, BdB and DFT with experimental pore size data (4V/S, $D_{Vmes} + XRD$). From [126].

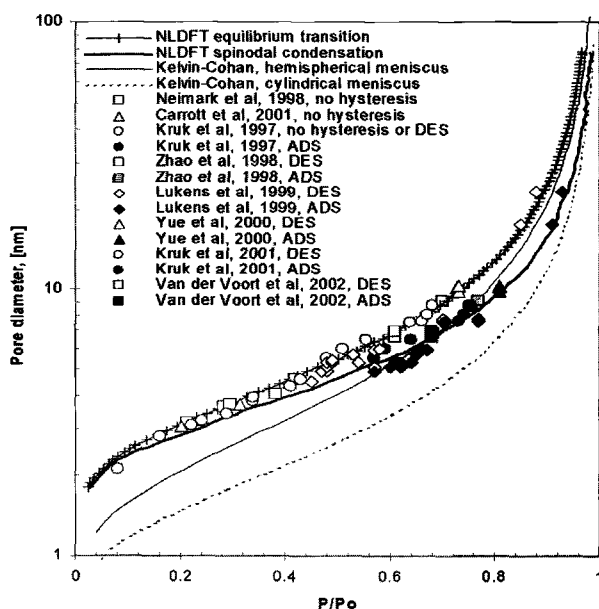


Figure 12. Pore size dependence of the relative pressure of condensation and evaporation for N_2 in cylindrical pores: Comparison of theoretical predictions (NLDFT- and BJH (Kelvin-Cohan) with experimental pore size data for MCM-41 and SBA 15. From [127].

4.2 Use of the adsorption or desorption branch for pore size calculation?

The presence of the hysteresis loop introduces a considerable complication, and of course the question arises whether the adsorption branch or the desorption branch of a hysteretic sorption isotherm should be used for the pore size analysis. The answer of this question depends on the texture of the adsorbent, and in case of highly disordered systems, where the nature of hysteresis is very complex, it might be even impossible to correlate the adsorption or the desorption branch of the hysteresis loop with the true pore size and pore size distribution. In the following we discuss the question whether the adsorption or desorption branch should be used for pore size calculations based on our discussion of the origin of hysteresis in section 3 of this review. However, the nature of hysteresis is still under investigation and a general agreement could not even be reached for simple systems. Hence, our conclusions have therefore to be considered as to be preliminary.

In case of ordered materials such as MCM-41 and SBA-15 a lot of progress was made with regard to the understanding of the nature of pore condensation and hysteresis. The typically observed H1 hysteresis can be modeled by the independent pore model (see section 3.3.2). Hysteresis can here be attributed to the occurrence of metastable states of the pore fluid associated with pore condensation. It is believed that the desorption branch of the hysteresis loop reflects the equilibrium phase transition, i.e., theories and methods which describe the equilibrium phase transition (e.g., BJH, NLDFT etc..) should be applied to the desorption branch in order to calculate the pore size correctly. The adsorption branch can also be taken for pore size analysis if a theory (method) is applied which takes metastability into account and provides a correlation between the relative pressure where spinodal condensation occurs and the pore size. As mentioned before (section 3.3) such a method, based on NLDFT (*NLDFT-spinodal condensation method*), was suggested by Ravikovitch and Neimark [89]. Another possibility is to apply an empirical method such as the KJS approach [36], which however can only be applied for pore size analysis over a limited pore size range, i.e., the range over which a kind of calibration curve exists, which represents a correlation between the pore size and the pore condensation pressure.

The situation is more complex for materials consisting of a three-dimensional network of pores. Based on our discussion in section 3.32(a) it appears that pore condensation hysteresis of type H1 as observed in ordered three dimensional pore systems (e.g MCM-48, some ordered sol-

gel glasses, CPG) is still dominantly caused by metastabilities associated with the pore condensation transition. Also here it is believed that the desorption branch of the hysteresis loop can be associated with the equilibrium gas-liquid phase transition, i.e., the desorption branch should be chosen for pore size analysis if theories/methods are applied which are based on the equilibrium transition (e.g., BJH, equilibrium transition NLDFT, see also section 3.3.2.a).

In case of highly disordered materials (e.g., porous vycor glass), the occurrence of hysteresis is as discussed before in section 3.3 associated with a variety of effects including metastable states of the pore fluid, potential pore blocking and percolation phenomena, effects from possible system-spanning transitions, long time dynamics etc. The significance of each mechanism for the shape of hysteresis depends on details of the texture of the porous material. Very often sorption hysteresis of type H2 is observed in such cases. In contrast to the situation in ordered materials, the desorption branch of the hysteresis loops can then not be used for pore size analysis by methods based on the equilibrium transition (e.g. BJH). This is also true if the evaporation of the pore liquid is caused by cavitation, i.e., evaporation occurs close to the lower limit of hysteresis as observed for instance in materials, which give rise to type H3 hysteresis (see Figure 10 in section 3.3.3 and discussion of so-called tensile strength effect). Here a more realistic pore size analysis can be obtained from an analysis of the adsorption branch. Again, the application of empirical methods based on experimental calibration (e.g., KJS approach [36]) is certainly a good way to assess the pore size, but a pore size analysis over the complete mesopore range can be performed by applying the *NLDFT-spinodal condensation method* [89].

It was further suggested to check the consistency of the pore size analysis by applying the conventional NLDFT method (describing the equilibrium condensation/evaporation transition) to the desorption branch and the NLDFT-spinodal condensation method to the adsorption data [89]. This allows to compare theoretical and experimental “widths” of the hysteresis loops. Hysteresis loops, which are wider than those predicted theoretically (i.e., the pore size distribution curves calculated from adsorption and desorption branch do not agree), indicate that hysteresis cannot be solely explained within the framework of the independent pore model (see section 3.3.2.(a)).

We applied this approach on nitrogen data obtained at 77 K on ordered SBA-15, controlled-pore glass (CPG) and porous vycor glass (which can be considered as a disordered system compared to SBA-15). The results

are shown in Figures 13 – 15. The observed hysteresis loops for SBA-15 as well as for controlled pore glass are of type H1, whereas the porous vycor glass clearly exhibits type H2 hysteresis. The pore size distribution curves obtained from the adsorption branch (by applying the NLDFT-spinodal condensation method) and desorption branch (by applying the NLDFT equilibrium method) are in perfect agreement for SBA-15. This confirms that sorption hysteresis in this SBA-15 silica sample is caused by delayed condensation (i.e., by metastable states of the pore fluid occurring during adsorption/condensation). Good agreement between the PSD's calculated from the adsorption and desorption branches can also be found for the controlled-pore glass sample. Although controlled-pore glasses consist of a network of cylindrical-like pores, the hysteresis appears to be mainly due to metastability effects, i.e., the observed hysteresis can be described to a large extent by applying the independent pore model. This conclusion is partially in agreement with results obtained by Findenegg et al, who applied the Saam-Cole theory to describe the H1 hysteresis observed for the adsorption of organic vapors in controlled-pore glasses [128]. Here, a semi-quantitative agreement with theoretical prediction of the Saam-Cole theory could be obtained.

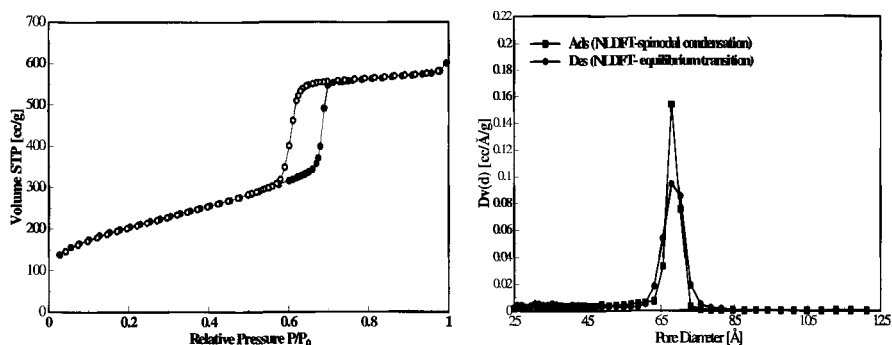


Figure 13. N_2 adsorption/desorption at 77 K in SBA-15 and pore size distributions from adsorption and desorption by applying NLDFT methods dedicated to describe the pore (spinodal) condensation (adsorption branch) and the equilibrium evaporation (desorption branch) transitions.

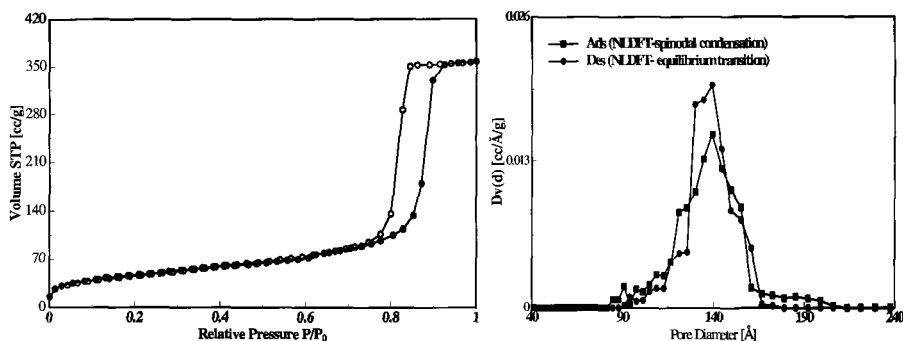


Figure 14. N₂ adsorption/desorption at 77 K in controlled pore glass and pore size distributions from adsorption and desorption branch by applying NLDFT methods dedicated to describe the pore (spinodal) condensation (adsorption branch) and the equilibrium evaporation (desorption branch) transitions.

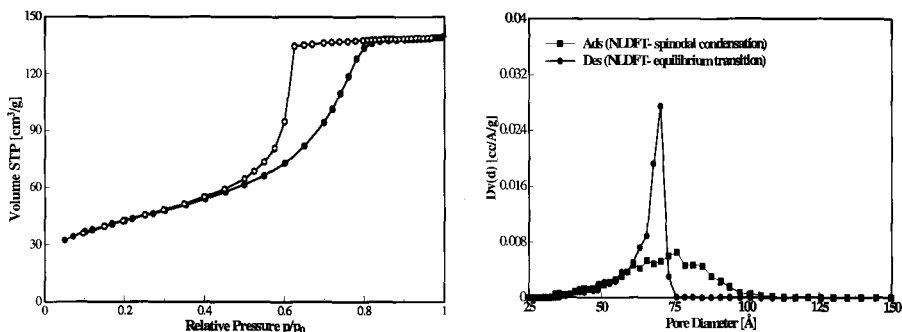


Figure 15. Nitrogen adsorption/desorption at 77 K in porous vycor glass and pore size distributions from adsorption and desorption branch by applying NLDFT methods dedicated to describe the pore (spinodal) condensation (adsorption branch) and the equilibrium evaporation (desorption branch) transitions.

However, the situation is different for the vycor glass sample. The pore size distribution obtained from the desorption branch is artificially sharp leading to the observed H2 type hysteresis. The disagreement between the pore size distribution curves obtained from adsorption and desorption branch indicates that hysteresis cannot be described within the single pore model. The mechanism of pore condensation and hysteresis in

vykor is in contrast to controlled pore glass much more complex and not fully understood (see section again sections 3.3.2 and 3.3.3). The observed H2 hysteresis in porous vykor is often attributed to the occurrence of pore blocking and percolation phenomena [e.g., 87,91,97], which however do not occur during adsorption (i.e. condensation). Hence, the pore size distribution calculated from the adsorption branch can here be considered as to be more realistic.

The examples discussed here and in section 3.3 confirm that the IUPAC classification of hysteresis loops can be in principle quite helpful to determine the “correct” branch of the hysteresis loop for pore size analysis. It seems that in ordered system very often H1 hysteresis occurs, whereas H2 and H3 hysteresis is typically observed for disordered mesoporous systems. There is some evidence that in many cases where type H1 hysteresis occurs – even if observed in materials consisting of three dimensional pore networks - the desorption branch is correlated with the equilibrium phase transition, and therefore with the pore size if methods based on the determination of the gas-liquid phase transition (e.g. BJH, equilibrium-NLDFT) are applied for pore size analysis. This is not the case for H2 and H3 hysteresis, and the analysis of the adsorption branch by applying a proper method (e.g., NLDFT-spinodal condensation method or Kelvin equation based approach calibrated for adsorption branch) may lead here to a more accurate pore size analysis.

However, it should be clearly stated, that the suggestions given above are certainly not justified for highly disordered materials, where a clear decision with regard to the type of hysteresis loop is not always possible. In such cases it is very helpful to include in the sorption experiment the measurement of so-called scanning curves (of the hysteresis loop), which allow to reveal details of the mechanisms of pore condensation and evaporation (e.g., effects of connectivity, existence of cooperative processes etc.) [86, 87,96]. In addition, the factors which determine the shape of the hysteresis loop are still not completely known for disordered, connected pore systems (see section 3.3.2). For instance, theoretical studies reveal the occurrence of H2 hysteresis without the implementation of pore blocking and percolation effects [105,106]. More work is needed to correlate such theoretical predictions with sorption experiments on disordered porous materials, where the texture can be explored by independent methods (e.g., SANS, SAXS [129]).

5 Concluding Remarks

Significant progress was achieved during recent years with regard to the understanding of sorption phenomena in narrow pores. The shape of sorption isotherms depends on pore size and temperature (which reflects differences in the thermodynamic states of the pore fluid and the bulk fluid) and on the chemical and geometrical heterogeneity (i.e. the degree of disorder) of the porous material. These factors have to be taken into account in order to obtain a comprehensive and accurate pore size characteristics from the analysis of sorption isotherms. From an experimental point of view, nitrogen sorption at liquid nitrogen temperature (77 K) and argon sorption at liquid argon temperature (87 K) can be used to obtain a pore size analysis over the complete range of micro- and mesopores. In contrast, pore size analysis with argon at 77 K is limited to pores of diameters smaller than ca. 15 nm.

Major improvements with regard to the pore size analysis of mesoporous materials could be achieved mainly because of the following reasons: (i) the discovery of novel ordered mesoporous materials, such as MCM-41, MCM-48, SBA-15, which exhibit a uniform pore structure and morphology and can therefore be used as model adsorbents to test theories of gas adsorption; (ii) carefully performed sorption experiments; (iii) the development of microscopic methods, such as the Non-Local-Density Functional Theory (NLDFT) or computer simulation methods, which allow to describe the configuration of adsorbed molecules in narrow pores on a molecular level. These methods allow to obtain an accurate pore size analysis over a wide pore size (i.e., combined micro/mesopore analysis). In contrast, classical methods based on macroscopic thermodynamic assumptions (e.g., BJH) underestimate the pore size up to 25 % (for pore sizes < 10 nm), if not properly corrected or calibrated. Microscopic methods for pore size analysis take into account details of the fluid-fluid interactions and the adsorption potential (which depends on the strength of the fluid-wall interactions and the pore geometry). However, appropriate methods for pore size analysis based on NLDFT and GCMC are meanwhile available for many important fluid/substrate systems.

Despite this progress, a satisfying verification of theoretical models for the pore size analysis of mesoporous materials could be achieved so far only for highly ordered materials (such as mesoporous molecular sieves), which can be modeled within the framework of an independent pore model.. It is found that methods and theories based on a single pore model are in some cases applicable (to some extent) to describe the sorption and

phase behavior of fluids in porous materials consisting of ordered three-dimensional pore networks. However, the phase and hysteresis behavior of fluids in disordered porous systems is still not well understood and more theoretical and experimental work is clearly required to understand the combined effects of confinement, pore geometry, connectivity, etc. on the origin pore condensation and hysteresis. Furthermore, more work is necessary to evaluate to which extent pore size analysis in terms of a pore size distribution curve (which is essentially based on the single pore model) is appropriate in order to characterize materials consisting of complex, disordered pore networks. Therefore, it is important to develop more realistic adsorbent models, which attempt to describe the microstructure of porous materials at length scales beyond that of a single pore model. Predictions of such advanced models should be evaluated in combination with carefully performed sorption experiments.

6 Acknowledgements

The author would like to thank R. Ahmad for his help with the sorption experiments and R. Swinson for his support in the preparation of the graphics. Helpful discussions with J. Jagiello, S. Lowell and M.A. Thomas are gratefully acknowledged.

7 References

1. Sing K.S.W., Everett D.H., Haul R.A.W., Mouscou L., Pierotti R. A., Rouquerol J. and Siemieniewska T., Reporting physisorption data for gas/solid systems with special reference to the determination of surface area and porosity, *Pure & Appl. Chem.* **57** (1985) pp. 603 – 619.
2. Kresge C.T., Leonowicz M.E., Roth W.J., Vartuli J.C. and Beck J.S., Ordered mesoporous molecular sieves synthesized by a liquid-crystal template mechanism, *Nature* **359** (1992) pp. 710-712.
3. Zhao X S., Lu G.Q. (Max) and Millar J. G., Advances in mesoporous molecular sieve MCM-41, *Ind.Eng.Chem. Res.* **35** (1996) pp. 2075-2090.
4. Linden M., Schacht S., Schueth F., Steel A. and Unger K., Recent advances in nano- and macroscale control of hexagonal, mesoporous materials, *Journal of Porous Materials* **5** (1998) pp. 177 – 193.
5. Yanagisawa T., Schimizu T., Kuroda K. and Kato C., The preparation of alkyltrimethylammonium-kanemite complexes and their conversion to mesoporous materials, *Bull. Chem. Soc. Jpn.* **63** (1990) pp. 988-992.
6. Inagaki S., Fukushima Y. and Kuroda K., Synthesis of highly ordered mesoporous materials from a layered polysilicate, *J. Chem. Soc. Chem Commun.* **22** (1993) pp. 680- 682.

7. Zhao D.Y., Feng J.L., Huo Q.S., Melosh N., Frederickson G., Chemelka B.F. and Stucky G.D., Triblock copolymer syntheses of mesoporous silica with periodic 50 to 300 angstrom pores, *Science* **279** (1998) pp. 548 – 552.
8. Ryoo R., Ko C.H., Kruk M., Antochuck V. and Jaroniec M., Block-Copolymer-Templated Ordered Mesoporous Silica: Array of Uniform Mesopores or Mesopore-Micropore Network? *J. Phys. Chem B* **104** (2000) pp. 11465 -11471.
9. Galarneau A., Cambon H., Martin T., De Menorval L. C., Brunel D. and Di Renzo Fajula F., SBA-15 versus MCM-41: Are they the same materials?, *Studies in Surface Science and Catalysis* **141** (2002) pp. 395-402.
10. Barton T.J., Bull M., Klemperer W.G., Loy D.A., McEnaney B., Misono M., Monson P.A., Pez G., Scherer G.W., Vartuli J.C. and Yagi M. O., Tailored porous materials, *Chem Mater.* **11** (1999) pp. 2633-2656.
11. Moeller K. and Bein T., Inclusion chemistry in periodic mesoporous hosts, *Chem Mater.* **10** (1998) pp. 2950 – 2963.
12. Fröba M., Köhn K., Bouffaud B., Richard O. and Tendeloo G.V., Iron (III) oxide within mesoporous MCM-48 silica phases: Synthesis and Characterization, *Mat. Res. Soc. Symp. Proc.* (1999) pp. 547- 552.
13. Inagaki S., Guan Y., Fukushima Y., Oshuna T., and Terasaki O., Novel mesoporous materials with a uniform distribution of organic groups and inorganic oxide in their frameworks, *J. Am. Chem. Soc.* **121** (1999) pp. 9611-9614.
14. Sefa T., Ozin G., Grondey H., Kruk M. and Jaroniec M., Recent developments in the synthesis and chemistry of periodic mesoporous organosilicas, *Studies in Surface Science and Catalysis* **141** (2002) p. 1.
15. Muth O., Schellbach C. and Froeba M., Triblock copolymer assisted synthesis of periodic mesoporous organosilicas (PMOs) with large pores, *Chem. Commun.* (2001) pp. 2032 – 2033.
16. Jun S., Joo S, Ryoo R., Kruk M, Jaroniec M, Liu Z., Ohsuna T. and Terasaki O., Synthesis of new, nanoporous carbon with hexagonally ordered mesostructure, *J.Am.Chem.Soc.* **122** (2000) pp. 10712-10713.
17. Joo S.H., Ryoo R., Kruk M. and Jaroniec M., Evidence for general nature of pore interconnectivity in 2-dimensional hexagonal mesoporous silicas prepared using block copolymer templates, *J. Phys. Chem. B* **106** (2002) p. 4640.
18. Eddaoudi M., Li Hailian and Yagi O.M., Highly porous and stable metal-organic frameworks: structure design and sorption properties, *J. Am. Chem. Soc.* **122** (2000) pp. 1391 – 1397.
19. Murata K., Kaneko K., Kokai F., Takahashi K., Yudasaka M. and Ijima S., Pore structure of single-wall carbon nanohorn aggregates, *Chemical Physics Letters* **331** (2000) pp. 14-20.
20. Thommes M., Koehn R. and Froeba M., Sorption and pore condensation behavior of pure fluids in mesoporous MCM-48 silica, MCM-41 silica, SBA-15 silica and controlled-pore glass at temperatures above and below the bulk triple point, *Applied Surface Science* **196** (2002) pp. 239-249.
21. Rouquerol J., Avnir D., Fairbridge C.W., Everett D.H., Haynes J.H., Pernicone N., Ramsay J.D.F. and Sing K.S.W., Unger K.K., Recommendations for the characterization of porous solids, *Pure & Appl. Chem.* **66** (1994) pp. 1739 -1748.
22. Keller J.U. and Robens E., du Fresne von Hohenesche, Thermogravimetric and Sorption Measurement Techniques/Instruments, *Studies in Surface Science and Catalysis* **144** (2002) pp. 387 – 394.

23. Kaneko K., Determination of pore size and pore size distribution 1. Adsorbents and catalysts, *Journal of Membrane Science* **96** (1994) pp. 59-89.
24. Kaneko K., Ohba T., Hattori Y., Sunaga M., Tanaka H. and Kanoh H., Role of gas adsorption in nanopore characterization, *Studies in Surface Science and Catalysis* **144** (2002) pp. 11 -18.
25. Chenite A., Le Page Y. and Sayari A., Direct TEM imaging of tubules in calcined MCM-41 type mesoporous materials, *Chem Mater.* **7** (1995) pp. 1015-1019.
26. Franke O., Schulz-Ekloff, G., Rathousky J., Starek J. and Zukal A., Unusual type of adsorption isotherm describing capillary condensation without hysteresis, *J. Chem. Soc., Chem. Commun.* (1993) pp. 724-726.
27. Branton P.J., Hall P.G. and Sing K.S.W., Physisorption of nitrogen and oxygen by MCM-41, a model mesoporous adsorbent, *J. Chem. Soc Chem. Commun.* (1993) pp. 1257-1258.
28. ^a Rathousky J., Zukal A., Franke O. and Schulz-Ekloff G., Adsorption on MCM-41 mesoporous molecular sieve, Part I. Nitrogen isotherms and parameters of the porous structure, *J. Chem Soc. Faraday Trans.* **90** (1994) pp. 2821 -2826;
^b Rathousky J., Zukal A., Franke O. and Schulz-Ekloff G., Adsorption on MCM-41 mesoporous molecular sieve, Part II, Cyclopentane isotherm and their temperature dependence, *J. Chem. Soc. Faraday Trans.* **91** (1995) p. 937.
29. Branton P.J., Hall P.G., Sing K.S.W., Reichert H. and Schueth F., Unger K.K., Physisorption of argon, nitrogen and oxygen by MCM-41, a model mesoporous adsorbent, *J. Chem. Soc. Faraday Trans.* **90** (1994) pp. 2965-2967.
30. Schmidt, Stoecker M., Hansen E., Akporiaye D. and Ellestad O.H., MCM-41: a model system for adsorption studies on mesoporous materials, *Microporous Materials* **3** (1995) pp. 443 -448.
31. Llewellyn P.L., Grillet Y., Schueth F. and Reichert H., Unger K., Effect of pore size on adsorbate condensation and hysteresis within a potential model adsorbent: M41S, *Microporous Mater.* **3** (1994) p. 345.
32. Llewellyn P.L., Grillet Y., Ruquerol J., Martin C. and Coulomb J.P., Thermodynamic and structural properties of physisorbed phases within the model mesoporous adsorbent M41S (pore diameter 2.5 nm), *Surf. Sci.* **352 - 354** (1996) pp. 468.
33. Ravikovitch P. I., Domhnail S.C.O., Neimark A.V. and Schueth F., Unger K.K., Capillary hysteresis in nanopores: Theoretical and experimental studies of nitrogen adsorption on MCM-41, *Langmuir* **11** (1995) pp. 4765 – 4772.
34. Zhu G.Y., Zhao X.S., Lu G.Q. (Max) and D.D.Do., Improved comparison plot method for pore structure characterization of MCM-41, *Langmuir* **12** (1996) pp. 6513-6517.
35. Maddox M.W., Olivier J.P. and Gubbins K.E., Characterization of MCM-41 using molecular simulation heterogeneity effects, *Langmuir* **13** (1997) pp. 1737-1745.
36. Kruk M., Jaroniec M. and Sayari A., Adsorption study of surface and structural properties of MCM-41 materials of different sizes, *J. Phys. Chem. B* **101** (1997) pp. 583-589.
37. Sonwane C.G., Bathia S.K. and Calos N., Experimental and theoretical investigation of adsorption hysteresis and criticality in MCM-41: Studies with O₂, Ar and CO₂, *Ind. Eng. Chem. Res.* **37** (1998) pp. 2271- 2283.
38. Lukens W.W. Jr., Schmidt-Winkel, Zhao D., Feng J. and Stucky G.D., Evaluating pore sizes in mesoporous materials: a simplified standard adsorption method and a

- simplified Broeckhoff-de Boer method, *Langmuir* **15** (1999) pp. 5403-5409.
39. Kruk M. and Jaroniec M., Characterization of the porous structure of SBA-15, *Chem. Mater.* **12** (2000) pp. 1961-1968.
40. Ravikovitch P.I. and Neimark A.V., Characterization of micro-and mesoporosity of SBA-15 materials from adsorption isotherms by the NLDFT method *J. Phys. Chem B* **105** (2001) pp. 6817 – 6823.
41. Romero A.A., Alba M.D., Zhou W. and Klinowski J., Synthesis and characterization of the mesoporous silicate molecular sieve MCM-48, *J. Phys. Chem B* **101** (1997) pp. 5294-5300.
42. Kruk M., Jaroniec M., Ryoo R. and Kim J.M., Characterization of MCM-48 silicas with tailored pore sizes synthesized via a highly efficient procedure, *Chem Mater.* **11** (1999) pp. 2568-2572.
43. Thommes M., Koehn R., Froeba M., Systematic sorption studies on surface and pore size characteristics of different MCM-48 silica materials, *Studies in Surface Science and Catalysis* **128** (2000) pp. 259-269.
44. Thommes M., Koehn R. and Froeba M., Sorption and pore condensation behavior, of nitrogen, argon and krypton in mesopores MCM-48 silica materials, *J. Phys. Chem B* **104** (2000) pp. 7932-7943.
45. Schumacher K., Ravikovitch P., Du Chesne A. and Neimark A.V., Unger K.K., Novel Characterization of MCM-48 materials, *Langmuir* **16** (2000) pp. 4648 – 4654.
46. Kruk M. and Jaroniec M., Characterization of MCM-48 silicas with tailored pore sizes synthesized via a highly efficient procedure, *Chem Mater.* **12** (2000) pp. 1414 – 1421.
47. Ravikovitch P.I. and Neimark A.V., Relations between structural parameters and adsorption characterization of templated nanoporous materials with cubic symmetry, *Langmuir* **16** (2000) pp. 2419 – 2423.
48. Thommes M., Koehn R. and Froeba M., Characterization of mesoporous solids: pore condensation and hysteresis phenomena in mesoporous molecular sieves. *Studies in Surface Science and Catalysis* **142** (2002) pp. 1695 -1702.
49. Kanda H., Myahara M., Yoshioko T. and Okazaki M., Verification of the condensation model for cylindrical nanopores. Analysis of the nitrogen isotherm for FSM-16 , *Langmuir* **16** (2000) pp. 6622-6627.
50. Inohue S., Hanzwa Y. and Kaneko K., Prediction of hysteresis disappearance in the adsorption isotherm of N₂ on regular mesoporous silica, *Langmuir* **14** (1998) pp. 3079-3081.
51. Darmstadt H., Roy C., Kaliaguine S., Choi S.J. and Ryoo R., Surface Chemistry of mesoporous carbon molecular sieves, *Carbon* **40** (2002) pp. 2673 – 2683.
52. Gregg S.J. and Sing K.S.W., *Adsorption, Surface Area and Porosity* (Academic Press, London, 1982).
53. Lowell S. and Shields J.E., *Powder Surface Area and Porosity* (Chapman & Hall, London , 1991).
54. Rouquerol F., Rouquerol J. and Sing K. S.W., *Adsorption by Powders & Porous Solids* (Academic Press, London, 1999).
55. Galarneau A., Desplandier D., Dutartre R. and Di Renzo F., Micelle-templated silicates as a test bed for methods of mesopore size evaluation, *Microporous Mesoporous Mater.* **27** (1999) pp. 297-308.
56. Rouquerol F., Rouquerol J., Peres C., Grillet Y. and Boudellal M., Calorimetric

- study of nitrogen and argon adsorption on porous silicas, In *Characterization of Porous Solids*, edited by Gregg S.J, Sing K.S.W, Stoeckli H.F. (The Society of Chemical Industry, Luton ,UK, 1979) pp. 107 – 116.
57. Jelinek L. and Kovats E.S., True surface area from nitrogen adsorption experiments, *Langmuir* **10** (1994) pp. 4225 – 4231.
 58. Pfeifer P., Avnir D. and Farin D., Scaling Behavior of Surface Irregularity in the molecular Domain: From Adsorption studies to fractal catalysts, *Journal of Statistical Physics* **36** (1984) pp. 699-717.
 59. Neimark A. V. and Unger K.K., Method of discrimination surface fractality, *Journal of Colloid and Interface Sci.* **158** (1993) pp. 412-419.
 60. Sonwane C.G., Bhatia S.K. and Calos N.J., Characterization of surface roughness of MCN-41 using methods of fractal analysis, *Langmuir* **15** (1999) pp. 4603-4612
 61. Barrett E. P., Joyner L. G., and Halenda P. P., The determination of pore volume and area distributions in porous substances. I Computations from Nitrogen Isotherms, *J. Amer. Chem. Soc.* **73** (1951) pp. 373-380.
 62. Broekhoff J.C.P., de Boer J.H., Studies on pore systems in catalysts. IX. Calculation of pore distributions from the adsorption branch of nitrogen sorption isotherm in the case of open cylindrical pores. A. Fundamental equations, *J. Catalysis* **9** (1967) pp. 8-14.
 63. Broekhoff J.C.P. and de Boer J.H., Studies on pore systems in catalysts XIII. Pore distributions from the desorption branch of a nitrogen sorption isotherm in the case of cylindrical pores, *J. Catalysis* **10** (1968) pp. 377 -380; XIV. Calculation of the cumulative distribution functions for slit-shaped pores from the desorption branch of a nitrogen isotherm, *J. Catalysis* **10** (1968) pp. 391-400.
 64. Broekhoff J.C.P., de Boer J.H., Calculation of pore distributions from the adsorption branch of nitrogen sorption isotherm in the case of open cylindrical pores. B. Applications *J. Catalysis* **9** (1967) pp. 15-27.
 65. Cole M. W. and Saam W. F., Excitation spectrum and thermodynamic properties of liquid films in cylindrical pores, *Phys.Rev.Lett.* **32** (1974) pp. 985-988.
 66. Evans R. J., Fluids adsorbed in narrow pores: phase equilibria and structure, *Phys. Condens Matter* **2** (1990) pp. 8989-9006.
 67. Votyakov E.V., Tovbin Y.U.K., MacElroy J.M.D. and Roche A., A theoretical study of the phase diagrams of simple fluids confined within narrow pores, *Langmuir* **15** (1999) pp. 5713 – 5721.
 68. Celstini F., Capillary condensation within nanopores of various geometries, *Physics Letters A* **228** (1997) pp. 84 -90.
 69. Gubbins K. E., Theory and simulation of adsorption in micropores, In *Physical Adsorption: Experiment, Theory and Application*, edited by J. Fraissard, (Kluwer, Dordrecht, 1997) pp. 65 -105.
 70. Gelb L.D., Gubbins K.E., Radhakrishnan R. and Sliwiska-Bartkowiak M., Phase separation in confined systems, *Rep. Prog. Phys.* **62** (1999) pp. 1573 -1659.
 71. Burgess C.G.V., Everett D.H. and Nuttall S., Adsorption hysteresis in porousmaterials, *Pure & Appl. Chem.* **61** (1989) pp. 1845-1853.
 72. De Keizer A., Michalski T. and Findenegg G.H., Fluids in pores: experimental and computer simulation studies of multilayer adsorption, pore condensation and critical-point shifts, *Pure & Appl. Chem.* **63** (1991) pp. 1495-1502.
 73. Thommes M. and Findenegg G.H., Pore condensation and critical-point shift of a fluid in controlled-pore glass, *Langmuir* **10** (1994) pp. 4270-4277.

74. Machin W. D., Temperature dependence of hysteresis and the pore size distribution of two mesoporous adsorbents, *Langmuir* **10** (1994) pp. 1235 – 1240.
75. Groß S. and Findenegg G.H., Pore condensation in novel highly ordered mesoporous silica, *Ber. Bunsenges. Phys. Chem.* **101** (1997) pp. 1726-1730.
76. ^aMorishige K. and Shikimi M., Capillary critical point of argon, nitrogen, oxygen, ethylene and carbon dioxide in MCM-41, *Langmuir* **13** (1997) pp. 3494-3498.
^bMorishige K. and Shikimi M., Adsorption hysteresis and pore critical temperature in a single cylindrical pore, *J. Chem Phys.* **108** (1998) pp. 7821-7824.
77. Sonwane C.G. and Bhatia S.K., Characterization of pore size distribution of mesoporous materials from adsorption isotherms, *J. Phys. Chem B* **104** (2000) pp. 9099-9110; Bhatia S.K., and Sonwane C.G., Capillary coexistence and criticality in mesopores: modification of the Kelvin theory, *Langmuir* **14** (1998) pp. 1521-1524.
78. Myahara M., Sakamoto M., Kandra H. and Higashitani K., Freezing point elevation in nanospace detected directly by atomic force spectroscopy, *Studies in Surface Science and Catalysis* **144** (2002) pp. 411 – 418.
79. Olivier J., Thermodynamic Properties of confined fluids I : Experimental measurement of krypton adsorbed by mesoporous silica from 80 K to 130 K, In *Proceedings of the Second Pacific Basin Conference on Adsorption Science and Technology*, edited by D.D. DO (World Scientific, Singapore, 2000) pp. 472 -476.
80. Fretwell H.M., Duffy J.A., Clarke A.P., Alam M.A. and Evans R., Phase Transitions of CO₂ confined in nanometer pores as revealed by positronium annihilation *J. Phys. : Condens Matter* **7** (1995) pp. L717-L717.
81. Coulomb J.P., Grillet Y., Lewellyn P.L., Martin C. and Andre G., Structural properties of krypton confined in MCM-41 ($\phi = 40 \text{ \AA}$) In *Fundamentals of Adsorption*, edited by F. Meunier (Elsevier, Paris, 1998) pp. 147 – 152.
82. Morishige K., Kawano K. and Hayashigi T., Adsorption isotherm and freezing of Kr in a single cylindrical pore, *J. Phys. Chem B* **104** (2000) pp. 10298-10303.
83. Huber P. and Knorr K., Adsorption-desorption isotherms and x-ray diffraction of Ar condensed into a porous glass matrix, *Phys. Rev. B* **60** (1999) pp. 12657 – 12665.
84. Dominguez H., Allen M.P. and Evans R., Monte Carlo Studies of the freezing and condensation transition of confined fluids, *Mol. Phys.* **96** (1998) pp. 209-229.
85. De Boer J. H., *The Structure and Properties of Porous Materials*, (Butterworth, London, 1958).
86. Everett D.H., Adsorption hysteresis, In *The Solid-Gas Interface Vol.2*, edited by E.A. Flood (Marcel Decker, New York, 1967).
87. Ball P.C. and Evans R., Temperature dependence of gas adsorption on a mesoporous solid : capillary criticality and hysteresis, *Langmuir* **5** (1989) pp. 714-723.
88. Neimark A.V., Ravikovitch P.I. and Vishnyakov A., Adsorption Hysteresis in nanopores, *Phys. Rev. E* **62**, (2000) p. R1493.
89. Neimark A.V. and Ravikovitch P.I., Capillary condensation in MMS and pore structure characterization, *Microporous and Mesoporous Materials* **44-56** (2001) pp. 697-707.
90. Awschalom D.D., Warnock J. and Shafer M.W., Liquid-film instabilities in confined geometries, *Phys. Rev. Lett.* **57** (1996) pp. 1607 -1610.
91. Mason G., The effect of pore space connectivity on the hysteresis of capillary

- condensation in adsorption-desorption isotherms, *J. Colloid Interface Sci.* **88** (1982) pp. 36-46.
92. Wall G. C. and Brown R. J. C., The determination of pore size distributions from sorption isotherms and mercury penetration in interconnected pores: the application of percolation theory, *J. Colloid Interface Sci.* **82** (1981) p. 141.
 93. Neimark A.V., Percolation theory of capillary hysteresis phenomena and characterization of porous solids, *Studies in Surf. Sci. & Catal.* **62** (1991) pp. 67-74.
 94. Parlar M. and Yortsos Y.C., Percolation theory of vapor adsorption-desorption processes in porous materials, *J. Colloid Interface Sci.* **124** (1988) pp. 162 – 176.
 95. Zhu H., Zhang L. and Seaton N. A., Sorption hysteresis as a probe of pore structure, *Langmuir* **9** (1993) pp. 2576 - 2582; Liu H., Seaton N.A., Determination of the connectivity of porous solids from nitrogen sorption measurements - III Solids containing large mesopores, *Chem. Eng. Sci.* **49** (1994) pp. 1869 - 1879.
 96. Rojas F., Kornhauser I., Felipe C., Esparza J.M., Cordero S., Dominguez A., and Riccardo J.L., Capillary condensation in heterogeneous mesoporous networks consisting of variable connectivity and pore-size correlation, *Phys.Chem.Chem.Phys.* **4** (2002) pp. 2346-2355.
 97. Page J.H., Liu L., Abeles B., Herbolzheimer E., Deckmann H.W. and Weitz D.A., Adsorption and desorption of a wetting fluid in vycor studied by acoustic and optical techniques, *Phys. Rev. E*, **52**, (1995) pp. 2763-2777.
 98. Hoinkis E. and Roehl-Kuhn B., The spatial distribution of vapor-filled voids on condensation and drainage of nitrogen at ~ 78 K in a mesoporous silica glass. In *Fundamentals of Adsorption 7*, edited by Kaneko K., Kanoh H., Hanzawa Y., (IK International ltd, Chiba City, Japan ,2002) pp. 601 -607.
 99. Sarkisov L. and Monson P.A., Modelling of adsorption and desorption in pores of simple geometry using molecular dynamics, *Langmuir* **17** (2001) pp. 7600 – 7604.
 100. Gubbins K.E., Molecular simulation of confined nano-phases. In *FundamentalsOf Adsorption 7*, edited by Kaneko K., Kanoh H., Hanzawa Y., (IK International Ltd, Chiba City, Japan , 2002) pp. 17-20.
 101. Page K.S. and Monson P.A., Monte Carlo calculations of phase diagrams for a fluid confined in a disordered porous material, *Phys. Rev. E*, **54** (1996) pp. 6557 - 6564.
 102. Pellenq R.J.M., Rousseau B. and Levitz P.E., A grand canonical monte carlo study of argon adsorption/condensation in mesoporous silica glasses, *Phys. Chem.Chem. Phys.* **3** (2001) pp. 1207 – 1212.
 103. Gelb L.D. and Gubbins K.E., Characterization of porous glasses: Simulation models, adsorption isotherms, and the BET analysis method, *Langmuir* **14** (1998) pp. 2097 – 2111.
 104. Gelb L.D., Molecular simulation of capillary phenomena in controlled pore Glasses, in *Fundamentals of Adsorption 7*, edited by Kaneko K., Kanoh H. and Hanzawa Y., (IK International ltd, Chiba City, Japan, 2002) pp. 333 – 340.
 105. Kierlik E., Rosinberg M.L., Tarjus G., and Viot P., Equilibrium and out-of equilibrium (hysteretic) behavior of fluids in disordered porous materials: Theoretical predictions, *Phys. Chem.Chem. Phys* **3** (2001) pp. 1201-1206.
 106. Woo H.J., Sarkisov L. and Monson P.A., Mean-field theory of fluid adsorption in a porous glass, *Langmuir* **17** (2001) pp. 7472-7475.
 107. Burgess C.G.V. and Everett D.H., The lower closure point in adsorption hysteresis

- of the capillary condensation type, *J. Colloid and Interface Sci* **33** (1970) p. 611.
108. Sonwane C.G. and Bhatia S.K., Analysis of criticality and isotherm reversibility in regular mesoporous materials, *Langmuir* **15** (1999) pp. 5347-5354.
109. Ravikovitch P.I. and Neimark A.V., Experimental confirmation of different mechanisms of evaporation from ink-bottle type pores: equilibrium, pore blocking, and cavitation, *Langmuir* **18** (2002) pp. 9830 – 9837.
110. Schreiber A., Reinhardt S. and Findenegg G.H., The lower closure point of the adsorption hysteresis loop of fluids in mesoporous silica materials, *Studies in Surface Science and Catalysis* **144** (2002) p. 177.
111. Zhu H.Y., Ni L.A. and Lu G.Q. (Max), A pore size dependent equation of state for multilayer adsorption in cylindrical mesopores, *Langmuir* **15** (1999) pp. 3632-3641.
112. Sonwane C.G. and Bhatia S.K., Determination of pore size distributions of mesoporous materials from adsorption isotherms, in *Fundamentals of Adsorption* **7**, edited by Kaneko K., Kanoh H. and Hanzawa Y., (IK International Ltd, Chiba City, Japan, (2002) pp. 999 – 1006.
113. Groen J.C., Doorn M.C. and Peffer L.A.A., MCM-41 and the BDB corrected Kelvin equation for accurate mesopore size distributions from gas adsorption data, in *Adsorption Science and Technology*, edited by D.D. Do (World Scientific, Singapore, 2000) pp. 229-233.
114. Kruk M. and Jaroniec M., Application of large pore MCM-41 molecular sieves to improve pore size analysis using nitrogen adsorption measurements, *Langmuir* **13** (1997) pp. 6267 – 6273.
115. Jaroniec M., Kruk M. and Choma J., The 50th anniversary of the Barrett-Joyner-Halenda method for mesopore size analysis: critical appraisal and future Perspective, in *Fundamentals of Adsorption* **7**, edited by Kaneko K., Kanoh H. and Hanzawa Y., (IK International Ltd, Chiba City, Japan, 2002) pp. 570 – 577.
116. Kruk M. and Jaroniec M., Accurate method for calculating mesopore size distributions from argon adsorption data at 87 K developed using model MCM-41 materials, *Chem. Mater.* **12** (2000) 222-230.
117. Kruk M. and Jaroniec M., Determination of mesopore size distributions from argon adsorption data at 77 K, *J. Phys. Chem B* **106** (2002) 4732 – 4739.
118. Kruk M., Antochshuk V., Jaroniec M. and Sayari A., New Approach to evaluate pore size distributions and surface areas for hydrophobic mesoporous solids *J. Phys. Chem B* **103** (1999) pp. 10670 – 10678.
119. Evans R., Marconi U. M. B., and Tarazona P., Fluids in narrow pores: adsorption, capillary condensation and critical points *J. Chem. Phys* **84** (1986) pp. 2376-2399; Evans R., Marconi U. M. B. and Tarazona P., Capillary Condensation and adsorption in cylindrical and slit-like pores, *Chem. Soc., Faraday Trans 2*, **82** (1986) pp. 1763-1787.
120. Seaton N.A., Walton J.R.B. and Quirke N., A new analysis method for the determination of the pore size distributions of porous carbons from nitrogen adsorption measurements, *Carbon* **27** (1989) p. 853.
121. Lastoskie C.M., Gubbins K. and Quirke N., Pore size distribution analysis of microporous carbons: a density functional theory approach, *J. Phys. Chem.* **97** (1993) p. 4786.
122. Olivier J.P., Conklin W.B. and v. Szombathley M., Determination of pore size distribution from density functional theory, in *Studies in Surface Science and*

- Catalysis* **87** (1994) p. 81.
123. Neimark A.V., Method of indeterminate Lagrange multipliers in the non-local density functional theory 124, *Langmuir* **11** (1995) p. 4183.
 124. Neimark A.V., Ravikovitch P.I., Grün M., Schüth F. and Unger K.K., Pore size analysis of MCM-41 type of adsorbents by means of nitrogen and argon adsorption, *J. Colloids and Interface Sci.* **207** (1998) pp. 159 – 169.
 125. Ravikovitch P.I. and Neimark A.V., Characterization of nanoporous materials from adsorption and desorption, *Colloids and Surfaces A: Physicochemical and Engineering Aspects* **187-188** (2001) pp. 11 – 21.
 126. Di Renzo F., Galarneu A., Trens P., Taunchoux N. and Fajula F., Confinement at nanometer scale: why and how? *Studies in Surface Science and Catalysis* **142** (2002) pp. 1057-1066.
 127. Neimark A.V., Ravikovitch P.I., and Vishnyakov A., Bridging scales from molecular simulations to classical thermodynamics: density functional theory of capillary condensation in nanopores, *J. Phys.: Condens. Matter* **1** (2003) pp. 347 – 365.
 128. Findenegg G.H., Gross S. and Michalski T., Pore condensation in controlled-pore glass. An experimental test of the Saam-Cole theory, *Studies in Surface Science and Catalysis* **87** (1994) pp. 71 -80.
 129. Smarsly B., Goeltner C., Antonietti M., Ruland W. and Hoinkis E., SANS Investigation of nitrogen sorption in porous silica, *J. Phys. Chem. B* **105** (2001) pp. 831-840; Smarsly B., Thommes M. and Ravikovitch P., manuscript in preparation.

MOLECULAR SIMULATION OF ADSORPTION IN POROUS MATERIALS

DAVID NICHOLSON

*Computational and structural group, Department of Chemistry, Imperial College,
London SW7 2AY, United Kingdom.*

E-mail: d.nicholson@ic.ac.uk

Simulation studies of adsorption have increased steadily in number since the 1970's. The many advantages of modelling include the insights to be gained into the behaviour of complex real systems by probing the effects of well-defined modifications of model adsorbents, and the promise that specific tailoring of new materials if understood in sufficient detail, may improve performance in applications such as catalysis and separation. The Chapter begins with an overview of some of the more recent innovations in methodology, particular attention being given to biasing methods that improve sampling efficiency in Monte Carlo studies of large molecules in highly confined spaces, and the dual control volume (DCV) method that has found use, for example, in examining the nature of mesopore hysteresis. The increased application of simulation, especially to more recent high temperature adsorption, has highlighted the distinction between the absolute adsorption quantities that result from simulation and theory, and excess adsorption that is always measured in experiments. This in turn has encouraged a re-examination of thermodynamic concepts that underlie the interpretation of data from both sources. Much insight into the molecular processes that occur in real adsorbents has been achieved by studying simple ideal geometry such as slits or cylinders. Amongst the more recent investigations of this type, the nature of packing in micropores and insight into hysteresis in mesopores are highlighted. The existence of unusual states of matter, such as the plastic phase that can occur under particular conditions of temperature and confinement, is an example of the kind of detail that can be extracted from simulation studies. Heterogeneity is another long-standing problem in adsorption, where simulation has been fruitful. Several models where particular forms of heterogeneity may exist, such as striped and stepped surfaces, have been studied in some detail, and the increasing importance of this type of structure in nanotechnology is likely to inspire further work of this nature. The distinction between geometrical and structural heterogeneity has also been clarified by simulation of suitably chosen model pores. A somewhat different form of heterogeneity occurs in zeolites where it is well known that the introduction of extra-framework cations can have dramatic effects on adsorption behaviour of polar molecules. Simulation of nitrogen adsorption in chabazite, using high level potential energy models, have been taken as an example of the way in which an improved understanding of such processes can be gained. The continued confirmation that simulation is a powerful tool for elucidating and clarifying the molecular mechanisms involved in the adsorption process, especially in porous materials where high confinement can lead to unusual states of matter, will ensure that it will find many uses in this field in the foreseeable future.

1 Introduction

Since the late 1970's, simulation has played an increasing role in the interpretation of adsorption phenomena in porous materials. One reason for the attractiveness of simulation in this field is that one is dealing with inherently small systems; another is the atypical states of adsorbate phases encountered in highly confined spaces. Added to these is the geometrical and chemical complexity of adsorbent matrices. All these factors suggest that it may be advantageous to study highly idealised model adsorbents containing realistic adsorbate molecules in order to gain insight into the underlying nature of the physical phenomena. Many simulation studies begin from this position, with slit pore and cylindrical pore models being especially popular. However, simulations of random sphere models, and more recently of reconstructed porous materials have gained popularity, as computers become more powerful.

The gap between highly idealised models and real materials continues to prove difficult to bridge, and the search for well defined porous structures has been spurred by the goal of creating highly tailored, and therefore controlled, structures as well as by the desire to produce simple structures with a one-to-one correspondence with simplified models [1]. Amongst several possibilities, the zeolites are perhaps the oldest; favoured because their crystalline structure promises clearly defined, reproducible and replicated pore spaces [2,3]. However, geometrical complexity, chemical heterogeneity and small crystallite sizes have frustrated some of the optimism of earlier work in this area. The great majority of zeolite simulations have been made with silicalite, the pure silica form of ZSM, although this has few practical uses compared to the ionic form. Amongst the newer materials that continue to attract attention are the silica based MCM types of adsorbent, pillared clays and carbon nanotubes. All these materials have also found, or show promise for industrial application, which adds to the motivation for their study.

Early simulation used mainly spherical models for adsorbate species. With the increase in computing power, there has been a move towards modelling more complicated polyatomic structures.

2 Simulation Techniques

The majority of adsorption experiments focus on adsorption isotherms. By far the largest number of standard measurements use the volumetric method to measure the adsorption of nitrogen at 77K as a characterisation technique. However, most applications of porous materials are made at

ambient or higher temperature, and high-pressure gravimetric measurements are becoming more common. In open systems, the grand canonical Monte Carlo (GCMC) method is the most natural simulation technique. In single-component systems, there are three basic types of trial move: random translation or reorientation of a molecule in space and creation or destruction of molecules at randomly selected locations. In mixture simulations, there is significant advantage in adding exchange trials between different adsorbate species in the system, in which an attempt is made to change the molecular identity of a randomly selected molecule to that of a different component in the mixture. When a flexible molecular model is used, trial movement of the individual atoms (or united atoms) are also included, taking account of bond-stretching, bond-bending and torsion potential energy. The basic methodology has been well documented [4,5].

A major difficulty in open-system simulations is that acceptance probability becomes lower as density increases, and it is generally advisable to examine control charts of running mean against configuration number to check for convergence. Cavity biasing techniques have been devised to improve acceptance of trial insertions in dense fluids and energy biasing [6]. When non-spherical or polar species are involved, other problems arise. For example insertion of highly polar species, such as water, may be rejected when a random orientation leads to repulsion between like charges. Similarly, random attempts to insert long chain molecules into a confined space, such as a zeolite cavity, are likely to be frustrated by repulsive overlap of part of the chain with adsorbent atoms.

The requirement of detailed balance in a Monte Carlo simulation leads to the equality

$$P_o^B P_o^{ins} P_o^{acc} = P_n^B P_n^{ins} P_n^{acc}$$

where P^B is the Boltzmann probability of the configuration in the given ensemble, P^{ins} is the a priori probability of generating a new configuration and P^{acc} is the acceptance probability which must be corrected for bias. The subscripts o and n refer to old and new states for the system respectively.

In rotation insertion bias [7], several orientations are sampled, and the most favourable accepted subject to correction for the bias. In the case of long chain molecules, with n_a atoms (or pseudo atoms) the chain is grown atom by atom [7,8]. A distinction is made between internal (*int*) (such as

bond-stretching, bending etc) and external (*ext*) contributions to the interaction potential. Trial positions in a configuration *b* are generated with the probability

$$p(b) = \exp[-\beta U^{\text{int}}(b)]$$

where U^{int} is the part of the potential energy due to internal interactions [7,8]. The normalised Rosenbluth factor W^{ext} is computed from the external interaction u_j^{ext} on adding atom *j* at trial position *i* out of *k* trial positions.

$$W^{\text{ext}} = \frac{1}{k^{n_a-1}} \exp[-\beta u_1^{\text{ext}}] \prod_{j=2}^{n_a} \sum_{i=1}^k \exp[-\beta u_j^{\text{ext}}(i)]$$

The use of internal interactions to generate the trial positions is equivalent to a shift in the chemical potential, relative to that of the “ideal” chain that is related to the average Rosenbluth factor by:

$$\langle W^{\text{ext}} \rangle = \exp[-\beta(\mu - \mu^{\text{id}})]$$

Here “ideal” refers to a chain with internal interactions only and it is to be noted that this differs from the real chain in the ideal gas phase.

In an open system, the chemical potential in the reservoir (μ_B) must be included in the probability P^{acc} equal to that of the adsorbate (μ), and the acceptance condition should be computed using,

$$\mu = \mu_B + \mu_{\text{id}}^{\text{ext}}$$

Configurational bias significantly improves the acceptance of creation and destruction trials for long chain molecules. For aromatic species, cavity bias in combination with orientational bias [6,9], has proved effective in improving acceptance probability.

A new hybrid method, known as dual control volume (DCV) or grand canonical molecular dynamics (GCMD) [10,11,12] has recently found use in both equilibrium and non-equilibrium investigations of adsorption. In this technique, a model adsorbent is included in a sequence of volumes (usually 3 or 4). Creation and destruction of molecules is carried out in the outer volumes (the control volumes) in a sequence of Monte Carlo steps, and molecular dynamics steps are performed on the whole system at

frequent intervals. In this way, molecules can only enter or leave the adsorbent by dynamic steps. If the end volumes are maintained under different chemical potentials, the fluid is driven through the adsorbent under a gradient.

3 Thermodynamics

The treatment of adsorption thermodynamics goes back at least to the 50's but is still remains a topic of interest [13,14,15,16,17,18,19].

The most general approach is to treat the system as a solution of adsorbate species in a solvent of adsorbent. The natural choice of free energy in an open system is the grand free energy, defined by

$$\Omega = U - TS - \sum \mu_i N_i = -kT \ln \Xi \quad (1)$$

where Ξ is the grand canonical partition function.

The change in internal energy of the system is given by:

$$dU = TdS - pdV + \sum \mu_i dN_i + \sum \mu_j dN_j^s$$

where p is the pressure in the external bulk gas phase, N_i the number of molecules of adsorbate of type i , and N_j^s the number of adsorbent atoms of type j and V is the total volume including void and solid (the solute).

These expressions lead to a Gibbs-Duhem equation [17,19,20]:

$$\sum N_i d\mu_i = 0 \quad (2)$$

at constant temperature and grand free energy. Equation (2) forms the basis of the Gibbs adsorption isotherm and the ideal adsorption isotherm approximation for mixture adsorption [19,20]. This formulation avoids any specific reference to the pressure in the adsorbate fluid, a quantity that can only be defined in relationship to a specific geometry in a rigid adsorbent.

When properties related to pressure dependent terms are discussed, such as capillary condensation, it is useful to reformulate these thermodynamic equations in terms of the pore space itself, though this has the drawback that it necessitates reference to a specific geometry for the

pore space. In a slit shaped or cylindrical pore space of internal volume V_p , the change in internal free energy can be expressed in terms of the normal and transverse components of the pressure tensor, p_N , p_T . For example in a slit pore of width h , formed from two surfaces of area A (such that $V_p = hA$),

$$dU = TdS - dA \int p_T(z)dz - dh \int \int p_N(x, y)dx dy + \sum \mu_i dN_i$$

This equation can be rewritten [21,20]

$$dU = TdS - p dV_p - (\bar{p}_T - p)h dA - (\bar{p}_N - p)A dh + \sum \mu_i dN_i$$

Insertion of the total derivative of the grand free energy from equation (1), leads to the expression

$$d\Omega = -SdT - p dV_p - (\bar{p}_T - p)h dA - (\bar{p}_N - p)A dh - \sum N_i d\mu_i \quad (3)$$

From which, various properties may be defined [20]. For example the surface tension, γ ,

$$\left(\frac{\partial \Omega}{\partial A} \right)_{T, V_p, \mu_i, h} = \gamma = - (\bar{p}_T - p)h$$

and the disjoining pressure Π ,

$$\frac{1}{A} \left(\frac{\partial \Omega}{\partial h} \right)_{T, V_p, \mu_i, A} = \Pi = - (\bar{p}_N - p)$$

Equation (3) also yields the Gibbs-Duhem expression in equation (2).

Simulations always yield absolute quantities such as the mean value of the absolute amount adsorbed, which can be calculated from the number of molecules of a given species in the simulation box, or the absolute value of the mean potential energy which is equivalent to the mean configurational part, $\langle U^{conf} \rangle$, of the internal energy. The latter may be usefully divided into molecule-wall and molecule-molecule contributions. The absolute configurational energy, $\langle U \rangle$, may be obtained by adding the kinetic

energy contribution for the adsorbate components; equivalent to their energy in a perfect gas state.

Experimental measurements, whether gravimetric or volumetric, give excess quantities, for example the excess number of molecules adsorbed N_i^{Σ} is given by:

$$N_i^{\Sigma} = N_i - N_i^g$$

where N_i^g is the number of non-adsorbed molecules of the adsorptive that would occupy the adsorption space. The adsorption space must always be calibrated prior to a measurement, ideally with a non-adsorbed gas. In practice, all real gases are adsorbed to some small extent, and N_i^g is calculated from the number of molecules of a weakly adsorbed gas (usually He room temperature) that occupies the adsorption space, V , from $N_i^g = V\rho_g y_i$ where ρ_g is the density of the calibration gas, and y_i the mole fraction of species i . The true adsorption excess is therefore inaccessible experimentally. To make a comparison of experiment with simulation, a separate simulation should be made to reproduce the calibration process [22]. In practice this procedure is frequently unnecessary, since at low temperatures and pressures, absolute and excess quantities are nearly identical. At high pressures and ambient temperatures, there can be very substantial differences between absolute and excess quantities. For example, the excess isotherm may pass through a maximum at high pressure, when it becomes easier to compress gas into the external phase, than to force additional molecules into the pore space.

The excess enthalpy is given by

$$H^{\Sigma} = H - H^g$$

where $H^g = V\rho_g h_g$ and h_g the enthalpy per molecule of the gas phase. Since $V^{\Sigma} = V - V_g = 0$, H^{Σ} and U^{Σ} are the same.

The differential heat (or more correctly the differential enthalpy) of adsorption is defined as the partial derivative of the enthalpy of adsorption, relative to an ideal gas phase. The quantity commonly known as the isosteric heat of adsorption is

$$q_{st} = -\Delta\bar{u} = kT - \left(\frac{\partial U^{conf}}{\partial N} \right)_{T,V} \quad (4)$$

In a simulation, this can be calculated either from fluctuations [23] or by taking appropriate derivatives of the configurational energy [13], calculated from the total potential energy of interaction of the adsorbate with other adsorbate species and with the adsorbent.

The corresponding excess function must be obtained by differentiation of the appropriate excess quantities

$$q_{ST}^{\Sigma} = -\Delta \overline{U^{\Sigma}} = KT - \left(\frac{\partial u^{\Sigma_{conf}}}{\partial N^{\Sigma}} \right)_{T,V} \quad (5)$$

As is the case for adsorption isotherms, there may be substantial differences between absolute differential heats and excess differential heats calculated from experimental adsorption isotherms [18] or from calorimetry [24] at ambient temperatures. Even at zero coverage, this difference can be of the order of 8% and increases with coverage [18]. Non-ideality of the gas phase, can be included, by adding a residual enthalpy term to the right hand side in equations (4) and (5) [18].

From the standpoint of a molecular interpretation of heats, it is the absolute heat quantities that are relevant, since there can be no statistical distinction between molecules at equivalent positions in the pore space, whether they are counted as part of the excess or part of the gas phase population. Absolute heats from simulation can be divided into adsorbate-adsorbate contributions, and adsorbent-adsorbate contributions and this gives useful insight into the energetics underlying the adsorption process. For example, a differential heat that remains constant over a range of adsorbate densities does not necessarily imply adsorption into an energetically uniform environment. The adsorbent wall component of the heat may decrease as favourable sites are occupied at low coverage, but this decrease can be compensated by an increase in the contribution from adsorbate interactions as adsorbate density increases [25].

4 Adsorption in spaces with simple geometries

Many real porous adsorbents have structures that incorporate both a degree of order and a degree of random complexity that may also extend over a wide range of pore sizes. For example, many carbon-based adsorbents are believed to consist of elementary spaces resembling slit pores with graphitic walls in random orientation and with a distribution of slit width sizes. A standard classification of pore sizes distinguishes between mesopores with dimensions above 2nm and micropores below this size

[26], based on the adsorption of nitrogen at 77K. However, it has become clearer that the distinction between micropore and mesopore isotherm types depends on the characterising probe [27,28] and not simply on pore size.

A useful strategy for simulation is to study simplified or idealised geometries that may be claimed to have some resemblance to real structures such as slits, cylinders or sphere packs. The properties of real materials can then be approached, in principle, through size distributions, and pore connectivities. Conversely, characterisation techniques reverse this approach, and attempt to extract statistical properties. A major advantage of studying simple geometries is that a clearer understanding of the physics underlying adsorption processes in real materials may emerge. On the other hand, it can be reasonably claimed that the view that a real material is simply the sum of essentially independent units of simple geometry, is naïve and is likely to miss important aspects of the processes in real systems.

The distinction between mesopores and micropores is perhaps best founded on the observation of adsorption isotherms, and is thus dependent on both temperature and adsorptive. Typically, mesopore isotherms comprise a two stage filling process. In the first stage, layers of adsorbate are formed at the pore walls, followed by capillary condensation [29], identified by an abrupt riser, and accompanied experimentally by hysteresis. However, as temperature is raised, the riser section becomes shorter, and the hysteresis loop narrower, until it finally disappears at the capillary critical temperature. This behaviour is typical of adsorption below the critical temperature where the adsorbate-adsorbent interaction is strong compared to the molecule-molecule interaction, and is typified by the adsorption of nitrogen or argon at liquid nitrogen temperature, frequently used in characterisation.

In cases where the adsorbate-adsorbate interaction is relatively strong (for example water adsorption) capillary condensation can occur before adsorbate layers are formed [30]. When the ratio of adsorptive size to pore size is increased, or when the temperature is above critical, the capillary condensation and hysteresis, that are typical of mesopore behaviour, is not observed. Adsorption isotherms may still exhibit inflections or other features associated with transitions, related to reorganisation of adsorbate structures.

4.1 Packing in micropores

An important feature of micropore behaviour that has been highlighted by simulation, is the strong sensitivity to packing. Several simulations of simple fluids in model pores over a range of pore sizes show crossing of isotherms or heats curves [31, 32, 33, 34, 35, 36, 37]. In micropores of critical width a sharp (first order) transition from a gas-like to a solid-like state can occur. Transitions of this type have been observed for adsorbates modelled as spheres, and for diatomic molecules, and it may be conjectured that the phenomenon is general [38,39,20]. Isotherms re-plotted as constant pressure isosteres against pore width, reveal packing transitions. In slit pores, the intensity of the transitions increases with pressure [33, 20], but in cylinders the trend is complicated by geometrical constraints as illustrated in figure 1, where the strong transition that appears at around 1.0nm radius, fades at higher pressures when the ordering of the adsorbed layers becomes dominated by the curvature of the cylinder.

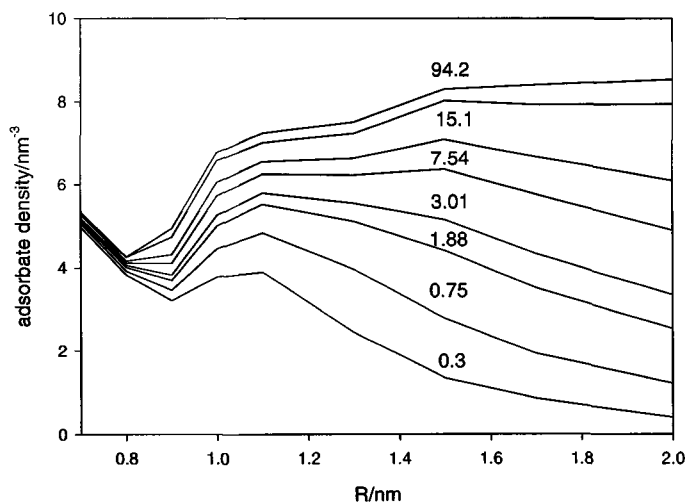


Figure 1. Adsorbate density for methane at 273K, as a function of pore radius in a series of graphitic cylinders. The numbers on the isosteres are fugacities in bar.

Heat curves, re-plotted at constant densities, exhibit similar phenomena [36]. In mixture adsorption, packing facility can be an important factor in determining selectivity [37, 40, 41]. The transitions observed over three adsorbed layers at saturation density in slit pores have been rationalised,

using a lattice model version of density functional theory, in terms of the solid-like structures available to the molecules as the pore width is expanded to accommodate successive layers of adsorbate [42]. Single particle and pair distributions were found to exhibit characteristic features that correspond to the sequence of buckling and rhombic transitions that occur as the slit pore width is increased. An examination of pair distribution functions, [35] taken at a relative pressure of 1.0, from simulations at 303K of a spherical model of CCl_4 in graphitic slit pores, revealed that a new set of peaks labelled as X, Y, Z in Figure 2, appears close to the first density maximum in pores of width around 1.0nm. This anomalous structure was interpreted as belonging to a plastic crystal phase [43], possessing long-range positional order but no orientational order. Experimental evidence for the existence of this type of phase for CCl_4 in the micropores of carbon fibres has been reported [44]. The radial distribution peaks corresponding to the plastic structure disappeared at fractional filling below 0.84.

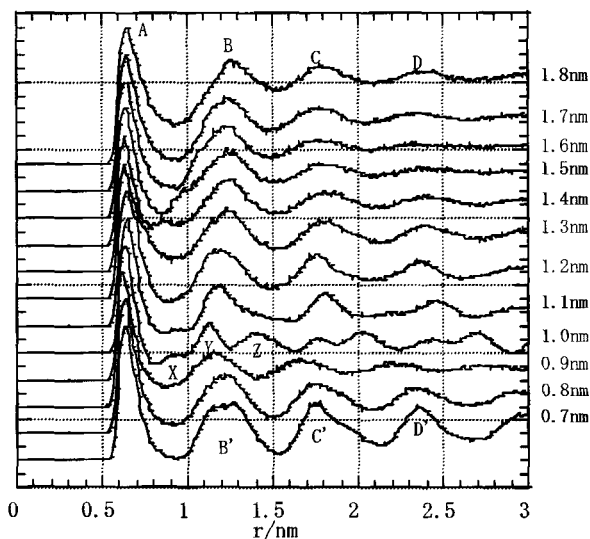


Figure 2. Pair distribution functions for a spherical model of CCl_4 at 303K in graphitic slit pores. A plastic phase appears at slit widths around 1.0nm. (From reference [35], with permission).

4.2 Mesopores, capillary condensation and hysteresis

Many adsorption measurements and applications are made in mesoporous systems where subcritical adsorbates show capillary condensation and hysteresis phenomena. In particular, this behaviour is common in characterisation procedures using nitrogen adsorptive at 77K. Nevertheless, the mechanism of condensation and hysteresis has been discussed extensively over several decades and continues to attract attention. Recently the coexistence curves for capillary fluids have been investigated, both experimentally and using simulation [45]. Confinement lowers the critical temperature and the low-density branch of the temperature-density co-existence region is shifted to a higher density than that of the corresponding bulk gas adsorptive, resulting in an overall narrowing of the coexistence curves.

Hysteresis can occur when two similar free energy minima are separated by a free energy barrier and may be accessed by different paths. In a single mesopore, the filling mechanism depends on a phase transition at the interface between one or two adsorbed layers and a lower density phase in the core of the pore space. Different mechanisms have been proposed for emptying, including the formation of a critical nucleus or cavity within the dense adsorbate fluid [46] and the Kelvin criticality of the spherical meniscus formed at the end of a filled pore [47]. Cohan showed that, in a cylindrical pore, the combination of condensation at a cylindrical meniscus formed by adsorbed layers, followed by the second of these emptying mechanisms, resulted in a parallel sided hysteresis loop [47]. This theory has been further developed and elaborated by taking into account the contribution from the external field due to the adsorbent [48, 49, 50, 51]. However, it is insufficient to account for the range of typical loop shapes observed in experimental studies [52]. Recent refinements of this type of approach have been successful in predicting experimental adsorption data for nitrogen adsorption in independent and near cylindrical pores of MCM41 [51].

GCMC simulation at temperatures below the critical temperature generally shows the expected type of condensation phenomenon [45, 29] accompanied by hysteresis. However, the GCMC method suffers from a fundamental uncertainty because the method allows creation and destruction of molecules through the capillary wall. Clearly, this is physically unrealistic and it is observed that hysteresis loops obtained in this way are often unrealistically broad. The technique has also been criticised on the grounds that it fails to sample the large fluctuations responsible for the phase change [53]. The recently developed gauge-cell

technique [54,55] overcomes the latter objection by tracing out the profile of the hysteresis loop and shows that conventional GCMC in single pores closely follows the true spinodal when Arrhenius factors for the free energy barriers between the stable and metastable states become non-vanishing. Multiple histogram reweighting is another technique that has been applied to this and other phase transition problems [56], and has been successful in demonstrating a crossover from Ising-like to mean field type of coexistence curve close to the critical point.

Simple single-capillary models are not applicable to many real mesoporous materials (MCM type of materials may be an exception) since these generally comprise interlinked voids of varying dimension and geometry. A less simplified view is to consider a model of a network of simple pores having a distribution of sizes. In the limit, one may consider two linked pores of different width, referred to as an “ink-bottle” pore. The assumption is that in this kind of geometry, filling and emptying of the network depends on accessibility of the large pore that may be blocked by a small pore that is filled with adsorbate fluid and may therefore be treated as a percolation phenomenon. According to the Cohan hypothesis, the larger pore would not empty until a spherical meniscus (assuming cylindrical pores) at the mouth of the small pore becomes subcritical. One problem encountered by network models is that small pore spaces may include micropores as well as mesopores. Since there is no simple thermodynamic model to handle the former, molecular theories or simulation, rather than thermodynamic theories, are essential. More elaborated dual site-bond network models have been developed take account of overlap in pore size distribution [57] and are capable of reproducing a range of hysteresis types [58].

With the increasing availability of larger computing power, modelling of porous materials has been extended to the construction of models with more general internal geometry, such as random sphere packs [59,60,61,62], that approach more nearly the expected structure of real materials. More recently, models for porous glasses have been constructed by a simulated etching process that closely mimics the preparation of the experimental material [63,64]. Reverse Monte Carlo and simulated annealing have also been used as a basis on which to construct model materials [65,66]. Here basic structural units, such as spheres, or in the case of carbons, graphitic plates, are used as building blocks. The removal, movement or addition of material to the model adsorbent is controlled by global parameters such as porosity and distribution functions from X-ray scattering data for real materials that can be determined by methods that are independent of adsorption. When used as adsorbents in

simulated adsorption experiments, these models demonstrate that network effects do indeed play a role in the overall shape of the hysteresis loop. However, since the models have highly complex pore geometry, they can only provide limited insight into the underlying mechanism of adsorption and desorption. Moreover, it is possible that kinetic limitations contribute to hysteresis, since experimental measurements often take hours to reach equilibrium. On the other hand, experimental hysteresis loops are usually highly reproducible implying that a true thermodynamic equilibrium has been achieved.

The issue of mechanism has been largely resolved by using DCV (or GCMD) simulation [67,68] (see section 2). Both of these studies used a model of serially linked slit pores with a wide pore sandwiched between two narrower pores. This configuration may be regarded as a network element, in the spirit of the inkbottle model, designed to test the percolation hypothesis. The DCV method ensures that only diffusion effects control the entry and exit of adsorptive to the adsorbent. However, in the earlier work [67] the end pores, which were of micropore size, were used as control volumes, whilst Sarkisov and Monson [68] studied pores of mesopore width, and included an end volume, containing adsorptive vapour phase, as control volume. Hysteresis was observed in this model, but cannot be attributed to a pore blocking effect since the larger central pore empties whilst the remaining end pores (which are still supercritical) remain filled (Figure 3). Molecules evaporated from the smaller pore at the vapour-adsorptive meniscus, are replaced by diffusion from the larger pore. It was suggested that desorption from the larger pore begins when the adsorbate in it reaches a thermodynamic state where spontaneous fluctuations can nucleate to form a cavity. The filling mechanism on the other hand was shown to follow essentially the classical Cohan path of layer formation followed by condensation, and occurs at a higher relative pressure than cavitation as illustrated in Figure 3.

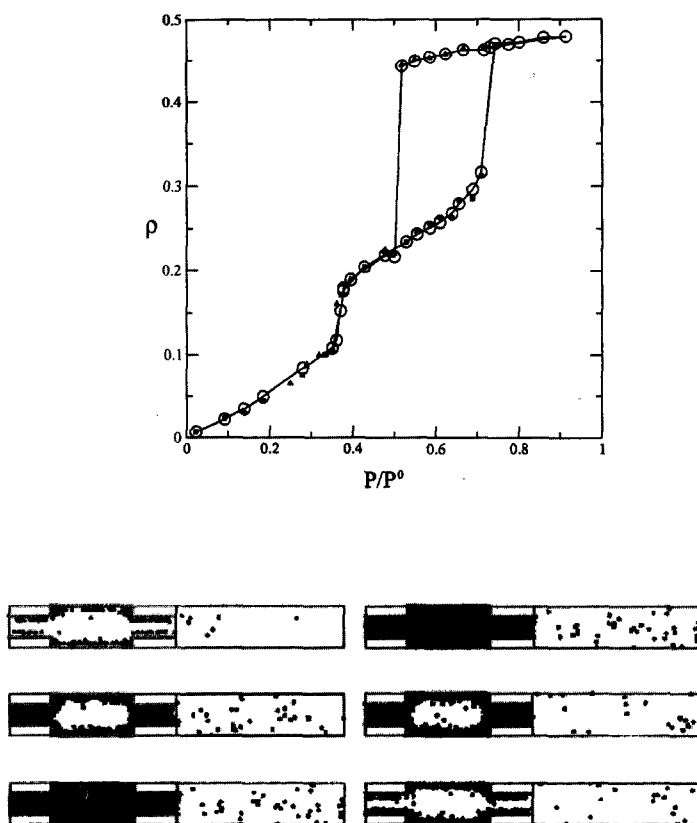


Figure 3. Filling and emptying of an “inkbottle” pore, studied by DCV (grand canonical molecular dynamics). The molecular pictures show three stages in the filling process (on the left), and three stages of emptying (on the right). The isotherm has a low-pressure step – without hysteresis - corresponding to filling and emptying of the small pore. The larger pore fills at a relative pressure of 0.75, but critical nucleation, leading to emptying, does not occur until a relative pressure of 0.5. (From reference [68], with permission).

Nevertheless, pore blocking may play a role in adsorption and desorption [67] when solid like layers form in micropores [38,39,67] that control percolation paths. DCV simulations in single open-ended slit pores also show hysteresis [68], but in this case, emptying is controlled by the collapse of the meniscus formed at the ends of the filled pore. Again

filling was found to follow a process of layering and capillary condensation. DCV simulations in closed pores do not show any hysteresis [68]. It is also important to note that GCMC simulations on the same models [61,62,68] are in excellent agreement with the DCV simulations, confirming that thermodynamic states and not kinetics underlie capillary condensation and hysteresis phenomena in mesopores, and that standard GCMC, applied to suitable pore models, can correctly predict the course of the hysteresis loop.

It may be concluded from this work there are two possible mechanisms that can contribute to hysteresis in networks of pores. When only mesopores are present, the classical Cohan type of mechanism applies to openings that are directly in contact with the adsorptive. However, its correct thermodynamic description necessitates the inclusion of the adsorbent field [51]. On the other hand, the emptying of spaces trapped by smaller pores can be controlled by a cavitation process, where the relative pressure for desorption is not, in general, the same as that for emptying via a meniscus in contact with a vapour phase. A third possibility, when micropore size spaces are present, is that frozen adsorbate in spaces of critical width can block the exit of adsorbate fluid from wider spaces trapped by these micropores, even though the trapped fluid is sub-critical and would desorb through any mesoporous path connected to the external adsorptive phase. However, it is not clear in this case how the filling process can occur through the already blocked micropore. Although network and percolation effects are important in determining the form of the hysteresis loop, quantitative interpretation for characterisation or other purposes is complex [64] and not yet fully resolved.

5 Adsorption heterogeneity

The classical Langmuir equation is based on a flat surface with sites having equal energies. Many earlier developments of adsorption theory retained this basic model. Whilst Langmuirian (or type I) isotherm shapes are commonly observed in adsorption experiments on materials with very small pores, it was soon appreciated that this is an insufficient condition to validate the Langmuir model, except as a convenient fitting equation. The lack of agreement between theory and experiment is most clearly manifested by experimental differential heat curves, which often show a sharp decrease at low adsorbate coverages. The Langmuir model, since it takes no account of interaction between adsorbate molecules, predicts an invariant heat over the whole range of coverage. If adsorbate interactions are taken into account, the isosteric heat curves would be expected to

increase steadily with coverage. Simulation has modified this simple picture, even for pores with energetically uniform surfaces, by showing that the adsorbate-adsorbent contribution to the heat may decline as adsorbate-adsorbate contributions increase with coverage so that the overall heat curve may have positive, negative or zero slope, dependent on pore geometry [20]. The lack of agreement between simple theory and experiment is customarily attributed to heterogeneity in experimental systems. The fundamental equation describing the observed adsorption isotherm, $\Gamma(p)$ is:

$$\Gamma(p) = \int \Gamma(p, \varepsilon) f(\varepsilon) d\varepsilon \quad (6)$$

where, $\Gamma(p, \varepsilon)$ is a local isotherm for sites with energy ε . Several points arise from this simple picture. First, it is now well established that simple pores of different width have different adsorption energies. Due to overlap effects, pores of the same, energetically homogeneous, material will behave as energetically different sites. So that, if no other factors affect adsorption, equation (6) may be mapped onto an identical expression in which ε is replaced by pore size. Secondly, as pointed out above, adsorbate-adsorbate interaction energy should be accounted for in the correct description of adsorption. When heterogeneity is considered, this becomes a particularly difficult problem, since mean-field theories cannot account for the local concentration of adsorbate at low energy sites in the initial stages of adsorption. A third aspect of heterogeneity, which is sometimes referred to as chemical heterogeneity, occurs when relatively isolated foreign species are embedded in the adsorbent. An important example is the presence of ions in zeolite pores. Typically, there may be one, (or possibly two) positive ions in a zeolite cage to compensate for the negative charges that result from substituting Si T-atoms by atoms of lower valency (often aluminium).

An extreme example of heterogeneity, that has considerable practical importance in nanotechnology, is the striped surface where nano-scale patterns of different chemistry are in close proximity. A recent approach [69] to this type of problem is to construct a supersite model that takes account of the realistic structure of a heterogeneous surface that is intermediate between a random distribution of sites and a patchwise surface. The model enables interactions between adsorbate molecules to be included in the theory. Simulations of xenon adsorption on stepped surfaces were used to test the theory. Extensive simulations studies of

both adsorption and wetting have been made on model systems of pores with patterned walls [70,71].

Simulations of adsorption of 12-6 molecules on roughened surfaces inside both cylindrical [29] and slit [72] pores constructed from 12-6 atoms, do not show the steep decline in initial energy or isosteric heats expected for heterogeneous surfaces, despite a decrease in the adsorbate-adsorbent part of the heat with coverage. On the other hand, this characteristic feature was found in similar systems where the adsorbent is modelled as a matrix of solid particles [73]. Similarly, isotherms and heat curves have been calculated using a database of model pores ranging in size from 0.7nm to 2.0nm width, and a distribution of pore sizes [74]. The characteristic signature of rapidly decreasing initial heats appears when the distribution is skewed towards the wide pore sizes. One may deduce from these simulations, that one cause of strongly decreasing initial heats in real materials may be the initial adsorption of molecules in crevices that are very close to molecular size and in relatively low concentration. Spaces between agglomerated particles, as well as micropores and surface defects may be sites for these optimally adsorbed molecules. Crevices of molecular size may, of course occur on highly roughened surfaces, and it is clear that the distinction between severe surface roughening and microporous structure can become blurred.

6 Adsorption in zeolites

Zeolites are mainly, though not exclusively, alumina-silica crystalline materials that are widely used in industry for separations and catalysis. Their well-defined intracrystalline structure makes them attractive subjects for theoretical study. A great variety of zeolite architectures exists [75] with channels and cages in the micropore size range, and a wide range of interconnected pore widths and shapes is possible. Further variety is added when Si T-atoms are substituted by other species. The substitution of one or more Si, typically by Al, leaves negative charges on the silica-alumina framework that are neutralised by extra-framework ions such as Na^+ or Ca^{2+} etc. In many structures, the exact position of these ions is difficult to locate.

When neutral, or weakly polar, molecules are adsorbed, or when cations are absent from the zeolite framework, the attractive part of the adsorbate-adsorbent interaction is dominated by dispersion interactions. These are difficult to evaluate accurately. Direct quantum mechanical calculations require large basis sets, and calculations at least at the MP2 level or higher, since the dispersion is no more than 10^{-5} of the total

energy. Furthermore, a number of positions, and - in the case of non-spherical neutral species - orientations, are needed in order to construct a complete potential energy surface. Physical adsorption phenomena do not generally involve deep interpenetration of electron shells, and a Born-Mayer representation of the repulsive side of the potential in the form:

$$u_{rep} = A \exp(-br)$$

for centres separated by r , is usually adequate. For large hydrocarbon molecules, centres are most often represented by united atoms of CH_2 , CH_3 etc.

Some progress towards the goal of building reliable transferable potential functions has been achieved by combining a perturbation theory approach for dispersion, electrostatic and induced interactions, with Born-Mayer repulsion [76]. Damped dispersion terms up to and including C_{10} were include in the dispersion contribution which is expressed by:

$$u_{disp} = - \sum_{n=3} \frac{f_{2n} C_{2n}}{r^{2n}}$$

and summations were made over O, Si and Al framework atoms. Dispersion contributions from extra framework ions must also be included when these are present. In pure silica forms such as silicalite [77], pure silica chabazite [78] and in $\text{AlPO}_4\text{-5}$, the C_8 and the Si or Al contributions to the potential are by no means unimportant.

For a highly polarisable species, such as Xe, the 3-body terms can also contribute significantly to the interaction potential. Due to the 4th order 3-body term, the 3-body contribution can be attractive overall, rather than repulsive. In Figure 4 the interaction potentials energy of Ar and Xe in the cross section of the straight channel in silicalite are shown, calculated with and without 3-body terms. The 3-body contribution for Ar makes a small repulsive contribution to the overall interaction, but for Xe the total of the 3-body terms deepens the attractive potential well [79]. In many cases however, it is safe to omit 3-body terms, and the computational labour in calculating them is a considerable deterrent, even for contemporary computers.

It has been shown [76,80] that a potential model constructed along the lines outlined above, can be evaluated from a knowledge of polarisabilities, and the effective number of electrons together with A , b Born-Mayer parameters which can be calculated through combining rules [81].

Where adsorbate-adsorbate interactions or electrostatic interactions assume greater importance, it is reasonable to neglect C_8 , C_{10} and 3-body terms in the PN potential. Later work [82] has demonstrated that this modified TrAZ (transferable potential for adsorption in zeolites) strategy can be successful.

A popular simplification is based in the Kiselev model [83] in which only oxygen framework atoms are included in the potential sums, and a simple L-J 12-6 model is used to model the dispersion repulsion terms. In its original form, this type of model does not give particularly good results [77,78]. An example is the adsorption of methane in $\text{AlPO}_4\text{-5}$, where a step in the isotherm is missed in simulations using this model [78]. However, a stepped isotherm can be reproduced in simulations using this simplified model, if suitable adjustment is made to the parameters [84,85]. However, the step is shifted to a higher relative pressure than that predicted by experiment. Fig. 4 illustrates the very different pore space predicted by the PN and Kiselev models where the narrow single minimum well of the PN potential, through a cross section in the straight pore of silicalite, is replaced by a wider double potential well in the Kiselev model. Nevertheless, parameter adjustment for the 12-6 type of potential can give quite close agreement with the PN model [79]. One may conclude, that parameter adjustment in a simple potential model is capable of producing reasonable agreement between simulation and experiment, but not capable of producing transferable potentials.

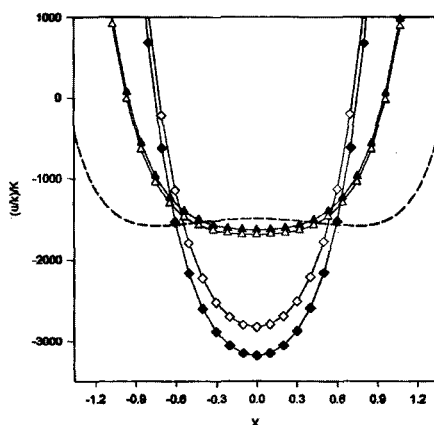


Figure 4. Adsorption energy for argon (triangles) and xenon (squares) at the central cross section of a silicalite straight pore, as a function of position in nanometres. The filled points are the complete potential energy, including 3-body interactions; the empty points are the same potential omitting the 3-body interactions. The broken curve is the potential energy calculated according to the Kiselev model. (From reference [76], with permission).

The zeolites ZSM, mordenite and faujasite, are amongst the most frequently used materials in hydrocarbon processing such as separation and cracking, and many simulations of single and mixture adsorption of hydrocarbon and aromatic adsorptives in these and other zeolites have been reported. A useful tabulation of simulations carried before 2001 is given in reference [3]. Biasing techniques are usually necessary to improve efficiency and to converge the simulations to equilibrium.

For example, orientational bias improves the percentage of acceptance for creation of xylene isomers in FAU zeolites by several orders of magnitude [82], whilst configurational bias is effective for chain molecules, particularly in labyrinthine zeolites such as silicalite, [86,87]. Energy bias has been used in GCMC simulation of methanol and cyclohexane in silicalite [88]. Comparisons between these simulations and experiment, predominantly adsorption isotherms, generally show satisfactory agreement, especially for smaller molecules.

The presence of cations in zeolites can dramatically alter their adsorption behaviour [89,90]. Typically, there are one or two cations per unit cell so that there is a wide spatial separation between their positive charge centres in contrast to ionic crystals where positive and negative centres alternate on an atomic size scale. Zeolites with extra framework cations are thereby highly heterogeneous with respect to molecular adsorbate species carrying permanent multipoles. For example, cationic zeolites are used on an industrial scale for separation of air into O₂ and N₂ components by exploiting the much stronger quadrupole in N₂.

The sensitivity of N₂ adsorption to the number of Ca²⁺ cations in chabazite is illustrated by the simulated isotherms for N₂ adsorption at 77K shown in Figure 5 [91]. The chabazite framework is constructed from eight double 6-rings (D6R units), enclosing an ellipsoidal cavity. Six 8-ring windows access the cavity in three orthogonal directions. The D6R units and 4-ring windows are inaccessible to the nitrogen adsorbate. The negative charges resulting from substitution of 2 or 4 Si by Al at the T-sites can be neutralised by one or by two Ca²⁺ ions respectively. Calcium ions may be sited centrally within the D6R units (N position), on the faces of the D6R unit (A position), or close to the windows (B position). The isotherms shown are for Ca in A positions, the most probable location for Ca in real chabazite. In this location, the nitrogen quadrupole has easy access to the Ca charge. When one Ca is present in each unit cell, a single N₂ molecule adsorbs close to the ion at very low pressure; a second isotherm step, corresponding to the adsorption of two nitrogens close to the ion, occurs at a pressure about 8 orders of magnitude higher. At higher pressures, an ordered cluster of nitrogen molecules gradually builds up

within the cage. With two Ca ions present, two nitrogen molecules are adsorbed at each end of the cage, and the first isotherm step corresponds to two molecules per unit cell. The next step corresponds to the adsorption of two molecules at each Ca ion, and a third diffuse step completes the filling of the cavity to 6 molecules at the saturation pressure. When no Ca ions are present, the nitrogen initially adsorbs at the centre of the cavity, in such a way as to maximise the dispersion interactions with the oxygen ions in the D6R ring. There are two equivalent sites, as shown by the constant adsorbate-adsorbent contribution to the heat of adsorption below two molecules per unit cell. In the pure silica form, adsorption does not begin until a pressure that is almost 20 orders of magnitude higher than in the Ca forms and only four nitrogen molecules are adsorbed at saturation vapour pressure instead of six in the Ca forms. Placement of Ca in the B sites results in modifications to the isotherms [89,90,91], but the adsorption is similar to that in the A forms. On the other hand, when the Ca^{2+} ion is buried in a D6R ring, isotherms very similar to the pure silica isotherm results, since the distance between the Ca charge and the quadrupole is then too great for the electrostatic and induced interactions to make any substantial contribution to the potential energy. In practice of course, pressures as low as 10^{-24} bar are not measurable, even with the highest resolution adsorption equipment, and nearly all the detail shown in these simulated isotherms would be obscured in a single initial step when conventional nitrogen adsorption at 77K is measured experimentally. Similar arguments apply in general for any adsorbents with very tight pores or strong sites for nitrogen, and raise the question of whether this technique is suitable for characterisation of such materials.

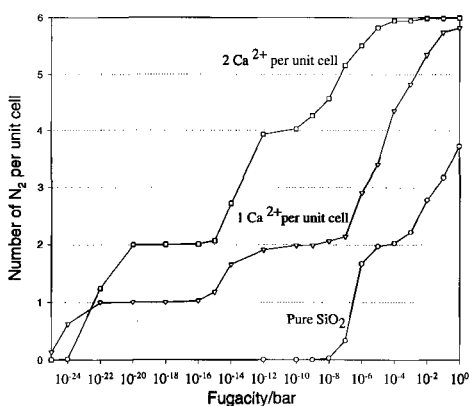


Figure 5. Simulated isotherms for nitrogen adsorbed at 77K in chabazite with extra framework calcium in the A site (see text) and for the pure silica form.

Conclusions

Simulation has proved to be a powerful tool in elucidating and clarifying the molecular mechanisms involved in the adsorption process. Porous materials are an especially suitable subject for investigation by simulation since conventional thermodynamic theories often breakdown when applied to adsorption in highly confined spaces.

A wide variety of simulation techniques is now available, although the now conventional GCMC method is suitable for the majority of investigations, supplemented by biasing techniques when larger molecules or complicated spaces are involved. Once the methodology and pore model have been decided, the sole input to a simulation is the choice of potential energy model. Precise representation of experimental adsorption isotherms for well-defined materials by simulation is still difficult to achieve in many cases, although good semi-quantitative modelling is generally achievable. Apart from improvements in potential energy modelling, other aspects of real porous media still need to be addressed. Prominent amongst these is the complexity and inherent heterogeneity of the majority of real materials, and the question of whether rigid adsorbent models are always adequate. Much of the progress made over the last three decades has resulted from the rapid increase in computing power, and one may be optimistic that research in this field will exploit future improvements to good advantage.

References

1. Barton T. J., Bull L. M., Klemperer W. G., Loy D. A., McEnaney B., Misono M., Monson P. A., Pez G., Scherer G. W., Vartuli J. C. and Yaghi O., Tailored porous materials, *Chem. of Materials* **11** (1999) pp. 2633-2656 .
2. Demontis P. and Suffriti B., Structure and dynamics of zeolites investigated by Molecular Dynamics, *Chem. Rev.* **97** (1997) pp. 2845-2878.
3. Fuchs A. H. and Cheetham A. K., Adsorption of guest molecules in zeolitic materials: Computational aspects, *J. Phys Chem. B* **105** (2001) pp. 7375-7383.
4. Allen M. and Tildesley D.J., *Molecular Simulation of Liquids*, Oxford, 1986.
5. Frenkel D. and Smit B., *Understanding Molecular Simulation*, A.P., 1992.
6. Snurr, R. Q., Bell, A. T. and Theodorou, D. N., Prediction of adsorption of aromatic hydrocarbons in silicalite from grand canonical Monte Carlo simulations with biased insertions, *J. Phys. Chem.* **97** (1993) pp. 13742-13752.
7. Cracknell R. F., Nicholson D., Parsonage N. G. and Evans H., Rotational insertion bias: a novel method for simulating dense phases of structured particles, with particular reference to water, *Mol. Phys.* **71** (1990) pp. 931-943.

8. Vlugt J. H., Krishna R. and Smit B., Molecular simulations of adsorption isotherms for linear and branched alkanes and their mixtures in silicalite, *J. Phys Chem. B* **103** (1999) pp. 1102-1118.
9. van Tassel P. R., Davis H. T. and McCormick A. V., Adsorption simulations of small molecules and their mixtures in a zeolite micropore, *Langmuir* **10** (1994) pp. 1257-1267.
10. Heffelfinger G. S. and van Swol F., Diffusion in Lennard-Jones fluids using dual control volume grand canonical dynamics simulation DCV-GCMD, *J. Chem. Phys.* **100** (1994) pp. 7548-7552.
11. Macelroy J. M. D., Nonequilibrium molecular dynamics simulation of diffusion and flow in a thin microporous membrane, *J. Chem. Phys.* **101** (1994) pp. 5274-5280.
12. Cracknell R. F., Nicholson D. and Quirke N., Direct molecular simulation of flow down a chemical potential gradient in a slit shaped pore, *Phys. Rev. Lett.* **74** (1995) pp. 2463-2466.
13. Vuong T. and Monson P. A., Monte Carlo simulation studies of heats of adsorption in heterogeneous solids, *Langmuir* **14** (1996) pp. 1-35.
14. Vuong T. and Monson P. A., Surface roughness effects in molecular models of adsorption in heterogeneous porous solids, *Langmuir* **16** (1998) pp. 4880-4886.
15. Keirlik E., Rosinberg M. L., Tarjus G. and Monson, P. A., The pressure of a fluid confined in a disordered porous material, *J. Chem. Phys.* **103** (1995) pp. 4256-4260.
16. Vega C., Kaminsky R. D. and Monson P. A., Adsorption of fluids in disordered porous media from integral equation theory, *J. Chem. Phys.* **99** (1993) pp. 3003-3013.
17. Cracknell R. F. and Nicholson D., Adsorption of gas mixtures on solid surfaces, theory and computer simulation, *Adsorption* **1** (1995) pp. 7-16.
18. Myers A. L., Calles J. A. and Calleja G., Comparison of molecular simulation of adsorption with experiment, *Adsorption* **3** (1997) pp. 107-115.
19. Myers A. L. and Monson P. A., Adsorption in porous materials at high pressure: Theory and experiment., *Langmuir* in press (2002).
20. Nicholson D. and Stubos A. K., Simulation of adsorption in micropores, *Recent advances in gas separation by porous media*, ed N. Kanellopoulos, Elsevier, Amsterdam (2000) pp. 231-256.
21. Magda J. J., Tirrell M. and Davis H. T., Molecular dynamics of narrow, liquid filled pores, *J. Chem. Phys.* **83** (1985) pp. 1888-1901.
22. Neimark A. V. and Ravikovitch P. I., Calibration of pore volume in adsorption experiments and theoretical models, *Langmuir* **13** (1997) pp. 5148-5160.
23. Nicholson D., and Parsonage N. G., Computer simulation and the statistical mechanics of adsorption, Academic Press, 1982.
24. Dunne J. A., Rao M., Sircar S., Gorte R. J. and Myers A. L., Calorimetric heats of adsorption and adsorption isotherms. 3. Mixtures of CH₄ and C₆H₆ in silicalite and mixtures of CO₂ and C₂H₆ in NaX, *Langmuir* **13** (1997) pp. 4333-4341.
25. Douget D., Pellenq R. J.-M., Boutin A., Fuchs A. H. and Nicholson D., The adsorption of argon and nitrogen in silicalite-1 zeolite: A grand canonical Monte Carlo study, *Molecular Simulation* **17** (1996) pp. 255-288.
26. Rouquerol F., Rouquerol J. and Sing K. S. W., Adsorption by powders and porous solids : principles, methodology and applications, Academic Press, San Diego, (1999).

27. Sweatman M. B. and Quirke N., Characterisation of porous materials by gas adsorption at ambient temperatures and high pressure, *J. Phys Chem. B* (2002) pp. 1403-1411.
28. Scaife S. and Quirke N., Characterisation of porous materials by gas adsorption: Do molecular probes give different pore structures? *J. Phys Chem. B* **104** (2000) pp. 313-318.
29. Steele W. A. and Bojan M. J., Simulation studies of sorption in model cylindrical pores, *Adv. in Colloid & Interface Sciences* (1998) pp. 153-178.
30. Brennan J. K., Thomson K. T. and Gubbins K. E., Adsorption of water in activated carbons: Effect of pore blocking and connectivity., *Langmuir* **18** (2002) pp. 5438-5447.
31. Keffer D., Davis H. T. and McCormick A. V., The effect of nanopore shape on the structure and isotherms of adsorbed fluids, *Adsorption* **2** (1996) pp. 9-22.
32. Davies G. M. and Seaton N. A., The effect of choice of pore model on the characterization of the internal structure of microporous carbons using pore size distributions, *Carbon* **36** (1998) pp. 1473-1490.
33. Olivier J. P., Improving the models used for calculating the size distribution of micropore volume of activated carbons from adsorption data, *Carbon* **36** (1998) pp. 1469-1472.
34. Samios S., Stubos A. K., Kanellopoulos N. K., Cracknell R. F., Papadopoulos G. K. and Nicholson D., Determination of micropore size distribution from grand canonical Monte Carlo simulations and experimental CO₂ isotherm data, *Langmuir* **13** (1997) pp. 2795-2802.
35. Suzuki T., Kaneko K. and Gubbins K. E., Pore width sensitive filling mechanism for CCl₄ in a graphitic micropore by computer simulation, *Langmuir* **13** (1997) pp. 2545-2549.
36. Nicholson D. and Quirke N., The role of enthalpy of adsorption in micropore characterisation: A simulation study, *Studies in Surf Sci. and Catalysis* **128** (2000) pp. 11-20.
37. Nicholson D., A simulation study of pore size dependence of transport selectivity in cylindrical pores, *Mol. Phys.* **100** (2002) pp. 2151-2163.
38. Lastoskie C., Gubbins K. E. and Quirke N., Pore size distribution analysis and networking: Studies of microporous sorbents, *Studies in Surf Sci. and Catalysis* **87** (1994) pp. 51-60.
39. Nicholson D., Freeman N. A. and Day M. A., A simulation study of nitrogen adsorption in magnesium oxide pores, *Characterisation of Porous Materials: Royal Society of Chemistry, Special Publication Number 213* (1998) pp. 549-557.
40. Nicholson D., Using computer simulation to study the properties of molecules in micropores, *J. Chem. Soc. Faraday Trans.* **92** (1996) pp. 1-9.
41. Nicholson D. and Cracknell R. F., Molecular selectivity in slit shaped pores, *Fundamentals of Adsorption V* (1996), ed D. Le Van, Kluwer, pp. 675-682.
42. Nguyen T.X., Bhatia S. K., and Nicholson D., Close packed transitions in slit-shaped pores: a density functional theory study of methane adsorption capacity in Carbon, *J. Chem. Phys.* In press (2002).
43. Nishikawa K., Murata Y., *Bull Chem Soc Japan* **2** (1979) pp. 293-300.
44. Iiyama T., Suzuki T. and Kaneko K., *Chem. Phys Lett.* **259** (1996) pp. 37-48.
45. Gelb L. D., Gubbins K. E., Radhakrishnan R. and Sliwinski-Bartowiak M., Phase separation in confined systems, *Rep. Prog. Phys.* **62** (1999) pp. 1573-1659.

46. Hill T.L., *J. Chem. Phys.* **15** (1947) 767-774.
47. Cohan L.H., *JACS* **60** (1938) 433.
48. Broekhoff J.C.P. and de Boer J. H., Studies on pore systems in catalysis ix. Calculation of pore distribution from the adsorption branch of nitrogen sorption isotherm in the case of open cylindrical pores: a fundamental equation, *J. Catalysis* **9** (1967) pp. 8-14.
49. Saam W. F. and Cole M. W., Excitations and thermodynamics for liquid helium films, *Phys Rev. B* **11** (1975) pp. 1086-1105 .
50. Bhatia S. K. and Sonwane C. G., Capillary coexistence and criticality in mesopores: modification of the Kelvin theory, *Langmuir* **14** (1998) pp. 1521-1524 .
51. Sonwane C. G. and Bhatia S. K., Adsorption in mesopores: A molecular-continuum model with application to MCM-41, *Chem. Eng. Sci.* **53** (1998) pp. 3143-3156 .
52. Sing K. S. W., Everett D. H., Haul R., Moscou L., Pierrotti R. A., Rouquerol J. and Siemieniowska T., Reporting physisorption data for gas/solid systems, *Pure and Appl. Chem* **57** (1985) pp. 603-625 .
53. Schoen M., Rhykerd C. L., Cushman J. H. and Diestler D. J., Slit-pore sorption isotherms by the grand-canonical Monte Carlo method: Manifestations of hysteresis, *Mol. Phys.* **66** (1989) pp. 1171-1182 .
54. Neimark A. V. and Vishnyakov A. M., Gauge cell method for simulation of phase transitions in confined spaces, *Phys Rev. E.* **62** (2000) pp. 4611-4622.
55. Vishnyakov A. M. and Neimark A. V., Studies of liquid-vapour equilibria, criticality and spinodal transitions in nanopores by the gauge cell Monte Carlo simulation method, *J. Phys. Chem. B* **105** (2002) pp. 7009-7020 .
56. Shi W., Zhao X. and Johnson J. K., Phase transitions of adsorbed fluids computed from multiple histogram reweighting, *Mol. Phys.* **100** (2002) pp. 2139-2150.
57. Mayagoitia V., Rojas F., Kornhauser I. and Perez-Aguilar H., Modeling of porous media and surface structures: Their true essence as networks, *Langmuir* **13** (1997) pp. 1327-1331 .
58. Kornhauser I., Cordero S., Felipe F. and Rojas F., On comparing pore characterisation results from sorption and intrusion processes, *Fundamentals of adsorption 7* (2002) eds. K. Kaneko, H. Kanoh and Y. Hanzawa, (IK International, Chiba) pp. 1030-1037.
59. Macelroy J. M. D. and Raghavan K., Transport of an adsorbing vapour in a model silica system, *J. Chem. Soc. Faraday Trans.* **87** (1991) pp. 1971-1987.
60. Raghavan K. and Macelroy J. M. D., Molecular dynamics simulations of adsorbed alkanes in silica micropores at low-to moderate loadings, *Molecular Simulation* **15** (1995) pp. 1-33.
61. Sarkisov L. and Monson P. A., Capillary condensation and hysteresis in disordered porous materials, *Studies in Surf Sci. and Catalysis* **128** (2000) pp. 21-29.
62. Sarkisov L. and Monson P. A., Hysteresis in Monte Carlo and molecular dynamics simulations of adsorption in porous materials, *Langmuir* **16** (2000) pp. 9857-9860.
63. Gelb L. D. and Gubbins K. E., Characterisation of porous glasses: Simulation models, adsorption isotherms, and the BET analysis method, *Langmuir* **14** (1998) pp. 2097-2111.
64. Gelb L. D. and Gubbins K. E., Molecular simulation of capillary phenomena in controlled pore glasses, *Fundamentals of adsorption 7* (2002) eds. K. Kaneko, H. Kanoh and Y. Hanzawa, (IK International, Chiba) pp. 333-340.

65. Pikunic J., Pellenq R. J.-M., Thomson K. T., Rouzaud J.-N., Levitz P. and Gubbins K. E., Improved molecular models for porous carbons, *Studies in Surf. Sci. and Catalysis* **132** (2001) pp. 647-652.
66. Thomson K. T. and Gubbins K. E., Modeling structural morphology of micro-porous carbons by reverse Monte-Carlo, *Langmuir* **16** (2000) pp. 5761-5774.
67. Maddox, M. W., Quirke, N. and Gubbins K. E., A molecular simulation study of pore networking effects, *Molecular Simulation* **19** (1997) pp. 267-283.
68. Sarkisov L. and Monson P. A., Modelling of adsorption and desorption in pores of simple geometry using molecular dynamics, *Langmuir* **17** (2001) pp. 7600-7604.
69. Steele, W. A. The supersite approach to adsorption on heterogeneous surfaces, *Langmuir* **15** (1999) pp. 6083-6090.
70. Schoen M. and Diestler D. J., Ultrathin fluid films confined to a chemically heterogeneous slit-shaped nanopore, *Phys Rev. E* **56** (1997) pp. 4427-4440.
71. Schneemilch M. and Quirke N., Wetting of nanopatterned surfaces: The striped surface, *J. Chem. Phys.* In press 2002.
72. Nicholson D., A simulation study of energetic and structural heterogeneity in slit shaped pores, *Langmuir* (1999) pp. 2508-2515.
73. Vuong T. and Monson P. A., Monte Carlo Simulation Studies of Heats of Adsorption in Heterogeneous Solids, *Langmuir* **14** (1996) pp. 1-35.
74. Nicholson D. and Quirke N., The role of enthalpy of adsorption in micropore characterisation: A simulation study, *Studies in Surf. Sci. and Catalysis* **128** (2000) pp. 11-20.
75. Meier W. M. and Olson D., Atlas of zeolites, *Zeolites* **12** (1992) pp. 453.
76. Nicholson D. and Pellenq R. J.-M., Adsorption in zeolites: intermolecular interactions and computer simulation, *Adv. in Colloid & Interface Sciences* **76-77** (1998) pp. 179-202.
77. Pellenq R. J.-M. and Nicholson D., Grand ensemble Monte Carlo simulation of simple molecules adsorbed in silicalite-1 zeolite, *Langmuir* **11** (1995) pp. 1626-1635.
78. Boutin A., Pellenq R. J.-M. and Nicholson D., Molecular simulation of the stepped adsorption isotherm of methane in AlPO₄-5, *Chem. Phys. Letts.* **219** (1994) pp. 484-490.
79. Nicholson D., Boutin A. and Pellenq R. J.-M., Intermolecular potential functions for adsorption in zeolites: State of the art and effective potentials, *Molecular Simulation* **17** (1996) pp. 217-238.
80. Pellenq R. J.-M. and Nicholson D., A simple method to calculate dispersion coefficients for isolated and in-condensed-phase species, *Mol. Phys.* **95** (1998) pp. 549-570.
81. Bohm H. J. and Ahlrichs R., A study of short range repulsions, *J. Chem. Phys.* **77** (1982) pp. 2028-2034.
82. Lachet V., Boutin A., Tavitiyan B. and Fuchs A. H., Computational study of p-Xylene/m-Xylene mixtures adsorbed in NaY zeolite, *J. Phys Chem. B* **102** (1998) pp. 9224-9233.
83. Kiselev A. K., Lopatkin A. A. and Shulga A. A., Molecular statistical calculation of gas adsorption in silicalite, *Zeolites* **5** (1985) pp. 261.

84. Maris T., Vlugt J. H. and Smit B., Simulation of alkane adsorption in the aluminophosphate molecular sieve AlPO₄-5, *J. Phys. Chem.* **102** (1998) pp. 7183-7189.
85. Boutin A., Buttefey S., Cheetham A. K. and Fuchs A. H., *Mol. Simul.*, in press (2002)
86. Smit B. and Siepmann J. I., Simulating the adsorption of alkanes in zeolites, *Science* **264** (1994) pp. 1118-1120.
87. Smit B. and Siepmann J. I., Computer simulations of the energetics and siting of n-alkanes in zeolites, *J. Phys. Chem.* **98** (1994) pp. 8442-8452.
88. Gupta A. R., Clark L. A. and Snurr R. Q., Grand canonical Monte Carlo simulations of non-rigid molecules; siting and segregation in silicalite zeolite, *Langmuir* **16** (2000) pp. 3910-3919.
89. Grey T. J., Gale J. G. and Nicholson D., Simulation studies of Nitrogen in zeolites: Comparison of ionic and pure silica forms, *Fundamentals of adsorption 7*, Eds. K. Kaneko, H. Kanoh, Y. Hanzawa, IK International (2002) pp. 360-367.
90. Grey T., Nicholson D., Gale J. D. and Peterson B. K., A simulation study of the adsorption of nitrogen in Ca-chabazite, *Appl. Surf. Sci.* (2002).
91. Grey T., Travis K. P., Gale J. D. and Nicholson D., A Comparative Simulation Study of the Adsorption of nitrogen and Methane in siliceous heulandite and chabazite, *Micropor. and Mesopor. Mater.* **31** (2001) pp. 45-59.

SURFACE FUNCTIONALIZATION OF ORDERED NANOPOROUS SILICATES

X. S. ZHAO AND A. S. MARIA CHONG

Department of Chemical and Environmental Engineering, National University of Singapore, 10 Kent Ridge Crescent, Singapore 119260

E-mail: chezxs@nus.edu.sg

G. Q. (MAX) LU

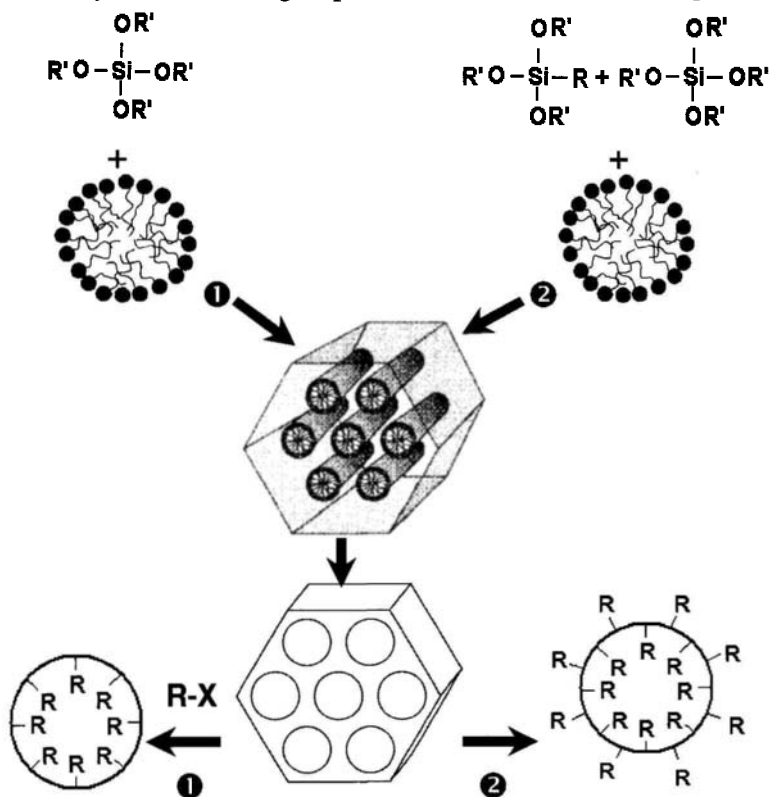
Department of Chemical Engineering, The University of Queensland, St Lucia, Brisbane, Qld 4072, Australia

E-mail: m.lu@uq.edu.au

The combination of organic and inorganic properties at the nanosize level in a composite material is an emerging area of materials science that has unprecedented implications in the development of functional materials for advanced technologies. In the past few years, surface functionalization of ordered nanoporous silicates designed M41S, FSM-16, HMS/MSU, and SBA, etc. prepared with the assistance of surfactant micelles has received rapidly growing interest and potential applications of the functionalized materials have been envisaged in many fields, including catalysis, adsorption, optics, electronics, sensors, nanotechnology, biology, and many others. In general, there are two approaches to the functionalization, namely grafting (also known as post-modification) and co-condensation or direct synthesis. The first approach enables one to obtain a variety of surface functional groups with limited density and non-uniform distribution of the functionalities (at least in some cases) while the original nanostructures can be substantially maintained. The second approach affords an inorganic-organic composite with relatively uniformly distributed organic species both on the surface and throughout the pore walls at the expense of loss in long-range structure ordering because of the disruption of the functionalities to local structures (particularly when relatively a large amount of functional groups is desired). With the availability of periodic mesoporous organosilicas, in which organic functionalities are built in the pore walls of the materials, prepared by employing organic-bridged silsesquioxanes as a precursor, surface functionalization is becoming more and more sophisticated, allowing control over the type and position of the functional groups at a molecular level. This chapter provides a brief overview of the grafting and direct synthesis methods. With an introduction to the surface chemistry of ordered nanoporous silicates, we first discuss surface grafting of various functionalities such as organosilanes, metal-organic complexes, and catalytically active species, etc. with an emphasis on silylation. Then, we present our recent experimental data on functionalization of nanoporous SBA-15 materials by the co-condensation method. Finally, we offer a concluding remark to highlight research opportunities and perspectives in this field. We hope this chapter could shed light on technological aspects of functionalization of ordered nanoporous silicates.

1 Introduction

Since the discoveries of ordered nanoporous silicates (ONSs) of types M41S [1,2], FSM-16 [3], HMS [4], MSU [5], and SBA [6], synthesized in the presence of ionic, neutral, and nonionic surfactants, respectively, surface functionalization has played a vital role in various technological aspects such as improvement of thermal/hydrothermal stability, development of new catalyst and adsorbent, nanotechnology, and novel materials for advanced applications [7-11]. In general, there are two approaches to surface functionalization of ONSs as illustrated in Scheme 1, namely grafting also known as post-synthesis and co-condensation or direct synthesis. With the availability of periodic nanoporous organosilicas (PNOs) prepared by using organic-bridged silsesquioxanes as the Si precursor [12-14], surface functionalization of ONSs is becoming more and more sophisticated, allowing one to control over the type, location, and density of functional groups at a molecular level [15-18].



Scheme 1. Grafting and co-condensation approaches to surface functionalization.

The grafting method refers to post-modification of a pre-synthesized ONS material by attachment of a functional moiety via terminal hydroxyl groups or silanol groups (Si-OH) [19-21]. In this way, the silanol groups are replaced by the functional groups, which are pendent on the pore surface whereas the pore structure is maintained at the expense of a decreased pore diameter and pore volume. The grafting method affords an organic-inorganic composite with desirable functionalities of almost any kinds but with a limited density of the functionalities due to the limited number of surface accessible silanols [21], as well as heterogeneity of the functionalities [9]. On the other hand, direct synthesis is a one-pot method consisting of co-condensation of a tetraalkoxysilane such as tetraethylorthosilicate (TEOS) with an organosiloxane such as 3-aminopropyltriethoxysilane (APTES) via a sol-gel process by controlling hydrolysis and condensation rates in the presence of a template under either basic, neutral or acidic conditions. This method offers a better control over the density and uniformity of the organic functional groups but suffers the loss in long-range structure ordering (in particular when the organosiloxane is present in initial synthesis mixture in a relatively large amount) because the functionalities are present both on the pore surfaces and inside the pore walls, leading to a disrupted local structure of the silicate framework.

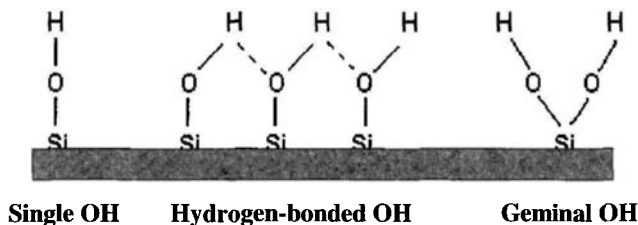
Functionalized ONS materials possess novel properties that cannot be observed on pure-silicate counterparts, enabling them to be novel catalysts, adsorbents, and advanced materials. Through the development of functionalized ONS materials, a great deal of research breakthroughs has been made in the past few years towards applications. For examples, by introducing organic functionalities on the surface and/or inside the pore walls, surface hydrophobicity can be dramatically enhanced, leading to a more hydrothermally stable material for catalytic and adsorptive applications in an aqueous medium. The use of functionalized ONS as a carrier for immobilization of catalytic species such as enzymes and Lewis acids for reducing process cost and minimizing environmental pollution has been demonstrated to be very promising. Thiol-functionalized ONS materials have been shown to be a superior selective adsorbent for removal of mercury present in wastewater.

In this chapter, we discuss surface functionalization of ONSs through grafting and direct synthesis. With an elaboration of the surface nature of ONSs, surface functionalization via grafting is described with an emphasis on silylation, followed by the direct synthesis method for functionalization of SBA-15 materials. Finally, concluding remarks are given.

2 Functionalization of ONSs by grafting

2.1 Surface chemistry of ONSs

As the pore walls of ONSs are amorphous [22], it is not unexpected that their surface properties are very similar to that of amorphous silicas [23,24]. A comprehensive study by Zhao et al. [21] has demonstrated that there are three types of surface silanol groups on the surface of ONSs. They are free, geminal, and hydrogen-bonded hydroxyl groups as illustrated in Scheme 2, whereas only free and geminal silanol groups are reactive towards a functional reagent. The types and number are dependent on the way of how template is removed and post-treatments [21,25].



Scheme 2. Schematic representation of SiOH groups on pure-silica MCM-41 surface.

A number of spectroscopic techniques have been employed to investigate the surface chemistry of ONSs [21]. The FTIR spectra of a pure-silica MCM-41 sample depicted in Fig. 1 reveal the evolution of IR intensity against temperatures in vacuum. The two main absorption bands at about 3738 and 3222 cm^{-1} observed at room temperature are due to free and hydrogen-bonded silanol groups perturbed by physically adsorbed water, respectively. With increasing degassing temperatures, the intensity of the absorption band at 3738 cm^{-1} increased while the intensity of the

broad absorption band decreased accompanied by a gradual shift to the high wave-number region. These observations are explained in terms of the different behaviors of free and hydrogen bonded silanol groups: increase in the degassing temperatures resulted in dehydration of the hydrogen-bonded SiOH groups, leading to a gradual decrease in intensity of the peak at 3222 cm^{-1} , and simultaneously the formation of more free silanol groups, thus the intensity of the peak at 3738 cm^{-1} was increased. The IR data indicate that there are at least two types of surface silanol groups, i.e. free and hydrogen-bonded ones. The later can be partially converted to the former simply by heat treatments. However, IR provides no information on the density of the silanol groups. By employing other techniques, the silanols can be quantified.

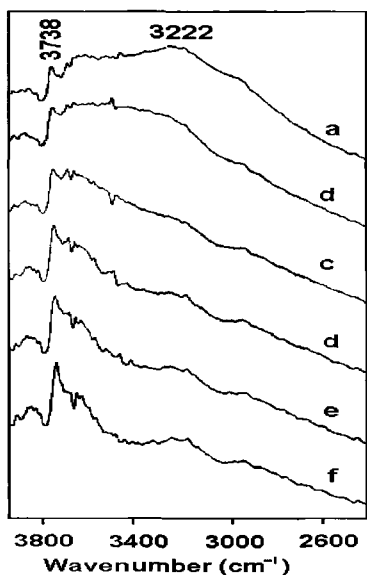


Figure 1. FTIR spectra of pure-silica MCM-41 degassed at (a) 298, (b) 373, (c) 473, (d) 573, (e) 673 and (f) 773 K, respectively.

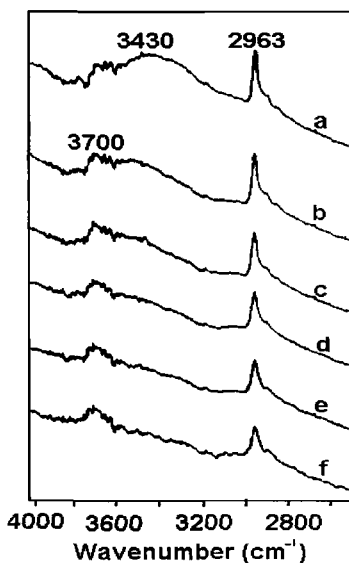


Figure 2. FTIR spectra of surface-silylated MCM-41 silica measured at (a) 298, (b) 373, (c) 472, (d) 573, (e) 673 and (f) 773 K, respectively.

Upon silylation, the FTIR spectra shown in Fig. 2 are significantly different to that in Fig. 1. The absorption band at 3738 cm^{-1} is no longer seen. The broad absorption band at 3222 cm^{-1} observed on the pure-silica MCM-41 sample now is seen at about 3430 cm^{-1} . Such a left-hand shift of hydrogen-bonded silanol groups is understood because of the total removal of the physically adsorbed during the pre-treatment before silylation. The silanol groups are still substantially hydrogen-bonded at room temperature because of the appearance of the peak at 3430 cm^{-1} . Two new absorption bands at 2963 and 3700 cm^{-1} , respectively, can be seen. The band at 2963 cm^{-1} is ascribed to attached trimethylsilyl (TMS) groups while the band at 3700 cm^{-1} can be attributed to single SiOH groups derived from geminal SiOH groups because of silylation, i.e. $\text{=Si(OH)}_2 + \text{TMCS} \rightarrow (\text{CH}_3)_3\text{SiO-Si-OH}$. These results demonstrate that free SiOH groups are highly accessible to the silylating agent, TMCS, while hydrogen-bonded SiOH groups are not inactive in this reaction. In addition, one OH groups in geminal silanols can also react with TMCS.

Temperature-programmed desorption (TPD) of pyridine can be used to detect the weak acidic silanol groups. Fig. 3 shows representative pyridine-TPD curves collected at different heating rates. These curves are expressed as DrTGA against temperature. Two desorption peaks in the temperature range of $323\text{--}523\text{ K}$ can be seen, which are ascribed to pyridine desorption from two energetically different adsorption sites, respectively. Considering the similarities of pure-silica MCM-41 surface to amorphous silica and the literature data of pyridine desorption from the amorphous silica [26], the first peak at about $323\text{--}373\text{ K}$ corresponds to the desorption of pyridine from hydrogen-bonded silanols, whilst the second peak, at about $393\text{--}443\text{ K}$, is associated with the desorption of pyridine from free SiOH groups.

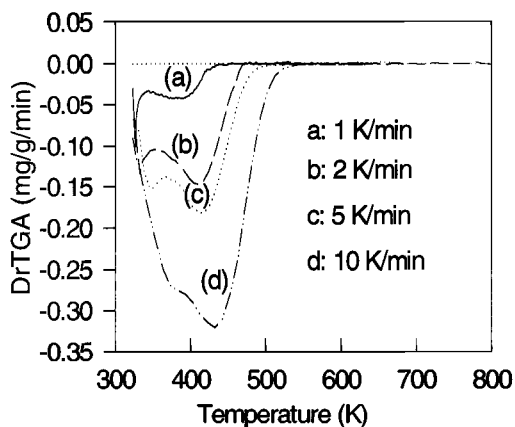


Figure 3. Pyridine-TPD profiles of pure-silica MCM-41 at different heating rates.

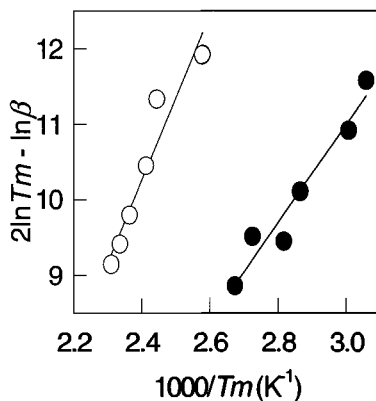


Figure 4. Plots of $\ln(T_m^2/\beta)$ as a function of $1/T_m$.

An energetic analysis using equation (1) proposed by Cvetanovic and Amenomiya [27] allows calculation of the activation energies of the two adsorption sites.

$$2\ln T_m - \ln \beta = \frac{E_d}{RT_m} + \ln \frac{E_d}{AR} \quad (1)$$

where T_m is the temperature (K) at which the maximum desorption rate for a given adsorption site is found, β is the heating rate (K/min) during desorption, E_d is the activation energy of the desorption sites, R is the gas constant, and A is a pre-exponential factor. The plots of $(2\ln T_m - \ln \beta)$ as a function of $1/T_m$ for the two different desorption sites are shown in Fig. 4. Two types of silanol sites are distinguished by their different activation energies of desorption, calculated to be 54.2 and 91.4 kJ/mol for hydrogen-bonded and free SiOH groups, respectively.

Solid-state nuclear magnetic resonance (NMR) at magic angle spinning (MAS) has been widely used for determination of silanol groups on silica gel surface [28,29]. It has also been used to study MCM-41 silica surface [21]. Fig. 5 shows the ^{29}Si CP/MAS NMR spectra of various MCM-41 samples treated using different methods and of an amorphous silica sample. For the samples without silylation, three peaks can be observed. According to Sindorf and Maciel [28], the lowest intensity peak observed at -92 ppm corresponds to surface silicon atoms with two siloxane bonds and two silanol groups, namely geminal silanol sites, $(\text{SiO})_2\text{Si}(\text{OH})_2$,

often denoted as Q^2 . The resonance at -101 ppm is attributed to surface silicon atoms with three siloxane bonds and one silanol group, i.e. isolated silanol sites, $(SiO)_3*SiOH$, designed as Q^3 . The resonance at -110 ppm is ascribed to surface silicon atoms with four siloxane bonds, i.e. $(SiO)_4*Si$, designed Q^4 . For the two silylated MCM-41 samples, a strong resonance peak at about 14 ppm, assigned to the Si atoms of the attached $*Si(CH_3)_3$ moiety, is seen. Because of the consumptions of free and geminal silanol groups, the intensities for the Q^2 and Q^3 silicon resonances were significantly decreased while the intensity of the Q^4 silicon resonance was substantially increased. The intensity redistribution of the different Si sites is due to the reactions of surface SiOH groups with chlorotrimethylsilane.

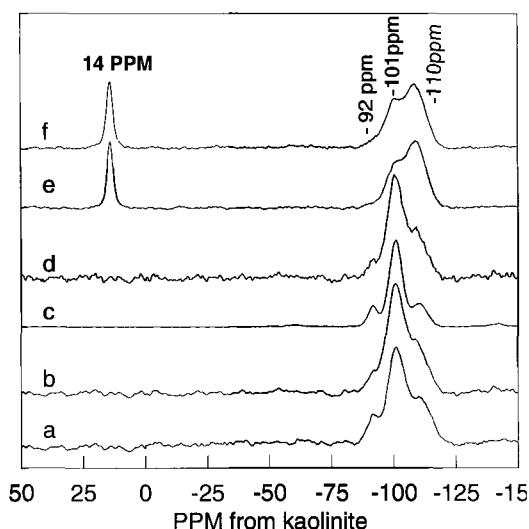


Figure 5. ^{29}Si CP/MAS NMR spectra (a) amorphous silica; (b) as-synthesized pure-silica MCM-41; (c) templated-extracted MCM-41; (d) calcined MCM-41-C; (e) sample *c* after being silylated with TRMS; and (f) sample *d* after being silylated with TMCS.

The resolution of the ^{29}Si CP/MAS NMR spectra obtained is sufficiently high for accurate curve fittings to provide the relative peak intensities of the different Si sites except for the Q^4 sites because of the long distance between Si atoms deeper in pore walls and the surface H atoms. The peak assignments and the relative peak areas after curve fitting with a series of Gaussian peaks are listed in Table 1.

Table 1. Relative peak area (%) of different Si sites*

Sample	Q ² Si sites	Q ³ Si sites	Q ⁴ Si sites	TMS Si sites
Amorphous silica	14.7	59.2	26.1	
As-synthesized MCM-41	5.2	68.9	26.0	
Calcined MCM-41	4.8	64.3	30.9	
Calcined MCM-41 after silylation with TMCS	3.3 (2.6)	38.3 (35.3)	57.9 (47.3)	(14.8)
Solvent-extracted MCM-41	11.0	71.8	17.2	
Solvent-extracted MCM-41 after silylation with TMCS	3.1 (2.0)	29.6 (36.8)	67.3 (47.5)	(13.7)

*Areas in parenthesis are the sum of the four peaks used for quantitative calculations.

From these relative peak areas, one can calculate the number of surface SiOH groups per nm², α_{OH} , using equation (2),

$$\alpha_{OH} = \frac{S \times (1 + f + f_g^r)}{f} \quad (2)$$

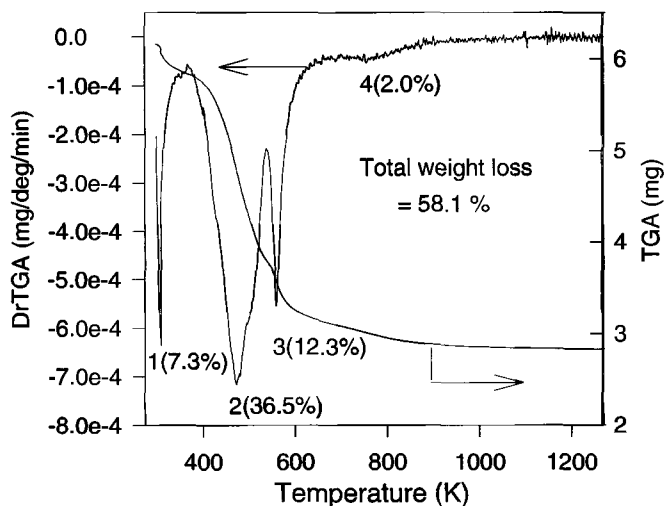
where $f = I_s^r / (I_g^r + I_l^r)$, $f_g^r = I_g^r / (I_g^r + I_l^r)$. I_s^r , I_g^r , and I_l^r denote the ²⁹Si peak areas at 14 ppm (attached trimethylsilyl silicon atoms), - 92 ppm (unreacted geminal silicon sites), and - 101 ppm (unreacted single SiOH sites), respectively; f is the ratio of attached silane silicons to the remaining silanol silicons in modified sample; f_g^r is the fraction of residual geminal silanols in the modified sample; S is the concentration of attached TMS groups, i.e. the number of chemically bonded TRMS groups per nm² of MCM-41 surface which can be obtained by the following equation (3):

$$S = \frac{\Delta W\% \times N_A}{EMW \times S_{BET}} \times 10^{-20} \text{ (number/nm}^2\text{)} \quad (3)$$

where $\Delta W\%$ represents the weight gain after silylation (%), N_A is Avogadro's number, EMW is the effective molar weight of the attached TRMS groups (72 g/mol), and S_{BET} is the BET surface area (m²/g). The calculated results are given in Table 2.

Table 2. Parameters for α_{OH} for two pure-silica MCM-41 samples.

Template removal method	S_{BET} (m^2/g)	f_g^r	f	S	$W\%$	α_{OH} ($/nm^2$)
Calcination	1180	0.069	0.390	0.668	9.42	2.5
Solvent extraction	1153	0.052	0.353	0.754	10.39	3.0

**Figure 6.** TGA and DrTGA curves of as-synthesized pure-silica MCM-41.

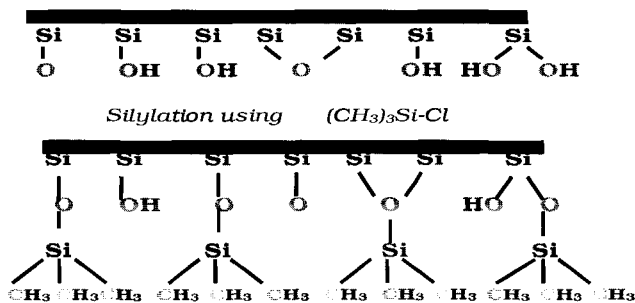
Thermal gravimetric analysis (TGA) provides some voluble information of surface silanol groups [21]. Fig. 6 shows the weight loss curves of an as-synthesized pure-silica MCM-41 sample. Four maxima in the rate of weight loss (peak 1, 2, 3, and 4) can be observed. Peak 1, centered at 323 K, is associated with physically adsorbed water, constituting about 7.3% weight loss; peak 2, at about 473 K, related to the decomposition of the template, i.e. the Hoffman elimination reaction, $C_{16}H_{33}(CH_3)_3N^+ \rightarrow C_{16}H_{32} + N(CH_3)_3 + H^+$, contributes to about 36.5% of the weight loss; peak 3, at 563 K, assigned to the combustion of remaining carbon species (e.g. adsorbed trimethylamine, residual carbons), contributes to 12.3% weight loss; and the last peak, peak 4, at about 753 K, which is due to the dehydroxylation of SiOH groups, gives a weight loss of about 2.0%. Based on anhydrous silica, the total organic content in the as-synthesized MCM-41 sample is about 53.8 %. The stoichiometric molar ratio of Si/N is thus calculated to be 3.79. As a result, the theoretical number of silanol groups attached to the internal surface is about 2.4 per nm^2 (based on the internal surface area is $1025 m^2/g$). Justified by the

weight loss event because of dehydroxylation of hydrogen-bonded SiOH groups (1.9 %), the concentration of hydrogen-bonded SiOH groups can be estimated to be about 2.1 per nm², which is in good agreement with the NMR results (1.8-2.3 per nm²) and the theoretical value.

In summary, it can be concluded that the three types of surface SiOH groups display the following characteristics: single SiOH groups with an IR absorption band at 3738 cm⁻¹ and magnetic resonance peak at -101 ppm; hydrogen-bonded SiOH groups with an IR absorption band at 3200 - 3600 cm⁻¹ and magnetic resonance peak at -101 ppm; and geminal SiOH groups with an IR absorption band at 3738 cm⁻¹ and magnetic resonance peak at -92 ppm, respectively. The value of the SiOH number, α_{OH} , namely in the range of 2.5 and 3.0 depending upon template removal method, is less than that determined by Ishikawa et al. [30] while slightly more than that measured by Llewellyn et al. [31]. We believe that the range of 2.5-3.0 obtained from the NMR data is more acceptable as it is further supported by the TGA data in Fig. 6 and the theoretical calculation. Depending on demanding, the density of silanol groups can be enhanced by rehydration of surface siloxane bonds [32].

2.2 Grafting of organosilanes – silylation

Silylation was the first to be used to functionalize ONSs as was originally described by Mobil scientists [2]. Reaction of a suitable organosilane reagent such as chlorosilanes, alkoxysilanes, silylamines, and disilazane, etc. with the ONSs via the surface silanol groups using an appropriate solvent under reflux conditions yields an organic-inorganic composite with the organosilane pendent on the pore surface [7,8]. As illustrated in Scheme 3 by using TMCS as the silylating reagent as an example, the reaction of TMCS with surface free and geminal groups occurs under dry conditions, producing a surface-TMS-covered organic-inorganic composite. The surface coverage of the TMS groups is determined by the density of the accessible free and geminal silanol groups with a maximum surface coverage of about 85 % [25]. Anwender and co-workers [33,34] demonstrated that the steric size and shape of silylating agents also play a role in determining the surface coverage. Having examined a number of organosilanes, the authors concluded that the best surface coverage was obtained with the sterically less demanding silyl groups. Nevertheless, the accessible surface silanol groups, namely free and geminal silanols, play a key role in grafting.



Scheme 3. Schematic illustration of surface silylation of ONSs with TMCS.

If a high surface coverage of surface functionalities is desired, attempt may be made to increase the population of the surface silanol groups as described by a number research groups [32,35–37]. Instead of silylation using organosilanes, Yamamoto and Tatsumi [38] developed a strategy leading to methyl groups covalently bonded to surface silicon atoms. The first step the authors used was esterification of the surface hydroxyl groups with butanol to form Si-OBu, followed by reaction with the Grignard reagent CH_3MgI , leading to the formation of Si- CH_3 species.

Simultaneous surfactant removal and surface derivatization via the formation of strong siloxane bonds was demonstrated [39]. The displacement reaction is possible so long as the organosilane exhibits at least one reactive group such as Cl-Si, EtO-Si, or MeO-Si. According to Lin et al. [40], the surfactant-silyl exchange process is greatly favored when applied to nanoporous silica prepared under acidic conditions because of the weaker interactions between the silica walls and the surfactant compared to those materials prepared under basic conditions. Using alkyl and alkoxysilanes, namely, TMCS, MPTMS, and APTMS, higher surface coverage (3.5–4.5 mmol/g) were obtained in ethanol under milder conditions. However, Lim and Stein [41] observed that grafting of vinyl groups takes place mostly at the external surface and near the pore openings of the ONS materials.

Site-selective grafting was attempted as well [42–44]. Shephard and co-workers [42] modified the external surface of MCM-41 silica with Ph_2SiCl_2 first, assuming that the external surface is more accessible to Ph_2SiCl_2 because of its large kinetic diameter. Then, they functionalized the internal surface with $(\text{MeO})_3\text{Si-(CH}_2)_3\text{-NH}_2$ as an anchor for a Ru cluster. High-resolution transmission electron microscopy (HRTEM) measurements revealed that the amine tethers were almost entirely

attached to the internal surface. Interestingly, Zhao et al. [43] were able to selectively silylate the external surface of a MCM-41 silica by employing an as-synthesized material whose pores were still filled with cationic surfactant cetyltrimethylammonium, making the pores inaccessible to the silylating agent TMCS. Then the authors manipulated to remove the surfactant molecules occupying the pore mouths, followed by deposition of controllable layers of inorganic species on the pore mouths, enabling them to engineer the pore-opening sizes of ONSs. Similarly, de Juan and Ruiz-Hitzky [44] functionalized as-synthesized ONS by using TMCS. Then the surfactant was removed by solvent extraction. Finally, the internal pore surfaces were functionalized with PPDMCS.

Esterification of surface silanol groups with alcohols have also been shown to be an alternative approach to silylation [45,46]. Further modification of esterificated ONSs with Grignard reagent CH_3MgI allowed Yamamoto and Tatsumi to obtain $-\text{CH}_3$ -terminated materials [47].

Upon silylation, both the hydrothermal stability and the mechanical stability of ONSs can be drastically improved because of the very hydrophobic nature of the attached organic silanes [25,37,38 45-53]. This offers a greater opportunity in development of novel catalyst and adsorbent used in the presence of water vapor or in an aqueous medium. For example, Zhao and co-workers found that TMCS-modified MCM-41 materials are promising adsorbent for the removal of volatile organic compounds (VOCs) in the presence of high-concentration of water vapor [53]. As can be seen from Figure 7, silylation of MCM-41 resulted in a very hydrophobic nature (left), more hydrophobic than dealuminated zeolite Y, and a reasonable adsorption capacity of benzene (right), higher than zeolite Y and activated carbon BPL [53].

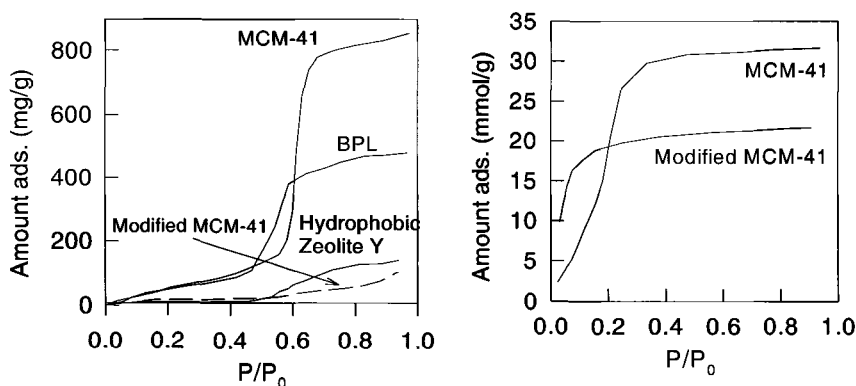
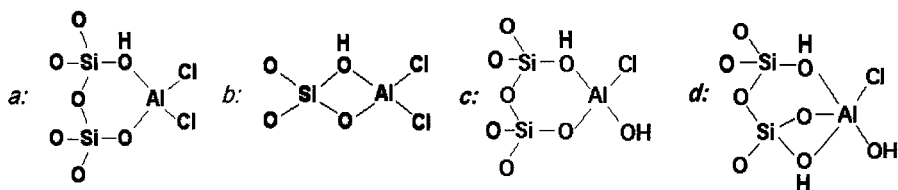


Figure 7. Adsorption isotherms of water (left) and benzene (right) [54].

2.3 Grafting of catalytic species

Redox catalysts such as Ti and V species play a remarkable role in catalysis. Since the availability of ONS materials, grafting of redox catalysts has been studied extensively [54-61]. Titanocene (Cp_2Ti) grafted on MCM-41 materials were shown to possess remarkable catalytic properties [54-56]. Modification of MCM-48 via grafting of VO_x species on the surface using DMDCS as a coupling agent was reported by Van Der Voort and co-workers [56,57]. The authors first silylated the material with DMDCS and then hydrolyzed it to create $\text{Si-O-Si}(\text{CH}_3)_2\text{OH}$ surface species, which were used to anchor $\text{VO}(\text{acac})_2$. Calcination of the obtained material led to surface VO_x supported mesoporous silica.

Immobilization of Lewis acids such as AlCl_3 and BF_3 on ONS supports via grafting method has received growing interest [62-72]. Of particular interest is the immobilization of AlCl_3 because of its high catalytic activity towards many alkylation reactions, ready availability, environmental unfriendliness, and lack of selectivity. Upon immobilization, the acidity and catalytic activity are maintained whereas selectivity can be drastically enhanced because of the effect of the mesoporous supports [62,66,67]. Most importantly, immobilized aluminum chloride species have been found to be stable against leaching during reaction and regeneration. Spectroscopic studies showed the presence of the following four possible aluminum species as illustrated in Scheme 4 [67].



Scheme 4. Possible Al species of AlCl_3 grafted on mesoporous silica surface [67].

A number of metal complexes have been grafted or tethered to the internal surface of mesoporous silicas [73-88]. Grafting of homogeneous chiral catalysts has attracted a great deal of attention as well [89-94]. Acidic species such as sulfonic groups and sulfated zirconia species have also been attached to ONS surfaces [95-98]. In addition to acidic functionalities, basic functional groups have been immobilized and tested in terms of basic catalysis [99-105]. The details of the grafting of acidic and basic species for catalytic applications are described Macquarrie. In another chapter, Choudhary and Uphade discuss grafting of Lewis acids and bases on nanoporous silicas and their environmental applications.

3 Functionalization by co-condensation

The apparent advantage of the grafting method is the good preservation of the mesostructure after functionalization. However, it has several shortcomings. First, attachment of a layer of organic species on the pore surface results in a reduced pore size and pore volume, causing a stronger resistance to diffusion of molecules having a kinetic diameter of a similar size to the reduced pore size. Second, limited loading of a functionality can be grafted because of the limited number of surface silanol groups [14]. Third, grafting is a time consuming process as it involves two steps: pre-synthesis of a parent mesostructure and post-treatment with a functionality, during which complete drying of both the mesostructure and the reaction solvent prior to the grafting reaction are required in order to avoid the formation of unwanted polycondensation byproducts [106,107]. Fourth, control over the loading level and uniformity of functional groups is difficult to achieve [41,107]. Fifth, the grafted functionalities are unstable due to partial cross-linking of the organosiloxane with silica surface [108]. Finally, poor control over the position of the functionalities [41].

In comparison with grafting, co-condensation, which is a method involving one-step co-polymerization of a tetraalkoxysilane such as tetraethyl orthosilicate (TEOS) with an organosiloxane such as 3-aminopropyltriethoxysilane (APTES), offers a higher and more uniform surface coverage of functionality and a better control over the surface properties. It was first used by two research groups [109,110] to prepare organically functionalized MCM-41 materials. Subsequently, this method has been employed to functionalize other nanoporous materials such as MSU and SBA series and many functionalities have been incorporated into silicate framework [9,41, 106,107,111-135].

In this section, we present our recent experimental data of surface functionalization of nanoporous SBA-15 materials by co-condensation of TEOS with APTES, 3-mercaptopropyltrimethoxysilane (MPTMS), phenyltrimethoxysilane (PTMS), vinyltriethoxysilane (VTES), and 4-triethoxybutyronitrile (TSBN), respectively [135, 136].

3.1 Synthesis of functionalized SBA-15 materials by co-condensation

A range of molar ratio of organosilane to TEOS was used to prepare a series of samples, denoted 1Z:x, where Z represents APTES, MPTMS, PTMS, VTES, and TSBN, respectively, and $x = 2 - 20$, which varies

depending on the organosiloxanes. For example, 1APTES:10 denotes a sample which was prepared with a molar ratio of APTES to TEOS = 1:10. Surfactant P123 was removed from the functionalized samples using ethanol extraction at 70 °C for about 6 h. The samples involved, together with their BET surface area (S_{BET}), BJH pore diameter (D_{BJH}) and pore volume (V_{Pore}) are compiled in Table 3.

Table 3. Physical properties of various SBA-15 materials functionalized by co-condensation

Sample	R:TEOS*	S_{BET} (m ² /g)	D_{BJH} (Å)		V_{Pore} (cm ³ /g)
			Ads.	Des.	
1APTES:8	1:8	460	13.5	10.6	0.310
1APTES:10	1:10	550	13.5	36.2	0.370
1APTES:15	1:15	550	90.0	60.8	1.10
1APTES:20	1:20	599	90.3	60.6	1.08
1MPTMS:5	1:5	369	25.0	35.0	0.300
1MPTMS:10	1:10	489	60.0	46.1	0.620
1MPTMS:15	1:15	670	66.0	50.0	0.900
1MPTMS:20	1:20	625	66.2	50.0	0.83
1PTMS:5	1:5	434	13.2	33.6	0.330
1PMTS:10	1:10	619	50.0	39.1	0.660
1PTMS:15	1:15	537	66.1	46.1	0.720
1PTMS:20	1:20	584	76.1	60.7	1.00
1TEVS:2	1:2	588	45.0	38.5	0.67
1TEVS:3	1:3	605	53.4	40.8	0.88
1TEVS:5	1:5	711	66.0	50.2	0.920
1TEVS:10	1:10	592	76.2	55.0	1.03
1TEVS:15	1:15	632	89.8	54.9	0.920
1TEVS:20	1:20	555	89.8	60.6	1.00
1TSBN:5	1:5	512	60.0	36.2	0.600
1TSBN:10	1:10	673	76.4	54.6	0.980
1TSBN:15	1:15	721	89.7	60.6	1.05
1TSBN:20	1:20	715	89.7	60.6	1.12

* R = organosiloxane

3.2 N_2 physisorption isotherms

Fig. 8 shows the N_2 adsorption/desorption isotherms of the various organosiloxane-functionalized SBA-15 samples. It is seen that for all

1Z:15 and 1Z:20 samples, their isotherms are characteristic of monolayer-multilayer adsorption followed by capillary condensation at $P/P_0 = 0.75$ or in the vicinity, indicating that all the samples prepared using low-concentration of organosilanes are order nanoporous materials.

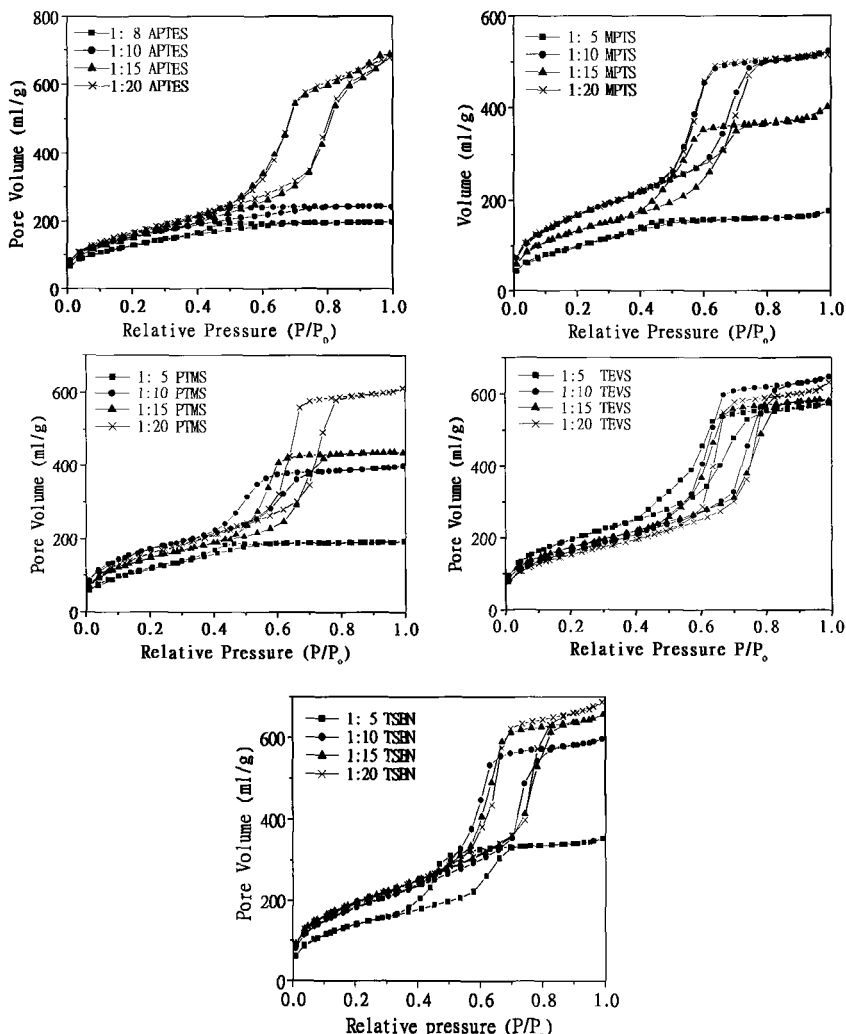


Figure 8. N_2 adsorption-desorption isotherms of SBA-15 samples functionalized with various organosiloxanes of different amount (solid line: adsorption; dash line: desorption).

With increasing the amount of the organosiloxanes present in the initial synthesis mixtures, the isotherms of some samples began to change shapes – from Type IV to Type I, indicating an adverse effect of the organosiloxanes on the formation of SBA-15 mesostructure. From the isotherms it can also be seen that TEVS, amongst, has the least adverse effect while APTES has the most adverse effect. As the concentration of organosiloxanes was increased to about 17 % (samples 1Z:5), the type IV isotherm can not be observed on samples functionalized with MPTS and PTMS while it can still be seen on samples 1TEVS:5 and 1TSBN:5. As for sample 1TSBN:5, though its isotherm is characteristic of type IV, the amount adsorbed at the platform region was substantially lower than that of sample 1TSBN:10, showing a substantial loss in mesostructure. The insignificant effect of the presence of 17 % TEVS or less on the formation of SBA-15 is in agreement with the SAXS results shown in Fig. 9, which will be discussed in next section. When the concentration of TEVS was increased to 25 % (sample 1TEVS:3), Type I isotherm instead of type IV is seen, showing the observed effect of TEVS on the formation of SBA-15 at this concentration. Such different effects of the organosiloxanes on SBA-15 mesostructure are considered to be related to their different behaviors under the experimental conditions (strongly acidic). We will elaborate this point later on after SAXS data are discussed. The nitrogen adsorption data show that there are different concentration limitations for different organosilanes that could be co-condensed with TEOS while a good mesostructure can be maintained. When the concentration of organosilane is higher than the limitation, the mesostructure no longer exists but a mixed structure, perhaps including both microstructure and mesostructure, is obtained.

3.3 SAXS characterization

Structural characterization of mesoporous silica materials by using SAXS technique has proven very reliable [136-139]. Scattering vector q employed in SAXS analysis can be related to the diffraction angle (θ) by using the Bragg equation $\lambda = 2d\sin\theta$ with $q = 4\pi \sin \theta / \lambda$, where $\lambda = 1.5418$ Å. Fig. 9 (left) compares the SAXS patterns of organically functionalized SBA-15 samples synthesized in the presence of about 4.8 % organosiloxanes with that of a pure-silica SBA-15 sample. All samples except for 1APTES:20 display three well-resolved peaks, which can be indexed according to a two-dimensional $p6mm$ hexagonal symmetry, suggesting the presence of a highly ordered hexagonal array of pores,

characteristic of SBA-15 phase [6]. In the presence of 4.8 % organosiloxane, the functionalized SBA-15 samples except for 1APTES:20 possess a similar SAXS pattern to that of pure-silica SBA-15, indicating a negligible effect of organosiloxanes MPTS, PTMS, TEVS, and TSBN in the synthesis mixture on the formation of SBA-15 mesostructure under such a low concentration. From the positions of the (100) peaks, the d_{100} spacing of the samples were calculated to be in the range of 80 – 100 Å. The d_{100} spacing can be used in estimation of the pore size of the samples by deducting the pore wall thickness that can be obtained from TEM images. It should be particularly mentioned that sample 1APTES:20 displays only one very broad diffraction peak yet its isotherm is of Type IV (see Fig. 8). This again indicates that APTES has a strong effect on the local structure of the silicate framework.

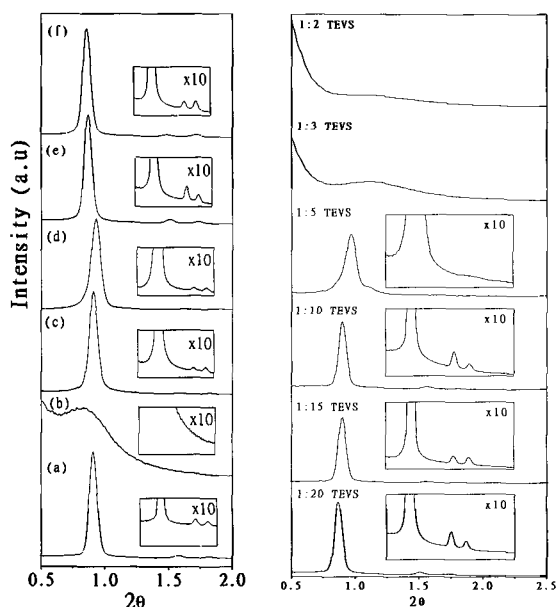


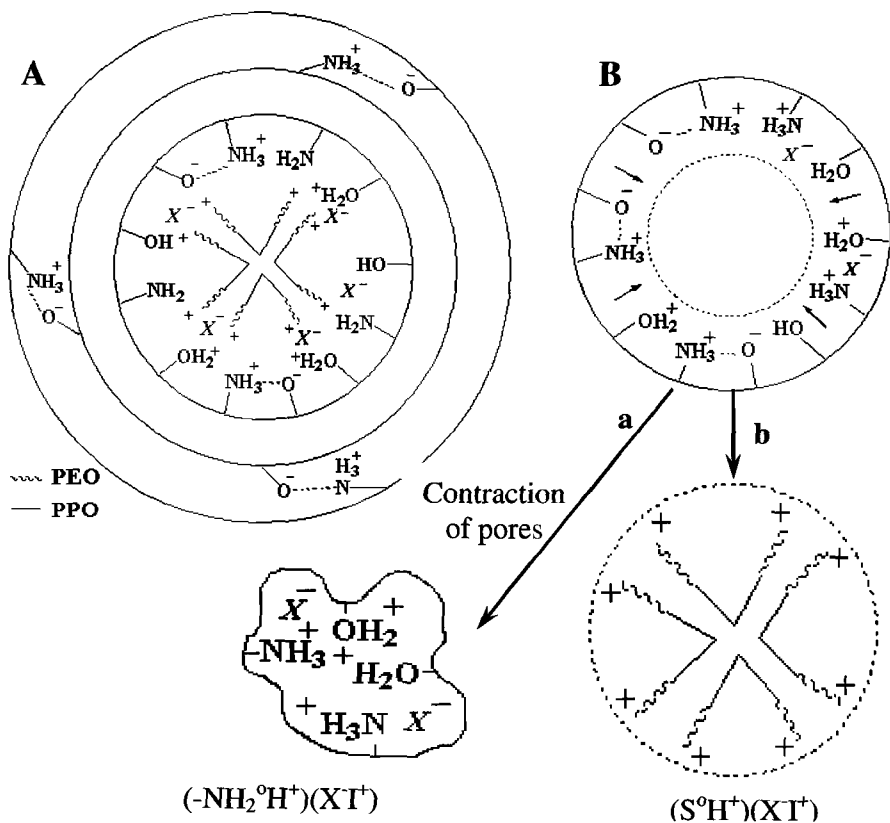
Figure 9. Left: SAXS spectra of (a) pure-silica SBA-15, (b) 1APTES:20, (c) 1MPTS:20, (d) 1PTMS:20, (e) 1TEVS:20, and (f) 1TSBN:20. Right: SAXS spectra of 1TEVS:x.

A noticeable observation from Fig. 9 is the highest SAXS resolution of sample 1TEVS:20 among the samples presented. It should be particularly mentioned that the SAXS resolution of sample 1TEVS:20 is even better than that of the pure-silica SBA-15 sample. This was not expected because the presence of TEVS in the initial synthesis mixture would be more or

less disruptive to mesostructure ordering as reported previously in a similar synthetic system or in a neutral synthetic system [121,123,127]. Such an interesting phenomenon encouraged us to further examine the structure ordering of TEVS-functionalized samples prepared in the presence of higher molar ratio of TEVS to TEOS. Compared in Fig. 9 (right) are the SAXS patterns of samples 1TEVS: x , where $x = 2, 3, 5, 10, 15$, and 20. It can be seen that the SAXS resolution of sample 1TEV:5 is similar to that of 1TEVS:20, indicating that as high as about 17 % TEVS can be co-condensed with TEOS without perturbing the structural ordering, which is consistent with the nitrogen adsorption data discussed earlier. This observation could be reasoned by the length of TEVS chain, which is relatively short with only two double bonded carbons. As such, it becomes easier for TEVS to co-condense with TESO without provoking profound disruptions to silicate network. The short carbon chain nature could also make TEVS itself easily be included into the micelles as proposed by Mercier and Pinnavaia [106]. Another possible reason for the better structure ordering could be due to the fast hydrolysis rate of TEVS compare to TEOS and other organosiloxanes.

The strong adverse effect of APTES on the formation of mesostructure has not observed in previous studies carried out under basic or neutral conditions [15,107,132]. This is believed to be related to the following aspects. First, as illustrated in Scheme 5 (A), amine groups of APTES are known to be easily protonated under acidic conditions [108,141], such protonated amine groups would have cross-linked with silanol groups of the silicate species, resulting in local disruptions of the silicate walls as reflected by the SAXS patterns with only one very broad peak. On the other hand, as suggested by Walcarius and co-workers [141], protonated terminal amine groups can interact with silanol groups to form zwitterions ($-\text{NH}_3^+ \cdots ^-\text{OSi}$). The formation of such zwitterions on the pore surface would have prevented direct interactions of surfactant P123 with the silicates, leading to a less ordered pore structure. Second, it is known that the formation of mesoporous SBA-15 silica under acidic conditions is via a mechanism of $(\text{S}^0\text{H}^+)(\text{X}^-)$ [6,142]. In the presence of APTES, it is believed that competitive interactions have taken place as illustrated in Scheme 5B. Those silicate species connected with APTES having protonated amine groups ($-\text{NH}_2\text{H}^+$) would have competed with those positively charged silicate species (SiOH_2^+) for surfactant P123 to form $(-\text{NH}_2\text{H}^+)(\text{X}^-\text{SiOH}_2^+)$, leading to microporosity as revealed by the nitrogen adsorption data. Third, the interactions of the amine groups with the hydrophilic EO moieties were disrupted by a contrast matching of the

surfactant head group with organosilane APTES [106,129]. The long-chain aminopropyl groups with a hydrophilic tail of protonated amine groups directing towards the micelle cores caused a repulsion as the micelle cores are composed of hydrophobic PPO blocks [6]. Fourth, because APTES is basic in nature, an increase in the percentage of APTES added to the synthesis medium resulted in pH increase (it was observed that the pH increased from -0.25 to 0.33 as the amount of APTES was increased from 5 to 17 %, resulting in structure disordering as has been observed by Choi and co-workers on SBA-15 silicas [140]).



Scheme 5. (A) An illustration of local structure disordering of silicate walls because of cross-linking of protonated amines with silanols and the weaker interactions between P123 and silicate species because of zwitterions. (B) A scheme showing pore contraction because of the presence of protonated amine groups (a) in comparison with the absence of organosilane APTES. I = silicate precursor; S^0 = neutral surfactant; X^- = mediated counterions.

3.4 TEM observation

The mesostructural ordering and symmetry inferred from the SAXS data can be confirmed by the TEM images shown in Fig. 10. The two-dimensional $p6mm$ hexagonal symmetry can be seen on all samples. The poorest structure ordering of 1APTES:20 among the samples is evident.

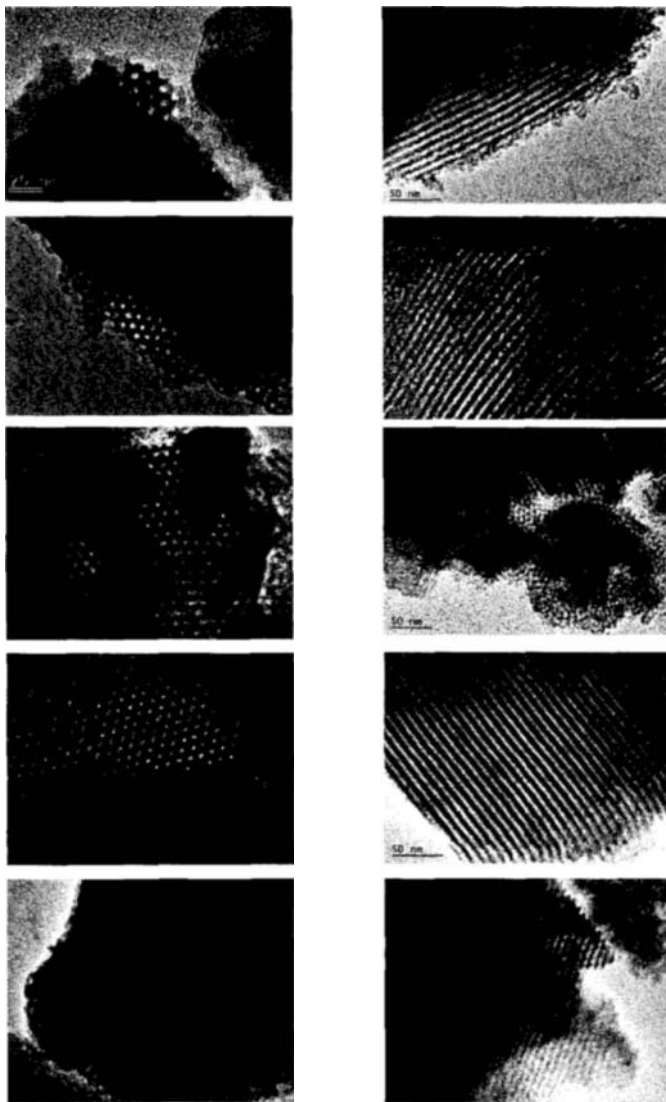


Figure 10. TEM images of (a) 1APTES:20, (b) 1MPTS:20, (c) 1PTMS:20, (d) 1TEVS:20, and (e) 1TSBN:20 taken along the direction of the pore axis (left-hand) and perpendicular to the pore axis (right-hand).

3.5 NMR characterization

Fig. 11 shows the ^{13}C CP/MAS NMR and ^{29}Si MAS NMR spectra respectively for samples 1Z:20. The ^{13}C CP/MAS NMR spectra for TEVS- and PTMS-modified samples show the presence of carbon species due to $-\text{CH}=\text{CH}-$ and phenyl groups respectively, indicating the incorporation of ethylene and phenyl functionalities. Incorporation of TSBN, MPTS and APTES is evident from the ^{29}Si MAS NMR spectra because of the presence of T sites. Extra peaks observed on the ^{13}C CP/MAS NMR spectra such as 59 ppm and 13 ppm are probably due to residual ethoxy groups from incomplete hydrolysis of TEOS. FTIR measurements indicated that ethoxy groups are present in some of the samples. The resonance peaks with chemical shifts in the range of 65-75 ppm is due to residual surfactant that was not totally removed. TGA data did demonstrate some 3-5 wt.% of surfactant P123 remained after solvent extraction.

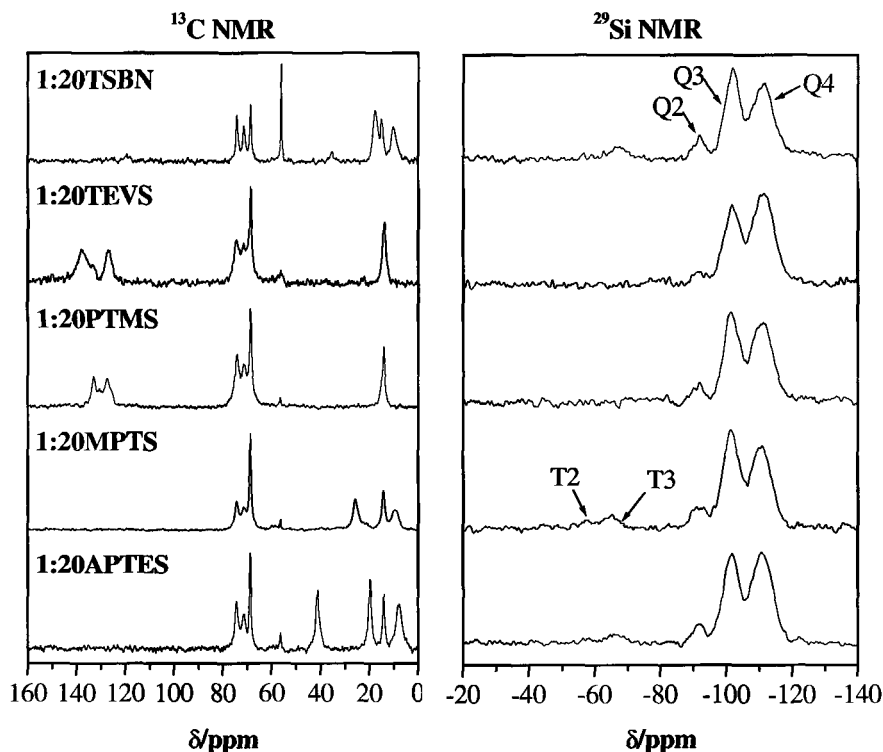


Figure 11. ^{13}C CP/MAS NMR and ^{29}Si MAS NMR spectra of functionalized SBA-15.

3.6 Elemental analysis and XPS characterization

Table 4. Elemental and XPS analysis data of organosiloxane-functionalized SBA-15 samples.

Sample	Elemental analysis				XPS			
	C %	N %	S %	Density (mmol/g)	C %	N %	S %	Density (mmol/g)
1APTES:8	6.2	2.6	-	1.2	27.7	1.70	-	1.18
1APTES:10	16.2	1.3	-	0.9	23.4	1.58	-	1.13
1APTES:15	10.6	1.1	-	0.8	16.0	1.43	-	1.02
1APTES:20	3.1	0.9	-	0.7	16.7	1.43	-	1.02
1TSBN:5	14.2	1.9	-	1.34	34.0	2.3	-	1.64
1TSBN:10	10.4	1.7	-	1.24	35.4	1.33	-	0.95
1TSBN:15	8.0	0.78	-	0.56	28.0	1.22	-	0.87
1TSBN:20	7.8	0.71	-	0.51	22.4	1.29	-	0.92
1MPTS:5	15.4	-	5.41	1.69	30.2	-	4.63	1.45
1MPTS:10	11.5	-	2.10	0.66	26.9	-	2.85	0.89
1MPTS:15	9.97	-	2.10	0.66	36.2	-	1.26	0.39
1MPTS:20	8.65	-	1.65	0.52	23.7	-	1.34	0.42
1PTMS:5	19.2	-	-	2.7	30.4	-	-	4.22
1PTMS:10	13.4	-	-	1.9	21.0	-	-	2.92
1PTMS:15	15.4	-	-	2.1	22.6	-	-	3.14
1PTMS:20	10.3	-	-	1.4	18.7	-	-	2.60
1TEVS:5	9.26	-	-	3.9	19.0	-	-	7.90
1TEVS:10	7.49	-	-	3.1	15.7	-	-	6.53
1TEVS:10	8.21	-	-	3.4	21.2	-	-	8.82
1TEVS:20	6.19	-	-	2.6	22.8	-	-	9.50

Table 4 shows the N and S contents of APTES-, MPTMS- and TSBN-functionalized SBA-15 samples analyzed by using both elemental analysis and XPS. The density of TEVS and PTMS were solely derived from C. The C contents obtained from XPS and elemental analysis can be attributed to the surfactant that was left after the ethanol extraction or the ethanol itself. Hence, XPS and elemental analysis will not provide a very

accurate analysis to the organosilane incorporated. The organic content in samples detected using XPS was slightly higher than the CHNS elemental analysis. This strongly indicated the distribution of these organosilanes concentrated on the surface of the functionalized SBA-15. The loading of organosilanes was basically proportion to the concentration of organosilane employed in the synthesis.

4 Concluding remarks

While both grafting and co-condensation allow one to obtain various surface-functionalized nanoporous materials, there are pros and cons for each method. The grafting method affords the preservation of the mesostructure after functionalization while suffers a relatively low density and non-uniformity of functionality. The co-condensation method allows one to obtain a high loading of the functionality at the expense of loss in structure ordering. Various chemical functionalities including both inorganics and organics can be anchored on the surfaces of ONSs via grafting approach. With regard to the co-condensation method, the choice is limited. In addition, removal of template during solvent extraction might result in partial loss in the co-condensed functionalities. With all these in mind, one should be able to select which method is suitable for his/her purposes of functionalization.

With the availability of more approaches to surface modification in addition to that have been discussed, functionalization of ONSs is becoming more and more sophisticated, allowing one to obtain materials with controlled synergy of inorganic and organic properties, opening up unprecedented opportunities for development of novel catalysts, adsorbents, optical and electronic materials, etc. For example, the co-condensation of titanium alkylloxide with organosiloxane might offer an oxidation catalyst with a high surface hydrophobicity, positioning the materials to be a novel catalyst. Another example is aluminum-containing PMO materials, which are believed to possess not only surface acidity required by most of hydrocarbon conversion reactions but also surface hydrophobicity. The use of periodically ordered inorganic-organic nanoporous and macroporous materials as a low-dielectric optical material or photonic bandgap material with waveguide properties would be a area to explore. A final example is the use of functionalized nanoporous or macroporous materials with imprinted properties made by combining template strategy with molecular imprinting technique as a molecular recognizer for biomolecules such as protein or DNA.

5 Acknowledgements

XSZ thanks ARF of NUS and A*STAR for supporting part of the work presented here.

References

1. Kresage C. T., Leonowicz M. E., Roth W. J., Vartuli J. C. and Beck J. S., Ordered mesoporous molecular sieves synthesized by a liquid-crystal template mechanism, *Nature* **359** (1992) pp. 710-712.
2. Beck J. S., Vartuli C., Roth W. J., Leonowicz M. E., Kresge C. T., Schmitt K. D., Chu T-W., Olson D. H., Sheppard E. W., McCullen S. B., Higgins J. B. and Schlenker J. L., A new family of mesoporous molecular sieves prepared with liquid crystal templates, *J. Am. Chem. Soc.* **114** (1992) pp. 10834-10843.
3. Inagaki S., Fukushima Y., Kuroda K., Synthesis of highly ordered mesoporous materials from a layered polysilicate, *J. Chem. Soc., Chem. Commun.* (1993) pp. 680-682.
4. Tanev P. T. and Pinnavaia T. J., A neutral templating route to mesoporous molecular sieves, *Science* **267** (1995) pp. 865-867.
5. Bagshaw S. A., Prouzet E. and Pinnavaia T. J., Templating of mesoporous molecular-sieves by nonionic polyethylene oxide surfactants, *Science* **269** (1995) pp. 1242-1244.
6. Zhao D., Huo Q., Feng J., Chmelka B. F. and Stucky G. D., Nonionic triblock and diblock copolymer and oligomeric surfactant syntheses of highly ordered, hydrothermally stable, mesoporous silica structure, *J. Am. Chem. Soc.* **120** (1998) pp. 6024-6036.
7. Moller K. and Bein T., Inclusion chemistry in periodic mesoporous hosts, *Chem. Mater.* **10** (1998) pp. 2950-2963.
8. Clark J. H. and Macquarrie D. J., Catalysis of liquid phase organic reactions using chemically modified mesoporous inorganic solids, *Chem. Commun.* (1998) pp. 853-860.
9. Stein A., Melde B. J. and Schroden R. C., Hybrid inorganic-organic mesoporous silicates – nanoscopic reactors coming of age, *Adv. Mater.* **12** (2000) pp. 1403–1419.
10. Sayari A. and Hamoudi S., Periodic mesoporous silica-based organic-inorganic nanocomposite materials, *Chem. Mater.* **13** (2001) pp. 3151-3168.
11. Wight A. P. and Davis, M. E., Design and preparation of organic-inorganic hybrid catalysts, *Chem. Rev.* **102** (2002) pp. 3589-3614.
12. Inagaki S., Guan S., Fukushima Y., Ohsuna T. and Terasaki O., Novel mesoporous materials with a uniform distribution of organic groups and inorganic oxide in their framework, *J. Am. Chem. Soc.* **121** (1999) pp. 9611-9614.
13. Asefa T., MacLachlan M. J., Coombs N. and Ozin G. A., Periodic mesoporous organosilicas with organic groups inside the channel walls, *Nature* **402** (1999), pp. 867-871.
14. Melde B. J., Holland B. T., Lanford C. F. and Stein A., Mesoporous sieves with unified hybrid inorganic/organic frameworks, *Chem. Mater.* **11** (1999) pp. 3302-3308.

15. Hall S. R., Fowler C. E., Lebeau, B. and Mann S., Template-directed synthesis of bi-functionalized organo-MCM-41 and phenyl-MCM-48 silica mesophases, *Chem. Commun.* (1999) pp. 201-202.
16. Asefa T., Kruk M., MacLachlan M. J., Coombs N., Grondy H., Jaroniec M. and Ozin G. A., Novel bifunctional periodic mesoporous organosilicas, BPMOs: Synthesis, characterization, properties and in-situ selective hydroboration-alcoholysis reactions of functional groups. *J. Am. Chem. Soc.* **123** (2001) pp. 8520-8530.
17. Burleigh M. C., Markowitz M. A., Spector M. S. and Gaber B. P., Direct synthesis of periodic mesoporous organosilicas: Functional incorporation by co-condensation with organosilanes. *J. Phys. Chem. B* **105** (2001) pp. 9935-9942.
18. Burleigh M. C., Markowitz M. A., Spector M. S. and Gaber B. P., Amine-functionalized periodic mesoporous organosilicas. *Chem. Mater.* **13** (2001) pp. 4760-4766.
19. Chen J., Li Q., Xu R. and Xiao, F., Distribution of the silanol groups in the mesoporous molecular sieve MCM-41, *Angew. Chem. Int. Ed. Engl.* **34** (1995) pp. 2694-2696.
20. Jentys A., Pham N. H. and Vinek H., Nature of hydroxy groups in MCM-41, *J. Chem. Soc., Faraday Trans.* **92** (1996) pp. 3287-3291.
21. Zhao X. S., Lu G. Q., Whittaker A. J., Miller G. J. and Zhu H. Y., A comprehensive study on the surface chemistry of mesoporous MCM-41, *J. Phys. Chem. B* **101** (1997) pp. 6525-6531.
22. Chen C. Y., Li H. Y. and Davis M. E., Studies on mesoporous materials. I. Synthesis and characterization of MCM-41, *Micropor. Mesopor. Mater.* **2** (1993) pp. 17-26.
23. Iler R. K., *The chemistry of silica*, Wiley, New York, 1979.
24. Vansant E. F., Van Der Voort, P. and Vrancken K. C., Characterization and modification of the silica surface, *Stud. Surf. Sci. Catal.* **93** (1995) pp. 109-125.
25. Zhao X. S. and Lu G. Q., Modification of MCM-41 by surface silylation with trimethylchlorosilane and adsorption study, *J. Phys. Chem. B* **102** (1988) pp. 1556-1561.
26. Nikiel L. and Zerda T. W., Adsorption of pyridine on silica gels, *J. Phys. Chem.* **95** (1991) pp. 4063-4069.
27. Cvetanovic R. J. and Amenomiya Y., Application of a temperature-programmed desorption technique to catalyst studies, *Adv. Catal.* **17** (1967) pp. 103-149.
28. Sindorf D. W. and Maciel G. E., Cross-polarization/magic-angle-spinning silicon-29 nuclear magnetic resonance study of silica gel using trimethylsilane bonding as a probe of surface geometry and reactivity, *J. Phys. Chem.* **86** (1982) pp. 5208-5219.
29. Fyfe C. A., Gobbi G. C. and Kennedy G. J., Quantitatively reliable silicon-29 magic-angle spinning nuclear magnetic resonance spectra of surfaces and surface-immobilized species at high field using a conventional high-resolution spectrometer, *J. Phys. Chem.* **89** (1985) pp. 277-281.
30. Ishiikawa T., Matsuda M., Yasukawa A., Kandori K., Inagaki S., Fukushima T. and Kondo S., Surface silanol groups of mesoporous silica FSM-16, *J. Chem. Soc., Faraday Trans.* **92** (1996) pp. 1985-1989.

31. Llewellyn P. L., Schüth F., Grillet Y., Rouquerol F., Rouquerol J. and Unger K. K., Effect of pore size on adsorbate condensation and hysteresis within a potential model adsorbent: M41S, *Micropor. Mater.* **3** (1994) pp. 345–349.
32. Feng X., Fryxell G. E., Wang L.-Q., Kim A. Y., Liu J. and Kemner K. M., Functionalized monolayers on ordered mesoporous supports, *Science* **276** (1997) pp. 923–926.
33. Anwender R., SOMC@PMS. Surface organometallic chemistry at periodic mesoporous silica, *Chem. Mater.* **12** (2001) pp. 4419–4438.
34. Anwender R., Nagl I., Widenmeyer M., Engelhardt G., Groeger O., Palm C. and Röser, T., Surface characterization and functionalization of MCM-41 silicas via silazane silylation, *J. Phys. Chem. B* **104** (2000) pp. 3532–3544.
35. Liu J., Feng X., Fryxell G. E., Wang L.-Q., Kim A. Y. and Gong M., Hybrid mesoporous materials with functionalized monolayers, *Adv. Mater.* **10** (1998) pp. 161–165.
36. Mercier L. and Pinnavaia T. J., Heavy metal ion adsorbents formed by the grafting of a thiol functionality to mesoporous silica molecular sieves: factors affecting Hg(II) uptake, *Environ. Sci. Technol.* **32** (1998) pp. 2749–2754.
37. Kimura T., Saeki S., Sugahara Y. and Kuroda K., Organic modification of FSM-type mesoporous silicas derived from Kanemite by silylation, *Langmuir* **15** (1999) pp. 2794–2798.
38. Yamamoto K. and Tatsumi T., Remarkable improvement in hydrothermal stability of MCM-41 by surface modification with Grignard reagents, *Chem. Lett.* **6** (2000) pp. 624–625.
39. Antochshuk V. and Jaroneic M., Functionalized mesoporous materials obtained via interfacial reactions in self-assembled silica-surfactant systems, *Chem. Mater.* **12** (2000) pp. 2496–2501.
40. Lin H. P., Yang L. Y., Mou C. Y., Liu S. B. and Lee H. K., A direct surface silyl modification of acid-synthesized mesoporous silica, *New J. Chem.* **24** (2000) pp. 253–255.
41. Lim H. M. and Stein A., A comparative studies of grafting and direct syntheses of inorganic-organic hybrid mesoporous materials, *Chem. Mater.* **11** (1999) pp. 3285–3295.
42. Shephard D. S., Zhou W., Maschmeyer T., Matters J. M., Roper C. L., Parsons S., Johnson B. F. G. and Duer M. J., Site-directed surface derivatization of MCM-41: use of high-resolution transmission electron microscopy and molecular recognition for determining the position of functionality within mesoporous materials, *Angew. Chem. Int. Ed.* **37** (1998) pp. 2719–2723.
43. Zhao X. S., Lu G. Q. and Hu X., A new method for tailoring the pore-opening size of MCM-41, *Chem. Commun.* (1999) pp. 1391–1392.
44. de Juan F. and Ruiz-Hitzky E., Selective functionalization of mesoporous silica, *Adv. Mater.* **12** (2000) pp. 430–432.
45. Kimura T., Kuroda K. and Sugahara Y., Esterification of the silanol groups in the mesoporous silica derived from Kanemite, *J. Porous Mater.* **5** (1998) pp. 127–132.
46. Zhao X. S., Lu G. Q. and Hu X., Characterization of the structural and surface properties of chemically modified MCM-41 materials, *Micropor. Mesopor. Mater.* **41** (2000) pp. 37–47.

47. Zhao X. S., Audsley F. and Lu G. Q., Irreversible change of pore structure of MCM-41 during rehydration/dehydration at room temperature, *J. Phys. Chem. B* **102** (1998) pp. 4143-4146.
48. Koyano K. A., Tatsumi T., Tanaka Y. and Nakata S., Stabilization of mesoporous molecular sieves by trimethylsilylation, *J. Phys. Chem. B* **101** (1997) pp. 9436-9440.
49. Antochshuk V. and Jaroniec M., Adsorption, thermogravimetric, and NMR studies of FSM-16 material functionalized with alkylmonochlorosilanes, *J. Phys. Chem. B*, **103** (1999) pp. 6252-6261.
50. Matsumoto A., Tsutsumi K., Schumacher K. and Unger K. K., Surface functionalization and stabilization of mesoporous silica spheres by silanization and their adsorption characteristics, *Langmuir* **18** (2002) pp. 4014-4019.
51. Park M. and Komarneni S., Stepwise functionalization of mesoporous crystalline silica materials, *Micropor. Mesopor. Mater.* **25** (1998) pp. 75-80.
52. Shigeno T., Nagao M., Kimura T. and Kuroda K., Direct silylation of a mesostructured precursor for novel mesoporous silica KSW-2, *Langmuir* **18** (2002) pp. 8102-8107.
53. Zhao X. S., Ma Q. and Lu G. Q., VOC removal: comparison of MCM-41 with hydrophobic zeolites and activated carbons, *Energy & Fuels* **12** (1998) pp. 051-1054.
54. Mashmeyer T., Rey F., Sankar G. and Thomas J. M., Heterogeneous catalysts obtained by grafting metallocene complexes onto mesoporous silica, *Nature* **378** (1995) pp. 159-162.
55. Marchese L., Gianotti E., Dellarocca V., Mashmeyer T., Rey F., Coluccia S. and Thomas J. M., Structure-functionality relationship of grafted Ti-MCM-41 silicas. Spectroscopic and catalytic studies, *PCCP* **1** (1999) pp. 585-592.
56. Kageyama K., Tamazawa J.-I. and Aida T., Extrusion polymerization: catalyzed synthesis of crystalline linear polyethylene nanofibers within a mesoporous silica, *Science* **285** (1999) pp. 2113-2115.
57. Van Der Voort P. and Vansant E. F., The synthesis of stable, hydrophobic MCM-48/VO_x catalysts, using alkylchlorosilanes as coupling agents for the molecular designed dispersion of VO(acac)₂, *Micropor. Mesopor. Mater.* **38** (2000) pp. 385-390.
58. Van Der Voort P., Morey M., Stucky G. D., Mathieu M. and Vansant E. F., Creation of VO_x surface species on pure-silica MCM-48 using gas-phase modification with VO(acac)₂, *J. Phys. Chem. B* **102** (1998) pp. 585-590.
59. Wu P. and Iwamoto M., Metal-ion-planted MCM-41. Part 3. Incorporation of titanium species by atom-planting method, *J. Chem. Soc., Faraday Trans.* **94** (1998) pp. 2871-2875.
60. Zheng S., Gao L., Zhang Q., Zhang W. and Guo J., Preparation, characterization and photocatalytic properties of singly and doubly titania-modified mesoporous silicate MCM-41 by varying titanium precursors, *J. Mater. Chem.* **11** (2001) pp. 578-583.
61. Ahn W. S., Lee D. H., Kim T. J., Kim J. H., Seo G. and Ryoo R., Post-synthetic preparations of titanium-containing mesoporous molecular sieves, *Appl. Catal. A* **181** (1999) pp. 39-49.

62. Price P. M., Clark J. H. and Macquarrie D. J., Modified silicas for clean technology, *J. Chem. Soc., Dalton Trans* (2000) pp. 101-110.
63. Clark J. H., Price P. M., Martin K., Macquarrie D. J. and Bastock T. W., Environmentally friendly catalysis using supported reagents: enhanced selectivity without loss in activity in the alkylation of benzene using hexagonal mesoporous silica (HMS)-supported aluminium chloride, *J. Chem. Res.* (1997) pp. 430-431.
64. Clark J. H., Monks G. L., Nightingale D. J., Price P. M. and White J. F., A new solid acid-based route to linear alkylbenzenes, *J. Catal.* **193** (2000) pp. 348-350.
65. Sage V., Clark J. H. and Macquarrie D. J., Cationic polymerization of styrene using mesoporous silica supported aluminium chloride, *J. Mol. Catal. A* **198** (2003) pp. 349-358.
66. Zhao X. S., Lu G. Q. and Song C., Mesoporous silica-immobilized aluminum chloride as a new catalyst system for the isopropylation of naphthalene, *Chem. Commun.* (2001) pp. 2306-2307.
67. Zhao X. S., Lu G. Q. and Song C., Immobilization of aluminum chloride on MCM-41 as a new catalyst system for liquid-phase isopropylation of naphthalene, *J. Mol. Catal. A* **191** (2003) pp. 67-74.
68. Choudhary V. and Mantri K., AlCl_3 -grafted Si-MCM-41: Influence of thermal treatment conditions on surface properties and incorporation of Al in the structure of MCM-41, *J. Catal.* **205** (2002) pp. 221-225.
69. Choudhary V., Mantri K. and Jana S. K., Highly selective Si-MCM-41 supported InCl_3 , GaCl_3 , FeCl_3 , and ZnCl_2 catalysts for low temperature esterification of *tert*-butanol by acetic anhydride, *Micropor. Mesopor. Mater.* **47** (2001) pp. 179-183.
70. Hu X., Chuan G. K. and Jaenicke S., Room temperature synthesis of diphenylmethane over MCM-41 supported AlCl_3 and other Lewis acids, *Appl. Catal. A* **217** (2001) pp. 1-9.
71. Hu X., Foo M. L., Chuan G. K. and Jaenicke S., Pore size engineering on MCM-41: Selectivity tuning of heterogenized AlCl_3 for the synthesis of linear alkyl benzenes, *J. Catal.* **195** (2000) pp. 412-415.
72. Anwender R., Palm C., Groeger O. and Engelhard G., Formation of Lewis acidic support material via chemisorption of trimethylaluminum on mesoporous silicate MCM-41, *Organometal.* **17** (1998) pp. 2027-2036.
73. Possemiers K., Impens N. R. E. N. and Vansant E. F., Synthesis of a covalently bound polymeric borazine structure on a mesoporous silica gel, *J. Chem. Soc., Faraday Trans.* **93** (1997) pp. 2309-2314.
74. Huber C., Moller K. and Bein T., Reactivity of a trimethylstannyl molybdenum complex in mesoporous MCM-41, *J. Chem. Soc., Chem. Commun.* (1994) pp. 2619-1620.
75. O'Brien S., Tudor J., Barlow S., Drewitt M. J., Heyes S. J. and O'Hare D., Modification of MCM-41 via ring opening of a strained [1]ferrocenophane, *Chem. Commun.* (1997) pp. 641-642.
76. Liu C.-J., Li S.-G., Wang W.-Q., Che C.-M., Ruthenium porphyrin encapsulated in modified mesoporous molecular sieve MCM-41 for alkene oxidation, *Chem. Commun.* (1997) pp. 65-66.
77. Tudor J. and O'Hare D., Stereospecific propene polymerization catalysis using an organometallic modified mesoporous silicate, *Chem. Commun.* (1997) pp. 603-604.
78. Van Looveren L. K., Geysen D. F., Vercruysse K. A., Wouters B. H., Grobet P. J. and Jacobs P. A., Methylalumoxane MCM-41 as support in the co-oligomerization

- of ethane and propene with $[\{C_2H_4(1\text{-indenyl})_2\}Zr(CH_3)_2]$, *Angew. Chem. Int. Ed. Eng.* **37** (1998) pp. 517-520.
79. Holland B. T., Walkup C. and Stein A., Encapsulation, stabilization, and catalytic properties of flexible metal porphyrin complexes in MCM-41 with minimal electronic perturbation by the environment, *J. Phys. Chem. B* **102** (1998) pp. 4301-4309.
80. Rao R. R., Weckhuysen B. M. and Schoonheydt R. A., Ethylene polymerization over chromium complexes grafted onto MCM-41 materials, *Chem. Commun.* (1999) pp. 445-446.
81. Shyu S.-G., Cheng S.-W. and Tzoi D.-L., Immobilization of $Rh(PPh_3)_3Cl$ on phosphinated MCM-41 for catalytic hydrogenation of olefins, *Chem. Commun.* (1999) pp. 2337-2338.
82. Ernst S. and Selle M., Immobilization and catalytic properties of perfluorinated ruthenium phthalocyanine complexes in MCM-41-type molecular sieves, *Micropor. Mesopor. Mater.* **27** (1999) pp. 355-363.
83. Bleloch A., Johnson B. F. G., Ley S. V., Price A. J., Shephard D. S. and Thomas A. W., Modified mesoporous silicate MCM-41 materials: immobilized perruthenate – a new highly active heterogeneous oxidation catalyst for clean organic synthesis using molecular oxygen, *Chem. Commun.* (1999) pp. 1907-1908.
84. Anwender R., Görlitzer H. W., Gerstberger G., Palm C., Runte O. and Spiegler M., Grafting of bulky rare earth metal complexes onto mesoporous silica MCM-41, *J. Chem. Soc., Dalton Trans.* (1999) pp. 3611-3615.
85. Nagl I., Widenmeyer M., Grasser S., Kohler K. and Anwender R., Surface confined ketyl radicals via samarium(II)-grafted mesoporous silicas, *J. Am. Chem. Soc.* **122** (2000) pp. 1544-1545.
86. Fang M., Wang Y., Zhang P., Li S. and Xu R., Spectroscopic and vapochromic properties of MCM-48-entrapped trisbipyridineruthenium (II), *J. Luminescence* **91** (2000) pp. 67-70.
87. Ferreira P., Goncalves I. S., Kuhn F. E., Pillinger M., Rocha J., Thursfield A., Xue W.-M. and Zhang G., Synthesis and characterization of MCM-41-supported dimolybdenum complexes, *J. Mater. Chem.* **10** (2000) pp. 1395-1401.
88. Melis K., Vos D. D., Jacobs P., Verpoort F., ROMP and RCM catalyzed by $(R_3P)_2Cl_2Ru=CHPh$ immobilized on mesoporous support, *J. Mol. Catal. A* **169** (2001) pp. 47-56.
89. Kim G.-J. and Shin J.-H., The synthesis of new chiral salen complexes immobilized on MCM-41 by grafting and their catalytic activity in the asymmetric borohydride reduction of ketones, *Catal. Lett.* **63** (1999) pp. 205-212.
90. de Rege F. M., Morita D. K., Ott K. C., Tumas W. and Broene R. D., Non-covalent immobilization of homogeneous cationic chiral rhodium-phosphine catalysts on silica surfaces, *Chem. Commun.* (2000) pp. 1797-1798.
91. Abramson S., Lasperas M., Galarneau A., Desplantic-Giscard D. and Brunel D., Best design of heterogenized β -aminoalcohols for improvement of enantioselective addition of diethylzinc to benzaldehyde, *Chem. Commun.* (2000) pp. 1773-1774.
92. Piaggio P., Langham C., McMorn P., Bethell D., Bulman-Page P. C., Hancock F. E., Sly C. and Hutchings G. J., Catalytic asymmetric epoxidation of stilbene using a chiral salen complex immobilized in Mn-exchanged Al-MCM-41, *J. Chem. Soc., Perkin Trans. 2* (2000) pp. 143-148.

93. Clark R. J. and Shannon I. J., Mesoporous immobilized copper bis(oxazoline) complexes for enantioselective catalysis, *Chem. Commun.* (2001) pp. 1936-1937.
94. Wagner H. H., Hausmann H. and Holderich W. F., Immobilization of rhodium diphosphine complexes on mesoporous Al-MCM-41 materials: catalysts for enantioselective hydrogenation, *J. Catal.* **203** (2001) pp. 150-156.
95. Van Rhijn W. M., De Vos D. E., Sels B. F., Bossaert W. D. and Jacobs P. A., Sulfonic acid functionalized ordered mesoporous materials as catalysts for condensation and esterification reactions, *Chem. Commun.* (1998) pp. 317-318.
96. Iengo P., Aprile G., Di Serio M., Gazzoli D. and Santacesaria E., Preparation and properties of new acid catalysts obtained by grafting alkoxides and derivatives on the most common supports. Part III – grafting titanium alkoxides and sulphate derivatives on silica, *Appl. Catal. A* **178** (1999) pp. 97-109.
97. Ghanbari-Siahkali A., Philippou A., Dwyer J. and Anderson M. W., The acidity and catalytic activity of heteropoly acid on MCM-41 investigated by MAS NMR, FTIR and catalytic tests., *Appl. Catal. A* **192** (2000) pp. 57-69.
98. Diaz I., Marquez-Alvarez C., Mohino E., Perez-Pariente J. and Sastre E., Combined alkyl and sulfonic acid functionalization of MCM-41-type silica, *J. Catal.* **193** (2000) pp. 283-294.
99. Diaz I., Mohino E., Perez-Pariente J. and Sastre E., Synthesis, characterization and catalytic activity of MCM-41-type mesoporous silicas functionalized with sulfonic acid, *Appl. Catal. A* **205** (2001) pp. 19-30.
100. Sutta P. and Brunel D., Preparation of MCM-41 type silica-bound manganese(III) Schiff-base complexes, *Chem. Commun.* (1996) pp. 2485-2486.
101. Cauvel A., Renard G. and Brunel D., Monoglyceride synthesis by heterogeneous catalysis using MCM-41 type silicas functionalized with amino groups, *J. Org. Chem.* **62** (1997) pp. 749-751.
102. Macquarrie D. and Jackson D. B., Aminopropylated MCMs as base catalysts: a comparison with aminopropylated silica, *Chem. Commun.* (1997) pp. 1781-1782.
103. Sercheli R., Vargas R. M., Sheldon R. A. and Schuchardt U., Guanidines encapsulated in zeolite Y and anchored to MCM-41: synthesis and catalytic activity, *J. Mol. Catal. A* **148** (1999) pp. 173-181.
104. Zhou X.-G., Yu X.-Q., Huang J.-S., Li S.-G., Li L.-S. and Che C.-M., Asymmetric epoxidation of alkenes catalyzed by chromium binaphthyl Schiff base complex supported on MCM_41, *Chem. Commun.* (1999) pp. 1789-1790.
105. Inagaki Y., Kajita Y., Yoshida H., Ito K. and Hattori T., New basic mesoporous silica catalyst obtained by ammonia grafting, *Chem. Commun.* (2001) pp. 1358-2359.
106. Mercier L. and Pinnavaia T. J., Environmentally friendly catalysis using supported reagents - evolution of a highly-active form of immobilized aluminum-chloride, *Chem. Mater.* **12** (2000) pp. 188-196.
107. Macquarrie D., Jackson D. B., Mdoe J. E. and Clark J. H., Organomodified hexagonal mesoporous silicates, *New J. Chem.* **23** (1999) pp. 539-544.
108. White L. D. and Tripp C. P., Reaction of (3-aminopropyl)dimethylethoxysilane with amine catalysts on silica surfaces, *J. Colloid Interface Sci.* **232** (2000) pp. 400-407.
109. Burkett S. L., Sims S. D. and Mann S., Synthesis of hybrid inorganic-organic mesoporous silica by co-condensation of siloxane and organosiloxane precursors, *Chem. Comm.* (1996) pp. 1367-1368.

110. Macquarrie D. J., Direct preparation of organically modified MCM-type materials. Preparation and characterization of aminopropyl-MCM and 2-cyanoethyl-MCM, *Chem. Commun.* (1996) pp1961-1962.
111. Fowler C. E., Burkett S. L. and Mann S., Synthesis and characterization of ordered organo-silica-surfactant mesophases with functionalized MCM-41-type architecture, *Chem. Commun.* **18** (1997) pp. 1769-1770.
112. Lim M. H., Blanford C. F. and Stein A., Synthesis and characterization of a reactive vinyl-functionalized MCM-41: Probing the internal pore structure by a bromination reaction, *J. Am. Chem. Soc.* **119** (1997) pp. 4090-4091.
113. Richer R. and Mercier L., Direct synthesis of functionalized mesoporous silica by non-ionic alkylpolyethyleneoxide surfactant assembly, *Chem. Commun.* (1998), pp. 1775-1776.
114. Corma A., Jordá J. L., Navarro M. T. and Rey F., One step synthesis of highly active and selective epoxidation catalysts formed by organic-inorganic Ti containing mesoporous composites, *Chem. Commun.* (1998) pp. 1899-1900.
115. Fowler C. E., Lebeau B. and Mann S., Covalent coupling of an organic chromophore into functionalized MCM-41 mesophases by template-directed co-condensation, *Chem. Commun.* (1998) pp. 1825-1826.
116. Mercier L. and Pinnavaia T. J., Functionalized porous clay heterostructure for heavy metal ion (Hg^{2+}) trapping, *Micropor. Mesopor. Mater.* **20** (1998) pp. 101-106.
117. Van Rhijn W. M., De Vos D. E., Sels B. F., Bossaert W. D. and Jacobs P. A. Sulfonic acid functionalized ordered mesoporous materials as catalysts for condensation and esterification reactions, *Chem. Commun.* (1998) pp. 317-318.
118. Bambrough C. M., Slade R. C. T. and Williams R. T., Synthesis of a large pore phenyl-modified mesoporous silica and its characterization by nitrogen and benzene sorption, *J. Mater. Chem.* **8** (1998) pp. 569-571.
119. Brown J., Mercier L. and Pinnavaia T. J., Selective adsorption of Hg^{2+} by thiol-functionalized nanoporous silica, *Chem. Commun.* (1999) pp. 69-70.
120. Bossaert W. D., De Vos D. E., Van Rhijn W. M., Bullen J., Grobet P. J. and Jacobs P. A., Mesoporous sulfonic acids as selective heterogeneous catalysts for the synthesis of monoglycerides, *J. Catal.* **182** (1999) pp. 156-164.
121. Babonneau F., Leite L. and Fontlupt S., Structural characterization of organically-modified porous silicates synthesized using CTA(+) surfactant and acidic conditions, *J. Mater. Chem.* **9** (1999) pp. 175-178.
122. Diaz I., Marquez-Alvarez C., Mohino F., Pérez-Pariente J and Sastre E., Combined alkyl and sulfonic acid functionalization of MCM-41-Type silica - Part 2. Esterification of glycerol with fatty acids, *J. Catal.* **193** (2000) pp. 295-302.
123. Margolese D., Melero J. A., Christiansen S. C., Chmelka B. F. and Stucky G. D., Direct syntheses of ordered SBA-15 mesoporous silica containing sulfonic acid groups, *Chem Mater.* **12** (2000) pp. 2448-2459.
124. Bhaumik A. and Tatsumi T., Organically modified titanium-rich Ti-MCM-41, efficient catalysts for epoxidation reactions, *J. Catal.* **189** (2000) pp. 31-39.
125. Hall S. R., Davis S. A. and Mann S., Cocondensation of organosilica hybrid shells on nanoparticle templates: A direct synthetic route to functionalized core-shell colloids, *Langmuir.* **16** (2000) pp. 1454-1456.

126. Bambrough C. M., Slade R. C. T. and Williams R. T., Steric effects in the sorption of n-butanol and tert-butanol by tailored phenyl-modified porous silicas, *PCCP* **2** (2000) pp. 3499-3502.
127. Mori Y. and Pinnavaia T. J., Optimizing organic functionality in mesostructured silica: direct assembly of mercaptopropyl groups in wormhole framework structures *Chem. Mater.* **13** (2001) pp. 2173-2178.
128. Burleigh M. C., Markowitz M. A., Spector M. S. and Gaber, B. P., Imprinted polysilsesquioxanes for the enhanced recognition of metal ions, *Chem. Mater.* **13** (2001) pp. 2537-2546.
129. Melero J. A., Stucky G. D., Grieken R. and Morales G., Direct syntheses of ordered SBA-15 mesoporous materials containing arenesulfonic acid groups, *J. Mater. Chem.* **12** (2002) pp. 1664-1670.
130. Shen J. G., Herman R. G. and Klier K., Sulfonic acid-functionalized mesoporous silica: Synthesis, characterization, and catalytic reaction of alcohol coupling to ethers, *J. Phys. Chem. B* **106** (2002) pp. 9975-9978.
131. Bibby A. and Mercier L., Mercury(II) ion adsorption behavior in thiol-functionalized mesoporous silica microspheres, *Chem. Mater.* **14** (2002) pp. 1591-1597.
132. Liu N., Assink R. A., Smarsly B. and Brinker C. J., Synthesis and characterization of highly ordered functional mesoporous silica thin films with positively chargeable -NH₂ groups, *Chem. Commun.* (2003) pp. 1146-1147.
133. Beaudet L., Hossain K.-Z. and Mercier L., Direct synthesis of hybrid organic-inorganic nanoporous silica microspheres. 1. Effect of temperature and organosilane loading on the nano and micro-structure of mercaptopropyl-functionalized MSU silica, *Chem. Mater.* **15** (2003) pp. 327-334.
134. Chong A. S. M. and Zhao X. S., Functionalization of SBA-15 with APTES and characterization, *J. Phys. Chem. B* (2003) in press.
135. Chong A. S. M. and Zhao X. S., Functionalization of SBA-15 with organosiloxanes by direct synthesis, unpublished results.
136. Cho Y. S., Park J. C., Lee B., Kim Y., Yi J., *Catal. Lett.* **81** (2002) pp. 89-96.
137. Jang J., Lim B., Lee J., Hyeon T., *Chem. Commun.* (2001) pp. 83-84.
138. Li Z. H., Gong Y. J., Wu D., Sun Y. H., Wang J., Liu Y. and Dong B. Z., *Surf. Interface Anal.* **31** (2001) pp. 897-900.
139. Sassi Z., Bureau J.C. and Bakkali A., *Vib. Spectrosc.* **28** (2002) pp. 251-262.
140. Choi D. and Yang S. J., *J. Colloids Interface Sci.* **261** (2003) pp. 127-132.
141. Walcarius A., Etienne M. and Lebeau B. *Chem. Mater.* **15** (2003) pp. 2161-2173.
142. Zhao D., Feng J., Huo Q., Melosh N., Fredrickson G. H., Chmelka B. F. and Stucky, G. D., *Science* **279** (1998) pp. 548-552

SURFACE ALUMINATION OF MESOPOROUS SILICATES

ROBERT MOKAYA

*School of Chemistry, University of Nottingham, University Park,
Nottingham NG7 2RD, UK*

E-mail: r.mokaya@nottingham.ac.uk

The primary aim of introducing Al onto mesoporous silicates is to create acid and ion exchange sites. The traditional method of preparing mesoporous aluminosilicates is via direct (mixed-gel) synthesis during which an aluminosilicate framework is formed directly from aluminate and silicate ions. An alternative and increasingly popular method of introducing Al onto mesoporous silicates is the so-called post-synthesis alumination, in which the Al is grafted onto an already formed silica framework. This is possible due to the presence of silanol groups on the mesoporous silica pore walls, which act as anchoring sites for the Al. Post-synthesis alumination generates aluminosilicate materials with readily accessible acid or ion exchange sites on the inner walls of the mesoporous framework and generally offers distinct advantages over direct synthesis with respect to accessibility to active sites, structural ordering and stability.

1 Introduction

Mesoporous silicas possess uniform channels of diameter in the range 20Å to 500Å and are synthesised via a mechanism in which supramolecular assemblies of surfactant micelles act as structure directors for the organisation of inorganic silicate precursors [1]. There is currently considerable research interest in the preparation and use of heteroatom containing mesoporous silicas as heterogeneous catalysts, ion exchangers, molecular/supramolecular sieves or templates for the preparation of mesostructured non-silica materials or other nanostructured arrays [1,2]. The incorporation of Al is particularly important as it gives rise to solid acid materials with acid sites associated with the presence of Al in framework positions within the silica pore walls. Mesoporous aluminosilicates have therefore been the focus of many recent studies [3-6], because of their potential application in solid acid/base catalysis and adsorption technology and in particular as acid catalysts for bulk hydrocarbon conversion. The traditional method of introducing Al into mesoporous silicates is by direct (mixed-gel) synthesis during which an aluminosilicate framework is formed directly from aluminate and silicate ions.

An alternative method of introducing Al onto mesoporous silicates is via post-synthesis alumination, in which the Al is grafted onto an already formed silica framework. Silanol groups on the pore walls of the 'host' silica framework act as anchoring sites for the Al. This review covers the developments in post-synthesis alumination of mesoporous silica since the first reports appeared about five years ago. It also contains a brief mention of directly prepared materials and draws comparisons between the two methods of preparing mesoporous aluminosilicates.

2 Direct mixed-gel synthesised mesoporous aluminosilicates

The primary aim of introducing Al onto mesoporous silicas is to create acid sites and ion exchange capacity associated with tetrahedrally coordinated Al located within the aluminosilicate framework. In the case of direct mixed-gel synthesis, once the Al is incorporated into the silica framework, the acid (Bronsted and Lewis) and ion exchange sites are generated via one of two ways; (i) cation exchange of the calcined material with ammonium ions followed by further calcination or (ii) calcination for as-synthesised materials that do not contain any alkali ions. The amount of Al incorporated (usually given by the molar Si/Al ratio) is governed by the concentration of aluminate species in the synthesis gel. Varying the Si/Al ratio can therefore control the number of acid or ion exchange sites generated. In general, the number of acid sites increases with the Al content (or more precisely the accessible tetrahedral Al content). The acid strength tends to be largely independent of the Al content. The acid strength of directly prepared aluminosilicates is generally low and comparable to that of amorphous aluminosilicas.

A number of studies and recent reviews have dealt with the preparation and characterization of direct (mixed-gel) synthesised mesoporous aluminosilicates [3-26]. In general, directly prepared mesoporous aluminosilicates exhibit the highest acidity and catalytic activity for acid catalysed reactions at high Al contents. High Al contents however have the disadvantage of compromising the structural ordering and are usually accompanied by a significant degradation of structural ordering especially after thermal treatments (e.g. calcination during template removal) [7,13-16]. The degradation in structural ordering is usually an indication of poor thermal stability of the aluminosilicate framework and in particular low stability of tetrahedrally co-ordinated (framework) Al. Aluminium in tetrahedral framework positions is crucial for the generation of acid sites. The extent of Al incorporation into framework (as opposed to non-

framework) positions can, to some extent, be controlled since it is dependent of the Al source used [17-26]. Once incorporated into framework positions it is desirable that the Al is stable (especially to thermal and hydrothermal treatments) within tetrahedral positions. The decrease in structural ordering with Al content in mesoporous aluminosilicates is usually accompanied by an increase in the amount of non-framework Al. The increase of non-framework Al is occasioned by dealumination – the extraction of Al from the framework due mainly to local heating effects. Dealumination is associated with a decrease in the ion exchange capacity and the number of Bronsted acid sites.

3 Methods for the surface aluminations of mesoporous silicas

The direct mixed-gel synthesis of mesoporous aluminosilicates suffers from irreproducible preparation routes which result in materials with poor structural ordering and low thermal stability (especially with respect to the stability of Al in framework positions). Another disadvantage of direct mixed-gel synthesis of mesoporous aluminosilicates is that some of the Al is incorporated deep within the pore walls where it is not readily accessible and does not generate acid or ion exchange sites. These disadvantages can be addressed by preparing the mesoporous aluminosilicates via routes which graft Al onto an already prepared silica host matrix. Klinowski and co-workers [27] aluminated pure silica MCM-41 using an aqueous solution of sodium aluminate (NaAlO_2) and obtained materials with framework Si/Al ratio as low as 1.9. ^{27}Al and ^{29}Si magic-angle-spinning (MAS) NMR showed that all the aluminium was incorporated in the framework. Their aluminated materials retained good structural ordering as indicated by well-resolved X-ray diffraction (XRD) patterns. The pore size of the aluminated MCM-41 was observed to decrease at high Al contents. Both the NaAlO_2 concentration and temperature were found to be key variables in the aluminations. Treatment with a concentrated ($>1 \text{ mol l}^{-1}$) solution of NaAlO_2 at ca. 100°C transformed the pure silica MCM-41 into crystalline zeolite Na-A. It is worth noting that due to the presence of Na in the aluminating reagent, these materials required an extra ammonium ion exchange and calcination step to generate acid sites [28].

Two groups independently reported the first preparation of aluminated mesoporous silicates where acid sites were generated simply by calcination without the need for ammonium exchange [29-31]. Mokaya and Jones reported the preparation of Al-containing MCM-41 materials by grafting Al onto purely siliceous MCM-41 [29,30]. The grafting was performed

using aluminium isopropoxide as Al source and hexane as solvent. ^{27}Al MAS NMR and XPS were used to confirm that the Al was incorporated (before and especially after calcination) into the solid framework where it adopted 4-coordinate symmetry as shown in Figure 1. The resulting Al-grafted MCM-41 materials retained the structural ordering (with no loss of long range ordering) and physical properties of the parent pure silica MCM-41 [29,30]. Ryoo and co-workers [31] on the other hand, reported a post-synthesis route, through which various metal elements could be grafted onto pure silica mesoporous frameworks using non-aqueous solutions of various metal salts to obtain mesoporous metallosilicates with superior structural integrity, acidity and catalytic activity compared to equivalent materials prepared via direct mixed-gel synthesis. Calcination of AlCl_3 -grafted MCM-41 yielded mesoporous aluminosilicates with a high proportion of Al in tetrahedral positions as shown in Figure 2.

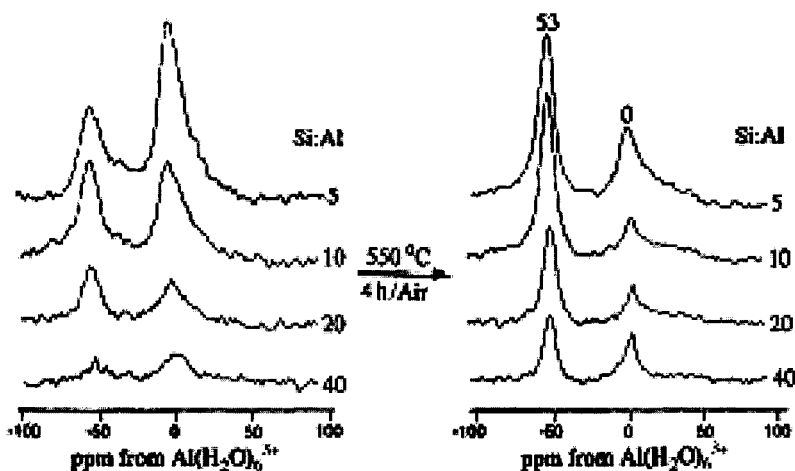


Figure 1. ^{27}Al MAS NMR spectra of dry (left) and calcined (right) Al-grafted MCM-41 materials prepared by reacting pure silica MCM-41 with aluminium isopropoxide in hexane [30].

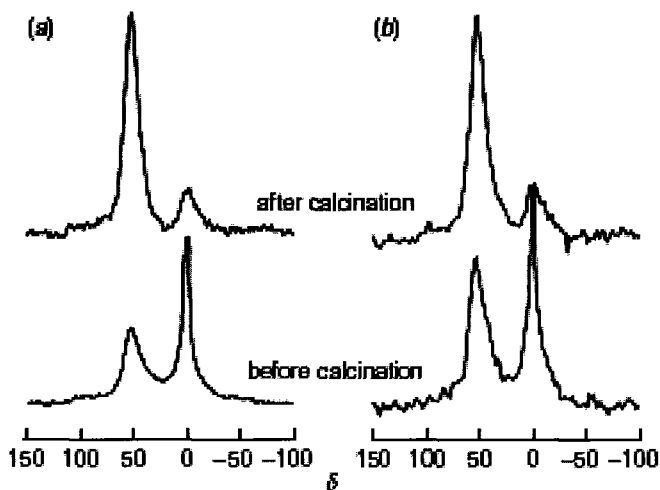


Figure 2. ^{27}Al MAS NMR spectra for Al-grafted samples: (a) Al-MCM-41 ($\text{Si}/\text{Al} = 32$) (b) AIKIT ($\text{Si}/\text{Al} = 33$). The NMR spectra show transitions from octahedral to tetrahedral Al upon calcination [31].

Mokaya and Jones extended post-synthesis alumination of mesoporous silicas to aqueous solutions [32,33]. Aluminosilicate MCM-41 materials were prepared by reacting purely siliceous MCM-41 with dilute aqueous solutions of aluminium chlorohydrate (ACH) [32,33]. The ACH solutions, which contain Al polycations (such as the Al_{13}^{7+} Keggin ion) as the main Al species were found to be an efficient source of Al for alumination of MCM-41. The amount of Al grafted onto the MCM-41 was largely dependent on the concentration of Al in the grafting solution as shown in Table 1. In general, higher concentrations of Al in the grafting solution result in greater Al incorporation. However, the amount of grafted Al levelled off at high ACH concentrations suggesting the existence of a limiting factor, which was thought to be the number of available and accessible silanol groups present on parent MCM-41. The resulting aluminosilicate materials had textural properties similar to those of the parent pure silica MCM-41 (PSMCM) as shown in Table 1. The aluminated samples also retained the structural integrity of the parent pure silica MCM-41 as shown in Figure 3.

Table 1. Elemental composition (Si/Al ratio) and textural properties of pure silica (PSMCM) and Al-MCM-41 materials prepared by post-synthesis alumination of PSMCM using aqueous solutions of aluminium chlorohydrate (ACH) [33].

Sample	[Al] ^a	Si/Al	d_{100} ^b (Å)	Surface Area (m ² /g)	Pore Volume (cm ³ /g)	APD ^c (Å)	a_0 ^d (Å)	WT ^e (Å)
PSMCM			41.2	887	0.85	31.6	47.6	16.0
AlMCM1	0.034	17.0	41.6	793	0.73	30.4	48.0	17.6
AlMCM2	0.12	9.8	42.0	760	0.69	29.3	48.5	19.2
AlMCM3	0.24	7.4	42.5	771	0.70	28.0	49.1	21.1
AlMCM4	0.30	6.5	42.8	767	0.65	26.5	49.4	22.9
AlMCM5	0.48	6.1	43.0	753	0.62	25.8	49.7	23.9

^aConcentration of Al (mol l⁻¹) in grafting ACH solution. ^b d_{100} = basal (100) spacing. ^cAPD = Average Pore Diameter (determined using BJH analysis).

^d a_0 = The lattice parameter from XRD data, using the formula $a_0 = 2d_{100}/\sqrt{3}$. ^eWall thickness, given by $a_0 - \text{APD}$.

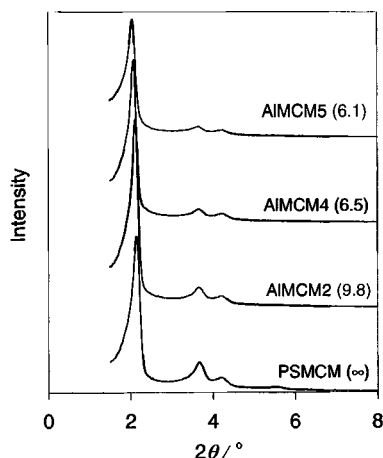


Figure 3. Powder XRD patterns of calcined pure silica MCM-41 (PSMCM) and Al-grafted MCM-41 materials prepared by reaction of PSMCM with an aqueous solution of aluminium chlorohydrate. Values in parenthesis are the Si/Al ratio of the Al-grafted samples [33].

Post-synthesis aluminations are generic and may be applied to all types of mesoporous silicas. For example, Cheng *et al* [34] aluminated pure silica SBA-15 through reaction with aluminum chloride. Al was incorporated into the framework of the SBA-15 with no deterioration in structural ordering. Luan and co-workers [35] performed post-synthesis aluminations of mesoporous silica SBA-15 via three different procedures, i.e., reaction with (i) AlCl_3 in dry ethanol [31] (ii) aluminum isopropoxide in dry hexane [29,30] and (iii) an aqueous solution of sodium aluminate [28]. They evaluated the efficiency of the aluminations and their effect on the pore structure and ion exchange capacity of the resulting Al-SBA-15. They compared the amount of framework and non-framework Al, at various Si/Al ratios for samples prepared via the three aluminations and found that, in general, aluminations by aqueous sodium aluminate was the most effective in grafting the Al into tetrahedral positions. Materials prepared using sodium aluminate however had the disadvantage of the presence of Na, which hindered the generation of acid sites via simple calcination. Aluminations by AlCl_3 in ethanol maintained the mesoporous structure of SBA-15 best. Electron-spin resonance studies revealed that the incorporated Al in the tetrahedral framework serve as ion exchange sites [35]. In a similar comparative study, Chen *et al* [36] prepared Al-MCM-41 materials via post-synthesis aluminations of pure silica MCM-41 using various Al sources, i.e., AlCl_3 , aluminum isopropoxide and NaAlO_2 . They found that irrespective of the preparation method, the surface area, pore diameter, crystallinity and thermal stability of the Al-MCM-41 materials decreased with increasing Al content. The aluminated materials had better thermal stability and could incorporate higher amounts of Al without disintegration of the mesoporous structure compared to Al-MCM-41 prepared by direct synthesis. For example, directly prepared samples did not exhibit mesoporous structural ordering at Si/Al ratios lower than 5 while for post-synthesis aluminations with AlCl_3 or Al isopropoxide it was possible to achieve Si/Al ratios lower than 5 with retention of the mesoporous structure.

Post-synthesis aluminations of pure silica MCM-41 and SBA-15 may also be performed using trimethylaluminum (TMA) as Al source and dry toluene as solvent [37,38]. Sano *et al* found that with TMA as aluminating reagent, Al was easily incorporated (without the need for calcination) into the silica framework of MCM-41 and SBA-15 without severe structural degradation. However, the basal (d_{100}) spacing, surface area and pore volume of the aluminated SBA-15 decreased monotonously with the extent of aluminations (Table 2). The incorporation of Al into tetrahedral

positions was higher for MCM-41 as shown in Figure 4, which compares the ^{27}Al MAS NMR of TMA aluminated, SBA-15 and MCM-41.

Table 2. Characteristics of pure silica SBA-15 and AISBA-15 prepared by post-synthesis alumination with trimethylaluminium (TMA) followed by calcination at 773 K for 5 hours [37].

Sample	[TMA] ^a	Si/Al ^b	d_{100} ^c (nm)	Surface Area (m ² /g)	Pore Volume ^d (cm ³ /g)	Pore Size ^d (nm)	a_0 ^e (nm)	WT ^f (nm)
SBA-15			9.80	770	0.811	6.16	11.31	5.15
AISBA-15	1	14.6	9.52	613	0.693	6.16	10.99	4.83
AISBA-15	2	8.4	9.52	526	0.654	6.16	10.99	4.83
AISBA-15	3	5.7	9.43	457	0.598	6.16	10.89	4.73
AISBA-15	4	4.9	9.43	432	0.585	5.80	10.59	5.09
AISBA-15	5	4.8	9.43	410	0.564	5.80	10.89	5.09

^a Amount of TMA (mmol) in alumination mixture. ^b Bulk Si/Al determined by X-ray fluorescence. ^c d_{100} = basal (100) spacing. ^d Determined by the Dollimore-Heal method. ^e a_0 = Lattice parameter from SAXS data, using the formula $a_0 = 2d_{100}/\sqrt{3}$. ^f Wall thickness = a_0 – pore size

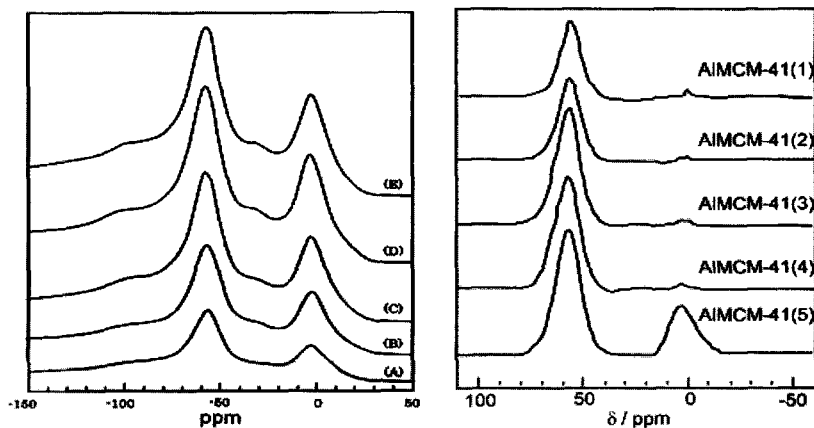


Figure 4. ^{27}Al MAS NMR spectra for TMA-grafted SBA-15 (left) and MCM-41 (right). For SBA-15; (A) 1 mmol TMA, Si/Al = 14.6, (B) 2 mmol TMA, Si/Al = 8.4, (C) 3 mmol TMA, Si/Al = 5.7, (D) 4 mmol TMA, Si/Al = 4.9, (E) 5 mmol TMA, Si/Al = 4.8 and for MCM-41; (1) 1 mmol TMA, Si/Al = 14.3, (2) 2 mmol TMA, Si/Al = 9.0, (3) 3 mmol TMA, Si/Al = 6.3, (4) 4 mmol TMA, Si/Al = 4.3 and (5) 5 mmol TMA, Si/Al = 4.0 [37,38].

Dwyer and co-workers [39] carried out a detailed study of the vapour phase alumination (using AlCl_3 vapour) of pure silica MCM-41 and compared the resulting materials with directly prepared Al-MCM-41. Al was successfully incorporated into pure silica MCM-41 via post-synthesis reaction with AlCl_3 vapour as grafting reagent. ^{27}Al and ^{29}Si MAS NMR studies indicated that presence of both framework and extra-framework Al sites in the AlCl_3 vapour aluminated samples. Ryoo and co-workers [40] prepared three different types of Al-containing materials, KIT-1, MCM-41 and MCM-48 in which the Al was incorporated by various routes such as direct syntheses, grafting of the Al species with anhydrous AlCl_3 , and impregnation with an aqueous solution of AlCl_3 . ^{27}Al MAS NMR spectroscopy indicated that, for impregnated samples, the co-ordination of Al sites lost tetrahedral symmetry upon complete dehydration, suggesting the possible existence of three-coordinated Al catalytic sites.

Mokaya investigated the effect of particle size on the post-synthesis alumination of pure silica MCM-41 [41]. Aluminosilicate MCM-41 materials derived from pure silica MCM-41 materials of varying particle size were prepared via post-synthesis grafting routes. Particle size was found to have no effect on the take-up and retention of Al (similar Si/Al molar ratios were obtained for various particle sizes) but influenced the distribution of Al with larger particles having a higher concentration of surface Al. Small particles were therefore 'penetrated' by Al to a much greater extent than large particles. Physical characterisation (XRD and N_2 sorption studies) indicated that particle size played a key role in determining whether or not structural integrity is retained after Al insertion; large particle pure silica MCM-41, with long range ordering, was more likely to retain structural ordering and retain textural properties after Al insertion. The acid content (and therefore proportion of Al sites giving rise to acid sites) was, however, higher in smaller particle samples than in large particle samples. However particle size had no effect on acid strength. The activity for acid catalysed reactions (cracking of cumene) was higher for small particle samples. This was attributed to the higher efficiency with which reactant and product molecules access or exit the shorter pores in small particles as opposed to the longer (one-dimensional for MCM-41) pores in the larger particles.

The temperature at which alumination is performed is also an important factor which influences the properties of resulting mesoporous aluminosilicates. Mokaya [42] probed the influence of temperature on the alumination process. Al-grafted MCM-41 materials were obtained by reacting pure silica MCM-41 with aqueous solutions of aluminium chlorohydrate (ACH) at either room temperature (RT) or 80°C [42]. The

grafting temperature was found to have a profound effect on physical, chemical and catalytic properties. Good retention of structural integrity was achieved after grafting at 80°C while materials prepared at RT suffered much greater structural degradation. Incorporation of Al was up to four times higher at 80°C than at RT. The large variation between the amounts of Al incorporated at 80°C and RT was ascribed to differences in the mobility of the rather bulky Al species found in ACH solutions. The higher Al content of materials grafted at 80°C translated to higher acid content and higher total conversions for the cracking of cumene. However the catalytic activity per active site (TOF values) was higher for RT grafted materials presumably due to better site isolation occasioned by a lower Al content [42].

Alumination of mesoporous silicas via post-synthesis grafting procedures in aqueous or non-aqueous media normally results in uniform incorporation of Al with little control of its spatial distribution. Increasing the Al content in the alumination gel generally results in a uniform increase in the amount of incorporated Al throughout the surface of the entire sample. Using a template-directed alumination procedure, Mokaya [43] described an unusual stepwise alumination procedure in which increasing proportions of pure silica MCM-41 are aluminated depending on the amount of Al available in the alumination gel. In the so-called template-directed alumination of MCM-41, the Al was introduced onto pure silica MCM-41 during secondary synthesis (i.e., recrystallisation). The extent of alumination, up to full alumination, increased with the amount of Al in the recrystallisation gel. Evidence from several characterisation techniques indicated that during the recrystallisation in the presence of an Al source, the proportion of aluminated MCM-41 increased with increase in the content of Al in the recrystallisation gel and that beyond a certain gel Si/Al ratio (determined by synthesis conditions) the whole sample was aluminated. The findings hinted at the possibility of full alumination a portion of the pores of pure silica MCM-41 before alumination of other pores has started resulting in an apparently mixed-phase material with clearly defined basal spacings as shown in Figure 5 [43].

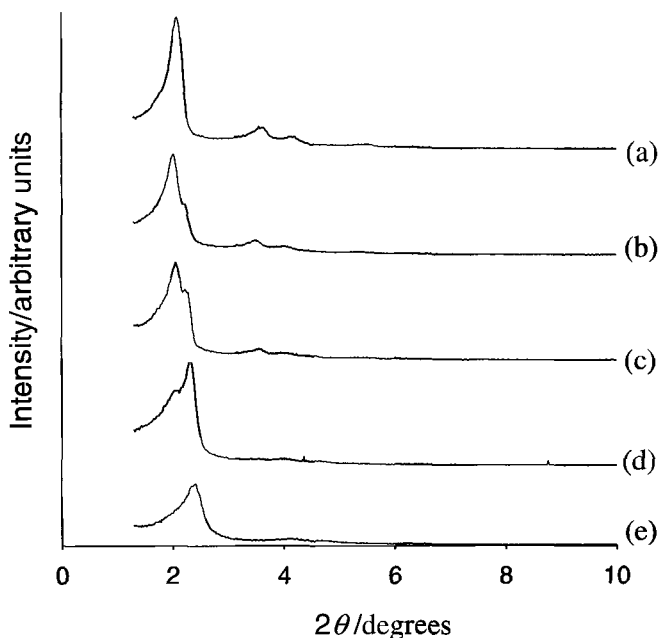


Figure 5. Powder XRD patterns of (a) pure silica Si-MCM-41 and recrystallised (b) Al-MCM41-80, Si/Al = 40.1; (c) Al-MCM41-40, Si/Al = 28.3; (d) Al-MCM41-20, Si/Al = 16.9 and (e) Al-MCM41-10, Si/Al = 8.8, materials [43].

Mesoporous aluminosilicates prepared via surface alumination tend to have significant amounts of extra-framework Al (EFAL). Reinsertion of such EFAL into the framework is desirable. Indeed the reinsertion of EFAL into framework positions is a well-known phenomenon for dealuminated Y zeolites and is achieved via, for example, hydrothermal treatment of the zeolite in an aqueous solution of KOH [44]. However, such treatment is not feasible for mesoporous aluminosilicates because it is too severe. The relatively fragile mesoporous frameworks would readily dissolve in the highly basic (pH = 13.5) KOH solution. Mokaya [45] reported on a modified 'insertion' method suitable for mesoporous aluminosilicates. The method allowed for virtually all octahedrally coordinated (extra-framework) Al in calcined Al-grafted MCM-41 materials (designated CAP5, Si/Al = 4.6 and CAH5, Si/Al = 4.7) to be inserted into (tetrahedral) framework positions as shown in Figure 6. The method involved treatment of the Al-grafted materials with an aqueous solution of NH_4OH (pH ~ 11.1) and could be performed at either room temperature

(30°C) or at a range of temperatures up to 80°C. The insertion of EFAL into the Al-grafted MCM-41 framework increased the proportion of tetrahedrally coordinated Al with a concomitant increase in acidity and ion exchange capacity [45].

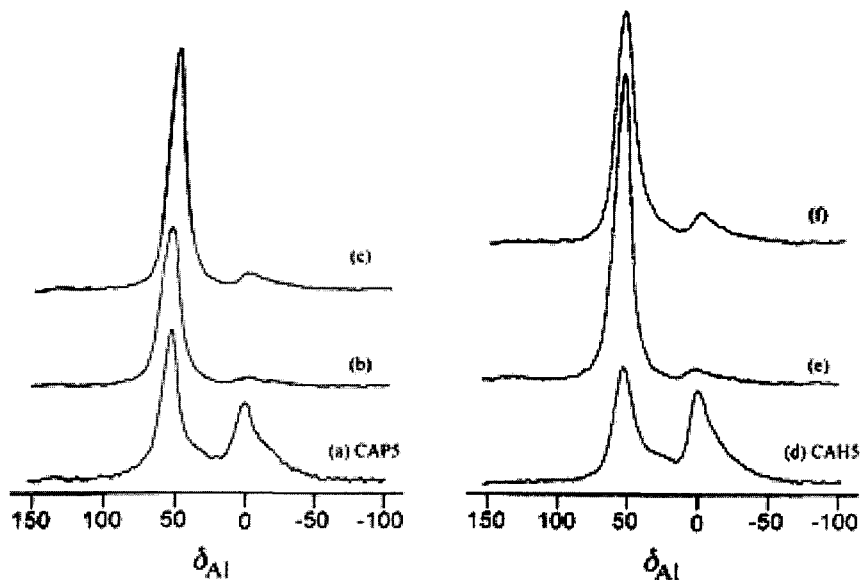


Figure 6. ^{27}Al MAS NMR spectra of Al-grafted materials before and after treatment with NH_4OH ; (a) CAP5, (b) CAP5 treated at 30°C, (c) CAP5 treated at 80°C, (d) CAH5, (e) CAH5 treated at 30°C and (f) CAH5 treated at 80°C [45].

Post-synthesis alumination has been extended to a new class of materials known as porous clay heterostructures (PCH) [46,47]. PCH are obtained by introducing a surfactant template into the interlayer region of clays (monmorillonites or saponites) and subsequently polymerizing a silica source around them to obtain a mesostructured silica framework within the clay inter-gallery region. Pinnavaia and co-workers [46] performed post-synthesis grafting of Al into the intragallery silica framework of a PCH precursor derived from a synthetic saponite clay. The resulting aluminated PCH materials exhibited basal spacings of 32–34.8 Å, surface areas of 623–906 m^2/g , pore volumes of 0.32–0.45 cm^3/g , and pore sizes in the 14–25 Å range. The Al content was determined by the Si/Al ratio of the alumination mixture. Nearly all of the grafted Al was

incorporated into tetrahedral sites in the intragallery silica framework. Sodium aluminate was found to be more effective (compared to aluminum chloride) for achieving higher loading of tetrahedral Al without forming (extra-framework) octahedral Al or collapsing the intercalated galleries. However the best retention of textural properties was achieved when the alumination was carried out under acidic conditions using aqueous AlCl_3 as the aluminum source. On the other hand, Vansant *et al* [47] performed post-synthesis grafting of Al onto montmorillonite-PCH using an aluminium acetylacetonate complex as grafting reagent followed by a calcination step to anchor the Al. In this way, Brønsted acid sites, that were stable to thermal treatment at 300°C, were created.

4 Acidity and catalytic activity of Al-grafted mesoporous silicates

Early studies on Al-MCM-41 materials prepared by grafting Al onto pure silica MCM-41 [29-33] found that the materials exhibited considerable Brønsted acidity. An example is shown in Figure 7 [30]. The acid content in the Al-grafted MCM-41 materials was attributed to the presence of Brønsted acid generating Al in accessible sites on (rather than within) the pore walls [30,33]. The Al-grafted MCM-41 also possessed considerable catalytic activity for the cracking of cumene as shown in Figure 8 for ACH-grafted materials [33]. Chen and co-workers [36] prepared Al-MCM-41 materials via post-synthesis alumination of pure silica MCM-41 using various Al sources, i.e., AlCl_3 , aluminum isopropoxide and sodium aluminate and compared their acidity to that of direct mixed-gel synthesised materials. The aluminated Al-MCM-41 had moderate acidity, comparable to that of the directly synthesized material. The acidity and catalytic activity of the aluminated materials are compared in Table 3. Dwyer *et al* [39] on the other hand investigated vapour phase alumination of MCM-41. Over a similar range of Al content, the concentration of both Brønsted and Lewis acid sites (accessible to pyridine) was higher for the aluminated materials compared to directly prepared samples. This was reflected in catalytic activity, which was also higher for the post-synthesis aluminated MCM-41 materials [39].

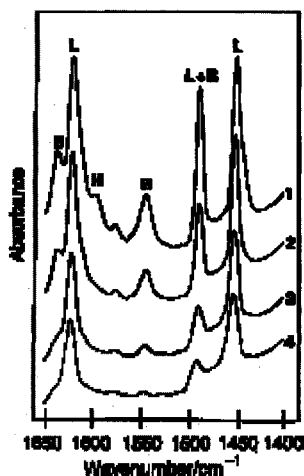


Figure 7. IR spectra of pyridine adsorbed on Al-grafted (using aluminium isopropoxide as Al source and hexane as solvent) MCM-41 (Si/Al = 6.1) following pyridine adsorption and thermal treatment at (1) 100°C, (2) 200°C, (3) 300°C and (4) 400°C. H denotes hydrogen-bonded pyridine; B Brønsted bound pyridine; L Lewis bound pyridine [30].

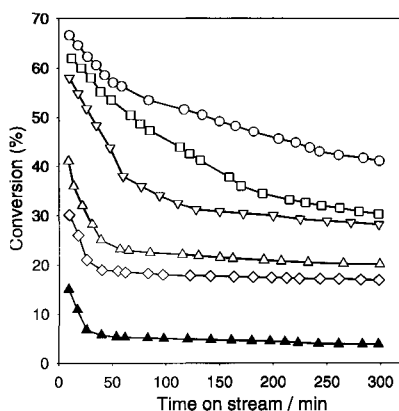


Figure 8. Deactivation behaviour during cumene conversion over Al-MCM samples and a reference material (ACH-grafted (0.24 mol l^{-1}) amorphous silica, AlSA, Si/Al = 9.9) at 300°C. AIMCM5, Si/Al = 6.1, (o); AIMCM4, Si/Al = 6.5, (\square); AIMCM3, Si/Al = 7.4, (∇); AIMCM2, Si/Al = 9.8, (Δ); AIMCM1, Si/Al = 17.0, (\diamond) and AlSA (\blacktriangle) [33].

Table 3. Acidity of various Al-containing MCM-41 samples and correlation with cumene activity at 300°C [36].

Sample no.	Si/Al	Bronsted acidity ($\mu\text{mol g}^{-1}$)	Lewis acidity ($\mu\text{mol g}^{-1}$)	Total acidity ($\mu\text{mol g}^{-1}$)	Cumene conv. (%)
Direct synthesis					
1	15.3	37.7	78.9	116.6	39.1
2	7.3	78.7	116.1	194.8	46.4
3	5.0	92.2	148.8	241.1	54.8
AlCl ₃ grafted					
6	6.4	79.6	117.8	197.4	40.9
7	4.9	69.9	119.8	189.7	33.8
8	1.3	30.8	132.4	163.2	25.4
Al-isopropoxide grafted					
9	11.8	0.5	28.6	28.6	2.5
10	3.3	5.6	100.8	106.4	33.1
11	1.3	64.5	95.7	160.4	41.8
NaAlO ₂ grafted					
12	3.2	78.1	93.8	171.9	49.7
Al(NO ₃) ₃ grafted					
13	62.7	28.6	88.5	117.1	19.5

The IR spectra of the pyridine adsorbed on TMA aluminated AlMCM-41 (Si/Al = 6.3) and protonated mordenite (MOR, Si/Al = 7.7) after evacuation at various temperatures is shown in Figure 9 [38]. The TMA aluminated MCM-41 was found by Sano and co-workers to have both Bronsted and Lewis acid sites [38]. The Bronsted acid sites of TMA aluminated MCM-41 were fewer and weaker than those of mordenite [38]. The catalytic activity of TMA aluminated MCM-41 was lower than that of mordenite and the rate of deactivation was also lower for the MCM-41 as shown in Figure 10. Sano and co-workers also compared the acidity and catalytic activity of Al-SBA-15 and Al-MCM-41 obtained via aluminations with TMA [37]. Data from cumene cracking and pyridine adsorption experiments, shown in Figure 11 and 12, indicated that the Bronsted acid sites of Al-SBA-15 prepared via aluminations with TMA were stronger than those of Al-MCM-41 prepared by the same method.

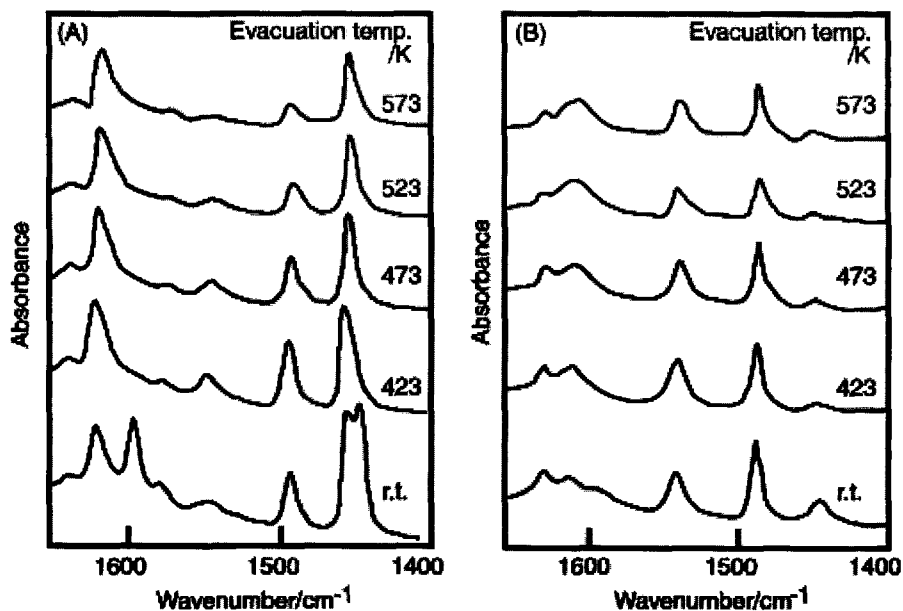


Figure 9. IR spectra of pyridine adsorbed on (A) TMA-grafted Al-MCM-41 ($\text{Si}/\text{Al} = 6.3$) and (B) mordenite ($\text{Si}/\text{Al} = 7.7$) at various evacuation temperatures [38].

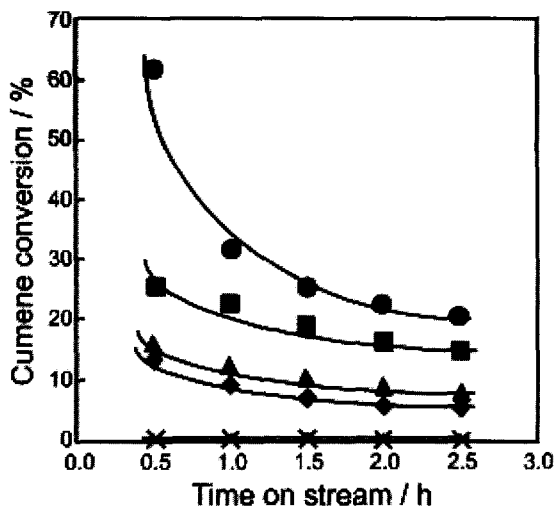


Figure 10. Conversion profiles of cumene on various TMA-grafted Al-MCM-41 samples and mordenite ($\text{Si}/\text{Al} = 7.7$). Reaction conditions: Temperature = 623 K, $\text{W}/\text{F} = 0.20$ h, (X) parent pure silica MCM-41; (◆) Al-MCM-41(1), $\text{Si}/\text{Al} = 14.3$; (▲) Al-MCM-41(2), $\text{Si}/\text{Al} = 9.0$; (■) Al-MCM-41(3), $\text{Si}/\text{Al} = 6.3$ and (●) mordenite [38].

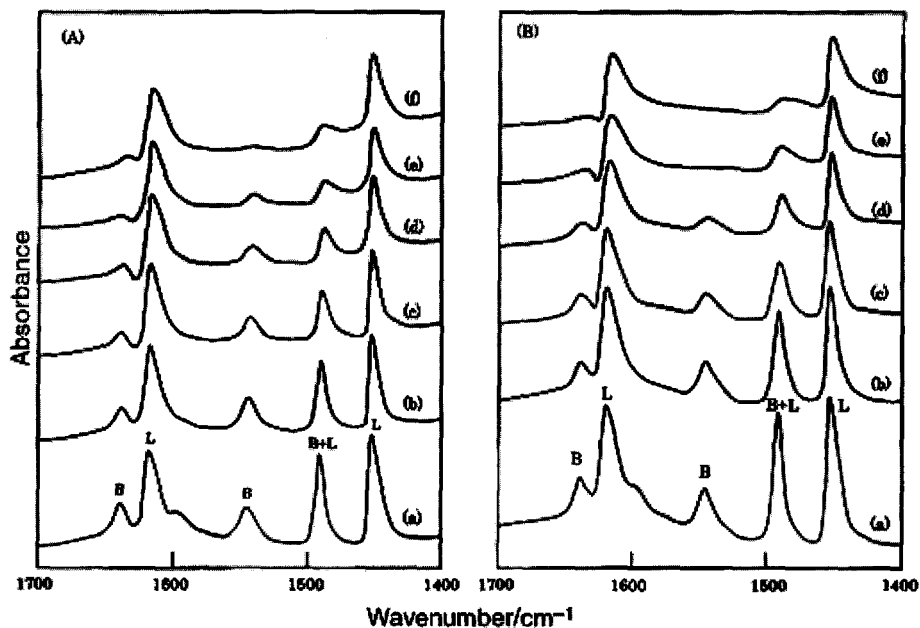


Figure 11. IR spectra of pyridine adsorbed on TMA-grafted (A) AlSBA-15 ($\text{Si}/\text{Al} = 5.7$) and (B) Al-MCM-41 ($\text{Si}/\text{Al} = 6.3$) at various evacuation temperatures. (a) 423 K, (b) 473 K, (c) 523 K, (d) 573 K, (e) 623 K and (f) 673 K. B and L denote Brønsted and Lewis-bound pyridine respectively [37].

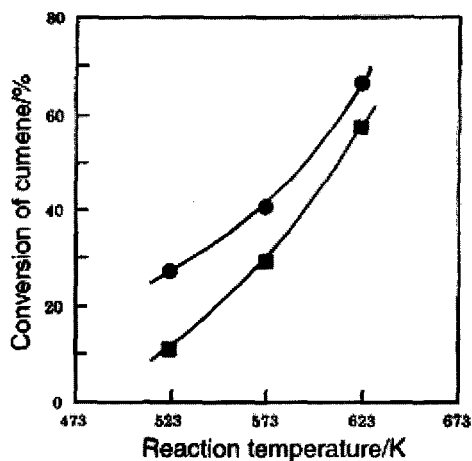


Figure 12. Initial activity for conversion of cumene at various reaction temperatures on TMA-grafted Al-SBA-15 ($\text{Si}/\text{Al} = 5.7$), (●) and Al-MCM-41 ($\text{Si}/\text{Al} = 6.3$), (■). Reaction conditions: $W/F = 0.20$ h, nitrogen carrier gas flow rate = 40 ml min^{-1} [37].

Ryoo and co-workers [40] studied the Friedel-Crafts alkylation of benzene, toluene, and *m*-xylene with benzyl alcohol over three different types of materials, KIT-1 (disordered three-dimensional channel network), MCM-41 (hexagonal packing of one-dimensional channels), and MCM-48 (cubic Ia3d structure composed of two independent three-dimensional channel systems). Aluminum was incorporated into the mesoporous materials by various routes such as direct syntheses, grafting of the Al species with anhydrous AlCl_3 , and impregnation with an aqueous solution of AlCl_3 . Post-synthesis impregnation was found to be the most effective method of generating catalytic activity. A series of Al-SBA-15 materials with different Si/Al ratios were prepared via a post-synthesis alumination using aluminium isopropoxide in dry hexane by Nie and co-workers [48]. Al was incorporated into the SBA-15 framework to generate acid sites of medium strength. The number of acid sites generated were dependent on the amount of Al incorporated, i.e., acid content increased with decreasing Si/Al ratio. The Al-grafted SBA-15 samples were impregnated with 1% Pt and used for the hydroisomerisation of *n*-dodecane. The catalytic data indicated that Al-grafted SBA-15 was a suitable material as acid component for bifunctional catalysts, which may be used for the hydroisomerization of long chain *n*-paraffins [48].

Post-synthesis alumination of so-called porous clay heterostructures (PCH) generates Bronsted acid sites that increase in number as the Si/Al ratio decreases. The Al-grafted PCH derivatives were reported by Pinnavaia *et al* [46] to exhibit high catalytic activity for cumene cracking in comparison to the parent non aluminated PCH. It is interesting to note that the acidity and catalytic activity of direct mixed-gel synthesised mesoporous aluminosilicates can also be improved further by grafting of more Al. For example, Bastardo-Gonzalez and co-workers [49] prepared primary amine templated Al-MMS (Al-HMS) mesoporous aluminosilicates and then subjected them to alumination using ACH as Al source. In addition to decreasing the pore size, Al-grafting increased the acid content and catalytic activity as shown in Table 4. The increase in acid content after Al grafting was greatest (~ 60%) for the 'parent' sample with the least initial Al content (Al-MMS40) and lowest for Al-MMS10 (~ 12%) which had a much higher initial Al concentration. The introduction of extra Al created new acid sites. This was possible since the parent Al-MMS materials possessed exposed and accessible silanol groups, which acted as anchoring points for the extra Al. The samples grafted with extra Al (i.e., AlAl-MMS samples in Table 4) were more active than their corresponding Al-MMS samples for the conversion of cumene. The increase in activity for cumene conversion after grafting mirrored the increases in Al content

and acidity. Furthermore since the cumene was converted to benzene and propene (which occurs on Bronsted acid sites), it was inferred that there was an increase in the number of Bronsted acid sites after grafting. A different reaction, the alkylation of toluene with benzyl chloride indicated that, Al-grafting also increased the number of Lewis acid sites [49].

Table 4. Elemental composition, acid content and catalytic activity of primary amine templated mesoporous aluminosilicates before (Al-MMSX) and after (AlAl-MMSX) grafting with extra Al [49].

Sample	Si/Al	Acid content (mmol H ⁺ /g)	Cumene conv. (%)	
			50 min.	150 min.
Al-MMS40	39.0	0.36	35	28
AlAl-MMS40	22.8	0.57	53	47
Al-MMS20	22.0	0.56	47	41
AlAl-MMS20	14.9	0.75	59	54
Al-MMS10	9.0	0.73	59	51
AlAl-MMS10	7.4	0.82	67	60

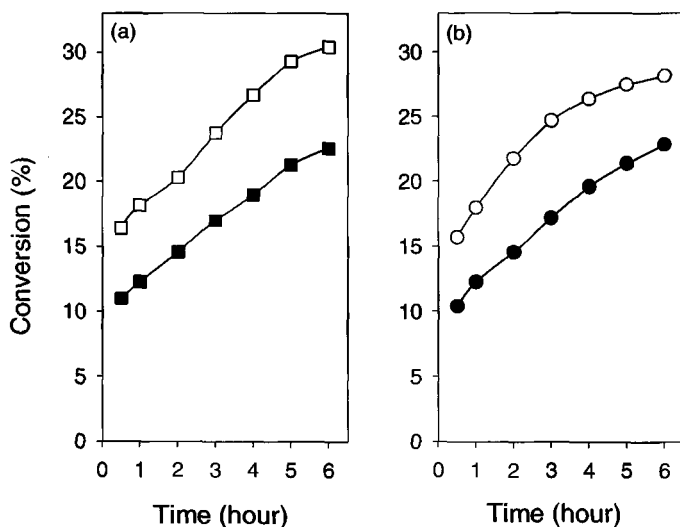


Figure 13. Conversion as a function of reaction time in the alkylation of toluene using (a) benzyl alcohol and (b) benzyl chloride on a primary amine templated mesoporous aluminosilicate before, Al-MMS20, (dark symbols, ■ and ●) and after, AlAl-MMS20, (open symbols, □ and ○) grafting with extra Al [49].

5 Stability of Al-grafted mesoporous aluminosilicates

Aluminosilicate MCM-41 materials prepared by post-synthesis alumination using aluminium chlorohydrate (ACH) were found to exhibit high mechanical and hydrothermal stability as shown in Table 5 [32]. Compaction at 185 MPa did not have any significant effect on the textural properties of an ACH-grafted sample, AIMCM4 (Si/Al = 6.5). Compaction at 370 MPa resulted in a 29% decrease in surface area and 25% decrease in pore volume. The mechanical stability was considered remarkable given that pure silica MCM-41 is destroyed at a compaction pressure of 224 Mpa [50]. Steaming of ACH-grafted AIMCM5, (Si/Al = 6.1), at 750°C for 4 hours decreased the surface area and pore volume by only 25%. Refluxing of AIMCM5 in boiling water for 16 hours had virtually no effect on textural properties [32]. The enhanced mechanical and hydrothermal stability of the ACH-grafted materials was attributed to recrystallisation effects, involving the grafted Al, which act to heal defect sites in the structure of the parent pure silica MCM-41.

Table 5. Basal (d_{100}) spacing and textural properties ACH-grafted MCM-41 materials before and after compaction at high pressure or various hydrothermal treatments [32].

Sample	d_{100} (Å)	Surface Area (m ² /g)	Pore Volume (cm ³ /g)	APD (Å)	a_0 (Å)	WT (Å)
AIMCM4 (Si/Al = 6.5)	42.8	767	0.65	26.5	49.4	22.9
AIMCM4 (185 Mpa) ^a		755	0.57	27.4		
AIMCM4 (370 Mpa) ^a		547	0.49	28.5		
AIMCM4 (740 Mpa) ^a		284	0.26	30.6		
AIMCM5 (Si/Al = 6.1)	43.0	753	0.62	25.8	49.7	23.9
ST-AIMCM5 ^b		558	0.45	22.6		
REF-AIMCM5 ^c		834	0.70	24.9		

APD = Average Pore Diameter (from BJH analysis). a_0 = The lattice parameter, from the XRD data using the formula $a_0 = 2d_{100}/\sqrt{3}$. WT = Wall thickness = a_0 - APD. ^aSample AIMCM4 compressed at the pressures shown in parenthesis. ^bSample AIMCM5 steamed at 750°C for 4 hours. ^cSample AIMCM5 refluxed in distilled water for 16 hours.

An interesting observation was that after steaming at high temperature (750°C), the steamed ACH-grafted MCM-41 samples possessed (on the evidence from catalytic activity for cumene cracking) stronger Brønsted acid sites compared to the parent materials [32]. The acid content of a steamed ACH-grafted sample, ST-*Al*MCM5 was 0.257 mmol H⁺/g compared to 0.605 mmol H⁺/g for parent *Al*MCM5 (Si/*Al* = 6.1). However, despite the lower acid content, the conversion of cumene was higher for the steamed sample; ST-*Al*MCM5 had an initial rate (in mmol/g/hr and taken at 10 min time on stream) of 1.225 compared to a rate of 0.843 for *Al*MCM5. This corresponded to an apparent turnover frequency (TOF) of 4.75 over ST-*Al*MCM5 and 1.4 over *Al*MCM5. This result indicated that acid sites on the steamed sample (though fewer in number) were stronger than those on the non-steamed *Al*MCM5 sample.

Aluminosilicate MCM-41 materials with remarkable stability and enhanced acidity and catalytic activity were prepared via a combination of post-synthesis alumination and hydrothermal treatment [51]. The materials were prepared via two methods involving the reaction of pure silica MCM-41 with aqueous aluminium chlorohydrate (ACH) solution (the 'wet' grafted sample CAH5, Si/*Al* = 6.1) or with aluminium isopropoxide in non-aqueous (hexane) media ('dry' grafted sample CAP10, Si/*Al* = 9.8). Both CAH5 and CAP10 exhibited well-resolved higher order (110), (210), and (200) peaks and retained most of their textural properties after boiling in water for 150 hours as shown in Table 6 and Figure 14. There were no significant changes in *d*₁₀₀ spacing after the hydrothermal treatments. Nitrogen sorption isotherms (Figure 15) indicated that the mesoporous structure of CAH5 and CAP10 was maintained after refluxing in water for 48 hours. The pore size distribution of CAH5 and CAP10 was broadened after exposure to boiling water for 150 hours. Refluxing in distilled water was beneficial with regard to the use of the *Al*-grafted materials (CAH5 and CAP10) as solid acid catalysts. The amount of *Al* per unit mass of material was higher for the refluxed samples and increased with the extent of refluxing. This was accompanied by a considerable increase in acid content for the refluxed samples, which was manifested in higher catalytic activity for the cracking of cumene as shown in Table 6 [51]. The increase in *Al*/Si ratio of CAH5 and CAP10 was attributed to the dissolution of non-framework silica during the hydrothermal treatment. Consistent with elemental analysis, an increase in the *Al* concentration on the framework walls was observed by XPS analysis. ²⁷*Al* NMR also was used to verify the nature of *Al* in the *Al*-grafted samples before and after refluxing and indicated that most of the *Al* remained in tetrahedral position [51].

Table 6. Elemental composition, textural properties, acidity and catalytic activity of Al-grafted materials before and after various hydrothermal treatments [51].

Sample	Si/Al	Surface Area (m ² /g)	Pore Volume (cm ³ /g)	APD ^a (Å)	WT ^b (Å)	Acidity ^c	Cumene conv. ^d
CAH5	6.1	753	0.62	25.8	23.9	0.88	0.98
CAH5-R16	5.1	834	0.70	24.9	23.4	1.25	1.33
CAH5-R48	4.5	902	0.70	26.8	22.2	1.38	1.34
CAH5-R150	4.2	724	0.65	31.0	19.1	1.29	1.32
CAP10	9.8	850	0.76	30.9	16.9	0.63	0.64
CAP10-R16	8.1	894	0.81	31.0	16.3	1.18	1.29
CAP10-R48	7.1	864	0.80	32.5	16.6	1.28	1.32
CAP10-R150	6.5	810	0.77	33.7	15.5	1.30	1.36

^aAPD = Average Pore Diameter (obtained using BJH analysis of the desorption isotherm). ^bWall thickness = lattice parameter (a_0) - APD, where a_0 was obtained from the XRD data using the formula $a_0 = 2d_{100}/\sqrt{3}$. ^cMmol H⁺ per gram of sample. ^dCumene cracking rate, in mmol (g catalyst)⁻¹ h⁻¹, after 20 min time on stream. Total conversion equals a rate of 1.52. Under similar conditions the conversion rate over USY zeolite (CBV 740, Si/Al = 21) and HY zeolite (Si/Al = 3.6) was 1.34 and 0.54 respectively.

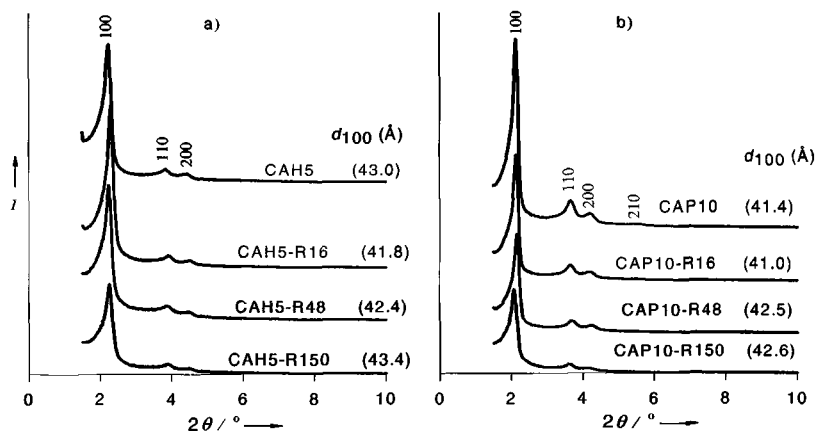


Figure 14. X-Ray diffraction patterns of (a) ‘wet’-grafted, CAH5 and (b) ‘dry’-grafted, CAP10 mesoporous aluminosilicates before and after various hydrothermal treatments in boiling water. The R values indicate the time in hours that the sample was exposed to boiling water [51].

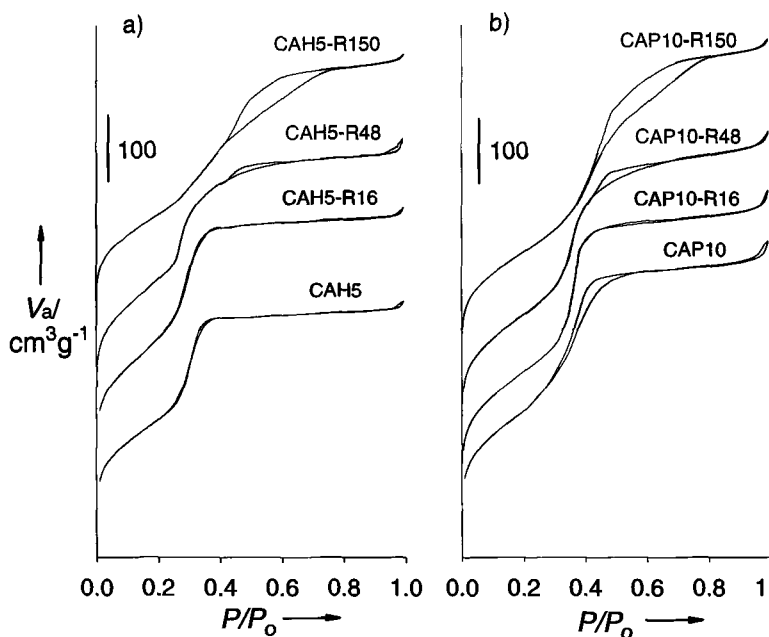


Figure 15.4 Nitrogen sorption isotherms for (a) 'wet'-grafted CAH5 and (b) 'dry'-grafted CAP10 mesoporous aluminosilicates before and after various hydrothermal treatments in boiling water [51].

Mesoporous aluminosilicate MCM-41 with improved steam stability may also be prepared by grafting Al onto pure silica MCM-41 materials that possess thick pore walls. Mokaya reported that Al-grafted MCM-41 prepared from pure silica MCM-41 with thick pore walls was hydrothermally more stable than materials with thinner pore walls as shown in Figure 16 [52]. Pure silica MCM-41 synthesised at 145°C and a reaction time of 96 hours (with walls 2.2 nm thick) gave Al-grafted MCM-41 with the best hydrothermal stability. As shown in Figure 16c, the exposure of the resulting Al-grafted material to steaming at 800 and 900°C for 4 h did not significantly alter the XRD pattern [52]. As indicated by the nitrogen sorption isotherms shown in Figure 16, the sample steamed at 800°C still exhibited a relatively sharp mesopore filling step. Upon steaming at 900°C, 68% of the initial surface area and 50% of the initial pore volume was retained. The improved hydrothermal stability was attributed to the combination of thicker pore walls and improved framework crosslinking prior to Al grafting. The improvement in structural steam stability was accompanied by a higher retention of acidity, which is important for the use of these materials as solid acid catalysts [52].

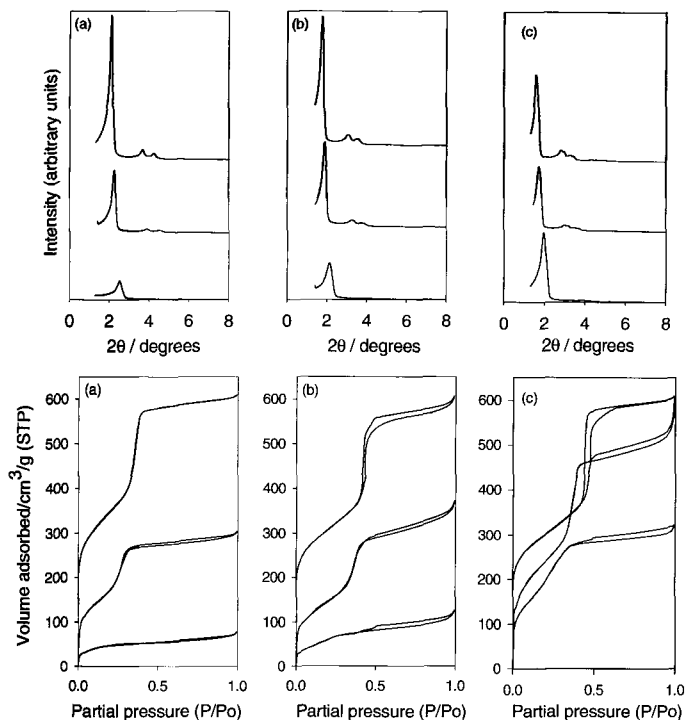


Figure 16. Powder XRD patterns and nitrogen sorption isotherms for Al-grafted MCM-41 samples after calcination (top curves) and before and after hydrothermal treatments at 800 (middle curves) and 900 °C (bottom curves); the parent pure silica MCM-41 materials were prepared at (a) 150 °C, 48 h, (b) 140 °C, 96 h, and (c) 145 °C, 96 h [52].

The post-synthesis alumination pathway is a critical factor in determining the steam stability of Al-grafted MCM-41 [53,54]. Remarkable improvements in steam stability that can be achieved by careful choice of the alumination pathway and materials that exhibit high temperature hydrothermal stability, which is unprecedented for Al-MCM-41, have been prepared [53,54]. Al-grafted MCM-41 materials prepared via supercritical fluid mediated alumination of pure silica MCM-41 or via so-called ‘dry’ grafting (i.e., pure silica MCM-41 grafted with Al in hexane) exhibit remarkably higher steam stability compared to materials grafted in aqueous media [54]. The order of steam stability is, supercritical grafted > dry grafted > wet grafted as shown in Figure 17 and 18 and Table 7 which shows the textural properties of the three samples before and after steaming. After steaming, the wet-grafted sample retained only 10% of its original surface area and 20% of pore volume. The dry grafted sample, on

the other hand, retained 78% of its original surface area and 53% of pore volume. The supercritically grafted sample retained much of its surface area (88%) and pore volume (79%) after steaming. Another indicator of stability is the extent to which the pore size reduces after steaming. As shown in Table 7, steaming induced reduction in pore size is lowest for the supercritically grafted sample. It was proposed that the difference in steam stability between supercritical, dry and wet grafted Al-MCM-41 materials is due to the way in which the Al interacts with the host silica framework and in particular the extent to which the Al is sorbed onto rather than into the framework [53,54]. Under dry grafting conditions the Al is sorbed mainly on the outermost surface of the host Si-MCM-41 while under wet (aqueous) grafting conditions the Al may penetrate the framework (due to greater hydrolysis of the host silica framework) and occupy both surface and near surface sites. For supercritically grafted samples, the low solvating power of SCFs ensures even more efficient deposition of Al onto rather than into the silica framework. No hydrolysis of the host silica framework occurs during the SCF mediated alumination. Furthermore, better dispersion of Al achieved under SCF conditions can be expected to coat efficiently the surface of the host Si-MCM-41 with a protective aluminosilicate layer. Removal of Al (i.e., dealumination) which occurs during steaming is therefore more detrimental to the structural integrity of wet grafted samples due to extraction of Al sited deeper within the framework. Steam stable Al-grafted MCM-41 materials are therefore best prepared via alumination pathways that efficiently coat the outermost parts (i.e., pore wall surfaces) of the host pure silica material with Al without introducing Al deep into the silica (pore wall) framework.

Table 7. Textural properties and acidity of Al-grafted materials before and after steaming at 900°C for 4 hours

Sample	Surface Area (m ² /g)	Pore Volume (cm ³ /g)	APD ^a (Å)
Wet grafted (H10)	835	0.73	35.0
Steamed H10	86	0.15	
Dry grafted (P10)	902	0.83	36.8
Steamed P10	705	0.44	25.0
Supercritically grafted (S10)	833	0.92	36.0
Steamed S10	729	0.73	33.1

^aAPD = Average Pore Diameter estimated using the relation $APD = 4V/S$, where V is the mesopore volume and S is surface area.

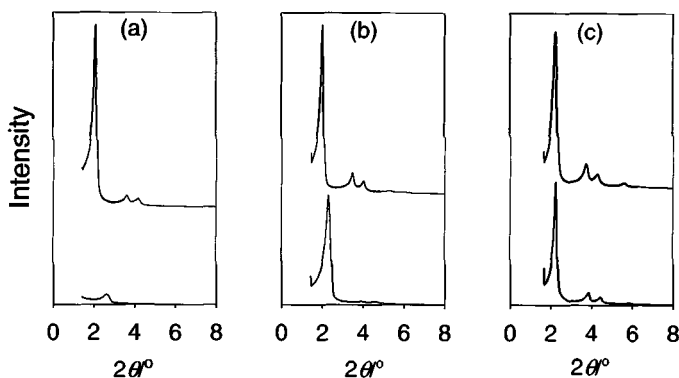


Figure 17. Powder XRD patterns of (a) wet-grafted, (b) dry-grafted and (c) supercritically grafted Al-MCM-41 before (top) and after (bottom) steaming at 900°C for 4 hours.

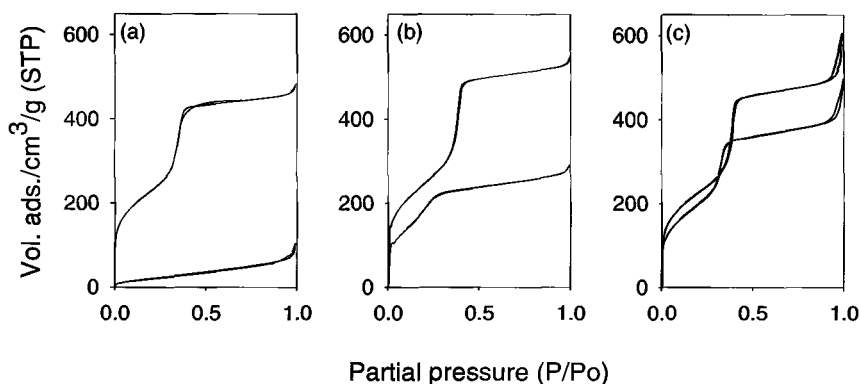


Figure 18. Nitrogen sorption isotherms of (a) wet-grafted, (b) dry-grafted and (c) supercritically grafted Al-MCM-41 before (top) and after (bottom) steaming at 900°C for 4 hours.

Shen and Kawi [56] have also reported that post-synthesis alumination substantially enhanced the hydrothermal stability (in boiling water and under steaming conditions), mechanical stability and chemical stability (in high pH aqueous solutions) of MCM-41. They also found that the boiling water stability of the pure silica MCM-41 was remarkably improved by introducing non-structural Al species onto the pore surface [57,58]. They

attributed the improved stability, in part, to a protective layer of non-framework Al species, which protected surface hydroxyl groups from hydrolysis. Shen and Kawi also investigated the effect of Al content of the stability of aluminosilicate MCM-41 and found that post-synthesis alumination prevented the formation of structural defects and that it was an effective method to prepare Al-containing MCM-41 with uniform pore structure [59]. Moreover, the resulting uniform mesoporous structure of alumina-modified MCM-41 was maintained without the formation of structural defects, upon hydrothermal treatment in boiling water for 1 week. The hydrothermal stability, in boiling water, of SBA-15 and MCM-41 was considerably improved after post-synthesis alumination with trimethylaluminium in toluene as shown in Figure 19 [37].

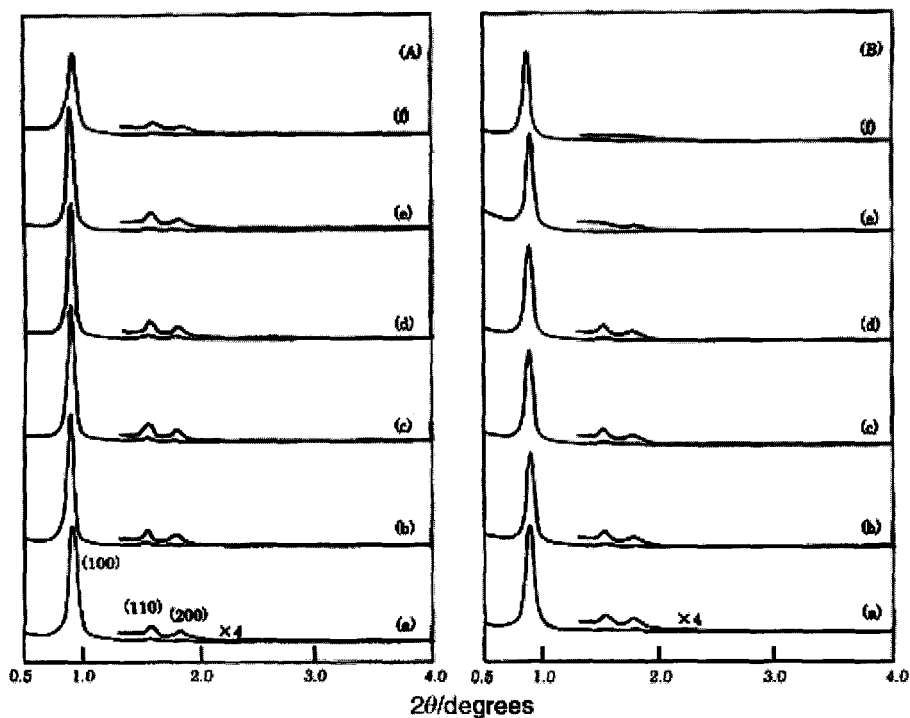


Figure 19. SAXS patterns of (A) Al-grafted, Al-SBA-15 and (B) pure silica SBA-15 after treatment in boiling water for various periods of time; (a) 0 h, (b) 6 h, (c) 12 h, (d) 24 h, (e) 48 h and (f) 72 h [37].

Mesoporous MSU-G molecular sieve silica, prepared through a H bonding assembly mechanism in the presence of a $C_{12}H_{25}NH(CH_2)_2NH_2$

gemini surfactant as the structure director are known to be stable under thermal (up to 1000°C) and hydrothermal conditions. Aluminosilicate MSU-G containing 2% Al were prepared through post-synthesis grafting reactions with aluminum nitrate, aluminum iso-butoxide or sodium aluminate [60]. The Al was incorporated into the framework to various degrees, depending on the grafting reagent as shown in Figure 20 [60]. In addition to their stability, the Al-grafted MSU-G materials were more efficient acid catalysts compared to 2% Al-grafted MCM-41 for the conversion of 2,4-di-tert-butylphenol and cinnamyl alcohol to a bulky flavan as the primary alkylation product. The improved catalytic activity of Al-MSU-G (compared to Al-MCM-41) was attributed to its vesicular particle morphology, which facilitates reagent access to catalytic centers in the lamellar framework of the Al-containing MSU-G.

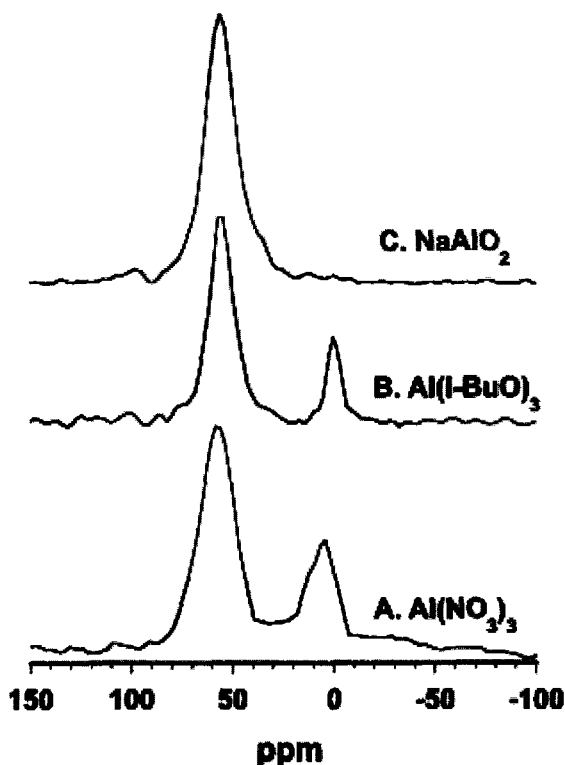


Figure 20. ^{27}Al MAS NMR spectra of calcined 2% Al-MSU-G prepared through post-synthesis alumination reactions with (A) aluminum nitrate, (B) aluminum iso-butoxide, and (C) sodium aluminate [60].

6 Alumination of mesoporous silica via composite materials

In an effort to increase the acidity and stability of mesoporous aluminosilicates, composite zeolite/mesoporous silica materials have been prepared [61-68]. The resulting materials are basically mixtures of the two components with varying degrees of intergration. For example a zeolite Beta/MCM-41 composite was prepared by Gou *et al* [61-63] through a two-step crystallization process in which a colloidal gel of lowly crystallised zeolite beta was first prepared and then added to a solution of cetyltrimethylammonium bromide. The composite material possessed a well-ordered mesoporous MCM-41 phase and a zeolite Beta phase. The mesopore walls of the composite were reported to contain secondary building units characteristic of zeolite Beta. The composite material had a higher proportion of stronger Bronsted acid sites and higher activity for the cracking of heptane compared to a physical mixture of MCM-41 and zeolite Beta. Zeolites may also be used as silica-alumina source to prepare zeolite/mesoporous molecular sieve composites (denoted ZMC) [69]. The XRD patterns of the ZMC composites exhibited peaks due to both the zeolite and mesoporous molecular sieve phases. The ZMC composites had strong acidity similar to that of zeolites and a considerable activity for the cracking of n-hexane [69].

Kaliaguine and co-workers [70] have extended the concept of zeolite/mesoporous composite materials and transformed the walls of a mesoporous aluminosilicate into a semi-crystalline pseudo-zeolitic framework. The resultant composite material exhibited both zeolite and mesoporous characteristics, as shown in Figures 21 and 22, which are consistent with the presence of zeolitic and mesoporous material. The materials, denoted UL-ZSM-5, were prepared via hydrothermal treatment of the parent mesoporous aluminosilicate in the presence of tetrapropylammonium hydroxide [70]. Evidence for the presence of ZSM-5 nanocrystallites was provided by bright- and dark-field TEM images - the bright spots in the image corresponded to ZSM-5 nanocrystals embedded in the particles of the UL-ZSM-5 [70]. ^{27}Al MAS NMR spectra exhibited only one resonance peak at 54–58 ppm attributed to tetrahedrally coordinated (framework) Al. The acidity of UL-ZSM-5 was found to be higher and stronger than that of the parent mesoporous aluminosilicate. Kaliaguine *et al* [71] have also used zeolite seeds as grafting reagents to prepare strongly acidic and stable mesoporous aluminosilicates. Clear zeolite seed solutions were used to perform hydrothermal (130°C for 24 hours) grafting of zeolite seeds onto the walls of Al-SBA-15. The resultant composite material, denoted ZC MeosAS, exhibited much improved

acidity and hydrothermal stability due to coating of nanosized ZSM-5 seeds on the walls of the parent SBA-15. The increase in Brønsted acid sites in ZC MesoAs in comparison to the parent Al-SBA-15 was probed by FTIR as shown in Figure 23. The order of acidic strength was H-ZSM-5 > ZC MesoAS > parent Al-SBA-15. One-phase mesoporous aluminosilicate materials may also be prepared if nanoclustered zeolite seeds are used as framework precursors [72-77].

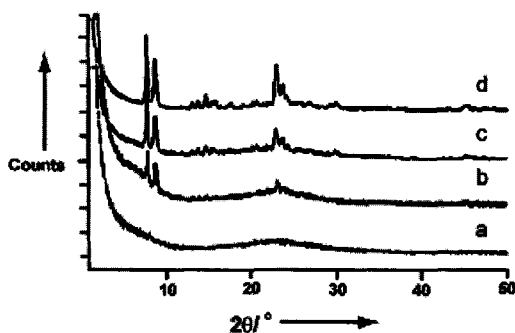


Figure 21. XRD patterns of calcined UL-ZSM-5 reaction products (a) before crystallization and after crystallization times of (b) 1, (c) 2, and (d) 5 days [70].

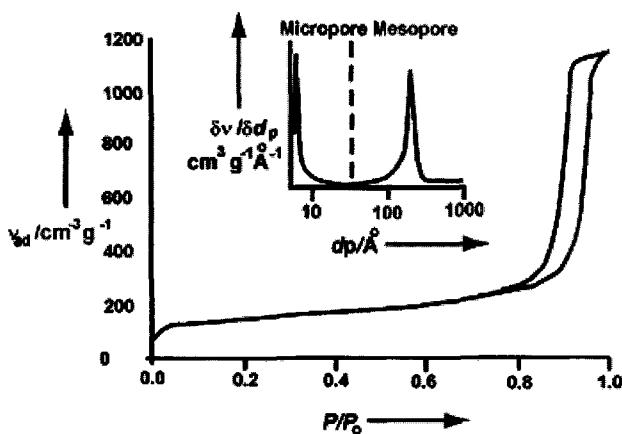


Figure 22. Nitrogen sorption isotherms of UL-ZSM-5 after 2 days crystallization time. Inset: HK micropore and BJH mesopore distributions; dp is the pore diameter [70].

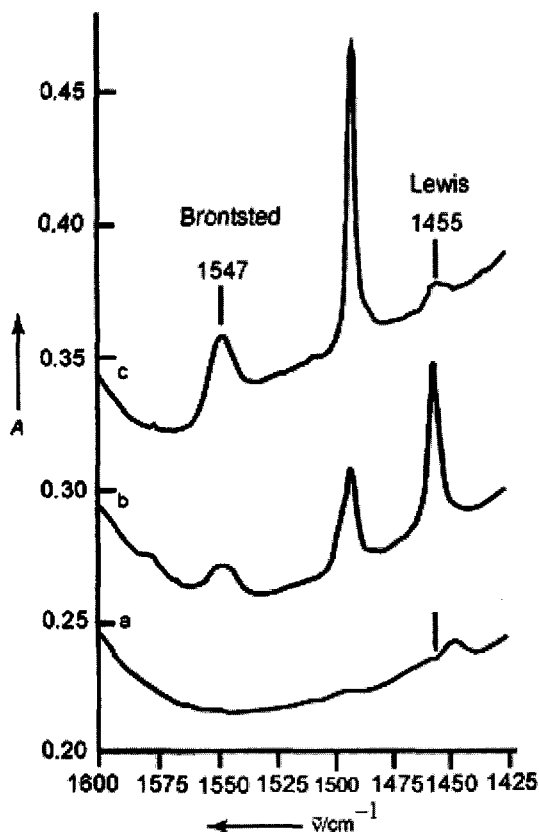


Figure 23. FTIR spectra of adsorbed pyridine in the 1350–1600 cm^{-1} range after pyridine was adsorbed and then desorbed at 150 °C: (a) parent MesoAS in H-form; (b) ZSM-5-coated MesoAS; (c) H-ZSM-5 [71].

7 Concluding remarks

The need to prepare well ordered and stable mesoporous aluminosilicates with accessible active (i.e., acid or ion exchange) sites has inspired the developments in surface alumination of mesoporous silicas seen over the last few years. It is now possible to prepare well ordered materials that are also exceptionally stable. Surface alumination avoids the presence of Al deep within the aluminosilicate framework. The presence of Al within the framework of directly prepared mesoporous aluminosilicates is known to cause undesirable reduction in structural ordering and a lowering in

thermal and hydrothermal stability A further key advantage of surface alumination is that, unlike direct mixed-gel synthesis, it generates aluminosilicate materials with readily accessible active sites on the inner walls of the mesoporous framework [78,79]. Surface alumination of lumination of mesoporous silica therefore offers distinct advantages over direct synthesis with respect to accessibility to active sites, structural ordering and stability. The preparation of mesoporous aluminosilicates via surface alumination is not restricted by ‘templated synthesis’, which can be expensive, irreproducible and in some cases inimical to the incorporation of Al. The starting point for is the mesoporous silica, which may take any form (hexagonal, cubic, lamellar) and can be prepared via a range of inexpensive synthesis routes employing cationic, neutral, non-ionic or non-surfactant templates and cheap sources of silica.

8 Acknowledgements

The author is grateful to co-workers, past and present, who have contributed to some of the work reviewed here and to the EPSRC and the University of Nottingham for financial support.

References

1. Kresge C. T., Leonowicz M. E., Roth W. J., Vartuli J. C. and Beck J. S., Ordered mesoporous molecular sieves synthesized by a liquid-crystal template mechanism, *Nature* **359** (1992) pp. 710-712.
2. Ying J. Y., Mehnert C. P. and Wong M. S., Synthesis and applications of supramolecular-templated mesoporous materials, *Angew. Chem. Int. Ed.* **38** (1999) pp. 56-77.
3. Biz S. and Occelli, M. L., Synthesis and characterization of mesostructured materials, *Catal. Rev.-Sci. Eng.* **40** (1998) pp 329-407.
4. Corma A., From microporous to mesoporous molecular sieve materials and their use in catalysis, *Chem. Rev.* **97** (1997) pp. 2373-2419.
5. Sayari, A., Catalysis by crystalline mesoporous molecular sieves, *Chem. Mater.* **8** (1996) pp. 1840-1852
6. On D. T., Desplandier-Giscard D., Danumah C. and Kaliaguine S., Perspectives in catalytic applications of mesostructured materials, *Appl. Catal. A*, **222** (2001) pp. 299-357
7. Corma A., Fornés V., Navarro, M. T. and Pérez-Pariente, J., Acidity and stability of MCM-41 crystalline aluminosilicates, *J. Catal.* **148** (1994) pp. 569-574.
8. Mokaya R., Jones W., Luan Z., Alba M. D. and Klinowski, J., Acidity and catalytic properties of mesoporous aluminosilicate MCM-41, *Catal. Lett.* **37** (1996) pp. 113-120
9. Mokaya R. and Jones, W., Physicochemical characterisation and catalytic activity of primary amine templated aluminosilicate mesoporous catalysts, *J. Catal.* **172** (1997) pp. 211-221.

10. Mokaya R and Jones W., Synthesis of acidic aluminosilicate mesoporous molecular sieves using primary amines, *Chem. Commun.* (8) (1996) pp. 981-982.
11. Mokaya R and Jones W., Acidity and catalytic activity of aluminosilicate mesoporous molecular sieves prepared using primary amines', *Chem. Commun.* (8) (1996) pp. 983-984.
12. Mokaya R and Jones W., Direct synthesis of acidic aluminosilicate mesoporous molecular sieves, *Mat. Res. Soc. Symp. Proc.* **431** (1996) pp. 83-88.
13. Kosslick H., Lischke G., Landmesser H., Parltitz B., Storek W. and Fricke J., Acidity and catalytic behaviour of substituted MCM-48, *J. Catal.* **176** (1998) pp. 102-114.
14. Kosslick H., Landmesser H and Fricke R., Acidity of substituted MCM-41-type mesoporous silicates probed by ammonia, *J. Chem. Soc., Faraday Trans.* (1997) pp. 1849-1854.
15. Mokaya, R., Al content dependent hydrothermal stability of directly synthesised aluminosilicate MCM-41, *J. Phys. Chem. B*, **104** (2000) pp. 8279-8286.
16. Kima J. H., Tanabe M. and Niwa M., Characterization and catalytic activity of the AlMCM-41 prepared by a method of gel equilibrium adjustment, *Micropor. Mater.* **10** (1997) pp. 85-93
17. Chakraborty B. and Viswanathan. B., Surface acidity of MCM-41 by in situ IR studies of pyridine adsorption, *Catal. Today* **49** (1999) pp. 253-260.
18. Busio M., Jänchen J. and van Hooff J. H. C., Aluminum incorporation in MCM-41 mesoporous molecular sieves, *Micropor. Mater.* **5** (1995) pp. 211-218.
19. Reddy K. M. and Song C., Synthesis and catalytic applications of novel mesoporous aluminosilicate molecular sieves, *Mater. Res. Soc. Symp. Proc.* **454** (1997) pp. 125-137.
20. Occelli M. L., Biz S., Auroux A. and Ray G. J., Effects of the nature of the aluminum source on the acidic properties of some mesostructured materials, *Micropor. Mesopor. Mater.* **26** (1998) pp. 193-213.
21. Biz S and White M. G., Syntheses of aluminosilicate mesostructures with high aluminum content, *J. Phys. Chem. B* **103** (1999) pp. 8432-8442.
22. Badamali S. K., Sakthivel A. and Selvam P., Influence of aluminium sources on the synthesis and catalytic activity of mesoporous AlMCM-41 molecular sieves, *Catal. Today* **63** (2000) pp. 291-295.
23. Cesteros Y. and Haller G. L., Several factors affecting Al-MCM-41 synthesis, *Micropor. Mesopor. Mater.* **43** (2001) pp. 171-179.
24. On D. T., Zaidi, S. M. J. and Kaliaguine, S., Stability of mesoporous aluminosilicate MCM-41 under vapor treatment, acidic and basic conditions, *Micropor. Mesopor. Mater.* **22** (1998) pp. 211-224.
25. Janicke M. T., Landry C. C., Christiansen S. C., Birtalan S., Stucky G. D. and Chmelka B. F., Low silica MCM-41 composites and mesoporous solids, *Chem. Mater.* **11** (1999) pp. 1342-1351; Janicke M. T., Landry C. C., Christiansen S. C., Kumar D., Stucky G. D. and Chmelka B. F., Aluminum incorporation and interfacial structures in MCM-41 mesoporous molecular sieves, *J. Am. Chem. Soc.* **120** (1998) pp. 6940-6951.
26. Zhao X. S., Lu G. Q., Whittaker A. K., Millar G. J. and Zhu H. Y., Comprehensive study of surface chemistry of MCM-41 using ^{29}Si CP/MAS NMR, FTIR, pyridine-TPD, and TGA, *J. Phys. Chem. B* **101** (1997) pp. 6525-6531.
27. Hamdan H., Endud S., He H. Y., Muhid M. N. M. and Klinowski J., Alumination of the purely siliceous mesoporous molecular sieve MCM-41 and its hydrothermal

- conversion into zeolite Na-A, *J. Chem. Soc. Farad. Trans.* **92** (1992) pp. 2311-2315.
28. Endud S., Nur H. and Hamdan H., Probing the active sites of aluminated mesoporous molecular sieve MCM-41 by secondary synthesis in the conversion of cyclohexanol, *Stud. Surf. Sci. Catal.* **117** (1998) pp. 453-459.
 29. Mokaya R. and Jones W., Post-synthesis grafting of Al onto MCM-41, *Chem. Commun.* **22** (1997) pp. 2185-2186.
 30. Mokaya R. and Jones W., Grafting of Al onto purely siliceous mesoporous molecular sieves, *Phys. Chem. Chem. Phys.* **1** (1999) pp. 207-213.
 31. Ryoo R., Jun S., Kim J. M., Kim M. J., Generalised route to the preparation of mesoporous metallosilicates via post-synthetic metal implantation, *Chem. Commun.* (1997) pp. 2225-2226.
 32. Mokaya R. and Jones W., Aluminosilicate mesoporous molecular sieves with enhanced stability obtained by reacting MCM-41 with aluminium chlorohydrate, *Chem. Commun.* **17** (1998) pp. 1839-1840.
 33. Mokaya R. and Jones W., Efficient post-synthesis alumination of MCM-41 using aluminium chlorohydrate containing Al polycations', *J. Mater. Chem.* **9** (1999) pp. 555-561.
 34. Cheng M. J., Wang Z. B., Sakurai K., Kumata F., Saito T., Komatsu T., Yashima T., Creation of acid sites on SBA-15 mesoporous silica by alumination, *Chem. Lett.* **28** (1999) pp. 131-132.
 35. Luan Z. H., Hartmann M., Zhao D. Y., Zhou W. Z. and Kevan L., Alumination and ion exchange of mesoporous SBA-15 molecular sieves, *Chem. Mater.* **11** (1999) pp. 1621-1627.
 36. Chen L. Y., Ping Z., Chuah G. K., Jaenicke S. and Simon G., A comparison of post-synthesis alumination and sol-gel synthesis of MCM-41 with high framework aluminum content, *Micropor. Mesopor. Mater.* **27** (1999) pp. 231-242.
 37. Sumiya S., Oumi, Y., Uozumi T. and Sano T., Characterization of AlSBA-15 prepared by post-synthesis alumination with trimethylaluminium, *J. Mater. Chem.* **11** (2001) pp. 1111-1115.
 38. Oumi Y., Takagi S., Sumiya S., Mizuno R., Uozumi T. and Sano T., Novel post-synthesis alumination method for MCM-41 using trimethylaluminium, *Micropor. Mesopor. Mater.* **44-45** (2001) pp. 267-274.
 39. Ghanbari-Siahkali A., Philippou A., Garforth A., Cundy C. S., Anderson M. W. and Dwyer J., A comparison of direct synthesis and vapour phase alumination of MCM-41, *J. Mater. Chem.* **11** (2001) pp. 569-577.
 40. Jun S. and Ryoo R., Aluminum impregnation into mesoporous silica molecular sieves for catalytic application to Friedel-Crafts alkylation, *J. Catal.* **195** (2000) pp. 237-243.
 41. Mokaya R., The effect of particle size on aluminosilicate MCM-41 catalysts prepared via grafting routes, *J. Catal.*, **186** (1999) pp. 470-477.
 42. Mokaya R., Al_x^{nt}-grafted MCM-41 catalysts: probing the influence of temperature on the alumination process. *J. Catal.*, **193** (2000) pp. 103-107.
 43. Mokaya R., Template-directed stepwise post-synthesis alumination of MCM-41 mesoporous silica, *Chem. Commun.* (2000) pp. 1451-1452.
 44. Hamdan H., Sulikowski B. and Klinowski J., Hydrothermal isomorphous substitution of aluminum in Faujasitic frameworks – 2nd generation zeolite catalysts, *J. Phys. Chem.* **93** (1989) pp. 350- 356.

45. Mokaya R., Insertion of extra-framework Al into the framework of mesoporous MCM-41 aluminosilicate, *Chem. Commun.* **19** (2000) pp. 1891-1892.
46. Polverejan M, Pauly T. R and Pinnavaia T. J., Acidic porous clay heterostructures (PCN): Intragallery assembly of mesoporous silica in synthetic saponite clays, *Chem. Mater.* **12** (2000) pp. 2698-2704.
47. Ahenach J., Cool P. and Vansant E. F., Enhanced Bronsted acidity created upon Al-grafting of porous clay heterostructures via aluminium acetylacetonate adsorption, *Phys. Chem. Chem. Phys.* **2** (24) (2000) pp. 5750-5755.
48. Nie C., Huang L., Zhao D. Y. and Li Q., Performance of Pt/Al-SBA-15 catalysts in hydroisomerization of n-dodecane, *Catal. Lett.* **71** (2001) pp. 117-125.
49. Bastardo-Gonzalez E., Mokaya R. and Jones W., Super-microporous aluminosilicate catalysts via primary amine templating, *Chem. Commun.* **11** (2001) pp. 1016-1017; Bastardo-Gonzalez E., Mokaya R. and Jones W., Synthesis and characterisation of super-microporous aluminosilicates prepared via primary amine templating, *Stud. Surf. Sci. Catal.* **141** (2002) pp. 141-150.
50. Gusev V. Y., Feng X. B., Bu Z., Haller G. L. and O'Brien J. A., Mechanical stability of pure silica mesoporous MCM-41 by nitrogen adsorption and small-angle X-ray diffraction measurements, *J. Phys. Chem.* **100** (1996) pp. 1985-1988.
51. Mokaya R., Ultrastable mesoporous aluminosilicates by grafting routes, *Angew. Chem. Int. Ed.* **38** (1999) pp. 2930-2934.
52. Mokaya R., Influence of pore wall thickness on the steam stability of Al-grafted MCM-41, *Chem. Commun.* **7** (2001) pp. 633-634.
53. Mokaya R., Alumination pathways to mesoporous aluminosilicates with high temperature hydrothermal stability, *Chem. Phys. Chem.* **3** (2002) pp. 360-363.
54. O'Neil A. S., Mokaya R., and Poliakoff M., Supercritical fluid mediated alumination of mesoporous silica and its beneficial effect on hydrothermal stability, *J. Am. Chem. Soc.* **124** (2002) pp. 10636-10637.
55. Mokaya R., Synthesis of mesoporous aluminosilicates with enhanced stability and ion-exchange capacity via a secondary crystallization route, *Adv. Mater.* **12** (2000) pp. 1681-1685.
56. Shen S. C. and Kawi S., Improvement of both the acidity and stability of MCM-41 by post-synthesis alumination, *Chem. Lett.* **28** (1999) pp. 1293-1294.
57. Kawi S. and Shen S. C., Effects of structural and non-structural Al species on the stability of MCM-41 materials in boiling water, *Mater. Lett.* **42** (2000) pp. 108-112.
58. Shen S. C. and Kawi S., Understanding of the effect of Al substitution on the hydrothermal stability of MCM-41, *J. Phys. Chem. B* **103** (1999) pp. 8870-8876.
59. Shen S. C. and Kawi S., MCM-41 with improved hydrothermal stability: Formation and prevention of Al content dependent structural defects, *Langmuir* **18** (2002) pp. 4720-4728.
60. Kim S. S., Liu Y. and Pinnavaia T. J., Ultrastable MSU-G molecular sieve catalysts with a lamellar framework structure and a vesicle-like particle texture, *Micropor. and Mesopor. Mater.* **44-45** (2001) pp. 489-498.
61. Guo W. P., Huang L. M., Deng P., Xue Z. Y. and Li Q. Z., Characterization of Beta/MCM-41 composite molecular sieve compared with the mechanical mixture, *Micropor. and Mesopor. Mater.* **44-45** (2001) pp. 427-434.
62. Guo W. P., Xiong C. R., Huang L. M. and Li Q. Z., Synthesis and characterization of composite molecular sieves comprising zeolite Beta with MCM-41 structures, *J. Mater. Chem.* **11** (2001) pp. 1886-1890.

63. Guo W. P., Huang L. M., Chen H. Y. and Li Q. Z., A novel MCM-41-beta-zeolite composite molecular sieve with mesoporous and microporous structure, *Chemical Journal of Chinese Universities-Chinese* **20** (1999) pp. 356-358.
64. Huang H. Y., Shen B. J., Xu C. M. and Pan H., Study on a novel composite molecular sieve with mesoporous and microporous structure, *Acta Chimica Sinica* **60** (2002) pp. 1350-1352.
65. Huang L. M., Guo W. P., Deng P., Xue Z. Y. and Li Q. Z., Investigation of synthesizing MCM-41/ZSM-5 composites, *J. Phys. Chem. B* **104** (2000) pp. 2817-2823.
66. Lee D. S. and Liu T. K., Synthesis of micropore/mesopore composite materials, *React. Kinet. Catal. Lett.* **72** (2001) pp. 209-218.
67. Li G., Kan Q. B., Wu T. H. and Zhang H.J., Synthesis and catalytic performance of mesoporous material with pore wall composed of the primary structure units of zeolite, *Acta Chimica Sinica* **60** (2002) pp. 759-763.
68. Poladi P. H. R. P. and Landry C. C., Synthesis, characterization, and catalytic properties of a microporous/mesoporous material, MMM-1, *J. Solid State Chem.* **167** (2002) pp. 363-369.
69. Goto Y., Fukushima Y., Ratu P., Imada Y., Kubota Y., Sugi Y., Ogura M. and Matsukata M Mesoporous material from zeolite, *J. Por. Mater.* **9** (2002) pp. 43-48.
70. On D. T and Kaliaguine S., Large-pore mesoporous materials with semi-crystalline zeolitic frameworks, *Angew. Chem. Int. Ed.* **40** (2001) pp. 3248-3251.
71. On D. T. and Kaliaguine S., Ultrastable and highly acidic, zeolite-coated mesoporous aluminosilicates, *Angew. Chem. Int. Ed.* **41** (2002) pp. 1036-1040.
72. Liu Y., Zhang W. and Pinnavaia T. J., Steam-stable aluminosilicate mesostructures assembled from zeolite type Y seeds, *J. Am. Chem. Soc.* **122** (2000) pp. 8791-8792.
73. Liu Y., Zhang W. and Pinnavaia T. J., Steam-stable MSU-S aluminosilicate mesostructures assembled from zeolite ZSM-5 and zeolite Beta seeds, *Angew. Chem., Int. Ed.* **40** (2001) pp. 1255-1258.
74. Liu Y. and Pinnavaia T. J., Assembly of hydrothermally stable aluminosilicate foams and large-pore hexagonal mesostructures from zeolite seeds under strongly acidic conditions, *Chem. Mater.* **14** (2002) pp. 3-5.
75. Zhang Z. T., Han Y., Xiao F. S., Qiu S. L., Zhu L., Wang R. W., Yu Y., Zhang Z., Zou B. S., Wang Y. Q., Sun H. P., Zhao D. Y. and Wei Y., Mesoporous aluminosilicates with ordered hexagonal structure, strong acidity, and extraordinary hydrothermal stability at high temperatures, *J. Am. Chem. Soc.* **123** (2001) pp. 5014-5021.
76. Zhang Z. T., Han Y., Zhu L., Wang R. W., Yu Y., Qiu S. L., Zhao D. Y. and Xiao F. S., Strongly acidic and high-temperature hydrothermally stable mesoporous aluminosilicates with ordered hexagonal Structure, *Angew. Chem. Int. Ed.* **40** (2001) pp. 1258-1253.
77. Han Y., Wu S., Sun Y., Li D., Xiao F.-S., Liu J. and Zhang X., Hydrothermally stable ordered hexagonal mesoporous aluminosilicates assembled from a triblock copolymer and preformed aluminosilicate precursors in strongly acidic media, *Chem. Mater.* **14** (2002) pp. 1144-1148.
78. Serwicka E. M., Mokaya R., Poltowicz J. and Jones W., New insights into the spatial distribution of Al in various mesoporous aluminosilicates, *Chem. Phys. Chem* **3** (2002) pp. 892 – 896.

79. Du H., Terskikh V. V., Ratcliffe C. I. and Ripmeester, J. A., Distinguishing surface versus buried cation sites in aluminosilicate mesoporous materials, *J. Am. Chem. Soc.* **124** (2002) pp. 4216-4217.

ACIDITY MEASUREMENT OF NANOPOROUS ALUMINOSILICATES – ZEOLITES AND MCM-41

J. ZHENG, C. SONG, X. XU AND U. T. TURAGA

Clean Fuels and Catalysis Program, Energy Institute and Department of Energy & Geo-Environmental Engineering, Pennsylvania State University, University Park, PA 16802, USA Email: csong@psu.edu

X. S. ZHAO

*Department of Chemical and Environmental Engineering, National University of Singapore, Kent Ridge Crescent, Singapore 119260
Email: chezxs@nus.edu.sg*

The purpose of this paper is to briefly review the methods for measuring the acidity of zeolites and MCM-41 based nanoporous aluminosilicates. Emphasis has been laid on the introduction of techniques such as titration in non-aqueous solvents, microcalorimetric measurement of the heats of adsorption of probe molecules, temperature-programmed desorption of ammonia and alkylamines as comparison for reliability, FTIR and NMR as powerful methods especially with various probe molecules, and some other spectroscopic techniques like XPS, PAS, and EPR.

1 Introduction

Zeolites [1-4] having pore sizes ranging from 0.2 to 1.0 nm, and mesoporous molecular sieves of the M41S family [5-8], from which MCM-41 is the most popular, having pore sizes in a wide range (2–10 nm), are all nanoporous aluminosilicates. They share the similarity in their regular system of pores with uniform width. There is, however, one significant difference besides the pore sizes and channel structure between zeolites and MCM-41, namely the crystallinity of the silica or silica-alumina pore walls.

As discovered in 1756 by Swedish mineralogist, Alex Cronstedt, the name of “zeolite” was derived from two Greek words, i.e., zeo and lithos, which means boiling and stones, respectively [1]. Zeolites are crystalline aluminosilicates with a framework consisting of SiO_4 and AlO_4 tetrahedra connected via the oxygen atoms at the corner points of the tetrahedron. The negative framework charge due to the net building tetrahedral $\text{AlO}_{4/2}^-$ is compensated by small cations, usually alkali or alkaline ions. Such an alkali or alkaline ion can be replaced by other cationic ions such as NH_4^+ through ion exchange. Upon calcination, Brønsted acidic (proton donating) sites can be generated due to the thermal decomposition of NH_4^+ species. A zeolite can also possess Lewis acidic (electron attracting) sites

because of lattice defects, extra-framework Al and/or six-coordinated Al species. The presence of both Brønsted acid and Lewis acid sites having different strengths, densities, distributions and stabilities, in combination with the unique crystal structures, makes zeolites very attractive for a large number of chemical reactions and enables them to play significant roles in modern petroleum refining, petrochemical industry, and energy and fuel technology such as fluid catalytic cracking (FCC), dewaxing, and Fischer-Tropsch (F-T) synthesis processes.

By using surfactant arrays instead of small alkylammonium molecules as templates, Mobil scientists in 1992 made a breakthrough synthesis of an important family of mesoporous aluminosilicates, specifically MCM-41 [5]. MCM-41 is a hexagonal aluminosilicate material containing a regular array of nonintersecting pore system with only long-range crystallinity. The mesopore walls however are of non-crystalline nature. The acidity of these mesoporous aluminosilicates is not as strong as that of crystalline zeolites, but is still strong enough for certain acid-catalyzed reactions [6]. Furthermore, the acidity of MCM-41 can be modified or improved by (1) proper selection of aluminum sources and preparation methods, (2) incorporation of heteroatoms other than aluminum (such as Ga-, B-, Fe-, etc.), and (3) surface grafting of acidic groups ($-\text{AlCl}_2$, $-\text{HSO}_3$) and/or chemically loading of super-strong acids, etc. These, coupled with its uniform mesopores, make MCM-41 a promising catalytic material for processing large molecules.

The characterization and measurement of acidity of zeolites and MCM-41 based nanoporous aluminosilicates are of vital interest in order to gain a detailed understanding of the chemistry of acid-catalyzed reactions. To describe surface acidity, the following factors need to be determined:

- The nature of the acid sites (i.e. Brønsted or Lewis),
- The density of the acid sites (the number of acid sites per unit mass or surface area),
- Their acid strengths or strength distribution, and
- The precise location of the acid sites.

No single method is available that provides all the above information; therefore several approaches must be combined. Many techniques have been developed, which include titration, thermodynamic methods with pre-adsorption of base molecules, vibrational spectroscopy, nuclear magnetic resonance, photoelectron spectroscopy, positron annihilation methods, catalytic reactions, etc. The following sections will be focused on the brief introduction and discussion of these methods for acid

measurement. Efforts have been made to update new trends in each technique based on excellent recent reviews.

2 Titration Methods

The acidity of a material is defined relative to a base used in acid-base interaction. Based on this, the simplest and most widespread method of the acid strength determination for a solid catalyst involves the use of a suitable color indicator adsorbed on it's the catalyst surface by means of titration [9-13].

The acid strength of a surface is the ability of the surface to convert an adsorbed neutral base B (the indicator) into its conjugate acid BH^+ and is expressed in terms of the Hammett acidity function H_0 , which is defined by the following equations:

Brønsted acidity:

$$H_0 = -\log \left\{ a_{H^+} \frac{f_B}{f_{BH^+}} \right\} = pK_a + \log \frac{[B]}{[BH^+]}$$

where a_{H^+} is the activity of the Brønsted acid, f_B and f_{BH^+} are the activity coefficients for the neutral base and conjugate acid, respectively, and $[B]$ and $[BH^+]$ are their concentrations.

Lewis acidity:

$$H_0 = -\log \left\{ a_A \frac{f_B}{f_{AB}} \right\} = pK_a + \log \frac{[B]}{[AB]}$$

where a_A is the activity of the Lewis acid, f_B is the activity coefficient of the base B and f_{AB} is the activity coefficient of the Lewis acid–base adduct AB.

An indicator will be converted into its conjugate acid only by acid sites which have an acid strength equal to or higher than that of the indicator. Therefore, the acid strength of a solid catalyst can be estimated by noting which members of a series of Hammett indicators (as seen in Table 1 [13]) are adsorbed in the acid form.

Table 1. Basic Indicators Used for Measurement of Acid Strength [13].

Indicators	Color in Base	Color in Acid	pK _a	Equivalent (H ₂ SO ₄)%
Neutral red	Yellow	Red	+6.8	8 x 10 ⁻⁸
Methyl red	Yellow	Red	+4.8	
Phenylazonaphthylamine	Yellow	Red	+4.0	5 x 10 ⁻⁵
<i>p</i> -(Dimethylamino)-azobenzene	Yellow	Red	+3.3	3 x 10 ⁻⁴
2-Amino-5-azotoluene	Yellow	Red	+2.0	5 x 10 ⁻³
Benzeneazo-diphenylamine	Yellow	Purple	+1.5	2 x 10 ⁻²
Crystal violet	Blue	Yellow	+0.8	0.1
Dicinnamalacetone	Yellow	Red	-3.0	48
Benzalacetophenone	Colorless	Yellow	-5.6	71
Anthraquinone	Colorless	Yellow	-8.2	90
2,4,6-Trinitroaniline	Colorless	Yellow	-10.1	90
<i>m</i> -Nitrotoluene	Colorless	Yellow	-12.0	
<i>p</i> -Nitrochlorobenzene	Colorless	Yellow	-12.4	
2,4-Dinitrofluorobenzene	Colorless	Yellow	-14.5	
1,3,5-Trinitrotoluene	Colorless	Yellow	-16.0	

Non-aqueous titration should be used since the acidity of solid materials can be modified in the presence of water. The method consists, in practice, of titrating with *n*-butylamine a solid acid suspended in benzene using an indicator, and the result colors are noted. If the color is that of the acid form of the indicator, the value of the H₀ function of the surface is the same or lower than the pK_a of the conjugate acid of the indicator. The lower the pK_a of the color-changing indicator is, the greater the acid strength of the solid.

Besides its simplicity, the traditional titration method suffers from some limitations as listed below:

- The equilibrium for the titration reaction is rarely achieved.
- The method is limited for white samples.
- The visual determination of the color changes are often inaccurate.
- The color changes on solids alone are problematic since almost every reaction on a zeolite or MCM-41 produces some degree of visual color change that does not have an obvious relationship to the acidity [14].

In order to overcome the above limitations, spectrophotometric methods (such as utilization of UV-visible spectroscopy, fluorescence

spectroscopy, etc.) and thermometric titration of solid acids with amine have been developed. In the latter case, the solid sample as suspended in benzene is commonly titrated with *n*-butylamine by controlling the slight changes of temperature using a Beckman thermometer connected to a galvanometer [15]. Therefore, the equilibrium condition during titration can be more accurately monitored due to advanced techniques.

So far, this method works well for larger-pore materials (pore size > 0.5 nm) with 3-dimensional channel systems [9]. But it is unsuccessful with small-pore zeolites (< 0.5 nm) due to the blockage of the channels by strongly adsorbed *n*-butylamine. Thus this method is of limited utility but could possibly be extended by use of more competitive solvents or higher reaction temperatures to provide greater mobility of the titrant. Extension of the experimental techniques to permit the use of thermometric titration with a wider variety of zeolites, and also for MCM-41, would be quite valuable.

It should be mentioned that, the use of the H_0 function is adequate for homogeneous acids, however, in the case of heterogeneous acids, neither a_{H^+} nor the surface acidity function H_0 have an explicit physical meaning [11, 14]. Therefore, care should be taken on the application of Hammett function and indicators to characterize the acidity and catalytic properties of nanoporous aluminosilicates.

3 Thermodynamic Methods

3.1 Calorimetry

The main phenomenon that accompanies adsorption at solid–gas or solid–liquid interfaces is heat evolution. The heat effects can be caused either by a single process or, more generally, by a combination of physical adsorption (reversible), chemical adsorption (irreversible at the experimental temperature), and sometimes an associated reaction (such as polymerization or formation of a complex).

The use of calorimetric methods of measuring acid strength distributions is well established, based on the assumption that the acid strength is directly related to the heat of adsorption (or desorption). These techniques include DTA (differential thermal analysis), TG-DTG (differential thermogravimetry), DSC (differential scanning calorimetry), and microcalorimetry. They can be used either by themselves, or coupled with other techniques (for instance, TG-DSC, calorimetry-volumetry, DSC-chromatography, etc.).

Techniques such as DTA, DTG or DSC study the thermal behavior of a catalyst as it undergoes heating at a constant rate. On the contrary, in the adsorption microcalorimetry technique, the sample is kept at a constant temperature while certain amount of a probe basic molecule adsorbs onto its surface, and a heat-flow detector emits a signal proportional to the amount of heat transferred per unit time. Dosing of the probe molecule is continued until saturation (or half saturation) coverage is reached. The calorimetric data are usually displayed as a plot of heat of adsorption/desorption versus coverage of specific basic molecules.

The selection of probe molecule for calorimetric studies depends on the following factors: (1) the strength of basicity, (2) the molecular size, and (3) its diffusion inside the porous structure of aluminosilicate materials. Ammonia is among the smallest and strongly basic molecules, and its diffusion is hardly affected by nanoporous structures. This makes it the most commonly used probe in calorimetry. Larger molecules such as pyridine, a series of amines, ring-substituted pyridine, nitriles and alcohols, and even non-polar molecules like hexane, are also frequently used.

Extensive studies of the acidity of zeolites by adsorption calorimetry have been carried out over the past decade [16]. Recently, there are also growing numbers of calorimetric studies on mesoporous aluminosilicates MCM-41 [17, 18].

The influence of the nature of the aluminum source on the acidic properties of mesostructured materials MCM-41 has been studied by microcalorimetry experiments with ammonia as the probe molecule [17]. Aluminum insertion into the mesoporous silicate framework was found to affect both strength and distribution of the acid sites in a manner controlled by synthesis conditions. Aluminum acidic sites with strengths in the 130–150 kJ mol⁻¹ range can be found either on the surface of the pore wall, where they interact directly with the basic probe molecule, or sandwiched between silica layers within the pore wall (~3–4 Si layers thick), or in the pore (or within the pore walls) as extra-framework Al species.

The acidic and sorption properties of Al containing MCM-41 molecular sieves in comparison with relevant FAU and MFI zeolites have also been investigated by microcalorimetry of *n*-hexane, benzene, acetonitrile, and water adsorption [18]. While the heats of adsorption of acetonitrile are mainly influenced by a specific interaction on the acidic sites in the meso- and micro-porous molecular sieves (MCM-41 and zeolites, respectively), the adsorption heat of a non-polar molecule like *n*-hexane is determined by the pore size or density of those materials.

Overall, the contribution of the pore size effects in MCM-41 is smaller than that in the narrower channels of MFI zeolites.

Figure 1 shows the acidity scale of some acidic nanoporous aluminosilicate materials in terms of average heat of desorption (with ammonia as common probe molecule) at plateau or half coverage [16]. It can be found that crystalline zeolites have stronger acidity than that of MCM-41, except for those very small pore zeolites where steric hindrance may take effect due to channel blockage.

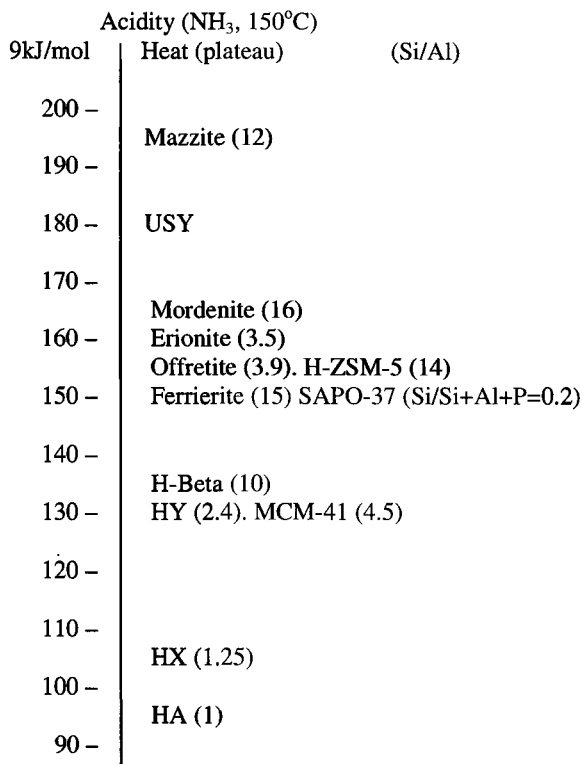


Figure 1. Acidity scale (average heat of NH₃ adsorption/desorption at plateau or half coverage) [16].

3.2 Temperature programmed desorption (TPD) of base molecules

3.2.1 Ammonia-TPD

Temperature programmed desorption of ammonia (NH₃-TPD) is an easy, practical and thus frequently used method to determine the number of

Brønsted acid sites (e.g., Si-OH-Al groups or bridging OH groups in nanoporous aluminosilicates) as well as their strength.

NH₃-TPD typically involves saturation of the surface with ammonia under some set of adsorption conditions, followed by linear ramping of the sample temperature in a flow of inert gas. Ammonia concentration in the effluent gas may be followed by gas chromatography or mass spectroscopy or adsorption/titration as combined with spectroscopic analysis. Alternatively, the experiment may be carried out in a microbalance (such as that used for TGA) and changes in sample mass instead are recorded continuously. The temperature profile during NH₃ desorption itself can consist of a series of isothermal periods separated by steps of constant heating, so called stepwise TPD [19].

The desorbed amount of ammonia gives information about the number of OH groups. A quantitative analysis of the characteristic desorption curves (calculation of the effective desorption energy via certain mathematical transformations) provides information about the acid strength and the distribution of the interaction strengths, respectively [20, 21].

Unfortunately there are some limitations about this method, despite its simplicity:

- It is incompletely supported by the theory, because NH₃-TPD experiments involve complex behaviors relating to the re-adsorption and diffusion of ammonia in the nanopores of aluminosilicates [18, 20].
- The interaction between ammonia and a solid acidic or non-acidic surface is not always an accurate measurement of acid strength. It has been reported that ammonia adsorption on non-Brønsted sites may be even stronger than on Brønsted sites [12, 22].
- The temperature at which desorption occurs from both Brønsted and non-Brønsted sites depends strongly on conditions used for the experiments [12].
- Qualitative analysis may be difficult, as well-separated peaks can result from changes in the particle size of the catalysts and not necessarily from different types of sites [9, 12].

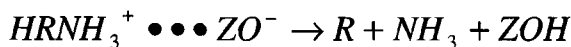
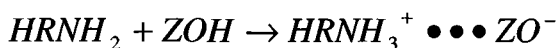
3.2.2 *n*-Butylamine TPD

The use of alkylamines (such as *n*-propylamine, *n*-butylamine etc) as probe molecules has been used for both zeolites [12, 22-24] and MCM-41 [25-27], and shows significant advantages over ammonia TPD as listed below:

- Unlike ammonia, which is strongly basic, the alkylamines have modest basicity and do not interact with sites that are not normally thought to be acidic.
- The ambiguities in the choice of the temperature used to discriminate weakly and strongly adsorbed species in NH_3 -TPD can also be avoided.
- Certain amine molecules, such as *n*-butylamine, have molecular sizes and lengths closer to those of hydrocarbons, so the acid sites detected by *n*-butylamine desorption may be more useful at a practical level [25].

A typical TPD of *n*-butylamine experiment begins by degassing physisorbed air and water off a known amount of nanoporous aluminosilicate sample. The sample is then saturated adsorption with vapors of *n*-butylamine, followed by temperature programmed desorption.

For acidic nanoporous aluminosilicates, *n*-butylamine adsorbs onto Brønsted and Lewis acid sites with varying strengths. *n*-Butylamine (HRNH_2) reacts with the proton of a Brønsted acid site to form a *n*-butylammonium (HRNH_3^+) ion intermediate. Within a well-defined temperature range of 300-475°C, this intermediate dissociates and desorbs as ammonia and *n*-butene via a reaction similar to the Hoffman elimination as shown below [12]:



where Z stands for nanoporous aluminosilicates such as zeolites.

Lewis acid sites do not react with *n*-butylamine and allow the latter to merely physisorb on them. Thus, molecules of *n*-butylamine physisorbed on Lewis acid sites desorb at temperatures lower than those chemisorbed on Brønsted acid sites. Molecules desorbing at lower temperatures (below 250°C) could also be associated with hydroxyl defects, internal silanols, and molecules hydrogen-bonded to protonated amines at Brønsted sites [22, 28].

The profiles of the *n*-butylamine TPD of USY zeolites ($\text{SiO}_2/\text{Al}_2\text{O}_3=40$) and MCM-41 having varying $\text{SiO}_2/\text{Al}_2\text{O}_3$ ratios are shown in Figure 2 [29, 30]. All the samples show a desorption feature below 250°C which is attributed predominantly to Lewis acidity or weak acidity. The strong Brønsted acidity on MCM-41 samples, as determined

by the desorption feature of 300–470°C, increases with decreasing $\text{SiO}_2/\text{Al}_2\text{O}_3$ ratio of MCM-41, but is still less acidic than USY zeolite.

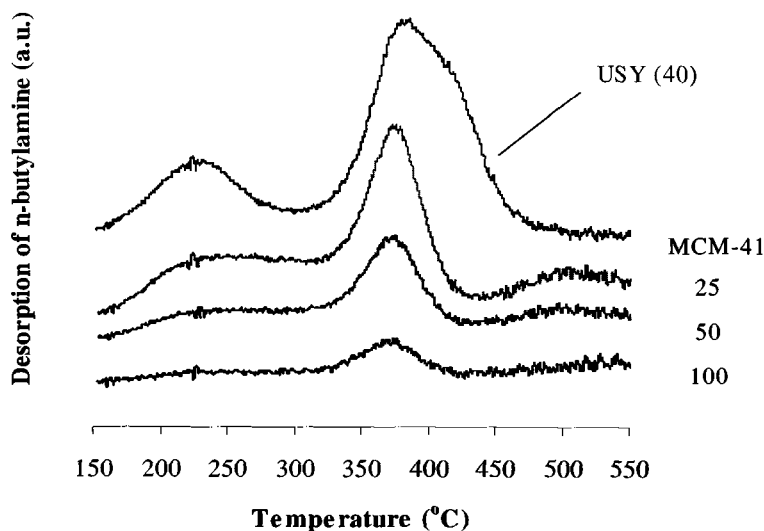


Figure 2. N-butylamine TPD profiles of USY zeolite ($\text{SiO}_2/\text{Al}_2\text{O}_3=40$) and MCM-41 of varying $\text{SiO}_2/\text{Al}_2\text{O}_3$ ratios.

4 Infrared Spectroscopic (IR) Methods

4.1 FTIR hydroxyl groups of zeolites.

Infrared (IR), in most cases as Fourier transform infrared spectroscopy (FTIR), has been widely used to characterize the intrinsic acid strength of zeolites and MCM-41 because it is a very powerful technique allowing one to measure directly the hydroxyl bond strength.

The interpretation of most prominent bands to the hydroxyl groups of nanoporous aluminosilicate materials has been widely accepted. For zeolite OH groups, the observed bands can be assigned as follows [31, 32]:

- Terminal silanol groups, at 3745 cm^{-1} .
- Internal silanol groups due to structural defects, at 3700 cm^{-1} .
- OH groups located on extra-framework aluminum or partially hydrolyzed framework aluminum species (EFAL), at 3670 cm^{-1} .
- Acidic bridged OH groups connected to the framework of the zeolite (SiOHAl), which include two bands for FAU zeolites:

- a) SiOHAl groups in the supercage, at higher frequency (HF) of 3630 cm^{-1} , and
- b) SiOHAl groups in the sodalite cage, the small pore of FAU zeolites, at lower frequency (LF) of 3566 cm^{-1} .

Similarly, the bands for MCM-41 OH groups can be assigned as follows [33, 34], the first two of which appear on all MCM-41 samples while the last two are observed with increasing Al concentration,

- Terminal silanol groups, sharp band at 3745 cm^{-1} .
- Silanol groups inside the channels of MCM-41 with strong hydrogen-bonding interactions, broad band at 3530 cm^{-1} .
- Silanol groups inside the channels of MCM-41 without strong hydrogen-bonding interactions, shoulder band at 3715 cm^{-1} .
- Hydroxyl groups on aluminum oxide species, which are most likely not belonging to the mesoporous structure, shoulder band at 3660 cm^{-1} .

With the advances of FTIR technology, the sensitivity of this method has been enhanced to detect very low concentrations of OH species. Recently, an additional pair of bands have been reported for the SiOHAl groups in strongly acidic USY zeolites [19, 35, 36], i.e., the band at about 3601 cm^{-1} (HF) and the other at 3523 cm^{-1} (LF), corresponding to the stronger acidic hydroxyls vibrating in the supercages and that pointing into the sodalite cages, respectively.

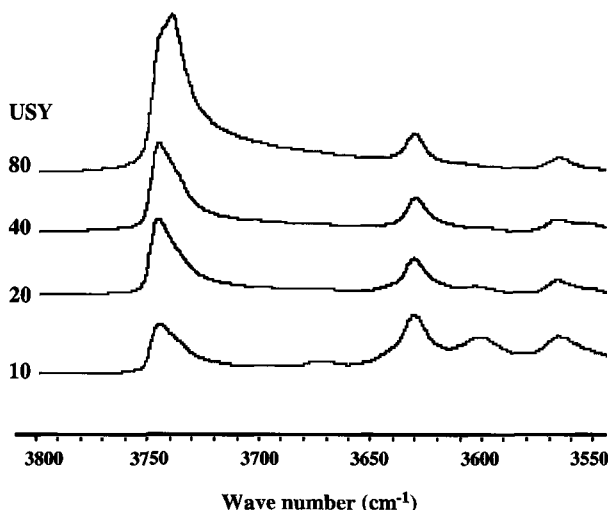


Figure 3. FTIR of USY zeolites with SiO₂/Al₂O₃ ratio varying between 10 and 80.

Figure 3 shows the FTIR spectra of four USY zeolites having $\text{SiO}_2/\text{Al}_2\text{O}_3$ ratio between 10-80 [29]. It can be seen that, with the decreasing of $\text{SiO}_2/\text{Al}_2\text{O}_3$ in this range, the intensities of both the common SiOHAl groups (HF at 3630 cm^{-1} and LF at 3566 cm^{-1}) and the new pair (HF at 3601 cm^{-1} and LF at 3523 cm^{-1}) increase significantly, showing the increasing of the acidic strength of USY zeolites.

4.2 FTIR of zeolite and MCM-41 adsorbed probe molecules

In principle, the concentration of hydroxyl groups, and therefore the concentration of potential Brønsted acid sites, could be obtained from the intensity of the corresponding FTIR band, as mentioned above. However, for quantitative estimation the extinction coefficients of the different types of hydroxyls contributing to the FTIR bands are required, which is seldom possible [11].

Two main approaches for FTIR studies of Brønsted acidity in nanoporous aluminosilicates were developed long time ago and use adsorption of chemical compounds to either (1) measure the low-frequency shifts of the O-H bond stretching vibrations upon H-bonding with adsorbed molecules or (2) test the reactivity of Brønsted acids upon chemical transformations with adsorbed molecules. For the analysis of Lewis acid sites, the interactions between these centers and adsorbed molecular species are even more important since unlike Brønsted acid site, Lewis acid sites reveal no specific features in FTIR spectra [37].

Different types of probe molecules as chosen will influence the obtained characteristics and the structure-activity relationship of the probed nanoporous aluminosilicates. Therefore, the choice of the appropriate probe molecule is very important. The most important criteria can be summarized as follows [37-39]:

- The probe molecule should have dominating and rather weak acidic properties.
- The IR spectrum of the sorbed probe molecule should allow distinction between sorption and protonic (Brønsted) and aprotic (Lewis) acid sites.
- The probe molecule should allow differentiation between acid sites of the same type, but of different strength.
- The size of the probe molecule should be comparable to the size of the reactant to probe the concentration of acid sites relevant for a particular reaction.

- The spectral measurement must not be complicated; therefore, molecules adsorbed at 300 K are more preferable than those adsorbed at low or high temperatures.

The most frequently used probe molecules are pyridine and substituted pyridines, ammonia, aliphatic amines, nitriles, benzene and substituted benzenes, and carbon monoxide. Less frequently used probe molecules are ketones, aldehydes, ethers, alkanes, and alkenes. Some inert molecules such as N₂ and H₂ have also been utilized as probe molecules. Table 2 summarizes the most suitable and utilized probe molecules and their respective ranges of FTIR frequency.

Table 2. Comparison of Suitable Probe Molecules.

Probe molecule	Type of sites*	Frequency cm ⁻¹	Reference
Pyridine	B, L	1450-1650	11
Lutidine	B	1450-1650	30
NH ₃	B, L	1400-1500	37
CH ₄	L	2800-3020	41
CH ₃ Cl	B	2800-3800	42
Benzene	B	1700-2100	43
CH ₃ CN	B, L	1700-2900	44
CO	B, L	2140-2240	45
N ₂ O	L	2225-2275	37
N ₂	L	2340-2370	46
H ₂	B, L	3850-4160	37

* B = Brønsted acid sites, L = Lewis acid sites.

The IR spectra of adsorbed nitrogen bases (especially pyridine) on acidic catalyst surfaces have been established as an accurate and reliable method for determining the nature of the individual sites presented because of the spectral differences observed for the adsorbate on Lewis and Brønsted acid sites. The characteristic bands of pyridine protonated by Brønsted acid sites (pyridinium ions) appear at ~1540 cm⁻¹ and 1640 cm⁻¹, while the bands from pyridine coordinated to Lewis acid sites appear at ~1450 cm⁻¹ and 1620 cm⁻¹ [11].

The use of a large probe molecule like 2,6-dimethylpyridine (also known as lutidine) and di-tert-butyl-pyridine is thought to be a more selective probe of Brønsted acidity than pyridine for the characterization of the acid sites located at the external surface of zeolites and in MCM-41 [30, 40]. While lutidine is more basic than pyridine, it cannot coordinate with Lewis acid sites because of the steric hindrance imposed on

nitrogen's lone pair of electrons by the methyl groups at the 2 and 6 positions. Therefore, lutidine was used in a recent study as a probe molecule to definitively determine Brønsted acidity on the MCM-41-supported catalysts [30]. The temperature programmed desorption of lutidine was monitored using an on-line FTIR spectrometer. Figure 4 shows the TPD of lutidine from a CoO-MoO₃ catalyst supported on MCM-41 with a SiO₂/Al₂O₃ of 25. Small concentrations of lutidinium ion (IR bands at 1645 cm⁻¹ and 1628 cm⁻¹) are observed even at temperatures as high as 400°C indicating good Brønsted acid strength of the support.

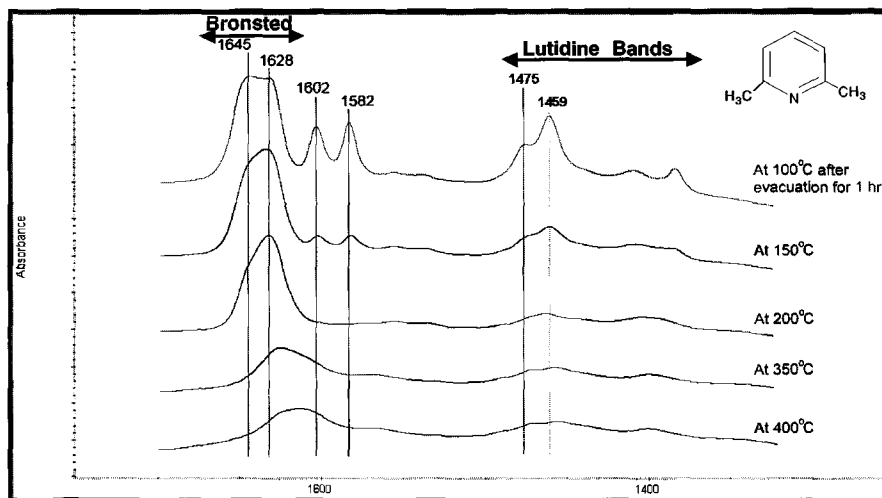


Figure 4. Temperature-programmed desorption of lutidine over CoO-MoO₃ supported MCM-41 (SiO₂/Al₂O₃ ratio=25).

5 Nuclear Magnetic Resonance (NMR) Methods

High-resolution solid-state nuclear magnetic resonance (NMR) spectroscopy is another powerful tool in characterization of solid acid catalyst. ¹H, ¹³C, ¹⁵N, ¹⁹F, ²⁷Al, ²⁹Si and ³¹P NMR are widely used. The most direct evidence for the nature of zeolite acidity is from ¹H NMR. Freude *et al.* was the first to discuss the zeolite acidity by ¹H magic angle spinning NMR [47]. Afterward, extensive studies have been carried out [47-50]. By correlating the quantum chemical calculations and the experiment results, a relationship between the acid sites and its chemical shift was established, as shown in Figure 5 [11].

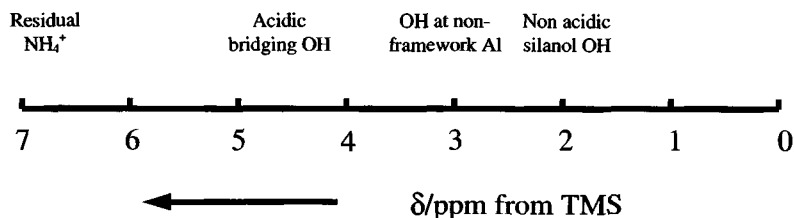


Figure 5. The ^1H chemical shifts (δ) of various protonic species in aluminosilicates.

The Brønsted and Lewis acid can also be easily distinguished by solid state NMR of amines (using ^{15}N) and phosphines (using ^{31}P) [51, 52]. The formation of protonated (Brønsted) or non-protonated (Lewis) complexes with the acid site was evidenced by the chemical shift difference. Depending on the accessibility, type or acid strength of the site, different probes characterize different subsets of acid sites. In addition, ^{13}C NMR can distinguish the types of complex formation (strongly or weakly complexed to the acid site) between Brønsted acid and probes [53].

For the analysis of zeolite acidic strength, NMR spectra are far more quantitative and far more easily interpreted than UV-visible spectral changes on solid powders by selecting some Hammett indicators as probe molecules [14]. Figure 6 shows the ^{19}F NMR spectra of *p*-fluoroaniline and *p*-fluoronitrobenzene in zeolite HY and HZSM-5 [14]. *p*-Fluoroaniline is a strong base and will only be protonated by acids of modest strength, while *p*-fluoronitrobenzene is a weak base and will be only protonated by superacid or near-super acid. From the results, it is clearly seen that *p*-fluoroaniline was protonated in each zeolite, and the *p*-fluoronitrobenzene is not, which indicated that the both HY and HZSM-5 is not superacid.

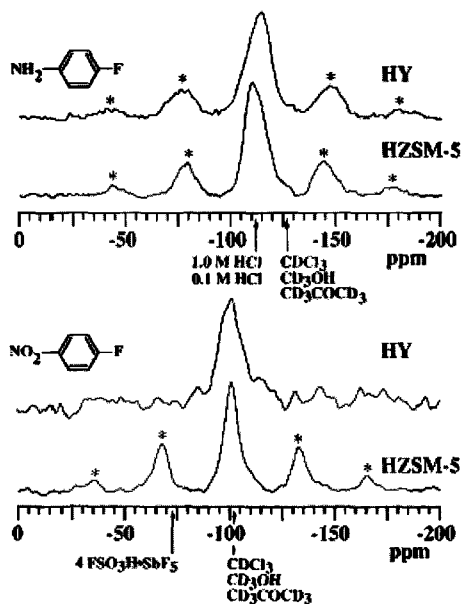


Figure 6. Representative 188 MHz ^{19}F NMR spectra of p-fluoroaniline (top) and p-fluoronitrobenzene (bottom) obtained in zeolites HY and HZSM-5. Solution chemical shifts in non-acidic and acidic solvents are transcribed to the axes for reference. Spinning sidebands reflecting chemical shift anisotropy are denoted by *. Spectra were acquired (several thousand scans) using magic angle spinning (4 mm rotors), cross polarization (2 ms) and proton dipolar decoupling.

The concentration of the acid sites can be quantified by the ^{27}Al MAS NMR [30]. Aluminum (^{27}Al) MAS NMR provides conclusive information about the coordination of Al in the MCM-41 framework. Tetrahedrally coordinated Al, the precursor for Brønsted acidity, shows a chemical shift of 55 to 80 ppm, while chemical shifts for octahedral Al are observed from 0 to 22 ppm [2]. By quantifying tetrahedral Al concentration using a ^{27}Al MAS NMR spin count standard of pure AlPO_4 , the concentration of acid sites can be determined, as recently done for a comprehensive study on MCM-41 [30].

Figure 7 shows the ^{27}Al MAS NMR spectra of MCM-41 with different $\text{SiO}_2/\text{Al}_2\text{O}_3$ ratios. The number of moles of tetrahedral Al for each sample is listed in Table 3. It was measured that 64–72% of all Al in the MCM-41-supported catalysts used in this study are tetrahedrally coordinated and, therefore, the Brønsted acidity of the MCM-41-supported catalysts was determined [30].

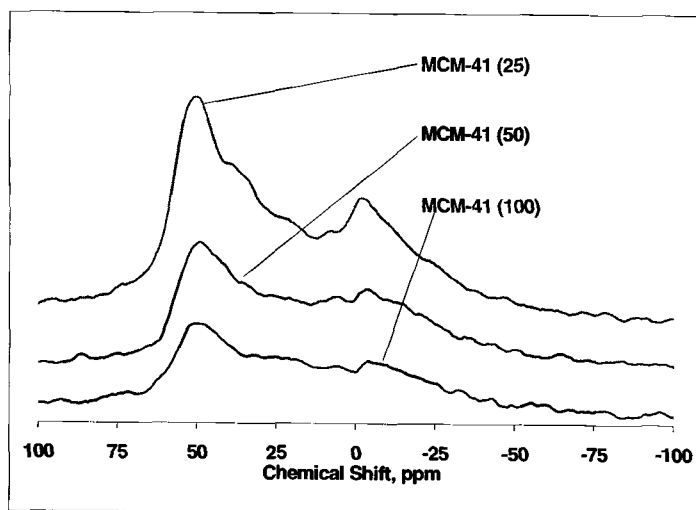


Figure 7. Aluminum (^{27}Al) MAS NMR traces of MCM-41-supported catalysts of varying $\text{SiO}_2/\text{Al}_2\text{O}_3$ ratios.

6 Other Spectroscopic Methods

6.1 X-ray Photoelectron Spectroscopy (XPS)

Since XPS measures the kinetic energy of photoelectrons emitted from the core levels of surface atoms upon X-ray irradiation of the uppermost atomic layers, it can be used to characterize surface acid sites, in combination with probe molecules [11, 54].

Table 3. Tetrahedral Al in MCM-41 samples of varying $\text{SiO}_2/\text{Al}_2\text{O}_3$ ratio.

Samples	Tetrahedral Al (mmol/g)	Tetrahedral Al (%)
MCM-41 (25)	3.62	64.2
MCM-41 (50)	1.96	65.0
MCM-41 (100)	1.33	72.7

When pyridine is adsorbed on acid sites of nanoporous aluminosilicates, the $\text{N}(1s)$ peak is substantially broader than the corresponding $\text{Si}(2p)$, $\text{Al}(2p)$ and $\text{O}(1s)$ peaks suggesting a composite peak for nitrogen. The $\text{N}(1s)$ for pyridine on H-ZSM-5 zeolite can be deconvoluted into three components having different binding energies but

similar peak widths. The peaks at higher binding energy are assigned to two Brønsted sites and third peak to a Lewis site.

However, it can be realized that this technique cannot be as powerful as IR and NMR spectroscopies [11, 54]. It is difficult to obtain accurate measurements due to the charging and contamination problems. A more complete database of binding energy values is also in need for comparison of acid strength using several bases of varying strength. Moreover, it cannot be used to determine the total acidity of nanoporous solid acids since it only focus on the external surface.

6.2 Positron Annihilation Spectroscopy (PAS)

Positron annihilation spectroscopy (PAS) has seldom been applied to the study of nanoporous aluminosilicates [55]. Positrons are antiparticles of electrons that can be formed from the decay of neutron-deficient radioisotopes such as ^{22}Na . They combine with electrons of the medium to form positronium atoms (Ps). Ps exists in two ground states, the singlet Ps (*para*-Ps) and the triplet Ps (*ortho*-Ps). The intrinsic lifetime of *p*-Ps is long enough for positronium-medium interactions. The interactions shorten the intrinsic lifetime of *o*-Ps and an accurate measurement of the positron or positronium lifetime spectrum can provide information about the chemical and physical properties of the medium.

Positron lifetime measurements of NaY and HY zeolites show that the lifetime of *o*-Ps in HY is much shorter than those in NaY, indicating that the annihilation of *o*-Ps is accelerated by its oxidation reaction with the strong Brønsted acidity in zeolites. Angular correlation of gammas from positron annihilation in pyridine-adsorbed Y-zeolite were measured as a function of temperature. These experiments again reveal that positronium, being the smallest atom, is capable of detecting minute changes in the chemistry of the internal surfaces of porous substances [55].

6.3 Electron Paramagnetic Resonance (EPR)

Lewis acid sites can be cations or different aluminum species located in defect centers. The electric field of an electron deficient site is able to quench the orbital magnetic moment of an adsorbed molecule. If, as a consequence, the molecule exhibits a magnetic moment, like in the case of the nitric oxide (NO), one may use this interaction to identify and characterize the Lewis acid sites in nanoporous aluminosilicates with electron paramagnetic resonance (EPR).

EPR of adsorbed NO probes only the sites strong enough to quench the orbital magnetic moment of NO molecule. However, the method can

provide an estimation of the strength of the detected Lewis acid sites. A correlation was established between the amount of non-framework Al and the spin concentrations of adsorbed NO. These absolute concentrations are lower than the expected number of Lewis acid sites [56].

Some other spectroscopic methods, such as Frequency-response technique [57] and laser-induced fluorescence spectroscopy [58] have also been utilized for acidity measurements.

Last but not the least, acidity catalyzed reactions with well-developed and understood mechanisms can also serve as probe reactions for measuring the acidity of nanoporous materials. Details can be found in some recent reviews [6, 11, 14].

7 Concluding Remarks

A precise and accurate description of the acidity of nanoporous aluminosilicates (including type, number, strength and environment of the sites) should allow a correlation to be made with the catalytic activity, if not a forecast. Many disagreements still exist among the various characterization methods and between these and measurements of catalytic activity. The understanding and measurement of the acidity of nanoporous aluminosilicates are still persistent, particularly in the field of zeolite chemistry, where the micropores can play a role through confinement or steric effects. A goal for the characterization of the acidity of nanoporous aluminosilicates is to develop an understanding of their catalytic behavior during acid-catalyzed reactions.

Various techniques that could be used for measuring acidity of nanoporous materials can be summarized in the following list:

- Titration method can be used only to get approximate idea on the acid strength distribution of a given nanoporous aluminosilicate.
- Calorimetric methods provide the most quantitative data on the acid strength of nanoporous aluminosilicates.
- NH_3 -TPD is simple and versatile, but is strongly affected by heat and mass transfer. These effects must be carefully taken into consideration for high accuracy and reliability.
- TPD of alkylamine adsorption seems to be a promising alternative to NH_3 -TPD due to the alkylamines' weaker basicities and more suitable molecular sizes.
- IR of hydroxyl groups on zeolites and MCM-41 can provide direct, yet mostly qualitative, information on the strengths of potential Brønsted acidic sites.

- IR study using suitable probe molecules, either strong or slightly basic, are particularly useful in distinguishing Brønsted and Lewis acid sites, providing many useful and semi-quantitative data on both the strength and the distribution of acid sites.
- NMR is also a powerful method for detecting the type, strength, and environments of acid sites by selecting various probe molecules.
- Other spectroscopic methods are being developed as supplements for FTIR and NMR.

In general, it appears that a single technique is not sufficient for the characterization and interpretation of acid sites in nanoporous aluminosilicates, and for the prediction of catalysis or other applications. Therefore, the combination of these experimental techniques, such as FTIR, NMR, thermodynamic methods, etc., should be preferred. Independent experimental methods should be used and also be coupled, if possible, with theoretical methods, to provide better understanding and new insights into the properties of nanoporous aluminosilicates.

8 Acknowledgements

Various portions of our research were supported by US Department of Energy, national Energy Technology Laboratory, and US Department of Defense, Air Force Office of scientific Research via research grants (to CS at PSU). We also thank Mr. Ashok Mishra for his assistance in collecting a part of FTIR data.

References

1. Barrer R. M., *Zeolites and clay minerals as sorbents and molecular sieves*, Academic Press, London, (1978).
2. Szostak R., *Molecular Sieves: Principles of synthesis and identification*. New York, NY, Van Nostrand Reinhold, (1989).
3. Van Bekkum H., Flanigen E.M. and Jansen C., *Zeolites and molecular sieves*, New York; Elsevier, (1991).
4. Nagy J. B., Bodart P., Hannus I. and Kiricsi I., *Synthesis, Characterization and Use of Zeolite Microporous Materials*, DecaGen Ltd., (1998).
5. Beck J. S., Vartuli J. C., Roth W. J., Leonowicz M. E., Kresge C. T., Schmitt K. D., Chu C. T. W., Olson D. H., Sheppard E. W., McCullen S. B., Higgins J. B. and Schlenker J. L. A new family of mesoporous molecular sieves prepared with liquid crystal templates, *J. Am. Chem. Soc.* **114** (1992) pp. 10834-10843.
6. Corma A., From microporous to mesoporous molecular sieve materials and their use in catalysis, *Chem. Rev.* **97** (1997) pp. 2373-2419.

7. Biz S. and Occelli M. L., Synthesis and characterization of mesostructured materials, *Cat. Rev. Sci. Eng.* **40** (1998) pp. 329-407.
8. Selvam P., Bhatia S. K. and Sonwane C. G., Recent advances in processing and characterization of periodic mesoporous MCM-41 silicate molecular sieves, *Ind. Eng. Chem. Res.* **40** (2001) pp. 3237-.
9. Rabo J. A. and Gajda G. J., Acid function in zeolites: recent progress, *Catal. Rev. Sci. Eng.* **31** (1989-90) pp. 385-430.
10. Farneth W. E. and Gorte R. J., Methods for characterizing zeolite acidity, *Chem. Rev.* **95** (1995) pp. 615-635.
11. Corma A., Inorganic solid acids and their use in acid-catalyzed hydrocarbon reactions, *Chem. Rev.* **95** (1995) pp. 559-614.
12. Gorte R. J., What do we know about the acidity of solid acids, *Catal. Lett.* **62** (1999) pp. 1-13.
13. Tanabe K., Misono M., Ono Y. and Hattori H., *Stud. Surf. Sci. Catal.* **51** (1989) p. 6.
14. Haw J. F., Zeolite acid strength and reaction mechanism in catalysis, *Phys. Chem. Chem. Phys.* **4** (2002) pp. 5431-5441.
15. Micek-Ilnicka A., Characterization of acid catalysts by thermometric titration, *Catal. Lett.* **81** (2002) pp. 233-236.
16. Auroux A., Microcalorimetry methods to study the acidity and reactivity of zeolites, pillared clays and mesoporous materials, *Top. Catal.* **19** (2002) pp. 205-213.
17. Occelli M.L., Biz S., Auroux A. and Ray G.J., Effects of the nature of the aluminum source on the acidic properties of some mesostructured materials, *Micropor. Mesopor. Mater.* **26** (1998) pp. 193-213.
18. Janchen J., Stach H., Busio M. and van Wolput J. H. M. C., Microcalorimetric and spectroscopic studies of the acidic- and physisorption characteristics of MCM-41 and zeolites, *Thermo. Acta* **312** (1998) pp. 33-45.
19. Zhang W., Burckle E. C. and Smirniotis P. G., Characterization of the acidity of ultrastable Y, mordenite, and ZSM-12 via NH₃-stepwise temperature programmed desorption and Fourier transform infrared spectroscopy, *Micropor. Mesopor. Mater.* **33** (1999) pp. 173-185.
20. Niwa M. and Katada N., Measurements of acidic property of zeolites by temperature programmed desorption of ammonia, *Catal. Surv. Japan* **1** (1997) pp. 215-226.
21. Hunger B., Heuchel M., Clark L. A. and Snurr R. Q., Characterization of acidic OH groups in zeolites of different types: an interpretation of NH₃-TPD results in the light of confinement effects, *J. Phys. Chem. B*, **106** (2002) pp. 3882-3889.
22. Biaglow A. I., Parrillo D. J. and Gorte R. J., Characterization of H, Na-Y using amine desorption, *J. Catal.* **144** (1993) pp. 193-201.
23. Kresnawahjuesa O., Heussner R., Lee C. C., Kuehl G. and Gorte R. J., An examination of acid sites in H-LTA zeolites, *Appl. Catal. A: Gen.* **199** (2000) pp. 53-60.
24. Maesen T. L. M. and Hertzberg E. P., Proton distribution in modified FAU-type zeolites, *J. Catal.* **182** (1999) pp. 270-273.
25. Reddy K. M. and Song C., Effect of Al sources on the synthesis and acidic characteristics of mesoporous aluminosilicates of MCM-41 type, *Stud. Surf. Sci. Catal.* **117** (1998) pp. 291-299.
26. Yiu H.H.P., Brown D.R. and Barnes P.A., Mesoporous solid acid catalysts: relationship between amine TPD data and catalytic activities, *Catal. Lett.* **59** (1999) pp. 207-211.
27. Araujo A. S., Fernandes V. J. Jr. and Verissimo S. A., Acid properties of SiMCM-41 mesoporous molecular sieve, *J. Ther. Ana. Calor.* **59** (2000) pp. 649-655.

28. Woolery G. L., Alemany L. B., Dessau R. M. and Chester A. W., Spectroscopic evidence for the presence of internal silanols in highly siliceous ZSM-5, *Zeolites* **6** (1986) pp. 14-16.
29. Zheng J., Ming G. and Song C., Influence of the surface acidity of commercial USY zeolites on the Pd supported catalysts for the hydrogenation of naphthalene in the presence of benzothiophene, in preparation.
30. Turaga U. T., MCM-41-supported cobalt-molybdenum catalysts for deep hydrodesulfurization of diesel and jet fuel feedstocks, *Ph.D. Thesis*, Pennsylvania State University, (2002).
31. Huehne M. A., Babitz S. M., Kung H. H. and Miller J. T., *Appl. Catal.* **166** (1998) pp. 293-299.
32. Kotrel S. Lunsford J. H. and Knolzinger H., Characterizing zeolite acidity by spectroscopic and catalytic means: a comparison, *J. Phys. Chem. B* **105** (2001) pp. 3917-3921.
33. Kosslick H., Landmesser H. and Fricke R., Acidity of substituted MCM-41-type mesoporous silicates probed by ammonia, *J. Chem. Soc., Faraday Trans.* **93** (1997) pp. 1849-1854.
34. Jentys A., Kleestorfer K. and Vinek H., Concentration of surface hydroxyl groups on MCM-41, *Micropor. Mesopor. Mater.* **27** (1999) pp. 321-328.
35. Makorova M., Garforth A., Zholobenko V. L., Dwyer J., Earl G. J. and Rawlence D., *Stud. Surf. Sci. Catal.* **84** (1994) pp. 365-372.
36. Morin S., Ayrault P., Gnep N. S. and Guisnet M., *Appl. Catal. A: Gen.* **166** (1998) pp. 281-292.
37. Kustov L.M., New trends in IR-spectroscopic characterization of acid and basic sites in zeolites and oxide catalysts, *Top. Catal.* **4** (1997) pp. 131-144.
38. Lercher J.A., Grundling Ch. and Eder-Mirth G., Infrared studies of the surface acidity of oxides and zeolites using adsorbed probe molecules, *Catal. Today* **27** (1996) pp. 353-376.
39. Ryczkowski J., IR spectroscopy in catalysis, *Catal. Today* **68** (2001) pp. 263-381.
40. Corma A., Fornes V., Forni L., Marquez F., Martinez-Triguero J. and Moscotti D., 2,6-Di-Tert-Butyl-Pyridine as a probe molecule to measure external acidity of zeolites, *J. Catal.* **179** (1998) pp. 451-458.
41. Yamazaki T., Hasegawa K., Honma K. and Ozawa S., Infrared spectroscopic studies on cations in zeolite pores using as CH₄ a probe molecule, *Phys. Chem. Chem. Phys.* **3** (2001) pp. 2686-2691.
42. Jaumain D. and Su B. L., Monitoring the Brønsted acidity of zeolites by means of in situ FT-IR and catalytic testing using chloromethane as probe molecule, *Catal. Today* **73** (2002) pp. 187-196.
43. Su B. L. and Barthomeuf D., Quantitative measurement by infrared spectroscopy of the protonic acidity of H-SAPO-37 and HY using benzene as a probe, *J. Catal.* **139** (1993) pp. 81-92.
44. Thibault-Starzyk F., Travert A., Saussey J. and Lavalley J. C., Correlation between activity and acidity on zeolites: a high temperature infrared study of adsorbed acetonitrile, *Top. Catal.* **6** (1998) pp. 111-118.
45. Knozinger H. and Huber S., IR spectroscopy of small and weakly interacting molecular probes for acidic and basic zeolites, *J. Chem. Soc., Faraday Trans.* **94** (1998) pp. 2047-2060.

46. Wakabayashi F. and Domen K., A new method for characterizing solid surface acidity – an infrared spectroscopic method using probe molecules such as N_2 and rare gases, *Catal. Surv. Japan* **1** (1997) pp. 181–193.
47. Freude D. Hunger M. and Pfeifer H. Study of Brønsted acidity of zeolites using high-resolution proton magnetic resonance with magic-angle spinning, *Chem. Phys. Lett.* **91** (1982) pp. 307–310.
48. Pfeifer H., Brønsted and lewis acidity of zeolites and related catalysis studied by nuclear magnetic-resonance spectroscopy, *Coll. Surf.* **36** (1989) pp. 169–177.
49. Datka J., Geerlings P., Mortier W. and Jacobs P. Influence of the overall composition on zeolite properties. 2. Framework hydroxyls: a quantum chemical study, *J. Phy. Chem.* **89** (1985) pp. 3488–3493.
50. Pfeifer H., Freude D. and Karager J., Nuclear magnetic-resonance studies of zeolites, *Z. Phys. Chem. Leipzig* **269** (1988) pp. 320–330.
51. Lunsford J.H., Rothwell W.P. and Shen W.X., Acid sites in zeolite Y: a solid-state NMR and infrared study using trimethylphosphine as a probe molecule. *J. Am. Chem. Soc.* **107** (1985) pp. 1540–1547.
52. Earl W.L., Fritz P.O., Gibson A.A.V. and Lunsford J.H., A solid-state NMR study of acid sites in zeolite-Y using ammonia and trimethylamine as probe molecules, *J. Phys. Chem.* **91** (1987) pp. 2091–2095.
53. Rabo J.A. and Gajda G.J., Acid function in zeolites-recent progress, *Catal. Rev.* **31** (1989) pp. 385–430.
54. Johansson M. and Klier K., Surface acidity (Brønsted and Lewis) by high resolution X-ray photoelectron spectroscopy, *Top. Catal.* **4** (1997) pp. 99–108.
55. Huang W.F., Hung K.J., Huang D.C., Huang C.C. and Tseng P.K., Positron spectroscopy of base-adsorbed Y-zeolite, *Phys. Lett. A* **266** (2000) pp. 430–434.
56. Catana G., Baetens D., Mommaerts T., Schoonheydt R. A. and Weckhuysen B. M., Relating structure and chemical composition with Lewis acidity in zeolites: a spectroscopic study with probe molecules, *J. Phys. Chem. B* **105** (2001) pp. 4904–4911.
57. Rees L. V. C. and Onyestyak G., Frequency-response characterization of acid sites in zeolite catalysts using NH_3 as the probe molecule, *Micropor. Mesopor. Mater.* **28** (1999) pp. 293–303.
58. El-Rayyes A. A., Perzanowski H.P., Klein U. K.A. and Barri S. A.I., Acidity of zeolite Y-probed by adsorption of 1-naphthylamine and studied by laser-induced fluorescence spectroscopy, *Catal. Lett.* **78** (2002) pp. 161–170.

NANOCATALYSTS PREPARED BY THE MOLECULARLY DESIGNED DISPERSION PROCESS

P. COOL, M. BALTES AND E.F. VANSANT

*University of Antwerpen (U.I.A.), Department of Chemistry,
Laboratory of Adsorption and Catalysis, Universiteitsplein 1, 2610 Wilrijk, Belgium
E-mail: pegie.cool@ua.ac.be*

Molecular Designed Dispersion (MDD) of metal complexes on a highly porous support is a novel synthesis method to obtain high quality heterogeneous catalysts. The aim of the method is to decorate surfaces of porous powders with a monolayer of metal-oxides having the desired structures. The process basically consists of two steps: (1) the anchoring of the complex onto the support in a controlled way, and (2) the mild oxidation of the grafted complex towards catalytically active metal-oxide surface structures. In this way a high dispersion of the supported metal oxide can be obtained. The main principles of the designed dispersion approach will be presented here, as well as typical case studies, leading to superior supported vanadium oxide and vanadium-tantalum mixed oxide catalysts. Detailed chemical, structural and catalytical analyses of these catalysts are discussed.

1 Introduction

In heterogeneous catalysis the surface structure of the catalyst determines the catalytic properties. To satisfy the demands of activity and selectivity, a catalyst system needs to be prepared that catalyzes the desired reaction and eliminates all side reactions. This 'designing' of a catalyst system requires a thorough control of the surface morphology, and for this purpose a novel synthesis method, the molecular designed dispersion, has been developed.

In the past, the preparation of supported metal oxides mainly proceeded by aqueous impregnation of a ceramic support, having the appropriate porosity properties, with a solution containing the desired metal salt(s). Water-soluble salts of the metal are used for which the counter ion may be decomposed easily by heating (e.g. nitrates, acetates, or amine complexes), or the salt is selected for which the counter ion (such as chloride) may be removed upon washing the solid with de-ionized water. However, this technique of impregnation implies important disadvantages: (a) the amount of solution may be in excess of that required to fill the pores, so that a filtration step is necessary to separate the solid from the supernatant liquid; (b) metals are forced onto the ceramic from solution by decreasing the solubility of the metal ions, which can be altered by removing the solvent, adding a co-solvent or by changing the solution pH.

In all cases, the mechanism by which the metal ions attach to the ceramic surface is not known completely and the resulting surface morphology is not well-controlled in all systems. Slight variations in the preparation method results in large changes in the resulting catalytic properties.

Suitable catalysts are prepared by the state-of-the-technology; however, there is a continuing need to develop catalyst preparations allowing precise control over surface structure and hence ensure quality control of catalyst properties with a minimum amount of testing. This quality control will be necessary for the new generation of catalysts required for the future catalytic reactions which demand control of the critical ensemble size and structure. For these new catalysts, control of the catalyst synthesis must be linked directly to surface structure. Such control of the synthesis must be more sophisticated than the known techniques such as manipulation of the metal ion solubility by pH and the rate of catalyst dehydration. It is for these reasons that researchers started to develop new catalyst preparation methods.

2 Molecular designed dispersion approach

2.1 Introduction

A 'designed dispersion' is a surface arrangement of metal ions prepared in a controlled manner so that the metal ions are grouped into ensembles. The ensemble size and the minimum distance between ensembles can be regulated. The metal ion dispersion is created by first adsorbing or ion exchanging metal complexes onto the support. The complex employed, contains metal ions bound to organic ligands and must show a strong affinity for the surface. The nuclearity of the complex determines the ensemble size, the size of the organic ligands determines the minimum distance between ensembles, and the strong affinity for the surface ensures monolayer coverage. The number of metal ions in the ensembles, the internuclear distance between metal ions, and the geometric arrangement of metal ions in the complex are determined by the choice of metal complex for the impregnation. Surfaces may be prepared in which all of the ensembles have the same size [1-8]. This result is important and stands in contrast to some metal catalysts prepared by aqueous impregnation techniques as these samples contain sites of different types and show a distribution of catalytic properties. The ability to create a uniform surface is one advantage of the designed dispersion approach.

2.2 Surface-metal complex interactions

The goal in designing a catalyst system is to prepare a surface which catalyzes only those desired reactions and to eliminate all side reactions, if possible. Thus, the structure of the surface is dictated by the demands of the desired reactions. The ideal catalyst is one having only one type of surface structure replicated over the surface as a monolayer. To realize this goal, a good control over the morphology of the surface is required. This can be done by mounting stable metal complexes on the surface so that only a single layer is formed. The formation of a single layer of complexes requires a strong interaction between the complex and the surface.

The strength of the surface-metal complex interaction depends upon the mechanism by which the complex attaches to the surface. For example, a very weak attachment results from a mechanism involving only Van Der Waals forces. Clearly another mechanism is required to attach metal complexes to ceramic surfaces. Among the mechanisms resulting in strong interactions are the following: (1) hydrogen bonding, (2) ion exchange and (3) ligand exchange. For hydrogen bonding to occur, one species must provide the proton (hydrogen), and the other must provide the nucleophile. Ceramic surfaces terminate with OH groups which are the source of the hydrogens. Thus, for a hydrogen-bonding to occur, the complex must provide the nucleophile, in the form of a functional group to the organic ligands. In the case of ion exchange, surface proton(s) of the ceramic must be replaced by a cationic metal complex. Clearly, one must be able to synthesize as a cation the complex containing the desired metals; but moreover, the surface protons must be removed during the ion exchange with the aid of a strong base either as a part of the complex or as a part of the solvent system. Finally, the ligand exchange mechanism requires that the metal complex be able to surrender a ligand concurrent with the surface losing a proton so that the surface anion (e.g. SiO^-) may replace the ligand to the metal ion. In the following, the chemistries of each component in the process will be discussed.

2.2.1 Chemistry of ceramic surfaces

One necessary condition for fixing metal complexes to ceramic oxides is the presence of surface-OH groups which may react with functional groups in the metal complex. The ceramic metal oxides such as silica and alumina

may contain a large amount of surface hydroxyl groups (-OH), as evidenced by infrared spectroscopy.

For example, van Roosmalen [9] and Hertl [10] showed that the surfaces of silica gel and Cab-O-Sil, respectively, are populated with silanol groups showing distinctive vibrational stretch and deformation. These silanol groups react with active chemicals such as disilazanes to form surface silyl ethers [10, 11]. The reaction shows that even weakly acidic silanol protons may react with sufficiently strong bases such as the nitrogen in the disilazanes. These results suggested that the silanol protons may also interact with strong base groups in metal complexes.

Alumina is another ceramic known to have surface-OH groups [12]. The chemical properties of these Al-OH groups are not equivalent for all species as shown by the rich IR spectrum in the stretching region [12]. As the OH bond strengths depends on the coordination of the neighboring Al^{3+} atoms, the proton acidity also changes with position on the alumina surface; thus the reactivity of these surface-OH groups changes with position. Unlike the silica surface described above, the alumina surface shows a rich variety of surface properties. As many as five different OH groups exist on the surface (figure 1). The Type Ia OH group is attached to a tetrahedral Al ion; whereas, the Type IIa OH group bridges between a tetrahedral Al ion and an octahedral Al ion. In case of Type Ib, the OH is coordinated to one octahedral Al, for Type IIb the OH is coordinated to two octahedral Al's and for Type III to three octahedral Al's. The Type III structure bears a positive charge and therefore is the most acidic since proton abstraction will lead to a negative charge on the resulting structure. Conversely, OH groups bearing net negative charges are considered basic and thus subject to become good 'leaving' groups. Thus the Ia and Ib structures give rise to the basic OH groups on the surface.

This discussion on surface-OH chemistry can be extended to include the crystalline ceramics such as the zeolites. The aluminosilicates are one sub-group of zeolites which show surface-OH groups that can interact with metal complexes. However, the strong protonic acidity of the hydrogen-forms of the aluminosilicates may initiate decomposition of the complex as it contacts the surface. Such acid-catalyzed decomposition of the complex may be inhibited with the use of either more stable complexes, such as ethylenediamines, or with the use of base-exchanged forms of the zeolite. The ammonium-forms of the zeolites may be used if the metal complex will not accept as ligands the ammonium ion or the ammonia molecule.

The microporous network of the zeolites presents a problem for the use of metal complexes having dimensions greater than the pore size of the zeolite. If one wants to introduce metals inside the pore network, then the choice of metal complexes is limited by the size of the available metal complexes; however, this consideration can be exploited to selectively decorate the exterior of the zeolite crystal with an inert, but very large complex (e.g. tetraethoxysilaan) so that the smaller, metal complex is introduced into the interior of the crystal, only. By excluding the metal complexes from the external parts of the crystal, it is possible to exploit the shape-selective effects of the catalysts.

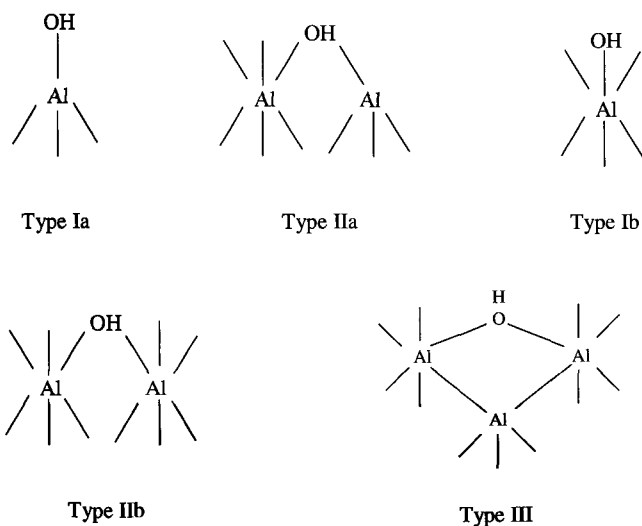


Figure 1. Different types of OH-groups on the alumina surface.

2.2.2 Chemistry of metal complexes

From the foregoing discussion, it appears that the metal complex should contain nucleophilic ligands to participate in hydrogen-bonding and perhaps even in ion exchange interactions. Examples of such ligands include acetylacetonate (acac) anions $(C_5H_7O_2)^{1-}$, aminoalkoxide (ae) anions $(-NR_1R_2CH_2CH_2O-)$, diethanolamine (Deta) anions $\{NH(C_2H_5OH)_2\}^{1-}$, and bipyridil (bipy) anions $\{(NC_5H_4)_2\}^{1-}$. These ligands show nucleophilic functional groups having the required basicity to

interact with the surface protons such as those found on silica. However, for ligand exchange reactions, the basic character of the ligand is not sufficient to ensure the affinity of the complex for the surface. The intrinsic stability of the metal complex also determines the nature of the surface-complex interaction. For a sufficiently basic nucleophile in a rather unstable metal complex, the acidic surface proton may initiate an acid-catalyzed substitution reaction for which the ligand leaves the metal complex as a stable molecule to be replaced by a group from the surface such as $\{\text{SiO}\}^{1-}$.

Neutral metal complexes-metal acetylacetonates

The tautomerism of β -diketones offers a rich chemistry which permits a large number of the transition metal ions to be chelated as neutral complexes known as metal acetylacetonates having the formula $[\text{M}^{n+}(\text{acac})_n]$. Fackler [13] summarized much of this chemistry more than 30 years ago. He reported that all of the elements to the left of Group III metals combined to form metal acetylacetonates with the exception of Nb, Ta, W, Au. Thus, almost all of the catalytically interesting transition metals formed metal acetylacetonates. The β -diketones which chelated these metals included the following: acetylacetonates (acac), dibenzoylmethane (dbm), benzoylacetone (ba), dipivaloylmethane (dpm), diisobutylmethane (dibm), trifluoroacetylacetone (tfac), hexafluoroacetylacetone (hfac), and others. Thus the size of the metal β -diketonol can be altered by proper size of the ligands.

The structure of many metal β -diketonols was elucidated and reported in literature. Mainly, the oxygen atoms of the β -diketonol coordinated to the metal ion and the structure of the resulting complex followed from the oxidation state of the metal ion. This means that divalent metal ions showed coordination numbers restricted to four with a particular ligand and the arrangement of the oxygens were either square planar or tetrahedral. Metal ions known to have planar or square planar structure include the following: Cu^{2+} , Pd^{2+} , Pt^{2+} , VO^{2+} , TiO^{2+} . The trivalent metal ions formed nearly octahedral arrangements of the oxygen atoms about the metal ion with the exception of B^{3+} and Au^{3+} . Some metal complexes form polynuclear species as a result of sharing of β -diketonols between adjacent metal ions. Metals known to form such polymer structures include Mg^{2+} , Ni^{2+} , Co^{2+} , Mn^{2+} , Fe^{2+} and Ln^{3+} . Examples of some metal acetylacetonate complex structures are depicted in figure 2.

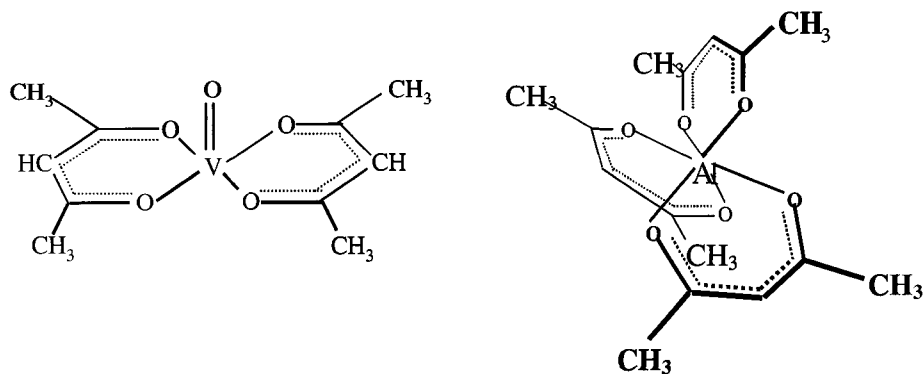


Figure 2. The square pyramidal structure of $\text{VO}(\text{acac})_2$ (left) and the octahedral structure of $\text{Al}(\text{acac})_3$ (right).

Cationic metal complexes

Other types of metal complexes may be used as precursors to supported catalysts. These precursors include stable, cationic complexes with nucleophilic ligands, such as the perchlorate salts of copper bipyridil dimer $\{[\text{Cubipy}]_2\}$, copper diaminopropoxide trimer $\{[\text{Cudap}]_3\}$, copper diethanolamine $\{\text{Cu}(\text{H}_2\text{DetaHDeta})\}$ monomer and dimer, and the hexameric M^{3+} μ -hydroxy copper diethylaminoethoxide where $\text{M} = \text{Al}, \text{Cr}$ or Fe . Other cationic metal complexes have been grafted to the surface of silica using nickel (II) ethylenediamine $[\text{Ni}\{(\text{H}_2\text{N}-\text{CH}_2\text{CH}_2-\text{NH}_2)_3\}]^{2+}$ and nickel (II) cyclohexanediamine $[\text{Ni}\{\text{C}_6\text{H}_{12}(\text{NH}_2)_2\}_3]^{2+}$ [14]. The charge of the complex, the nature of the ligands, the pH and temperature of the solvent, the competitive ions, and adduct formation were important factors in the formation of a monolayer of the metal complex on the silica. The mechanisms for interaction between the support and the metal complexes were as follows: ligand screened electrostatic adsorption, grafting by reaction with the support to liberate a ligand, and hydrogen bonding.

2.2.3 Liquid-phase deposition vs. gas phase deposition: the role of the solvent

The proper choice of solvent in case of a liquid-phase deposition is important to the goal of achieving a monolayer dispersion of complex onto the support surface. The solvent must allow a favorable interaction

between the complex and the surface. The main function of the solvent is to bring into solution the molecules or ions of the metal complex so that these species may diffuse to the surface and become affixed to it. In that connection the solvent must possess the proper chemical properties to solvate the crystal of the metal complex without interfering with the process of decorating the surface. The solvent should not coordinate to the metal complex nor should it bond with the surface. Thus, the solvent must be non-coordinating and non-hydrogen bonding. van Ommen et al. [15] used both toluene and acetonitrile to dissolve a family of metal acetylacetonates on ceramic oxides. Different results were obtained in the ultimate catalytic properties of the supported metal oxides after thermolysis to remove the organic ligands. Also Kenvin [16] reported striking differences in the chemical composition of the $\text{Cu}(\text{acac})_2$ system on silica when using either acetonitrile or methanol as the solvent. The results showed that methanol did become involved in the dimerisation of the complex over silica. So the choice of solvent is dictated by the need to solvate the metal complex crystal without interfering with the process.

Another way to adsorb the complex onto the support, is to carry out the reaction in the gas phase, without the use of a solvent. Modification of the support in the gas phase eliminates the use of toxic solvents. For example, most acetylacetonate complexes sublime around 200°C in an inert atmosphere. As a result of the elevated temperatures the complexes will have a higher reactivity, so that gas phase reactions can be much more successful. This gas phase deposition of metal complex onto the support can be carried out in a flow-type reactor at atmospheric pressure or in a vacuum deposition reactor.

2.2.4 Models of surface-complex interactions

Several factors influence the interaction between the complex and the surface: shape, charge, stability and functional groups in the complex.

Shape. The shape of the complex influences the orientation of the complex with respect to the surface of the support. Consider the work of Kenvin [16] who prepared supported catalysts by the deposition of neutral metal acetylacetonates on silica. The $\text{Cu}(\text{acac})_3$ complex, having a spherical shape, did not show any affinity for the surface; whereas, the equally stable, planar shaped $\text{Cu}(\text{II})(\text{acac})_2$ was attracted to the surface. This emphasizes the importance of the orientation of the (acac) ligands with respect to the surface silanol groups. The $\text{Cr}(\text{III})(\text{acac})_3$, having the

octahedral arrangement of the ligands, does not permit the surface silanols to hydrogen bond to the (acac) ligands; whereas, the planar $\text{Cu}(\text{acac})_2$ permits easy access of silanols into the (acac) groups. In another study, Beckler [2] reported the steric hindrance effects of bulky substituent groups on a cationic complex. The n-butyl groups of the complex prevented a close association of the complex with the surface such that ion exchange did not occur; whereas, the ion exchange readily occurred with a complex having the smaller ethyl groups [2].

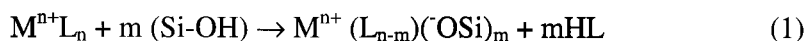
Charge, ion-exchange. In the ion exchange mechanism, a surface species such as the silanol, must lose a proton and the resulting siloxide must hydrogen bond to a proton on the ligand or bond directly to the metal ion. Thus the activation of the surface-OH species is a necessary step in the ion exchange mechanism which anchors the cationic complex to the surface siloxides. The charge on the complex has a secondary effect on the affinity of the complex with the surface compared to the effects of stability of the complex relative to ligand exchange reactions or compared to the functional groups present in the complex. Both cationic and neutral metal complexes form monolayers on the surface of silica when the complexes show functional groups such as OH which interact with $(\text{SiO})^{1-}$ [2] or O which hydrogen bond to SiOH [16]. Obviously, the charge on the complex is not sufficient to ensure a strong interaction with the surface as the cationic $\text{Cu}(\text{en})_2^{2+}$ will not ion exchange with the surface [17,18]; whereas, the hexameric cationic complex reported by Beckler [2] readily ion exchanges with the surface as a result of the hydrogen-bonding groups present in the complex. Thus, the charge of the complex plays a secondary role to that of the functional groups in anchoring the complexes to the surface of silica.

Hydrogen bonding. For cationic complexes to hydrogen bond, they need either an electron-pair (hydrogen bond acceptor) or a proton (hydrogen bond donor). When acetylacetonate complexes are used as precursors for supported metal oxide catalysts, the formation of an adsorbed complex on the support is a necessary first step. The complex can be stabilized as an intact species on the surface by hydrogen bonding interactions with, for example, surface OH groups, or can react to form a chemisorbed species, via a ligand exchange reaction in the simplest case. On silica, the primary interaction is one of hydrogen bonding, and this has been demonstrated using infrared spectroscopy of the supported complex to investigate the

nature of the adsorbed species [19-21]. The small shifts observed in the infrared spectra make it easy to assign the bands to different vibrational modes of the complex, but also serve to indicate the limited interaction of the complex with the support. Another recent study by Porbeni [22] showed that the copper acetylacetonate interacts with an aluminum oxide surface in a way that appears to be very similar to the mode of interaction with the silica surface.

Neutral metal acetylacetonates have been attached as a monolayer film to silica surfaces without the benefit of ion exchange or ligand exchange reactions [7, 8, 16]. These materials showed the tendency to maintain monolayer dispersions even at high loadings of the complexes. The mechanism for binding some of these metal acetylacetonates to the surface is hydrogen bonding between the surface silanols and the π -electrons of the acac ligands. Thus, surface silanol protons are necessary functional groups to affix neutral metal complexes to the surface of a ceramic.

Ligand exchange. The ability of the complex to surrender ligands also shows an effect on the affinity of the complex to the surface. Kenvin [16] reported on the affinity of Fe(III)(acac)_3 and Mn(III)(acac)_3 for the silica surface as a result of ligand loss. These complexes were known to have low stabilities relative to the copper and chromium complexes [23, 24]. The loss of a ligand affords the possibility of forming a direct bond between the metal of the complex and the surface siloxide as shown in eq. (1).



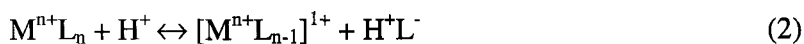
The anionic ligand present in the complexes (e.g. acac) reacts with a proton to become the stable molecule (e.g. pentanedione). Thus, protons from the surface silanols are activated during the impregnation to form the stable molecules from the ligands which were surrendered from the parent complex when the stability of the complex permits this ligand exchange reaction [23, 24].

2.3 Thermolysis of supported polynuclear metal complexes

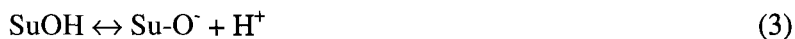
Before use, the catalyst needs to be activated by heating (calcining) at high temperature. The ligands of the metal complexes must be removed to allow reactants access into the orbitals of the catalytic metals. One way to remove the ligands is by controlled thermolysis in the appropriate

atmospheres. Another method is for a surface species to replace the ligand(s) by a reaction similar to Eq. (1). This reaction serves as a mechanism to anchor the complex firmly to the surface which may play an important role in resisting the effects of heat in sintering the metal ions.

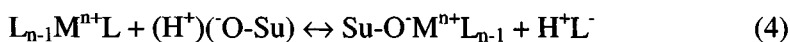
Proton-assisted thermolysis. The ligands in many complexes are anionic, bidentate chelating agents (e.g. aminoalkoxide and acetylacetonate). Under the proper conditions, a ligand reacted with a proton to form the stable molecule of the anion, such as pentanedione from acetylacetonate.



However, the source of protons is the ceramic surface as a result of the following reaction where Su denotes a surface metal ion of the ceramic oxide, SuO.



For ceramics such as silica and alumina, reaction (3) is unlikely to occur without the aid of a strong base B. In the case of some metal complexes, the ligand L contained a functional group having the proper basicity. Thus, it is likely that Eqs. (2) and (3) occur simultaneously as given by Eq. (4).



By this scheme, the activation of the surface proton, Eq. (4), is made possible by a sufficiently basic nucleophile in the ligand (L), and the surface proton reciprocated by rendering the ligand a better leaving group as a stable molecule of the anion. This symbiotic process results in the introduction of the surface oxide (^-O-Su) into the metal complexes which then anchors the residue of the complex to the surface. The process continues according to Eq. (2) to give full ligand replacement provided that the density of surface-OH groups was sufficiently high.

Thus, the mechanism to remove ligands, such as $(acac)^{1-}$, $(HDeta)^{1-}$ and aminoalkoxide anions, at mild temperatures (less than 200°C) is to supply surface protons to these ligands. Each of them will combine then with a proton to produce the corresponding neutral molecule: pentanedione, diethanol amine, and aminoalkyl alcohol. This procedure facilitates the

process of ligand removal followed by introduction of the surface siloxide into the metal complex. The process is called proton-assisted thermolysis and does not require oxygen. At higher temperatures, the remaining (non-hydrogen-bond-interacting) ligands are oxidized, yielding typical oxidation products, such as CO_2 , acetone, water,

2.4 Reaction scheme of the molecular designed dispersion process

In order to visualize the process of molecular designed dispersion, consider the creation of MO_x catalysts onto the surface of a porous silica support by the reaction with metal acetylacetonate complexes.

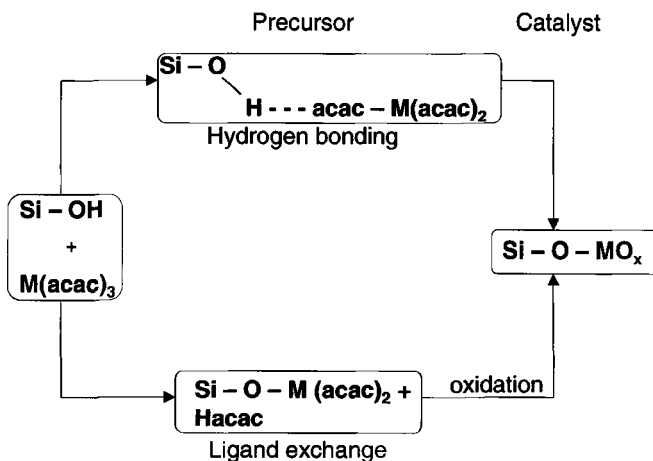


Figure 3. Visualization of the creation of a heterogeneous MO_x catalyst by the 'Molecular Designed Dispersion' process

The MDD process clearly consists of two steps (figure 3): in a first step, a neutral transition metal acetylacetonate complex ($\text{M}^{n+}(\text{acac})_n$) is anchored to the surface of the high-surface area oxide support. In a consecutive step, the adsorbed complex is decomposed in an oxygen-containing atmosphere at elevated temperatures, yielding the supported transition metal oxide catalyst. The adsorption of the complex can occur in two distinct ways: (1) by hydrogen bonding between an acetylacetonate ligand and the surface hydroxyls and (2) by a ligand-exchange mechanism, with formation of a covalent metal-oxygen support bonding and loss of a ligand as acetylacetonate (Hacac).

The actual reaction mechanism can be determined by calculating the ratio R:

$$R = \frac{\text{mmol}(\text{acac}) \cdot (\text{g support})^{-1}}{\text{mmol M} (\text{g support})^{-1}} = \frac{n_{\text{acac}}}{n_{\text{M}}} \quad (5)$$

In this formula, M is the central metal ion of the acetylacetonate complex. The surface concentration of acac ligands (n_{acac}) can be determined by measuring the weight loss of the modified support in the thermogram after heating in an oxygen flow at 500°C. The metal loading n_{M} is obtained by chemical analysis.

If the complex interacts by hydrogen bonding, the R-value should equal the number of acetylacetonate ligands. For instance, R should be 2 for $\text{VO}(\text{acac})_2$ and 3 for $\text{Al}(\text{acac})_3$. A lower value is an indication of the ligand-exchange mechanism, involving the loss of one or more acac ligands during the reaction.

3 Applications: designed dispersions of metal oxides on porous solids

In what follows, some typical examples will be discussed of superior nanocatalysts prepared by the molecularly designed dispersion method, using metal acetylacetonate complexes. As porous supports, both amorphous silica and the mesoporous templated silicate structure MCM-48 have been used.

3.1 MCM-48 and silica supported vanadium oxide catalysts prepared by the reaction with $\text{VO}(\text{acac})_2$

Mesoporous molecular sieve MCM-48 is a unique member of the M41S family (as defined by Mobil), first described in 1992 [25, 26]. Based on its three-dimensional pore structure, the substrate is potentially very interesting and a promising support for heterogeneous catalysts by grafting the surface of the support with catalytic active VO_x -species. The preparation of MCM-48 supported vanadium oxide catalyst by means of the MDD process of $\text{VO}(\text{acac})_2$ will be compared to the preparation of silica supported VO_x .

3.1.1 Preparation methods

The MCM-48 support in this study was prepared using TEOS ($\text{Si}(\text{OC}_2\text{H}_5)_4$) and the 16–12–16 gemini surfactant, with the formula $[\text{C}_{16}\text{H}_{33}\text{-N}^+(\text{CH}_3)_2\text{-(CH}_2\text{)}_{12}\text{-N}^+(\text{CH}_3)_2\text{-C}_{16}\text{H}_{33}]\cdot 2\text{Br}^-$. The synthesis of MCM-48 has already been optimized and reported in previous publications [27, 28].

Silica gel (Kieselgel 60, Merck) was thermally pretreated in air for 17 h at 700°C. The specific surface area of the silica (S_{BET}) was 340 m²/g. The surface modification reaction with HMDS (1,1,1,3,3,3-hexamethyldisilazane) is performed in fully methylated glassware (three neck bottle and reflux condenser). The HMDS is allowed to reflux during 30 min, before the silica or MCM-48 samples are introduced. Subsequently, the HMDS reaction is carried out for 5 h.

The deposition of the $\text{VO}(\text{acac})_2$ complex is carried out in a liquid phase reaction at room temperature. The support was stirred for 1 h in a solution of the $\text{VO}(\text{acac})_2$ complex in zeolite dried toluene. The reaction vessel was purged with a stream of dry nitrogen. After the reaction the modified support was filtered, washed with fresh solvent, and dried under vacuum. One washing cycle consists of washing 1 g of the reacted substrate with an aliquot of 25 mL of solvent, before drying.

The samples obtained after modification were stored in a nitrogen glove box to avoid hydration until analysis was completed and subsequently calcined to form the supported vanadium oxide catalysts. Calcination was performed in a programmable oven (25–500°C; heating rate 2°C/min; isothermal period 17 h) in air.

3.1.2 Discussion

Porosity characteristics of MCM-48 supported vanadium oxide. The optimized synthesis of the mesoporous silica molecular sieve, MCM-48, enables the creation of a highly porous material with surface area of 1275 m²/g and a pore volume exceeding 1.0 mL/g. The maximum of the very narrow pore size distribution is found at $r_p = 1.63$ nm. The XRD pattern indicates the cubic unit-cell with a dimension of 7.92 nm.

The deposition of $\text{VO}(\text{acac})_2$ on the MCM-48 material reduces the surface area and the porosity, due to the bulky acetylacetonate ligands of the complex. After the thermal conversion of the adsorbed complex both the surface area and porosity features are restored to a certain extent, due to the removal of the acetylacetonate ligands (Table 1).

Table 1. XRD and BET characteristics of the MCM-48-supported vanadium oxide in comparison to the blank MCM-48 support

	V mmol/g	V/nm ²	S _{BET} m ² /g	r _p nm	V _p mL/g	a nm
MCM-48	0	0	1275	1.63	1.15	7.92
VO _x -MCM-48	0.2	0.1	1189	1.64	1.09	7.97
	0.4	0.2	1077	1.6	1.05	7.98
	0.7	0.31	821	1.43	1.01	7.90
	1.3	0.63	804	1.34	0.90	7.98

S_{BET}: BET specific surface area; r_p: pore radius; V_p: pore volume; a: unit-cell parameter

Table 1 summarizes the characteristics of the MCM-48-supported vanadium oxides, obtained after deposition of VO(acac)₂ and subsequent thermal conversion. Samples are prepared with increasing vanadium loading (0–1.3 mmol g⁻¹ or 0–6.5 wt% V). The change in unit cell parameter is negligible, which shows that the cubic MCM-48 structure is maintained. The pore radius, pore volume, and surface area shift to lower values as a function of the vanadium loading. This reduction is due to the narrowing of the pores after the deposition of the vanadium oxide layer. The results reveal that the deposition of the VO(acac)₂ complex and the subsequent thermal conversion results in a supported vanadium oxide catalyst with the characteristic MCM-48 properties.

The interaction between VO(acac)₂ with silica and MCM-48. Following equation (5), the R-values of the vanadium modified MCM-48 materials equal 1.8, suggesting that the complex reacts both by hydrogen bonding and ligand exchange. This means that a part of the acac ligands are evolved and covalently bonded vanadium species are present, besides the hydrogen bonded VO(acac)₂. This is a quite interesting observation as the liquid phase deposition of VO(acac)₂ on amorphous silica proceeds exclusively by hydrogen bonding [29–31], the corresponding R value is 2. A ligand exchange reaction with silica occurs only during the gas phase modification [29, 30] (sublimation of the complex in vacuum at 120–180°C and subsequent reaction with the substrate; the elevated temperatures increase the reactivity of the complex and the support).

Additional information on the interaction mechanism of VO(acac)₂ with MCM-48 can be provided by ESR spectroscopy [32]. ESR is a powerful technique for detecting the presence and the coordination

geometry of the paramagnetic V^{4+} (d^1) species. The ESR spectra of the $VO(acac)_2$ -modified MCM-48 material are typical for V^{4+} in an axial to slightly rhombic environment with the characteristic number of hyperfine lines due to its nuclear spin I of $7/2$. In the ESR signal, there is no indication for the presence of a broad background signal, which could be due to clustered V^{4+} -species. This indicates that V^{4+} is well-dispersed on the MCM-48 surface after synthesis. The V^{4+} -species observed at the surface of MCM-48 have a clear vanadyl character [VO^{2+}], which means that one of the vanadium-oxygen bonds is particularly short and can be described in terms of a $V=O$ bond. The ESR results indicate typical 5- and 6-coordinated vanadyl species; i.e. $(VO^{2+})_{5c}$ and $(VO^{2+})_{6c}$, respectively. Both species are difficult to distinguish by ESR because the sixth ligand is only weakly interacting. Thus, the distorted octahedral coordination is one in which an additional ligand is completing the coordination sphere. This axial coordination is expected to be the most pronounced for a V^{4+} species with g and A values close to axial symmetry. This is indeed the case for the ESR parameters of the $VO(acac)_2$ -modified MCM-48 material. Therefore, a distorted square pyramidal coordination is the most likely coordination model for V^{4+} on MCM-48.

The ESR measurements reinforce our conclusion that the MCM-48 surface exhibits higher reactivity in comparison to the amorphous silica support. The surface of silica terminates in either a siloxane group ($\equiv Si-O-Si \equiv$) with oxygen on the surface or one of several forms of silanol groups ($\equiv Si-OH$; free, bridged and/or geminal silanols). The calcination procedure of the as-synthesized MCM-48 precursor, which is carried out to remove the gemini surfactant molecules, leaves the substrate covered only with siloxane bridges and isolated hydroxyl groups [28]. It has been reported that the OH groups on the surface of MCM-48 exhibit only weak acidity, comparable with the OH groups on silica [33].

This can also be inferred from Figs. 4a and 4e, which present the infrared spectra of the pure MCM-48 support after pretreatment at $550^\circ C$, and of the pure silica support pretreated at $700^\circ C$, respectively. Pretreatment of the silica support at $700^\circ C$ results in dehydration and dehydroxylation reactions, leaving the silica surface also covered only with isolated silanols and siloxane bridges. The spectra in Figs. 4a and 4e exhibit a band at 3747 cm^{-1} , attributed to the isolated OH. A differing acid-base character between the OH groups on silica and MCM-48 would result in a different position of this characteristic band.

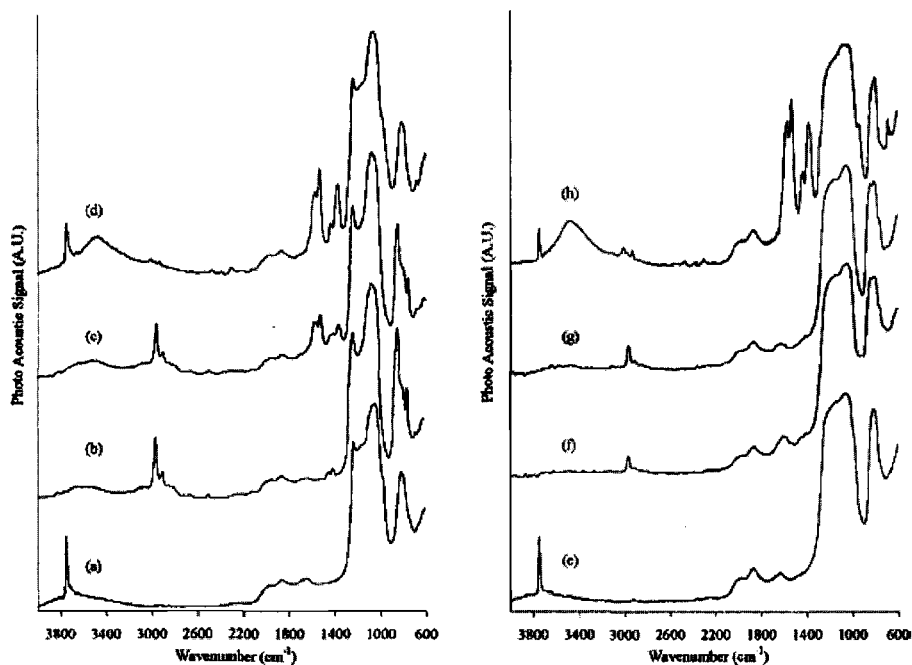
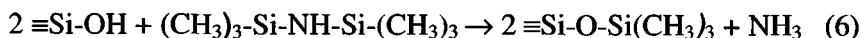


Figure 4. FTIR-PA spectra of (a) pure MCM-48 after pretreatment at 550°C, (b) MCM-48 modified with HMDS, (c) MCM-48 after modification with HMDS and VO(acac)₂, (d) MCM-48 after modification with VO(acac)₂, without HMDS pretreatment, (e) pure silica support after pretreatment at 700°C, (f) silica modified with HMDS, (g) silica after modification with HMDS and VO(acac)₂, (h) silica after modification with VO(acac)₂, without HMDS pretreatment.

In order to study the surface properties of the support materials and to compare the interaction mechanism of the VO(acac)₂ complex with both MCM-48 and silica, an additional set of experiments was performed. First, the silanol groups on both supports (after pretreatment at 550°C and 700°C for MCM-48 and silica, respectively) were deactivated prior to the reaction with VO(acac)₂, in order to study the influence on the deposition of the complex. Therefore, a typical chemical modification technique has been performed, being the reaction of the silica surface with hexamethyldisilazane (HMDS) [34]. HMDS reacts readily with the silanols, yielding very stable trimethylsilyl groups according to the following reaction [34]:



The on-line determination of the liberated NH_3 directly yields the number of silanols reacted with HMDS. However, after modification of the silica surface with HMDS all the hydroxyls are converted into trimethylsilyl groups. This is also shown in Fig. 4. Figures 4b and 4f present the infrared spectra of respectively the MCM-48 and the silica support after reaction with HMDS. The band at 3747 cm^{-1} has disappeared, whereas in the region around 2950 cm^{-1} the methyl bands are present. If these pretreated samples are subsequently modified with $\text{VO}(\text{acac})_2$ it can be inferred if the complex reacts selectively with the OH groups of the support. The vanadium modified samples are presented in Figs. 4c and 4g, respectively. In spectrum 4c the IR bands between 1200 and 1600 cm^{-1} are attributed to the acetylacetonate ligands of the adsorbed complex. The vanadium determination reveals a loading of 0.12 mmol g^{-1} (0.6 wt\% V) and the corresponding R value is 2. The vanadium loading of the modified MCM-48 support using the same reaction conditions, without the HMDS pretreatment is 0.4 mmol g^{-1} (2 wt\% V). In Fig. 4g the spectrum of the HMDS pretreated silica support is shown after modification with $\text{VO}(\text{acac})_2$ under the same reaction conditions. No acac bands are observed in the IR and the chemical analysis traced only a negligible amount of vanadium. In comparison, the infrared spectra of the $\text{VO}(\text{acac})_2$ -modified MCM-48 and silica supports, without the HMDS pretreatment, are shown in Figs. 4d and 4h, respectively. The broad band between 3600 and 3200 cm^{-1} is assigned to hydrogen bonded silanol groups, indicating the presence of hydrogen bonded $\text{VO}(\text{acac})_2$.

It can be inferred that the $\text{VO}(\text{acac})_2$ reacts selectively with the OH groups of the support, but on MCM-48 there are also other surface sites, in particular the siloxane groups, contributing to the adsorption process of the complex. It was already established earlier [35] that on silica the concentration of the siloxane bridges increases with rising pretreatment temperatures, as the remaining free silanol groups dehydroxylate. Simultaneously, the reactivity enhances, as structural changes occur, giving rise to the so-called *strained* siloxane bridges. This site is assumed to be an unsymmetrical siloxane bridge consisting of one silicon atom being more electron deficient than the other. The MCM-48 support is only covered with 0.9 OH/nm^2 [27, 28]. A part of the siloxane bridges are probably strained groups, resulting in a much higher reactivity in comparison to amorphous silica, and the $\text{VO}(\text{acac})_2$ can interact with this surface site too. It is particularly interesting to elucidate the nature of the interaction of the $\text{VO}(\text{acac})_2$ complex with the strained Si–O–Si sites, as this provides valuable information on the surface properties of the MCM-48. A ligand

exchange mechanism with the strained Si–O–Si groups on MCM-48 would result in the formation of a covalently bonded Si–O–VO(acac) species and simultaneously the formation of Si(acac). However, it is generally known that Si(acac) compounds are extremely unstable, and therefore, a formation of Si(acac) species is very unlikely. Moreover, the R value of the reaction of VO(acac)₂ with the pure (non-HMDS-pretreated) MCM-48 is 1.8, suggesting the release of acac ligands. However, the reaction of the complex with the HMDS pretreated support is 2. The explanation for this difference was revealed by studying the effect of water on the formation of the various surface species. When the HMDS pretreated MCM-48 was modified with VO(acac)₂ under “wet” conditions (i.e. the complex and the solvent were not dried prior to the reaction), the R value of the reaction was 1.1. Furthermore, the IR spectra of the sample prepared under wet conditions (not shown here), still exhibits the characteristic acac bands, but it is obvious that some OH groups are generated as well. A control experiment to elucidate the formation of these Si–OH groups is carried out by stirring the HMDS pretreated sample in “wet” toluene, in the absence of VO(acac)₂. The IR spectrum of this control experiment showed no significant generation of Si–OH groups. The hydrophobic trimethylsilyl groups prevent the surface from direct rehydroxylation. Indeed, the rather low stability of MCM-48 toward moisture can be improved drastically by trimethylsilylation. Apparently, even with the hydrophobic nature of the sample, water can still interact with the surface sites involving vanadium species. It is anticipated that the presence of traces of H₂O will result in a conversion of the strained siloxane–VO(acac)₂ system, with the formation of a covalently bonded vanadium species and the simultaneous generation of Si–OH species and release of acetylacetone (Hacac). Similarly, the VO(acac)₂ modified MCM-48 sample (without HMDS pretreatment) is sensitive to exposure to air or traces of water, which results in the immediate conversion of the surface species involving a strained siloxane–VO(acac)₂ system. This explains the lower R values for non-HMDS-pretreated MCM-48, as the HMDS-pretreated samples are stabilized by the trimethylsilyl groups. The hydrophobic nature prevents the uptake of water before characterization. However, the presence of water during the modification of the HMDS pretreated MCM-48 with VO(acac)₂, also results in lower R values, due to the *in situ* conversion of the strained siloxane–VO(acac)₂ system.

In conclusion, the reaction of MCM-48 with VO(acac)₂ yields two types of adsorbed complexes. The VO(acac)₂ can interact by hydrogen bonding with the surface silanols. In addition, a part of the complexes can interact

with the very reactive strained siloxane groups of the MCM-48 as well. This results in the formation of a strained siloxane-VO(acac)₂ system, which is envisaged in Figure 5. Exposure to air (water) converts this system, with formation of a covalently bonded species and generation of Si-OH groups.

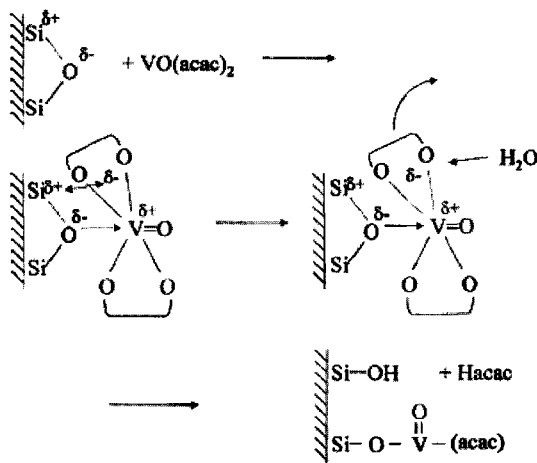


Figure 5. Schematic presentation of the reaction mechanism of the adsorption of VO(acac)₂ on MCM-48.

The difference in reactivity between the MCM-48 and the silica surface can be explained by the number of strained siloxane groups and the difference in surface area. In the case of MCM-48, there are more strained groups, and the surface area is approximately four times higher than the surface area of silica. Accordingly, the reactivity per gram is much higher for MCM-48.

In addition, a full spectroscopic characterization of the supported VO_x/MCM-48 by FTIR, Raman, and UV-vis-DR spectroscopy (not shown here) indicates the presence of different VO_x structures as a function of the surface loading [32]. At loadings up to 0.7 mmol g⁻¹ (3.5 wt% V) the MCM-48 surface is uniformly covered with tetrahedral (SiO)₃V=O monomers. With increasing loadings, polymer chains of tetrahedral VO_x appear, which are linked to each other with V-O-V bridges. At surface loadings of 1.33 mmol g⁻¹ (6.7 wt% V) also a small fraction of crystalline V₂O₅ is formed. Nevertheless, due to the high surface area of the MCM-48 support, higher vanadium loadings can be obtained in comparison to an amorphous silica support before crystalline vanadium oxide appears.

Oxidation of methanol. Supported vanadium oxides possess unique properties in several heterogeneous catalytic processes, e.g., the oxidation of sulfur dioxide to sulfur trioxide [36] in the preparation of sulfuric acid, the oxidation of *o*-xylene to phthalic anhydride [37], and the selective catalytic reduction of NO_x [36]. The oxidation of methanol is an important probe reaction to study the catalytic properties of surface vanadium oxide species. The product selectivity reflects the reaction pathways that depend on the acidic, basic, or redox sites on the catalyst surface. Acidic sites give rise to dimethyl ether, basic sites produce carbon oxides (CO_x) and redox sites produce formaldehyde, methyl formate, and dimethoxymethane.

In this study the influence of the vanadium loading on the catalytic properties has been studied for the oxidation of methanol and the results are shown in Table 2.

Table 2. Oxidation of methanol at 400°C: the catalytic performance of the MCM-48 and silica-supported vanadium oxides as a function of the vanadium loading.

V (mmol/g)	Conversion (%)	Selectivity (%) / Yield (%)		
		CO+CO ₂	HCHO	CH ₃ OCH ₃
VO _x /MCM-48				
0.0	15	0.0 / 0.0	2.7 / 0.4	97.3 / 14.9
0.2	31	0.0 / 0.0	98.1 / 30.4	1.9 / 0.6
0.4	61	3.4 / 2.1	94.7 / 57.7	1.9 / 1.2
0.7	75	5.0 / 3.8	92.8 / 69.6	2.2 / 1.7
1.3	68	46.8 / 31.9	33.9 / 23.1	19.3 / 13.1
VO _x /silica				
0.0	9	0.0 / 0.0	11.1 / 1.3	88.9 / 10.7
0.2	21	0.0 / 0.0	79.3 / 16.6	20.7 / 4.4
0.4	45	8.0 / 3.6	88.0 / 39.6	4.0 / 1.8
0.7	58	20.3 / 11.8	72.5 / 42.0	7.2 / 4.2
1.3	31	41.2 / 12.7	38.5 / 12.1	20.3 / 6.2

The conversion, selectivity, and yield are presented as a function of the vanadium loading. The reaction was carried out at 400°C at atmospheric pressure. The pure MCM-48 exhibits rather low activity (15% conversion). However, the conversion level is significantly higher than that of amorphous silica (9% conversion). The reaction of methanol on the MCM-48 surface yields dimethylether, which suggests the presence of acidic

sites. This is an additional indication that the surface of MCM-48 contains sites with higher reactivity in comparison with silica. This was attributed to the presence of strained siloxanes, which indeed can act as Lewis acid center [34]. The conversion level increases with increasing loading of vanadium. The major product is formaldehyde, produced at the $(\text{SiO})_3\text{V}=\text{O}$ redox sites. The spectroscopic study evidenced that with higher vanadia coverage (on MCM-48, the sample with $0.7 \text{ mmol g}^{-1} \text{ V}$) polymeric chains with V–O–V bridges appear. However, the conversion and selectivity level still increases, which means that these V–O–V bridges do not affect the reaction. It has already been reported [36, 38] that the active sites on supported vanadium oxide catalysts for the oxidation of hydrocarbons, are rather the V–O–support bonds than the terminal $\text{V}=\text{O}$ or bridging V–O–V. Therefore, the catalytic properties of the vanadium oxide layer can be altered by varying the oxide support. Titania and alumina for example give rise to much stronger V–O–support bonds and simultaneously the activity for the methanol oxidation enhances too.

The samples containing a fraction of crystalline vanadium oxide (for a V- concentration of 1.3 mmol/g) show a decreased activity (only a slight effect on the MCM-48 sample), as the vanadium sites in the crystal lattice of V_2O_5 are less or not accessible. In addition, the formaldehyde yield is drastically reduced, and carbon oxides (CO and CO_2) are formed. The increased conversion to dimethylether (on acidic sites) is due to the aggregation of V_2O_5 crystals, leaving a part of the support surface uncovered. Vanadium oxide itself only shows a weak acidic character [38]. Basically, on both MCM-48 and silica, the VO_x centers are linked to the surface via Si–O–V bonds. However, the supported $\text{VO}_x/\text{MCM-48}$ catalysts exhibit a better catalytic performance. Especially higher yields of formaldehyde can be obtained on the supported MCM-48 catalysts in comparison to the silica samples with the same vanadium loading (Table 2).

3.2 Silica supported vanadium-tantalum mixed oxides

In this study, the structural, chemical, and catalytic properties of silica-supported vanadium-tantalum mixed oxide catalysts will be discussed, using the vanadium oxide case for comparison.

3.2.1 Preparation methods

The preparations of the supported vanadium-tantalum mixed oxides were carried out by successive modification of the silica support (followed by calcination before the next modification).

In the liquid phase reactions, the thermally treated silica was stirred at room temperature for 1 h in a zeolite-dried toluene solution containing tantalum ethoxide ($\text{Ta}(\text{OC}_2\text{H}_5)_5$) or vanadyl acetylacetonate ($\text{VO}(\text{acac})_2$) for modification with Ta or V, respectively. The reaction vessel was purged with a stream of dry nitrogen. After the reaction the modified support was filtered, washed with fresh solvent and dried under vacuum at room temperature. Subsequently, the samples were calcined in air at 500 °C for 16 h.

For the gas-phase reactions, the thermally pretreated silica (3 g) was additionally preheated at the reaction temperature for 3 h in a fixed-bed flow-type reactor, under a pressure of 5-10 kPa in a nitrogen flow. After this pretreatment, the reactant vapors were passed through the support bed, with nitrogen used as carrier gas. Vaporization of the reactants was carried out by sublimation of $\text{VO}(\text{acac})_2$ at 160 °C and evaporation of $\text{Ta}(\text{OC}_2\text{H}_5)_5$ at 200 °C, respectively. $\text{VO}(\text{acac})_2$ was deposited at a reaction temperature of 160 °C, $\text{Ta}(\text{OC}_2\text{H}_5)_5$ at 200 °C. After the reaction, the modified support was purged with nitrogen at the reaction temperature for 2 h. Subsequently, calcination was performed in the reactor at 500 °C, in an airflow for 6h.

3.2.2 Discussion

Structural characterization. (A) UV-Vis Diffuse Reflectance Spectroscopy. UV-vis-DRS is used to investigate the coordination of the supported oxide species. The spectral features of the supported vanadium and supported tantalum catalysts are summarized in table 3.

Table 3. UV-VIS-DR charge transfer band assignments.

Nature of species	CT band position (nm)	
	VO_x	TaO_x
tetrahedral monomer	250,300	233
tetrahedral chains	350	
square pyramidal	410	
octahedral	470	265

Silica-supported tantalum exhibits at low loading (<0.5 mmol/g Ta) a strong band with maximum at 233 nm. With higher loadings an additional band is present at 265 nm. Supported vanadium oxides show several CT bands as a function of the vanadium loading, according to the presence of three main types of configurations: tetrahedrally coordinated monomers and polymeric chains (characterized by CT bands between 200 and 400 nm), two-dimensional ribbons with a square pyramid coordination geometry (CT band at 410 nm) and octahedrally coordinated species (CT band at 470 nm). The spectra of the supported vanadium-tantalum mixed oxides (not shown here) show the same evolution as the spectra obtained for supported vanadium oxides. Increasing the vanadium concentration (with constant Ta concentration) results in typical charge-transfer transitions at higher wavelength, which shows that more polymerized VO_x species occur. However, increasing the Ta concentration does not result in an appreciable change of the UV-vis-DRS spectra. In addition, there is no change when the sequence of grafting of vanadium oxide and tantalum oxide is reversed.

(B) FTIR Spectroscopy. (i) OH Stretching Region. Infrared spectroscopy yields information on the interaction of the surface metal oxide species with the support, by examining the surface hydroxyl region. After the modification with TaO_x and/or VO_x , the IR intensity of the OH bands of the SiO_2 support decreases gradually with increasing loading, due to the consumption of the surface hydroxyls in the reaction with the respective transition metal precursors. Accordingly, the deposited oxide is linked to the support by support-oxygen-metal bonds. However, even at considerably high coverages, not all the surface OH groups are removed. With increasing V and Ta coverage new bands appear at 3660 or 3680 cm^{-1} (spectra not shown), revealing the presence of V-OH and Ta-OH species, respectively.

(ii) Metal-Oxygen Region. The infrared spectra also show important vanadium-oxygen and tantalum-oxygen IR vibrations. In Figure 6, the IR spectra of the metal-oxygen region of the modified silica catalysts are shown.

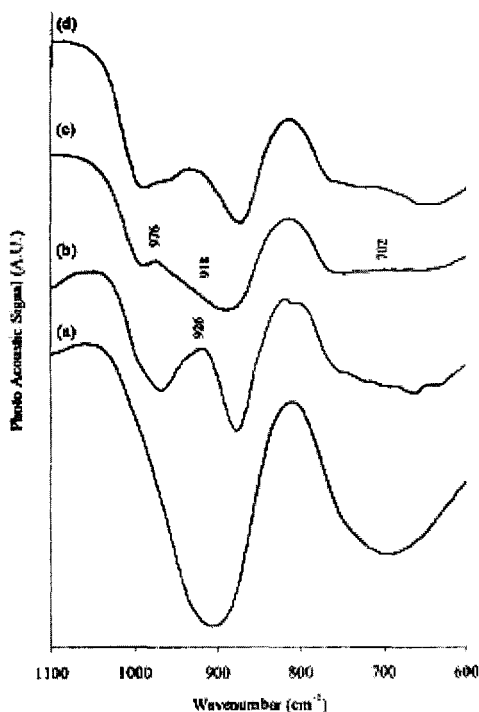


Figure 6. FTIR-PAS spectra of the liquid phase prepared supported silica catalysts studied in the metal oxygen region: (a) pure SiO_2 support after pretreatment at 500°C ; (b) VO_x/SiO_2 (0.36 mmol/g); (c) $\text{TaO}_x/\text{SiO}_2$ (0.47 mmol/g); (d) $\text{VO}_x\text{-TaO}_x/\text{SiO}_2$ with respective V and Ta loading of 0.35 and 0.20 mmol/g.

In the case of the silica-supported vanadium oxide (spectrum b), a band around 926 cm^{-1} is attributed to the presence of Si-O-V bonds. Both liquid- and gas-phase-prepared $\text{TaO}_x/\text{SiO}_2$ samples show broad bands centered around 702 and 918 cm^{-1} (spectrum c). The former corresponds to Ta-O stretching vibration modes. The latter can be attributed to the presence of Si-O-Ta linkages in accordance to the vanadia case. Additionally, a clearly resolved band is observed at 976 cm^{-1} , attributed to Ta=O. The supported vanadium-tantalum mixed oxide samples exhibit several bands of both the vanadia and tantalum, showing the same evolution as a function of the loading as in the case of the supported oxides as such.

(C) *Raman spectroscopy.* Figure 7 shows the FT-Raman spectra of the modified silica. Pure silica exhibits Raman modes at 430, 488, 605, 800, and 980 cm^{-1} (spectrum a). Silica-supported vanadia in spectrum b exhibits

a strong Raman band at 1042 cm^{-1} , assigned to the stretching mode of $\text{V}=\text{O}$ in a tetrahedral species with three $\text{V}-\text{O}-\text{Si}$ bonds to the silica surface. At V loadings of $>0.6\text{ mmol/g}$, strong Raman features at 994, 697, 286, and 147 cm^{-1} (spectrum c) reveal the formation of crystalline V_2O_5 (the XRD patterns could not evidence the presence of V_2O_5 , which means that Raman spectroscopy is much more sensitive to small crystalline clusters). Silica-supported tantalum (spectrum d) shows a band at 974 cm^{-1} . The infrared study also showed a distinct band around 976 cm^{-1} . These bands are probably arising from $\text{Ta}=\text{O}$ vibrations. Samples with Ta loadings of up to 0.8 mmol/g still show no bands of crystalline Ta_2O_5 (Raman bands at 105, 253, and 627 cm^{-1}).

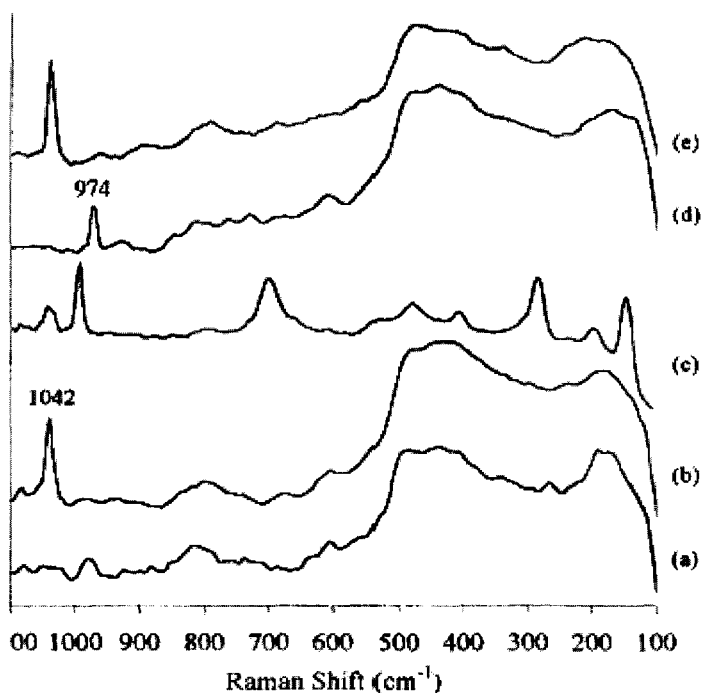


Figure 7. FT-Raman spectra of the silica-supported oxide catalysts; (a) pure SiO_2 ; (b) VO_x/SiO_2 (0.36 mmol/g); (c) VO_x/SiO_2 (1.03 mmol/g); (d) $\text{TaO}_x/\text{SiO}_2$ (0.47 mmol/g); (e) $\text{VO}_x\text{-TaO}_x/\text{SiO}_2$ with respective V and Ta loading of 0.35 and 0.59 mmol/g .

The spectra of the supported vanadia-tantalum mixed oxide catalysts (spectrum e) are similar to the supported vanadia samples. Surprisingly, they show no Raman features arising from the tantalum phase. This is probably due to the low cross-section of the tantalum-oxygen vibrations

compared to the vanadium-oxygen vibrations, as reported for the niobia-vanadia system [39]. No changes in the Raman spectra are observed upon addition of tantalum oxide to the silica-supported vanadia samples, nor when the vanadia phase is deposited on a previously prepared silica-supported tantalum phase (the $\text{V}=\text{O}$ band is observed at 1042 cm^{-1}). In addition, the vanadia-tantalum samples exhibit no bands attributed to polymeric $\text{V}-\text{O}-\text{V}$ species (at 930 cm^{-1}), which means that the vanadia phase rests well-dispersed over the support surface and is not forced to aggregate upon Ta addition.

To conclude, the spectroscopic study of the silica-supported tantalum catalyst shows at low Ta loading a highly uniform surface structure, characterized by a charge-transfer band in the UV-vis-DRS spectra at 233 nm, and $\text{Ta}=\text{O}$ bands at 974 and 976 cm^{-1} in Raman and infrared, respectively. The $\text{Ta}=\text{O}$ species are linked to the silica support by $\text{Si}-\text{O}-\text{Ta}$ bridges. A recent EXAFS study of silica-supported tantalum oxide [40] revealed that the surface oxide species are present as isolated tantalate species with one short $\text{Ta}-\text{O}$ bond and three long $\text{Ta}-\text{O}$ bonds. This means that at low loadings the deposited TaO_x species are in an isolated tetrahedral configuration. However, at a higher loadings an additional surface configuration occurs, which gives rise to a CT band around 260 nm and exhibits $\text{Ta}-\text{OH}$ species (IR band at 3680 cm^{-1}). On the other hand, the octahedrally coordinated Ta in pure Ta_2O_5 shows similar spectroscopic features. Therefore, the second surface structure is attributed to octahedrally coordinated tantalum, which is probably polymerized via $\text{Ta}-\text{O}-\text{Ta}$ bridges.

In case of silica-supported vanadia catalysts, at low surface coverages, the vanadia species are present in an isolated tetrahedral VO_4 coordination, possessing a terminal $\text{V}=\text{O}$ and three bridging $\text{V}-\text{O}$ -support bonds. At higher surface vanadia coverages, the vanadia species are polymerized through bridging $\text{V}-\text{O}-\text{V}$ bonds. With increasing surface coverage square pyramidal and octahedrally coordinated (and even crystalline) vanadia species occur.

The spectroscopic study of the supported mixed oxides leads to similar conclusions as in the case of the supported tantalum and supported vanadia as such. Interestingly, the structure and dispersion of one metal oxide species is nearly unaffected by the presence of the other metal oxide species nor by the grafting sequence of the oxides.

Catalytic performance in the oxidation of methanol. In table 4, the activity and selectivity of the silica supported TaO_x and $\text{VO}_x\text{-TaO}_x$ catalysts for the

oxidation of methanol is summarized. These results can be compared to the catalytic performance of pure $\text{VO}_x\text{-SiO}_2$ catalysts, as reported in table 2.

Table 4. Activity and selectivity of the SiO_2 supported TaO_x and $\text{VO}_x\text{-TaO}_x$ catalysts.

Catalyst	V mmol/g	Ta mmol/g	Activity* 10^{-3} mol/g h	Selectivity (%)			
				CO_x	FA	DME	MF
$\text{TaO}_x/\text{SiO}_2$	0.00	0.24	3.99	0.00	0.00	100.0	0.0
$\text{TaO}_x/\text{SiO}_2$	0.00	0.47	5.28	0.00	14.0	70.0	16.0
$\text{VO}_x\text{-TaO}_x/\text{SiO}_2$	0.36	0.20	5.48	0.00	74.8	25.2	0.0
$\text{VO}_x\text{-TaO}_x/\text{SiO}_2$	0.35	0.59	6.03	0.00	54.8	40.3	4.9
$\text{VO}_x\text{-TaO}_x/\text{SiO}_2$	0.24	0.60	5.08	0.00	47.5	26.6	25.9
$\text{TaO}_x\text{-VO}_x/\text{SiO}_2$	0.37	0.20	5.98	0.00	74.3	25.0	0.7

*: Activity, moles of methanol converted per gram of catalyst and per hour; FA: formaldehyde, DME: dimethylether, MF: methyl formate.

As could be deduced from table 2, VO_x/SiO_2 produces mainly oxidation products, such as formaldehyde. The catalyst surface exhibits an even distribution of vanadia and residual hydroxyl groups of the silica support. Methanol is adsorbed and transformed to formaldehyde on the vanadium sites. However, methanol can react with the residual surface hydroxyl sites as well, which results in adsorbed methoxy groups. Therefore, during the methanol conversion, the formaldehyde formed on the vanadia sites is in close interaction with methoxy groups on the silica sites. Via a hemiacetal intermediate, methyl formate can be produced as well [41]. With increasing loadings, the formaldehyde selectivity increases, as the surface density of the residual Si-OH groups decreases. For the silica samples with high V loadings at which crystalline V_2O_5 is observed (>0.6 mmol/g), the formation of redox products markedly decreases, in favor of the formation of dimethyl ether and carbon oxides.

Silica-supported tantalum oxide catalysts show activities comparable to the VO_x/SiO_2 . However, the main reaction product this time is dimethyl ether, indicating the acidic properties of the TaO_x phase. Indeed, the infrared study of the adsorption of pyridine showed the Lewis acidic characteristics of the tantala species [42]. However, at high loadings, also Brönsted acidity occurs, due to the presence of Ta-OH groups. At these

higher Ta loading the $\text{TaO}_x/\text{SiO}_2$ samples produce methyl formate and formaldehyde along with the formation of dimethyl ether. This suggests that the interaction of tantalum with the silica support gives rise to a considerable redox activity too. This may be due to the ease of hydrolysis of the bridging Ta-O-Si bonds during the methanol oxidation, however, a detailed understanding for this redox behaviour is not yet established and a thorough oxidation study is required in order to clarify this issue.

The difference in reactivity between vanadia and tantalum is also reflected in the supported mixed oxide catalysts. The addition of tantalum to silica-supported vanadia increases the total activity and the selectivities toward formaldehyde and dimethyl ether. In addition, reversing the sequence of deposition of VO_x and TaO_x does not lead to significant changes in activity and selectivity.

To conclude, silica-supported vanadia-tantalum catalysts exhibit high selectivity toward formaldehyde and dimethylether, according to the presence of both active redox and active acid centers.

4 Conclusions

Supported catalysts and adsorbents with unique and controlled properties can be prepared following the molecular designed dispersion (MDD) process with the use of polynuclear metal complexes as the precursors. The deleterious effects of sintering upon thermolysis are ameliorated with the proper choice of metal complex, solvent and support. Thus, by the MDD method it becomes possible to graft highly dispersed metal oxide layers on the support surface. Systematic changes in the types and sizes of the metal complexes can be exploited to produce a series of supported catalysts with variable, predictable properties. Two typical case studies leading to superior supported vanadium oxide and vanadium-tantalum mixed oxide catalysts are discussed.

5 Acknowledgement

P. Cool acknowledges the FWO-Flanders Belgium (Fund for Scientific Research-Flanders) for financial support as a post-doctoral fellowship.

References

1. Babb K.H. and White M.G., Polynuclear metal complexes as model mixed oxide catalysts, *J. Catal.* **98** (1986) p. 343-354.
2. Beckler R.K. and White M.G., Polynuclear metal complexes as model mixed oxide catalysts: an ion exchange support interaction, *J. Catal.* **102** (1986) p. 252-256.
3. Beckler R.K. and White M.G., Effects of adsorbate coverage on the infrared spectrum of chemisorbed ammonia, *Langmuir* **3** (6) (1987) p. 1074-1080.
4. Beckler R.K. and White M.G., Polynuclear metal complexes as model mixed oxide catalysts: selective chemisorption of ammonia and nitric oxide, *J. Catal.* **109** (1988) p. 25-36.
5. Beckler R.K. and White M.G., Polynuclear metal complexes as model mixed oxide catalysts: isomerization activity, *J. Catal.* **110** (1988) p. 364-374.
6. Beckler R.K. and White M.G., Preparation and characterization of supported mixed metal oxides: thermal decomposition of heteropoly metal complexes immobilized on silica, *J. Catal.* **112** (1988) p. 157-167.
7. Kenvin J.C. and White M.G., Preparation and characterization of supported mononuclear metal complexes as model complexes. In *Proceedings of the 198th ACS National Meeting* (Miami Beach, FL, 1989).
8. Kenvin J.C., White M.G. and Mitchell M.B., Hydrogen bonding of mononuclear metal complexes to Cab-O-Sil. In *Proceedings of the 200th ACS National Meeting* (Washington D.C., 1990).
9. Van Roosmalen A.J. and Mol J.C., An infrared study of the silica gel surface. 1. Dry silica gel, *J. Phys. Chem.* **82**(25) (1978) p. 2748-2751.
10. Hertl W. and Hair M.L., Reaction of hexamethyldisilazane with silica, *J. Phys. Chem.* **75** (14) (1971) p. 2181-2185.
11. Rosenthal D.J., White M.G. and Parks G.D., Estimating the relative acid site density of silica-alumina by infrared spectroscopy using a selective reactant poison, *AIChE Journal* **33** (2) (1987) p. 336-340.
12. Peri J.B., A model for the surface of γ -alumina, *J. Phys. Chem.* **69** (1) (1965) p. 220-230.
13. Fackler J.P., Metal beta-ketoenolate complexes, *Progress in Inorg. Chem.* **7** (1966) p. 361.
14. Che M., Concepts and relevance to catalysis phenomena. In *Proceedings 10th ICC Budapest*, Elsevier, Amsterdam, 1993; Lepetit C., Che M., Interfacial coordination chemistry: current status & applications, *J. Mol. Catal.* **100** (1995), pp. 147-150
15. van Hengstum A.J., van Ommen J.G., Bosch H. and Gellings P.J., Selective gas phase oxidation of toluene by vanadium oxide/TiO₂ catalysts, *Appl. Catal.* **8** (1983) p.369-382.
16. Kenvin J.C., White M.G. and Mitchell M.B., Preparation and characterization of supported mononuclear metal complexes as model catalysts, *Langmuir* **7** (6) (1991) p.1198-1205.
17. White M.G., Bruce D., Choksi H. and Bertrand J.A., The catalytic properties of supported CuO catalysts prepared from mononuclear, dinuclear, and trinuclear Cu complexes. In *AIChE Annual meeting*, paper 99 Ci (1991).
18. Bertrand J.A., Bruce D.A., White M.G., The effects of molecular structure upon complex-support interactions. In *AIChE Journal* **39** (12) (1993), p. 1966.

19. Van Der Voort P., Possemiers K., Vansant E.F., Preparation of supported vanadium oxide catalysts: Adsorption and thermolysis of vanadyl acetylacetonate on a silica support, *J. Chem. Soc., Faraday Trans.* **92**(5) (1996) p.843-848.
20. Rao S.N.R., Waddell E., Mitchell M.B., White M.G., Selective sulfur dioxide adsorbents prepared from designed dispersions of groups IA and IIA metal oxides on alumina, *J. Catal.* **163** (1) (1996) p. 176-185.
21. Mitchell M.B., Chakravarthy V.R., White M.G., Interaction of single and multiple layers of copper acetylacetonate complexes with silica surfaces: an infrared diffuse reflectance study, *Langmuir* **10** (12) (1994) p. 4523-4529.
22. Gole J.L., White M.G., Nanocatalysis. Selective conversion of ethanol to acetaldehyde using mono-atomically dispersed copper on silica nanospheres, *J. Catal.* **204** (1) (2001) p. 249-252.
23. Rollison C.L., Chromium, Molybdenum & Tungsten in Comprehensive coordination chemistry, Pergamon Press, New York (1987) p.390.
24. Kemmet R.D.W., Manganese in Comprehensive coordination chemistry, Pergamon Press, Austria (1973), p. 872.
25. Kresge C.T., Leonowicz M.E., Roth W.J., Vartuli J.C., Beck J.S., Ordered mesoporous molecular sieves synthesized by a liquid-crystal template mechanism, *Nature* **359** (1992) p. 710-712.
26. Kresge C.T., Leonowicz M.E., Roth W.J., Vartuli J.C., Synthetic mesoporous crystalline material, US Patent 5098684 (1992).
27. Van Der Voort P., Mathieu M., Mees F., Vansant E.F., Synthesis of high-quality MCM-48 and MCM-41 by means of the gemini surfactant method, *J. Phys. Chem. B* **102** (1998), p. 8847-8851.
28. Van Der Voort P., Morey M., Stucky G.D., Mathieu M., Vansant E.F., Creation of VO_x surface species on pure silica MCM-48 using gas-phase modification with $\text{VO}(\text{acac})_2$, *J. Phys. Chem. B* **102** (1998), p. 585-590.
29. Baltes M., Van Der Voort P., Collart O., Vansant E.F., The adsorption of $\text{VO}(\text{acac})_2$ on a mesoporous silica support by liquid phase and gas phase modification to prepare supported vanadium oxide catalysts, *J. Porous Mater.* **5** (1998), p. 317-324.
30. Baltes M., Collart O., Van Der Voort P., Vansant E.F., Synthesis of supported transition metal oxide catalysts by the designed deposition of acetylacetonate complexes, *Langmuir* **15** (1999), p. 5841-5845.
31. Baltes M., Van Der Voort P., Weckhuysen B.M., Rao R.R., Schoonheydt R.A., Vansant E.F., Synthesis and characterization of alumina-supported vanadium oxide catalysts prepared by the molecular designed dispersion of $\text{VO}(\text{acac})_2$ complexes, *Phys. Chem. Chem. Phys.* **2** (2000), p. 2673-2680.
32. Baltes M., Cassiers K., Van Der Voort P., Weckhuysen B.M., Schoonheydt R.A. and Vansant E.F., MCM-48 supported vanadium oxide catalysts, prepared by the molecular designed dispersion of $\text{VO}(\text{acac})_2$: a detailed study of the highly reactive MCM-48 surface and the structure and activity of the deposited VO_x , *Journal of Catalysis* **197** (2001) p.160-171.
33. Jentys A., Pham N.H., Vinek H., Nature of hydroxy groups in MCM-41, *J. Chem. Soc., Faraday Trans.* **92** (17) (1996), p. 3287-3291.
34. Vansant E.F., Van Der Voort P., Vrancken K.C., Characterization and chemical modification of the silica surface, *Studies in Surface Science and Catalysis*, Elsevier, Amsterdam (1995).

35. Haukka S., Root A., The reaction of hexamethyldisilazane and subsequent oxidation of trimethylsilyl groups on silica studied by solid-state NMR and FTIR, *J. Phys. Chem.* **98** (6) (1994) p. 1695-1703.
36. Deo G., Wachs I.E., Haber J., Vanadium oxide monolayer catalysts, *Crit. Rev. Surf. Chem.* **4** (1994), p. 141.
37. Dias C.R., Portela M.F., Bond G.C., Oxidation of o-xylene to phthalic anhydride over V_2O_5/TiO_2 catalysts: I. Influence of catalyst composition, preparation method and operating conditions on conversion and product selectivities, *J. Catal.* **157** (2) (1995) p. 344-352.
38. Wachs I.E., Weckhuysen B.M., Structure and reactivity of surface vanadium oxide species on oxide supports, *Appl. Catal. A*, **157** (1-2) (1997), p. 67-90.
39. Deo G., Wachs I.E. Effect of additives on the structure and reactivity of the surface vanadium oxide phase in V_2O_5/TiO_2 catalysts, *J. Catal.* **146** (2) (1994), p. 335-345.
40. Tanaka T., Nojima H., Yamamoto T., Takenaka S., Funabiki T., Yoshida S., Structure of surface tantalate species and photo-oxidation of carbon monoxide over silica-supported tantalum oxide, *Phys. Chem. Chem. Phys.*, **1** (1999), p. 5241-5251.
41. Louis C., Tatibouët J.M., Che M., Catalytic properties of silica-supported molybdenum catalysts in methanol oxidation: the influence of molybdenum dispersion, *J. Catal.* **109** (1988), p. 354-366.
42. Baltes M., Kytökiivi A., Weckhuysen B.M., Schoonheydt R.A., Van Der Voort P., Vansant E.F., Supported tantalum oxide and supported vanadia-tantala mixed oxides: structural characterization and surface properties, *J. Phys. Chem. B*. **105** (2001) p. 6211-6220.

ACIDITY-ENHANCED NANOPOROUS CATALYTIC MATERIALS

FENG-SHOU XIAO* AND YU HAN

Department of Chemistry & State Key Laboratory for Inorganic Synthesis and Preparative Chemistry, Changchun 130023, China
E-mail: fsxiao@mail.jlu.edu.cn

Mesoporous molecular sieves such as hexagonally ordered MCM-41 have been attracted much attention because of their potential use as versatile catalysts and catalyst supports for conversion of large molecules. However, as compared with conventional zeolites, these mesostructured materials have relatively low acidity, which severely hinders their practical applications in catalytic reactions for petroleum industry. This chapter will review the development for acidity-enhanced mesoporous materials, which include (1) heteropolyacids (HPAs) were supported into the mesopores; (2) superacids such as $\text{SO}_4^{2-}/\text{ZrO}_2$ were formed in the mesopores; (3) acidic sites were enhanced by post-treatments; (4) strongly acidic sites were prepared from assembly of preformed nanosized zeolite precursors.

1 Introduction

Nanoporous solids are of scientific and technological interest because of their ability to interact with atoms, ions, and molecules not only at their surface, but also in the bulk of the materials. Generally, nanoporous solids include microporous crystals of zeolites and ordered mesoporous materials [1]. Traditional microporous zeolites have strong acidic sites, which have been widely applied in industrial processes as versatile catalysts, catalyst supports, ion exchangers, and absorbents [1-4]. Ordered mesoporous materials such as MCM-41 and SBA-15 have large uniformed pores and high surface areas, promising many potential applications such as catalysis, separation, adsorption, and fabrication of nanostructured materials [5-7].

Ordered mesoporous materials were first reported by Mobil scientists [5], and since the first discovery, a series of novel ordered mesoporous materials have been shown [5-19]. For examples, mesoporous SBA-15 with thick pore walls have been prepared using triblock copolymers as templates [6]. The synthesis of MSU materials have been achieved using neutral gemini surfactants as the templates [8]. The preparation of KIT-1 involves the use of inorganic salts as additives [9,10]. Through the grafting route, mesoporous aluminosilicates have been obtained [11]. In spite of many encouraging progresses in recent years, the acidity of the current mesoporous materials are yet generally lower than those of microporous

aluminosilicate zeolites, which can be attributed to the amorphous nature of the mesoporous walls [7].

In this chapter, we review recent development for acidity-enhanced mesoporous materials, which include (1) heteropolyacids (HPAs) supported in the mesopores; (2) superacids such as $\text{SO}_4^{2-}/\text{ZrO}_2$ formed in the mesopores; (3) acidic sites generated by post-treatment; and (4) strongly acidic mesoporous materials prepared from assembly of preformed nanosized zeolite precursors.

2 Heteropolyacids (HPAs) supported on mesoporous materials

The use of relatively stable and strongly acidic heteropolyacids in acid-catalyzed reactions has attracted much attention for processes requiring higher acidity than that of the zeolites and mesoporous materials. In particular, 12-tungstophosphoric acid $\text{H}_3\text{PW}_{12}\text{O}_{40}$ (HPW) is the most acidic of the Keggin series [20], and this has led many recent researches to focus on HPW acid. However, the extremely small surface area of these nonporous heteropolyacids strongly limits their wide application in catalytic reactions. On the other hand, the relatively weak acidity of ordered mesoporous materials also severely hinders their practical applications for the petroleum industry [7]. Heteropolyacides supported on mesoporous materials are expected to exhibit bifunctional catalysts including both large surface area and strongly acidic strength [7, 21,22].

Heteropolyacids (HPAs) supported on pure silica MCM-41 were first reported by Kresge et al. [23]. This was also done by Kozheunikov et al. [24] and Kawi et al. [25] by supporting $\text{H}_3\text{PW}_{12}\text{O}_{40}$ on a mesoporous pure silica MCM-41. In this case, the HPW retained the Keggin structure on the MCM-41 surface and formed highly dispersed HPW species without HPA crystals even at HPW loadings as high as 50 wt%. Textural characterization of the samples clearly showed that the BET surface area and the pore volume reduced rapidly with increasing HPW loading, but it still much higher than that of pure HPW (Table 1). For example, pure HPW is a nonporous crystalline materials with a BET surface area smaller than $10 \text{ m}^2/\text{g}$; however, once loaded onto pure silica MCM-41 with a loading of 50 wt%, the resulting HPW/MCM-41 mesoporous materials have a BET surface area above $500 \text{ m}^2/\text{g}$, with a pore volume of more than $0.40 \text{ cm}^3/\text{g}$. The strong reduction of BET surface area for HPW/MCM-41 samples indicates that some pores in the samples are blocked by HPW, indicating a non-uniform distribution of the acid species on the surface.

Table 1. The parameters of BET surface area and pore volume of various mesoporous samples [25].

Sample	BET surface area (m ² /g)	Pore volume (cm ³ /g)	Pore size (Å)	
MCM-41	1311	1.03	31.4	
HPW(15%)/MCM-41	1128	0.98	30.0	Amorphous
HPW(30%)/MCM-41	632	0.53	29.7	Amorphous
HPW(50%)/MCM-41	499	0.40	29.5	Amorphous
Pure HPW	<10			Crystalline

Heteropolyacids (HPAs) supported on mesoporous materials such as MCM-41 are quite active as catalysts for alkylation of isobutene by butene [26,27], 4-*tert*-butylphenol by isobutene and styrene [24], cracking of 1,3,5-triisopropylbenzene (TIPB) [28], and *n*-C₄ isomerization [29]. For example, HPW supported on MCM-41 is more active than the bulk HPA and H₂SO₄ for the liquid phase alkylation of 4-*tert*-butylphenol (TBP) with isobutene. Figure 1 shows proposed reaction pathways, and Table 2 presents the catalytic activities and selectivities over these HPW supported on MCM-41 samples.

Table 2. Alkylation of TBP with isobutene in benzene (70 °C, TBP/C₆H₆ 50/50 wt/wt) [24].

Catalyst ^a	Amount (wt %) ^b	$\tau_{1/2}$ (min) ^c	Selectivity (mol %) ^d	
			DTBP	TTB
97% H ₂ SO ₄	2.5	21	46	54
HPW(20%)/MCM-41	2.5	20	89	11
HPW(40%)/MCM-41	2.5	11	87	13
HPW(50%)/MCM-41	2.5	8	91	9
HPW(20%)/SiO ₂ ^e	2.5	20	89	11

^a All the HPW catalysts were prepared by impregnation, dried at room temperature in vacuum, and stored over P₂O₅. ^b The percentage of the catalyst based on the total amount of the reaction mixture. ^c The half-time of the TBP conversion. ^d The selectivity based on TBP at 95% TPB conversion, 0.5-1h. ^e As a carrier Aerosil 380 (Degussa AG) was used.

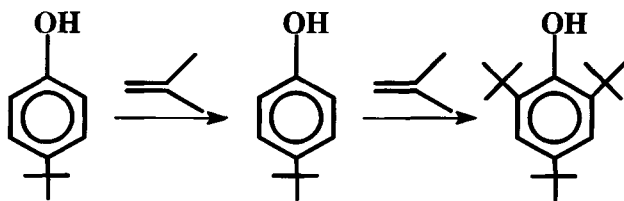


Figure 1. Proposed reaction pathways of Alkylation of TBP with isobutene in benzene.

Nevertheless, these catalysts have a tendency to lose HPA molecules by elution [30] and to form large HPA clusters on the external surface of the supporting materials during liquid phase esterification reaction [31]. When the HPA modified MCM-41 samples were treated with cesium or ammonium carbonates to obtain HPA salts inside MCM-41 pores, the heteropoly anions were more strongly bonded to the support. Obviously, the success for HPAs supported in mesoporous materials is limited because HPA molecules are easily lost and surface area of the materials is reduced significantly. Therefore, ordered mesoporous materials with strong acidity and large surface area are still being sought.

3 Sulfated zirconia supported on mesoporous materials

3.1 Sulfated zirconia supported on mesoporous materials by solution containing zirconium salts

It is well known that sulfated zirconia is a superacid catalyst characterized by Hammett indicators [32,33], which is suitable for catalyzing reactions such as hydrocarbon isomerization and etherification [34-36]. Sulfated zirconia supported in mesopores is one of the good ways for increasing acidity of mesoporous materials, and recently these works have been investigated extensively [37-43].

Matsushashi et al. [37] reported that a mesoporous solid acid with ordered mesopores was prepared by modification of FMS-16 with sulfated zirconia ($\text{SO}_4^{2-}/\text{ZrO}_2/\text{FMS-16}$). FMS-16 precalcined at 850°C was soaked with an ethanol solution of zirconyl chloride, followed by exposure of H_2SO_4 and calcination at 650°C in air. X-ray diffraction measurement shows that $\text{SO}_4^{2-}/\text{ZrO}_2/\text{FMS-16}$ basically retained its ordered mesostructure. Nitrogen isotherms of the samples show that the surface area and pore volume of $\text{SO}_4^{2-}/\text{ZrO}_2/\text{FMS-16}$ reduce significantly as compared with those

of unmodified FMS-16, indicating that some pores are blocked by and $\text{SO}_4^{2-}/\text{ZrO}_2$ species.

Kawi *et al* [38,39] reported the preparation of superacid catalyst for $\text{SO}_4^{2-}/\text{ZrO}_2/\text{MCM-41}$. In this case, pre-dried silica MCM-41 was dispersed into a mixed solution of $\text{Zr}(\text{OPr})_4$ and *n*-hexane under vigorous stirring, followed by removal of organic solvent, hydrolysis by water at room temperature, immersion by H_2SO_4 , and calcination at 600°C . The acidic strength of $\text{SO}_4^{2-}/\text{ZrO}_2/\text{MCM-41}$ was measured by Hammett indicator, giving H_0 value at around -13.8 , a typical value of superacid catalyst. Catalytic tests show that $\text{SO}_4^{2-}/\text{ZrO}_2/\text{MCM-41}$ is *ca.* 2.5-3 times more active than the conventional $\text{SO}_4^{2-}/\text{ZrO}_2$ superacid catalyst for MTBE and *n*-pentane isomerization (Table 3). Additionally, Mou *et al.* [40,41] also reported the synthesis of superacid of $\text{SO}_4^{2-}/\text{ZrO}_2$ supported on MCM-41 by using a one-step incipient wetness impregnation method with zirconium sulfate as the precursor in methanol solution, followed by thermal decomposition of the precursor in air.

Table 3. Catalytic activities of $\text{SO}_4^{2-}/\text{ZrO}_2$ and $\text{SO}_4^{2-}/\text{ZrO}_2/\text{MCM-41}$ superacid catalysts [38].

Reactant	<i>t</i> /min	$\text{SO}_4^{2-}/\text{ZrO}_2$		$\text{SO}_4^{2-}/\text{ZrO}_2/\text{MCM-41}$	
		TON ^a	Selec. %	TON ^a	Selec. %
<i>n</i> -Pentane	60	0.27	98 ^b	0.81	100 ^b
	200	0.41	98	1.19	99
	360	0.50	98	1.36	99
	600	0.54	98	1.42	99
MeOH + Bu ^t OH	60	4.11	100 ^c	10.10	100 ^c
	180	4.13	100	10.13	100
	360	4.11	100	10.12	100
	600	4.12	100	10.10	100

^aTON: mol of products/mol of Zr in the catalyst. ^bSelectivity of isopentane. ^cSelectivity of MTBE.

Notably, the preparation of $\text{SO}_4^{2-}/\text{ZrO}_2$ supported on mesoporous materials is generally employed by organic solution such as methanol and hexane because the impregnation of zirconium salts on mesoporous materials of MCM-41 and subsequent treatments usually take more than several hours at relative high temperature (100°C), which result in the

mesostructures being significantly destroyed [37-41]. Recently, Gao *et al.* [42] reported a successful preparation of superacid of $\text{SO}_4^{2-}/\text{ZrO}_2$ supported on newly stable mesoporous materials of SBA-15 by using incipient wetness impregnation method in a aqueous solution, followed by dryness, sulfation, and calcination.

3.2 Sulfated zirconia supported on mesoporous materials by solid/solid monolayer dispersion

More recently, Xiao *et al.* [43] have prepared $\text{SO}_4^{2-}/\text{ZrO}_2/\text{MCM-41}$ by monolayer dispersion of dispersion of $\text{ZrOCl}_2 \cdot 8\text{H}_2\text{O}$ into the mesopores, followed by the hydrolysis and sulfation, which have been characterized by X-ray diffraction, nitrogen adsorption isotherms, infrared spectroscopy, and catalytic cracking of *n*-hexane, cumene, and 1,3,5-triisopropylbenzene. The results show that $\text{ZrO}_2/\text{SO}_4^{2-}$ was successfully loaded into the inner pores of MCM-41 and the as-synthesized catalyst showed favorable catalytic properties. In this case, $\text{SO}_4^{2-}/\text{ZrO}_2/\text{MCM-41}$ retained well-ordered mesoporous structures due to the avoid of impregnation of zirconium salts with mesoporous materials in a aqueous solution.

Figure 2 shows XRD patterns in the region of $1\text{--}10^\circ$ for $\text{ZrOCl}_2 \cdot 8\text{H}_2\text{O}$, MCM-41, and a ground mixture of $\text{ZrOCl}_2 \cdot 8\text{H}_2\text{O}$ and MCM-41 for 20 min as well as heating of 80°C for 12 h, respectively. $\text{ZrOCl}_2 \cdot 8\text{H}_2\text{O}$ (Fig. 2A) exhibits two peaks at 7.1 and 8.6° . MCM-41 (Fig. 2B) exhibits four peaks at 2.2 , 3.8 , 4.4 , and 5.8° . The mixture of $\text{ZrOCl}_2 \cdot 8\text{H}_2\text{O}$ and MCM-41 (Fig. 2C) ground for 20 min exhibits both the peaks assigned to $\text{ZrOCl}_2 \cdot 8\text{H}_2\text{O}$ and the peaks assigned to MCM-41. Notably, after heating the mixture of $\text{ZrOCl}_2 \cdot 8\text{H}_2\text{O}$ and MCM-41 (Fig. 2D) at 80°C for 12 h, the sample results show disappearance of peaks at 7.1 and 8.6° assigned to $\text{ZrOCl}_2 \cdot 8\text{H}_2\text{O}$ crystalline, indicating that $\text{ZrOCl}_2 \cdot 8\text{H}_2\text{O}$ highly disperses into the mesopores of MCM-41, where $\text{ZrOCl}_2 \cdot 8\text{H}_2\text{O}$ no longer exists in crystalline state; these results are good agreement with those published in literature [44-46].

Furthermore, all treatments of the samples including the hydrolysis at room temperature for 5 min, activation at 140°C for 5 h, sulfation at room temperature for 10 min, and calcination at 600°C for 3 h (Fig. 2E), show that the characteristic peaks assigned to hexagonally mesoporous materials are almost unchanged, and no peaks in the region of $30\text{--}50^\circ$ assigned to ZrO_2 crystals could be observed. These results suggest that the mesostructured materials are stable and that no ZrO_2 crystals are formed under the treatments of dispersion, hydrolysis, activation, sulfation, and calcination.

Interestingly, although MCM-41 is not stable in boiling water, it is stable under the above treatments, suggesting that the solid dispersion method is useful for preparation of sulfated zirconia in the mesopores of MCM-41.

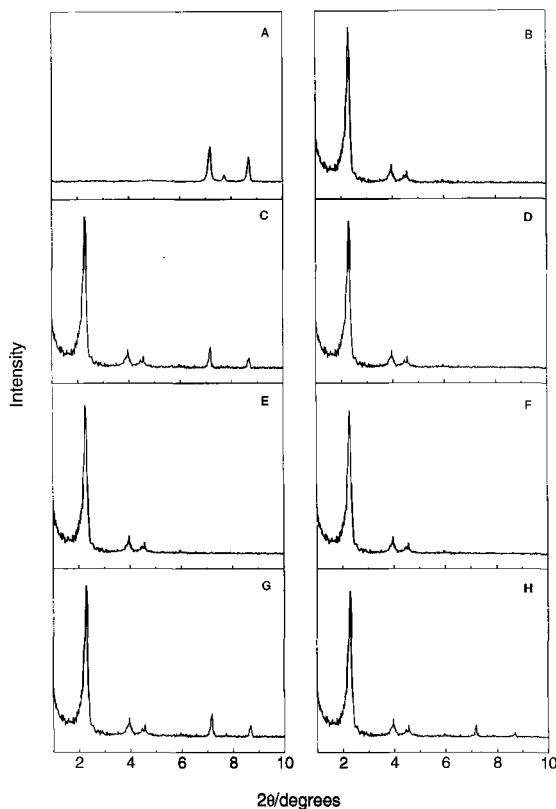


Figure 2. XRD patterns of (A) $\text{ZrOCl}_2 \cdot 8\text{H}_2\text{O}$, (B) MCM-41, (C) mechanical mixture of $\text{ZrOCl}_2 \cdot 8\text{H}_2\text{O}$ and MCM-41 ($\text{ZrOCl}_2 \cdot 8\text{H}_2\text{O}/\text{MCM-41}=0.16$ g/g and $\text{Zr}/\text{Si}=0.063$), (D) after C, the mixture was heated at 80°C for 24 h, (E) after D, the sample was hydrolyzed in 0.5 M of $\text{NH}_3 \cdot \text{H}_2\text{O}$ at room temperature, activated at 140°C for 5 h, and sulfated in 0.5 M of H_2SO_4 at room temperature for 10 min, (F) mechanical mixture of $\text{ZrOCl}_2 \cdot 8\text{H}_2\text{O}$ and MCM-41 ($\text{ZrOCl}_2 \cdot 8\text{H}_2\text{O}/\text{MCM-41}=0.23$ g/g and $\text{Zr}/\text{Si}=0.084$), followed by heating at 80°C for 24 h, (G) mechanical mixture of $\text{ZrOCl}_2 \cdot 8\text{H}_2\text{O}$ and MCM-41 ($\text{ZrOCl}_2 \cdot 8\text{H}_2\text{O}/\text{MCM-41}=0.34$ g/g and $\text{Zr}/\text{Si}=0.126$) for 20 min, (H) after G, the mixture was heated at 80°C for 24 h. Reprinted with permission from ref 43. Copyright 2002 Elsevier.

When the weight value of $\text{ZrOCl}_2 \cdot 8\text{H}_2\text{O}/\text{MCM-41}$ was increased into 0.23 g/g (molar ratio of Zr/Si at 0.084), we still cannot observe the XRD peaks of $\text{ZrOCl}_2 \cdot 8\text{H}_2\text{O}$ crystalline, as shown in Fig. 2F. Upon further

increase of $\text{ZrOCl}_2 \cdot 8\text{H}_2\text{O}$ loading in MCM-41 sample over 0.23 g/g, the characteristic peaks assigned to $\text{ZrOCl}_2 \cdot 8\text{H}_2\text{O}$ appeared again, indicating the presence of crystalline $\text{ZrOCl}_2 \cdot 8\text{H}_2\text{O}$ in the sample, as given in Figs. 2G and 2H. These results indicate that maximum content of $\text{ZrOCl}_2 \cdot 8\text{H}_2\text{O}$ supported in MCM-41 is about 0.23 g/g.

Table 4. Catalytic activities of various samples in cracking of cumene and 1,3,5-triisopropylbenzene.

Sample	Si/Al	Cumene Conv. (%) at 250°C	TIPB ^a Conv. % at 250°C
HMCM-41	∞	5.4	65.8
SZ+MCM-41	∞	8.4	5.6
SZ/MCM-41	∞	69.3	99.9
SZ		75.2	98.1
HZSM-5	60	68.4	2.7

^a TIPB: 1,3,5-triisopropylbenzene.

Catalytic activities of various catalysts in cracking of cumene and 1,3,5-triisopropylbenzene at the reaction temperature of 250–320°C are presented in Table 4. In catalytic cumene cracking, MCM-41 is inactive (5.4% at 250°C) because there is no acidic site in the MCM-41 sample. However, after supporting of sulfated zirconia in the MCM-41 materials ($\text{Zr/Si}=0.042$), the sample activity ($\text{SO}_4^{2-}/\text{ZrO}_2/\text{MCM-41}$) increased significantly, giving the conversion at 69.3% at 250°C, which is a little higher than that of HZSM-5 sample. In contrast, the same amount of sulfated zirconia mechanically mixed with MCM-41 ($\text{Zr/Si}=0.042$) shows very low conversion at 8.4% at 250°C. These results suggest the SZ/MCM-41 is much more active due to larger surface area than that of SZ in cumene cracking.

In catalytic cracking of 1,3,5-triisopropylbenzene at the reaction temperature of 250°C, MCM-41 is inactive (0.1 %); HZSM-5 is very low conversion because of the small pore size of MFI zeolite, and catalytic reaction can occur only on the external surface of ZSM-5 crystals. However, after supporting of sulfated zirconia in the MCM-41 materials, the sample ($\text{SO}_4^{2-}/\text{ZrO}_2/\text{MCM-41}$) shows the highest catalytic activity (99.9%), which is much higher than that of mechanical mixture of sulfated zirconia with MCM-41 (16.8%). These results suggest that the SZ/MCM-41 is an excellent candidate as catalyst for catalytic cracking of large

molecules, particularly of the petroleum residues for which high reaction temperatures are required.

As observed in all superacid catalysts of $\text{SO}_4^{2-}/\text{ZrO}_2$ supported on mesoporous materials, it is very interesting to note that catalytic activity for *n*-butene isomerization (typical model reaction for superacid catalysts) over $\text{SO}_4^{2-}/\text{ZrO}_2/\text{MCM-41}$ reduces extensively as compared with that over $\text{SO}_4^{2-}/\text{ZrO}_2$, which is reasonably assigned that acidic strength of $\text{SO}_4^{2-}/\text{ZrO}_2/\text{MCM-41}$ is much lower than that of $\text{SO}_4^{2-}/\text{ZrO}_2$ due to the absence of tetragonal phase of crystalline ZrO_2 in the limited mesopores of MCM-41. Therefore, ordered mesoporous materials with strongly acidic sites and large surface area are always desirable.

4 Acidity-enhanced mesoporous materials by post-treatments

In order to increase acidic strength of mesoporous materials, various post-treatments have been used, which include alumination by grafting route [47-52, 55-61], functionalization by phosphoric acid and sulfonic acid [62-72], and hydrothermal recrystallization [73-85].

4.1 Alumination of mesoporous materials by grafting route

Mokaya [47] reported that Al-containing MCM-41 materials are successfully prepared by grafting aluminum species onto purely siliceous MCM-41 in hexane solution containing aluminum isopropoxide; the resulting materials retain the hexagonal order and physical properties of the purely siliceous parent MCM-41 and exhibit higher Brønsted acid content compared to Al-MCM-41 prepared by direct hydrothermal synthesis. Later, he [48-50] also reported that aluminosilicate MCM-41 materials prepared by post-synthesis alumination using aqueous aluminum chlorohydrate possess stronger Brønsted acid sites as compared to the parent material.

Ryoo et al. [51,52] reported a post-synthesis route, through which aluminum species can be grafted onto siliceous frameworks using non-aqueous solutions of AlCl_3 and $\text{Al}(\text{NO}_3)_3$ etc., is developed as a generalised means to obtain mesoporous aluminosilicates molecular sieves with various structures such as MCM-41 (hexagonal), MCM-48 (cubic Ia3d), SBA-1 (cubic Pm3n), KIT-1 (disordered) and MSU-1 (disordered) with superior structural integrity, acidity and catalytic activity to those of materials having metals incorporated during synthesis. For example, NH_3 -TPD for the resulting Al-implanted samples (Al-MCM-41) gave higher TPD peak centered around 400°C assigned to strong Lewis acidity of

the extraframework Al species, which was not reported previously [53,54]. The Al implanted samples exhibited 2-3 times higher catalytic activity for *n*-butane cracking under 0.5 kPa butane and 110 kPa He at near 528°C. Furthermore, Ryoo et al [55] also investigated Friedel–Crafts alkylation of benzene, toluene, and *m*-xylene with benzyl alcohol over Al-MCM-41, Al-MCM-48, and Al-KIT-1 prepared from grafting route, and it is found that these catalysts are very active for Friedel–Crafts alkylation. Table 5 presents catalytic activities of these catalysts with various Si/Al ratio.

Table 5. Catalytic conversion (%) of benzyl alcohol after 3 h in Friedel–Crafts alkylation of benzene [55].

Sample	Si/Al ratio ^a			
	9	19	38	60
Al-MCM-41		32	77	
Al-KIT-1	9.5	51	65	95
Al-MCM-48		48	45	

^a Aluminum was incorporated by AlCl₃ impregnation. The Si/Al ratio was determined by inductively coupled plasma emission spectroscopy. The molar composition of the reaction mixture was 1 benzene : 0.025 benzyl alcohol : 0.65×10⁻³ Al. The reaction was measured at 80 °C with stirring under reflux conditions.

Furthermore, Dwyer et al. [56] reported mesoporous Al-MCM-41 materials were prepared by the reaction of siliceous MCM-41 with aluminum chloride vapor. Characterization of samples demonstrated that aluminum could be successfully incorporated into purely siliceous mesoporous MCM-41 (Si-MCM-41) by a post-synthesis reaction with aluminum chloride vapor. Materials prepared by this post synthesis reaction were compared with a series of Al-MCM-41 catalysts where aluminum was incorporated during synthesis. The ²⁷Al MAS NMR spectra clearly show that both methods yield materials where aluminum species are located at both tetrahedral and octahedral.

Notably, although the Al species are successfully incorporated into mesoporous materials by grafting routes, the formation of extra-framework aluminum species (octahedral sites) are still observed. Sano *et al.* [58] reported novel post-synthesis alumination method for MCM-41 using trimethylaluminum (TMA). By using this route, aluminum species in mesoporous materials are tetrahedral, which are well confirmed by ²⁷Al MAS NMR spectra of the samples, giving a single peak at near 54 ppm.

SBA-15 molecular sieve is newly discovered mesoporous silica with large uniform pore size (up to 30 nm) and thicker walls than MCM-41,

resulting in much higher stability [6]. However, incorporation of aluminum into the siliceous framework of SBA-15 by direct synthesis seems difficult because SBA-15 is synthesized in strong acid media (2 M HCl) and most aluminum sources dissolve under these conditions. Therefore, alumination of SBA-15 by post-synthesis have been paid much attention [58-60].

Kevan et al. [59] reported that mesoporous silica SBA-15 molecular sieve has been incorporated with aluminum *via* three different post-synthesis procedures by reacting SBA-15 with AlCl_3 in dry ethanol (route 1), with aluminum isopropoxide in dry hexane (route 2) and with an aqueous solution of sodium aluminate (route 3), followed by calcination. The Si/Al ratios in the resulting materials are in close agreement with the composition in the postsynthesis mixtures over a range of 40-10, indicating that the aluminum is mostly incorporated into silica SBA-15. The silanol groups on the internal wall surfaces of SBA-15 are suggested to be the sites for aluminum incorporation. The incorporation procedure has a strong effect on the aluminum coordination, pore structure, and ion exchange capacity of the resulting materials. At comparable Si/Al ratios around 20, the percentage of aluminum with tetrahedral symmetry in the synthesized materials is about 100% (route 3) > 76% (route 1) > 71% (route 2), indicating that alumination by aqueous sodium aluminate is most effective. The BET specific surface areas are 85% (route 1) > 60% (route 2) > 42% (route 3), showing that alumination by AlCl_3 in ethanol best maintains the mesoporous structure of SBA-15.

Sano et al. [60] reported alumination of mesoporous siliceous SBA-15 molecular sieve was carried out using trimethylaluminium (TMA). It is found that the aluminum could be easily incorporated into the siliceous SBA-15 without serious structure deformation. The hydrothermal stability of SBA-15 was considerably improved by the TMA processing. The results of the cumene cracking reactions and the pyridine adsorption experiments indicated that the Bronsted acid sites of Al-SBA-15 are stronger than those of Al-MCM-41 prepared by the same method.

4.2 Functionalization of mesoporous materials by phosphoric acid and sulfonic acid

In order to continuously increase acidity, mesoporous materials functionalized by phosphoric acid and sulfonic acid have been investigated [62-72]. Li *et al.* [62] firstly reported that post-treatment of mesoporous materials by phosphoric acid will greatly improve their thermal stability and acidity. The P-modified Al-MCM-41 shows potential application in the

cracking of long-chain alkane for producing gas olefins, especially iso-butene. Furthermore, Kawi *et al.* [63] reported that phosphorus species could be grafted onto the surface of MCM-41 by simply treating MCM-41 with phosphoric acid for a very short period, followed by high temperature calcination. The existence and state of surface phosphorus species grafted on MCM-41 are confirmed by XPS measurement. Using XRD and N₂ adsorption measurements, the uniform mesoporous structure of MCM-41 is shown to be quite stable under phosphoric acid treatment. FTIR results show that the surface phosphorus species grafted onto the surface of MCM-41 can selectively increase the number of Brønsted acidic sites on the surface without forming any Lewis acid sites. Using NH₃-TPD, the mild acidity of the generated Brønsted acidic sites on phosphorus-containing MCM-41 significantly enhances its catalytic activity for the dehydration of isopropanol. Figure 3 proposed two possible reaction pathways for the generation of Brønsted acid sites of the grafted phosphorus species, formed from the dehydration of phosphoric acid attached on the hydroxy groups of MCM-41, and Table 6 presents conversion (%) of isopropanol to propylene over MCM-41 and mesoporous materials modified by phosphoric acid (PM-25).

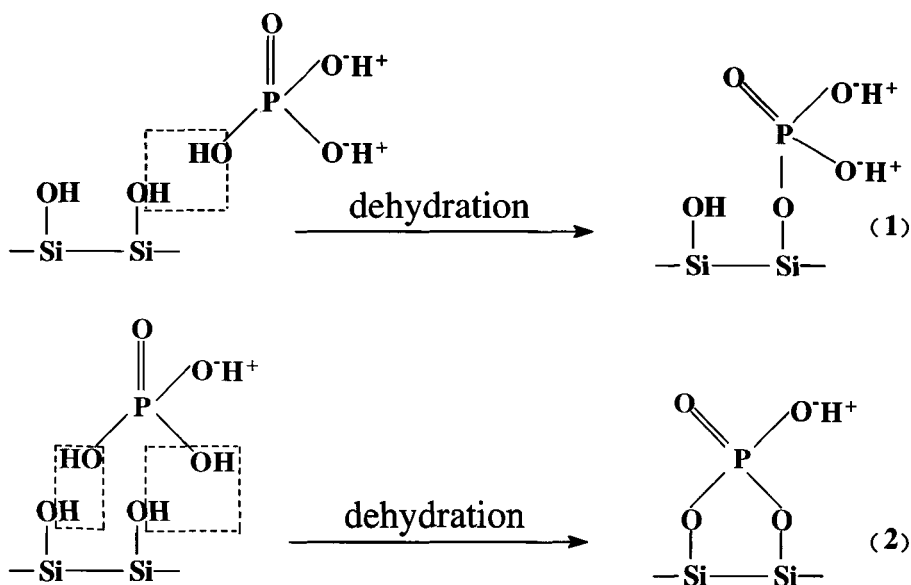


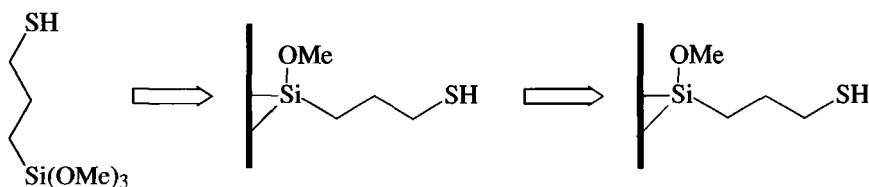
Figure 3. Two possible reaction pathways for the generation of Brønsted acid sites of the grafted phosphorus species [63].

Table 6. Conversion ^a (%) of isopropanol to propylene over Si-MCM-41 and PM 25 catalysts [63].

	150°C	175°C	200°C	250°C	300°C
Si-MCM-41	0	0	0.44	3.02	13.8
PM-25	5.6	10.1	47.1	97.3	99.9

^a the catalytic activity of the phosphorus containing MCM-41 catalysts for the dehydration of isopropanol was studied in a quartz microreactor containing 0.2 g of catalyst. Isopropanol was introduced to the reactor by flowing 20 ml/min of He saturated with isopropanol vapor at 20 °C.

Functionalization of mesoporous materials by sulfonic acid is also interesting method for increasing acidity [64-72]. Jacobs et al [64] firstly reported the functionalization of mesoporous materials by sulfonic acid. In this case, ordered mesoporous materials are modified with a 3-mercaptopropyl group using (3-mercaptopropyl)trimethoxysilane (MPTS, Fluka) as the organosulfonic acid precursor. Then, the mesoporous materials with immobilized mercaptopropyl groups were oxidized with H₂O₂ in a methanol–water mixture. Finally, the materials were extensively rinsed with H₂O, dried at 60°C. These acid-activated materials are denoted with the suffix -SO₃H. ¹³C-MAS-NMR proves that the current procedure leaves no -SH or -S-S groups on the surface; the only signals are those of heterogenized -(CH₂)₃SO₃H. Figure 4 shows proposed the grafting of MPTS and the formation of -(CH₂)₃SO₃H groups.

**Figure 4.** Proposed grafting of MPTS and formation of -(CH₂)₃SO₃H groups. Reprinted with permission from ref 64. Copyright 1999 Elsevier.

Furthermore, functionalization by sulfonic acid is also applied to mesoporous materials of SBA-15, which involve the co-condensation of tetraethoxysilane and mercaptopropyltrimethoxysilane in the presence of block copolymers and hydrogen peroxide under acidic conditions [65]. The

modified SBA-15 materials show hexagonal mesoscopic order and pore sizes up to 60 Å, surface areas up to 800 m²/g, and excellent thermal and hydrothermal stabilities. The formation of the sulfonic groups during co-condensation of the silica species coincides with enhanced mesoscopic ordering and changes in the adsorption properties of the final materials. ³¹P MAS NMR measurements of chemically adsorbed triethylphosphine oxide confirm the presence of Bronsted acid centers that are stronger than those found in Al-MCM-41 [65].

More recently, Inagaki et al. [66, 67] reported the surfactant-mediated synthesis of an ordered benzene–silica hybrid material; this material has an hexagonal array of mesopores with a lattice constant of 52.5 Å and crystal-like pore walls that exhibit structural periodicity with a spacing of 7.6 Å along the channel direction. The periodic pore surface structure results from alternating hydrophilic and hydrophobic layers, composed of silica and benzene. They also have sulfonated the mesoporous benzene–silica while preserving both the meso- and molecular-scale ordered structures. The sulfonic acid-functionalized mesoporous material might find use as a solid acid catalyst that can be readily recovered and reused [68]. The sulfonate groups were kept at pore walls up to 500 °C in air or nitrogen, as confirmed by mass spectroscopy. In contrast, the sulfonic acid on mesoporous materials of MCM-41 and SBA-15 will be decomposed at over 400°C. This unusually high thermal stability would allow the use of this solid acid catalyst not only in liquid-phase reactions, but also in gas-phase reactions at high temperature. Because the sulfonic acid groups serve as carriers of protons, the sulfonated mesoporous benzene–silica might also find use as an electrolyte for fuel cells [69].

The ordered mesoporous materials functionalized by sulfonic acid are very catalytically active for organic reactions such as esterification [65-71] and condensation of phenol and acetone to Bisphenol-A [72]. As a typical example, Figure 5 shows condensation of phenol and acetone to Bisphenol-A and Table 7 presents catalytic conversion of phenol and product selectivity.

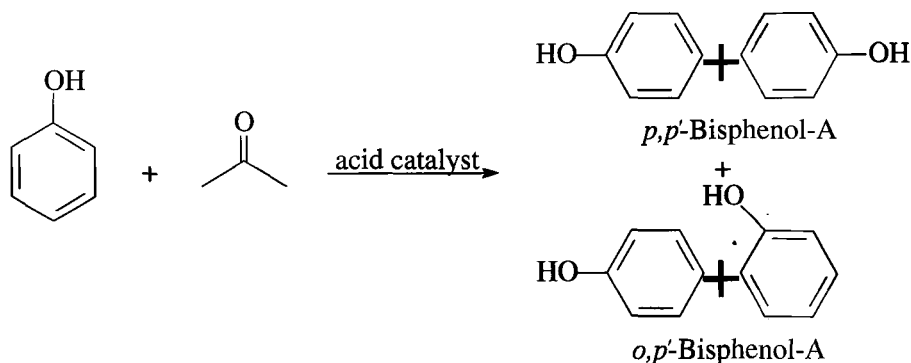


Figure 5. Proposed condensation of phenol and acetone to Bisphenol-A. Reprinted with permission from ref 72. Copyright 2001 Royal Society of Chemistry.

Table 7. Synthesis of Bisphenol-A with sulfonic acid functionalized MCM-41 silicas ^a [72].

Catalyst	Phenol conversion, %	Selectivity ^b , %
HBeta ^c	5	55
HY ^d	7	---
HZSM-5 ^e	<5	10
MCM-SO ₃ H	30	92
MCM-SO ₃ H ^f	17	90

^a Reagents and conditions: Phenol 4.7 g, acetone 0.58 g, (molar ratio =5/1), catalyst 50 mg, 70 °C, 24 h. ^b Selectivity to *p,p*A-Bisphenol-A. ^c Si/Al= 50. ^d Si/Al = 10.6. ^e Si/Al = 80. ^f Incomplete oxidation (from XANES).

4.3 Hydrothermal Recrystallization

As observed by alumination of mesoporous materials, grafting route indeedly increases the Al amount including tetrahedral and octahedral sites, but it is difficult to improve acidic strength of these Al species because the wall of mesoporous materials is still amorphous nature. Therefore, the hydrothermal recrystallization of mesoporous materials has been attracted much attention [73, 77-84].

Jansen et al. [73] reported the hydrothermal recrystallization of mesoporous MCM-41 and HMS for the first time. Their approach is based on the idea to recrystallize partially the amorphous framework of MCM-41 and HMS. By attachment of TPA cations, the template for ZSM-5 onto the

mesopore walls *via* an ion-exchange procedure a high dispersion of the TPA in the mesoporous material is achieved. This should result in a nucleation of ZSM-5 species and controlled conversion of MCM-41 and HMS. According to this idea, calcined Al-MCM-41 or Al-HMS was converted to TPA-MCM-41 or TPA-HMS by ion-exchange with a excess of aqueous TPAOH, followed by hydrothermal recrystallization at 120 °C. After filtration, washed with water, and dried at 100 °C, the materials designed as PNAs were calcined at 500 °C for removal of the organic templates.

Characterization of XRD patterns of the parent MCM-41 and HMS materials and the corresponding PNAs do not differ significantly. FTIR spectroscopy reveals only for the PNA samples show a distinct vibration at 550–560 cm⁻¹, which is a characteristic asymmetric stretching mode of the five-membered ring present in ZSM-5 [74–76]. The parent MCM-41 and HMS which have both an amorphous framework do not absorb at this wavenumber and therefore the 550 cm⁻¹ vibration is a good probe for detecting the degree of crystallinity of a siliceous MFI-type material even at this initial stage of ZSM-5 formation giving very small tectosilicate structures [74].

The substantial improvement of the catalytic activity, and thus the acidity, of the PNAs compared to the parent materials is demonstrated by the cracking of cumene, as presented in Table 8. As compared with that over parent MCM-41 and HMS materials, the enhanced cumene conversion over the PNAs is exclusively the result of a higher cracking activity. The improved activity is therefore assigned to enhanced Brønsted acidity which is also reflected by the initial *n*-hexane cracking activity of the PNAs which is about four times higher than that of the MCM-41 and HMS materials.

Table 8. Conversion of cumene at 300 °C over PNAs and related parent materials [73].

Sample	Cumene conversion (%) at time on stream	
	10 min	3 h
MCM-41 ^a	14.7	13.6
PNA-1	41.3	37.5
HMS ^a	24.8	26.8
PNA-2	47.6	42.4
ZSM-5 ^b	95.1	93.7

^a MCM-41 and HMS in the H⁺-form. ^b H-ZSM-5 with Si/Al at 78.

Mokaya [77,78] reported alumination of MCM-41 mesoporous silica by hydrothermal recrystallization. In this case, calcined pure silica MCM-41 and the required amount of Al (as aluminum isopropoxide) were added to the solution under stirring. Then, the resulting gel was aged at room temperature, followed by hydrothermal recrystallization at 150 °C in a Teflon-lined autoclave. The solid product was obtained by filtration, washed with distilled water, dried in air at room temperature and calcined in air at 550 °C. The sample composition analysis shows that Al species are effectively incorporated into mesoporous materials, and characterization of XRD and TEM techniques shows that these samples are still ordered hexagonal mesopores. Probing catalytic reactions such as cumene and hexane cracking show that the activity over these recrystallized samples is higher than that over conventional mesoporous aluminosilicates, indicating the stronger acidic sites in the samples. More recently, they [79] reported the use of supercritical fluids (SCFs) as carriers/solvents for postsynthesis alumination of mesoporous silica. The low viscosity and high diffusivity inherent to SCFs are ideally suited for rapid transport of Al into mesoporous silica and should achieve better Al dispersion. Another motivation for carrying out alumination under supercritical fluid conditions is that a better dispersion (and surface coverage) of Al should result in improved hydrothermal stability. They have demonstrated that the use of SCFs (as compared to aqueous or organic solvents) leads to Al-grafted MCM-41 materials that exhibit exceptional hydrothermal (steam) stability even for relatively highly aluminated materials.

Karlsson et al. [80,81] reported stepwise hydrothermal crystallization of MFI/MCM-41 like phases by co-templates of $C_6H_{13}(CH_3)_3NBr$ and $C_{14}H_{29}(CH_3)_3NBr$ in the temperature of 100-200°C. At first, the mesoporous phase was hydrothermally synthesized from the aluminosilicate gels in the temperature of 100-140 °C. Then, the sample was hydrothermally recrystallized at higher temperature of 150-200°C, and in this condition the MFI phase was formed. Characterization of XRD patterns for these samples shows typical peaks assigned to both microporous crystals of MFI and hexagonal mesopores of MCM-41, suggesting the mixed phases of MFI/MCM-41. The relative amounts of the two structures MFI and MCM-41 in the final products can be controlled by varying the ratio of the templates and by tuning the synthesis temperature.

Similarly, Li et al. [82-84] reported MCM-41/ZSM-5 composites, and Kaliaguine et al. [85] reported UL-ZSM-5, which were prepared using a dual templating method through a process of two-step crystallization.

Mesoporous MCM-41 was first synthesized using the self-assembling of surfactant cetyltrimethylammonium bromide and subsequently the amorphous wall of MCM-41 was recrystallized with a template of tetrapropylammonium bromide, which was introduced into the MCM-41 wall through a pretreatment process. Two kinds of stable MCM-41/ZSM-5 composites can be synthesized during the course of recrystallization. Crystallized mesoporous MCM-41 containing only short-range ordered ZSM-5 structure was first synthesized in the early stage of the recrystallization. With the increase of recrystallization time, some discrete micron-sized ZSM-5 crystals were produced and firmly attached to the loose aggregates of crystallized MCM-41, and another kind of MCM-41/ZSM-5 composite containing interconnected mesopore and micropore was therefore obtained. TPD-NH₃ measurement shows that the acidic strength of MCM/ZSM-5 composites is improved greatly, and catalytic tests show that MCM-41/ZSM-5 composites are more advantageous than amorphous MCM-41 and a mechanical mixture of MCM-41 and ZSM-5 in acid catalysis. Figure 6 shows proposed model for the structural transformation during the recrystallization.

Mesoporous aluminosilicates of UL-zeolites are also prepared from two step procedures [85]. At first, an amorphous mesoporous aluminosilicate was synthesized using SiCl₄ and AlCl₃ in ethanol. Secondly, the dried surfactant-containing mesoporous precursor was impregnated with a solution of TPAOH, followed by crystallization at 130 °C. In this process, the highly dispersed amorphous material of a mesoporous molecular sieve as a precursor phase was used to generate unusual mesostructured semizeolitic materials (UL-zeolites) by secondary solid-phase crystallization. Zeolite nanoparticles are grown from the mesopore walls and at the same time the end product retains some of the mesopore surface of the precursor.

Nevertheless, BET surface area of MCM-41/ZSM-5 composites is reduced significantly, as compared with that of mesoporous MCM-41. For example, MCM-41/ZSM-5 composites exhibit BET surface area at 400-600 m²/g, which is much lower than that of MCM-41 (900-1200 m²/g).

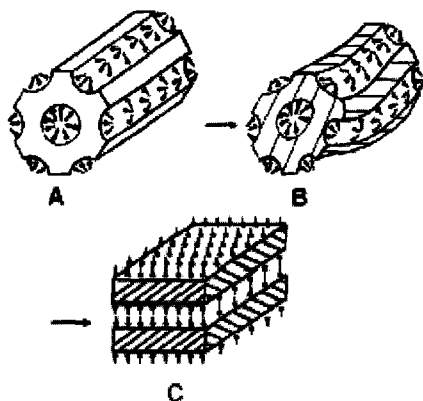


Figure 6. Schematic model for the structural transformation during the recrystallization: (A) hexagonal mesoporous, (B) disordered mesoporous, and (C) lamellar. •, amorphous; ///, crystallized. Reprinted with permission from ref 84. Copyright 2000 American Chemical Society.

5 Strongly acidic mesoporous aluminosilicates assembled from preformed nanosized zeolite precursors

5.1 Strongly acidic mesoporous aluminosilicates synthesized in alkaline media

As discussed in last sections, mesoporous aluminosilicates exhibit relatively weak acidity as compared with that of zeolites. On the other hand, after hydrothermal recrystallization, the acidity of MFI/MCM-41 composites is greatly enhanced, but their BET surface area is reduced significantly as compared with mesoporous aluminosilicates. To synthesize mesoporous aluminosilicates with strongly acidic sites and large surface area, a novel route for preparation of mesoporous aluminosilicates assembled from preformed zeolite precursors or zeolite seeds solution has been reported by Pinnavaia et al. [86-88] and Xiao et al. [89-99].

Pinnavaia et al. [86] reported steaming stable mesoporous aluminosilicates with strongly acidic sites are assembled from nanoclustered precursors that normally nucleate the crystallization of microporous zeolites. These precursors, also known as “zeolite seeds”, are presumed to promote zeolite nucleation by adopting AlO_4 and SiO_4 tetrahedra connectivities that resemble the secondary structural elements in a crystalline zeolite. Assembling these same zeolite seeds into a mesostructure imparts acidity and hydrothermal stability that begin to

approach zeolites, even though the framework walls remain atomically disordered.

The hexagonal mesoporous aluminosilicates (MSU-S) have been synthesized from zeolite seeds of faujasitic type Y [86], followed by synthesis from zeolite seeds solution of ZSM-5 and Beta in basic media [87]. Both XRD and nitrogen adsorption isotherms shows that the mesoporous materials of MSU-S are hydrothermally stable. Catalytic tests in cumene cracking show that MSU-S is much more active than conventional mesoporous aluminosilicates, indicating that the acidic strength of MSU-S is greatly enhanced, as compared with that of MCM-41. Table 9 presents textural properties and cumene conversions for mesoporous aluminosilicate sieves assembled from zeolite seeds solution of MFI and Beta.

Interestingly, the mesoporous wall of MSU-S is very thin, only at 9-12Å, but MSU-S is hydrothermally stable. On the other hand, it has been reported that the particle size of preformed seeds in the solution is at 2-3 nm (*e.g.* particle size at 2.8 nm for ZSM-5 seeds templated by tetrapropylammonium ions) [99-101]. Obviously, it is difficult that mesoporous wall of MSU-S is assembled from zeolite seeds because the zeolite seeds are much thicker than the mesoporous wall of MSU-S. Therefore, the idea of mesoporous aluminosilicates assembled from zeolite seeds is insufficient.

Table 9. Textural properties and cumene conversions [87].

Sample	Unit cell dimension a_0 [Å]	Surface area [m ² /g]	Pore volume [cm ³ /g]	Pore size [Å]	Cumene conv. ^b [%]
1.5%Al-MSU-S _(MFI)					
calcined	45.3	1231	1.06	36.8	32.2
steamed 600°C, 5h	44.5	1192	0.93	34.7	
steamed 800°C, 5h	36.6	849	0.44	24.3	
1.5%Al-MSU-S _(BEA)					
calcined	47.3	1124	1.06	39.1	31.5
steamed 600°C, 5h	46.7	1065	0.94	38.0	
steamed 800°C, 5h	37.0	885	0.46	26.4	
1.5%Al-MCM-41					
calcined	46.4	1013	1.08	38.7	11.7
steamed 600°C, 5h	35.2	639	0.39	20.1	
steamed 800°C, 5h		55			

^aReaction conditions: 6 mm i.d. fixed bed quartz reactor; 200 mg catalyst; cumene flow rate, 4.1 mmol/min; N₂ carrier gas, 20 cm³/min; conversions reported after 60 min on-stream at 300 °C. ^b1.5%Al-MCM-41 was prepared by the direct assembly of conventional aluminosilicate anions formed from sodium aluminate, fumed SiO₂, and TMAOH.

Xiao et al. [89,90] reported that ordered hexagonal mesoporous aluminosilicates (MAS-5) with uniform pore sizes have been successfully synthesized from assembly of pre-formed aluminosilicate precursors with cetyltrimethylammonium bromide (CTAB) surfactant. The aluminosilicate precursors were obtained by heating at 100-140°C for 2-10 hours from alumina-silica gels at the $\text{Al}_2\text{O}_3/\text{SiO}_2/\text{TEAOH}/\text{H}_2\text{O}$ molar ratios of 1.0/7.0-350/10.0-33.0/500-2000. Mesoporous MAS-5 shows extraordinary stability both in boiling water (over 300 hours) and in steam (800 °C for 2 hours). Temperature-programmed-desorption of ammonia shows that acidic strength of MAS-5 is much higher than that of MCM-41 and is comparable to that of microporous Beta zeolite, as shown in Figure 7. In catalytic cracking of 1,3,5-tri-isopropylbenzene and alkylation of isobutane with butene, MAS-5 exhibits greater catalytic activity and selectivity, as compared with MCM-41 and HZSM-5. Figure 8 shows catalytic conversion of 2-butene in alkylation of isobutane with butene vs. reaction time over various catalysts.

The MAS-5 samples were characterized with infrared, UV-Raman, and NMR spectroscopy and numerous other techniques. The results suggest that the pore walls of MAS-5 contains primary and secondary structural building units, similar to those of microporous zeolites. Such unique structural features might be responsible for the observed strong acidity and high thermal stability of the mesoporous aluminosilicates with ordered hexagonal symmetry.

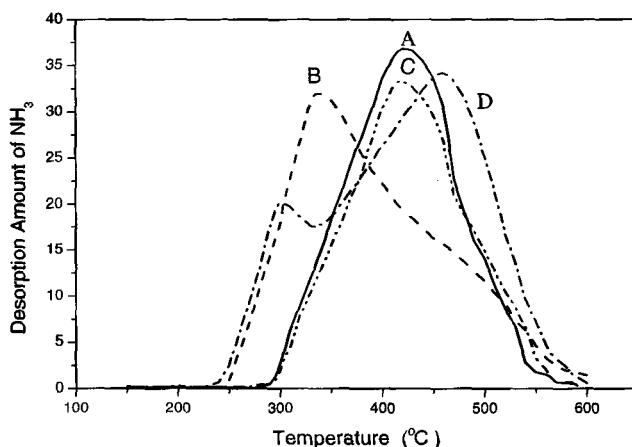


Figure 7. Temperature-programmed-desorption of ammonia (NH_3 -TPD) curves for various samples of (A) MAS-5, (B) MCM-41, (C) HBeta, and (D) HZSM-5. Reprinted with permission from ref 89. Copyright 2001 Wiley.

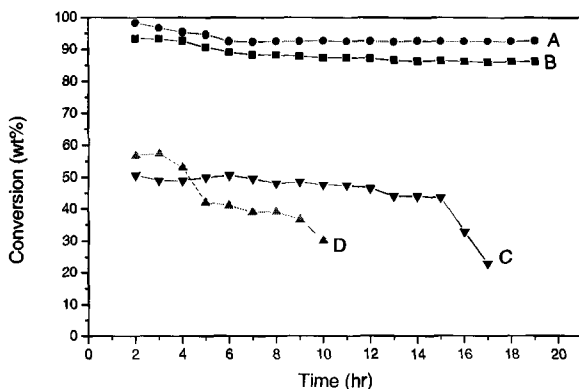


Figure 8. Catalytic conversion of 2-butene in alkylation of isobutane with butene vs. reaction time over various catalysts (each of 0.5 g) of (A) MAS-5, (B) HBeta, (C) MCM-41, and (D) HZSM-5 at a reaction temperature of 25 °C with isobutane/butene molar ratio of 12/1, 1-butene/2-butene molar ratio of 8/1, and WHSV of 9 h⁻¹. Reprinted with permission from ref 89. Copyright 2001Wiley.

The aluminosilicate precursors were prepared from heating aluminosilicate gel in the presence of TEAOH at 100–140 °C for 2–3 hours. TEAOH is known to be a very good structure-directing agent in the synthesis of Beta zeolite [103,104]. Addition of a small amount of aluminosilicate precursors (3% wt.) into alumina-silica gel (Al₂O₃/SiO₂/Na₂O/H₂O=1/10–40/2.8–12/500–900) at 140 °C for 2–4 days leads to Beta zeolite with high crystallinity in the absence of organic templates [103,104]. The aluminosilicate precursors appear to serve as seeds for the formation of Beta zeolite. IR characterization of these aluminosilicate precursors shows a clear band at 520–600 cm⁻¹, which is characteristic of 5-membered rings, indicating that aluminosilicate precursors contain zeolite primary and secondary structure building units [74–76].

Table 10 shows textural properties of MAS-5 prepared from preformed Beta zeolite precursors and conventional MCM-41. Interestingly, the thickness of mesoporous wall for MAS-5 is much thicker than that of MCM-41, which is assigned that since the aluminosilicate precursors contain zeolite primary and secondary structure building units, the size of aluminosilicate precursor particles (or nanoclusters) should be larger than that of SiO₄ or AlO₄ tetrahedron for constructing the walls of mesopores.

Table 10. Textural properties for mesoporous aluminosilicate of MAS-5 prepared from preformed Beta zeolite precursors [88,89].

Sample	Unit cell dimension a_0 [Å]	Surface area [m ² /g]	Pore volume [cm ³ /g]	Pore size [Å]	Thickness of mesoporous wall [Å]
MAS-5	52.1	1150	1.17	28.1	24.0
MCM-41	44.4	940	0.68	27.9	16.5

The tetrahedral aluminum species in the MAS-5 is thermally and hydrothermally stable. Figure 9 shows ²⁷Al NMR spectra of as-synthesized, calcined, and hydrothermally treated MAS-5 and MCM-41 samples. Interestingly, the MAS-5 samples gives only one peak at 61 ppm assigned to tetrahedral aluminum sites in mesoporous aluminosilicates. In contrast, after calcination of as-synthesized MCM-41 in air at 550 °C, the sample NMR spectrum shows a new peak at 0 ppm assigned to 6-coordinated aluminum, in addition to the peak at 55 ppm. The formation of 6-coordinated aluminum in the sample is possibly from dealumination of MCM-41.

More recently, the assembly of preformed zeolite precursors with surfactants in basic media is applied to synthesize cubic mesoporous aluminosilicates, and TPD-NH₃ measurements also show similar acidic strength to that of corresponding zeolites [107,108].

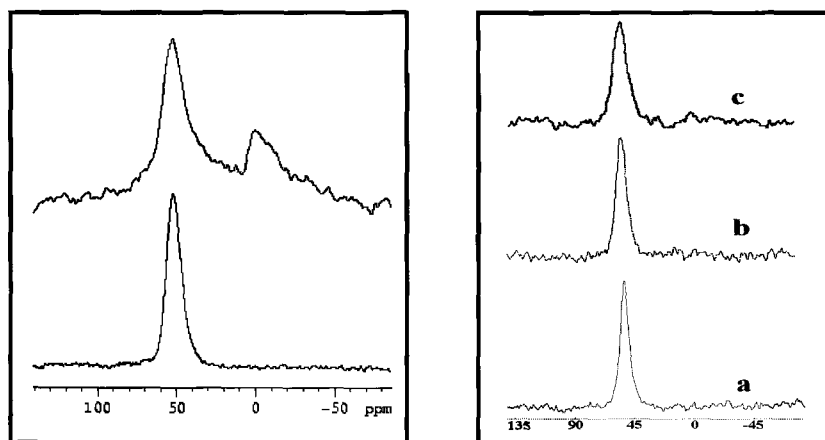


Figure 9. [A] ²⁷Al NMR spectra of (a) as-synthesized MCM-41 and (b) calcined MCM-41 at 550°C for 4 h; [B] ²⁷Al NMR spectra of (a) as-synthesized MAS-5, (b) calcined MAS-5 at 550°C for 4 h; (c) MAS-5 after treatment with 100% water vapor at 600°C for 4h.

5.2 Strongly acidic mesoporous aluminosilicates synthesized in strongly acidic media

It is well known that both microporous crystals of zeolites and mesoporous materials are easily synthesized in alkaline media. If the conditions were not controlled very well, mixed phases would be often obtained. On the other hand, in the strongly acidic condition, the preformed zeolite nanoclusters would not grow continuously into large crystal and the appearance of metal oxides can also be avoided. The products therefore would be pure mesoporous materials without zeolite crystals or metal oxides as byproducts.

The first example for preparation of ordered mesoporous aluminosilicates assembled from preformed zeolite precursors in strongly acidic media is reported by Xiao et al. [93-96]. They reported that heteroatoms of Al are effectively introduced into the framework of ordered mesoporous silica materials (designated as MAS-7) in strong acidic media ($\text{pH} < 0$) by a two-step procedure. Characterization of nitrogen adsorption isotherms and TEM shows that the mesoporous wall (4-5 nm) of MAS-7 is much thicker than that of SBA-15, which is enough for assembly of preformed zeolite precursors (2-3 nm). Recently, Pinnavaia et al. [88] reported assembly of hydrothermally stable and strongly acidic aluminosilicate foams and large-pore hexagonal mesostructures from zeolite seeds under strongly acidic conditions.

Catalytic activities in cracking of cumene and 1,3,5-tri-isopropylbenzene over various catalysts are summarized in Table 11. Although HZSM-5 show strong acidity and give very high conversion for cumene, it is almost inactive for 1,3,5-tri-isopropylbenzene due to its relative small pore size and the large diameter of reactant molecules. At the same conditions, Al-SBA-15 [59] prepared from “post-synthesis” shows relatively low activity, as a result of amorphous connective way of the Al species in its framework. Additionally, Al-SBA-15[105] synthesized from “direct synthesis” shows higher catalytic activities (conversion at 25.5 and 52.4 % for cumene and 1,3,5-tri-isopropylbenzene, respectively) than those of Al-SBA-15 prepared by “post-synthesis”, but still much lower than those of MAS-7. Only MAS-7 shows the highest activities for both reactions (conversion at 43.2 and 96.6 % for cumene and 1,3,5-tri-isopropylbenzene) because it combine the advantages of both zeolite beta (strong acidity) and SBA-15 (large pores). More significantly, after the treatment in boiling water for 50 h, MAS-7 still shows large surface area and high catalytic activity.

Table 11. Properties and catalytic activities in cracking of cumene and 1,3,5-tri-isopropylbenzene of various samples ^a.

Sample	Pore size (nm)	Wall thickness (nm)	Conv. of cumene (%)	Conv. of 1,3,5-tri-isopropylbenzene (%)
MAS-7	7.6	5.4	43.5	96.6
SBA-15	7.6	3.2	Inactive	Inactive
Al-SBA-15 ^b	---	---	7.8	36.5
Al-SBA-15 ^c	---	---	25.5	52.4
H-ZSM-5	---	---	94.4	1.7

^a Pore size distributions and pore volumes were determined from N₂ adsorption isotherms at 77K. The wall thickness were calculated as: a_0 -pore size ($a_0 = 2 \times d(100)/3^{1/2}$). Catalytic reactions were performed at 300 °C. In each run, 50 mg of catalyst was used, pulse injection of the reactant was 0.4 μ ml, and reaction flow rate was 53.7 ml/min. ^b Al-SBA-15 was prepared according to the method reported by Ref. [59]. ^c Al-SBA-15 was prepared according to the method reported by Ref. [105].

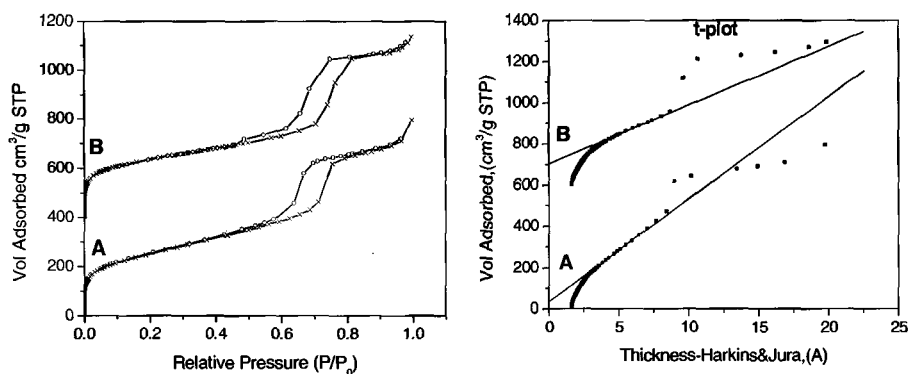


Figure 10. N₂ adsorption/desorption isotherms (left) and *t*-plots (right) for calcined: (A) SBA-15 and (B) MAS-7. The isotherm and *t*-plot for B are respectively offset from 400 and 600 cm³/g to begin for clarity.

Mesoporous aluminosilicates assembled from preformed zeolite precursors in strongly acidic media show large amount of micropores, which are well-characterized by nitrogen adsorption isotherms, TEM, and probing catalytic reactions [93,96].

Fig. 10 shows the *t*-plots of the MAS-7 sample and the SBA-15 sample, respectively. Generally, the *t*-plots of conventional mesoporous materials

should pass zero of axis, meaning no micropores in them. Miyazawa *et al* reported that there are some micropores in the wall of SBA-15 formed by penetration of hydrophilic poly (ethylene oxide) chains of triblock copolymer in the silica wall. [106]. The SBA-15 sample prepared in this work also show the character of containing micropores. However, it is very interesting to note that the micropore volume of the MAS-7 sample ($0.16 \text{ cm}^3/\text{g}$) is much more than that of the SBA-15 sample prepared from the same conditions ($0.05 \text{ cm}^3/\text{g}$). Even we considered the fact that MAS-7 has thicker walls than SBA-15, the ratio of micropores volume to the thickness of the walls in MAS-9 is still much more than that in SBA-15. The larger micropore volume in MAS-7 may be attributed to the existence of zeolite MFI primary units in the mesoporous walls.

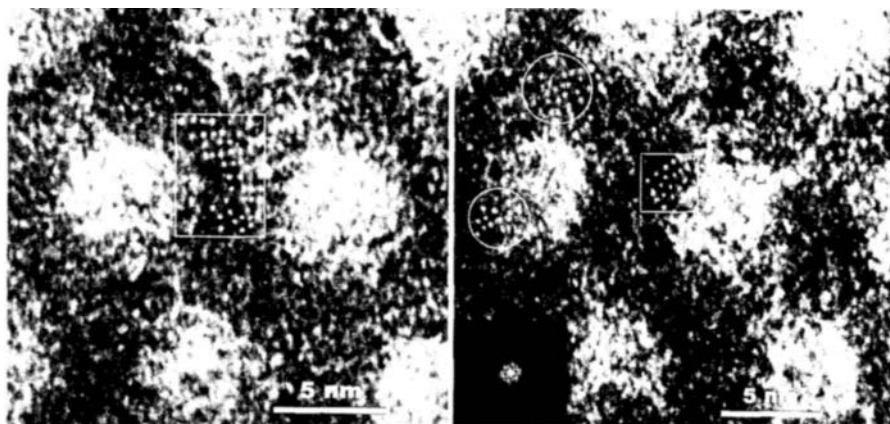


Figure 11. HRTEM image of MAS-7. The marked area presents fairly ordered micropore arrays. Inset is the Fourier diffractogram of the square area. Reprinted with permission from ref 96. Copyright 2002 American Chemical Society.

Figure 11 is HRTEM images of MAS-7, which clearly show some micropores. This further confirms the presence of microporosity within such mesoporous materials prepared from assembly of preformed zeolite precursors with triblock copolymer templates. What is more important is that within the mesoscale pore walls, micropore arrays with more or less periodicity are found (especially in those areas marked with circles or rectangles in Figures 11). These micropore arrays are mostly around 2 nm in size (marked areas in Figure 11), which is similar to the size of preformed zeolite nanoclusters reported previously [100-102]. The Fourier

diffraction pattern (Figure 11, inset) corresponding to the micropore array presents a discernible hexagonal diffraction pattern, which convincingly confirms the existence of nanorange hexagonally ordered microporosity within the pore walls of MAS-7. This further confirms the existence of micropore nanoarrays and also suggests that the zeolite structure units might be the origin of these micropores because MAS-7 was prepared from precursors containing zeolite nanoclusters.

Microporosity of ordered mesoporous aluminosilicates assembled from zeolite nanoclusters is investigated by catalytic reactions with various probing molecules. At first, the samples are treated by bulky basic organic molecular (5,7-Dibrom-8-hydroxy-chinolin with size of 8.7 Å). In this case, the acidic sites in mesopores are killed and the acidic sites in micropores less than molecular diameter of 5,7-Dibrom-8-hydroxy-chinolin are still active. Cracking of 1,3,5-triisopropylbenzene (size of 7.4 Å) shows that the treated MAS-7 is still catalytically active. In contrast, the treated Al-SBA-15 are almost inactive. These results show that MAS-7 contains micropores, whose size is similar to that of Beta.

Table 12. Catalytic activities of various samples without treatment of (5,7-Dibrom-8-hydroxy-chinolin) DBHC molecules.

Catalyst (Si/Al)	Conversion (%) of 1,3,5-triisopropylbenzene (TIPB) cracking ^a	
	Without DBHC treatment	After DBHC treatment
Beta (30)	100	100
Al-SBA-15 (30)	--- ^b	92.5
Al-SBA-15 (20)	---	98.4
MAS-7 (30)	12.5	97.3

^a 1,3,5-triisopropylbenzene (TIPB) cracking reactions were performed at 573 K by pulse injections. In each run, 50 mg of catalyst was used, pulse injection of reactant was 0.4 μL, and nitrogen was used as the carrier gas at a flow rate of 53.7 mL/min. ^b undetectable.

More recently, the assembly of preformed zeolite nanoclusters with surfactants has been investigated extensively. Table 13 [98] summarized Xiao's results for strongly acidic mesoporous aluminosilicates assembled from various preformed zeolite precursors.

Table 13. Summary of novel ordered mesoporous aluminosilicates assembled from various zeolite precursors.

Zeolite precursors	Basic media		Acidic media	
	Sample	Symmetry	Sample	Symmetry
Beta	MAS-5 [88-91]	hexagonal	MAS-7[92-94]	hexagonal
ZSM-5	MAS-4 [98]	hexagonal	MAS-9[92-94]	hexagonal
	MAS-6 [98]	cubic	MAS-10 [98]	cubic
L	MAS-3 [98]	hexagonal	MAS-8 [98]	hexagonal
FAU	MAS-2 [98]	hexagonal	MAS-11 [98]	hexagonal
M	MAS-1 [98]	hexagonal	MAS-13 [98]	hexagonal
Silicalite-I	MPS-4 [98]	hexagonal	MPS-9 [98]	hexagonal

6 Acknowledgements

This work was supported by the National Natural Science Foundation of China (29825108, 20173022, and 20121103), the State Basic Research Project (G2000077507), and the National Advanced Materials Committee of China.

References

1. Van Bekkum H., Flanigen E. M., Jacobs P. A., and Jansen J. C. (Eds), *Introduction to Zeolite Science and Practice*, Elsevier, Amsterdam, 2001.
2. Breck D. W. (Ed.), *Zeolite Molecular Sieves*, Wiley, New York, 1974.
3. Rabo J. A. (Ed), *Zeolite Chemistry and Catalysis*, ACS Monograph 171, Am. Chem. Soc., Washington, DC, 1976.
4. Barrer R. M.(Ed), *Hydrothermal Chemistry of Zeolites*, Academic Press, London, 1982.
5. Kresge C. T., Leonowicz M. E., Roth W. J., Vartuli J. C. and Beck J. S., Ordered mesoporous molecular-sieves synthesized by a liquid-crystal template mechanism, *Nature* **352** (1992) pp. 710-712; Beck J.S., *et al.*, A new family of mesoporous molecular-sieves prepared with liquid-crystal templates, *J. Am. Chem. Soc.* **114** (1992) pp. 10834-10843.
6. Zhao D., Feng J., Huo Q., Melosh N., Fredrickson G. H., Chmelka B. F. and Stucky G. D., Triblock copolymer syntheses of mesoporous silica with periodic 50 to 300 angstrom pores, *Science* **279** (1998) pp. 548-552.
7. Corma A., From microporous to mesoporous molecular sieve materials and their use in catalysis, *Chem. Rev.* **97** (1997) pp. 2373-2420.
8. Kim S. S., Zhang W. and Pinnavaia T. J., Ultrastable mesostructured silica vesicles, *Science* **282** (1998) pp.1032-1035.
9. Ryoo R., Kim J. M. and Shin C. H., Disordered molecular sieve with branched mesoporous channel network, *J. Phys. Chem.* **100** (1996) pp. 17718-17721.

10. Ryoo R., Jun S., Kin J. M., and Jim M. J., Generalised route to the preparation of mesoporous metallosilicates via post-synthetic metal implantation, *Chem. Commun.* (1997) pp. 2225-2226.
11. Mokaya R. and Jones W., Post-synthesis grafting of Al onto MCM-41, *Chem. Commun.* **22** (1997) pp. 2185-2186.
12. Huo Q. S., et al., Generalized synthesis of periodic surfactant inorganic composite-materials, *Nature* **368** (1994) pp. 317-321.
13. Yang P. D., Zhao D.Y., Margolese D. I., Chmelka B. F., and Stucky G.D., Generalized syntheses of large-pore mesoporous metal oxides with semicrystalline frameworks, *Nature* **396** (1998) pp. 152-155.
14. Antonelli D. M. and Ying J. Y., Mesoporous materials, *Curr. Opin. Colloid Interface Sci.* **1** (1996) 523-529; Sun T. and Ying J. Y., Synthesis of microporous transition-metal-oxide molecular sieves by a supramolecular templating mechanism, *Nature* **389** (1997) pp. 704-706.
15. Chen C., Li H., and Davis M. E., Studies on mesoporous materials, *Microporous Mater.* **2** (1993) pp. 17-26.
16. Khushalani D., Kuperman A., Coombs N. and Ozin G. A., Mixed surfactant assemblies in the synthesis of mesoporous silicas, *Chem. Mater.* **8** (1996) pp. 2188-2193.
17. Zhao X. S. and Lu G. Q., Modification of MCM-41 by surface silylation with trimethylchlorosilane and adsorption study, *J. Phys. Chem. B* **102** (1998) pp. 1556-1561.
18. Kim J. M., Jun S. & Ryoo R., Improvement of hydrothermal stability of mesoporous silica using salts: reinvestigation for time-dependent effects, *J. Phys. Chem. B* **103** (1999) pp. 6200-6205.
19. Yang P., Zhao D., Margolese D. J., Chmelka B. F. and Stucky G. D., Generalized synthesis of large-pore mesoporous metal oxides with semicrystalline frameworks, *Nature* **396** (1998) pp. 152-155.
20. Misono M., Mizuno N., Katamura K., Kasei A., Konishi Y., Sakata K., Okuhara T. and Yoneda Y., Catalysis by heteropoly compounds. III. The structure and properties of 12-heteropolyacids of molybdenum and tungsten and their salts pertinent to heterogeneous catalysis, *Bull. Chem. Soc. Jpn.* **55** (1982) p. 400.
21. Okuhara T., Mizuno N. and Misono M., Catalytic chemistry of heteropoly compounds, *Adv. Catal.* **41** (1996) p. 113.
22. Kozhevnikov I. V., Heteropoly acids and related compounds as catalysts for fine chemical synthesis, *Catal. Rev.-Sci. Eng.* **95** (1995) p. 311.
23. Kresge C. T., Marler D. O., Rav G. S. and Rose B. H., Supported heteropoly acid catalysts, US Patent, 5,366,945, 1994.
24. Kozhevnikov I. V., Sinnema A., Jansen R. J. J., Pamin K. and Van Bekkum H., New acid catalyst comprising heteropoly acid on a mesoporous molecular sieve MCM-41, *Catal. Lett.* **30** (1995) p. 241.
25. Xia Q.-H., Hidajat K. and Kawi S., Structure, acidity, and catalytic activity of mesoporous acid catalysts for the gas-Phase synthesis of MTBE from MeOH and ButOH, *J. Catal.* **209** (2002) p. 433.
26. Blasco T., Corma A., Martinez A. and Martinez-Escolano P., Supported heteropolyacid (HPW) catalysts for the continuous alkylation of isobutane with

- 2-butene: the benefit of using MCM-41 with larger pore diameters, *J. Catal.* **177** (1998) p. 306.
27. Chu W., Zhao Z., Sun W., Ye X., and Wu Y., Isobutane/butene alkylation over supported heteropoly acid catalysts, *Catal. Lett.* **55** (1998) p. 57.
 28. Ghanbari-Siahkali A., Philippou A., Dwyer J., and Anderson M. W., The acidity and catalytic activity of heteropoly acid on MCM-41 investigated by MAS NMR, FTIR and catalytic tests, *Appl. Catal. A* **192** (2000) p. 318.
 29. Yang W., Billy J., Ben Tarrit Y., Vedrine J. C., and Essayem N., $H_3PW_{12}O_{40}$ supported on Cs modified mesoporous silica: catalytic activity in n-butane isomerisation and in situ FTIR study: Comparison with microporous $Cs_xH_{3-x}PW_{12}O_{40}$, *Catal. Today* **73** (2002) p. 153.
 30. Chu W., Yang X., Shan Y., Ye X., and Wu Y., Immobilization of the heteropoly acid (HPA) $H_4SiW_{12}O_{40}(SiW_{12})$ on mesoporous molecular sieves (HMS and MCM-41) and their catalytic behavior, *Catal. Lett.* **42** (1996) p. 201.
 31. Verhoef M. J., Kyooman P. J., Peters J. A. and van Bekkum H., A new synthesis route to the microporous tin sulfide TMA-SnS-1 at room temperature in quasi non-aqueous systems, *Microporous Mesoporous Mater.* **27** (1999) p. 57.
 32. Arata K., Solid superacids, *Adv. Catal.* **37** (1990) p. 165.
 33. Song X. M. and Sayari A., Sulfated zirconia-based strong solid –acid catalysts: recent progress, *Catal. Rev.-Sci. Eng.* **38** (1996) p. 329.
 34. Jin T., Yamaguchi T., and Tanabe K., Mechanism of acidity generation on sulfur-promoted metal oxides, *J. Phys. Chem.* **90** (1986) p. 4797.
 35. Hino M. and Arata K., Reaction of butane and isobutane catalyzed by titanium oxide treated with sulphate ion: Solid superacid catalyst, *Chem. Commun.* (1979) p. 1148; Synthesis of solid superacid catalyst with acid strength of $H_0 > -16.04$, (1980) p. 851.
 36. Yadav G. D. and Nair J. J., Sulfated zirconia and its modified versions as promising catalysts for industrial processes, *Micropor. Mesopor. Mater.* **33** (1999) p. 1.
 37. Matsushashi M., Tanaka M., Nakamura H., and Arata K., Formation of acid sites in ordered pores of FSM-16 by modification with sulfated zirconia, *Appl. Catal. A* **208** (2001) p. 1.
 38. Xia H.-Q., Hidajat K., and Kawi S., $SO_4^{2-}/ZrO_2/MCM-41$ as a new superacid catalyst, *Chem. Commun.* **22** (2000) p. 2229.
 39. Xia H.-Q., Hidajat K., and Kawi S., Effect of ZrO_2 loading on the structure, acidity, and catalytic activity of the $SO_4^{2-}/ZrO_2/MCM-41$ acid catalyst, *J. Catal.* **205** (2002) p. 318.
 40. Chen C.-L., Cheng S., Lin H.-P., Wong S.-T. and Mou C.-Y., Sulfated zirconia catalyst supported on MCM-41 mesoporous molecular sieves, *Appl. Catal. A* **215** (2001) p. 21.
 41. Chen C.-L., Li T., Cheng S., Lin H.-P., Bhongale C. J., and Mou C.-Y., Direct impregnation method for preparing sulfated zirconia supported on mesoporous silica, *Micropor. Mesopor. Mater.* **50** (2001) p. 201.
 42. Hua W., Yue Y., and Gao Z., Acidity enhancement of SEA mesoporous molecular sieve by modification with SO_4^{2-}/ZrO_2 , *J. Mol. Catal. A* **170** (2001) p. 195.
 43. Y. Sun, Zhu L., Lu H., Wang R., Lin S., Jiang D. and Xiao F.-S., Sulfated zirconia supported in mesoporous materials, *Appl. Catal. A* **237** (2002) p. 21.
 44. Xiao F.-S., Zhang W., Jia M., Yu Y., Fang C., Guoxingbatu, Zheng S., Qiu S. and Xu R., Higher activity of $CuCl_2/HZSM-5$ prepared by dispersion method in

- selective catalytic reduction of NO by propylene (SCR-HC) at lower temperature, *Catal. Today* **50** (1999) p. 117.
45. Xie Y. C. and Tang Y.-Q., Spontaneous monolayer dispersion of oxides and salts onto surface of supports: applications to heterogeneous catalysis, *Adv. Catal.* **37** (1990) p. 1
 46. Xiao F.-S., Zheng S., Sun J., Yu R., Qiu S. and Xu R., Dispersion of Inorganic Salts into Zeolites and Their Pore Modification, *J. Catal.* **176** (1998) p. 474.
 47. Mokaya R. and Jones W., Post-synthesis grafting of Al onto MCM-41, *Chem. Commun.* **22** (1997) p. 2185.
 48. Mokaya R. and Jones W., Aluminosilicate mesoporous molecular sieves with enhanced stability obtained by reacting MCM-41 with aluminium chlorohydrate, *Chem. Commun.* **17** (1998) p. 1839.
 49. Mokaya R. and Jones W., Grafting of Al onto purely siliceous mesoporous molecular sieves, *Phys. Chem. Chem. Phys.* **1** (1999) p. 207.
 50. Mokaya R. and Jones W., Efficient post-synthesis alumination of MCM-41 using aluminium chlorohydrate containing Al polycations, *J. Mater. Chem.* **9** (1999) p. 555.
 51. Ryoo R., Jun S., Kim J. M. and Kim M. J., Generalised route to the preparation of mesoporous metallosilicates via post-synthetic metal implantation, *Chem. Commun.* **22** (1997) p. 2225.
 52. Ahn W. S., Lee D. H., Kim T. J., Kim J. H., Seo G. and Ryoo R., Post-synthetic preparations of titanium-containing mesopore molecular sieves, *Appl. Catal. A* **181** (1999) p. 39.
 53. Corma A., Fornés V., Navarro M. T., and Pérez-Pariente J., Acidity and stability of MCM-41 crystalline aluminosilicates, *J. Catal.* **148** (1994) p. 569.
 54. Kosslick H., Landmesser H., and Fricke R., Acidity of substituted MCM-41-type mesoporous silicates probed by ammonia, *J. Chem. Soc., Faraday Trans.* **93** (1997) p. 1849.
 55. Jun S. and Ryoo R., Aluminum impregnation into mesoporous silica molecular sieves for catalytic application to Friedel-Crafts alkylation, *J. Catal.* **195** (2000) p. 237.
 56. Ghanbari-Siahkali A., Philippou A., Cundy C. S., Anderson M. W., and Dwyer J., A comparison of direct synthesis and vapour phase alumination of MCM-41, *J. Mater. Chem.* **11** (2001) p. 569.
 57. Chen L. Y., Ping Z., Chuah G.K., Jaenicke S., and Simon G., A comparison of post-synthesis alumination and sol-gel synthesis of MCM-41 with high framework aluminum content, *Micropor. Mesopor. Mater.* **27** (1999) p. 231.
 58. Oumi Y., Takagi H., Sumiya S., Mizuno R., Uozumi T., and Sano T., Novel post-synthesis alumination method for MCM-41 using trimethylaluminum, *Micropor. Mesopor. Mater.* **44-45** (2000) p. 267.
 59. Z. Luan, M. Hartmann, D. Zgao, W. Zhou and L. Kevan, Alumination and ion exchange of mesoporous SBA-15 molecular sieves, *Chem. Mater.* **11** (1999) p. 1621.
 60. Sumiya S., Oumi Y., Uozumi T., and Sano T., Characterization of AISBA-15 prepared by post-synthesis alumination with trimethylaluminum, *J. Mater. Chem.* **11** (2000) p. 1111.

61. Morey M. S., Stucky G. D., Schwarz S., and Froba M., Isomorphic substitution and postsynthesis incorporation of zirconium into MCM-48 mesoporous Silica, *J. Phys. Chem. B* **103** (1999) p. 2037.
62. Huang L. M. and Li Q. Z., Enhanced acidity and thermal stability of mesoporous materials with post-treatment with phosphoric acid, *Chem. Lett.* (1999) p. 829.
63. Kawi S., Shen S. C. and Chew P. L., Generation of Bronsted acid sites on Si-MCM-41 by grafting of phosphorus species, *J. Mater. Chem.* **12** (2002) p. 1582.
64. Bossaert W. D., De Vos D. F., Van Rhijin W. M., Bullen J., Grobet P. J., and Jacobs P. A., Mesoporous sulfonic acids as selective heterogeneous catalysts for the synthesis of monoglycerides, *J. Catal.* **182** (1999) p. 156.
65. Margolese D., Melero J. A., Christiansen S. C., Chmelka B. F. and Stucky G. D., Direct syntheses of ordered SBA-15 mesoporous silica containing sulfonic acid groups, *Chem. Mater.* **12** (2000) p. 2448.
66. Inagaki S., Guan S., Ohsuna T. and Terasaki O. An ordered mesoporous organosilica hybrid material with a crystal-like wall structure, *Nature* **416** (2002) p. 304.
67. Yang Q., Kapoor M. P. and Inagaki S., Sulfuric acid-functionalized mesoporous benzene-silica with a molecular-scale periodicity in the walls, *J. Am. Chem. Soc.* **124** (2002) p. 9694.
68. Harmer M. A., Farneth W. E. and Sun Q. Tailored fiber cross sections, *Adv. Mater.* **10** (1998) p. 1255.
69. Mikhailenko S., Desplantier-Giscard D., Danumah C. and Kaliaguine S., Solid electrolyte properties of sulfonic acid functionalized mesostructured porous silica, *Micropor. Mesopor. Mater.* **52** (2002) p. 29.
70. Diaz I., Marquez-Alvarez C., Mohino F., Perez-Pariente J., and Sastre E., Combined alkyl and sulfonic acid functionalization of MCM-41-type silica: part 2. esterification of glycerol with fatty acids, *J. Catal.* **193** (2000) p. 295.
71. Diaz I., Marquez-Alvarez C., Mohino F., Perez-Pariente J., and Sastre E., Combined alkyl and sulfonic acid functionalization of MCM-41-type silica: part 1. synthesis and characterization, *J. Catal.* **193** (2000) p. 283.
72. Das D., Lee J.-F. and Cheng S., Sulfonic acid functionalized mesoporous MCM-41 silica as a convenient catalyst for bisphenol-a synthesis, *Chem. Commun.* **21** (2001) p. 2178.
73. Kloetstra K. R., van Bekkum H. and Jansen J. C., Mesoporous material containing framework tectosilicate by pore-wall recrystallization, *Chem. Commun.* **23** (1997) p. 2281.
74. Jacobs A., Derouane E. G. and Weitkamp J., Evidence for X-ray amorphous zeolites, *Chem. Commun.* (1981) p. 591.
75. Scholle K. F. M. G. J., Veeman W. S., Frenken P. and Velden G. P. M., Characterization of intermediate TPA-ZSM-5 type structure during crystallization, *Appl. Catal.* **17** (1985) p. 233.
76. Jansen J. C., van der Gaag F. J. and van Bekkum H., Identification of ZSM-type and other 5-ring containing zeolites by i. r. Spectroscopy, *Zeolites* **3** (1984) p. 369.
77. Mokaya R., Template-directed stepwise post-synthesis alumination of MCM-41 mesoporous silica, *Chem. Commun.* (2000) p. 1451.
78. Mokaya R., Ultrastable mesoporous aluminosilicates by grafting routes, *Angew. Chem. Int. Ed.* **38** (1999) p. 2930.

79. Mokaya R., Supercritical fluid-mediated alumination of mesoporous silica and its beneficial effect on hydrothermal stability, *J. Am. Chem. Soc.* **124** (2002) p. 10636.
80. Karlsson A., Stocker M. and Schmidt R., Composites of micro- and mesoporous materials: simultaneous syntheses of MFI/MCM-41 like phases by a mixed template approach, *Micropor. Mesopor. Mater.* **27** (1999) p. 181.
81. Karlsson A., Stocker M. and Schafer K., Composites of micro- and mesoporous materials of MFI/MCM-41 like phases, *Stud. Surf. Sci. Catal.* **129** (2000) p. 106.
82. Chen X., Huang L. and Li Q., Hydrothermal transformation and characterization of porous silica templated by surfactants, *J. Phys. Chem. B* **101** (1997) p. 8460.
83. Guo, W., Huang, L. and Li Q., A novel MCM-41-beta-zeolite composite molecular sieve with mesoporous and microporous structure, *J. Chem. Chin. Univ.* **20** (1999) p. 356.
84. Huang L., Guo W., Deng P., Xue Z. and Li Q., Investigation of synthesizing MCM-41/ZSM-5 composites, *J. Phys. Chem. B* **104** (2000) p. 2817.
85. On D. T. and Kaliaguine S., Ultrastable and highly acidic, zeolite-coated mesoporous aluminosilicates, *Angew. Chem. Int. Ed. Engl.* **41** (2002) p. 1036.
86. Liu Y., Zhang W. Z. and Pinnavaia T. J., Steam-stable aluminosilicate mesostructures assembled from zeolite type Y seeds, *J. Am. Chem. Soc.* **122** (2000) p. 8791.
87. Liu Y., Zhang W. Z., Pinnavaia T. J., Steam-stable MSU-S aluminosilicate mesostructures assembled from zeolite ZSM-5 and zeolite Beta seeds, *Angew. Chem. Int. Ed. Engl.* **40** (2001) p. 1255.
88. Liu Y. and Pinnavaia T. J., Assembly of hydrothermally stable aluminosilicate foams and large-pore hexagonal mesostructures from zeolite seeds under strongly acidic conditions, *Chem. Mater.* **14** (2002) p. 3.
89. Zhang Z., Han Y., Zhu L., Wang R., Yu Y., Qiu S., Zhao D. and Xiao F.-S., Strongly acidic and high-temperature hydrothermally stable mesoporous aluminosilicates with ordered hexagonal structure, *Angew. Chem. Int. Ed. Engl.* **40** (2001) p. 1258.
90. Zhang Z., Han Y., Xiao F.-S., Qiu S., Zhu L., Wang R., Zou B., Sun H., Zhang Z., Zhao D. and Yen W., Mesoporous aluminosilicates with ordered hexagonal structure, strong acidity, and extraordinary hydrothermal stability at high temperatures, *J. Am. Chem. Soc.* **123** (2001) p. 5014.
91. Han Y., Yu Y., Xiao F.-S., Liu X.-C., Han X.-W. and Bao X.-H., Stable tetrahedral aluminum sites in hexagonal mesoporous aluminosilicates, *Chinese J. Chem.* **20** (2002) p. 711.
92. Xiao F.-S., Han Y. and Qiu S., Acidity and hydrothermal stability of mesoporous materials, *Chemical J. Chinese Univ.* **23** (2002) p. 1847.
93. Xiao F.-S., et al., 13th IZC, Strong acidic and high temperature hydrothermally stable mesoporous aluminosilicates with well-ordered hexagonal structure, *Stud. Surf. Sci. Catal.* **135** (2001) p. 06-P-07.
94. Han Y., Xiao F.-S., Wu W., Sun Y., Meng X., Li D., Lin S., Deng, F. and Ai X., A novel method for incorporation of heteroatoms into the framework of ordered mesoporous silica materials synthesized in strong acidic media, *J. Phys. Chem. B* **105** (2001) p. 7963.
95. Han Y., Wu S., Sun Y., Li D., Xiao F.-S., Liu J. and Zhang X., Hydrothermally stable ordered hexagonal mesoporous aluminosilicates assembled from a triblock

- copolymer and preformed aluminosilicate precursors in strongly acidic media, *Chem. Mater.* **14** (2002) p. 1144.
96. Liu J., Zhang X., Han Y. and Xiao F.-S., Direct observation of nanorange ordered microporosity within mesoporous molecular sieves, *Chem. Mater.* **14** (2002) p. 2536.
97. Xiao F.-S., Han Y., Yu Y., Meng X., Yang M. and Wu S., Hydrothermally stable ordered mesoporous titanosilicates with highly active catalytic sites, *J. Am. Chem. Soc.* **124** (2002) p. 888.
98. Sun Y., Han Y., and Xiao F.-S., Novel stable mesoporous materials synthesized in strongly acidic media, unpublished results.
99. Xiao F.-S., 11th National Catalytic Meeting of China, Novel mesoporous materials assembled from preformed nanosized zeolite precursors, Plenary Lecture, Hangzhou, China, Nov. 14-18, 2002.
100. Watson J. N., Brown A. S., Iton L. E. and White J. W., Detection of TPA-silicalite precursors nucleated during the room temperature aging of a clear homogeneous synthesis solution, *J. Chem. Soc. Faraday Trans.* **94** (1998) p. 2181.
101. de Moor P. P. E. A., Beelen T. P. M., Komanschek B. U. and van Santen R. A., Nanometer scale precursors in the crystallization of Si-TPA-MFI, *Micropor. Mesopor. Mater.* **21** (1998) p. 263.
102. de Moor P. E. A., Beelen T. P. M. and van Santen R. A., In situ observation of nucleation and crystal growth in zeolite synthesis. a small-angle X-ray scattering investigation on Si-TPA-MFI, *J. Phys. Chem. B* **103** (1999) p. 1639.
103. Zhou Q., Pang W., Qiu S. and Jia M., Synthesis of Beta zeolite by structure-directing agent, *CN Patent*, ZL 93 1 17593.3, 1996.
104. Zhou Q., Li B., Qiu S. and Pang W., Synthesis of low Si Al beta-zeolite by using nucleation gel, *Chemical J. Chinese Univ.* **20** (1999) p. 693.
105. Yue Y., Cedeon A., Bonardet J.-L., Melosh N., D'Esinose J.-B. and Fraissard J., Electron induced modification of the surface electrochemical properties of diamond electrodes, *Chem. Commun.* **17** (1999) p. 1697.
106. Miyazawa K. and Inagaki S., Control of the microporosity within the pore walls of ordered mesoporous silica SBA-15, *Chem. Commun.* **21** (2000) p. 2121.
107. Li G., Kan Q.-B., Wu T.-H., Hou C.-M., Huang J.-H., Wu S.-J. and Li C., Synthesis and catalytic performances of mesoporous aluminosilicates of cubic and hexagonal structure with stronger acid sites, *Chem. J. Chinese Univ.* **23** (2002) p. 1171.
108. Shih P.-C., Lin H.-P. and Mou C.-Y., Ultrastable acidic mesoporous aluminosilicates with ordered cubic structure assembled from zeolite seeds, in Proceedings of 3rd International Symposium on Mesoporous Materials, Jeju, Korea, July 7-11, 2002.

MODIFIED MESOPOROUS MATERIALS AS ACID AND BASE CATALYSTS

DUNCAN J MACQUARRIE

*Centre for Clean Technology, University of York, Heslington, YORK, YO10 5DD,
England.
E-mail: djm13@york.ac.uk*

The development of modified mesoporous materials, mainly silicas, as acid and basic catalysts is reviewed. Over the last decade, great strides have been made in both the use of mesoporous acid and base catalysts, and also in the understanding of how to generate the most appropriate system for a given application. Excellent activity is seen in a wide range of reactions, and it is expected that the momentum driving the whole area of nanoscopic materials will continue to ensure a thriving future for these catalysts.

1 Introduction

The ability to fabricate nanostructured materials with high degrees of control over pore structure has developed extremely rapidly in the last decade. The inspiration of many groups worldwide was the ground-breaking work at Mobil [1] which led to the MCM-41 groups of materials, a series of highly regular pore size silicas and aluminosilicates. While others may lay claim to the first synthesis of such structures [2,3], it is the Mobil work which recognised the enormous potential of the materials, and gave the impetus for the huge number of structures which have been produced subsequently [4,5,6,7,8,9,10,11,12].

One of the major driving forces behind the development of mesoporous molecular sieves as catalysts is the necessity to develop better, cleaner manufacturing processes for the multitude of chemicals which are required for daily life. The substitution of e.g. AlCl_3 with a solid acid is one of many major challenges – for small molecules the zeolites have provided some answers, and many petrochemical transformations are carried out using these microporous reactors; for larger molecules pore sizes have to be increased in order to allow access to the pore system. (It should be recognised that some liquid phase reactions can be successfully carried out in zeolitic reactors

[13,14,15,16,17]). This became possible with the MCM-41 class of materials, and since then, enormous strides have been made in this area.

The ability to produce aluminosilicates with pore sizes in excess of 1nm led to initial thoughts that these materials were indeed larger pore analogues of zeolites in every sense, and that the levels of acidity would parallel those found in the zeolites themselves. Interestingly, that has not been the case and although the acidity of the Al-MCM-41 series has been increased by careful control over several key reaction parameters, it still falls short of many zeolites. The second major feature of zeolite activity, shape selectivity, has only been touched upon. A few examples exist where this has been observed, but in others the possibility of other explanations lies open.

This chapter will focus on the development and use of Micelle Templated Silicas (MTS) as acid and basic catalysts. These materials include the MCM-41 series of materials, but also include other mesoporous inorganic materials (and hybrid organic-inorganic analogues) which are finding use as novel catalysts for a range of applications.

2 Synthesis of materials

There exists a wide range of systems which can deliver MTS systems and non-silica analogues. These have been classified by Stucky et al. [18] depending on the nature of the inorganic species (I) and the template (S, N – where S refers to surfactant, and N to non-ionic surfactant) and the interaction between them (Figure 1).

Essentially, most of the possibilities have been successfully utilised in the production of stable materials with extensive porosity and high surface area. The major groups of materials relevant to catalysis have been the S^-I^+ group (the MCM series), the S^0I^0 group (usually utilising a neutral amine template; what was originally called HMS – Hexagonal Mesoporous Silica, but now referred to as MTS with a wormhole pore system), and the N^0I^0 (neutral block copolymer systems utilising poly(ethylene oxide) – block-poly(propylene oxide)-block polyethylene oxide or polyethylene oxide endcapped with e.g. a C_{12} chain – the so-called MSU-X series [19]). Many other variants have been explored, some of which are showing promise in various applications [20].

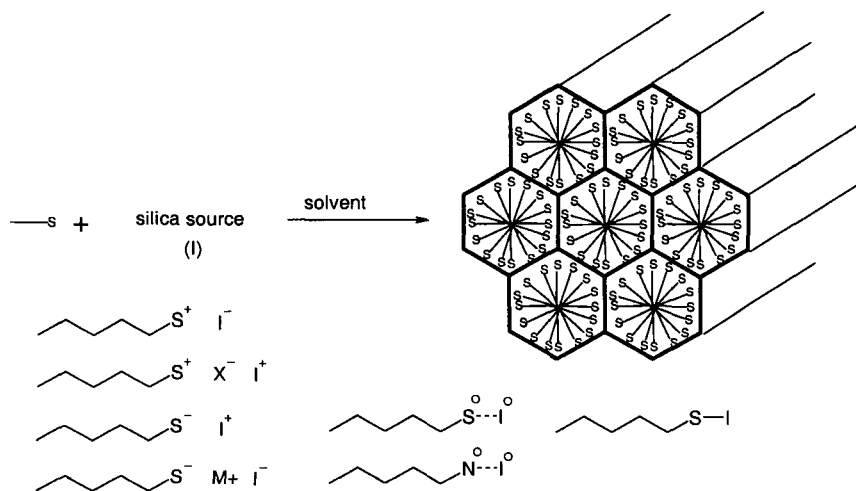


Figure 1. Schematic of the possible surfactant-template combinations. I represents the inorganic species, and can be positively or negatively charged or neutral; S represents the surfactant head group, and can likewise be positive or negative or neutral. Dotted lines represent H-bonding interactions, full lines are covalent bonds.

The majority of research has focussed on materials synthesised by the original MCM route, with appropriate attachment of catalytic groups either during or after synthesis. The other variant which has been followed most actively utilises the neutral amine templating route. This has the advantage of a very convenient synthesis and template recovery, as well as mild synthesis conditions, which allow the direct incorporation of organics, as an alternative to post-synthesis grafting [21]. This is also possible using the polyether route [22,23], but little catalytic work has been published on this route. The direct co-condensation route has been exploited as a method for the incorporation of functionality [24,25], although the acidity of the template extraction step imposes some limitations on its generality. Recent discoveries by Antochshuk and Jaroniec have subsequently allowed the mild removal of quaternary templates from either all-inorganic MCM's [26,27], Ce substituted MCM [28] or from organically modified systems[29] opening up a new range of catalytic materials. The general routes for catalyst preparation are summarised in Figure 2.

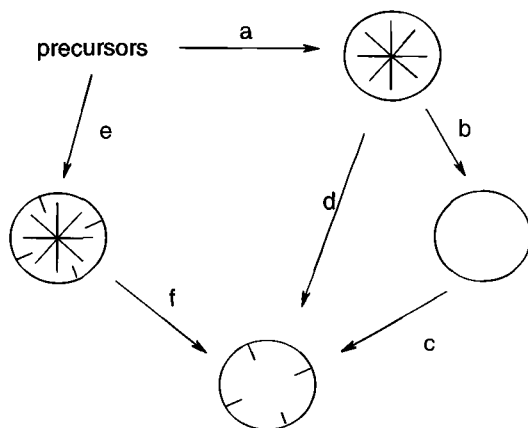


Figure 2. Routes for the preparation of catalysts based on templated synthesis of materials. a + b – templated synthesis of silica. c – grafting of functionality onto preformed silica; d – reactive extraction; e + f – templated synthesis of a functionalised silica. Step f may also include a reactive extraction to provide a more highly functional material, or a bifunctional system.

There has been little in the way of systematic study of the different routes to these catalysts in terms of their relative activities in a given reaction. This type of study will shed light on the often subtle differences in materials, some of which are being teased out by careful studies on the synthesis of the materials.

For example, Brunel has shown that grafting of organic groups, by the reaction of the calcined MTS with trialkoxysilanes in toluene, leads to selective attachment of the organics in patches on the surface of the material, rather than as an even coverage over the whole surface[30]. This corresponds to a selective reaction on the hydrophobic patches present on the surface, leading to a catalyst which is almost certainly different at this level to a material prepared by co-condensation route.

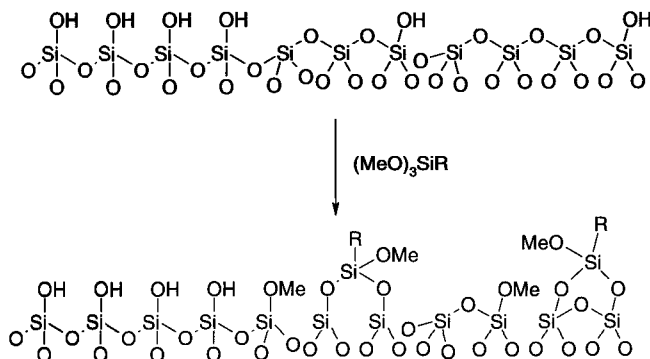


Figure 3. Non-uniform distribution of organic units on the surface of a grafted MTS material.

Stein has investigated the distribution of vinyl groups in both vinyl-grafted MCM-41 and the analogous material prepared by direct sol-gel synthesis [31]. He found that the majority of grafted vinyl groups were to be found at the edges of pores, and on the external surface, indicating that the diffusion of the functionality into the pores is slow relative to the rate of attachment to the surface. By contrast, the vinyl groups in the co-condensed material exist predominantly in the pores in a relatively uniform distribution.

Similarly, it has been shown that the template extraction stage of the direct co-condensation route can be critical for control over surface chemistry. It has been found that template extraction of silicas with dilute HCl leads to a material with no alkoxy groups on the surface of the material [32]. By contrast, extraction of template with alcohols leads to a substantial number of the surface silicon atoms to have alkoxy groups attached.[29] This study also indicated that the as-synthesised, template-containing material has no discernable quantity of alkoxy groups present. This indicates that the hydrolysis of the precursors is complete, and that all the alkoxy groups are attached during extraction. Extraction with acetone and acetic acid lead to materials without alkoxy groups. Reviews on the syntheses of these materials are given [4,5, 6,7,8,9,10,11].

3 Acid catalysts

The Al-MCM-41 materials initially prepared by Mobil have bulk compositions similar to those of the zeolites, that is a silica framework containing aluminium in tetrahedral environments. This led to the hope

that these materials would be equivalent in acidity to the zeolites, and would represent large pore strongly acidic catalysts. Early attempts in this area were disappointing, as the materials displayed acidity equivalent only to dilute mineral acids. One of the first examples of the acidity of these applications was from van Bekkum [33], who showed that the H^+ -Al-MCM-41 was capable of smoothly forming tetrahydropyranyl acetals from alcohols [33] and the acetalisation of aldehydes [34].

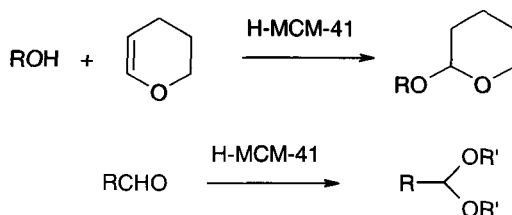


Figure 4. Reactions catalysed by original versions of H^+ -Al-MCM-41.

Such reactions are typically carried out with a trace of HCl in the alcohol being protected, indicating the relatively weak nature of the sites. However, progress has been made in the development of acidity in these materials, and it is now known that the acidity of these materials depends on a variety of factors, such as the source of Al used [35], the adjustment of pH during synthesis [36, 37], and the detailed nature of the template removal / calcination step [38]. Such details have led to variations in the acidity reported by different groups, but it seems that the Al-MCM-41s formed from these variations generally display acidity similar to the amorphous aluminosilicates. This is no doubt related to the amorphous nature of the walls, and the effect of developing analogous materials with (partly) crystalline walls remains to be seen. Some initial results in this area have been reported by several groups and it does seem that the incorporation of crystalline zones into the walls of the materials has a positive effect on the acidity of the materials. Further work is required to push this effect to its limit.

The use of seed particles has been shown to dramatically improve the stability of H^+ -exchanged Al-MCM-41. Pinnavaia et al. [39] have demonstrated that the formation of zeolite Y seeds directly before formation of Al-MCM-41 leads to a material with acidity comparable to the original material, but which retains both its structure and acidity after high temperature steam treatment, a necessary regeneration treatment for petrochemical cracking catalysts. An alternative preparative route which involves the grafting of Al_{13} polycations [40] had a similarly well-

defined diffraction pattern before steaming, but lost this during the steaming process. Cumene cracking activity was reduced only slightly with the seeded catalyst, but others investigated lost most of their activity upon steaming. The additional stability was attributed in part to the presence of seeded crystalline species in the walls of the material, but also partly to the presence of occluded carbon. The same workers have subsequently provided evidence of a more stable material, which has exceptional high temperature stability without occluded carbon, indicating that the stability resides in an intrinsically stable inorganic framework [41].

A slightly different approach was taken by Qiu, Xiao et al [42]. They used a mixed template system to prepare an ultrastable Al-MCM-41 system. One template (tetraethylammonium hydroxide) seems to form nanoclusters of a zeolite beta precursor, and the other, cetyltrimethyl ammonium bromide generates the MCM-41 structure from these nanoclusters. The resultant material is stable even after 2 hours in steam at 800°C, and has an acidity (as measured by ammonia desorption) considerably higher than a standard Al-MCM-41 of the same bulk composition, and similar to zeolite Beta. Pyridine titration results confirm a larger number of stronger Bronsted sites than for the standard preparation route. The new material dramatically outperforms the standard material in the alkylation of butane with butene.

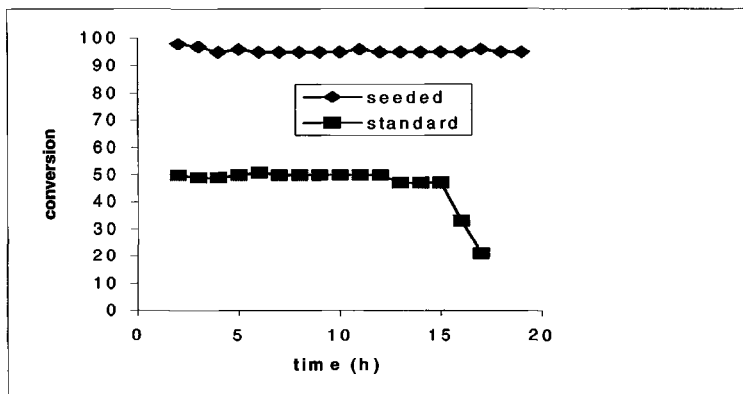


Figure 5. Comparison of standard and “beta-seeded” Al-MCM-41 catalysts in the alkylation of butane with butene.

It is clear that the acidity of the first examples of Al-MCM-41 is substantially lower than the maximum obtainable, and that hydrothermal stability as well as activity can be improved dramatically by correct organisation of the walls of the material. Thus, H^+ - Al-MCM-41 materials have been successfully applied to more challenging reaction types than the pyranlation of alcohols and important new applicational areas are now available for these materials, such as the cracking and treatment of heavy hydrocarbons too large to be processed using conventional catalysts.

The synthesis of jasminealdehyde is a subtle and elegant example of the use of a relatively mild acidic H-MCM-41. Jasminealdehyde is a perfumery intermediate which can be prepared by the condensation of heptanal with benzaldehyde. One of the major difficulties in such cross-couplings is the self condensation of the aliphatic aldehyde. In a clever twist to the direct route, Corma et al protected the aldehyde in situ as a dimethyl acetal [43].

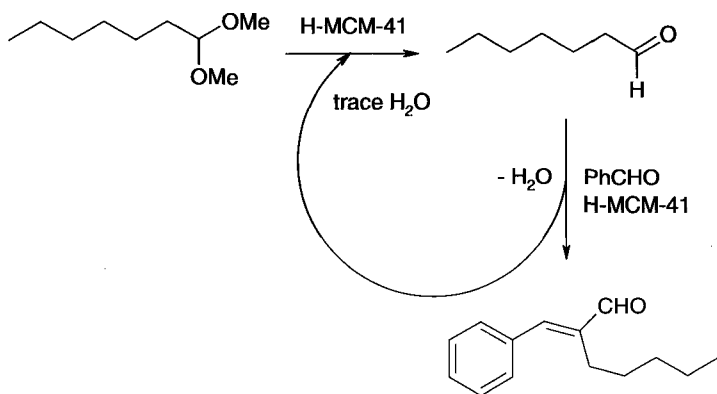


Figure 6. Synthesis of jasminaldehyde.

Traces of water in the system continually generated a small concentration of heptanal which then condensed selectively with the larger quantity of benzaldehyde. All the steps of the reaction, including the formation of the acetal, were catalysed by H^+ - Al-MCM-41. H-MCM-41 with a low Si: Al ratio of 16 were substantially better than those with higher ratios (50 or 83).

Alkylation and especially acylation of aromatics are two areas where progress in new catalytic systems is required. The alkylation of toluene

with ethene and propene has been described in a gas phase system at 180°C. The results obtained from both an activity study and spectroscopic probing indicate that the materials used were of an acidity higher than amorphous silica-aluminas, but lower than zeolite beta [44]. The levels of acidity found while being sufficient for alkylation, were incapable of promoting transalkylation under the conditions used. Benzene can also be alkylated by short chain alkenes [45,46].

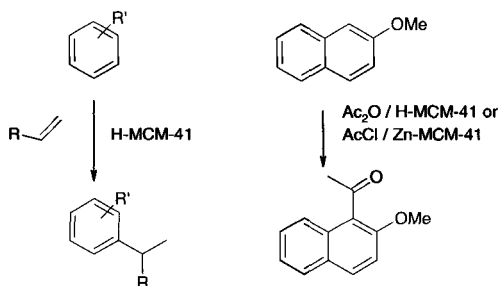


Figure 7. Friedel Crafts reactions catalysed by H^+ - Al-MCM-41.

Work is ongoing in these areas with H^+ - Al-MCM-41 systems; while results are interesting, more needs to be done before a really satisfactory catalytic system is found. 2-Methoxynaphthalene can be efficiently acetylated with acetic anhydride in the 1 position to give an intermediate in the synthesis of Naproxen [47]. A Zn exchanged MCM-41 was also found to be a reasonable catalyst for this reaction. Fries rearrangement has also been reported [48].

An alternative approach to increasing the acidity of MCM-41 type materials is the grafting of acidic centres onto the surface of the solid. A range of materials have been prepared, typically from the chemisorption of strong Lewis acids such as $AlCl_3$, as well as the physisorption of weaker Lewis acids such as $ZnCl_2$.

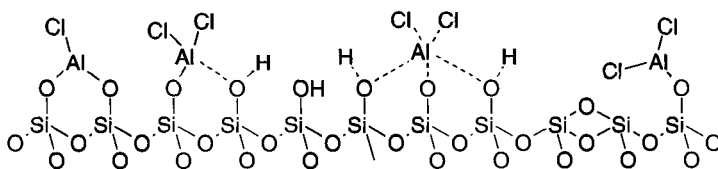


Figure 8. Surface structures postulated for MTS+ $AlCl_3$ based catalysts [49].

The attachment of aluminium chloride, one of the most powerful Lewis acids known, to the hydroxylic surface of silicas and related materials is a reaction which must be very closely controlled in order not to deactivate completely the resulting solid. The optimal attachment requires the formation of one Al-O-Si unit, providing the attached group with sufficient stability towards dissolution, without reducing acidity significantly. If this can be achieved, then the catalyst will have activity close to that of AlCl₃ itself. Over-vigorous attachment routes will cause the replacement of further Cl atoms, and lead to the formation of two or more Si-O-Al units, something which will drastically reduce the acid strength of the catalyst. Obviously, the sensitivity of the resultant material to basic contaminants such as water is relatively high, and this must be taken into account when the material is prepared. Nonetheless, it is possible to reproducibly prepare highly acidic materials using this route, and Clark et al have demonstrated their utility in typical AlCl₃-catalysed reactions such as Friedel-Crafts alkylation [50,51].

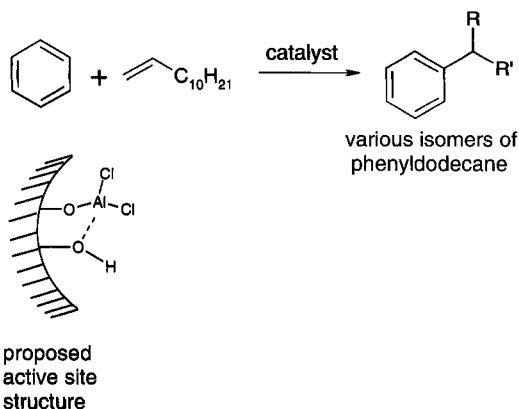


Figure 9. Alkylation of benzene with long chain alkenes using MTS-AlCl₂. Crosses – AlCl₂-HMS₂₄-Ph₃N ; triangles - AlCl₂-HMS₂₄-Ph₃N ; squares – AlCl₂-K10 ; diamonds AlCl₃.

This work related to the alkylation of benzene with long chain alkenes, leading to important precursors to the linear alkylbenzene sulfonate class of surfactants. Their work demonstrated that the activity of the materials was high, and that tuning the pore size to the length of the alkene could

bring about considerable improvements in the selectivity to mono-alkylation.

The suppression of the (relatively facile) double and polyalkylation which can plague Friedel-Crafts alkylation is an important advance and was explained as being due to shape selectivity. Certainly, diffusional effects would be expected to be important in these systems. The selectivity improvements noted as a function of chain length and pore size, and the variations in reaction rates are both consistent with shape selectivity. Interestingly, the importance of the external sites (i.e. out-of-pore) was shown by selective blocking of these sites. The method used was to poison the active sites with a large, bulky base. This was claimed to deactivate the external sites selectively, leading to an increase in shape selectivity. How selective this process is remains open to debate, but the improvement in selectivity obtained suggests that it does discriminate relatively effectively between in-pore and out-of-pore sites. The benefits of this increase of selectivity manifest themselves in the higher utilisation of the alkene, and in considerable reductions in the dilution of the alkene in benzene, the commonest method for suppressing dialkylation. Similar results were reported by Jaenicke's group,[52] with alkenes ranging from C_6 to C_{16} and pore sizes of 20 to 40Å. In similar studies [53] they showed that the $AlCl_3$ -O-Si based catalyst was capable of the benzylation of benzene, but little evidence of shape selectivity was seen. Other supported Lewis acids were investigated and the order of reactivity was found to be as follows: $AlCl_3 > ZnCl_2 \gg FeCl_3, NiCl_2, CuCl_2$. Similarly, 1,3-difluorobenzene can be readily propylated with 2-chloropropane with the Al-based catalyst under mild conditions, although alkylation with propene led to rapid deactivation [54].

Not surprisingly, no activity was found with isopropanol as reagent, presumably due to the conversion of Al-Cl bonds to Al-OH under the influence of water or isopropanol.

Interestingly, in a reaction system which produces water as a by-product, the ^{27}Al MAS-NMR spectrum indicated no change to the catalyst after reaction. It may be that the high temperature reduces the opportunity for the water to attack the catalytic centre, or that slight reductions in the catalytic activity brought about by the presence of water are insufficient to slow the reaction significantly at the high temperatures used here, whereas the much milder conditions used in the benzene propylation does discriminate between the two catalysts. The purely siliceous H-MCM-41 analogue showed modest activity.

One of the by-products in such reactions is the formation of small amounts of alkene oligomers. This activity has been exploited by Clark and co-workers for the polymerisation of 1,3-pentadiene [56,57]. They found that their results were consistent with the presence of both a Lewis-catalysed polymerisation and a Bronsted-catalysed route.

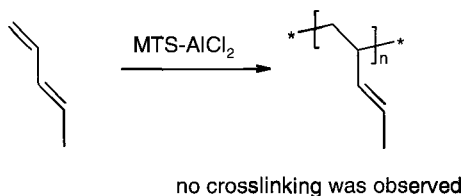


Figure 12. Polymerisation of 1,3-pentadiene with MTS- AlCl_3 .

The unmodified catalyst therefore gave a bimodal dispersion of molecular weight. Evidence was provided which suggests that the Bronsted site is a silanol proton polarised by interaction with an adjacent O-AlCl_3 unit. While HCl itself does not induce polymerisation, the addition of HCl to the catalyst produces an almost 3-fold increase in polymer yield. Addition of the bulky proton acceptor 2,6-di-*t*-Bu-4-Me pyridine effectively blocks the proton sites, which account for ca. 67% of the active sites of the catalyst. The blocked catalyst then produces a monodisperse polymer.

The polymer obtained from the mesoporous catalyst is free from the crosslinking of the polymer through pendant double bonds. With homogeneous aluminium chloride, this crosslinking is a serious problem, even at low conversions [58,59].

Using the related BF_3 -MTS catalyst [60] allows the efficient polymerisation of α -methylstyrene and indene [56]. α -Methylstyrene reacts very rapidly (reaction is complete within 10mins) and follows relatively straightforward kinetics ($E_A = 20\text{kJ mol}^{-1}$). Indene, on the

other hand, shows an induction period and, subsequently, a slow polymerisation with $E_A = 135\text{kJ mol}^{-1}$. Copolymerisation of the two monomers together at various ratios is always rapid, and gives copolymers in every case.

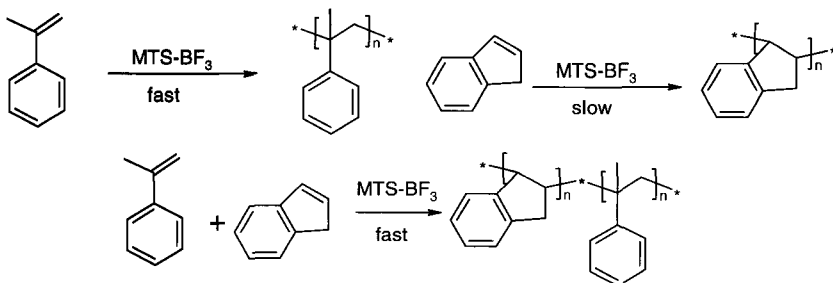


Figure 13. Polymerisation of alkenes with MTS- BF_3 .

A second class of polymerisation has been reported using mesoporous materials. This is the acid-catalysed ring opening polymerisation of lactones, and is efficiently catalysed by Al-MCM-41 materials [61]. This process, which yields polyesters, is an example of the so-called “immortal polymerisation” [62] in which very narrow molecular weight distributions can be attained, and the number of polymer chains formed exceeds greatly the number of initiator molecules.

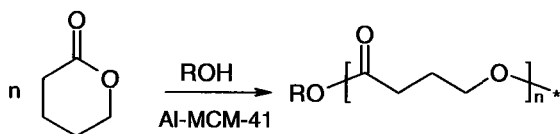


Figure 14. Ring-opening polymerisation of lactones using Al-MCM-41.

The latter phenomenon is achieved by the presence of e.g. an alcohol as an efficient, reusable chain transfer agent. In this case, the protonic sites of the MCM were able to activate the attack of butanol onto the lactone (valerolactone or caprolactone) to initiate the polymerisation,

giving butyl encapped polymers, with exceptionally well-controlled molecular weight distribution (P_D is typically ≤ 1.1). the number average molecular weight M_n is furthermore equal to the theoretical value expected for a completely uniform polymer. These effects ere assigned to the elimination of scrambling effects often seen with homogeneous initiators, but which are suppressed due to confinement of polymerisation to the interior of the catalyst. Similar results were also reported with MCM-41 and a titanium-containing MCM-41, with the latter giving a polymer containing some very high molecular weight material [63].

Cationic polymerisation of vinyl ethers and vinyl carbazoles has been effected by acidic MCM-41 and MCM-48 materials [64,65,66]. The common theme is the ability of the acidic centre in the materials to abstract chloride from either diarylmethyl chlorides or triarylmethyl chlorides, with the resulting cation initiating a cationic polymerisation.

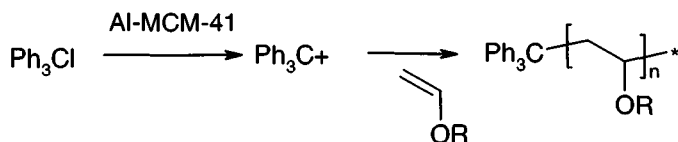


Figure 15. Polymerisation of vinyl ethers by generation of trityl cationic initiators.

An alternative source of active solid acids has been described by Hölderich and his group. They have developed a series of routes to supported imidazolium tetrachloroaluminates [67], (Figure 16) inspired by the use of tetrachloroaluminate ionic liquids as powerfully acidic reaction media [68,69,70].

A series of different preparative methods has been investigated, including incipient wetness (pore filling by a liquid, followed by removal of excess liquid). This resulted in the loss of integrity of the support, although methods involving the pre-supporting of AlCl_3 and subsequent addition of the imidazolium chloride, were developed to get round this problem [71,72]. However, it is reported that there is a strong interaction of the support silanols with the anion, which lowers its activity. Grafting of imidazolium chloride silanes is, however, straightforward, and subsequent reaction of these tethered salts with AlCl_3 leads to very acidic tetrachloroaluminates. Supporting the pre-formed tetrachloroaluminate itself is also possible. Sol-gel routes fail to

give high quality materials [72], something which is presumably due to the ionic nature of the silane[73].

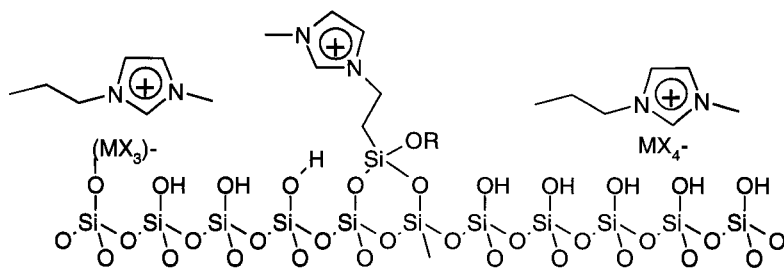


Figure 16. Routes to the preparation of immobilised imidazolium tetrachloroaluminates.

The supported catalysts have been evaluated in the acid catalysed reaction of alkenes with benzene [67]. Excellent activity was noted with MCM supported species, outperforming significantly the same species supported on amorphous silicas, and dramatically outstripping the unsupported salt, whose activity was considerably different. The grafted materials were by far the most active, with those simply adsorbed (and suffering from surface-anion interactions) and the direct sol-gel materials (which have poorly ordered structures) being less active. Extension to acylation reactions (using chloroferrates and chlorostannates instead of chloroaluminates) failed due to extensive leaching, thought to be of the product ketone – Lewis acid complex.

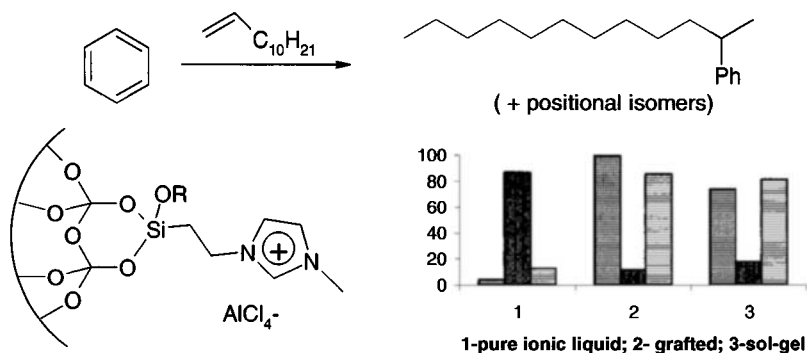


Figure 17. Comparative reactivity of different imidazolium tetrachloroaluminates in the alkylation of benzene. A – olefin conversion ; B – olefin isomers; C – selectivity to monoalkylated product.

Heteropolyacids (HPA) are polyanionic clusters, typically consisting of twelve MO_4 tetrahedra surrounding a central P or Si atom. This is known as the Keggin structure, and the most widely investigated HPAs are those where $\text{M} = \text{W}$ or Mo . This is partly due to the fact that the overall charge on the anion is 3- (P) or 4- (Si), leading to three or four charge-balancing protons, providing in turn a very high acidity, and to the interesting redox behaviour of the M centres, which imparts a bifunctionality on the systems, making them particularly interesting in a range of applications [74]. It is possible to support HPAs onto acidic or neutral supports such as silica and related materials, but adsorption onto basic surfaces such as MgO can lead to decomposition [75,76]. While low loadings of HPA can decompose on silica and on mesoporous silicas [77,78,79,80], higher loadings appear to be both stable and well-dispersed [81]. These materials have been examined in liquid-phase acid catalysed reactions. A shape selective alkylation of phenol was observed with a P-W HPA supported on MCM-41, where the activity was higher than sulfuric acid and also higher than bulk HPA, probably due to dispersion of the species in the pores of the mesoporous host [82]. The related Si-W-MCM-41 catalyst was active in the esterification of acetic acid with *n*-butanol [83]. These materials can also be used in butane isomerisation [84], where it is shown that MCMs are superior as supports to clays, and in the alkylation of isobutane with 2-butene[85]. Activity was improved by utilising larger pore MCM supports, as the deactivation method involved the deposition of carbonaceous deposits on the support.

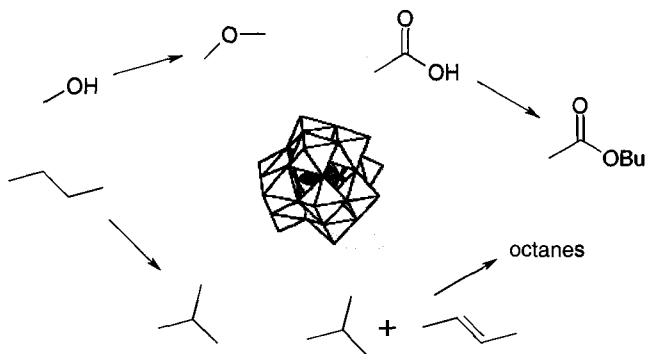


Figure 18. A general structure for HPA and their use in selected acid catalysed reactions.

The aromatisation of α -pinene to p-cymene has also been investigated using HPAs supported on a mesoporous silica [86]. This reaction appears to utilise both the acidic sites, in the catalyst for the initial ring-opening and the oxidative ability of the HPA to help the (relatively facile) aromatisation step.

One of the drawbacks of the HPA catalysts immobilised in mesoporous matrices is their ready loss into polar solutions. This leaching of the active site is a serious difficulty with those catalysts simply physisorbed to the inorganic support (despite the presence of a relatively strong interaction [74]). One method which has been used to alleviate this difficulty is the use of modified materials for the anchoring of the HPA. To this end, aminopropyl-containing MCM-41 has been used as a host matrix, and it was shown that the stability towards leaching was much improved during liquid phase oxidation of cyclohexane [87], where oxidation activity was not affected compared to unmodified MCM-41 support, and in the esterification of acetic acid with isoamyl alcohol, where no leaching was found, and where the activity was described as excellent [88]. Unfortunately, no data was presented on the relative activities of the amine supported HPA and the pure silica-supported material, so that it is difficult to ascertain the drop (if any) in activity caused by the attachment via an amine group.

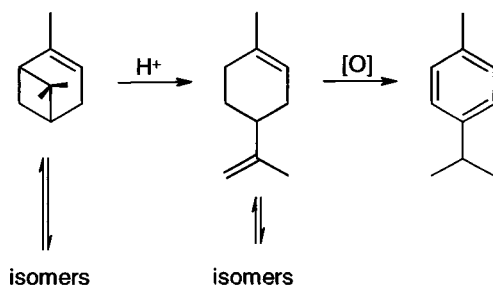


Figure 19. Aromatisation of α -pinene using HPA on mesoporous silica.

The formation of bisphenol A from phenol and acetone has also been investigated using leaching resistant HPA-MCM catalysts [89].

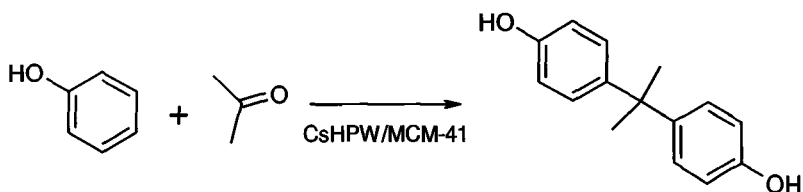


Figure 20. Catalysis of bisphenol A formation with insolubilised HPA materials.

These authors used the insolubility of the ammonium and cesium salts of the HPA to eliminate leaching in the reaction, and this was achieved successfully. The activity was reduced somewhat compared to the supported HPA itself, due to the less acidic nature of the system, but selectivity towards the desired *p,p* isomer was highest for the Cs sample.

Sulphonic acids are amongst the strongest Bronsted acids, and immobilisation of these functions has been achieved successfully via a two-step process. The first example of this was given by Van Rhijn et al [90,91]. The preparation consisted of a one pot co-condensation of 3-mercaptopropyltrimethoxysilane and TEOS [92,93]. After template extraction, the thiol groups were oxidised by hydrogen peroxide. Acidification / washing by aqueous sulfuric acid led to the final material. Other groups have prepared very similar materials based on the same synthetic principle, but with variations such as the removal of the acidification step [94] and the utilisation of nitric acid as oxidant [95]. Stucky et al. have also published a route whereby the as-synthesised material is oxidised at the same time as material synthesis to give the sulfonic acid directly [96].

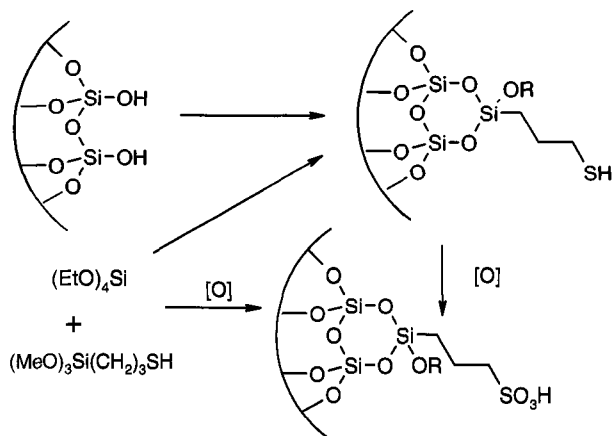


Figure 21. Different routes for the formation of supported sulfonic acids.

A considerable amount of effort has been put into the analysis of these materials. The incorporation of the thiol is straightforward, although most authors report that the product also contains disulfide, most probably formed due to oxidation prior to material formation. The mildly basic nature of the synthesis solution should favour thiol oxidation to disulfide [97], and the presence of significant amounts of this product even at low thiol loadings is consistent with a solution phase dimerisation, prior to solid formation. Additionally, ^{13}C NMR spectra seem to support this conclusion [90,98]. Interestingly, Wilson et al. have analysed the thiol material by Raman spectroscopy [94], which is uniquely able to see the disulfide directly via its Raman active vibration at $500\text{--}550\text{cm}^{-1}$. No evidence for disulfide could be found in their system. The similarity of their synthetic procedure to others in the literature casts into some doubt the presence of disulfide in these materials.

The subsequent oxidation step leads to a material with considerably fewer acidic sites than would be expected. Despite the complete disappearance of spectral features due to the thiol, there appears to be incomplete oxidation to the sulphonic acid. For example, the H^+/S ratio of a range of bifunctional sulfonic acids lie in the range $0.94 - 0.39$ [98]. Nitric acid oxidation appears to be less suitable for the oxidation than hydrogen peroxide, with a very low H^+/S ratio of 0.37 [95]. The one step materials synthesis and oxidation route of Stucky [96] gave H^+/S ratios of $0.66\text{--}0.82$, somewhat higher than the same authors obtained for synthesis of the thiol material and subsequent oxidation ($0.25\text{--}0.77$). Explanations

for these discrepancies may be due to accessibility of the acid sites during titration (access may be slow for such materials[99]), although all S(II) sites were accessed by the oxidant, and neither similar amine-containing materials nor high-loading nitriles, carboxylic acids or peracids suffer such problems, even at very high loadings[100,101]. While XPS analysis suggests that little or no S(II) species are present [94, 102], and the presence of partially oxidised species such as thiosulfonate cannot be excluded, it is not clear what the oxidised, non-acidic component is.

A related arene-sulfonic acid has been synthesised by Stucky et al [103]. This material, prepared by a route which does not involve the oxidation of thiols, gives a very powerfully acidic material with significant thermal stability. The ratio $H^+/S = 1$ in each case, and the acidity of the material (as measured by the triethylphosphine oxide ^{31}P NMR probe [104,105]) is higher than that of the alkylsulfonic acids, and of that of Al-MCM41. It approaches that of Amberlyst 15, a sulfonic acid ion-exchange resin. However, in water, sulfonic acid groups are lost, presumably as a consequence of the proto-desulfonylation reaction (a retro-Friedel-Crafts process) known to occur for arene sulfonic acids [106]. Hot toluene does not cause loss of sulfonic acid groups. Sastre et al have also published a route to arene sulfonic acids based on the sulfonylation of phenyl and methy/phenyl-derivatised mesoporous materials [107]. Sulfonylation led to the functionalisation of the rings, but appeared to remove some of the functional groups at the same time. These sulfonic acid catalysts have been evaluated in a range of Bronsted acid catalysed reactions, including esterification, Friedel-Crafts reactions, and Claisen-Schmidt reaction. Simple esterification reactions (1-butanol and acetic acid) have been used by Wilson et al [94] who have shown that conversions up to 85% can be achieved at high S loadings (7.02 - 11.62wt% S). For esterifications, conversion increased with S content, but initial rate of reaction remained relatively steady. By contrast, conversion in the Claisen-Schmidt reaction of benzaldehyde and acetophenone was independent of S loading except at the lower end, whereas initial rate increased approximately linearly with S content.

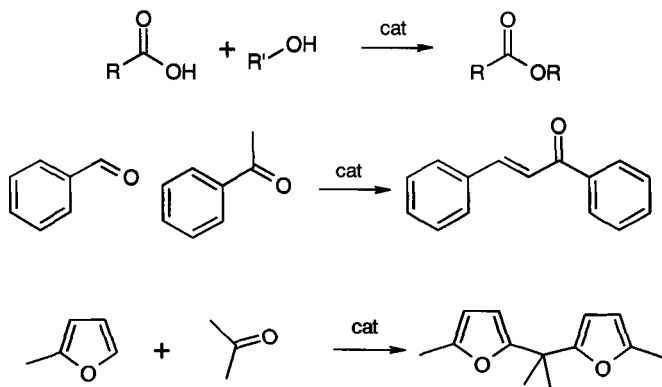


Figure 22. Reactions catalysed by supported sulfonic acids.

More complex esterification processes have been attempted, in particular the esterification of glycerol, which brings the challenge of selectivity. Bossaert et al. have studied the monoesterification of glycerol with lauric acid [91]. They found that the reaction proceeds well with the mesoporous sulfonic acids, much better than with USY zeolites, which, while giving excellent selectivity to the desired monoester, especially with shorter ($<C_{10}$) acids, are very slow due to pore size limitations [108,109,110,111].

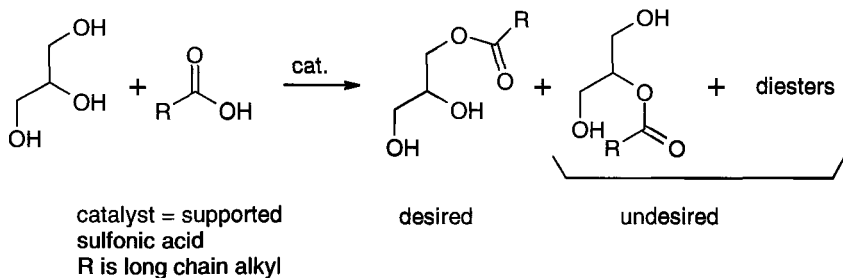


Figure 23. Monoesterification of glycerol using supported sulfonic acids.

The reaction profile is complicated by two factors, a non-catalysed background rate which is significant, and the immiscibility of the reaction partners, which leads to a relatively slow initial rate, followed by a burst of activity after sufficient product has been formed to emulsify the system. Selectivity in the best cases exceeds 50% and

yields of ca. 50% monoglyceride are obtained. Reuse gives identical results. There is evidence that access to the pore structure is limited, since more open pore structures give somewhat faster rates. Selectivity is higher with the mesoporous catalysts than with homogeneous, but the effect is not dramatic.

Pérez-Pariente et al. have shown that the activity of these materials can be improved by the incorporation of secondary organic groups such as Me [112]. A similar effect of methyl groups is seen in the arene sulfonic acids, with best selectivity being 74% at 50% conversion [107]. Friedel-Crafts activity has also been seen with the coupling of acetone with two molecules of 2-methylfuran to give the bis-furylpropane [90].

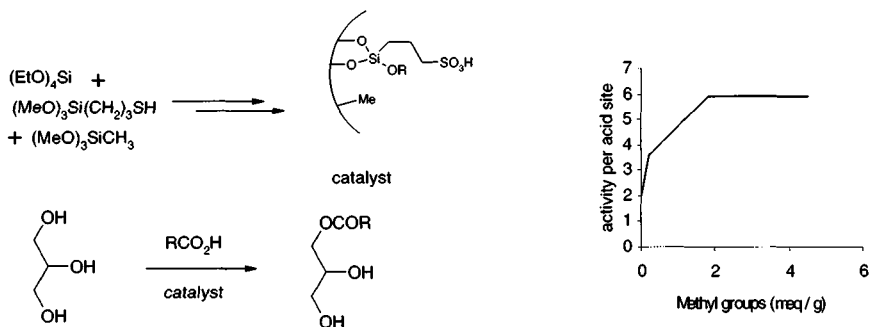


Figure 24. Effect of additional methyl groups on catalytic activity of supported sulfonic acids.

4 Base Catalysis

Base catalysis using mesoporous materials is also an active field of research. Over the last quarter century, much more effort has been placed on the development of solid acids than solid bases, presumably due to the impetus given to solid acids by the success of the zeolites in large scale petrochemical cracking. These solid acid have functioned as a cornerstone of the chemical industry for decades with enormous success, and it is not surprising that many attempts have been made to extend their influence to other reaction types. Solid bases on the other hand have little precedent on such a large scale. Nonetheless, the number of processes which could benefit from solid base catalysts, especially in the fine chemicals sector, makes this area well worth pursuing. Additionally, in an increasingly environmentally conscious industry,

many base-catalysed processes have the benefit of being inherently relatively clean, with a large number of important C-C bond forming reactions such as Knoevenagel and aldol condensations taking place with only the production of water as a co-product. Michael additions and e.g. the Baylis-Hillman reaction produce no co-products and are thus particularly attractive, given the often high functionality of the products. A range of mesoporous bases have been prepared and utilised in a series of these reaction types, and substantial progress has been made, both in terms of synthetic application and in the understanding of the details of the process and the requirements for an effective catalyst.

The basicity of as-synthesised Al-MCM-41 has been studied. This material, after calcination, has O^-Na^+ units on its surface and thus might be expected to be mildly basic. Indeed, this has been shown to be the case [113,114]. The Knoevenagel reaction is effectively catalysed by this material, with good conversions being achieved in reasonable timescales. The addition of Cs^+ ions or Cs_2O nanocrystals, led to materials with enhanced basicity, but with limited stability [114,115], the latter problem being overcome by the incorporation of Ln, leading to binary CsLn oxide species. These materials were shown to be effective in the Michael and aldol reactions, indicating their ability to activate molecules with pK_a 's of 13 and above.

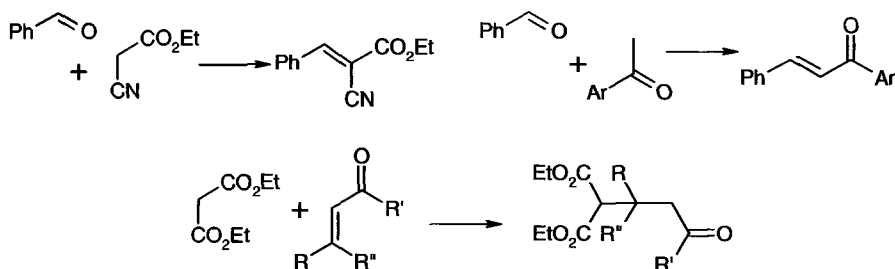


Figure 25. Reactions catalysed by Cs substituted MCM-41.

A wide range of materials has been prepared using amine substituted materials. The diversity of these materials comes about from the flexibility of using different synthetic protocols – grafting versus direct co-polymerisation of the amine-silane during material synthesis (along with different variations of this procedure) – the use of different

materials as inorganic hosts, and the variations possible on the amine itself (primary, secondary, tertiary, diamine etc).

The simplest systems were first published in 1995, when Brunel et al showed that MCMs could be functionalised by grafting of aminopropylsilanes onto the surface of the mesoporous host matrix [116,117,118]. The resultant materials were more active in the Knoevenagel reaction of benzaldehyde and ethyl cyanoacetate than the metal substituted systems discussed above, and their activity was proportional to loading of amine groups over a considerable range. It was further proposed (and subsequently confirmed) that the active site is actually the imine, formed extremely rapidly by the condensation of the amine and benzaldehyde. A second catalyst, prepared by the displacement of chloride from chloropropyl-MCM by piperidine, was found to be considerably less reactive, as might be expected if the imine were indeed the active site.

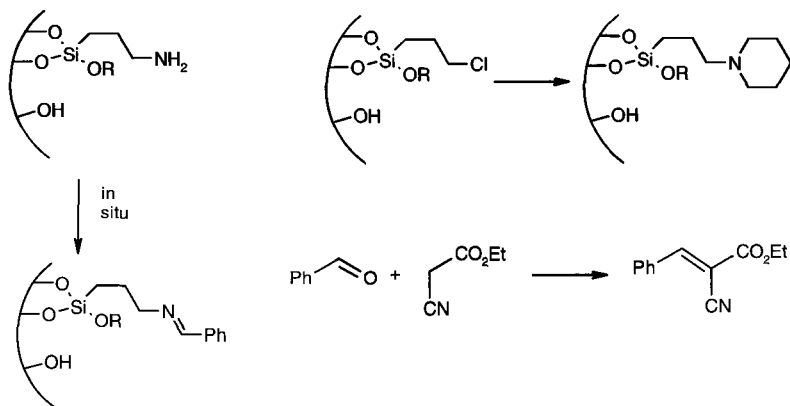


Figure 26. Base catalysis of the Knoevenagel reaction using amine grafted mesoporous silicas. The lower activity of the piperidine catalyst is presumed to be due to its inability to form an imine.

However, as discussed below, the nature of the amine can play a major role in the activity of these systems, and structure-activity relationships are often not simple. For example it is known that supported secondary amines, prepared by imine formation on aminopropyl-amorphous silica supports and subsequent reduction, display significantly different activities dependent on the nature of the alkyl group attached to the amine centre. The bulkier the group, the more active the catalyst, although the reason for this is not well understood, it

may relate to the degree of interaction of the amine centre with the silica surface.

The same aminopropyl group was also incorporated into a material made by the direct co-condensation route [21,119,120].

These materials are excellent catalysts of the Knoevenagel condensation of ketones with e.g. ethyl cyanoacetate, but surprisingly poor for the reactions involving aldehydes. This odd behaviour is not understood, but is partly due to the low nucleophilicity of the amine groups in these materials [121,122], which leads to an inability to form imines, the active groups in the grafted materials. Fortunately, this low nucleophilicity also has a positive effect: The poisoning of grafted amino groups in such systems is due to the formation of amide groups on the surface of the catalysts from a slow reaction of the amine with the ester of the cyanoacetate. This does not happen in the co-condensed materials, and thus catalyst lifetime is extended, typically by a factor of 4-5.

Loading studies on the latter catalysts have been more limited, although again there is an increase in activity with increased loading [120]. A further increase in both activity and lifetime was also observed by the incorporation of non-catalytically active phenyl groups into the catalyst by co-condensation of TEOS, aminopropyl trimethoxysilane and phenyl trimethoxysilane. This procedure leads to a material with smaller pores (2.0nm) than that without the phenyl silane (2.4nm) because of co-surfactancy effects, but nonetheless higher activity and lifetime.

A fuller comparative study of the relative behaviours of these two classes of aminopropyl materials would be fascinating, not least due to the potential for different distribution of sites in the two classes of compounds, and the different surface chemistries likely to exist in the two materials. For example, Brunel has shown that grafting on mesoporous silicas takes place predominantly on the hydrophobic patches of the surface, giving patches of relatively concentrated organic groups, surrounded by hydrophilic hydroxyl-rich areas [123]. While few distribution studies have been carried out on in-situ materials,[124] it is quite possible that this patch-like distribution may not be present, instead a more random distribution may pertain, surrounded by a hydroxyl / alkoxy-rich surface. Removal of template with alcohols has been shown to lead to significant loadings (1-3mmol/g) of alkoxy groups in a range of functional materials [29].

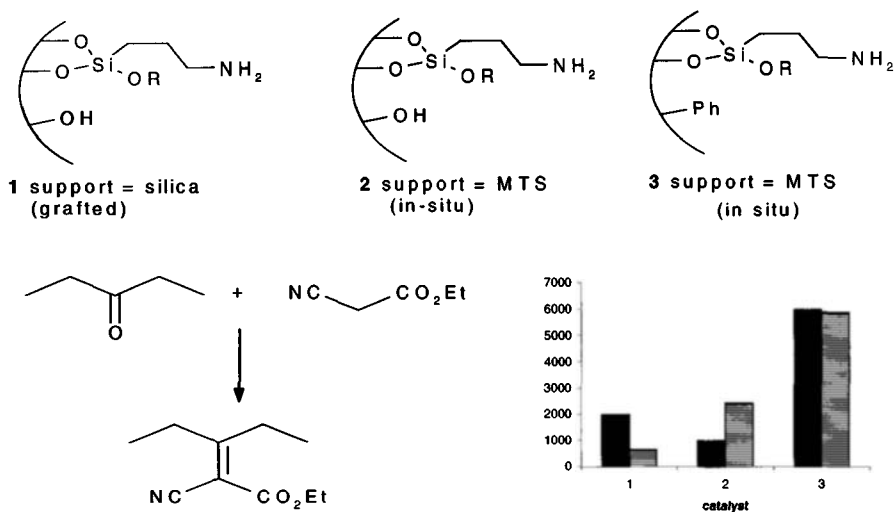


Figure 27. Comparative study on various aminopropyl-micelle templated silicas in the Knoevenagel reaction.

The closely related aminoethylaminopropyl-MTS has also been prepared and it appears to be more basic than the simple aminopropyl system [125]. For example, it is capable of catalysing the Knoevenagel reaction effectively (as expected), but also the aldol condensation of aldehydes with acetone, yielding mixtures of the aldol product and the dehydrated compound in varying proportions. The mild conditions (50°C , and a few hours reaction time) are impressive. The catalyst could be reused.

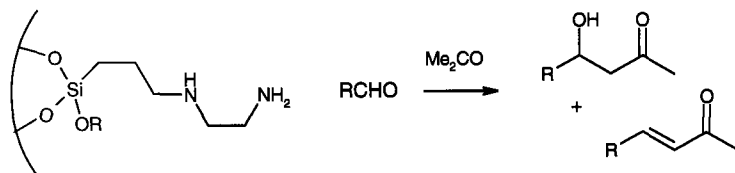


Figure 28. Aldol condensation catalysed by diamino-micelle templated silicas.

Secondary amines have been utilised in a novel direct synthesis of 5-ketoaldehydes [126]. They have shown that *N*-methyl aminopropyl-FSM-16[127] is an excellent catalyst for the direct Michael addition of aldehydes to vinyl ketones. (Figure 29) This reaction is usually carried out in indirect ways, usually involving protection / deprotection steps and, although a secondary amine route was recently published [128,129], it involves the use of large amounts of the amine catalyst. Yields are good, and reaction periods are moderate. Interestingly, the catalyst was extremely specific, with unsupported secondary amines showing very low activity, and other solid bases such as MgO and other inorganic oxides being inactive. These results are consistent with a nucleophilic role for the nitrogen, probably forming an iminium-type intermediate, possibly aided by surface interactions with silanols.

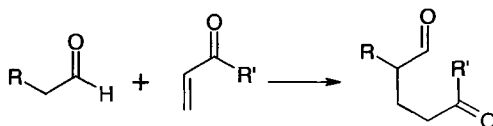


Figure 29. Direct Michael addition of aldehydes to enones catalysed by supported secondary amines.

Tertiary amines have also proved of great value in the Michael addition. *N,N*-dimethylaminopropyl-MTS was found to be an excellent catalyst for the Michael addition of nitroalkanes to enones [130]. Yields of a range of products were high, and it was shown that the intrinsic activity of sites within a co-condensed material was considerably higher than that achieved with a similar material prepared from grafted functions on an amorphous silica support.

A target reaction type which is currently of great interest involves the preparation of monoglycerides of fatty acids. These materials are biodegradable surfactants which are prepared from renewable resources, and thus are seen as attractive alternatives to many of the petrochemical-based surfactants currently in use [131,132]. Their synthesis may be approached with both acid and base catalysts, with each having strengths and weaknesses. The major advantage of the base-catalysed route is the reduced likelihood of formation of diesters from two fatty acids and one glycerol unit. This is because, unlike the acid catalysed esterifications [109,133], the base-catalysed route involves the ring opening of glycidol by basic activation of an acid. This means that the monoglyceride cannot undergo further condensation to give the diester. Enzymatic

routes are available, but they involve complex separations and conversion rates are often slow [134,135,136,137].

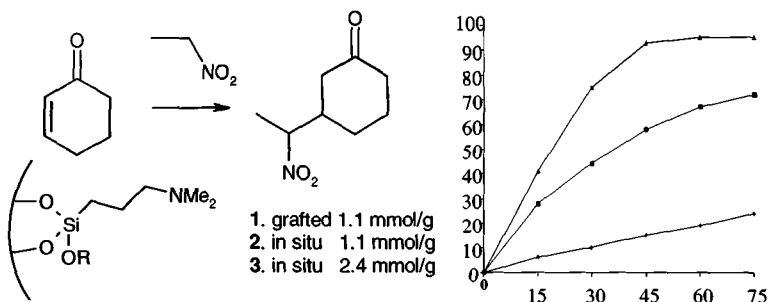


Figure 30. Michael additions catalysed by various supported tertiary amines.

Therefore, approaches to this involving mesoporous base catalysts have appeared. Aminopropyl and piperidine-based catalysts have been investigated [118,138]. These materials showed good reactivity in the initial run, and were, surprisingly, more active in the second and subsequent runs with recovered catalyst. The authors explained this phenomenon to a reaction between surface silanols and glycidol, leading to a more organophilic surface, probably encouraging ingress of reactants. Passivation of catalysts with trimethylsilyl groups gave greater improvements, and the best system (a trimethylsilylated piperidine catalyst) gave 90% yields, significantly higher than those obtained by acid catalysis.

Jaenicke has also investigated this reaction using a range of solid bases. His group looked at supported primary and tertiary amines, pyrimidines and a guanidine, from both the point of view of basicity and activity [139]. He demonstrated that the expected trend in base strength was apparent (i.e. pyrimidine < amine < guanidine), but that the differences were smaller than would be expected for the free, solution-phase species. This indicates that there is some “damping” of the basicity, presumably via H-bonding interactions with the relatively acidic surface, but not a complete neutralisation of the more basic sites. The most basic catalyst, based on the supported guanidine, was the most effective. Again, activity increased on reuse, with conversion changing from 84% to 95%.

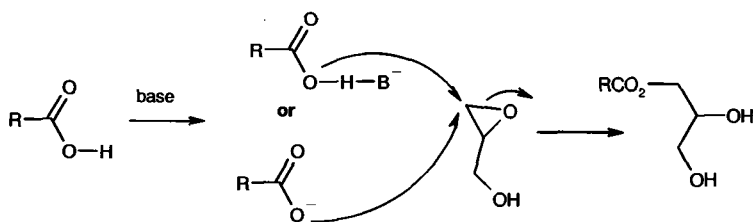


Figure 31. Base catalysed esterification of glycidol.

Guanidine catalysts have been the subject of a significant amount of effort in several reaction types. Not surprisingly, reactions such as the Knoevenagel work well with such catalysts, but there is no advantage over simple amine systems. Michael reactions Linstaad-Knoevenagel, epoxidations, and transesterifications do, however, benefit from the additional base strength. As mentioned above, there is a reduction in basic strength due to interaction with the support on simple guanidine-micelle templated silica systems, but no work has yet been done to quantify the changes in basicity which can be achieved by surface passivation. Indirectly, however, work has been done to look at the variations in activity of supported guanidines.

Transesterifications are an important group of reactions, which have substantial industrial significance. The formation of synthetic lubricants is a key area, and the product ester must be completely neutral to be of value in typical lubrication applications. Thus the use of homogeneous acid and base catalysts is difficult, due to the need for aqueous washing of the catalysts, since the catalyst is not only active in transesterifications, but also hydrolysis. Solid, filterable catalysts are thus of particular importance.

Brunel has demonstrated the efficiency of a triazabicyclodecene (TBD) supported on a micelle templated silica for the transesterification of ethyl propionate with short chain alcohols [140]. Transesterification of soybean oil with methanol, catalysed by guanidines supported on MCMs has also been carried out by Schuchardt [141]. This reaction allows the valorisation of this abundant renewable resource. As with Brunel's catalyst, conversions were good, but the rate of conversion was somewhat slower than other catalysts reported. It should be noted that transesterification reactions are equilibria, whose rate of progress is the sum of the forward and reverse reaction. Removal of the (preferably

more volatile) product alcohol can thus make a significant difference to the observed rate, and thus comparisons can be difficult.

A more challenging version of the Knoevenagel reaction is the Linstead variation, whereby malonic acid is condensed with an aldehyde.

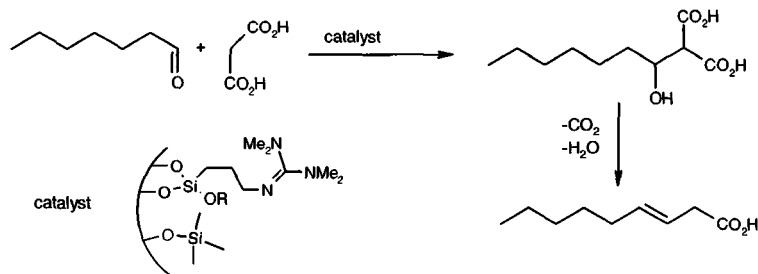


Figure 32. Linstead-Knoevenagel condensation.

The initial β-hydroxy diacid then undergoes decarboxylation and dehydration to generate the unexpected β,γ-unsaturated acid [142,143,144]. This can be carried out with bulk triethanolamine as solvent and catalyst, but this is unattractive, and we have shown that supported tetramethyl guanidine can be used in THF as solvent to carry out this reaction [145]. Conversions are good, but two problems exist. Firstly, there is a small amount of self-condensation of heptanal, but this is a minor problem. The more tricky problem is that the hydroxy-diacid forms readily, but does not decarboxylate and dehydrate at the temperatures possible in THF. This can be solved by carrying out the condensation and then changing solvent, but this is a cumbersome procedure, and requires the addition of a trace of homogeneous tetramethyl guanidine.

Jacobs and his co-workers have also studied supported guanidines. They used the related 1,5,7-triazabicyclo[4.4.0]dec-5-ene (TBD) system supported by ring opening of the supported glycidyl functionality by the guanidine to give the tethered basic catalyst.[146] This catalyst is an effective catalyst for the Knoevenagel, aldol and Michael reaction, with excellent yields and selectivities under mild conditions and short reaction times. The efficient addition of diethyl malonate to Michael acceptors indicates that the material is more basic than the majority of supported amines. They also found that cyclohexenone and similar unsaturated ketones could be epoxidised using their catalyst, at relatively low conversions.

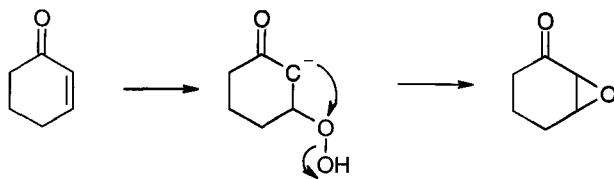


Figure 33. Epoxidation catalysed by supported guanidines.

The mechanism is effectively a Michael addition of the hydroperoxide anion followed by elimination of hydroxide. It was interesting to note that the selectivity towards hydrogen peroxide was relatively low (ca. 20%) indicating an inefficient use of the oxidant. Further work has subsequently been carried out by Brunel and Macquarrie, who have carried out a comparison of both grafted and co-condensed materials, using tetramethylguanidine as catalyst.[145] The most effective materials were found to be those formed by a stepwise attachment of tetramethyl guanidine to the surface, by attachment of chloropropyl groups, surface passivation and finally attachment of the guanidine unit. This work showed that the decomposition of hydrogen peroxide can be substantially reduced (from >90% to ca. 50%) by the passivation step, and that the selectivity towards both organics and hydrogen peroxide can be improved significantly.

Yields were also good. Thus, the passivation of the surface is again an important factor in the development of an active selective catalyst. The non-productive decomposition of hydrogen peroxide by the surface of mesoporous silicas and related materials has been noted before. In the case of Ti-substituted mesoporous silicas [147,148] the decomposition of hydrogen peroxide was more or less eliminated by surface passivation, when these materials were used as large-pore versions of the microporous TS-1 zeolite.

It is possible that the true active site in these catalysts (when used in water-containing systems) is the hydroxide anion. Free guanidines are capable of deprotonating water, and indeed a silyl-guanidine appeared to exist as a guanidinium hydroxide in aqueous ethanol. Similarly, the co-product of the epoxidation reaction is hydroxide, and thus this species should certainly be generated during the reaction.

Micelle templated silicas have been produced which have grafted quaternary ammonium chlorides attached. These can readily be exchanged for the hydroxide, and have been shown to be powerful base catalysts [149,150]. Their catalysts are active in the simple Knoevenagel reaction of benzaldehyde with ethyl cyanoacetate, and are also active in the Michael addition of ethyl cyanoacetate or ethyl 2-oxo-cyclopentane

carboxylate with methyl vinyl ketone or cycloalkenones. The ketoester reacted smoothly to give high yields and excellent selectivity towards the adduct, but the cyanoacetate reacted further to give the double Michael product resulting from a second addition of acceptor onto the first product.

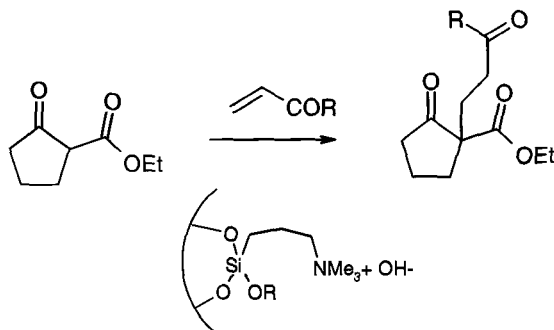


Figure 34. Michael reaction catalysed by a supported hydroxide.

This is a common problem which is difficult to solve for C-acids such as cyanoacetate, and, while it was possible to control the extent of the reaction by varying concentration and reaction conditions, it was not possible to suppress entirely. Diethyl malonate could also be reacted successfully. The aldol condensation of *o*-hydroxyacetophenones and benzaldehydes was also possible, leading to good yields of 2-hydroxychalcone and flavanone. A variation on this reaction type was studied, which combines both Knoevenagel and Michael reactions. This is the condensation of *o*-hydroxyphenols with, in this case, diethyl pentene dicarboxylate. The condensation-addition sequence can lead to either a chromene or a coumarin. The supported catalyst produced very different results to those obtained with a piperidine catalyst, where the major product was the coumarin. In this case, the supported hydroxide, the major product was the chromene. Two possible mechanisms can be put forward: the first involves a Knoevenagel condensation leading to a mixture of E and Z products, which then undergo either a Michael reaction to give the chromene, or a transesterification to yield the coumarin.

The product distribution would then be determined by the E/Z ratio of the Knoevenagel products (given that they cannot interconvert rapidly). This mechanism was favoured by the authors over the alternative, in which a Michael addition occurs first, leading to a symmetrical adduct,

which then can only give the chromene product. This was partly due to the fact that the expected aldehyde intermediate in the latter reaction could not be detected. Whether the anionic product of the Michael addition could trap the aldehyde product before being protonated is not clear. It would be expected that the intramolecular Knoevenagel reaction might be very rapid under the conditions used, and therefore the aldehyde intermediate may be consumed at the active site without being detected. Against this possibility is, however, the fact that high chromene yields can be obtained even in ethanol, which would facilitate extremely rapid proton transfer. Whatever the exact details of the mechanism, it is an interesting example of the ability of a supported catalyst to direct reactions in a selective manner, and one opposite to those found in homogeneous systems.

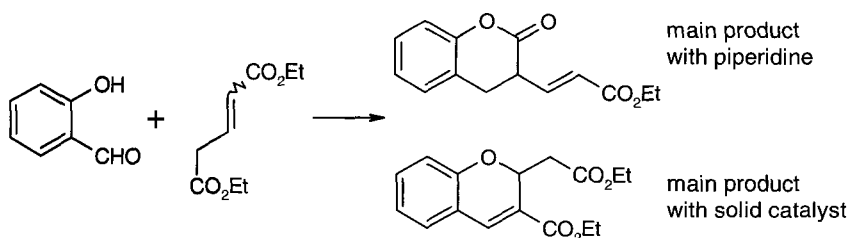


Figure 35. Variation in product distribution between homogeneous and heterogeneous base catalysis

5 Conclusions and perspectives for future directions

The first few years of accessible and highly controllable mesoporous silicas have led to the production of a wide range of catalytic species. We have already seen fundamental studies on material properties lead to a considerable increase in the acidity of Al-MCM systems, as well as many developments in the organically modified area. Increased control over surface functionality is leading to a better understanding of what is required and what is possible, and these advances are making rational design more attainable. The breadth of species supported and studied is still lower than that on amorphous materials, but this will change, and the improved control over surface and pore properties will eventually lead to considerably better materials and catalysts.

It is also clear that many newer materials (e.g. mesoporous aluminas, metal oxides and carbons) will begin to play a more active role in

catalysis – many are known, but their catalytic applications have not yet been exploited. These advances, as well as the ability to produce ever larger pore sizes, bimodal porosity, and fundamental studies on the processes occurring within pores, will mean that the future of these materials is very bright.

6 Acknowledgements

The author would like to thank the Royal Society for funding of a University Research Fellowship.

References

1. Kresge C.T., Leoniwicz M. E., Roth W. J., Vartuli J. C. and Beck J. S., Ordered Mesoporous Molecular sieves synthesised by a Liquid-Crystal Template Mechanism, *Nature* **359** (1992) pp. 710-712.
2. Yanigisawa T., Shimizu T., Kuroda K. and Kato C., Trimethylsilyl Derivatives of Alkyltrimethylammonium-Kanemite Complexes and their Conversion to Microporous Materials, *Bull. Chem. Soc. Japan*. **63** (1990) pp. 988-990.
3. Chiola V., Ritsko J. E. and Vanderpool C. D., US Patent 3556725, 1971.
4. Brinker C. J., Porous inorganic materials, *Curr. Opin. Solid State Mater. Sci.* **1** (1996) pp. 798-806.
5. Vartuli J. C., Kresge C. T., Roth W. J. and McCullen S. B. in *Advanced Catalysts and Nanostructured Materials*, ed. W R Moser, Academic Press, New York, (1996) pp. 1-19.
6. Stucky G. D., Huo Q., Firouzi A. and Chmelka B. F., Directed Synthesis of Organic/Inorganic Hybrid Structures, *Stud. Surf. Sci., Catal.* **105** (1997) pp. 3-28.
7. Raman N. K., Anderson M. T. and Brinker C. J., Template Based Approach to the Preparation of Amorphous, Nanoporous Silicas, *Chem. Mater.* **8** (1996) p. 1682.
8. Antonelli D. M. and Ying J. Y., Mesoporous Materials, *Curr. Opin. Coll. Interface. Sci.* **1** (1996) pp. 523-529.
9. Behrens P., *Angew. Chem. Int. Ed.* **108** (1996) pp. 515-523.
10. Zhao X. S., Lu G. Q. and Millar G. J., Advances in Mesoporous Molecular Sieve MCM-41, *Ind. Eng. Chem. Res.* **35** (1996) pp. 2075-2090.
11. Stein A., Melde B. J. and Schroden R. C., Hybrid inorganic organic mesoporous silicas. Nanoscopic reactors coming of age, *Adv. Mater.* **12** (2000) pp. 1403-1419.
12. Ying J. Y., Mehnert C. P. and Wong M. S., Synthesis and applications of supramolecular templated materials, *Angew. Chem. Int. Ed.* **38** (1999) pp. 56-77.
13. Hölderich W. F. and Heinz D., Research and development of zeolite catalysts in the 80s and 90s as well as forthcoming trends, *Res. Chem. Intermed.* **24** (1998) pp. 337-348.
14. Davis M. E., Zeolite based catalysts for chemicals synthesis, *Micropor. Mesopor. Mater.* **21** (1998) pp. 73-182.

15. Venuto P. B., Organic catalysis over zeolites. A perspective on reaction paths within micropores, *Microp. Mater.* **2** (1994) pp. 297-411.
16. Corma A. and Garcia H., Organic acids catalysed over solid acids, *Catal. Today* **38** (1997) pp. 257-308.
17. Harmer M. A., Industrial Processes using Solid Acid Catalysts, in *Handbook of Green Chemical Technology*, ed. J. H. Clark and D. J. Macquarrie, Blackwell Science (2002) pp. 86-119.
18. Huo Q., Margolese D. I., Ciesla U., Feng P., Gier T. E., Sieger P., Leon R., Petroff P. M., Schüth F. and Stucky G. D., Generalised Synthesis of Periodic Surfactant Inorganic composite Materials, *Nature* **368** (1994) pp. 317-321.
19. Tanev P. T. and Pinnavaia T. J., A neutral templating route to mesoporous molecular sieves, *Science* **267** (1995) pp. 865-867.
20. Ciesla U. and Schüth F., Ordered mesoporous materials, *Micropor. Mesopor. Mater.* **27** (1999) pp. 131-149.
21. Macquarrie D. J., Direct preparation of organically modified MCM-type materials. Preparation and characterisation of aminopropyl-MCM and 2-cyanoethyl-MCM, *Chem. Commun.* (1996) pp. 1961-1962.
22. Richer R. and Mercier L., Direct synthesis of functional mesoporous silica by neutral pH nonionic surfactant assembly: Factors affecting framework structure and composition, *Chem. Mater.* **13** (2001) pp. 2999-3008.
23. Richer R. and Mercier L., Direct synthesis of functionalised mesoporous silica by nonionic alkylpolyethyleneoxide surfactant assembly, *Chem. Commun.* (1998) pp. 1775-1776.
24. Sims S. D., Burkett S. L. and Mann S., Synthesis of hybrid inorganic-organic mesoporous silica by co-condensation of siloxane and organosiloxane precursors, *Chem. Commun.* (1996) pp. 1367-1368.
25. Lim M. H., Blanford C. F. and Stein A., Synthesis and characterisation of a reactive vinyl-functionalised MCM-41: Probing the internal pore structure by a bromination reaction, *J. Am. Chem. Soc.* **119** (1997) pp. 4090-4091.
26. Antochshuk V. and Jaroniec M., Functionalised mesoporous materials obtained via interfacial reactions in self-assembled silica-surfactant systems, *Chem. Mater.* **12** (2000) pp. 2496-2501.
27. Antochshuk V. and Jaroniec M., Simultaneous modification of mesopores and extraction of template molecules from MCM-41 with trialkylchlorosilanes, *Chem. Commun.* (1999) pp. 2373-2374.
28. Antochshuk V., Araujo A. S. and Jaroniec M., Functionalised MCM-41 and CeMCM-41 materials synthesised via interfacial reactions, *J. Phys. Chem. B* **104** (2000) pp. 9713-9719.
29. Macquarrie D. J., Jackson D. B., King B. L. and Watson A., Preparation of novel inorganic-organic hybrid micelle templated silicas. Comparison of different routes for materials preparation, *Stud. Surf. Sci., Catal.* **142** (2001) pp. 1125-1132.
30. Brunel D., Cauvel A., di Renzo F., Fajula F., Fubini B., Onida B. and Garrone E., Preferential grafting of alkoxysilane coupling agents on the hydrophobic portion of the surface of micelle templated silica, *New. J. Chem.* **24** (2000) pp. 807-813.
31. Lim M. H. and Stein A., Comparative studies of grafting and direct syntheses of inorganic-organic hybrid mesoporous materials, *Chem. Mater.* **11** (1999) pp. 3285-3295.

32. Cassiers K., Van Der Voort P. and Vansant E. F., Synthesis of stable and directly usable hexagonal mesoporous silica by efficient amine extraction with acidified water, *Chem. Commun.* (2000) pp. 2489-2490.
33. Kloetstra K. R. and van Bekkum H., Catalysis of the tetrahydropyranylation of alcohols and phenols by the H-MCM-41 mesoporous molecular sieve, *J. Chem. Res. (S)* (1995) pp. 26-27.
34. Climent M. J., Corma A., Iborra S., Navarro M. C. and Primo J., Use of mesoporous MCM-41 aluminosilicates as catalysts in the production of fine chemicals. Preparation of dimethyl acetals, *J. Catal.* **161** (1996) pp. 783-789.
35. Ocelli M. L., Biz S., Auroux A. and Ray G. J., Effects of the nature of the aluminium source on the acidic properties of some mesostructured materials, *Micropor. Mesopor. Mater.* **26** (1998) pp. 193-213.
36. Kim J. H., Tanabe M. and Niwa M., Characterisation and catalytic activity of the AlMCM-41 prepared by a method of gel equilibrium adjustment, *Microp. Mater.* **10** (1997) pp. 85-93.
37. Lindlar B., Kogelbauer A. and Prins R., Chemical structural and catalytic characteristics of Al-MCM-41 prepared by pH-controlled synthesis, *Micropor. Mesopor. Mater.* **38** (2000) pp. 167-176.
38. Hitz S. and Prins R., Influence of template extraction on structure, activity and stability of MCM-41 catalysts, *J. Catal.* **168** (1997) pp. 194-206.
39. Liu Y., Zhang W. and Pinnavaia T. J., Steam-stable aluminosilicate mesostructures assembled from zeolite Y seeds, *J. Am. Chem. Soc.* **122** (2000) pp. 8791-8792.
40. Mokaya R., Ultrastable mesoporous aluminosilicates by grafting routes, *Angew. Chem. Int. Ed.* **38** (1999) pp. 2930-2934.
41. Liu Y., Zhang W. and Pinnavaia T. J., Steam-stable MSU-S aluminosilicate mesostructures assembled from zeolite ZSM-5 and zeolite beta seeds, *Angew. Chem. Int. Ed.* **40** (2001) pp. 1255-1258.
42. Zhang Z., Han Y., Zhu L., Wanh R., Yu Y., Qiu S., Zhao D. and Xiao F-S., Strongly acidic and high temperature hydrothermally stable mesoporous aluminosilicates with ordered hexagonal structure, *Angew. Chem. Int. Ed. Int.* **40** (2001) pp. 1258-1262.
43. Climent M. J., Corma A., Guil-Lopez R., Iborra S. and Primo J., Use of mesoporous MCM-41 aluminosilicates as catalysts in the preparation of fine chemicals – A new route for the preparation of jasminaldehyde with high selectivity, *J. Catal.* **175** (1998) pp. 70-79.
44. Perego C., Amarilli S., Carati A., Flego C., Pazzuconi G., Rizzo C. and Bellussi G., Mesoporous silica-aluminas as catalysts for the alkylation of aromatic hydrocarbons with olefins, *Micropor. Mesopor. Mater.* **27** (1999) pp. 345-354.
45. Bellussi G., Perego C., Carati A., Peratello S., Previde Massara E. and Perego G., Amorphous mesoporous silica-alumina with controlled pore size as acid catalysts, *Stud. Surf. Sci. Catal.* **84** (1994) pp. 85-92.
46. Lee Q. N., Hill C. US Pat., 5 118 894, 1992.
47. Gunnewegh E. A., Gopie S. S. and van Bekkum H., MCM-41 type molecular sieves as catalysts for the Friedel Crafts acylation of 2-methoxynaphthalene, *J. Mol. Cat. A* **106** (1996) pp151-158.
48. van Bekkum H., Hoefnagel A. J., van Koten M. A., Gunnewegh E. A., Vogt A. H. G. and Kouwenhoven H. W., Zeolite catalysed aromatic acylation and related reactions, *Stud. Surf. Sci. Catal.* **83** (1994) pp. 379-390.
49. Shorrocks J K, D.Phil Thesis, University of York, 2000

50. Price P. M., Clark J. H., Martin K., Macquarrie D. J. and Bastock T. W., Enhanced selectivity in the preparation of linear alkylbenzenes using hexagonal mesoporous silica supported aluminium chloride, *Org. Proc. Res. Dev.* **2** (1998) pp. 221-225.
51. Clark J. H., Price P. M., Martin K., Macquarrie D. J. and Bastock T. W., Environmentally friendly catalysis using supported reagents. Enhanced selectivity without loss of activity in the alkylation of benzene using hexagonal mesoporous silica (HMS) supported aluminium chloride, *J. Chem. Res. (S)* (1997) pp. 430-431.
52. Hu X., Foo M. L., Chuah G. K. and Jaenicke S., Pore size engineering on MCM-41: Selectivity tuning of heterogenised AlCl_3 for the synthesis of linear alkylbenzenes, *J. Catal.* **195** (2000) pp. 412-415.
53. Hu X., Chuah G. K. and Jaenicke S., Room temperature synthesis of diphenylmethane over MCM-41 supported AlCl_3 and other Lewis acids, *App. Cat. A Gen.* **217** (2001) pp. 1-9.
54. Hu X., Chuah G. K. and Jaenicke S., Solid acid catalysts for the efficient synthesis of 2-(2,4-difluorophenyl) propane, *App. Cat. A Gen.* **209** (2001) pp. 117-123.
55. Zhao X. S., Lu G. Q. and Song C., Mesoporous silica-immobilised aluminium chloride as a new catalyst system for the isopropylation of naphthalene, *Chem. Commun.* (2001) pp. 2306-2307.
56. Clark J. H., Shorrock K., Budarin V. and Wilson K., Chemically modified mesoporous solids and their use in the polymerisation of hydrocarbon monomers, *J. Chem. Soc. Dalton Trans* (2002) pp. 423-427.
57. Shorrock J. K., Clark J. H., Wilson K. and Chisem J., Use of a supported aluminium chloride catalyst for the production of hydrocarbon resins, *Org. Proc. Res. Dev.* **5** (2001) pp. 249-253.
58. Santerella J. M., These de Doctorat, Institut Polytechnique de Grenoble, 1994.
59. Peng Y. X., Nguyen H. A., Macedo A. and Cheradame H., Electrophilic polymerisation of 1,3-pentadiene initiated by aluminium triflate, *Eur. Polym. J.* **340** (1994) pp. 69-77.
60. Wilson K. and Clark J. H., Synthesis of a novel supported BF_3 solid acid catalyst, *Chem. Commun.* (1998) pp. 2135-2136.
61. Kageyama K., Ogino S., Aida T. and Tatsumi T., Mesoporous zeolites as a new class of catalyst for the controlled polymerisation of lactones, *Macromolecules* **31** (1998) pp. 4069-4073.
62. Isoda M., Sugimoto H., Aida T. and Inoue S., Lewis-acid driven accelerated living polymerisation of lactones initiated with aluminium porphyrins. Chemoselective activation of ester groups by Lewis acid, *Macromolecules* **30** (1997) pp. 57-62.
63. Kageyama K., Tatsumi T. and Aida T., Mesoporous zeolite as new catalyst for polymerisation of lactones, *Polym. J.* **31** (1999) pp. 1005-1008.
64. Spange S., Graesser A., Rehak P., Jager C. and Schulz M., Cationic Polymerisation of cyclohexyl vinyl ether within MCM-41 channels, *Macromol. Rapid. Commun.* **21** (2000) pp. 146-150.
65. Spange S., Graesser A., Huwe A., Kremer F., Timtemann C. and Behrens P., Cationic Host-Guest Polymerisation of N-vinylcarbazole and Vinyl Ethers in MCM-41, MCM-48 and Nanoporous Glasses, *Chem. Eur. J.* **7** (2001) pp. 3722-3728.

66. Spange S., Graeser A., Muller H., Zimmerman Y., Rehak P., Jager C., Fuess H. and Baetz C., Synthesis of inorganic/organic host-guest hybrid materials by cationic vinyl polymerisation within Y zeolites and MCM-41, *Chem. Mater.* **13** (2001) pp. 3698-3708.
67. Valkenberg M. H., deCastro C., Hölderich W. F., Immobilisation of ionic liquids on solid supports, *Green Chem.* **4** (2002) pp. 88-93.
68. Boon J. A., Levisky J. A., Pflug J. L. and Wilkes J. S., Friedel Crafts reactions in ambient temperature molten salts, *J. Org. Chem.* **51** (1986) pp. 480-483.
69. Adams C. J., Earle M. J., Roberts G. and Seddon K. R., Friedel-Crafts reactions in room temperature ionic liquids, *Chem. Commun.* (1998) pp. 2097-2098.
70. Earle M. J., McCormac P. and Seddon K. R., Diels Alder reactions in ionic liquids: A safe recyclable alternative to lithium perchlorate-diethylether mixtures, *Green Chem.* **1** (1999) pp. 23-25.
71. Valkenberg M. H., deCastro C. and Hölderich W. F., Novel Lewis acid catalysts (NLACs): their properties, characterisation and use in catalysis, *Stud. Surf. Sci. Catal.* **135** (2001) pp. 179-185.
72. Valkenberg M. H., deCastro C. and Hölderich W. F., Novel Lewis acids by immobilisation of ionic liquids, in *Supported Catalysts and their Applications – Proceedings of the 4th International Symposium on Supported Reagents and Catalysts*, ed. D C Sherrington and A P Kybett, RSC, Cambridge, 2001, pp. 242-246.
73. Corriu R. J. P., Mehdi A. and Reyé C., Synthesis by neutral surfactant assembly of ordered mesoporous organic-inorganic hybrid materials incorporating phosphorus centres, *C R Acad. Sci. Paris*, t.2, Sé Ilc (1999) pp. 35-39.
74. Kozhevnikov I. V., Catalysis by heteropolyacids and multi component polyoxometalates in liquid phase reactions, *Chem. Rev.* **98** (1998) pp. 171-198.
75. Kozhevnikov I. V., Catalysis of organic reactions by heteropoly acids, *Russ. Chem. Rev.* **56** (1987) pp. 811-824.
76. Kozhevnikov I V, Heteropoly acids as catalysts for organic reactions *Stud. Surf. Sci. Catal.* **90** (1994) pp. 21-34.
77. Brückmann K., Che M., Haber J. and Tatibouet J. M., On the physicochemical and catalytic properties of $H_5PV_2Mo_{10}O_{40}$ supported on silica, *Catal. Lett.* **25** (1994) pp. 225-240.
78. Rocchiccioli-Deltcheff C., Amirouche M., Herve G., Fournier M., Che M. and Tatibouet J. M., Structure and catalytic properties of silica-supported polyoxomolybdates. 2. Thermal behaviour of unsupported and silica-supported 12-molybdosilicic acid from IR and catalytic activity studies, *J. Catal.* **126** (1990) pp. 591-599.
79. Tatibouet J. M., Che M., Amirouche M., Fournier M. and Rocchiccioli-Deltcheff C., Catalytic oxidation of methanol by 12-molybdosilicic acid supported on silica – dispersion effect, *J. Chem. Soc. Chem. Commun.* (1988) pp. 1260-1261.
80. Rocchiccioli-Deltcheff C., Aouissi A., Launey S. and Fournier M., Silica-supported 12-molybdosilicic acids catalysts. Influence of the thermal treatments and of the Mo contents on their behaviour, from IR, Raman, X-ray diffraction studies and catalytic reactivity in the methanol oxidation, *J. Mol. Cat. A* **114** (1996) pp. 331-342.
81. Kozhevnikov I. V., Kloetstra K. R., Sinnerna A., Zandbergen H. W. and van Bekkum H., Study of catalyst comprising heteropolyacid $H_3PW_{12}O_{40}$ supported on MCM-41 molecular sieve and amorphous silica, *J. Mol. Cat. A* **114** (1996) pp. 287-298.

82. Kozhevnikov I. V., Sinnerna A., Jansen R. J. J., Parnin K. and van Bekkum H., New acid catalyst comprising heteropolyacid on a mesoporous molecular sieve MCM-41, *Catal. Lett.* **30** (1995) pp. 241-252.
83. Chu W.L., Yang X.G., Shan Y.K., Ye X. and Wu Y., Immobilisation of the heteropolyacid (HPA) $\text{H}_3\text{SiW}_{12}\text{O}_{40}$ on mesoporous molecular sieves (HMS and MCM-41) and their catalytic behaviour, *Catal. Lett.* **42** (1996) pp. 201-208.
84. Marme F., Coudurier G. and Vedrine J. C., Acid type catalytic properties of heteropolyacid $\text{H}_3\text{PW}_{12}\text{O}_{40}$ supported on various porous silica-based materials, *Micropor. Mesopor. Mater.* **22** (1998) pp. 151-163.
85. Blasco T., Corma A., Martinez A. and Martinez-Escolano P., Supported heteropolyacid (HPA) catalysts for the continuous alkylation of isobutane with 2-butene: The benefit of using MCM-41 with larger pore diameters, *J. Catal.* **177** (1998) pp. 306-313.
86. Jaramillo H., Palacio L. A. and Sierra L., Characterisation of a heteropolyacid supported on mesoporous silica and its application in the aromatisation of alpha-pinene, *Stud. Surf. Sci. Catal.* **142** (2001) pp. 1291-1298.
87. Kaleta W. and Nowinska K., Immobilisation of heteropoly anions in Si-MCM-41 channels by means of chemical bonding to aminosilane groups, *Chem. Commun.* (2001) pp. 535-536.
88. Pizzio L., Vasquez P., Kikot A. and Basadella E., Amine functionalised SiMCM-41 as a carrier for heteropolyacid structures, *Stud. Surf. Sci. Catal.* **142** (2001) pp. 1411-1418.
89. Nowinska K. and Kaleta W., Synthesis of bisphenol A over heteropoly compounds encapsulated into mesoporous molecular sieves, *App. Cat. A* **203** (2000) pp. 91-100.
90. Van Rhijn W. M., De Vos D. E., Sels B. F., Bossaert W. D., Grobet P. J. and Jacobs P.A., Sulfonic acid functionalised ordered mesoporous materials as catalysts for condensation and esterification reactions, *Chem. Commun.* (1998) pp. 317-318.
91. Bossaert W. D., De Vos D. E., Van Rhijn W. M., Bullen J., Grobet P. J. and Jacobs P.A., Mesoporous sulfonic acids as selective heterogeneous catalysts for the synthesis of monoglycerides, *J. Catal.* **182** (1999) pp. 156-164.
92. Feng X., Fryxell, G. E., Wang L. Q., Kim A. Y., Liu J. and Kemner K. M., Functionalised monolayers on ordered mesoporous supports, *Science* **276** (1997) pp. 923-926.
93. Mercier L. and Pinnavaia T. J., Access in mesoporous materials: Advantages of a uniform pore structure in the design of a heavy metal adsorbent for environmental remediation, *Adv. Mater.* **9** (1997) pp. 500-503.
94. Wilson K., Lee A.F., Macquarrie D. J. and Clark J. H., Structure and activity of sol-gel sulphonic acid silicas, *App. Catal. A* **228** (2002) pp. 127-133.
95. Lim M.H., Blanford C. F. and Stein A., Synthesis of ordered microporous silicates with organosulfur surface groups and their applications as solid acid catalysts, *Chem. Mater.* **10** (1998) p. 467.
96. Margolese D., Melero J. A., Christiansen S. C., Chmelka B. F. and Stucky G. D., Direct Syntheses of ordered SBA-15 mesoporous silica containing sulfonic acid groups, *Chem. Mater.* **12** (2000) pp. 2448-2459.
97. *Advanced Organic Chemistry* 4th Ed., J March, J Wiley and Son, New York (1992), p. 1204-5.

98. Díaz I., Márquez-Alvarez. F.M., Pérez-Pariente J. and Sastre E., Combined alkyl and sulfonic acid functionalisation of MCM-41-type silica – Part 1. Synthesis and characterisation, *J. Catal.* **193** (2000) pp. 283-294.
99. Walcarius A., Etienne M. and Bessiere J., Rate of access to the binding sites in organically modified silicates. Amorphous silicas grafted by amine or thiol groups, *Chem. Mater.* **14** (2002) pp. 2757-2766.
100. Macquarrie D. J. and Rousseau H., High loading aminopropyl silicas as novel scavenger resins for high throughput synthesis, Synlett, in press
101. Elings J. A., Ait-Meddour R., Clark J. H. and Macquarrie D. J., Preparation of a silica supported peroxycarboxylic acid and its use in the epoxidation of alkenes, *Chem. Commun.* (1998) pp. 2707-2708.
102. Díaz I., Márquez-Alvarez. F.M., Pérez-Pariente J. and Sastre E., *J. Catal.* **193** (2000) pp. 283-294.
103. Melero J. A., Stucky G. D., van Grieken R. and Morales G., Direct Syntheses of ordered SBA-15 mesoporous silica containing arene sulfonic acid groups *J. Mater. Chem.* **12** (2002) pp. 1664-1670.
104. Osegovic J. P. and Drago R. S., A solid acidity scale based on the P-31 MAS-NMR shift of chemisorbed triethyl phosphine oxide, *J. Catal.* **182** (1999) pp. 1-4.
105. Osegovic J. P. and Drago R. S., Measurement of the global acidity of solid acids by P-31 MAS-NMR of chemisorbed triethylphosphine oxide, *J. Phys. Chem. B* **104** (2000) pp. 147-154.
106. *Advanced Organic Chemistry* 4th Ed., J March, J Wiley and Son, New York (1992) p. 566.
107. Mohino F., Diaz I., Perez-Pariente J. and Sastre E., Synthesis, characterisation and catalytic activity of SO₃H-phenyl-MCM-41 materials, *Stud. Surf. Sci. Catal.* **142** (2002) pp. 1275-1282.
108. Corma A., Garcia H., Iborra S. and Primo J., Modified Faujasite zeolites as catalysts in organic reactions – esterification of carboxylic acids in the presence of HY zeolites, *J. Catal.* **120** (1989) pp. 78-87.
109. Heykants E., Verrelst W. H., Parton R. F. and Jacobs P. A., *Stud. Surf. Sci. Catal.* **105** (1996) p. 1277.
110. Machado M. da S., Cardoso D., Sastre E. and Perez-Pariente J., Selective synthesis of glycerol monolaurate with zeolitic molecular sieves, *App. Catal. A General* **203** (2000) pp. 321-328.
111. Abro S., Pouilloy Y. and Barrault J., Selective synthesis of monoglycerides from glycerol and oleic acid in the presence of solid catalysts, *Stud. Surf. Sci. Catal.* **108** (1997) pp. 539-546.
112. Díaz I., Márquez-Alvarez. F.M., Pérez-Pariente J. and Sastre E., *J. Catal.* **193** (2000) pp. 283-294; Díaz I., Márquez-Alvarez F.M., Pérez-Pariente J. and Sastre E., Combined alkyl and sulfonic acid functionalisation of MCM-41-type silica – Part 2. Esterification of glycerol with fatty acids *J. Catal.* **193** (2000) pp. 295-302.
113. Kloetstra K. R. and van Bekkum H., Base and acid catalysis by the alkali-containing MCM-41 mesoporous molecular sieve, *Chem. Commun.* (1995) pp. 1005-6.
114. Kloetstra K. R., van Laren M. and van Bekkum H., Binary caesium-lanthanum oxide supported on MCM-41: A new stable heterogeneous basic catalyst, *J. Chem. Soc. Faraday Trans.* (1997) pp. 1211-1220.
115. Kloetstra K. R. and van Bekkum H., Solid mesoporous basic catalysts comprising of MCM-41 supported caesium oxide, *Stud. Surf. Sci. Catal.* **105** (1997) pp. 431-438.

116. Brunel D., Cauvel A., Fajula F. and DiRenzo F., MCM-41-type silicas as supports for immobilised catalysts, *Stud. Surf. Sci. Catal.* **97** (1995) pp. 173-180.
117. Laspéras M., Lloret T., Chaves L., Rodriguez I., Cauvel A. and Brunel D., Amine functions linked to MCM-41 silica as a new class of solid base catalysts for condensation reactions, *Stud. Surf. Sci. Catal.* **108** (1997) pp. 75-82.
118. Brunel D., Functionalised micelle templated silicas (MTS) and their use as catalysts for fine chemicals, *Micropor. Mesopor. Mater.* **27** (1999) pp. 329-344.
119. Macquarrie D. J. and Jackson D. B., Aminopropylated MCMs as base catalysts: a comparison with aminopropylated silica, *Chem. Commun.* (1997) pp. 1781-1782.
120. Macquarrie D. J., Organically modified hexagonal mesoporous silicas: clean synthesis of catalysts and the effect of high loading and non-catalytic second groups on the catalytic activity of amine-containing materials, *Green Chem.* **1** (1999) pp. 195-198.
121. Macquarrie D. J., Mdoe J. E. G., Jackson D. B. and Clark J. H., Organomodified Hexagonal Mesoporous silicates, *New. J. Chem.* **23** (1999) pp. 539-544.
122. Brunel D., Blanc A. C., Garrone E., Onida B., Rocchia, M., Nagy J. B. and Macquarrie D.J., Spectroscopic studies on aminopropyl-containing micelle templated silicas. Comparison of grafted and co-condensation routes, *Stud. Surf. Sci. Catal.* **142** (2002) pp. 1395-1402.
123. Brunel D., Cauvel A., di Renzo F., Fajula F., Fubini B., Onida B. and Garrone E., Preferential grafting of alkoxysilane coupling agents on the hydrophobic portion of the surface of micelle templated silica, *New. J. Chem.* **24** (2000) pp. 807-813.
124. Lim M. H., Blanford C. F. and Stein A., Synthesis and characterisation of a reactive vinyl-functionalised MCM-41: Probing the internal pore structure by a bromination reaction, *J. Am. Chem. Soc.* **119** (1997) pp. 4090-4091.
125. Choudary B. M., Lakshmi Kantam M., Sreekanth P., Bandopadhyay T., Figueras F. and Tuel A., Knoevenagel and aldol condensations catalysed by a new diamino-functionalised mesoporous material *J. Mol. Cat.* **142** (1999) pp. 361-365.
126. Shimizu K., Suzuki H., Hayashi E., Kodama T., Tsuchiya Y., Hagiwara H. and Kitayama Y., Catalytic direct 1,4-conjugate addition of aldehydes to vinyl ketones on secondary amines immobilised in FSM-16 silica, *Chem. Commun.* (2002) pp. 1068-1069.
127. Inagaki S., Fukushima Y. and Kuroda K., Synthesis of highly ordered mesoporous materials from a layered polysilicate, *J. Chem. Soc. Chem. Commun.* (1993) pp. 680-681.
128. Hagiwara H., Okabe T., Hakoda K., Hoshi T., Ono H., Kamat V. P., Suzuki T. and Ando M., Catalytic enamine reaction: an expedient 1,4-conjugate addition of naked aldehydes to vinylketones and its application to the synthesis of cyclohexenone from Stevia purpurea, *Tetrahedron Lett.* **42** (2001) pp. 2705-2707.
129. Hagiwara H., Komatsubara N., Ono H., Okabe T., Hoshi T., Suzuki T., Ando M. and Kato M., Diethylamino(trimethyl)silane mediated direct 1,4-addition of naked aldehydes to electron-deficient olefins, *J. Chem. Soc. Perkin Trans 1* (2001) pp. 316-322.
130. Mdoe J. E. G., Macquarrie D. J. and Clark J. H., Michael additions catalysed by N,N-dimethylaminopropyl-derivatised amorphous silica and hexagonal mesoporous silica, *Synlett* (1998) pp. 625-8.
131. Johansson I. and Svensson M., Surfactants based on fatty acids and other natural hydrophobes, *Current Opinion Colloids and Interface Sci.* **6** (2001) pp. 178-188.
132. Fiechter A., Biosurfactants: moving towards industrial applications, *Trends Biotechnol.* **10** (1992) pp. 208-217.

133. Mattson F. H. and Volpenhein R. A., Synthesis and properties of glycerides, *J. Lipid Res.* **3** (1962) pp. 281-296.
134. Yeh Y.C. and Gulari E., Enzymatic glyceride synthesis in a foam reactor, *J. Am. Oil Chem. Soc.* **75** (1998) pp. 643-650.
135. US Patent 5747305 (to US Dept, of Agriculture)
136. US Patent 5316927 (to Opta Food Ingredients)
137. Reetz M. T., Zonta A. and Simpelkamp J., Efficient heterogeneous biocatalysis by entrapment of lipases in hydrophobic sol-gel materials, *Angew. Chem. Int. Ed.* **34** (1995) pp. 301-303.
138. Cauvel A., Renard G. and Brunel D., Monoglyceride synthesis by heterogeneous catalysis using MCM-41 type silicas functionalised with amino groups, *J. Org. Chem.* **62** (1997) pp. 749-751.
139. Lin X., Chuah G. K. and Jaenicke S., Base functionalised MCM-41 as catalysts for the synthesis of monoglycerides, *J. Mol. Cat.* **150** (1999) pp. 287-294.
140. Derrien A., Renard G. and Brunel D., Guanidine linked to micelle templated mesoporous silicas as a base catalyst for transesterification, *Stud. Surf. Sci. Catal.* **117** (1998) pp. 445-452.
141. Sercheli R., Vargas R. M. and Schuchardt U., Alkylguanidine catalysed heterogeneous transesterification of soybean oil, *J. Am. Oil Chem. Soc.* **76** (1999) pp. 1207-1210.
142. Linstead R.P., Noble E.G. and Boorman E.J., Investigations of the olefinic acids, Part VII. The preparation of the Δ β -acids, *J. Chem. Soc.* (1933) pp. 557-561.
143. Corey E. J., The mechanism of the Decarboxylation of α,β - and β,γ -. *Am. Chem. Soc.* **74** (1952) pp. 5897-5905.
144. Ragoussis N., Modified Knoevenagel condensations – synthesis of (E)-3-alkenoic acids, *Tetrahedron Lett.* **28** (1987) pp. 93-96.
145. Macquarrie D. J., Blanc A., Brunel D., Renard G. and Quinn C. R., the preparation and use of novel immobilised guanidine catalysts in base-catalysed epoxidation and condensation reactions, *Green Chem.* **2** (2000) pp. 283-288.
146. Subba Rao Y. V., De Vos D. E. and Jacobs P. A., 1,5,7-triazabicyclo[4.4.0]dec-5-ene immobilised in MCM-41. A strongly basic porous catalyst, *Angew. Chem. Int. Ed. Engl.* **23** (1997) pp. 2661-2663.
147. Tatsumi T., Koyama K. A. and Igarishi N., Remarkable activity enhancement by trimethylsilylation in oxidation of alkenes and alkanes with H_2O_2 catalysed by titanium containing mesoporous molecular sieves, *Chem. Commun.* (1998) pp. 325-326.
148. D'Amore M. B. and Schwarz S., Trimethylsilylation of ordered and disordered titanosilicates: improvements in epoxidation with aqueous H_2O_2 from micro to mesopores and beyond, *Chem. Commun.* (1999) pp. 121-122.
149. Rodriguez I., Iborra S., Rey F. and Corma A., Heterogenised Bronsted base catalysts for fine chemicals production: grafted quaternary ammonium hydroxides as catalysts as catalysts for the production of chromenes and coumarins *App. Cat. A General* **194-5** (2000) pp. 241-252.
150. Rodriguez I., Iborra S., Corma A., Rey F. and Jordà J. L., MCM-41-quaternary organic tetraalkylammonium hydroxide composites as strong and stable Bronsted base catalysts, *Chem. Commun.* (1999) pp. 593-594.

LEWIS ACID/BASE CATALYSTS SUPPORTED ON NANOPOROUS SILICA AS ENVIRONMENTAL CATALYSTS

V.R. CHOUDHARY AND B.S. UPHADE

*Chemical Engineering Division, National Chemical Laboratory, Pune 411 008,
INDIA*

E-mail: vrc@ems.ncl.res.in

A number of Lewis acid/base catalysts can be supported on different types of mesoporous silicas. Unlike microporous zeolite-based catalysts, mesoporous silica-based catalysts have a high potential for their applications as catalysts in a number of organic syntheses involving Friedel-Crafts type reactions, oxidation, reduction and other Lewis acid/base catalyzed reactions, with no bar on the molecular size of reactants and/or products. The presence of surface silanol groups at high concentration in the channels of mesoporous silicas provides sites for chemical bonding or grafting of metal halides or oxides, thus producing novel mesoporous silica-based Lewis acid/base catalysts. Incorporation of heterometallic elements in the structure of mesoporous silicas also leads to Lewis acidic metal oxide finely dispersed throughout the mesoporous channels. This article covers and provides source of references for the various methods employed in the preparation of mesoporous silica supported Lewis acid/base catalysts and the applications of these versatile and environ-friendly (easily separable and reusable) catalysts for the synthesis of fine chemicals, involving both the small size and large size molecules.

1 Introduction

After the disclosure in 1992 by Mobil group of MCM-41 [1,2], containing hexagonal arrays of uniform mesoporous (1.5 to 10 nm) channels, and MCM-48 [3], having three dimensional interconnected mesoporous channels, further extensive research activities have been focused on the synthesis of other novel mesoporous materials, such as MSU [4], HMS [5], SBA-3 [6], SBA-15 [7], KSW-2 [8], CMK-1 [9]. Research on the modifications and applications of the mesoporous silicas increased dramatically in the recent years [10]. A number of reviews, covering the synthesis and characterization [11-19], modification [20-26] and catalytic applications [11-14, 17, 19, 20, 27-31] of mesoporous materials, particularly mesoporous silicas, appeared during the last six years.

Catalytically active sites, such as acidic and/or redox sites, for various reactions could be created in the channels of the mesoporous silicas during

their hydrothermal synthesis by incorporating heteroatoms or by their post-synthesis modification. Because of this and the larger pore size than that of the microporous zeolites, mesoporous silica based catalysts have provided very high promises and potential as substitutes for zeolites to carry out catalytic conversions involving large size reactant(s) and/or product molecules. One of the most important applications of these novel mesoporous solid catalysts is to replace environmentally hazardous, corrosive, difficult to separate and dispose-off homogeneous catalysts (viz. mineral and Lewis acids, organic and inorganic bases and toxic metallic compounds) employed in the liquid-phase synthesis of bulk and fine chemicals, and thereby bringing in practice a green chemistry [25].

One of the major tasks to practice green chemistry is to replace the currently used stoichiometric alkylations and oxidations for the production of fine chemicals by environmentally benign solid catalyzed reactions. Solid Lewis acids are expected to play a crucial role for accompanying this goal. Very recently, Corma and Garcia [32] has thoroughly reviewed Lewis acids as catalysts in the homogeneous and heterogeneous oxidation reactions, with a particular emphasis on the use of solid Lewis acids to promote catalytic oxidations.

In the last 3–4 years a large number of studies have been reported on the preparation and use of a number of novel mesoporous Lewis acid/base catalysts (viz. heteroatom substituted Lewis acid/base supported mesoporous silica) as environmentally benign catalysts useful for Friedel–Crafts type alkylation/acylation reactions, oxidation/epoxidation, hydrodesulfurization and other reactions. This article is focused on these recent studies, particularly on the preparation and characterization of Lewis acid/base supported on mesoporous silicas and their applications as environmentally benign catalysts. Our objective was not to cover all the literature but the important ones and we have tried our best to cover most of the important publications on this topic.

2 Synthesis of mesoporous silicas with or without heterometallic elements

Hydrothermal synthesis and characterization of mesoporous silicates, MCM-41 (hexagonal), MCM-48 (cubic) and other mesoporous silicas have been described in details in the reviews by Sayari [12], Biz and Occelli [15], Ciesla and Schüth [16] and Corma [19]. Recent developments in the synthesis and chemistry of periodic mesoporous organosilicas containing bridging organic groups integrated within a well-ordered

mesoporous silicas-based framework structure have been described by Tewodros et al. [33].

Recently, a number of studies have been reported on the synthesis of mesoporous silicas with or without containing heterometallic elements in their mesoporous framework.

Borade and Clearfield [34] reported the hydrothermal synthesis of MCM-41 with Si/Al ratio of ≥ 2.0 without observing the presence of octahedral Al in ^{27}Al MAS NMR. The MCM-41 material in the protonated form was found to contain both the Brönsted and Lewis acid sites. The extent of Al incorporation in the framework of MCM-41 was influenced by the source of aluminium used [35].

As compared to MCM-41, only a few studies have been reported on MCM-48, mostly because of the difficulty of the synthesis and controlling the pore size of MCM-48. Recently, Corma et al. [36,37] and Koyano and Tatsumi [38-40] have reported the hydrothermal synthesis and characterization of mesoporous Si-MCM-41 [37,38], Si-MCM-48 [37,39,40], Ti-Si-MCM-41 [36,38] and Ti-Si-MCM-48 [37,39,40]. Si and Ti-Si-MCM-41 with controlled pore sizes can be obtained without using polar organic additives and alkali metal anions [36,37].

Klinowski and coworkers have reported the hydrothermal synthesis and characterization of gallosilicate [41] and galloaluminosilicate [42] mesoporous MCM-41. The unit cell parameter of Ga-Si-MCM-41 is found to be much smaller than that of Si-MCM-41 [41].

A few studies have also been reported on the room temperature synthesis of Si-MCM-41 [43,44], Al-Si-MCM-41 [45], Ga-Si-MCM-41 [46], V-Si-MCM-41 [47], Fe-Si-MCM-41 [48] and heterometallic element (viz. Al, Ga, Fe, B, Ti, Zr and V) incorporated HMS [49].

3 Preparation and characterization of Lewis acid/base containing mesoporous silica catalysts

Lewis acids (viz. transition and Gr. IIIA metal oxides and halides) and bases (basic metal oxides) held on the surface of mesoporous silica by physisorption, chemical bonding or by both. Mesoporous silica-supported Lewis acid/base catalysts are prepared by post-synthesis modification of mesoporous silica, with or without containing heterometallic elements, by demetallation of heterometal from heterometallic element containing mesoporous material, by impregnating metal halides or oxides on mesoporous silica or by chemically grafting the catalytically active species (viz. metal oxide or halide) on the surface of mesoporous silica.

3.1 Demetallation of heterometal containing mesoporous silica

During the calcination, Brönsted acid sites are converted into Lewis acid sites and/or a part of the heterometal (viz. Al, Ga, Fe and other transition elements) present in the framework of mesoporous silica is expelled in a form of finely dispersed metal oxide in the channels of the mesoporous material, producing strong Lewis acid sites. Thus thermal and/or hydrothermal treatment under controlled condition provides a method for creating strong Lewis acid sites in mesoporous material.

Kossilick et al. [50] investigated acidity and active sites of Al-Si-MCM-41 and observed the formation of strong Lewis acid sites at the expense of Brönsted acid sites due to the calcination of Al-Si-MCM-41. ^{27}Al MAS NMR of the calcined samples of Al-Si-MCM-41 [34,35,50,51] showed the presence of octahedral alumina. Both Brönsted and Lewis acid sites of different strengths were observed in the Al-, Ga-, and Fe-substituted MCM-41 [52]; the calcination of Al-Si-MCM-41 caused the formation of octahedrally coordinated Al at the expense of framework Al [52]. Landmesser et al. [53] have also observed the formation of Lewis acid sites at the expense of tetrahedrally coordinated heterometal after the calcination of Al-, Ga-, and Fe-substituted MCM-48. Two types of Lewis acid sites, one absorbing at 1610 cm^{-1} (L1) and second absorbing at 1300 cm^{-1} (L2) were observed for Al-Si-MCM-48 and Ga-Si-MCM-48. However, only one type of Lewis acidity (L1) was observed for Fe-Si-MCM-48. Lewis acidity was found to decrease in the order $\text{Ga} \approx \text{Al} \gg \text{Fe}$. From their comprehensive characterization, Yuan et al. [54] suggested the presence of small nanocrystals of iron oxide linked with silica wall through oxygen in Fe-Si-MCM-41.

From the structural characterization techniques Gao et al. [55] also demonstrated similar surface niobium oxide species (isolated NbO_4 unit) are present in Nb-Si-MCM-41 and $\text{Nb}_2\text{O}_5/\text{SiO}_2$ catalysts.

3.2 Metal oxides/halides impregnated on mesoporous silica

Incipient wetness impregnation is a commonly practiced technique for the preparation of supported catalysts. This technique has also been extensively used for the preparation of mesoporous silica supported metal oxides or halides.

3.2.1 Mesoporous silica supported metal oxides

Metal oxides can simply be supported on mesoporous silica by the incipient wetness impregnation of a water-soluble precursor metal compound (e.g. nitrate, acetate, citrate, oxalate, etc., which on calcinations/thermal decomposition is converted into metal oxide) from its aqueous solution, followed by filtration, washing, drying and calcination.

Abe et al. [56] reported the preparation by the incipient wetness method and characterization of Fe_2O_3 nanoparticles in Si-MCM-41; nanoparticles of Fe_2O_3 are encapsulated into the uniform pores of the MCM-41. Huang et al (57) have carried out in-situ study of MCM-41 supported iron oxide catalyst by XANES and EXAFS under different catalyst pretreatment conditions and observed the formation of different iron oxide species in the different pretreatments. Köhn et al [58] synthesized ternary Co(II) iron(III) oxide nano-particles within mesoporous Si-MCM-48. Their XRD and EXAFS studies revealed the existence of the nanoparticles without the destruction of the MCM-48 host structure. Lensveld et al. [59] have shown that incipient wetness impregnation with a nickel citrate precursor is an excellent method to prepare Si-MCM-41 supported nickel catalyst combining both a high metal loading and a high dispersion of the active phase. Cheng et al. [60] reported the preparation by incipient wetness impregnation of an aqueous solution of ammonium heptamolybdate on a series of Al-Si-MCM-41/ $\gamma\text{-Al}_2\text{O}_3$ extrudate supports and characterization of molybdena catalyst, having high thiophene conversion activity.

Recently, Choudhary et al. [61-65] have reported Si-MCM-41 supported Ga_2O_3 and In_2O_3 (which is basic in nature), prepared by incipient wetness impregnation technique, as reusable and highly active/selective catalyst for Friedel-Crafts benzylation and acylation reactions. Unlike other Lewis acid catalysts, these catalysts do not demand stringent moisture-free conditions for their use in the Friedel-Crafts reactions.

3.2.2 Mesoporous Silica supported metal halides

Metal halide Lewis acid catalysts can be supported on mesoporous silica by incipient wetness impregnation on pre-dried mesoporous silica of anhydrous metal halides from their moisture-free non-aqueous solution, followed by removing the solvent by evaporation.

Recently, Choudhary et al. [65-72] have reported highly active, reusable and less moisture sensitive Si-MCM-41 supported ZnCl_2 [65-68], FeCl_3 [65,66,68,69], GaCl_3 [65-68,70] and InCl_3 [65-68,70-72] catalysts,

useful for the Friedel-Crafts benzylation and acylation reactions. These catalysts were prepared by incipient wetness impregnation of the respective anhydrous metal chloride from its acetonitrile solution; the solvent was removed by evaporation under vacuum (at 80 °C).

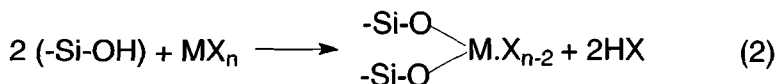
In the preparation of a mesoporous silica supported metal oxide catalysts, the mesoporous silica is subjected to a low pH (generally the aqueous solution of metal nitrates has very low pH) and hydrothermal treatment during drying and calcination, which may affect the structure of the mesoporous silica. Choudhary and Sansare [73] have studied in detail the effects of calcination temperature, in hydrothermal treatment (at different steam concentrations and temperatures) and treatment at high pH (8.5-13.5) and low pH (0.5-2.2) on the stability of Si-MCM-41.

3.3 Chemically bonded/grafted metal halides/oxides on mesoporous silica

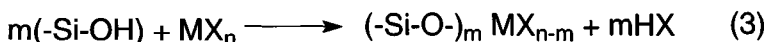
Metal halides and oxides can be immobilized by chemically grafting them on the surface of mesoporous silica. Their grafting can be accomplished by reacting anhydrous metal halides or alkoxides with the surface hydroxyl groups of mesoporous silica by gas-solid, liquid-solid or solid-solid reaction. Mesoporous Si-MCM-41 has a highly defective structure with different types of terminal silanol (Si-OH) groups [74,75]. Terminal Si-OH groups are also expected to be present in the other mesoporous silicas.

3.3.1 Grafting by Liquid-Solid Reaction

Grafting of Metal Halides: Metal halide can be heterogenized by grafting it on the surface of inorganic solids by reacting anhydrous metal halide from its non-aqueous solution with the surface hydroxyl groups, leading to the formation of hydrogen halide, as follows:



Or



The halogenated metal species are grafted on the solid surface through $(\text{-O-Si-})_m$ chemical bond(s). Such chemically bonded Lewis acid species are, however, expected to be different from the corresponding chemically non-bonded or free metal halide.

A few studies have been reported on the preparation and characterization of AlCl_3 (an important Lewis acid catalyst) grafted on KIT-1 (a mesoporous aluminosilicate molecular sieve with a disordered three-dimensional channel network) [76] and Si-MCM-41 [77-81]. The grafting of AlCl_3 according to the above reactions has been confirmed by measuring quantitatively the amount of HCl evolved as function of time (Fig. 1) in the reaction of anhydrous AlCl_3 dissolved in dry CCl_4 with Si-MCM-41 at 80 °C [78,79]. Similarly, GaCl_3 -grafted or Ga-incorporated MCM-41 can also be prepared by the above grafting method [82].

SnCl_2 [81], FeCl_2 [83], FeCl_3 [83], ZnCl_2 [84] and TiCl_4 [85] grafted Si-MCM-41 have also been prepared and characterized for their surface and catalytic properties.

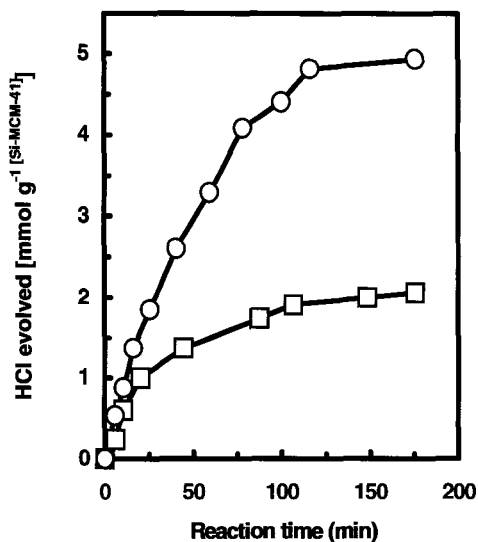


Figure 1. HCl evolved in the grafting of AlCl_3 on Si-MCM-41 at two different concentrations of AlCl_3 in the reaction mixture [O: $3.45 \text{ mmol g}^{-1} (\text{Si-MCM-41})$, \square : $1.0 \text{ mmol g}^{-1} (\text{Si-MCM-41})$]

Grafting of metal oxides: Metal oxide can also be immobilized by grafting it on the surface of mesoporous silica by reacting generally a metal alkoxide dissolved in non-aqueous solvent with the surface hydroxyl group.

Preparation and characterization of Al-grafted Si-MCM-41 by the reaction with Si-MCM-41 of Al-isopropoxide or Al-chlorohydrate from n-hexane solution [86] and Al-alkoxide from non-aqueous media [87] have been reported by Mokaya [86,87] and Mokaya and Jones [88]. Al-grafted MCM-41 has also been prepared by reacting Si-MCM-41 with aqueous solution containing Al-polycondensations at 80 °C and even at room temperature [89].

Kim et al. [90] reported post-synthesis incorporation of Ga into Si-MCM-41 by reacting repeatedly gallium nitrate from its ethanol solution with Si-MCM-41.

A few studies have also been reported on the preparation and characterization of transition metal oxide grafted Si-MCM-41. Titania-grafted mesoporous silica catalysts have been prepared by reacting Ti-butoxide from its ethanol solution with Si-MCM-41 [91,92], Si-MCM-48 [91] and KIT-1 [91] and also by reacting Ti-isopropoxide from its isopropyl alcohol solution with Si-MCM-41, Si-MCM-48, HMS, KIT-1 and SBA-1 [93]. Post-synthesis modification of mesoporous silicas by grafting Ti on Si-MCM-41 [94], Co on Si-MCM-41 or Si-MCM-48 [95], and Mn-oxo species on MCM-41 [96] has also been reported.

3.3.2 Grafting by gas-solid reaction

Metal halide grafted mesoporous silica catalysts can also be prepared by reacting vapors of volatile metal chloride (e.g. BF_3 , SiCl_4 , TiCl_4 , AlCl_3 , etc.) or complex with the surface hydroxyl groups under moisture-free conditions, leading to the formation of hydrogen halide with or without structural metal halide.

VO_x species were grafted on Si-MCM-48 [97] by anchoring vanadyl–acetylacetonate from gas phase on the surface of mesoporous silica by the reaction with surface silanol groups, followed by the thermolysis of the anchored complex at higher temperature (500 °C) in air.

Yang et al. [98] prepared titania-silica catalysts by chemical grafting involving a reaction of TiCl_4 vapors with surface hydroxyl groups of silica. Hagen et al. [94] also employed chemical vapor deposition method for the grafting of Ti on MCM-41 using different Ti-alkoxides as Ti precursors.

3.3.3 Grafting by Solid-Solid Reaction

Metal halide or oxide grafted mesoporous silica catalysts can also be prepared reacting the physically deposited (impregnated) or the chemically

grafted metal halide with surface hydroxyl groups of the mesoporous silica or with water vapors.

Titania-grafted silica catalyst, developed by Shell [99,100], was prepared by impregnating TiCl_4 or organic titanium containing compounds, followed by calcination at high temperatures. Ti/SiO_2 with isolated titanium ions was prepared by reacting TiCl_4 vapors with silica and then treating the TiCl_4 grafted silica with water vapors [98]. Choudhary et al. [101] prepared a number of highly active metal chloride (e.g. FeCl_3 , GaCl_3 , InCl_3 , etc.) grafted Si-MCM-41 catalysts, useful for the Friedel-Crafts reactions, by first impregnating the metal chloride from its acetonitrile or chlorohydrocarbon solution on Si-MCM-41 and then calcining the dried impregnated catalyst mass at higher temperatures under inert or oxidizing atmosphere.

Apart from the metal chlorides and oxides grafted mesoporous silicas, organometallic complex (metallocene complex viz. titanocene dichloride) grafted mesoporous Si-MCM-41 catalyst, which is a shape selective catalyst with a large concentration of accessible, well spaced and structurally well defined active sites, has also been reported [102].

3.4 Other Lewis acid containing MCM-41 catalysts

Bourlinos et al. [103] have prepared and characterized Fe-containing Si-MCM-41 using the exchange method of the template with $\text{FeCl}_3 \cdot 6\text{H}_2\text{O}$ and $(\text{Fe}_3\text{Ac}_6\text{O} \cdot 0.3\text{H}_2\text{O})\text{NO}_3$. Their IR, EPR and Mössbauer studies indicated that Fe is integrated into the mesoporous silica network after the calcinations. Yiu and Brown [104] compared the H^+ , Fe^{3+} , and Al^{3+} -exchanged Al-Si-MCM-41 and Al-mesoporous molecular sieves and observed that Fe^{3+} -exchanged forms exhibit the higher Lewis acid catalytic activities.

4 Application of Lewis acid catalysts supported on mesoporous silica

4.1 Mesoporous silica supported Group-III A acidic metal oxides/chlorides

These catalysts have been mainly used for the Friedel-Crafts type reactions and other acid catalyzed reactions, as follows.

Corma and coworkers [105] found that mesoporous Al-Si-MCM-41 is a convenient acid catalyst for Friedel-Crafts alkylation of a bulky compound, such as 2,4-di-tert-butylphenol with cinnamyl alcohol.

Recently, Choudhary et al. [61,62,64] reported that $\text{Ga}_2\text{O}_3/\text{Si-MCM-41}$ shows high activity for the benzylation by benzyl chloride and acylation by benzoyl chloride of benzene and other aromatic compounds. This catalyst is reusable and shows high activity even in the presence of moisture; the moisture has a beneficial effect, particularly for the acylation reactions. Okumura et al. [106] observed that, as compared to Ga-Si-MCM-41 , the Ga-impregnated MCM-41 shows better performance in the benzylation of benzene. A number of studies have been reported on the use of Si-MCM-41 supported (by impregnation or grafting) chlorides of aluminum, gallium or indium. Clark and coworkers [107–109] used AlCl_3 supported on hexagonal mesoporous silica (HMS) as an environ-friendly catalyst for the alkylation of benzene by linear alkenes and obtained good selectivity for monoalkylated linear alkyl benzenes without loss of the catalytic activity. AlCl_3 grafted on Si-MCM-41 showed high activity and selectivity to monoalkylated products in the alkylation of benzene with $\alpha\text{-C}_{6-16}$ olefins [77] and also in the benzylation and acylation reactions [79].

Hu et al [110] studied room temperature benzylation of benzene over AlCl_3 supported on Si-MCM-41. Jun and Ryoo [76] also investigated activity in Friedel–Crafts alkylation of benzene, toluene and m-xylene with benzyl alcohol over AlCl_3 -impregnated and grafted MCM-41, MCM-48 and KIT-1. Same surface character with regard to the catalytic reaction, independent of the different structure and AlCl_3 deposition conditions, were observed for the three types of mesoporous silica supported AlCl_3 catalysts.

It may be noted that, the supported and grafted AlCl_3 catalysts are very sensitive to moisture and their activity in the Friedel–Crafts alkylation reactions is almost totally killed because of their exposure to moisture containing gas or the presence of moisture in the reaction mixture.

Recently, Choudhary et al. [67,68,70,71] reported high activity and selectivity with little or no moisture sensitivity for Si-MCM-41 supported GaCl_3 and InCl_3 catalysts in the benzylation [68,70] and acylation [67,71,72] of aromatic compounds. These catalysts also showed high selectivity in the esterification of tert-butanol by acetic anhydride [66] and activity in the polycondensation of benzyl chloride [62].

Processes for the Friedel–Crafts type alkylation [65,72,111,112] and esterification [113] reactions using the environ-friendly Si-MCM-41 supported Ga_2O_3 , GaCl_3 and InCl_3 catalysts are described in a number of recent US patents [65,72,111–113].

Takeguchi et al. [114] used Ga-MCM-41 catalyst for the aromatization of hexane. Kosslick et al. [50,52] observed remarkable acetone-to-isobutene conversion activity for the Al- and Ga-substituted MCM-41 catalysts, both containing Brönsted and Lewis acid sites of different strengths. The activity of Al-substituted MCM-41 was, however, higher.

Although, the Si-MCM-41 supported Ga_2O_3 , GaCl_3 and InCl_3 catalysts [61,64,68,70,71] are Lewis acidic ones, their catalytic activity in the Friedel–Crafts reaction is influenced only to a small extent due to their exposure to moisture or the presence of moisture in the reaction mixture. Also, unlike with the Lewis acidic catalysts [115], the benzene benzylation activity of these catalysts is comparable to or even higher than that observed for the benzylation of substituted benzene having electron donating groups [61,68]. These two observations and a correlation between the redox potential of the metal (Zn, Ga, In and Fe) present in the catalyst and the catalytic activity [61,68], led Choudhary et al. [67,68,116] to suggest a probable redox mechanism for the benzylation and acylation reactions over the catalysts. The redox mechanism is presented in Fig. 2.

4.2 Mesoporous silica containing transition metal elements

These mesoporous catalysts have been employed for various catalytic reactions such as Friedel–Crafts type reactions, polymerization/polycondensation, complete and partial oxidations, epoxidation, oxidative dehydrogenation, selective catalytic reduction, and hydrodesulfurization reactions. Their catalytic action involves their acidic and/or redox functions.

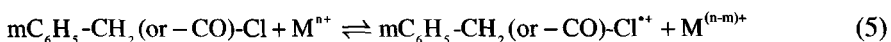
4.2.1 Friedel–Crafts Type Reactions

Among the metal (viz. Fe, Zn, Cr, Ni, Al and Co) containing MCM-41 and HMS catalysts, CaO et al. [117] found that the Fe-containing MCM-41 possesses highest activity for the benzylation of benzene with benzyl chloride [117]. No relationship was observed between the activity and acidity of the different catalysts. By comparing the results on the benzylation of toluene (by benzyl chloride) over H^+ -, Al^{3+} -, and Fe^{3+} -exchanged Al-Si-MCM-41, Yiu and Brown [104] concluded that Fe^{3+} forms exhibit highest Lewis acid catalytic activities. However, it may be noted that the observed high activity in these two cases is likely to be attributed not to the Lewis acidity but to the redox function of the

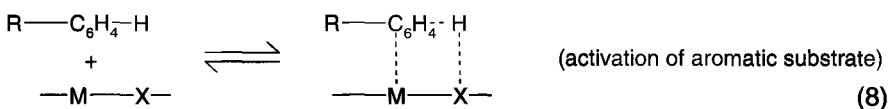
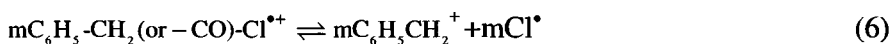
Fe-containing catalysts. Recently, Choudhary et al. [68,69] investigated a number of Fe-containing solid catalysts, including Si-MCM-41 supported FeCl_3 and Fe_2O_3 catalysts, for the benzylation of benzene. The supported Fe_2O_3 or FeCl_3 catalysts showed high benzene benzylation activity even in the presence of moisture. Similar to that observed by CaO et al. [117], there was no direct relationship between the acidity and benzylation activity of the catalysts. The activity of the Fe-containing catalysts seems to be controlled by their redox properties ($\text{Fe}^{3+} + \text{e}^- \rightleftharpoons \text{Fe}^{2+}$) and the benzylation reaction over these catalysts essentially involves a redox mechanism [69], as described in Fig. 2.

Although, the Fe-containing catalysts shows high benzylation activity, they are also very good benzyl chloride polycondensation catalysts [118], much better than the Ga- or In-containing ones [62], and hence always lead to the polycondensation of benzyl chloride to an appreciable extent in the benzylation with benzyl chloride [69].

Si-MCM-41 supported zinc chloride catalyst also shows activity in the benzylation [68] and acylation [67] of benzene. However, it is less active than the Si-MCM-41 supported GaCl_3 and InCl_3 catalysts.



[where M=In, Ga, Fe or Zn, n=3 (for In, Ga and Fe) or 2 (for Zn) and m=2 (for In and Ga) and 1 (for Fe and Zn)]



(X=O or Cl)

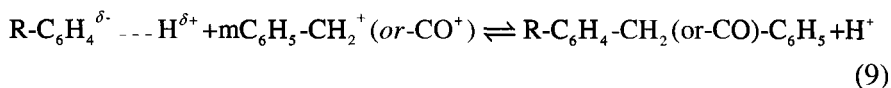


Figure 2. Probable redox mechanism for the benzylation and acylation of aromatic compounds over Si-MCM-41 supported Ga_2O_3 , GaCl_3 and InCl_3 catalysts.

4.2.2 Polymerization/polycondensation reactions

Choudhary and coworkers [118] have found that Fe-containing solid catalysts, including Si-MCM-41 supported Fe_2O_3 and FeCl_3 , show high activity for the polycondensation of benzyl chloride. The solvent employed in the polycondensation play an important role; the reaction rate for $\text{Fe}_2\text{O}_3/\text{Si-MCM-41}$ in the different solvents is in the following decreasing order: ethylene dichloride \gg n-hexane $>$ n-octane \gg ethanol.

He et al [119] have investigated the application of Cr/MCM-41 as a catalyst for the ethylene polymerization. Polyethylene with a certain conformation was formed within the nanosize one-dimensional channels of MCM-41 without destroying the pore structure of MCM-41.

4.2.3 Epoxidation of olefinic compounds

Thomas and coworkers [102] have shown that titanocene grafted on the pore walls of MCM-41 is a good catalyst for the epoxidation of cyclohexene and more bulky cyclic alkenes.

Koyano and Tatsumi [38-40] investigated the application of Ti-Si-MCM-41 [38] and Ti-Si-MCM-48 [39,40] for the epoxidation of bulky alkene (e.g. cyclododecene and α -terpineol) and unsaturated alcohols with H_2O_2 and/or t-butyl hydroperoxide. The stability of Ti-Si-MCM-41 against water was low compared to Si-MCM-41 [38] and Ti-Si-MCM-48 [39] was found to be more active than Ti-Si-MCM-41. Nemeth et al [120] have demonstrated that the selectivity and activity of Ti-MCM-41 for the epoxidation of cyclohexene is significantly improved after silylation or removal of water from the reaction medium. Yang et al [98] observed that better activity and selectivity to epoxide in the epoxidation of styrene are obtained when the Ti-SiO₂ catalyst contains more number of isolated Ti-O-Si species.

Kaliaguine and coworkers [121] have reported bifunctional Ti-MCM-41 containing different trivalent ions (e.g. B^{3+} , Al^{3+} or Fe^{3+}) for the epoxidation of α -pinene. These catalysts contained both acidic and oxidizing sites and showed high selectivity for diol formation and also good stability and reusability. Epoxidation of large size molecules such as terpineol [36,85], norbornene [36,49] and α -pinene [94,122] over Ti-Si-MCM-41 [36,94], Ti-HMS and Zr-HMS [49], Nb- or Ti-grafted Si-MCM-41 or Si-MCM-48 [85,122] have also been reported.

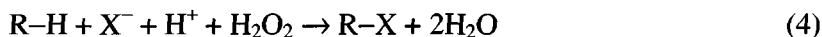
4.2.4 Oxidative dehydrogenation and halogenation reactions

Vanadium-containing MCM-41 and MCM-48, prepared by grafting using VOSO_4 or VOCl_3 as vanadium source, showed selectivity to propylene higher than SiO_2 supported vanadia in the oxidative dehydrogenation of propane (at 500 – 550 °C) [123]. Vanadium oxide supported MCM-41 was also found to be active and selective catalyst in the oxidative dehydrogenation of propane and ethane [124].

Chromium oxide supported Si-MCM-41 was found to be active in the oxidative dehydrogenation of propane at a lower temperature (350 °C) [125]. Chromium oxide supported Zr- or La-doped MCM-41 catalysts [126] and chromium impregnated Si-MCM-41 [127] catalyst have also been reported for the oxidative dehydrogenation of propane. The high activity of the vanadia or chromium oxide containing mesoporous MCM-41 is attributed to the high dispersion of catalytically active species in the mesoporous channels [124,125,127]. Chromium is a toxic and hence chromium-containing catalysts are to be prepared and handled very carefully.

Si-MCM-41 supported iron oxide catalyst [57] has been used for the ethyl benzene dehydrogenation and characterized for its structural evolution under the reducing environment of catalyst pretreatment and the dehydrogenation reaction.

Walker et al. [128] have found that Ti-MCM-48 effectively catalyses peroxidative halogenation reactions. Apart from Ti (IV), other transition metal (viz., V and W) grafted MCM-48 materials were also found to catalyse peroxidative halogenation reactions such as peroxidative chlorination or bromination of phenolsulfonaphthalein, 2,3-dimethoxy toluene, using hydrogen peroxide. The oxidative halogenation of organic substrate involves following stoichiometric reaction:



4.2.5 Other Oxidation Reactions

Complete oxidation: Manganese-oxo species grafted on Si-MCM-41 showed high redox catalytic activity for the total oxidation of propane to CO_2 [96]. Si-MCM-41 supported chromia catalyst has also been used for the air oxidation of organic compounds [129].

Partial oxidation: Transition metal containing mesoporous MCM-41 catalysts have been used in a number of partial oxidation reactions, such as

methanol oxidation over Nb-MCM-41 [55], oxidation of methane to formaldehyde over $\text{VO}_x/\text{Si-MCM-41}$ or Si-MCM-48 [130], liquid-phase oxidation of ethyl benzene to acetophenone over Cr-containing MCM-41 and MCM-48 [131], selective oxidation of 2,6-di-tert-butyl phenol with H_2O_2 over titanium incorporated different silicas (the catalytic activity of the Ti-grafted mesoporous silica for the oxidation decrease in the order of $\text{MCM-48} > \text{HMS} > \text{KIT-1} > \text{MCM-41} > \text{SBA-1}$) [93], and oxidative coupling of naphthol to binaphthol by molecular oxygen using Cu^{2+} - or Fe^{3+} -doped MCM-41 aluminosilicate [132].

Hydroxylation: Liquid phase oxidation of benzene with H_2O_2 to phenol using $\text{FeCl}_3/\text{Mesoporous SiO}_2$ [133], V-Si-MCM-41 [47,134] and FeCl_2 or FeCl_3 -grafted Si-MCM-41 [83] catalysts has been investigated. The catalytic activity of V-Si-MCM-41 was found to increase with increasing the acidity of the catalyst and the reaction temperature [134]. In the oxidation of toluene with H_2O_2 over V-Si-MCM-41 [47], both the partial oxidation and hydroxylation products (viz. benzaldehyde, o-cresol and p-cresol) have been observed. As compared to Ti-HMS, Cu-HMS [135] showed high activity in the hydroxylation of phenol to dihydroxybenzene using aqueous H_2O_2 as an oxidant.

4.2.6 Photocatalytic reactions

Ti-Si-MCM-41 and Ti-Si-MCM-48 zeolites [136] exhibited high and unique photocatalytic activity for the reduction of CO_2 by H_2O to methane and methanol in gas phase (at 50 °C). This is attributed to the charge transfer excited state of the highly dispersed titanium oxide species in the mesoporous zeolites. Titanium dioxide supported on HMS also showed high photocatalytic activity in the degradation of 2,4,6-trichlorophenol [137]. The photocatalytic activity of TiO_2 was enhanced after its deposition on HMS; the supported structure was the main factor responsible for the observed enhanced photocatalytic activity of TiO_2 .

Transition metal (viz. V, Cr, Fe and Cd) substituted TiO_2 loaded MCM-41 catalysts were also used as photocatalysts for the degradation of aqueous organics, such as formic acid and phenolic compounds [138,139].

4.2.7 Selective catalytic reduction

A few studies have been reported on the catalytic reduction of nitrogen monoxide with propene over $\text{CuCl}/\text{MCM-41}$ [140], NO_x by ammonia [141,142] or propene [143] over MnCl_2 -impregnated Si-MCM-41 and Al-

MCM-41 [141], Zr-doped mesoporous silica supported CoO [142] and Pt/MCM-41 (Al_2O_3) [143].

4.2.8 Desulfurization /hydrotreating reactions

A number of studies have been reported on the use of acidic transition metal oxide/sulfide containing mesoporous silicates as desulfurization/hydrodesulfurization catalysts, such as Mo/Al-MCM-41/ $\gamma\text{-Al}_2\text{O}_3$ [60], NiMo/MCM-41- Al_2O_3 [144], Ni,Mo/MCM-41 [145], Co-Mo/MCM-41 [146,147], Ni-Nb-MCM-41 and Cu-Nb-MCM-41 [148], Ni,Nb-supported MCM-41 [149], sulfided Co-Mo/MCM-41 [150], Ni-W/MCM-41 and Co-W/MCM-41 [151], Ni- or Nb-MCM-41 [152] and Mo/Ti-MCM-41 [153].

4.2.9 Miscellaneous applications

Rh-Mn supported on MCM-41 has been used for the synthesis of C_2 -oxygenated (acetaldehyde and ethanol) from syngas [154]. SnO_2 /MCM-41 has been used as a gas sensor [155].

5 Applications of basic catalysts supported on mesoporous Silica

As compared to the acidic catalysts, applications of only a few basic catalysts supported on mesoporous silica have been reported.

5.1 Friedel-Crafts type benzylation/acylation reactions

Between the Ga_2O_3 (which is amphoteric) and In_2O_3 (which is basic in nature) supported on various catalyst carriers (viz. silica-alumina, zirconia, H-ZSM-5, Si-MCM-41 and Al-Si-MCM-41), the In_2O_3 /Si-MCM-41 showed the highest activity for the liquid-phase benzylation (with benzyl chloride) [61,156] and acylation (with acyl chloride) of benzene and substituted benzenes. The high activity of this basic catalyst is attributed to its redox properties and the benzylation and acylation reactions involve redox mechanism and activation of aromatic substrate, as described in Fig. 2. Apart from its high activity and selectivity, the In_2O_3 /Si-MCM-41 catalyst is moisture insensitive and/or less sensitive; it shows high benzylation or acylation activity even in the presence of moisture and the moisture has a beneficial effect, more particularly for the acylation reactions [61,63].

Thallous oxide (which is highly basic in nature) supported on catalyst carriers with little or no surface hydroxyl groups also showed very high activity in the benzylation and benzylation of benzene [157]. However, when thallium oxide was deposited on Si-MCM-41, there was a total collapse of the MCM-41 structure with a very large decrease in the surface area due to very strong metal oxide-support interactions. It would be interesting to study the performance of thallium oxide supported on dehydroxylated mesoporous silica. However, it may be noted that thallium is a highly toxic metal and hence is not environ friendly.

5.2 Michael addition and Knoevenagel or Aldol condensation

Kloetstra and van Bekkum [158] have shown that Na^+ - or Ca^+ -exchanged MCM-41 is selective, water stable and recyclable catalyst for the base catalysed Aldol and Knoevenagel condensation and cesium acetate-impregnated MCM-41 catalyst is a strong base catalyst for the Michael addition. van Bekkum and coworkers [159] employed a binary CsLa-oxide/MCM-41, a new stable heterogeneous basic catalyst, for the liquid-phase Michael addition of Et cyanoacetate to Et acrylate and Knoevenagel addition or enolates to benzaldehyde. This catalyst can be reused after its high temperature regeneration without loss of activity. MCM-41 supported MgO showed catalytic activity for propene photo-oxidation [160].

6 Concluding remarks

Mesoporous silica supported Lewis acid/base catalysts have a high potential as versatile and environ-friendly catalysts, easily separable and generally reusable. Their large size channels allow the entry and exit of reactant and product molecules of almost all the sizes encountered in the synthesis of fine/speciality chemicals. The potential of these catalysts has been explored for the number of organic synthesis reactions and the scope of their applications is increasing day-by-day. Because of their uniform channels and high concentration of surface silanol groups present in the channels, mesoporous silicas are excellent supports for the preparation of chemically bonded or grafted Lewis acid/base catalysts (e.g. acidic metal chlorides and acidic/basic metal oxides) and also for hydrogenising or immobilizing other homogeneous catalysts. Although, a number of metal- or metal chloride-grafted mesoporous silica catalysts have been reported, the potential of mesoporous silicas for the preparation of chemically bonded or grafted catalytically active species has not yet been fully utilized/explored.

7 Acknowledgement

Dr. B. S. Uphade thanks Council of Scientific and Industrial Research (CSIR), New Delhi, India for the award of Senior Research Associateship/Scientist's Pool.

References

1. Kresge C.T., Leonowicz M.E., Roth W.J., Vartuli J.C. and Beck J.S., Ordered mesoporous molecular sieves synthesized by a liquid-crystal template mechanism, *Nature* **359** (1992) pp. 710-712.
2. Beck J.S., Vartuli J.C., Roth W.J., Leonowicz M.E., Kresge C.T., Schmitt K.D., Chu C.T.-W., Olson D.H., Sheppard E.W., McCullen S.B., Higgins J.B. and Schlenker J.L., A new family of mesoporous molecular sieves prepared with liquid crystal templates, *J. Am. Chem. Soc.* **114** (1992) pp. 10834-10843.
3. Kresge C.T., Leonowicz M.E., Roth W.J., Vartuli J.C. and Beck J.S., Synthetic mesoporous crystalline material having high adsorption capacity for benzene, *US Patent 5,098,684* (1992) pp. 41.
4. Bagshaw S.A., Prouzet E. and Pinnavaia T.J., Templating of mesoporous molecular sieves by nonionic polyethylene oxide surfactant, *Science* **269** (1995) pp. 1242-1244.
5. Tanev P.T. and Pinnavaia T.J., A neutral templating route to mesoporous molecular sieves, *Science* **267** (1995) pp. 865-867.
6. Huo Q.S., Margolese D.I. and Stucky G.D., Surfactant control of phases in the synthesis of mesoporous silica-based materials, *Chem. Mater.* **8** (1996) pp. 1147-1160.
7. Zhao D.Y., Feng J.L., Huo Q.S., Melosh N., Fredrickson G.H., Chmelka B.F. and Stucky G.D., Triblock copolymer synthesis silica with periodic 50 to 300 angstrom pores, *Science* **279** (1998) pp. 548-552.
8. Kimura T., Kamata T., Fuziwara M., Takanao Y., Kaneda M., Sakamoto Y., Terasaki O., Sugihara Y. and Kuroda K., Formation of novel ordered mesoporous silicas with square channels and their direct observation by transmission electron microscopy, *Angew. Chem. Int. Ed. Engl.* **39** (2000) pp. 3855-3859.
9. Ryoo R., Joo S.H. and Jun S., Synthesis of highly ordered carbon molecular sieves via template-mediated structural transformation, *J. Phys. Chem. B*: **103** (1999) pp. 7743-7746.
10. Schüth F., Ordered Mesoporous Materials- state of the art and prospects, *Stud. Surf. Sci. Catal.* **135** (2001) pp. 1-12.
11. Sayari A., Catalysis by crystalline mesoporous molecular sieves, *Chem. Mater.* **8** (1996) pp. 1840-1852.
12. Sayari A., Periodic mesoporous materials: synthesis, characterization and potential applications, *Stud. Surf. Sci. Catal.* **102** (1996) pp. 1-46.
13. Corma A., Preparation and catalytic properties of new mesoporous materials, *Topics in Catal.* **4** (1997) pp. 249-260.
14. Ying J.Y., Synthesis and applications of nanoporous materials, *Stud. Surf. Sci. Catal.* **117** (1998) pp. 85-87.

15. Biz S. and Occelli M.L., Synthesis and characterization of mesostructured materials, *Cat. Rev. –Sci. Eng.* **40** (1998) pp. 329-407.
16. Ciesla, U. and Schüth F., Ordered Mesoporous Materials, *Micro. Meso. Mater.* **27** (1999) pp. 131-149.
17. He X. and Antonelli D., Recent advances in synthesis and applications of transition metal containing mesoporous molecular sieves, *Angew. Chem. Int. Ed. Engl.* **41** (2001) pp. 214-229.
18. Fryxess G.E. and Liu J., Designing surface chemistry in mesoporous silica, *Surfactant Sci. Ser.* **90** (2000) pp. 665-687.
19. Corma A., From microporous to mesoporous molecular sieve materials and their use in catalysis, *Chem. Rev.* **97** (1997) pp. 2373-2419.
20. Brunel D., Blanc A.C. Galarneau A. and Fajula F., New trends in the design of supported catalysts on mesoporous silicas and their applications in fine chemicals, *Catal. Today* **73** (2002) pp. 119-152.
21. Cool P. and Vansant E.F., Chemical modification of oxide surfaces, *Trends in Phys. Chem.* **7** (1999) pp. 145-158.
22. Raja R. and Thomas J.M., Catalyst design strategies for controlling reactions in microporous and mesoporous molecular-sieves, *J. Mol. Catal. A: Chem.* **181** (2002) pp. 3-14.
23. Choi S., Wang Y., Nie Z., Khambapati D., Liu J. and Peden C.H.F., Mesoporous silica supported solid acid catalysts, *Stud. Surf. Sci. Catal.* **130B** (2000) pp. 965-970.
24. Tuel A., Modification of mesoporous silicas by incorporation of heteroelements in the framework, *Micro. Mesopor. Mater.* **27** (1999) pp. 151-169.
25. Clark J.H., Macquarrie D.J. and Wilson K., Functionalised mesoporous materials for green chemistry, *Stud. Surf. Sci. Catal.* **129** (2000) pp. 251-264.
26. De Vos D.E., Dams M., Sels B.F. and Jacobs P.A., Ordered mesoporous and microporous molecular sieves fictionalized with transition metal complexes as catalysts for selective organic transformations, *Chem. Rev.* **102** (2002) pp. 3615-3640.
27. van Bekkum H. and Kloetstra K.R., New organic chemical conversions over MCM-41 type materials, *Stud. Surf. Sci. Catal.* **117** (1998) pp. 171-182.
28. Tuel. A., Transition metal-modified mesoporous silicas as catalysts for oxidation reactions, *Stud. Surf. Sci. Catal.* **117** (1998) pp. 159-170.
29. Corma A. and Kumar D., Possibilities of mesoporous materials in catalysis, *Stud. Surf. Sci. Catal.* **117** (1998) pp. 201-222.
30. Clark J.H. and Macquarrie D.J., Catalysis of liquid phase organic reactions using chemically modified mesoporous inorganic solids, *Chem. Commun.* (1998) pp. 853-860.
31. Choudary B.M., Lakshmi Kantam M. and Lakshmi Santhi P., New and ecofriendly options for the production of speciality and fine chemicals, *Catal. Today* **57** (2000) pp. 17-32.
32. Corma A. and Garcia H., Lewis acids as catalysts in oxidation reactions: From homogeneous to heterogeneous systems, *Chem. Rev.* **102** (2002) pp. 3837-3892.
33. Asefa T., Ozin G.A., Grondey H., Kruk M. and Jaroniec M., Recent developments in the synthesis and chemistry of periodic mesoporous organosilicas, *Stud. Surf. Sci. Catal.* **141** (2002) pp. 1-26.
34. Borade R.B. and Clearfield A., Synthesis of aluminum rich MCM-41, *Catal. Lett.* **31** (1995) pp. 267-272.

35. Badamali S.K., Sakthivel A. and Selvam P., Influence of aluminum sources on the synthesis and catalytic activity of mesoporous AlMCM-41 molecular sieves, *Catal. Today* **63** (2000) pp. 291-295.
36. Corma A., Navarro M.T. Pérez-Pariente J. and Sánchez F., Preparation and properties of Ti-containing MCM-41, *Stud. Surf. Sci. Catal.* **84** (1994) pp. 69-75.
37. Corma A., Kan Q. and Rey F., Synthesis of Si and Ti-Si-MCM-48 mesoporous materials with controlled pore sizes in the absence of polar organic additives and alkali metal ions, *Chem. Commun.* (1998) pp. 579-780.
38. Koyano K.A. and Tatsumi T., Synthesis of titanium-containing MCM-41, *Micropor. Mater.* **10** (1997) pp. 259-272.
39. Koyano K.A. and Tatsumi T., Synthesis of titanium-containing mesoporous molecular sieves with a cubic structure, *Chem. Commun.* (1996) pp. 145-146.
40. Koyano K.A. and Tatsumi T., Synthesis of titanium-containing mesoporous molecular sieves with a cubic structure, *Stud. Surf. Sci. Catal.* **105** (1997) pp. 93-100.
41. a) Cheng C.-F., He H., Zhou W., Klinowski J., Sousa Gonsalves J.A. and Gladden L.F., Synthesis and characterization of the gallosilicate mesoporous molecular sieve MCM-41, *J. Phys. Chem.* **100** (1996) pp. 390-396; b) Cheng C.-F., Alba M.D. and Klinowski J., The unit cell of the gallosilicate mesoporous molecular sieve [Si,Ga]-MCM-41 is significantly smaller than in the purely silicious [Si]-MCM-41, *Chem. Phys. Lett.* **250** (1996) pp. 328-334.
42. Cheng C.-F. and Klinowski J., Synthesis and characterization of the galloaluminosilicate molecular sieve MCM-41, *J. Chem. Soc., Faraday Trans.* **92** (1996) pp. 289-292.
43. Edler K.J. and White J.W., Room-temperature synthesis of molecular sieve MCM-41, *Chem. Commun.* (1995) pp. 155-156.
44. Voegtlin A.C., Matijasic A., Patarin J., Sauerland C., Grillet Y. and Huve L., Room-temperature synthesis of silicate mesoporous MCM-41-type materials: Influence of the synthesis pH on the porosity of the materials obtained, *Micro. Mater.* **10** (1997) pp. 137-147.
45. Chatterjee M., Iwasaki T., Hayashi H., Onodera Y., Ebina T. and Nagase T., Room-temperature formation of thermally stable aluminium-rich mesoporous MCM-41, *Catal. Lett.* **52** (1998) pp. 21-23.
46. Chatterjee M., Iwasaki T., Onodera Y., Nagase T., Hayashi H. and Ebina T., Characterization of ordered mesoporous gallium MCM-41 synthesized at room temperature, *Chem. Mater.* **12** (2000) pp. 1654-1659.
47. Chatterjee M., Iwasaki T., Hayashi H., Onodera Y., Ebina T. and Nagase T., Characterization of tetrahedral vanadium-containing MCM-41 molecular sieves synthesized at room temperature, *Chem. Mater.* **11** (1999) pp. 1368-1375.
48. He N.-Y., Cao J.-M., Bao S.-L. and Xu Q.-H., Room-temperature synthesis of an Fe-containing mesoporous molecular sieves, *Mater. Chem.* **31** (1997) pp. 123-136.
49. Tuel A., Modification of mesoporous silicas by incorporation of heteroelements in the framework, *Micro. Mesopor. Mater.* **27** (1999) pp. 151-169.
50. Kosslick H., Lischke G., Parltitz B., Storek W. and Fricke R., Acidity and active sites of Al-MCM-41, *Appl. Catal. A: Gen.* **184** (1999) pp. 49-60.
51. Hunger M., Schenk U., Breuninger M., Gläser R. and Weitkamp J., Characterization of the acid sites in MCM-41-type materials by spectroscopic and catalytic techniques, *Micro. Mesopor. Mater.* **27** (1999) pp. 261-271.

52. Kosslick H., Lischke G., Walther G., Storek W., Martin A. and Fricke R., Physico-chemical and catalytic properties of Al-, Ga- and Fe-substituted mesoporous materials related to MCM-41, *Micro. Mesopor. Mater.* **9** (1997) pp. 13-33.
53. Landmesser H., Kosslick H., Kurschner U. and Fricke R., Acidity of substituted mesoporous molecular sieve MCM-48, *J. Chem. Soc., Faraday Trans.* **94** (1998) pp. 971-977.
54. Yuan Z.Y., Zhou W., Zhang Z.L., Chen Q., Su B.-L. and Peng L.-M., Comprehensive characterization of iron containing mesoporous molecular sieve MCM-41, *Stud. Surf. Sci. Catal.* **141** (2002) pp. 403-416.
55. Gao X., Wachs I.E., Wong M.S. and Ying J.Y., Structural and reactivity properties of Nb-MCM-41: Comparison with that of highly dispersed Nb₂O₅/SiO₂ catalysts, *J. Catal.* **203** (2001) pp. 18-24.
56. Abe T., Tachibana Y., Uematsu T. and Iwamoto M., Preparation and characterization of Fe₂O₃ nanoparticles in mesoporous silicate, *Chem. Commun.* (1995) pp. 1617-1618.
57. Wong S.-T., Lee J.-F., Cheng S. and Mou C.-Y., In-situ study of MCM-41-supported iron oxide catalysts by XANES and EXAFS, *Appl. Catal., A:Gen.* **198** (2000) pp. 115-126.
58. Köhn R., Brieler F. and Fröba M., Ternary transition metal oxides within mesoporous MCM-48 silica phases: Synthesis and characterization, *Stud. Surf. Sci. Catal.* **129** (2000) pp. 341-348.
59. Lensveld D.J., Mesu, J.G., van Dillen A.J. and de Jong K.P., Synthesis and characterization of MCM-41 supported nickel oxide catalysts, *Micro. Mesopor. Mater.* **44-45** (2001) pp. 401-407.
60. Cheng M., Kumata F., Saito T., Komatsu T. and Yashima T., Preparation and characterization of Mo catalysts over AlMCM-41/ γ -Al₂O₃ extruded supports, *Appl. Catal., A:Gen.* **183** (1999) pp. 199-208.
61. Choudhary V.R., Jana S.K. and Kiran B.P., Highly active Si-MCM-41-supported Ga₂O₃ and In₂O₃ catalysts for Fridel-Crafts-type benzylation and acylation reactions in the presence or absence of moisture, *J. Catal.* **192** (2000) pp. 257-261.
62. Choudhary V.R., Jana S.K. and Chaudhari M.K., Polycondensation of benzyl chloride over Ga- and In-modified ZSM-5 type zeolites and Si-MCM-41 or monmorillonite-K10 supported GaCl₃ and InCl₃ catalysts, *J. Mol. Catal., A:Chem.* **170** (2001) pp. 251-259.
63. Choudhary V.R. and Jana S.K., Benzoylation of benzene and substituted benzenes by benzoyl chloride over In₂O₃/Si-MCM-41 catalyst, *J. Mol. Catal., A:Chem.* **184** (2002) pp. 247-255.
64. Choudhary V.R. and Jana S.K., Acylation of aromatic compounds using moisture insensitive mesoporous Si-MCM-41 supported Ga₂O₃ catalyst, *Synth. Commun.* **32** (2002) pp. 2843-2848.
65. Choudhary V.R., Jana S.K. and Kiran B.P., Supported catalyst useful for Fridel-Crafts reactions and process for the preparation of aralkylated aromatic compounds using the catalyst, *US Patent* 6,180,557 (2001).
66. Choudhary V.R., Mantri K. and Jana S.K., Highly selective Si-MCM-41 supported InCl₃, GaCl₃, FeCl₃ and ZnCl₂ catalysts for low temperature esterification of tert-butanol by acetic anhydride, *Micro. Mesopor. Mater.* **47** (2001) pp. 179-183.
67. Choudhary V.R., Jana S.K. and Patil N.S., Acylation of benzene over clay and mesoporous Si-MCM-41 supported InCl₃, GaCl₃ and ZnCl₂ catalysts, *Catal. Lett.* **76** (2001) pp. 235-239.

68. Choudhary V.R. and Jana S.K., Benzylolation of benzene and substituted benzenes by benzyl chloride over InCl_3 , GaCl_3 , FeCl_3 and ZnCl_2 supported on clays and Si-MCM-41, *J. Mol. Catal. A: Chem.* **180** (2002) pp. 267-276.
69. Choudhary V.R., Jana S.K. and Mamman A.S., Benzylolation of benzene over Fe-modified ZSM-5 and H- β zeolites and Fe_2O_3 or FeCl_3 deposited on Micro-, Meso-, and Macroporous solids, *Micro. Mesopor. Mater.* **56** (2002) pp. 65-71.
70. Choudhary V.R., Jana S.K. and Kiran B.P., Highly active and moisture-insensitive solid catalysts- GaCl_3 and InCl_3 supported on montmorillonite-K10 and Si-MCM-41 for benzylolation of benzene, *Catal. Lett.* **64** (2000) pp. 223-226.
71. Choudhary V.R., Jana S.K. and Patil N.S., Acylation of aromatic compounds using moisture insensitive InCl_3 impregnated mesoporous Si-MCM-41 catalysts, *Tetrahedron Lett.* **43** (2002) pp. 1105-1107.
72. Choudhary V.R., Jana S.K. and Patil N.S., Process for the acylation of aromatic compounds using a reusable solid catalysts comprising indium halide, *US Patent 6,437,191* (2002).
73. Choudhary V.R. and Sansare S.D., Thermal, hydrothermal and acid-base stability of highly silicious MCM-41 mesoporous materials, *Proc. Ind. Acad. Sci. (Chem. Sci.)* **109** (1997) pp. 229-233.
74. Chen J., Li Q., Xu R. and Xiao F., Distinguishing the silanol groups in the mesoporous molecular sieve MCM-41, *Angew. Chem. Int. Ed. Engl.* **34** (1995) pp. 2694-2696.
75. Jentys A., Phan N.H. and Vinek H., Nature of hydroxyl groups in MCM-41, *J. Chem. Soc., Faraday Trans.* **92** (1996) pp.3287-3291.
76. Jun S. and Ryoo R., Aluminum impregnation into mesoporous silica molecular sieves for catalytic application to Friedel-Crafts alkylation, *J. Catal.* **195** (2000) pp. 237-243.
77. Hu X., Foo M.-L., Chuah G.K. and Jaenicke S., Pore size engineering on MCM-41: selectivity tuning of heterogeneous AlCl_3 for the synthesis of linear alkyl benzenes, *J. Catal.* **195** (2000) pp. 412-415.
78. Choudhary V.R. and Mantri K., AlCl_3 -grafted Si-MCM-41: Influence of thermal treatment conditions on surface properties and incorporation of Al in the structure of MCM-41, *J. Catal.* **205** (2002) pp. 221-225.
79. Choudhary V.R. and Mantri K., AlCl_x -grafted Si-MCM-41 prepared by reacting anhydrous AlCl_3 with terminal Si-OH groups: An active solid catalyst for benzylolation and acylation reactions, *Micro. Mesopor. Mater.* (in press).
80. Chen L.Y., Ping Z., Chuah G.K., Jaenicke S. and Simon G., A comparison of post-synthesis alumination and sol-gel synthesis of MCM-41 with high framework aluminum content, *Micro. Mesopor. Mater.* **27** (1999) pp. 231-242.
81. Ryoo R., Jun S., Kim J.M. and Kim M.J., Generalized route to the preparation of mesoporous metallosilicates via post-synthetic metal implantation, *Chem. Commun.* (1997) pp. 2225-2226.
82. Choudhary V.R., A.G. Gaikwad and Mantri K., A novel method for the incorporation of Ga in mesoporous Si-MCM-41 (Unpublished work).
83. Lee C.W., Ahn D.H., Wang B., Hwang J.S. and Park S.-E., Hydroxylation of phenol over surface functionalised MCM-41 supported metal catalysts, *Micro. Mesopor. Mater.* **44-45** (2001) pp. 587-594.
84. Zhang W.-H., Shi J.-L., Wang L.-Z. and Yan D.-S., The post-preparation of mesoporous Zr-MCM-41 via grafting reaction, *Mater. Lett.* **46** (2000) pp. 35-38.

85. Aronson B.J., Blanford C.F., Christopher F. and Stein A., Solution-phase grafting of titanium dioxide onto the pore surface of mesoporous silicates: synthesis and structural characterization, *Chem. Mater.* **9** (1997) pp. 2842-2851.
86. Mokaya R., Ultrastable mesoporous aluminosilicates by grafting routes, *Angew. Chem. Int. Ed. Engl.* **38** (1999) pp. 2930-2934.
87. Mokaya R., The effect of particle size on aluminosilicate MCM-41 catalysts prepared via grafting routes, *J. Catal.* **186** (1999) pp. 470-477.
88. Mokaya R. and Jones W., Grafting of Al onto purely silicious mesoporous molecular sieves, *Phys. Chem. Chem. Phys.* **1** (1999) pp. 207-213.
89. Mokaya R., Al_x^{n+} -grafted MCM-41 catalysts: probing the influence of temperature on the alumination process, *J. Catal.* **193** (2000) pp. 103-107.
90. Kim J.Y., Lee S.J. and Yu J.-S., Post-synthesis incorporation of Ga into mesoporous siliceous MCM-41, *Bull. Korean Chem. Soc.* **21** (2000) pp. 544-546.
91. Ahn W.S., Lee D.H., Kim T.J., Kim J.H., Seo G. and Ryoo R., Post-synthesis preparation of titanium-containing mesopore molecular sieve, *Appl. Catal., A: Gen.* **181** (1999) pp. 39-49.
92. Kim T.J., Kim J.-H. and Seo G., Physico-chemical state of titania impregnated on MCM-41 mesoporous material upon liquid-phase reaction of titania alkoxide, *React. Kinet. Catal. Lett.* **73** (2001) pp. 275-282.
93. Kang K.K., Byun C.S. and Ahn W.S., Titanium iso-propoxide grafting on M41S type hosts: catalytic and adsorption study, *Stud. Surf. Sci. Catal.* **129** (2000) pp. 335-340.
94. Hagen A., Schueler K. and Voskamp M., Post-synthetic preparation of Ti-MCM-41 oxidation catalysts with titanium alkoxides, *Stud. Surf. Sci. Catal.* **130C** (2000) pp. 3059-3064.
95. Echchahed B., Badiei A.-R., Beland F. and Bonneviot L., Fe and Co modifications of silicious MCM-41 and -48 using direct or post-synthetic methods, *Stud. Surf. Sci. Catal.* **117** (1998) pp. 559-566.
96. Burch R., Cruise N., Gleeson D. and Tsang S.C., Surface-grafted manganese-oxo species on the walls of MCM-41 channels-A novel oxidation catalyst, *Chem. Commun.* (1996) pp. 951-952.
97. van der Voort P., Mathieu M., Morey M., Stucky G.D. and Vansant E.F., Creation of MOx surface species on pure silica MCM-48 using gas- and liquid-phase modifications with M-acetylacetone complexes, *Stud. Surf. Sci. Catal.* **117** (1998) pp. 333-341.
98. Yang Q., Wang S., Lu J., Xiong G., Feng Z., Xin Q. and Li C., Epoxidation of styrene on Si/Ti/SiO₂ catalysts prepared by chemical grafting, *Appl. Catal., A: Gen.* **194-195** (2000) pp. 507-514.
99. Wulff H.P., Silicon dioxide/titanium dioxide-based catalysts for converting olefins to oxiranes, *Ger. Offen.* **2,102,597** (1971), to Shell, (CA: 75: p 131488m).
100. Wulff H.P., Epoxidation with improved heterogeneous catalyst, *US Patent* **3,923,843** (1975), to Shell, (CA: 84: p 89977d).
101. Choudhary V.R. and Gaikwad A.G., (Unpublished work).
102. Maschmeyer T., Rey F., Sankar G. and Thomas J.M., Heterogeneous catalysts obtained by grafting metallocene complexes onto mesoporous silica, *Nature* **378** (1995) pp. 159-162.
103. Bourlinos A.B., Karakassides M.A. and Petridis D., Synthesis and characterization of iron-containing MCM-41 porous silica by the exchange method of the template, *J. Phys. Chem. B* **104** (2000) pp. 4375-4380.

104. Yiu H.H.P. and Brown D.R., Lewis and Brönsted acid catalysis with Al-MCM-41 and Al-MMS: Dependence on exchange cation, *Catal. Lett.* **56** (1998) pp. 57-64.
105. Armengol E., Cano M.L., Corma A., Garcia H. and Navarro M.T., Mesoporous aluminosilicates MCM-41 as a convenient acid catalyst for Fridel-Crafts alkylation of a bulky aromatic compound with cinnamyl alcohol, *Chem. Commun.* (1995) pp. 519-520.
106. Okumura K., Nishigaki K. and Niwa M., Prominent catalytic activity of Ga-containing MCM-41 in the Fridel-Crafts alkylation, *Micro. Mesopor. Mater.* **44-45** (2001) pp. 509-516.
107. Clark J.H., Price P.M., Keith M., Macquarrie D.J. and Bastock T.W., Environmentally friendly catalysis using supported reagents; enhanced selectivity without loss in activity in the alkylation of benzene using hexagonal mesoporous silica (HMS)-supported aluminum chloride, *J. Chem. Res., Synop.* (1997) pp. 430-431.
108. Price P.M., Clark J.H., Keith M., Macquarrie D.J. and Bastock T.W., Enhanced selectivity without loss of activity in the alkylation of benzene using hexagonal mesoporous silica (HMS)-supported aluminum chloride, *Spec. Publ. -R. Soc. Chem.* **216** (1998) pp. 229-230.
109. Price P.M., Clark J.H., Keith M., Macquarrie D.J. and Bastock T.W., Enhanced selectivity in the preparation of linear alkylbenzenes using hexagonal mesoporous silica supported aluminum chloride, *Org. Process Res. Dev.* **2** (1998) pp. 221-225.
110. Hu X., Chuah G.K. and Jaenicke S., Room temperature synthesis of diphenylmethane over MCM-41 supported $AlCl_3$ and other Lewis acids, *Appl. Catal., A: Gen.* **217** (2001) pp. 1-9.
111. Choudhary V.R., Jana S.K. and Kiran B.P., Process for the preparation of aralkylated aromatic compounds using heterogeneous catalyst, *US Patent 6,215,035* (2001).
112. Choudhary V.R. and Jana S.K., A process for the liquid phase acylation of aromatic compounds, *US Patent 6,459,000* (2002).
113. Choudhary V.R., Mantri K. and Jana S.K., A process for the selective esterification of t-alcohol by an acid anhydride using a reusable solid catalyst, *US Patent 6,420,596* (2002).
114. Takeguchi T., Kim J.-B., Kang M., Inui T., Cheuh W.-T. and Haller G.L., Synthesis and characterization of alkali-free, Ga-substituted MCM-41 and its performance for n-hexane conversion, *J. Catal.* **175** (1998) pp. 1-6.
115. Olah G.A., in *Fridel-Crafts and Related Reactions* (Wiley-Interscience, New York, 1963).
116. Choudhary V.R., Jana S.K., Patil N.S. and Bhargava S., Fridel-Crafts type benzylation and benzoxylation of aromatic compounds over H β zeolite modified by oxides or chlorides of gallium and indium, *Micro. Mesopor. Mater.* **57** (2002) pp. 21-35.
117. Cao J., He N., Li C., Dong J. and Xu Q., Fe-containing mesoporous molecular sieves as benzylation catalysts, *Stud. Surf. Sci. Catal.* **117** (1998) pp. 461-467.
118. Jana S.K., Kiran B.P. and Choudhary V.R., Polycondensation of benzyl chloride over Fe-containing micro-, meso- and macroporous solid catalysts, In *Recent Trends in Catalysis*, ed. by V. Murugesan, B. Arabindoo and M. Palanichamy (Narosa Publishing House, New Delhi, India, 1999) pp. 106-111.

119. He J., Duan X. and Howe R.F., Structural characterization of Cr/MCM-41 and polymerization of ethylene within its nanoscale channels, *Huaxue Xuebao* **57** (1999) pp. 125-131.
120. Nemeth L., McCulloch B., Jensen R., Wilson S. and Moscoso, New transition metal-containing molecular sieves for selective liquid phase oxidation, *Stud. Surf. Sci. Catal.* **125** (1999) pp. 473-480.
121. On D.T., Kapoor M.P., Joshi P.N., Bonnevot L. and Kaliaguine S., Catalytic epoxidation of α -pinene over bifunctional mesoporous molecular sieves, *Catal. Lett.* **44** (1997) pp. 171-176.
122. Kapoor M.P. and Raj A., Epoxidation over niobium and titanium grafted MCM-41 and MCM-48 mesoporous molecular sieves, *Stud. Surf. Sci. Catal.* **129** (2000) pp. 327-334.
123. Peña M.L., Dejoz A., Fornés V., Rey F., Vázquez M.I. and López Nieto J.M., V-containing MCM-41 and MCM-48 catalysts for the selective oxidation of propane in gas phase, *Appl. Catal., A: Gen.* **209** (2001) pp. 155-164.
124. Solsona B., Blasco T., López Nieto J.M., Peña M.L., Rey F. and Vidal-Moya A., Vanadium oxide supported on mesoporous MCM-41 as selective catalysts in the oxidative dehydrogenation of alkanes, *J. Catal.* **203** (2001) PP. 443-452.
125. Santamaria-Gonzalez J., Merida-Robles J., Alcantara-Rodriguez M., Maireles-Torres P., Rodriguez-Castellon E. and Jimenez-Lopez A., Catalytic behavior of chromium supported mesoporous MCM-41 silica in the oxidative dehydrogenation of propane, *Catal. Lett.* **64** (2000) pp. 209-214.
126. Jimenez-Lopez A., P., Rodriguez-Castellon E., Maireles-Torres P., Diaz L. and Merida-Robles J., Chromium oxide supported on zirconium- and lanthanum-doped mesoporous silica in oxidative dehydrogenation of propane, *Appl. Catal., A: Gen.* **218** (2001) pp. 295-306.
127. Merida-Robles J., Alcantara-Rodriguez M., Rodriguez-Castellon E., Santamaria-Gonzalez J., Maireles-Torres P. and Jimenez-Lopez A., Chromium-impregnated mesoporous silica as catalyst for the oxidative dehydrogenation of propane, *Stud. Surf. Sci. Catal.* **130B** (2000) pp. 1865-1870.
128. Walker J.V., Morey M., Carlsson H., Davidson A., Stucky G.D. and Butler A., Oxidative halogenation catalysed by transition-metal-ion-grafted mesoporous silicate, *J. Am. Chem. Soc.* **119** (1997) pp. 6921-6922.
129. Pradier C.M., Rodrigues F., Marcus P., Landau M.V., Kaliya M.L., Gutman A. and Herskowitz M., Supported chromia catalysts for oxidation of organic compounds: The state of chromia phase and catalytic performance, *Appl. Catal., B: Environ.* **27** (2000) pp. 73-85.
130. Berndt H., Martin A., Bruckner A., Schreier E., Muller D., Kosslick H., Wolf G.-U. and Lucke B., Structure and catalytic properties of VO_x/MCM materials for the partial oxidation of methane to formaldehyde, *J. Catal.* **191** (2000) pp. 384-400.
131. Sakthivel A., Dapurkar S.E. and Selvam P., Mesoporous (Cr)MCM-41 and (Cr)MCM-48 molecular sieves: Promising heterogeneous catalysts for liquid phase oxidation reactions, *Catal. Lett.* **77** (2001) pp. 155-158.
132. Armengol E., Corma A., Garcia H. and Primo J., A highly selective synthesis of 1,1'-bi-2-naphthol by oxidative coupling of naphthol on mesoporous Fe, Cu/MCM-41 aluminosilicates, *Eur. J. Org. Chem.* (1999) pp. 1915-1920.
133. Seo Y.J., Tagawa T. and Goto S., Liquid-phase oxidation of benzene to phenol over $\text{FeCl}_3/\text{SiO}_2$ catalyst, *J. Chem. Eng. Jpn.* **27** (1994) pp. 307-308.

134. Lee C.W., Lee W.J., Park Y.K. and Park S.-E., Catalytic hydroxylation of benzene over vanadium-containing molecular sieves, *Catal. Today* **61** (2000) pp. 137-141.
135. Fu Z., Chen J., Yin D., Yin D., Zhang L. and Zhang Y., Highly effective Cu-HMS catalyst for hydroxylation of phenol, *Catal. Lett.* **66** (2000) pp. 105-108.
136. Anpo M., Yamashita H., Ikeue K., Fujii Y., Zhang S.G., Ichihashi Y., Park D.R. Suzuki Y., Koyano K. and Tatsumi T., Photocatalytic reduction of CO₂ with H₂O on Ti-MCM-41 and Ti-MCM-48 mesoporous zeolite catalysts, *Catal. Today* **44** (1998) pp. 327-332.
137. Dai Q., He N., Weng K., Lin B., Lu Z. and Yuan C., Enhanced photocatalytic activity of titanium dioxide supported on hexagonal mesoporous silica at lower coverage, *J. Inclusion Phenom. Macrocyclic Chem.* **35** (1999) pp. 11-21.
138. Davydov L., Reddy E.P., France P. and Smirniotis P.G., Transition-metal-substituted titania-loaded MCM-41 as photocatalysts for the degradation of aqueous organics in visible light, *J. Catal.* **203** (2001) pp. 157-167.
139. Reddy E.P., Davydov L. and Smirniotis P.G., Synthesis, characterization and photocatalytic activity of titania loaded Cd-MCM-41, *Catal. Lett.* **79** (2002) pp. 183-189.
140. Jia M.J., Lin W.Y., Zhang W.X., Xiao F.S., Pang W.Q. and Wu T.H., Selective catalytic reduction of nitrogen monoxide with propene over CuCl/MCM-41 catalysts, *React. Kinet. Catal. Lett.* **67** (1999) pp. 353-358.
141. Iojoiu, E.-E., Onu P., Schmitzer S. and Weisweiler W., Selective catalytic reduction of NO_x by NH₃ over Mn supported MCM-41 mesoporous materials, *Stud. Surf. Sci. Catal.* **135** (2001) pp. 4948-4955.
142. Moreno-Tost R., Santamaria-Gonzalez J., Maireles-Torres P., Rodriguez-Castellon E. and Jimenez-Lopez A., Cobalt supported on zirconia doped mesoporous silica: A selective catalyst for reduction of NO with ammonia at low temperatures, *Appl. Catal., B: Environ.* **38** (2002) pp. 51-60.
143. Schiesser W., Vinek H. and Jentys A., Surface species during catalytic reduction of NO by propene studied by in-situ IR-spectroscopy over Pt supported on mesoporous Al₂O₃ with MCM-41 type structure, *Appl. Catal., B: Environ.* **33** (2001) pp. 263-274.
144. Klimova T., Ramirez J., Calderon M. and Dominguez J.M., New Mo and NiMo catalysts supported on MCM-41/alumina for thiophene hydrodesulfurization, *Stud. Surf. Sci. Catal.* **117** (1998) pp. 493-500.
145. Cui J., Yue Y.-H., Sun Y., Dong W.-Y. and Gao Z., Characterization and reactivity of Ni,Mo-supported MCM-41 catalysts for hydrodesulfurization, *Stud. Surf. Sci. Catal.* **105A** (1997) pp. 687-694.
146. Reddy K.M., Wei B. and Song C., Mesoporous molecular sieve MCM-41 supported Co-Mo catalyst for hydrodesulfurization of petroleum resids, *Catal. Today* **43** (1998) pp. 261-272.
147. Song C. and Reddy K.M., Mesoporous molecular sieve MCM-41 supported Co-Mo catalyst for hydrodesulfurization of dibenzothiophene in distillate fuels, *Appl. Catal., A: Gen.* **176** (1999) pp. 1-10.
148. Ziolek M., Nowak I., Sobczak I., Lewandowska A., Decyk P. and Kujawa J., Physico-chemical and catalytic properties of MCM-41 mesoporous molecular sieves containing transition metals (Cu, Ni, and Nb), *Stud. Surf. Sci. Catal.* **129** (2000) pp. 813-822.
149. Cui J., Yue Y.-H., Sun Y., Dong W.-Y. and Gao Z., Hydrodesulfurization of thiophene on Ni, Mo-supported MCM-41 catalysts, *Chem. Res. Chin. Uni.* **14** (1998) pp. 284-288.

150. Song C. and Reddy K.M., Mesoporous zeolite-supported Co-Mo catalyst for hydrodesulfurization of dibenzothiophene in distillate fuels, *Prepr. -Am. Chem. Soc., Div. Pet. Chem.* **41** (1996) pp. 567-573.
151. Li X., Wang A.-J., Han D.-F. Wang Y. and Hu Y.-K., Preparation of W-based catalysts supported by siliceous MCM-41 for deep hydrodesulfurization, *Shiyou Xuebao, Shiyou Jiagong* **17** (2001) pp. 11-15.
152. Ziolek M., Nowak H., Poltorak H., Lewandowska A. and Sobczak I., The possible use of mesoporous molecular sieves for deodorization, *Stud. Surf. Sci. Catal.* **125** (1999) pp. 691-698.
153. Klimova T., Rodriguez E., Martinez M and Ramirez J., Synthesis and characterization of hydrotreating Mo catalysts supported on titania-modified MCM-41, *Micro. Mesopor. Mater.* **44-45** (2001) pp. 357-365.
154. Ma H., Yuan Z., Wang Y. and Bao X., Temperature-programmed surface reaction study on C₂-oxygenate synthesis over SiO₂ and nanoporous zeolitic material supported Rh-Mn catalysts, *Surf. Interf. Anal.* **32** (2001) pp. 224-227.
155. Li G. and Kawi S., MCM-41 modified SnO₂ gas sensors: sensitivity and selectivity properties, *Sen. Actuators, B:* **B59** (1999) pp. 1-8.
156. Choudhary V.R. and Jana S.K., Benzylation of benzene by benzyl chloride over Fe, Zn-, Ga- and In-modified ZSM-5 type zeolite catalysts, *Appl. Catal., A: Gen.* **224** (2002) pp. 51-62.
157. Choudhary V.R. and Jana S.K., Highly active and low moisture sensitive supported thallium oxide catalysts for Friedel-Crafts type benzylation and acylation reactions: strong thallium oxide-support interactions, *J. Catal.* **201** (2001) pp. 225-235.
158. Kloetstra K.R. and van Bekkum H., Base and acid catalysis by the alkali-containing MCM-41 mesoporous molecular sieve, *Chem. Commun.* (1995) pp. 1005-1006.
159. Kloetstra K.R., van Laren M. and van Bekkum H., Binary cesium-lanthanum oxide supported on MCM-41: A new stable heterogeneous basic catalyst, *J. Chem. Soc., Faraday Trans.* **93** (1997) pp. 1211-1220.
160. Martra G., Yoshida H., Dellarocca V., Murata C., Hattori T., Coluccia S. and Marchese L., Spectroscopic characterization and photocatalytic properties of Mg²⁺-modified MCM-41, *Stud. Surf. Sci. Catal.* **140** (2001) pp. 331-340.

NANOPOROUS CATALYSTS FOR SHAPE-SELECTIVE SYNTHESIS OF SPECIALTY CHEMICALS: A REVIEW OF SYNTHESIS OF 4,4'-DIALKYLBIIPHENYL

JIAN-PING SHEN

Cabot Superior MicroPowders, 3740 Hawkins NE, Albuquerque, New Mexico 87109, USA

Email: jian-ping_shen@carbot-corp.com; Tel: 505-342-1492 ext.55; Fax: 505-342-2168

CHUNSHAN SONG*

Clean Fuels and Catalysis Program, The Energy Institute, and Department of Energy & Geo-Environmental Engineering, The Pennsylvania State University, 206 Hosler Building, University Park, PA 16802, USA

Email: csong@psu.edu

Shape-selective synthesis of polycyclic organic chemicals can be achieved using nanoporous catalysts with pore structure, channel diameter, and acidic features that may be tuned to suit the needs of specific reactions. This chapter discusses the shape-selective synthesis of 4,4'-dialkylbiphenyl with the substituents ranging from isopropyl to methyl groups on the bicyclic structure. Matching the alkylating agent with a desired pore structure of molecular sieves is critical. To fully exploit concepts of reactant, product and transition-state shape selectivities, one can first use steric hindrance to eliminate unnecessary isomers that have adjacent substituted groups, and simplify isomer composition, then fine-tune the relationship between the desired product and zeolite pore channels by selecting appropriate alkyl groups and molecular sieve catalysts with modifications. The control of catalytic sites on internal and external surface is also important. If possible, eliminating the active sites on external surface to the extent possible is highly beneficial for selective synthesis of 4,4'-dimethylbiphenyl and 4,4'-diisopropylbiphenyl.

1 Introduction

Mono- and dialkylated binuclear aromatic compounds such as 4-alkylbiphenyl (4-ABP) or 2-alkylnaphthalene (2-AN) and 4,4'-dialkylbiphenyl (4,4'-DABP) or 2,6-dialkylnaphthalene (2,6-DAN) are valuable industrial intermediates for polyester fibers, engineering plastics, and liquid crystalline polymers. Therefore, they have drawn much attention from industrial and academic research organizations [1-3]. The dialkylbiphenyls or dialkylnaphthalenes can be oxidized into the corresponding carboxylic acids, followed by step-growth polymerization to synthesize polymers such as polyethylene biphenyl (PEBP) and polyethylene naphthalene (PEN), which are far superior to current polymers made from *terephthalic* acid such as (PET) (Fig. 1) [4].

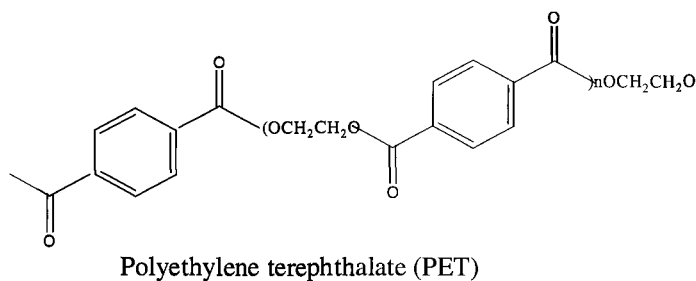
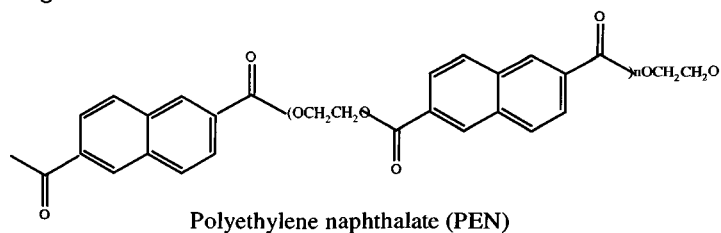
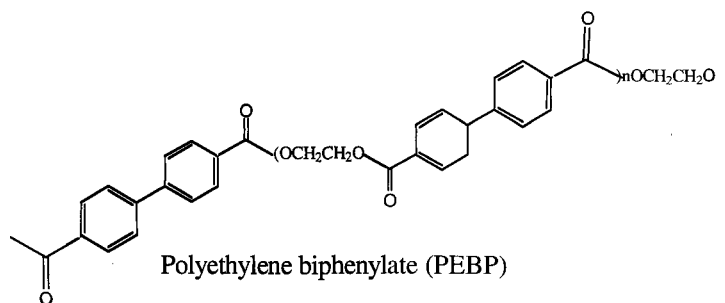


Figure 1. Polymers made from 2,6-dinaphthalenedicarboxylic acid, 4,4'-dibiphenyldicarboxylic acid and terephthalic acid.

The focus of initial work to synthesize 4,4'-dialkylbiphenyl (4,4'-DABP) was Friedel-Crafts chemistry by using Lewis acid catalysts such as AlCl_3 and silica-alumina. However, such catalysts have low selectivity for the *para*-product, 4,4'-DABP, and multiple recycle operations have to be employed to completely convert all reactants and other isomers. Furthermore, these catalysts are liquid acids and thus limited by environmental requirements. Therefore, attempts are currently underway to replace Lewis acids with solid acid catalysts having uniform pore systems.

Molecular sieves are widely applied for petroleum chemistry, fine chemicals, and specialty chemicals because their unique pore structures result in high selectivity for desired products. Typically, there are three types of selective mechanisms over molecular sieve catalysts as proposed by Weisz and Csicsery et al. [5], namely, reactant selectivity, product selectivity, and restricted transition state selectivity mechanisms. They are distinguished depending on whether the pore size limits the entrance of reactant molecules, the departure of product molecules, or the formation of certain transition states:

1. The reactant selectivity mechanism occurs when some of the molecules in a reaction mixture can enter the pores and react in the pores. However, molecules that are too large to diffuse through the pores cannot be excluded from the pores and thereby reaction.
2. The product selectivity mechanism occurs when some of products formed in the catalyst pores are too bulky to diffuse out, being forced to undergo further conversion to less bulky molecules (by equilibration or cracking). The large product molecules, which cannot diffuse out, may eventually deactivate the catalytic sites by blocking pores.
3. The restricted transition-state selectivity mechanism occurs when certain reactions are prevented because the corresponding transition state would require more space than that available inside the pores. Reactions requiring smaller transition states proceed unhindered to form desired product molecules.

Unlike mononuclear aromatics such as dialkylbenzene, which has just three isomers, i.e., *p*-, *o*-, and *m*-dialkylbenzene, polynuclear aromatics like dialkylbiphenyls have complicated isomers. Fig. 2 demonstrates, for example, the complex isomers of methylbiphenyl and dimethylbiphenyl.

Among these, the most thermodynamically stable isomers are those with substituents at the 3-positions [6], and the desired product, 4,4'-DABP, is only a small portion among all isomers. Thus, to selectively obtain 4,4'-DABP requires better understanding of molecular sieve acidity/basicity and structure and their correlation with alkylating agents. For example, to eliminate unnecessary isomers, one can use an alkylating reagent that results in products having large substituents which can prohibit isomer formation such as ortho-isomers like 3,4-, 2,3-, 2,6- and 2,2'-DABP because of steric hindrance, as a result, the selectivity to 4,4'-DABP increases. The combination of zeolite with suitable pore structure will further increase the selectivity to the linear molecule, 4,4'-DABP owing to the presence of shape selectivity. 4,4'-dialkylbiphenyl with large

substituted group like isopropyl, however, has disadvantage during the oxidation into dicarboxylic acid such as severe oxidation and carbon loss. Instead, the oxidation of 4,4-dimethylbiphenyl has obviously benefit during ease controlling of reaction conditions and no carbon loss, nevertheless, it is much more difficult to be selectively prepared. Thus, up to date there are three common routines to prepare 4,4'-DABP in terms of substituted alky groups:

- Preparation of 4,4'-diisopropylbiphenyl (4,4'-DIBP) over zeolites with 12 member ring structure such as mordenite and SAPO.
- Ethylation and transethylation into 4,4'-diethylbiphenyl (4,4'-DEBP) over zeolites mordenite and HY.
- Synthesis of 4,4'-dimethylbiphenyl (4,4'-DMBP) through methylation, transmethylation and carbon-carbon coupling of substituted toluene.

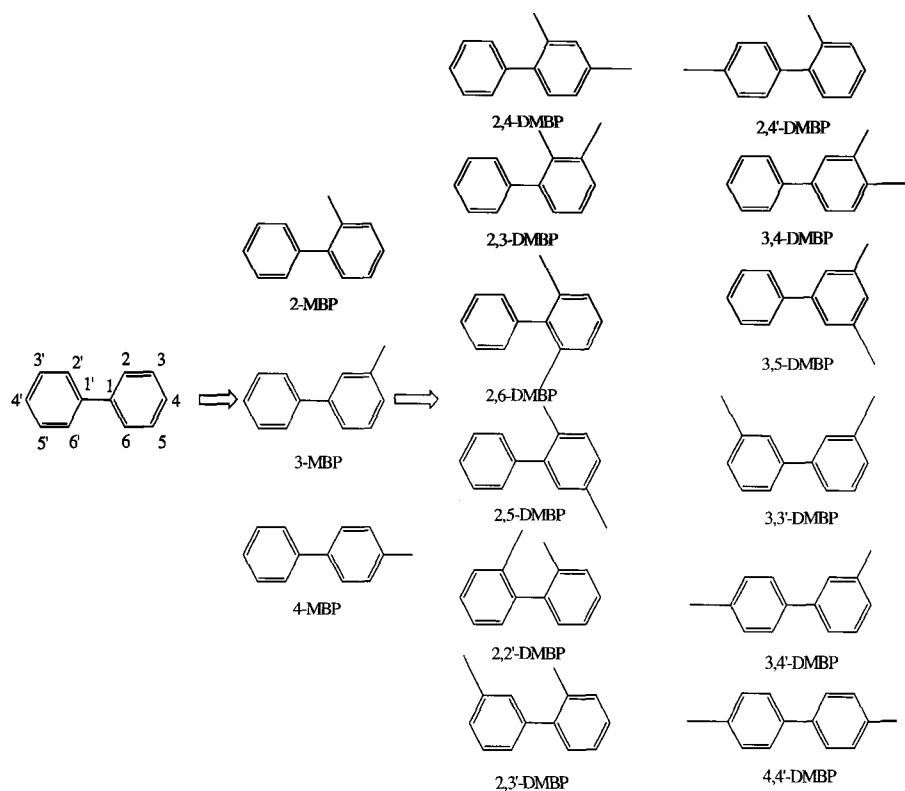


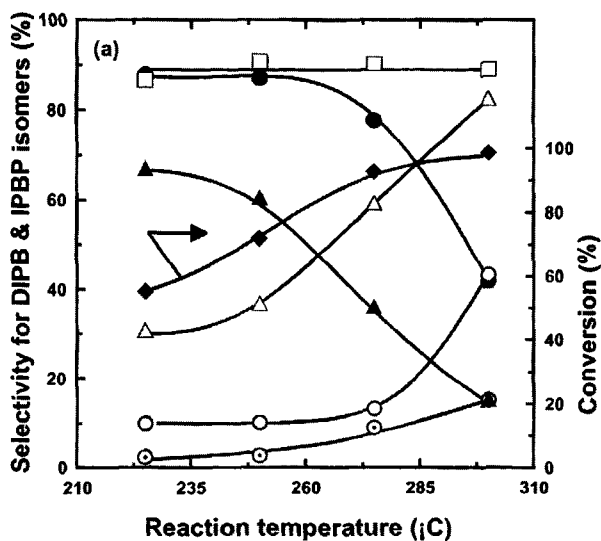
Figure 2. The complex of possible methylbiphenyl and dimethylbiphenyl isomers

2 Shape-selective preparation of 4,4'-diisopropylbiphenyl (4,4'-DIBP)

Many studies have focused on isopropylation of biphenyl with propylene to synthesize 4,4'-DIBP over mordenite-type zeolite because the combined mechanisms of reactant and restricted transition state selectivities can simultaneously take place in mordenite's unique pore structure [7-12]. Thus, a high selectivity for 4,4'-DIBP can be achieved. The selectivity of 4,4'-DIBP in the isopropylation of BP over HM zeolite catalyst was not only influenced by reaction parameters such as temperature, propylene pressure, $\text{SiO}_2/\text{Al}_2\text{O}_3$ ratio, and the degree of ion-exchange, but also by zeolite structure and acid site distribution, particularly internal and external surface acid sites. The following summarizes how reaction conditions and catalyst structure influences the product distribution and identifies ways to effectively enhance 4,4'-DIBP selectivity.

2.1 Effects of reaction conditions on BP isopropylation over HM catalyst

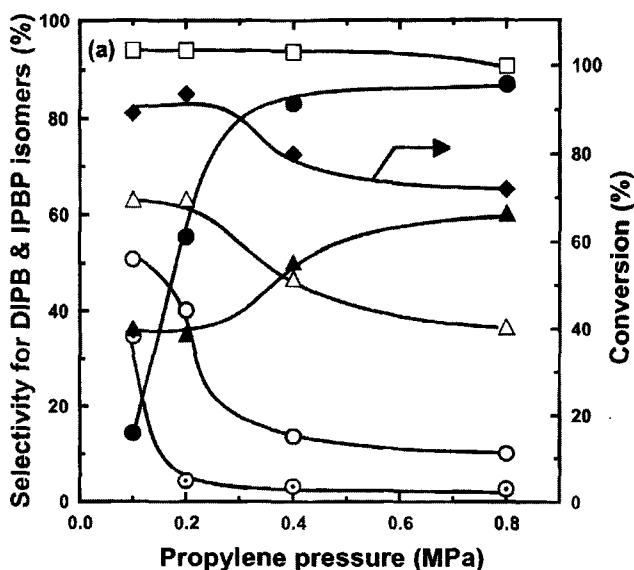
Research groups represented by Sugi et al. [11] have published a series of studies on the effects of reaction conditions on BP isopropylation. Fig. 3 shows the effects of reaction temperature on the selectivity for DIPB and IPBP isomers in the isopropylation of BP over unmodified HM (128). The selectivity for these DIBP isomers in bulk products varied with reaction temperature. The isopropylation produced 4,4'-DIBP selectively at moderate temperatures up to 250 °C but decreased with the increase in the selectivity for 3,4'-DIPB, at temperatures higher than 275°C, in part because this more thermodynamically stable isomer (3,4'-DIPB) is obtained from the 4,4'-isomer. Interestingly, the features of encapsulated products, which are contained in the catalyst used for the reaction, are quite different from those of bulk products in the isopropylation of BP. The selectivity for 4,4'-DIBP was higher than 80% at all temperatures, even at temperature as high as 300°C. These results indicate that shape selective formation of 4,4'-DIBP occurs inside the pores of HM (128) and isomerization of 4,4'-DIPB in the bulk products at high temperature occurs on external acid sites.



●:4,4'-DIPB ○:3,4'-DIPB ○:other DIPBs ▲:4-IPBP △:3-IPBP □:4,4'-DIPB(encapsulated) ◆:Conversion

Figure 3. Effects of reaction temperature on the isopropylation of BP over HM (128). Reaction conditions: BP 200mmol; catalyst, 1g; propylene pressure, 0.8MPa; period, 4h.

Effect of propylene pressure on the selectivity for DIPB and IPBP in the isopropylation of BP over HM (128) revealed the variation of 4,4'-DIPB with propylene pressure (Fig. 4). When pressure reaches higher than 0.4Mpa, the selectivity to the slimmer isomers, 4-IBP and 4,4'-DIPB, are greatly improved. For example, under high pressure of 0.8Mpa, the selectivity to 4,4'-DIPB is as high as 90%, while that of the other isomers such as 3,4'-DIPB are low. However, 4,4'-DIPB in encapsulated products is exclusively formed during this isopropylation, which means that the isomerization of 4,4'-DIPB into other isomers or alkylation of BP into other isomers have been effectively prevented by preferential adsorption of propylene on acid sites.



●: 4,4'-DIPB ○: 3,4'-DIPB ○: other DIPBs ▲: 4-IPBP △: 3-IPBP □: 4,4'-DIPB(encapsulated) ◆: Conversion

Figure 4. Effects of propylene pressure on the isopropylation of BP over HM (128). Reaction conditions: BP 200mmol; catalyst, 1g; temperature, 250°C; period, 4h.

2.2 Effect of Si/Al ratio of HM

Effect of $\text{SiO}_2/\text{Al}_2\text{O}_3$ ratio of HM on isopropylation of BP was reported in literature [9,12] under 0.8MPa of propylene at 250°C, and the results for bulk products and encapsulated products showed that at higher Si/Al ratio, mordenite favors the isopropylation of BP into IPBP and DIPB. A small portion of TriBP was also found in the products. On the other hand, the percentage of BP in encapsulated products was much lower than that in bulk products. DIPB isomers were predominant in encapsulated products, particularly so with highly dealuminated HMs, indicating that dealumination favors isopropylation of DIPB in the pores. Further analysis of DIPB distribution shown in Fig. 5 revealed that, in bulk products, 4,4'-DIPB selectivity increases with increasing Si/Al ratio, particularly when Si/Al ratio is higher than 50. Over all catalysts the thermodynamically favorable 3,4'-isomer is much lower than 4,4'-isomer, clearly showing high selectivity for the desired product 4,4'-DIPB. As compared with the encapsulated product 4,4'-DIPB over HM with Si/Al ratio less than 50,

one can deduce the occurrence of non-regioselective alkylation or isomerization of 4,4'-DIBP into other isomers.

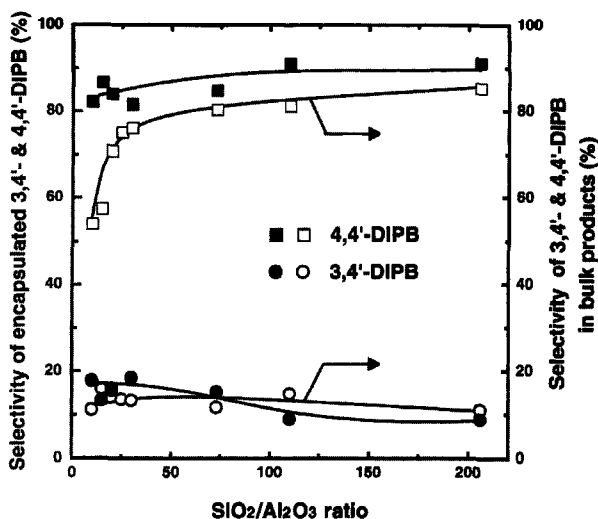


Figure 5. Effects of Si/Al ratios of HM on the selectivity for 3,4'- and 4,4'-DIBP in bulk and encapsulated products in the isopropylation of BP. Reaction conditions: BP 200mmol, HM 1g; propylene, 0.8Mpa; temperature 250°C; period 4h.

2.3 Surface modification and 4,4'-DIBP selectivity

By comparison of the bulk and encapsulated products over HM with different Si/Al ratios and under different reaction conditions, as shown in Figures 2.1.1, 2.1.2, and 2.2.1, one can find that HM-type zeolites have a natural tendency to shape selectively enable the formation of 4,4'-diisopropylbiphenyl. The presence of active sites on external surface seem responsible for the equilibration or the non-selectivity to the slim isomer. The enhanced selectivity to 4,4'-DIBP could be achieved if the removal or poisoning of active sites on external surface take place. There are several ways to reach this goal: dealumination of Al species by extraction using acid solution or hydrothermal treatment with water vapor [13]; modification with metal oxides such as ceria and calcium oxide [11,14,15]; selective poisoning of external acid sites by large organic molecules such as triphenylphosphate [9,16]. For example, Fig. 6 shows effect of the amount of cerium over HM (128) on the isopropylation of BP at 300°C.

The 4,4'-DIBP selectivity was only 50% over unmodified HM (128) where it is increased into 80% by the modification with 10% cerium oxide due to depression of the formation of 3,3'- and 3,4'-DIBP isomers although it is accompanied by a small decrease in catalytic activity.

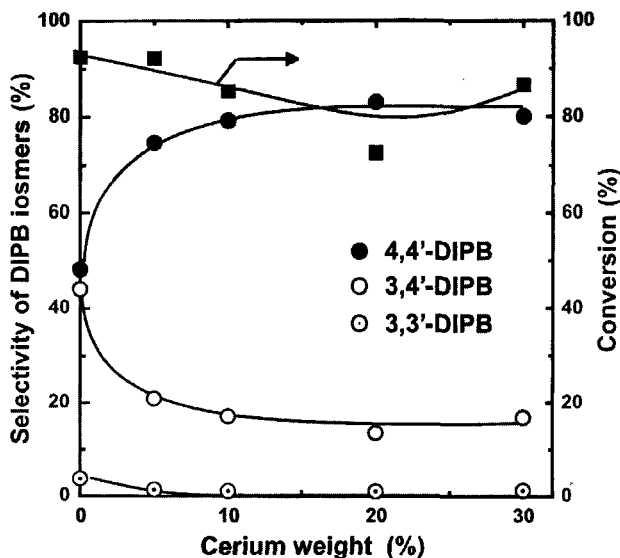


Figure 6. Effect of Ce amount over HM (128) on the isopropylation of BP. Reaction conditions: BP, 200mmol; catalyst, 1g; temperature, 250°C; propylene pressure, 0.8Mpa; time, 4h

Several researchers examined the modification effects of metal oxides by using probe molecules such as triisopropylbenzene (IPB) and 1,3,5-triisopropylbenzene (1,3,5-TIPB) as reactants over mordenite before and after modification [9,11], results of which studies are shown in Table 1. As follows from the cracking functionality over parent HM (128) and Ce(30)HM(128), modified with 30% of ceria, the conversion of large molecule, 1,3,5- TriBP, has been greatly depressed over modified mordenite, indicating coverage of active sites on the external surface and the narrowing of pore windows. During isopropylation of BP over Ce(30)HM(128), the highly selective product, 4,4'-DIBP, will have less chance to isomerize into other DIBPs once it diffuses out of the pores of mordenite, thus, enabling the high selectivity for 4,4'-DIBP in the products. Kikuchi et al. drew similar conclusions when they used tributylphosphite instead of Ce for modification of HM external surface.

Table 1. Cracking of 1,3,5-TIPB and IPB over HM and CeO₂-HM.

Catalyst	Conversion (%)	
	1,3,5-TIPB	IPB
HM(128)	60.9	98.5
Ce(30)HM(128)	3.9	65.5

^a Reaction conditions: catalyst, 10mg (as HM); temperature, 300°C; carrier gas flow rate, 50mlmin⁻¹(N₂); injection amount, 0.02 ul

2.4 Isopropylation of BP over silicoaluminophosphate molecular sieves

Because of less or weak acidity, SAPO are inactive for many reactions such as intermolecular hydrogen-transfer. However, SAPO molecular sieves were used as effective catalysts for some olefin transformations. SAPO such as SAPO-5 can have acidity mainly due to the replacement of P by Si in neutral aluminophosphate framework. Since their pore window opening is in the range of 0.6–0.7nm, similar to zeolites like HM and HY, they could also be the candidates for isopropylation of BP.

Some researchers [17,18] have reported BP isopropylation over SAPO molecular sieves. For example, Sugi et al. [19] recently synthesized a series of SAPO molecular sieves, SAPO-5, SAPO-11, SAPO-25 and SAPO-34, through a dry-gel conversion method and carried out BP isopropylation over the synthesized samples.

Like over zeolite HM [9,11,19], the products of BP isopropylation over SAPO also consist of IBP, DIPB, and TriBP. The comparison of their performance is depicted in Fig. 7. Among them, SAPO-11 showed higher selectivity for 4-IPBP and 4,4'-DIPB. It was observed that the selectivity for 4,4'-DIPB depends on pore size and structure. Molecular sieves with pore size of about 0.6–0.7 nm are suitable for selective synthesis of 4,4'-DIPB. The pore size of SAPO-11 (0.63 nm X 0.39 nm) closely resembles the molecular size of 4,4'-DIPB; thus SAPO-11 shows the highest selectivity for 4,4'-DIPB among SAPO molecular sieves. On the other hand, SAPO-5, being larger in size (0.73 nm), shows comparatively lower selectivity; however, it possesses the highest acidity among the catalysts, as shown in the TPD profile (Fig. 8), where the acid strength is much weaker than HY and HM, as indicated by the peak at high temperature. Clearly this is one of the factors for higher BP conversion. SAPO-34 is smaller in size and is not suitable for the formation of 4,4'-DIPB. Similar to SAPO-5, BP conversion was observed over SAPO-11 due to the similarity in

acidity. SAPO-20, being the smallest in size among all the catalyst is inactive for the isopropylation of BP. Thus, it can be seen that the reaction is governed by two factors: the pore geometry of the catalyst and acidity. Similar work on the influence of reaction time, Si/Al ratio, propylene pressure and modification with ceria has also been conducted in BP isopropylation and the results demonstrated that modification of external surface with ceria can effectively improve 4,4'-DIBP selectivity.

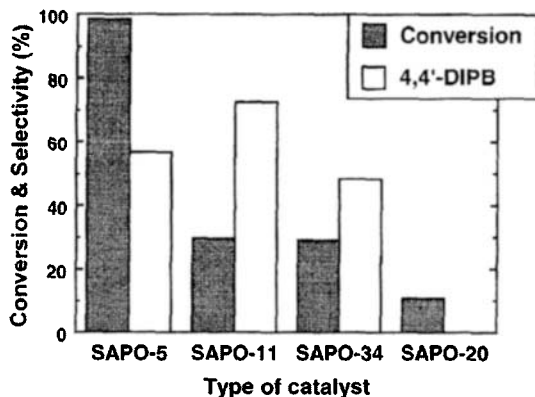


Figure 7. Isopropylation of BP over SAPO molecular sieves catalysts. Reaction conditions: BP, 100 mmol; propylene, 0.8 MPa; catalyst, 0.5 g; temperature, 300 °C; reaction time, 4 h.

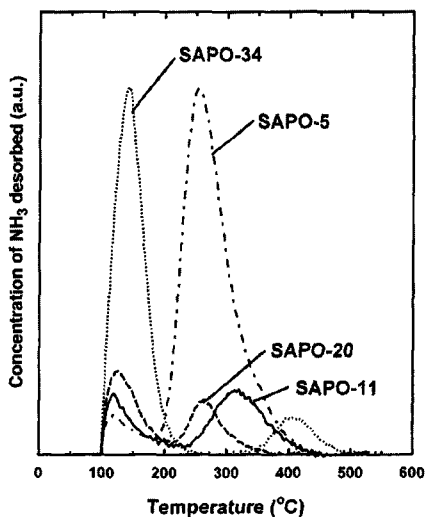


Figure 8. NH₃-TPD profiles of SAPO-5, SAPO-11, SAPO-20 and SAPO-34.

3 Ethylation and transethylation of biphenyl and its derivate into 4,4'-diethylbiphenyl (4,4'-DEBP)

Compared to the number of reports on preparation of 4,4'-diisopropylbiphenyl (4,4'-DIBP), the synthesis of 4,4'-DEBP through ethylation of biphenyl with ethylene or ethanol in literature has been rarely seen because of the lack of shape selectivity.

Xu et al. [20] conducted stepwise ethylation of biphenyl with ethylene under pressure 10 kg/cm^2 and temperature of 250°C over HM220 with high $\text{SiO}_2/\text{Al}_2\text{O}_3$ of 220. The ethylation resulted in a conversion of biphenyl ca. 90% after 12 hr; the product was composed of 60% EBP, 25% DEBP and 15% PEBP, including tri and tetraethylbiphenyls. From Fig. 9 it may be seen that three EBP isomers, 2-, 3-, and 4-EBP, were formed in different rates in the first stage and their behavior is also quite different in the second-stage ethylation yielding DEBP isomers. 2-EBP showed a linear increase with conversion. The yield of 4-EBP decreased after reaching a maximum at 50% conversion, the decrease corresponded to an increase of 4,4'- and 3,4'-DEBP. The yield of 3-EBP also increased linearly with increasing conversion, but decreased after reached a conversion of ca. 70%. These results indicate that 4-EBP preferentially participated in the ethylation, and that 3-EBP was gradually alkylated with decreasing amounts of 4-EBP. However, 2-EBP was excluded from further ethylation. The pore of HM differentiated the diffusion of EBP isomers in terms of reaction type shape-selective catalysis.

The slim isomer 4-EBP formed initially with only 17% selectivity (Fig. 10), as compared to approximately 40% for both 2- and 3-EBP, indicates the lack of shape selectivity in the first alkylation step from biphenyl to 4-EBP. The change in the distribution of EBP isomers is due to the preferential consumption of 4-EBP to form DEBP isomers. As for DEBP isomers, the most slim isomer 4,4'-DEBP obtained in highest selectivity was only ca. 30% and kept constant during the reaction, which indicated that the ethylation was governed by restricted transition state-type shape-selective catalysis and 4-ethyl group in 4-DEBP enhances steric restriction at the transition states inside pores to increase the shape selectivity in the second-stage alkylation. Compared with high isopropylation [7-14], the lack of shape selectivity for the formation of 4-EBP is due to the low steric restriction by the pores at the transition state of the ethylation of 4-EBP. The ethylation of biphenyl over HY zeolite further proves that the space available for ethylation plays a key role in selectivity to 4,4'-DEBP. When the space is large enough for ethylation of biphenyl, like Y zeolite, the formation of possible isomers was governed by thermodynamics. For

example, the high selectivity to 2-EBP is ascribed to the high electron density at the 2-position of biphenyl [20].

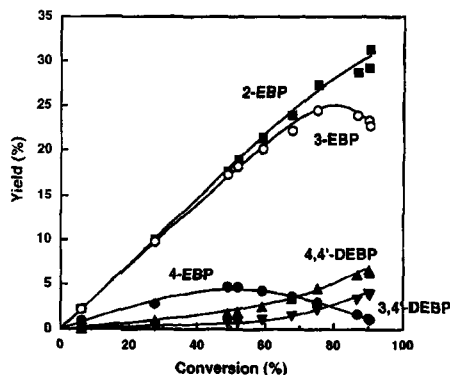


Figure 9. Yield of the products obtained after ethylation of biphenyl over HM220 at conditions of biphenyl, 400mmol, HM220 (2g), ethylene pressure, 10kg/cm², reaction temperature 250°C.

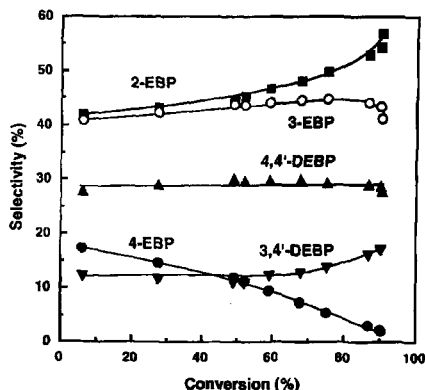


Figure 10. Selectivity of the ethylation of biphenyl over HM220 at the same reaction conditions as Fig. 9.

Since it is difficult to get high selectivity for 4,4'-DEBP over molecular sieves through ethylation, some researchers [21] have explored alternative methods to solve this problem. A successful example is the research conducted by Takeuchi et al. [22], in which 4,4'-DEBP at high ratio and with good yield was accomplished over HY zeolite by transethylation of biphenyl with triethyl- or tetraethylbenzene at relatively low temperature. The authors conducted ethylation of BP with ethylene over three types of catalysts, silica-alumina, HY, and HM and obtained, not surprisingly, non-selective 4,4'-DEBP. However, when the reaction was carried out by transethylation of BP with diethylbenzene over silica-alumina at 300-350 °C, 4,4'-DEBP formation, interestingly, shows moderate selectivity. At very low temperatures (160-170 °C), 4,4'-DEBP isomer selectivity over HY can reach 86% with a yield of 53 mol%, far higher than its equilibrium composition of 7%. The selectivity can be further improved to as high as 95% through a mixture of BP and 4-EBP (2:1 by weight); this high selectivity is attributed to reaction transition state selectivity. Low reaction temperature will minimize isomerization of 4,4'-DEBP into thermodynamically stable 3,x'-isomers. These results indicate that HY is more suitable than silica-alumina catalyst in transethylation, which probably occurs because of the more space available for HY zeolite and its stronger acid strength.

4 Preparation of 4,4'-dimethylbiphenyl (4,4'-DMBP)

At present the industrial scale production of 4,4'-biphenyldicarboxylic acid is achieved through the oxidation of 4,4'-diisopropylbiphenyl at rather severe conditions and accompanying decarboxylation [23]. In comparison with this method, the oxidation of 4,4'-dimethylbiphenyl appears to be highly advantageous as there is no decarboxylation and therefore, no carbon loss. As demonstrated above, high 4,4'-DIBP selectivity can be achieved through isopropylation of BP over modified zeolites with pore dimension of 0.6–0.7 nm such as mordenite, SAPO-5 [17,18] and SSZ-31 [8]. By contrast, ethylation of biphenyl over highly dealuminated mordenite showed rather low selectivity for the formation of para-substituted biphenyls. The selectivity can be achieved only through transethylation of BP with polyalkylbenzene. Therefore, one could deduce that the shape selective methylation of biphenyl, although preferable because of the reaction mentioned above, would be more difficult to achieve. It should be emphasized that the current method for preparation of 4,4'-DIBP and 4,4'-DEBP have been carried out under batch conditions by using autoclave reactors.

To develop an effective method to prepare 4,4'-DMBP, some alternative ways were reported, the most promising are:

- Carbon-carbon coupling of halogen-substituted toluene and toluene
- Transmethylation of BP with polymethylbenzene
- Methylation of BP or 4-MBP under fixed-bed conditions.

4.1 *Carbon-carbon coupling of halogen-substituted toluene and toluene into 4,4'-DMBP*

Halobenzene or halotoluene can be reduced to benzene or toluene by using Pd-based catalyst and a reducing agent such as hydrogen gas or formate salts [24,25]. The selectivity is generally high due to thermodynamics which favor aromatics. Under similar conditions, the addition of a surface-active agent and base can shift the selectivity to the coupling product, biphenyl or dimethylbiphenyl [26]. The former is also a building block for numerous agrochemicals and pharmaceuticals. To meet market needs, several synthetic approaches towards biphenyl-based coupling have been developed from the classic general Ullmann, Suzuki, and Stille reactions to custom-tailored catalytic transformations aimed at specific molecules. Amongst the variety of developed methods the most attractive one is the

Pd-catalyzed reductive coupling of haloaromatic as it benefits from simple reactor design, easy catalyst separation, and recycling. Fig. 11 shows the promising reaction scheme [27].

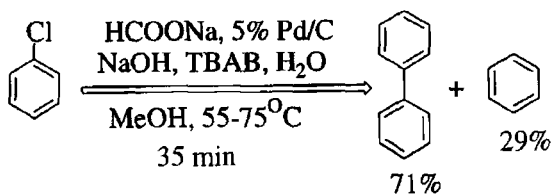


Figure 11. The coupling of chlorobenzene into biphenyl

If the starting material is para-chlorotoulene instead of chlorobenzene one can expect that 4,4'-DIBP can be selectively prepared, as shown in Table 2. From this table it can be seen that the selectivity to 4,4'-DMBP can be achieved at 64% by carefully selecting reaction conditions and reaction media.

Table 2. Pd-catalyzed reductive reaction with various starting materials.

Substrate	t, min	% conv.	% selec., Coupling	% selec., reduction
chlorobenzene	35	100	71	29
bromobenzene	20	100	73	27
4-chlorotoluene	100	100	64	36
2-chlorotoluene	120	100	32	68
4-chloro-1,1,1,-trifluorotoluene	55	100	70	30

**reaction conditions:* substrate, 22 nunol; NaOH, 62.5 nunol; HCOON_a, 26.4 nunol; catalyst, PdC, 0.53 mol% of substrate on Pd basis; TBAB, 4.9 mol % of the substrate; H₂O, 3.5g; temperature, 65°C; agitation speed, 900 rpm; solvent, MeOH (total volume) 25 ml.

Many researchers [28,29] have also conducted the preparation of 4,4'-DMBP by using toluene instead of halotoulene. The comparison of the results from literature is shown in Table 4.2. From this summary it can be seen that the effective catalysts are Pd-based compounds such as Pd (OAc)₂, PdCl₂ and Pd(OTf)₂ plus co-catalysts such as H(acac), HOAc, NaOAc, HClO₄, and HOTf. The most effective catalysts are Pd(OTf)₂ and HOTf, which can operate at low temperature and achieve relatively high toluene conversion. However, in all cases, the selectivity to 4,4'-DMBP is relatively low because in the presence of strong acid or high temperature,

the formed product 4,4'-DMBP will convert into the thermodynamically stable isomer like 3,4'-DMBP. A general proposed mechanism was proposed for aryl coupling in the following Fig. 12.

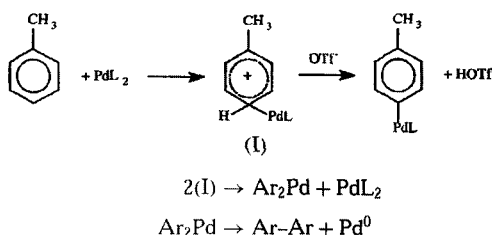


Figure 12. The reaction mechanism for Pd-catalyzed aryl coupling reaction

High selectivity to 4,4'-DMBP through carbon-carbon coupling can be achieved by carefully selecting reaction conditions and catalyst systems. If the methyl group can be replaced by other functional groups such as MeOOC and MeO during coupling reaction and the product can sustain high selectivity, then this routine could be a promising way for 4,4'-substituted biphenyl including 4,4'-biphenyldicarboxylic acid. However, The drawback for this coupling is that chemical reactions are conducted under either liquid-solid or strong acid conditions, thus, in practice, the cost for separation and recycling processing, and the potential environmental issues should be kept in mind.

4.2 Transmethylation of BP with polymethylbenzene into 4,4'-DMBP

Emig et al. [21] reported methylation with methanol and transmethylation of BP with polymethylbenzene over different type zeolites by using autoclave as a reactor. The reaction conditions applied for all experiments are listed in Table 3.

Table 3. Reaction conditions

Initial volume of reaction mixture	300 ml
Catalyst loading	2.8 wt%
Reaction temperature	523 K
Reaction pressure	3 MPa
Initial biphenyl concentration	0.19 mol/l
Initial alkylating agent concentration	80 mol/l
Internal reference concentration	0.09 mol/l

The basic aim of the investigation was to determine whether it is possible to synthesize 4- or 4,4'-methylated biphenyl in high selectivity during the methylation of biphenyl by simultaneously varying the catalyst type and the alkylating agent and the results are summarized in Table 4.

The definition of Y_{para} and S_{para} in the table is as follows:

- Yield of para-isomers

$$Y_{\text{para}} = Y_{4\text{-MBP}} + Y_{4,4'\text{-DMBP}} = \frac{n_{4\text{-MBP}}}{n_{\text{BP},0}} + \frac{n_{4,4'\text{-DMBP}}}{n_{\text{BP},0}}$$

where n_i represents the moles of species i .

- Selectivity of para-isomers

$$S_{\text{para}} = Y_{\text{para}} / X_{\text{BP}}$$

$$\text{where } X_{\text{BP}} = (n_{\text{BP},0} - n_{\text{BP}}) / n_{\text{BP},0}$$

Table 4. Evaluation of effects on catalyst structures and alkylating agents on selectivity of 4- and 4,4'-DMBP

Zeolite catalyst	Alkylating agent ($\gamma_{\text{para}} S_{\text{para}}$ [%])		
	Methanol	Durene	Pentamethylbenzene
HY-5	9.4/27.0	22.3/51.9	21.7/35.9
HY-11	-	15.6/40.4	23.8/41.1
US-HY-25	-	21.1/35.3	28.8/44.5
HM-5	9.3/15.3	3.4/19.9	-
HM-11	11.9/16.3	11.2/16.1	-
H-ZSM-5/50	0.0/0.0	-	-
H-ZSM-5/100	0.0/0.0	-	-
H-ZSM-5/400	0.0/0.0	-	-

As can be seen from the above Table, the alkylation of biphenyl with methanol over HY, HM and HZSM-5 resulted in low values for both Y_{para} and S_{para} , indicating low catalyst activity and the absence of shape selective catalysis. Under batch conditions, zeolite ZSM-5 shows totally inactivity for alkylation.

The performance of the catalysts, however, increased when using bulkier alkylating agents and changing the mechanism of the reaction from alkylation to transalkylation. The relatively low values for Y_{para} and S_{para} for durene/mordenite combination indicated that 2D framework of mordenite is not able to host such a bulky transition state. Only by using catalysts with a 3D framework, including spacious supercages such as faujasite, is there enough space for poplymethylbezene-biphenyl transition state complex to be formed.

Figs. 13-15 show the transmethylation of BP with pentamethylbenzene over unmodified and modified US-HY-26, the later was prepared by 10% aqueous solution of tributylphosite (US-HY-26-TBP), by 1M aqueous phosphoric acid (US-HY-26-P) and by an atmosphere saturated with water vapor (US-HY-26-H₂O).

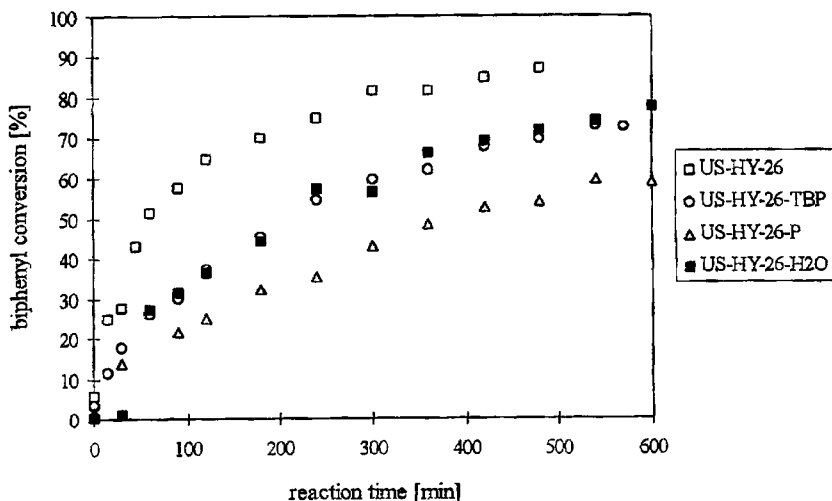


Figure 13. Effect of catalyst modification on biphenyl conversion

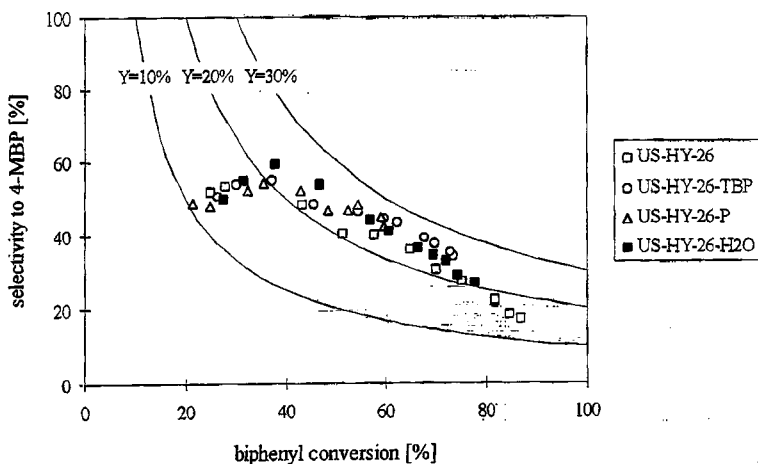


Figure 14. Effect of catalyst modification of US-HY-26 on 4-MBP selectivity

All modified catalysts show decreased activity (Fig. 13), which is in agreement with the decrease in acidity after modification. While using untreated US-HY-26 biphenyl conversion approached nearly 90% after 8h of reaction time. Even after 10 h the modified catalysts showed a conversion which is 20~30% lower. The least active catalyst turned out to be US-HY-26-P.

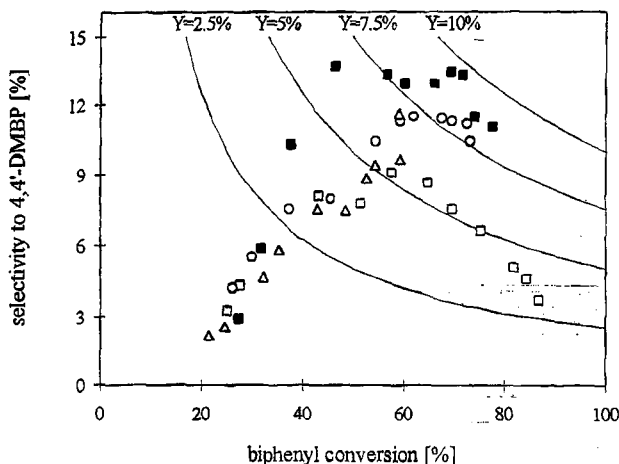


Figure 15. Effect of catalyst modification of US-HY-26 on 4,4'-DMBP selectivity

The selectivity to 4-MBP as a function of biphenyl conversion in Fig. 14 reveals that with increasing conversion selectivity decreases because of the consecutive reaction to dimethylbiphenyl and the isomerization to 3-MBP, the former was also confirmed in Fig. 15 by the changes in 4,4'-DMBP with biphenyl conversion. It is interesting to note that the catalyst modified with water vapor (US-HY-26-H₂O) shows the highest selectivity to 4,4'-DMBP perhaps because of the utilization of Bronsted acid sites on the zeolite surface in the presence of water vapor.

By comparison of 4,4'-DEBP selectivity obtained from transethylation of BP over HY zeolite (as high as 90%), one can, however, find out that high selective preparation of 4,4'-DMBP with transmethylation is much more challenging.

4.3 Selective methylation over ZSM-5 zeolite in a fixed bed

Methylation for 4,4'-DMBP was not achieved under the batch conditions. The benefits of 4,4'-DMBP as the precursor of 4,4'-biphenyldicarboxylic

acid against other 4,4'-isomers and the curiosity of science, however, still motivated the authors to explore the possible way to selectively obtain 4,4'-DMBP. Based on the accumulated experience in polyaromatics, the researchers at Pennsylvania State University have published a series of papers [13,14,15,16, 30] on selective synthesis of 4,4'-DMBP through methylation over ZSM-5 type zeolite under fixed-bed conditions.

Table 5 summarizes 4-MBP methylation with methanol over 12-member ring zeolites such as HY and HM and over the 10-member ring zeolite ZSM-5.

Table 5. Methylation of 4-MBP over various zeolite catalysts^a

	TOS (min)	Conv. (%)	Yield (%)				MBP composition (%)			DMBP composition (%)						
			BP	MBPs	DMBPs	Others	2-	3-	4-	2,2'-	3,3'-	3,4'-	4,4'-	2,3'-	Others	
Zeolite (SiO ₂ /Al ₂ O ₃)																
HY(40)	60	72.11	3.76	29.50	13.10	25.75	2.30	49.10	48.60	6.03	14.58	18.78	9.31	19.24	32.06	
HM(38)	63	80.44	0.96	29.04	21.16	29.28	8.37	51.38	23.37	0.33	16.07	17.06	12.05	20.70	33.79	
HZSM-5(50) ^b	63	38.22	0.96	19.02	7.49	10.75	0.17	12.29	76.46	0.70	5.90	42.31	26.42	9.00	15.66	
	120	19.13	0.68	3.87	14.33	0.25	0.09	4.47	95.43	0.00	1.54	42.85	37.15	10.12	8.35	
HZSM-5(50), temp. (°C) ^b																
280	120	25.32	1.13	9.44	13.15	1.60	0.08	11.14	88.74	0.46	3.57	46.16	36.05	10.04	3.75	
350	110	56.88	1.26	41.02	13.10	1.50	1.90	47.74	50.36	0.63	18.65	41.69	18.18	9.56	11.29	
400	110	68.18	1.31	53.28	12.31	1.28	7.26	55.35	37.39	0.49	23.64	35.01	10.64	7.55	22.66	
HZSM-5(50), gas flow (N ₂ , ml/min) ^b																
40	102	43.81	0.90	24.74	14.58	3.59	0.37	30.20	69.43	0.73	10.40	43.84	29.14	9.31	6.65	
60	110	35.78	1.25	19.33	14.22	0.98	0.34	22.79	76.87	0.99	8.38	38.18	37.50	8.52	5.82	
HZSM-5(50), feed (ml/h) ^b																
4.0	120	11.73	1.08	1.49	8.48	0.68	0.04	1.62	98.34	0.00	0.71	41.98	37.15	10.97	3.42	
6.0	110	6.79	1.10	0.74	4.68	0.27	0.00	0.79	99.21	0.00	0.00	42.31	37.15	11.75	5.98	
HZSM-5(50), modification (P, wt%) ^b																
TPP-CBV(8.2)	60	19.87	0.72	7.49	11.02	0.64	0.25	8.30	91.45	0.27	3.99	21.51	56.62	5.08	12.52	
	120	15.85	0.67	4.09	10.52	0.57	0.18	4.45	95.36	0.10	3.14	24.24	60.65	5.61	6.27	
AHP-CBV(2.6)	60	9.29	0.67	1.52	7.03	0.07	0.13	1.52	98.35	0.00	2.13	20.77	65.72	4.41	6.97	
	120	6.93	0.69	0.93	5.26	0.05	0.09	0.90	99.01	0.00	1.52	23.76	63.50	4.56	6.65	

^a Typical reaction conditions: reaction temperature 300 °C, feed 2 ml/h, methanol:4-MBP:mesitylene = 1:5:5 (mol), carrier gas N₂ 20 ml/min, catalyst 0.30 g.

^b The reaction over HZSM-5 and reaction conditions are the same if not specifically noted.

4-MBP methylation gave a whole range of products over 12-membered ring zeolites HY and HM including all the possible isomers such as IBP, DIBP and TriBP and polymethylbiphenyl. The products are very complex, and there is no sign of selectivity for the target product.

The typical results for methylation of 4-MBP over unmodified HZSM-5 revealed the quick deactivation of the parent zeolite. In the initial stage the isomerization of 4-MBP occurs significantly even though a high ratio of methanol to 4-MBP (5:1) was employed in the feed. Among MBP isomers, the main product is 3-MBP, which is in good agreement with the equilibrium. The close content (~40%) between 3,4'-DMBP and 4,4'-DMBP implies that HZSM-5 shows moderate selectivity to 4,4'-DMBP

(the percentage of thermodynamically favorable 3,4'-DMBP should be much higher than that of 4,4'-DMBP according to the equilibrium) under the conditions employed in this work. This observation is quite different from the observation in literature in a batch reactor.

Further investigations on reaction conditions (reaction temperature, feed rate and gas flow) and on modification were carried out to increase the selectivity of HZSM-5 (Table 5). It is clear that increasing temperature from 280 to 400 °C can significantly enhance 4-MBP isomerization (from yield of 9.44% to 53.28%, respectively) since the products from alkylation changes a little, around 13%. DMBP composition reveals that as reaction temperature increases higher than 300°C, the yield of the desired product, 4,4'-DMBP, is greatly suppressed, and the formation of 3,3'-DMBP is favored.

The carrier gas flow rate of 20–60 ml/min can increase the selectivity of 4,4'-DMBP, especially in the initial reaction stage. This may be attributed to the faster removal of 4,4'-isomer from the surface at higher gas flow. In the later stage of methylation, the portion of 4,4'-DMBP reaches almost the same value regardless of gas flow rate, this is due to the quick deactivation of external surface (see Fig. 16).

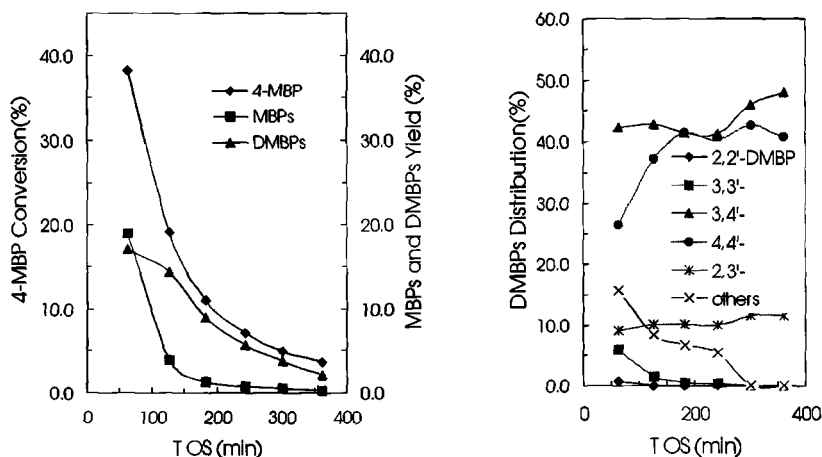


Figure 16. Catalyst activity and the product distribution of MBP and DMBP isomers from 4-MBP methylation over HZSM-5.

Modification of surface was initially carried out by using phosphors salts with different kinetic size, triphenyl phosphate (TPP) and ammonium phosphors acid (AHP). HZSM-5 modified with triphenyl phosphate, TPP-CBV(8.2), lowers conversion and depresses isomerization as compared to

the unmodified parent zeolite. The product distribution indicates that using larger P compound as a poison of external surface sites of HZSM-5 is an effective way to get the desirable product 4,4'-DMBP (up to 55%). A more effective way was found to improve 4,4'-DMBP selectivity by impregnation of ZSM-5 with ammonium hydrogen phosphate (2.6 wt%), as shown in Figs. 17 and 18. Even with the lower percentage of P (2.6 wt%), as compared to the sample of TPP-CBV(8.2), the conversion of 4-MBP over AHP-CBV(2.6) is much lower than that over TPP-CBV(8.2). This can be attributed to the different location of the phosphorus compounds on HZSM-5 zeolite. Because of its larger size, triphenyl phosphate is mainly located on the external surface of HZSM-5, and the internal surface area is still relatively high even with higher P content (357 m²/g TPP-CBV(8.2)). In the case of ammonium hydrogen phosphate, it can enter the internal surface in addition to the external surface, and can cause surface area decrease even at the lower P content (293 m²/g AHP-CBV(2.6)). Moreover, over AHP-CBV(2.6) the isomerization of 4-MBP is further suppressed, and the selectivity of 4,4'-DMBP is further improved. Distribution of DMBP isomers over AHP-CBV can reach as high as 65%. Thus, the target molecule can be enhanced dramatically by simultaneous modification of the internal and external surface of HZSM-5.

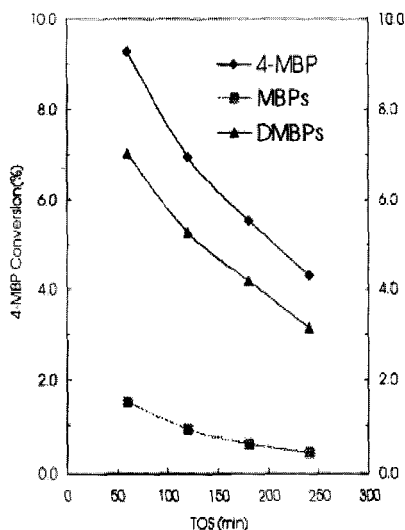


Figure 17. Conversion and the production yield from 4-MBP methylation over CBV(2.6)

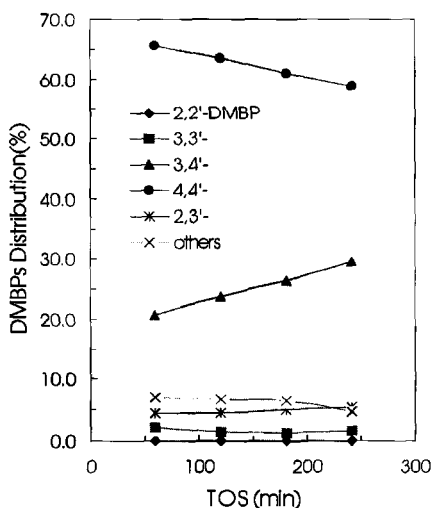


Figure 18. DMBP distribution from 4-MBP methylation over AHP-AHP-CBV(2.6)

ZSM-5 modified with a series of metal oxides such as MgO, CaO, SrO, BaO and ZnO with different content through impregnation method was also employed for 4-MBP methylation and the results demonstrated that proper MgO content (5.6wt%) can be very effective for biphenyl methylation and the selectivity can be increased as high as 80%. The correlation of characterization techniques of XRD, TGA, TPD and chemical analysis with catalytic reaction revealed that the high selectivity of 4,4'-DMBP over MgO samples largely results from the depression of second reaction of formed 4,4'-isomers such as isomerization, dealkylation and further alkylation into polymethylbiphenyls.

5 Conclusion

Specialty chemicals 4,4'-dialkylbiphenyl can be obtained selectively from alkylation and transalkylation of biphenyl and its derivatives with corresponding alkylating agents using nanoporous acidic solids as catalysts. One should bear in mind the following issues when dealing with shape-selectivity of 4,4'-isomers (as well as other polycyclic hydrocarbons):

- The relation of isomer composition with its transformation into other thermodynamically stable isomers like 3,4'- and 3,4'-isomers. The desired specialty chemicals such as 4,4'-dialkylbiphenyl and 2,6-dialkylnaphthalene are usually the slimmest or the most linear molecules and not necessarily favored by thermodynamics among its numerous isomers.
- Matching the alkylating agent with pore structure of molecular sieves is critical for this research. To fully exploit concepts of reactant, product and transition state shape selectivities, one can first use steric hindrance to eliminate unnecessary isomers that have adjacent substituted groups, and simplify isomer composition, then fine-tune the relationship between the desired product and zeolite pore channels by selecting appropriate alkyl groups and molecular sieve catalysts.
- The control of catalytic sites on internal and external surface is also important. If possible, eliminating the active sites on external surface to the extent possible is of great value. The presence of active sites on external surface will shift the selective product out from the channels into thermodynamic and non-regioselective composition through secondary isomerization besides the undesired side reactions such as cracking, dealkylation and alkylation. One can minimize side reactions

by selectively covering active sites by using oxides, lowering acid strength by using isomorphous substitution of Al, by transition metals and poisoning acid sites by using large modifiers.

- The desired alkylating groups (e.g., methyl or isopropyl group), or the desired product from alkylation, also depends on the needs of polymer applications. There are multiple choices of precursors for introducing the same alkyl groups, which in turn, also affect the catalyst activity, selectivity, and stability.

6 Acknowledgments

CS wishes to acknowledge Prof. Yoshihiro Sugi of Gifu University, Japan, for helpful discussions on the alkylation of polycyclic hydrocarbons, and Dr. Uday T. Turaga for his helpful comments on the draft manuscript.

References

1. Song C. and Schobert H. H., Opportunities for developing specialty chemicals and advanced materials from coals, *Fuel Processing Technol.*, **34** (1993) pp. 157-196.
2. Sugi, Y. and Toba M., Shape-selective alkylation of polynuclear aromatics, *Catal. Today* **19** (1994) p. 187.
3. Song C., Selective conversion of polycyclic hydrocarbons to specialty chemicals over zeolite catalysts, *Cattech.* **6** (2002) pp. 64-77.
4. Song C., Garces J. M and Sugi Y. (Eds), Shape-Selective Catalysis. Chemicals Synthesis and Hydrocarbon Processing, American Chemical Society, Washington DC, ACS Symposium Series, Vol. **738**, (1999) p. 410.
5. (a) Weisz P. B., Molecular shape selective Catalysis, *Pure Appl. Chem.* **52** (1980) pp 2091-2103; (b) Csicsery S. M., Catalysis by shape selective zeolites - science and technology, *Pure Appl. Chem.* **58** (1986) pp. 841-856.
6. Song C., Recent advances in selective conversion of polycyclic hydrocarbons into specialty chemicals over zeolite catalysts, *Catalysis*, Royal Society of Chemistry, **16** (2002) pp. 272-321.
7. Sugi Y., Tu X-L., Matsuzaki T., Hanaoka T-A., Kubota Y., Kim J-H., Matsumot M, Nakajima K. and Igarashi A., The effect of propylene pressure on shape-selective isopropylation of biphenyl over H-mordenite, *Catal. Today*, **31** (1996) pp. 3-10.
8. Ahedi R. K., Tawasa S., Kubota U., Sugi Y. and Kim J. H., Shape-selective alkylation of biphenyl catalyzed by H-[Al]-SSZ-31 zeolite, *J. Mol. Catal. A: Chem.* **389** (2002) pp. 1-14.
9. Matsuda T., Urata T., Saito U. and Kikuchi E., Effect of SiO₂/Al₂O₃ ratio on the catalytic properties of mordenite for alkylation of biphenyl with propene, *Appl. Catal. A: General* **131** (1995) pp. 215-224.

10. Tu, X., Matsumoto M., Maeda T., Sugi Y., Matsuzaki T., Hanaoka T., Kubota Y. and Kim J-H., Shape-selective ethylation of biphenyl over a highly dealuminated H-mordenite, *Micropor. Mater.* **3** (1995) pp. 593-595.
11. Tawada S., Sugi Y., Kubota Y., Imada Y., Hanaoka T., Matsuzaki T., Nakajima K., Kunimori K., and Kim J-H., Ceria-modification of H-mordenites The deactivation of external acid sites in the isopropylation of biphenyl and the isomerization of 4,4'-diisopropylbiphenyl, *Catal. Today* **60** (2000) pp. 243-253.
12. Sugi. Y., Tawada, Sugimura, T., Kubota Y., Hanaoka T., Matsuzaki T., Nakajima, K. and Kunimori K., Shape-Selective isopropylation of biphenyl over H-mordenites Relationships of bulk products and encapsulated products in the pores, *Appl. Catal. A: General* **189** (1999) pp. 251-261.
13. Guo X. W., Shen J. P., Sun L. and Song C. S., Effects of hydrothermal treatment conditions on the catalytic activity of HZSM-5 zeolites in the methylation of 4-methylbiphenyl with methanol, *Abstracts of Papers of the American Chemical Society* **224**: 006-CATL, 2002.
14. Guo X. W., Shen J. P., Sun L. and Song C. S., Methylation of 4-methylbiphenyl with methanol over modified HZSM-5 zeolite catalysts, *Abstracts of Papers of the American Chemical Society* **223**: 177-IEC, 2002.
15. Guo X. W., Shen J. P., Sun L., Song C. S. and Wang X. S., Shape-selective methylation of 4-methylbiphenyl into 4,4'-dimethylbiphenyl over zeolite HZSM-5 modified with metal oxides of MgO, CaO, SrO, BaO and ZnO, *Catal. Lett.* in press
16. Shen J. P., Sun L. and Song, C. S. Shape-selective synthesis of 4,4'-dimethylbiphenyl. 1. Methylation of 4-methylbiphenyl over modified zeolite catalysts, *Catal. Lett.* **65** (2000) pp. 147-151.
17. Bandyopadhyay M., Bandyopadhyay B., Tawada S., Kubota Y. and Sugi Y., Catalytic performance of silicoaluminophosphate (SAPO) molecular sieves in the isopropylation of biphenyl, *Appl. Catal. A: General* **225** (2002) pp. 51-62.
18. Matsuda T., Kimura T., Herawati E., Kobayashi C. and Kikuchi E., Shape selective alkylation of biphenyl with propene on SAPO-11 catalysts, *Appl. Catal.* **136** (1996) pp. 19-28.
19. Sugi Y. and Kubota Y., in: J.J. Spivey (Ed.), *Catalysis*, volume 13, a Specialist Periodical Report, Royal Society of Chemistry, 1997, **Chapter 3**, pp. 55-84.
20. Tu X., Matsumoto M., Maeda T., Sugi Y., Matsuzaki T., Hanaoka T., Kubota Y. and Kim J-H., Shape-selective ethylation of biphenyl over a highly dealuminated H-mordenite, *Micropor. Mater.*, **3** (1995) pp. 593-595.
21. Brechtelsbauer C. and Eming G., Shape selective methylation of biphenyl within zeolites: An example of transition state selectivity, *Appl. Catal. A: General* **161** (1997) pp. 79-92.
22. Takeuchi G., Shimoura Y. and Hara T., Selective transalkylation of biphenyl over solid acid catalysts, *Appl. Catal. A: General* **137**(1) (1996) pp. 87-91.
23. Lee G.S. Burdett K.A., and Maj J.J., Process for the preparation of para, para'-polyphenyldicarboxylic acid, US patent 4996353, 1991.
24. Weiner H., Blum J. and Sasson Y., Transfer hydrogenolysis of aryl halides and other hydrogen acceptors by formate salts in the presence of palladium/carbon catalyst, *J. Org. Chem.* **56** (1991) pp. 6145-6148.
25. Marques C. A., Selva M. and Tundo P., Facile Hydrodehalogenation with H₂ and Pd/C Catalyst under Multiphase Conditions. Part 2. Selectivity and Kinetics, *J. Org. Chem.* **59** (1994) pp. 3830-3837.

26. Hassan J., Penalva V., Lavenot L., Gozzi C., and Lemaire M., Catalytic alternative of the Ullmann reaction, *Tetrahedron* **54** (1998) pp. 13793-13804.
27. Mukhopadhyay S., Ratner S., Spornat A., Qafisheh N. and Sasson Y. Heterogeneous Pd-Catalyzed biphenyl synthesis under moderate conditions in a solid-liquid two phase system, *Organic Process & Development*, **6** (2002) pp. 297-300.
28. Stille J. K. Palladium-catalyzed coupling reactions: mechanism of reductive elimination, progress report, US Department of Energy, DE-AC02-78ER04903. A003.
29. Xu B. Q., Sood D., Iretskii A.V. and White M. G., Direct synthesis of dimethylbiphenyls by toluene coupling in the presence of palladium triflate and triflic acid, *J. Catal.* **187** (1999) pp. 358-366.
30. Shen J. P., Sun L. and Song C., Shape-selective methylation of 4-methylbiphenyl into 4,4'-dimethylbiphenyl over modified ZSM-5 catalysts, *Stud. Surf. Sci. Catal.* **135** (2001) p. 4055.

CATALYSIS INVOLVING MESOPOROUS MOLECULAR SIEVES

W.S. AHN AND G.J. KIM

School of Chemical Science and Engineering, Inha University, Incheon, Korea 402-751

E-mail: whasahn@inha.ac.kr

G. SEO

*Department of Chemical Technology, Chonnam National University, Kwang Ju, Korea
500-757*

Surfactant-templated mesoporous silicas discovered by Mobil research group, due to extremely high surface areas and large uniform pores, have attracted explosive interests in recent years. In this work, an overview of the research activities reported on the applications of the mesoporous materials in catalysis is presented. These will be narrated in the sequence of acid-base, redox, and chiral catalysis, in which either directly synthesized MCM-41 type materials embedded with various hetero-atoms or post-synthetically grafted with a suitable transition metal precursors are employed as catalysts. Organic functionalization is another very important synthesis protocol to prepare such catalysts. Applications of the mesoporous materials as supports in relatively minor class of reactions were treated in a concise tabular form summarizing important findings only. Enzyme catalysis using mesoporous material as immobilization matrix was not included in this review. Much attention was devoted explaining the logic behind the catalyst preparation for catalytic applications, and a short summary of the characterization results was included when necessary.

1 Introduction

Mesoporous (alumino) silicate molecular sieves such as MCM-41, -48, HMS and SBA-15, due to extremely high surface areas ($> 1000 \text{ m}^2/\text{g}$) and large uniform pores which can be subjected to precise pore size control ($15\text{-}100 \text{ \AA}$), have a wide range of potential applications in catalysis and sorption of large organic molecules. High dispersion of active sites, reduction in diffusion resistances, and accommodation of relatively large guest molecules in the mesoporous channel are the envisioned advantages of the material.

In addition, the surface of the mesoporous materials is usually covered with a significant portion of silanol groups, which can be used as anchoring sites for further organic functionalization. If necessary, hydrophobicity/hydrophilicity of the surface can also be adjusted by manipulating the silanol group density of the mesoporous material by conducting a suitable post-synthetic silylation treatment. These are the fundamental motivations behind the active research activities on mesoporous silicates for catalytic applications. In this chapter, attention will be given to an inspection of recent open literatures dealing with the utilization of mesoporous molecular sieves as catalysts or as support material for catalytic applications. Excellent reviews on the topic by Corma [1] and Arends et al [2] are already available, and it is attempted in this work to point out the important findings of relatively early work and to extend the review work covering the outcome of the more up to date research activities. For convenience and clarity, it is decided to present the contents of this review in the sequence of 1) acid-base catalysis, 2) redox catalysis, 3) asymmetric catalysis, and 4) others.

2 Acid/base catalysis

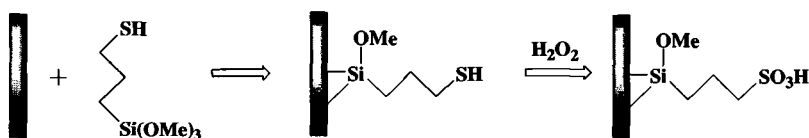
2.1. Preparation and applications in acid-catalyzed reactions

The pure silica MCM-41 has only weak acid sites on its surface, which are generated either by water molecules hydrogen-bonded to the surface hydroxyl groups or by protons exchanged with surface cations, much like in amorphous silica [3]. Al-MCM-41, on the other hand, is made of $\text{Si}(\text{OH})\text{Al}$ and $\text{Si}-\text{O}-\text{Al}(\text{OH})-\text{O}-\text{Si}$ species which act as Brönsted acid sites, and trigonal Al atoms formed by calcination, which behave as strong Lewis acid sites. The reversible conversion between Brönsted and Lewis acid sites along with calcination and hydration treatments is similar to that in zeolites or amorphous silica-alumina.

Al-containing mesoporous materials are generally prepared from the mixtures of Si and Al sources in the presence of quaternary ammonium surfactants as templates. Al-MCM-41 prepared using Al-isopropoxide, rather than chloride or nitrate, was found to be the more promising acidic catalyst and good support for platinum catalyst for hydrocracking [4]. Post-synthetic grafting with Al-isopropoxide in hexane is another way to prepare them [5]. Grafted Al atoms are initially octahedrally coordinated and converted to tetrahedral form after calcination. AlCl_3 or $\text{Al}(\text{NO}_3)_3$ has also been employed for grafting, and aluminum content in the grafted samples is usually higher than that in those prepared via the conventional direct synthesis.

According to IR observation, the intensities of the bands of Al-MCM-41 at 3715 and 3530 cm^{-1} increase with Al concentration, and a broad band at ca. 3660 cm^{-1} shows the same trend, indicating the formation acid sites [6]. The relative intensities of Brönsted to Lewis acid sites increase with Al incorporation, indicating that Brönsted acid sites are directly proportional to Si-O-Al-O-Si surface structure [7]. While the Brönsted acid sites of the H-Al-MCM-41 with lower Si/Al ratios retain a considerable amount of pyridine even after high temperature evacuation, the acidity of H-Al-MCM-41 is reported to be lower than zeolites and more comparable to those of amorphous aluminosilicates. The preparation of mesoporous molecular sieves with strong acid sites has not been successful yet. But recently, Al-MCM-41 in which the surface of mesopores is consisted of zeolite fragments was prepared by assembling the MFI-zeolite framework dissolved in alkaline solution using cetyltrimethylammonium bromide [8]. This dual structured material was active in the catalytic conversion of cumene to benzene, which proceeds only on strong Brönsted acid sites.

Anchoring acidic groups on the pore wall surface by post-synthetic grafting was also used to prepare acidic mesoporous materials (scheme 1) [9,10]. Alternatively, direct co-condensation of mercaptopropyltrimethoxy-silane (MPTMS) with tetraethylorthosilicate (TEOS) in the presence of a surfactant produces mesoporous materials with thiol groups. Extraction of surfactant species from the as-synthesized material by acidified ethanol under reflux, followed by subsequent oxidation of thiol to sulfonic acid using hydrogen peroxide, produces a mesoporous material containing sulfonic acid groups. Mesoporous materials prepared in this way had shown strong acidity, but has a poor long range order. Considerable decreases in pore volume and surface areas were observed after oxidation treatment.



Scheme 1. Anchoring of sulfonic acid groups [9].

SBA-15 containing a sulfonic acid group was prepared directly from the mixture composing of TEOS, MPTMS, and hydrogen peroxide in the

presence of a block copolymer template [11]. Average pore diameter of 60 Å and surface area of 800 m²/g were measured together with enhanced hydrothermal stability. It has a considerable amount of sulfonic groups, 1-2 mequiv of H⁺g⁻¹ of SiO₂. The presence of Brönsted acid sites was confirmed from the ³¹P MAS NMR spectra of adsorbed triethylphosphine, which are stronger than those present in the conventionally prepared H-Al-MCM-41. SBA-2 [12] and SBA-12 [13] containing sulfonic acid groups were also prepared, but stacking faults in the structure resulted in low catalytic activities in the esterification of fatty acid with glycerol. SBA-15 containing an arenesulfonic acid group [14] was produced via the co-condensation of 2-(4-chlorosulfonyl phenyl) ethyltrimethoxysilane and TEOS. Mesoporous materials containing phosphonic acid groups was prepared following the same procedure: the co-condensation of TEOS and trimethoxysilylpropyldiethylphosphonate in the presence of triblock copolymers under acidic conditions [15]. Direct sulfonation of phenylene group in the pore walls of uniform benzene-containing hybrid mesoporous silica was also attempted, recently [16].

The application of heteropoly acids (HPA) in the catalytic reactions involving non-polar reactants is limited because non-polar reactants are adsorbed on extremely small surface area of the HPA acids. However, finely dispersed HPA supported on a mesoporous material can provide high activity in acid-catalyzed reactions of bulky non-polar reactants due to their large exposed surface area and mesopores of the host. HPA's impregnated on mesoporous materials do not show any diffraction peaks at low loading, but UV-Vis and IR absorption bands verify their existence [17]. The abnormally small diffraction peaks indicate that HPA is dispersed in mesopores as Keggin units without keeping their secondary structure. At high loadings, on the other hand, some of the impregnated HPA are aggregated on the external surface and exhibit sharp diffraction peaks. Spectroscopic studies strongly suggest that the acidity of HPA supported on MCM-41 is the result of the complexation between HPA molecules and the hydroxyl groups of mesoporous material [18]. Whilst a notable increase in acidity is observed at low loadings (up to 23%), it decreases somewhat at higher loadings of HPA, depending on the dispersion. The dispersed state of HPA in mesoporous materials can be deduced from the differences in adsorption behaviors of polar and non-polar materials [19]. The adsorbed amount of polar materials such as methanol and ethanol does not change after HPA impregnation, only its adsorption rate becomes considerably slow, because polar materials can be adsorbed as pseudo-liquid phase in mesopores. On the other hand, the adsorbed amount of a non-polar material such as butene or pentene increases considerably with HPA impregnation. Since non-polar materials are adsorbed only on the external surface of HPA, a significant increase in

the amount of butene adsorbed indicates that HPA is dispersed in the mesopores as fine aggregates. However, mesoporous materials suffer severe structural distortion at high HPA loadings, which leads to a considerable loss in long range order, and a partial blocking of mesopores with HPA can result in a small decrease in the amount of butene adsorbed. A reduction in the amount of benzene adsorbed on MCM-41 after HPA impregnation was explained as a consequence of narrowing of pore entrance and the occupation of pore volume by HPA, but no clear evidence was presented [20].

Acidic mesoporous materials are promising catalysts in several acid-catalyzed reactions involving large organic molecules: cracking of middle distillates, alkylation of bulky organic substrates, and production of fine chemicals. While the activity of Al-MCM-41 in catalytic cracking of *n*-heptane, which is catalyzed by strong acid sites, was much lower than with ultra-stable zeolite Y [21], the increased accessibility of large molecules to acid sites in mesoporous materials achieve conversions similar levels to zeolites in the case of gas oil cracking. Extensive studies on cracking and hydrocracking over mesoporous materials were undertaken [4,21], but the low acidity and large carbon deposit on mesoporous materials remain as problems. The higher isomerization selectivity of platinum catalysts supported on MCM-41 relative to that on silica-alumina suggested that mesoporous materials are more suitable for the hydroisomerization as a catalyst support rather than for hydrocracking [23]. The catalytic activity of Al-containing mesoporous material in the alkylation of benzene with isobutene was again low compared to that of BEA zeolite [23]. Al-MCM-41 catalyst with weak acidity gives a lower selectivity to cymenes in the liquid phase alkylation of toluene with propylene [24]. Mesopores enhance the formation of polyalkylates, but weak acid sites do not accelerate cracking sufficiently. However, Al-MCM-41 showed high selectivity to branched dimers in the oligomerization of butene [25].

Friedel-Crafts alkylation and acylation of bulky chemicals were carried out on Al-MCM-41 catalysts, and the shape selectivity of the Al-MCM-41 was demonstrated [26]. Jasminaldehyde was synthesized through three consecutive reactions in one-pot synthesis using Al-MCM-41; acetalization of heptanal with methanol followed by hydrolysis of acetal and finishing with aldol condensation. The high selectivity to jasminaldehyde is achieved by maintaining low concentration of heptanal delivered by slow hydrolysis of acetal, which prevents the undesirable self-condensation of heptanal. Al-MCM-41 does not show improved activity in the benzylation of biphenyl with benzyl chloride compared to amorphous silica-alumina catalyst [27]. Although Al-MCM-41 is more active due to its large surface area, the amorphous silica-alumina catalyst shows longer catalyst life because larger pores of the amorphous catalyst

are not easily blocked by deposited carbon. MCM-41 was also used as a support for AlCl_3 in the Friedel-Crafts alkylation of difluorobenzene with 2-chloropropane [28]. The long lifetime and superior catalytic activity of the AlCl_3 supported catalyst demonstrated its high potential for industrial applications.

Since mesoporous materials have large enough pores to eliminate the influence of pore structure on product distribution, the effect of acid site concentration on the selectivity to the skeletal isomerization of *n*-butene can be more clearly verified [29,30]. High selectivity to *iso*-butene is observed on the mesoporous KIT-1 with low aluminium content in the skeletal isomerization of *n*-butene. The distant location of activated 1-butene molecules due to the low concentration of acid sites in KIT-1 is expected to suppress the formation of dimer and trimer which would be cracked to various hydrocarbons and lowers the selectivity to *iso*-butene. Elevated reaction temperature was required to achieve high conversions to *iso*-butene due to its weak acidity. The skeletal isomerization of 1-butene was also studied over SBA-2 [31]. Although the conversion and selectivity to butenes were high, the catalyst deactivated due to carbon filling on the pores.

The catalytic activity of tungstophosphoric acid (HPW) supported on the pure silica MCM-41 has been evaluated in the cracking of *n*-hexane [20], which showed a very high activity at a temperature as low as 200 °C. However, the catalyst deactivated rapidly due to coke deposition on the catalyst. HPW supported on mesoporous materials also showed high catalytic activity in alkylation and isomerization reactions. To increase the resistance to leaching by solvents, Cs-substituted HPW catalyst supported on MCM-41 mesoporous material was employed in the alkylation of 1,3,5-trimethylbenzene with cyclohexene [32]. This well-dispersed, supported HPW catalyst showed improved catalytic performance and high thermal stability as well as higher resistance to leaching. Gas phase alkylation of 2-isopropyl-naphthalene with isopropylalcohol was also carried out over HPW catalysts supported on KIT-1 mesoporous material [33]. The conversion and the selectivity to β,β -diisopropyl-naphthalene were high over the HPW catalyst with moderate loading. However, the selectivity of zeolite MCM-22 was much higher and the product shape selectivity attributable to mesopores was not observed in this alkylation reaction. Supporting HPW catalyst over Cs-modified MCM-41 was found to be more active in the reaction of *n*-C₄ isomerization than the conventionally prepared catalyst by impregnating a cesium salt of HPA; Cs-modified MCM-41 improved the dispersion of HPW, resulting in better catalytic activity [34]. HWP catalyst supported on MCM-41 also showed excellent catalytic activity and on-stream stability in the gas-phase synthesis of MTBE at quite low temperature, <100 °C [17]. Further

treatment of dispersed HPA by cesium or ammonium carbonates produces their salts, which can bind HPA more tightly and stably on the pore surface. Supporting HPW on mesoporous materials, however, does not always provide positive results for catalytic application, since strong interaction between HPW and the host material can adversely affect the catalytic activity of HPW. The lower activity of HPW catalyst supported on MCM-41 in the alkylation of *iso*-butane with 2-butene compared to that of silica was explained by the stronger interaction of HPW with the former, lowering both the number and the average acid strength of Brönsted acid sites of the catalyst [35]. In addition, the large amount of HPW loading in mesopores may have led to a partial blockage, which decreases the accessibility of reactants to the acid sites.

Esterification of glycerol with a fatty acid (Fig.1) was studied over the mesoporous material containing anchored sulfonic acid groups [9]. The catalytic activity of the catalyst in the esterification was not dependent on the concentration of acid sites, and a good accessibility of active sites to reactants proved to be more important. Although product shape selectivity was not observed, fast reaction rates and high monoglyceride yields suggest that this type catalyst is adequate for the esterification of various polyols and acids. Improved selectivity to monoglyceride was obtained from the catalyst prepared using a hexadecyltrimethylammonium and dodecyltrimethylammonium bromides as a mixed-template, achieving



Figure 1. Single esterification of glycerol.

the higher order in channel packing [36]. Similarly, high activity and selectivity to the monoglyceride over SBA-12 and SBA-15 was interpreted as a consequence of good arrangement of pores with appropriate size without defects [13].

Sulfonic acid groups attached to the mesoporous materials were also active in the condensation reaction between phenol and acetone producing Bisphenol-A (Fig.2) [10]. Although optimization of the catalyst preparation was essential to achieve good catalytic performance, high catalytic activity with >90% selectivity toward *p,p'*-Bisphenol-A was obtained. Zeolites such as H-MFI, H-FAU and H-BEA showed negligible activity. High selectivity to the linear molecule rather than *o,p'*-Bisphenol-A was interpreted as a result of shape selective catalysis in mesoporous materials.

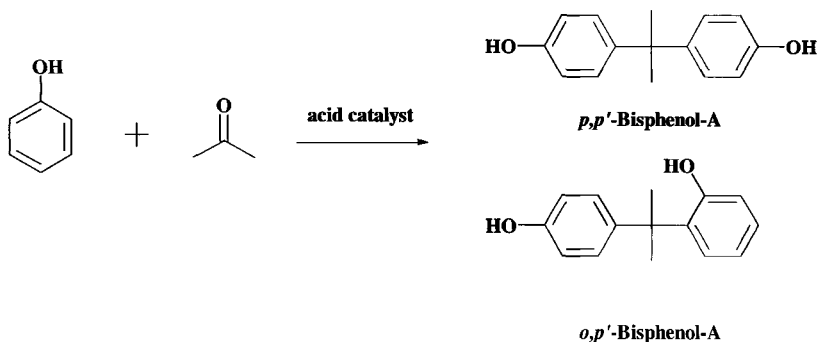


Figure 2. Synthesis of Bisphenol-A from phenol and acetone.

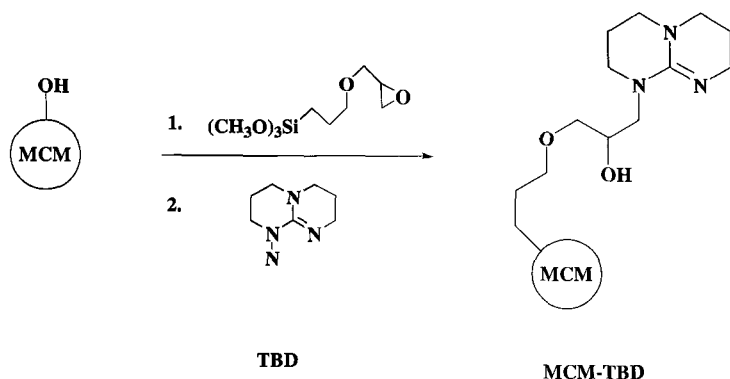
Acidic mesoporous materials were also applied to the catalytic degradation of polyethylene and polypropylene [21]. Although the amounts of valuable liquid products produced are larger over MCM-41 than MFI zeolite, the former deactivates rapidly due to carbon deposit. In order to reduce carbon deposit and to enhance liquid yield, catalytic degradation of polyethylene was studied on mesoporous folded silica (FSM) with no acid sites [37,38]. The initial rate of polyethylene degradation over FSM was similar to that over other solid acid catalysts such as silica-alumina and zeolites, but the yield of liquid products was much higher. This finding concerning the FSM catalyst strongly suggest that the mesopores surrounded by the silica sheet may act as reservoir for radical species, which accelerate the degradation of plastic melt. Neither MCM-41 nor bulk HPA was active in the catalytic degradation of polyethylene, but HPA supported on MCM-41 using water and methanol as solvent was active [39]. The formation of isobutene, which is not produced in the thermal degradation, indicates the change in the reaction path but its degradation mechanism over the supported HPA catalyst was not sufficiently explained.

2.2. Preparation and applications in base-catalyzed reactions

Basic MCM-41 catalysts are usually prepared by the incorporation of soluble salts of alkaline metals followed by calcination to remove the anionic species [40]. No diffraction peaks attributed to metal hydroxide/oxide are observed on the MCM-41 catalysts containing K_2O , BaO and K_2O/La_2O_3 , if metal oxide particles are highly dispersed. Surface

area after impregnation of metal oxide shows little change. CsLaO_x/MCM-41 is prepared by wet or solid-state impregnation of MCM-41 with cesium acetate and lanthanum nitrate followed by thermal decomposition [41]. The mild basic strength of this catalyst was demonstrated by its ability to remove a proton from enolate having a $pK_a < 10.2$. Ion-exchanging of Al-containing mesoporous material with Cs⁺ ion is another way to prepare a basic catalyst [42]. Cs modification on MCM-41 or MCM-48 brings about drastic increases in the conversions of base-catalyzed reactions, while the host material suffers a considerable loss in surface area, pore volume and pore diameter. Since the acid strength of Al-MCM-41 is not high, the basicity of the mesoporous material after alkaline metal ion exchange is not expected to be strong. Microwave irradiation, however, converts the ion-exchanged Cs⁺ to highly dispersed cesium oxide aggregates, which results in high catalytic activity for the dehydrogenation of 2-propanol [43]. Basic mesoporous materials can also be prepared by a simple treatment of evacuated silica with ammonia [44]. The ammonia-grafted FSM-16 has pair sites of SiNH₂ and SiOH, which exhibit higher turnover frequency in some base-catalyzed reactions than SiNH₂ single site alone.

More widely studied method for the preparation of basic mesoporous materials is the grafting of organic bases on the mesopore surface. A strong guanidine base 1,5,7-triazabicyclo[4,4,0]dec-5-ene (TBD) with pK_b value of ca. 25, can be immobilized on MCM-41 mesoporous material as shown in Scheme 2 [45]. The grafting of guanidine moiety into MCM-41 structure by the covalent bonding provides a useful route for the preparation of strong, nonionic basic catalysts. Furthermore, the glycidylation route prevents the evolution of harmful and corrosive acids.



Scheme 2. Grafting of TBD on mesoporous material.

Organic bases such as propylamine, piperidine, TBD, pyrrolidine, pyrimidine, imidazole, 1,2,4-triazole, 1,8-diaza-bicyclo[5,4,0]undecene-7 (DBU) were grafted on a various mesoporous silica supports [46-49]. 3-Aminopropyltriethoxysilane, 3-chloropropyltriethoxysilane and 3-glycidyl-oxypropyltrimethoxysilane were usually used as coupling reagents, and IR absorption bands attributed to these bases show the formation of covalent bonds between bases and coupling silanes attached on the host materials. Grafted bases have generally lower basicity than corresponding free bases, and also show a wide distribution of basic strength. Hydroxyl groups remained on the surface can be capped by the vapor phase treatment with hexamethyldisilazane to prevent the interaction between base moieties and hydroxyl groups and to increase the strength of grafted bases. Heterogeneized Brönsted base catalysts can also be prepared by grafting [49,50]. Tetraalkylammonium groups have been covalently bound to the MCM-41 surface by anchoring trimethoxysilyl-propyl-*N,N,N*-trimethyl ammonium chloride followed by the reaction with a methanol solution of tetramethylammonium hydroxide. No leaching of the anchored ammonium ions occurs during the anionic exchange of chloride with hydroxide.

The number of catalytic reactions studied over basic mesoporous materials is rather limited, and typical reactions studied over the basic mesoporous materials are Knoevenagel condensations and Michael additions, in which reactions are initiated by the deprotonation of a substrate by base catalysts [42-45]. Synthesis of chromenes and coumarins, which involves the combination of Michael addition and Knoevenagel condensation, was also studied [49].

Knoevenagel condensation refers to the condensation of aldehyde or ketone with an active methylene compound to yield carbon-carbon bond formation (Fig.3), and condensation reaction of benzaldehyde (BA) with ethylcyanoacetate (ECA) or with malonitrile is usually employed. In Knoevenagel condensation, the difficulty in deprotonation from donors dictates the basicity demanded in catalytic action. Ion exchange of Al-MCM-41 with Cs^+ ions considerably increases the conversion of the Knoevenagel condensation between BA and ECA [42]. Since the activity of the Al-MCM-41 also drastically increases by loading with a small amount of cesium acetate followed by calcination in air, it is not certain whether the basic character of Cs-modified MCM-41 is attributed to the exchanged Cs^+ ions or impregnated cesium oxide clusters. Several donor and acceptor species were employed to investigate the catalytic property of base-immobilized mesoporous materials, and the linear relationship between the initial rate of the condensation and the amount of amine grafted showed that the grafted amines act as active sites [45,46]. Most reactants tested in the condensation were not bulky, and no significant

effect of pore size and pore arrangement of mesoporous materials on conversion were demonstrated [48]. Since the Knoevenagel condensation is usually initiated by removing a proton from donors to produce anions, strong base catalysts are expected to be more active. However, grafted primary amine shows higher activity than tertiary amine in the Knoevenagel condensation between BA and ECA [46]. This disagreement between basicity and catalytic activity is due to the difference in the reaction mechanism; primary amines react with BA and form imine intermediates, which subsequently react with ECA. Therefore, basic strength for the deprotonation alone does not work as a determining factor for the reaction over the primary amine-grafted mesoporous materials.

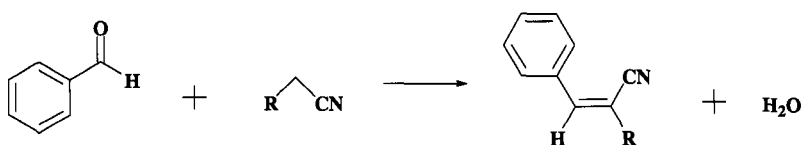


Figure 3. Knoevenagel condensation of BA and ECA.

Michael addition is one of the traditionally used carbon-carbon bond formation reactions over base catalysts in organic synthesis, in which 1,4-addition of an enolate anion to an α,β -unsaturated carbonyl compound yields a 1,5-dicarbonyl compound. Michael additions need high basicity, and suitable for the investigation of the catalytic role of grafted strong bases, whereas the Knoevenagel condensation between BA and ECA is not very demanding from the point of base strength. Mesoporous materials with grafted quaternary ammonium hydroxide [50,51] and TBD [45] showed high activity in the Michael addition of ECA to methyl vinyl ketone, indicating their strong basicity.

Bases catalyze the nucleophilic ring-opening of glycidol with fatty acid, and the preparation of monoglycerides from fatty acids and glycidol is a good example of base catalysis in the production of fine chemicals [47,52]. MCM-41 grafted with TBD shows lower activity at moderate temperature compared to ion-exchanged resin type catalyst because of mass transfer limitation. On the other hand, the former has higher thermal stability and can be used repeatedly at higher temperature if proper care is taken for the maintenance of the reaction atmosphere [40].

The application of basic mesoporous materials in commercial catalytic processes is not reported yet [53], because of the problem of activity control and high cost of preparation. However, small scale

applications of base-grafted mesoporous materials in fine chemical production are expected to emerge soon.

3 Redox catalysis

Titanium silicalite-1(TS-1) prepared by Enichem in the middle of 1980's has been proven to be an excellent catalyst for selective oxidation of relatively small organic molecules in the presence of H_2O_2 [54, 55]. Larger pore Ti-Beta was synthesized afterwards [56], but its application was still limited to molecules smaller than 7 Å. Soon after the Mobil discovery of M41S materials eventually came the synthesis of titanium containing mesoporous material with regular pore sizes greater than 35 Å. Subsequently, the synthetic utility of mesoporous molecular sieves has been considerably extended by the incorporation of various redox metals or metal complexes into their framework or pore wall surfaces. Blasco et al [57] prepared a series of Ti-MCM 41 by hydrothermal heating of Ti- and Si- alkoxide precursor mixtures with cationic surfactants at 408 K. Ti-MCM-41 showed significantly superior oxidation performances to microporous counterparts in oxidations of α -terpineol, 1-naphthol, norbornylene, cyclododecanol, 2,6 DTBP(di-tert-butyl phenol), and even large organic sulfide [58-60]. Tanev et al [61], on the other hand, made Ti-HMS with neutral primary amine surfactants at room temperature. For 2,6 DTBP oxidation, Ti-HMS was significantly more active than Ti-MCM-41, as a consequence of the former presenting less diffusion resistances due to the small crystallite size and the higher textual mesoporosity ; the textual mesopore volume in the 10-30 nm range for Ti-HMS was 1.11 ml/g compared with 0.03 ml/g for Ti-MCM-41 [62]. Ti-HMS exhibited better H_2O_2 selectivity compared to Ti-MCM 41 [59]. Ti-HMS was also applied to the one-pot synthesis of campholenic aldehyde, an intermediate for the fragrance santalol, from α -pinene using its oxidation and Lewis acid sites [63]. Furthermore, Ti-MCM-48 with its three dimensional pore system was found to be more active than Ti-MCM-41 with one dimensional pores in the epoxidation of bulky alkenes using H_2O_2 [64,65].

The successful incorporation of titanium into the framework in direct synthesis route is usually claimed by observing enlargements of unit cell parameter by ca 2-4 Å and by increases in wall thickness, which can be estimated by subtracting the pore size from the unit cell parameter. On the other hand, pore size of the calcined samples in most cases remains constant after Ti incorporation. Enhancement of cross-linking in the wall structure by Ti incorporation can be seen in increases in Q4 population in ^{29}Si MAS NMR spectra [62]. The presence of ca 960 cm^{-1} band in IR spectra can not be considered as a conclusive evidence for the Ti-

incorporation, since the same band is also found in pure silica materials. However, the ratio of the band at 960 cm^{-1} to the symmetric stretching vibration of SiO_4 at 800 cm^{-1} is higher for Ti-incorporated mesoporous materials than pure silica analogs [59]. Persistent 960 cm^{-1} IR band after high temperature calcination also support Ti-incorporation to the mesostructure, since Si-O^- species condenses out under such harsh conditions. UV-Vis diffuse reflectance spectra for Ti-incorporated mesoporous materials usually show an absorption band at about 220 nm and a weak shoulder in the range of 250-320 nm. The former is known to occur as a consequence of oxygen to tetrahedral titanium (IV) ligand to metal charge transfer. Isolated tetrahedral Ti(IV) species in ordered silicate framework position in TS-1 is known to produce an absorption band at 212 nm, and a slight shift to higher wavelength usually takes place due to the presence of water molecules adsorbed in the coordination sphere of Ti [62]. The shoulder at 270 nm is usually assigned to oligomerized hexacoordinated Ti species containing Ti-O-Ti bonds in silicon rich amorphous phase, which becomes more prominent with increasing Ti loading. Absence of absorption band at 330 nm means that anatase phase is absent in the sample. XPS spectrum of Ti(IV) in tetrahedral coordination shows Ti ($2\text{P}_{3/2}$) binding energy at 459.8 eV, whilst Ti in octahedral coordination in titanium oxide has the binding energy at 458.6 eV [59]. XANES and EXAFS analysis [57] also generate useful information probing the chemical and structural environment surrounding titanium. XANES of Ti-K edge gives rise to a strong pre-edge peak at 4968 eV for tetrahedrally coordinated Ti, whereas Ti in a highly symmetric octahedral environment in anatase and rutile shows three weak undulating pre-edge peaks. Upon dehydration at the tetrahedral site, a sharper more intense pre-edge peak at lower energy is observed in XANES spectrum. According to the reported EXAFS analysis of various titanium containing compounds, Ti-O distances in octahedral coordination fall within the range of 0.194-0.196 nm whereas for tetrahedral Ti-O distances are 0.180-0.186 nm. These Ti-containing mesoporous materials were also examined by ESR spectroscopy after a thermal activation treatment followed by γ -irradiation at 77K; an axial signal with $g_{\parallel}=1.971$ and $g_{\perp}=1.901$ was explained as arising from trivalent Ti at a framework tetrahedral site, whereas an ESR signal characterized by reverse g values $g_{\parallel}=1.898$ and $g_{\perp}=1.967$ was explained as Ti(III) in distorted octahedral symmetry [66]. Photoluminescence spectra with excitation at 250 nm for Ti-MCM-41 generate two overlapped emission bands at 430 and 480 nm with shoulders at ca. 400 and 550-600 nm. Oligomerized Ti(IV) species were suspected to contribute towards 550-600 nm shoulder peak whereas tetrahedral Ti(IV) could be the cause of 430 and 480 nm bands [67].

Compared to the crystalline microporous materials, the mesoporous catalysts suffer two major disadvantages, low intrinsic catalytic activity due to the amorphous nature of pore walls and poor hydrothermal and mechanical stability due to the high hydrophilicity derived from abundant surface silanol groups. 1-Hexene epoxidation using H_2O_2 as oxidant showed intrinsic activity order of $\text{TS-1} > \text{Ti-Beta} > \text{Ti-MCM-41}$. Apparently, titanium atom in the amorphous silica wall of MCM-41 is less redox-active and some of Ti atoms are suspected to be buried inside the pore wall, remaining inaccessible to the reactant molecules in directly prepared samples. Large population of silanol groups in MCM-41 makes Ti-MCM-41 less adequate for water present reaction system. Indeed, epoxidation with *tert*-butyl hydroperoxide (TBHP) in water-free reaction media produced high oxidant selectivity and improved conversion. Ti-MCM-41 is, however, much less hydrophilic than amorphous $\text{TiO}_2\text{-SiO}_2$. Control of hydrophobicity of the molecular sieve allows the optimization of the adsorption of reactants and products. Tatsumi et al [68] modified Ti-MCM-41 and 48 by post-synthetic trimethylsilylation, reacting Me_3SiCl and $(\text{Me}_3\text{Si})_2\text{O}$ with the surface silanol species. These catalysts achieved substantially enhanced activity in the oxidation of cyclohexene with H_2O_2 and were much more moisture-resistant. BET surface area, pore volume, and pore diameter decreased upon trimethylsilylation whilst the d spacings in XRD remained virtually unchanged. Corma et al [69] claimed that a highly active and selective catalyst for epoxidation with TBHP needs above 40 % silylation of the surface. Alternatively, simple removal of water from the commercial TBHP was an equally effective method to improve the catalyst performance without silylation. They also reported one step synthesis of organo-silica containing Ti-MCM-41 by co-condensation of $\text{Si}(\text{OC}_2\text{H}_5)_4$ doped with $\text{Ti}(\text{OC}_2\text{H}_5)_4$ and $\text{CH}_3\text{Si}(\text{OC}_2\text{H}_5)_4$, which was highly active and selective for epoxidation reaction using TBHP as an oxidant [70]. Upto 35 mol % incorporation of hydrophobic organo-silica was possible without losing a well-ordered mesostructure. It was recently claimed that hydrophobic modification of Ti-MCM-41 improves the epoxidation performance with TBHP, but H_2O_2 alone interacts irreversibly with titanium leading to the transformation of isolated Ti into oligomeric and oxide-like Ti species, which make water effect rather minor [71].

Investigations of titanium incorporated epoxidation catalysts support the general consensus that the most active and selective sites are isolated, mononuclear, 4- coordinate Ti(IV) centers. Ti-MCM-41 type catalyst was thus prepared in the presence of fluoride ion using H_2SiF_6 as a silicon source [72]; acidic environment minimizes the chances for titanium species precipitated as hydroxide and can enhance hydrothermal stability. Soluble titanium peroxo solution [73] or TiCl_3 solution [74] was also

claimed useful avoiding the formation of anatase TiO_2 due to relatively low hydrolysis rates of the Ti precursors.

Ti-containing mesoporous molecular sieves can be prepared by post-synthetic grafting of suitable titanium precursors onto the pure silica mesoporous host materials. Maschmeyer et al [75] grafted titanocene dichloride onto the inner surfaces of siliceous MCM-41 and the resulting material exhibited high catalytic performance for cyclohexene and pinene oxidation with TBHP. The increased performance was rationalized by noting that all titanium centers are surface species and no detectable amounts of oligomeric and hence inactive species are present. This grafting approach was applicable for other metallocenes of V-, Zr-, Mo-grafted to MCM-48 [76]. All these metallocene grafted materials, however, showed some extent of metal leaching. Titanium alkoxide grafting on various mesoporous materials demonstrated that MCM-48 and HMS, due to 3 D channels and textual mesoporosity, prove to be useful in 2,6 DTBP oxidation. Activity increased with the amount of titanium grafted, irrespective of the titanium coordination states [77]. Grafting of $\text{Ti}(\text{OSiPh}_3)_4$ onto the internal surface of MCM-41 produced an epoxidation catalyst of high activity/selectivity by the presence of the phenyl group on each titanium center increasing the longevity of their catalytic activity towards attack from moisture [78]. Post-synthesis introduction of Ti to a surfactant-containing MCM-41 was claimed effective [79], and Titanium(IV) silsesquioxane was also anchored into MCM-41 either by physical adsorption [80] or via multi-step chemical bonding [81].

Incorporation of titanium into SBA-15 by direct synthesis appears unlikely because of the highly acidic synthesis condition, but Ti-SBA-15 was prepared in this route making use of TiCl_4 as a Ti source under microwave-hydrothermal conditions [82]. Ti-SBA-15, by post-synthetic grafting of Ti-alkoxide [83], titanocene dichloride [84] or by incipient wetness impregnation of Ti-isopropoxide in ethanol [85] was also reported. Grafting is expected to have an advantage of making more Ti sites being exposed to the reactants, especially for thicker-walled SBA-15, and simple impregnation also produced Ti-SBA-15 with fundamentally identical properties to more elaborately prepared samples by grafting. Ti-SBA-15 showed very similar catalytic properties to Ti-MCM-41 including the enhancement of activity/selectivity in epoxidation by silylation, but was substantially more stable and less prone to metal leaching [83].

Jarupatakorn and Tilley [86] used tris(tert-butoxy)siloxy titanium complexes such as $(^i\text{PrO})\text{Ti}[\text{OSi}(\text{O}^i\text{Bu})_3]_3$ to react with the hydroxyl groups in mesoporous materials. They concluded that the preexisting TiO_4 and SiO_4 environment of the double alkoxide molecular precursor provides a high degree of site isolation for the sterically protected Ti centers, which explains the high activity/selectivity of cyclohexene

epoxidation with cumene hydroperoxide. Steric hindrance of the $\text{-OSi(O}^t\text{Bu)}_3$ ligands, however, retards the grafting reaction, limiting the total number of Ti sites grafted. Mesoporous material with larger pore diameter such as SBA-15 was reported advantageous in this regard.

Several attempts were made to increase the titanium loading in the mesoporous materials. In one study, titanium content in Ti-MCM-41 was increased by using 2,2,2,-nitrile-triehanol as complexing agent to coordinate both Si and Ti atoms and harmonize the hydrolysis activity of the resulting precursors [87]. Si/Ti value of 1.9 was claimed. Ti-MSU prepared by Bagshaw et al [88] also utilized the hydrolytic control of Ti in the presence of non-ionic polyethylene oxide surfactants under ambient temperature; by using Ti-bis(ethyl acetoacetato) diisopropoxide, 1 to 10 mol % Ti could be incorporated. Solution phase grafting of TiCl_4 followed by calcination also produced Ti-MCM-41 with 5.3 to 9.7 wt % Ti loading [89]. Ti-MCM-48 was also prepared by titanylacetylacetonate as the Ti source to increase the titanium dispersion in grafting procedure, but formation of nanosized TiO_2 formation was inescapable at higher Ti loading above 10 wt % [90]. These materials with high Ti loadings are not expected to improve catalytic performance in liquid phase epoxidation reactions due to the limited number of tetrahedrally coordinated Ti sites, but may prove useful in photocatalytic decomposition of VOC's.

Finally, two recent works on titanium containing mesoporous molecular sieves deserve separate comments. Ti-TUD-1 was prepared using non-surfactant triethanolamine [91]. Triethanolamine easily forms complexes with titanium alkoxides, which together with free triethanolamine form meso-sized aggregates that template mesopores upon increasing the synthesis temperature. Ti-TUD-1 has uniform mesopores tunable from 2.5 to 25 nm and pores are randomly connected in three dimensions. In addition, the surface of the mesopore wall is covered with a titanium-enriched phase much like the Ti-grafted Ti-MCM-48. These combined features of Ti-TUD-1 were claimed to produce epoxidation activity ca 6 fold higher than directly synthesized Ti-MCM-41. MTS-9, hydrothermally synthesized in a triblock polymer(P123) surfactant solution with preformed precursors containing TS-1 nanoclusters in a strong acidic media ($\text{pH} < 1$) is another promising catalyst [92]. MTS-9 was active both in small phenol hydroxylation with comparable activity to TS-1 and also was very active for the oxidation of bulky 2,3,6 trimethyl phenol, which attributes to the TS-1 like environment of Ti species. Furthermore, hexagonal structure of the material was retained even after boiling in water for 120 h. This excellent hydrothermal stability is claimed due to the zeolite-like connectivity of TO_4 in the mesostructure and thicker walls.

Vanadosilicates are also known as good hydrocarbon oxidation catalysts using H_2O_2 as an oxidant. V-MCM-41 was prepared using vanadyl(IV) sulfate as a vanadium source and found to be efficient in 1-naphthol and cyclododecane partial oxidation [93]. A spectroscopic study of V-MCM-41 based on NMR and ESR analysis was reported [94], which indicates that vanadium in calcined samples is coordinated to four oxygen atoms in an approximately tetrahedral configuration and easily converted V^{5+} to V^{4+} and vice versa. V-HMS prepared using either vanadyl(IV) sulfate or vanadium(V) isopropoxide was active for liquid phase oxidation of large organic substrates. For 2,6 DTBP oxidation, V-HMS exhibited exceptional catalytic activity/selectivity and high H_2O_2 efficiency, far superior to Ti-HMS. However, significant leaching of vanadium species were observed in V-HMS and these dissolved species are believed to be involved in reaction [95]. The stability of vanadium remained as a serious problem and found to be dependent on the nature of substrate, solvent, and oxidant. Recently, V-MCM-41 was reported to oxidize alkanes to ketones without vanadium leaching using isobutylaldehyde/ O_2 , which is known to form, in situ, the anhydrous peracid and acylperoxo radical [96]. Gas phase propane oxidation using V-MCM-41, -48 was attempted [97]. Synthesis of V-SBA-1 [98] was also reported.

Other metal-incorporated mesoporous molecular sieve catalysts include Zr-HMS [99] and Nb-MCM-41 [100] which showed some mild acidity in addition to its oxidative property, and Fe-MCM-41 prepared using ferric nitrate for styrene epoxidation [101]. Cr-MCM-41 after pre-washing with ammonium acetate was recently claimed as a heterogeneous catalyst active for cyclohexane oxidation in acetic acid solvent [102]. W-MCM-41 was also prepared in direct synthesis in acidic medium using $(\text{NH}_4)_2\text{WO}_4$, which produced glycol and ester mostly in cyclohexene oxidation in acetic acid [103].

Development of efficient biomimetic heterogeneous oxidation catalysts containing metal complexes with Schiff base, phthalocyanine or porphyrin ligand, which mimic the catalytic activities of metalloenzymes, has received much attention. The grafted metal complexes can, by subsequent activation, also act as precursors for the preparation of highly dispersed transition metals. These works of utilizing immobilized transition metal complexes as oxidation catalysts are summarized in Table 1. An article by Arends and Sheldon [104] is recommended to gain an overview of recent development in selective liquid phase oxidations using heterogeneous catalysts, including the immobilized homogeneous catalysts.

Table 1. Transition metal complex immobilization on MCM-41 for liquid phase oxidation reactions.

Ref	Catalyst	Prep. Method	Reaction	Comments
105	Fe(II)-Phen/ MCM-41	[Fe(II)-(Phen) ₃]Cl ₂ ion-exchange with H-MCM-41	Hydroxylation of Phenol with H ₂ O ₂	• 9.5% loss of Fe complex after 10 repeat runs
106	Fe(II)-Phen/ MCM-41	Impregnation	Benzylalcohol oxidation with TBHP	• Protection effect of the matrix leading to higher TON
107	Fe,Cu/ MCM-41	Tethering	Cyclohexene oxidation with H ₂ O ₂	• Metal leaching serious
108	Fe/MCM-41	Tethering	Phenol hydroxylation with H ₂ O ₂	• Spacer(ATMS) significant contribution
109	Mn(II)-salen/ MCM-41	Tethering	Styrene/cyclic olefin epoxidation using PhIO or m-CPBA	• Direct anchoring of pre fabricated Mn-complex vs stepwise assembling
110	Mn(III)complex/ MCM-41	Tethering	Cyclohexene oxidation (to ether) with TBHP	• Improved ligand design
111	Mn(III)complex/ MCM-41	Grafting of Mn-Porphyrin complex	Styrene/cyclohexene epoxidation with PhIO	• Matrix protection effect • Mild deactivation after prolonged use
112	Mn-MCM-41	Template ion exchange using Mn(NO ₃) ₂ ·6H ₂ O	Styrene/stilbene epoxidation with TBHP	• Mn more active than V, Cr, Fe, Mo

Table 1. (continued)

Ref	Catalyst	Prep. Method	Reaction	Comments
113	Mn/MC M-41	Immobilization of gaseous $\text{Mn}_2(\text{CO})_{10}$ + calcination	Propene combustion	<ul style="list-style-type: none"> Onset temperature 100°C lower than with commercial SiO_2
114	Co complex/ MCM-41	Immobilization of monohydroxy-cobalt complex	Cyclohexane to cyclohexanone with TBHP	<ul style="list-style-type: none"> 3-bromopropyltrichlorosilane tethering improves TOF and selectivity
115	Cr(III) salen/ MCM-41	Grafting of Cr-salen complex	Norbornene/1-naphthol oxidation with TBHP	<ul style="list-style-type: none"> Stable after 5 runs (no leaching)
116	TEMPO/ MCM-41	Tethering	Oxidation of primary alcohols	<ul style="list-style-type: none"> Fine chemical synthesis Comparison of prep. methods
117	W complex/ MCM-41	Peroxo-W complex tethering	Bulky olefin epoxidation with H_2O_2	<ul style="list-style-type: none"> Phosphoramidate anchored MCM-41 most promising
118	W complex/ MCM-41	Grafting or direct synthesis using W- oxo(peroxo) species	Cyclooctene epoxidation with H_2O_2	<ul style="list-style-type: none"> Comparison of synthesis method Metal leaching
119	Ru/MC M-41	Ship in bottle/direct/grafting	n-hexane oxidation with TBHP	<ul style="list-style-type: none"> Comparison of prep. methods
120	Cu/MC M-41	Impregnation	2,6 DTBP oxidation in air	<ul style="list-style-type: none"> alkali metal additive necessary

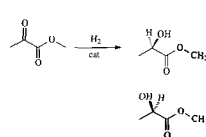
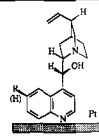
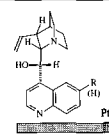
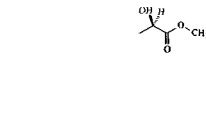
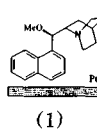
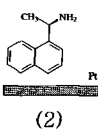
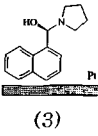
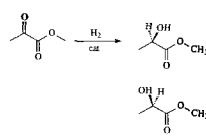
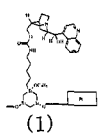
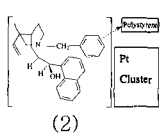
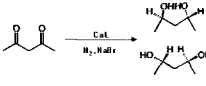
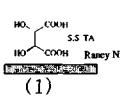
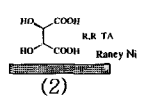
4 Enantioselective Catalysis

Heterogeneous catalytic syntheses of optically pure chemicals have gained significant potential over recent years. These chiral catalysts offer practical advantage of easy catalyst separation from the reaction mixtures and subsequent reuse, even though some penalties in reaction rate and enantioselectivity are frequently inevitable. Several immobilization strategies have been shown to give stable and active heterogeneous chiral catalysts. Attaching a chiral ligand covalently via a suitable functional linker or tether to a support is the most critical step, because optical purity of the product can vary with the length of and the flexibility of the spacer. Pore size can also affect the enantioselectivity. In this regard, silica based mesoporous molecular sieves are emerging as interesting support materials for immobilizing chiral functionalities for fine chemical synthesis. The pore system with a typical diameter of 3-10 nm offers large surface areas and the spaces necessary to accommodate the substrates of various sizes to avoid mass transport problems, although molecular sieving effect becomes less important. Ligands bearing a trimethoxysilane group can be immobilized via abundant surface silanol groups. In this section, various concepts of preparing immobilized chiral catalysts are discussed with examples.

4.1. *Metal-based chiral hydrogenation catalysts*

Hydrogenation has been one of the most important reactions in asymmetric catalysis and the heterogenization of chiral complexes on inorganic supports has been explored vigorously up to date. In principle, metal catalysts can be made enantioselective by rearrangement of the metal surface into a chiral morphology by adsorption of chiral modifier on the surface [121-127]. The adsorption of various cinchona-type alkaloids on Pt (entry 1, 2 in Table 2) or interaction of tartaric acid/NaBr with Raney nickel (entry 4) [127] leads to excellent asymmetric induction of the selected α - and β -ketoester substrates. An enantiomeric excess of 95% has been achieved over the cinchona-modified Pt under optimal conditions for ethyl and methyl pyruvate hydrogenation [121-126]. Blaser and Muller [125] have grafted cinchona alkaloids on silica-supported Pt catalysts via a spacer as shown in Table 2 (entry 3) and obtained excellent ee. A characteristic feature of α -ketoester hydrogenation is that the enantio-differentiation induced by the presence of the chiral modifier is accompanied by strong increase in reaction rates. The modifier structure was found to influence the optical yield. While silica was used as a support, the mesoporous materials such as MCM-41, -48 and SBA-15 can easily be adopted as supports under the same reaction conditions.

Table 2. Asymmetric hydrogenation using metal supported catalysts in the presence of chiral modifier.

Entry	Ref	Reactions	Catalyst	e.e.
1	121		  (1) (2)	(1) 95% (2) 95%
2	122- 124		   (1) (2) (3)	(1) 95% (2) 82% (3) 75%
3	125, 126		  (1) (2)	(1) >90% (2) >99%
4	127		  (1) (2)	(1) 97% (2) 99%

More recently, Pt-loaded MCM-41 has been used as a catalyst in enantioselective hydrogenation of 1-phenyl-1,2-propanedione [121]. The maximum enantiomeric excess of (R)-1-hydroxy-1-phenylpropanone was 44% with 15wt% Pt/MCM-41 modified with (-)-cinchonidine (compared to 54% ee obtained with 5wt% Pt/Al₂O₃).

Clays are also useful material as catalyst support, especially for immobilization of organic modifiers on their surfaces. Pt-montmorillonites modified with tartrates were reported to be very selective solid catalysts for the hydrogenation of ethyl pyruvate [128]. Only Pt and Rh were found to be active in this reaction, producing moderate to good enantioselectivities (up to 75% ee for the R-isomer). The cinchonidine containing catalysts showed an increase in basal spacing to ca 1.5 nm, indicating that the modifiers are, in part, included in the inter-lamellar space and on the outer surfaces.

The effects of metal particle size and the type of chiral modifier may be more important than those of the pore size and pore structure of the support on the enantioselectivity in these reaction systems mentioned above.

4.2. Chiral complexes attached covalently on mesoporous matrices

Corma et al [129] have used USY zeolite having some mesoporosity in 1-3 nm range as an inorganic support to immobilize pyrrolidine-based ligands on its surfaces. The mesoporosity of the USY host was sufficiently open to anchor new proline and pyrrolidine-based chiral Rh(I) complexes via $\text{Si}(\text{OEt})_3$ linkers. Various α -aminoinnamates were hydrogenated to corresponding substituted phenylalanine derivatives with 93 - 98% ee (entry 1 in Table 3). Chiral 1,2-diphosphines ligands were used in the fixation of $\text{Rh}(\text{COD})(\text{R,R})\text{DPP}^+\text{BF}_4^-$ on the silica surfaces as in Table 3 (entry 2) [130], which showed high ee comparable to those of their soluble counterparts (ee up to 100%). The optical purity of the product varied slightly with the length and flexibility of the spacer and, in the case of methyl ester, the pore size affected the enantioselectivity.

Recently, 1,1'-bis-diphenylphosphinoferrocene ligand bound to Pd and anchored via a molecular tether of precise length to the inner wall of MCM-41 (ca. 3 nm diameter), yielded catalytic regioselectivity and ee (99%) that is far superior to the homogeneous analogues in allylic amination of cinnamylacetate with benzylamine [131]. The complex attached on the mesoporous material produced enantioselectivity higher than the complex anchored on silica (Ca-O-Sil) due to confinement effect in mesopores.

Epoxides are versatile intermediates in organic synthesis because epoxides undergo various nucleophilic ring-opening reactions to give enantiomerically enriched products of high synthetic use. The covalent construction of chiral salen complexes on the silica gel (entry 3) and MCM-41 (entry 4) was performed by a stepwise approach analogous to that by Sherrington et al [132-135]. The immobilized chiral salen Mn(III) complexes were stable during the enantioselective epoxidation of aromatic cyclic olefins and exhibited a relatively high enantioselectivity. Salvadori et al [132] have reported that the findings obtained with the silica gel-bound catalyst (entry 3) differ from the results with an analogous polystyrene-supported Mn(III)-salen complex. While the *m*-CPBA/NMO oxidation of indene in the presence of the former afforded good stereo- and chemo-selectivity values (60% ee and 97% ee yield), latter proved far less effective to those substrates. On the other hand, the chiral salen complexes immobilized on MCM-41 resulted in enhanced enantioselectivity compared to those on amorphous silica.

Anchoring a chiral tetraazamacrocyclic ligand on the mesoporous materials (MTS) has been demonstrated by Brunel et al [136], which afforded 1*R*,2*R*-*trans*-1-phenylpropylene oxide with very high enantioselectivity (76% ee) in the epoxidation of *trans*- β -methylstyrene (entry 5). This enantioselectivity is the highest ever observed in the

heterogeneous epoxidation of *trans*- β -methylstyrene.

The use of the Sharpless Ti-tartrate ester-based asymmetric system has been known as a very important organic synthetic methodology in asymmetric catalysis. Xiang et al [137] have reported the synthesis of organic-inorganic hybrid materials by grafting chiral tartaric acid derivatives on the surface of silica and in the mesopore of MCM-41. Use of these chiral tartaric catalysts with $\text{Ti}(\text{O}^i\text{Pr})_4$ and TBHP under typical Sharpless conditions gave higher levels of induction in epoxidation of *trans*-allylic alcohols with ee up to 86%, which is as good as the homogeneous Sharpless system (entry 6).

The dramatic enantioselective effect of cinchona alkaloids is not limited to Pt surfaces only ; it is known that catalytic amounts of OsO_4 in the presence of cinchona alkaloids gave access to chiral vicinal diols through dihydroxylation of olefins [138-141]. A silica-supported alkaloid containing 1,4-bis(9-O-quininyl)-phthalazine ((QN)₂-PHAL) showed comparable reactivity and enantioselectivity to those in homogeneous solution in the Sharpless asymmetric dihydroxylation of olefins (entry 7) [138]. *Trans*-stilbene gave > 99% ee (*S,S*)-diol at high conversion.

Several methods have been reported for asymmetric alkylation of aldehydes with dialkylzincs using chiral aminoalcohols as catalysts in heterogeneous conditions [142-145]. Brunel et al have investigated the asymmetric catalytic activities of the supported (-)-ephedrine on the mesoporous material (MTS) in the enantioselective ethylation of benzaldehyde with diethylzinc [143]. The results clearly showed that supported catalysts (ee 33%; entry 8 in Table 3) are considerably less active and selective than in homogeneous conditions (ee 66%). On the other hand, new proline-derived ligands immobilized on mesoporous silicas (MCM-41 and SBA-15) showed excellent enantioselectivity [144]. The ee of product was found to be dependent on the pore size of the mesoporous silicas, capping of free silanol moiety with trimethylsilyl(TMS) group, and employment of *n*-BuLi as an additive. High enantioselectivity (ee 75% ; entry 9) was achieved when both TMS capping and *n*-BuLi addition were applied for the mesoporous SBA-15 based catalysts as compared to amorphous silica and MCM-41. It is observed that the chiral complexes immobilized on MCM-41 improves the activity compared to the one attached to amorphous silica. But in other instances, the mesoporous catalyst performs worse than the catalyst attached to a non-porous support, due to the limited accessibility of active sites in the mesopores. In such a case, improved performance can be expected by using mesoporous host material with larger mesopores such as SBA-15.

Table 3. Enantioselectivities of chiral catalysts immobilized on the surfaces of inorganic support in various reactions.

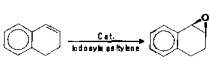
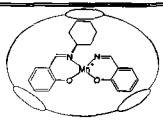
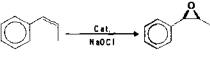
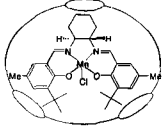
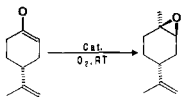
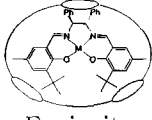
Entry	Ref.	Reactions	Catalyst	e.e.
1	129		 (Sep) = silica gel or USY	Silica 88% USY 97.9%
2	130	 R' = H, Me		Up to 100%
3	132	 a: CPBA / NMO, acetone, 0°C b: R' = R' = Ph	 a: R' = R' = Ph b: R' = R' = Ph	60% 62%
4	133	 Cat: NMO, CH2Cl2		59%
5	136	 Cat: PhIO		76%
6	137	 Cat: PhIO, CH2Cl2, 0°C	 (1) (2)	(1) 86% (2) 84%
7	138	 Cat: PhIO, CH2Cl2, 0°C		>99% 95.2%
8	143	 Cat: Et2Zn		Homogeneous (-)-ephedrine 66% Supported 33%
9	(1) 144, (2) 145	 Cat: Et2Zn	 (1) (2)	(1) up to 75% (2) 98%

4.3. Heterogenization via entrapment

This preparation method, often called the 'ship-in-bottle' approach, is based on building up a catalyst in well-defined cages of porous supports, and relies more on the size of the metal complex than on the specific adsorptive interaction with the support. The ship-in-bottle method is very useful for the fixation of homogeneous chiral catalysts without modification of environment around active chiral centers. Various host materials with small regular pores, especially microporous zeolites (X, Y, and DAY) having some mesopores generated by a post-synthetic dealumination, can be used for the entrapment of chiral complexes [146-148]. Recently, true encapsulation of enantioselective Mn(III) catalysts with different salen ligands in the cage of zeolites has been developed successfully and the results are summarized in Table 4.

In zeolite Y (entry 1) and in zeolite EMT (entry 2) ee's up to 58% and ~88% were obtained in *cis*- β -methylstyrene epoxidation, respectively [146,147]. It was necessary to enlarge the intra-zeolitic cavities by post-synthetic dealumination to generate a superior host for bulky homogeneous chiral complexes. The mesopores created were surrounded by micropores and the entrapped metal complexes can move freely and are more accessible during the catalysis. Such entrapped chiral salen complexes (entry 3) have been tested in the stereoselective epoxidation of *R*-(+)-limonene and (-)- α -pinene with molecular oxygen as an oxidant [148]. The best results so far-100 % conversion, 96 % selectivity and 91% ee -were achieved with the immobilized (*R,R*)-(*N,N'*)-bis(3,5-di-*tert*-butylsalicylidene)-1,2-diohenyl-ethylene-1,2-diaminocobalt complex in the epoxidation of (-)- α -pinene in mesoporous Y zeolites.

Table 4. Applications of ship-in-bottle method in asymmetric catalysis.

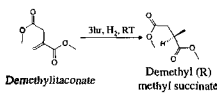
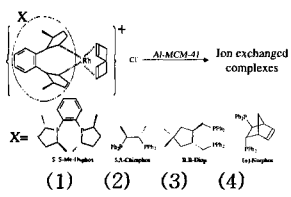
Entry	Ref.	Reactions	Catalyst	e.e.
1	146		 Y zeolite	58%
2	147		 EMT zeolite	~88%
3	148		 Faujasite	up to 91%

4.4. Immobilization of chiral complexes by ion-exchange

Electrostatic forces can also be used to bind cationic complexes to anionic supports. Both Frunza et al [149] and Piaggio et al [150] have used MCM-41 to immobilize chiral Mn(salen) complexes. Modification of the Mn-exchanged Al-MCM-41 with the salen ligand led to an enhancement in reactivity and the *cis* : *trans* ratio of the epoxide in olefin epoxidation. The *trans* epoxide is formed with an ee of 70%, which is very similar to that observed in the equivalent homogeneous reactions.

Recently, Wagner et al [151] have prepared a heterogeneous catalyst in which chiral rhodium diphosphine complexes are immobilized on Al-MCM-41 via ionic interaction of the cationic complex with the anionic MCM-41 host framework. When the hydrogenation of dimethylitaconate was studied as a test reaction, the immobilized catalysts showed high activity and excellent regio- and enantioselectivity as shown in Table 5. No reaction took place in the blank test when the carrier Al-MCM-41 itself was used as catalyst. The catalyst can be easily recovered and reused without further treatment. The conversion and the enantioselectivity of the catalyst remain at high levels after recycling.

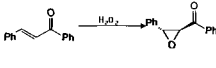
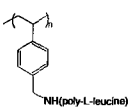
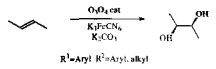
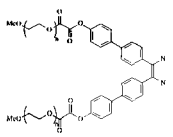
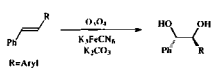
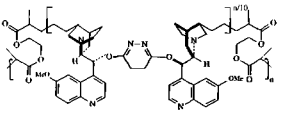
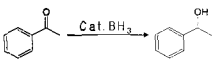
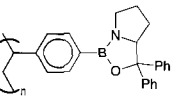
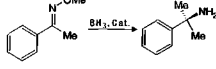
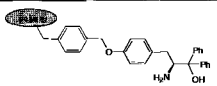
Table 5. Immobilization of rhodium diphosphine complexes on mesoporous MCM-41 and use in enantioselective hydrogenation.

Entry	Ref.	Reactions	Catalyst	e.e.
1	151	 <p>Demethylitaconate → Demethyl (R) methyl succinate</p>	 <p>Ion exchanged complexes</p> <p>X = (1) 1,5-naphthyl (2) 1,5-cyclohexadiene (3) 9,9'-bipyridine (4) 1,1'-binaphthalene</p>	(1) 92% (2) 47% (3) 35% (4) 48%

4.5. Organic polymer-supported chiral catalysts in asymmetric reactions

Covalent binding of ligands to organic polymer supports is by far the most frequently used strategy for the heterogenization of metal complexes and, in general, the successful catalytic systems are those immobilized by copolymerization or grafting method [124,125,129,141-143,152-154]. The results shown in Table 6 are not exhaustive but representative of the most active and enantioselective polymer-supported systems reported to date. Inorganic mesoporous materials can also be adopted instead of organic polymers for the various asymmetric reactions shown. It is well known that the polyamino acids grafted onto 2% cross-linked polystyrene (entry 1) are highly selective for the epoxidation of several substituted chalcones with optical yields up to 99%, and reuse was possible [152]. Together with the epoxidation of olefins, the dihydroxylation of olefins to 1,2-diols is one of the most interesting reactions to transform the olefinic bonds [129,140].

Table 6. Examples for heterogenized chiral catalysts in various reactions using polymer as a support.

Entry	Ref.	Reactions	Catalyst	e.e.
1	152			1 recycle 99% 2 recycle 94%
2	139			1 recycle 98% 2 recycle 98%
3	140			1 recycle 96% 2 recycle 96%
4	142, 153			1 recycle 98% 2 recycle 96%
5	154			99%

The polymeric systems can offer the advantages of heterogenized catalysts and the safety in handling a toxic reagent such as OsO_4 in the dihydroxylation of olefins. The highest enantioselectivity up to 99.9 % ee was obtained only using the polymer supports in the presence of two Cincona alkaloids (quinine and quinidine) [141]. Nevertheless, the drawback of the leaching expensive and toxic reaction component OsO_4 has not been completely overcome by using polymer-supported catalysts with alkaloid derivatives. Silica supported alkaloid, on the other hand, revealed very strong binding ability for OsO_4 and could be reused without any significant loss of reactivity and enantioselectivity after simple filtration.

The BH_3 hydrogenation reactions of ketones have been frequently used as a test reaction to investigate the heterogenized chiral catalysts [142,153,154]. Diphenyl amino alcohol derivatives grafted on polystyrene showed excellent performance for BH_3 hydrogenation reactions of ketones

and oxime ethers (with optical yields up to 99%; entry 4 and 5 in Table 6).

Copolymerization of functionalized ligands with a suitable monomer has been more frequently used than grafting. While the synthetic protocol is well established, it is difficult to predict and control the properties of the resulting polymer composed of a random sequence of the original monomer units. It is well known that the support properties (e.g. chemical composition, degree of cross-linking, porosity etc.) influence the catalytic performance of immobilized complexes. Mesoporous silicas, in contrast to organic polymers, do not swell and dissolve in organic solvents. The mesoporous catalysts differ significantly in many respects from the polymer supports. The choice of a support would be dependant on the catalytic system. The flexibility in choosing organic or inorganic catalysts can allow one to optimize them for each desired application. Immobilization of active homogeneous catalytic ingredient on a solid support is a fashionable topic in asymmetric catalysis. Many different techniques have been investigated to improve the enantioselectivity of products and to recycle the catalysts, but there is no general best method. Only in a few cases re-use of the recovered catalysts was possible without loss of performance. The chances of successful application of immobilized catalysts will improve with the development of new chiral ligands that have an anchoring group, efficient immobilization methods, and better understanding of the interactions between ligand-complexes and solid supports.

5 Other catalytic applications

Many other catalytic applications of M41S type mesoporous materials, utilizing the high surface areas, regular tunable pore sizes, and availability of surface sites available for further functionalization, have been reported. These were summarized in Table 7 with a comment.

6 Acknowledgements

This work was supported in part by grant No. R01-2000-000-00325-0 from the Basic Research Program of the Korea Science & Engineering Foundation.

and oxime ethers (with optical yields up to 99%; entry 4 and 5 in Table 6).

Copolymerization of functionalized ligands with a suitable monomer has been more frequently used than grafting. While the synthetic protocol is well established, it is difficult to predict and control the properties of the resulting polymer composed of a random sequence of the original monomer units. It is well known that the support properties (e.g. chemical composition, degree of cross-linking, porosity etc.) influence the catalytic performance of immobilized complexes. Mesoporous silicas, in contrast to organic polymers, do not swell and dissolve in organic solvents. The mesoporous catalysts differ significantly in many respects from the polymer supports. The choice of a support would be dependant on the catalytic system. The flexibility in choosing organic or inorganic catalysts can allow one to optimize them for each desired application. Immobilization of active homogeneous catalytic ingredient on a solid support is a fashionable topic in asymmetric catalysis. Many different techniques have been investigated to improve the enantioselectivity of products and to recycle the catalysts, but there is no general best method. Only in a few cases re-use of the recovered catalysts was possible without loss of performance. The chances of successful application of immobilized catalysts will improve with the development of new chiral ligands that have an anchoring group, efficient immobilization methods, and better understanding of the interactions between ligand-complexes and solid supports.

5 Other catalytic applications

Many other catalytic applications of M41S type mesoporous materials, utilizing the high surface areas, regular tunable pore sizes, and availability of surface sites available for further functionalization, have been reported. These were summarized in Table 7 with a comment.

6 Acknowledgements

This work was supported in part by grant No. R01-2000-000-00325-0 from the Basic Research Program of the Korea Science & Engineering Foundation.

Table 7. Other Catalytic Applications of Mesoporous Molecular Sieves.

Ref	Catalyst	Prep. Method	Reaction	Comments
155	Al-MCM-41	Grafting Al(Opr) ₃ in n-hexane	MVP reduction of cyclic ketones	<ul style="list-style-type: none"> Enhanced Lewis acidity due to low coordinated, distorted Al species
156	Al-Pc/MCM-41	Al phthalocyanine complex with NH ₂ tethering	CO ₂ cycloaddition to epoxides	<ul style="list-style-type: none"> High activity and stability Enhanced by n-Bu₄NBr addition
157	Co/SBA-15	Co(NO ₃) ₂ or Co(CH ₃ COO) ₂ impregnation	Fisch-Tropsch	<ul style="list-style-type: none"> Lower activity than conventional supports due to low reducibility
158	Co/SBA-15 MCM-41	Incipient wetness	Fisch-Tropsch	<ul style="list-style-type: none"> Pore size effect on particle size and reducibility
159	CoRu/MCM-41	Incipient Wetness	Fisch-Tropsch	<ul style="list-style-type: none"> Low catalyst reducibility No pore size effect observed
160	NiMo/MCM-41	Wet impregnation	Hydrosulfurization	<ul style="list-style-type: none"> Ni/Mo = 0.75 optimum

Table 7. (continued)

Ref	Catalyst	Prep. Method	Reaction	Comments
161	NiMo/Al-MCM-41	Impregnation	Hydrodesulfurization	<ul style="list-style-type: none"> • Metal support interaction exist with optimum $\text{SiO}_2/\text{Al}_2\text{O}_3 = 30$
162	Pt/Al-MCM-41	Wet impregnation	Naphthalene hydrogenation	<ul style="list-style-type: none"> • Bifunctional catalyst • Sulfur tolerance
163	Pt-Sn/MCM-41	Two step impregnation	Prostaglandin hydrogenation	<ul style="list-style-type: none"> • Effect of Sn content
164	Ru ₆ Pd ₆ /MCM-41	Mixed metal cluster carbonylate encapsulation	Hydrogenation	<ul style="list-style-type: none"> • Bimetallic nano particle catalysts
165	Rh-MCM-41	[RhCl(CO) ₂] ₂ immobilization with NH ₂ or PPh ₂ tethering	Hydrogenation of arenes	<ul style="list-style-type: none"> • PPh₂ ligand is much more active • No leaching
166	Rh-MCM-41	Rh(PPh ₃) ₃ Cl immobilization with (OEt ₃)Si(CH ₂) ₃ PPh ₂ tethering	Cyclohexene hydrogenation	<ul style="list-style-type: none"> • Induction period exists for best activity • Negligible leaching
167	Rh-MCM-41	Hydrothermal	NO reduction with CO	<ul style="list-style-type: none"> • RhOx particle (<3nm) size effect important

Table 7. (continued)

Ref	Catalyst	Prep. Method	Reaction	Comments
168	Pd-MCM-41	Pd-complex vapor grafting	Heck coupling of aryl halides	• Efficiency matches best homogeneous catalysts
169	Sn-MCM-41	Vapor phase grafting of SnEt ₄	Crotonaldehyde reduction	• Thin Sn-O ₂ overlayers function as active sites
170	Sn-HMS	Direct synthesis using Sn(IV) alkoxide	Ring – opening polymerization	• Poly (L-lactic acid) from Lewis acidity
171	Ni/H-MCM-41	Incipient Wetness	Isomerization of linolic acid	• Competing hydrogenation reaction
172	InCl ₃ /MCM-41 ¹	Impregnation	Acylation of aromatic compounds with acyl chloride	• Reaction insensitive to moisture
173	In ₂ O ₃ /MCM-41	Incipient Wetness	Benzoylation of benzene	• Redox function of basic In ₂ O ₃
174	CuCl/Al-MCM-41	Solid state ion exchange	Oxidative carbonylation of CH ₃ OH to DMC	• Si-O ⁺ Cu ⁺ active sites • 100% selectivity and high activity
175	Cu/MCM-41	Wet impregnation of Cu(NO ₃) ₂ + calcination	Wet oxidation of phenol	• Waste water treatment

Table 7. (continued)

Ref	Catalyst	Prep. Method	Reaction	Comments
176	MoO ₃ /HMS	Impregnation (NH ₄) ₆ Mo ₇ O ₂₄ ·4H ₂ O	Oct-1-ene metathesis	<ul style="list-style-type: none"> • Pore size & morphology strongly affect the products
177	Fe-MCM-41	Hydrothermal	Pinacol-type rearrangement	<ul style="list-style-type: none"> • Fe³⁺ redox property involved • Pore size effect observed
178	Fe ₂ O ₃ /MCM-41	Incipient wetness + calcinations	SO ₂ oxidation	<ul style="list-style-type: none"> • Superior performance to SiO₂ supported catalyst (Review)
179	V-HMS	Direct synthesis	2-butene isomerization NO decomposition	<ul style="list-style-type: none"> • Photocatalytic application (UV-irradiation)
180	V ₂ O ₅ /MCM-41	Incipient wetness + calcination	C oxidation with NO ₂	<ul style="list-style-type: none"> • Diesel soot oxidation
181	Ti-MCM-41 Ti-MCM-48	Hydrothermal	Gas phase CO ₂ + H ₂ O → CH ₄ + CH ₃ OH	<ul style="list-style-type: none"> • Photocatalytic reduction • Tetrahedral Ti⁴⁺ is active
182	Ti-HMS	Direct synthesis	Photocatalytic decomposition of NO	<ul style="list-style-type: none"> • V ion implantation enables photocatalysis under visible light irradiation

References

1. Corma A., From Microporous to Mesoporous Molecular Sieve Materials and Their Use in Catalysis, *Chem. Rev.* **97** (1997) pp. 2373-2419.
2. Arends I. W. C. E., Sheldon R. A., Wallau M. and Schuchardt U., Oxidative Transformations of Organic Compounds Mediated by Redox Molecular Sieves, *Angew. Chem. Int. Ed. Engl.* **36** (1997) pp.1144-1163.
3. Meziani M. J., Zajac J., Jones D. J., Rozière J. and Partyka S., Surface characterization of mesoporous silicoaluminates of the MCM-41 type: evaluation of polar surface sites using flow calorimetry, adsorption of a cationic surfactant as a function of pore size and aluminum content, *Langmuir* **13** (1997) pp. 5409-5417.
4. Reddy K. M. and Song C., Synthesis of mesoporous zeolites and their application for catalytic conversion of polycyclic aromatic hydrocarbons, *Catal. Today* **31** (1996) pp. 137-144.
5. Mokaya R. and Jones W., Post-synthesis grafting of Al onto MCM-41, *Chem. Commun.* (1997) pp. 2185-2186.
6. Jentys A., Pham N. H. and Vinek H., Nature of hydroxy groups in MCM-41, *J. Chem. Soc., Faraday Trans.* **92** (1996) pp. 3287-3291.
7. Chakraborty B. and Viswanathan B., Surface acidity of MCM-41 by *in situ* IR studies of pyridine adsorption, *Catal. Today* **49** (1999) pp. 253-260.
8. Ogura M., Kikuchi E. and Matsukata M., Synthesis of mesoporous materials using filtrate of alkali treatment of MFI zeolite, *Stud. Surf. Sci. Catal.* **135** (2001) 07-P-24.
9. Bossaert W. D., De Vos D. E., Van Rhijn W. M., Bullen J., Grobet P. J. and Jacobs P. A., Mesoporous sulfonic acids as selective heterogeneous catalysts for the synthesis of monoglycerides, *J. Catal.* **182** (1999) pp. 156-164.
10. Das D., Lee J. F. and Cheng S., Sulfonic acid functionalized mesoporous MCM-41 silica as a convenient catalyst for Bisphenol-A synthesis, *Chem. Commun.* (2001) pp. 2178-2179.
11. Margolese D., Melero J. A., Christiansen S. C., Chmelka B. F. and Stucky G. D., Direct syntheses of ordered SBA-15 mesoporous silica containing sulfonic acid groups, *Chem. Mater.* **12** (2000) pp. 2448-2459.
12. Díaz I., Mohino F., Perez-Pariente J., Sastre E., Wright P. A. and Zhou W., A direct synthesis route to the mesoporous silicate SBA-2 bearing thiol groups, *Stud. Surf. Sci. Catal.* **135** (2001) 07-P-17.
13. Díaz I., Mohino F., Sastre E. and Pérez-Pariente J., Synthesis and catalytic properties of SO₃H-mesoporous materials from gels containing non-ionic surfactants, *Stud. Surf. Sci. Catal.* **135** (2001) 08-P-10.
14. Melero J. A., Stucky G. D., van Grieken R. and Morales G., Direct syntheses of ordered SBA-15 mesoporous materials containing arenesulfonic acid groups, *J. Mater. Chem.* **12** (2002) pp. 1664-1670.
15. Corriu R. J. P., Datas L., Guari Y., Mehdi A., Reyé C. and Thieuleux C., Ordered SBA-15 mesoporous silica containing phosphonic acid groups prepared by a direct synthetic approach, *Chem. Commun.* (2001) pp. 763-764.
16. Yang Q., Kappor M. P. and Inagaki S., Sulfuric acid-functionalized mesoporous

- Benzene-silica with a molecular-scale periodicity in the walls, *J. Am. Chem. Soc.* **124** (2002) pp. 9694-9695.
17. Xia Q. H., Hidajat K. and Kawi S., Structure, acidity and catalytic activity of mesoporous acid catalysts for the gas-phase synthesis of MTBE from MeOH and Bu'OH, *J. Catal.* **209** (2002) pp. 433-444.
 18. Siahkali A. G., Philippou A., Dwyer J. and Anderson M. W., The acidity and catalytic activity of heteropoly acid on MCM-41 investigated by MAS NMR, FTIR and catalytic tests, *Appl. Catal. A: General* **192** (2000) pp. 57-69.
 19. Kim W. G., Kim M. W., Kim J. H. and Seo G., Dispersion measurement of heteropoly acid supported on KIT-1 mesoporous material, *Micropor. Mesopor. Mater.* in press.
 20. Jalil P. A., Al-Daous M. A., Al-Arfaj A. R. A., Al-Amer A. M., Beltrami J. and Barri S. A. I., Characterization of tungstophosphoric acid supported on MCM-41 mesoporous silica using *n*-hexane cracking, benzene adsorption and X-ray diffraction, *Appl. Catal. A: General* **207** (2001) pp. 159-171.
 21. Ying J. Y., Mehnert C. P. and Wong M. S., Synthesis and applications of supramolecular-templated mesoporous materials, *Angew. Chem. Int. Ed. Engl.* **38** (1999) pp. 57-77.
 22. Girgis M. J. and Tsao Y. P., Impact of catalyst metal-acid balance in *n*-hexadecane hydroisomerization and hydrocracking, *Ind. Eng. Chem. Res.* **35** (1996) pp. 386-396.
 23. Kodenev E. G., Shamakov A. N., Derevyankin A. Y., Lapina O. B. and Romannikov V. N., Highly-ordered aluminosilicate mesoporous mesophase materials: physico-chemical properties and catalytic behaviour, *J. Mol. Catal. A: Chemical* **158** (2000) pp. 349-354.
 24. Perego C., Amarilli S., Carati A., Flego C., Pazzuconi G., Rizzo C. and Bellussi G., Mesoporous silica-aluminas as catalysts for the alkylation of aromatic hydrocarbons with olefins, *Micropor. Mesopor. Mater.* **27** (1999) pp. 345-354.
 25. Chiche B., Sauvage E., Renzo F. D., Ivanova I. I. and Fajula F., Butene oligomerization over mesoporous MTS-type aluminosilicates, *J. Mol. Catal. A: Chemical* **134** (1998) pp. 145-157.
 26. Brunel D., Blanc A. C., Galarneau A. and Fajula F., New trends in the design of supported catalysts on mesoporous silicas and their applications in fine chemicals, *Catal. Today* **73** (2002) pp. 139-152.
 27. Beltrame P., Zuretti G. and Demartin F., Benzylolation of biphenyl with benzyl chloride over crystalline, amorphous and MCM-41 solid acid catalysts, *Ind. Eng. Chem. Res.* **39** (2000) pp. 1209-1214.
 28. Hu X., Chuah G. K. and Jaenicke S., Solid acid catalyst for the efficient synthesis of 2-(2,4-difluorophenyl)propane, *Appl. Catal. A: General* **209** (2001) pp. 117-123.
 29. Seo G., Park S. H. and Kim J. H., The reversible skeletal isomerization between *n*-butenes and *iso*-butene over solid acid catalysts, *Catal. Today* **44** (1998) pp. 215-222.
 30. Seo G., Kim N. H., Lee Y. H. and Kim J. H., Skeletal isomerization of 1-butene over mesoporous materials, *Catal. Lett.* **57** (1999) pp. 209-215.
 31. Hunter H. M. A. and Wright P. A., Synthesis and characterisation of the mesoporous silicate SBA-2 and its performance as an acid catalyst, *Micropor.*

- Mesopor. Mater.* **43** (2001) pp. 361-373.
32. Choi S., Wang Y., Nie Z., Liu J. and Peden C. H. F., Cs-substituted tungstophosphoric acid salt supported on mesoporous silica, *Catal. Today* **55** (2000) pp. 117-124.
33. Kim M. W., Kim W. G., Kim J. H., Sugi Y. and Seo G., Alkylation of isopropyl naphthalene over heteropoly acid catalysts supported on mesoporous materials, *Stud. Surf. Sci. Catal.* **135** (2001) 25-P-16.
34. Yang W., Billy J., Taarit Y. B., Védrine J. C. and Essayem. N., $\text{H}_3\text{PW}_{12}\text{O}_{40}$ supported on Cs modified mesoporous silica: catalytic activity in *n*-butane isomerisation and *in situ* FTIR study comparison with microporous $\text{Cs}_x\text{H}_{3-x}\text{PW}_{12}\text{O}_{40}$, *Catal. Today* **73** (2002) pp. 153-165.
35. Blasco T., Corma A., Martínez A. and Matínez-Escolano P., Supported heteropolyacid (HPW) catalysts for the continuous alkylation of isobutane with 2-butene: the benefit of using MCM-41 with larger pore diameters, *J. Catal.* **177** (1998) pp. 306-313.
36. Díaz I., Mohino F., Perez-Pariente J. and Sastre E., Synthesis, characterization and catalytic activity of MCM-41-type mesoporous silicas functionalized with sulfonic acid, *Appl. Catal. A: General* **205** (2001) pp. 19-30.
37. Sakata Y., Uddin M. A., Muto A., Kanada Y., Koizumi K. and Murata K., Catalytic degradation of polyethylene into fuel oil over mesoporous silica (KFS-16) catalyst, *J. Anal. Appl. Pyrolysis* **43** (1997) pp. 15-25.
38. Uddin M. A., Sakata Y., Muto A., Shiraga Y., Koizumi K., Kanada Y. and Murata K., Catalytic degradation of polyethylene and polypropylene into liquid hydrocarbons with mesoporous silica, *Micropor. Mesopor. Mater.* **21** (1998) pp. 557-564.
39. Jalil P. A., Investigations on polyethylene degradation into fuel oil over tungstophosphoric acid supported on MCM-41 mesoporous silica, *J. Anal. Appl. Pyrolysis* **65** (2002) pp. 185-195.
40. Jaenicke S., Chuah G. K., Lin X. H. and Hu X. C., Organic-inorganic hybrid catalysts for acid-and base-catalyzed reactions, *Micropor. Mesopor. Mater.* **35-36** (2000) pp. 143-153.
41. Kloetstra K. R., van Laren M. and van Bekkum H., Binary caesium-lanthanum supported on MCM-41: a new stable heterogeneous basic catalyst, *J. Chem. Soc., Faraday Trans.* **93** (1997) pp. 1211-1220.
42. Ernst S., Bongers T., Casel C. and Munsch S., Cesium-modified mesoporous molecular sieves as basic catalysts for Knoevenagel condensations, *Stud. Surf. Sci. Catal.* **125** (1999) pp. 367-374.
43. Yan X. W., Han X. W., Huang W. Y., Zhu J. H. and Min K., Attempts on generating basic sites on mesoporous materials, *Stud. Surf. Sci. Catal.* **142** (2002) pp. 1481-1488.
44. Inaki Y., Kajita Y., Yoshida H., Ito K. and Hattori T., New basic mesoporous silica catalyst obtained by ammonia grafting, *Chem. Commun.* (2001) pp. 2358-2359.
45. Subba Rao Y. V., De Vos D. E. and Jacobs P. A., 1,5,7-Triazabicyclo[4.4.0]dec-5-ene immobilized in MCM-41: a strongly basic porous catalyst, *Angew. Chem. Int. Ed. Engl.* **36** (1997) pp. 2661-2663.
46. Brunel D., Functionalized micelle-templated silicas (MTS) and their use as

- catalysts for fine chemicals, *Micropor. Mesopor. Mater.* **27** (1999) pp. 329-344.
47. Cauvel A., Renard G. and Brunel D., Monoglyceride synthesis by heterogeneous catalysis using MCM-41 type silicas functionalized with amino groups, *J. Org. Chem.* **62** (1997) pp. 749-751.
48. Lin X., Chuah G. K. and Jaenicke S., Base-functionalized MCM-41 as catalysts for the synthesis of monoglycerides, *J. Mol. Catal. A: Chemical* **150** (1999) pp. 287-294.
49. Choi Y., Kim K. S., Kim J. H. and Seo G., Knoevenagel condensation between ethylcyanoacetate and benzaldehyde over base catalysts immobilized on mesoporous materials, *Stud. Surf. Sci. Catal.* **135** (2001) 23-O-04.
50. Rodriguez I., Iborra S., Rey F. and Corma A., Heterogeneized Brønsted base catalysts for fine chemicals production: grafted quaternary organic ammonium hydroxides as catalyst for the production of chromenes and coumarins, *Appl. Catal. A: General* **194-195** (2000) pp. 241-252.
51. Rodriguez I., Iborra S., Corma A., Rey F. and Jorda J. L., MCM-41-Quaternary organic tetraalkylammonium hydroxide composites as strong and stable Brønsted base catalysts, *Chem. Commun.* (1999) pp. 593-594.
52. Corma A., Iborra S., Miguer S. and Primo J., Catalysts for the production of fine chemicals, *J. Catal.* **173** (1998) pp. 315-327.
53. Weitkamp J., Hunger M. and Rymas U., Base catalysis on microporous and mesoporous materials: recent progress and perspectives, *Micropor. Mesopor. Mater.* **48** (2001) pp. 255-270.
54. Notari B., Microporous crystalline titanium silicates, *Advances in Catalysis* **41** (1996) pp. 253-334.
55. Vayssilov G. N., Structural and physicochemical features of titanium silicalites, *Catal. Rev. Sci. Eng.* **39** (1997) pp. 209-251.
56. Corma A., Cambor M. A., Esteve P., Martines A. and Perezpariente J., Activity of Ti-beta catalyst for the selective oxidation of alkenes and alkanes, *J. Catal.* **145** (1994) pp. 151-158.
57. Blasco T., Corma A., Navarro M. T. and Peraz P. J., Synthesis, characterization and catalytic activity of Ti-MCM-41 structures, *J. Catal.* **156** (1995) pp. 65-74.
58. Koyano K. A. and Tatsumi T., Synthesis of titanium-containing MCM-41, *Micropor. Mater.* **10** (1997) pp. 259-271.
59. Reddy J. S., Dicko A. and Sayari A., Ti-Modified mesoporous molecular sieves, Ti-MCM-41 and Ti-HMS. In synthesis of microporous material: zeolites, clays and nanostructure, ed. by Occelli M. L. and Kessler H. (Marcel Dekker, New York, 1996) pp. 405-417.
60. Corma A., Iglesias M. and Sanchez F., Large pore Ti-zeolites and mesoporous Ti-silicalites as catalysts for selective oxidation of organic sulfides, *Catal. Lett.* **39** (1996) pp. 153-156.
61. Tanev P. T., Chibwe M. and Pinnavaia T. J., Titanium-containing mesoporous molecular sieves for catalytic oxidation of aromatic compounds, *Nature* **368** (1994) pp. 321-323.
62. Zhang W. Z., Froba M., Wang J. L., Tanev P. T., Wong J. and Pinnavaia T. J., Mesoporous titanosilicate molecular sieves prepared at ambient temperature by electrostatic (S^+T , $S^+X^-T^+$) and neutral (S^0T^0) assembly pathways: a comparison of physical properties and catalytic activity for peroxide oxidations, *J. Am. Chem.*

- Soc.* **118** (1996) pp. 9164-9171.
63. Suh Y. W., Kim N. K., Ahn W. S. and Rhee H. K., Redox-mesoporous molecular sieve as a bifunctional catalyst for the one-pot synthesis of campholenic aldehyde from α -pinene, *J. Mol. Catal. A: Chemical* **174** (2001) pp. 249-254.
 64. Koyano K. A. and Tatsumi T., Synthesis of titanium-containing mesoporous molecular sieves with a cubic structure, *Chem. Commun.* (1996) pp. 145-146.
 65. Corma A., Kan Q. and Rey F., Synthesis of Si and Ti-Si-MCM-48 mesoporous materials with controlled pore sizes in the absence of polar organic additives and alkali metal ions, *Chem. Commun.* (1998) pp. 579-580.
 66. Parkash A. M., Sung-suh H. M. and Kevan L., Electron spin resonance evidence for isomorphous substitution of titanium into titanosilicate TiMCM-41 mesoporous molecular sieve, *J. Phys. Chem. B* **102** (1998) pp. 857-864.
 67. Marchese L., Maschmeyer T., Gianotti E., Coluccia S. and Thomas J. M., Probing the titanium sites in Ti-MCM-41 by diffuse reflectance and photoluminescence UV-Vis spectroscopy, *J. Phys. Chem. B* **101** (1997) pp. 8836-8838.
 68. Tatsumi T., Koyano K. A. and Igarashi N., Remarkable activity enhancement by trimethylsilylation in oxidation of alkenes and alkanes with H_2O_2 catalyzed by titanium-containing mesoporous molecular sieves, *Chem. Commun.* (1998) pp. 325-326.
 69. Corma A., Domine M., Gaona J. A., Jorda J. L., Navarro M. T., Rey F., Perez-Pariente J., Tsuji J., McCulloch B. and Nemeth L. T., Strategies to improve the epoxidation activity and selectivity of Ti-MCM-41, *Chem. Commun.* (1998) pp. 2211-2212.
 70. Corma A., Jorda J. L., Navarro M. T. and Rey F., One step synthesis of highly active and selective epoxidation catalysts formed by organic-inorganic Ti containing mesoporous composites, *Chem. Commun.* (1998) pp. 1899-1900.
 71. Hagen A., Schueler K. and Roessner F., The performance of Ti-MCM-41 in aqueous media and after mechanical treatment studied by *in situ* XANES, UV/Vis and test reactions, *Micropor. Mesopor. Mater.* **51** (2002) pp. 23-33.
 72. Ahn W. S., Kim N. K. and Jeong S. Y., Synthesis, characterization and catalytic properties of Ti-containing mesoporous molecular sieves prepared using a fluorosilicon compound, *Catal. Today* **68** (2001) pp. 83-88.
 73. Luo Y., Lu G. Z., Guo Y. L. and Wang Y. S., Study on Ti-MCM-41 zeolites prepared with inorganic Ti sources: synthesis, characterization and catalysis, *Catal. Commun.* **3** (2002) pp. 129-134.
 74. Yu J. Q., Feng Z. C., Xu L., Li M. J., Xin Q., Liu Z. M. and Li C., Ti-MCM-41 synthesized from colloidal silica and titanium trichloride: synthesis, characterization and catalysis, *Chem. Mater.* **13** (2000) pp. 994-998.
 75. Maschmeyer T., Rey F., Sanker G. and Thomas J. M., Heterogeneous catalysts obtained by grafting metallocene complexes onto mesoporous silica, *Nature* **378** (1995) pp. 159-162.
 76. Kang K. K., Ahn W. S., Physicochemical properties of transition metal-grafted MCM-41 prepared using metallocene precursors, *J. Mol. Catal. A: Chemical* **159** (2000) pp. 403-410.
 77. Ahn W. S., Lee D. H., Kim. T. J., Kim J. H., Seo G. and Ryoo R., Post-synthetic preparations of titanium-containing mesopore molecular sieves, *Appl. Catal. A:*

General **181** (1999) pp. 39-49.

78. Attfilee M. P., Sankar G. and Thomas J. M., Facile heterogenisation of molecular $\text{Ti}(\text{OSiPh}_3)_4$ to form a highly active epoxidation catalyst, *Catal. Lett.* **70** (2000) pp. 155-158.
79. Lang N., Delichere P. and Tuel A., Post-synthesis introduction of transition metals in surfactant-containing MCM-41 materials, *Micropor. Mesopor. Mater.* **56** (2002) pp. 203-217.
80. Krijnen S., Abbenhuis H. C. L., Hanssen R. W. J. N., van Hooff J. H. C. and van Santen R. A., Solid-phase immobilization of a new epoxidation catalyst, *Angew. Chem. Int. Ed.* **37** (1998) pp. 356-358.
81. Smet P., Riondato J., Pauwels T., Moens L. and Verdonck L., Preparation and characterization of a titanium(IV) silsesquioxane epoxidation catalyst anchored into mesoporous MCM-41, *Inorg. Chem. Commun.* **3** (2000) pp. 557-562.
82. Newalkar B. L., Olanrewaju J. and Komarneni S., Direct synthesis of titanium-substituted mesoporous SBA-15 molecular sieve under microwave-hydrothermal conditions, *Chem. Mater.* **13** (2001) pp. 552-557.
83. Wu P. and Tatsumi T., Postsynthesis, Characterization and catalytic properties in alkene epoxidation of hydrothermally stable mesoporous Ti-SBA-15, *Chem. Mater.* **14** (2002) pp. 1657-1664.
84. Calleja G., van Grieken R., Garcia R., Melero J.A. and Iglesias J., Preparation of titanium molecular species supported on mesostructured silica by different grafting methods, *J. Mol. Catal. A: Chemical* **182-183** (2002) pp. 215-225.
85. Luan Z. H., Maes E. M., van der Heide P. A. W., Zhao D. U., Czernuszewicz R. S. and Kevan L., Incorporation of titanium into mesoporous silica molecular sieve SBA-15, *Chem. Mater.* **11** (1999) pp. 3680-3686.
86. Jarupatrakorn J. and Don Tilley T., Silica-supported, single-site titanium catalysts for olefin epoxidation. A molecular precursor strategy for control of catalyst Structure, *J. Am. Chem. Soc.* **124** (2002) pp. 8380-8388.
87. Haskouri J. E., Cabrera S., Gutierrez M., Beltran-Porter A., Beltran-Porter D., Dolores Marcos M. and Amoros P., Very high titanium content mesoporous silicas, *Chem. Commun.* (2001) pp. 309-310.
88. Bagshaw S. A., Di Renzo F. and Fajula F., Preparation of metal-incorporated MSU mesoporous silica molecular sieves. Ti Incorporation via a totally non-ionic route, *Chem. Commun.* (1996) pp. 2209-2210.
89. Aronson B. J., Blanford C. F. and Stein A., Solution-phase grafting of titanium dioxide onto the pore surface of mesoporous silicates: synthesis and structural characterization, *Chem. Mater.* **9** (1997) pp. 2842-2851.
90. Schrijnemakers K. and Vansant E. F., Preparation of titanium oxide supported MCM-48 by the designed dispersion of titanylacetylacetonate, *J. Porous Mater.* **8** (2001) pp.83-90.
91. Shan Z., Gianotti E., Jansen J. C., Peters J. A., Marchese L. and Maschmeyer T., One-step synthesis of a highly active, mesoporous, titanium-containing silica by using bifunctional templating, *Chem. Eur. J.* **7** (2001) pp. 1437-1443.
92. Xiao F. S., Han Y., Yu Y., Meng X. G., Yang M. and Wu S., Hydrothermally stable ordered mesoporous titanosilicates with highly active catalytic sites, *J. Am. Chem. Soc.* **124** (2002) pp. 888-889.
93. Reddy K. M., Moudrakovski I. and Sayari A., Synthesis of mesoporous

- vanadium silicate molecular sieves, *J. Chem. Soc. Chem. Commun.* (1994) pp. 1059-1060.
94. Sayari A., Moudrakovski I. L., Ratcliffe C. I. Ripmeester J. A. and Preston K. F., Synthesis and spectroscopic studies of vanadium-containing molecular sieves. In *Synthesis of microporous material: zeolites, clays and nanostructure*, ed. by Occelli M. L. and Kessler H. (Marcel Dekker, New York, 1996) pp. 417- 430.
95. Reddy J. S., Liu P. and Sayari A., Vanadium containing crystalline mesoporous molecular sieves leaching of vanadium in liquid phase reactions, *Appl. Catal. A: General* **148** (1996) pp. 7-21.
96. Neumann R. and Khenkin A. M., Vanadium-substituted MCM-41 zeolites as catalysts for oxidation of alkanes with peroxides, *Chem. Commun.* (1996) pp. 2643-2644.
97. Pena M. L., Dejoz A., Fornes V., Rey F., Vazquez M. I. and Lopez Nieto J. M., V-containing MCM-41 and MCM-48 catalysts for the selective oxidation of propane in gas phase, *Appl. Catal. A* **209** (2001) pp. 155-164.
98. Dai L. X., Tabata K. J., Suzuki E. J. and Tatsumi T., Synthesis and characterization of V-SBA-1 cubic mesoporous molecular sieves, *Chem. Mater.* **13** (2001) pp. 208-212.
99. Gontier S. and Tuel A., Novel zirconium containing mesoporous silicas for oxidation reactions in the liquid phase, *Appl. Catal. A: General* **143** (1996) pp. 125-135.
100. Ziolk M., Sobczak I., Nowak I., Decyk P., Lewandowska A. and Kujawa J., Nb-containing mesoporous molecular sieves—a possible application in the catalytic processes, *Micropor. Mesopor. Mater.* **35-36** (2000) pp. 195-207.
101. Zhang Q. H., Wang Y., Itsuki S., Shishido T. and Takehira K., Fe-MCM-41 for selective epoxidation of styrene with hydrogen peroxide, *Chem. Lett.* (2001) pp. 946-947.
102. Sakthivel A. and Selvam P., Mesoporous (Cr)MCM-41: a mild and efficient heterogeneous catalyst for selective oxidation of cyclohexane, *J. Catal.* **211** (2002) pp. 134-143.
103. Zhang Z. R., Suo J. H., Zhang X. M. and Li S. B., Synthesis, characterization and catalytic testing of W-MCM-41 mesoporous molecular sieves, *Appl. Catal. A: General* **179** (1999) pp. 11-19.
104. Arends I. W. C. E. and Sheldon R. A., Activities and stabilities of heterogeneous catalysts in selective liquid phase oxidations: recent developments, *Appl. Catal. A: General* **212** (2001) pp. 175-187.
105. Liu C., Ye X. and Wu Y., Hydroxylation of phenol by iron(II)-phenanthroline(Phen)/MCM-41 zeolite, *Catal. Lett.* **36** (1996) pp. 263-266.
106. Ganesan R. and Viswanathan B., Synthesis, characterization and catalytic activity of μ -oxo bridged dinuclear iron 1,10 phenanthroline complex encapsulated in MCM-41, *J. Mol. Catal. A: Chemical* **181** (2002) pp. 99-107.
107. Carvalho W. A., Wallau M. and Schuchardt U., Iron and copper immobilised on mesoporous MCM-41 molecular sieves as catalysts for the oxidation of cyclohexane, *J. Mol. Catal. A* **144** (1999) pp. 91-99.
108. Lee C. W., Ahn D. H., Wang B., Hwang J. S. and Park S. E., Hydroxylation of phenol over surface functionalized MCM-41 supported metal catalyst, *Micropor. Mesopor. Mater.* **44-45** (2001) pp. 587-594.

109. Choudary B. M., Kantam M. L., Bharathi B., Sreekanth P. and Figueras F., Epoxidations of olefins catalysed by new Mn(II) salen immobilized mesoporous materials, *J. Mol. Catal. A: Chemical* **159** (2000) pp. 417-421.
110. Lau S. H., Caps V., Yeung K. W., Wong K. Y. and Tsang S. C., A novel MCM-41-supported manganese(III) complex with nitrogen donor ligand for cyclohexene oxidation, *Micropor. Mesopor. Mater.* **32** (1999) pp. 279-285.
111. Li Z., Xia C. G. and Zhang X. M., Preparation and catalysis of DMY and MCM-41 encapsulated cationic Mn(III)-porphyrin complex, *J. Mol. Catal. A* **185** (2002) pp. 47-56.
112. Zhang Q. H., Wang Y., Itsuki S., Shishido T. and Takehira K., Manganese-containing MCM-41 for epoxidation of styrene and stilbene, *J. Mol. Catal. A* **188** (2002) pp. 189-200.
113. Burch R., Cruise N., Gleeson D. and Tsang S. C., Surface-grafted manganese-oxo species on the walls of MCM-41 channels-a novel oxidation catalyst, *Chem. Commun.* (1996) pp. 951-952.
114. Maschmeyer T., Oldroyd R. D., Sankar G., Thomas J. M., Shannon I. J., Beattie J. K. and Catlow C. R. A., Designing a solid catalyst for the selective low-temperature oxidation of cyclohexane to cyclohexanone, *Angew. Chem. Int. Ed. Engl.* **36** (1997) pp. 1639-1642.
115. Konor S., Chaudhari K., Das T. K. and Sivasanker S., Immobilization of Cr(salen) moiety in MCM-41 and studies on its catalytic properties, *J. Mol. Catal. A: Chemical* **150** (1999) pp. 295-297.
116. Brunel D., Fajula F., Nagy J. B., Deroide B., Verhoef M. J., Veum L., Peters J. A. and van Bekkum H., Comparison of two MCM-41 grafted TEMPO catalysts in selective alcohol oxidation, *Appl. Catal. A: General* **213** (2001) pp. 73-82.
117. Hoegaerts D., Sels B. F., de Vos D. E., Verpoort F. and Jacobs P. A., Heterogeneous tungsten-based catalysts for the epoxidation of bulky olefins, *Catal. Today* **60** (2000) pp. 209-218.
118. Bregeault J. M., Piquemal J. Y., Briot E., Duprey E., Launay F., Salles L., Vennat M. and Legrand A. P., New approaches to anchoring or insertion highly dispersed tungsten oxo(peroxo) species in mesoporous silicates, *Micropor. Mesopor. Mater.* **44-45** (2001) pp. 409-417.
119. Ernst S. and Selle M., Immobilization and catalytic properties of perfluorinated ruthenium phthalocyanine complexes in MCM-41-type molecular sieves, *Micropor. Mesopor. Mater.* **27** (1999) pp. 355-363.
120. Fujiyama H., Kohara I., Iwai K., Nishiyama S., Tsuruya S. and Masai M., Liquid-phase oxidation of 2,6-di-tert-butylphenol with Cu-impregnated MCM-41 catalysts in the presence of alkali metals, *J. Catal.* **188** (1999) pp. 417-425.
121. Collier P. J., Goulding T., Iggo J. A. and Whyman R., Studies of the platinum cinchona alkaloid catalyst for enantioselective α -ketoester hydrogenation, in *Chiral Reactions in Heterogeneous Catal.*, ed. by Jannes G. and Dubois V. (Plenum Press, 1995) pp. 105-110.
122. Blaser H. U. and Wiehl H. P. J., Enantioselective hydrogenation of α -ketoesters with cinchona-modified platinum catalysts: Effect of acidic and basic solvents and additives, *J. Mol. Catal.* **68** (1991) pp. 215-222.
123. Minder B., Schurch M., Mallat T., Baiker A., Heinz T. and Pfaltz A., Enantioselective hydrogenation of ethyl pyruvate over Pt/Alumina modified by

- (R)-1-(1-naphthyl)ethylamine derivatives, *J. Catal.* **160** (1996) pp. 261-268.
124. Minder B., Mallat T., Baiker A., Wang G., Heinz T. and Pfaltz A., A novel aminoalcohol modifier for the enantioselective hydrogenation of ethyl pyruvate on Pt/Alumina, *J. Catal.* **154** (1995) pp. 371-378.
125. Blaser H. U. and Pugin B., Scope and limitations of the applications of heterogeneous enantioselective catalyst, in *Chiral Reactions in Heterogeneous Catal.*, ed. by Jannes G. and Dubois V. (Plenum Press, 1995) pp. 33-57.
126. Bhaduri S., Darshane V. S., Sharma K. and Mukesh D., Carbonyl cluster derived polystyrene supported platinum for asymmetric hydrogenation of alpha-ketoesters, *J. Chem. Soc., Chem. Commun.* (1992) pp. 1738-1740.
127. Augustin R. L., Chapter 14 Hydrogenation I: Selectivity, in *Heterogeneous Catalysis for the Synthetic Chemist* (Marcell Dekker, 1996) pp. 313-343.
128. Balazsik K., Torok B., Szakonyi G. and Bartok M., Homogeneous and heterogeneous asymmetric reactions. Part X: Enantioselective hydrogenations over K-10 montmorillonite supported noble metal catalysts with immobilized modifier, *Appl. Catal. A: General* **182** (1999) pp. 53-63.
129. Corma A., Iglesias M., del Pino C. and Sanchez F., New rhodium complexes anchored on modified USY zeolites. A remarkable effect of the support on the enantioselectivity of catalytic hydrogenation of prochiral alkenes, *J. Chem. Soc. Chem. Commun.* (1991) pp. 1253-1255.
130. Nagel U. and Kinzel E., The first stereospecific catalytic hydrogenation with a polymer supported optically active rhodium complex, *J. Chem. Soc. Chem. Commun.* (1986) 1098-1099.
131. Shephard D. S., Nano-clusters, enantioselective catalysis and molecular recognition contrast agents in MCM-41. part II., *Stud. Surf. Sci. Catal.* **129** (2000) pp. 797-805.
132. Pini D., Mandoli A., Orlandi S. and Salvadori P., First example of a silica gel-supported optically active Mn(III)-salen complex as a heterogeneous asymmetric catalyst in the epoxidation of olefins, *Tetrahedron: Asymmetry* **10** (1999) pp. 3883-3886.
133. Kim G. J. and Shin J. H., The catalytic activity of new chiral salen complexes immobilized on MCM-41 by multi-step grafting in the asymmetric epoxidation, *Tetrahedron Lett.* **40** (1999) pp. 6827-6830.
134. Sherrington D.C., Polymer-supported metal complex alkene epoxidation catalysts, *Catal. Today* **57** (2000) pp. 87-104.
135. Canali L., Cowan E., Deleuze H., Gibson C. L. and Sherrington D. C., Remarkable matrix effect in polymer-supported Jacobsen's alkene epoxidation catalysts, *Chem. Commun.* **23** (1998) pp. 2561-2562.
136. Brunel D., Sutra P., and Fajula F., New chiral hybrid organic-inorganic mesoporous materials for enantioselective epoxidation, *Stud. Surf. Sci. Catal.* **129** (2000) pp. 773-780.
137. Xiang S., Zhang Y., Xin Q. and Li C., Asymmetric epoxidation of allyl alcohol on organic-inorganic hybrid chiral catalysts grafted onto the surface of silica and in the mesoporous of MCM-41, *Angew. Chem. Int. Ed.* **41** (2002) pp. 821-824.
138. Song C. E., Yang J. W. and Ha H. J., Silica gel supported bis-cinchona alkaloid: a highly efficient chiral ligand for heterogeneous asymmetric dihydroxylation of olefins, *Tetrahedron: Asymmetry* **8** (1997) pp. 841-844.

139. Bolm C. and Gerlach A., Polymer supported catalytic asymmetric Sharpless dihydroxylations of olefins, *Eur. J. Org. Chem.* (1998) pp. 21-27.
140. Lohray B. B., Nandan E. and Bhushan V., Unprecedented reactivity and selectivity in heterogeneous asymmetric catalytic dihydroxylation of alkenes, *Tetrahedron Lett.* **35** (1994) pp. 6559-6562.
141. Song C. E., Yang J. W., Ha H. J. and Lee S. G., Efficient and practical polymer catalysts for heterogeneous asymmetric dihydroxylation of olefins, *Tetrahedron: Asymmetry* **7** (1996) 645-648.
142. Kragl U. and Dwars T., The development of new methods for the recycling of chiral catalysts, *TRENDS in Biotechnology* **19** (2001) pp. 442-449.
143. Brunel D., Bellocq N., Sutra P., Cauvel A., Lasperas M., Moreau P., Renzo F. D., Galarneau A. and Fajula F., Transition-metal ligands bound onto the micelle-templated silica surface, *Coordination Chemistry Reviews* **178** (1998) pp. 1085-1108.
144. Kim S. W., Bae S. J., Hyeon T. and Kim B. M., Chiral proline-derivative anchored on mesoporous silicas and their application to asymmetric diethylzinc addition to benzaldehyde, *Micropor. Mesopor. Mater.* **44** (2001) pp. 523-529.
145. Heckel A. and Seebach D., Immobilization of TADDOL with a high degree of loading on porous silica gel and first applications in enantioselective catalysis, *Angew. Chem. Int. Ed. Engl.* **39** (2000) pp. 163-165.
146. Sabater M. J., Corma A., Domenech A., Fornes V. and Garcia H., Chiral salen manganese complex encapsulated within Zeolite Y: a heterogeneous enantioselective catalyst for the epoxidation of alkenes, *Chem. Commun.* (1997) pp. 1285-1286.
147. Ogunwumi S. B. and Bein T., Intrazeolite assembly of a chiral manganese salen epoxidation catalyst, *Chem. Commun.* (1997) pp. 901-902.
148. Schuster C. and Holderich W. F., Modification of faujasites to generate novel host for "Ship-in-bottle" complexes, *Catal. Today* **60** (2000) pp. 193-207.
149. Frunza L., Kosslick H., Landmesser H., Hoft E. and Fricke R., Host/guest interactions in nanoporous materials I. The embedding of chiral salen manganese(III) composites into mesoporous silicates, *J. Mol. Catal. A: Chemical* **123** (1997) pp. 179-187.
150. Piaggio P., McMorn P., Langham C., Bethell D., Bulman-Page P. C., Hancock F. E. and Hutchings G. J., Asymmetric epoxidation of stilbene by manganese(III) chiral salen complex immobilized in Al-MCM-41, *New J. Chem.* (1998) pp. 1167-1169.
151. Wagner H. H., Hausmann H. and Holderich W. F., Immobilized of rhodium diphosphine complexes on mesoporous Al-MCM-41 materials: catalysts for enantioselective hydrogenation, *J. Catal.* **203** (2001) pp. 150-156.
152. Itsuno S., Sakakura M. and Ito K., Polymer-supported poly(amino acids) as new asymmetric epoxidation catalyst of α,β -unsaturated ketones, *J. Org. Chem.* **55** (24) (1990) pp. 6047-6049.
153. Franot C., Stone G. B., Engeli P., Spondlin C. and Waldvogel E., A polymer-bound oxazaborolidine catalyst: enantioselective borane reductions of ketones, *Tetrahedron: Asymmetry* **6** (1995) pp. 2755-2766.
154. Itsuno S., Sakurai Y. and Ito K., Asymmetric reduction of acetophenone O-methyloxime with the reagent prepared from borane and polymer-supported (S)-

- (-)-2-amino-3-(4-hydroxyphenyl)-1,1-diphenylpropan-1-ol, *Polymer* **28** (1987) pp. 1005-1008.
155. Anwender R., Palm C., Gerstberger G., Groeger O. and Engelhardt G., Enhanced catalytic activity of MCM-41-grafted aluminium isopropoxide in MPV reductions, *Chem. Commun.* (1998) pp. 1811-1812
156. Lu X. B., Wang H. and He R., Aluminium phthalocyanine complex covalently bonded to MCM-41 silica as heterogeneous catalyst for the synthesis of cyclic carbonates, *J. Mol. Catal. A: Chemical* **186** (2002) pp. 33-42.
157. Wang Y., Noguchi M., Takahashi Y. and Ohtsuka Y., Synthesis of SBA-15 with different pore sizes and the utilization as supports of high loading of cobalt catalysts, *Catal. Today* **68** (2001) pp. 3-9.
158. Khodakov A. Y., Griboval-Constant A., Bechara R. and Zholobenko V. L., Pore size effects in Fischer Tropsch synthesis over cobalt-supported mesoporous silicas, *J. Catal.* **206** (2002) pp. 230-241.
159. Panpranot J., Goodwin Jr. J. G. and Sayari A., Synthesis and characteristics of MCM-41 supported CoRu catalysts, *Catal. Today* **77** (2002) pp. 269-284.
160. Wang A., Wang Y., Kabe T., Chen Y. Y., Ishihara A., Qian W. H. and Yao P. J., Hydrodesulfurization of dibenzothiophene over siliceous MCM-41-supported catalysts, *J. Catal.* **210** (2002) pp. 319-327.
161. Klimova T., Calderon M. and Ramirez J., Ni and Mo interaction with Al-containing MCM-41 support and its effect on the catalytic behavior in DBT hydrodesulfurization, *Appl. Catal. A: General* **6225** (2002) pp. 1-12.
162. Park K. C., Yim D. J. and Ihm S. K., Characteristics of Al-MCM-41 supported Pt catalysts: effect of Al distribution in Al-MCM-41 on its catalytic activity in naphthalene hydrogenation, *Catal. Today* **74** (2002) pp. 281-290.
163. Coman S., Cocu F., Parvulescu V. I., De Vos D. and Jacobs P. A., Chemoselective reduction of prostaglandin intermediates by liquid-phase hydrogen transfer on Pt-Sn/MCM-41 catalysts, *Micropor. Mesopor. Mater.* **44-45** (2001) pp. 477-482.
164. Johnson B. F. G., Raynor S. A., Brown D. B., Shephard D. S., Mashmeyer T., Thomas J. M., Hermans S., Raja R. and Sankar G., New catalysts for clean technology, *J. Mol. Catal. A: Chemical* **182-183** (2002) pp. 89-97.
165. Liu A. M., Hidajat K. and Kawi S., Combining the advantages of homogeneous and heterogeneous catalysis: rhodium complex on functionalized MCM-41 for the hydrogenation of arenes, *J. Mol. Catal. A: Chemical* **168** (2001) pp. 303-306.
166. Shyu S. G., Cheng S. W. and Tzou D. L., Immobilization of Rh(PPh₃)Cl on phosphinated MCM-41 for catalytic hydrogenation of olefins, *Chem. Commun.* (1999) pp. 2337-2338.
167. Mulukutla R. S., Shido T., Asakura K., Kogure T. and Iwasawa Y., Characterization of rhodium oxide nanoparticles in MCM-41 and their catalytic performances for NO-CO reactions in excess O₂, *Appl. Catal. A: General* **228** (2002) pp. 305-314.
168. Mehnert C. P. and Ying J. Y., Palladium-grafted mesoporous MCM-41 material as heterogeneous catalyst for Heck reactions, *Chem. Commun.* (1997) pp. 2215-2216.
169. Burch R., Caps V., Gleeson D., Nishiyama S. and Tsang S. C., Nanoscopic tin-oxygen linings on mesoporous silica as a novel catalyst for organic hydrogen transfer reaction, *Appl. Catal. A: General* **194-195** (2000) pp. 297-307.

170. Abdel-Fattah T. M. and Pinnavaia T. J., Tin-substituted mesoporous silica molecular sieve (Sn-HMS): synthesis and properties as a heterogeneous catalyst for lactide ring-opening polymerization, *Chem. Commun.* (1996) pp. 665-666.
171. Bernas A., Laukkanen P., Kumar N., Maki-Arvela P., Vayrynen J., Laine E., Holmbom B., Salmi T. and Murzin D. Y., A new heterogeneously catalytic pathway for isomerization of inoleic acid over Ru/C and Ni/H-MCM-41 catalysts, *J. Catal.* **210** (2002) pp. 354-366.
172. Choudhary V. R., Jana S. K. and Patil N. S., Acylation of aromatic compounds using moisture insensitive InCl_3 impregnated mesoporous Si-MCM-41 catalyst, *Tetrahedron Lett.* **43** (2002) pp. 1105-1107.
173. Choudhary V. R. and Jana S. K., Benzoylation of benzene and substituted benzenes by benzoyl chloride over $\text{In}_2\text{O}_3/\text{Si-MCM-41}$ catalyst, *J. Mol. Catal. A: Chemical* **184** (2002) pp. 247-255.
174. Li Z., Xie K. and Slade R. C. T., High selective catalyst $\text{CuCl}/\text{MCM-41}$ for oxidative carbonylation of methanol to dimethyl carbonate, *Appl. Catal. A: General* **205** (2001) pp. 85-92.
175. Wu Q., Hu X. J., Yue P. L., Zhao X. S. and Lu G. Q., Copper/MCM-41 as catalyst for the wet oxidation of phenol, *Appl. Catal. B: Environmental* **32** (2001) pp. 151-156.
176. Ookoshi T. and Onaka M., A remarkable Mo catalyst for olefin metathesis: hexagonal mesoporous silica-supported molybdenum oxide (MoO_3/HMS), *Chem. Commun.* (1998) pp. 2399-2400.
177. Hsien M., Sheu H. T., Lee T., Cheng S. and Lee J. F., Fe-substituted molecular sieves as catalysts in liquid phase pinacol rearrangement, *J. Mol. Catal. A: Chemical* **181** (2002) pp. 189-200.
178. Schuth F., Wingen A. and Sauer J., Oxide loaded ordered mesoporous oxides for catalytic applications, *Micropor. Mesopor. Mater.* **44-45** (2001) pp. 465-476.
179. Zhang S. G., Ariyuki M., Mishima H., Higashimoto S., Yamashita H., and Anpo M., Photoluminescence property and photocatalytic reactivity V-HMS mesoporous zeolites effect of pore size of zeolites on photocatalytic reactivity, *Micropor. Mesopor. Mater.* **21** (1998) pp. 621-627.
180. Liu S. T., Obuchi A., Uchisawa J., Nanba T. and Kushiya S., An exploratory study of diesel soot oxidation with NO_2 and O_2 on supported metal oxide catalysts, *Appl. Catal. B: Environmental* **37** (2002) pp. 309-319.
181. Anpo M., Yamashita H., Ikeue K., Fujii Y., Zhang S. G., Ichihashi Y., Park K. R., Suzuki Y., Koyano K. and Tatsumi T., Photocatalytic reduction of CO_2 with H_2O on Ti-MCM-41 and Ti-MCM-48 mesoporous zeolite catalysts, *Catal. Today* **44** (1998) pp. 327-332.
182. Anpo M., Takeuchi M., Ikeue K. and Dohshi S., Design and development of titanium oxide photocatalysts operation under visible and UV light irradiation. The applications of metal ion-implantation techniques to semiconducting TiO_2 and Ti/zeolite catalysts, *Current Opinion in Solid State and Materials Science* **6** (2002) 381-388.

ADSORPTION AND TRANSPORT IN NANOPOROUS MATERIALS

J. P. B. MOTA

Departamento de Química, Centro de Química Fina e Biotecnologia, Faculdade de Ciências e Tecnologia, Universidade Nova de Lisboa, 2829-516 Caparica, Portugal

E-mail: pmota@dq.fct.unl.pt

The basic equations governing the transport of single and multicomponent adsorbate mixtures through nanoporous materials are reviewed. The Maxwell-Stefan equations in the form of the dusty gas model are adopted and both viscous and diffusive terms are incorporated following the work of Mason and co-workers. Surface diffusion in microporous structures is addressed separately. The relationships between the various diffusivities, including the Fickian, Maxwell-Stefan and Onsager are elucidated. The limitations of Fick's law for describing intraparticle diffusion are discussed. Finally, we develop consistent methods of simplifying the particle uptake rate equations, which still take both structural and thermodynamic factors into consideration and properly account for the coupling of the fluxes of the various components in the mixture.

1 Introduction

The transport of adsorbate mixtures in porous materials is a topic of great importance in adsorption science and technology. Modelling of transport in many nanoporous materials has already attained a level of sophistication that allows even quantitative predictions of separation performance [35,50,66,72]. These models, when properly implemented, can play a vital role at the process design stage in the selection of adsorbent materials for specific separations by providing predictions of the expected behavior in the absence of defects in the porous structure of the adsorbent.

A key problem in modelling transport of guest phases in nanoporous materials is the development of realistic models of the pore morphology and topology, which is usually irregular to a greater or lesser extent. Whereas for well defined materials, such as zeolites, their atomic structure can be determined exactly, for non-crystalline porous materials, such as silica gels, silica aluminas and porous carbons, the problem is considerably more difficult. Molecular simulation is undoubtedly the most rigorous and general approach to modelling adsorption and transport in porous materials, and holds the greatest promise for the future [23]. (The reader is referred to the chapter by Nicholson for an excellent review of this topic.) However, whilst it seems improbable that continuum models can approach the accuracy of specific atomistic mod-

elling, they are currently the only viable route for incorporating adsorption equilibrium and kinetics at the process simulation level. (A recent attempt to incorporate molecular modelling in process simulation is given in [47,48].)

In this chapter we discuss the more popular continuum theories of transport of adsorbate mixtures in nanoporous materials. Our review is necessarily limited and does not address the full topic of adsorptive transport; the reader is referred to the references cited herein for further details. Transport in porous catalysts has been discussed by Jackson [24] and by Mason and Malinauskas [44]. Adsorbate transport is addressed by Nicholson [51], and by Yang [84] and Ruthven [65] in the introductory chapters of their books. The recent monograph of Do [17] provides an excellent review of the fundamental aspects of adsorption equilibria and dynamics in microporous solids. The specific topic of diffusion in zeolites has been addressed in two monographs [29, 12], one collection [9] and several reviews [3,16,30].

We shall focus on the Maxwell-Stefan formulation, since it seems to provide the most general, and convenient, approach for describing multicomponent mass transport within both micro- and macroporous materials. Using a few simple examples taken from the recent literature, we attempt to persuade the reader of the need to employ adsorption and transport models that take into consideration both structural and thermodynamic factors and properly account for the coupling of the fluxes of the various components in the mixture. The selected cases include exceptionally high transport rates in carbon nanotubes, multicomponent permeation in silicalite membranes, and pressure swing adsorption in bi-dispersed adsorbents.

The various intraparticle transport mechanisms which are introduced in Section 2, and their coupling, are discussed in detail in Sections 3 and 4. Surface diffusion is dealt separately in Section 5. Finally (Section 6), we give an overview of particle uptake rate models with emphasis on those that are suitable to bi-dispersed solids since most commercial adsorbents and catalysts fall into this category.

2 Intraparticle transport mechanisms

Within an adsorbent particle we may, in general, distinguish three fundamentally different types of diffusion mechanisms:

- Bulk diffusion that is significant for large pore sizes and high system pressures in which molecule-molecule collisions dominate over molecule-wall collisions.

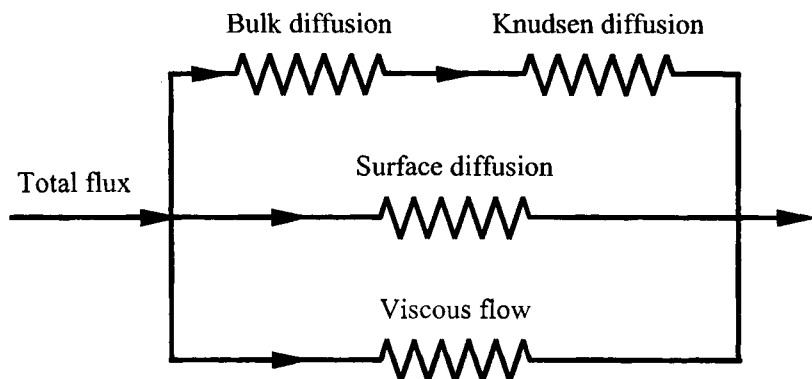


Figure 1. Electric analogue circuit picturing the distinct mechanisms by which a molecular species gets transported within an adsorbent. Adapted from Ref. [44].

- Knudsen diffusion that is the predominant mechanism when the mean-free path of the molecular species is much larger than the pore diameter and hence molecule-wall collisions become important.
- Surface diffusion of adsorbed molecular species along the surface of the pore wall; this mechanism becomes dominant for micropores and for strongly adsorbed species.

When the pressure gradient inside the particle is not negligible it gives rise to a fourth transport mechanism known as viscous, or Darcy flow. Bulk and Knudsen diffusion occur together whereas surface diffusion and viscous flow occur in parallel to the other two mechanisms (see Fig. 1).

Two theoretical formulations exist for modelling transport diffusion in nanoporous materials. The Fickian formulation relates macroscopic particle flows to concentration gradients, according to $N = -D\nabla c$, where N is the net particle flux through a surface S , D is the transport diffusivity, and ∇c is the local concentration gradient perpendicular to the surface S [10]. While this perspective is conceptually simple, it has been demonstrated that it breaks down even qualitatively in remarkably simple cases, such as phase equilibria in a closed system. In this case, Fick's law would predict a non-zero macroscopic flux due to the difference in phase density; however, no flux actually exists because the chemical potential gradient vanishes at equilibrium.

The other formulation of transport diffusion, which is discussed more extensively in this text, was developed independently by Maxwell and Stefan, and begins with the equation $N = -L\nabla\mu$, where L is the Onsager coefficient and $\nabla\mu$ is the local chemical potential gradient at the surface S . In this

approach, the flux is expressed either through an irreversible thermodynamics formulation [43] or in terms of the Maxwell-Stefan equations [38]. The two approaches are essentially equivalent, and the phenomenological coefficients of irreversible thermodynamics can be re-expressed in terms of the Maxwell-Stefan diffusion coefficients [54]. This formulation does not suffer from the qualitative shortcomings of Fick's law, and can be properly generalized for multicomponent systems [33].

We first discuss the Maxwell-Stefan formulation for combined bulk and Knudsen diffusion and then look at the viscous component of transport. When these three transport mechanisms are properly combined they give rise to the well-known *dusty gas* model developed by Mason and co-workers [42,43,45]. We then review the extension of the Maxwell-Stefan approach to describe the surface diffusion of adsorbate mixtures.

3 Combined bulk and Knudsen diffusion

For gaseous mixtures at operating conditions under which the mean free path of the molecules is much larger than the pore diameter, molecule-wall collisions are more frequent than molecule-molecule collisions and the prevailing transport mechanism is called Knudsen diffusion. In the other limit, when the mean free path of the molecules is much smaller than the pore diameter, molecule-molecule collisions predominate and bulk diffusion controls the diffusional transport. In the general case, both molecule-wall and molecule-molecule collisions contribute to the overall diffusional transport and the two mechanisms must be taken into account simultaneously.

Krishna [33] has argued convincingly that the most convenient approach to modelling combined bulk and Knudsen diffusion is the *dusty gas* model derived by Mason and co-workers [42,43,45]. The dusty gas model is basically an application of the Maxwell-Stefan diffusion equations for bulk systems [76] augmented by one additional component representing the porous solid. The latter is modelled as a collection of stationary giant molecules uniformly distributed in space, which are considered to be a dummy, or pseudo species in the mixture.

The Maxwell-Stefan description of diffusion is based on the principle that in order to cause relative motion between individual species in a mixture, a driving force has to be exerted on each of them. The driving force exerted on any particular species is due to the gradient of its chemical potential and is balanced by the friction that the species experiences with all species present in the mixture. Each of this friction contributions is considered to be proportional

to the corresponding difference in diffusion velocities and to the mole fraction of the other component.

Assuming that there are no external forces driving transport, the Maxwell-Stefan equations applied to the diffusion of an n -component mixture through a weakly interacting porous material can be written as [33]

$$-\frac{y_i}{R_g T} \nabla \mu_i = \sum_{\substack{j=1 \\ j \neq i}}^n \frac{y_j \mathbf{N}_i^d - y_i \mathbf{N}_j^d}{c \mathcal{D}_{ij}^e} + \frac{\mathbf{N}_i^d}{c \mathcal{D}_{iK}^e} \quad (i = 1, \dots, n), \quad (1)$$

where R_g is the gas constant, T is the temperature, c is the total concentration, $(y) \equiv (y_1, \dots, y_n)$ are the mole fractions, $(\mu) \equiv (\mu_1, \dots, \mu_n)$ are the chemical potentials, and $(\mathbf{N}^d) \equiv (\mathbf{N}_1^d, \dots, \mathbf{N}_n^d)$ are the individual fluxes with respect to a fixed coordinate frame. In (1) we have taken into account the fact that the solid is stationary ($\mathbf{N}_{n+1} = 0$).

For an ideal gas, $c = P/R_g T$, where $P = \sum_{i=1}^n p_i$ is the total pressure, and under isothermal conditions

$$\nabla \mu_i = R_g T \nabla \ln p_i \quad (i = 1, \dots, n), \quad (2)$$

which allows us to rewrite (1) as

$$-\frac{1}{R_g T} \nabla p_i = \sum_{\substack{j=1 \\ j \neq i}}^n \frac{y_j \mathbf{N}_i^d - y_i \mathbf{N}_j^d}{\mathcal{D}_{ij}^e} + \frac{\mathbf{N}_i^d}{\mathcal{D}_{iK}^e} \quad (i = 1, \dots, n). \quad (3)$$

For a non-ideal fluid mixture, the partial pressures p_i in (2) must be replaced by the corresponding mixture fugacities f_i .

Equation (3) can be cast into n -dimensional matrix notation to obtain the following explicit expression for the fluxes \mathbf{N}_i^d as a function of the gradients of partial pressure:

$$(\mathbf{N}^d) = -\frac{1}{R_g T} [\mathcal{B}^e]^{-1} \nabla(p), \quad (4)$$

where $(p) \equiv (p_1, \dots, p_n)$ and $[\mathcal{B}^e]$ is an n -dimensional square matrix with elements

$$B_{ii}^e = \frac{1}{\mathcal{D}_{iK}^e} + \sum_{\substack{j=1 \\ j \neq i}}^n \frac{y_j}{\mathcal{D}_{ij}^e}, \quad B_{ij(i \neq j)}^e = -\frac{y_i}{\mathcal{D}_{ij}^e} \quad (i, j = 1, \dots, n). \quad (5)$$

Equation (4) is the working equation for multicomponent transport diffusion in a weakly interacting porous material in the absence (or negligible contribution) of viscous flow.

The \mathcal{D}_{ij}^e represent the effective binary pair diffusion coefficients in the porous medium, while the \mathcal{D}_{iK}^e represent the effective Knudsen diffusion coefficients. The former are related to the corresponding free space values, D_{ij} , by

$$\mathcal{D}_{ij}^e = (\epsilon/\tau) D_{ij}, \quad (6)$$

where ϵ and τ are, respectively, the porosity and tortuosity factor of the porous matrix, both are functions of solid structure only. For gaseous components the binary diffusion coefficients D_{ij} are functions of the total pressure and temperature according to [59]

$$D_{ij} \propto T^{1.75}/P, \quad (7)$$

and so in the bulk controlled regime the fluxes N_i^d are independent of system pressure and pore size. On the other hand, the effective Knudsen diffusivities are given by [44]

$$\mathcal{D}_{iK}^e = (\epsilon/\tau) \frac{4K_0}{3} \sqrt{\frac{8R_g T}{\pi M_i}}, \quad (8)$$

where M_i is the molecular weight and K_0 is called the Knudsen diffusion parameter. K_0 is equal to $d_0/4$ for a cylindrical pore of diameter d_0 , and equal to $3h_0/16$ for a slit pore of width h_0 [53]. Therefore, in the Knudsen controlled regime the fluxes are directly proportional to the system pressure and pore size.

It follows from the above discussion that the Knudsen mechanism is important in small pores and low pressures, whereas bulk diffusion prevails in large pores and high pressures. Note also that, unlike bulk diffusion, the Knudsen mechanism contributes to the mass transport flux under both driving forces, that is, composition gradient and total pressure gradient.

4 Viscous flow

Mason and co-workers [42,43,45] demonstrated the importance of the viscous component of transport, pointing out that it should be included in the

formulation of the flux whenever transport occurs down a gradient of chemical potential. The individual viscous fluxes N_i^v can be written as

$$N_i^v = -cy_i \frac{B_0}{\eta} \nabla P \quad (i = 1, \dots, n), \quad (9)$$

where η is the viscosity of the mixture and B_0 is the permeability of the porous matrix, which is a function of solid structure only. For gases at moderate pressure, η can be calculated from the semi-empirical formula of Wilke [59]. Possible separation effects between species can be taken into account if the right-hand side of (9) is multiplied by a sieving coefficient α_i [42]; for example, $\alpha_i < 1$ allows for the possibility of semipermeable behavior, which might occur if one species is restrained by repulsive forces from passing through the pore ($\alpha_i = 0$).

In most cases the permeability has to be determined experimentally, along with K_0 and the porosity-tortuosity factor (ϵ/τ), since they all reflect solid characteristics such as pore size distribution, pore shape, pore orientation, pore surface roughness, etc. [17]. There are, however, some model structures of practical importance for which B_0 can be calculated theoretically. For example, the Poiseuille flow relationship for a cylindrical pore of diameter d_0 gives

$$B_0 = d_0^2/32, \quad (10)$$

which allows us to determine the permeability of a random arrangement of cylindrical pores with porosity ϵ :

$$B_0 = (\epsilon/\tau)d_0^2/32, \quad \tau = 3. \quad (11)$$

For parallel slit-shaped pores the term $d_0^2/32$ in (10) should be replaced by $h_0^2/12$, where h_0 is the width of the slit. For an aggregated bed of spheres the Karman-Kozeny relation gives

$$B_0 = \frac{d_0^2}{180} \frac{\epsilon^2}{(1 - \epsilon)^2}, \quad (12)$$

which is a reasonable approximation to the network of large pores in zeolite pellets.

Since the diffusive and viscous flow contributions are approximately additive, when both transport mechanisms are significant the total species flux is

$$N_i = N_i^d + N_i^v \quad (i = 1, \dots, n). \quad (13)$$

This equation, together with (9), can be inserted into (3) to give an explicit expression for the total fluxes as a function of the gradients of partial pressure:

$$(\mathbf{N}) = -\frac{1}{R_g T} [B^e]^{-1} \left\{ \nabla(p) + [\Lambda](p) \frac{B_0}{\eta} \nabla P \right\}. \quad (14)$$

$[\Lambda]$ is an n -dimensional diagonal matrix with elements

$$\Lambda_{ii} = 1/D_{iK}^e, \quad \Lambda_{ij(i \neq j)} = 0 \quad (i = 1, \dots, n) \quad (15)$$

and satisfies

$$[B^e](\gamma) = [\Lambda](\gamma). \quad (16)$$

Equation (14) is the final working form of the Mason formulation for intra-particle diffusion [42, 43] under the assumption that there are no external forces driving transport. The dusty gas model has been applied by Serbezov and Sotirchos [67, 68] to intraparticle transport in pressure swing adsorption under isothermal and non-isothermal conditions.

Equation (14) can be recast into the more familiar Fickian form as

$$(\mathbf{N}) = -[D^e] \nabla(c), \quad [D^e] = [B^e]^{-1} + \frac{B_0 R_g T}{\eta} [B^e]^{-1} [\Lambda] \begin{bmatrix} c_1 & \cdots & c_1 \\ \vdots & \ddots & \vdots \\ c_n & \cdots & c_n \end{bmatrix} \quad (17)$$

The elements D_{ij}^e of $[D^e]$ are effective Fickian transport diffusivities which account for both diffusive and viscous transport.

For the special case of single-component flow through a porous material, (14) reduces to

$$\mathbf{N} = - \left(\frac{D_K^e}{R_g T} + \frac{c B_0}{\eta} \right) \nabla P = -c \left(\frac{D_K^e}{R_g T} + \frac{c B_0}{\eta} \right) \nabla \mu, \quad (18)$$

which shows that viscous flow becomes the more important component of the flow at high density and in wide pores, since B_0 depends on the square of the pore width. For a single component with non-ideal behavior, (18) is replaced by

$$\mathbf{N} = - \left[D_K^e + R_g T \frac{c B_0}{\eta} \right] \left(\frac{\partial \ln f}{\partial \ln c} \right) \nabla c = -D^e \nabla c. \quad (19)$$

Travis and Gubbins [78] have recently developed a novel molecular simulation method in which the diffusive and viscous contributions to the total flux are determined separately. The method employs two non-equilibrium

molecular dynamics techniques: dual-control grand canonical molecular dynamics and an algorithm for simulating planar poiseuille flow. This technique was applied to study the combined viscous and diffusive transport of methane through single slit-shaped graphite pores of width 2.5, 5.0 and 10.0 methane diameters. It was found that the viscous contribution to the total intra-pore flux through each of these pores is 10%, 15% and 34%, respectively. This study lends support to the importance of the viscous flow contribution, even in very small pores [52].

Note, however, that in [78] the molecules are subjected to strong confinement and the assumption of a gaseous phase is not then a realistic model. As discussed in the next section, under these conditions the coefficient \mathcal{D}_K^e in (19) is no longer identified with the Knudsen diffusion coefficient but, in turn, expresses the mobility of the adsorbed phase.

For a two-component system, which is most often used experimentally, the explicit formulae for the fluxes are still easily manageable and the elements of $[D^e]$ are

$$[D^e] = [B^e]^{-1} + R_g T \frac{B_0}{\eta} \begin{bmatrix} c_1 & c_1 \\ c_2 & c_2 \end{bmatrix}, \quad (20)$$

$$[B^e]^{-1} = \frac{\begin{bmatrix} \mathcal{D}_{1K}^e & 0 \\ 0 & \mathcal{D}_{2K}^e \end{bmatrix}}{\mathcal{D}_{12}^e + y_1 \mathcal{D}_{2K}^e + y_2 \mathcal{D}_{1K}^e} \begin{bmatrix} \mathcal{D}_{12}^e + y_1 \mathcal{D}_{2K}^e & y_1 \mathcal{D}_{2K}^e \\ y_2 \mathcal{D}_{1K}^e & \mathcal{D}_{12}^e + y_2 \mathcal{D}_{1K}^e \end{bmatrix}. \quad (21)$$

Another special case that deserves discussion is when all effective Knudsen transport coefficients are equal and the same applies to the bulk diffusion coefficients. The most prominent example of this case are multicomponent mixtures of identical (isomers) or similar species. Under these conditions, the expression for the total molar flux

$$\mathbf{N} = - \left(\mathcal{D}_K^e + R_g T \frac{c B_0}{\eta} \right) \nabla c, \quad (22)$$

is identical to that for single-component flow, and the molar flux of a given species i can be written as

$$\mathbf{N}_i = -c \mathcal{D} \nabla y_i - y_i \left(\mathcal{D}_K^e + R_g T \frac{c B_0}{\eta} \right) \nabla c, \quad \mathcal{D} = \left(\frac{1}{\mathcal{D}^e} + \frac{1}{\mathcal{D}_K^e} \right)^{-1}. \quad (23)$$

Notice that the first term on the right-hand side of the definition of \mathbf{N}_i in (23) gives the pure diffusive flux of the species, $\mathbf{J}_i \equiv \mathbf{N}_i - y_i \sum \mathbf{N}_i$, which is the molar flux measured relative to a coordinate system that moves with the average velocity. The definition of \mathcal{D} in (23) is usually referred to as the Bosanquet formula [58].

5 Diffusion within micropores

Within micropores, the adsorbent potential field results in a large increase in adsorbate concentration in comparison with the adsorptive in the contiguous bulk phase. Furthermore, the surface forces are dominant and an adsorbed molecule never escapes from the force field of the surface. Diffusion becomes then an activated process, proceeding by a sequence of jumps between regions of low potential energy. Diffusion within this regime is generally termed configurational diffusion, intra-crystalline diffusion, micropore diffusion or simply surface diffusion [29].

Krishna [32,33,34] and Krishna and Wesselingh [38] have extended the Maxwell-Stefan approach to describe the surface diffusion of adsorbate mixtures. The theory has been recently adapted to diffusion of adsorbate mixtures wherein the individual components have different saturation loadings [28,35].

The Maxwell-Stefan approach applied to surface, or micropore, diffusion of an n -component mixture is usually written in terms of fractional occupancies θ_i as

$$-\frac{1}{R_g T} \nabla \mu_i = \sum_{\substack{j=1 \\ j \neq i}}^n \theta_j \frac{\mathbf{u}_i - \mathbf{u}_j}{\mathcal{D}_{ij}^s} + \frac{\mathbf{u}_i}{\mathcal{D}_i^s} \quad (i = 1, \dots, n), \quad (24)$$

where $-\nabla \mu_i$ is the force acting on species i tending to move it along the surface with a velocity \mathbf{u}_i . Since for different molecules different amounts may be needed to obtain similar levels of fractional occupancy, the θ_i are defined as

$$\theta_i = q_i / q_i^s \quad (i = 1, \dots, n), \quad (25)$$

where q_i is the individual loading of adsorbate i and q_i^s is the corresponding saturation value.

The first term on the right-hand side of (24) reflects the friction exerted by adsorbate j on the surface motion of species i , each moving with velocities \mathbf{u}_j and \mathbf{u}_i with respect to the surface. The second term reflects the friction between the species i and the surface. The coefficients \mathcal{D}_{ij}^s and \mathcal{D}_i^s represent the corresponding Maxwell-Stefan surface diffusivities; the \mathcal{D}_i^s is also called the corrected diffusivity in the literature [65]. Fig. 2 gives a pictorial representation of the three Maxwell-Stefan diffusivities describing diffusion of a binary mixture consisting of species 1 and 2. If there is no possibility of interchange between species 1 and 2, the first term on the right-hand side of (24) can be ignored.

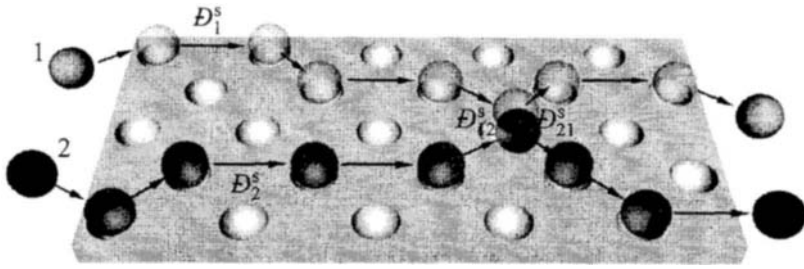


Figure 2. Conceptual model for surface diffusion of a binary adsorbate mixture. \mathcal{D}_1^s and \mathcal{D}_2^s are the Maxwell-Stefan surface diffusivities of components 1 and 2; \mathcal{D}_{12}^s represents the Maxwell-Stefan counter-sorption coefficient. Adapted from Ref. [32].

Based on the Vignes relationship for diffusion in bulk liquid mixtures, Krishna [32] has suggested that the counter-sorption diffusivity can be estimated as

$$\mathcal{D}_{ij}^s = (\mathcal{D}_i^s)^{\theta_i/(\theta_i+\theta_j)} (\mathcal{D}_j^s)^{\theta_j/(\theta_i+\theta_j)}. \quad (26)$$

Micropore diffusion is an activated process and this is evidenced by the fact that the Maxwell-Stefan micropore diffusivity follows an Arrhenius temperature dependence [27,29]:

$$\mathcal{D}^s = \mathcal{D}^{s(0)} \exp(-E^{\text{act}}/R_g T). \quad (27)$$

where E^{act} is the activation energy for surface diffusion. $\mathcal{D}^{s(0)}$ in general can be expected to be dependent on the total surface coverage but is, otherwise, temperature independent.

The surface fluxes, \mathbf{N}_i^s , of the diffusing adsorbed species are

$$\mathbf{N}_i^s = q_i \mathbf{u}_i = q_i^s \theta_i \mathbf{u}_i \quad (i = 1, \dots, n). \quad (28)$$

With this definition the Maxwell-Stefan surface diffusion equations can be recast in terms of the surface fluxes into a form analogous to (1):

$$-\frac{\theta_i}{R_g T} \nabla \mu_i = \sum_{\substack{j=1 \\ j \neq i}}^n \frac{q_j \mathbf{N}_i^s - q_i \mathbf{N}_j^s}{q_i^s q_j^s \mathcal{D}_{ij}^s} + \frac{\mathbf{N}_i^s}{q_i^s \mathcal{D}_i^s} \quad (i = 1, \dots, n) \quad (29)$$

or, alternatively,

$$-\frac{q_i}{R_g T} \nabla \mu_i = \sum_{\substack{j=1 \\ j \neq i}}^n \frac{q_j \mathbf{N}_i^s - q_i \mathbf{N}_j^s}{q_j^s \mathcal{D}_{ij}^s} + \frac{\mathbf{N}_i^s}{\mathcal{D}_i^s} \quad (i = 1, \dots, n). \quad (30)$$

To develop expressions for the diffusional fluxes, the gradients of the thermodynamic potentials are related to the gradients in loading through the partial pressures p_i (or mixture fugacities f_i) and the mixture adsorption isotherm. The left-hand side of (29) is usually expanded as follows

$$\frac{\theta_i}{R_g T} \nabla \mu_i = \sum_{j=1}^n \Gamma_{ij} \nabla \theta_j = \sum_{j=1}^n \Gamma_{ij} (q_j^s)^{-1} \nabla q_j \quad (i = 1, \dots, n), \quad (31)$$

where we have defined an n -dimensional matrix $[\Gamma]$ of thermodynamic factors

$$\Gamma_{ij} = \frac{\theta_i}{p_i} \frac{\partial p_i}{\partial \theta_j} = \left(\frac{q_j^s}{q_i^s} \right) \frac{q_i}{p_i} \frac{\partial p_i}{\partial q_j} \quad (i, j = 1, \dots, n). \quad (32)$$

$[\Gamma]$ includes the ratio of the saturation loadings of q_j^s and q_i^s , which are unequal for the off-diagonal terms.

Equations (29) and (31) can be cast into n -dimensional matrix notation as

$$(\mathbf{N}^s) = -[q^s][B^s]^{-1}[\Gamma]\nabla(\theta) = -[q^s][B^s]^{-1}[\Gamma][q^s]^{-1}\nabla(q), \quad (33)$$

where $\mathbf{N}^s \equiv (\mathbf{N}_1^s, \dots, \mathbf{N}_n^s)$, $\theta \equiv (\theta_1, \dots, \theta_n)$, $(q) \equiv (q_1, \dots, q_n)$, $[q^s]$ is a diagonal matrix of saturation loadings,

$$q_{ii}^s = q_i^s, \quad q_{ij}^s (i \neq j) = 0 \quad (i, j = 1, \dots, n), \quad (34)$$

and $[B^s]$ is an n -dimensional square matrix with elements

$$B_{ii}^s = \frac{1}{\mathcal{D}_i^s} + \sum_{\substack{j=1 \\ j \neq i}}^n \frac{\theta_j}{\mathcal{D}_{ij}^s}, \quad B_{ij}^s (i \neq j) = -\frac{\theta_i}{\mathcal{D}_{ij}^s} \quad (i, j = 1, \dots, n). \quad (35)$$

As stated above, knowledge of the mixture adsorption isotherm defines the relationship between the bulk fluid phase partial pressures p_i (or mixture fugacities f_i) and the fractional loadings θ_i . This relationship can be employed to calculate the elements of $[\Gamma]$. As an example, for the Langmuir equilibrium adsorption of an ideal gas mixture ($f_i = p_i$) on a solid adsorbent, whose model is given by

$$\theta_i = \frac{b_i p_i}{1 + \sum_{j=1}^n b_j p_j} \quad \text{or} \quad b_i p_i = \frac{\theta_i}{1 - \sum_{j=1}^n \theta_j} \quad (i = 1, \dots, n), \quad (36)$$

the elements Γ_{ij} are found to be

$$\Gamma_{ij} = \delta_{ij} + \frac{\theta_i}{1 - \sum_{j=1}^n \theta_j} \quad (i, j = 1, \dots, n), \quad (37)$$

where δ_{ij} is the Kronecker delta ($= 1$ if $i = j$; $= 0$ if $i \neq j$)

An alternative approach to surface diffusion is to use the Onsager formulation [56] of irreversible thermodynamics [29,85] in which the surface fluxes are written as linear functions of the chemical potential gradients. For an n -component adsorbate mixture the Onsager formulation can be written as

$$(\mathbf{N}^s) = -[q^s][L^s] \frac{1}{R_g T} \nabla(\mu). \quad (38)$$

Since the Onsager coefficients are postulated by microscopic reversibility [19] to obey the reciprocity conditions

$$L_{ij}^s = L_{ji}^s \quad (i, j = 1, \dots, n), \quad (39)$$

it may be concluded that the matrix $[L^s]$ is symmetric.

Taking into the account the definition of the matrix $[\Gamma]$ of thermodynamic factors, (38) can be rewritten as

$$(\mathbf{N}^s) = -[q^s][L^s] \begin{bmatrix} 1/\theta_1 & 0 & 0 \\ 0 & \ddots & 0 \\ 0 & 0 & 1/\theta_n \end{bmatrix} \frac{1}{R_g T} \nabla(\mu). \quad (40)$$

Comparison of (33) and (40) gives the relation between $[L^s]$ and $[B^s]$:

$$[B^s]^{-1} = [L^s] \begin{bmatrix} 1/\theta_1 & 0 & 0 \\ 0 & \ddots & 0 \\ 0 & 0 & 1/\theta_n \end{bmatrix}. \quad (41)$$

The Fickian formulation of multicomponent surface diffusion [41,57] employs an n -dimensional matrix of Fick diffusivities $[D^s]$ defined by

$$(\mathbf{N}^s) = -[q^s][D^s] \nabla(\theta) = -[q^s][D^s][q^s]^{-1} \nabla(q). \quad (42)$$

Comparing (33) and (42) we obtain the following inter-relation between the Fick and the Maxwell-Stefan surface diffusivities:

$$[D^s] = [B^s]^{-1} [\Gamma]. \quad (43)$$

Since the matrix $[\Gamma]$ of thermodynamic factors is generally non-diagonal, the matrix of Fick diffusivities is also generally non-diagonal. In general, the Maxwell-Stefan surface diffusivities \mathcal{D}_i^s are better behaved than the elements of the Fick diffusivity matrix $[D^s]$. The latter diffusivities are strongly influenced by the thermodynamic non-idealities in the system.

For single component diffusion, (33) and (42) degenerate to their scalar forms,

$$\mathbf{N}^s = -q^s \mathcal{D}^s \Gamma \nabla \theta = -\mathcal{D}^s \Gamma \nabla q \quad (\text{Maxwell-Stefan formulation}), \quad (44)$$

$$\mathbf{N}^s = -q^s D^s \nabla \theta = -D^s \nabla q \quad (\text{Fick formulation}), \quad (45)$$

where

$$\Gamma = \frac{\theta}{p} \frac{\partial p}{\partial \theta} = \frac{q}{p} \frac{\partial p}{\partial q} \quad \text{and} \quad D^s = \mathcal{D}^s \Gamma. \quad (46)$$

The thermodynamic factor Γ is often referred to as the Darken factor [13,65]. The product $D^s = \mathcal{D}^s \Gamma$ is then called the Fickian surface diffusivity.

Skoulidas *et al.* [73] have recently reported atomistic simulations for both self- and transport diffusivities of light gases in (10,10) and (6,6) single-walled carbon nanotubes (SWCNs) and in two siliceous zeolites with comparable pore sizes: silicalite and ZSM-12. A comparison of H_2 and CH_4 self- and transport diffusivities in (10,10) nanotubes, silicalite, and ZSM-12 at room temperature is presented in Fig. 3. The range of pressures studied spans loadings from infinitely dilute to near saturation. It is shown that D^s in SWNTs and ZSM-12 is almost independent of pore loading, whereas in silicalite it increases with increasing pore loading. Here, we show that by decoupling the transport diffusivity into the product of two separate contributions, \mathcal{D}^s and Γ , the Maxwell-Stefan formulation can explain the observed trends in the Fickian surface diffusivity.

The equilibrium adsorption isotherms for single-component H_2 and CH_4 in the three adsorbents were computed by Skoulidas *et al.* [73] using standard grand canonical Monte Carlo techniques, they not deviate appreciably from the Langmuirian behavior (see Fig. 1 of Ref. [73]). According to (37), the thermodynamic factor Γ for the Langmuir isotherm is

$$\Gamma = \frac{1}{1 - \theta} \quad (\text{Langmuir isotherm}), \quad (47)$$

which gives

$$D^s = \mathcal{D}^s \Gamma = \frac{\mathcal{D}^s}{1 - \theta}. \quad (\text{Langmuir isotherm}). \quad (48)$$

Mechanistically, the Maxwell-Stefan surface diffusivity \mathcal{D}^s may be related to the displacement of the adsorbed molecules, λ , and the jump frequency,

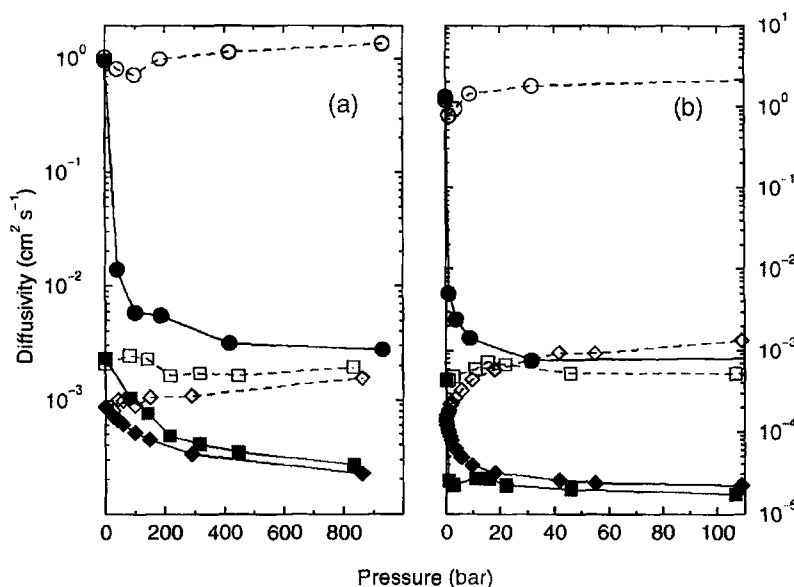


Figure 3. Diffusivities for (a) H_2 and (b) CH_4 in different adsorbents: (10,10) nanotubes (circles), ZSM-12 (squares), and silicalite (diamonds). The filled symbols and full lines represent the self-diffusivities and the open symbols and dashed lines are values for the transport diffusivities. Error bars are smaller than symbol sizes. Lines are a guide to the eye. Reprinted from Ref. [73] with permission from The American Physical Society.

$\nu(\theta)$, which in general can be expected to be dependent on the total surface coverage [80]:

$$D^s \propto \lambda^2 \nu(\theta). \quad (49)$$

ZSM-12 has roughly the same pore size as silicalite but has the same unidimensional pore topology as carbon nanotubes. The strong confinement of the molecules in this unidimensional pore topology does not favor them to overtake others along the pore, this is close to the situation known as single-file diffusion (SFD). For this situation the probability of a molecule being moved is proportional to the probability of an empty nearest neighbor vacancy. This means that under conditions of SFD the jump frequency decreases with increasing loading according to

$$D^s(\theta) = D^s(0)(1 - \theta) \quad (\text{SFD}), \quad (50)$$

where $D^s(0)$ is the zero-coverage value of the Maxwell-Stefan surface diffusivity. Therefore, for single-component Langmuirian adsorption in either

ZSM-12 or SWNT the Fickian transport diffusivity is expected to exhibit a rather weak loading dependence:

$$D^s(\theta) \approx \bar{D}^s(0) \quad (\text{Langmuirian adsorption in ZSM-12 or SWNT}). \quad (51)$$

On the other hand, the jump frequency in silicalite is much less dependent on loading because of its three-dimensional pore network and, as a first approximation, the diffusion process in silicalite can be described by a constant Maxwell-Stefan diffusivity, equal to the zero-coverage value $\bar{D}^s(0)$ [40]. In this case the transport diffusivity is expected to be strongly dependent on loading:

$$D^s(\theta) \approx \bar{D}^s(0) \frac{1}{1 - \theta} \quad (\text{Langmuirian adsorption in silicalite}). \quad (52)$$

Equations (51) and (52) are in very good agreement with the simulated data plotted in Fig. 3, and explain why D^s in SWNTs and ZSM-12 is almost independent of pore loading whereas in silicalite it increases with increasing pore loading. Fig. 3 shows a remarkable feature of nanotubes: the transport diffusivities in (10,10) SWNTs are 3–4 orders of magnitude larger than in the two zeolites over the entire range of pressures examined. According to Skoulidas *et al.* [73], the exceptionally high transport rates in SWNTs are shown to be a result of the inherent smoothness of the nanotubes. Based on these findings, the authors predict that carbon nanotube membranes will have fluxes that are orders of magnitude greater than crystalline zeolite membranes.

To further illustrate the strong influence that $[\Gamma]$ may have on the diffusion rate in certain zeolites, such as silicalite, we briefly review some of the recent work [36,37,82,83] on the diffusion behavior of several hydrocarbons in that zeolite. Broadly speaking, there are two distinct adsorption sites in silicalite: sites of type A, which represent the intersections between the straight channels and zig-zag channels, and sites of type B, which correspond to the channel interiors. Using Configurational-bias Monte Carlo simulation (CBMC), Vlught *et al.* [82,83] have shown that at low loading linear alkanes (with 6–8 carbon atoms) and branched alkanes (with C atoms ranging from 4 to 7) occupy preferentially the intersections (site A). However, since at high loadings the intersections are all fully occupied, these molecules are forced to reside in the channel interiors (site B) which is energetically more demanding. This leads to an inflection in the isotherm, as shown in Fig. 4(a) for the adsorption of *n*-hexane (*n*-C₆) and 2-methylpentane (2MP).

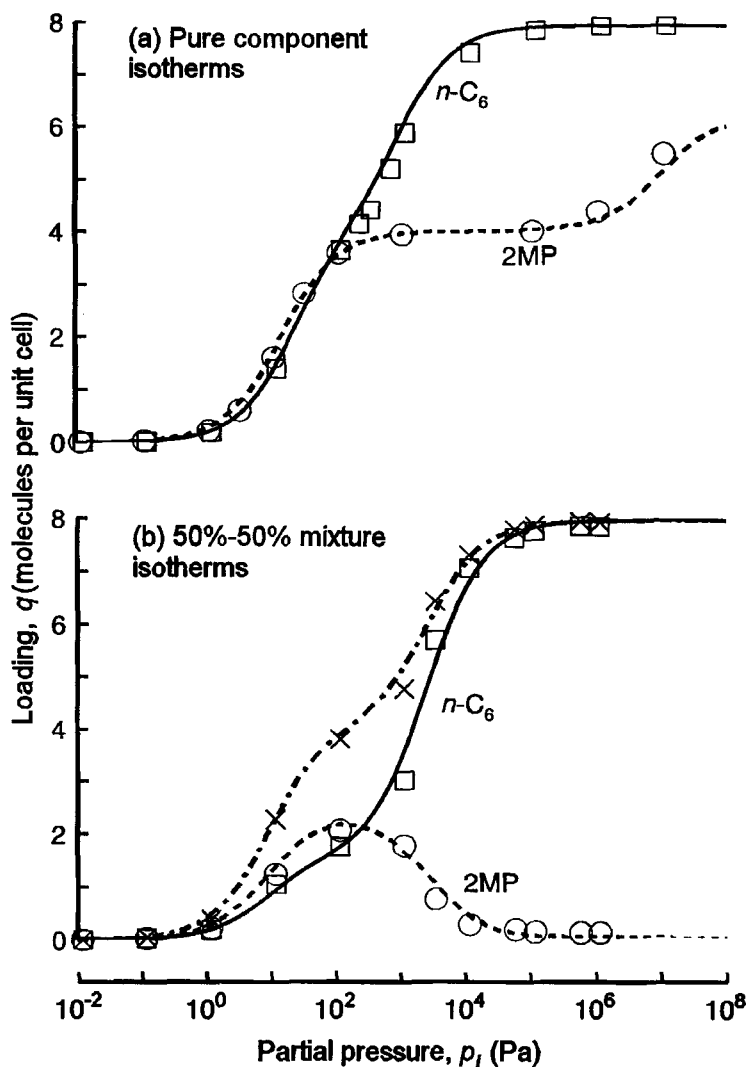


Figure 4. Pure component and 50%-50% mixture isotherms at 362 K in silicalite. The symbols represent the configurational-bias Monte Carlo (CBMC) simulations for (1, \square) *n*-hexane and (2, \circ) 2-methylpentane ($\{ \times \} = \{ \square \} + \{ \circ \}$). The statistical uncertainties in the simulations are smaller than the size of the symbols used. The continuous and dashed lines are the dual-site Langmuir (DSL) fits with the parameter values determined only from pure component CBMC simulation data. The DSL parameter values are for *n*-hexane, $q_1^s = 7.9$ molec./u.c., $\theta_{1A} = 0.51$, $\theta_{1B} = 0.49$, $k_{1A} = 4.5 \times 10^{-2} \text{ Pa}^{-1}$, $k_{1B} = 1.0 \times 10^{-3} \text{ Pa}^{-1}$, and for 2-methylpentane, $q_2^s = 6.2$ molec./u.c., $\theta_{2A} = 0.65$, $\theta_{2B} = 0.35$, $k_{2A} = 7.0 \times 10^{-2} \text{ Pa}^{-1}$, $k_{2B} = 1.0 \times 10^{-7} \text{ Pa}^{-1}$. Reprinted with permission from Ref. [36]. Copyright (1998) American Chemical Society.

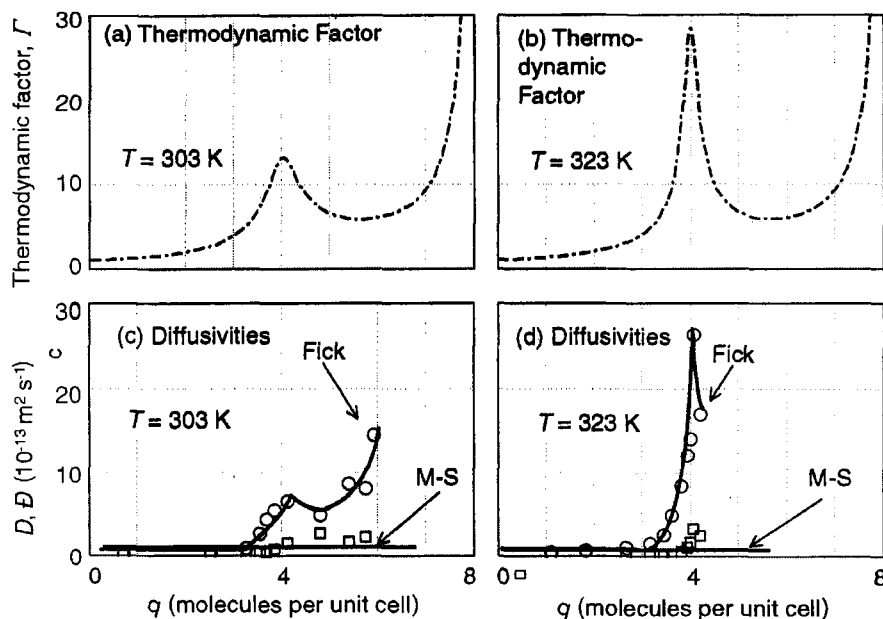


Figure 5. Thermodynamic correction factors (a, b) and diffusivities (c, d) for diffusion of benzene in Silicalite at (a, c) 303 K and (b, d) 323 K; experimental diffusivity data from Shah *et al.* (1995). Reprinted with permission from Ref. [37] copyright (1999) Elsevier Science.

This type of isotherm behavior can be described by a dual-site Langmuir (DSL) model [46,65,74], which for a single component can be written as

$$\theta = \frac{\theta_A k_A p}{1 + k_A p} + \frac{\theta_B k_B p}{1 + k_B p} = \frac{(\theta_A k_A + \theta_B k_B) p + (\theta_A + \theta_B) k_A k_B p^2}{1 + (k_A + k_B) p + k_A k_B p^2}. \quad (53)$$

Here, p is the partial pressure of the component, θ_A and θ_B are, respectively, the maximum fractional occupancies of the two types of sites A and B, and k_A and k_B are the corresponding DSL adsorption constants. As can be seen from Fig. 4(a), the DSL model provides a very good fit of the CBMC simulations of adsorption isotherms of n -C₆ and 2MP.

For the DSL isotherm model, the thermodynamic factor Γ can be determined by analytic differentiation of (53), see Krishna *et al.* [37]. This correction factor shows a maximum at the inflection point $\theta = \theta_A$ and a minimum at a higher loading $\theta_A < \theta < \theta_B$. This behavior is illustrated in Figs. 5(a) and 5(b) for adsorption of benzene on silicalite at two different temperatures. Since the Fick surface diffusivity D^s is proportional to the thermodynamic factor, it is also expected to exhibit the same non-monotonic behavior. As shown in Figs. 5(c) and 5(d), this is indeed verified by the experimental data of

Shah *et al.* [71] for Fick diffusivity at those two temperatures. The Maxwell-Stefan diffusivities, calculated from $\bar{D}^s = D^s / \Gamma$, are seen to be practically constant, emphasizing the importance of thermodynamic correction factors on the diffusion behavior.

For the description of binary diffusion we can follow the same approach as for one-component diffusion. However, in this binary situation the extra interaction between the adsorbed molecules represented by the counter-exchange coefficient \bar{D}_{12}^s should be taken into account. The relevant equations are

$$(\mathbf{N}^s) = - \begin{bmatrix} q_1^s & 0 \\ 0 & q_2^s \end{bmatrix} [D^s] \nabla(\theta), \quad (54)$$

$$[D^s] = \frac{\begin{bmatrix} \bar{D}_1^s & 0 \\ 0 & \bar{D}_2^s \end{bmatrix}}{\bar{D}_{12}^s + y_1 \bar{D}_2^s + y_2 \bar{D}_1^s} \begin{bmatrix} \bar{D}_{12}^s + y_1 \bar{D}_2^s & y_1 \bar{D}_2^s \\ y_2 \bar{D}_1^s & \bar{D}_{12}^s + y_2 \bar{D}_1^s \end{bmatrix} \begin{bmatrix} \Gamma_{11} & \Gamma_{12} \\ \Gamma_{21} & \Gamma_{22} \end{bmatrix}. \quad (55)$$

If the binary mixture is separated by means of permeation through a silicalite membrane, the fluxes can be written as

$$(N^s) = -\frac{1}{\delta} [q^s] [D^s] (\Delta\theta), \quad (56)$$

where δ is the thickness of the membrane layer and $(\Delta\theta)$ are the differences in the component loadings across the membrane. In this case the selectivity of separation is simply the ratio of the permeation rates, or fluxes, of the two components across the membrane:

$$S = \frac{N_1^s}{N_2^s} \equiv S_D S_\Gamma, \quad S_D = \frac{\bar{D}_1^s}{\bar{D}_2^s}, \quad S_\Gamma = \frac{q_1^s}{q_2^s} \left(\frac{\Gamma_{11} \Delta\theta_1 + \Gamma_{12} \Delta\theta_2}{\Gamma_{21} \Delta\theta_1 + \Gamma_{22} \Delta\theta_2} \right). \quad (57)$$

S is the product of two factors: S_D , which is the ratio of the Maxwell-Stefan diffusivities, and (ii) the thermodynamic selectivity factor S_Γ . Traditionally, S_D has been the focus of most attention and indeed achieving a high value of S_D is the basic principle used in size selective sieving processes with small pore zeolites. However, on the basis of (57), Krishna *et al.* [36] demonstrated that high selectivities can be realized with medium pore size silicalite by ensuring conditions such that S_Γ is large and supplements S_D . This is potentially interesting, because the diffusivities, and hence the fluxes, in medium pore size zeolites are considerably higher than in small pore zeolites [29].

In order to illustrate this concept, let us consider the permeation of a binary mixture of (1) *n*-hexane and (2) 2-methylpentane across a silicalite membrane. The pure component and 50%-50% mixture isotherms at 362 K are

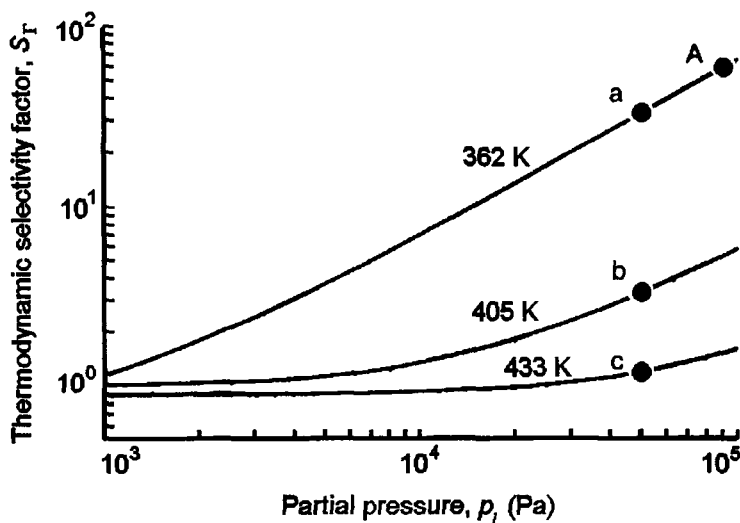


Figure 6. Thermodynamic selectivity factor S_T for permeation of a 50%-50% mixture of n -C₆ and 2MP across a silicalite membrane as a function of partial pressure of the components upstream of the membrane. The driving forces $\Delta\theta_i$ in (57) are calculated assuming that the downstream partial pressures are zero for both components. The DSL mixture isotherm (58) is used to calculate the molecular loadings at the upstream face of the membrane. Reprinted with permission from Ref. [36]. Copyright (1998) American Chemical Society.

shown in Fig. 4. The lines in Fig. 4(a) are DSL fits of the pure component isotherms; those in Fig. 4(b) are the mixture isotherm data predicted by the DSL mixture model, with parameters values determined only from pure component isotherm data. The extension of the DSL isotherm model to binary mixtures is

$$\theta_i = \frac{(\theta_{iA}k_{iA} + \theta_{iB}k_{iB})p_i + (\theta_{iA} + \theta_{iB})k_{iA}k_{iB}p_i^2}{1 + (k_{1A} + k_{1B})p_1 + k_{1A}k_{1B}p_1^2 + (k_{2A} + k_{2B})p_2 + k_{2A}k_{2B}p_2^2} \quad (i=1,2). \quad (58)$$

For hydrocarbon isomer separation, we may expect the branched isomer to have a lower mobility within the silicalite structure than the linear one, i.e. $\bar{D}_2^s < \bar{D}_1^s$. However, here we take a conservative approach and consider that the pure component Maxwell-Stefan diffusivities are identical for the two isomers, i.e. $\bar{D}_1^s = \bar{D}_2^s$. Under this assumption, $S = S_T$. Since the interchange coefficient \bar{D}_{12}^s has a value intermediate between \bar{D}_1^s and \bar{D}_2^s [32], we must also have $\bar{D}_1^s = \bar{D}_2^s = \bar{D}_{12}^s$. The Γ_{ij} required for calculation of the thermodynamic selectivity factor S_T , can be obtained by analytic differentiation of (58) [37,81].

Figure 6 shows the results for permeation of an equimolar mixture of n -C₆ and 2MP at temperatures of 362, 405, and 443 K. The driving forces $\Delta\theta_i$ in (57) were calculated assuming that the downstream partial pressures are zero for both components. The results show that large selectivities can be achieved by operating the system at high pressures and low temperatures. For example, at 362 K with an upstream partial pressure of 50 kPa for each of the components, $S_T = 32$ (point a), a value that drops to 3.3 (point b) and 1.2 (point c) for $T = 405$ and 443 K, respectively. Experimental values of the selectivity obtained by Funke *et al.* [20] for a 50%–50% mixture of n -hexane and 3-methylpentane through a silicalite confirm the 25-fold increase in selectivity as the temperature is decreased from 443 to 362 K. It is interesting to note that were S_T to be determined from the pure component data at low loading, a value close to unity would be obtained leading us to conclude that it is not possible to separate the isomers by permeation across a silicalite membrane.

6 Particle uptake rate models

The simplest approach to account for the solid structure is to lump all structural properties into constant factors that multiply the corresponding components of the flux. We have already discussed the three lumping parameters characterizing the medium for the three transport mechanisms, they are: the Knudsen flow parameter, K_0 ; the porosity-tortuosity ratio, ϵ/τ ; and the viscous flow parameter, B_0 .

A more rigorous approach is to model the solid structure in detail and then incorporate it into the transport model. Several examples of such approach have been proposed in the literature: Monte-Carlo simulation [1], effective medium theory [7,25,75], periodic capillary models [21], multi-scale approach [11], percolation model [60–62], averaging theorem [55], random capillary structure [14,77], and stochastic model [5,6]. Many of these models employ more or less complex kernel equations of the form

$$N_i = \int \frac{\epsilon(h)}{\tau(h)} N_i(h) f(h) dh, \quad (59)$$

where $f(h)$ is the pore size distribution, such that $f(h)dh$ is the fraction of pores with sizes between h and $h + dh$, and $N_i(h)$ is the mass flux for a model pore of characteristic size h . The integration is over all pore sizes and orientations believed to be present in the adsorbent.

Due to lack of space we cannot review these models in depth here; instead, we devote the rest of this section to the discussion of macroscopic

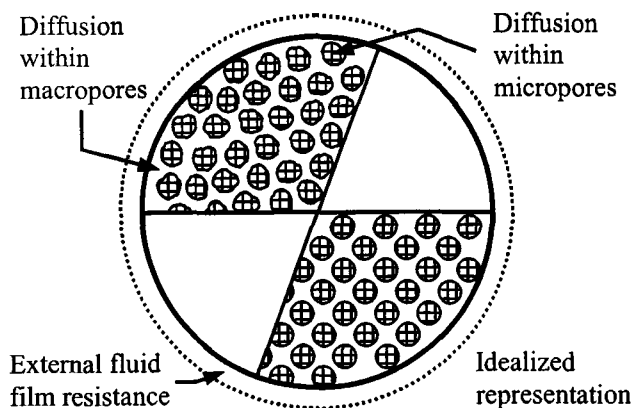


Figure 7. Schematic diagram of a bidisperse adsorbent particle consisting of small microporous crystals (e.g. zeolites) formed into a macroporous pellet. Adapted from Ref. [65].

uptake rate models applicable to bi-dispersed solids since most commercial adsorbents and catalysts fall into this category. Such solids usually have a network of large pores, which allows for fast transport and provide access to narrow pores, wherein diffusion occurs and most of the adsorption takes place. Examples of bidisperse adsorbents are activated carbons, activated aluminas and zeolite pellets. Because the pore structure has an important effect on intraparticle diffusion, transport models must reflect the bidisperse pore structure of the adsorbent. The use of single-pore models can lead to misinterpretations of experimental data and give erroneous predictions outside the operating conditions where the model parameters were fitted.

One approach to analyze intraparticle transport in a porous solid with a bimodal pore size distribution considers the macroscopic particle as an agglomeration of microscopic grains, with the inter-grain voids representing the macroporous network. A schematic of such conceptual model of a bi-dispersed adsorbent is given in Fig. 7. A somewhat similar approach to model the topology of bi-dispersed porous systems is to assume that the macropores and micropores are both cylindrical, with the latter originating from the lateral surface of the macropores. This pore structure was first proposed by Turner [79]. Both types of pore network model have been used extensively to model adsorption kinetics in adsorbents with bimodal pore-size distribution. One of the more recent examples is the work of Delgado and Rodrigues [15], who employed the Turner model to study the pressurization of gaseous adsorbate mixtures in a bi-dispersed pore structure by using the Maxwell-Stefan approach to describe intraparticle transport in both macro- and micropores.

For simplicity, here we assume that the system is isothermal and that most of the adsorption takes place in the narrow pores of the microparticles. The latter is usually a good approximation since the external surface of the microparticle is small compared to the capacity volume within it and, therefore, the adsorption capacity on its surface can be neglected. Under these assumptions, the diffusive transport within the microparticles is given by the Maxwell-Stefan surface diffusion equations (33), whereas the transport in the macroporous network of the pellet can be described by the Mason formulation for intraparticle diffusion, as expressed by (17).

The transient uptake process in a microparticle located at a radial position R in the spherical pellet is governed by

$$\frac{\partial(\theta)}{\partial t} = \nabla \cdot \{ [D^s] \nabla(\theta) \}, \quad (60)$$

where (θ) is the vector of fractional occupancies and $[D^s]$ is the matrix of Fickian surface diffusivities defined in (43). Assuming that the microparticles are also spherical with radius r_p , (60) can be written as

$$\frac{\partial(\theta)}{\partial t} = \frac{1}{r^2} \frac{\partial}{\partial r} \left\{ r^2 [D^s] \frac{\partial(\theta)}{\partial r} \right\} \quad (0 < r < r_p), \quad (61)$$

where r is the radial coordinate in the microparticle. Equation (61) is subjected to the following boundary conditions:

$$\frac{\partial(\theta)}{\partial r} = 0 \text{ for } r = 0 \quad \text{and} \quad (\theta) = (\theta^{\text{eq}}) \text{ for } r = r_p, \quad (62)$$

where (θ^{eq}) are the equilibrium fractional occupancies related through the mixture adsorption isotherm to the composition $(c) \equiv (c_1, \dots, c_n)$ of the fluid mixture in the contiguous macropore network located at radial position R in the pellet.

The average fractional occupancies inside the microparticle, $(\bar{\theta})$, are defined as

$$(\bar{\theta}) = \frac{3}{r_p^2} \int_0^{r_p} (\theta) r^2 dr. \quad (63)$$

From (61) and (63), the sorption rates may be related to the fluxes at the microparticle surface:

$$\frac{d(\bar{\theta})}{dt} = \frac{3}{r_p} \left\{ [D^s] \frac{\partial(\theta)}{\partial r} \right\}_{r=r_p}. \quad (64)$$

The differential material balances in the macropore network of the pellet can be written as

$$\epsilon \frac{\partial(c)}{\partial t} + (1 - \epsilon)[q^s] \frac{\partial(\bar{\theta})}{\partial t} = \frac{1}{R^2} \frac{\partial}{\partial R} \left\{ R^2 [D^e] \frac{\partial(c)}{\partial R} \right\} \quad (0 < R < R_p), \quad (65)$$

where ϵ is the macroporosity of the pellet and $[D^e]$ is the matrix of Fickian transport diffusivities defined in (17). This equation is subjected to the following boundary conditions:

$$\frac{\partial(c)}{\partial R} = 0 \text{ for } R = 0 \quad \text{and} \quad (c) = (c^b) \text{ for } R = R_p, \quad (66)$$

where $(c^b) \equiv (c_1^b, \dots, c_n^b)$ is the composition of the bulk fluid mixture surrounding the pellet. For simplicity, in (66) we have neglected the resistance of the film adjacent to the external surface of the pellet. Equation (65) can be averaged over the volume of the pellet to give

$$\epsilon \frac{d(\langle c \rangle)}{dt} + (1 - \epsilon)[q^s] \frac{d(\langle \bar{\theta} \rangle)}{dt} = \frac{3}{R_p} \left\{ [D^e] \frac{\partial(c)}{\partial R} \right\}_{R=R_p}, \quad (67)$$

where

$$\langle \phi \rangle \equiv \frac{3}{R_p^2} \int_0^{R_p} (\phi) R^2 dR \quad (68)$$

defines the mean value of (ϕ) in the pellet.

The set of equations (61–62) and (65–66) can be easily solved using collocation or finite difference methods. However, the numerical computations become bulky when those equations are simultaneously solved along with the transport equations in the bed. This is especially true when the purpose of modelling is to optimize the cyclic steady-state operation of a multi-bed adsorption process. It is therefore essential to consider carefully the possibility of introducing appropriate simplifying approximations at the particle level. Obviously, the biggest savings in numerical computations are achieved if the differential material balances could be appropriately replaced by ordinary differential equations. In this case the integration along the intraparticle spatial coordinates is no longer necessary. Several useful approaches have been suggested to achieve this goal: (LDF) linear driving force, nonlinear driving force, and parabolic concentration profile within the particle [84]. Each approach can save a tremendous amount of computation time in the model.

The assumption of parabolic concentration profile within the particle was first used by Liaw *et al.* [39] and by Rice [63], and is probably the most general approach to decrease the complexity of the uptake rate equations. It is a reasonable assumption, since the profiles obtained by exact solutions are almost parabolic in shape. We will show next how it can be used to simplify the uptake rate equations for the bi-dispersed model adsorbent discussed above. Since the parabolic-concentration-profile assumption can be regarded as a generalization of the original LDF approximation proposed by Glueckauf and Coates [22], we shall keep the LDF acronym when we refer to the simplified model.

To derive the LDF uptake rate equations it is first assumed that the fractional occupancies in a microparticle are well approximated by parabolic profiles satisfying the boundary conditions in (62):

$$(\theta) = (a) + (b)r^2, \quad (69)$$

where

$$(a) = (\theta)_{r=r_p} - (b)r_p^2 \quad \text{and} \quad (b) = \frac{5}{2r_p^2} \{(\theta)_{r=r_p} - (\bar{\theta})\}. \quad (70)$$

A straightforward substitution of (70) into (64) gives directly the generalized LDF approximation of the Maxwell-Stefan surface diffusion equations expressed in Fickian form:

$$\frac{d(\bar{\theta})}{dt} = 6[D^s]_{r=r_p}(b) = [k^s] \{(\theta)_{r=r_p} - (\bar{\theta})\}. \quad (71)$$

$[k^s]$ is an n -dimensional square matrix of LDF surface-diffusion rate constants given by

$$k_{ij}^s = \left\{ \frac{15}{r_p^2} D_{ij}^s \right\}_{r=r_p} \quad (i, j = 1, \dots, n). \quad (72)$$

According to (32), (35) and (43), the elements of $[k^s]$ are functions of the composition (c) of the fluid mixture in the contiguous macropore network. Therefore, the adsorption kinetics in the microparticle will be ultimately governed by the conditions prevailing at its external surface, since $[k^s]$ is determined by the values of D_{ij}^s at $r = r_p$.

Similarly, if the same approach is applied at the pellet level, the following generalized LDF approximation is obtained:

$$\epsilon \frac{d(\langle c \rangle)}{dt} + (1 - \epsilon)[q^s] \frac{d(\langle \bar{\theta} \rangle)}{dt} = [k^e] \{(\langle c \rangle)_{R=R_p} - (\langle c \rangle)\}, \quad (73)$$

where $[k^e]$ is an n -dimensional square matrix of LDF transport rate constants

$$k_{ij}^e = \left\{ \frac{15}{R_p^2} D_{ij}^e \right\}_{R=R_p} \quad (i, j = 1, \dots, n). \quad (74)$$

According to (5) and (17), the k_{ij}^e are functions of the composition (c^b) of the external fluid mixture surrounding the pellet. Equation (73) is equivalent to the lowest-order approximation derived by Serbezov and Sotirchos [70] for the dusty-gas model in a sorbent particle of uniform pore structure.

Note that $\{d(\bar{\theta})/dt\}$ is still undefined because $(\bar{\theta})$ has not yet been averaged. To do this, we must somehow integrate (71) over the volume of the pellet to obtain an expression for $\{d(\bar{\theta})/dt\}$, preferably as function of $(\langle\bar{\theta}\rangle)$ and $(\langle\theta\rangle)_{r=r_p}$, where the latter stands for the values of the loadings in equilibrium with an hypothetical fluid mixture of concentration $(\langle c \rangle)$. Although this can only be achieved exactly under highly simplified assumptions, it usually suffices to consider the elements of $[k^s]$ as constants when employing (68) to compute the average over the pellet. This gives rise to the following simplified uptake rate equation for the microparticles:

$$\frac{d(\langle\bar{\theta}\rangle)}{dt} = [\langle k^s \rangle] \{ (\langle\theta\rangle)_{r=r_p} - (\langle\bar{\theta}\rangle) \}, \quad (75)$$

where $[\langle k^s \rangle]$ stands for the matrix $[k^s]$ evaluated for $(\theta) = (\langle\theta\rangle)_{r=r_p}$ and $(c) = (\langle c \rangle)_{r=r_p}$.

Equations (73) and (75) are equivalent to adopting a double-LDF approximation [4] to account for intraparticle transport in the two sub-domains of the pellet. With this model simplification, the CPU time decreases by at least one order of magnitude thereby increasing the feasibility of performing the optimization of complex multicomponent adsorption processes under cyclic steady-state conditions.

To illustrate the applicability of the generalized double-LDF approximation, we apply the previous developed transport models to predict the isothermal uptake dynamics of a silicalite pellet exposed to an equimolar binary mixture of n -C₆ and 2MP, which is subjected to a cyclic change of the total pressure. Notice that since the two components are isomers, the simplified version of the dusty gas model given in (23) applies to the intraparticle transport in the macroporous network of the pellet.

The imposed cyclic pressure variation is a damped square wave with lower and upper pressure limits of $P_L = 1 \times 10^3$ Pa and $P_H = 5 \times 10^3$ Pa, respectively. The total pressure is ramped during $0.2r_p^2/\mathcal{D}^s$ time units (or, equivalently,

$3/k^s$) and then held constant for the same duration. It is intended to be representative of the conditions inside the adsorbing bed of a PSA unit. The values of the transport coefficients are listed in the caption of Fig. 8. For this set of values, both intracrystalline and macroporous mass transport mechanisms are significant, although the former is the more prevailing resistance.

Figure 8 compares the dynamic response curves at cyclic steady state obtained using the double-LDF approximation (dashed lines) and the exact solution (solid lines) of the corresponding distributed parameter model from which it results. The equilibrium solution, which neglects all mass transport resistances, is also included for reference (dash-dotted lines). The results show that the double-LDF approximation is in satisfactory agreement, both qualitatively and quantitatively, with the exact solution, whereas the equilibrium model deviates considerably from the correct result. In particular, it cannot predict even qualitatively the asymmetric shape of the response curve for the fractional loading and the observed overshoot (during adsorption) and undershoot (during desorption) in the concentration curve of the species with the smaller effective transport resistance (fast moving or weakly adsorbing species). In fact, it has been shown [70] that the latter phenomenon cannot be described by LDF approximations based on transport and adsorption models that do not account for the coupling of the fluxes of the various components in the mixture.

The results presented here are new and have not been published previously. Like many theoretical studies carried out in the past, they provide evidence for the need to properly account for intraparticle transport to correctly predict the adsorption kinetics of multicomponent adsorbate mixtures.

Note, however that Nakao and Suzuki [49] have shown that the conventional value of the rate constant, $k = 15D/R_p^2$, is not appropriate for processes with fast cycles, that is, those whose adsorption/desorption (half-cycle) stage is shorter than $1.5/k$. While this restriction is usually verified in fixed-bed adsorption experiments and standard swing adsorption processes [84], it should be applied carefully to simulate shorter cyclic adsorption processes like RPSA [31]. When applying a double-LDF approximation this restriction is expected to be more restrictive, this is supported by the results plotted in Fig. 8.

If the half-cycle length is shorter than $1.5/k$, it is still possible to employ the LDF approximation provided that the factor 15 in the definition of the LDF factor k is replaced by a time-dependent relationship that takes into account the duration of the cycle [2,8]. The validity of the LDF approximation in sorption/desorption cycles has been recently reviewed by Rodrigues and Dias [64].

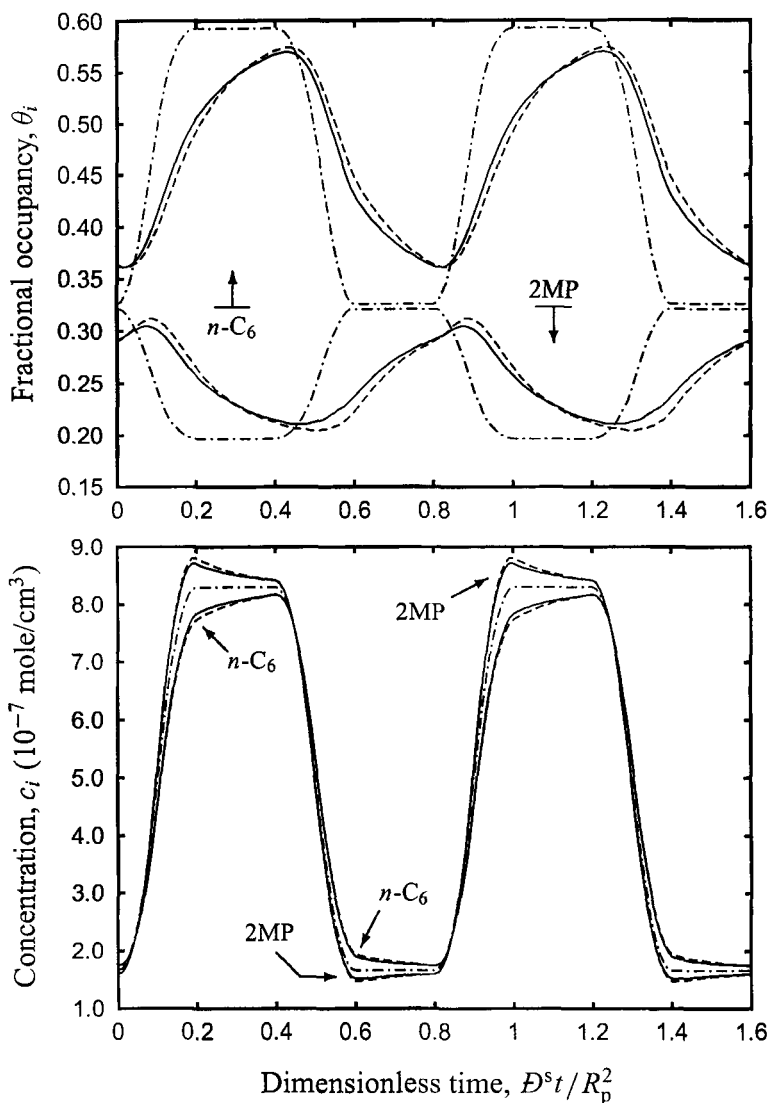


Figure 8. Cyclic steady-state response curves of partial concentration (bottom plot) and fractional loading (top plot) in an isothermal silicalite pellet subjected to a damped square-wave variation of the total pressure of an equimolar binary mixture of n -hexane ($n\text{-C}_6$) and 2-methylpentane (2MP). ---, equilibrium solution; —, numerical solution of; -.-, double-LDF approximation. The DSL mixture isotherm (58), with parameters given in Fig. 4 ($q_1^s = 2.45 \times 10^{-3}$, $q_2^s = 1.92 \times 10^{-3}$ mole/cm³), is used to calculate the fractional occupancies in the silicalite crystals. The temperature is $T = 362$ K and the pressure is cycled between $P_L = 1 \times 10^3$ and $P_H = 5 \times 10^3$ Pa. The main simulation parameters are: $\epsilon = 0.4$, $\tau = 3$, $\bar{D}^s / r_p^2 = 0.01$, $\bar{D}_K^c / R_p^2 = 36.7$, $\bar{D}_{12} / R_p^2 = 24.7$ and $B_0 \bar{P} / (\mu R_p^2) = 8.1$, where \bar{D}_{12} is evaluated at $\bar{P} = (P_L + P_H)/2$.

Provided that the adsorption unit is not subjected to strong pressure cycling, the generalized double-LDF approximation gives rise to a simple and convenient mathematical formulation of the intraparticle transport equations for bi-dispersed adsorbents. Note that the LDF equations are always used as part of a complex mathematical model (e.g. in conjunction with the partial differential equations for the adsorbent bed), the solution of which is obtained numerically. This means that in practice the LDF equations are always solved numerically regardless of whether an analytical solution is available or not. Therefore, by using rigorous transport models one can improve significantly the performance of the linear driving force approximation without making it computationally more involved than the simple Glueckauf LDF approximation.

7 Conclusions

In this paper we have reviewed the more popular continuum theories of transport of adsorbate mixtures in porous materials. Whilst it seems improbable that continuum models could approach the accuracy of specific atomistic modelling, they are currently the only viable route for incorporating adsorption kinetics at the process simulation level. We have focused on the Maxwell-Stefan formulation, since it seems to provide the most general, and convenient, approach for describing multicomponent mass transport within both micro- and macroporous materials. The working examples presented here demonstrate the need to employ transport and adsorption models that take into consideration both structural and thermodynamic selectivities and properly account for the coupling of the fluxes of the various components in the mixture.

References

1. Abbasi M. H. and Evans J. W., Diffusion of gases in porous solids - Monte-carlo simulations in the Knudsen and ordinary diffusion regimes, *AIChE J.* **29** (1983) pp. 617–624.
2. Alpay E. and Scott D. M., The linear driving force model for fast-cycle adsorption and desorption in a spherical particle, *Chem. Eng. Sci.* **47** (1992) pp. 499–502.
3. Auerbach S. M., Theory and simulation of jump dynamics, diffusion and phase equilibrium in nanopores, *Int. Rev. Phys. Chem.* **19** (2000) pp. 155–198.
4. Azevedo D. C. S. and Rodrigues A. E., Bilinear driving force approximation in the modelling of a simulated moving bed using bidisperse adsorbents, *Ind. Eng. Chem. Res.* **38** (1999) pp. 3519–3529.
5. Bhatia S. K., Stochastic theory of transport in inhomogeneous media, *Chem. Eng. Sci.* **41** (1986) pp. 1311–1324.

6. Bhatia S. K., Combined surface and pore volume diffusion in porous media, *AIChE J.* **34** (1988) pp. 1094–1105.
7. Burganos V. N. and Sotirchos S. V., Diffusion in pore networks - effective medium theory and smooth field approximation, *AIChE J.* **33** (1987) pp. 1678–1689.
8. Carta G., The linear driving force approximation for cyclic mass transfer in spherical particles, *Chem. Eng. Sci.* **48** (1993) pp. 622–625.
9. Catlow C. R. A., editor, *Modelling of Structure and Reactivity in Zeolites* (Academic Press, London, 1992)
10. Chandler D., *Introduction to Modern Statistical mechanics* (Oxford University Press, New York, 1987).
11. Chang H.-C., Effective diffusion and conduction in 2-phase media - a unified approach, *AIChE J.* **29** (1983) pp. 846–853.
12. Chen N. Y., Degnan T. F. and Smith C. M., *Molecular Transport and Reaction in Zeolites* (VCH, New York, 1994).
13. Darken L. S., Diffusion, mobility and their interrelation through free energy in binary metallic systems, *Trans. AIME* **175** (1948) pp. 184.
14. Deepak P. D. and Bhatia S. K., Transport in capillary network models of porous media - theory and simulation, *Chem. Eng. Sci.* **49** (1994) pp. 245–257.
15. Delgado J. A. and Rodrigues A. E., A Maxwell-Stefan model of bidisperse pore pressurization for Langmuir adsorption of gas mixtures, *Ind. Eng. Chem. Res.* **40** (2001) pp. 2289–2301.
16. Demonstis P. and Suffritti G. B., Structure and dynamics of zeolites investigated by molecular dynamics, *Chem. Rev.* **97** (1997) pp. 2845–2878.
17. Do D. D., *Adsorption Analysis: Equilibria and Kinetics* (Imperial College Press, London, 1998).
18. Do D. D. and Do H. D., Surface diffusion of hydrocarbons in activated carbon: comparison between constant molar flow, differential permeation and differential adsorption bed methods, *Adsorption* **7** (2001) pp. 189–209.
19. Elliot J. A. W., Elmoazzen H. Y. and McGann L. E., A method whereby Onsager coefficients may be evaluated *J. Chem. Phys.* **113** (2000) pp. 6573–6578.
20. Funke H. H., Argo A. M., Falconer J. L. and Noble R. M., Separations of cyclic, branched, and linear hydrocarbon mixtures through silicalite membranes, *Ind. Eng. Chem. Res.* **36** (1997) pp. 137–143.
21. Gavalas G. R. and Kim S., Periodic capillary models of diffusion in porous solids, *Chem. Eng. Sci.* **36** (1981) pp. 1111–1122.
22. Glueckauf E. and Coates J. J., Theory of Chromatography. Part IV. The influence of incomplete equilibrium on the front boundary of chromatograms and on the effectiveness of separation, *J. Chem. Soc.* (1947) pp. 1315.
23. Gubbins K. E., Molecular Simulation of Confined Nano-phases, In *Fundamentals of Adsorption* 7, ed. by Kaneko K., Kanoh H. and Y. Hanzawa Y. (IK International, Japan, 2002) pp. 13–20.
24. Jackson R., *Transport in Porous Catalysts* (Elsevier, Amsterdam, The Netherlands, 1977).
25. Kapoor A. and Yang R. T., Surface-diffusion on energetically heterogeneous surfaces - an effective medium approximation approach, *Chem. Eng. Sci.* **45** (1990) pp. 3261–3270.
26. Kapteijn F., Bakker W. J. W., Zheng G., Poppe J. and Moulijn J. A., The temperature and occupancy dependent diffusion of *n*-butane through a silicalite membrane, *Microporous*

- Mater.* **3** (1994) pp. 227–234.
27. Kapteijn F., Bakker W. J. W., Zheng G., Poppe J. and Moulijn J. A., Permeation and separation of light hydrocarbons through a silicalite-1 membrane. Application of the generalized Maxwell-Stefan equations, *Chem. Eng. Sci.* **57** (1995) pp. 145–153.
 28. Kapteijn F., Moulijn J. A. and Krishna R., The generalized Maxwell-Stefan model for diffusion in zeolites: sorbate molecules with different saturation loadings, *Chem. Eng. Sci.* **55** (2000) pp. 2923–2930.
 29. Kärger J. and Ruthven D. M., *Diffusion in Zeolites and Other Microporous Solids* (Wiley, New York, 1992).
 30. Keil F. J., Krishna R. and Coppens M.-O., Modeling of diffusion in zeolites, *Rev. Chem. Eng.* **16** (2000) pp. 71–197.
 31. Keller G. E. II and Jones R. L., Pressure swing parametric pumping—a new adsorption process, *J. Sep. Process Techn.* **2** (1981) pp. 17.
 32. Krishna R., Multicomponent surface diffusion of adsorbed species. A description based on the generalized Maxwell-Stefan diffusion equations, *Chem. Eng. Sci.* **45** (1990) pp. 1779–1791.
 33. Krishna R., Problems and pitfalls in the use of the Fick formulation for intraparticle diffusion, *Chem. Eng. Sci.* **48** (1993) pp. 845–861.
 34. Krishna R., A unified approach to the modelling of intraparticle diffusion in adsorption processes, *Gas Sep. & Purif.* **7** (1993) pp. 91–104.
 35. Krishna R. and Paschek D., Separation of hydrocarbon mixtures using zeolite membranes: a modelling approach combining molecular simulations with the Maxwell-Stefan theory, *Sep. Purif. Technol.* **21** (2000) pp. 111–136.
 36. Krishna R., Smit B. and Vlught T. J. H., Sorption-induced diffusion-selective separation of hydrocarbon isomers using silicalite, *J. Phys. Chem. A* **102** (1998) pp. 7727–7730.
 37. Krishna R., Vlught T. J. H. and Smit B., Influence of isotherm inflection on diffusion in silicalite, *Chem. Eng. Sci.* **54** (1999) pp. 1751–1757.
 38. Krishna R. and Wesselingh J. A., The Maxwell-Stefan approach to mass transfer, *Chem. Eng. Sci.* **52** (1997) pp. 861–911.
 39. Liaw C. H., Wang J. S. P., Greenkorn R. A. and Chao K. C., Kinetics of fixed-bed adsorption - new solution, *AIChE J.* **25** (1979) pp. 376–381.
 40. Maginn E. J., Bell A. T. and Theodorou D. N., Transport diffusivity of methane in silicalite from equilibrium and nonequilibrium simulations, *J. Phys. Chem.* **97** (1993) pp. 4173–4181.
 41. Marutovsky R. M. and Bülow M., Sorption kinetics of binary material mixtures in microporous zeolite structures, *Z. Phys. Chem.* **263** (1982) pp. 849–855.
 42. Mason E. A. and del Castillo L. F., The role of viscous flow in theories of membrane transport, *J. Mem. Sci.* **23** (1985) pp. 199–220.
 43. Mason E. A. and Lonsdale H. K., Statistical mechanical theory of membrane transport, *J. Membrane Sci.* **51** (1990) pp. 1–81.
 44. Mason E. A. and Malinauskas A. P., *Gas Transport in Porous Media: The Dusty Gas Model* (Elsevier, Amsterdam, The Netherlands, 1983).
 45. Mason E. A. and Viehland L. A., Statistical mechanical theory of membrane transport for multicomponent mixtures: passive transport through open membranes, *J. Chem. Phys.* **68** (1978) pp. 3562–3573.
 46. Micke A., Bülow M., Kocirik M. and Struve P., Sorbate immobilization in molecular sieves. Rate-limiting step for *n*-hexane uptake by silicalite-1, *J. Phys. Chem.* **98** (1994)

- pp. 12337–12344.
47. Mota J. P. B., Molecular simulation of gas separation by adsorption processes, In *Proceedings of 3rd Pacific Basin Conference on Adsorption Science and Technology*, ed. by Lee C.-H. (World Scientific Publishing, Singapore, 2003) pp. 296–300.
48. Mota J. P. B., Towards the atomistic description of equilibrium-based separation processes. 1. isothermal stirred-tank adsorber, In *European Symposium on Computer Aided Process Engineering - 13*, ed. by Kraslawski A. and Turunen I. (Elsevier, Amsterdam, The Netherlands, 2003) pp. 791–796.
49. Nakao S. and Suzuki M., Mass transfer coefficient in cyclic adsorption and desorption, *J. Chem. Eng. Japan* **16** (1983) pp. 114–119.
50. Nelson P. H. and Auerbach S. M., Self-diffusion in single-file zeolite membranes in Fickian at long times, *J. Chem. Phys.* **110** (1999) pp. 9235–9243.
51. Nicholson D., The transport of adsorbate mixtures in porous materials: basic equations for pores with simple geometry, *J. Membrane Sci.* **129** (1997) pp. 209–219.
52. Nicholson D., Cracknell R. F. and Quirke N., A transition in the diffusivity of adsorbed fluids through micropores, *Langmuir* **12** (1996) pp. 4050–4052.
53. Nicholson D. and Petropoulos J. H., Calculation of the surface flow of a dilute gas in model pores from first principles. Part III, *J. Colloid Interface Sci.* **106** (1985) pp. 538–546.
54. Nicholson D. and Travis K. P., Molecular simulation of transport in a single pore. In *Recent Advances in Gas Separation by Microporous Ceramic Membranes*, ed. by N. K. Kanellopoulos (Elsevier, Amsterdam, 2000) pp. 257–296.
55. Ochoa-Tapia A. J., Del Rio P. and Whitaker S., Bulk and surface-diffusion in porous media - an application of the surface-averaging theorem, *Chem. Eng. Sci.* **48** (1993) pp. 2061–2082.
56. Onsager L., Reciprocal relations in irreversible processes. I., *Phys. Rev.* **37** (1931) pp. 405–421.
57. Palekar M. G. and Rajadhyaksha R. A., Sorption in Zeolites—III. Binary sorption. *Chem. Eng. Sci.* **41** (1986) pp. 463–468.
58. Pollard W. G. and Present R. D., On gaseous self-diffusion in long capillary tubes, *Phys. Rev.* **73** (1948) pp. 762–774.
59. Reid R. C., Prausnitz J. M. and Poling B., *The Properties of Gases and Liquids*. 4th ed., McGraw-Hill, New York, U.S.A., 1987.
60. Reyes S. and Jensen K. F., Estimation of effective transport coefficients in porous solids based on percolation concepts, *Chem. Eng. Sci.* **40** (1985) pp. 1723–1734.
61. Reyes S. and Jensen K. F., Percolation concepts in modelling of gas solid reactions. 1. Applications to char gasification in the kinetic regime, *Chem. Eng. Sci.* **41** (1986) pp. 333–343.
62. Reyes S. and Jensen K. F., Percolation concepts in modelling of gas solid reactions. 2. Applications to char gasification in the diffusion regime, *Chem. Eng. Sci.* **41** (1986) pp. 345–354.
63. Rice R. G., Approximate solutions for batch, packed tube and radial flow adsorbers - comparison with experiment, *Chem. Eng. Sci.* **37** (1982) pp. 83–91.
64. Rodrigues A. E. and Dias M. M., Driving force approximation in cyclic adsorption processes: simple results from system dynamics based on frequency response analysis, *Chem. Eng. Process.* **37** (1998) pp. 489–502.
65. Ruthven D. M. *Principles of Adsorption and Adsorption Processes* (John Wiley, New

- York, 1984).
66. Sanborn M. J. and Snurr R. Q., Predicting membrane flux of CH₄ and CF₄ mixtures in Faujasite from molecular simulations, *AIChE J.* **47** (2001) pp. 2032–2041.
 67. Serbezov A. and Sotirchos S. V., Multicomponent transport effects in sorbent particles under pressure swing conditions, *Ind. Eng. Chem. Res.* **36** (1997) pp. 3002–3012.
 68. Serbezov A. and Sotirchos S. V., Mathematical modelling of the adsorptive separation of multicomponent gaseous mixtures, *Chem. Eng. Sci.* **52** (1997) pp. 79–91.
 69. Serbezov A. and Sotirchos S. V., Mathematical modelling of multicomponent non-isothermal adsorption in sorbent particles under pressure swing conditions, *Adsorption* **4** (1998) pp. 93–111.
 70. Serbezov A. and Sotirchos S. V., On the formulation of linear driving force approximations for adsorption and desorption of multicomponent gaseous mixtures in sorbent particles, *Sep. Purif. Technol.* **24** (2001) pp. 343–367.
 71. Shah D. B., Guo C. J. and Hayhurst D. T., Intracrystalline diffusion of benzene in silicalite: effect of structural heterogeneity, *J. Chem. Soc. Farad. Trans.* **91** (1995) pp. 1143–1146.
 72. Sholl D. S., Predicting single-component permeance through macroscopic zeolite membranes from atomistic simulations, *Ind. Eng. Chem. Res.* **39** (2000) pp. 3737–3746.
 73. Skoulidas A. I., Ackerman D. M., Johnson J. K. and Sholl D. S., Rapid transport of gases in carbon nanotubes, *Phys. Rev. Lett.* **89** (2002), pp. 185901(1–4).
 74. Song L. and Rees L. V. C., Adsorption and transport of *n*-hexane in silicalite-1 by the frequency response technique, *J. Chem. Soc. Farad. Trans.* **93** (1997) pp. 649–657.
 75. Sotirchos S. V. and Burganos V. N., Analysis of multicomponent diffusion in pore networks, *AIChE J.* **34** (1988) pp. 1106–1118.
 76. Taylor R. and Krishna R., Multicomponent Mass Transfer (Wiley, New York, 1993).
 77. Tomakadis M. M. and Sotirchos S. V., Ordinary, transition, and Knudsen regime diffusion in random capillary structures, *Chem. Eng. Sci.* **48** (1993) pp. 3323–3333.
 78. Travis K. P. and Gubbins K. E., Computer simulation of isothermal mass transport in graphitic slit pores, *Molec. Simulation* **27** (2001) pp. 405–439.
 79. Turner G. A., The flow-structure in packed beds - a theoretical investigation utilizing frequency response, *Chem. Eng. Sci.* **7** (1958) pp. 156–165.
 80. van den Broeke L. J. P., Simulation of diffusion in zeolitic structures, *AIChE J.* **41** (1995) pp. 2399–2414.
 81. Vlught T. J. H., Adsorption and Diffusion in Zeolites: A Computational Study (Ph.D. Thesis, University of Amsterdam, 2000).
 82. Vlught T. J. H., Krishna R. and Smit B., Molecular simulations of adsorption isotherms of linear and branched alkanes and their mixtures in silicalite, *J. Phys. Chem. B* **103** (1999) pp. 1102–1118.
 83. Vlught T. J. H., Zhu W., Kapteijn F., Moulijn J. A., Smit B. and Krishna R., Adsorption of linear and branched alkanes in the zeolite silicalite-1, *J. Am. Chem. Soc.* **120** (1998) pp. 5599–5600.
 84. Yang R. T., Gas Separation by Adsorption Processes (Butterworths, Boston, MA, 1987).
 85. Yang R. T., Chen Y. D. and Yeh Y. T., Predictions of cross-term coefficients in binary diffusion: diffusion in zeolite, *Chem. Eng. Sci.* **46** (1991) pp. 3089–3099.

ADSORPTION OF ORGANIC MOLECULES IN NANOPOROUS ADSORBENTS FROM AQUEOUS SOLUTION

R. DENOYEL

MADIREL, CNRS-Université de Provence, Centre de St Jérôme,

13 397 Marseille Cedex 20, France

E-mail: rdenoy@ctm.cnrs-mrs.fr

One of the main features of adsorption from solution is the variety and complexity of molecules that can be involved in the processes. Depending on the application, it may be needed to understand the adsorption mechanism of simple organic molecules as well as that of large molecules like proteins, surfactant or polymers that bear many chemical functions and may adopt a large number of different conformations at the interface. For all molecules, a good knowledge of both the surface chemistry and the accessibility of nanoporous materials are crucial to understand their adsorbing properties. In this review the methods of characterisation of nanoporous adsorbents in view of their use in aqueous solution is first presented. Then the adsorption from solution phenomenon is described with a special focus on the determination of adsorbed amounts and on energetic and kinetic aspects. Complementary methods are then quickly presented before finishing with an overview of applications and recent developments of nanomaterials in the field of adsorption from solution.

1 Introduction

Nanoporous materials are used in many industrial processes involving a liquid/solid interface. Water purification and chromatography are examples where adsorption of solutes at the solid/liquid interface governs the processes. The surface chemistry, pore size and distribution, and pore spatial organisation are the key factors in determining the efficiency of these processes. The surface chemistry and pore size distribution have an impact on thermodynamic parameters (adsorption energy, affinity) and accessibility while the pore size distribution and the spatial organisation of the pores including the connectivity, the tortuosity and the shape of the pores, are factors that affect the adsorption kinetics.

Microporous and mesoporous materials are the most widely used adsorbents. One can consider that the definition of "nanoporous material" encompasses both microporous and mesoporous adsorbents for which IUPAC has defined the following pore width ranges: 0 – 2 nm for microporous materials and 2 – 50 nm for mesoporous materials respectively. Microporous adsorbents may be needed for applications where molecular sieving functions such as separation/purification of small gaseous molecules. Other applications, like chromatography, need several

scales of controlled porosity from mesopores to macropores in order to achieve both high selectivity and fast transfer.

The adsorption phenomena occurring at the solid/liquid interface are generally more complicated than those at the solid/gas interface [1]. There are always competitive adsorptions of at least two components. If the two components are miscible, the adsorption can be studied in the whole composition range (from 0 to 1 expressed in molar fraction). Otherwise one component can be considered as a solvent and the other one as a solute. In the case of water solution the situation is extremely complex because water itself is a reactive solvent that is present under various forms (H_2O , H^+ or OH^-) the concentrations of which depend on pH. Moreover, in many cases the adsorption is studied in the presence of a salt that has also an influence on the adsorption process. It means that in many conditions (water, a salt and the solute), six components are present in a system. As a consequence, a reliable study of adsorption from aqueous solution may need to look upon the variation of many parameters: pH, ionic strength, temperature, etc. Moreover the concept of ionic strength may be not sufficient in the case where some ions can be specifically adsorbed.

The reactivity of water with many surfaces leads to the formation of a surface charge. The conditions of formation of the surface charge, its evolution as a function of pH, ionic strength and temperature have been extensively studied in the case of non-porous minerals [2]. As will be seen along this chapter, the surface charge of porous solids has been less studied.

Another feature of adsorption from solution is the variety and complexity of molecules that can be involved in the processes. One can be interested by simple organic molecule, like benzene and its derivatives for example, as well as by large molecules like proteins, surfactants or polymers that bear many different chemical functions and may adopt a large number of different configurations at the interface. For such molecules, a good knowledge of both the surface chemistry and the accessibility of nanoporous materials are crucial to understand their adsorption properties.

In order to give, as complete as possible, a description of adsorption from solution in nanoporous adsorbents, this chapter is divided in four parts. The first part discusses characterisation of nanoporous adsorbents in view of their use in aqueous solution. In the second part, the adsorption phenomenon from solution is described with a focus on the determination of adsorbed amounts and thermodynamics and kinetics. In the third part

other methods of studying adsorption from solution are presented. Applications and recent developments are overviewed in the fourth part.

2 Characterisation of nanoporous adsorbents in view of their use for adsorption in aqueous solution

In order to have a good understanding of the adsorption phenomena of a given nanoporous solid in aqueous solution, it is necessary to characterise the solid at different levels. The first one is the pore size distribution that allows assessing the accessibility to a given molecule. The second one is the surface chemistry that has consequences on the possibility of the interaction between the solute and the surface, as well as on the wettability of the pores by the solvent.

2.1 Pore size characterisation

Different from crystalline materials like zeolites for which the pore size can be deduced from structural measurements like X-ray diffraction, most nanoporous samples need to be characterised with suitable methods, even in the case of highly ordered materials like MCM-41 that have a diffraction pattern signature, the pore size cannot be deduced without an assumption for at least one of the parameters used in the calculation (for example the density of the walls has to be assumed [3]). Most of the methods for pore size characterisation are based on the analysis of gas adsorption isotherms. Nitrogen and argon, adsorbed at low temperatures, are the most used probes for such type of characterisation. Among the methods one can quote:

- the Brunauer, Joyner and Halenda (BJH) method [4], based on the Kelvin equation, which allows to determine mesopore size distribution;
- the Broekhoef –de Boer method [5] that is slightly more sophisticated and is probably more reliable for the small mesopores (3 – 8 nm) than the BJH method;
- the Density Functional Theory (DFT), that allows to use the same approach from micropores to mesopores and is then well suited for nanoporous materials [6].

Good agreement is obtained between DFT and the Broekhoef –de Boer method, whereas it is now admitted that the BJH method underestimates the pore size in the small mesopore range [7].

Because better information is obtained by using several complementary methods, it may be useful to derive pore size distributions from other approaches. For example, mercury porosimetry can be used to assess pore sizes above 3 nm. Nevertheless this method is destructive and many nanoporous materials with a poor mechanical strength like MCM-41 cannot withstand the high pressure that is imposed during measurement [8]. Another method that is interesting for characterising materials that are used in an aqueous medium is thermoporometry. This method, initially developed by Brun and Quinson [9], allows pore size distributions to be determined from the decrease of the melting or solidification temperature of a fluid confined inside a porous solid. The authors have derived the equations relating the solidification temperature of water (and other liquids like benzene) and the pore radius. The recording of the solidification enthalpy as a function of temperature with a DSC (differential scanning calorimeter) is then directly related to the pore size distribution since this enthalpy is proportional to the pore volume in which the solidification is observed and to the specific solidification enthalpy. This method is less used than gas adsorption, mainly because the parameters that are used (notably solid/liquid interfacial tensions) are not directly measurable and consequently a calibration with gas adsorption was done by Brun et al to get the suitable parameters. Nevertheless recent fundamental studies show that a parallel interpretation between capillary condensation and melting/solidification mechanisms can be done [10]. Moreover, in the case of water, the decrease of solidification temperature is so deep that it is possible to estimate pore size distributions until 2nm.

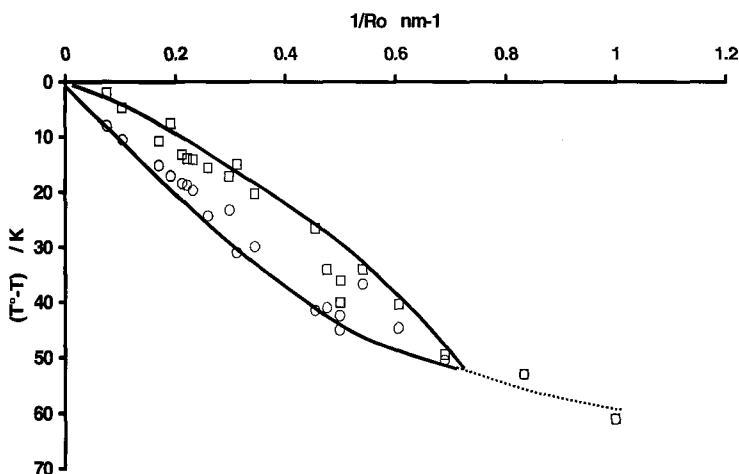


Figure 1. Temperature depression for water melting (squares) and solidification (circles) in nanopores as a function of the reverse of pore radius. Redrawn from ref. [10].

For example, in Figure 1, the melting and solidification temperatures are given as a function of the reverse of pore size for MCM-41 or SBA-15 materials. For very small pore sizes, there is no more hysteresis for the phase change. The decrease of water melting temperature may be 50K for a 2nm pore, then the sensitivity of the technique. Independently of theoretical questions about the mechanism of the process or the value of the parameters used for the calculation, this method has two advantages for studying solids that have to be used for adsorption from the aqueous phase. The first one is that it is not necessary to dry the material (this may be destructive in the case of soft gels or polymeric materials) which explains the use of this technique for characterising such materials [11]. In some cases, the pore size distribution evolution can be followed in situ during the material synthesis [12]. The second one is that it is a complementary characterisation with gas adsorption which can be useful notably if the pore size distribution and the pore volume that are derived are very different by the two methods. If the pore volume determined by thermoporometry is smaller than that from gas adsorption, it may indicate that the pore system is not fully wetted by water, showing that the hydrophilic nature of the surface may be not uniform in all porous system.

For nanoporous material having pores in the microporous range, it can be interesting to use immersion calorimetry to assess the real surface area accessible to a given molecule. The immersion energy of a solid into a liquid corresponds to the transfer energy of a dry solid into a liquid. If one considers only dispersive forces (see for example Everett and Powl calculations [13]), it can be shown that the energy of transfer of one molecule from the bulk to a micropore is enhanced as compared with the transfer to a non porous surface. For pores having a width close to the molecular size of the probe this enhancement may be as high as 2 or 3.6, for a slit-shaped pore or a cylindrical pore, respectively. These values are very close to the ratio of the actual area covered by the molecule in the micropore to its cross sectional area. As a consequence it is a reasonable approximation to consider that the immersion energy of a porous solid in a pure liquid is simply proportional to the surface area accessible to the probe molecule [14]. The question is to know if this approximation is still valuable when the pore size is larger than one molecular size. A theoretical answer can be given through the help of DFT. This latter method allows the calculation of adsorption isotherm for Lennard-Jones fluid for different pore sizes. Because this is a thermodynamic calculation based on the minimisation of the Grand Potential, the configurational energy is explicitly calculated in density functional theory [15]. Then it is possible

to calculate the integral energy of adsorption [1]. In the case of a nanoporous system, the integral energy of adsorption until total pore filling can be related to the immersion energy by the following equation:

$$\Delta_{imm}u = \Delta_{ads}u - n^a \Delta_{vap}u$$

where $\Delta_{imm}u$ is the immersion enthalpy, $\Delta_{ads}u$, the integral adsorption energy at saturation of the pore, n^a the amount adsorbed at saturation and $\Delta_{vap}u$ the vaporisation energy of the liquid. In figure 2, the integral adsorption energy per unit area calculated by DFT [16] is plotted as a function of the pore size as well as the corresponding immersion energy calculated by the preceding equation. This latter curve shows that the assumption of proportionality between the surface area and the immersion energy is reasonable for all pore size within an accuracy of $\pm 10\%$.

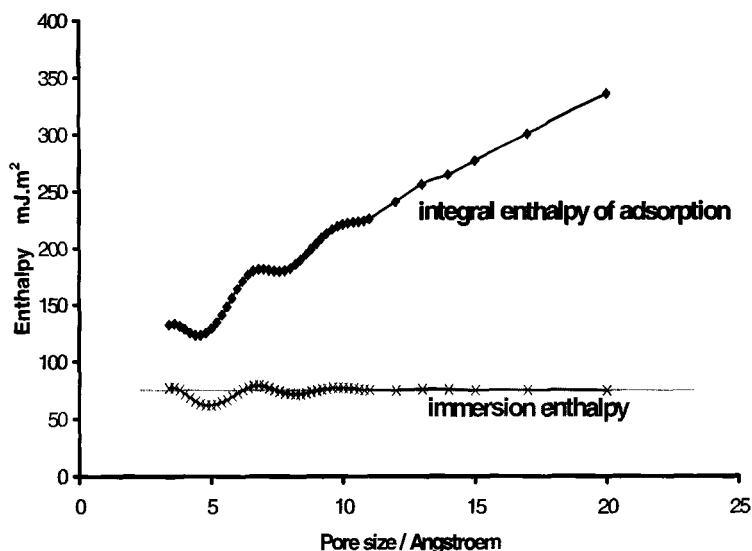


Figure 2. Integral adsorption enthalpy and corresponding immersion enthalpy as a function of pore size calculated by DFT for the filling of a slit-shaped pore by a mono-atomic fluid.

This method based on immersion calorimetry was assessed in the case of activated charcoals used for water treatment [14]. A non porous sample is used as a reference. Accessible surface areas for a set of organic molecules were deduced from the ratio of the immersion enthalpy of the unknown sample to that of the reference. A micropore size distribution can be then deduced from the size of the probes. This method has been

recently extended to zeolites [17]. Some attempts are now done at low temperature in order to use non-specific probes like nitrogen or argon [18].

Another method to characterise the pore size distribution and the surface area of porous solids in their application medium is to use the adsorption isotherm of probe molecules from solution. The idea is to transform the amount adsorbed at the plateau, when it is well defined, into an accessible surface area [19]. Some studies showed how iodine [20-23], p-nitrophenol [24,25] salicylic acid [26], surfactants [27] or dyes [28] can be used for such applications. The main difficulty comes from the fact that these molecules present an affinity for the surface that depends a lot on the experimental conditions. Among these molecules, many are ionic molecules and, because the surface is often charged, the resulting adsorption isotherm depends on pH.

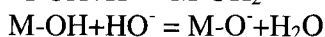
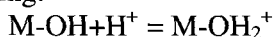
In the case of microporous solids, measurements with iodine [23] showed that methods like the α -s plot [1] could be extended to adsorption from solution. The reference adsorption isotherm is normalised by dividing the amount adsorbed by the amount adsorbed at the plateau thus allowing a reference curve to be plotted as α -s versus equilibrium concentration. The amounts adsorbed on the microporous sample that have to be characterised is plotted as a function of the α -s values. Plots similar to those for gas adsorption are obtained and allow a microporous pore volume and an external surface area to be calculated. The validity of the method is demonstrated by observing that the amount adsorbed at the end of the micropore filling corresponds to the point where the adsorption enthalpy becomes equal to that measured for the non-porous reference [23].

In the mesoporous range, much larger molecules are needed to characterise the porosity. The literature is very poor in this field. Polymers can be used to evaluate the porosity of a membrane. A molecular mass cut-off is thus defined rather than a real pore size. The solute exclusion technique has been also proposed to assess a pore size distribution [29]. Again, only the pore volume inaccessible to a given macromolecule is thus defined. No information is provided on the pore shape. This kind of method is adapted to wet porous materials and allows for example the in-situ characterisation of chromatographic phases. In a recent paper [30], Skvortsov and Fleer proposed a theory applicable to size exclusion chromatography that allows the determination of surface area and pore size of porous materials used in chromatography.

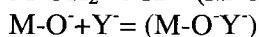
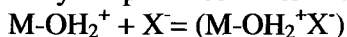
For all these approaches based on adsorption from solution a safe result cannot be obtained from only one experiment because of the possible, and generally unexpected, specific affinity between the probe and the surface.

2.2 Surface chemistry characterisation

The specific information on the chemical composition of the surface of nanomaterials should be obtained from spectroscopic techniques. These techniques are described in this book. So in this chapter only those used for measuring surface charge are discussed. Many solids get a surface charge when they are immersed in an aqueous solution. This surface charge has mainly two origins. The first one is the diffusion towards the solution of ions that are constitutive of the structure. This is the case of clays and zeolithes. The second one is due to the reaction of water with chemical groups on the surface. The most classical reactions are the following:



where M stands for atoms like silicon, titanium, aluminium etc. As underlined in the introduction, studies of the surface charge in porous media are rare in the literature. The simplest procedure to determine the surface charge of a solid is the potentiometric titration where the pH is followed as a function of the amount of acid or base that is added to an aqueous suspension of the powder [2]. The variations of the surface charge are thus deduced from the adsorption or desorption of protons. The surface charge depends on ionic strength. Usually an increase of the ionic strength leads to an increase of the surface charge. This latter can be considered as stabilised by the presence of ions following the binding reactions [31]:



When the electrolyte used to buffer the ionic strength is indifferent (non specific adsorption), the surface charge versus pH curves at various ionic strengths present a common intersecting point defining the point of zero charge PZC. The PZC may be equal to the isoelectric point PIE that is determined from electrophoretic mobility or streaming potential measurements (these measurements allows the so-called zeta-potential to be calculated). In these measurements the relative mobility between a liquid and a charged surface under the action of an electric field is analysed.

Two main experimental methods exist. In microelectrophoresis method, a diluted suspension of the particles is submitted to an electrical field E

between two electrodes. The speed of the particles, v , is measured to get the electrophoretic mobility $\mu=v/E$. This can be transformed into the so-called ζ -potential by applying Smolukowski-type equations [32]. For the second method - streaming potential experiment, particles are fixed in a bed and the pressure and voltage are measured during the flow of liquid. Again a ζ -potential can be calculated. Such potentials are more or less representative of the diffuse layer close to the charged interface that is usually described as a double layer [2]. By using models, a surface charge of the diffuse layer can be determined which is different from that obtained by potentiometric titration. This latter characterises the charge due to the chemical reaction with the solvent, whereas electrokinetics give access to an apparent charge that includes also adsorbed counter-ions. Recent models try to include both the chemical reactions at interface and the data of the diffuse layer issued from electrophoretic measurements [31]. The literature is very reach in that field because of the implications for the stability of non-porous colloid [2]. In the case of nanoporous solids one can expect that in most cases the interior of the pores are neutral as a whole. As a consequence the usual methods for studying the diffuse layer will give information on the electrical state of the external surface area. On the other side the methods, like potentiometric titration, that give access to the surface charge concentration can be used with porous solids. It has been shown that the porosity can affect the measurement of the surface charge inside the porosity. In micropores, the surface charge formation depends on the possibility for counter ions to penetrate inside the pore in order to neutralise and stabilise the charge [33]. Zhmud and Sonnefeld [34] showed how the surface charge, the surface potential and the effective equilibrium constant of charge formation reactions depend on the pore size for a set of mesoporous silicas. Notably the surface charge seems to decrease when the pore size decreases [34].

2.3 Wettability

The wettability of nanoporous solids used in aqueous solution applications is an important parameter. A non-wetting porous solid/liquid system is defined by the fact that the liquid cannot fill the porosity at saturation pressure. The first technical problem with such systems is that they are not easy to handle. The second problem is to know how the non-wetting character affects the adsorbing properties. One can indeed wonder whether the organic molecules that are in the aqueous solution can nevertheless be adsorbed on the unwetted surface of the pores. In a recent paper [36], the

adsorption of hydrophobic molecules onto nanoporous hybrid samples was studied. These samples were swelled MCM-41 type solids [37] while the walls of the pores were still covered by surfactant molecules. The powder, which is not wetted by water, floats on the liquid surface. Despite this fact, the hydrophobic molecules were adsorbed meaning that there was probably diffusion and adsorption of these molecules on the unwetted walls. At high surface concentration and equilibrium concentration the surface tension of the water solvent as well as that of the solid/vapour interface were sufficiently modified (lowered in the case of the liquid/vapour interface) to allow the full wetting of the porosity.

There is then a need to characterise the hydrophobic character of nanoporous solids. A way is to use probe molecules. For example, the adsorption of water vapour or other polar molecules can be used [38]. Another way is to directly study the interaction of liquid water with the solid. It can be done either by the standard immersion method [39] in the case of slightly hydrophobic solids, or by intrusion-extrusion of water under pressure in the case of very hydrophobic solids (say contact angles above 90°). This type of experiment has been developed recently in view of the possible application of nanoporous hydrophobic samples for shock dampers or energy storage [40]. Methods, based on the simultaneous determination of pressure/volume/heat of intrusion/extrusion [41], have been proposed to determine both the pore size distribution (in a way similar to the mercury porosimetry) and the apparent contact angle of water with the pore walls [42]. Many nanoporous hydrophobic materials have a high enough hydrophobic character for such applications : standard reverse phases for chromatography [40,42], grafted MCM-41 [43] or even non-organically modified samples like silicalite [44].

3 Thermodynamics and kinetics of adsorption in aqueous solution

3.1 Adsorption isotherm

The first step in any study of a physio-chemical phenomenon is the assessment of the thermodynamic properties. In the case of adsorption from solution, this is the determination of the adsorption isotherm. Whatever the interface, gas-solid or liquid-solid, experimental determination of the amount adsorbed leads to the concept of excess amount adsorbed. This is because the real structure of the interface is not known and the amount adsorbed is only deduced from the measurement of the variation of a macroscopic parameter that is measured far away from the interface. This parameter is the pressure for gas adsorption and the

concentration of species for adsorption from solution. The amount adsorbed is then deduced from the difference between the total amount of compound in the system and the amount that is present at equilibrium concentration in a volume that has to be defined. Experimentally this volume is taken equal to the volume of liquid that was introduced in the system. In gas adsorption it is deduced from a dead volume that is determined with a non-adsorbing gas. This is an approximation since the density of the liquid or of the gas in close vicinity of the interface is unknown. Various experimental methods can be found in the literature to determine the adsorption isotherm from the liquid phase. The simplest one is the immersion method [45] where the amount adsorbed is determined in a closed system. Other methods, like front chromatography, consider an open system. Whatever the method, closed or opened system, the same excess amount is determined provided the main parameters (temperature, pH, ionic strength) are fixed at the same value in the two types of experiments.

Theoretically it is necessary to introduce the concept of Gibbs Dividing Surface GDS [46]. Many papers can be found on this concept and the various ways to measure and present the adsorption data [47-50]. To summarise, it is generally propose to define the surface excess of component i as:

$$n_i^\sigma = n_i - c_i^l V^{l,0}$$

where n_i is the introduced amount of component i , c_i^l the concentration measured far away from the surface and $V^{l,0}$ is the volume of the fluid phase until the GDS. This equation can be written for any component in the system, including the solvent. This allows to eliminate $V^{l,0}$ in the preceding equation and to get the relative surface excess of 2 (the solute) with respect to 1 (the solvent):

$$n_2^{\sigma(1)} = n_2^\sigma - n_1^\sigma \frac{c_2^l}{c_1^l} = n_2 - n_1 \frac{c_2^l}{c_1^l} = n_2 - n_1 \frac{x_2^l}{x_1^l} = n^\circ \frac{\Delta x_2^l}{x_1^l}$$

where $n^\circ = n_1 + n_2$ and Δx_2^l is the composition change of 2 due to adsorption. The reduced surface excess can also be defined:

$$n_2^{\sigma(n)} = n_2^\sigma - n^\sigma x_2^l = n^\circ \Delta x_2^l$$

where $n^\sigma = n_1^\sigma + n_2^\sigma$ is the total surface excess. The relative surface excess of 2 with respect to 1 is equal to the surface excess of 2 when the GDS position is such that the surface excess of 1 is zero, whereas the reduced

surface excess of 2 is equal to the surface excess of 2 when the GDS position is such as the total surface excess is zero [1].

When possible, these various surface excesses are then reported to the surface area of the sample when it is well defined. Theoretically it should be measured at the place of the GDS to be significant. In the case of nanoporous solids or with curved surfaces, the concept of GDS reaches a limit because the value of the surface area depends on the position of the GDS. Nevertheless, the defined excess values are usable without any dividing surface concept. The surface excesses can be divided by the mass of adsorbent to get meaningful values that can be defined as “specific surface excess”. If two samples with the same pore size distribution but with different wall densities are compared, it is then necessary to divide the adsorbed amount either by a meaningful surface area or by the pore volume if one wants to compare the affinity of the solute towards the two adsorbents.

3.2 Energetic aspects

The adsorption equilibrium for a solution in contact with a flat surface is given by the Gibbs equation that is usually written at a constant temperature as:

$$d\gamma = -\sum_i \Gamma_i d\mu_i$$

where γ is the interfacial tension at the solid liquid interface, Γ_i the surface excess concentration of component i and μ_i its chemical potential. In the case of curved interfaces the influence of curvature has to be introduced. If a spherical interface is considered the Gibbs equation becomes [2]:

$$d\gamma = -\sum_i \Gamma_i d\mu_i + \left(\frac{\partial \gamma}{\partial R} \right)_{T, \mu_i} dR$$

where R is the radius of curvature. The second term on the right hand side of this equation is negligible when the curvature is much larger than the interfacial zone thickness [2]. In the case of nanoporous materials, it is probably no more negligible but, to our knowledge, it has not been considered until now in interpretation of results.

Another important aspect of adsorption energetics is the determination of adsorption enthalpies, which are characteristic of the interaction of the solute with the solid, bringing information on the nature of bonds and the configuration of the adsorbed phase. Adsorption enthalpies may be determined either directly by microcalorimetry or by the so-called isosteric method that uses several adsorption isotherms obtained at different

temperatures. The description of microcalorimetric methods for adsorption from solution can be found in the literature [51]. The simplest one is the titration method where a suspension of the solid under study is titrated by a stock solution. After correction for dilution effects, the adsorption enthalpy can be calculated as a function of the amount adsorbed. If the desorption study is needed or if large particle sized samples are used it is possible to use liquid-flow microcalorimetry. The comparison between the two approaches can be found elsewhere [52]. The calculation of the adsorption enthalpies by the isosteric methods is based on the two following equations than can be applied for dilute solutions or mixtures, respectively:

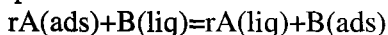
$$\Delta_{ads} \dot{h} = -RT^2 \left(\frac{\partial \ln x_i}{\partial T} \right)_{n_i^\sigma}$$

$$\Delta_{ads} h = -\frac{RT^2}{\Phi_1^I} \left(\frac{\partial \ln a_2^I}{\partial T} \right)_{n_2^a}$$

In the first equation, it is needed to derive at constant excess amount of all solutes, which is possible to ensure for the solute but not for the ions that are involved in adsorption process at the solid/aqueous solution interface. This is why it is always safer to use directly microcalorimetry. For the second equation a surface layer model is needed and the activity of the mixture has to be considered because of non-ideality when the full

range of composition is analysed. $\Phi_1^I = \frac{x_1^I}{x_1^I + r \cdot x_2^I}$ is the volume fraction of

component 1 and r can be considered as the displacement ratio of component 1 by component 2 [53,54]. In that case, adsorption, which is a displacement, can be considered as a chemical reaction involving the displacement of r molecules of component A by one molecule of component B:



This approach can be interesting for nanoporous materials, because the pore itself constitute a well defined volume for the adsorbed layer in which the displacement ratio is thus ascertained.

3.3 Kinetics of adsorption

Any thermodynamic study needs a preliminary kinetic study to check that the measurements are done at equilibrium. Nevertheless the number of quantitative kinetic studies is small in the literature, despite their great

importance. One of the reasons is that most adsorption studies are carried out by the solution depletion method, where the step of separation of the solid from the solution prevents to get information at a time shorter than a few minutes. In fact only studies on flat surfaces by optical methods like ellipsometry allows one to follow the rate of adsorption from the first second [55].

Generally, in the case of non-porous surfaces the adsorption is relatively quick. The adsorption rate is not only controlled by the transport to the surface (and then to the bulk diffusion coefficients) but also by the rate of exchange with the solvent at the interface. Consequently, contrary to the adsorption of one gas where the adsorption is not activated, adsorption from solution is always an activated process because the adsorption never occurs without desorption of the solvent. In the case of large molecules like polymer or surfactants slow kinetics were observed [56]. For such molecules, the time to reach the final conformation can also be very long even if the amount adsorbed does not change anymore. The phenomena of surface charge equilibration are generally very quick for non-porous surfaces. When a slow equilibration is observed, it is often related to the dissolution of the solid [2]. In the case of nanoporous solids, a slow kinetic of adsorption can be due to the diffusion of the solute through the pore network. For applications it is often sufficient to get breakthrough curves that give all needed information for both adsorption capacity and adsorption kinetic [57]. The study of desorption kinetics can also be very useful for other types of application. Recently nanoporous materials like MCM41 were proposed as drug delivery systems. In that case it is necessary to follow and model the release kinetic of molecules that were previously introduced inside the pores [58].

4 Other methods

Thermodynamics and kinetics approaches are macroscopic approaches that are needed for any application. In order to get a better understanding of the adsorption phenomenon it is necessary to have complementary methods that can bring information at the microscopic level. One may want information either on the conformation of adsorbed molecules or on the type of bonds that are involved between the solute, the solvent and the surface.

Information on the position of the molecule in the pores or on adsorbed layer thickness can be obtained from scattering techniques (X-ray or neutron) [59, 60], but the literature is poor in the case of adsorption

from solution on porous systems. In the case of polymers, both by NMR, IR or calorimetry it is possible to evaluate the fraction of segments that are either in contact with the surface or in the bulk [60]. NMR is sensitive to the mobility of the segments and then can discriminate between those that are in contact with the surface (low mobility) and those that are in loop and tails [61, 62]. Infra-red may evidence a band shift of the bond that is interacting with the surface allowing to evaluate the proportion of segments in contact with the surface (trains). Microcalorimetry is also sensitive to the number of segments that are in contact with the surface [63]. For other types of molecule, surfactants, peptides etc., the conformation at the interface and the aggregation state can be elucidated from NMR relaxation time measurements [64, 65].

The nature of bond between the solute and the surface can also be evidenced by spectroscopic techniques. By solid-state NMR it is thus possible to identify the bond between the adsorbed molecule and the surface. Examples can be found in the literature about organosilane adsorption [66], where the grafting of the molecules is obtained by siloxane bond formation, or polymer adsorption [67]. It must be kept in mind that the results are obtained for the dried sample, which means that both the conformation and the type of bond could have changed during the drying process. IR can be used to evidence the bonds that are formed when an organosilane molecule is grafted on a silica surface [68, 69]. Because water strongly absorbed infra red light it is generally necessary to use the attenuated total reflectance technique [70, 71], which means that the nanoporous material has to be deposited on a suitable support. Germanium wafers are often used because of their transparency in the infra-red wavelength range.

These spectroscopic experiments are not always easy to carry out but they really bring specific information on the state of the adsorbed phase. Moreover, one can see that in the quoted papers progresses are done at the quantitative level to determine the real composition of the adsorbed phase.

5 Applications

5.1 Adsorption of small molecules from aqueous solutions

Adsorption of small molecules can be found both in the case of mixtures (*i.e.* the adsorption is studied in the whole composition range) and in the case of dilute solutions.

5.1.1. Mixtures

For mixtures, most studies deal with water/alcohol systems. A typical problem is the separation of water and alcohol from their mixture. Nanoporous materials that give selectivity for one of the molecule can achieve this separation. The methods of separation include adsorption/desorption of the mixture [72] or pervaporation through nanoporous membranes [73]. It is then necessary to determine the competitive adsorption between water and alcohol from either their vapour or their liquid mixtures. For vapour pressures close to the saturation, where the porosity is filled by the mixture, the composition of the liquid filling the pores should be the same as that obtained from adsorption from liquid phase measurement [74]. As an example the specific excess adsorption isotherm for the system ethanol/water is given in figure 3 for silicalite. This adsorption isotherm is typical of what is obtained for systems studied in the whole composition range. U-shaped or S-shaped adsorption isotherms can be obtained [1]. In this case it is a U-shaped adsorption isotherm showing that ethanol is preferentially adsorbed in the all concentration range. In the same paper, to solve the problem underlined in the thermodynamics paragraph about the GDS location, the authors propose to rewrite the Gibbs equation under the form:

$$vd\phi = -\sum_i n_i^\sigma d\mu_i$$

where the bidimensional spreading pressure $d\gamma$ has been replaced by a tridimensional spreading pressure $d\phi$ and the surface area of the adsorbed phase by the its volume identified with the pore volume.

The adsorption isotherms shown in figure 3 show the high affinity of the organic molecule for the silicalite, which can be considered as a hydrophobic sample. Other types of zeolithes can be used for such applications: by varying the composition of the walls it is possible to modulate the affinity for the alcohol molecules [75, 76]. Hydrophobic nanoporous solids, like carbons [77], are also used for this separation.

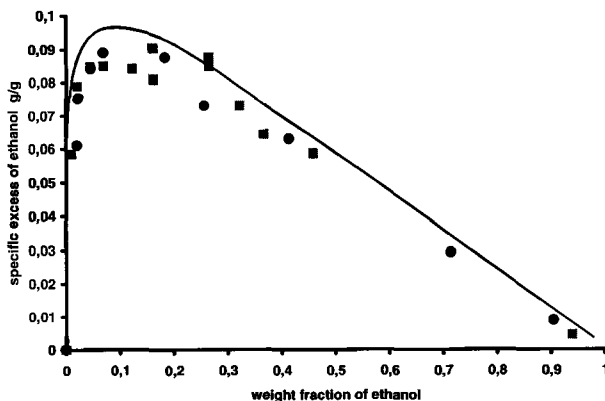


Figure 3. Adsorption of ethanol from aqueous solution on silicalite. The relative excess of ethanol with respect to water is determined by the conventional technique (circles) and by pycnometry (squares). Redrawn from ref. [74].

5.1.2. Dilute solutions

The adsorption from aqueous solution of small organic molecules in the low concentration range is often related to water treatment and environmental problems. In many cases, the considered organic molecules have a more or less pronounced hydrophobic character, which leads to a low solubility and a relatively easy partitioning towards hydrophobic phases. A large amount of work has been done on the adsorbing properties of activated charcoals, that are probably the most used nanoporous materials for all applications where the elimination of organic molecules from an aqueous solution is needed [78]. They generally have a broad distribution of pores from micropores to mesopores. Their micropores allow them to eliminate small organic molecules. Variations can be observed in their ability to adsorb a given molecule. The micropore size distribution and the surface chemistry should first be analysed. Because the surface chemistry of such sample is very complex, global test of the hydrophily like the determination of the water vapour adsorption isotherm can be useful. For example, a good correlation was obtained between the water adsorbed amount and the oxygen content of the charcoal [79]. Although they are adsorbents known for a long time, there are still many researches for improving the control of both the porosity and the surface chemistry of charcoals [80, 81]. The structural and chemical properties can be modified either by heating or by chemical treatment, including

chemical vapour deposition [81, 82]. The question of the mechanism of adsorption from solution by activated carbons is also often addressed. The important parameters that can be analysed are the reversibility of adsorption [83] or the relation between the adsorbing properties and the microscopic structure of the carbon. This latter is often difficult to define and, when the chemical sites at the interface are not really known, many interpretations are based on the interaction between the solute molecule and graphene layers [81, 84].

New types of nanoporous materials are systematically tested for the adsorption and elimination of small organic molecules from aqueous solution. For example zeolites are often proposed for separation applications, which led to many patents. Comparative studies between zeolites and carbons have been done [85]. Zeolites can be as efficient as charcoals to eliminate a given molecule but the rather hydrophobic surface of carbons and the dispersion in their pore size distribution give them a larger spectrum of possible organic molecules to be eliminated. Another problem connected with the pore size is the kinetic aspect. Because the zeolites have a uniform pore size, the diffusion through the network can be very slow. On the other side, heterogeneous networks that are present in charcoals can lead to fast adsorption because the largest pores (mesopores or macropores) that are efficient for the fast diffusion of molecules can connect the micropores, which are efficient for the adsorption of small pollutants [85]. Nevertheless, because of their well-defined structure, zeolites are model adsorbent that can be used as reference samples when complex systems are studied [86]. Any high surface area solid should be able to adsorb organic molecules at a certain level. When the solute is neutral, hydrophobic solids like carbon are very efficient. In the case where the solute is charged, various minerals may then be used [87,88]. Their efficiency depends on the pH conditions and on their point of zero charge.

Nanoporous adsorbents of the micelle templated silica type [89] could be also used in principle to adsorb organic molecules from aqueous solution. They can efficiently adsorb large molecules as we will see later, but in the case of small molecules they are not very efficient. Indeed on the one hand the pore size, which ranges between 2 and 10nm, is too large for an enhancement of the adsorption potential to be observed. On the other hand, the surface chemistry is that of a mineral, *i.e.* a polar surface, for which the water displacement by organic molecules that are less polar than water is generally difficult. Moreover, in many cases the organic molecules are rather negatively charged whereas most of these adsorbents are silica based, which means that they bear a negative charge in usual

conditions. A noticeable adsorption is then observed either if the solute molecule is positively charged or if lateral interactions between adsorbed molecules are strong (this is the case of surfactant adsorption that is presented later on). As a consequence, in order to make it efficient towards small organic molecule adsorption, the surface chemistry of nanoporous materials needs to be modified. Hybrid nanoporous materials are thus produced that can be tested for adsorption from aqueous solution of organic molecules. These hybrid materials are often organic-inorganic mesostructures which can be obtained by various synthesis routes. Pillared clays are such an example when the pillars are surfactant molecules [90]. One or two surfactant can be used in the same synthesis [91]. They can adsorb hydrophobic molecules that are probably solubilized between the surfactant chains [92, 93]. Surface modification by grafting has also been proposed either for clays [94] or zeolithes [95]. In the latter case, only the external surface is probably modified.

The same type of behaviour, i.e. solubilisation between the alkyl chains, should be obtained with micelle templated silica hybrid materials (MTS). Usually at the end of the synthesis such materials are treated in order to eliminate the surfactant phase that is confined between the mineral walls. It has been recently shown that the mesostructure surfactant/silica is able to eliminate hydrophobic molecules from aqueous solution [96]. The sorption isotherms of chlorophenol on such mesostructures prepared with surfactants varying by their chain length are presented in figure 4. As for pillared clays, the mechanism of abstraction is probably the solubilisation of the molecules between the confined chains of surfactant. This has been confirmed by calorimetric measurements that show very similar values between the sorption enthalpy of a set of hydrophobic molecules (chlorophenol derivatives) inside the confined surfactant phase and the solubilisation enthalpy in bulk micelles [36]. Various type of such mesostructure can be prepared [37]. They can be non-porous: the surfactant fills totally the porosity. They can be porous: a swelling agent is used during the synthesis and is removed by evaporation whereas the surfactant molecules stay on the surface. The other possibility with MTS nanomaterials is to remove the surfactant and to carry out a post modification with organosilane molecules. MCM-41 samples grafted with alkyl chains are able to remove organic molecules from solution [97]. Nevertheless, it seems that the as-synthesised MTS solubilise more small hydrophobic molecules than the post-grafted sample [98].

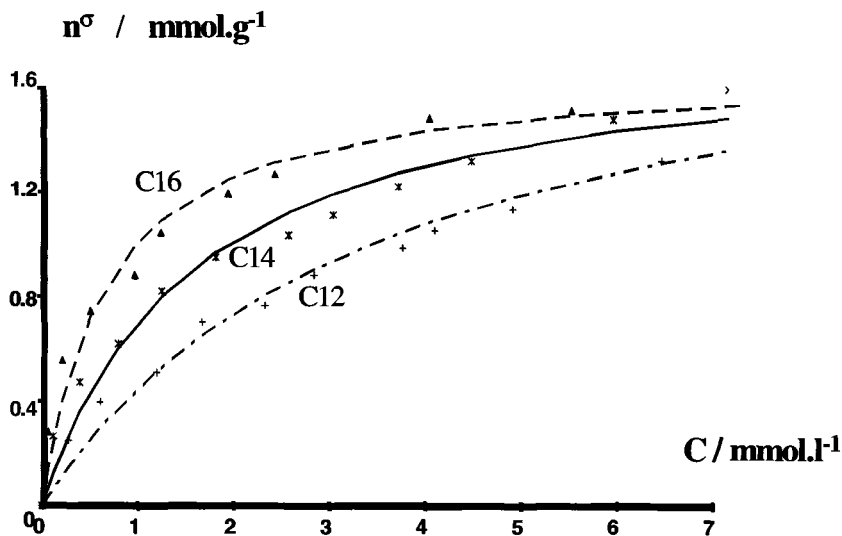


Figure 4. Adsorption of chlorophenol in MCM41-type hybrid mesostructures. C12, C14 and C16 correspond to silica mesostructures built around alkyltrimethyl ammonium bromide surfactants having 12,14 and 16 carbons in the alkyl chain, respectively (redrawn from [96]).

Nanoporous polymers can also be used to adsorb organic molecules from aqueous solution [99-101]. They are widely used in chromatography or catalysis. They offer many possibilities for surface modification then their use in molecular recognition [102]. Their porosity may be controlled at different levels, micropores or mesopores. In the mesopore range, mineral templates have been recently used [103].

Most of the adsorbents described in this paragraph are synthetic ones. Y. Tarasevich recently reviewed the possibilities of many natural adsorbents for elimination of organic pollutants from water [104].

5.2 Adsorption of polymers and macromolecules

The literature on adsorption of polymers by non-porous surfaces and suspensions is rich as compared to that dealing with porous system, even if interesting technical applications (for example coating of stationary phases for chromatography) can be found. A polymer can be introduced inside a porous system by two different ways. Frisch and Mark [105] have reviewed the methods to prepare nanocomposites based on zeolites as well as on mesoporous silica. Such nanocomposites can be prepared by in-situ synthesis of the polymer. The primary step is in fact the adsorption of the

monomer [106]. The other way is to let the chains diffuse into the pore structure. [107]. Polyethylene oxide, polyacrylic acid and dextran with molar masses up to 40000g were thus incorporated in MFI-type zeolites from their aqueous solution. As expected, the diffusion coefficients were found much lower than those in bulk solution (6 orders of magnitude lower). For controlled pore glasses with different pore sizes (around 8nm and 90nm), Gr  ll et al [108] showed how the adsorbed amount and the kinetic of adsorption depend on the pore size and the correlation length of the polymer.

For many applications involving biomolecules (proteins, polysaccharide, etc.), the good pore size range is within the mesopore range. The applications involving biomolecules encompass both separation process (purification, chromatography) and medical applications like extracorporeal techniques [109]. In this latter case it is needed to develop biocompatible adsorbents. Carbon based adsorbents can be useful under the form of polymeric adsorbent or activated carbons. There is then an interest in developing new mesoporous carbon adsorbents with well defined mesopore size distribution, for example by using mesoporous silica replica [110].

5.3 Adsorption of surfactants

The adsorption of surfactant from aqueous solution on various substrates has received much attention in the last decades. This is due to the fact that many applications involve surfactant molecules. Detergency, stability of suspension, enhanced oil recovery are among these applications. As for polymers, the adsorption of surfactants by porous samples is less studied than that by powders, suspensions or flat surfaces. The adsorption mechanism of surfactant is relatively well understood. It is now accepted that two steps can describe the formation of the adsorption layer. The initial adsorption in the low concentration range is generally due to the interaction between the polar head of the amphiphile molecule and some specific sites of the surface (H-bonds, electrostatic forces etc..). At higher concentrations, aggregates are formed at the interface as a result of lateral interactions between hydrophobic chains, which are similar to those responsible for bulk micelle formation. The concentration at which aggregates appear on the surface, the aggregate extent and thickness depend on i) the normal interaction (between the polar head and the surface), ii) the lateral interaction (between hydrophobic chains), and iii) the spatial and energetic distribution of adsorbing sites. It has been

observed that the porosity has an influence both on the adsorption of monomers and the formation of aggregates [111,112]. For example, there is a strong effect of the micropores on the adsorption of monomers when they can fit the size of the molecule. Activated charcoals adsorb non-ionic surfactants with a high affinity. The enthalpy part of the interaction may be found to be twice that on a non-porous surface [113,114]. If the pore size is not large enough, the aggregates cannot be formed on the surface. These aggregates are often micelle-like which need pores larger than 4nm to accommodate them. In a systematic study of surfactant adsorption on a set of porous silica (figure 5), Giordano et al [111] showed how the pore size distribution influences the surface concentration of monomers and aggregates. It was also shown that the notion of potential enhancement can be applied to the aggregates when they are in pores of similar size. Treiner et al [115] shown that the composition of the surface aggregate was not modified by the pore size (the non-ionic surfactant are generally polydisperse).

Micelle-templated silicas of the MCM41 type are prepared around cationic surfactants. Interestingly it is possible to adsorb a large amount of cationic surfactant inside organised mesoporous silica prepared with the same surfactant [116], showing that the decrease of pore radius during the calcination step is not so large.

6 Conclusions

As can be seen from the examples that are given all along this text, adsorption from aqueous solution on nanoporous materials encompasses a large variety of systems and it is not really possible to classify them in two or three categories obeying to simple laws. This is due to the diversity of organic molecules that can be met in industrial or natural processes. The modelling of adsorption has not been envisaged in the present paper. Because of the number of parameters, it is difficult to have models both easy to handle and containing a microscopic description. As a consequence many of the data of adsorption from solution by nanoporous systems are fitted with simple equations like that of Langmuir or Freundlich. All the classical equations and corresponding theories can be found in Lyklema's books [2] as well as models for macromolecule adsorption using mean-field concepts. The adsorption of surfactants in mesopores was modelled with this latter approach [117]. In most cases the classical equations were defined for non-porous systems and their extension to porous systems has to be done carefully. Monte-Carlo or Molecular Dynamics simulations have been extensively applied to gas

adsorption but much less to adsorption from aqueous solution. This is mainly due to the fact that to reproduce the properties of water alone is already a really difficult task. Then it is necessary to introduce ions and surface charge in the simulation [118] as well as the solute molecule with the question of the choice of the interaction potentials between the various components of the system [119].

References

1. Rouquerol F., Rouquerol J. and Sing K. S. W., *Adsorption by Powders and Porous Solids*, Academic Press, London (1999).
2. Lyklema J., *Fundamentals of Interface and Colloid Science. I Fundamentals. II. Solid-liquid Interfaces*, Academic Press, London (1995).
3. Kruk M., Jaroniec M., Kim J. M. and Ryoo R., Characterization of highly ordered MCM-41 silicas using X-ray diffraction and nitrogen adsorption, *Langmuir* **15** (1999) pp. 5279-5284.
4. Barrett E. P., Joyner L. G. and Halenda P. H., The determination of pore volume and area distributions in porous substances. I. Computations from nitrogen isotherms, *J. Am. Chem. Soc.* **73** (1951) pp. 373-380.
5. Broekhoff J.C.P. and Boer J. H. D., Pore systems in catalysts., XIII. Pore distributions from the desorption branch of a nitrogen sorption isotherm in the case of cylindrical pores. 2. Applications, *J. Catal.* **10** (1968) pp. 377-90.
6. Ravikovitch P.I., Vishnyakov A. and Neimark A.V., Density functional theories and molecular simulation of adsorption and phase transition in nanopores, *Phys.Rev. E*, **64** (2001) pp. 011602-1-20.
7. Neimark A.V. and Ravikovitch P.I., Capillary condensation in MMS and pore structure characterisation, Microporous and mesoporous materials, **44-45** (2001) pp. 697-707.
8. Sonwane C. G. and Bhatia S. K., Structural characterization of MCM-41 over a wide range of length scales, *Langmuir* **15** (1999) pp. 2809-2816.
9. Brun M., Lallemand A., Quinson J.F. and Eyraud C., A new method for the simultaneous determination of the size and the shape of pores: the thermoporometry, *Thermochimica Acta*, **21** (1977) pp. 59-88.
10. Denoyel R. and Pellenq R. J. M., Simple phenomenological models for phase transitions in a confined geometry. 1: melting and solidification in a cylindrical pore, *Langmuir* **18** (2002) pp. 2710-2716.
11. Iza M., Woerly S., Danumah C., Kaliaguine S. and Bousmina M., Determination of pore size distribution for mesoporous materials and polymeric gels by means of DSC measurements: thermoporometry, *Polymer*, **41** (2000) pp. 5885-5893.
12. Pauthe M., Quinson J.F., Ramsay J.D.F., Determination of porous texture in zirconia gels from adsorption isotherm measurements, small angle neutron scattering and thermoporometry, *Stud. Surf. Sci. Catal.* **87**, (1994) pp. 283-292.
13. Everett D.H. and Powl J.C., Adsorption in slit-like cylindrical micropores in the Henry's law region. A model for the microporosity of carbons, *J. Chem. Soc. Faraday Trans. I*, **72** (1976) pp. 619-36.

14. Denoyel R., Fernandez-Colinas J., Grillet Y. and Rouquerol J., Assessment of the surface area and microporosity of activated charcoals from immersion calorimetry and nitrogen adsorption data, *Langmuir*, **9** (1999) pp. 515-518.
15. Olivier J.P., Comparison of the experimental isosteric heat of adsorption on mesoporous silica with density functional theory calculations, *Stud. Surf. Sci. Catal.* **128** (2000) pp. 81-87.
16. Neugebauer N.N., PhD Dissertation, Leipzig University, Germany (1999).
17. Silvestre-Albero J., Gómez de Salazar C., Sepúlveda-Escribano A. and Rodríguez-Reinoso F., Characterization of microporous solids by immersion calorimetry, *Colloids and Surf. A: Physicochemical and Engineering Aspects* **187-188** (2001) pp. 151-165.
18. Rouquerol J., Llewellyn P., Navarette R., Rouquerol F. and Denoyel R., Assessing microporosity by immersion microcalorimetry into liquid nitrogen or liquid argon., *Stud. Surf. Sci. Catal.* **144** (2002) pp. 171-176.
19. Denoyel R. and Rouquerol F., Adsorption from the liquid phase, in *Handbook of porous solids*, Chap. 2.6., Wiley –VCH, in press.
20. Kipling J.J., in Adsorption from solution of non-electrolytes, Academic Press, London, 1965.
21. Puri B.R and Bansal R.C., Iodine adsorption method for measuring surface area of carbon blacks, *Carbon* **3** (1965) pp. 227-30.
22. Molina-Sabio M., Salinas-Martinez de Lecca C., Rodriguez-Reinoso F., Peunte-Ruiz C., Linares-Solano A., A comparison of different tests to evaluate the apparent surface area of activated carbons, *Carbon*, **23** (1985) pp. 91-96.
23. Fernandez-Colinas J., Denoyel R. and Rouquerol J., Adsorption of iodine from aqueous solutions onto activated carbons: correlation with nitrogen adsorption at 77K. *Ads. Sci. Technol.*, **6** (1989) pp. 18-26.
24. Giles C.H. and Nakhwa S.N., Adsorption. XVI. The measurement of specific surface areas of finely divided solids by solution adsorption, *J. Appl. Chem.*, **12** (1962) pp. 266-73.
25. Lopez-Gonzalez J. de D., Valenzuela-Calahorro C., Navarette-Guijosa A. and Gomez-Serrano V., Adsorption of p-nitrophenol by active carbons prepared from olive wood, *An. Chimica*, **84B** (1988) pp. 47-51.
26. Fernandez-Colinas J., Denoyel R., Rouquerol J., Characterization of activated charcoals by adsorption from solution, *Stud. Surf. Sci. Catal.* **62** (1991) pp. 399-408.
27. Somasundaran P. and Fuerstenau D.W., Mechanisms of alkyl sulfonate adsorption at the alumina-water interface, *J. Phys. Chem.*, **70** (1966) pp. 90-6.
28. Giles C.H., D'Silva A.P., Stridevi A., in "Proceedings of the International Symposium on Surface Area Determination", (D.H. Everett and R.H. Ottewill eds.), Butterworths, London (1969).
29. Lin J.K., Ladish M.R., Patterson J.A., Noller C.H., Determining pore size distribution in wet cellulose by measuring solute exclusion using a differential refractometer, *Biotechnologies and Bioengineering*, **29** (1987) pp. 976-981.
30. Skvortsov A. M. and Fleer G. J., End-functionalized polymer as a tool to determine the pore size and the interaction parameters in liquid chromatography, *Macromolecules* **35** (2002) pp. 8609-8620.
31. Venema P., Hiemstra T. and van Riemsduik W.H., Comparison of different site binding models for cation sorption: description of pH dependency, salt dependency, and cation-proton exchange, *J. Colloid Interface Sci.* **181** (1996) pp. 45-59.
32. Hunter R.J., Zeta Potential in Colloid Science, Academic Press, London, 1981.

33. De Keizer A., van der Ent E.M., Koopal L.K., Surface and volume charge densities of monodisperse porous silicas, *Colloids Surf. A*, **142** (1998) pp. 303-313.
34. Zhmud B.V. and Sonnefeld J., Charge regulation at the surface of porous silica, *J. Chem. Soc. Faraday Trans.* **91** (1995) pp. 2965-2970.
35. Zhmud B.V., Charge Regulation at the Surface of Porous Solids: A comparison between the results obtained using different potential-to-charge relations, *J. Colloid and Interface Sci.* **183** (1996) pp. 111-117.
36. Hanna K., Beurroies I., Denoyel R., Desplantier-Giscard D., Galarneau A. and Di Renzo F., Sorption of hydrophobic molecules by organic/inorganic mesostructures, *J. Colloid Interface Sci.* **252** (2002) pp. 276-283.
37. Desplantier-Giscard D., Galarneau A., di Renzo F. and Fajula F., Swelled micelle-templated silicas (MTS): structure control and hydrophobic properties, *Stud. Surf. Sci. Catal.*, **135** (2001) pp. 1105-1112.
38. Cauvel A., Brunel D., Di Renzo F., Garrone E. and Fubini B., Hydrophobic and hydrophilic behavior of micelle-templated mesoporous silica, *Langmuir* **13** (1997) pp. 2773-2778.
39. Everett D.H., Langdon A.G. and Maher P., Developments in immersion calorimetry: design and testing of an improved seal-breaking technique, *J. Chem. Thermodynamics*, **16** (1984) 981-992.
40. Fadeev A.Y. and Eroshenko V.A., Study of penetration of water into hydrophobized porous silicas, *J. Colloid Interface Sci.* **187** (1997) pp. 275-282.
41. Denoyel R., Beurroies I. and Vincent D., Microcalorimetric methods for studying vapour adsorption and wetting of powders, *J. Thermal Analysis and Calorimetry*, **70** (2002) pp. 483-492.
42. Gomez F., Denoyel R. and Rouquerol J., Determining the contact angle of a non-wetting liquid in pores by liquid intrusion calorimetry, *Langmuir* **16** (2000) pp. 3474-79.
43. Martin T., Lefevre B., Brunel D., Galarneau A., Di Renzo F., Fajula F., Gobin P.F., Quinson, J. F. and Vigier G., Dissipative water intrusion in hydrophobic MCM-41 type materials, *Chem Commun.* (2002) pp. 24-25.
44. Eroshenko V., Regis R.C., Soulard M. and Patarin J., Energetics: a new field of applications for hydrophobic zeolites, *J. Am. Chem. Soc.* **123** (2001) pp. 8129-8130.
45. Everett D.H., Reporting data on adsorption from solution at the solid/solution interface. Recommendations 1986, *Pure Appl. Chem.*, **58**(7) (1986) pp. 967-84.
46. Gibbs J.W., Collected (1877) Longmans Green and Co., New York.
47. Everett D.H., Reporting data on adsorption from solution at the solid/solution interface, *Pure Appl. Chem.*, **31** (1972) p. 579.
48. Defay R. and Prigogine I., Tension superficielle et adsorption, Desoer-Dunod, Liège-Paris (1951).
49. Schay G., in "Surface Area Determination", D.H. Everett and R.H. Otterwill, eds., Butterworth, London (1970) p. 273.
50. Kipling J.J., "Adsorption from solution of non-electrolytes", Academic Press, London (1965).
51. R. Denoyel, In situ methods for studying adsorbed phase at the solid/liquid interface: microcalorimetry and ellipsometry, *Comptes Rendus de l'Académie des Sciences, Geosciences*, **334** (2002) pp. 689-702.

52. Denoyel R., Rouquerol F., Rouquerol, J., Adsorption of anionic surfactants on alumina: complementarity of the informations provided by microcalorimetric experiments (Batch and Liquid Flow), *Colloids Surf.* **37** (1989) pp. 295-307.
53. Johnson I., Denoyel R., Everett D. H. and Rouquerol J., Adsorption at the liquid/graphite interface: comparison of enthalpy data obtained from three different methods, *Colloids Surf.* **49** (1990) p. 133.
54. Everett D.H. and Podoll R.T., Adsorption at the solid-liquid interface: non electrolytes systems, *Chem. Soc. Spec. Publ.*, **3** (1979) pp. 63-147.
55. Tiberg F., Jönsson B., Tang J.-A. and Lindman B., Ellipsometry Studies of the Self-Assembly of Nonionic Surfactants at the Silica-Water Interface: Equilibrium Aspects, *Langmuir* **10** (1994) pp. 2294-2300.
56. Fler G.J., Cohen Stuart M.A., Scheutjens J.M.H.M., Cosgrove T., Vincent B., Polymers at interfaces, Chapman et Hall, Cambridge (1993) pp. 286-297.
57. S.G.J. Heijman and R. Hopman, Activated carbon filtration in drinking water production: new developments and concepts, *Stud. Surf. Sci. Catal.* **120** (1998) pp. 723-43.
58. Vallet-Regi M., Ramila A., del Real R. P. and Perez-Pariente J., A new property of MCM-41: drug delivery system, *Chem. Mater.* **13** (2001) pp. 308-311.
59. Ramsay, J. D. F. Neutron scattering investigations of adsorption in microporous adsorbents having controlled pore geometry. *Stud. Surf. Sci. Catal.* **87** (1994) pp. 235-45.
60. Cohen Stuart M. A., Fler G. J. and Bijsterbosch B. H., Adsorption of poly(vinyl pyrrolidone) on silica. II. The fraction of bound segments, measured by a variety of techniques. *J. Colloid and Interface Sci.* **90** (1982) pp. 321-34.
61. Schonhoff M., Larsson A., Welzel P. B. and Kuckling D., Thermoreversible polymers adsorbed to colloidal silica: A ¹H NMR and DSC study of the phase transition in confined geometry, *J. Phys. Chem. B.* **106** (2002) pp. 7800-7808.
62. Larsson A., Kuckling D. and Schönhoff M., ¹H NMR of thermoreversible polymers in solution and at interfaces: the influence of charged groups on the phase transition, *Colloids Surf. A: Physicochemical and Engineering Aspects*, **190** (2001) pp. 185-192.
63. Trens P., Denoyel R., Conformation of poly(ethylene glycol) polymers at the silica/water interface: a microcalorimetric study, *Langmuir* **9** (1993) pp. 519-522.
64. Evenas, I. Furo, P. Stilbs, R. Valiullin, Adsorption isotherm and aggregate properties of fluorosurfactants on alumina measured by ¹⁹F NMR, *Langmuir* **18** (2002) pp. 8096-8101.
65. Long J. R., Oyler N., Drobný G. P. and Stayton P. S., Assembly of -helical peptide coatings on hydrophobic surfaces, *J. Am. Chem. Soc.* **124** (2002) pp. 6297-6303.
66. Plueddemann E. P, in Silane Coupling Agents, Plenum press, New york and London (1991).
67. El Mostafa Moujahid, Inacio J., Besse J.P. and Leroux F., Adsorption of styrene sulfonate vs. polystyrene sulfonate on layered double hydroxides, *Micropor. Mesopor. Mater.* **57** (2003) pp. 37-46.
68. Rivera D. and Harris J. M., In situ ATR-FT-IR kinetic studies of molecular transport and surface binding in thin sol-gel films: reactions of chlorosilane reagents in porous silica materials, *Anal. Chem.* **73** (2001) pp. 411-423.
69. Rivera D., Poston P. E., Uibel R. H. and Harris, J. M., In situ adsorption studies at silica/solution interfaces by attenuated total internal reflection fourier transform infrared spectroscopy: examination of adsorption models in normal-phase liquid chromatography, *Anal. Chem.* **72** (2000) pp. 1543-1554.

70. Neivandt D. J., Gee M. L., Tripp C. P. and Hair M. L., Coadsorption of poly(styrenesulfonate) and cetyltrimethylammonium bromide on silica investigated by attenuated total reflection techniques, *Langmuir* **13** (1997) pp. 2519-2526.
71. De Silva K. T. L. and McQuillan A. J., An in situ infrared spectroscopic study of ligand adsorption from aqueous solutions to cadmium telluride particle films, *Colloids Surf. A: Physicochemical and Engineering Aspects*, **194** (2001) pp. 189-195.
72. Nakai K., Development of automatic adsorption apparatus for binary mixture: measurement of individual adsorption isotherms of ethanol and water from their mixed vapours by active carbon fiber, *J. Colloid Interface Sci.* **240** (2001) pp. 17-23.
73. Asaeda M., Sakou Y., Yang J. and Shimasaki K., Stability and performance of porous silica-zirconia composite membranes for pervaporation of aqueous organic solutions, *J. Membrane Sci.* **209** (2002) pp. 163-175.
74. Farhadpour F. A. and Bono A., Adsorption from solution of nonelectrolytes by microporous crystalline solids: ethanol-water/silicalite system, *J. Colloid Interface Sci.* **124** (1988) pp. 209-27.
75. Dahl, I.M., Myhrvold E., Slagtern A., Stocker M., Adsorption of lower alcohols from water solutions on high silica zeolites, mesoporous MCM-41 and AlPO₄-5 *Adsorption Sci. Technol.*, **15** (1997) pp. 289-99.
76. Milestone N. and Bibby D.M., Adsorption of alcohols from aqueous solution by ZSM-5, *J. Chem.Tech. Biothecnol.* **34** (1983) pp. 73-79.
77. Biron E. and Evans M. J. B., Dynamic adsorption of water-soluble and insoluble vapours on activated carbon, *Carbon* **36** (1998) pp. 1191-1197.
78. Bansal R.P., Donnet J.P., Stoeckli F., in *Active Carbon*, Marcel Dekker, New York (1988).
79. Pendleton P., Wong S. H., Schumann R., Levay G., Denoyel R. and Rouquerol J., Properties of activated carbon controlling 2-methylisoborneol adsorption, *Carbon* **35** (1997) pp. 1141-1149.
80. Moreno-Castilla C. and Rivera-Utrilla J., Carbon materials as adsorbents for the removal of pollutants from the aqueous phase, *MRS Bull.* **26** (2001) pp. 890-894.
81. Park C., Engel E. S., Crowe A., Gilbert T. R. and Rodriguez N. M., Use of carbon nanofibers in the removal of organic solvents from water, *Langmuir* **16** (2000) pp. 8050-8056.
82. Villar-Rodill S., Denoyel R., Rouquerol J., Martinez-Alonzo A. and Tascon J. M. D., Fibrous carbon molecular sieves by CVD of benzene. Gas separation ability, *Chem. Mater.* **14** (2002) pp. 4328-4333.
83. Braidia W.J., Pignatello J.J., Lu Y., Ravikovitch P.J., Neimark A.V. and Xing B., Sorption hysteresis of benzene in charcoal particles, *Environ. Sci. Technol.*, in press.
84. Haghseresht F., Finnerty J. J., Nouri S. and Lu G. Q., Adsorption of aromatic compounds onto activated carbons: effects of the orientation of the adsorbates, *Langmuir* **18** (2002) pp. 6193-6200.
85. Okolo B., Park C. and Keane M. A., Interaction of phenol and chlorophenols with activated carbon and synthetic zeolites in aqueous media, *J. Colloid Interface Sci.* **226** (2000) pp. 308-317.
86. Li J. and Werth C., Evaluating competitive sorption mechanisms of volatile organic compounds in soils and sediments using polymers and zeolites, *Environ. Sci. Technol.* **35** (2001) pp. 568-574.

87. Flemming H. L., Adsorption on aluminas-current applications, *Stud. Surf. Sci. Catal.* **120A** (1998) pp. 561-585.
88. Vansant E.F., New composite adsorbents for the removal of pollutants from waste waters, *Stud. Surf. Sci. Catal.* **120B** (1998) pp. 381-396.
89. Beck J. S., Vartuli J. C., Roth W. J., Leonowicz, M. E. Kresge C. T., Schmitt K. D., Chu C. T. W., Olson D. H. and Sheppard E. W., A new family of mesoporous molecular sieves prepared with liquid crystal templates, *J. Am. Chem. Soc.* **114** (1992) pp. 10834-10843.
90. Boyd S.A., Lee J.F., Mortland M.M., Attenuating organic contaminant mobility by soil modification *Nature*, **333** (1988) pp. 345-347.
91. Zhu L. and Chen B., Sorption behaviour of p-nitrophenol on the interface between anion-cation organobentonite and water, *Environ. Sci. Technol* **34** (2000) pp. 2997-3002.
92. Lee J. F., Crum J. R. and Boyd S. A., Enhanced retention of organic contaminants by soils exchanged with organic cations, *Environ. Sci. Technol.* **23** (1989) pp. 1365-1372.
93. Stapleton G., Sparks D.L. and Dentel S.K., Sorption of pentachlorophenol to HDTMA-Clay as a function of ionic strength and pH, *Environ. Sci. Technol.* **28** (1994) pp. 2330-2335.
94. Huttenloch P., Roehl K.E., and Czurda K., Sorption of nonpolar aromatic contaminants by chlorosilane surface modified natural minerals, *Environ. Sci. Technol.*, **35** (2001) pp. 4260-4264.
95. Li Z., Burt T. and Bowman R. S., sorption of ionizable organic solutes by surfactant-modified zeolite, *Environ. Sci. Technol.*, **34** (2000) pp. 3756-3760.
96. Denoyel R. and Sabio Rey E., Solubilization in confined surfactant mesophases *Langmuir* **14** (1998) pp. 7321-7323.
97. Inumaru K., Kiyoto J. and Yamanaka S., Molecular selective adsorption of nonylphenol in aqueous solution by organo-functionalized mesoporous silica, *Chem. Commun.* (2000) pp. 903-904.
98. Cagnon B., Beurroies I., Boitard E., Dubes J.P. and Denoyel R., Adsorption from solution by hydrophobized MCM41, *In Fundamentals of adsorption*, K. Kaneko, H. Hanoh, Y. Hanzawa (eds.), International Adsorption Society, IK international, Chiba, Japan, (2002) 632.
99. Li A., Zhang Q., Chen J., Fei Z., Long C. and Li W., Adsorption of phenolic compounds on Amberlite XAD-4 and its acetylated derivative MX-4, *Reactive and Functional Polymers*, **49** (2001) pp. 225-233.
100. Derylo-Marczewska A., Goworek J. and Zgrajka W., Studies of melamine-formaldehyde resins by sorption from gas and liquid phases, *Langmuir* **17** (2001) pp. 6518-6523.
101. Derylo-Marczewska A., Goworek J., Pikus S., Kobylas E. and Zgrajka W., Characterization of melamine-formaldehyde resins by XPS, SAXS, and sorption techniques, *Langmuir* **18** (2002) pp. 7538-7543.
102. Nakano Y., Oya T. and Watanabe T., Selective adsorption of a guest molecule by heteropolymer gels, *In Fundamentals of adsorption*, K. Kaneko, H. Hanoh, Y. Hanzawa (eds.), International Adsorption Society, IK international, Chiba, Japan, (2002) p. 295.
103. Derylo-Marczewska A., Goworek J. and Zgrajka W., Investigations of sorption processes from liquid phase on new polymeric porous materials, *In Fundamentals of adsorption*, K. Kaneko, H. Hanoh, Y. Hanzawa (eds.), International Adsorption Society, IK international, Chiba, Japan, (2002) p. 303.

104. Tarasevich Y.I., Application of natural adsorbents and adsorption-active materials thereon in the processes of water purification, *Stud. Surf. Sci. Catal.* **120B** (1998) pp. 659-715.
105. Frisch H.L. and Mark J.E., Nanocomposites prepared by threading polymer chains through zeolites, mesoporous silica, or silica nanotubes, *Chem. Mater.* **8** (1996) pp. 1735-1738.
106. Matsumoto A., Kitajima T. and Tsutsumi K., Adsorption characteristics and polymerization of pyrrole on Y-Zeolites, *Langmuir* **15** (1999) pp. 7626-7631.
107. Buttersack C., Rudolph H., Mahrholz J. and Buchholz K., High specific interaction of polymers with the pores of hydrophobic zeolites, *Langmuir* **12** (1996) pp. 3101-3106.
108. Grull H., Shaulitch R. and Yerushalmi-Rozen R., Adsorption of PEO in highly confining porous glass, *Macromolecules* **34** (2001) pp. 8315-8320.
109. Murphy M. C., Patel S., Phillips G. J., Davies J. G., Lloyd A. W., Gun'ko V. M. and Mikhalevsky S. V., Adsorption of inflammatory cytokines and endotoxin by mesoporous polymers and activated carbons, *Stud. Surf. Sci. Catal.* **144** (2002) pp. 515-520.
110. Han S., Sohn K. and Hyeon T., Fabrication of new nanoporous carbons through silica templates and their application to the adsorption of bulky dyes, *Chem. Mater.* **12** (2000) pp. 3337-3341.
111. Giordano F., Denoyel R. and Rouquerol J., Influence of porosity on the adsorption of a non-ionic surfactant on silica, *Colloids Surf. A* **71** (1993) pp. 293-298.
112. Gu T. and Zhu B., The S-type isotherm equation for adsorption of nonionic surfactants at the silica gel-water interface, *Colloids Surf.* **44** (1990) pp. 81-87.
113. Gonzales-Garcia C.M., Denoyel R., Gonzalez-Martin M.L. and Gomez-Serrano V., Influence of porosity on the adsorption enthalpies of a non-ionic surfactant onto carbonaceous materials, *Thermochimica Acta* **375** (2001) pp. 177-185.
114. Thomas F., Bottero J.Y., Partyka S. and Cot D., Contribution of microcalorimetry to the study of adsorption mechanisms of ionic and non-ionic molecules at the solid-water interface, *Thermochimica Acta* **122** (1987) pp. 197-207.
115. Portet F., Desbène P. L. and Treiner C., Polydispersity of a non-ionic surfactant as related to its adsorption characteristics on porous silica particles in water, *J. Colloid Interface Sci.* **208** (1998) pp. 415-421.
116. Meziani M. J., Zajac J. and Partyka S., Adsorption and interfacial aggregation of a cationic quaternary ammonium surfactant on powdered mesoporous MCM-41 aluminosilicates from dilute aqueous solutions, *Langmuir* **16** (2000) pp. 8410-8418.
117. Huinink H.P., de Keizer A., Leermakers F.A., Lyklema J., Adsorption of Nonionic Surfactants in Hydrophilic Cylindrical Pores. 1. A Thermodynamic Analysis, *Langmuir* **13** (1997) pp. 6452-6460.
118. Lo W. Y., Chan K. Y., Lee M. and Mok K. L., Molecular simulation of electrolytes in nanopores, *J. Electroanal. Chem.* **450** (1998) pp. 265-272.
119. Nicholson D. and Parsonage N. G., Computer simulation and the statistical mechanics of adsorption, Academic Press (1982).

FUNCTIONALIZED NANOPOROUS ADSORBENTS FOR ENVIRONMENTAL REMEDIATION

MARK C. BURLEIGH

*Laboratory for Molecular Interfacial Interactions, Code 6930, Center for Bio/Molecular Science and Engineering, Naval Research Laboratory, Washington, DC 20375
E-mail: mcb@cbmse.nrl.navy.mil*

SHENG DAI

Chemical Sciences Division, Oak Ridge National Laboratory, P.O. Box 2008, Oak Ridge, TN 37831 E-mail: dais@ornl.gov

The key to the development of advanced adsorbents lies in the synthesis of functional porous materials. This chapter is focused on the subject related to methodologies for the functionalization of nanopores for remediation of potential environmental contaminants. The functionalization techniques covered include post-synthetic grafting, ion exchange functionalization, co-condensation, and assembly via periodic mesoporous organosilicas. The interface of the above techniques with molecular and ion imprinting methods is also discussed.

1 Introduction

The proliferation of human populations has led to environmental pollution of great proportions. Many pollutants are generated during power production or manufacturing and subsequent disposal of consumer products. Not all pollutants are man-made. Aquifers in the Western United States contaminated with toxic arsenic compounds are an example of natural pollution. Whether man-made or intrinsic to a given locality, pollutants can have harmful effects on plant and animal life. Of particular concern are highly toxic heavy metals and stable compounds such as phenols that persist in the environment. These may contaminate water supplies or re-enter the food chain and end up in human foodstuffs. For these reasons, the development of efficient separation technologies is a requirement for environmental quality and human health.

Adsorbent materials are used to separate contaminants from waste streams or remediation of contaminated sites. Requirements for efficient separations or cleanup include fast adsorption kinetics, high capacities, selectivity for specific contaminants, and the ability to easily regenerate and re-use the adsorbent material. Fast adsorption kinetics allow for the treatment of large quantities of waste in a reasonable amount of time. High

capacities permit the use of small amounts of adsorbent. Since the major components of most waste streams and contaminated sites are innocuous compounds, adsorbents must bind selectively to pollutants. The ability to regenerate loaded adsorbents allows them to be re-used, while the pollutants can be isolated and recycled. Since both adsorption and desorption occur on their surfaces, these materials are simply referred to as sorbents.

Sorbent technology has developed greatly over the past decade. Scientists are now able to create materials containing ordered arrays of nano-sized pore channels. In contrast, conventional materials such as activated carbon and silica are amorphous—molecular diffusion is limited by bottlenecks and dead volumes in their pore structures. This results in slow adsorption kinetics and lower capacities. The open pore structures of ordered nanoporous materials allow fast access of ions and small molecules to their large ($>1,000 \text{ m}^2/\text{g}$) surface areas. Moreover, nanoporous sorbents can be created with controlled pore size and tailored pore chemistries to enhance their selectivity. Herein, we provide an overview of nanoporous materials with emphasis on techniques for their functionalization and their use as sorbents for environmental remediation.

2 Synthesis of Ordered Materials

The discovery of a new family of porous silicon oxides (M41S) by Beck and co-workers at Mobil Oil Research and Development [1-5] has led to great interest in nanoporous materials. One member of this family, MCM-41 exhibits hexagonal arrays of uniform nanopores. These materials have large internal surface areas and narrow pore size distributions similar to those found in microporous zeolites. Unlike conventional zeolite materials with maximum pore dimensions $< 20 \text{ \AA}$, the pores of MCM-41 can be engineered with diameters between 15-100 \AA . The relatively large pore sizes in these materials make them attractive for sorbent applications, especially when adsorbate molecules are too large to penetrate microporous channels of zeolites. MCM-41 materials are synthesized using surfactant templating methods (Fig. 1).

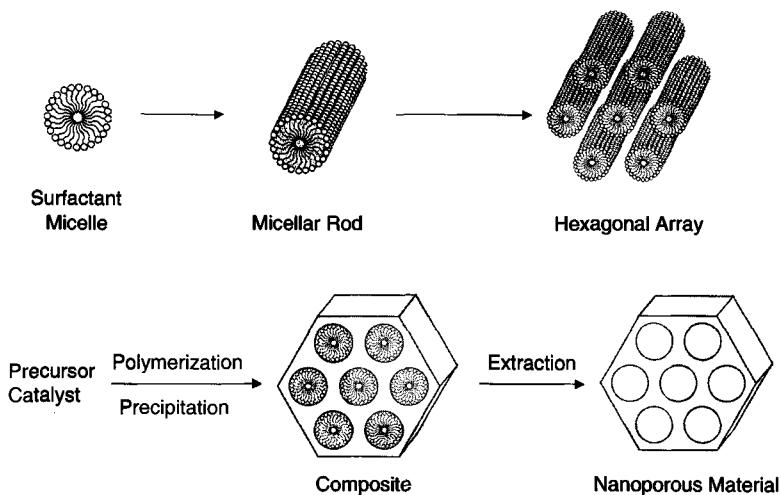


Figure 1. The surfactant template approach to nanoporous materials.

The surfactant template approach to porous materials utilizes the propensity of surfactants to form ordered supramolecular assemblies in solution. The addition of metal alkoxide precursors and subsequent hydrolysis and condensation reactions (at the appropriate pH) results in polymerization and the encapsulation of the surfactants. Removal of the surfactants by calcination, extraction, or ion exchange yields an ordered nanoporous material having pores shaped like the supramolecular assemblies. This nanocasting technique has proven to be very versatile. Colloid chemists have long known that different surfactants self-assemble to form supramolecular assemblies having different sizes and shapes. By using different surfactants, the templating approach allows the synthesis of materials with a wide variety of nanoporous structures.

Mobil scientists utilized alkyltrimethylammonium templates in basic media to produce both aluminosilicate and purely siliceous MCM-41. The head groups of these cationic surfactants (S^+) attract negatively charged inorganic precursors (I^-) to the surface of the supramolecular assemblies prior to polymerization. They demonstrated that increasing the length of the alkyl chain of the surfactant molecules increased the pore size of the resulting materials. The addition of the auxiliary organic mesitylene was also shown to expand the templates and increase pore sizes. Huo et al. reported a generalized synthetic approach to periodic surfactant/inorganic

composites by four separate electrostatic pathways [6]. In addition to using cationic surfactants in basic (S^+T) and acidic (S^+XT^+) media, ordered materials are also obtained using anionic surfactants in both acidic (ST^-) and basic (SM^+T) solutions.

Tanev and Pinnavaia have reported a template directed route to ordered nanoporous materials based on hydrogen bonding interactions [7]. This approach is based on the self-assembly of neutral primary amine templates (S^0) and neutral inorganic precursors (I^0). These HMS materials exhibit only short range hexagonal ordering and wormhole pore structures. The weaker (S^0I^0) interactions between the surfactants and inorganic species allow for facile extraction of the templates without the need for acidified solvents. Materials prepared by this synthetic approach have thicker pore walls, higher thermal stability, and smaller particle sizes than MCM-41 materials formed by electrostatic (S^+T) or (S^+XT^+) assembly pathways [8].

Stucky and co-workers synthesized a family of highly ordered nanoporous (20-300 Å) silicates using nonionic alkyl poly(ethylene oxide) surfactants and poly(alkylene oxide) block copolymers under acidic conditions [9]. They prepared silicas having cubic, 3-d hexagonal, 2-d hexagonal, and lamellar symmetries. In general, the silicas templated with the nonionic oligomeric surfactants formed cubic or 3-d hexagonal structures, while the nonionic triblock copolymers led to a 2-d hexagonal arrangement. One member of this family (SBA-15) exhibited large $d(100)$ spacings of 104-320 Å, pore sizes up to 300 Å, and thick pore walls (31-64 Å). Since nonionic templates were employed in acidic media, this is a (S^0H^+)(XT^+) assembly pathway. Block copolymer surfactants were also used in nonaqueous solvents to synthesize a wide variety of ordered nanoporous metal oxides from their respective metal chlorides [10].

In addition to MCM, HMS, and SBA materials, researchers have discovered a wealth of different synthetic strategies to produce nanoporous silicas with surfactant templates. Nanoporous silica referred to as FSM-16 has been derived from the sodium form of layered kanemite and cetyltrimethylammonium cations [11]. Bagshaw et al. used nonionic polyethylene oxide surfactants as structure directors for disordered MSU materials [12]. Ryoo and co-workers synthesized disordered silicas, designated KIT-1 by the addition of the tetrasodium salt of ethylenediaminetetraacetic acid to sodium silicate solutions containing cetyltrimethylammonium templates. These materials exhibit short interconnected wormlike pore structures [13].

3 Functionalization

Silica has many physical and chemical properties that make it an attractive solid support for adsorbent applications. It does not swell in water like many organic polymers, has good mechanical strength, and excellent thermal stability. For applications in aqueous media, the hydrophilic character of the silica surface allows for fast penetration of water to its internal pore spaces. Reactive surface silanol groups can be used to anchor organic functional groups that give the sorbent chemical selectivity for specific molecules and ions. The incorporation of organic functional groups into nanoporous silica has been accomplished by employing a number of different synthetic strategies.

3.1 *Post-synthetic Grafting*

Post-synthetic functionalization of nanoporous silica has been accomplished by refluxing organosilanes that contain alkoxysilyl groups in the appropriate solvent. The surface silanols undergo condensation reactions with the alkoxy groups of the functional silane to form covalent siloxane linkages. The careful exclusion of excess water avoids the hydrolysis of the alkoxy groups and subsequent homocondensation and polymerization of the organosilanes. Liu and co-workers synthesized thiol-silica hybrid materials by refluxing MCM-41 in a mixture of tris(methoxy)-mercaptopropylsilane and dry toluene [14]. Diaz and Balkus used a similar approach to functionalize MCM-41 with ethylenediamine, diethylenetriamine, and ethylenediaminetriacetic acid functional groups [15]. Likewise, Lim and Stein synthesized vinyl-functionalized MCM-41 [16] and Mercier and Pinnavaia reported thiol-functionalized HMS materials [17]. Since all of the functional groups are located on the nanopore surfaces sorbents made with post-synthetic grafting techniques exhibit rapid adsorption kinetics. High loadings of organosilanes can impart hydrophobicity due to the high concentration of organics at the solid-liquid interface.

3.2 *Ion Exchange Functionalization*

A novel approach to nanoporous organosilicas employing ion exchange functionalization was reported by Dai and co-workers [18]. This methodology eliminates the surfactant extraction step in the synthesis of functionalized nanoporous silica by treating the as-synthesized composites with a solution containing metal ion complexes of the appropriate

organosilane (Fig. 2). The cationic surfactants are displaced by the metal ion complexes and the alkoxysilyl groups then graft by reaction with the silica surface. Acid washing removes the metal ions and any residual surfactant giving the desired product. Although a complex between a divalent cation and two N-(2-aminoethyl)-3-aminopropyltrimethoxysilane molecules (AAPS) is illustrated, this versatile technique can be used with a wide variety of functional silanes.

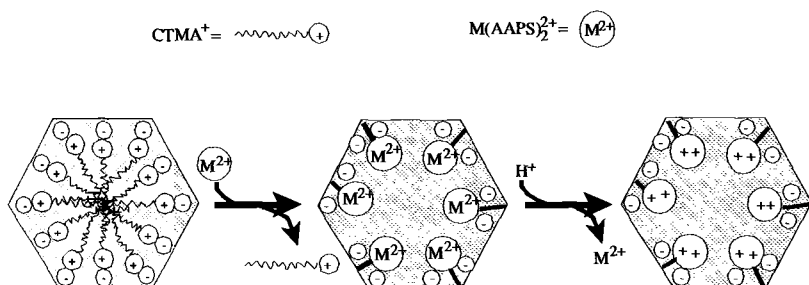


Figure 2. The ion exchange functionalization of nanoporous materials.

3.3 Co-condensation

The incorporation of functional groups into nanoporous materials can also be accomplished by adding the functional silanes during the initial synthetic step. They then undergo condensation with the metal alkoxide precursor (ie. tetramethylorthosilicate) and become part of the solid matrix that encapsulates the surfactant supramolecular assemblies. This co-condensation methodology is referred to as “direct synthesis” or “single pot synthesis” because it eliminates the need for an extra synthetic step to functionalize nanoporous materials. This approach has been employed by Mann and co-workers to produce ordered nanoporous silicas containing a variety of functional groups including: phenyl, *n*-octyl, thiol, amino, epoxy, allyl, and imidazole [19,20]. Although these materials were synthesized with only one functional silane, this method was later extended to produce bifunctional organosilicas containing allyl, thiol, or amine groups with phenyl moieties [21]. While Mann employed cationic cetyltrimethylammonium surfactants and basic conditions, Macquarrie successfully used a neutral amine templating strategy to produce cyano and amino-functionalized materials [22]. Mercier and Pinnavaia later

reported the incorporation of a variety of organosiloxane groups into nanoporous HMS materials by direct synthesis using the neutral amine assembly pathway [23]. Margolese et al. employed direct synthesis, triblock copolymer templates, and acidic media to produce large pore SBA-15 materials containing sulfonic acid groups [24].

Although post-synthetic grafting and ion exchange functionalization are effective, co-condensation has been the most popular method for functional incorporation in nanoporous materials. Key advantages include homogeneous distribution of organics in the product and single pot syntheses. Homogeneity alleviates the problem of hydrophobicity, a distinct disadvantage for applications that involve aqueous media. The simpler single pot synthesis e

liminates the multi-step synthesis required with post-synthetic grafting. A disadvantage of the co-condensation route is that the incorporation of high concentrations functional silanes results in disordered materials. Another problem inherent to co-condensation reactions is that of differing precursor hydrolysis rates. This can result in homocondensation of the precursor that hydrolyzes faster and an inhomogeneous distribution of functional groups in the resulting matrix.

3.4 Periodic Mesoporous Organosilicas

The difficulties associated with both post-synthetic grafting and co-condensation can be avoided by using bis(alkoxysilyl) precursors containing organic bridging groups. The resulting polysilsesquioxanes with large surface areas and ordered pore structures were first reported by Inagaki and co-workers [25]. These periodic mesoporous organosilicas (PMOs) put the organo- in organosilicas simply by the selection of the appropriate precursor [26]. The resulting materials are true molecular composites containing both inorganic siloxane groups and organic bridging functionalities in each monomer unit. This synthetic approach avoids the problems associated with different precursor hydrolysis rates incurred during co-condensation polymerizations and eliminates the multi step protocols required in post synthetic grafting techniques. Examples of PMO structures are shown in Figure 3.

Unfortunately, not all silsesquioxane precursors can be used to create PMOs. The lack of structural rigidity in the organic portion of the silsesquioxane precursor is the limiting factor. Too much flexibility will result in a material (similar to an organic polymer) that will not hold its shape once the surfactant template is removed. For this reason, all PMOs reported to date contain relatively short aliphatic or aromatic moieties.

Some very useful functional groups, including simple amines and thiols have not been incorporated into PMOs, due in part by the lack of available precursors that have the required rigidity. For instance, the organic bridging portions of known bis-trialkoxysilane precursors containing amine groups are too flexible to “stand alone” once the porogens are extracted. Surfactant removal from the ordered nanoscopic composites of these monomers results in a collapse of the polymer matrix [27]. In order to overcome this problem, co-condensation has been employed to produce a variety of bifunctional or multifunctional organosilicas [28,29,30].

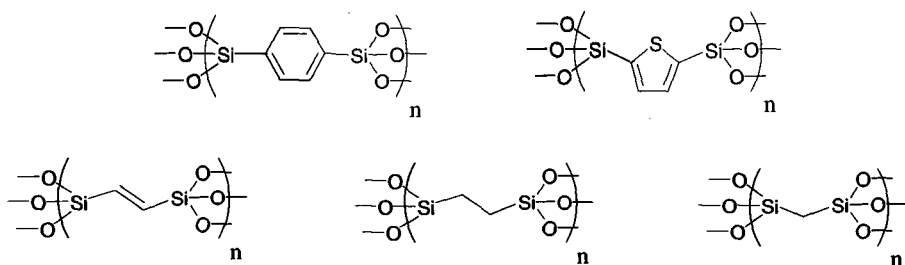


Figure 3. Chemical structures of some periodic mesoporous organosilicas.

4 Remediation

4.1 Metal Ion Sorbents

Man has harnessed the unique properties of metals since ancient times. Durability, ductility, and conductivity are some of the specific properties that make metals useful for a wide variety of applications. The mining, industrial processing and widespread use of metal-containing products has led to a redistribution of metals from geologic deposits to nearly every corner of the globe. While mankind has enjoyed the many benefits of metal applications, this redistribution has led to increased levels of many metals in aquatic, marine, and terrestrial ecosystems throughout the world. Many metals exhibit a high toxicity towards plant and animal life. Metal

ion sorbents are used to remove these toxins from waste streams and contaminated sites. Functionalized nanoporous materials can be designed with the combination of properties needed for the efficient removal of metal ions from aqueous systems.

Liu and co-workers designed a sorbent for mercury by post-synthetic grafting of mercaptopropylsilyl groups on calcined MCM-41. These thiol-functionalized organosilicas were loaded with a high concentration of immobilized ligands by repeated hydrolysis and silylation reactions [14]. Mercier and Pinnavaia used HMS materials as the solid support for similar thiol-functionalized sorbents for Hg(II) recovery [17]. Although the MCM-41 organosilicas exhibited higher mercury loading (505 mg/g) than the HMS materials (310 mg/g), both removed mercury to low enough concentrations to achieve federal drinking water standards. Furthermore, it was demonstrated that all of the thiol groups in both of these functionalized nanoporous adsorbents were accessible for metal ion binding.

While the metal ion adsorbents just described take advantage of the very high affinity of thiols for mercury, their ability to selectively bind other metal ions has not been demonstrated. In other words the selectivity series of these materials for various metal ions is purely dependent on the binding constants of the thiol-metal ion complexes. Since the binding constant of Hg(II) with thiol is many orders of magnitude greater than that of most metal ions these sorbents are very efficient. But this is a special case. Many waste streams and contaminated sites contain mixtures of metal ions with similar affinities for a given ligand and therefore selective adsorption of a particular metal ion is a difficult problem. For example, many areas contaminated with runoff from acid precipitation and mine drainage contain a mixture of metal ions [Cu(II), Ni(II), Zn(II), Pb(II)]. Selective metal ion sorbents are needed to remediate such sites.

In an attempt to develop more selective metal ion sorbents Dai and co-workers have employed a novel imprint coating methodology [31]. Instead of conventional grafting of functional silanes to the surface of nanoporous materials, metal ion complexes were formed prior to the grafting procedure. Removal of the metal ion templates gives materials that contain ligands that are arranged in orientations conducive to rebinding the metal ion template (Fig. 4).

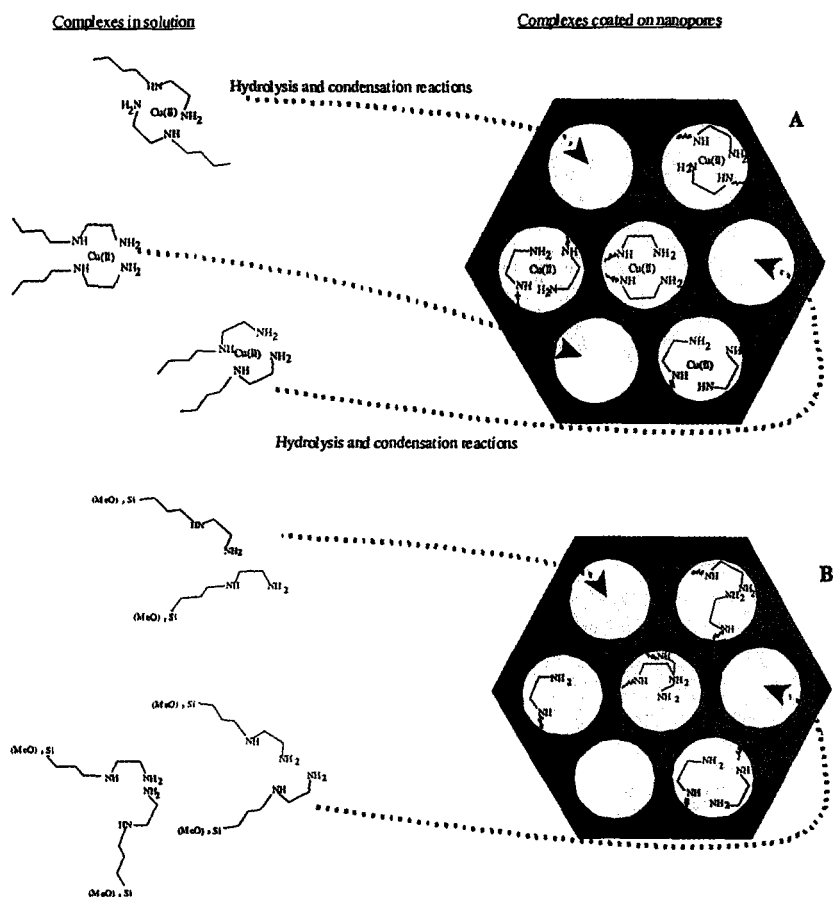


Figure 4. Mechanism of imprint coating (A) and conventional grafting (B).

It was demonstrated that sorbents synthesized by this imprinting approach have a higher affinity for the metal ion template than sorbents made with conventional grafting techniques containing ligands in more random orientations.

While the imprint coating methodology is a post-synthetic grafting technique, selective metal ion sorbents have also been synthesized by complex formation followed by co-condensation [32,33]. These hierarchically imprinted sorbents are made with a dual templating

technique where surfactant supramolecular assemblies form ordered nanopores and ligands create tailored metal ion binding sites. Enhanced distribution coefficients have been demonstrated for Cu(II) adsorption from mixed solutions of metal ions. This methodology has also been used to create a series of selective metal ion sorbents with bifunctional periodic mesoporous organosilicas [34]. Bis(triethoxysilyl)ethane monomers were copolymerized with metal ion complexes of N-(2-aminoethyl)-3-aminopropyl-trimethoxysilane in the presence of supramolecular assemblies of cetyltrimethylammonium chloride. Removal of the surfactant and metal ion templates gave ordered nanoporous sorbents that exhibited selectivity for the templated metal ions. Selective sorbent materials for Ni(II), Cu(II), and Zn(II) were synthesized and characterized. Unprecedented selectivity was demonstrated with an equimolar mixture of Ni(II) and Zn(II) ions. Despite the fact that all sorbents were made with the same precursor, functional silane, and surfactant they sequestered metal ions in much different ways. The Ni(II) imprinted sorbents adsorbed more Ni(II) than Zn(II) and the Zn(II) imprinted sorbents adsorbed more Zn(II) than Ni(II). This clearly illustrates how ligand orientation can be used to create specific coordination environments for selective sorbent materials in order to separate metal ions with similar ligand affinities.

4.2 Adsorption of Anions

Toxic metals such as arsenic and chromium form stable oxyanions in both groundwater and industrial effluents. Liu and co-workers have reported selective oxyanion sorbents by post-synthetic grafting of N-(2-aminoethyl)-3-aminopropyl-trimethoxysilane to nanoporous silica followed by treatment with Cu(II) salt solutions [35]. These sorbents demonstrated selectivity for chromate and arsenate in the presence of competing sulfate anions. Unfortunately, under the acidic conditions normally found where contamination of oxyanions exists the ethylenediamine functional groups become protonated and may release the toxic Cu(II) ions. Yoshitake et al. designed oxyanion sorbents by grafting amines to SBA and MCM nanoporous silicas [36]. The sorbent behavior of these materials was evaluated under acidic conditions. The protonated amines demonstrated efficient adsorption of both chromate and arsenate without the risk of Cu(II) contamination.

4.3 Radionuclide Adsorption

Due to their high toxicity and persistence in the environment the separation and isolation of radionuclides is a top priority for environmental quality. Ju et al. have developed anion sorbents by co-condensation functionalization of nanoporous silica with ammonium, butylammonium, and guanidine-containing functional silanes [37]. These materials exhibited high capacities for anionic thorium complexes in highly acidic media. Furthermore, they showed better selectivity for thorium from mixed solutions of thorium and uranyl ions than commercially available quaternary ammonium anion-exchange resins. Lin et al. have reported the synthesis of nanoporous sorbents for the selective removal of cesium from nuclear wastes and contaminated groundwater [38]. By immobilizing copper ferrocyanide complexes with surface grafted ethylenediamine functional groups selective sequestration of cesium from mixed solutions containing excess sodium or potassium has been demonstrated. Trens and co-workers prepared nanoporous adsorbent materials by grafting of malonamide-type molecules on the surface of MCM-41 [39]. These materials demonstrated high capacities for trivalent americium and europium. Facile regeneration was accomplished by washing with water at pH = 10.

4.4 Adsorption of Organics

The utility of functionalized nanoporous adsorbents for environmental remediation is not limited to metal ion recovery. Several studies have been reported on the adsorption of organic pollutants as well. Inumaru et al. synthesized octylsilane-functionalized nanoporous silica by post-synthetic grafting and demonstrated efficient removal of nonylphenol from water [40]. These materials exhibited nonylphenol capacities higher than conventional activated carbons and selectivity for nonylphenol over phenol. Nanoporous organosilicas with high affinities for phenols have been synthesized by Markowitz and co-workers [41]. Sorbents containing a diethylphenylene bridging functionality demonstrated higher capacities for *p*-nitrophenol, *p*-chlorophenol, and *p*-methyl phenol than an ethylene-bridged periodic mesoporous organosilica. Regeneration of these materials was accomplished by washing with ethanol. No measurable decrease in sorbent performance was detected after ten adsorption-desorption cycles.

A particularly interesting approach to the removal of organic pollutants from water is the use of the nanoscopic composite materials containing surfactant templates. This technique was first reported by

Denoyel and Rey [42] who demonstrated the removal of 3-chlorophenol by nanoscopic MCM-41 composites synthesized with cationic dodecyltrimethylammonium, tetradecyltrimethylammonium, and hexadecyltrimethylammonium surfactant templates. Surprisingly, IR analysis indicated the surfactants did not leach out of the composites until displaced by the chlorophenol molecules at very high equilibrium concentrations. The surfactants with longer chain lengths exhibited higher adsorption capacities at low concentrations of chlorophenol, but pseudo equilibrium values were very similar. Zhao et al. used nanoscopic composites to remove trichloroethylene and tetrachloroethylene from water [43]. The composites exhibited a higher capacity for the pollutants than calcined MCM-41. Structural aluminum was shown to increase the adsorption capacity.

5 Conclusions

We have provided an overview of nanoporous materials with emphasis on techniques for their functionalization and their use as sorbents for environmental pollutants. Recent advances make it possible to create selective sorbents by controlling pore sizes and tailoring the pore chemistries by incorporation of appropriate functional groups. Reviews on the synthesis and characterization of ordered nanoporous materials have been published recently [44, 45, 46]. Due to their many favorable properties functionalized nanoporous materials are having a significant impact in the field of adsorbent technology for environmental remediation.

6 Acknowledgements

The authors wish to thank Dr. David Beach, Dr. Michael Markowitz, and Dr. Bruce Gaber for many helpful discussions. We would also like to thank the Office of Naval Research for the support through a Naval Research Laboratory Accelerated Research Initiative and the Office of Basic Energy Sciences, U.S. Department of Energy for the support through the Oak Ridge National Laboratory under Contract DE-AC05-00OR22725 with UT-Battelle, LLC.

References

1. Kresge C. T., Leonowicz M. E., Roth W. J., Vartuli J. C. and Beck J. S., Ordered mesoporous molecular sieves synthesized by a liquid crystal template mechanism, *Nature* **359** (1992) pp. 710-712.
2. Beck J. S., Vartuli J. C., Roth W. J., Leonowicz M. E., Kresge C. T., Schmitt K. D., Chu C. T., Olsen D. H., Sheppard E. W., McCullen S. B., Higgins J. B. and Schlenker J. L., A new family of mesoporous molecular sieves prepared with liquid crystal templates, *J. Am. Chem. Soc.* **114** (1992) pp. 10834-10843.
3. Vartuli J. C., Schmitt K. D., Kresge C. T., Roth W. J., Leonowicz, M. E., McCullen S. B., Hellring S. D., Beck J. S., Schlenker J. L., Olsen D. H. and Sheppard E. W., Effect of surfactant/silica molar ratios on the formation of mesoporous molecular sieves: inorganic mimicry of surfactant liquid-crystal phases and mechanistic implications, *Chem. Mater.* **6** (1994) pp. 2317-2326.
4. Vartuli J. C., Kresge C. T., Leonowicz M. E., Chu A. S., McCullen S. B., Johnson I. D. and Sheppard E. W., Synthesis of mesoporous materials: liquid-crystal templating versus intercalation of layered silicates, *Chem. Mater.* **6** (1994) pp. 2070-2077.
5. Beck J. S., Vartuli J. C., Kennedy G. J., Kresge C. T., Roth W. J. and Schramm S. E., Molecular or supramolecular templating: defining the role of surfactant chemistry in the formation of microporous and mesoporous molecular sieves, *Chem. Mater.* **6** (1994) pp. 1816-1821.
6. Huo Q. S., Margolese D. I., Ciesla U., Feng P. Y., Gier T. E., Sieger P., Leon R., Petroff P. M., Schuth F. and Stucky G. D., Generalized synthesis of periodic surfactant inorganic composite-materials, *Nature* **368** (1994) pp. 317-321.
7. Tanev P. T. and Pinnavaia T. J., A neutral templating route to mesoporous molecular sieves, *Science* **267** (1995) pp. 865-867.
8. Tanev P. T. and Pinnavaia T. J., Mesoporous molecular sieves prepared by ionic and neutral surfactant templating: a comparison of physical properties, *Chem. Mater.* **8** (1996) pp. 2068-2079.
9. Zhao D., Huo Q. S., Feng J., Chmelka B. F. and Stucky G. D., Nonionic triblock and star diblock copolymer and oligomeric surfactant syntheses of highly ordered, hydrothermally stable, mesoporous silica structures, *J. Am. Chem. Soc.* **120** (1998) pp. 6024-6036.
10. Yang P. D., Zhao D. Y., Margolese D. I., Chmelka B. F. and Stucky G. D., Block copolymer templating syntheses of mesoporous metal oxides with large ordering lengths and semicrystalline framework, *Chem. Mater.* **11** (1999) pp. 2813-2826.
11. Yanagisawa T., Shimizu T., Kuroda K. and Kato C., The preparation of alkyltrimethylammonium-kanemite complexes and their conversion to mesoporous materials, *Bull. Chem. Soc. Jpn.* **63** (1990) pp. 988-991.
12. Bagshaw S. A., Prouzet E. and Pinnavaia T. J., Templating of mesoporous molecular-sieves by nonionic polyethylene oxide surfactants, *Science* **269** pp. 1242-1244.
13. Ryoo R., Kim J. M., Ko C. H. and Shin C. H., Disordered molecular sieve with branched mesoporous channel network, *J. Phys. Chem.* **100** (1996) pp. 17718-17721.
14. Feng X., Fryxell G. E., Wang L. Q., Kim A. Y., Liu J. and Kemner K. M., Functionalized monolayers on ordered mesoporous supports, *Science* **276** (1997) pp. 923-926.

15. Diaz J. F., Balkus K. J., Bedioui F., Kurshev V. and Kevan L., Synthesis and characterization of cobalt-complex functionalized MCM-41, *Chem. Mater.* **9** (1997) pp. 61-67.
16. Lim M. H. and Stein A., Comparative studies of grafting and direct syntheses of inorganic-organic hybrid mesoporous materials, *Chem. Mater.* **11** (1999) pp. 3285-3295.
17. Mercier L. and Pinnavaia T. J., Heavy metal ion adsorbents formed by the grafting of a thiol functionality to mesoporous silica molecular sieves: Factors affecting Hg(II) uptake, *Environ. Sci. Technol.* **32** (1998) pp. 2749-2754.
18. Dai S., Shin Y. S., Ju Y. H., Burleigh M. C., Lin J. S., Barnes C. E. and Xue Z. L., A new methodology to functionalize surfaces of ordered mesoporous materials based on ion exchange reactions, *Adv. Mater.* **11** (1999) pp. 1226-1230.
19. Burkett S. L., Sims S. D. and Mann S., Synthesis of hybrid inorganic-organic mesoporous silica by co-condensation of siloxane and organosiloxane precursors, *J. Chem. Soc., Chem. Commun.* (1996) pp. 1367-1368.
20. Fowler C. E., Burkett S. L. and Mann S., Synthesis and characterization of ordered organo-silica-surfactant mesophases with functionalized MCM-41-type architecture, *J. Chem. Soc., Chem. Commun.* (1997) pp. 1769-1770.
21. Hall S. R., Fowler C. E., Lebeau B. and Mann S., Template-directed synthesis of bi-functionalized organo-MCM-41 and phenyl-MCM-48 silica mesophases, *J. Chem. Soc., Chem. Commun.* (1999) pp. 201-202.
22. Macquarrie D. J., Direct preparation of organically modified MCM-type materials. Preparation and characterisation of aminopropyl-MCM and 2-cyanoethyl-MCM, *J. Chem. Soc., Chem. Commun.* (1996) pp. 1961-1962.
23. Mercier L. and Pinnavaia T. J., Direct synthesis of hybrid organic-inorganic nanoporous silica by a neutral amine assembly route: Structure-function control by stoichiometric incorporation of organosiloxane molecules, *Chem. Mater.* **12** (2000) pp. 188-196.
24. Margolese D., Melero J. A., Christiansen S. C., Chmelka B. F. and Stucky G. D., Direct syntheses of ordered SBA-15 mesoporous silica containing sulfonic acid groups, *Chem. Mater.* **12** (2000) pp. 2448-2459.
25. Inagaki S., Guan S., Fukushima Y., Ohsuna T. and Terasaki O., Novel mesoporous materials with a uniform distribution of organic groups and inorganic oxide in their frameworks, *J. Am. Chem. Soc.* **121** (1999), 9611-9614.
26. Yoshina-Ishii C., Asefa T., Coombs N., MacLachlan M. J. and Ozin G. A., Periodic mesoporous organosilicas, PMOs: fusion of organic and inorganic chemistry 'inside' the channel walls of hexagonal mesoporous silica, *J. Chem. Soc., Chem. Commun.* (1999) pp. 2539-2540.
27. Burleigh M. C., Markowitz M. A., Spector M. S. and Gaber B. P., Unpublished results. Base catalyzed polymerization of bis[3-(trimethoxysilyl)propyl]-ethylenediamine has been achieved with CTAC as the surfactant template. Nitrogen gas adsorption analyses of the surfactant-extracted product gave a calculated BET surface area of only 30 m²/g. No peaks were resolved in the powder XRD pattern.
28. Asefa T., Kruk M., MacLachlan M. J., Coombs N., Grondey H., Jaroniec M. and Ozin G. A., Novel bifunctional periodic mesoporous organosilicas, BPMOs: Synthesis, characterization, properties and in-situ selective hydroboration-alcoholysis reactions of functional groups, *J. Am. Chem. Soc.* **123** (2001) pp. 8520-8530.
29. Burleigh M. C., Markowitz M. A., Spector M. S. and Gaber B. P., Direct synthesis of periodic mesoporous organosilicas: Functional incorporation by co-condensation with organosilanes, *J. Phys. Chem. B* **105** (2001) pp. 9935-9942.

30. Burleigh M. C., Markowitz M. A., Spector M. S. and Gaber B. P., Amine-functionalized periodic mesoporous organosilicas, *Chem. Mater.* **13** (2001) pp. 4760-4766.
31. Dai S., Burleigh M. C., Shin Y., Morrow C. C., Barnes C. E. and Xue Z. L., Imprint coating: A novel synthesis of selective functionalized ordered mesoporous sorbents., *Angew. Chem. Int. Ed. Engl.* **38** (1999) pp. 1235-1239.
32. Dai S., Burleigh M. C., Ju Y. H., Gao H. J., Lin J. S., Pennycook S. J., Barnes C. E. and Xue Z. L., Hierarchically imprinted sorbents for the separation of metal ions, *J. Am. Chem. Soc.* **122** (2000) pp. 992-993.
33. Dai S., Hierarchically imprinted sorbents, *Chem. Eur. J.* **7** (2001) pp. 763-768.
34. Burleigh M. C., Dai S., Hagaman E. W. and Lin J. S., Imprinted polysilsesquioxanes for the enhanced recognition of metal ions, *Chem. Mater.* **13** (2001) pp. 2537-2546.
35. Fryxell G. E., Liu J., Hauser T. A., Nie Z. M., Ferris K. F., Mattigod S., Gong M. L. and Hallen R. T., Design and synthesis of selective mesoporous anion traps, *Chem. Mater.* **11** (1999) pp. 2148-2154.
36. Yoshitake H., Yokoi T. and Tatsumi T., Adsorption of chromate and arsenate by amino-functionalized MCM-41 and SBA-1, *Chem. Mater.* **14** (2002) pp. 4603-4610.
37. Ju Y. H., Webb O.F., Dai S., Lin J. S. and Barnes C. E., Synthesis and characterization of ordered mesoporous anion-exchange inorganic/organic hybrid resins for radionuclide separation, *Ind. Eng. Chem. Res.* **39** (2000) pp. 550-553.
38. Lin Y. H., Fryxell G. E., Wu H. and Engelhard M., Selective sorption of cesium using self-assembled monolayers on mesoporous supports, *Environ. Sci. Technol.* **35** (2001) pp. 3962-3966.
39. Trems P., Russell M. L., Spjuth L., Hudson M. J. and Liljenzin J. O., Preparation of malonamide-MCM-41 materials for the heterogeneous extraction of radionuclides, *Ind. Eng. Chem. Res.* **41** (2002) pp. 5220-5225.
40. Inumaru K., Kiyoto J. and Yamanaka S., Molecular selective adsorption of nonylphenol in aqueous solution by organo-functionalized mesoporous silica, *J. Chem. Soc., Chem. Commun.* (2000) pp. 903-904.
41. Burleigh M. C., Markowitz M. A., Spector M. S. and Gaber B. P., Porous polysilsesquioxanes for the adsorption of phenols, *Environ. Sci. Technol.* **36** (2002) pp. 2515-2518.
42. Denoyel R. and Rey E. S., Solubilization in confined surfactant mesophases, *Langmuir* **14** (1998) pp. 7321-7323.
43. Zhao H. T., Nagy K. L., Waples J. S. and Vance G. F., Surfactant-templated mesoporous silicate materials as sorbents for organic pollutants in water, *Environ. Sci. Technol.* **34** (2000) pp. 4822-4827.
44. Selvam P., Bhatia S. K. and Sonwane C. G., Recent advances in processing and characterization of periodic mesoporous MCM-41 silicate molecular sieves, *Ind. Eng. Chem. Res.* **40** (2001) pp. 3237-3261.
45. Stein A., Melde B. J. and Schrodin R. C., Hybrid inorganic-organic mesoporous silicates - Nanoscopic reactors coming of age, *Adv. Mater.* **12** (2000) pp. 1403-1419.
46. Sayari A. and Hamoudi S., Periodic mesoporous silica-based organic - Inorganic nanocomposite materials, *Chem. Mater.* **13** (2001) pp. 3151-3168.

NANOPOROUS ADSORBENTS FOR AIR POLLUTANT REMOVAL

P. LE CLOIREC

*Ecole des Mines de Nantes, GEPEA UMR CNRS 6144, 4 rue Alfred Kastler,
BP 20722, 44307 Nantes cedex 03, France
E-mail: Pierre.Le-Cloirec@emn.fr*

Nanoporous material is commonly used for air treatments. Activated carbon, alumina, zeolites and resins are often chosen to remove pollutants present in gaseous emissions. This chapter presents a global approach to the purification of air by adsorbents. First, mechanisms and adsorption modeling are explained in order to provide good understanding of adsorption applied to air treatments. Adsorption parameters are given for a large range of pollutants found in industrial or domestic emissions. Secondly, examples of industrial filters packed with adsorbents are presented with their operating conditions. Then, the regeneration of adsorbents involving different ways of heating is described.

1 Introduction

Among the technologies useful for air treatment, the processes involving transfer phenomena and interactions of a pollutant present in gaseous phase with a solid surface are widely used. They may be applied to both water and air purification [1-7]. Thus, these adsorption systems can remove a large number of molecules and especially volatile organic compounds (VOC), odorous molecules or dioxins and furanes. The applications are possible for a high concentration of pollutant (g m^{-3}) to diluted air (some mg or $\mu\text{g m}^{-3}$). The adsorption processes are carried out for the treatment of industrial or domestic emissions. The installation design caters for airflow between some 1 to $100\,000\text{ m}^3\text{ h}^{-1}$.

The objective of this chapter is to present theoretical and practical approaches of air treatments by adsorption processes with emphasis on the following points:

- mechanisms and the transfers
- adsorbents used in air treatments
- processes carried out in different applications
- desorption and regeneration of saturated adsorbents

2 Mechanism approaches

2.1 Gas-solid transfer

Due to component concentration gradients (Fick's law) between a gaseous phase and a solid, molecules diffuse and tend to accumulate as a surface layer until the balance of surface forces is reached. The adsorption mechanisms, corresponding to solute transfer from air to solid and to interactions between molecules and the surface, are described by several steps that are schematically presented in Figure 1 [5][8].

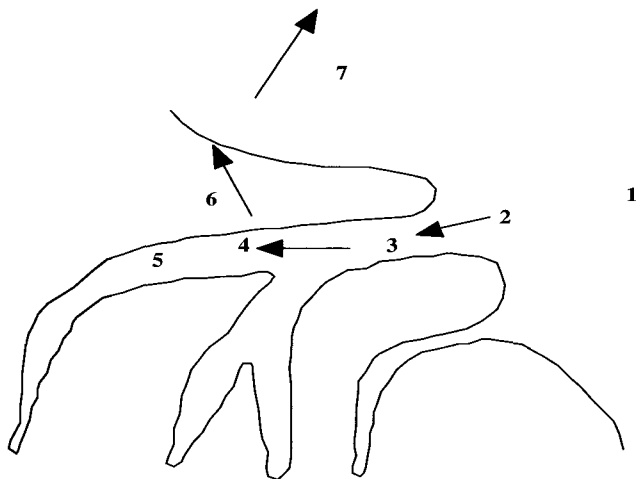


Figure 1. Schematic representation of adsorption onto a porous material.

1. Bulk diffusion. The molecules present in air diffuse to the external surface of the porous material. An agitated vessel minimizes the concentration gradient in the reactor and gives homogeneous gas in contact with the solid.
2. External mass transfer. The mass transfer occurs through the high concentration layer around the adsorbent. The layer thickness is a function of the turbulence in the system.
3. Diffusion in the porous volume. The diffusion coefficient evolution is a function of the pore diameter. The diffusivity is close to that found in a liquid for macropores while the values are smaller for micropores. In this case, depending on the diameter ratio between solute and pore size, Knudsen diffusion is found [9].
4. Adsorption. The molecule interacts very quickly with the solid surface and produces an exothermic reaction. The reaction energies are in the

range of 5 to 60 kJ mol⁻¹ depending on the compound molecular properties and the adsorbent structure [40].

5. **Slow surface diffusion.** After adsorption, the molecules diffuse on the adsorbent surface. In this case, the diffusivity is very low: about 10 000 times lower than the pore diffusion coefficient. This transfer limits the global kinetics of adsorption. This mechanism is important for solute adsorption in aqueous phase but seems to be negligible in gaseous phase.

6. **Thermal conduction inside the porous material.** Due to the adsorption reaction, heat is conducted through the solid to the solution.

7. **Thermal conduction through the gaseous phase.** Air has a very low volumetric thermal capacity compared to water, thus a temperature rise occurs. This phenomenon is found for adsorption of volatile organic compound where a significant effect is noted (see section 4.4.3.) [10-12].

2.2 Adsorption in a batch reactor

2.2.1 Mass balance

Consider a volume of air loaded with a molecule (A) which is in contact with a mass of adsorbent. The system is continuously stirred for a time. Assuming there is no chemical or biological reaction but only a mass transfer from the gas phase to the solid surface, the mass balance can be written:

$$m(q_t - q_0) = V(C_0 - C_t) \quad (1)$$

where

m	:	mass of adsorbent (g)
q_t	:	concentration of the solute on the solid at time t (mg g ⁻¹)
q_0	:	concentration of the solute on the solid at $t = 0$ (mg g ⁻¹) for a virgin adsorbent $q_0 = 0$
V	:	volume of the solution (L)
C_0	:	initial concentration in the solution (mg L ⁻¹)
C_t	:	concentration at time t in the solution (mg L ⁻¹)

2.2.2 Kinetics

Consider the same situation as above. A new adsorbent is used and the experiment is performed at constant temperature. The concentration of the pollutant (A) is analyzed as a function of time. A kinetic curve is obtained for the molecule being removed from the air as given in Figure 2.

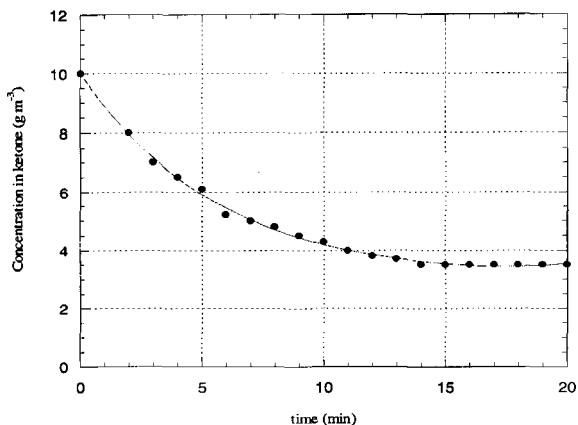


Figure 2. Acetone adsorption onto activated carbon grains (NC60) in a batch reactor ($V = 1$ L, $T = 20 \pm 1^\circ\text{C}$).

The Adams Bohart Thomas theory assumes that the adsorption is an equilibrated reaction between a solute (A) and a surface (σ) following the equation:



The authors have proposed a relation to model the evolution of the amount adsorbed:

$$\frac{dq}{dt} = k_1 C (q_m - q) - k_2 q \quad (3)$$

where

- k_1 : adsorption kinetic coefficient ($\text{L mg}^{-1}\text{h}^{-1}$)
- k_2 : desorption kinetic coefficient (h^{-1})
- q_m : maximal adsorption capacity (mg g^{-1})
- C : concentration in solution (mg L^{-1})
- q : adsorption capacity (mg g^{-1})

For $t \rightarrow 0$, $C \rightarrow C_0$ and $q \rightarrow 0$

Then, the previous kinetic relation (3) becomes:

$$\left(\frac{dq}{dt} \right)_{t \rightarrow 0} = k_1 C_0 q_m \quad (4)$$

i.e. a straight line equation corresponding to the initial velocity coefficient. For all organic pollutants, the initial adsorption coefficient on activated carbon fibers (ACF) is higher than on granular activated carbon (GAC) with a ratio from 4 to 20.

2.2.3 Equilibrium

2.2.3.1 Langmuir equation

Another specific zone of the kinetic curve is in the region $t \rightarrow \infty$.

where $\frac{dq}{dt} = 0$ $C \rightarrow C_e$ and $q \rightarrow q_e$

Equation (3) becomes:

$$k_1 C_e (q_m - q_e) = k_2 q_e \quad (5)$$

or

$$q_e = \frac{b q_m C_e}{1 + b C_e} \quad (6)$$

with $b = \frac{k_1}{k_2}$ is equilibrium constant and $\theta = \frac{q_e}{q_m}$ is the fraction of surface coverage.

This relation is applied to adsorption on a completely homogeneous surface with negligible interactions between adsorbed molecules.

From an experimental data set (C_e, q_e) , the constant b and q_m are determined by plotting $1/q_e$ vs. $1/C_e$. The straight-line slope is $1/bq_m$, and the intercept is $1/q_m$. Examples for activated carbon grains (NC60) are given in Table 1. An illustration of the application of the Langmuir equation to adsorption isotherm curves is presented in Figure 3.

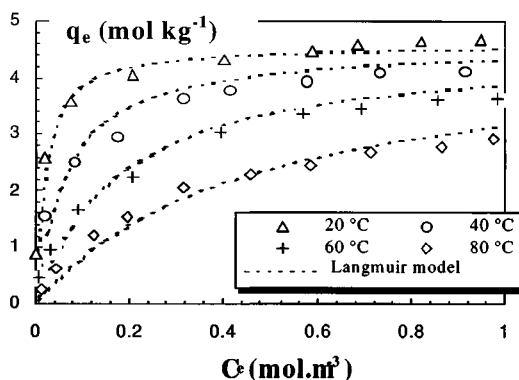


Figure 3. Adsorption isotherm curves of toluene on activated carbon (Pica NC60) - Comparison between experimental data and the Langmuir model.

Table 1. Langmuir equation parameters for some VOC adsorbed onto activated carbon grains (NC60) at $T = 20 \pm 1^\circ\text{C}$.

Compound	q_m (mol.kg ⁻¹)	b (m ³ .mol ⁻¹)	R^2
Acetone	5.92	$2.28.10^{-5}$	0.976
1,2-Dichloroethane	5.32	$1.63.10^{-7}$	0.942
Ethanol	8.46	$5.98.10^{-5}$	0.963
Ethyl acetate	4.41	$1.36.10^{-9}$	0.938
Methylethylketone	5.06	$1.27.10^{-6}$	0.931
Methylethyldioxolane	3.58	$2.79.10^{-7}$	0.945
Toluene	4.60	$4.06.10^{-7}$	0.980

2.2.3.2 Freundlich equation

The empirical Freundlich isotherm has been proposed to fit the adsorption data:

$$q_e = K_F C_e^{1/n} \quad (7)$$

where K_F and $1/n$ are constants and depend on the solute – adsorbent couple and temperature. If $1/n < 1$, adsorption is favorable. On the contrary, if $1/n > 1$, adsorption is unfavorable. This relation could correspond to an exponential distribution of adsorption heat. However, the form of the equation shows that there is no limit for q_e as C_e increases? which is physically impossible. This means that the Freundlich equation is useful for low C_e values.

Taking the logarithms of both sides of equation (7) gives:

$$\ln(q_e) = \ln(K_F) + \frac{1}{n} \ln(C_e)$$

From the straight line $\ln(q_e)$ vs. $\ln(C_e)$, one obtains the slope $1/n$ and the intercept $\ln(K_F)$. Table 2 gives a set of Freundlich equation parameters for some organics present in air adsorbed onto activated carbon grains or fibers.

Table 2. Parameters of the Freundlich equation for two kinds of activated carbon.

	Activated carbon grains		Activated carbon fibers	
	k (mg ^{1-1/n} m ^{3/n} g ⁻¹)	1/n	k (mg ^{1-1/n} m ^{3/n} g ⁻¹)	1/n
Acetone	587	0.45	37	0.374
Benzene	250	0.20	283	0.147
Carbon disulfide			139	0.206
Chloroform			315	0.202
1,2-dichloroethane	1198	0.32		
Dichloromethane	900	0.53	138	0.320
Ethyl acetate	696	0.19	253	0.187
Isopropanol	661	0.26		
Ethanol			184	0.254
Methanol	630	1.00	255	0.161
Methyl ethyl Ketone	663	0.24		
Tetrachloroethylene	700	0.175	679	0.216
Toluene	298	0.09	298	0.143
Trichloroethylene			427	0.141

Several authors HAVE tried to correlate the Freundlich parameters (K_F , $1/n$) with the molecular structure of the solute through quantitative structure activity relationships (QSAR). Classical multiple linear regressions were used to find equations between K_F or $1/n$ and molecular connectivity indexes or linear solvation energy parameters [13-15]. Original statistical tools like neural networks were also used for different adsorption data sets. Good agreements were found between calculated and experimental values [14,40].

2.2.3.3 Polanyi-Dubinin equation

Based on the Polanyi potential theory, Dubinin and Raduskevich or Dubinin and Asthakov proposed an adsorption equation giving a relation between the volume of solute adsorbed and the adsorption potential [4][16]. The latter is defined as the free-energy change required to move a molecule from the bulk solution to the adsorption space:

$$W = W_0 \exp \left[- \left(\frac{\xi}{E} \right)^b \right] \quad (8)$$

where

$$\xi = -RT \ln \left(\frac{P_s}{P_e} \right) \quad (9)$$

and

$$W = \frac{q_e}{\rho_l} \quad W_0 = \frac{q_m}{\rho_l} \quad (10)$$

b	:	constant ($1.5 < b < 3$)
P_e	:	pressure at equilibrium (Pa)
P_s	:	saturated vapor pressure (Pa)
E	:	adsorption energy (J mg^{-1} or J mol^{-1})
q_e	:	adsorption capacity at equilibrium (mg g^{-1})
q_m	:	maximal adsorption capacity (mg g^{-1})
R	:	ideal gas constant ($R = 8.32$ in IS unit)
T	:	temperature (K)
W	:	volume adsorbed per mass of adsorbent ($\text{cm}^3 \text{g}^{-1}$)
W_0	:	maximum volume adsorbed per mass of adsorbent ($\text{cm}^3 \text{g}^{-1}$)
ξ	:	adsorption potential (J mg^{-1} or J mol^{-1})
ρ_l	:	liquid pure compound density (g mL^{-1} or mol mL^{-1})

An application of such equations produces parameters, which are given in the Table 3. An illustration of the application of the Dubinin-Radushkevich equation ($b = 2$) to adsorption isotherm curves is presented in Figure 4.

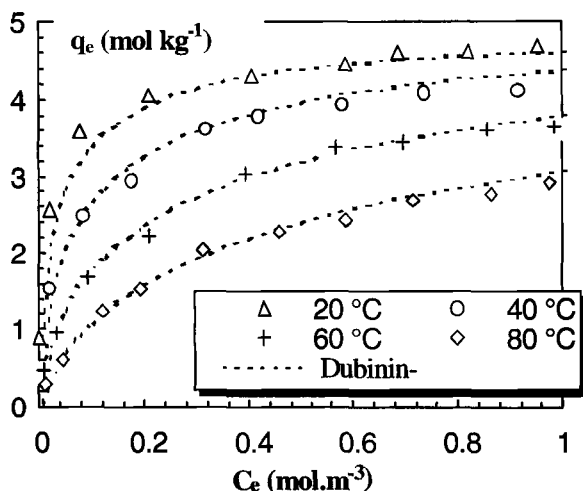


Figure 4. Adsorption isotherm curves of toluene on activated carbon (Pica NC60) - Comparison between experimental data and THE Dubini-Raduskevich model.

Table 3. Dubinin-Radushkevich equation parameters for some volatile organic compounds adsorbed on microporous activated carbon.

Compound	W_0 ($\text{cm}^3 \cdot \text{g}^{-1}$)	E ($\text{kJ} \cdot \text{mol}^{-1}$)	Correlation coefficient
Acetone	0.454	15.4	0.954
1,2-Dichloroethane	0.514	18.9	0.969
Ethanol	0.506	13.1	0.943
Ethyl acetate	0.482	15.8	0.974
Methylethylcetone	0.508	16.9	0.992
Methylethyldioxolane	0.425	12.4	0.978
Toluene	0.511	13.3	0.986

2.2.3.4 Other equilibrium equations

Tien [4] mentions various expressions that can be used to describe adsorption isotherms (concentration C could be replaced by pressure P):

- The linear isotherm

$$q_e = KC_e \quad (11)$$

- The Toth isotherm

$$q_e = \frac{q_m C_e}{(b' + C_e^t)^{1/t}} \quad (12)$$

- The Langmuir-Freundlich isotherm

$$q_e = \frac{b q_m C_e^{1/n}}{1 + b C_e^{1/n}} \quad (13)$$

- The BET isotherm

$$q_e = \frac{q_m \frac{C_e}{C_s}}{\left(1 - \frac{C_e}{C_s}\right) \left[1 + (\alpha - 1) \frac{C_e}{C_s}\right]} \quad (14)$$

Where

- b, b', t : equation parameters
- C_e : gas phase concentration at equilibrium (mg L^{-1} or mol L^{-1})
- C_s : saturation concentration of the compound (mg L^{-1})
- q_e : adsorption capacity at equilibrium (mg g^{-1} or mol g^{-1})
- q_m : maximal adsorption capacity (mg g^{-1} or mol g^{-1})
- α : equation parameter

2.3 Multi-component adsorption

In some cases, gaseous emissions are complex mixtures of solutes. Thus, with several species present in air, mechanisms and theoretical approaches are required to predict and estimate multi-component adsorption equilibria from pure component isotherm data. Several theories and equations have been proposed introducing the adsorption competition between the different adsorbates.

2.3.1 Mass balance

Considering a similar experimental approach to that for a pure component system, the mass balance can be written for a solute i in solution with N compounds ($1 \leq i \leq N$):

$$m(q_i(t) - q_{i0}) = V[C_{i0} - C_i(t)] \quad (15)$$

where

C_{i0}	:	initial concentration of the solute i in the solution (mg L^{-1})
$C_i(t)$:	concentration of solute i at time t in the solution (mg L^{-1})
m	:	mass or amount of adsorbent (g)
$q_i(t)$:	concentration of the solute i on the solid at time t (mg g^{-1})
q_{i0}	:	concentration of the solute on the solid at $t = 0$ (mg g^{-1}) for a virgin adsorbent $q_{i0} = 0$
V	:	volume of reactor

2.3.2 Extended Langmuir equation

Analogous to the Langmuir equation written for a pure component, an expression is generalized for multi - component adsorption isotherms:

$$q_i = \frac{b_i q_{mi} C_i}{1 + \sum_{j=1}^N b_j C_j} \quad (16)$$

b_i are q_{mi} are the single component adsorption isotherm parameters of the i^{th} adsorbate.

C_i	:	concentration of the solute i in the solution (mg L^{-1})
C_j	:	concentration of solute j in the solution (mg L^{-1})

2.3.3 Ideal adsorbed solution (IAS) theory

The IAS theory was established for gas mixtures and then extended to liquids and especially water. Tien [4] describes the thermodynamic principles for this theory, the equation set and the procedures to apply for adsorption calculations:

$$C_i = C_i^0 x_i \quad (17)$$

$$\frac{\pi_i A}{RT} = \int_b^{C_i^0} \frac{q_i^0}{C_i^0} dC_i^0 \quad (18)$$

$$q_t = \left[\sum_{i=1}^N \frac{x_i}{q_i^0} \right]^{-1} \quad (19)$$

$$q_i = q_t x_i \quad (20)$$

where

- C_i^0 : concentration of the i^{th} adsorbate in the solution being the only solute (mg L^{-1})
- q_i^0 : concentration of the i^{th} adsorbate in the adsorbed phase for a pure component solution (mg g^{-1})
- q_t : total amount of mole adsorbed on the solid (mg g^{-1})
- x_i : mole fraction of adsorbate in adsorbed phase $\left(\sum_{i=1}^N x_i \right)$
- π_i : spreading pressure of the i^{th} solute (Pa)
- R : gas law constant ($R = 8.32$ in IS units)
- T : temperature (K)

We have to note that it is difficult to apply this model to a very complex gaseous phase containing a large set of molecules. However, IAS equations have produced good results in agreement with experimental data for mixtures with 2 or 3 organics present in air [4].

2.4 Factors affecting adsorption

2.4.1 Specific surface area and pore diameter

In a first approach, the adsorption capacity of a molecule onto a porous medium is proportional to the adsorbent surface area. A microporous

material, with a pore diameter less than 2 nm, is generally used for air treatment. Mechanically, the pore diameter has to be much greater than the molecule size to get a quick diffusion inside the porous volume in order to reach the adsorption sites.

2.4.2 Pollutant structure

The transfer and the adsorption is strongly influenced by the size of the compound (surface and volume) and by the functional groups present in the molecule (alcohols, aldehydes, ketones, carboxylic acids, amines, mercaptans, halogenated molecule) inducing some polarization effects. Some studies have been reported finding a quantitative structure property relationship (QSPR) between molecular structure and adsorption parameters (adsorption capacities and energies) [14,17,40]. The reactivity of some compounds gives oxidations at the adsorbent surface, which play a catalytic role. A mixture of molecules in air gives an adsorption competition between the different molecules and then reduces the adsorption capacity of the molecule alone.

2.4.3 Humidity and temperature

The influence of air moisture is like a competition between water molecules and adsorbate. Activated carbon is generally useful at room temperature until a relative humidity of about 70 – 80 % for pollutant concentrations ranging from 1 to 1 000 mg m⁻³. However, the most important parameter is the ratio of molecule and water concentration. That is to say, a high humidity will be harmful for removing solvent traces. In contrast, it will have no effect on the removal of solvent at high concentration.

Due to the exothermal reactions, the temperature influences the adsorption. It is less efficient at high temperature thus an adsorption at low temperature is recommended (less than 40 °C).

2.5 Adsorption – desorption energies

The molecule-solid interaction energy is an important parameter for adsorption but also in terms of desorption and regeneration of the saturated porous material. These values are determined by different calorimetric analyses [10-12,18-20,40]. Some useful data are presented in Table 4 for calculating the adsorption exothermal heat or the energy needed to be introduced into the system in order to regenerate the porous media.

Table 4. Adsorption-desorption energies of VOC in a microporous activated carbon obtained by differential scanning calorimetry [40].

Volatile organic compound	Adsorption Energy $-\Delta H_{\text{ads}}^{\text{int}}$ (kJ.mol ⁻¹)	Desorption Energy $\Delta H_{\text{dés}}$ (kJ.mol ⁻¹)
Acetaldehyde	48.5	52.6
Acetone	50.6	55.2
Butylamine	74.9	85.6
Chloroform	50.5	56.3
Cyclohexane	55.4	65.1
Dichloromethane	48.6	53.2
Ethanol	48.6	54.7
Ethyl acetate	61.2	70.4
Formaldehyde	42.3	49.3
Heptane	72.9	70.4
Hexane	61.4	78.7
Isopropyl acetate	68.5	78.7
Isopropyl ether	62.2	70.5
Methanol	40.8	85.6
Methylethylketone	56.2	65.5
Methylethyldioxolane	70.9	56.3
Methylisobutylketone	67.6	68.5
Pentane	57.9	73.2
Propanol	50.0	60.1
Tetrachloroethylene	70.2	67.3
Toluene	63.1	71.4
Trichloroethylene	65.6	54.7
Triethylamine	81.9	70.5

2.6 Some specific cases

2.6.1 Ketones

Akubuiro and Wagner [21] [22] proposed ketone oxidation mechanisms at the surface of an activated carbon. Ketones are oxidized to produce peroxides which are very unstable and are decomposed in strong exothermal reactions. These by-products give carboxylic acids, aldehydes

and/or diketones. An example of the reaction pathways is proposed in Figure 5.

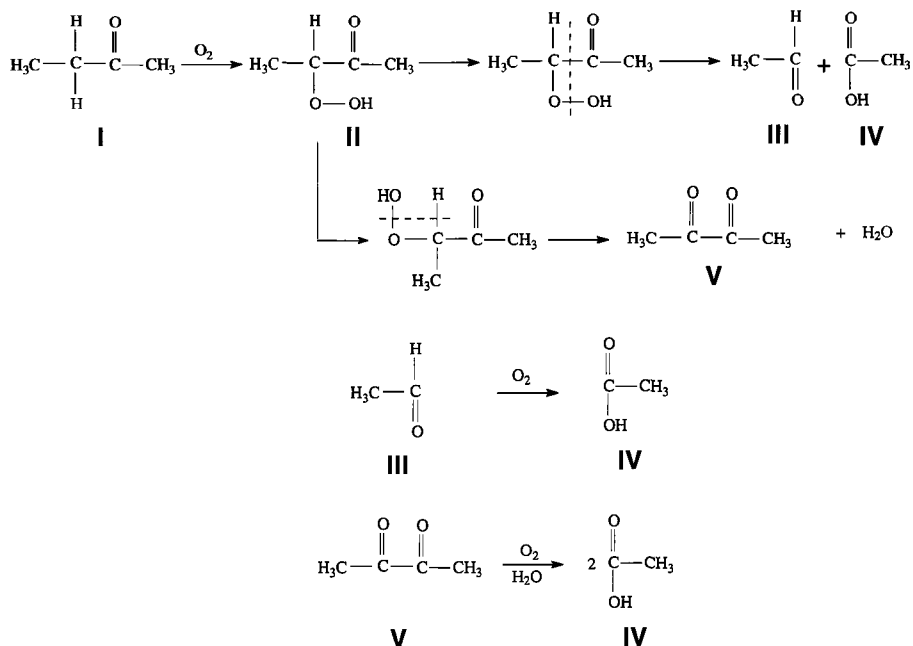


Figure 5. Probable oxidation mechanisms of methyl ethyl ketone [21].

2.6.2 Hydrogen sulfide and ammonia

Hydrogen sulfide, always found in odorous gaseous emissions, is removed by physisorption on activated carbons with an adsorption capacity less than 3 % [23]. An oxidation reaction generally occurs, with oxygen of the air at room temperature catalyzed by the surface of the medium:



Hydrogen sulfide is transformed into sulfur, which stays on the porous structure. In the case of wastewater treatment plant emissions, the amount of sulfur removed by adsorption and oxidation is about 900 mg/g. Activated carbon does not seem to be a good adsorbent of ammonia present in air. Thus, in order to increase the adsorption capacities of such a material an impregnation with metal or metal oxides is performed. Iron or copper on activated carbons are commonly used.

3 Some adsorbents used in air treatments

Adsorbents used for air treatments are generally microporous solids like activated carbon, zeolites or resins. They are used in the form of powders, grains, cloths, felts, extrudates or pellets, and in a size consistent with the applications being considered.

3.1 Activated carbons

Activated carbon is the most widely used adsorbent in the world. Its production rate ranges between 400 000 and 500 000 t yr⁻¹. It is obtained from carbonaceous substances, which are converted into porous materials through carbonization and activation steps. The final properties of carbon depend on the original material and the specific manufacturing process [16,23,24].

Table 5. Some characteristics of activated carbons used in air treatments.

Parameter	Unit	Symbol	Data range
Origin			Coconut, wood, peat, coal, bituminous coal
Size	mm	d_g	
- Powder			0.1 – 0.5
- Grains			0.5 – 5
- Fibers, cloth, felt			0.01
External porosity	-	ϵ	0.3 – 0.5
Bulk density	kg m ⁻³	ρ_a	
- Coconut, Coal			500 - 600
- Wood			250 - 350
Particle density	kg m ⁻³	ρ_p	700 - 1000
Real density	kg m ⁻³	ρ_r	2000 - 2500
Pore diameter	nm	–	
- Macropores			> 50
- Mesopores			2 < d < 50
- Micropores			< 2
Pore volume	cm ³ g ⁻¹	–	0.3 – 0.7
Specific surface area	m ² g ⁻¹	S_{BET}	
- non-activated			2 - 20
- activated			500 - 2000
Ash	wt. %	–	3 - 10
Moisture	wt. %	–	3 - 30
Acid soluble	wt. %		0.5 - 1
Water soluble	wt. %		0.1 – 0.5
Hardness	wt. % (weight)	–	65 – 80
Surface functional groups (acidic or basic functions)	meq g ⁻¹		0.5 - 5

3.2 Zeolites

The basic unit of a zeolitic structure is a TO_4 tetrahedron, where T is a Si or Al atom/ion. The general formula is $\text{M}_{x/n}[(\text{AlO}_2)_x(\text{SiO}_2)_y]\text{mH}_2\text{O}$, where M is an exchangeable cation with the valency n [13]. Zeolites can be described in various crystallographic terms reported in the Atlas of Zeolite Structure Types [18,25]. Some of the most common zeolites are:

- type A with a typical unit cell composition $[\text{Na}_{12}\{\text{Al}_{12}\text{Si}_{12}\text{O}_{48}\}.27\text{H}_2\text{O}]_8$
- types X and Y such as faujasite $(\text{Na}_2,\text{Ca},\text{Mg})_{29}\{\text{Al}_{58}\text{Si}_{134}\text{O}_{384}\}.240\text{H}_2\text{O}$.

The tetrahedrons are arranged in the form of truncated-octahedrons (sodalite units or β -cages) with an effective diameter of about 0.6 nm. The structures of zeolites A and X,Y are generated by linking the sodalite units via quadratic and hexagonal prisms respectively. These arrangements give α -cages and supercages respectively, which are responsible for molecule sequestration. Some zeolite characteristics are presented in Table 6.

Table 6. Some zeolite characteristics.

Zeolite	Type A	Type X	Type Y
Si/AL	1	1 – 1.5	1.5 – 3
Framework density (atom nm^{-3})	12.9	12.7	
Diameter of large cage (nm)	1.14	1.3	
Free pore aperture (nm)	0.42	0.74	

3.3 Some other adsorbents

Some other porous materials are used in air treatments. Silica gel is a dry colloidal silicic acid with the following chemical composition: $\text{SiO}_2, n\text{H}_2\text{O}$. Its specific surface area ranges between 300 and 800 m^2g^{-1} and the pore diameters are between 2 and 14 nm. It is generally used for air-drying.

Activated alumina is produced by a thermal treatment of bauxite ($\text{Al}_2\text{O}_3, 3\text{H}_2\text{O}$). Its surface is strongly polar with an acid or basic character due to the amphoteric behavior of the metal. This adsorbent is used to dry air but is in competition with molecular sieves.

Macro-reticulated polymers are more recent organic materials developing a specific surface area from 700 to 1400 m^2g^{-1} with pore diameters between 0.5 and 1.3 nm.

4 Adsorption and fixed bed adsorbers

In continuous adsorption processes, the adsorbent is packed in a column or in cylindrical filters as presented in Section 5.1 (Figures 10 and 11). In order to describe the global adsorption in such a system, the flow and the mass transfer have to be defined.

4.1 Flow through a fixed bed

The flow of a compressible single fluid through a bed packed with adsorbent granules is approached using different concepts. Equations have been developed to characterize the flow in terms of velocity, residence time, and pressure drop.

4.1.1 Velocities and residence times

In a filter, two velocities can be defined for a fluid flowing through a porous medium:

- the empty bed velocity:

$$U_0 = \frac{Q_v}{A} \quad (21)$$

where

- U_0 : fluid velocity in the empty filter (m s^{-1})
- A : total cross sectional area of the bed (m^2)
- Q_v : volumetric flow ($\text{m}^3 \text{s}^{-1}$)

- the real velocity or velocity in a cross - section of a bed packed with irregular materials:

$$U = \frac{Q_v}{\varepsilon_0 A} \quad (22)$$

where

- ε_0 : fractional voidage or porosity defined by $\varepsilon_0 = \frac{V_e}{V}$
- U : fluid velocity in the packed bed (m s^{-1})
- V_e : empty volume in the packed bed (m^3)
- V : total bed volume (m^3)

Generally, the velocity in the empty bed (U_0) is used in a large number of equations to determine pressure drop or other flow characteristics.

The average residence time $(\bar{\theta})$ in an empty column is given by the following simple equation:

$$\bar{\theta} = \frac{V}{Q_v} \quad (23)$$

In the case of a bed packed with an adsorbent, a real average residence time $(\bar{\theta}_r)$ can be defined as:

$$\bar{\theta}_r = \frac{\varepsilon_0 V}{Q_v} \quad (24)$$

Of these two relations, equation (23) is generally used for adsorbers. The residence time distribution is not presented in this chapter. For more information, a large number of books may be consulted [26-28].

4.1.2 Pressure drops

4.1.2.1 Darcy's law

In 1830 in Dijon (France), Darcy determined a relation between the pressure drop and operating conditions. This equation, confirmed by a number of researchers, can be written as follows:

$$\frac{\Delta P}{H} = \frac{\mu}{B} U_0 \quad (25)$$

where

ΔP	:	pressure drop (Pa)
H	:	bed thickness (m)
μ	:	dynamic viscosity of fluid ($1.8 \cdot 10^{-3}$ Pl for air at 20 °C)
B	:	permeability coefficient (m^2)
U_0	:	empty bed velocity (m s^{-1})

The permeability coefficient (B) values are a function of the material used in the adsorbers. Some data are presented in Table 7. It should be noted that the Darcy equation applies only to laminar flow (cf. Reynolds number in Section 4.1.2.2).

Table 7. Characteristics and permeability coefficients of some materials (Adapted from [29]).

Packing material	Size		Specific surface area $S \text{ m}^2 \text{ m}^{-3}$	Bed porosity	Permeability coefficient $B \text{ m}^2$
	(inch)	(mm)			
Sphere	1/32	0.8	7600	0.393	$6.2 \cdot 10^{-10}$
	1/16	1.6	3759	0.405	$2.8 \cdot 10^{-9}$
	1/8	3.18	1895	0.393	$9.4 \cdot 10^{-9}$
Cylinder	1/8 x 1/8	3.18 x 3.18	1840	0.401	$1.1 \cdot 10^{-8}$
	1/8 x 1/4	3.18 x 6.36	1595	0.397	$1.2 \cdot 10^{-8}$
	1/4 x 1/4	6.36 x 6.36	945	0.410	$4.6 \cdot 10^{-8}$
Plates	1/4 x 1/4 x 1/32	6.36 x 6.36 x 0.8	3033	0.410	$5.0 \cdot 10^{-9}$
	1/4 x 1/4 x 1/16	6.36 x 6.36 x 1.6	1984	0.409	$1.1 \cdot 10^{-8}$

4.1.2.2 Carman – Kozeny – Ergun equations

In order to obtain general expressions for the pressure drop, operating conditions and characteristics of the packing material, a new concept of flow through beds has been proposed by Carman and co-workers. In a laminar flow regime, an analogy between streamline flow through a tube and flow through pores constituted by packing adsorbent is given as:

$$\frac{\Delta P}{H} = K'' \frac{(1 - \varepsilon_0)^2}{\varepsilon_0^3} S^2 \mu U_0 \quad (26)$$

where

- K'' : dimensionless constant ($3.5 < K'' < 5.5$)
 U : average velocity through pore channels (m s^{-1})
 ΔP : pressure drop (Pa)
 H : length of the column (m)
 S : specific surface area ($\text{m}^2 \text{m}^{-3}$)
 ε_0 : fractional voidage or porosity (dimensionless)

In a large variety of materials, $3.5 < K'' < 5.5$ was obtained [29]. An average value close to 5 is often used. In this case, the error in the results

is less than $\pm 10 \%$. For spheres, $S = \frac{A_g}{V_g} = \frac{6}{d_g}$, the equation becomes:

$$\frac{\Delta P}{H} = 180 \frac{(1 - \varepsilon_0)^2}{\varepsilon_0^3} \frac{1}{d_g^2} \mu U_0 \quad (27)$$

When the packing material grains present an irregular shape, the sphericity (ϕ) is defined as the ratio between the surface area of a sphere

of the same volume as a particle and the surface area of the particle ($0 \leq \phi \leq 1$). In this case, the particle size is introduced into the equation as ϕd_g , $\phi = 1$ for a sphere.

In a turbulent flow, $Re = \frac{d_g U_0 \rho}{\mu} \geq 1$, different research workers (Carman, Kozeny, Ergun) have extended the equations (26 and 27) with a first term due to viscous forces (skin friction) and a second term, obtained for high flow rate by dimension analysis [30][31]:

$$\frac{\Delta P}{H} = 4.17 \frac{(1 - \epsilon_0)^2}{\epsilon_0^3} S^2 \mu U_0 + 0.29 \frac{(1 - \epsilon_0)}{\epsilon_0^3} S \rho U_0^2 \quad (28)$$

or for a spherical grain (diameter d):

$$\frac{\Delta P}{H} = 150 \frac{(1 - \epsilon_0)^2}{\epsilon_0^3} \frac{1}{d^2} \mu U_0 + 1.75 \frac{(1 - \epsilon_0)}{\epsilon_0^3} \frac{1}{d} \rho U_0^2 \quad (29)$$

4.1.2.3 Comiti – Renaud model

More recently, Comiti and Renaud [32] have proposed an equation with a similar shape to the previous relations but with values for tortuosity (τ) and dynamic surface area (a_{vd}) in contact with the fluid:

$$\frac{\Delta P}{H} = 2\tau^2 \frac{(1 - \epsilon_0)^2}{\epsilon_0^3} a_{vd}^2 \mu U_0 + 0.0968 \frac{(1 - \epsilon_0)}{\epsilon_0^3} \tau^3 a_{vd} \rho U_0^2 \quad (30)$$

with

τ : tortuosity (dimensionless)

a_{vd} : specific surface area of the material in contact with the fluid (m^{-1})

This equation has been successfully applied to experimental data obtained with parallelepiped particles or activated carbon fabrics [33][34].

4.2 Breakthrough curves

Fixed beds are generally used in air treatment. Polluted air is applied directly to one end and forced through the packing adsorbent by pressure. The molecules present in the air are removed by transfer onto the adsorbent. The region of the bed where the adsorption takes place is called the mass transfer zone, adsorption zone or adsorption wave. As a function of time, for a constant inlet flow, the saturated zone moves through the contactor and approaches the end of the bed. Then, the effluent

concentration equals the influent concentration and no more removal occurs. This phenomenon is termed breakthrough. An illustration is given in Figure 6.

Some information can be extracted from the breakthrough curve. The breakthrough time is reached when the ratio $C_b/C_0 = 0.05$ or 0.1 , i.e. when the pollutant outlet concentration is between 5 to 10 % of the inlet concentration. This percentage is a function of the desired air quality.

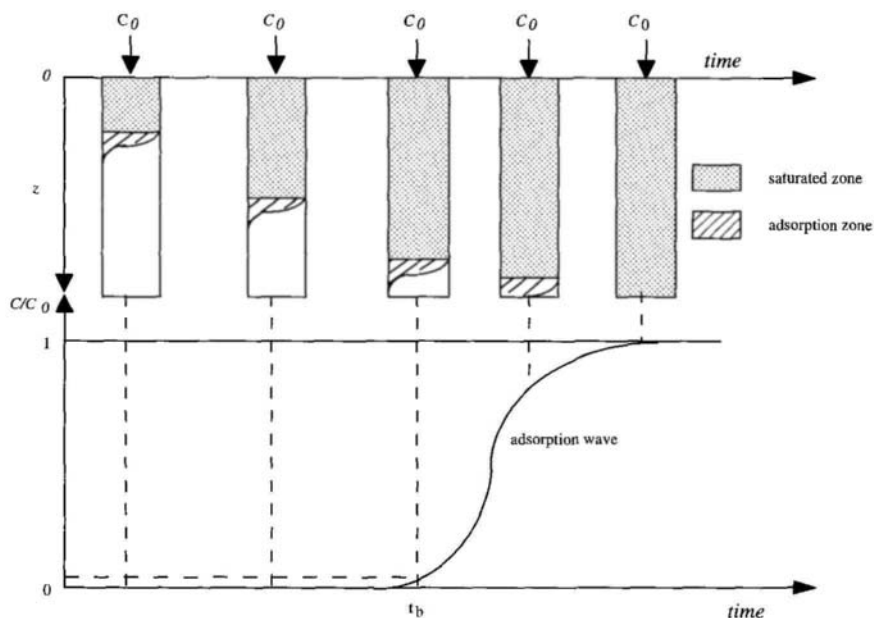


Figure 6. Schematic breakthrough curve in a fixed bed.

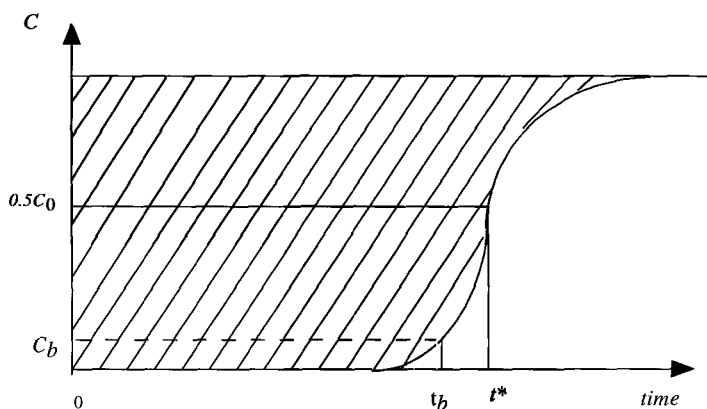


Figure 7. Determination of the total pollution removed from the feed stream by integration of the breakthrough curve.

The total amount of solute removed ($S_{T \text{ removed}}$) from the feed stream upon complete saturation is given by the area under the effluent curve (C vs. t ; Figure 7), that is:

$$S_{T \text{ removed}} = Q_v \int_0^\infty (C_0 - C) dt = \varepsilon_0 SHC_0 + (1 - \varepsilon_0) SHq_0 \quad (31)$$

The pollutant removed at $t = t_b$ is given approximately by:

$$S_{t=t_b \text{ removed}} = Q(C_0 - C)t_b \quad (32)$$

where

Q_v	:	volumetric flow ($\text{m}^3 \text{ h}^{-1}$)
q_0	:	adsorption capacity in equilibrium with C_0 (mg g^{-1})
S	:	surface of the reactor (m^2)
H	:	height of the adsorber (m)
ε_0	:	fractional voidage (dimensionless)
t_b	:	breakthrough time (h)

The stoichiometric time (t^*) is the time at which a perfectly sharp (i.e. a step function) breakthrough curve exists. Thus, it corresponds to the instant of time at which complete saturation of the adsorption capacity of the bed occurs. Its value is approached for a symmetrical profile (C, t^*) = ($0.5 C_0, t^*$) as shown in Figure 7. For a non-symmetrical profile, Cooney [35] gives some simple numerical methods based on the mass balance between the solute concentration in the fluid and the solute adsorbed. From the t^* value, the length of unused bed (LUB) is calculated by the following equation:

$$LUB = \left(1 - \frac{q_b}{q_0}\right)H = \left(1 - \frac{t_b}{t^*}\right)H \quad (33)$$

q_b : adsorption capacity at $t = t_b$ (mg g^{-1}), and the column efficiency (E) is given by :

$$E = \frac{LUB}{H} \quad (34)$$

4.3 Adsorption capacities

From the breakthrough curves, data of adsorption capacities have been determined for a large set of volatile organic compounds adsorbed onto activated carbons. These values are presented in Table 8.

Table 8. Vapor adsorption of different solvents onto activated carbon in a dynamic system, $T = 20\text{ }^{\circ}\text{C}$, $P = 1\text{ atm}$ [adapted from 23].

Compound	Maximal adsorption capacity (%)
Acetaldehyde	7
Acetic acid	30
Acetone	15
Acetylene	2
Acrylic acid	20
Amyl acetate	34
Butyl acetate	28
Ethyl acetate	19
Methyl acetate	16
Isopropyl acetate	23
Bromhydric acid	12
Butyric acid	35
Acryaldehyde	15
Amylic alcohol	35
Ammonia	negligible
Benzene	24
Butane	8
Butanol	30
Butylene	8
Butyl chloride	25
Butyne	8
Butaraldehyde	21
Camphor	20
Caprylic acid	35
Carbon disulfide	15
Carbon tetrachloride	45
Chlorhydric acid	12
Chlorine	15
Chloroform	40
Cresol	30
Crotonaldehyde	30
Decane	25
Diethyl ketone	30
Ethanol	21
Ethyl chloride	12
Butyl ether	20

Table continued

Table 8. Vapor adsorption of different solvents onto activated carbon in a dynamic system, $T = 20\text{ }^{\circ}\text{C}$, $P = 1\text{ atm}$ [adapted from 23]*

Ethyl ether	15
Ethylene	3
Ethyl mercaptan	23
Eucalyptol	20
Fluorhydric acid	10
Formaldehyde	negligible
Formic acid	7
Heptane	23
Hexane	16
Hydrogen sulfide	3*
Indole	25
Iodhydric acid	15
Iodine	40
Iodoform	30
Isopropanol	26
Methanol	10
Methylene chloride	25
Methyl ethyl ketone	25*
Methyl isobutyl ketone	30*
Methyl mercaptan	20
Naphtalene	30
Nicotine	25
Nitric acid	20
Nitrobenzene	20
Nitrogen dioxide	10*
Nonane	25
Octane	25
Ozone	Decomposition*
Palmitic acid	35
Pentane	12
Phenol	30
Propane	5
Propionic acid	30
Propylene	5
Propyl mercaptan	25
Propyne	5
Pyridine	25

Table continued

Table 8. Vapor adsorption of different solvents onto activated carbon in a dynamic system, $T = 20\text{ }^{\circ}\text{C}$, $P = 1\text{ atm}$ [adapted from 23]

Skatole	25
Sulfur dioxide	10
Sulfuric acid	30
Sulfur trioxide, oleum	10
Toluene	29
Valeric acid	35
Xylene	34

4.4 Modeling breakthrough curves

Several equations are available in the literature. Only three approaches and models of breakthrough curves are proposed in this section.

4.4.1 The breakthrough time modeling

This model is based on two kinetic equations of transfer from the fluid phase and accumulation in the pore volume of the material. A simple equation is obtained giving the breakthrough time (t_b) as a function of the operating conditions:

$$t_b = \frac{N_0}{C_0 U_0} (z - z_0) \quad (35)$$

where

t_b	:	breakthrough time (h)
C_0	:	inlet concentration (mg L^{-1})
U_0	:	velocity in the empty bed (m h^{-1})
N_0	:	adsorption capacity (mg L^{-1})
z	:	filter length (m)
z_0	:	adsorption zone (m)

The adsorption capacity is expressed as mass per volume, i.e. for example, mg pollutant removed per liter of bed. Using the bed density, it is easy to calculate this parameter in a common dimension (mg g^{-1} , for example) and to compare this calculated value to the maximum adsorption capacity at equilibrium (q_m) in a batch adsorber. The two parameters (N_0

and z_0) are experimentally determined. In air treatment, z_0 ranges from 1 to 10 cm depending on the adsorbed molecules and the adsorbent.

4.4.2 A simple mass transfer model [36]

The relations used for this model are :

- a mass balance between the aqueous phase and the solid phase,
- a mass transfer equation assuming a linear driving force approximation,
- the Freundlich equation (Eq. (7) Section 2.2.3.2).

The equation for the breakthrough curves is found :

$$C(t) = \left[\frac{C_0^{n-1}}{1 + A e^{-rt}} \right]^{1/n-1} \quad (36)$$

where

- n : Freundlich equation parameter
- $C(t)$: concentration at time t (mg L^{-1})
- C_0 : initial concentration (mg L^{-1})
- A, r : equation parameters determined experimentally

This approach has been successfully applied to pilot unit adsorption.

4.4.3 Modeling mass and heat transfers [10-12]

The adsorption of VOC vapor with activated carbon is modeled by a set of 3 partial differential equations (PDEs): the energy balance and the adsorbate mass balances within the gas and solid phases. The following assumptions are made to develop the model:

- The pressure drop through the bed is negligible.
- The flow pattern is described by the plug flow model. Temperature, adsorbate concentration, gas flow and porosity are uniform at any cross-section of the bed.
- The physical properties of the adsorbent are considered constant and the accumulation of energy in the gas phase is negligible.
- Heat loss is negligible in large industrial columns, which operate under near adiabatic conditions contrary to laboratory scale columns. An overall heat transfer coefficient is used to express heat loss.

- Heats of adsorption are usually considered as constant in mathematical models. However, values of adsorption energies are dependent on the surface loading so this phenomenon must be introduced into the energy balance. Variations of adsorption energies with temperature are weak and are not considered in the model.

- The mass transfer rate is represented by the linear driving force (LDF) model. Because of the high VOC concentration range, grain external surface diffusion is generally considered to be the main contribution to the mass transfer. However, the mass transfer coefficient is an effective lumped-resistance coefficient.

Based on the assumptions made above, the mathematical model could be written as follows:

- Mass balance for the gas phase

$$\{ \text{mass flux} \} + \left\{ \begin{array}{c} \text{mass accumulation} \\ \text{in the gas phase} \end{array} \right\} + \left\{ \begin{array}{c} \text{mass adsorbed} \\ \text{in the solid phase} \end{array} \right\} = 0$$

$$U_o \frac{\partial C}{\partial z} + \varepsilon \frac{\partial C}{\partial t} + \rho_b \frac{\partial q}{\partial t} = 0 \quad (37)$$

- Mass balance for the solid phase

$$\frac{\partial q}{\partial t} = k (q_e - q) \quad (38)$$

- Heat balance

$$\{ \text{heat flux} \} + \left\{ \begin{array}{c} \text{accumulation of} \\ \text{heat in the bed} \end{array} \right\} - \left\{ \begin{array}{c} \text{heat generated by} \\ \text{the adsorption} \end{array} \right\} + \{ \text{heat loss} \} = 0$$

$$U_o \rho_g C_g \frac{\partial T}{\partial z} + \rho_b (C_s + q C_a) \frac{\partial T}{\partial t} - \rho_b [-\Delta H_d] \frac{\partial q}{\partial t} + \frac{4h_o}{D} (T - T_0) = 0 \quad (39)$$

The mass transfer coefficient k is usually expressed [9] as:

$$k = \frac{60 D_s}{d_p^2} \quad (40)$$

External surface diffusion is an activated carbon process which can be expressed [37-39]:

$$D_s = \frac{1.61 \times 10^{-6}}{\tau} \exp\left(\frac{0.45 \Delta H_{int}}{RT}\right) \quad (41)$$

The 0.45 coefficient was proposed to obtain the activation energy of surface diffusion from the mean adsorption heat [10]. The pre-exponential term is an empirical factor and the uncertainty of the tortuosity value is great. The ratio $1.61 \cdot 10^{-6} / \tau$ was then replaced by an adjustable parameter. The diffusion coefficient is then written as follows:

$$D_s = \alpha \exp\left(\frac{0.45 \Delta H_{int}}{RT}\right) \quad (42)$$

where α is the only adjustable parameter of the model.

The adsorption equilibrium is described by the temperature-dependent form of the Langmuir equation:

$$q_e = \frac{q_m b_o \exp\left(\frac{A}{RT}\right) C}{1 + b_o \exp\left(\frac{A}{RT}\right) C} \quad (43)$$

The set of PDEs was written in dimensionless form. The spatial discretisation is performed using the Keller box scheme and the method of lines is employed to reduce the PDEs to a system of ordinary differential equations. The resulting system is solved using a backward differentiation formula method.

The initial conditions used are:

$$C(z, 0) = 0 \quad q(z, 0) = 0 \quad T(z, 0) = T_0$$

The boundary conditions for $t > 0$ are:

$$C(0, t) = C_0 \quad T(0, t) = T_0 \\ \partial q(L, t) / \partial z = 0$$

The calorific capacity and the energies of interactions between molecules and adsorbent are determined using a thermal gravimetric analysis coupled with differential scanning calorimetry (TGA/DSC) [40].

An example of applications of such a model is given in Figures 8 and 9. In this case, ethanol at high concentration is removed from air by an activated carbon grain filter.

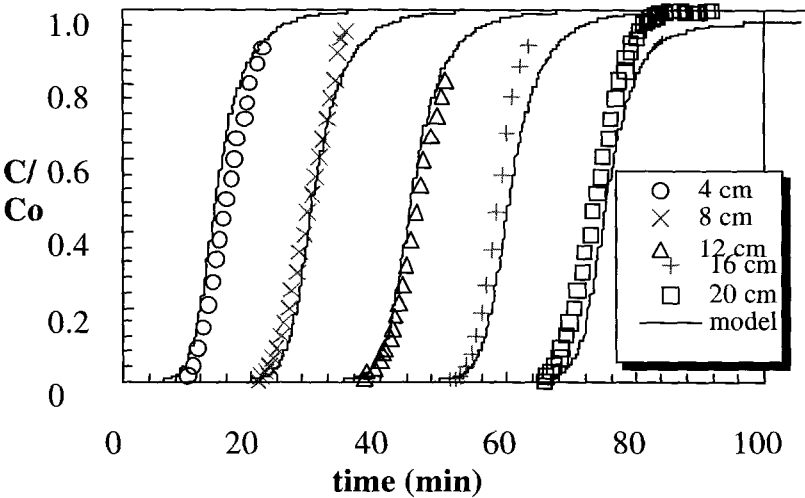


Figure 8. Breakthrough data and simulation of ethyl alcohol adsorption on Picatif NC 60 ($C_0=47\text{ g.m}^{-3}$; $U_0=0.139\text{ m.s}^{-1}$).

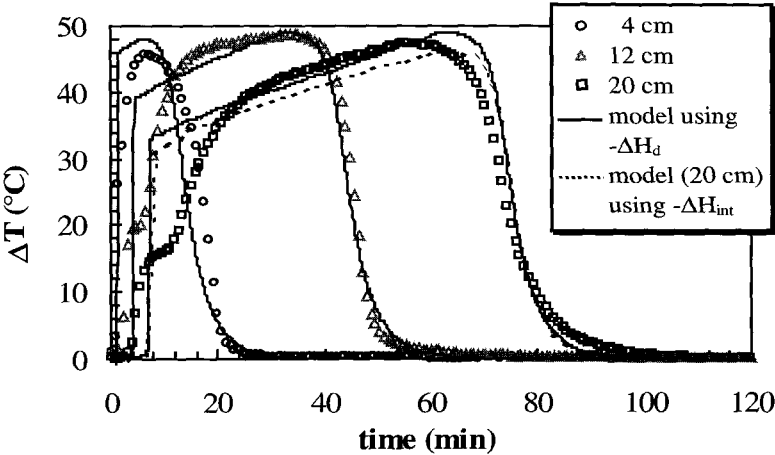


Figure 9. Temperature data and simulation of ethanol adsorption on Picatif NC 60 ($C_0 = 47\text{ g.m}^{-3}$; $U_0 = 0.139\text{ m.s}^{-1}$).

5 Industrial systems and design approaches

5.1 Fixed bed adsorbents

Some fluidized beds are used, but fixed beds, packed with an adsorbent, are the most popular for air treatments. The air flows from the bottom to the top of the reactor. A schematic presentation of a VOC treatment process is given in Figure 10. Two adsorbers are put in parallel, one is working and the other one is in regeneration by steam. The desorbate is condensed in a heat exchanger and the non soluble solvent is recovered in a settling tank.

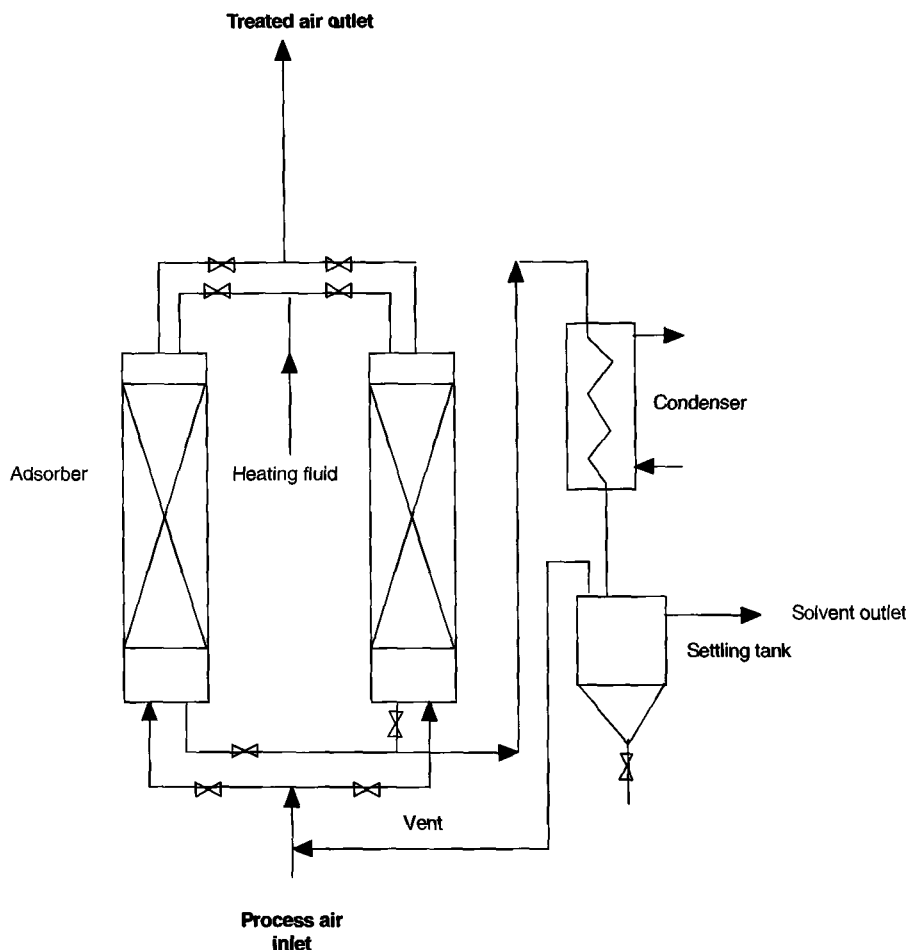


Figure 10. Schematic presentation of an industrial VOC adsorber with in situ regeneration by steam and solvent recovery.

In order to illustrate the previous description, an industrial treatment used in VOC control in gaseous emissions is presented in Figure 11. Some design data and operating conditions are given in Table 8. The working procedure of adsorption and regeneration is shown in Figure 12.

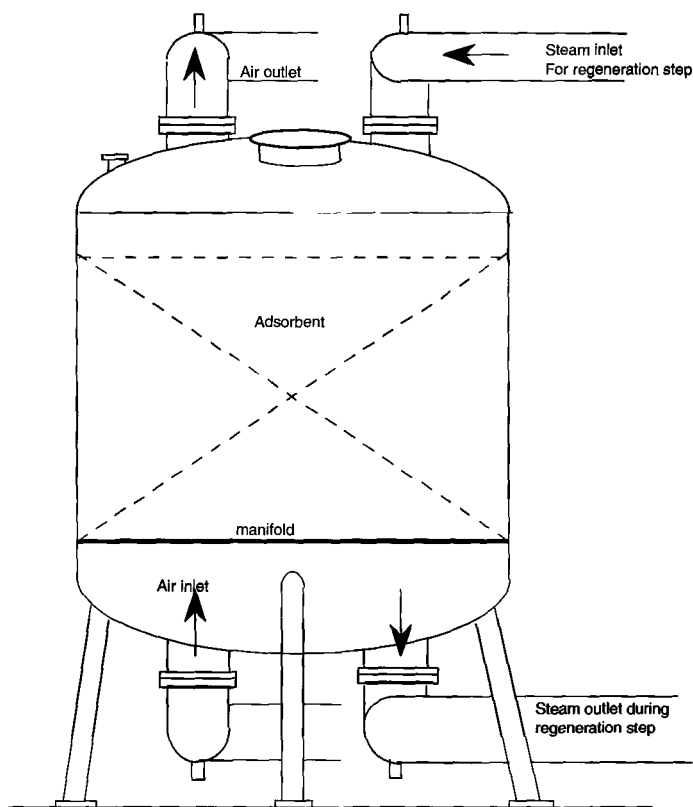


Figure 11. Industrial fixed bed adsorber packed with activated carbon used for VOC emission control.

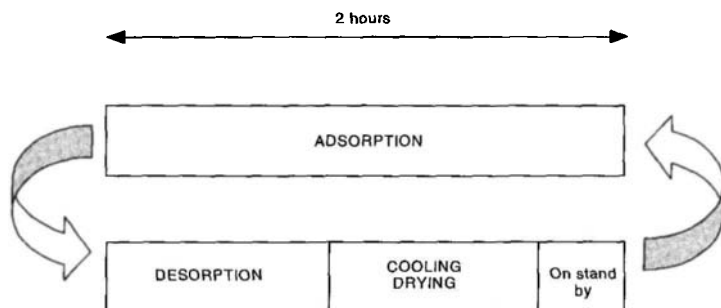


Figure 12. Adsorption – desorption procedure.

Table 9. Design & operating conditions for an industrial adsorber packed with activated carbon for dichloromethane emission control.

Initial data	
Emission flow	5 500 – 7500 m ³ h ⁻¹
Initial concentration of dichloromethane	3 000 mg m ⁻³
Temperature	20 – 40 °C
Relative humidity	50 – 70 %
Adsorber design	
Bed length	1.9 m
Diameter	2.8 m
Adsorber surface	6.15 m ²
Adsorbant volume	11.67 m ³
Operating conditions	
Air velocity	890 – 1220 m h ⁻¹
Residence time	5.6 – 7.6 s
Adsorbent	
Adsorbent	Microporous activated carbon
Extruded grain size	3 mm
Specific surface area	1 100 m ² g ⁻¹
Adsorbant mass	5 000 kg
Adsorption	
Adsorption capacity (chosen)	5 – 7 % (weight)
Adsorption cycle time	2 h
Regeneration	
Heating fluid	Steam
Relative pressure	0,5 bar
Steam amount used for a regeneration step	1300 kg h ⁻¹
Desorption time	1 h
Steam consumption	3.7 TO 5.2 kg kg ⁻¹ solvent recovered
Drying and cooling time	About 1 h

5.2 Practical operating conditions

The design of an adsorber for air treatment is achieved as a function of three main variables: i) the air flow, ii) the kind of the molecule and iii) the concentration of the pollutant. Some practical design values can be obtained using the methodology presented in Figure 13.

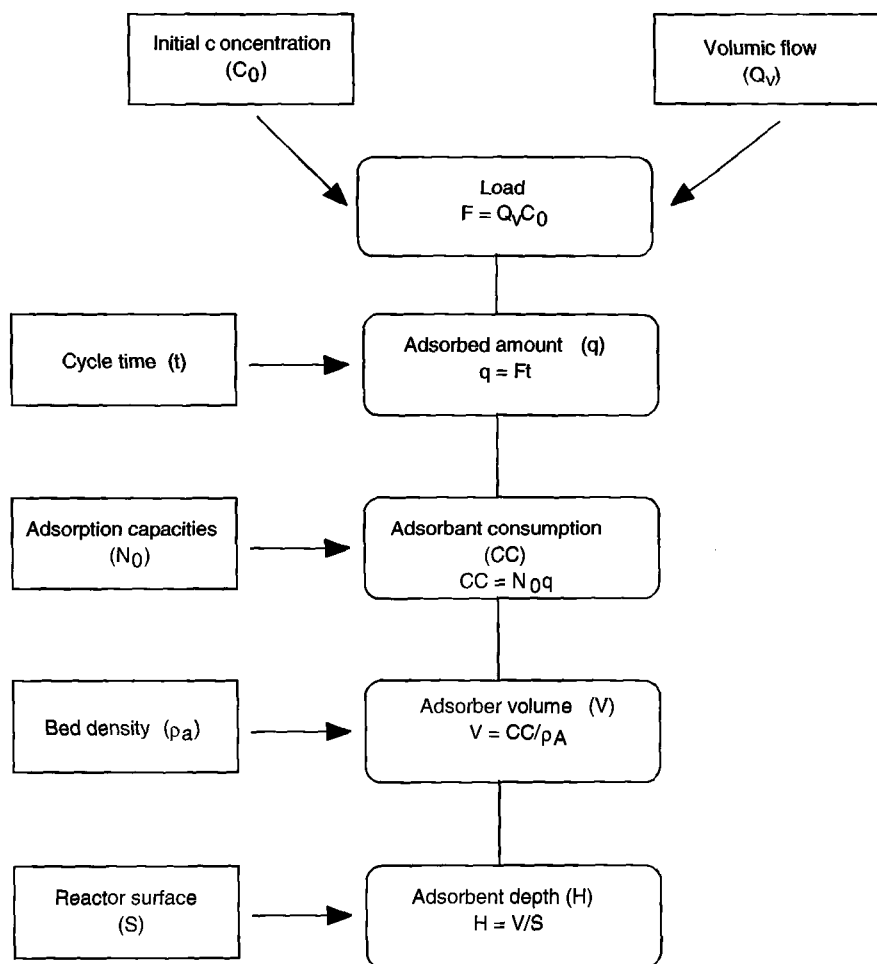


Figure 13. Numerical methodology to provide the simple design parameters of an adsorber.

The velocity is chosen as a function of the molecule to be adsorbed and its inlet concentration. Commonly, the velocities range between 500 and 600 m h⁻¹, i.e. 0.140 to 0.170 m s⁻¹. In the case of well-adsorbed compounds, velocities reach 1 000 to 2 000 m h⁻¹ (0.28 to 0.56 m s⁻¹).

The bed depth is defined from the mean residence time ($\bar{\theta}$) or from adsorption capacities which depend on the cycle time. The residence time ranges between 0.1 and 5 s.

5.3 Safety of the process

The adsorbents are safe processes. However, we have to pay special attention to some specific cases:

- Activated carbon is a reducing agent; thus, it is not suitable for adsorbing an oxidant. A strong oxido-reduction reaction with an increase in temperature could be produced.
- The exothermal reaction due to adsorption of high concentration solvent (more than 100 g/m³) and especially ketones has to be taken into account.

6 Activated carbon regeneration

Regeneration of adsorbents is an interesting operation economically but is only applied to volatile compounds. It is carried out in the activated carbon producers or *in situ*.

6.1 Reactivation of activated carbon

A simple method of regeneration consists of reactivating the spent material in a reactivation oven at the producers. A temperature between 900 and 1200 °C is required with the presence of an oxidant such as steam or CO₂. The method is applied to activated carbons saturated with organic volatile compounds. This operation gives a loss of carbon estimated at 5 to 20 %.

6.2 *In situ* thermal regeneration

The adsorption reaction is exothermal and thus the regeneration of saturated porous materials is performed with heat. Different ways are used either with the supply of an external heat source or with an intrinsic heating of the adsorbent. However, whatever the technologies used, several operations are required as shown in Figure 12.

6.2.1 Heating fluid regeneration

6.2.1.1 Utilization of steam

The regeneration with steam is the most common technique for regeneration of activated carbon saturated with solvents. The steam, at temperatures ranging between 105 and 140 °C, flows through the packing material and cleans the activated carbon. The desorbate is then condensed.

Of course, the solvent has to be non-miscible in water. The steam consumption is between 3 and 14 kg kg⁻¹ of recuperated VOC. Table 9 gives the steam consumption for different VOC and activated carbons of different origins.

Table 10. Examples of steam consumption for activated carbon regeneration (kg of steam kg⁻¹ recuperated solvent).

Activated carbon origin	Carbon tetrachloride	Perchloro -ethylene	Trichloro -ethylene	Toluene	Chloro-benzene
Coconut	3.5	7.3	4.8	9.8	7.6
Peat	6.3	7.0	8.7	12.8	13.9
Wood	3.4	3.1	4.1	6.0	5.5

Heat recuperation is often interesting in order to improve the global heat balance of the installation. Some difficulties are sometimes met with steam regeneration:

- The solvent has to be non-miscible in order to obtain an easy separation between the solvent and water.
- The condensed water has to be treated due to a solubilization of a small part of the solvent during the condensation and separation steps.
- A decomposition of some chlorinated solvent gives chlorhydric acid and thus a corrosion of the installation.

6.2.1.2 Utilization of hot gas

Regeneration with hot air or inert gas avoids some hydrolysis of desorbed solvent. The desorption sequences are similar to those of steam regeneration. Due to low specific heat (about 1 kJ kg⁻¹ K⁻¹ for air), this technique requires large volumes of gas and then a dilution of the desorbate.

6.2.2 Low pressure regeneration

Due to a reduction of pressure, the equilibrium between the adsorbed phase and the fluid is shifted. The desorbed pollutant is recovered by condensation in a cold trap. This technology is applied to very volatile organic compounds or when the adsorption energies are weak.

An interesting example is given by the adsorption and the desorption of gas. The filling of a tank or a truck tank with gas gives an emission of pollutants in air. The treatment is achieved with filters of activated carbon grains or cloths and the desorption is performed at low pressure between 200 and 500 mm Hg. The solvent stream is then absorbed in liquid gas.

6.2.3 Heating the adsorbent

In order to improve the energy balance of the regeneration systems, the direct heating of the porous material can be performed in different ways.

6.2.3.1 Joule effect regeneration [41,42]

The principle of this technique is to consider the adsorbent as an electrical resistance, which is heated by the joule effect when an alternating current is applied. This regeneration is particularly suitable for activated carbon cloths or felts. After saturation of the adsorbent, the filter is heated by the joule effect and the desorbate is flushed out of the reactor with an inert gas. Then, the solvent is condensed in a cold trap to be recycled.

An industrial system using an activated carbon cloth filter (Figure 14) has been used to remove a mixture of ethanol and ethyl acetate from a gaseous emission. Table 10 resumes the operating conditions of adsorption and desorption.

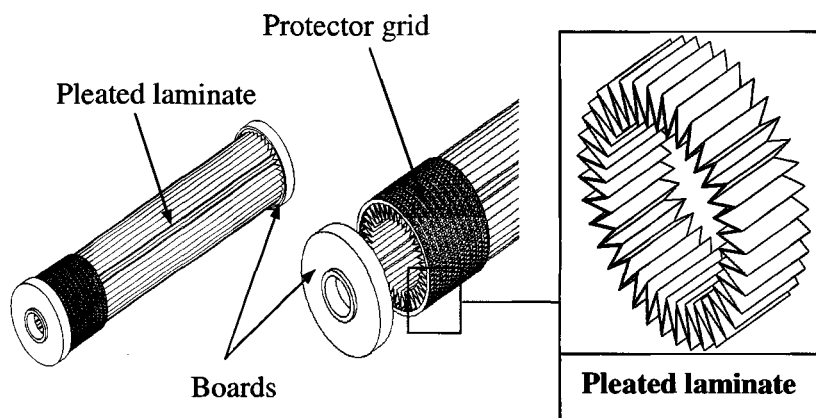


Figure 14. Mechanical drawing of pleated activated carbon cloth filter [42,43].

Table 11. Some operating conditions for an industrial system using adsorption of a mixture of ethanol and ethyl acetate (50/50) onto activated carbon cloths and desorption by the joule effect.

Operating condition	Adsorption phase	Desorption phase
Velocity (m h^{-1})	500	2
Residence time (s)	9	270
Inlet concentration (g m^{-3})	1.5	-
Outlet concentration (g m^{-3})	< 0.020	80
Adsorption temperature ($^{\circ}\text{C}$)	25	
Desorption temperature ($^{\circ}\text{C}$)		150
Cold trap temperature ($^{\circ}\text{C}$)		-40

6.2.3.2 Infrared regeneration

Another technique to desorb pollutants from an adsorbent is to heat it by infra red radiation. Some examples are published for the regeneration of hydrophobic zeolites saturated by organic volatile compounds coming from the painting industry gaseous emissions [44].

6.2.3.3 Electromagnetic induction regeneration [5,45]

The Electromagnetic induction heating has been recently studied to regenerate an activated carbon filter without any contact between the heat source and the adsorbent. The heat production is generated by Foucault's currents induced by an alternating magnetic field.

The process consists in putting the filter in a solenoid, i.e. a spiral metallic tube. When the filter is saturated, a current at high frequency (1 – 100 kHz) is applied. It generates a magnetic and electrical field inside the filter and the activated carbon grain temperature increases up to 100 – 200 $^{\circ}\text{C}$ as a function of the electrical power applied.

6.2.3.4 Micro-wave regeneration

Using micro-waves is an alternative method to heat an adsorbent. A high frequency generator is necessary and focusing the waves is required to produce heating on a determined adsorbent volume. This technology is applicable to grains and for more recent porous material such as activated carbon clothes or felts.

References

1. Montgomery J.M., *Water Treatment, Principles & Design*, John Wiley & Sons, New York, USA, (1985) pp. 174-197.
2. Young D.M., Crowell A.D., *Physical Adsorption of Gases*, Butterworths, London, UK (1962).
3. Ruthven D.M., *Principles of adsorption and adsorption processes*, John Wiley & Sons, New York, USA (1984).
4. Tien C., *Adsorption Calculations and Modeling, Series in Chemical Engineering*, Butterworth Heinemann, Boston USA (1994).
5. Le Cloirec P., *Les composés organiques volatils (COV) dans l'environnement*, Tec & Doc Lavoisier, Paris (1998).
6. Bicocchi S., *Les polluants et les techniques d'épuration des fumées*, Tec & Doc Lavoisier, Paris (1998).
7. Popescou M., Blanchard J.M. and Carré J., *Analyse et traitement physicochimique des rejets atmosphériques industriels*, Tec & Doc Lavoisier, Paris (1998).
8. Kast W. and Otten W., The breakthrough in fixed bed adsorbents: method of calculation and the effect of process parameters, *Intern. Chem. Eng.* **29** (1987) pp. 197-211.
9. Treybal R.E., *Mass-Transfer Operations*, McGraw Hill Intern. Ed., Boston, USA, (1981).
10. Delage F., Pré P. and Le Cloirec P., Effects of moisture on warming of activated carbon bed during VOC adsorption, *J. Environ. Eng.* **125** (1999) pp. 1160-1167.
11. Delage F., Pré P. and Le Cloirec P., Mass transfer and warming during adsorption of high concentrations of VOCs on an activated carbon bed: experimental and theoretical analysis, *Environ. Sci. Technol.* **34** (2000) pp. 4816-4821.
12. Pré P., Delage F. and P. Le Cloirec, A model to predict the adsorber thermal behavior during treatment of volatile organic compounds onto wet activated carbon, *Environ. Sci. Technol.* **36** (2002) pp. 4816-4821.
13. Brasquet C. and Le Cloirec P., QSAR for organic adsorption onto activated carbon in water: What about the use of neural networks? *Water Res.*, **33** (1999) pp. 3603-3608.
14. Brasquet C., Bourges B., Le Cloirec P., Quantitative Structure Properties Relationship (QSPR) for the adsorption of organic compounds onto activated carbon cloth: comparison between multilinear regression and neural networks, *Environ. Sci. Technol.* **33** (1999) pp. 4226-4231.
15. Crittenden J.C., Sanongraj S., Bulloch J.L., Hand D.W., Rogers T.N., Speth T.F. and Ulmer M., Correlation of aqueous phase adsorption isotherms, *Environ. Sci. Technol.*, **33**, (1999) pp. 2926-2933.
16. Suzuki M., *Adsorption Engineering*, Elsevier, Amsterdam, The Netherlands (1990).
17. Kier L.B. and Hall L.H., *Molecular Connectivity in Structure Activity Analysis*, John Wiley & Sons Inc., New York, USA (1986).
18. Rouquerol F., Rouquerol J. and Sing K., *Adsorption by powders & porous solids*, Academic Press, San Diego, USA (1999).
19. Imelik B. and Védrine J.C., *Les techniques physiques d'étude des catalyseurs*, Edition Technip, Paris (1998).

20. Baudu M., Le Cloirec P. and Martin G., First approach of desorption energies of water and organic molecules onto activated carbon by Differential Scanning Calorimetry studies, *Water Res.* **27** (1993) pp 69-76.
21. Akubuiro E.C. and Wagner N.J., Assessment of activated carbon stability toward adsorbed organics, *Ind. Eng. Chem. Res.* **31** (1992) pp. 339-346.
22. Akubuiro E.C., Potential mechanistic routes for the oxidative disintegration of ketones on carbon adsorbents, *Ind. Eng. Chem. Res.* **32** (1993) pp. 2960-2968.
23. Cheremisinoff P.N. and Ellerbusch F., *Carbon Adsorption Handbook*, Ann Arbor Science Publisher Inc, Ann Arbor, Mi, USA (1978).
24. Bansal R.C., Donnet J.B. and Stoeckli F., *Active Carbon*, Marcel Dekker Inc. New York, USA (1988).
25. Meier W.M. and Olson D.H., *Atlas of Zeolite Structure Types*, Intern. Zeolite Ass., Butterworth-Heinemann, London, UK, (1992).
26. Levenspiel O., *Chemical Reaction Engineering*, 2nd Edition, John Wiley & Sons, New-York, USA, (1972).
27. Trambouze P., Van Landeghem H. and Wauquier J.P., *Les réacteurs chimiques*, Technip, Paris, France, (1984).
28. J. Villiermaux, *Génie de la réaction chimique*, Tec & Doc, Lavoisier, Paris, France, 1993.
29. Coulson J.M., Richardson J.F., Backhurst J.R. and Harker J.H., *Chemical engineering*, Butterworth, 4th Edition, Vol 2, Butterworth Heinemann, Oxford, UK, (1991).
30. Zlokarnik M., *Dimensional Analysis and Scale-up in Chemical Engineering*, Springer-Verlag, Berlin, Germany, (1991).
31. Baléo J.N., Bourges B., Courcoux Ph., Faur-Brasquet C. and Le Cloirec P., *Méthodologie expérimentale*, Tec & Doc, Lavoisier, Paris, France (2003).
32. Comiti J. and Renaud M., A new model for determining mean structure parameters of fixed bed from pressure drop measurements, *Chem. Engn. Sc.* **44** (1989) pp. 1539-1545.
33. Baléo J.N., Subrenat A. and Le Cloirec P., Numerical simulation of flow in air treatment devices using activated carbon cloth filters, *Chem. Engn. Sci.* **55** (2000) pp. 1807-1816.
34. Brasquet C. and Le Cloirec P., Pressure drop through textile fabrics – experimental data modelling using classical models and neural networks, *Chem. Engn. Sci.* **55** (2000) pp. 2767-2778.
35. Cooney D.O., *Adsorption Design for Wastewater Treatment*, Lewis Publishers, Boca Raton, USA, (1999).
36. Clark R.M., Evaluating the cost and the performance of field scale granular activated carbon system, *Environ. Sci. Technol.* **21** (1987) pp. 574-581.
37. Crittenden J.C., *Mathematical modeling of adsorber : single and multicomponents*, PhD Thesis, University of Michigan, USA, 1976.
38. Crittenden J.C. and Weber W.J. Jr, *J. Environ. Eng.* **104** (1978) pp.185-192.
39. Crittenden J.C., Wong B.W.C., Thacker W.E., Someyink V.L. and Hinrichs R.L., Mathematical modeling of sequential loading in fixed bed adsorbents, *J. Water Pollut. Control Fed.* **52** (1980) pp. 2780-2795.
40. Pré P., Delage F., Faur-Brasquet C. and Le Cloirec P., Quantitative structure activity relationships for the prediction of VOCs adsorption and desorption energies onto activated carbon, *Fuel Process. Technol.* **77-78** (2002) pp. 345-351.
41. Le Cloirec P. and Martin G., Thermal regeneration by the Joule effect of activated carbon used for air treatment, *Environ. Technol.* **13** (1992), pp. 423-435.

42. Subrenat A., Baléo J.N., Le Cloirec P. and Blanc P.E., Electrical behavior of activated carbon cloth heated by the Joule effect : desorption application, *Carbon* **39** (2001) pp. 707-716.
43. Subrenat A., Baléo J.N. and Le Cloirec P., Analysis of pressure drops in pleated activated carbon cloth filters, *J. Environ. Engn.*, **6** (2000) pp. 562-568.
44. Davis W.T., *Air Pollution Engineering Manual*, John Wiley & Sons, New York, USA (2000).
45. Mocho P., Bourhis J.Ch. and Le Cloirec P., Heating activated carbon by electromagnetic induction, *Carbon* **34** (1996) pp. 851-856.

BIOADSORPTION AND SEPARATION WITH NANOPOROUS MATERIALS

ANTJE DAEHLER, GEOFFREY W. STEVENS AND ANDREA J.O'CONNOR

*Particulate Fluids Processing Centre, Department of Chemical and
Biomolecular Engineering, University of Melbourne, Victoria 3010, Australia*

E-mail: andrea.jo@unimelb.edu.au

Recently developed nanoporous materials have properties which make them ideal as adsorbents for biochemical separations. In particular, their narrow pore size distributions with pore diameters that can be tailored to suit particular biochemical applications promise high selectivity via size exclusion. Recent research has demonstrated this promise, along with insights into other important properties including adsorption capacity, selectivity, kinetics and mechanisms. This chapter reviews the research in this area to date and identifies the challenges remaining for commercial application of these materials in bioadsorption and separations to be achieved.

1 Introduction

The selective separation of biological molecules via adsorption is important for a number of applications, for example in the food and pharmaceutical industries where high yields and purities are often crucial. Molecular sieves, such as zeolites, have narrow pore size distributions and large specific surface areas, and can provide efficient separation based on size differences of the solute molecules (size exclusion). However, the pores in conventional microporous molecular sieves are generally too small to allow access to biological molecules, and therefore are not suitable for bioseparations. Conversely, the smaller surface area of nonporous materials severely limits their capacity. Concerns with some the adsorbents currently in use include lack of selectivity, swelling and leaching of undesirable materials out of the adsorbent (e.g. aluminium from bentonite, a clay commonly used for protein removal in food applications [1]). Certain chromatography media overcome some of these limitations; however they are often polymeric, which has the disadvantages of the media swelling in some solvents and the presence of micropores that can reduce their separation efficiency [2].

The development of a new class of nanoporous silica materials in the early 1990s expanded the pore size range of molecular sieves into the mesoporous region (pore dimensions of 2 - 50 nm [3]). This development was lead by the groundbreaking work of two groups. Researchers at Mobil reported the synthesis and properties of a new class of synthetic materials, which they identified as mesoporous molecular sieves and named M41S [4, 5]. M41S materials, including MCM-41 and MCM-48, are synthesised by the polymerisation of silica in aqueous surfactant solutions. Control of the pore size is achieved via selection of surfactant chain length and/or addition of organic swelling agents. Similarly to zeolite syntheses, the organic molecules (surfactants) function as structure directing agents or templates. However, in contrast to zeolites, structure is determined not by single organic molecules but micelles, liquid-crystalline self-assembled surfactant aggregates. The ordered micelles act as templates for the silica structure, a process termed Liquid Crystal Templating (LCT) [5]. Though it has been pointed out that it is not strictly correct to say that aggregates of these molecules act as “templates” for the porous structure, since liquid crystal formation involved in the synthesis is believed to occur co-operatively with the silica species, rather than independently, M41S and related materials are often referred to as “supramolecular templated materials”.

Almost at the same time as the synthesis of MCM-41 was first published, Yanagisawa *et al.* [6] described an alternative synthesis pathway for preparing mesoporous silicate from a layered silicate, kanemite. The resulting material is called FSM-16 (Folded Sheet Mesoporous Material). The preparation is similar to MCM-41 but uses a layered silicate as the silica source. Instead of a liquid crystal templating mechanism, a “folded sheet” mechanism was proposed to describe the synthesis mechanism of FSM materials [7, 8].

A rich variety of further mesoporous materials has since been developed, with prominent examples including the larger pore SBA-15 (Santa Barbara Amorphous) [9] and MCF (Mesostructured Cellular Foams) [10].

Research in the field of nanoporous materials has steadily increased over the past decade, with hundreds of publications per year devoted to mesoporous or mesostructured silica materials alone [11]. Their specific properties, including high surface areas ($\sim 1000 \text{ m}^2/\text{g}$), uniform pore size and shape, and tuneable mesopore sizes make them attractive for a number of applications, either as purely inorganic materials or modified with

functional groups to create hybrid inorganic-organic silica materials targeted for specific applications.

The main application targeted for nanoporous silica materials since their development has been catalysis, and a large number of articles have been published in this field, including some recent review articles [8, 12, 13]. A number of other applications have also been suggested, among them adsorption and separation. A “Method for Separation of Substances” with M41S materials has been patented [14]. The adsorption isotherms for a range of hydrocarbons on MCM-41 have been reported, and it has been found to have potential for the separation of acidic, neutral and basic polycyclic hydrocarbons using high performance liquid chromatography (HPLC) [15]. The ion exchange capacity of pure-silica MCM-41 is known to be low [16], but hybrid nanoporous materials can provide the desired functional groups such as ion exchangers. The use of such hybrid materials has been successfully demonstrated for the adsorption of heavy metal ions [17-19].

Development in the expanding field of nanoporous materials has not been limited to supramolecular templated silica materials. Analogues of the pure silica materials with a wide range of inorganic compositions have been reported, as well as nanoporous polymers [20] and carbons [21]. The various synthesis procedures for nanoporous silica materials include sol-gel methods in the presence of water-soluble organic polymers, yielding monolithic silica with a double pore system [22].

The silica materials are particularly interesting for biological separations: silica is considered safe for food and pharmaceutical applications, and the surface chemistry of silica with surface silanol (hydroxyl) groups provided anchor points for further surface modification. Therefore, this review focuses on developments in the area of nanoporous silica materials related to bioadsorption and separation.

These materials have a range of properties, as shown in Table 1, which would make them suitable for the adsorption of biological molecules. The adjustable pore sizes could provide selectivity in separation processes by size exclusion in the mesoporous size range. This range is ideal for many biological molecules, such as vitamins, amino acids, and some polypeptides and proteins, among others, which are frequently processed and purified in aqueous solutions. In contrast to typical porous adsorbents, which have fairly broad distributions of pore sizes, these materials have narrow pore size distributions which will improve access to the pores for species close to the size exclusion limit, and hence improve their capacity for these species. The large specific surface areas and high specific pore

volumes also could provide high adsorption capacities. Being rigid, these materials will not swell in solution, thus avoiding the problems of swelling found with many polymeric and layered inorganic adsorbents. Swelling can lead to maldistribution and consequent loss of performance of media in packed columns, as well as loss of significant amounts of valuable product by entrainment in the media. Nanoporous silica materials are usually synthesized in particulate form, and the small primary particles usually form larger agglomerates. This leads to a bimodal pore structure (regular intraparticle mesopores and larger, irregular interparticle pores), which could facilitate diffusion of the solute to the intraparticle pores and thus enhance adsorption kinetics.

Despite the promising properties of nanoporous silica materials for the separation of biological molecules, only limited work in this area has been reported. Some researchers have focused on the related field of enzyme immobilisation, investigating some adsorption processes, regarding access to the pores and adsorption capacity, but primarily considered other factors, like the activity of the immobilised enzyme. Kinetics, desorption, elution, repeated use and lifetime of the nanoporous silica materials, factors important for their use as adsorbents for separations, are generally not considered particularly relevant for immobilisation studies. Thus, information about such properties relevant to application of nanoporous silica materials in the separation of biological molecules is relatively limited.

Table 1. Promising Features of Nanoporous Silica for Bioadsorption and Separations

Property	Potential benefit for adsorption processes
Tuneable pore sizes	Pore sizes can be tailored for macromolecules
High surface area and pore volume	High adsorption capacity
Uniform pore size and shape	High capacity for solutes close to the size-exclusion limit, shape selectivity
Bimodal pore structure	Enhanced adsorption kinetics
Silanol groups on surfaces	Ability to functionalise surfaces
Rigidity	Minimal swelling, easier column operation, reduced product losses

In this chapter, an overview of the work published so far involving biological molecules is given in Section 2, Separations, Adsorption and Solutes. Articles focussing on separation are reviewed in further detail. The aspects relevant to adsorption are detailed in Section 3, Adsorption – Capacity and Kinetics. Section 4, Access to Pores, discusses ways to verify the access of the solute molecules into pores. Section 5, Size Exclusion, investigates the adsorption selectivity of nanoporous silica based on solute size. The surface interactions of solutes and adsorbents are the topic of Section 6, Adsorption Mechanisms. Considerations involving the performance and lifetime of nanoporous silica adsorbents in industrial applications are discussed in Section 7, Regeneration and Reuse. Section 8, Stability, discusses stability in general, and more specifically, under adsorption conditions. The issues which will need to be addressed for commercial application of nanoporous silica in bioseparations are identified in Section 9, Challenges Remaining. Finally, a summary of the current state of research together with a perspective for future development in this area are given at the end of the chapter in Section 10, Concluding Remarks.

2 Separations, Adsorption and Solutes

In recent years, only a few articles have demonstrated separations of biological molecules from mixed solutions using nanoporous silica materials. Han *et al.* [23] reported the size dependent sequestration of anionic proteins from mixtures in aqueous solutions by SBA-15 and MCF (in both materials, the surface silanol groups were derivatised with (3-aminopropyl)-triethoxysilane, APTS), as well as the release of the sequestered proteins by increasing the ionic strength.

Zhao *et al.* [24] demonstrated the use of large pore SBA-15, modified with dimethyloctadecylchlorosilane (C_{18} -SBA-15), as a substrate in high performance liquid chromatography (HPLC) to separate biomolecules including peptides and proteins. They found that a C_{18} -SBA-15 packed HPLC capillary column showed symmetric and baseline separated chromatographic peaks in trials with both peptides and proteins. For the separation of four small biomolecules (cysteine, glutathione, 6-thiopurine and dopamine), they demonstrated that the chromatographic peaks achieved with the C_{18} -SBA-15-packed HPLC column were narrower and more symmetric than for a commercial C_{18} column (Figure 1).

Minakuchi *et al.* tested a continuous mesoporous silica rod column for the reversed-phase acetonitrile-water linear gradient elution of

polypeptides (in the presence of trifluoroacetic acid), and found that it showed much higher separation efficiency for this application than conventional columns packed with 5 μm silica particles with 30 nm pores. The continuous silica rod used in this work was synthesised by methods reported by Nakanishi and co-workers [22, 25, 26] and had a double pore system with 1.1 μm through-pores as well as 26 nm nanopores. Similar monolithic silica columns are now commercially available from Merck under the trade name Cromolith.

Most publications concerned with the interactions of biological molecules and nanoporous silica have either concentrated on the adsorption process and stopped short of demonstrating separations, or are primarily concerned with enzyme immobilisation. These studies, however, can provide valuable information for bioadsorption and separation processes.

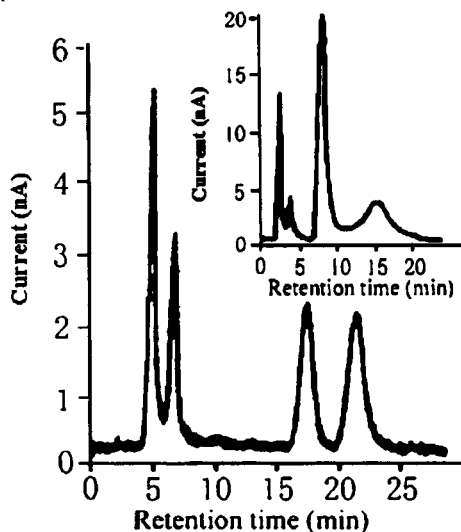


Figure 1: Chromatogram of four small biomolecules with a C18-SBA-15 capillary column. The inset shows the separation on a commercial C18 column. The four peaks represent, from left to right, cysteine, glutathione, 6-thiopurine and dopamine, respectively [24] - Reproduced by permission of The Royal Society of Chemistry.

Among the first to publish work showing enzyme immobilisation on supramolecular templated nanoporous silica were Balkus and co-workers [27]. They showed the immobilisation of globular enzymes (cytochrome c,

papain, trypsin) on MCM-41, and found a clear dependence of the achieved loading on enzyme size (Figure 2). Peroxidase (horseradish) was also investigated, and was not significantly retained by the MCM-41, indicating that the peroxidase molecules were too large to fit into the 4 nm pores.

Table 2 shows examples of the variety of biological molecules which have been adsorbed onto nanoporous silica materials (with or without modified surfaces). Most solutes listed can be either classified as being proteins (including enzymes), or “smaller biological molecules”, including amino acids, vitamins, and peptides, with the exception of one article which investigated the immobilisation of whole microbial cells [28].

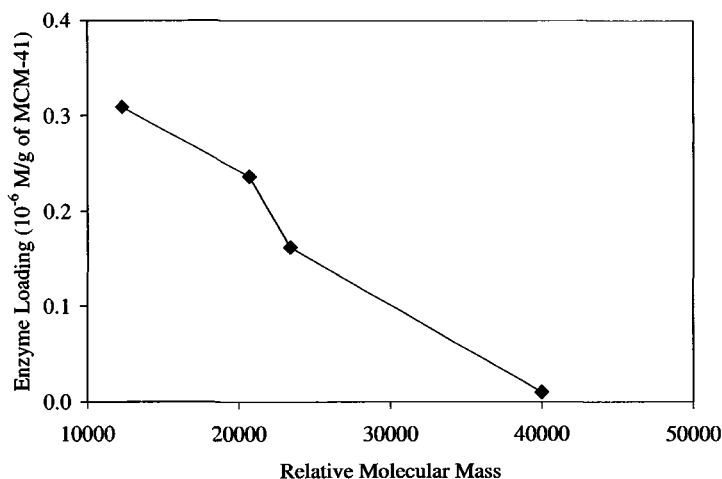


Figure 2. Effect of enzyme molecular weight on the loading onto MCM-41 Reprinted from [27] with permission from Elsevier Science.

The findings of these adsorption or immobilisation studies, which provide information relevant for the various aspects of separation processes, are discussed in the following sections.

Table 2. Adsorption of biological molecules on nanoporous silica materials - solutes and nanoporous supports used.

Solutes	Adsorbents*	
cytochrome c, trypsin, papain, peroxidase	MCM-41	[27]
conalbumin, ovalbumin, trypsin inhibitor protein	SBA-15, MCF (both APTS-silylated)	[23]
cytochrome c	MCM-41, CNS, MPS-F127	[29]
cytochrome c	MCM-41, MCM-48 MCM-41 (Al/Si), Nb-TMS1	[30]
cytochrome c	MCM-48, SBA-15, Nb-TMS4	[31]
horseradish peroxidase, subtilisin	FMS-16, MCM-41 and SBA-15	[32]
lysozyme, trypsin	MCM-41, trimethylsilane modified MCM-41	[33, 34]
lysozyme, bovin serum albumin, myoglobin, ovalbumin	SBA-15 (C ₁₈ surface modified)	[24]
trypsin	MCM-41, MCM-48, SBA-15	[35]
trypsin	SBA-15, surface modified with phenyl, amine, thiol, chloride and carboxylic acid functional groups	[36, 37]
lysozyme, trypsin	MCM-41, SBA-15	[38]
peptides (trypsin-digested myoglobin)	SBA-15 (C ₁₈ surface modified)	[24]
glycyltyrosine, leucine-enkephaline, insulin, cytochrome c, lysozyme, transferrin, bovin serum albumin, β -lactoglobulin, polypeptides	monolithic porous silica (C ₁₈ surface modified)	[39]

Table continued

Adsorbents are pure silica, without surface modification unless otherwise specified; MCM-41 = hexagonal M41S material, MCM-48 = cubic M41S material, SBA-15 = Santa Barbara Amorphous Material, hexagonal, MCF = Mesoporous Cellular Foam, APTS = (3-aminopropyl)-triethoxysilane, CNS = cyano-modified nanoporous silica, MCM-41(C₁₄) = MCM-41 synthesised with surfactant containing 14 carbon atoms, Nb-TMS1 & 4 = Niobium Transition Metal Oxide Molecular Sieves, MPS-F127 = mesoporous silica, synthesised with non-ionic triblock-copolymer, Al/Si = aluminosilicate, FSM = Folded Sheet Material

Solutes	Adsorbents*	
Small biological molecules		
lysine, phenylalanine, histidine, glutamic acid, aspartic acid, glutamine, asparagine, etc. (amino acids and related amides)	MCM-41 (C ₁₄)	[40]
lysine (amino acid)	MCM-41	[41]
L-glutamic acid and L-alanine (amino acids)	zirconium phosphate-modified porous silica	[42]
chlorophyll α	FSM	[43]
riboflavin (vitamin B ₂)	MCM-48	[44]
riboflavin (vitamin B ₂)	MCM-41, MCM-48	[33]
cysteine, glutathione, 6-thiopurine, dopamine	SBA-15 (C ₁₈ surface modified)	[24]
Microbial cells		
<i>Arthrobacter</i> sp., <i>Bacillus subtilis</i> and <i>Micrococcus luteus</i>	MCM-41 (Al/Si)	[28]

3 Adsorption Capacity and Kinetics

One of the important aspects for application of an adsorbent is its capacity. A number of the articles listed in Table 2 report loadings of various biological molecules onto nanoporous silica materials. However, it is difficult to compare their results or make predictions of performance in other situations, because the pore size distributions, pore volumes and specific surface areas of the adsorbents vary. The surface chemistry of the silica materials, such as the silanol group density, may also vary depending on the preparation method for the adsorbent, potentially altering the adsorbent/adsorbate interactions, and so also affecting the capacity. In addition, the solution conditions (pH, ionic strength, solute concentration and temperature) affect the extent of adsorption and these have also varied in the reported experiments. Furthermore, the contact time between the solution and adsorbent varies, and while some authors state that equilibrium was reached, few present evidence of this or data on the adsorption kinetics. Some of the higher loadings reported are 189 mg/g for adsorption of lysozyme onto SBA-15 and 104 mg/g for lysozyme adsorbed onto MCM-41[38], and 180 mg/g for horse radish peroxidase (HRP) on a FSM-16 material with 8.9 nm pore size [32]).

Adsorption behaviour can be described with various models, the most commonly used in this field being the theoretically derived Langmuir model and the empirical Freundlich equation. According to the Langmuir theory, the equilibrium loading, q , is a function of the equilibrium concentration of the adsorbate in solution, c , and is further determined by the maximum capacity, Q (monolayer coverage), and a temperature dependent term, K_L , which depends on the affinity of the adsorbate to the surface [45, 46].

$$q = Q \frac{K_L c}{1 + K_L c} \quad (1)$$

The Freundlich equation describes the loading, q , as an exponential function of the concentration, c , with the pre-exponential parameter K_f and the exponent β [45, 46].

$$q = K_f c^\beta \quad (2)$$

For cases of very strong affinity of solute and adsorbent (large K_L value), the Langmuir isotherm approaches a rectangular shape, where at low concentrations, the loading is close to the maximum capacity. This rectangular type of isotherm is sometimes called an irreversible isotherm. It can be modelled by a Langmuir type isotherm with a large affinity term [45]. Figure 3 shows an example of a rectangular type isotherm (lysozyme adsorption on MCM-41) together with a more typical shape for Langmuir or Freundlich type reversible isotherms (trypsin adsorption on MCM-41).

Adsorption capacity depends on the affinity, or interactions, between the solute and adsorbent surface, which govern the mechanism by which the solutes are adsorbed, and which are affected by solution conditions (see Section 6). Figure 4 shows an example of lysozyme adsorption onto MCM-41 before and after surface modification. MCM-41 was surface modified with HMDS (hexamethyldisilazane), resulting in trimethylsilane moieties attached to the silica surface. This affects the surface interactions between the lysosyme and the MCM-41 surface, and results in a higher loading for the HMDS-modified MCM-41, despite the reduction in pore size [34].

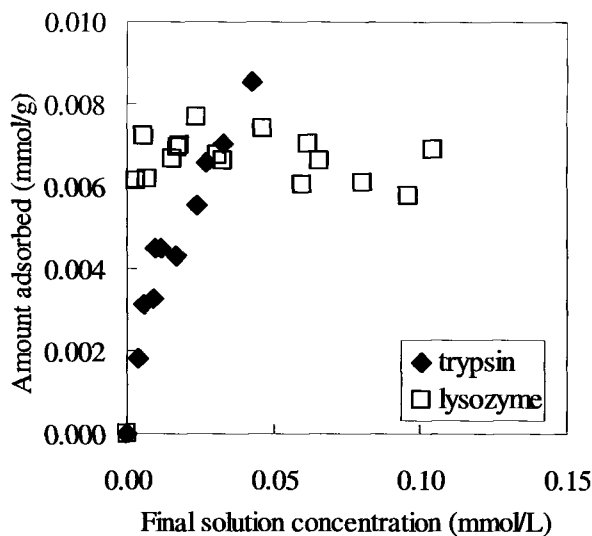


Figure 3. Adsorption isotherms for lysozyme and trypsin on MCM-41 in 0.1 M MES (2-[N-morpholino] ethane-sulfonic acid) buffer, pH 6, 48 h contact [38].

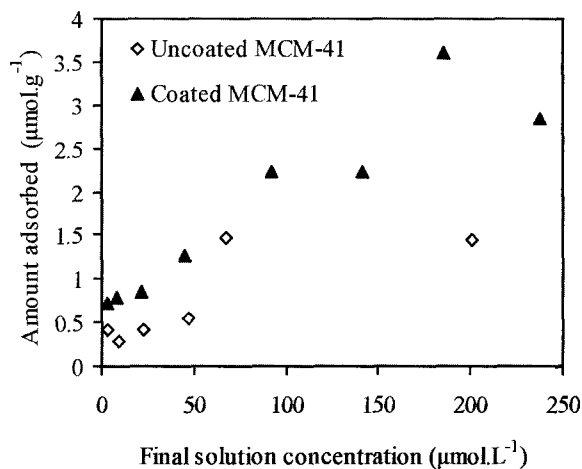


Figure 4. Amount of lysozyme adsorbed onto MCM-41 with and without surface modification with HMDS (96 h, pH 6) [34].

The capacity can also be influenced by other factors, for example, accessible surface area of the adsorbent. In porous solids, steric hindrance can limit the quantity of large molecules that can be adsorbed. Thus, the capacity will depend on the relation between the solute and pore sizes (see Sections 4 and 5).

Both the Langmuir and Freundlich equations describe equilibrium adsorption, i.e. when sufficient time has passed for the system to reach a point where the amount of solute adsorbed stays constant. For adsorption applications it is also important to study the adsorption kinetics, i.e., the rate of increase of loading as the system approaches equilibrium. Adsorption kinetics are important in both batch and column adsorption operations as they effect the required contact times and the time to breakthrough, respectively. These factors in turn influence the size of the contactors and the frequency of regeneration required.

Three steps can influence the rate of adsorption in porous particles:

1. Diffusion to the particle
2. Diffusion within the particle, i.e. in the pores
3. Reaction of the solute with the surface

The third step is generally only important for chemisorption, but not for physisorption, where no chemical reaction takes place. Therefore, adsorption in porous particles is generally diffusion controlled. Both diffusion towards, as well as within, the particle occur in a real system, but the slower step determines the rate of adsorption. [47][48].

Few authors have commented on the kinetics of adsorption of biological molecules on nanoporous silica. Some have tested adsorption at fixed contact times, while others have tried to establish that equilibrium was reached by making repeated measurements until the concentration remained constant. Studies investigating adsorption kinetics [33, 34, 38, 49, 50] found that the kinetics are faster for small solutes and slower for molecules close to pore size, as would be expected. Figure 5 shows lysozyme adsorption kinetics on MCM-41 and SBA-15. For both materials, equilibrium was reached after ca. 48 hours. It is also interesting to note the large capacity difference between these two adsorbents, attributed to the much larger pore size of the SBA-15 sample.

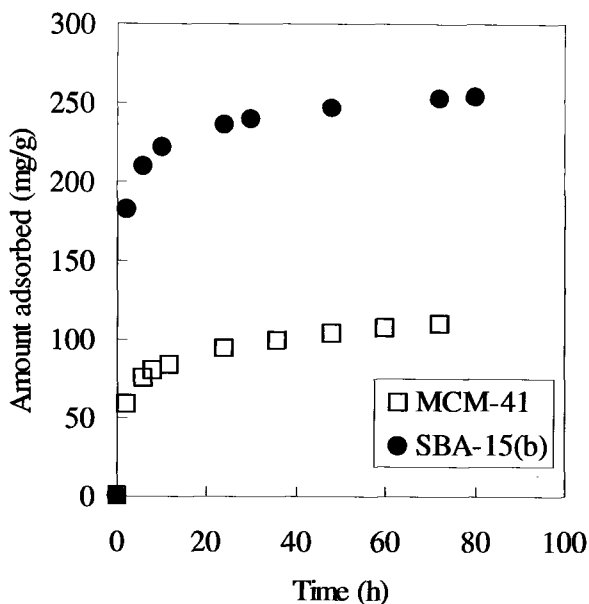


Figure 5. Kinetics of lysozyme adsorption on MCM-41 and SBA-15 [38].

4 Access to Pores

In the adsorption of biological molecules into nanoporous materials, the molecular dimensions often approach the pore diameter. Furthermore, there has been some uncertainty in determining the exact diameter of the nanoporous solids investigated by gas adsorption methods because the models used, such as the BJH model, did not adequately describe the materials' pore structures. For example, the BJH model was found to underpredict the diameter of MCM-41 by 25 - 30 % [51-53]. While more accurate models have been developed in recent years [54-56], these are not always applied.

The solute dimensions are also not straightforward to determine. Much of the data available on biomolecule sizes comes from crystallography data, and so the dimensions measured may differ from the actual dimensions of the molecules in solution. Moreover, some molecules undergo significant changes in size and shape depending on solution conditions (e.g., serum albumin may almost double its equivalent spherical radius if the solution pH decreases from 5 to 2.5) [57]. Proteins may also form dimers or higher aggregates under certain solution conditions which greatly alters their dimensions. Estimates of molecular sizes in solution

can be derived from measurements of partial specific volumes or diffusion coefficients of the molecules but these generally assume that the molecule is spherical, resulting in a calculated diameter that may not be a good representation of the molecular size for non-spherical molecules.

Whether or not a solute adsorbs into the pores of the adsorbent, or merely to the external surface of the particles remains a question that needs to be addressed. Surface access of the adsorbed molecule into the pores is inferred by some authors by comparing the loading of different pore size materials with the same solute or different size solutes on the same material. (see Section 5) or by calculating a theoretical loading, based on the area taken up by the molecule and comparing this to the internal and external surface areas of the adsorbent.

In an attempt to evaluate the extent of exterior surface adsorption of a protein onto MCM-48, Washmon-Kriel *et al.* [31] stirred a cytochrome c solution with as-synthesized MCM-48, which had its pores completely blocked with the surfactant template. It was determined that only a small amount was adsorbed onto the external surfaces (0.6mg/g as opposed to 11.8 mg/g on MCM-48 after calcination). Thus it was confirmed that only a small portion of the cytochrome c was adsorbed to the outer surfaces of the 0.5-1.0 μm diameter molecular sieve particles.

Another, more direct method to determine whether or not a solute was adsorbed into the pores of an adsorbent is the analysis of the material before and after adsorption by nitrogen physisorption to indicate the extent of pore filling [58-60]. It should be noted that material instability upon contact with water can also cause changes in gas adsorption isotherms, including decreases in pore volumes [40, 44, 61]. Drying the loaded adsorbent for gas adsorption analysis also alters the adsorbate volume and so changes in pore volumes cannot be used to quantitatively determine the amount of solute loaded. These factors need to be considered when investigating the loading of the solute into the pores by gas adsorption.

Adsorption of the protein, lysozyme, into the pores of MCM-41 was investigated by Yang *et al.* using nitrogen adsorption [60]. The molecular dimensions of the ellipsoidal lysozyme (4.3 x 2.5 x 1.9 nm [62] were similar to the pore diameter of the MCM-41 (BJH pore diameter 3.3 nm).

Figure 6 shows the nitrogen adsorption isotherms of MCM-41 before protein adsorption or solution contact, after 48 h in buffer solution and after protein adsorption from the same buffer solution [60]. It can be seen clearly that the volume of nitrogen adsorbed decreased markedly after protein adsorption, but did not decrease significantly after buffer contact in

the absence of the protein, indicating that the protein was adsorbed into the pores, causing a decrease in the pore volume.

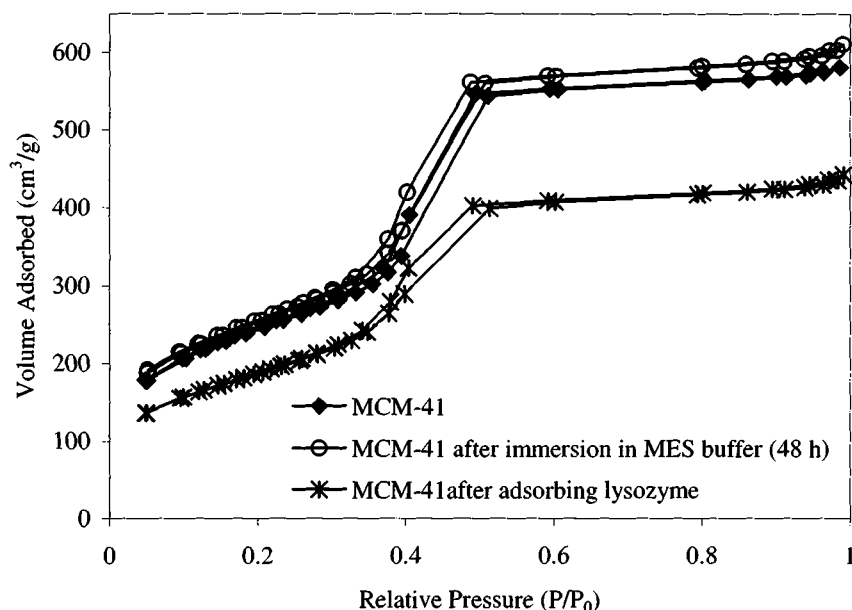


Figure 6. Nitrogen adsorption isotherms of MCM-41 before and after adsorption (48 h contact time) of lysozyme from MES buffer (0.1M, pH6) and after immersion in MES buffer (0.1M, pH6) alone for 48 hours [60].

Takahashi *et al.* [59] used of nitrogen adsorption isotherms to investigate the adsorption of an enzyme, horse radish peroxidase (HRP), into the pores of FSM. They showed that for the of varying pore diameters, smaller pore FSM materials did not change their pore volume upon adsorption, indicating that HRP could not enter the pores, whereas the larger pore materials showed decreased pore volumes, indicating that HRP was adsorbed in the pores. Furthermore, they reported that XRD confirmed that the FSM structure remained intact after adsorption.

Several authors have predicted better access into the three-dimensional, interconnected pore system of the cubic MCM-48 than into the parallel, unconnected channels of the hexagonal MCM-41 [63-66]. This would primarily be expected to influence diffusion and thus adsorption kinetics, but may also affect the adsorption capacity via pore blocking in the one dimensional structures. Studies comparing cytochrome c adsorption onto MCM-48, SBA-15 and MCM-41 under similar adsorption conditions (e.g.

contact time, solution concentration) found that MCM-48 adsorbed up to 50% more of the protein than the two hexagonal structures [30][31]. This was attributed to the pore structure being three-dimensional instead of one-dimensional. However, the surface area of the MCM-48 was significantly higher than that of the MCM-41 or SBA-15 samples used, which could at least partly explain the higher loadings observed.

5 Size Exclusion

The potential for size exclusion due to the narrow pore size distribution, one of the most distinguishing features of supramolecular templated nanoporous silica, has been investigated by a number of authors. Diaz *et al.* showed this via a strong correlation between enzyme size and loading onto MCM-41 (Figure 1) [27].

In a study previously discussed (see Section 2), Han *et al.* [23] investigated the size exclusion properties of APTS derivatized SBA-15 (5.9 nm pore size) and MCF (16 nm pore size). From a mixture of three anionic proteins of varying size with similar isoelectric points: conalbumin (MW 77,000, pI 6.0), chicken egg ovalbumin (MW 44,000, pI 4.9) and soybean trypsin inhibitor protein (MW 14,000, pI 5.2), APTS-SBA-15 sequestered and released the small trypsin inhibitor, while APTS-MCF sequestered and released all three proteins. APTS-SBA-15 also sequestered and released the large conalbumin to a small degree, and this was attributed to adsorption on the functionalised external surfaces of the particles.

Itoh *et al.* [43] demonstrated size exclusion by adsorption of chlorophyll a on FSM materials of varying pore size. Figure 7 clearly shows the influence of pore size on the amount adsorbed – the quantity adsorbed increased with the FSM pore diameter. Although the FSMs with different pore diameters had almost the same surface area, the amount of chlorophyll a adsorbed by FSM increased sharply above a pore diameter of 2 nm. This indicates a distinct size exclusion effect with chlorophyll a only adsorbing significantly into the pores of FSM when the pore diameter was greater than 2 nm.

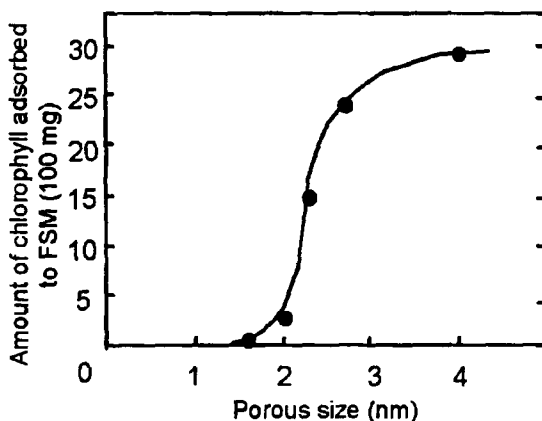


Figure 7: Relationship between the amount of chlorophyll adsorbed on FSM samples and the pore diameter of the FSM [43] - Reproduced by permission of The Royal Society of Chemistry.

The size selectivity of thiol-functionalized SBA-15 was demonstrated by Yiu *et al.* [37] using a number of proteins of varying diameter. Figure 8 shows the dimensions of the proteins, estimated from the Protein Databank [62], compared to the pore dimensions of the thiol-functionalized SBA-15.

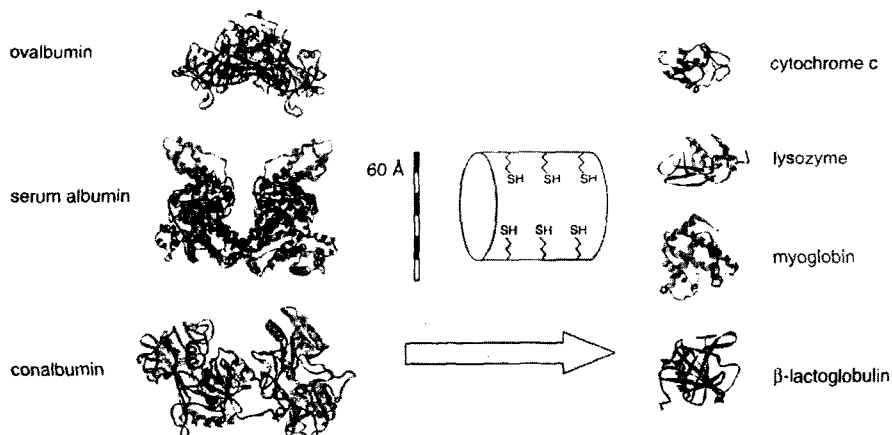


Figure 8. Schematic representation (to scale) comparing the proteins examined with the functionalised pores of SBA-15. The dimensions of the proteins were estimated from crystal structures available in the Protein Databank [62, 67]. Figure reproduced from [37] by permission of The Royal Society of Chemistry.

Figure 9 shows the extent of adsorption of these proteins on the nanoporous solid after contact overnight. Adsorption was found to increase dramatically with decreasing molecular size, with no significant amount of the three larger proteins, whose dimensions appear to be larger than the pore diameter, adsorbed.

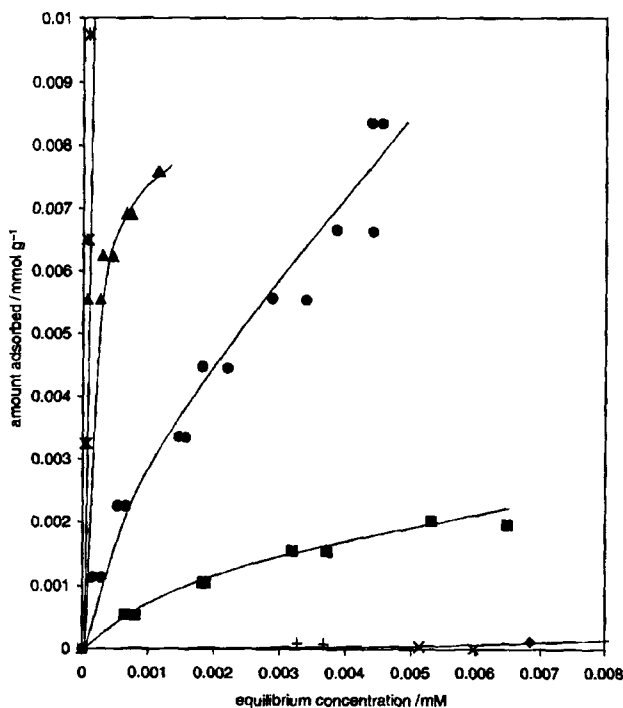


Figure 9: Adsorption of proteins on thiol-functionalised SBA-15 (pore size 5.1 nm) at 37°C. (Key: * cytochrome c, ▲ lysozyme, ● myoglobin, ■ β-lactoglobulin, ◆ ovalbumin, + bovine serum albumin, × conalbumin [37] - Reproduced by permission of The Royal Society of Chemistry.

These studies clearly indicate that separations based on size exclusion should be possible with nanoporous silica materials featuring narrow pore size distributions.

6 Adsorption Mechanisms

The mechanism involved in the adsorption of a particular kind of molecule onto an adsorbent material has implications both for the selectivity of the

adsorbent material, as well as the desorption of the molecule and regeneration of the material. While enzyme immobilisation studies are not particularly concerned with selectivity, they do tend to investigate desorption as an important and undesirable process: the leaching of immobilised enzyme into the treated solution has to be prevented as much as possible. One way of achieving this is silylation of the pore openings after adsorption of the enzyme into the pores [27], but this is obviously not applicable when the adsorbents are to be used for separations. Of more relevance here are studies of the interactions between enzymes and adsorbent surfaces, undertaken by looking at the factors influencing leaching or desorption.

Adsorption of biomolecules may occur through a range of attractive forces including electrostatic and hydrophobic interactions. For example, proteins are zwitterionic, meaning their net charge can be positive, negative or neutral, depending on the solution pH, and the way in which their charge varies with pH depends on their particular amino acid composition. They also contain hydrophobic amino acid residues to differing degrees which can interact with hydrophobic surfaces. However, it must be noted that proteins can be denatured by interactions with surfaces causing changes to their 3D conformation.

The silica surface can show both hydrophilic and organophilic (hydrophobic) characteristics, behaviour attributed to surface heterogeneity [68]. Furthermore, the surface silanol (hydroxyl) groups present on silica can carry a negative charge, depending on pH, and the pKa of these groups is about 6.5 [69]. Thus, the silica surface can interact with solute molecules in different ways, which may be classified as either hydrophobic/hydrophilic or electrostatic (i.e., related to the charges on silica surface and solute molecule). If the silica has been surface modified with functional groups these entities interact with the solute, potentially changing the affinity and adsorption mechanism. The adsorption mechanism of different solutes on nanoporous silica has been discussed in several studies, some of which are detailed below.

O'Connor *et al.* found that the adsorption of the amino acid lysine onto silicate MCM-41 (at pH 5.5 where the lysine is positively charged and the silica negatively charged) [41] decreased as the ionic strength of the solution was increased, Figure 10. This is consistent with an electrostatic adsorption mechanism, as added salt causes increased electrostatic shielding and competition for binding sites, and so reduces the amount of the cationic amino acid adsorbed.

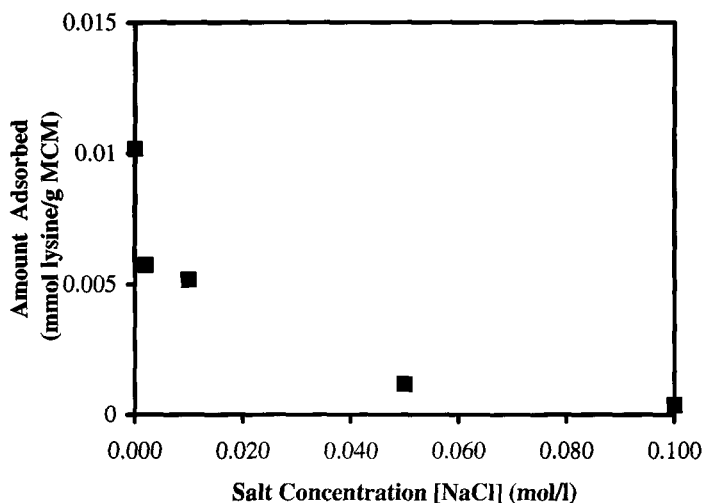


Figure 10. Lysine adsorption onto MCM-41 with different background salt concentrations (initial pH = 5.5, initial [lysine] = 0.30 mmol/L) [41].

Yiu *et al.* [35] found that trypsin was readily adsorbed onto MCM-41, MCM-48 and SBA-15 (although results suggested that for MCM-48 and MCM-41, adsorption only took place on the exterior particle surfaces, and trypsin did not fit into the pores). However, they found that large amounts of trypsin were leached from the supports upon contact with a pH 8 buffer solution, indicating only a weak interaction between the trypsin molecules and the surface of the supports. In order to achieve stronger binding for enzyme immobilization, Yiu *et al.* [36] derivatized SBA-15 samples with phenyl, amine, thiol, chloride or carboxylic acid functional groups. Upon contact with pH 8 buffer solution, strong retention of adsorbed trypsin was observed for acid and chloride functionalised solids, and moderate improvement for amine and thiol, whereas no difference in leaching was observed for phenyl-functionalized SBA-15. While a strong retention may prove difficult for separation applications, these results are relevant in terms of selectivity and binding mechanism. Yiu *et al.* discussed the surface interaction in particular for two of the attached groups. The alkyl chloride groups were thought to react with amine groups, which are available on the surface of the trypsin molecule. The -S-S-bonds on the surface of a trypsin molecule were thought to interact with the thiol groups on the molecular sieve surface, reducing the leaching.

Takahashi *et al.* [32] recently observed that larger levels of HRP (horse radish peroxidase) adsorption occurred on nanoporous silica templated with cationic surfactants (MCM-41 and FSM-16) than on materials templated with non-ionic triblock copolymers (SBA-15). They suggested that this was due to the higher level of negatively charged groups on the surface of the cationic-templated materials. To test this theory, Takahashi *et al.* [59] measured the amounts of cationic and anionic pigments adsorbed on the nanoporous silica materials. The adsorbed amounts of cationic methylene blue (MB) for the FSM-16 and MCM-41 materials were larger than those for the SBA-15 material. The adsorbed amounts of anionic sodium anthraquinone-2-sulfonic acid (ASS) were approximately equal for the three types of nanoporous silica materials. The adsorbed amounts of MB for the FSM-16 and MCM-41 materials were 2-3 times greater than those of ASS, while significant differences in the adsorbed amounts were not observed between MB and ASS for SBA-15. These results indicated that FSM-16 and MCM-41 tend to adsorb large amounts of cationic molecules, probably due to their synthesis with cationic surfactants.

In order to further investigate the electrostatic interactions, Takahashi *et al.* measured [59] amounts of HRP adsorbed on FSM-16 and SBA-15 across a wide range of solution pH values (Figure 11). They again found significant differences in the adsorption of HRP on cationic (FSM-16) and non-ionic (SBA-15) templated material. The large adsorbed amount of HRP in the lower pH regions decreased steeply with increasing pH from 3 to 6 and decreased more gradually in the higher pH region from 6 to 9. In the case of SBA-15, the adsorbed amounts were again much lower and no significant changes in the adsorbed amount with pH were observed. The titration curve for HRP showed that HRP molecules have a positive charge below pH 6 and the charge density decreases with increasing pH. Therefore, these results are consistent with electrostatic attraction between the positive charges on the HRP and negative charges on the FSM-16 surface.

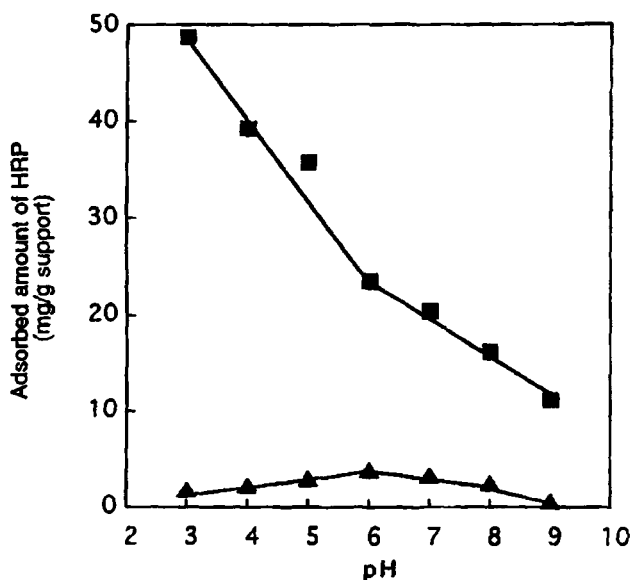


Figure 11. pH profiles of HRP adsorption to FSM-16/51 (■, pore diameter 5.1 nm) and SBA-15/50 (▲, pore diameter 5.0 nm). Reprinted with permission from [59], American Chemical Society.

These results demonstrate that the surface charges of nanoporous silica as well as those of the protein under the solution conditions in use must be taken into account in designing an adsorption process. Deere *et. al* [58] remarked that for adsorption to occur, the surface charges of the protein and of the MPS must be complementary, in addition to the requirement that the pore diameter be sufficiently large. In the solute/adsorbent combinations investigated, they found further evidence for electrostatic interactions being strong. Pepsin at pH 6.5, for example, is negatively charged and did not adsorb onto cyano-modified silicate (CNS) whereas subtilisin, which is of a similar size and bears an overall positive charge, was adsorbed. They also found that the amount of cytochrome c adsorbed on CNS decreased with increasing ionic strength. Furthermore, they reported that for protein adsorption on CNS, the iso-electric point (IEP) of a protein was an important factor, though other aspects contributed as well. They measured the adsorption of various proteins from solutions of known concentration and ionic strength at pH 6.5 as a function of the proteins' isoelectric points. At this pH, the CNS surface was negatively charged. For proteins with an IEP below 6.5, no significant

adsorption was recorded, while for proteins with an IEP above 6.5, the amount adsorbed generally increased with increasing IEP.

Ernst *et al.* [40] found evidence of electrostatic interactions being most important for amino acid adsorption on pure silica MCM-41C₁₄ (synthesised using surfactant with a 14 carbon chain). They investigated the influence of the pH value on the uptake of amino acids with an acidic (glutamic acid, pI = 3.24), a neutral (phenylalanine, pI = 5.48) and a basic side chain (lysine, pI = 9.82) by silica mesoporous MCM-41C₁₄ (Figure 12). A value of 3.2 for the point of zero charge (pzc) was determined for the nanoporous adsorbent. The adsorption of lysine starts at pH values of about 4 and increases up to pH = 10, where the limited stability of silica in alkaline solutions restricts further investigations. This behaviour was explained by electrostatic interactions between the amino acid and the adsorbent. For pH values above the pzc, the surface of MCM-41 becomes negatively charged. Because of its high pI of 9.82, lysine was positively charged over the whole pH range investigated in this study. This combination provided optimum conditions for ionic interactions. For phenylalanine, a maximum adsorption was reached for pH 4. The silica surface becomes more negatively charged with increasing pH, but for pH > pI the anionic form of phenylalanine predominates, which results in an increasing repulsion. Glutamic acid was hardly adsorbed over the whole pH range, because its isoelectric point almost coincides with the pzc of MCM-41. Only at pH 3 a minor adsorption could be detected. Hence, electrostatic interactions between deprotonated silanol groups on the surface of MCM-41 and the amino groups of the amino acid were proposed. This was in-line with the experimental findings in the same study that amino acids with negatively charged side chains were hardly adsorbed, whereas basic amino acids show very high affinities to MCM-41.

While Ernst *et al.* concluded from these result that electrostatic interactions dominated the adsorption mechanism, they found that hydrophobic interactions complement the electrostatic forces. They reported that the amount of amino acids bearing non-polar side chains adsorbed to MCM-41 increased with the chain length. These hydrophobic interactions were tentatively explained by the favourable geometry of the adsorption complex, which promotes interactions to neighbouring adsorbate molecules due to the marked curvature of the nanopores.

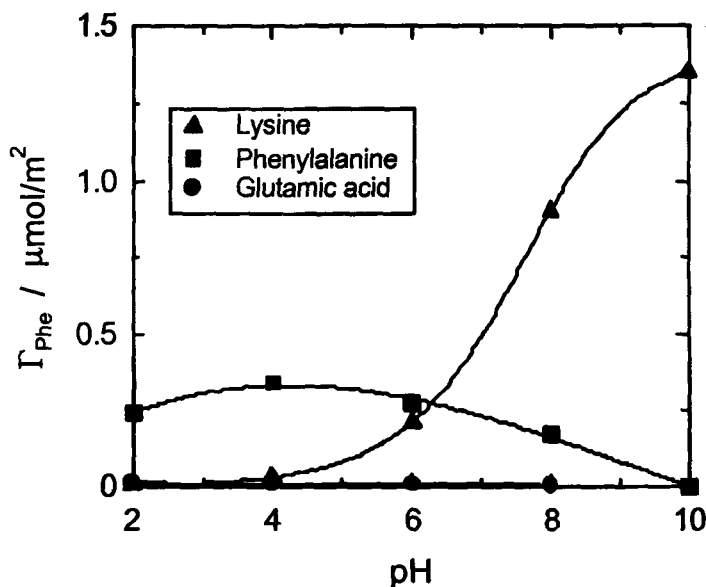


Figure 12. Influence of the pH on the adsorption of lysine, phenylalanine and glutamic acid on MCM-41C₁₄. Reprinted from [40], with permission from Elsevier Science.

As detailed in Section 2, *Han et al.* [23] demonstrated adsorption (sequestration) of anionic proteins onto SBA-15 and MCF, both surface modified by silylation with (3-aminopropyl)-triethoxysilane. The anionic proteins were absorbed readily, while lysozyme, a cationic protein at pH 7 was not adsorbed, demonstrating charge-based selectivity. The conalbumin was tightly associated with the MCF material, since repeated washing with H₂O failed to release any conalbumin. However, when the ionic strength was raised (0.5M phosphate buffer, pH 7), the sequestered protein was fully released back into solution, confirming an electrostatic adsorption mechanism.

In contrast to *Deere et al.* in their investigation of cytochrome c adsorption on cyano-modified nanoporous silica (CNS)[58], *Gimon-Kinsel et al.*[30] suggested for cytochrome c adsorption onto silica materials (MCM-48, MCM-41) that the enzyme-support interaction was dominated by hydrophobic/hydrophilic properties rather than electrostatic interactions. This was concluded from the fact that in leaching tests, silica MCM-41 exhibited a stronger retention of cytochrome c than aluminosilicate MCM-41.

For lysozyme adsorption on MCM-41 with and without trimethylsilane moieties on the surface, *Kisler et al.* reported increased loading for the

surface modified material (Figure 4). Since trimethylsilane moieties increase the hydrophobic character of the silica surface, this would indicate the importance of hydrophobic interactions..

From this variety of findings concerning adsorption mechanisms, it can be seen that for pure silica materials, both electrostatic and hydrophobic/hydrophilic interactions can play an important role, and that the exact nature of the interaction varies depending on the individual solutes, adsorbents, and solution conditions used. For surface modified materials, the nature of the attached group also strongly influences the interactions.

7 Regeneration and Reuse

In the development of a new adsorbent for separation processes, it is not enough to demonstrate its capacity and selectivity for adsorption of the target solutes. Methods also need to be developed to remove the adsorbed solute and regenerate the adsorbent. For biological solutes, methods like removal by calcination at high temperature could be possible. In a study on the immobilisation of microbial cells on aluminosilicate MCM-41, Tope *et al.* [28] reported that the cells could be removed and the material was regenerated by calcination at 600°C for 12 hours. They further reported that retention of the structural features of MCM-41 was confirmed by XRD after calcination, wherein no changes were observed.

While regeneration by calcination appears possible, it is likely not only to result in high energy costs, but also destroys the solute. This would only be acceptable if the aim was the removal of the solute as an impurity from a solution, or if further use of the solute is not desired. It would however not be feasible if, as is often the case, the solute it is a desired product that is adsorbed with the intent of recovery. Also, in the case of surface modified materials, any organic moieties attached to the surface would be damaged by high temperatures, and the surface modification would have to be repeated.

A more common and promising method is the elution of the adsorbed solute with an appropriate solvent or solution, with the aim of obtaining a concentrated solution. If an adsorption process is fully reversible, the desorption process follows the same isotherm as that for adsorption, whereas irreversible adsorption causes hysteresis between the adsorption and desorption isotherms.

For the selection of an efficient eluent, it is important to know the adsorption mechanism (see Section 6. Adsorption Mechanism). Where electrostatic interactions dominate, elution of the adsorbed solute may be facilitated by changing the pH or ionic strength of the eluent. In the case of hydrophobic interactions, it may be favourable to use eluents with a more hydrophobic character, e.g. organic solvents.

As described in Section 6, Han *et al.* [23] achieved elution by increasing the ionic strength to release sequestered proteins from APTS-SBA-15. Zhao *et al.* [24] have shown elution of biological molecules from C₁₈-SBA-15 in an HPLC column using phosphate buffer (pH 3.0) and Minakuchi *et al.* successfully separated polypeptides with a continuous silica rod column by reversed-phase acetonitrile-water linear gradient elution.

However, these articles have not discussed the effects of repeated use or the lifetime of the materials used. This is of major concern for the separation of biological molecules with nanoporous silica materials, since many biological molecules are processed in aqueous solutions, and nanoporous silica materials have been reported to lack stability, especially upon contact with moisture, as discussed below.

8 Stability

A key factor limiting the range of applications of nanoporous silica materials in general and M41S materials in particular, is their lack of stability [70]. Instability in this context is understood as irreversible damage to the structure of the material, most commonly shown by changes to the X-ray diffraction patterns and nitrogen adsorption isotherms.

The thermal, mechanical, chemical and hydrothermal stability of nanoporous silica materials have been investigated by a number of authors, with varying results, depending on a number of factors, e.g., wall thickness, synthesis conditions (pH, temperature, silica precursor). Some nanoporous silica materials showed a high thermal stability, with no damage to the structure for calcination temperatures up to 750°C [71] while others were shown to degrade at calcination temperatures above 550°C [70].

The mechanical stability of M41S materials at ambient conditions was shown to be low, which is problematic, e.g., for its application as chromatographic column packing [72]. However, it has been shown that damage to the structure of MCM-48 and MCM-41 under mechanical

compression is due adsorbed water, and that the structure was retained when the materials were compressed under nitrogen [73, 74].

The hydrolysis of Si-O-Si bonds, called siloxane bridges has been identified as the main mechanism causing structural damage to nanoporous silica materials. This mechanism has been confirmed, e.g., by the increase in the Q^3 (silanol group) signal in ^{29}Si MAS NMR after contact with water vapour overnight [75] and also after compression under air, but not under nitrogen [73]. It is believed that the hydrolysis takes place at so-called “strained” siloxane bridges, with energetically unfavourable bond angles, resulting for example from the condensation of neighbouring silanol groups upon calcination [11, 70, 76-78]. The formation of strained siloxane bridges is influenced by synthesis conditions (e.g. silica precursor, pH) and treatment of the materials. Efforts to increase the hydrothermal stability of these materials often involve strategies that facilitate a relaxation of the framework structure, e.g. pH control [77], post-synthesis restructuring [79] or the use of salt solution during synthesis [80, 81].

The wall thickness has also been identified as an important factor, with thicker walls enhancing the stability of the materials, and synthesis procedures resulting in thicker walls have been developed [76-78, 82]. Improved hydrothermal stability has been reported for a number of materials, usually tested by boiling the samples in water [79, 83, 84]. Pyrolytic carbon deposition has also been shown to increase stability of MCM-41 [85].

Structural damage has been reported when the hydrothermal stability of nanoporous silica materials was studied in contact with moist air or water vapour [72, 86-88] and upon storage at ambient conditions [77]. Some studies have focussed on the hydrothermal stability of the materials by assessing their structure before and after treatment in boiling water for up to 48 h [79, 80, 89-91].

However, for the application of nanoporous silica materials as adsorbents involving aqueous solutions, it is important that the pore structure is retained throughout repeated adsorption and regeneration cycles, generally performed around room temperature. Recent work has shown that the M41S materials are modified by prolonged exposure to water and water vapour, showing decreased structural regularity, pore shape uniformity, pore size and pore volume [75, 78, 87, 90, 92-94].

On solution contact, basic solutions in particular cause major loss of structure with much larger pores and decreased surface areas found in materials immersed for periods as short as several hours [76, 95]. This is consistent with the increased solubility of silica at basic pH [96]. Little

change was observed in the properties for materials exposed to neutral or acidic solutions over periods up to 48 hours [76, 95]. Water immersion was found to have greater impact on the structure as the temperature of the solution was increased in the range 298 - 373 K [97].

It appears that the low stability restricts the life of nanoporous silica materials, especially M41S materials, in aqueous solutions, and could limit the range of applications for these materials. Whether the increased stability of materials with thicker pore walls or improved synthesis procedures is sufficient to provide stability under separation conditions remains to be fully determined.

Modification of mesoporous silicates to include hydrophobic organic components on the pore surfaces or within the walls, either by co-condensation or post-synthesis grafting, has been found to improve their stability in the presence of water. Lim and Stein demonstrated that a vinyl-functionalised MCM-41 sample, prepared by post-synthesis grafting, had greater hydrothermal stability than untreated MCM-41 when placed in boiling water for 24 h [89]. However, the functionalised sample was still noticeably degraded in this time.

The most promising modification in terms of enhancing the stability seems to be the attachment of trimethylsilane moieties [73, 75, 82, 86, 93, 94]. This has also been shown to improve the materials' structural stability and thereby their mechanical stability under compression [78, 86, 92].

Organic modification of the surfaces of M41S materials appears to be a promising route for structural stabilisation as well as providing control over the surface chemistry of the materials, which may be used to enhance their separation selectivity.

9 Challenges Remaining

While nanoporous silica materials show promise for the separation of biological molecules, and monolithic silica columns developed by Nakanishi and co-workers [22] (see Section 2) are now commercially available, a number of challenges on the way to many commercial applications remain to be addressed.

Some separations have been demonstrated, but further data is needed, especially on separations from real process liquids. One of the major problems to be solved is the stability and lifetime of nanoporous silica materials upon prolonged exposure to aqueous solutions. Improved

materials will have to be tested under solution conditions relevant to biological processing and the lifetime of potential adsorbent materials will have to be investigated.

Reliable methods for regeneration of particular adsorbent materials with particular solutes need to be developed, based on the adsorption mechanisms in effect. The potential for re-use of the adsorbents also needs to be investigated, both in terms of the lifetime of the materials and maintenance of the adsorption capacity and selectivity of the materials over repeated cycles of adsorption and regeneration.

In industrial separation applications, it is likely that these materials will be used as packing for chromatography columns. In this case, particle sizes and morphology are important, as small particles would lead to large pressure drops and thus high energy requirements. While work on investigating different particle morphologies of nanoporous silica materials has been published by a number of authors [71, 98-106], the implications for separation processes remain to be studied. In addition, particle attrition needs to be limited and mechanical stability of the particles confirmed so that the pressure drop across the beds does not increase significantly during operations.

Finally, commercial issues including the costs and scale-up issues involved in the synthesis and surface modification processes, as well as the economics of the application of nanoporous materials as adsorbents competing with existing adsorbents and chromatography media will have to be investigated.

10 Concluding Remarks

Nanoporous silica materials, both with and without surface modification, have potential for the separation of biological applications. This is apparent from the variety of biological molecules that have been adsorbed onto various nanoporous silica materials. The ability of these adsorbent materials to separate molecules by size exclusion has been demonstrated clearly by a number of authors. Stability, especially for unmodified materials and control of particle morphology remain among the challenges that will need to be overcome for commercial application of these materials in separation processes to proceed. Further investigation of equilibrium adsorption and kinetics is necessary to fully understand the processes involved.

Though adsorption capacity has been shown to vary with the properties of the adsorbed molecule and the adsorbent in particular cases, the mechanisms governing adsorption for complex molecules require further elucidation. The selectivity of nanoporous adsorbents for particular solutes from mixtures has been demonstrated but the resolution achievable between molecules with similar properties has yet to be fully tested. Separations from real process liquors also remain to be demonstrated, but it seems that this is likely to be just a matter of time.

Once these challenges have been overcome and separations from real process liquors have been demonstrated, it will then be factors like costs involved and selectivity achieved that will determine whether adsorption of biological molecules with nanoporous materials can compete with or even replace the processes currently employed.

References

1. Keller W.D., *Clays*, in *Kirk-Othmer Encyclopaedia of Chemical Technology*, Wiley-Interscience: NY., 1979, pp. 190-206
2. Cabrera K., Lubda D., Eggenweiler H.M., Minakuchi H. and Nakanishi K., A new monolithic-type HPLC column for fast separations, *HRC Journal of High Resolution Chromatography* **23** (1)2000 pp. 93-99
3. IUPAC, M.o.S.a.T., IUPAC Manual of Symbols and Terminology, Appendix 2, Part 1, Colloid and Surface Chemistry, in *Pure Appl. Chem.* 1972, p. 578.
4. Kresge C.T., Leonowicz M.E., Roth W.J., Vartuli J.C. and Beck J.S., Ordered mesoporous molecular sieves synthesized by a liquid-crystal template mechanism, *Nature* **359** (1992) pp. 710-712.
5. Beck J.S. et al., A new family of mesoporous molecular sieves prepared with liquid crystal templates, *J. Am. Chem. Soc.* **114** (1992) pp. 10834-10843.
6. Yanagisawa T., Shimizu T., Kuroda K. and Kato C., The Preparation of Alkyltrimethylammonium-Kanemite Complexes and Their Conversion to Microporous Materials, *Bull. Chem. Soc. Jpn.* **63** (4) (1990) pp. 988-992.
7. Inagaki S., Fukushima Y. and Kuroda K., Synthesis of highly ordered mesoporous materials from a layered polysilicate, *J. Chem. Soc., Chem. Commun.* **8** (1993) p. 680
8. Ciesla U. and Schuth F., Ordered mesoporous materials, *Micropor. Mesopor. Mat* **27** (2-3) (1999) pp. 131-149.
9. Zhao D.Y., Feng J.L., Huo Q.S., Melosh N., Fredrickson G.H., Chmelka B.F. and Stucky G.D., Triblock Copolymer Syntheses of Mesoporous Silica With Periodic 50 to 300 Angstrom Pores, *Science* **279** (5350) (1998) pp. 548-552.
10. Schmidt-Winkel P., Lukens W.W. Jr., Zhao D., Yang P., Chmelka B.F., Stucky G.D., and U.o.C.S.B.C.A.U.S.A. Department of Chemistry Materials Research Laboratory, Mesocellular siliceous foams with uniformly sized cells and windows, *J. Am. Chem. Soc.* **121**(1) (1999) pp. 254-255.

11. Davidson A., Modifying the walls of mesoporous silicas prepared by supramolecular-templating, *Current Opinion in Colloid & Interface Science*, **7**(1-2) (2002) pp. 92-106.
12. Corma A., From Microporous to Mesoporous Molecular Sieve Materials and Their Use in Catalysis, *Chem. Rev.* **97**(6) (1997) pp. 2373 -2420.
13. Brunel D., Blanc A.C., Galarneau A. and Fajula F., New trends in the design of supported catalysts on mesoporous silicas and their applications in fine chemicals, *Catalysis Today* **73**(1-2) (2002) pp. 139-152.
14. Herbst J.A., Kresge C.T., Olson D.H., Schmitt K.D., Vartuli J.C. and Wang D.I.C., Method for separation of substances, 1995, Mobil Oil Corporation: US.
15. Grun M., Kuraganov A.A., Schacht S., Schuth F. and Unger K.K., Comparison of an ordered mesoporous aluminosilicate, silica, alumina, titania and zirconia in normal-phase high performance liquid chromatography, *Journal of Chromatography* **740** (1996) pp. 1-9.
16. Kim J.M., Kwak J.H., Jun S. and Ryoo R., Ion Exchange and Thermal Stability of Mcm-41, *Journal of Physical Chemistry* **99** (45) (1995) pp. 16742-16747.
17. Mercier L. and Pinnavaia T.J., Access in mesoporous materials: Advantages of a uniform pore structure in the design of a heavy metal ion adsorbent for environmental remediation, *Adv. Mater.* **9** (6) (1997) pp. 500-503.
18. Lee B., Kim Y., Lee H. and Yi J., Synthesis of functionalized porous silicas via templating method as heavy metal ion adsorbents: the introduction of surface hydrophilicity onto the surface of adsorbents, *Micropor. and Mesopor. Mater.* **50** (1) (2001) pp. 77-90.
19. Chen X.B., Feng X.D., Liu J., Fryxell G.E. and Gong M.L., Mercury separation and immobilization using self-assembled monolayers on mesoporous supports (SAMMS), *Sep. Sci. Technol.* **34** (6-7) (1999) pp. 1121-1132.
20. Valkama S., Maeki-Ontto R., Stamm M., ten Brinke G. and Ikkala O., eds. Mesoporous Polymeric Materials Based on Comb-Coil Supramolecules, *Studies in Surface Science and Catalysis*, ed. A. Sayari and M. Jaroniec, **141** (2002) Elsevier: Amsterdam.
21. Joo S.H., Jun S. and Ryoo R., Synthesis of ordered mesoporous carbon molecular sieves CMK-1, *Microporous and Mesoporous Materials* **44** (2001) pp. 153-158.
22. Nakanishi K., Minakuchi H., Soga N. and Tanaka N., Double pore silica gel monolith applied to liquid chromatography, *J. Sol-Gel Sci. Technol.* **8** (1-3) (1997) pp. 547-552.
23. Han Y.-J., Stucky G.D. and Butler A., Mesoporous Silicate Sequestration and Release of Proteins, *J. Am. Chem. Soc.* **121** (42) (1999) pp. 9897-9898.
24. Zhao J., Gao F., Fu Y., Jin W., Yang P. and D. Zhao D., Biomolecule separation using large pore mesoporous SBA-15 as a substrate in high performance liquid chromatography, *Chem. Commun.* **7** (2002) pp. 752-753.
25. Nakanishi K., Minakuchi H., Soga N. and Tanaka N., Structure design of double-pore silica and its application to HPLC, *J. Sol-Gel Sci. Technol.* **13** (1-3) (1998) pp. 163-169.
26. Nakanishi K., Shikata H., Ishizuka N., Koheiya N. and Soga N., Tailoring mesopores in monolithic macroporous silica for HPLC, *HRC Journal of High Resolution Chromatography* **23** (1) (2000) pp. 106-110.
27. Diaz J.F. and Balkus K.J., Enzyme Immobilization in Mcm-41 Molecular Sieve, *Journal of Molecular Catalysis B-Enzymatic* **2** (2-3) (1996) pp. 115-126.

28. Tope A.M., Srivinas N., Kulkarni S.J. and Jamil K., Mesoporous molecular sieve (MCM-41) as support material for microbial cell immobilization and transformation of 2,4,6-trinitrotoluene (TNT): a novel system for whole cell immobilization, *Journal of Molecular Catalysis B-Enzymatic* **16** (2001) pp. 17-26.
29. Deere J., Magner E., Wall J.G. and Hodnett B.K., Adsorption and activity of cytochrome c on mesoporous silicates, *Chem. Commun* **5** (2001) pp. 465-466.
30. Gimón-Kinsel M.E., Jiménez V.L., Washmon L. and Balkus K.J., Mesoporous Molecular Sieve Immobilized Enzymes, in *1st International Symposium on Mesoporous Molecular Sieves*, 1998. Baltimore: Elsevier Science.
31. Washmon-Kriel L., Jiménez V.L. and Balkus K.J., Cytochrome c immobilization into mesoporous molecular sieves, *J. Mol. Catal. B: Enzym* **10** (5) (2000) pp. 453-469.
32. Takahashi H., Li B., Sasaki T., Miyazaki C., Kajino T. and Inagaki S., Immobilized enzymes in ordered mesoporous silica materials and improvement of their stability and catalytic activity in an organic solvent, *Micropor. and Mesopor. Mater.* **44** (2001) pp. 755-762.
33. Kisler J., Daehler A., Stevens G.W. and O'Connor A.J., Separation of Biological Molecules using Mesoporous Molecular Sieves, *Micropor. and Mesopor. Mater.* **44-45** (2001) pp. 769-774.
34. Kisler J., Stevens G.W. and O'Connor A.J., Adsorption of Proteins on Mesoporous Molecular Sieves, *Materials Physics and Mechanics* **4** (2) (2001) pp. 89-93.
35. Yiu H.H.P., Wright P.A. and Botting N.P., Enzyme immobilisation using siliceous mesoporous molecular sieves, *Micropor. Mesopor. Mater.* **44** (Special Issue SI) (2001) pp. 763-768.
36. Yiu H.H.P., Wright P.A., and Botting N.P., Enzyme immobilisation using SBA-15 mesoporous molecular sieves with functionalised surfaces, *Journal of Molecular Catalysis B-Enzymatic* **15** (1-3) (2001) pp. 81-92.
37. Yiu H.H.P., Botting C.H., Botting N.P. and Wright P.A., Size selective protein adsorption on thiol-functionalised SBA-15 mesoporous molecular sieve, *Phys. Chem. Chem. Phys* **3** (15) (2001) pp. 2983-2985.
38. Yang J., Daehler A., Stevens G.W. and O'Connor A.J., Adsorption of Lysozyme and Trypsin onto Mesoporous Silica Materials, in *3rd International Mesoporous Materials Symposium (IMMS 2002)*, 2002. Jeju, Korea.
39. Minakuchi H., Ishizuka N., Nakanishi K., Soga N. and Tanaka N., Performance of an octadecylsilylated continuous porous silica column in polypeptide separations, *Journal of Chromatography* **828** (1-2) (1998) pp. 83-90.
40. Ernst S., Harmann M. and Munsch S., Adsorption of selected amino acids from aqueous solutions on mesoporous molecular sieves. in 13th International Zeolite Conference, 2001, Montpellier, France.
41. O'Connor A.J., Hokura A., Kisler J.M., Shimazu J., Stevens G.W. and Komatsu Y., Amino acid adsorption from solution onto siliceous MCM-41, in preparation.
42. El Shafei G.M.S., Effect of pore structure on surface characteristics of zirconium phosphate-modified silica, *Journal of Colloid & Interface Science* **250** (2) (2002) pp. 394-399.

43. Itoh T., Yano K., Inada Y. and Fukushima Y., Stabilization of chlorophyll a in mesoporous silica and its pore size dependence, *Journal of Materials Chemistry* **12** (11) (2002) pp. 3275-3277.
44. Daehler A., Stevens G.W. and O'Connor A.J. Biochemical Separations via Mesoporous Molecular Sieves, in *6th World Congress of Chemical Engineering*, September 2001. 2001, Melbourne, Australia: IEAust.
45. Do D.D., Adsorption Analysis: Equilibria and Kinetics, 1998, London: Imperial College Press.
46. Coulson J.M., Richardson J.F., Backhurst J.R. and Harker J.H., *Chemical Engineering, Volume 2, Particle Technology & Separation Processes*, 4th ed. Chemical Engineering. 1991.
47. Helfferich F.G., *Ion exchange*. 1962, New York: McGraw-Hill.
48. Levenspiel O., Chapter 25 Fluid-Particle Reactions: Kinetics, in *Chemical Reaction Engineering*, 1999, John Wiley & Sons: New York .
49. Kisler J., Stevens G.W. and O'Connor A.J., Protein Adsorption on Mesoporous Silicates, in *Chemeca '99*. 1999. Newcastle: The Institution of Engineers Australia.
50. Kisler J., Stevens G.W. and O'Connor A.J., Mesoporous Molecular Sieves as Adsorbents for Bioseparations, in *13th International Zeolite Conference*, 2001. Montpellier, France.
51. Schumacher K., Ravikovitch P.I., Chesne A.D., Neimark A.V. and Unger K.K., Characterization of MCM-48 Materials, *Langmuir* **16** (10) (2000) pp. 4648-4654.
52. Ravikovitch P.I., Wei D., Chueh W.T., Haller G.L. and Neimark A.V., Evaluation of Pore Structure Parameters of MCM-41 Catalyst Supports and Catalysts By Means of Nitrogen and Argon Adsorption, *J. Phys. Chem. B* **101** (19) (1997) pp. 3671-3679.
53. Neimark A.V., Ravikovitch P.I., Grun M., Schuth F. and K.K. Unger K.K., Pore Size Analysis of MCM-41 Type Adsorbents By Means of Nitrogen and Argon Adsorption, *J. Colloid Interface Sci.* **207** (1) (1998) pp. 159-169.
54. Kruk M. and Jaroniec M., Accurate method for calculating mesopore size distributions from argon adsorption data at 87 K developed using model MCM-41 materials, *Chemistry of Materials* **12** (1) (2000) pp. 222-230.
55. Kruk M., Jaroniec M., Sakamoto Y., Terasaki O., Ryoo R. and Ko C.H., Determination of pore size and pore wall structure of MCM-41 by using nitrogen adsorption, transmission electron microscopy, and X-ray diffraction, *J. Phys. Chem. B* **104** (2) (2000) pp. 292-301.
56. Sonwane C.G. and Bhatia S.K., Characterization of pore size distributions of mesoporous materials from adsorption isotherms, *J. Phys. Chem. B* **104** (39) (2000) pp. 9099-9110.
57. Tanford C., Buzzell J.G., Rands D.G. and Swanson A., The reversible expansion of bovine serum albumin in acid solutions, *J. Am. Chem. Soc.* **77** (1955) pp. 6421.
58. Deere J., Magner E., Wall J.G. and Hodnett B.K., Mechanistic and Structural Features of Protein Adsorption onto Mesoporous Silicates, *J. Phys. Chem. B* **106** (29) (2002) pp. 7340-7347.

59. Takahashi H., Li B., Sasaki T., Miyazaki C., Kajino T. and Inagaki S., Catalytic activity in organic solvents and stability of immobilized enzymes depend on the pore size and surface characteristics of mesoporous silica, *Chemistry of Materials* **12** (11) (2000) pp. 3301-3305.
60. Yang J., Stevens G.W. and O'Connor A.J., *Unpublished data*.
61. Chen L.Y., Jaenicke S. and Chuah G.K., Thermal and hydrothermal stability of framework-substituted MCM-41 mesoporous materials, *Micropor. Mater.* **12** (4-6) (1997) pp. 323-330.
62. The dimensions of the protein molecules were measured using Swiss-PdbViewer v3.51 (Glaxo Wellcome Experimental Research) and the structures of the molecules were downloaded from Protein Databank (www.pdb.org).
63. Oye G., Sjoblom J. and Stocker M., Synthesis and characterization of siliceous and aluminum-containing mesoporous materials from different surfactant solutions, *Micropor. Mesopor. Mater.* **27** (2-3) (1999) pp. 171-180.
64. Morey M.S., Davidson A. and Stucky G.D., Silica-based, cubic mesostructures: Synthesis, characterization and relevance for catalysis, *Journal of Porous Materials* **5** (3-4) (1998) pp. 195-204.
65. Gallis K.W. and Landry C.C., Synthesis of Mcm-48 By a Phase Transformation Process, *Chemistry of Materials* **9** (10) (1997) pp. 2035 ff.
66. Xu J., Luan Z.H., He H.Y., Zhou W.Z. and Kevan L., A Reliable Synthesis of Cubic Mesoporous Mcm-48 Molecular Sieve, *Chemistry of Materials* **10** (11) (1998) pp. 3690-3698.
67. Berman H.M., Westbrook J., Feng Z., Gilliland G., Bhat T.N., Weissig H., Shindyalov I.N. and Bourne P.E., The Protein Data Bank, (Research Collaboratory for Structural Bioinformatics Protein Data Bank, RCSB PDB, <http://www.pdb.org/>). *Nucleic Acids Research*, 2000 **28** (2000) pp. 235-242.
68. Zhao X.S., Lu G.Q., and Hu X., Organophilicity of MCM-41 adsorbents studied by adsorption and temperature-programmed desorption, *Colloid Surf. A-Physicochem. Eng. Asp.* **179** (2-3) (2001) pp. 261-269.
69. Falcone J.S. Jr, Silcon Compounds, in *Kirk-Othmer Encyclopaedia of Chemical Technology* 1982, Wiley-Interscience: NY. pp. 855-880.
70. Cassiers K., Linssen T., Mathieu M.B.M., Schrijnemakers K., Van Der Voort P., Cool P. and Vansant E.F., A Detailed Study of Thermal, Hydrothermal, and Mechanical Stabilities of a Wide Range of Surfactant Assembled Mesoporous Silicas, *Chem. Mater.* **14** (5) (2002) pp. 2317-2324.
71. Schumacher K., Grun M. and Unger K.K., Novel synthesis of spherical MCM-48, *Micropor. Mesopor. Mater.* **27** (2-3) (1999) pp. 201-206.
72. Broyer M. and Valange J.P.B.S., Bertrand O., Weber G. and Gabelica Z., Influence of Aging, Thermal, Hydrothermal, and Mechanical Treatments on the Porosity of MCM-41 Mesoporous Silica, *Langmuir* **18** (13) (2002) pp. 5083-5091.
73. Tatsumi T., Koyano K.A., Tanaka Y. and Nakata S., Mechanical stability of mesoporous materials, MCM-48 and MCM-41, *Journal of Porous Materials* **6** (1) (1999) pp. 13-17.
74. Tatsumi T., Koyano K.A., Tanaka Y. and Nakata S., Mechanochemical Collapse of M41s Mesoporous Molecular Sieves Through Hydrolysis of Siloxane Bonds, *Chemistry Letter*, **5** (1997) pp. 469-470.

75. Zhao X.S., Audsley F. and Lu G.Q., Irreversible Change of Pore Structure of Mcm-41 Upon Hydration At Room Temperature, *J. Phys. Chem. B* **102** (21) (1998) pp. 4143-4146.
76. Landau M.V., Varkey S.P., Herskowitz M., Regev O., Pevzner S., Sen T. and Luz Z., Wetting stability of Si-MCM-41 mesoporous material in neutral, acidic and basic aqueous solutions, *Micropor. Mesopor. Mater.* **33** (1-3) (1999) pp. 149-163.
77. Edler K.J. and White J.W., Preparation dependent stability of pure silica MCM-41, *Journal of Materials Chemistry* **9** (10) (1999) pp. 2611-2615.
78. Van der Voort P., Mathieu M. and Vansant E.F., Active MCM-48 supported catalysts: different strategies to increase the structural and chemical stability, in *13th International Zeolite Conference: Zeolites and Mesoporous Materials at the Dawn of the 21st Century*, 2001, Montpellier, France: Elsevier.
79. Chen L.Y., Horiuchi T., Mori T. and Maeda K., Postsynthesis hydrothermal restructuring of M41S mesoporous molecular sieves in water, *J. Phys. Chem. B* **103** (8) (1999) pp. 1216-1222.
80. Kim J.M., Jun S. and Ryoo R., Improvement of hydrothermal stability of mesoporous silica using salts: reinvestigation for time-dependent effects, *J. Phys. Chem. B* **103** (30) (1999) pp. 6200-6205.
81. Yu J., Shi J.L., Chen H.R., Yan J.N. and Yan D.S., Effect of inorganic salt addition during synthesis on pore structure and hydrothermal stability of mesoporous silica, *Micropor. and Mesopor. Mater.* **46** (2-3) (2001) pp. 153-162.
82. Stein A., Melde B.J. and Schroden R.C., Hybrid inorganic-organic mesoporous silicates - nanoscopic reactors coming of age, *Adv. Mater.* **12** (19) (2000) pp. 1403-1419.
83. Mokaya R., Hydrothermally stable restructured mesoporous silica, *Chem. Commun.* **10** (2001) pp. 933-934.
84. Zhang Z.T. et al., Mesoporous aluminosilicates with ordered hexagonal structure, strong acidity, and extraordinary hydrothermal stability at high temperatures, *J. Am. Chem. Soc.* **123** (21) (2001) pp. 5014-5021.
85. Carrott M., Candeias A.J.E., Carrott P.J.M., Sing K.S.W. and Unger K.K., Stabilization of MCM-41 by pyrolytic carbon deposition, *Langmuir* **16** (24) (2000) pp. 9103-9105.
86. Koyano K.A., Tatsumi T., Tanaka Y. and Nakata S., Stabilization of Mesoporous Molecular Sieves By Trimethylsilylation, *J. Phys. Chem. B* **101** (46) (1997) pp. 9436-9440.
87. Carrott M., Candeias A.J.E., Carrott P.J.M. and Unger K.K., Evaluation of the stability of pure silica MCM-41 toward water vapor, *Langmuir* **15** (26) (1999) pp. 8895-8901.
88. Zhao X.S., Lu G.Q., and Hu X., Characterization of the structural and surface properties of chemically modified MCM-41 material, *Micropor. and Mesopor. Mater.* **41**(1-3) (2000) pp. 37-47.
89. Lim M.H. and Stein A., Comparative studies of grafting and direct syntheses of inorganic-organic hybrid mesoporous materials, *Chemistry of Materials* **11** (11) (1999) pp. 3285-3295.
90. Yamamoto K. and Tatsumi T., Organic functionalization of mesoporous molecular sieves with Grignard reagents, *Micropor. and Mesopor. Mater.* **44** (2001) pp. 459-464.

91. Jun S., Kim J.M., Ryoo R., Ahn Y.S. and Han M.H., Hydrothermal stability of MCM-48 improved by post-synthesis restructuring in salt solution, *Micropor. Mesopor. Mater.* **41** (1-3) (2000) pp. 119-127.
92. Igarashi N., Tanaka Y., Nakata S. and Tatsumi T., Increased Stability of Organically Modified MCM-41 Synthesized by a One-step Procedure, *Chemistry Letters* **1** (1999) pp. 1-2.
93. Kisler J.M., Stevens G.W. and O'Connor A.J., Adsorption of proteins on mesoporous molecular sieves, *Materials Physics and Mechanics* **4** (2) (2001) pp. 89-93.
94. Yang J., Daehler A., Stevens G.W. and O'Connor A.J., Improving the Hydro-Stability of MCM-41 by Post-Synthesis Treatment and HMDS Coating, in *NANOPOROUS MATERIALS-III*. 2002. Canada: Elsevier, Amsterdam.
95. Trong On D., Zaidi S.M.J., and Kaliaguine S., Stability of mesoporous aluminosilicate MCM-41 under vapor treatment, acidic and basic conditions, *Micropor. and Mesopor. Mater.* **22** (1-3) (1998) pp. 211-224.
96. Iler R.K., The chemistry of silica : solubility, polymerization, colloid and surface properties, and biochemistry, 1979, New York: Wiley,.
97. Ryoo R. and Jun S., Improvement of Hydrothermal Stability of MCM-41 Using Salt Effects During the Crystallization Process, *J. Phys. Chem. B* **101** (3) (1997) pp. 317-320.
98. Ogawa M. and Yamamoto N., Preparation of blow-molded macroscopic bubbles of mesoporous silica by a supramolecular templating approach, *Langmuir* **15** (6) (1999) pp. 2227-2229.
99. Lin H.P., Cheng Y.R. and Mou C.Y., Hierarchical order in hollow spheres of mesoporous silicates, *Chemistry of Materials* **10** (12) (1998) pp. 3772 ff.
100. Grun M., Unger K.K., Matsumoto A. and Tsutsumi K., Novel pathways for the preparation of mesoporous MCM-41 materials: control of porosity and morphology, *Micropor. Mesopor. Mater.* **27** (2-3) (1999) pp. 207-216.
101. Grun M., Lauer I. and Unger K.K., The Synthesis of Micrometer- and Submicrometer-Size Spheres of Ordered Mesoporous Oxide MCM-41, *Adv. Mater.* **9** (3) (1997) p. 254
102. Schulz-Ekloff G., J. Rathousky J. and Zukal A., Controlling of morphology and characterization of pore structure of ordered mesoporous silicas, *Micropor. Mesopor. Mater.* **27** (2-3) (1999) pp. 273-285.
103. Tanev P.T. and Pinnavaia, T.J., Mesoporous Silica Molecular Sieves Prepared By Ionic and Neutral Surfactant Templating - a Comparison of Physical Properties, *Chemistry of Materials* **8** (8) (1996) pp. 2068-2079.
104. Yu J., Shi J.L., Wang L.Z., Ruan M.L. and Yan D.S., Preparation of high thermal stability MCM-41 in the low surfactant/silicon molar ratio synthesis systems, *Mater. Lett.* **48** (2) (2001) pp. 112-116.
105. Zhang W.Z., Pauly T.R. and Pinnavaia T.J., Tailoring the framework and textural mesopores of HMS molecular sieves through an electrically neutral (s-degrees-i-degrees) assembly pathway, *Chemistry of Materials* **9** (11) (1997) pp. 2491-2498.

106. Pauly T.R., Liu Y., Pinnavaia T.J., Billinge S.J.L. and Rieker T.P., Textural mesoporosity and the catalytic activity of mesoporous molecular sieves with wormhole framework structures, *J. Am. Chem. Soc.* **121** (38) (1999) pp. 8835-8842.

NANOPOROUS MATERIALS AS SUPPORTS FOR ENZYME IMMOBILIZATION

HUMPHREY H.P. YIU AND PAUL A. WRIGHT

*School of Chemistry, the Purdie Building, University of St Andrews, St. Andrews, Fife,
Scotland, U.K. KY16 9ST
E-mail: paw2@st-and.ac.uk*

The investigation of the potential use of mesoporous molecular sieves in biochemistry and biotechnology began in the late 1990s when the mesoporous silica MCM-41 was used to immobilize selected enzymes. The synthesis of a range of well defined, ordered mesoporous solids with pore sizes of up to 100 Å and beyond has further stimulated research in this area. The pore dimensions of these solids match the molecular size of many biomolecules, and they have potential applications in the size selective separation of proteins and the immobilization of enzymes. As supports for enzyme immobilization, mesoporous solids provide high surface areas and pore volumes to permit relatively high enzyme loading whilst permitting the enzymes to retain their activity. The materials chemistry of these solids has been extensively researched, giving rise to mesoporous solids with a range of different physical and chemical properties that make 'tailored' supports for enzyme immobilization a real possibility. In particular, the surface properties can be modified by functionalization to improve the retention of the enzyme molecules within the pore space. Examples of enzymes that have been successfully immobilized include proteases, lipases and peroxidases.

1 Introduction

Efforts have been made to immobilize enzymes since the 1950s [1]. The continuing aim of such work is to permit the use, recovery and re-use of expensive enzymes in chemical transformations and fine chemicals syntheses.

Immobilized enzymes can be considered to be heterogeneous catalysts. Supported catalysts of this type are convenient to handle compared with free enzymes. Also, they can readily be separated from the reaction solution and can be stored and recycled. Immobilization can improve stability in the case of protease enzymes by reducing the effects of autolysis, and can more generally reduce protein aggregation. Immobilized enzymes may show improved stability to the effects of heat and chemical deactivation. Furthermore, it should be possible to use immobilized enzymes to catalyze transformations in organic solvents in which the native enzyme would be insoluble. This will lead to alternative product

distributions to those available in aqueous media. In some cases, an increase in activity can be observed upon immobilization [2] but in general immobilization causes a loss in activity due to restricted mass transfer of reactants and products. It is therefore of great interest to control the surface area, surface chemistry and porosity of the support. Although production costs of tailored supports are likely to be higher than for standard high area silicas, they could readily be compensated for by improved performance.

Supports for enzyme immobilization can be organic or inorganic. Inorganic carriers include silica gel, glass, alumina, clay minerals and zeolites, and oxides of transition metals (e.g. NiO, TiO₂, ZrO₂). Natural polymers (e.g. carbohydrates) and functionalized synthetic polymers (e.g. polystyrene and nylon) are employed as organic carriers. [3]

The discovery of mesoporous solids by Mobil [4,5] and separately by Yanagisawa et. al. in the early 1990s, [6] followed by research at Santa Barbara [7, 8] and elsewhere has given rise to a range of well ordered porous solids with pore sizes in the nanometer size range. It was quickly realized that such materials could possess ideal characteristics as well defined enzyme supports. [9] In this chapter, the current state of research into the immobilization of enzymes onto nanoporous inorganic solids is reviewed.

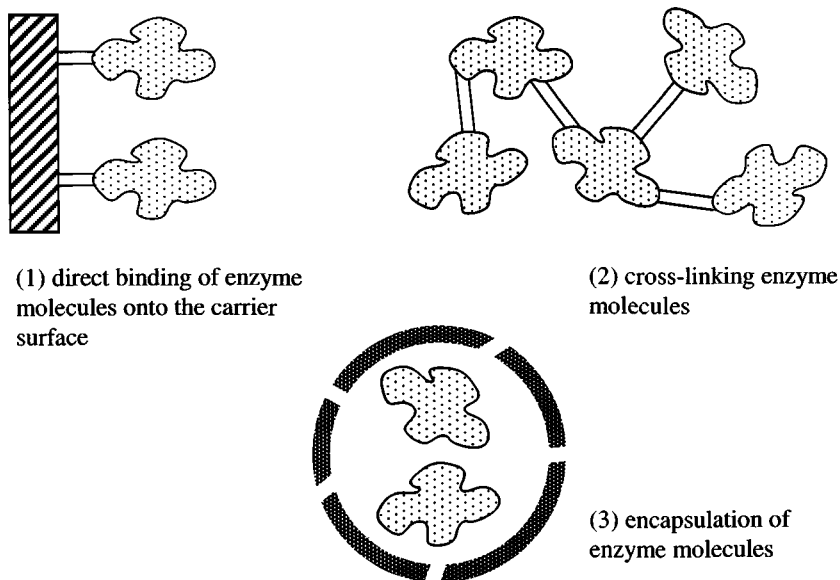


Figure 1. Three commonly used methods for enzyme immobilization.

2 Immobilization methods for enzymes

There is considerable literature on methods for enzyme immobilization since the 1980's [3, 10, 11]. Figure 1 shows three of the most commonly used immobilization method for enzymes: (1) direct binding of enzyme molecules to the carrier surface, (2) cross-linking enzyme molecules, and (3) encapsulation of enzyme molecules. All methods have their advantages and disadvantages and the choice depends on the nature of the target enzyme and the reaction conditions. In addition to these methods, it is also possible to support enzymes by physically adsorbing them on supports, for example by electrostatic interactions where the enzyme and the support carry opposite charges under the conditions of immobilization and use.

Table 1. Parameters to be considered for enzyme immobilization.

	Parameters to be considered	Examples
Enzyme	Biochemical properties	MW, functional groups on the molecule surface, surface charge, purity
	Kinetic parameters	Specific activity, pH and temperature profiles, solvents
Carrier	Chemical characteristics	Compositions, functional groups, pore size, stability, surface charge
	Mechanical properties	Flow resistance, single particle compression behavior
Immobilized enzyme	Immobilization methods	Yield of active enzyme
	Mass transfer effects	External and internal diffusion
	Stability	Operational stability, storage stability
	Performance	Productivity, enzyme consumption

In enzyme immobilization, a suitable choice for a carrier is critical and the activity of the final composite could be affected. The chemical and physical properties of the carriers must be considered in making the correct choice. These properties include the chemical basis of the carrier, their functional groups on the surface, porosity, particle size and morphology. Table 1 summarizes the basic parameters for enzyme immobilization.

There are several ways to immobilize an enzyme molecule onto the surface of a carrier:

1. The enzyme molecule is carefully modified and activated before binding. This method may cause denaturation of the enzyme due to the chemical process involved during modification.
2. The surface of the carrier is modified and activated. An unmodified enzyme is then bound to the carrier surface by simple adsorption or covalent bonding. This is the most popular method in enzyme immobilization.
3. A multi-functional agent is used as a *bridge* to link between the surface of the carrier and the enzyme molecules.
4. With the use of recombinant DNA technology, the enzyme is modified to possess bio-specific groups which allow the enzyme molecule to be adsorbed onto specific carriers via *bio-affinity* binding.

In this chapter we concentrate on method 2, in which the enzyme is bound to the internal surface of the nanoporous carrier by adsorption or covalent bonding.

3 General considerations in the application of nanoporous materials for enzyme immobilization

The development of nanoporous materials has provided a new class of potential carriers for immobilized enzymes. The range of materials with their wide variation of chemical and physical properties gives scientists a wide choice. As well as pore size (below), material may be prepared with different framework compositions (silica, titania, etc.) and a range of surface functionalities (such as thiol, carboxylic acid, amines, etc.).

Since nanoporous materials all have well defined pore dimensions, the use of any particular material as a high surface area carrier is limited to enzyme molecules smaller than the pore size, or, if the solid contains cages, smaller than the size of the connecting windows between cages.

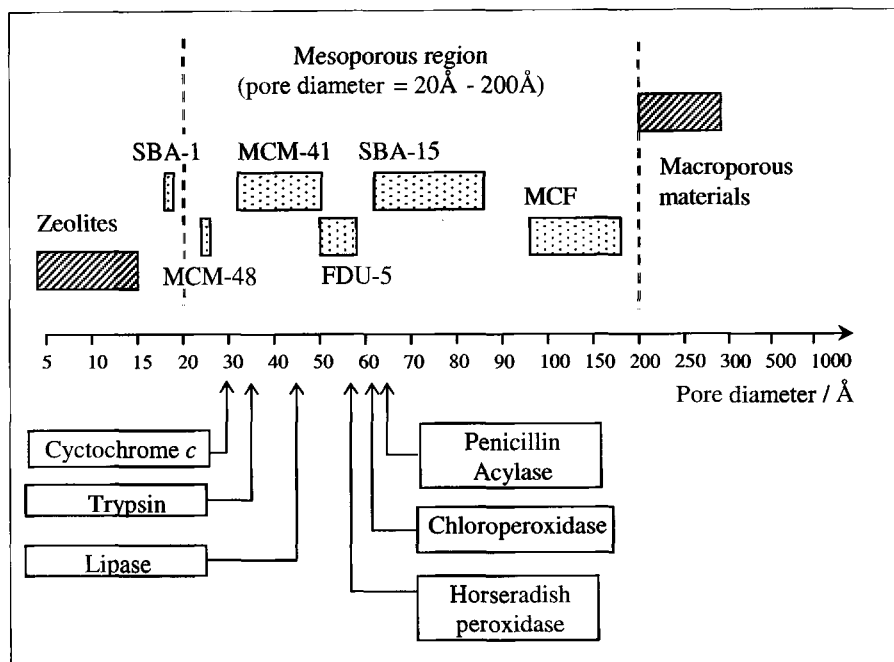


Figure 2. Comparison of the pore size of some nanoporous materials and the average molecular size of some commonly used enzymes. The average molecular size of the enzymes was measured with Swiss pdb view v7 software (available from ca.expasy.org).

If the size of the enzyme molecules is considerably larger than the pore size of the carrier, then immobilization can only occur on its outer surface. The ideal choice of nanoporous carriers to permit high loadings of a target enzyme on the internal surfaces must take into account the unique character of their porosity. Figure 2 shows the pore size of the some well-known nanoporous materials and compares them with the average spherical dimension of a few selected enzymes. In some cases, however, microporous solids have been used as supports. In these cases it is the interaction of the enzymes with the external surfaces that are important.

4 Microporous molecular sieves as carriers

Zeolites have been used to immobilise enzymes, their use as carriers for enzymes being limited to their outer surfaces, which provide hydrophilic groups suitable for enzyme immobilization. Some commonly used zeolites such as zeolites A and X are commercially available and not costly.

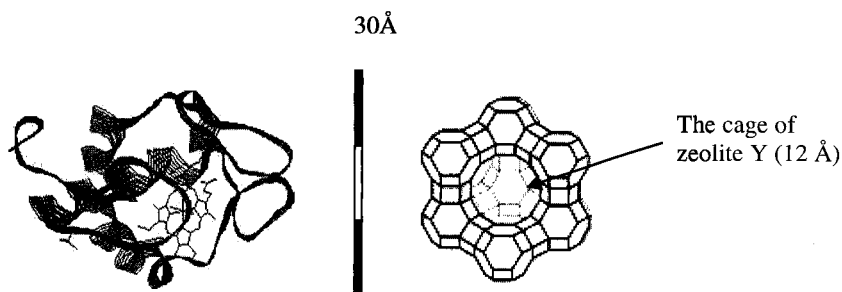


Figure 3. The comparison of the size of a cytochrome *c* molecule and a 12 Å cage of zeolite Y. Cytochrome *c* is one of the smallest enzyme molecules.

Zeolites are well known for their surface acidity and they have been extensively used in chemical industries as solid acid catalysts. In general, when zeolites are used as carriers for enzyme immobilization, higher surface acidities lead to lower enzyme activities, the enzyme molecules being thought to be denatured by the acid sites on the surface [12]. Another study showed that the pH of the buffer was altered by the presence of zeolite during immobilization process so that the pH dropped by up to 4 units over a 24-hour immobilization process.[13] This increase in acidity appeared to denature pH-sensitive enzymes such as thermolysin, which is stable over the pH range 6.0 to 9.0, but the effect was reduced for less pH-sensitive enzymes such as α -chymotrypsin.

In enzyme catalysis, water content is always vital to the enzyme activity. Enzymes are usually inactive in the absence of water but high water content can promote unwanted reactions such as enzyme autolysis, the reversal of alcoholysis and hydrolysis, and secondary hydrolysis of products. [14] Zeolites adsorb water strongly and can act to buffer the thermodynamic activity of the water. Enzymes immobilized on zeolites tend to have a residual level of water available to them, which can be enough to activate the enzyme even in a dry organic medium. [15] When the solvent initially contains a range of water concentrations, the zeolite support can adsorb most of the water from solution and maintain the activity of the enzyme. This explains why enzyme/zeolite composites retain high activities over a broad range of solution water contents.

Furthermore, the activity of enzyme/zeolite composites is affected by the surface hydrophilicity. This is a complicated aspect because different surface properties favor different reactions. For example, Lie and Molin [16] have supported lipase on zeolites with different surface hydrophilicity and the lipase activity in hydrolysis and esterification was studied. The results showed that carriers with a hydrophilic surface were preferred to

hydrophobic supports in hydrolysis reaction while the opposite was observed for esterification.

5 Mesoporous molecular sieves as carriers

Since the early 1990s, the discovery of a new class of ordered materials, M41S, [4, 5] has provided a new area of research in enzyme immobilization. [17, 18] These materials have a highly ordered mesoporous structure which allows the entrapment of macromolecules with dimensions $< 100 \text{ \AA}$. Simple hexagonal mesoporous silicas such as MCM-41 and also FSM-16 and SBA-15 are among the most popular materials as enzyme supports. All these solids possess cylindrical channels aligned along a common axis and ordered in a hexagonal array. There is compelling evidence that in the larger pore SBA-15 materials these channels may be interconnected by mesopores. The first report using mesoporous molecular sieves as carriers in enzyme immobilization was published in 1996 by Díaz and Balkus [19]. Since 1996, research in this area has developed quite rapidly (see figure 4).

Within these studies, three main methods have been used to immobilize enzyme molecules inside the mesopores of the carriers.

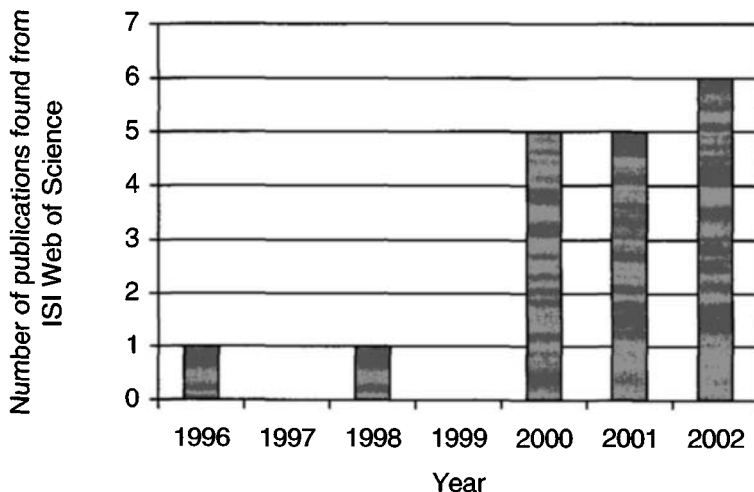


Figure 4. The number of publications found from ISI Web of Science database (wos.mimas.ac.uk) on enzyme immobilization with the use of mesoporous molecular sieves as carriers.

5.1 Encapsulation of enzyme molecules

In the first publication of mesoporous molecular sieves in enzyme immobilization, the encapsulation method was applied to immobilize the enzyme molecules inside the mesopores of pure siliceous MCM-41. [19] Figure 5 shows a simplified scheme of this mechanism. In this method, the enzyme molecules were first dissolved in a buffer solution and MCM-41 was then suspended in the solution to permit uptake of the enzyme. Finally the opening of the mesopores was reduced in size through silanation with the use of 3-aminopropyltriethoxysilane in order to prevent subsequent leaching out of the enzymes during reaction. After silanation, the diameter of the mesopore openings was reduced by *ca.* 12 Å.

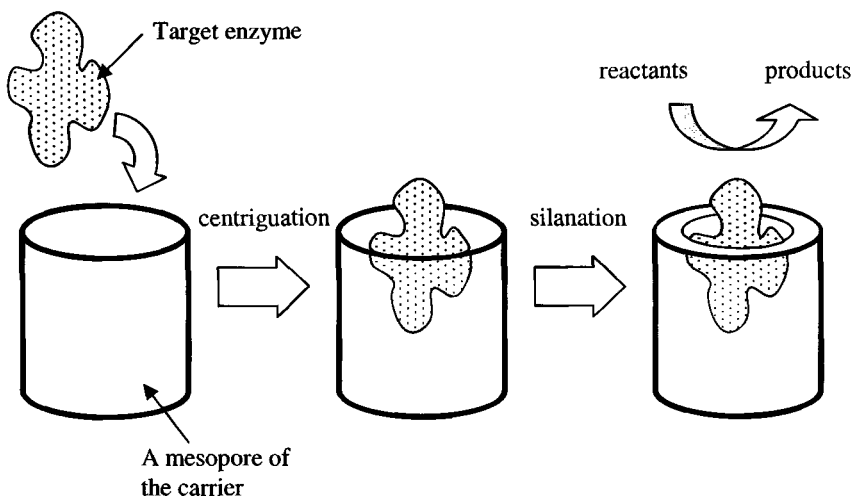


Figure 5. The mechanism of entrapment of an enzyme molecule inside the mesoporous channel of the carrier.

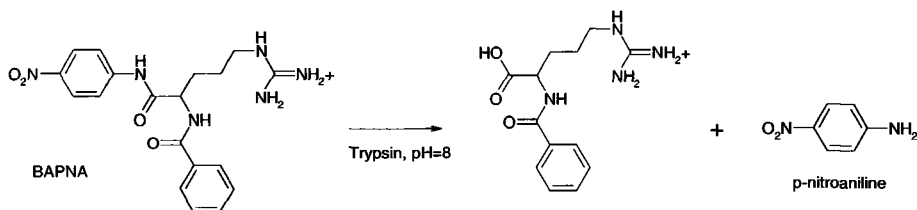
In this work of Balkus *et al.*, four enzymes with a range of molecular sizes (cytochrome *c* 30 Å, papain 36 Å, trypsin 38 Å and horseradish peroxidase, HRP, 46 Å) were chosen as target enzymes. The enzyme size was found to have a significant effect on the immobilization efficiency of the MCM-41 carrier. The enzyme loading decreased from 0.3 µM for cytochrome *c* to 0.01 µM for HRP, indicating that the HRP molecule was too large to enter the mesopores of the MCM-41. Without closing the pore entrances, major leaching of trypsin and papain occurred, the magnitude of which depended on the solution pH. To minimize this, the solid was silanated to reduce the opening of the mesopore. Unfortunately, this

process also strongly reduced the activity of the immobilized enzyme, probably due to denaturing of trypsin during silanation and reduction in the accessibility of the substrate to the active site of the trypsin molecules inside the mesopores.

Besides using pure silica MCM-41, aluminosilicate MCM-41, pure siliceous MCM-48 and niobium oxide mesoporous molecular sieves Nb-TMS1 and Nb-TMS4 were used as carriers for the immobilization of cytochrome *c* by the same research group [20, 21]. Among these, MCM-48 showed the highest loading capacity for cytochrome *c* probably because of its 3-dimensional pore structure and high surface area. The activity of the immobilized cytochrome *c* was tested using cyclic voltammetry (CV) and the results showed the enzyme remained active after immobilization.

5.2 Physical adsorption of enzyme onto the surface of carriers

The simplest method of immobilizing enzyme onto mesoporous carriers is by adsorption. This avoids denaturing the enzyme during further treatments such as silanation. In this method, the mesoporous carrier is suspended in a buffered enzyme solution for a certain length of time, usually overnight, and the solution separated from the composite by centrifugation.



Scheme 1. The hydrolysis of *N*-α-benzoyl-DL-arginine-4-nitroanilide (BAPNA) [22].

Trypsin has been immobilized onto pure siliceous MCM-41, MCM-48 and SBA-15 [22] and the effect of pore size on the activity had been studied. The hydrolysis of *N*-α-benzoyl-DL-arginine-4-nitroanilide (BAPNA) was used as a model reaction. The formation of *p*-nitroaniline (scheme 1) is followed spectrophotometrically at 405 nm. The activity of the immobilized enzyme was found to increase as the pore size increased probably because the diffusion of the reactants and the products was enhanced with larger pore openings. However, there was major loss of enzyme due to leaching. It is likely that the only way to avoid such loss from leaching is in those cases where it is possible to choose an

operational pH where the enzyme and the support have opposite charges, and the enzyme remains active. Examples of this are described later.

Pure silica MCM-41 has also been used as a carrier for the immobilization of Penicillin acylase (PA) via simple adsorption. [23, 24] With the use of a hydrolysis reaction as the activity test, the activity of immobilized PA decreased with an increase in pH from 6.3 to 7.7. A significant decrease of activity was recorded when the length of the immobilization process increased from 12 hours to 24 hours, thought to be due to the denaturation of PA after a long period of time. The immobilized PA was also recycled and a loss of 26% and 10% in activity was recorded from the first and second reuse respectively. Since the molecular size of PA ($80 \text{ \AA} \times 76 \text{ \AA} \times 40 \text{ \AA}$) is rather large compared with the mesopores of MCM-41 (see figure 6), the enzyme molecules would only be immobilized on the exterior surface rather than inside the mesopores.

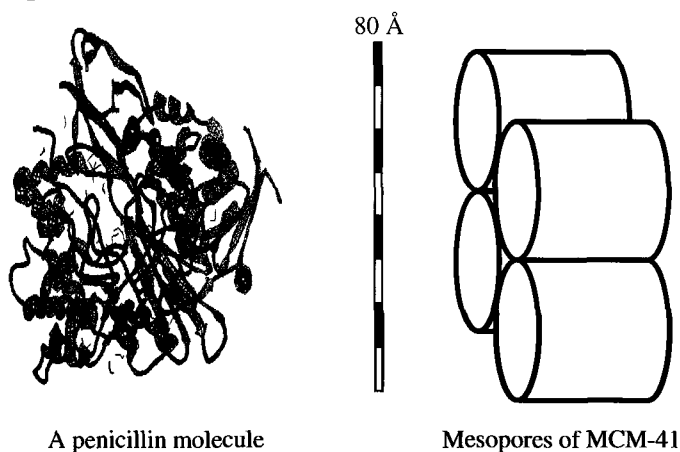


Figure 6. A visual comparison on the size of a penicillin molecule (from Protein Databank, www.pdb.org) and the mesopores of MCM-41.

Most of these immobilized enzymes have been examined in aqueous medium. However, for applications in chemical industries, establishing their activity in non-aqueous medium would be an important step forward for enzyme immobilization. [25] An example of this is given below for Horseradish peroxidase.

Horseradish peroxidase (HRP) has been used extensively in industry as an environmental friendly catalyst for oxidation reactions with hydrogen peroxide as the most common oxidant. [26] The enzyme is of an

appropriate size to adsorb within the pores of large pore mesoporous solids.

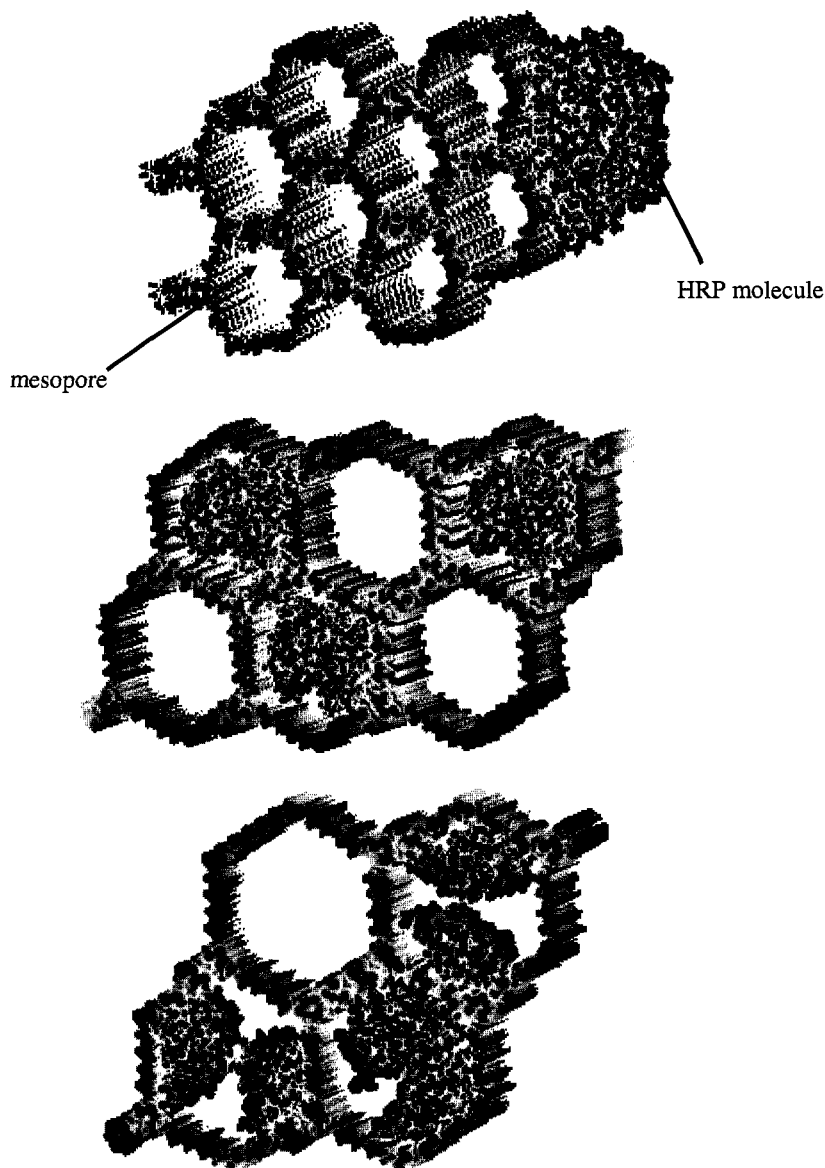


Figure 7. Image models of immobilized HRP in FSM-16 with various pore sizes using computer simulation. The FSM-16 model was constructed in accordance with the folded sheet formation mechanism. The pore diameters of the FSM-16 model selected were 30, 50, and 90 Å for models b-d, respectively (Reproduced from ref. 27).

Takahashi *et al.* immobilized HRP onto FSM-16, MCM-41 and SBA-15 with different pore sizes and their activity was tested in an organic

medium, using toluene as a solvent. [27, 28] The HRP molecule has an oval shape with dimensions $37 \text{ \AA} \times 43 \text{ \AA} \times 64 \text{ \AA}$ which are commensurate with the mesoporosity of these carriers. The results showed SBA-15 had a much lower capacity for HRP than FSM-16 and MCM-41 (10 to 24 mg g^{-1} for SBA-15 compared with 89 to 183 mg g^{-1} for FSM-16 and MCM-41). This was attributed to the difference in the surfactant template used in the preparation of these materials. (A non-ionic co-block polymer was used as a template for the preparation of SBA-15 while cationic surfactant templates were used for FSM-16 and MCM-41.) This result was in contrast with that from Diaz and Balkus [19] probably because the MCM-41 used in this work had a pore size of 50 \AA (20 \AA larger than the material used by Balkus).

The activity of the immobilized HRP was monitored with the catalytic oxidation of 1,2-diaminobenzene in toluene at 37°C with *tert*-butylhydroperoxide as the oxidant. HRP immobilized onto FSM-16 with a pore size of 51 \AA exhibited the highest activity, some ten times the activity of free HRP. The increase in activity was possibly due to the size of the mesopores which matches the dimensions of the HRP molecules (see figure 7). This was thought to prevent the HRP being exposed to environmental changes that arise when fully immersed in the organic medium. A simple test for the thermal stability of the immobilized HRP was also carried out. The most active sample, HRP immobilized on FSM-16, showed a 20% loss in activity upon exposure to a buffer solution at 70°C for 120 minutes while the free HRP showed a 60% loss in activity after 30 minutes. This shows the thermal stability of the HRP was improved upon immobilization.

Enzymes immobilised on mesoporous molecular sieves have also been used in reactions where the reactants are supplied in the form of vapours in a carrier gas. [29] Pure siliceous and aluminosilicate MCM-41 have been used carriers for lipase and the enzyme/MCM-41 composites were found active in the esterification of acetic acid with ethanol at 25°C and 45°C . By appropriate immobilization, enzymatic catalysis in flowing gas streams is therefore possible.

Recently, Chen et. al. [30] reported the use of siliceous SBA-15 as a carrier for a crude lipase, Newlase F, which contains lipase and acid protease from *Rhizopus niveus*. A simple adsorption method was employed in this research and the lipase activity was found to be 50% to 300% higher than the free enzyme with less than 10% of the activity recorded from the supernatant. This indicated that more than 90% of the lipase was adsorbed onto the SBA-15 carrier. An increase in lipase

activity upon immobilization is not uncommon, possibly because the hydrophilic surface of the carrier aids the adsorption of reactants. [31] Interestingly, in the same experiment, the protease activity of the supernatant was 80% of that of the free enzyme, much more than that of the enzyme/SBA-15 composite. This indicates that the SBA-15 carrier selectively adsorbed lipase (49 Å x 49 Å x 46 Å) rather than acid protease (65 Å x 53 Å x 40 Å). Therefore, in this work, SBA-15 functioned not only as a carrier for enzyme immobilization but also as the stationary phase for enzyme separation. The true molecular sieving behavior of SBA-15 in protein separation has been convincingly shown in previous publications [32, 33].

5.3 Chemical binding of enzyme onto the surface of carriers

Although simple adsorption is the easiest method to immobilize enzyme molecules onto mesoporous molecular sieves, leaching remains a major drawback for this method. One way to overcome this is by strengthening the weak interaction between the enzyme molecules and the pore surface of the mesoporous molecular sieves. Increasing the strength of electrostatic interactions is one approach, enzyme immobilization via chemical bonding onto the internal surface is another. Since the preparation procedures for inorganic-organic hybrid mesoporous molecular sieves are now well established in the literature [34, 35] there is a choice of immobilisation methods using this approach. Figure 8 shows a schematic mechanism for enzyme immobilization via chemical bonding that may be electrostatic or covalent.

A variety of functional groups is available in inorganic-organic hybrid mesoporous molecular sieves. The most potentially useful functional groups for enzyme immobilization are thiols, carboxylic acids, alkyl chlorides and amines. Other functional groups such as alkyl, phenyl and vinyl can be added to modify the pore surface and consequently the enzyme's environment by increasing the hydrophobicity.

Inorganic-organic hybrid mesoporous molecular sieves can be prepared by two routes: (1) one-pot *in situ* functionalization (scheme 2) or (2) post-synthesis functionalization (see scheme 3). The former route involves the co-condensation of a functionalized and an unfunctionalized alkoxysilane (e.g. 3-aminopropyltriethoxysilane with tetraethoxysilane, or tetraethyl- orthosilicate TEOS). The alkoxysilanes must hydrolyze at a similar rate to the tetraethoxysilane or a heterogeneous gel will form and the functional groups will not be evenly distributed. Once formed, the surfactant template of these materials must be removed by solvent

extraction and 100% extraction is rarely achieved (see scheme 2). For *in situ* functionalized mesoporous molecular sieves, the percentage of functional groups is limited to *ca.* 20% and a loss of structural order usually occurs with high functional group contents as the number of Si–O–bonds available for linkage is reduced.

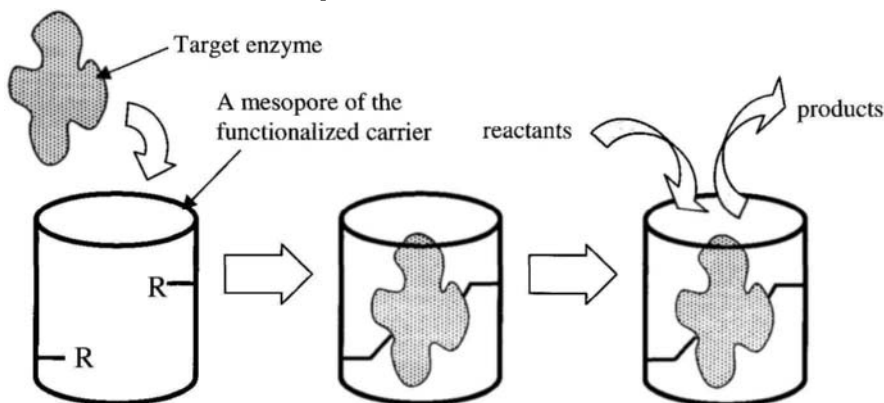
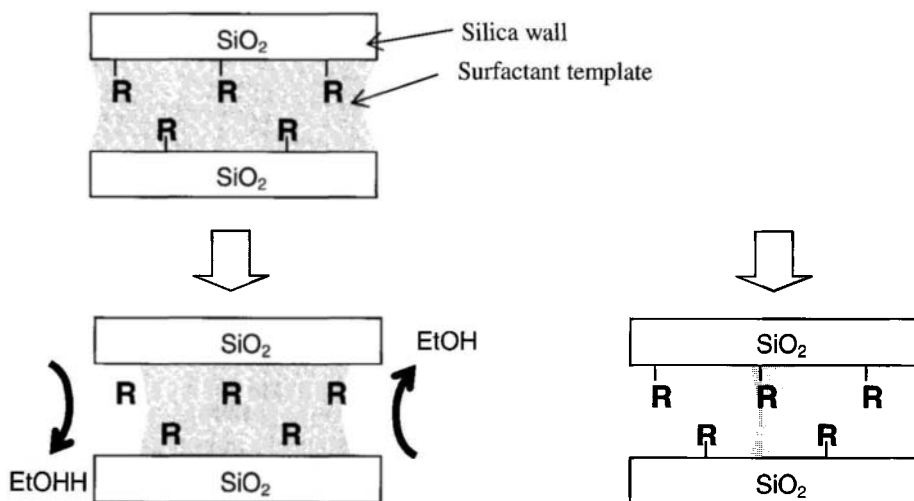


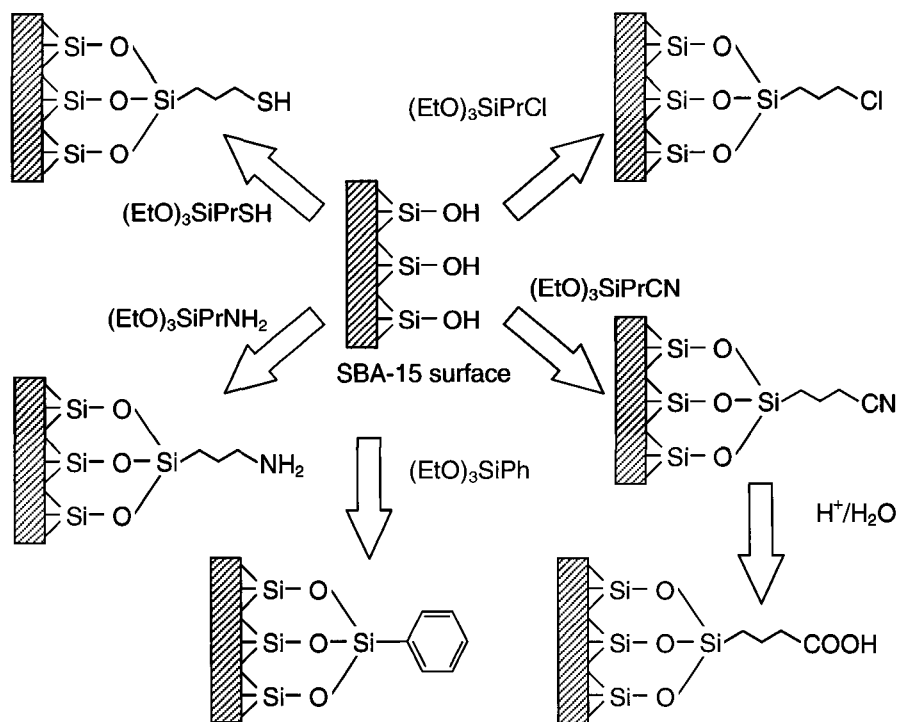
Figure 8. The mechanism of chemical binding of an enzyme molecule onto the surface of a mesopore of the carrier.



Scheme 2. The removal of surfactant template of *in situ* functionalized mesoporous materials using solvent (ethanol) extraction.

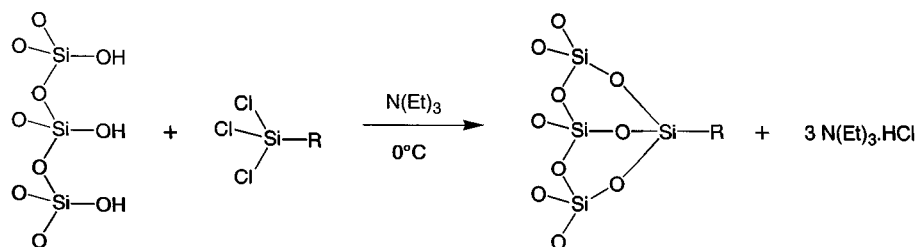
The post-synthesis route involves a reaction of the functionalized silane with a calcined mesoporous molecular sieve. Since all the template

molecules have been removed during calcination before functionalization, there is no residual template in the hybrid mesoporous molecular sieve. However, the procedure tends to be more complicated and the siloxane attached to the surface by less than three groups. Scheme 3 shows preparation routes for post-synthesis functionalization of a mesoporous molecular sieve.



Scheme 3 Idealised preparation of post-synthesis functionalized SBA-15.

As with the *in situ* route, the hydrolysis of functionalized alkoxysilanes can be used in the post-synthesis functionalization route. The conditions for these reactions are widely available in the literature. [34] In another route, functionalized chlorosilanes can also be used in presence of a base, usually a trialkylamine (see scheme 4).



Scheme 4. Functionalization using a chlorosilane.

Our research was first to use organic-inorganic hybrid mesoporous molecular sieves in enzyme immobilization. [36] In this work, the enzyme trypsin was used, with its activity assayed as described previously. SBA-15 materials with different surface functional groups ($-\text{SH}$, $-\text{Ph}$, $-\text{Cl}$, $-\text{NH}_2$, and $-\text{COOH}$), prepared via *in situ* and post synthesis routes, were studied. Leaching of the enzyme enzyme was largely solved by using SBA-15 functionalised with groups such as $-\text{SH}$, $-\text{Cl}$ and $-\text{COOH}$.

Table 2. Initial rate of BAPNA hydrolysis and immobilization and catalysis efficiencies of supported and free trypsin.

Catalysts	Initial rate for BAPNA hydrolysis ($\mu\text{moles of } p\text{-nitroaniline per mg protein per min}$)	Immobilization and catalysis efficiency ^a
Free trypsin	0.46	1.00
calcined SBA-15	0.25	0.26
<i>Post-synthesis</i>		
<i>psPrSH-SBA-15</i>	0.05	0.06
<i>psPrCl-SBA-15</i>	0.11	0.22
<i>psPrNH₂-SBA-15</i>	0.03	0.04
<i>psPrCOOH-SBA-15</i>	0.08	0.15
<i>psPh-SBA-15</i>	0.20	0.17
<i>In situ</i>		
<i>isPrSH-SBA-15</i>	0.44	0.84
<i>isPrCl-SBA-15</i>	0.14	0.28
<i>isPrNH₂-SBA-15</i>	0.02	0.03
<i>isPrCOOH-SBA-15</i>	0.39	0.59
<i>isPh-SBA-15</i>	0.27	0.43

^a immobilization and catalysis efficiency was calculated as the fraction of protein retained on the solid during immobilisation multiplied by the relative specific activity compared with free trypsin. [35]

The activity of the immobilized enzymes is shown in table 2. Trypsin immobilised on *is*PrSH-SBA-15 (prepared via *in situ* route) showed the highest catalytic activity. This immobilized enzyme retained 96% activity of the free trypsin with negligible leaching. After recovery, the immobilized enzyme was reused, giving 66% of the original activity.

An aldehyde-functionalized SBA-15 material has also been used as a carrier for immobilizing an enzyme, α -chymotrypsin. [37] Aldehyde functionalized supports have been a popular choice for protein immobilization [38] because an imine binding can form easily between the surface aldehyde groups and the amine groups on the protein molecules. Unfortunately, aldehyde-functionalized alkoxysilane is not commercially available and can only be synthesized in the laboratory with the use of a rhodium phosphine catalyst. [39] In this work, the aldehyde-functionalized SBA-15 was prepared via a post-synthesis route with trimethoxysilylpropanal. The activity of immobilized enzyme in the hydrolysis of *N*-succinyl-Ala-Ala-Pro-Phe *p*-nitroanilide (SAAPPN) was found to decrease to only *ca.* 5% of that of the free enzyme. However, the activity in transesterification of *N*-acetyl-L-phenylalanine ethylester (APEE) in organic media increased by more than 200% when compared with the free enzyme. It seems that the SBA-15 carrier protects the enzyme molecules from denaturation in organic media. To prove this assumption, the α -chymotrypsin/SBA-15 composite was suspended in pure methanol at room conditions. The half-life of the immobilized enzyme was found to increase over 100-fold. Moreover, the thermal stability of this immobilized enzyme was also shown to be improved.

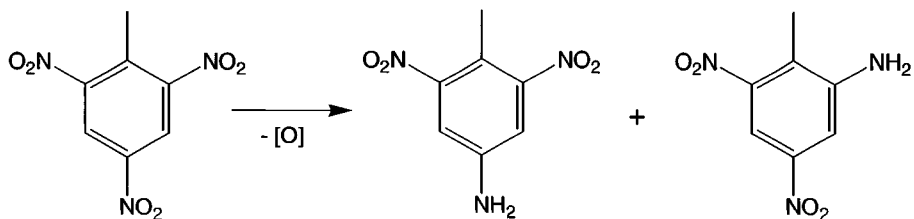
In more recent research, SBA-15 materials with -NH_2 and -COOH functional groups were used as carriers for the immobilization of organophosphorus hydrolase (OPH), an enzyme that has been widely investigated for biosensing and the decontamination of poisonous agents. [40] The carrier with 2% -COOH functional group exhibited the highest protein loadings (4.7% w/w) and the highest activity (4182 units mg^{-1} support). By contrast, the carrier with 20% -NH_2 was found to have a very low loading and the composite inactive. These trends mirror our own work on Trypsin. Another important finding from this work was that the immobilized OPH on carboxy-functionalized SBA-15 was found to retain 62% of its activity after a lengthy 145 days while the free OPH could only retain 23%, indicating the immobilized OPH had improved stability.

The results on OPH can be rationalised by the effect of surface charge. The immobilisation and the activity measurements were performed at pH 7.5. At this pH the OPH (isoelectric point, $\text{pI} = 8.3$) will possess an

overall positive charge, whereas carboxylic acid groups on the solid will be negatively charged and amine groups on the surface will be positively charged, giving rise to net attraction and repulsion of the enzyme.

5.4 Other examples

A rather different approach in enzyme immobilization onto mesoporous molecular sieve was published by Tope et. al. [41] In this study, aluminosilicate MCM-41 was used as a carrier to immobilize the whole cell for the reductive transformation of 2,4,6-trinitrotoluene (TNT, see scheme 5). The whole microbial cells of *Arthrobacter* sp., *Bacillus subtilis* and *Micrococcus luteus* were studied in this work. A flow-reactor system was used for immobilization and testing the cell activity.



Scheme 5. The reductive transformation of TNT to 2-aminodinitrotoluene and 4-aminodinitrotoluene as major products.

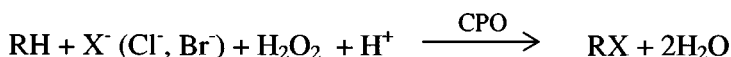
The results indicated that the cells of all three species were adsorbed onto the surface of MCM-41. The tolerance level of the cell of *Arthrobacter* sp. was increased from 60 mg l^{-1} to 400 mg l^{-1} upon immobilization onto MCM-41. A 100% conversion was recorded after 2 days when the immobilized cell was used. It was also found that the immobilized cell retained its activity even after 10 cycles. The suitability of MCM-41 as a carrier was compared with the zeolites HY and HZSM-5. The zeolites gave 4% immobilization compared with over 99% for MCM-41, indicating that MCM-41 was much more efficient carrier for cell immobilization than the zeolites.

6 Mesocellular foam (MCF) materials as carriers

The pore size of the mesoporous molecular sieves is limited by the dimensions of the micelle templates and, to date, the largest pore size claimed for a well ordered mesoporous molecular sieves is around 100 \AA .

[42] With this restriction, only relatively small enzymes can be immobilized inside the mesoporous channels of the molecular sieves. The discovery of mesocellular foam (MCF) materials in 1999 allows a much wider choice of enzymes to be studied in this area of research. These materials are prepared using emulsions as templates and the pore size varies from 150 Å to 400 Å. [42, 43] Moreover, MCF materials exhibit very similar chemical properties to MCM-41 and SBA-15 and functionalization is also possible.

Until very recently, the application of MCF materials has not been studied extensively. There is no report on the catalytic properties of MCFs or MCF-based catalysts, for example. However, MCF has been used in protein separations [32] and more recently in enzyme immobilization. [45] Han *et al.* have reported the use of MCF as a carrier for immobilization of chloroperoxidase from *Caldariomyces fumago*. Chloroperoxidase is a very useful enzyme which catalyzes halogenation in the presence of halide ions (Cl^- and Br^-) and peroxides (see scheme 6). In the absence of halide ions, it also catalyzes oxidation reaction with a remarkable enantioselectivity [46].



Scheme 6.

In the work of Han *et al.*, pure silica MCF with a pore size of 150 Å was used to immobilize CPO (SBA-15, SBA-16 and MCM-48 were also studied for comparison). The activity of the immobilized CPO was monitored using the monochlorodimedone (MCD) assay. [47] CPO remained active in MCF and SBA-15 (pore size = 70 Å) but low activities were recorded from the immobilized CPO on MCM-48 (32 Å) and SBA-16 (82 Å). The pore size of MCM-48 was too small for CPO (77 Å x 65 Å x 46 Å) immobilization while SBA-16 was also unsuitable. Although SBA-16 has a pore size of 82 Å, the size of the openings between cages is only 47 Å which inhibits immobilization. This highlights an important consideration in the use of some of the new mesoporous structures, where the window size may be much smaller than the pore size. Besides the pore structure of the carrier, the loading of CPO was also affected by the pH of the solution during the immobilization process with a maximum loading at pH = 3.5. At this pH, which is slightly below the isoelectric point of CPO (pI = 4), the enzyme has a net positive charge and the silica (isoelectric point pI = 2) a net positive charge, accounting for the high loading of CPO on MCF (12.2 wt %). CPO remains active at these pH's and the specific

activity of CPO supported on MCF was around one half of that of the free enzyme. The decrease in activity was attributed to steric constraints preventing free access to the active site of the enzyme molecule.

The stability of the immobilized CPO was also studied and CPO was found to leach out from MCF but not from the SBA-15. This was accounted for the relatively small pore size which restricted the mobility of the CPO molecules. The pore size of the MCF is likely to be an advantage, however, in supporting larger enzymes.

7 Future developments

It has been proved that nanoporous materials can be used as carriers for enzyme immobilizations. As a result of the rapid growth of research in the preparation of nanostructure materials with new physical and chemical properties, materials can be almost tailor-made, with desired pore size, connectivity and surface chemistry to suit specific applications. The synthesis of a unique carrier for target enzymes will soon be possible. This is part of the new exciting area of “materials design”.

So far, there have been many successful cases of enzyme immobilization using nanoporous materials with retention of enzymatic activity. Table 3 summarizes the published literature in this area of research. However, most of the research published only uses standard activity assays to monitor the activity of the immobilized enzymes. There is little research so far on the applications of these enzyme/nanomaterials in real catalytic reactions, and demonstration of their utility remains a pressing concern. HRP, for example, has been already recommended as an alternative oxidation catalyst to transition metal complexes.

In addition, it would be a significant improvement if the support could be chosen or manipulated to improve the catalytic action of the enzyme. For example, it may be possible to improve selectivities of reaction by introducing a molecular sieving ability to the enzyme / nanomaterials composites.

Finally, one of the most unique characters of enzymes is their ability to catalyse reactions with highly enantioselectivity. If enzyme / nanomaterials composites can be prepared that retain their enantioselectivity, their applications in pharmaceutical and fine chemical industries can be exploited.

Table 3. A summary of published research in enzyme immobilization using mesoporous molecular sieves as supports.

Support	Method	Enzyme	Test	Loading (mg g ⁻¹)	Ref
MCM-41	encapsulation	cytochrome <i>c</i> trypsin papain horseradish peroxidase	cyclic voltammetry hydrolysis of BAPNA	0.4 – 5.8	19
MCM-41, MCM-48, Al-MCM-41, Nb-TMS1	encapsulation	cytochrome <i>c</i>	cyclic voltammetry	5.7 – 8.7	20
MCM-48, SBA-15, Nb-TMS4	encapsulation	cytochrome <i>c</i>	cyclic voltammetry	6.2 - 11.8	21
SBA-15, MCM-41, MCM-48	adsorption	trypsin	hydrolysis of BAPNA	24	22
MCM-41	adsorption	penicillin acylase	hydrolysis of phenylacetic acid	230	23, 24
FSM-16, MCM-41, SBA-15	adsorption	horseradish peroxidase	oxidation of diaminobenzene	10 - 183	27
FSM-16 (-CH ₃)	adsorption	horseradish peroxidase	oxidation of diaminobenzene	130 - 180	28
MCM-41, Al-MCM-41	adsorption	lipase	esterification of acetic acid with ethanol	2.1 – 4.6	29
SBA-15	adsorption	crude lipase	hydrolysis transesterification	40	30
SBA-15 (-SH, -Cl, -COOH, etc)	chemical binding	trypsin	hydrolysis of BAPNA	24	36
SBA-15 (-CHO)	chemical binding	α -chymotrypsin	hydrolysis of SAAPPN transesterification of APEE	5.4	37
SBA-15 (-COOH)	chemical binding	organophosphorus hydrolase	paraoxon assay	31	40
MCF	chemical binding	chloroperoxidase	MCD assay	122	45
MCM-41	whole cell adsorption	microbial cells	reductive transformation of TNT	N/A	41

It is only a few years since the first results describing enzymes supported on nanoporous solids were published. The scope for fine tuning the pore size and the chemical nature of the support to complement the enzyme being immobilised suggests this is a young area of considerable promise.

8 Acknowledgements

We gratefully acknowledge the input of Dr. Nigel Botting and the support of the EPSRC.

References

1. Hartmeier. W., Immobilized biocatalysts (Springer, Berlin, 1988).
2. Kreiner M., Moore B. D. and Parker M. C., Enzyme-coated micro-crystals: a 1-step method for high activity biocatalyst preparation, *J. Chem. Soc. Chem. Commun.* **12** (2001) pp. 1096-1097.
3. Tischer W. and Kasche V, Immobilized enzymes: methods and applications, *Topics Curr. Chem.* **200** (1999) pp. 95-126.
4. Beck J. S., Vartuli J. C., Roth W. J., Leonowicz M. E., Kresge C. T., Schmitt K. D., Chu C. T.-W., Olson D. H., Sheppard E. W., McCullen S. B., Higgins J. B. and Schlenker J. L., A new family of mesoporous molecular sieves prepared with liquid crystal templates, *J. Am. Chem. Soc.* **114** (1992) pp. 10834-10843.
5. Kresge C. T., Leonowicz M. E., Roth W. J., Vartuli J. C. and Beck J. S., Ordered mesoporous molecular sieves synthesized by a liquid-crystal templated mechanism, *Nature* **359** (1992) pp. 710-712.
6. Yanagisawa T., Shimizu T., Kuroda K. and Kato K., The preparation of alkyltrimethylammonium-kanemite complexes and their conversion to microporous materials, *Bull Chem. Soc. Jpn.* **63** (1990) pp. 988-992.
7. Zhao D.Y., Feng J.L., Huo Q.S., Melosh N., Fredrickson G.H., Chmelka B.F. and Stucky G.D., Triblock copolymer syntheses of mesoporous silica with periodic 50 to 300 angstrom pores, *Science* **279** (1998) pp. 548-552.
8. Zhao D.Y., Huo Q.S., Feng J.L., Chmelka B.F. and Stucky G.D., Nonionic triblock and star diblock copolymer and oligomeric surfactant syntheses of highly ordered, hydrothermally stable, mesoporous silica structures, *J. Am. Chem. Soc.* **120** (1998) pp. 6024-6036.
9. Thomas J. M., Molecular-sieves – the chemistry of crystalline sponges, *Nature* **368** (1994) pp. 289-290.
10. Tischer W. and Kasche V, Immobilized enzymes: crystals or carriers?, *Trends Biotechnol.* **17** (1999) pp. 326-335.
11. Katchalski-Katzir E., Immobilized enzymes – learning from past successes and failures, *Trends Biotechnol.* **11** (1993) pp. 471-478.
12. Serralha F. N., Lopes J. M., Lemos F., Prazeres D. M. F., Aires-Barros M. R., Cabral J. M. S. and Ramôa Ribeiro F., Zeolites as supports for an enzymatic alcoholysis reaction, *J. Mol. Catal. B: Enzym.* **4** (1998) pp. 303-311.

13. Xing G.-W., Li X.-W., Tian G.-L. and Ye Y.-H., Enzymatic peptide synthesis in organic solvent with different zeolites as immobilization matrixes, *Tetrahedron* **56** (2000) pp. 3517-3522.
14. Yan A. X., Li X. W. and Ye Y. H., Recent progress on immobilization of enzymes on molecular sieves for reactions in organic solvents, *Appl. Biochem. Biotech.*, **101** (2002) pp. 113-129.
15. Ullmann D., Bordusa F., Salchert K. and Jakubke H.-D., A New simple route to the synthesis of protease substrates in ice, *Tetrahedron: Asymmetry* **7** (1996) pp. 2047-2054.
16. Lie E. and Molin G., Hydrolysis and esterification with immobilized lipase on hydrophobic and hydrophilic zeolites, *J. Chem. Tech. Biotechnol.* **50** (1991) pp. 549-553.
17. Ciesla U. and Schüth F., Ordered mesoporous materials, *Microporous Mesoporous Mater.* **27** (1999) pp. 131-149.
18. Trong On D., Desplandier-Giscard D. and Kaliaguine S., Perspectives in catalytic applications of mesostructured materials, *Appl. Catal. A: Chemical* **222** (2001) pp. 299-357.
19. Díaz J. F. and Balkus Jr. K. J., Enzyme immobilization in MCM-41 molecular sieves, *J. Mol. Catal B: Enzym.* **2** (1996) pp. 115-126.
20. Gimon-Kinsel M. E., Jimenez V. L., Washmon L. and Balkus Jr. K. J., Mesoporous molecular sieve immobilized enzyme, *Stud. Surf. Sci. Catal.* **117** (1998) pp. 373-380.
21. Washmon-Kriel L., Jimenez V. L. and Balkus Jr. K. J., Cytochrome *c* immobilization into mesoporous molecular sieve, *J. Mol. Catal B: Enzym.* **10** (2000) pp. 453-469.
22. Yiu H. H. P., Wright P. A. and Botting N. P., Enzyme immobilisation using siliceous mesoporous molecular sieves, *Microporous Mesoporous Mater.* **44** (2001) pp. 763-768.
23. Li X.-F., He J., Ma R.-Y. and Duan X., The immobilization of penicillin G Amidase on mesoporous molecular sieves MCM-41, *Acta Chim. Sinica* **58** (2000) pp. 167-171.
24. He J. Li X., Evans D. G., Duan X. and Li C., A new support for the immobilization of penicillin acylase, *J. Mol. Catal. B: Enzym.* **11** (2000) pp. 45-53.
25. Carrea G. and Riva S., Properties and synthetic applications of enzymes in organic solvents, *Angew. Chem. Int. Ed.* **39** (2000) pp. 2226-2254.
26. Colonna S., Gaggero N., Richelmi C. and Pasta P., Recent biotechnological developments in the use of peroxidases, *Trends Biotechnol.* **17** (1999) pp. 163-168.
27. Takahashi H., Li B., Sasaki T., Miyazaki C., Kajino T. and Inagaki S., Catalytic activity in organic solvents and stability of immobilized enzymes depend on the pore size and surface characteristics of mesoporous silica, *Chem. Mater.* **12** (2000) pp. 3301-3305.
28. Li B. and Takahashi H., New immobilization method for enzyme stabilization involving a mesoporous material and an organic/inorganic hybrid gel, *Biotechnol. Lett.* **22** (2000) pp. 1953-1958.
29. Pires E. L., Miranda E. A. and Valenca G. P., Gas-phase enzymatic esterification on immobilized lipases in MCM-41 molecular sieves, *App. Biochem. Biotech.* **98** (2002) pp. 963-967.

30. Chen Z. Z., Li Y. M., Peng X., Huang F. R. and Zhao Y.F., The use of crude lipase in deprotection of C-terminal protecting groups, *J. Mol. Catal B: Enzym.* **18** (2002) pp. 243-249.
31. Tweddell R. J., Kermasha S., Combes D. and Marty A., Immobilization of lipase from *rhizopus niveus*: a way to enhance its synthetic activity in organic solvent, *Biocatal. Biotransfor.* **16** (1999) pp. 411-426.
32. Han Y.-J., Stucky G. D. and Butler A., Mesoporous silicate sequestration and release of proteins, *J. Am. Chem. Soc.* **121** (1999) pp. 9897-9898.
33. Yiu H. H. P., Botting C. H., Botting N. P. and Wright P. A., Size selective protein adsorption on thiol-functionalised SBA-15 mesoporous molecular sieve, *Phys. Chem. Chem. Phys.* **3** (2001) pp. 2983-2985.
34. Stein A., Melde B. J. and Schroden R. C., Hybrid inorganic-organic mesoporous silicates - Nanoscopic reactors coming of age, *Adv. Mater.* **12** (2000) pp. 1403-1419.
35. Lim M. H. and Stein A., Comparative studies of grafting and direct syntheses of inorganic-organic hybrid mesoporous materials, *Chem. Mater.* **11** (1999) pp. 3285-3295.
36. Yiu H. H. P., Wright P. A. and Botting N. P., Enzyme immobilisation using SBA-15 mesoporous molecular sieves with functionalised surfaces, *J. Mol. Catal B: Enzym.* **15** (2001) pp. 81-92.
37. Wang P., Dai S., Waezsada S. D., Tsao A. Y. and Davison B. H., Enzyme stabilization by covalent binding in nanoporous sol-gel glass for nonaqueous biocatalysis, *Biotechnol. Bioeng.* **74** (2001) pp. 249-254.
38. Wong S. S., Chemistry of protein conjugation and cross-linking (CRC Press, Boca Raton, 1993).
39. Takeuchi R. and Sato N., Hydroformylation of alkenes having organosilicon substituents, *J. Organomet. Chem.* **393** (1990) pp. 1-10.
40. Lei C., Shin Y., Liu J. and Ankerman E. J., Entrapping enzyme in a functionalized nanoporous support, *J. Am. Chem. Soc.* **124** (2002) pp. 11242-11243.
41. Tope A. M., Srinivas N., Kulkarni S. J. and Jamil K., Mesoporous molecular sieve (MCM-41) as support material for microbial cell immobilization and transformation of 2,4,6-trinitrotoluene (TNT): a novel system for whole cell immobilization, *J. Mol. Catal. B: Enzym.* **16** (2001) pp. 17-26.
42. Kruk M. and Jaroniec M., Determination of mesopore size distributions from argon adsorption data at 77 K, *J. Phys. Chem. B* **106** (2002) pp. 4732-4739.
43. Schmidt-Winkel P., Lukens P. P., Zhao D., Yang P., Chmelka B. F. and Stucky G. D., Mesocellular siliceous foams with uniformly sized cells and windows, *J. Am. Chem. Soc.* **121** (1999) pp. 254-255.
44. Lettow J. S., Han Y. H., Schmidt-Winkel P., Yang P., Zhao D., Stucky G. D. and Ying J. Y., Hexagonal to mesocellular foam phase transition in polymer-templated mesoporous silicas, *Langmuir* **16** (2000) pp. 8291-8295.
45. Han Y.-J., Watson J. T., Stucky G. D. and Butler A., Catalytic activity of mesoporous silicate-immobilized chloroperoxidase, *J. Mol. Catal B: Enzym.* **17** (2002) pp. 1-8.
46. Franssen M. C. R., Haloperoxidases: useful catalysts for halogenation and oxidation reactions, *Catal. Today* **22** (1994) pp. 441-457.
47. Meister Winter G. E. and Butler A., Inactivation of Vanadium Bromoperoxidase: Formation of 2-Oxohistidine, *Biochemistry* **35** (1996) pp. 11805-11811.

A NOVEL NONSURFACTANT ROUTE TO NANOPOROUS MATERIALS AND ITS BIOLOGICAL APPLICATIONS

YEN WEI*

Department of Chemistry, Drexel University, Philadelphia, PA 19104, USA

E-mail: weiyen@drexel.edu

KUN-YUAN QIU

Department of Polymer Science & Engineering, Peking University, Beijing 100871 China

We have developed a novel, biocompatible nonsurfactant-templating pathway to mesoporous materials with high surface area ($\sim 1000 \text{ m}^2/\text{g}$) and pore volume ($\sim 0.5\text{--}1.0 \text{ cm}^3/\text{g}$) as well as pore size in the range of 2–12 nm with narrow size distributions. Nonsurfactant molecules such as glucose, maltose, dibenzoyl-L-tartaric acid, fructose, cyclodextrins, urea, glycerol, soluble starch, citric acid, hydroxyethyl methacrylate, ascorbic acid, oligopeptides, etc. can be used as templates to direct the mesostructure formation. The pore parameters are adjustable by varying template concentration. The entire preparation can be performed at room temperature and near neutral pH. This has enabled us to encapsulate a variety of bioactive substances including enzymes, proteins, nucleic acids and cells directly in mesoporous host materials of designable pore diameters. The host matrix can be tuned for various hydrophobicity-hydrophilicity by making organic- (or polymer-) modified hybrid materials. Activity, denaturing (or unfolding) and/or re-naturing (or refolding) of various proteins, such as phosphatases, lipase, horseradish peroxidase, glucose oxidase, hemoglobin, organophosphorus acid anhydrolase, and cytochrome *c*, in the mesoporous host have been investigated. Our ability to confine protein molecules in cages with designable size and internal surface properties provides a unique tool for studying the protein folding pathway, folding intermediates, conformation change, and probably single molecule activity as well as the protein-protein interactions. A broad spectrum of potential applications of the nonsurfactant-templated nanoporous materials have explored including catalysis, enzyme immobilization, biosensors, nanobioreactor, fabrication of nanoparticles, drug-delivery, molecular imprinting, and nanocomposites.

1 Introduction

Since the discovery of the ordered mesoporous MCM-41 materials in 1992, numerous mesoporous (or, more generally, *nanoporous*) silicate and other metal oxides with narrowly distributed pore diameters in the range 2 to ~ 10 nm or greater have been synthesized based on the template-directed reactions of inorganic precursors [1–6]. This new class of materials has been explored for many potential applications in catalysis, separation, ion exchange, catalytic support, molecular imprinting, fabrication of

nanoparticles or nanowires, etc. [3-10] So far, most mesoporous materials have been prepared using ionic or neutral *surfactants* or block copolymers as the templates to direct the mesophase formation [1-11]. These approaches, while successful in producing new materials with beautiful nanostructures, suffer a number of drawbacks. As examples, some cationic surfactants are toxic and expensive. There has been limited success in the synthesis of mesoporous materials in the forms of large monoliths or membranes with desired channel orientations. In particular, the synthesis is often achieved under harsh conditions during the reactions and/or the template-removal process, such as high temperature and pressure, strongly acidic or alkaline media, which are undesirable for any inclusion of bioactive substances like proteins and nucleic acids. To solve some of these problems, we have developed a new *nonsurfactant-templating* approach to the synthesis of mesoporous materials.

In this article, we will give a brief account of *our* work in the past several years and also currently in progress on the nonsurfactant-templating approach and its related applications in nanotechnology and in biochemistry. More extensive literature reviews and experimental details are avoided here but they can be found in the publications cited in the reference section.

2 Nonsurfactant-Templating Route to Mesoporosity

Since the early 1990s, we have been interested in the preparation of inorganic materials with chiral cavities for asymmetric synthesis and chiral separations [12,13]. We introduced small organic chiral compounds such as D-glucose and dibenzoyl-L-tartaric acid to the sol-gel synthesis of silica in hope that removal of these chiral compounds would result in chiral cavities in the silica. It turned out we could not detect any significant chiral cavities in the sol-gel silica matrix after complete removal of the chiral compounds by solvent extraction. However, interestingly the materials were found to be nonporous optically rotatory monoliths with excellent optical properties before the extraction [12] and *mesoporous* after the extraction. This led to the discovery of a novel, low-cost, environmental friendly, biocompatible nonsurfactant-templating pathway to mesoporous materials with high surface area (e.g. 1000 m²/g) and pore volume (e.g. 0.5-1.0 cm³/g) as well as pore size in the range of 2-12 nm with narrow size distributions [14,15].

The nonsurfactant molecules such as glucose, maltose, dibenzoyl-L-tartaric acid (DBTA), fructose, cyclodextrins, urea, glycerol, soluble starch, citric acid, hydroxyethyl methacrylate, ascorbic acid, oligopeptides, etc., can be used as templates in directing the mesostructure formation during the sol-gel reactions [14-47]. In general, the nonsurfactant-templated synthesis starts with the sol-gel reactions of inorganic precursors, e.g. tetraethyl orthosilicate (TEOS) for silica, in the presence of a nonsurfactant compound, e.g. DBTA. Upon gelation and drying, the template-silica composites are obtained usually as *nonporous*, transparent and monolithic solids. The template molecules are removed by solvent extraction (e.g. ethanol for DBTA). As the template is removed, the porosity of the materials increases (Fig. 1), leading to the final mesoporous materials after complete removal of the template.

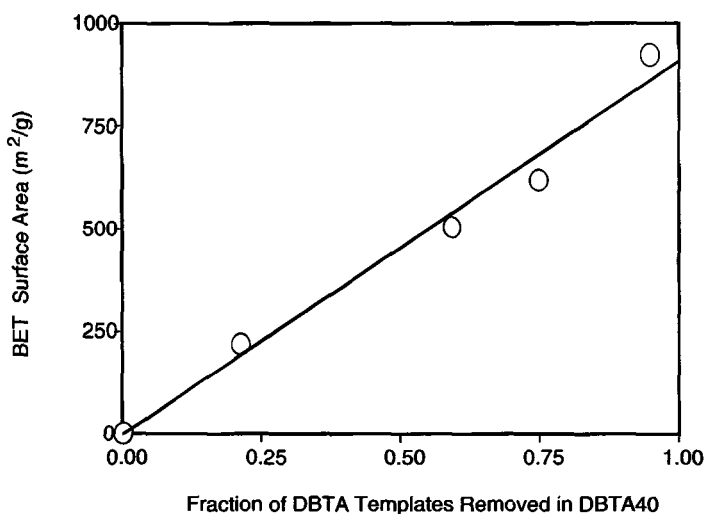


Figure 1. Relationship between the surface area and the fraction of DBTA template removed from the sol-gel silica containing 40 wt% of DBTA (Sample DBTA40)[15,16].

The pore size, pore volume and specific surface area are adjustable to a certain extent simply by varying concentration of the templating compounds in the preparations. Generally the values of these pore parameters increase with the template concentration (Fig. 2). Mesoporosity is usually achieved at high template contents of about 30% by weight or higher. The template-removal is achieved by solvent extraction, calcinations or other methods. Using appropriate procedures, the entire preparation can be performed at room temperature and near neutral pH.

Besides silica, other mesoporous oxides such as titania, alumina, zirconia and multi-metal oxides can be prepared similarly [19-21, 29, 31-33]. The mesoporosity has been supported by nitrogen adsorption-desorption isotherms, X-ray diffraction (XRD), transmission electron microscopy (TEM) and atomic force microscopy (AFM).

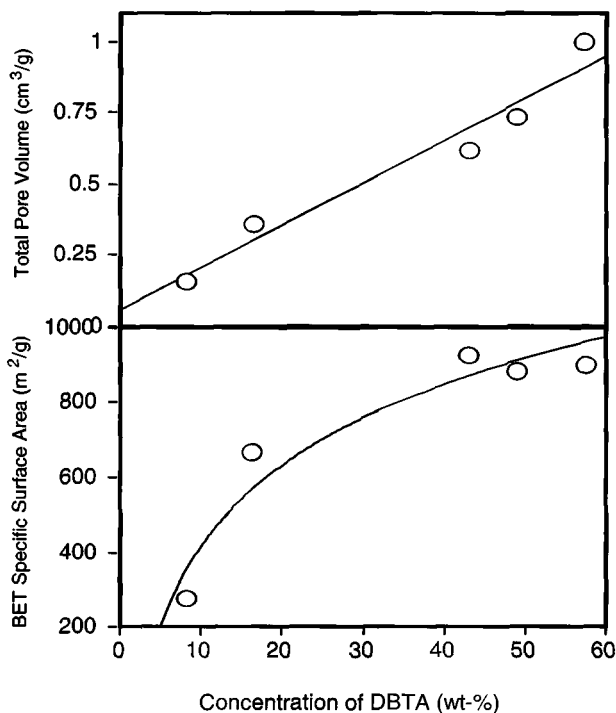


Figure 2. Effect of concentration of DBTA template on total pore volume (top) and surface area (bottom – the curve in the plot meant to serve as eye guide only) [15,16].

Under controlled extraction conditions, transparent monoliths of mesoporous silica with relatively large dimensions (e.g. 2x2x1 mm) could be obtained [30,31]. We have also prepared a series of organic-inorganic hybrid mesoporous materials [37-44,47]. Particularly, using the sol-gel chemistry developed in our laboratories for the synthesis of nonporous polymer-inorganic hybrid materials [48,49], we have achieved the first synthesis of hybrid mesoporous materials, in which organic polymers such as polystyrene, poly(methyl methacrylate), etc., are *covalently* bonded with silicate [40-44]. These polymer-modified mesoporous materials are of interest because the polymer chains may provide otherwise fragile silica matrix with some toughness. Furthermore, the pore parameters could be tuned by physical stimuli such as heating because the segmental motions

of polymer chains increase with temperature, leading to a decreased pore size.

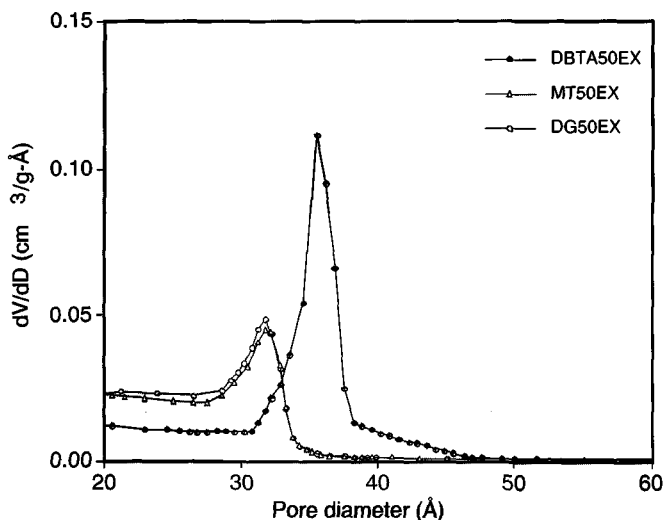


Figure 3. BJH pore size distributions obtained from the nitrogen adsorption-desorption isotherms for mesoporous silicas templated with 50 wt% of DBTA, maltose (MT) and glucose [15,16].

In an effort to elucidate the mechanism for the mesophase formation, we have investigated nearly 100 compounds. Apparently, only those compounds that contain highly polar functional groups can work as the templates to afford materials with narrowly distributed mesopores. The template molecules must work with some collectivity (i.e. as aggregates or assemblies) because the sizes of mesopores are much greater than those of template molecules and maltose (a dimer of glucose) exhibited essentially the same templating effect as glucose (Fig. 3). We believe that strong polar interactions and hydrogen bonding between the nonsurfactant molecules or their aggregates and the inorganic species (e.g. silicate intermediates) may play an important role in directing the mesophase formation. The nanophase separation between the nonsurfactant aggregates and the forming inorganic matrix during the gelation would lead to a bicontinuous-like phase structures. The removal of the templates results in mesoporous inorganic (e.g. silica) matrix with interconnected channels of regular diameters. Indeed, such an isotropic worm-hole structure was

observed in the TEM images of all mesoporous materials prepared via the nonsurfactant templating route (Fig. 4). Further theoretical and experimental studies are in progress to gain a detailed understanding of the templating mechanism. Unlike many surfactant-templated mesoporous materials, the nonsurfactant-templated materials have no discernable packing or orientation of the mesopores/channels. We attempted to induce ordered structures using electric, magnetic and mechanical force fields but have not achieved any significant ordering so far. It is interesting to note that the lack of packing could be advantageous for many applications because the mesoporosity is accessible in all directions. The effects of other additives (e.g. metal halides [25]) and the use of mixtures of nonsurfactant templates [21,27] on mesopore structure have also been investigated.

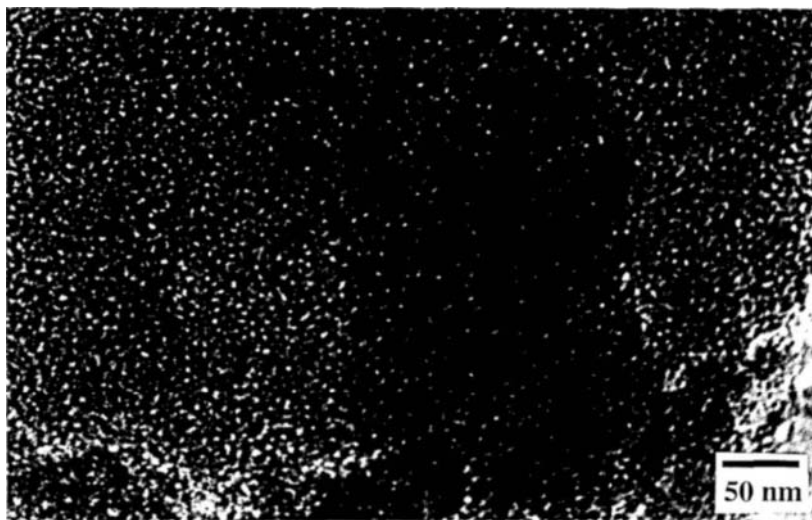


Figure 4. TEM image of D-glucose-templated mesoporous silica. The lighter features are “worm hole”-like mesopores/channels and the darker features are silica matrix [17,18].

3 Selected Applications of Nonsurfactant-Templating Approach

Nanotechnology has been a subject of worldwide attention in the research communities recently. We have been exploring a number of potential applications of the nonsurfactant-templated nanoporous materials, such as catalysis, separation, chromatography, substrate for solid phase peptide synthesis, molecular imprinting, drug-release, enzyme immobilization, biosensors, nanobioreactor, etc. As examples, mesoporous Ti-incorporated

silica was found catalytically active for the ring-opening polymerization of ϵ -caprolactone [50]. The gold nanoparticles were prepared within the nanopores of silica matrix [51,52]. Since vinyl monomers such as 2-hydroxyethyl methacrylate (HEMA) were found to be good nonsurfactant templates, novel nanocomposite materials were prepared by the sol-gel reactions of tetraalkyl orthosilicate in the presence of HEMA and a free radical initiator. Upon the formation of HEMA-silica gels, instead of removing HEMA by extraction to afford mesoporous silica, the free-radical polymerization of HEMA was initiated thermally or photochemically to yield novel polymer-silica nanocomposites [35,53]. The applications of the nanocomposites in dentistry are currently under investigation. Recently, we have also developed a new approach to prepare silver nanoparticles in the glucose-templated silica materials. Thus, after obtaining glucose-silica gel, silver nitrate solution was allowed to diffuse into the materials and silver ion was reduced by glucose to form silver nanoparticles (i.e. the “mirror reaction”) inside the mesoporous silica matrix [54]. Nanospheres with mesoporosity have also been prepared (Fig. 5), which, along with other nonsurfactant-templated mesoporous materials, could be used to host various synthetic or natural therapeutic agents for controlled delivery applications [52, 55].

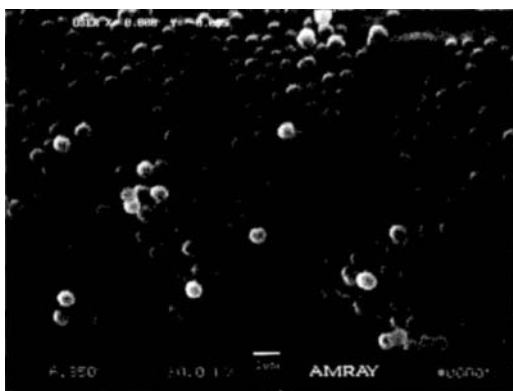


Figure 5. Scanning electron microscopy (SEM) image of mesoporous silica spheres after removal of fructose templates [52,55].

4 Nanoencapsulation of enzymes and other bioactive substances

One of the most unique advantages of our nonsurfactant approach to mesoporous materials is its biocompatibility. The synthesis can readily be accomplished at room temperature and near neutral pH. Nonsurfactants such as sugar compounds are highly biocompatible. These enabled us to develop a novel nanobiotechnology: one-step direct encapsulation of bioactive substances, such as proteins, nucleic acids, cells, etc., inside nanoporous matrices [18,35,47,56-67]. The encapsulation is effected by direct introduction of bioactive substances to nonsurfactant-templating sol-gel reactions prior to the system gelation with pH adjusted to near neutral and partial removal of organic byproducts (e.g. methanol or ethanol).

Immobilization of enzymes is of great importance because of its immense potentials for biocatalysis, biosensors, bioreactor, and pharmaceutical applications. A popular current method is formation of covalent bonds between enzymes and a solid support, which often alters the enzymatic activities adversely. Encapsulation is another widely studied method (Fig. 6). Various enzymes have been encapsulated in inorganic oxides such as silica through conventional sol-gel process. However, because of the *microporous* nature (i.e. pore diameter of 1.5 nm or smaller with broad pore size distributions) of conventional sol-gel materials, the catalytic activities of enzymes are hindered by low diffusion rates of substrate and product molecules and by poor accessibility of enzymes inside the materials (Fig. 6, top) [68,69]. On the other hand, enzymes can be entrapped in *macroporous* materials such as hydrogels that have pore sizes usually in micrometers. There is no problem in diffusion and accessibility. However, the enzyme molecules can easily leach out of the hosts (Fig. 6, bottom), particularly when pH of media is changed, resulting in the loss of charge interactions between the enzyme and matrix.

In a sharp contrast, in our method of encapsulating enzymes in *mesoporous* hosts, the pore diameters (e.g. ~3-6 nm or higher and tunable) are greater than those in microporous materials and the diffusion of substrates and products is facilitated significantly (Fig. 6, middle). As a consequence, the apparent enzymatic activity is increased drastically by 2-1000 times [56-64]. Compare to *macroporous* materials, the diameter of interconnecting pores/channels is designed to be small enough to prevent the enzyme molecules from leaking out of the mesoporous host matrix. As biocatalysts, the enzymes are re-usable. Because of confinement in the host cage, the thermal and operational stability of enzymes are greatly enhanced over the same free enzymes in solutions. There is a general trend that the

smaller the pores the greater the thermal stability. The protein molecules are also protected from recognition and/or attacks by other biomacromolecules such as antibodies and proteases in the surrounding media. This new method has been demonstrated by encapsulating alkaline phosphatase, acid phosphatase, horseradish peroxidase (HRP), glucose oxidase (GOx), lipase, hemoglobin, alcohol dehydrogenase, organophosphorus acid anhydrolase (OPAA), DNA, collagen, red blood cells, etc., in mesoporous silica or hybrid materials [18,35,47,56-67].

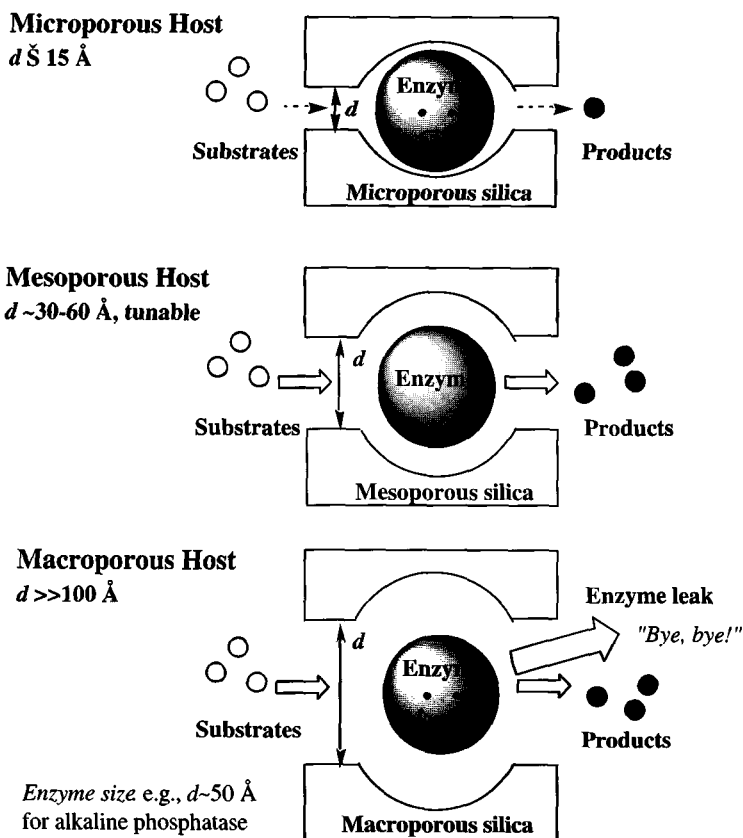


Figure 6. Cartoon illustration of enzyme immobilization by encapsulation in microporous (top), mesoporous (middle) and macroporous (bottom) host materials.

We have been exploring various potential applications of this new technology in biocatalysis, biosensors, bioreactors and pharmaceuticals. It is noteworthy that multiple enzymes (e.g. HRP and GOx) can be encapsulated in one mesoporous host matrix, where the product (e.g. H_2O_2) of one enzyme (GOx) serves as the substrate of another (HRP) [62]. Such a system could be used as nanobioreactors and as biosensors. Indeed, the nanoencapsulated GOx-HRP was found to be a good sensor for glucose with fast response time [62]. Recently, we have demonstrated that OPAA immobilized in mesoporous matrix exhibited excellent resistance to organic solvents. Significant OPAA activity was observed in the presence of 20% acetone or dimethyl formamide [65]. It should be noted that OPAA is a potentially useful enzyme for safe, non-corrosive decontamination of a variety of organophosphorus compounds, including the fluoride-containing nerve agents such as Sarin and Soman. Enhanced environmental stability of OPAA by nanoencapsulation would allow for its use under harsh but practical conditions. Furthermore, the thermodynamic properties, such as hydrophobicity, etc., can be tuned by incorporating organic moieties and polymers into the inorganic framework to yield hybrid mesoporous materials [37-44,47,60,65]. For some enzymes whose substrates include organic compounds (e.g. lipase and OPAA), a more hydrophobic environment would be favorable.

5 Protein folding/unfolding in nanoporous host materials and rigid matrix artificial chaperones

As mentioned in the previous section, the stability of proteins increases significantly upon encapsulation. Such an increase could be attributed to the confinement effect of host matrices on denaturation including reversible unfolding of the protein molecules [56-66]. Protein folding is amongst the most studied subjects in modern biochemistry. Full understanding of protein folding is probably one of few remaining fundamental problems in life science (another is the molecular understanding of consciousness or free will or soul). Besides the great academic interest, the knowledge about the protein folding/unfolding will find many practical industrial applications. Numerous theoretical and experimental approaches have been derived to solve the protein folding problem. Our ability to directly encapsulate protein molecules in mesoporous matrix provides a new tool to the study of protein folding and

unfolding in view of that the average size of a large number of non-membrane-bound proteins in their native states is about 2-10 nm.

The space confinement effect on protein unfolding is illustrated in Figure 7. Assume the hydrodynamic volume (or space) required for unfolding of a protein molecule is V_H , the protein cannot or is very difficult to unfold if the cage size (V_1) is much smaller than V_H . It may partially unfold or completely unfold at an increased cage size, i.e. $V_1 < V_2 < V_H$ or $V_3 \gg V_H$, respectively. Hence, it is expected that the protein stability should increase as the pore size of the porous host matrix is decreased. Our experimental data on based on enzymatic activity assays are indeed in agreement with such a general trend [56-66]. The extent and rate of protein denaturing upon heat treatment were found to decrease generally as the pore size became smaller [59,62]. Using a minimalist two-dimensional HP lattice model, we have carried out Monte Carlo simulations to study confinement effects on protein stability. Heat capacity was calculated as a function of temperature using the histogram method and results obtained show that confinement tends to stabilize the folded conformations, consistent with experimental results. We have also investigated the effects of confinement on the kinetics of the refolding and unfolding processes as functions of temperature and box size. As expected, unfolding time increases as cage size decreases [66].

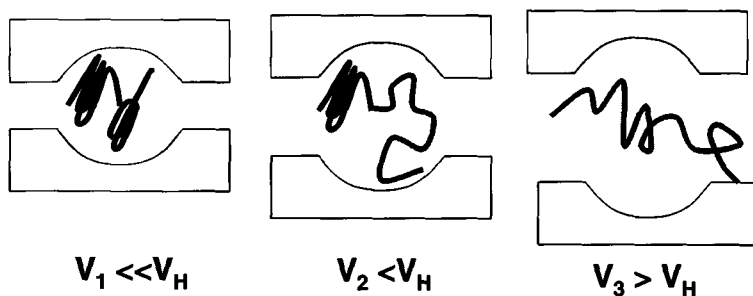


Figure 7. Cartoon illustration of protein unfolding in confined space having excluded volumes V_1 , V_2 and V_3 without considering the interactions between the protein molecule and the internal surface of the nanoporous matrix materials: protein may not unfold if $V_1 \ll V_H$, partially unfold if $V_1 < V_2 < V_H$, or completely unfold if $V_3 \gg V_H$.

Currently we are exploring the possibility of observing the catalytic activity of single enzyme molecule in mesoporous matrix. It is known that conformation change in an enzyme molecule affects its catalytic activity significantly and conventionally measured activity might be just an

average value over a variety of conformational states of the enzyme in a given time period [70]. Since the conformation change would result in variation in the size of enzyme molecule, we should be able to control the number of allowable conformation states by encapsulating the enzyme in mesoporous matrix with controlled pore size. Observation of activity of single enzyme molecule in controlled space confinement would enable us to gain significant insights into the relations of protein folding-unfolding and conformation fluctuation with the functions of the protein.

It should be noted that besides the physical confinement there are many factors that may affect protein denaturation including reversible unfolding. Among them are the interactions between the protein molecules and the internal surface of the nanoporous matrix materials. Some of our preliminary results indeed suggest that the hydrophilic silica surface (Si-OH) exerts significant influence on protein unfolding and refolding and that organic modification of the host matrix [37-44,47,60,65] could allow for an assessment of contributions by such interactions.

Besides protein unfolding, we have also studied protein refolding in mesoporous host materials. Urea is a well known denaturant for many proteins. Very interestingly we have found that it is also a good nonsurfactant template for mesoporosity [28-30]. Therefore, we are able to encapsulate proteins in their denatured or unfolded states in mesoporous materials prepared with urea as the template. As shown in Figure 8, upon removal of urea template by extraction, the unfolded protein molecules should be able to refold back towards their native state. The extent of refolding should be influenced by, and increase with, the pore size. Indeed, our results on cytochrome *c* (Cc) show that the extent of Cc refolding, as evaluated by fluorescence spectroscopic measurements, tends to increase as the pore size (Fig. 9) [67]. Recently, further measurements with circular dichroism (CD) and resonance-Raman spectroscopy also support such a trend [71]. Such an ability of mesoporosity to influence protein folding is of great significance. In biological systems, protein folding is often mediated by chaperones. The Anfinsen cage in chaperonins is believed to provide a space confinement to influence protein folding. Again, the thermodynamic properties of internal surface of mesoporous host matrix can be modified by introducing various organic moieties [37-44,47,60,65]. As a result, these rigid mesoporous host materials function, in many ways, similar to chaperones (hence the term “rigid matrix artificial chaperones”).

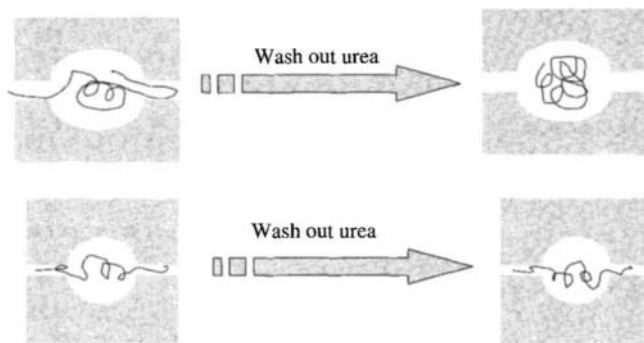


Figure 8. A cartoon illustration of urea-denatured protein refolding upon removing the urea by water-extraction: protein may refold when the cage is large (top) or may not completely refold in a small cage (bottom).

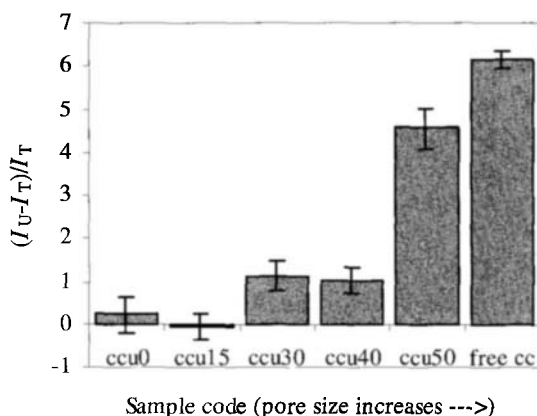


Figure 9. Plot of relative extent of refolding of cytochrome c (Cc), as represented by the relative difference, $(I_U - I_T)/I_T$, in fluorescence intensity between unfolded (I_U) and refolded (I_T) Cc, for the samples with pore sizes increasing up to free Cc in solution.[67].

According to a very popular funnel model for protein folding (or refolding) [72], unfolded protein chains with high energy may have a huge number of possible conformational states (and hence a same huge number of radii of gyration). As folding proceeds, the energy decreases through many local energy minima till a single global energy minimum is reached in the native state of folded protein. By using mesoporous materials of controlled pore sizes to host unfolded protein molecules as we have conceptualized [67], the number of starting conformational states of unfolded protein should be drastically reduced because as limited by the pore size of the host materials, those molecules with large radii of gyration may not be able to commence refolding to any significant extent. This may

make experimental testing of the model much less formidable. In addition, it is highly possible that with appropriate design of pore parameters and properties the folding intermediates could be trapped or even isolated for detailed studies. Our preliminary results from Raman spectroscopic study of Cc refolding in mesoporous matrices suggest that under certain conditions the refolding of Cc might have stayed at the molten globule states [71]. Recently we have also encapsulated a series of hemoglobin molecules with quaternary structures (monomer, dimer and tetramer) in various mesoporous host materials prepared by nonsurfactant-templated synthesis [73]. Since the protein molecules have no or very limited mobility in the host matrix, association-dissociation becomes virtually impossible which should allow us to probe the structure-function of proteins at the quaternary structure level. It is recognized that so far the triggers for the unfolding or refolding (i.e. thermal treatment, pH and solvent changes or solvent extraction) in our work are too slow to conduct useful kinetic measurements. We will explore the applicability of many other elegantly established techniques such as T-jump, photochemical and electrochemical methods in our systems.

6 Summary

Starting from attempts to make materials with chiral cavities, we have found a novel, low-cost, environmental friendly, biocompatible nonsurfactant-templating pathway to mesoporous materials with high surface area and pore volume as well as narrowly distributed pore size in the range of 2-12 nm. Nonsurfactant molecules, such as glucose, dibenzoyl-L-tartaric acid, fructose, cyclodextrins, urea, glycerol, soluble starch, etc., can be used as templates to direct the mesostructure formation. Unlike the surfactant-templating and block-polymer pathways, the possible candidates for nonsurfactant templates are virtually unlimited. The pore parameters are tunable to some extent by varying template concentration. Thermodynamic properties such as hydrophilicity can be incorporated into the mesoporous framework by making organic- (or polymer-) modified hybrid materials. The entire preparation by the nonsurfactant pathway is achievable under mild conditions, e.g. room temperature and near neutral pH. Besides many potential applications in nanotechnology, this has led to the development of a new bio-immobilization technique that enables a one-step, direct encapsulation of a variety of bioactive substances including enzymes, proteins, nucleic acids and cells in mesoporous host

materials for potential biocatalysis, biosensor, bioreactor and pharmaceutical applications. Various enzymes including phosphatases, horseradish peroxidase, glucose oxidase, and organophosphorus acid anhydrolase in mesoporous host matrices exhibit significantly enhanced catalytic activities over those in microporous hosts. Observation of enhanced stability of encapsulated enzymes prompted us to study the protein unfolding and refolding in confined space as determined by the pore sizes in the host matrix. The extent of refolding of cytochrome *c* in the mesoporous host was found to increase with the pore sizes. With further research this method could be established as a unique tool for studying the protein folding pathway, folding intermediates, conformation change, and probably single molecule activity as well as the protein-protein interactions.

7 Acknowledgements

This work has been supported in part by the National Institutes of Health (Grant No. DE09848), the Commonwealth of Pennsylvania through a grant to the Nanotechnology Institute of Southeastern Pennsylvania, the US Army Research Office, the US Army Research Laboratory, the US Department of Energy, and the National Natural Science Foundation of China (NSFC Nos. 29874002, 19810760343 and 29825504). The authors wishes to thank a cadre of students, associates and collaborators for their contributions to the work described in this article.

References

1. Kresge C. T., Leonowicz M. E., Roth W. J., Vartuli J. C. and Beck J. S., Ordered mesoporous molecular sieves synthesized by a liquid-crystal template mechanism, *Nature* **359** (1992) pp. 710-12.
2. Beck J. S., Vartuli J. C., Roth W. J., Leonowicz M. E., Kresge C. T., Schmitt K. D., Chu C. T. W., Olson D. H. and Sheppard E. W., A new family of mesoporous molecular sieves prepared with liquid crystal templates, *J. Am. Chem. Soc.* **114** (1992) pp. 10834-43.
3. Ying J.Y., Mehnert C.P. and Wong M.S., Synthesis and applications of supramolecular-templated mesoporous materials, *Angew. Chem. Int. Ed.* **38** (1999) pp. 56-77.
4. Carati A., Ferraris G., Guidotti M., Moretti G., Psaro R., and Rizzo C., Preparation and characterisation of mesoporous silica-alumina and silica-titania with a narrow pore size distribution, *Catal. Today* **77** (2003) pp. 315-323.
5. Ciesla U. and Schuth F., Ordered mesoporous materials, *Micropor. Mesopor. Mater.* **27** (1999) pp. 131-149.

6. Raman N.K., Anderson M.T. and Brinker C.J., Template-based approaches to the preparation of amorphous, nanoporous silicas, *Chem. Mater.* **8** (1996) pp. 1682-1701.
7. Zhang Z.T., Han Y., Xiao F.S., Qiu S.L., Zhu L., Wang R., Yu Y., Ze Zhang Z., Zou B., Wang Y., Sun H., Zhao D.Y., and Wei Y., Mesoporous aluminosilicates with ordered hexagonal structure, strong acidity, and extraordinary hydrothermal stability at high temperatures, *J. Am. Chem. Soc.* **123** (2001) pp. 5014-5021.
8. Zhu G.S., Qiu S.L., Terasaki O. and Wei Y., Polystyrene beads assisted self-assembly of microstructured silica hollow spheres in highly alkaline media, *J. Am. Chem. Soc.* **123** (2001) pp. 7723-7724.
9. Zhang Z.T., Dai S., Fan X., Pennycock S. J., and Wei Y., Controlled synthesis of CdS nanoparticles inside ordered mesoporous silica using ion-exchange reaction, *J. Phys. Chem. B* **105** (2001) pp. 6755-6758.
10. Zhang Z.T., Dai S., Wei Y. and Qiu S.L., Ion-imprinted zeolite: a surface functionalization methodology based on the 'ship-in-bottle' technique, *Adv. Mater.* **13** (2001) pp. 493-496.
11. Chan V. Z.-H., Hoffman J., Lee V.Y., Latrou H., Avgeropoulos A., Hadjichristidis N., Miller R.D., and Thomas E.L. Ordered bicontinuous nanoporous and nanorelief ceramic films from self assembling polymer precursors, *Science* **286** (1999) pp. 1716-1719.
12. Wei Y., Jin D. and Ding T., Optical rotatory silica materials prepared via sol-gel process, *J. Phys. Chem. B* **101** (1997) pp. 3318-3323.
13. Yin H.P. and Wei Y., An effort to make chiral cavity in sol-gel materials by using large molecules as templates, *Polym. Mater. Sci. Eng.* **87** (2002) pp. 271-272.
14. Wei Y., Jin D., Ding T., Shih W.H., Liu Q., and Cheng S.Z.D., A novel synthesis of mesoporous materials, In *Proc. Symp. Frontiers of Chemistry*, ed by Wu Y.D. and Yan Y.J., (Hong Kong University of Science & Technology, CWCYC-2, Hong Kong, (1997) pp. 21-24.
15. Wei Y., Jin D., Ding T., Shih W.H., Liu Q., Cheng S.Z.D., and Fu Q., A Novel Templating Route to Mesoporous Materials, *Adv. Mater.* **10** (1998) pp. 313-316.
16. Jin D., Novel organic-inorganic hybrid and nano-structured materials, PhD Dissertation, Drexel University 1997.
17. Wei Y., Xu J., Dong H., Dong J.H., Qiu K.Y., and Jansen-Varnum S.A., Preparation and physisorption characterization of D-glucose-templated mesoporous silica materials via base-catalyzed sol-gel process, *Chem. Mater.* **11** (1999) pp. 2023-2029.
18. Xu J., Immobilization of Enzymes in Mesoporous Materials via the Nonsurfactant-Templated Sol-Gel Chemistry, PhD Dissertation, Drexel University 2000.
19. Liu X., Wei Y., Jin D. and Shih W.H., Synthesis of mesoporous aluminum oxide with aluminum alkoxide and tartaric acid derivative, *Mater. Lett.* **42** (2000) pp. 143-149.
20. Zheng J.Y., Qiu K.Y., Feng Q.W., Xu J., and Wei Y., Sol-gel synthesis of mesoporous titania using nonsurfactant organic compounds as templates, *Mol. Cryst. Liq. Cryst.* **354** (2000) pp. 183-194 [771-782].
21. Zheng J.Y., Pang J.B., Qiu K.Y., and Wei Y., Synthesis of mesoporous titanium dioxide materials by using mixture of organic compounds as nonsurfactant template, *J. Mater. Chem.* **11** (2001) pp. 3367-3372.

22. Pang J.B., Qiu K.Y., and Wei Y., A novel nonsurfactant pathway to hydrothermally stable mesoporous silica materials, *Micropor. Mesopor. Mater.* **40** (2000) pp. 299-304.
23. Pang J.B., Qiu K.Y., and Wei Y., Synthesis of mesoporous silica materials with ascorbic acid as template via sol-gel process, *Chinese J. Chem.* **18** (2000) pp. 693-697.
24. Zheng J.Y., Pang J.B., Qiu K.Y., and Wei Y., Synthesis of mesoporous silica materials with hydroxyacetic acid derivatives as templates via a sol-gel process, *J. Inorg. Organomet. Polym.* **10** (2000) pp. 103-113.
25. Pang J.B., Qiu K.Y., and Wei Y., A new nonsurfactant pathway based on tartaric acid in conjunction with metal halides to mesoporous silica materials, *Chem. Mater.* **13** (2001) pp. 2361-2365.
26. Pang J.B., Qiu K.Y., and Wei Y., Preparation of mesoporous silica materials with hydroxy-carboxylic acid compounds as templates via sol-gel process, *J. Non-Crystal. Solids* **283** (2001) pp. 101-108.
27. Zheng J.Y., Pang J.B., Qiu K.Y., and Wei Y., Synthesis of mesoporous silica materials via nonsurfactant templated sol-gel route by using mixture of organic compounds as template, *J. Sol-Gel Sci. Technol.* **24** (2002) pp. 81-88.
28. Pang J.B., Qiu K.Y., Xu J., Wei Y., and Chen J., Synthesis of mesoporous silica materials with pore diameters of 2-6 nm via urea-templated sol-gel reactions, *J. Inorg. Organomet. Polym.* **10** (2000) pp. 39-49.
29. Zheng J.Y., Pang J.B., Qiu K.Y., and Wei Y., Synthesis and characterization of mesoporous titania and silica-titania materials by urea templated sol-gel reactions, *Micropor. Mesopor. Mater.* **49** (2001) pp. 189-195.
30. Pang J.B., Qiu K.Y., Wei Y., Lei X.J., and Liu Z.F., A facile preparation of transparent and monolithic mesoporous silica materials, *Chem. Commun.* (2000) pp. 477-478.
31. Pang J.B., Qiu K.Y., and Wei Y., Preparation of monolithic Ti-incorporated mesoporous silica materials via tartaric acid-templated sol-gel process, *Chin. J. Chem.* **19** (2001) pp. 198-201.
32. Zheng J.Y., Pang J.B., Qiu K.Y., and Wei Y., The effects of template contents on the physicochemical sorption properties of Zr-incorporated mesoporous titania materials, *Chinese J. Chem.* **20** (2002) pp. 951-957.
33. Zheng J.Y., Qiu K.Y., and Wei Y., Investigation of Zr-incorporated mesoporous titania materials via nonsurfactant templated sol-gel route: Synthesis, characterization and stability, *J. Mater. Sci.* **38** (2003) pp. 437-444.
34. Pang J.B., Preparation and characterization of mesoporous silica materials via a nonsurfactant-templated route, PhD Dissertation, Peking University 2001.
35. Feng Q.W., Novel organic-inorganic hybrid mesoporous materials and nanocomposites, PhD Dissertation, Drexel University 2001.
36. Zheng J.Y., Synthesis and characterization of mesoporous materials via nonsurfactant small molecules templated sol-gel process, PhD Dissertation, Peking University 2002.
37. Dong H., Xu J., Jansen S.A., Qiu K.Y., and Wei Y., Synthesis of nonsurfactant-based hybrid mesoporous materials, *Polym. Prepr. (Am. Chem. Soc., Div. Polym. Chem.)* **41**[1] (2000) pp. 194-195.

38. Dong H., Xu J., Jansen S.A., Qiu K.Y., and Wei Y., Synthesis of phenyl-modified mesoporous materials via the nonsurfactant route, *Polym. Prepr. (Am. Chem. Soc., Div. Polym. Chem.)* **41**[1] (2000) pp. 602-603.
39. Wu Q.H., Pang J.B., Qiu K.Y., and Wei Y., Organic-inorganic hybrid mesoporous materials with methacrylamine modification, *Acta Polymerica Sinica* **4** (2001) pp. 538-540.
40. Feng Q.W., Xu J., Dong H., and Wei Y., Synthesis of polymer-modified mesophases via the nonsurfactant-templated sol-gel process. *Polym. Prepr. (Am. Chem. Soc., Div. Polym. Chem.)* **41**[1] (2000) pp. 515-516.
41. Wei Y., Feng Q.W., Xu J., Dong H., Li S., Qiu K.Y., Jansen S.A., Yin R., and Ong K.K., Polymethacrylate-silica hybrid mesoporous materials: a bridge between the inorganic and polymeric molecular sieves, *Adv. Mater.* **12** (2000) pp. 1448-1450.
42. Feng Q.W., Xu J., Dong H., Li S., and Wei Y., Synthesis of polystyrene-silica hybrid mesoporous materials via the nonsurfactant-templated sol-gel process, *J. Mater. Chem.* **11** (2000) pp. 2490-2494.
43. Pang J.B., Qiu K.Y., and Wei Y., Synthesis of mesoporous poly(styrene-co-maleic anhydride)/silica hybrid materials via nonsurfactant-templated sol-gel process, *Chin. J. Polym. Sci.* **18** (2000) pp. 469-472.
44. Bai J., Zheng J.Y., Qiu K.Y., and Wei Y., Synthesis of hybrid mesoporous polystyrene-silica materials with non-surfactant citric acid as template via sol-gel process, *Chinese J. Polym. Sci.* **20** (2002) pp. 565-572.
45. Pang J.B., Qiu K.Y., and Wei Y., Recent progress in research on mesoporous materials I: Synthesis, *J. Inorg. Mater.* **17** (2002) pp. 407-414.
46. Pang J.B., Qiu K.Y., and Wei Y., Progress in mesoporous materials research, Part II: Applications, *J. Inorg. Mater.* **17** (2002) pp. 665-671.
47. Dong H., Organic-inorganic hybrid mesoporous silica materials and their applications as hosts for protein molecules, PhD Dissertation, Drexel University 2002.
48. Wei Y., Bakthavatchalam R. and Whitecar C.K., Synthesis of new organic- inorganic hybrid glasses, *Chem. Mater.* **2** (1990) pp. 337-339.
49. Wei Y., Polymer-modified ceramics, In *Encyclopedia of Materials: Science and Technology*, ed by Buschow K.H.J., Cahn R.W., Flemings M.C., Hschner B., Kramer E.J. and Mahajan S. (Elsevier Science Ltd., Oxford, UK 2001) pp. 7594-7605.
50. Pang J.B., Dong C.M., Qiu K.Y., and Wei Y., Tartaric acid templated synthesis of mesoporous Ti-incorporated silica and its catalytic activity for the ring-opening polymerization of ϵ -caprolactone, *Chinese J. Polym. Sci.* **20** (2002) pp. 361-368.
51. Cheng S., Wei Y., Feng Q.W., Qiu K.Y., Pang J.B., Jansen S.A., Yin R., and Ong K.K., A facile synthesis of mesoporous gold-silica nanocomposite materials via sol-gel process with nonsurfactant templates, *Chem. Mater.* **15** (2003) pp. 1560-1566.
52. Cheng S., Nanostructured, Electroactive and Bioapplicable Materials, PhD Dissertation, Drexel University 2002.
53. Wei Y., Feng Q.W., Cheng S., Qiu K.Y., Pang J.B., Yin R., and Ong K.K., Synthesis of polymer-silica nanocomposites via sol-gel process with polymerizable templates, *Macromolecules* Submitted.
54. Patel A., Sun Z.F. and Wei Y., Sol-gel synthesis and characterization of silver nanoparticles in D-glucose- templated mesoporous silica materials, Abstract in *Am. Chem. Soc.-MARM'03*, Princeton, NJ, June 2003.
55. Cheng S. and Wei Y., Mesoporous silica nanospheres synthesized by a nonsurfactant templated sol-gel pathway, *Polym. Mater. Sci. Eng.* **87** (2002) pp. 302-303.

56. Wei Y., Xu J., Jin D., Lin M., and Feng Q.W., 'Room with a view': novel immobilization of enzymes in mesoporous host materials, *Proc. North Am. Catal. Soc.* (Tech. NAM'99, Boston 1999) pp. 14-15.
57. Wei Y., Xu J., Feng Q.W., Dong H., and Lin M., Encapsulation of enzymes in mesoporous host materials via the nonsurfactant-templated sol-gel process, *Mater. Lett.* **44** (2000) pp. 6-11.
58. Feng Q.W., Xu J., Lin M., Dong H., and Wei Y., One-step direct immobilization of acid phosphatase in mesoporous silica sol-gel materials. *Polym. Mater. Sci. Eng.* **83** (2000) pp. 502-503.
59. Wei Y., Xu J., Feng Q.W., Lin M., Dong H., Zhang W.J., and Wang C., A novel method for enzyme immobilization: direct encapsulation of acid phosphatase in nanoporous silica host materials. *J. Nanosci. Nanotech.* **1** (2001) pp. 83-94.
60. Xu J., Dong H., Feng Q.W. and Wei Y., Direct immobilization of horseradish peroxidase in hybrid mesoporous sol-gel materials", *Polym. Prepr. (Am. Chem. Soc., Div. Polym. Chem.)* **41**[1] (2000) pp. 1044-1045.
61. Xu J., Dong H., Feng Q.W. and Wei Y., Immobilization and activity assay of horseradish peroxidase in mesoporous sol-gel silica materials, *Polym. Prepr. (Am. Chem. Soc., Div. Polym. Chem.)* **41**[1] (2000) pp. 1042-1043.
62. Wei Y., Dong H., Xu J., and Feng Q.W., Simultaneous immobilization of horseradish peroxidase and glucose oxidase in mesoporous sol-gel host materials, *Chem. Phys. Chem.* **3** (2002) pp. 803-808.
63. Wei Y. and Qiu K.Y., Synthesis and biotechnological applications of vinyl polymer-inorganic hybrid and mesoporous materials, *Chin. J. Polym. Sci.* (Springer-Verlag) **18** (2000) pp. 1-7.
64. Xu J., Feng Q.W., Dong H., and Wei Y., Stability of immobilized horseradish peroxidase in mesoporous sol-gel silica materials, *Polym. Prepr. (Am. Chem. Soc., Div. Polym. Chem.)* **41**[1] (2000) pp. 1046-1047.
65. Ong K., Cheng T-c, Yin R., Dong H., and Wei Y., Nanoencapsulation of OPAA with mesoporous materials for chemical agent decontamination in organic solvents, (DoD Joint Service Scientific Conf on Chem & Bio Defense Research (CB), November 19-21, 2002, Hunt Valley, MD) *Proc. US DoD Sci. Conf.*, in press, 2003.
66. Ping G., Yuan J. M., Vallieres M., Sun Z., Dong H., Wei Y., Li F. Y., and Lin S. H., Effects of confinement on protein folding and protein stability, *J. Chem. Phys.* **118** (2003) pp. 8042-8048.
67. Wei Y., Sun Z.F., Zheng J.Y., Dong H., Yuan J.M. and Ping G., Rigid matrix artificial chaperone (RMAC)-mediated refolding of heme proteins, *Polym. Mater. Sci. Eng.* **87** (2002) pp. 252-253.
68. Avnir D., Braun S., Lev O., and Ottolenghi M., Enzymes and other proteins entrapped in sol-gel materials, *Chem. Mater.* **6** (1994) pp. 1605-14.
69. Dave B.C., Dunn B., Valentine J.S., and Zink J.I., Sol-gel encapsulation methods for biosensors, *Anal. Chem.* **66** (1994) pp. 1120A-1127A.
70. Xie S., Single-molecule approach to enzymology, *Single Molecules* **2** (2001) pp. 229-236.
71. Wei Y., Sun Z.F., Spiro T., Yuan J.M. et al. Using resonance Raman spectroscopy to monitor the folding states of cytochrome *c* encapsulated in mesoporous matrices, Manuscript in preparation.

72. Onuchic J. N., Wolynes P. G., Luthey-Schulten Z. and Socci N. D., Toward an outline of the topography of a realistic protein-folding funnel, *Proc. Nat. Acad. Sci. USA* **92** (1995) pp. 3626-30.
73. Sun Z. and Wei Y., Unpublished results.

Author Index

A		K	
Ahn W.S.	649	Kaliaguine S.	47
		Kim G.J.	649
		Knowles W.V.	125
B		L	
Baltes M.	487	Le Cloirec P.	772
Burleigh M.C.	756	Li F.	263
		Li Z-C	188
C		Liu C.	263
Cheng H-M.	263	Liu X.	14
Chong A.S.M.	393	Lu G.Q.	1, 237, 393
Choudhary V.R.	596		
Cool P.	487		
D		M	
Daehler A.	812	Macquarrie D.J.	553
Dai S.	756	Mokaya R.	427
Denoyel R.	727	Mota J.P.B.	694
Diniz da Costa J.C.	237		
Dong H.	188		
F		N	
Fan J.	14	Nangia A.	165
Fang H-T	263	Nicholson D.	365
Feng Q.	188		
G		O	
Giessler S.	237	O'Connor A.J.	812
		On Do Trong	47
H		Q	
Han Y.	519	Qiu K-Y	188, 873
J		S	
Jansen S.A.	188	Selvam P.	101
		Seo G.	649
		Shen J-P.	623
		Song C.	464, 623
		Stevens G.W.	812

T

Thommes M.	317
Tian B.	14
Turaga U.T.	464

U

Uphade B.S.	596
-------------	-----

V

Vansant E.F.	487
--------------	-----

W

Wang C.E.	188
Wei Y.	188, 873
Wong M.S.	125
Wright P.A.	849

X

Xiao F-S.	519
Xu J.	188
Xu X.	464

Y

Yang H.	14
Yang Q-H	263
Yiu H.H.P.	849
Yu C.	14

Z

Zhao D.Y.	14
Zhao X.S.	1, 206, 393, 464
Zheng J.	464
Zhou Z.C.	206

Index

<u>Index terms</u>	<u>Links</u>				
A					
acid catalysis	74	536	557		
acid-base pairs	31				
acidity	85	439	519	633	645
	651	653			
acidity					
Brönsted	479				
Lewis	480				
adsorbent – environmental remediation	757	767			
adsorption					
capacity	812	815			
physical	383				
equilibria	781				
kinetics	775	820			
thermodynamics	380				
alkylation	628	630			
B					
base catalysis	575				
basity	657	659			
BET	324				
bioadsorption	812				
biocompatible nonsurfactant template	874				
bioadsorption	812				
BJH	329				
breakthrough curve	791				

<u>Index terms</u>	<u>Links</u>				
C					
calorimetry	468				
canonical Monte Carlo (GCMC)	367				
capillary condensation	331	369			
carbon nanotubes	266				
catalysis	102	427	519		
catalyst	487				
chiral catalyst	668				
chromium catalyst	102				
clathrate	168				
co-condensation	188	407	555	556	761
	861				
colloidal microspheres	214				
composite materials	51				
corona	22				
cracking	435	436			
crystal engineering	179				
crystallization	48				
D					
density function theory	729	731			
diffusion	697				
E					
encapsulation of enzyme	880				
environmental catalysts	596				
enzyme	815	817			
enzyme immobilization	851				
EPR	481				
F					
Friedel-Crafts alkylation	562				
FTIR	473				

Index terms**Links**

functionalization	394	573	760	861	863
-------------------	-----	-----	-----	-----	-----

G

gas separation	237	241			
gas storage	182	293			
grafting	403	446	555	663	664
	760				
graphite	269				

H

host-guest compounds	165				
hydrogen					
bonding	169				
energy	308				
hydrophobicity	248	395	418		
hydrothermal stability	78	394	405		
hysteresis	317	322			

I

immobilization	649	668			
isopropylation	632				

K

Kelvin equation	328	329			
-----------------	-----	-----	--	--	--

L

Langmuir isotherm	748				
Lewis acid	561	563	598		
Lewis base	598				
linear driving force (LDF)	722				
liquid-phase adsorption	742				

<u>Index terms</u>	<u>Links</u>		
M			
macroporous materials	225		
membrane reactor	251		
membranes	237		
mesoporous			
carbons	147		
materials	126		
metal oxides	144		
silica spheres	879		
metal oxides	499		
microporosity	22	23	
molecular-dynamic (MD) simulations	321	368	
molecularly designed dispersion	488		
monolayer	487	488	
Monte-carlo (MC) simulation	317		
N			
nanocatalysts	499		
nanosized zeolite	537		
NMR	477		
non-ionic block copolymer	14	16	
non-local-density-functional theory (NLDFT)	317	321	355
non-silicate mesoporous materials	129		
nonsurfactant fructose template	190		
O			
oxidation	113		
P			
particle uptake rate equation	713		
phenyl groups	193		
physical adsorption	322		
PMO	762		

Index terms**Links**

positron annihilation spectroscopy (PAS)	481			
post-alumination	429			
post-treatment	527	528		
protein refolding and unfolding	882			
proteins	812	814	816	849

R

redox catalysis	660
-----------------	-----

S

self assembly	207		
SEM	220		
separation	816		
shape selective catalysis	635		
silylation	398		
size exclusion	827		
sol-gel	238		
structural stability	125		
superacid	521	522	523
supported catalysts	599		
surface			
chemistry	727	729	
modification	499	500	
structure	271		
surfactant-templating routes	127		
synthesis	126		
3D photonic crystals	211		

T

template	207
templating mechanism titration	466
TPD	470
Transport	694

Index terms

Links

V

volumetric adsorption 323

Z

zeolite 48 366 630 632

Series on Chemical Engineering

NANOPOROUS MATERIALS: SCIENCE AND ENGINEERING

edited by **G Q Lu** (*University of Queensland*) & **X S Zhao** (*National University of Singapore*)

Porous materials are of scientific and technological importance because of the presence of voids of controllable dimensions at the atomic, molecular, and nanometer scales, enabling them to discriminate and interact with molecules and clusters. Interestingly the big deal about this class of materials is about the "nothingness" within — the pore space. International Union of Pure and Applied Chemistry (IUPAC) classifies porous materials into three categories — micropores of less than 2 nm in diameter, mesopores between 2 and 50 nm, and macropores of greater than 50 nm. In this book, nanoporous materials are defined as those porous materials with pore diameters less than 100 nm.

Over the last decade, there has been an ever increasing interest and research effort in the synthesis, characterization, functionalization, molecular modeling and design of nanoporous materials. The main challenges in research include the fundamental understanding of structure-property relations and tailor-design of nanostructures for specific properties and applications. Research efforts in this field have been driven by the rapid growing emerging applications such as biosensor, drug delivery, gas separation, energy storage and fuel cell technology, nanocatalysis and photonics. These applications offer exciting new opportunities for scientists to develop new strategies and techniques for the synthesis and applications of these materials.

This book provides a series of systematic reviews of the recent developments in nanoporous materials. It covers the following topics: (1) synthesis, processing, characterization and property evaluation; (2) functionalization by physical and/or chemical treatments; (3) experimental and computational studies on fundamental properties, such as catalytic effects, transport and adsorption, molecular sieving and biosorption; (4) applications, including photonic devices, catalysis, environmental pollution control, biological molecules separation and isolation, sensors, membranes, hydrogen and energy storage, etc.

Imperial College Press

www.icpress.co.uk

P181 hc

ISBN 1-86094-210-5



9 781860 942105